

Computational Methods in Applied Sciences

Manolis Papadrakakis
Michalis Fragiadakis
Vagelis Plevris *Editors*

Computational Methods in Earthquake Engineering

Volume 2



 Springer

Computational Methods in Earthquake Engineering

Computational Methods in Applied Sciences

Volume 30

Series Editor

E. Oñate

International Center for Numerical Methods in Engineering (CIMNE)

Technical University of Catalonia (UPC)

Edificio C-1, Campus Norte UPC

Gran Capitán, s/n

08034 Barcelona, Spain

onate@cimne.upc.edu

www.cimne.com

For further volumes:

www.springer.com/series/6899

Manolis Papadrakakis • Michalis Fragiadakis •
Vagelis Plevris
Editors

Computational Methods in Earthquake Engineering

Volume 2

 Springer

Editors

Manolis Papadrakakis
School of Civil Engineering
Inst. Struct. Analysis & Antiseismic Res.
National Technical University of Athens
Athens, Greece

Vagelis Plevris
Dept. of Civil Engineering Educators
School of Pedagogical & Technol. Educ.
Athens, Greece

Michalis Fragiadakis
School of Civil Engineering
Laboratory for Earthquake Engineering
National Technical University of Athens
Athens, Greece

ISSN 1871-3033 Computational Methods in Applied Sciences

ISBN 978-94-007-6572-6

ISBN 978-94-007-6573-3 (eBook)

DOI 10.1007/978-94-007-6573-3

Springer Dordrecht Heidelberg New York London

Library of Congress Control Number: 2013940929

© Springer Science+Business Media Dordrecht 2013

This work is subject to copyright. All rights are reserved by the Publisher, whether the whole or part of the material is concerned, specifically the rights of translation, reprinting, reuse of illustrations, recitation, broadcasting, reproduction on microfilms or in any other physical way, and transmission or information storage and retrieval, electronic adaptation, computer software, or by similar or dissimilar methodology now known or hereafter developed. Exempted from this legal reservation are brief excerpts in connection with reviews or scholarly analysis or material supplied specifically for the purpose of being entered and executed on a computer system, for exclusive use by the purchaser of the work. Duplication of this publication or parts thereof is permitted only under the provisions of the Copyright Law of the Publisher's location, in its current version, and permission for use must always be obtained from Springer. Permissions for use may be obtained through RightsLink at the Copyright Clearance Center. Violations are liable to prosecution under the respective Copyright Law.

The use of general descriptive names, registered names, trademarks, service marks, etc. in this publication does not imply, even in the absence of a specific statement, that such names are exempt from the relevant protective laws and regulations and therefore free for general use.

While the advice and information in this book are believed to be true and accurate at the date of publication, neither the authors nor the editors nor the publisher can accept any legal responsibility for any errors or omissions that may be made. The publisher makes no warranty, express or implied, with respect to the material contained herein.

Printed on acid-free paper

Springer is part of Springer Science+Business Media (www.springer.com)

Preface

The book provides an insight on advanced methods and concepts for the design and analysis of structures against earthquake loading. This second volume of the series is a collection of 28 chapters written by leading experts in the field of structural analysis and earthquake engineering. Emphasis is given on the current state-of-the-art methodologies and concepts in computational methods and their application in engineering practice. The book content is suitable for both practicing engineers and academics, covering a wide variety of topics in an effort to assist the timely dissemination of research findings for the mitigation of seismic risk. Due to the devastating and socioeconomic consequences of seismic events, the topic is of great scientific interest and is expected to be of valuable help to scientists and engineers. The chapters of this volume are extended versions of selected papers presented at the COMPDYN 2011 conference, held in the island of Corfu, Greece, under the auspices of the European Community on Computational Methods in Applied Sciences (ECCOMAS).

In the introductory chapter of [Mylonakis et al.](#) the seismic response of inhomogeneous soils is explored analytically using one-dimensional viscoelastic wave propagation theory. The authors treat the problem analytically obtaining the exact solution of the Bessel type for the natural frequencies, mode shapes and base-to-surface response transfer function. The model proposed is validated using available theoretical solutions and finite-element analyses. The chapter presents results that demonstrate the effect of salient model parameters such as layer thickness, impedance contrast between surface and base layer, surface-to-base shear wave velocity ratio in the inhomogeneous layer, rate of inhomogeneity and hysteretic damping ratio.

[Lekidis et al.](#) study the Evripos bridge, a famous structure in central Greece that connects the island of Evia to the mainland. The bridge is cable stayed and its behavior to seismic excitations has been continuously monitored. The authors investigate the dynamic response of the bridge due to asynchronous base excitations along its supports and make comparisons with the conventional design procedure of assuming a synchronous base excitation at all supports. Valuable conclusions are drawn regarding the impact of spatially variable ground motion on the seismic response of cable-stayed bridges.

In the chapter of [Kostic et al.](#), the authors present a novel beam-column element formulation for the inelastic three-dimensional analysis of frames. Beam-column elements with section resultant plasticity for the hysteretic behavior of the end plastic hinges are widely used for numerical simulations in earthquake engineering because they offer a good compromise between accuracy and computational cost. The chapter presents a lumped plasticity beam-column element with significant capabilities for the description of the global and local response of frames under monotonic and cyclic loads. The proposed element accounts for the interaction of the axial force with the bending moments about the principal section axes with suitably defined yield and limit surfaces that permit the description of the gradual yielding and the post-yield hardening behavior of the end sections. Comparisons of the hysteretic response of structural elements and small structural models between the proposed element and the more accurate, but computationally much more intensive fiber section description of the cross section demonstrate the capabilities of the proposed model.

[Adam et al.](#) present a methodology for predicting the seismic peak response of vibratory non-structural elements. The non-structural elements may be attached to both elastic and ductile load-bearing frame structures. The proposed methodology is based on modified modal superposition of floor response spectra for single-degree-of-freedom (SDOF) oscillators on SDOF supporting structures. For several example problems, the “exact” results are contrasted with the outcomes of the proposed methodology. The comparison provides evidence that the proposed methodology delivers sufficiently accurate predictions of the seismic peak response.

[Lignos et al.](#) discuss the effectiveness of simplified nonlinear models for the seismic assessment of steel moment frames using single and multi-mode nonlinear static methods. It is demonstrated that the nonlinear static procedure (NSP), also known as pushover analysis, has much value in understanding important behavior characteristics that are not being explored in a nonlinear response history analysis (NRHA) in which engineers usually focus on a “blind” demand/capacity assessment rather than interpretation and visualization of the steel frame behavior. It is also shown that NSP procedures have many limitations for quantitative assessment of steel moment frame demands even for low-rise frames. The authors conclude that both NSP and NRHA have intrinsic value and that it is advisable to employ a combination of both to understand seismic performance of steel moment frames and to quantify important engineering demand parameters for these lateral resisting structural systems.

[Pardalopoulos et al.](#) propose a new approach for the rapid preliminary assessment of the seismic vulnerability of reinforced concrete buildings. The method determines the columns’ limiting shear resistance at the critical story of the structure by applying a strength assessment procedure associated with typical column details representative of the state of practice from the time that the building was constructed. The severity of the seismic displacement demand and the maximum seismic acceleration that the building can sustain is evaluated with the aid of a stiffness index assessment. The presented method requires prior knowledge only of the basic geometric and material properties of the building. The method is verified on two reinforced concrete buildings that failed during the 1999 Athens earthquake,

proving that this approach allows engineers to immediately identify the most vulnerable buildings that are likely to collapse in a potentially strong earthquake and also to assist them on setting objectives for the rehabilitation of RC buildings.

Existing structures have lightly reinforced shear walls and in most cases, especially under cycling loading, shear cracks will appear, reducing the shear capacity of the wall. The aim of the work of [Panagouli et al.](#) is to estimate the post-cracking strength of shear walls, taking into account the geometry of existing cracks and the mixed friction-plastification mechanisms that develop in the vicinity of a crack. In this chapter, Panagouli et al. examine a typical shear wall of an existing structure where a crack has been formed. The authors propose a new approach for modeling the geometry of the crack, using the notion of fractal geometry. Due to the significance of the crack geometry, a multi-resolution analysis is performed. The materials (steel and concrete) are assumed to have elastic-plastic behavior, while for concrete both cracking and crushing are taken into account in an accurate manner. On the interface unilateral contact and friction conditions are assumed to hold. For every structure resulting for each resolution of the interface, a classical Euclidean problem is solved. The obtained results lead to valuable conclusions concerning the post-cracking strength of lightly reinforced shear walls.

[Mergos and Kappos](#) investigate the seismic behavior of existing RC buildings designed and constructed in accordance with standards that do not meet current seismic code requirements. In these structures, not only flexure, but also shear and bond-slip deformation mechanisms need to be considered, both separately and in combination. The authors have developed a novel finite-element model for the inelastic seismic analysis of planar RC frames. The proposed model is able to capture the gradual spread of inelastic flexural and shear deformations as well as their interaction at the end regions of RC members. Additionally, it is capable of predicting shear failures caused by degradation of shear strength in the plastic hinges of RC elements, as well as pullout failures caused by inadequate anchorage of the reinforcement in the joint regions. The proposed element is verified against experimental results involving individual column and plane frame specimens with non-ductile detailing, showing that satisfactory correlation is established between the model predictions and the experimental evidence.

[Taiebat et al.](#) investigate the seismic response and design of basement walls. The authors examine the current state of practice that is based on the Mononobe-Okabe (M-O) method and perform a series of dynamic numerical analyses on a typical basement wall designed with the M-O earth pressures. The wall is subjected to three ground motions spectrally matched to the Uniform Hazard Spectrum prescribed by the NBCC2010 guidelines and the seismic performance of the wall under this level of demand is discussed. The authors give emphasis on peak ground acceleration (PGA) levels appropriate for the design of such structures, since the provisions of current standards tend to overestimate the demand. Particular attention is also given to the resulting drift ratio in the walls.

In the chapter of [Asteris et al.](#), the authors discuss the seismic modeling of in-filled framed structures. The feasibility of possible immediate implementation for practical design of some recent developments both in analysis and design of in-filled frames is first investigated. Moreover, contemporary seismic design codes and

guidelines introduce provisions for the calculation of the stiffness of solid infilled frames mainly through modeling the infill walls as “diagonal struts.” However, the case of infilled frames with openings is still an open issue. This chapter uses available finite-element results to propose an analytical equation in order to obtain a reduction factor for the case of frames with openings against solid frames. The validity of the methodology is demonstrated by comparing the results of the proposed equation with the results of various researchers in the literature.

[Dasiou et al.](#) deal with the topic of seismic efficiency of restored ancient colonnades using fragments of architectural members. As a common practice, restoration projects of ancient colonnades have to deal with joining together fragments of architectural members using threaded titanium bars (as reinforcement) fixed into place with cement mortar. The basic criterion for the design of such connections is that, in case of a seismic event, the reinforcement should absorb the seismic energy and fail before the marble suffers any damage. The efficiency of the reinforcement of the connection calculated with this methodology is investigated, while two case studies with different geometries: a column of the Parthenon Pronaos and the Southern colonnade of the Ancient Agora of Kos in Greece, are examined. The induced forces were calculated using the distinct element method.

[Dimitrakopoulos and DeJong](#) investigate the seismic response of rocking structures and discuss their retrofit with external viscous dampers. Stand-alone rocking structures have been thoroughly investigated, but there are relatively few theoretical studies on the response of retrofitted rocking structures. In this chapter emphasis is given in optimizing the rocking behavior, instead of preventing it, with the aid of viscous dampers. A single rocking block analytical model is utilized to determine the optimal viscous damping characteristics which exploit the beneficial aspects of rocking motion while dissipating energy and preventing overturning collapse. To clarify the benefits of damping, overturning envelopes for the damped rocking block are presented and compared with the pertinent envelopes of the free rocking block. Preliminary experimental work to verify analytical modeling is also presented. In the end of the chapter, the principles of controlling rocking behavior with damping are extended to a particular class of rocking problems, the dynamics of masonry arches. A pilot application of the proposed approach to masonry arches is also presented.

[Perus et al.](#) present a web-based methodology for the prediction of approximate IDA curves. The proposed methodology consists of two independent processes. The first process results to a response database of the single-degree-of-freedom model, whereas the second process involves the prediction of approximate IDA curves from the response database by using n -dimensional linear interpolation. The web application utilizes a response database of IDA curves, which was calculated for thirty ground motion records and the discrete values of the six parameters, which describe the period, damping and the force-displacement relationship of a building’s pushover curve. The web application enables quadrilinear idealization of the pushover curve, including strength degradation. Structural collapse capacity can therefore also be estimated. A very good agreement between the computed and the approximated IDA curves is observed, demonstrating that this tool can be a valuable aid for earthquake engineering practice in the future.

[De Luca et al.](#) discuss the issue of bilinear fitting of static pushover curves. The authors propose an improvement of codes' bilinear fit for static pushover curves aimed at decreasing the error introduced in the conventional pushover analysis by the piecewise linear fitting of the capacity curve. The error introduced by the bilinear fit of the force-deformation relationship is quantified by studying it at the single-degree-of-freedom (SDOF) system level. Incremental Dynamic Analysis (IDA) is employed to enable a direct comparison of the actual curved backbones versus their piecewise linear approximations. A near-optimal elastic-plastic bilinear fit can be an enhanced solution to decrease systematically the error introduced in pushover analysis, compared to the fit approaches provided by most codes. The main differences are (a) closely fitting the initial stiffness of the capacity curve and (b) matching the maximum strength value, rather than disregarding them in favor of balancing areas or energies. The proposed approach is shown to reduce the conservative bias observed for systems with highly curved force-deformation backbones.

[Gkimousis and Koumouis](#) investigate the inelastic behavior of reinforced concrete structures subjected to a number of strong ground motions of escalated Intensity Measure, by monitoring the characteristic Engineering Demand Parameters (EDPs). This provides the necessary data to estimate the overall performance of a structure at a particular site of specified seismic hazard within the framework of Incremental Dynamic Analysis. A series of plane frames of different number of spans and stories is investigated. Moreover, the authors examine also the effect of some general design code provisions on the collapse capacity of the frames studied, such as stiffness distribution along the building height and the strong column-weak beam design principle.

[Borzi et al.](#) study the seismic risk assessment of Italian school buildings. The work is based on the idea of defining a methodology that implements an analysis in successive steps with an increasing level of detail in an attempt to identify the most seismically vulnerable school buildings in Italy. The school building location, the exposure data and the seismic input information are implemented in a WebGIS platform through interactive maps and tabs. By means of the developed WebGIS tools, the seismic risk analyses of the school buildings are performed and the obtained results are presented in terms of maps and tables.

[Vassilopoulou and Gantes](#) investigate the geometric nonlinear dynamic response of saddle-shaped cable nets subjected to uniform harmonic loads using an equivalent SDOF model. The transformation from the MDOF cable net to the SDOF system is obtained with the aid of similarity relationships. The comparison between the two models by means of the steady-state amplitude of the central node demonstrates that the behavior of the SDOF model describes satisfactorily the response of the MDOF, predicting the dominant nonlinear phenomena.

[Naprstek et al.](#) present a work on the nonlinear dynamic behavior of a ball vibration absorber, modeled as a holonomous system. Using Lagrange equations of the second type, the governing nonlinear differential system is derived. The solution procedure combines analytical and numerical processes, where the 2nd Lyapunov method is used as the main tool for the dynamic stability investigation. The function and effectiveness of an absorber identical to those installed at the existing TV

towers was examined in the laboratory of the Institute of Theoretical and Applied Mechanics. The response spectrum demonstrates a strongly nonlinear character of the absorber.

[Casarotti et al.](#) attempt to evaluate the response of an isolated system based on double curved surface sliders. The objective is to study the response of a particular installation system for Double Curved Surface Sliders for buildings with large plan development in case of construction defects related to the non-perfect co-planarity of the devices. A case study is presented, in which the effects of randomly simulated construction defects are analyzed. Preliminary results showed that the simulated construction defects have only limited influence on the global hysteretic behavior of the system and that the simultaneous loss of contact may occur only for a limited number of devices.

During strong earthquakes, structural poundings may occur between adjacent buildings due to deformations of their stories. In the case of seismically isolated buildings, pounding may occur with the surrounding moat wall due to the insufficient seismic gap at the base of the building. [Polycarpou and Komodromos](#) investigate numerically the effectiveness of rubber shock-absorbers as a mitigation measure for earthquake-induced structural poundings. The study presents a methodology that can be used to numerically simulate the use of rubber layers between neighboring structures with relatively narrow seismic gaps in order to act as collision bumpers and mitigate the detrimental effects of earthquake-induced poundings. The efficiency of this potential impact mitigation measure is parametrically investigated considering both cases of conventionally fixed-supported and seismically isolated buildings subjected to various earthquake excitations.

[Lavan and Daniel](#) present a methodology for sizing, tuning and allocating multiple tuned-mass dampers in 3D irregular structures. The methodology is based on a two-step iterative analysis/redesign algorithm, which allows obtaining a very efficient amount of added dampers' mass while converging to an allowable response of the structure. This performance-based design methodology is simple, relies on analysis tools only, and is fast converging and thus its use is attractive for the engineering practice. The proposed method allows reducing absolute accelerations to a desirable level following the performance-based design principles. This is achieved using several TMDs located at different places and tuned to several frequencies. The methodology is general in scope and suitable for all types of structures, regardless of the amount of irregularity.

[Melkumyan](#) presents three remarkable projects on retrofitting buildings using base isolation. The first is about retrofitting of a five-story stone apartment building without resettlement of the occupants. The second involves the retrofitting of a 60-year-old, three-story stone historical school building and the third project is about the development of the design on retrofitting by base isolation of a 180-year-old historical building. The retrofitting scheme is described and detailed results of the earthquake response analysis for two cases, i.e. when the building is base isolated and when it has a fixed base, are given. For all three buildings comparative analyses of the cost of innovative base isolation retrofitting technology versus the costs of the different methods of conventional retrofitting are presented.

[Manos and Mitoulis](#) present an expert system developed for the preliminary design of the seismic isolation of bridges, assumed to respond as a SDOF system. The expert system and the developed software include a series of checks of Eurocode 8-2, in order to ensure the satisfactory seismic “optimum” performance of the selected isolation scheme. In doing so, the software accesses a specially created database of the geometrical and the mechanical characteristics of commercially available cylindrical or prismatic elastomeric bearings, than can be easily enriched by relevant data from laboratory tests on isolation devices. The proposed methodology is validated through rigorous 2D and 3D MDOF parametric numerical analyses and with the case study of a real bridge.

[Burczyński et al.](#) investigate new soft-computing techniques in structural dynamics where one tries to study, model, analyze and optimize very complex phenomena, for which more precise scientific tools of the past were not able to give low-cost and complete solutions. The paper deals with various applications on optimization problems of bio-inspired methods, such as evolutionary algorithms (EA), artificial immune systems (AIS) and particle swarm optimizers (PSO). Structures considered in this work are analyzed using the finite-element method (FEM) and the boundary element method (BEM). The bio-inspired methods are applied to optimize shape, topology and the material properties of 3D structures modeled by the FEM and to optimize location of stiffeners in 2D reinforced plates modeled by the coupled BEM/FEM. The structures are optimized using criteria that depend on frequency, displacements or stresses. Numerical examples demonstrate that methods based on soft-computing can be very effective for solving optimal design problems.

[Gencturk and Hossain](#) study the optimal design of RC frames, a widely used structural type around the world, considering both the initial cost and structural performance as problem objectives. Initial cost comprises the total cost of materials and workmanship for structural components, while structural performance is measured by a two-level approach. First, each design is checked for acceptability according to existing codes, and next performance is quantified in terms of maximum inter-story drift obtained from nonlinear inelastic dynamic analysis. This multi-objective, multi-level approach allows one to investigate the implications of the selection of design parameters on the seismic performance while minimizing the initial cost and satisfying the design criteria. The results suggest that structural performance varies significantly within the acceptable limits of design codes and lower initial cost could be achieved for similar structural performance.

[Moutsopoulou et al.](#) present their work on nonsmooth and nonconvex optimization for the design and the order reduction of robust controllers used in smart structures. H-infinity controller design for linear systems is a difficult, nonconvex typically nonsmooth optimization problem when the controller is fixed to be of order less than the one of the open-loop plant, an important requirement in embedded smart systems. A new optimization package is used, aiming at solving fixed-order stabilization and local optimization problems, based on a new hybrid solution algorithm. The problem is to reduce the vibration of the smart system using H-infinity control and nonsmooth and nonconvex optimization.

Decision-making for infrastructure systems is a difficult task to perform because of the complexity and the variety of the types of risks that may occur in

the different phases of the life-cycle of an infrastructure system. In their chapter [Xenidis and Angelides](#) propose a new methodology for risk-based decision making for planning and operating infrastructure systems. The methodology integrates the variability of impact upon risk occurrence, the available risk-response strategies, and the preference of the decision maker over these strategies with regard to the criticality of the various impacts upon risk occurrence. It considers four risk-response strategies, namely: acceptance, mitigation, transfer, and avoidance. Three approaches are applied, in order to determine the preference margins between these strategies: Compliance with regulations and specifications, determination based on data elaboration, and subjective judgment. Once the expected value of the impact upon risk occurrence is estimated, the decision maker is able to decide for the respective risk-response.

In the last chapter, [Soroushian et al.](#) investigate the practical performance of a recent technique for more efficient dynamic analysis of bridge structures with direct time integration. A typical multi-span concrete bridge is considered, in two structural cases (original and upgraded with nonlinear elements), and subjected to four major earthquakes. The analyses are carried out with the Newmark average acceleration method, and the modified Newton Raphson method for nonlinearity iterations, once conventionally (not implementing the recently proposed technique), and then again with implementing the technique proposed. Having implemented the proposed technique in time integration analysis, the responses obtained are very close to the responses of the conventional analyses, while the computational cost is considerably reduced.

The aforementioned collection of chapters provides an overview of the present thinking and state-of-the-art developments on the computational techniques in the framework of structural dynamics and earthquake engineering. The book is targeted primarily to researchers, postgraduate students and engineers working in this scientific field. It is hoped that this collection of chapters in a single book will be found a useful tool for both researchers and practicing engineers.

The book editors would like to express their deep gratitude to all authors for the time and effort they devoted to this volume. Furthermore, we are most appreciative to the reviewers for their effective comments that helped the authors to improve their contributions. Finally, the editors would like to thank the personnel of Springer Publishers for their kind cooperation and support for the publication of this book.

Athens, Greece
December 2012

Manolis Papadrakakis
Michalis Fragiadakis
Vagelis Plevris

Contents

1D Harmonic Response of Layered Inhomogeneous Soil: Exact and Approximate Analytical Solutions	1
George E. Mylonakis, Emmanouil Rovithis, and Haralambos Parashakis	
Monitored Incoherency Patterns of Seismic Ground Motion and Dynamic Response of a Long Cable-Stayed Bridge	33
Vassilios Lekidis, Savvas Papadopoulos, Christos Karakostas, and Anastasios Sextos	
An Efficient Beam-Column Element for Inelastic 3D Frame Analysis . . .	49
Svetlana M. Kostic, Filip C. Filippou, and Chin-Long Lee	
Floor Response Spectra for Moderately Heavy Nonstructural Elements Attached to Ductile Frame Structures	69
Christoph Adam, Thomas Furtmüller, and Lukas Moschen	
Seismic Assessment of Steel Moment Frames Using Simplified Nonlinear Models	91
Dimitrios G. Lignos, Christopher Putman, and Helmut Krawinkler	
Preliminary Seismic Assessment Method for Identifying R.C. Structural Failures	111
Stylianos J. Pardalopoulos, Georgia E. Thermou, and Stavroula J. Pantazopoulou	
Numerical Determination of the Seismic Strength of Reinforced Concrete Shear Walls with Fractal Cracks	129
O. Panagouli, E. Mistakidis, and K. Iordanidou	
Damage Analysis of Reinforced Concrete Structures with Substandard Detailing	149
Panagiotis E. Mergos and Andreas J. Kappos	

Seismic Evaluation of Existing Basement Walls	177
Mahdi Taiebat, W.D. Liam Finn, Alireza Ahmadnia, Elnaz Amirzehni, and Carlos E. Ventura	
Modeling of Infilled Framed Structures	197
Panagiotis G. Asteris, Christis Z. Chrysostomou, Ioannis Giannopoulos, and Paolo Ricci	
Numerical Evaluation of the Seismic Efficiency of Connections of Fractures and Complements of Ancient Colonnades	225
Maria-Eleni Dasiou, Ioannis N. Psycharis, and Antigone Vrouva	
Seismic Overturning of Rocking Structures with External Viscous Dampers	243
Elias G. Dimitrakopoulos and Matthew J. DeJong	
Innovative Computing Environment for Fast and Accurate Prediction of Approximate IDA Curves	259
Iztok Peruš, Robert Klinc, Matevž Dolenc, and Matjaž Dolšek	
Improving Static Pushover Analysis by Optimal Bilinear Fitting of Capacity Curves	273
Flavia De Luca, Dimitrios Vamvatsikos, and Iunio Iervolino	
Collapse Fragility Curves of RC Frames with Varying Design Parameters	297
Ilias A. Gkimousis and Vlasis K. Koumousis	
Seismic Risk Assessment of Italian School Buildings	317
Barbara Borzi, Paola Ceresa, Marta Faravelli, Emilia Fiorini, and Mauro Onida	
Nonlinear Dynamic Response of MDOF Cable Nets Estimated by Equivalent SDOF Models	345
Isabella Vassilopoulou and Charis J. Gantes	
Non-linear Model of a Ball Vibration Absorber	381
Jiří Náprstek, Cyril Fischer, Miroš Pirner, and Ondřej Fischer	
Evaluation of Response of an Isolated System Based on Double Curved Surface Sliders	397
Chiara Casarotti, Marco Furinghetti, and Alberto Pavese	
Numerical Investigation of the Effectiveness of Rubber Shock-Absorbers as a Mitigation Measure for Earthquake-Induced Structural Poundings	417
Panayiotis C. Polycarpou and Petros Komodromos	
Seismic Design Methodology for Control of 3D Buildings by Means of Multiple Tuned-Mass-Dampers	437
Oren Lavan and Yael Daniel	

Comparison of Innovative Base Isolation Retrofitting Technology with Conventional Retrofitting of Existing Buildings 461
Mikayel Melkumyan

Preliminary Design of Seismically Isolated R/C Bridges—Features of Relevant Expert System and Experimental Testing of Elastomeric Bearings 491
George C. Manos and Stergios A. Mitoulis

Soft Computing in Structural Dynamics 521
T. Burczyński, R. Górski, A. Poteralski, and M. Szczepanik

Optimal Design of RC Frames Using Nonlinear Inelastic Analysis 545
Bora Gencturk and Kazi Ashfaq Hossain

Nonsmooth and Nonconvex Optimization for the Design and Order Reduction of Robust Controllers Used in Smart Structures 569
A.J. Moutsopoulou, A.T. Pouliezos, and G.E. Stavroulakis

A Risk-Based Decision Making Methodology for Planning and Operating Safe Infrastructure Systems Against Various Hazards . . . 591
Yiannis Xenidis and Demos C. Angelides

On Practical Performance of a Technique for More Efficient Dynamic Analysis in View of Real Seismic Analysis of Bridge Structures . . . 613
Aram Soroushian, Akbar Vasseghi, and Mahmood Hosseini

Author Index 635

1D Harmonic Response of Layered Inhomogeneous Soil: Exact and Approximate Analytical Solutions

George E. Mylonakis, Emmanouil Rovithis, and Haralambos Parashakis

Abstract The seismic response of inhomogeneous soils is explored analytically by means of one-dimensional viscoelastic wave propagation theory. The system under investigation comprises of a continuously inhomogeneous layer over a homogeneous one of higher stiffness. The excitation is specified at the bottom of the base layer in the form of vertically propagating harmonic S waves. Shear wave propagation velocity in the inhomogeneous layer is described by a generalized parabolic function, which allows modeling of soil having vanishing shear modulus at the ground surface. The problem is treated analytically leading to an exact solution of the Bessel type for the natural frequencies, mode shapes and base-to-surface response transfer function. The model is validated using available theoretical solutions and finite-element analyses. The exact analytical solution is compared with energy-based Rayleigh techniques and equivalent homogeneous soil approximations. The latter are defined by means of alternative definitions for the representative shear wave velocity in the inhomogeneous layer. Results are presented in the form of normalized graphs demonstrating the effect of salient model parameters such as layer thickness, impedance contrast between surface and base layer, surface-to-base shear wave velocity ratio in the inhomogeneous layer, rate of inhomogeneity and hysteretic damping ratio. Harmonic response of inhomogeneous soils with vanishing shear wave velocity near soil surface is explored by asymptotic analyses.

Keywords Inhomogeneous soil · Wave propagation · Rayleigh method · Shape functions

G.E. Mylonakis (✉)

Department of Civil Engineering, University of Patras, Rio, 26500, Greece

e-mail: mylo@upatras.gr

E. Rovithis

Earthquake Planning and Protection Organization (EPPO-ITSAK), Thessaloniki, 55102, Greece

e-mail: rovithis@itsak.gr

H. Parashakis

Department of Civil Works, Technological Educational Institute of Crete, Heraklion, Greece

e-mail: parashaki_m@hotmail.com

1 Introduction

Under certain conditions such as those encountered in thick and soft soil deposits, conventional one-dimensional analysis procedures based on discretizing the soil in a multi-layer system with constant properties within each layer, may underestimate soil amplification with respect to the actual response of a continuously inhomogeneous medium, depending primarily on frequency content of input motion. Based on a detailed in-situ investigation of dynamic properties of soft deposits, Towhata [1] demonstrated analytically that shear wave propagation velocity may vary continuously with depth even for complex stratifications involving different soil materials and geologic environments. In this case, pertinent analytical solutions reveal the possibility of higher amounts of seismic energy reaching the ground surface with respect to soils with discontinuous variation in shear modulus.

Continuously inhomogeneous soils have been studied for different types of soil inhomogeneity or of seismic waves in multiple directions providing closed-form solutions for natural frequencies, modal shapes and base-to-surface amplification functions. Following the early work of Ambraseys [2] and Seed and Idriss [3], Dobry et al. [4] studied the dynamic response of inhomogeneous soils with shear wave propagation velocity of the form $V_s = cz^n$, z being depth and n a positive inhomogeneity coefficient associated with zero shear modulus at the ground surface. A special case of the above equation, corresponding to $n = 2/3$, was adopted by Travasarou and Gazetas [5] as part of an investigation of seismic response of soft marine clay sediments. Based on earlier suggestions by Dobry et al. [4] and Towhata [1], the above authors showed analytically that seismic strains may tend to infinity at soil surface depending on the rate of increase of shear wave velocity with depth. Heterogeneous soils with shear wave velocity increasing from a non-zero value at the free surface were examined by Ambraseys [2], Toki and Cherry [6], Schreyer [7] and Gazetas [8], focusing on the effect of rate and type of heterogeneity. An extended one-dimensional model was later developed by Towhata [1], who investigated the behavior of the medium for the whole set of positive inhomogeneity coefficients ($0 < n < \infty$) considering zero or finite stiffness at the surface. More recently, Parashakis [9] and Semblat and Pecker [10] presented analytical solutions of the wave equation for a heterogeneous soil profile with shear wave velocity increasing with depth according to a generalized power law and different boundary conditions at the base.

The effect of soil inhomogeneity has also been studied for different types of seismic waves in multiple dimensions. For instance, the late Professor Vardoulakis [11] considered the case of torsional waves in an inhomogeneous half space. Later, Vrettos [12] solved the eigenvalue problem of dispersive SH-surface waves propagating in an inhomogeneous half-space for both bounded and unbounded variation of shear modulus with depth. In a very recent publication [13], the same author treated analytically, by means of infinite series, a soil layer with exponential variation of soil shear modulus with depth with a bounded value at infinity. A set of solutions pertaining to 1D- and 2D-viscoelastic wave propagation problems has been presented in a

series of publications by Manolis and Shaw [14–16]. A collection of available solutions for wave propagation in inhomogeneous media can be found in Brekhovskikh and Bayer [17].

On the other hand, design practice often requires knowledge of the vibrational characteristics of soil deposits by means of simplified approximations. In support of the above, modern seismic codes [18–20] classify sites according to the average shear wave propagation velocity within the top 30 meters (termed $V_{s,30}$) of the soil profile, referring to homogeneous or inhomogeneous profiles without strong gradients in shear wave velocity with depth. However, in case of a moderately-to-strongly inhomogeneous soil, the choice of a pertinent, “representative” shear wave velocity is not straightforward especially when thick and soft deposits are encountered. In this context, Dobry et al. [21] investigated alternative approximate methods to estimate the fundamental period of a layered soil profile, following the early work of Madera [22]. Based on an extensive parametric investigation performed for an ample range of representative soil profiles the above author showed the efficiency of the Rayleigh procedure [23] in predicting the first natural frequency of the system, leading to comparable results with respect to the exact values. A series of energy-based Rayleigh solutions have been reported recently by Miha [24] encompassing different types of soil inhomogeneity.

In the herein reported study, seismic response of inhomogeneous soil is investigated in the realm of one-dimensional viscoelastic wave propagation theory, based on a recent publication by the authors [25]. Following the work by Towhata [1], a generalized parabolic function is adopted to describe the wave propagation velocity in the inhomogeneous soil, thus allowing both for zero and finite shear modulus at the surface. The surficial inhomogeneous zone is followed by a homogeneous layer supported on a rigid base, leading to bounded shear wave propagation velocity at large depths. Soil mass density and material damping are assumed to be constant within each layer, but could be different between the upper and the lower one. Thereby, the proposed model is capable of describing a much wider set of geometric and material configurations over earlier models considering a single layer. Furthermore, inhomogeneous soils having vanishing values of shear modulus at ground surface can be modeled, thus allowing study of dependence of near-surface displacements and strains to corresponding soil stiffness. Single- and two-layer inhomogeneous deposits are examined considering free or forced harmonic oscillations. The problem is treated analytically leading to a closed-form solution for the vibrational characteristics and the base-to-surface transfer function of the system. The model is thoroughly validated by means of both analytical and finite-element solutions. The exact solution for single- and two-layer systems is compared with simple approximations derived using the Rayleigh technique and equivalent homogeneous soil considerations. The latter are defined by means of alternative definitions for the representative shear wave velocity in the inhomogeneous layer corresponding to: (i) the shear wave propagation velocity at the base of the inhomogeneous layer, (ii) the shear wave velocity in the middle of the inhomogeneous layer, (iii) the mean shear wave velocity within the inhomogeneous layer, (iv) the shear wave velocity

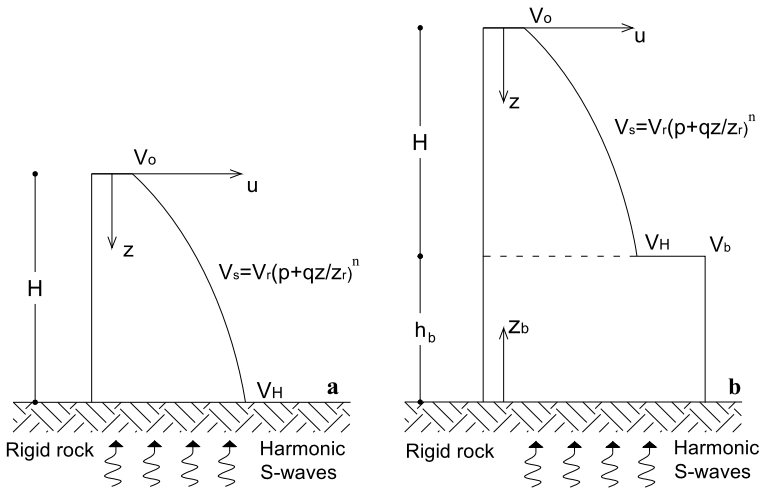


Fig. 1 (a) Single inhomogeneous layer over rigid rock. (b) Two-layer deposit comprising of an inhomogeneous surface layer followed by a homogeneous layer over a rigid base

providing equal travel time from base to surface between homogeneous and inhomogeneous soil and (v) the shear wave velocity leading to an equivalent homogeneous soil having the same fundamental frequency as the inhomogeneous profile. The dependence of near-surface shear strains for inhomogeneous soils with very small surface-to-base shear wave velocity ratios is investigated by means of asymptotic analyses.

2 Continuously Inhomogeneous Soils: Analytical Investigation

A continuously inhomogeneous viscoelastic soil zone of thickness H over a rigid base (Fig. 1a) is considered as a basis of the layered inhomogeneous soil examined. Soil mass density, ρ and hysteretic damping ratio, ξ , are considered constant with depth, while shear wave propagation velocity is assumed to increase with depth according to the generalized power law function:

$$V_s = V_r \left(b + q \frac{z}{z_r} \right)^n \quad (1)$$

where n , b , q are dimensionless inhomogeneity factors and z is the vertical coordinate (depth) measured from ground surface. V_r and z_r stand for a reference shear wave velocity and a reference depth, respectively. For positive values of b , Eq. (1) results in non-zero shear wave velocity at the surface ($z = 0$). Introducing the shear wave velocities at the surface (V_o) and base (V_H) and setting $q = (1 - b)$, $z_r = H$, the model can be cast in the more convenient form:

$$V_s = V_H \left[b + (1 - b) \frac{z}{H} \right]^n \quad (2)$$

where $b = (V_o/V_H)^{1/n}$. Evidently, for small values of the inhomogeneity factor n , the velocity model simplifies to a uniform distribution, whereas for values of n close to unity the model converges to a linear distribution. Setting $b = 0$ in Eq. (2), the variation reduces to one starting from a zero value at the surface. This special case yields some important results as to the amplitude of near surface shear strains and displacements which are discussed in the ensuing.

A more general case of an inhomogeneous surface layer underlain by a homogeneous one of finite thickness h_b and shear wave propagation velocity V_b is examined as a generalized two-layer deposit (Fig. 1b). This extended model allows for different soil properties between the inhomogeneous and the homogeneous layer to be accounted for. A similar two-layer model has been studied by Afra and Pecker [26], considering the lower layer as a viscoelastic half space.

The input motion is specified at the base of the system in the form of a harmonic horizontal displacement, $u = u_o \exp(i\omega t)$, ω being the cyclic excitation frequency, thereby generating S waves propagating vertically up and down in the profile.

2.1 Single Inhomogeneous Layer

Under harmonic oscillations, one-dimensional shear waves in a soil layer with constant mass density ρ and variable shear modulus $G(z)$ are described by the ordinary differential equation

$$\frac{d}{dz} \left[G(z) \frac{du}{dz} \right] + \rho \omega^2 u = 0 \quad (3)$$

Substituting $G(z) = \rho V_s^2(z) = \rho V_r^2(b + qz/z_r)^{2n}$ into the above expression yields:

$$\frac{d^2u}{dz^2} + 2n \frac{q}{z_r} \left(b + q \frac{z}{z_r} \right)^{-1} \frac{du}{dz} + k_r^2 \left(b + q \frac{z}{z_r} \right)^{-2n} u = 0 \quad (4)$$

where $k_r = \omega/V_r$ is a reference wave number. Introducing the linear transformation $x = b + qz/z_r$ and employing the chain rule of differentiation, Eq. (4) simplifies to

$$\frac{d^2u}{dx^2} + 2nx^{-1} \frac{du}{dx} + \left(\frac{k_r z_r}{q} \right)^2 x^{-2n} u = 0 \quad (5)$$

which is a differential equation of the Bessel type. Upon substituting $u = x^s$ and $u = \exp[i\lambda z^{\ell/2}]$, it is easy to establish by dominant balance, that $x = 0$ is a regular singular point with two power-law behaviors and $x = \text{infinity}$ is an irregular one with two exponential behaviors. Restricting our interest to the most common case $0 < n < 1$ [9, 27, 28], the general solution to Eq. (5) is given by [29]:

$$u(x) = x^\mu [C_1 J_\nu(\lambda x^{\ell/2}) + C_2 N_\nu(\lambda x^{\ell/2})] \quad (6)$$

where $J_\nu(\cdot)$ and $N_\nu(\cdot)$ denote the Bessel functions of the first and second kind and order ν , respectively, while $\ell = 2(1 - n)$ is a dimensionless parameter representing

the step of the associated power series solutions [30]. Parameters μ and ν are obtained from the asymptotic behavior near the origin ($x = 0$), which is satisfied for $\mu = (1 - 2n)/2$ and $\nu = (2n - 1)/2(1 - n)$, while the asymptotic behavior of the solution at infinity requires $\lambda = 2k_r z_r / \ell q$. Accordingly, the solution to Eq. (6) takes the form:

$$u(x) = x^\mu \left[C_1 J_\nu \left(\frac{1}{1-n} \frac{k_r z_r}{q} x^{\ell/2} \right) + C_2 N_\nu \left(\frac{1}{1-n} \frac{k_r z_r}{q} x^{\ell/2} \right) \right] \quad (7)$$

where C_1 and C_2 are integration constants to be determined from the boundary conditions. Of these, $\tau(0) = G(z)\gamma(z)|_{z=0} = 0$ describes the physical restriction of zero shear tractions at the soil surface. Using $\gamma(z) = du/dz = q/z_r du/dx$ and considering a layer with finite shear modulus at the surface ($b > 0$), this condition yields a proportionality relation between constants C_1 and C_2 :

$$C_2 = -C_1 J_{\nu+1} \left(\frac{1}{1-n} \frac{k_r z_r}{q} b^{\ell/2} \right) \left[N_{\nu+1} \left(\frac{1}{1-n} \frac{k_r z_r}{q} b^{\ell/2} \right) \right]^{-1} \quad (8)$$

Upon eliminating constant C_2 in Eq. (7) by means of the above expression yields a standing wave that satisfies the boundary condition of a traction-free surface. Recalling that $x = b + qz/z_r$, the solution to the differential equation is

$$u(z) = \frac{C_1 (b + qz/z_r)^\mu}{N_{\nu+1} (\lambda b^{\ell/2})} \left\{ J_\nu \left[\lambda \left(b + q \frac{z}{z_r} \right)^{\ell/2} \right] N_{\nu+1} [\lambda b^{\ell/2}] \right. \\ \left. - J_{\nu+1} [\lambda b^{\ell/2}] N_\nu \left[\lambda \left(b + q \frac{z}{z_r} \right)^{\ell/2} \right] \right\} \quad (9)$$

which describes the variation of displacement within the layer.

Shear stresses are obtained upon differentiation of Eq. (9) with respect to z :

$$\tau(z) = \frac{C_1 \omega^2 \rho}{k_r N_{\nu+1} (\lambda b^{\ell/2})} \left\{ J_{\nu+1} \left[\lambda \left(b + q \frac{z}{z_r} \right)^{\ell/2} \right] N_{\nu+1} [\lambda b^{\ell/2}] \right. \\ \left. - J_{\nu+1} [\lambda b^{\ell/2}] N_{\nu+1} \left[\lambda \left(b + q \frac{z}{z_r} \right)^{\ell/2} \right] \right\} \quad (10)$$

2.1.1 Natural Frequencies and Mode Shapes

In the absence of earthquake disturbances at the base of the layer, wave amplitude at $z = H$ must vanish. Enforcing this condition to Eq. (9) yields the characteristic equation:

$$J_{\nu+1} (\lambda_m b^{\ell/2}) N_\nu (\lambda_m) - J_\nu (\lambda_m) N_{\nu+1} (\lambda_m b^{\ell/2}) = 0 \quad (11)$$

the solution of which provides the natural frequencies of the layer, ω_m ; these can be written in normalized form as

$$\bar{\omega}_m = \frac{\omega_m}{\omega_{1n}} = \frac{2}{\pi} (1-n)(1-b)\lambda_m, \quad m = 1, 2, 3, \dots \quad (12)$$

where $\omega_{1n} = \pi V_H/2H$ is the fundamental natural frequency of a homogeneous soil layer of same thickness as the inhomogeneous one, and shear wave propagation velocity equal to wave velocity at the base, V_H .

Employing Lommel's identity [30]:

$$J_{\nu+1}(\lambda b^{\ell/2})N_{\nu}(\lambda b^{\ell/2}) - J_{\nu}(\lambda b^{\ell/2})N_{\nu+1}(\lambda b^{\ell/2}) = \frac{2}{\pi \lambda b^{\ell/2}} \quad (13)$$

the solution for the displacement at soil surface ($z = 0$) simplifies to:

$$u(0) = \frac{-2C_1 b^{\mu-\ell/2}}{\pi \lambda N_{\nu+1}(\lambda b^{\ell/2})} \quad (14)$$

Normalizing Eq. (9) by $u(0)$ in Eq. (14) yields the modal shape $\Phi_m(z) = u_m(z)/u_m(0)$ of the layer:

$$\begin{aligned} \Phi_m(z) = \frac{\pi \lambda_m (b + qz/z_r)^\mu}{2b^{\mu-\ell/2}} & \left\{ J_{\nu+1}[\lambda_m b^{\ell/2}] N_{\nu} \left[\lambda_m \left(b + q \frac{z}{z_r} \right)^{\ell/2} \right] \right. \\ & \left. - N_{\nu+1}[\lambda_m b^{\ell/2}] J_{\nu} \left[\lambda_m \left(b + q \frac{z}{z_r} \right)^{\ell/2} \right] \right\} \end{aligned} \quad (15)$$

which can be readily evaluated, as function of depth, for any given eigenvalue λ_m .

2.1.2 Steady State Harmonic Response

Under harmonic base excitation, the base-to-surface transfer function is defined in terms of the familiar amplification factor [31, 32]:

$$F(\omega) \equiv \frac{u(0)}{u(H)} \quad (16)$$

Taking the ratio of Eqs. (14) and (9) and setting $z = H$, the transfer function of the inhomogeneous soil layer is obtained as

$$F(\omega) = \frac{2b^{\mu-\ell/2}}{\pi \lambda} \left[J_{\nu+1}(\lambda b^{\ell/2})N_{\nu}(\lambda) - J_{\nu}(\lambda)N_{\nu+1}(\lambda b^{\ell/2}) \right]^{-1} \quad (17)$$

where λ is now a continuous function of excitation frequency ω . Note that soil damping can be accounted for in the above analysis by means of the correspondence principle of viscoelasticity using the standard substitutions $G \rightarrow G^* = G(1 + 2i\xi)$ and $V_s(z) \rightarrow V_s^*(z) = V_s(z)\sqrt{1 + 2i\xi}$ [31, 32]. Also, the solution is equally applicable to the case of vertically-propagating P waves if the appropriate wave velocity and damping ratio are employed.

2.2 Two-Layer Inhomogeneous Soil

Referring to the generalized two-layer inhomogeneous soil in Fig. 1b, the above analytical solution can be extended to account for the presence of an underlying

homogeneous layer of thickness h_b and shear wave propagation velocity V_b . The response of the homogeneous layer due to a harmonic horizontal displacement applied at the base is given by the elementary function [31, 32]:

$$u_b(z_b) = A_1 \sin(k_b z_b) + A_2 \cos(k_b z_b) \quad (18)$$

where z_b is the vertical coordinate measured upwards from the base of the layer, A_1 and A_2 represent the amplitudes of the waves traveling upward and downward in the layer, respectively; $k_b (= \omega / V_b)$ is the corresponding wave number.

Upon enforcing the continuity of stresses and displacements at the base of the system and the interface of the surface and the base layer:

$$\begin{aligned} u_b(0) &= u_o \\ u_b(h_b) &= u(H) \\ \tau_b(h_b) &= -\tau(H) \end{aligned} \quad (19)$$

the analytical expressions for $u(z)$, $\tau(z)$ and $u_b(z_b)$ in Eqs. (9), (10) and (18), yield the following simultaneous algebraic equations in A_1 and C_1 :

$$\begin{aligned} &A_1 \sin(k_b h_b) + u_o \cos(k_b h_b) \\ &= C_1 \left[(1-n) \frac{q\theta_H}{k_r z_r} \right]^{\frac{1-2n}{2(1-n)}} \frac{J_v(\theta_H) N_{v+1}(\theta_o) - N_v(\theta_H) J_{v+1}(\theta_o)}{N_{v+1}(\theta_o)} \end{aligned} \quad (20)$$

$$\begin{aligned} &\rho_b \frac{\omega^2}{k_b} [A_1 \cos(k_b h_b) - u_o \sin(k_b h_b)] \\ &= C_1 \rho_H \omega^2 \left((1-n) \frac{q\theta_H}{k_r z_r} \right)^{\frac{1}{2(1-n)}} \frac{1}{k_r} \frac{J_{v+1}(\theta_H) N_{v+1}(\theta_o) - J_{v+1}(\theta_o) N_{v+1}(\theta_H)}{N_{v+1}(\theta_o)} \end{aligned}$$

where $\theta_o = \lambda b^{\ell/2}$, $\theta_H = \lambda(b + qH/z_r)^{\ell/2}$; ρ_H and ρ_b stand for soil mass density of the inhomogeneous and the homogeneous layer, respectively.

The solution to Eqs. (20) yields the following expressions for parameters A_1 and C_1 :

$$\begin{aligned} A_1 &= C_1 \left[(1-n) \frac{q\theta_H}{k_r z_r} \right]^{\frac{1-2n}{2(1-n)}} \frac{J_v(\theta_H) N_{v+1}(\theta_o) - N_v(\theta_H) J_{v+1}(\theta_o)}{\sin(k_b h_b) N_{v+1}(\theta_o)} \\ &\quad - \frac{u_o}{\tan(k_b h_b)} \end{aligned} \quad (21)$$

and

$$\begin{aligned} C_1 &= u_o N_{v+1}(\theta_o) \left\{ \left[(1-n) \frac{q\theta_H}{k_r z_r} \right]^{\frac{1-2n}{2(1-n)}} [J_v(\theta_H) N_{v+1}(\theta_o) \right. \right. \\ &\quad \left. \left. - N_v(\theta_H) J_{v+1}(\theta_o) \right] \cos(k_b h_b) \right\} \end{aligned}$$

$$\begin{aligned}
& - \frac{\rho_H k_b h_b}{\rho_b k_r H} \left[(1-n) \frac{q \theta_H}{k_r z_r} \right]^{\frac{1}{2(1-n)}} \left\{ J_\nu(\theta_H) N_{\nu+1}(\theta_o) \right. \\
& \left. - N_\nu(\theta_H) J_{\nu+1}(\theta_o) \right\} \sin(k_b h_b) \Big\}^{-1} \quad (22)
\end{aligned}$$

2.2.1 Natural Frequencies and Mode Shapes

For the free vibrations of the soil column one obtains the following frequency equation:

$$\tan(k_b h_b) = \left(b + \frac{q}{z_r} H \right)^{-n} \frac{\rho_b k_r}{\rho_H k_b} \frac{J_\nu(\theta_H) N_{\nu+1}(\theta_o) - N_\nu(\theta_H) J_\nu(\theta_o)}{J_{\nu+1}(\theta_H) N_{\nu+1}(\theta_o) - N_{\nu+1}(\theta_H) J_{\nu+1}(\theta_o)} \quad (23)$$

from which the natural frequencies of the two-layer system can be numerically evaluated in terms of λ_m or θ_{om} and θ_{Hm} . The normalized mode shapes are obtained from Eq. (15) and

$$\begin{aligned}
\Phi_m(z_b) &= \frac{\pi \theta_o}{2} \left(1 + \frac{1-b}{b} H \right)^{\frac{1-2n}{2}} \frac{\sin(k_b z_b)}{\sin(k_r h_b)} \\
&\times \left[J_\nu(\theta_H) N_{\nu+1}(\theta_o) - J_{\nu+1}(\theta_o) N_\nu(\theta_H) \right] \quad (24)
\end{aligned}$$

within the inhomogeneous and the homogeneous layer, respectively, for the pertinent values of λ_m (or θ_{om} and θ_{Hm}).

2.2.2 Steady State Harmonic Response

Under harmonic base excitation, the base-to-surface transfer function for the two-layered inhomogeneous soil is defined in the same spirit as in Eq. (16):

$$F(\omega) \equiv \frac{u(0)}{u_b(0)} \quad (25)$$

where $u_b(0)$ denotes the soil displacement at base level. After some lengthy algebra, Eq. (25) yields the solution:

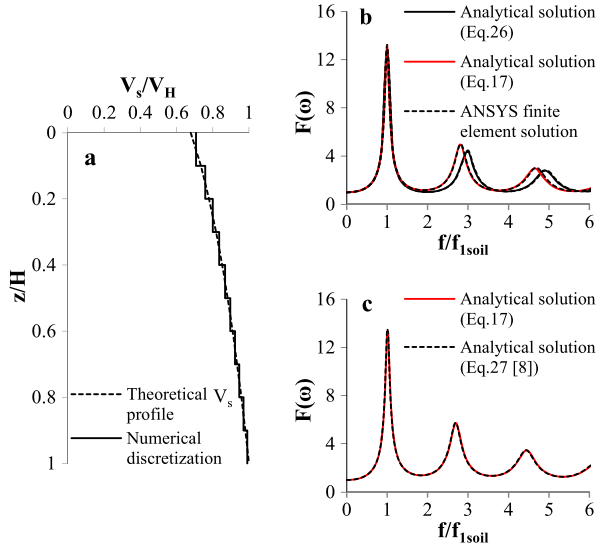
$$\begin{aligned}
F(\omega) &= \left[\frac{2(1-n)(1-b)\rho_b}{\pi b^{1/2} H} \right] \left\{ k_H \rho_b \left[J_\nu(\theta_H) N_{\nu+1}(\theta_o) \right. \right. \\
&\quad \left. \left. - J_{\nu+1}(\theta_o) N_\nu(\theta_H) \right] \cos(k_b h_b) \right. \\
&\quad \left. - k_b \rho_H \left[J_{\nu+1}(\theta_H) N_{\nu+1}(\theta_o) \right. \right. \\
&\quad \left. \left. - J_{\nu+1}(\theta_o) N_{\nu+1}(\theta_H) \right] \sin(k_b h_b) \right\}^{-1} \quad (26)
\end{aligned}$$

As already mentioned, material damping in the soil can be readily incorporated in the above equations by replacing the real wave numbers k_H ($= \omega/V_H$) and k_b ($= \omega/V_b$) with the complex counterparts $k_H^* = \omega/V_H^*$ and $k_b^* = \omega/V_b^*$, respectively.

Fig. 2 (a) Numerical discretization of the idealized V_s profile within the inhomogeneous layer.

(b) Comparison of the analytical solution against a rigorous numerical solution for $V_o/V_H = 0.7$, $h_b/H = 4$, $V_b/V_H = 1$, $\rho_b/\rho_H = 1$, $n = 0.25$, $\xi = 0.05$.

(c) Comparison of the proposed analytical solution with the solution in Ref. [8] for the case of a single inhomogeneous layer with wave propagation velocity varying linearly with depth; $V_o/V_H = 0.5$, $\xi = 0.05$



3 Model Validation

A comparison against a rigorous numerical finite-element analysis was undertaken to validate the analytical solution. To this end, a two-dimensional finite-element model was developed using a general-purpose finite-element platform [33]. The soil stratum was discretized with 4-noded planar elements, with the length of each element established according to the anticipated wavelength of the shear waves propagating in the medium. A sufficiently fine discretization was adopted, aiming at a good discrete approximation of the continuously varying velocity profile (Fig. 2a). Shear wave velocity ratios at the surface and the base of the inhomogeneous layer and the inhomogeneity factor were selected at $V_o/V_H = 0.7$ and $n = 0.25$ respectively. For the two-layer case, ratios h_b/H , V_b/V_H and ρ_b/ρ_H were taken at 4, 1 and 1 respectively. Following the proposed solution, the FE model was analyzed in the frequency domain for harmonic base excitation. The numerical solution in the form of base-to-surface transfer function was compared to the analytical model for both single- (Eq. (17)) and two-layer (Eq. (26)) inhomogeneous soil, with the abscissa normalized by the fundamental resonant frequency, f_{1soil} . Based on the comparative results shown in Fig. 2b, it is evident that the analytical and numerical solutions provide very similar results.

Available solutions from the literature were also employed within the validation scheme. To this end, the solution obtained in [8]

$$F(\omega) = \frac{2s}{(-1/2 + s)(1 + \tilde{b})^{-1/2-s} + (1/2 + s)(1 + \tilde{b})^{-1/2+s}} \quad (27)$$

was utilized, corresponding to a heterogeneous soil layer with shear wave velocity varying linearly with depth in the form $V_s = V_o(1 + qz)$. In the above expression,

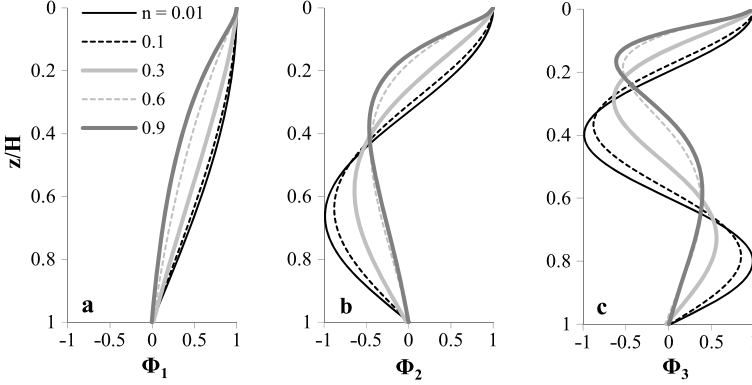


Fig. 3 Normalized shapes of the first (a), second (b) and third (c) natural mode of an inhomogeneous layer over rigid rock. Note the different curvatures of the modes for high values of the inhomogeneity factor n near the surface; $V_o/V_H = 0.1$

\tilde{b} stands for the dimensionless rate of heterogeneity ($\tilde{b} = qH$) and the parameter s is given by:

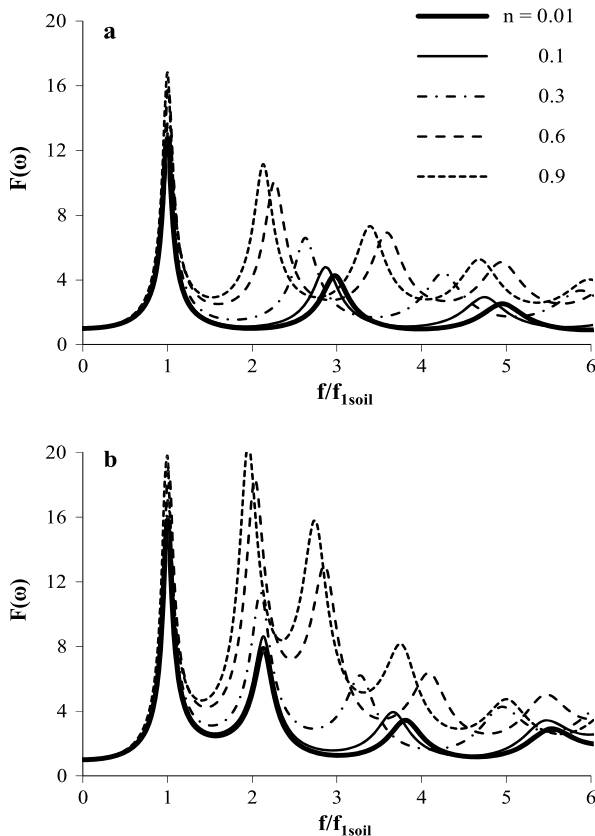
$$s = \left[\frac{1}{4} - \frac{\omega^2}{V_o^2 s^2 (1 + 2i\xi)} \right]^{1/2} \quad (28)$$

Base-to-surface transfer functions computed from Eq. (17) and Eq. (27), respectively, are compared in Fig. 2c for a V_o/V_H ratio of 0.5. The observed amplification patterns are nearly identical.

4 Parametric Investigation: Effect of Salient Parameters

Vibrational characteristics of the system and base-to-surface transfer functions were explored, as affected by salient model parameters such as inhomogeneity factor n , surface-to-base shear wave velocity ratio (V_o/V_H), shear wave velocity contrast (V_b/V_H), relative layer thickness (h_b/H) and hysteretic damping ratio ξ . Figure 3 compares the shapes of the first, second and third modes of the single inhomogeneous layer computed from Eq. (15) for different values of the inhomogeneity factor n in the range 0 to 1. Shear wave velocity at the free surface was taken as a small fraction of the base value ($V_o/V_H = 0.1$), that represents an inhomogeneous soil with significantly reduced shear modulus near the ground surface. As expected, for values of the inhomogeneity factor close to zero ($n = 0.01$), mode shapes closely resemble those of a homogeneous deposit, approaching ground surface tangent to vertical that is, at zero shear strain. On the contrary, when the inhomogeneity factor n is above 0.5, modal amplitudes exhibit a sharp increase near the surface, approaching ground surface tangent to horizontal that is, at infinite shear strain. Similar observations have been reported in Ref. [5] for soils of this type. This behavior is associated

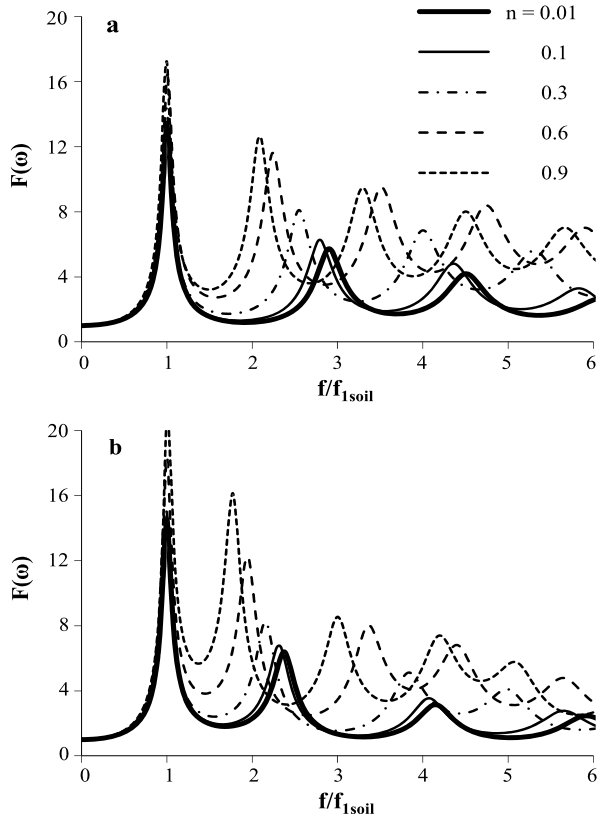
Fig. 4 Effect of inhomogeneity factor n on base-to-surface transfer function of (a) a single inhomogeneous layer and (b) a two-layer inhomogeneous soil with $V_b/V_H = 3$, $h_b/H = 2$, $\rho_b/\rho_H = 1$ as function of frequency. In all plots $V_o/V_H = 0.1$, $\xi = 0.05$



with large shear strains near the free surface, in agreement with interpretations of earthquake data [34].

The analytical base-to-surface transfer function obtained for the single inhomogeneous layer (Eq. (17)) is plotted in Fig. 4, referring to the combined effect of inhomogeneity factor n and shear wave velocity ratio V_o/V_H , with the abscissa normalized by the fundamental frequency of the soil, f_{1soil} . It is observed that for small V_o/V_H ratios ($V_o/V_H = 0.1$), increasing the inhomogeneity factor amplifies response (Fig. 4a) and shifts higher mode resonances to lower frequencies [24, 35]. For the above range of soil inhomogeneity, the response of the two-layer soil obtained for high shear wave velocity contrasts (V_b/V_H) at the interface of the surface and the base layer presents particular interest. Contrary to the well-known response of a piece-wise homogeneous two-layer soil, where the role of higher soil modes progressively diminishes, response of inhomogeneous soil exhibits significant resonant amplitudes at higher modes, a behavior akin to decreasing soil damping with increasing frequency (Fig. 4b). The important role of higher modes is evident regardless of thickness of the underlying homogeneous layer (h_b). Relative layer thickness (h_b/H) referring to the two-layer system was set at 0.5, 1, 2 and 3, re-

Fig. 5 Effect of h_b/H ratio on base-to-surface transfer functions of a two-layer inhomogeneous soil for (a) $h_b/H = 0.5$, (b) $h_b/H = 3$. In both graphs $\xi = 0.05$, $V_o/V_H = 0.1$, $V_b/V_H = 2$, $\rho_b/\rho_H = 1$



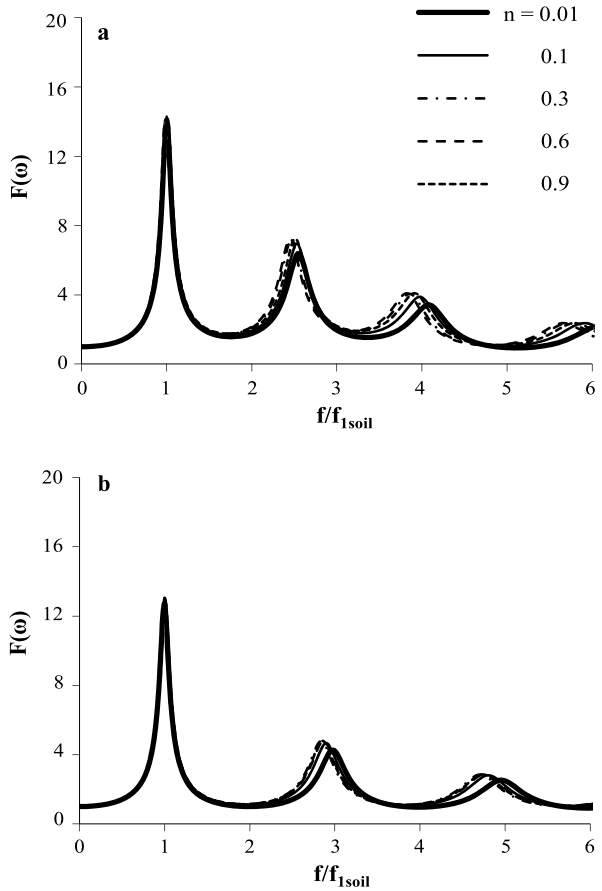
spectively. Figures 5a and 5b show representative base-to-surface transfer functions corresponding to the inhomogeneous two-layer deposit for a h_b/H ratio of 0.5 and 3, respectively. In both cases, strong amplification is observed at higher resonant frequencies with respect to the homogeneous case ($n = 0.01$). Evidently, deeper deposits tend to respond at lower frequencies with larger peak amplitudes (Fig. 5b).

For larger V_o/V_H surface-to-base wave velocity ratios (e.g. $V_o/V_H = 0.75$) corresponding to mild variations of shear wave propagation velocity within the surface inhomogeneous layer, the effect of the inhomogeneity factor is understandably diminished. In this case, the harmonic response of the single- and two-layer inhomogeneous system resembles that of the homogeneous soil ($n = 0.01$). This is clearly demonstrated in Figs. 6a and 6b where Eqs. (26) and (17) are plotted, respectively, for a V_o/V_H ratio of 0.75 providing comparable base-to-surface transfer functions.

5 Comparison with “Equivalent” Homogeneous Soil

Five equivalent homogeneous layers are examined using the following alternative definitions for the representative propagation velocity V_{hom} :

Fig. 6 Effect of inhomogeneity factor n on base-to-surface transfer function of (a) a two-layer inhomogeneous soil with $V_b/V_H = 2$, $h_b/H = 1$, $\rho_b/\rho_H = 1$ and (b) a single inhomogeneous layer as function of frequency. In both graphs $\xi = 0.05$, $V_o/V_H = 0.75$



- V_{hom1} , equal to the shear wave propagation velocity V_H at the base of the inhomogeneous soil

$$V_{hom1} = V_H \quad (29)$$

This is a reference case corresponding to an always-stiffer soil with respect to the actual one.

- V_{hom2} , equal to the shear wave propagation velocity $V_s(H/2)$ at the mid depth of the inhomogeneous layer. This is an elementary, yet potentially useful averaging approach following Ref. [8]

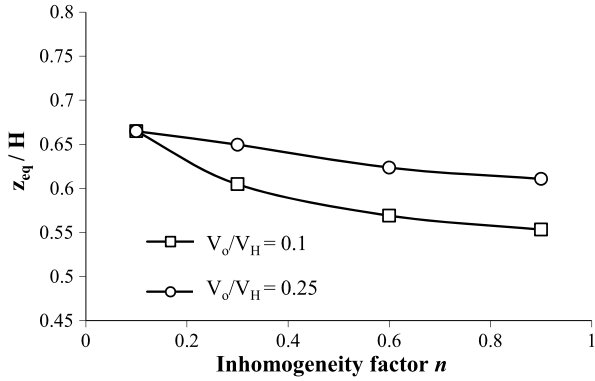
$$V_{hom2} = V_s(H/2) \quad (30)$$

- V_{hom3} , equal to the mean shear wave propagation velocity within the inhomogeneous layer:

$$V_{hom3} = \frac{1}{H} \int_0^H V_s(z) dz \quad (31)$$

where $V_s(z)$ is given by Eq. (2).

Fig. 7 Variation of normalized “equivalent” depth (z_{eq}/H) with inhomogeneity factor n for moderately to strongly inhomogeneous soil



- V_{hom4} , providing equal base to surface travel times between homogeneous and inhomogeneous soil [36]

$$V_{hom4} = H \left[\int_0^H \frac{1}{V_s(z)} dz \right]^{-1} \quad (32)$$

- V_{hom5} , corresponding to an equivalent homogeneous soil having the same fundamental frequency as the inhomogeneous profile

$$V_{hom5} = f_{1Inhom} 4H \quad (33)$$

This is another reference case, which requires knowledge of the actual natural frequency. Alternatively, V_{hom5} may be viewed as the shear wave propagation velocity in the inhomogeneous soil corresponding to the “equivalent” depth (z_{eq}) proposed by Dobry et al. [21]. For the single layer system, z_{eq} normalized by the layer thickness H may be computed from Eq. (2) as

$$\frac{z_{eq}}{H} = \frac{1}{1-b} \left[\left(\frac{V_{hom5}}{V_H} \right)^{\frac{1}{n}} - b \right] \quad (34)$$

Based on the above expression, the dependence of z_{eq}/H to the inhomogeneity factor n is plotted in Fig. 7, referring to a moderately to strongly inhomogeneous soil. For this range of soil inhomogeneity (i.e. V_o/V_H ratio lower than approximately 0.5 and an inhomogeneity factor n above 0.3), Eq. (34) yields a normalized equivalent depth in the range of 0.55 to 0.65.

5.1 Single Layer System

The above shear wave velocity profiles are compared to the generalized parabola $V_s(z)$ (Eq. (2)) in Figs. 8a and 8b referring to V_o/V_H ratios of 0.1 and 0.75 respectively. The inhomogeneity factor n has been taken in these graphs equal to 0.6. It is observed that for large V_o/V_H ratios, the above expressions yield comparable

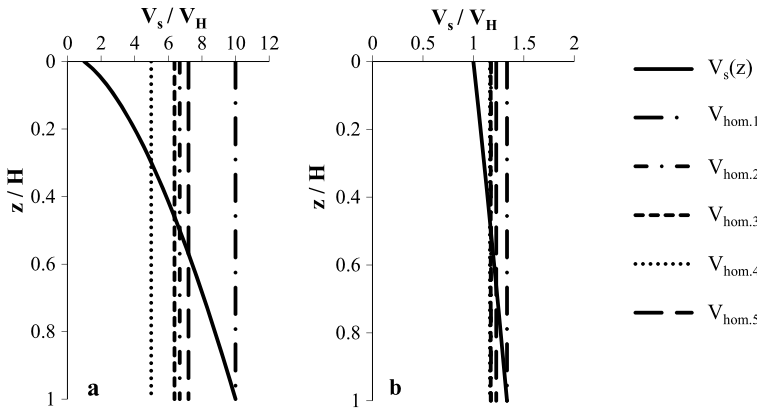


Fig. 8 Comparison of the parabolic function $V_s(z)$ in an inhomogeneous soil to the shear wave velocities of five equivalent homogeneous profiles for (a) $V_o/V_H = 0.1$ and (b) $V_o/V_H = 0.75$ and an inhomogeneity factor $n = 0.6$

results due to the smooth variation of $V_s(z)$ with depth; small V_o/V_H ratios lead to larger deviations among the computed V_{hom} profiles (Fig. 8a).

In Fig. 9, the inhomogeneous system is compared to the above equivalent homogeneous soils in terms of its natural vibrational characteristics. To this end, the ratio of the fundamental frequency of the equivalent homogeneous profile to the first natural frequency of the inhomogeneous soil (f_{1hom}/f_{1Inhom}) is plotted against the inhomogeneity factor n for the examined V_o/V_H ratios. Each plot in Fig. 9 corresponds to a different equivalent homogeneous soil according to Eqs. (29)–(33). The same results are shown in Fig. 10 referring to the second natural frequency of the deposit (i.e. f_{2hom}/f_{2Inhom}). Recall in this regard that for a homogeneous viscoelastic layer of thickness H , resonant frequencies are given by the well-known formula [32]:

$$f_m = \frac{V_s}{4H}(1 + 2m), \quad m = 0, 1, 2, 3, \dots \quad (35)$$

Based on the comparative results of Figs. 9 and 10 several trends are worthy of note. First, insignificant deviations of the analytical solution from the equivalent homogeneous layers are observed for V_o/V_H ratios above 0.75. In these cases, the prescribed frequency ratios are close to unity regardless of the adopted equivalent homogeneous soil scenario. On the contrary, for small V_o/V_H ratios and inhomogeneity factors n close to unity, replacing a continuously inhomogeneous soil with an equivalent homogeneous may lead to substantial over- or under-estimation of the resonant frequencies depending on the value of V_{hom} . Note, for example, that for a strongly inhomogeneous soil (i.e. $V_o/V_H = 0.1$, $n = 0.9$), f_{1hom}/f_{1Inhom} ratio based on Eq. (32) can be about 0.6 (Fig. 9d), which suggests an underestimation of the fundamental frequency of the inhomogeneous deposit, whereas Eq. (29) yields a value of 1.7 (Fig. 9a), which indicates a strong overestimation of the fundamental natural frequency of the system. Naturally the use of V_H as the shear wave propa-

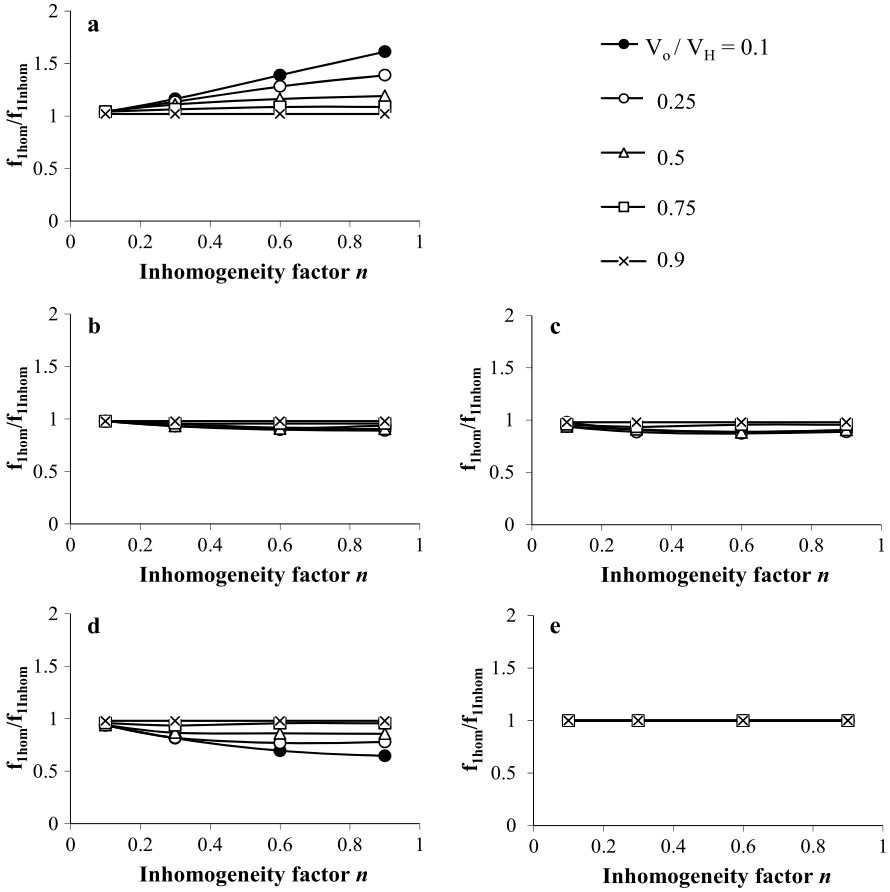


Fig. 9 Ratio of fundamental frequency of the equivalent homogeneous soil (f_{1hom}) to first natural frequency of the inhomogeneous soil (f_{1Inhom}) as function of inhomogeneity factor n : (a) $V_{hom} = V_{hom1}$, (b) $V_{hom} = V_{hom2}$, (c) $V_{hom} = V_{hom3}$, (d) $V_{hom} = V_{hom4}$, (e) $V_{hom} = V_{hom5}$. In all plots, $\xi = 0.05$

gation velocity of an equivalent homogeneous soil through Eq. (29) always results in a stiffer soil, leading to frequency ratios above unity independent of both V_o/V_H and n (Figs. 9a and 10a).

Of particular interest is the case of low V_o/V_H ratios, where the fundamental frequency of the inhomogeneous soil is well predicted by an equivalent homogeneous layer having the same propagation velocity at the mid depth of the deposit (Eq. (30)). In this case the f_{1hom}/f_{1Inhom} ratios are close to unity, exhibiting a slight underestimation of the fundamental frequency with increasing inhomogeneity factor (Fig. 9b). This should be correlated to the continuous nature of the generalized parabola adopted for describing the wave propagation velocity in the inhomogeneous layer. Similar trends can be seen in Fig. 9c, where the equivalent homoge-

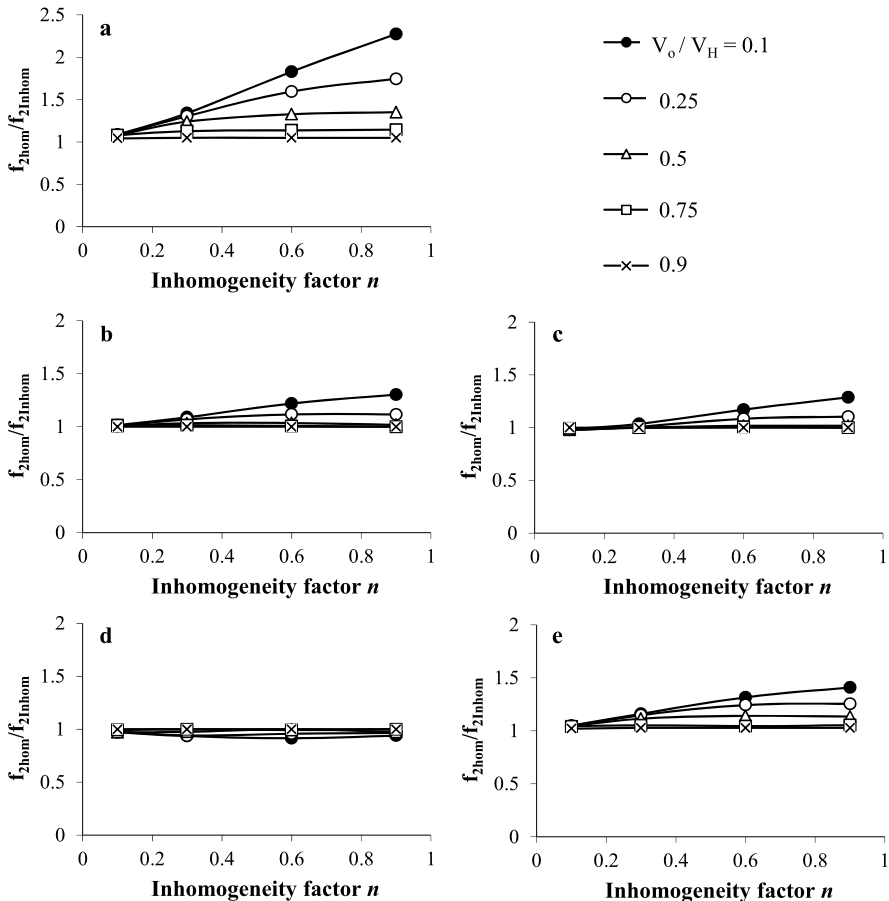


Fig. 10 Ratio of second natural frequency of the equivalent homogeneous soil (f_{2hom}) to second resonance frequency of the inhomogeneous soil (f_{2Inhom}) as function of inhomogeneity factor n : (a) $V_{hom} = V_{hom1}$, (b) $V_{hom} = V_{hom2}$, (c) $V_{hom} = V_{hom3}$, (d) $V_{hom} = V_{hom4}$, (e) $V_{hom} = V_{hom5}$. In all plots, $\xi = 0.05$

neous soil is defined by Eq. (31). At higher resonant frequencies, Eqs. (30) and (31) provide a good approximation when V_o/V_H ratios above 0.25 are considered (Figs. 10b and 10c). However, for low V_o/V_H ratios ($V_o/V_H = 0.1$) high resonant frequencies are not well captured, leading to overestimated values especially for high levels of the inhomogeneity factor n . Considerable deviations from the exact solution are also observed at high resonances (Fig. 10e) when the equivalent homogeneous soil is defined by Eq. (33). Recall that V_{hom5} computed by means of Eq. (33) corresponds to a homogeneous layer having the same fundamental frequency as the inhomogeneous one, leading to a f_{1hom}/f_{1Inhom} ratio of 1 (Fig. 9e).

Further comparisons between continuously inhomogeneous and equivalent homogeneous soils were performed, relating peak resonant amplitudes of base-to-

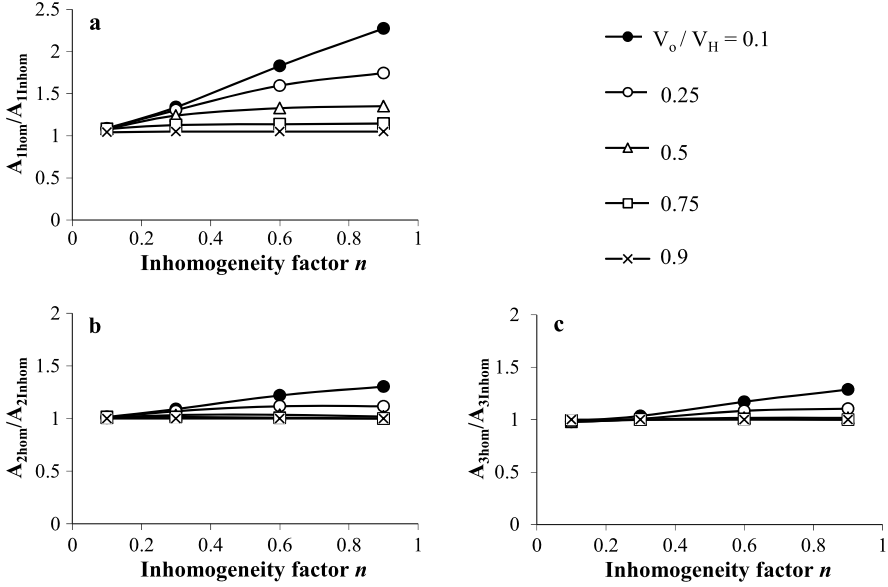


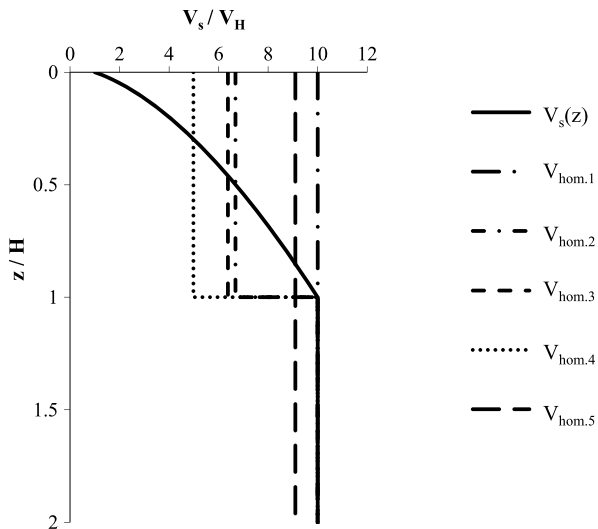
Fig. 11 Ratio of resonance amplitudes of the equivalent homogeneous soil (A_{hom}) to resonance amplitudes of the inhomogeneous soil (A_{Inhom}) against the inhomogeneity factor n for the first (a), second (b) and third (c) natural frequency of the soil deposit. In all plots, $\xi = 0.05$

surface transfer functions. Resonant amplitude ratios A_{hom}/A_{Inhom} defined in the same spirit as the resonant frequency ratios are plotted in Fig. 11 against the inhomogeneity factor n , corresponding to the first (Fig. 11a), second (Fig. 11b) and third (Fig. 11c) natural frequencies of the system. Linear hysteretic damping was taken at 0.05 for both inhomogeneous and equivalent homogeneous cases. The resonant amplitudes of the latter are computed from [32]:

$$A_m \approx \frac{2}{\pi} \frac{1}{\xi(2m-1)}, \quad m = 0, 1, 2, 3, \dots \quad (36)$$

which are independent of V_{hom} and, thereby, of the approach followed to define the equivalent homogeneous soil (Eqs. (29)–(33)). Based on the results of Fig. 11, it is observed that in terms of resonant amplitudes, the replacement of a continuously inhomogeneous soil layer with an equivalent homogeneous one may be valid only for sufficiently smooth variation of shear wave velocity with depth. Indeed, A_{hom}/A_{Inhom} ratios remain close to unity only for large V_o/V_H ratios or small inhomogeneity factors n . On the contrary, when strongly inhomogeneous soils are encountered (i.e. V_o/V_H ratios below 0.5 and inhomogeneity factors n larger than 0.3), use of an equivalent homogeneous soil may substantially underestimate resonant amplitudes with respect to the exact solution, especially at high resonances (Figs. 11b, 11c).

Fig. 12 Comparison of a two-layer inhomogeneous soil to the shear wave velocities of five equivalent homogeneous profiles ($V_o/V_H = 0.1$, $V_b/V_H = 1$, $h_b/H = 1$, $n = 0.6$)



5.2 Two-Layer System

Two-layer equivalent homogeneous systems defined by means of Eqs. (29)–(33) in the same spirit as in the single-layer case were also investigated as simplified approximations of continuously inhomogeneous such as that described in Eq. (2). Representative two-layer homogeneous profiles are presented in Fig. 12 referring to V_o/V_H , V_b/V_H , h_b/H ratios and inhomogeneity factor n at 0.1, 1, 1 and 0.6. For the purpose of this parametric investigation both V_b/V_H and h_b/H ratios were consecutively set at 1, 2 and 3. Recall that for a homogeneous viscoelastic two-layer soil, base-to-surface transfer function is given by the expression [31]:

$$F(\omega) = [\cos(q_{hom}H) \cos(q_b H_b) - I_R \sin(q_{hom}H) \sin(q_b H_b)]^{-1} \quad (37)$$

where $q_{hom} (= \omega/V_{hom})$ and $q_b (= \omega/V_b)$ stand for the wave numbers of the surface and the base layer, respectively, and $I_R (= \rho_b V_b / \rho_H V_{hom})$ is the impedance contrast between the two layers.

Ratio of the fundamental frequency of the equivalent two-layer homogeneous profile to the first natural frequency of the inhomogeneous soil (f_{1hom}/f_{1Inhom}) is plotted in Fig. 13 against the inhomogeneity factor n for the examined V_o/V_H ratios. In all graphs, V_{hom} is defined by Eq. (29) (i.e. $V_{hom} = V_H$) and V_b/V_H ratio was set at 3. Each plot corresponds to a different h_b/H ratio; 1, 2 and 3 respectively. Similar to the single-layer case, definition of the equivalent homogeneous case by means of V_H leads to frequency ratios above unity especially for moderately-to-strongly inhomogeneous soils (small V_o/V_H ratios and large inhomogeneity factors n). Larger h_b/H values corresponding to deeper soil deposits lead to lower f_{1hom}/f_{1Inhom} ratios (Figs. 13b–13c), indicating a prevailing contribution of the underlain inhomogeneous layer to the overall response. Mention has already been made to the good approximation of the resonant frequencies of smoothly-to-moderately

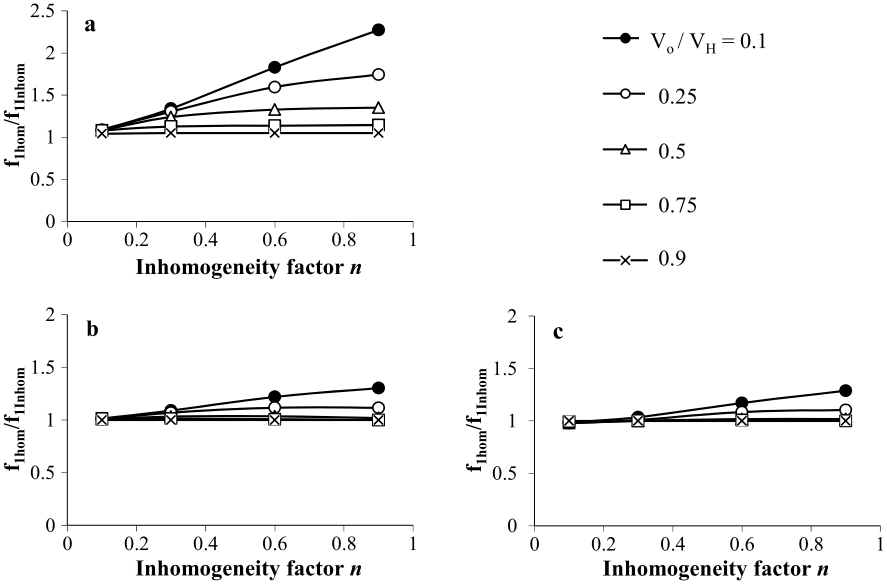


Fig. 13 Ratio of fundamental frequency of the equivalent two-layer homogeneous soil (f_{1hom}) to first natural frequency of the inhomogeneous soil (f_{1Inhom}) as function of inhomogeneity factor n : (a) $h_b/H = 1$, (b) $h_b/H = 2$, (c) $h_b/H = 3$. In all plots, $V_{hom} = V_{hom1}$, $V_b/V_H = 3$, $\rho_b/\rho_H = 1$, $\xi = 0.05$

inhomogeneous soils (i.e. $V_o/V_H > 0.25$) when an equivalent homogeneous soil of either equal shear wave propagation velocity at the mid depth of the inhomogeneous deposit, or of equal mean wave propagation velocity within the whole layer is implemented. Similar trends were observed in the case of the two-layer system leading to resonant frequencies ratios close to unity. This is demonstrated in Figs. 14a and 14b showing f_{1hom}/f_{1Inhom} and f_{2hom}/f_{2Inhom} frequency ratios, respectively, computed by means of Eqs. (30) and (31) referring to the two-layer system for different V_b/V_H and h_b/H ratios. Insignificant deviations from the exact solution are observed for low V_o/V_H ratios ($V_o/V_H = 0.1$) leading to slightly overestimated frequencies with increasing inhomogeneity factor n , especially at high resonances (Fig. 14b). On the contrary, when the equivalent homogeneous soil is defined through Eq. (32) ($V_{hom} = V_{hom4}$) the actual fundamental frequency of the inhomogeneous deposit is underestimated (Fig. 14c). The above trend was also observed when Eq. (33) was implemented within definition of the equivalent homogeneous soil.

In terms of peak resonant amplitudes, the equivalent two-layer homogeneous approximation deviates substantially with respect to the actual response, in agreement with the conclusions derived from the single-layer case. In support of the above, resonant amplitude ratios corresponding to the second natural frequency (i.e. A_{2hom}/A_{2Inhom}) of a two-layer deposit with $V_b/V_H = 3$ and $h_b/H = 2$, are plotted in Fig. 15. Contrary to the single-layer system, resonant amplitudes of a two-layer system depend on the specific value of the equivalent shear wave velocity (V_{hom}).

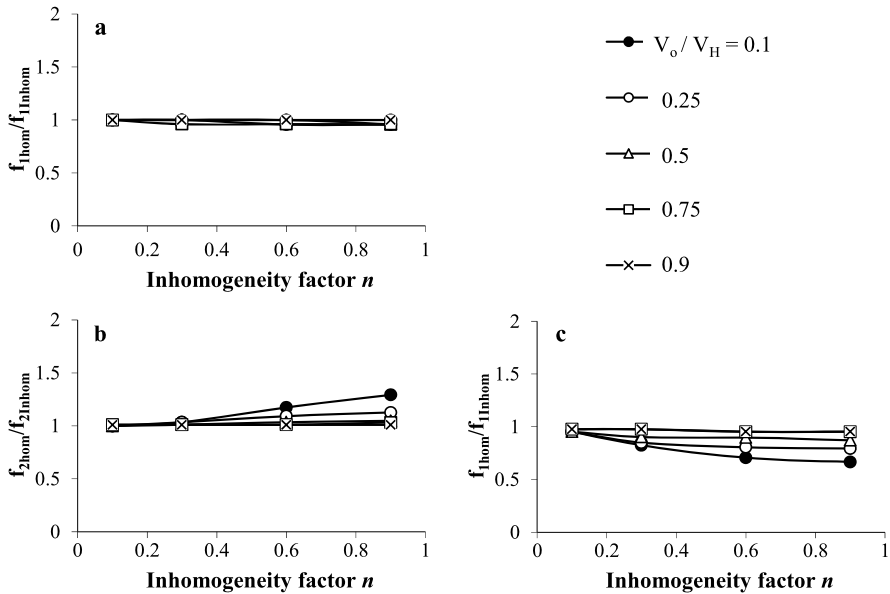


Fig. 14 (a) f_{1hom}/f_{1Inhom} ratios as function of inhomogeneity factor n for $V_b/V_H = 1$ and $V_{hom} = V_{hom2}$. (b) f_{2hom}/f_{2Inhom} ratios as function of inhomogeneity factor n for $V_b/V_H = 2$ and $V_{hom} = V_{hom3}$. (c) f_{1hom}/f_{1Inhom} ratios as function of inhomogeneity factor n for $V_b/V_H = 3$ and $V_{hom} = V_{hom4}$. In all plots $h_b/H = 1$, $\rho_b/\rho_H = 1$, $\xi = 0.05$

Thus, each plot in Fig. 15 refers to a different equivalent homogeneous soil based on Eqs. (29)–(33). The effect of replacing a continuously inhomogeneous soil with an equivalent homogeneous is evident leading to over- or under-estimated resonant amplitudes, especially at higher resonances of moderately-to-strongly inhomogeneous soils. Note, for example, that A_{2hom}/A_{2Inhom} ratios vary in the range 0.4 (Fig. 15a) to 4.5 (Fig. 15e). The above trend was observed independently of the V_b/V_H and h_b/H values.

6 Comparison with Energy-Based Solutions: Rayleigh Method

Within an approximate analysis framework, the Rayleigh procedure is implemented to compute the fundamental natural frequency of inhomogeneous soils based on the principle of virtual work. For this purpose, both left- and right-hand side of Eq. (3) are multiplied by an arbitrary function $u^*(z)$ that satisfies the displacement boundary conditions of the problem in the same manner as $u(z)$:

$$\frac{d}{dz} \left[G(z) \frac{du(z)}{dz} \right] u^*(z) = -\rho(z) \omega^2 u(z) u^*(z) \quad (38)$$

Upon integrating by parts the first term in Eq. (38), yields:

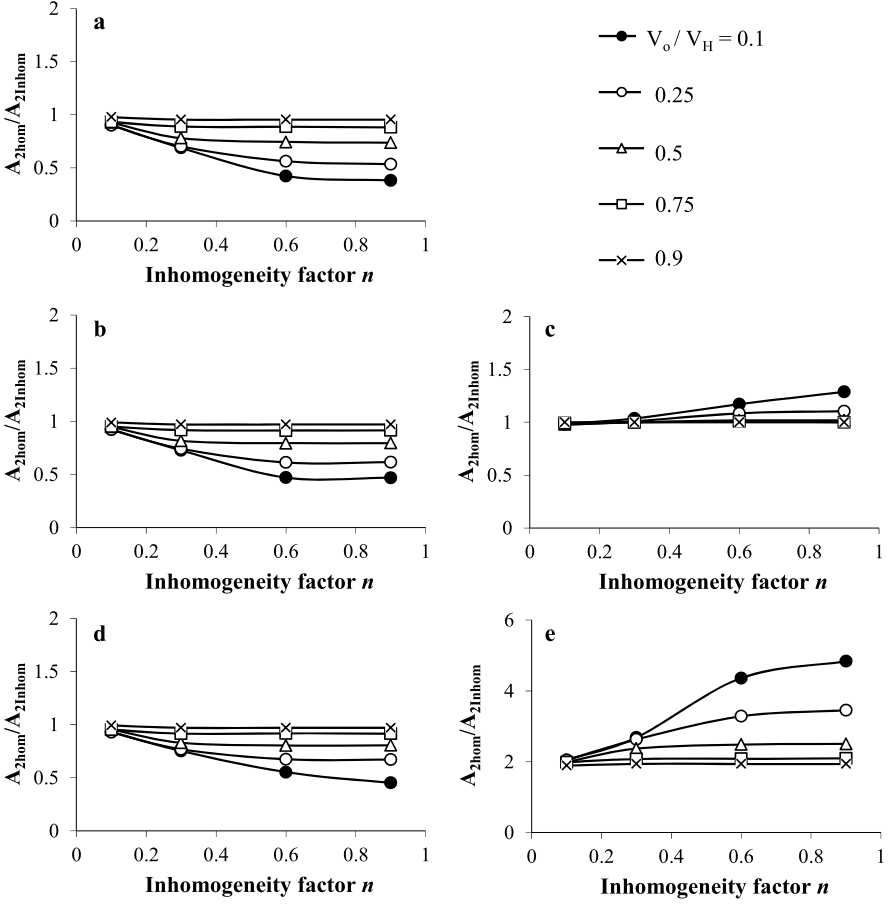


Fig. 15 Resonant amplitude ratios (A_{2hom}/A_{2Inhom}) corresponding to the second natural frequency of the system as function of inhomogeneity factor n : (a) $V_{hom} = V_{hom1}$, (b) $V_{hom} = V_{hom2}$, (c) $V_{hom} = V_{hom3}$, (d) $V_{hom} = V_{hom4}$, (e) $V_{hom} = V_{hom5}$. In all plots, $V_b/V_H = 3$, $h_b/H = 2$, $\rho_b/\rho_H = 1$, $\xi = 0.05$

$$G(z) \frac{du(z)}{dz} u^*(z) \Big|_0^H - \int_0^H G(z) \frac{du(z)}{dz} \frac{du^*(z)}{dz} dz = -\omega^2 \int_0^H \rho(z) u(z) u^*(z) dz \quad (39)$$

The first term in the left-hand side of the above expression is zero due to the stress-free ground surface and the boundary condition at the base of the system (i.e., $u(H) = 0$). Taking into consideration that $u^*(z) = u(z)$, Eq. (39) simplifies to:

$$\int_0^H G(z) \left(\frac{du(z)}{dz} \right)^2 dz = \omega^2 \int_0^H \rho(z) u^2(z) dz \quad (40)$$

from which the natural frequencies of the system may be extracted in the form of the Rayleigh quotient:

$$\omega^2 = \frac{\int_0^H G(z) \left(\frac{du(z)}{dz} \right)^2 dz}{\int_0^H \rho(z) u^2(z) dz} \quad (41)$$

Substituting $u(z) = u_o \psi(z)$, $G(z) = \rho(z) V_s^2(z)$ and $\rho(z) = \rho$, referring to constant soil mass density within the layer, Eq. (41) yields:

$$\omega_1^2 = \frac{\int_0^H V_s^2(z) \left(\frac{d\psi(z)}{dz} \right)^2 dz}{\int_0^H \psi^2(z) dz} \quad (42)$$

where $\psi(z)$ is a unitary dimensionless shape function representing the mode shape corresponding to the fundamental natural frequency ($f_{1,Inhom}$) of the inhomogeneous layer. Introducing depth and shear wave propagation velocity as dimensionless variables by means of the expressions:

$$\bar{z} \equiv z/H \quad (43)$$

and

$$\bar{V}_s(\bar{z}) \equiv V_s(z)/V_H = b + (1-b)\bar{z} \quad (44)$$

respectively, and employing the chain rule of differentiation Eq. (42) may be rewritten as:

$$\omega_1^2 = \frac{V_H}{H} \frac{\int_0^1 \bar{V}_s^2(\bar{z}) \left(\frac{d\psi(\bar{z})}{d\bar{z}} \right)^2 d\bar{z}}{\int_0^1 \psi^2(\bar{z}) d\bar{z}} \quad (45)$$

Recalling that $\omega_{1n} = \pi V_H/2H$, ω_{1n} being the fundamental natural frequency of a homogeneous soil of thickness H and shear wave propagation velocity equal to V_H , the Rayleigh expression for the normalized fundamental frequency (i.e. $\bar{f}_{1,Inhom}$) of the inhomogeneous layer is

$$\bar{f}_{1,Inhom} = \frac{\omega_1}{\omega_{1n}} = \frac{2}{\pi} \left[\frac{\int_0^1 \bar{V}_s^2(\bar{z}) \left(\frac{d\psi(\bar{z})}{d\bar{z}} \right)^2 d\bar{z}}{\int_0^1 \psi^2(\bar{z}) d\bar{z}} \right]^{1/2} \quad (46)$$

6.1 Sensitivity of Rayleigh Predictions on Selection of Shape Function

As evident from the foregoing, the accuracy of the fundamental frequency predicted by means of the Rayleigh method depends entirely on the selected shape function $\psi(\bar{z})$. In order to investigate the effect of $\psi(\bar{z})$ on $\bar{f}_{1,Inhom}$, a linear, a parabolic and a sinusoidal shape function were examined respectively. For a linear shape function described by:

$$\psi(\bar{z}) = 1 - \bar{z} \quad (47)$$

the solution (Eq. (46)) for the normalized fundamental frequency of an inhomogeneous layer with normalized shear wave velocity given by Eq. (44) is [24]

$$\bar{f}_{1,Inhom,lin} = \frac{2\sqrt{3}}{\pi} \left[\frac{b^{1+2n} - 1}{(1+2n)(b-1)} \right]^{1/2} \quad (48)$$

It is reminded here that n stands for the inhomogeneity factor and $b = (V_o/V_H)^{1/n}$. For the parabolic shape function

$$\psi(\bar{z}) = 1 - \bar{z}^2 \quad (49)$$

the corresponding solution yields, after some straightforward algebra [24]:

$$\begin{aligned} \bar{f}_{1,Inhom,par} &= \frac{\sqrt{30}}{\pi} \\ &\times \left[\frac{b^{3+2n} - 1 - 3n - 2n^2 + 3b + 8nb + 4n^2b - 3b^2 - 5nb^2 + 2n^2b^2}{(1+n)(1+2n)(3+2n)(b-1)^3} \right]^{1/2} \end{aligned} \quad (50)$$

Finally, for the sinusoidal shape function

$$\psi(\bar{z}) = \cos\left(\frac{\pi}{2}\bar{z}\right) \quad (51)$$

Equation (46) takes the following form by means of Eqs. (44) and (51) [24]:

$$\bar{f}_{1,Inhom,sin} = \sqrt{2} \left[\int_0^1 [b + (1-b)\bar{z}]^{2n} \sin\left(\frac{\pi\bar{z}}{2}\right)^2 d\bar{z} \right]^{1/2} \quad (52)$$

The above Rayleigh-based equations are compared to the exact solution (Eq. (11)) in Fig. 16 in terms of the normalized fundamental frequency of the system against the inhomogeneity factor n . Each plot corresponds to a different V_o/V_H ratio set at 0.1, 0.5 and 0.9 in Figs. 16a, 16b and 16c, respectively. It is observed that for smoothly-to-moderately inhomogeneous soils, the Rayleigh method provides reliable predictions of the fundamental frequency showing a slight sensitivity on the selected shape function (Figs. 16b and 16c). However, for low V_o/V_H ratios and large inhomogeneity factors referring to strongly inhomogeneous soils (Fig. 16a), the above method deviates from the exact solution leading to a stiffer response.

7 Special Case: Vanishing Stiffness at Soil Surface

For an inhomogeneous soil layer having zero stiffness at the surface ($b = 0$), it can be shown [24, 35] that the displacement and stress fields are given by the expressions:

$$\begin{aligned} u(z) &= C_1 z^{-\mu} \left[J_\nu(\lambda z^{\ell/2}) - \frac{\omega H}{V_H} \left(\frac{z}{H}\right)^{1-n} J_{\nu+1}(\lambda z^{\ell/2}) \right] \\ &+ C_2 z^{-\mu} \left[N_\nu(\lambda z^{\ell/2}) - \frac{\omega H}{V_H} \left(\frac{z}{H}\right)^{1-n} N_{\nu+1}(\lambda z^{\ell/2}) \right] \end{aligned} \quad (53)$$

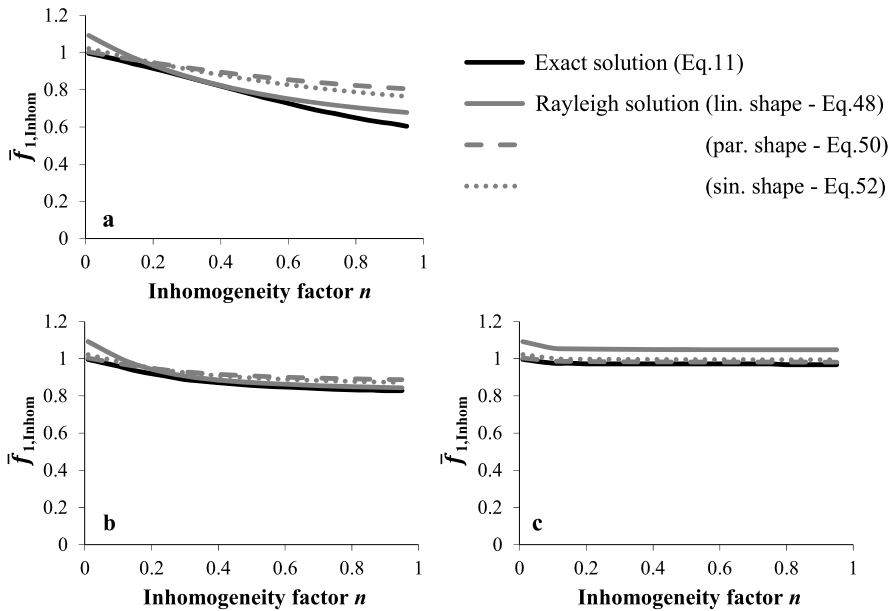


Fig. 16 Normalized fundamental frequency of the inhomogeneous layer as function of inhomogeneity factor n . Comparison of the exact solution with approximate Rayleigh solutions for (a) $V_o/V_H = 0.1$, (b) $V_o/V_H = 0.5$, and (c) $V_o/V_H = 0.9$. In all plots $\xi = 0.05$

and

$$\tau(z) = -\rho\omega^2 z^\mu [C_1 J_\nu(\lambda z^{\ell/2}) + C_2 N_\nu(\lambda z^{\ell/2})] \quad (54)$$

where $\nu = 1/2(1 - n)$, $\ell = 2(1 - n)$ and $\mu = 1/2$. Enforcing the boundary condition of zero shear tractions at the surface yields the equation:

$$\lim_{z \rightarrow 0} [-C_1 \rho\omega^2 z^{1/2} J_\nu(\lambda z^{\ell/2}) - C_2 \rho\omega^2 z^{1/2} N_\nu(\lambda z^{\ell/2})] = 0 \quad (55)$$

For values of z close to zero, the first term inside the brackets becomes asymptotically equal to [37]:

$$z^{1/2} J_\nu(\lambda z^{\ell/2}) \sim z^{1/2} \frac{1}{\Gamma(1 + \nu)} \left(\frac{\lambda z^{\ell/2}}{2} \right)^\nu \quad (56)$$

Since $z^{1/2} z^{\nu\ell/2} = z^{1/2} z^{1/2} = z$ [recall that $\nu\ell = 2(1 - n)/2(1 - n) = 1$ in this solution], the expression in Eq. (56) vanishes at the surface, thereby satisfying the stress boundary condition.

For the second term the corresponding asymptotic expression near the origin is [37]:

$$z^{1/2} N_\nu(\lambda z^{\ell/2}) \sim z^{1/2} \frac{-1}{\sin(\nu\pi)\Gamma(1 - \nu)} \left(\frac{2}{\lambda z^{\ell/2}} \right)^\nu \quad (57)$$

As $z^{1/2}z^{-\nu\ell/2} = z^{1/2}z^{-1/2} = z^0 = 1$ the second term in Eq. (55) is finite at the surface unless integration constant C_2 is zero. Accordingly, setting $C_2 = 0$, the solution compatible with the stress-free boundary condition at the surface is:

$$u(z) = C_1 z^{-1/2} \left[J_\nu(\lambda z^{\ell/2}) - \frac{\omega H}{V_H} \left(\frac{z}{H} \right)^{1-n} J_{\nu+1}(\lambda z^{\ell/2}) \right] \quad (58)$$

From Eqs. (56) and (58) the displacement at ground surface is [24, 35]:

$$u(0) = \lim_{z \rightarrow 0} C_1 \left[\frac{(\lambda/2)^\nu}{\Gamma(1+\nu)} - \frac{\omega}{V_H H^{-n}} \frac{(\lambda/2)^{\nu+1}}{\Gamma(2+\nu)} z^{2(1-n)} \right] \quad (59)$$

The above result suggests that as long as n is smaller than 1 (as assumed in this study), surface displacement would be finite. This finding contradicts the assertion in Ref. [1] that displacement at ground surface is infinite when $V_o/V_H = 0$.

Shear strain $\gamma(z)$ in the soil is obtained by differentiating Eq. (58)

$$\gamma(z) = -\frac{\omega^2 H}{V_H^2} \left(\frac{z}{H} \right)^{-2n} C_1 z^{1/2} J_\nu(\lambda z^{\ell/2}) \quad (60)$$

Repeating the asymptotic analysis for small z 's yields the expression:

$$z^{-2n+1/2+\nu\ell/2} = z^{-2n+1/2+1/2} = z^{1-2n} \quad (61)$$

which indicates that for $n > 1/2$ the exponent $(1 - 2n)$ becomes negative and, thereby, the magnitude of shear strain at the surface is infinite. This holds regardless of frequency and excitation amplitude, and despite the fact that the corresponding shear stress is zero and the displacement is finite. On the contrary, for $n < 1/2$ the exponent is positive and shear strain is zero at the surface. In other words, strain amplitude at the surface can be either zero or infinite, but never finite. These findings are in agreement with those obtained in Ref. [5] for the special case where $n = 2/3$.

The effect of vanishing shear wave propagation velocity near the soil surface is further investigated in terms of base-to-surface transfer function in Fig. 17, for a single layer described by four different inhomogeneity factors and three different damping ratios. For values of the inhomogeneity factor less than 0.5, the response strongly resembles that of a homogeneous layer. On the other hand, a remarkably amplified response is evident when the inhomogeneity factor is higher than 0.5. This behavior becomes more pronounced as the inhomogeneity factor approaches 1, leading to considerably stronger amplification at higher resonances with respect to the fundamental one.

As real soils almost invariably possess a finite amount of stiffness at the surface, the behavior of the solution at very small V_o/V_H 's is further investigated in Fig. 18. Significant amplification patterns are evident at higher mode resonances, as V_o/V_H and n tend to 0 and 1, respectively. This suggests that strong amplification will develop even for finite surface stiffness (under zero shear strain), which will merely get maximized at the theoretical limit $V_o/V_H = 0$. From a practical viewpoint, a V_o/V_H ratio of less than 0.1 and an inhomogeneity coefficient n of over 0.5 suffice to trigger this effect. An explanation is that the strong amplification is

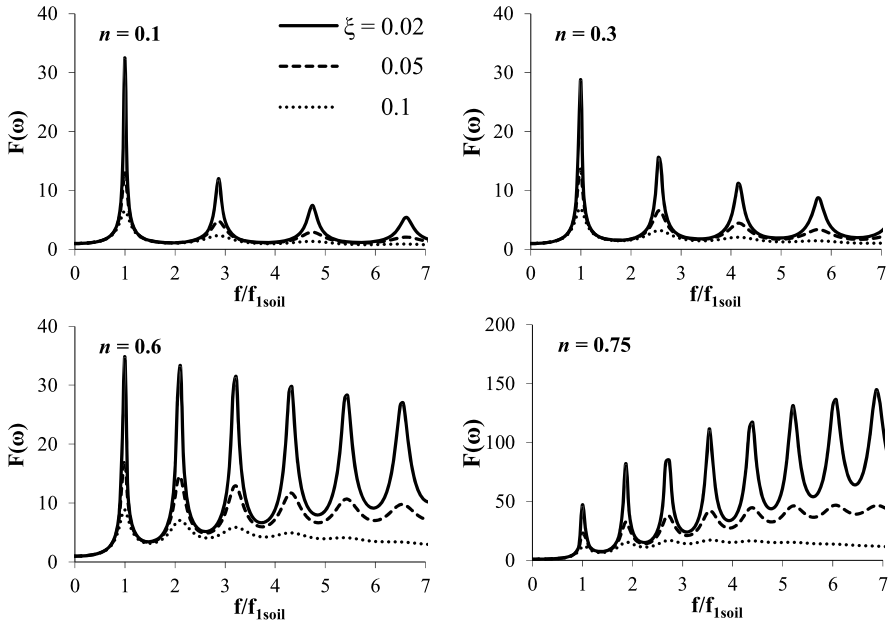


Fig. 17 Effect of inhomogeneity factor n on base-to-surface transfer functions for a single inhomogeneous layer having zero stiffness at the surface and damping ratio ξ of 0.02, 0.05 and 0.10

associated with *transition* phenomena (i.e., accumulation of wave energy in areas of progressively smaller elastic modulus near the surface leading to an increase in wave amplitude) as opposed to *reflection* phenomena associated with development of resonance in the layer.

As a final remark, it is worth mentioning that for values of ν of the semi-integer type (i.e., $\nu = p + 1/2$, $p = 0, 1, 2, \dots$), the Bessel functions simplify to expressions involving trigonometric functions. For the single layer system, this condition requires $n = 2(p + 1)/(2p + 3)$ that is $n = 2/3, 4/5, 8/9, 10/11$, etc. For the first two cases (i.e., $n = 2/3, 4/5$), the amplification function in Eq. (17) can be shown to reduce to:

$$F(\omega) = \lambda [\lambda b^{1/3} \cos(\lambda b^{1/3} - \lambda) - \sin(\lambda b^{1/3} - \lambda)]^{-1} \quad (62)$$

and

$$F(\omega) = \lambda^3 [(3\lambda b^{1/5} - 3\lambda + \lambda^3 b^{2/5}) \cos(\lambda b^{1/5} - \lambda) - (3 - \lambda^2 b^{2/5} + 3\lambda^2 b^{1/5}) \sin(\lambda b^{1/5} - \lambda)]^{-1} \quad (63)$$

respectively, which can be evaluated by elementary means.

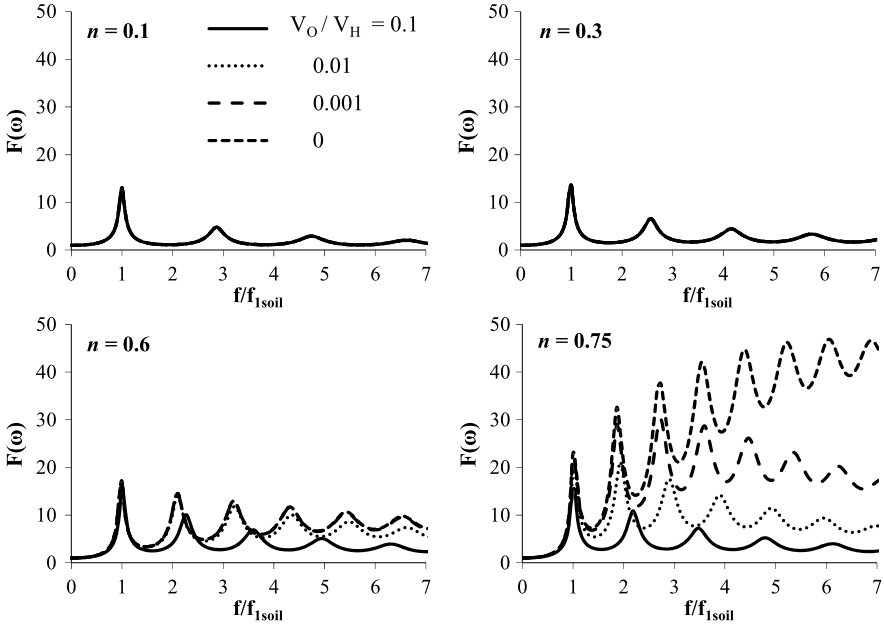


Fig. 18 Effect of inhomogeneity factor n on base-to-surface transfer functions for a single inhomogeneous layer having V_o/V_H ratio of 0.1, 0.01, 0.001 and 0. In all plots, $\xi = 0.05$

8 Conclusions

An analytical closed-form solution was derived for one-dimensional viscoelastic harmonic wave propagation in layered inhomogeneous soil over a rigid base, when the propagation velocity is described by means of a generalized parabolic function of depth. The vibrational characteristics and base-to-surface transfer functions of the system were examined, as affected by salient model parameters. Equivalent homogeneous soil approaches and approximate Rayleigh solutions were investigated in terms of both resonant frequencies and response amplitudes. The special case of an inhomogeneous soil having zero stiffness at the surface was explored as to the variation of shear strain with depth.

The main conclusions of the study are:

- Modal amplitudes in soft inhomogeneous soils exhibit strong gradients near the ground surface, which correspond to large shear strains. This is important for inhomogeneity factors n larger than 0.5.
- For soils with low shear modulus at ground surface, an increase in inhomogeneity factor n will tend to shift higher mode resonances to lower frequencies resulting in amplified seismic response. This may have significant practical implications for input motions of low frequency content.

- Two-layer inhomogeneous soils demonstrate significant resonant amplitudes, even at higher modes, regardless of thickness of the underlying homogeneous layer.
- Resonant frequencies of moderately inhomogeneous soil ($V_o/V_H > 0.25$) may be adequately captured by an equivalent homogeneous layer of either equal shear wave propagation velocity at the mid depth of the inhomogeneous deposit, or of equal mean wave propagation velocity within the whole layer. On the contrary, resonant amplitudes of a moderately-to-strongly inhomogeneous soil ($V_o/V_H < 0.5$ and inhomogeneity factor above 0.3) may be significantly underestimated when an equivalent homogeneous soil is adopted, especially at higher resonances.
- Approximate energy-based solutions derived by means of the Rayleigh procedure may lead to reliable estimates of the fundamental natural frequency of smoothly-to-moderately inhomogeneous soils. For strongly inhomogeneous soils the Rayleigh method results in stiffer soil response yielding larger values of the fundamental natural frequency with respect to the exact solution.
- For the special case of vanishing shear wave velocity at the free surface ($V_o/V_H = 0$), near surface shear strain may be either zero (for $n < 0.5$) or infinite (for $n > 0.5$) but never finite. This holds regardless of excitation frequency and amplitude. On the other hand, surface displacements are always finite.
- Following up on the above conclusion, strong amplification will develop even for finite surface stiffness (under zero shear strain), which will merely get maximized at the theoretical limit $V_o/V_H = 0$. From a practical viewpoint, a V_o/V_H ratio of less than 0.1 combined with an inhomogeneity coefficient n of over 0.5 will suffice to trigger this effect. An explanation is that the strong amplification is associated with *transition* phenomena (i.e., accumulation of wave energy in areas of progressively smaller elastic modulus near the surface leading to an increase in wave amplitude) as opposed to *reflection* phenomena associated with development of resonance in the layer.

Acknowledgements The corresponding author would like to acknowledge the contributions of Ms Vasiliki Miha and Ms Kathleen Schulze, former students at University of Patras and the City University of New York, respectively, for numerically evaluating the single-layer solution presented in this paper as part of their Diploma and Master's theses conducted under his supervision (Refs. [24] and [35]).

References

1. Towhata I (1996) Seismic wave propagation in elastic soil with continuous variation of shear modulus in the vertical direction. *Soils Found* 36(1):61–72
2. Ambraseys NN (1959) A note on the response of an elastic overburden of varying rigidity to an arbitrary ground motion. *Bull Seismol Soc Am* 49(3):211–220
3. Seed HB, Idriss IM (1969) The influence of ground conditions on ground motions during earthquakes. *J Soil Mech Found Div* 94:93–137
4. Dobry R, Whitman R, Roesset JM (1971) Soil properties and the one-dimensional theory of earthquake amplification. Research report R71-18, MIT

5. Travararou T, Gazetas G (2004) On the linear response of soils with modulus varying as a power of depth—the Maliakos marine clay. *Soils Found* 44(5):85–93
6. Toki K, Cherry S (1972) Inference of subsurface accelerations and strain from accelerograms recorded at ground surface. In: *Proceedings of the 4th European symposium on earthquake engineering*, London
7. Schreyer H (1977) One-dimensional elastic waves in inhomogeneous media. *J Eng Mech Div* 103(5):979–990
8. Gazetas G (1982) Vibrational characteristics of soil deposits with variable wave velocity. *Int J Numer Anal Methods Geomech* 6:1–20
9. Parashakis H (2009) 1D seismic wave propagation in a class of inhomogeneous soil deposits. Master thesis, Hellenic Open University (in Greek)
10. Semblat JF, Pecker A (2009) *Waves and vibrations in soils: earthquakes, traffic, shocks, construction works*. IUSS Press, Pavia
11. Vardoulakis I (1984) Torsional surface waves in inhomogeneous elastic media. *Int J Numer Anal Methods Geomech* 8:287–296
12. Vrettos C (1990) Dispersive SH-surface waves in soil deposits of variable shear modulus. *Soil Dyn Earthq Eng* 9(5):255–264
13. Vrettos C (2012) Dynamic response of soil deposits to vertical SH waves for different rigidity depth-gradients. *Soil Dyn Earthq Eng*. doi:[10.1016/j.soildyn.2012.04.003](https://doi.org/10.1016/j.soildyn.2012.04.003)
14. Manolis GD, Shaw RP (1997) Harmonic elastic waves in continuously heterogeneous random layers. *Eng Anal Bound Elem* 19(3):181–198
15. Manolis GD, Shaw RP (1999) Numerical simulation of transient waves in a heterogeneous soil layer. *Comput Mech* 23:75–86
16. Manolis GD, Shaw RP (2000) Fundamental solutions for variable density two-dimensional elastodynamic problems. *Eng Anal Bound Elem* 24(10):739–750
17. Brekhovskikh LM, Bayer R (1976) *Waves in layered media*. Academic Press, New York
18. Building Seismic Safety Council (1997) NEHRP recommended provisions for seismic regulations for new buildings, part 1—Provisions (FEMA 302)
19. National Research Council Canada (2005) *National building code of Canada (NBCC)*
20. CEN, European Committee for Standardization (2004) EN 1998-1:2004 Eurocode 8: design of structures for earthquake resistance, part 1: General rules, seismic actions and rules for buildings. Brussels
21. Dobry R, Oweis I, Urzua A (1976) Simplified procedures for estimating the fundamental period of a soil profile. *Bull Seismol Soc Am* 66(4):1293–1321
22. Madera GA (1971) *Fundamental period and amplification of peak acceleration in layered systems*. Research report R70-37, MIT
23. Biggs JM (1964) *Introduction to structural dynamics*. McGraw-Hill, New York
24. Miha V (2007) Seismic response of inhomogeneous soil deposits. Master thesis, University of Patras (in Greek)
25. Rovithis E, Parashakis Ch, Mylonakis G (2011) 1D harmonic response of layered inhomogeneous soil: analytical investigation. *Soil Dyn Earthq Eng* 31(7):879–890
26. Afra H, Pecker A (2002) Calculation of free field response spectrum of a non-homogeneous soil deposit from bed response spectrum. *Soil Dyn Earthq Eng* 22:157–165
27. Muir Wood D (2004) *Geotechnical modelling*. E & FN Spon, London
28. Dakoulas P, Gazetas G (1985) A class of inhomogeneous shear models for seismic response of dams and embankments. *Soil Dyn Earthq Eng* 4(4):166–182
29. Abramowitz M, Stegun I (1970) *Handbook of mathematical functions*. Dover, New York
30. Wylie CR, Barrett LC (1995) *Advanced engineering mathematics*. McGraw-Hill, New York
31. Roesset JM (1976) Soil amplification of earthquakes. In: *Numerical methods in geotechnical engineering*. McGraw-Hill, New York
32. Kramer LS (1996) *Geotechnical earthquake engineering*. Prentice Hall international series
33. ANSYS Inc. ANSYS user's manual, version 11. SAS IP, Houston

34. Lu L, Katayama T, Yamazaki F (1991) Soil amplification based on array observation in Chiba, Japan. In: Proceedings of the 2nd international conference on recent advances in geotechnical earthquake engineering and soil dynamics, Missouri
35. Schulze K (2005) Vibrational characteristics and seismic response of inhomogeneous soils. Master thesis, City University of New York
36. Zhao JX (1997) Modal analysis of soft-soil sites including radiation damping. *Earthq Eng Struct Dyn* 26(1):93–113
37. Hildebrand FB (1962) *Advanced calculus for applications*. Prentice Hall, Englewood Cliffs

Monitored Incoherency Patterns of Seismic Ground Motion and Dynamic Response of a Long Cable-Stayed Bridge

Vassilios Lekidis, Savvas Papadopoulos, Christos Karakostas,
and Anastasios Sextos

Abstract The Evripos bridge in central Greece, connects the island of Evia to the mainland. The cable-stayed section of the bridge is 395 m in length, with a central span of 215 m and side-spans of 90 m each. The deck, 13.5 m in width, is at 40 m above sea-level, suspended by cables from two, 90 m high pylons. A permanent accelerometer special array of 43 sensors was installed on the bridge in 1994 by the Institute of Engineering Seismology and Earthquake Engineering. Two triaxial sensors have been monitoring the free-field (near pier M4) and pier M5 base response on the mainland (Boeotian) coast and two others the respective locations (pier base M6 and free-field near pier M7) on the Euboean coast. Since then the bridge's behavior to seismic excitations has been continuously monitored and investigated. From various earthquake events recorded at the site, it became obvious that the excitation at each of the aforementioned locations differs, with the lowest peak acceleration values observed at site M7 for all three components, independently of magnitude, azimuth and epicentral distance of the earthquake, a fact that can be attributed to local site conditions. In the present research effort, an investigation of the dynamic response of the Evripos bridge due to the asynchronous base excitations along its supports is carried out. Comparisons are made with the conventional design procedure of assuming a common (synchronous) base excitation at all supports and interesting conclusions are drawn regarding the impact of spatially variable ground motion on the seismic response of the particular bridge.

V. Lekidis · C. Karakostas
Earthquake Planning and Protection Organization (EPPO-ITSAK), 5 Agiou Georgiou Str.,
Patriarchika Pylaias, GR55535 Thessaloniki, Greece

V. Lekidis
e-mail: lekidis@itsak.gr

C. Karakostas
e-mail: christos@itsak.gr

S. Papadopoulos · A. Sextos (✉)
Department of Civil Engineering, Aristotle University of Thessaloniki, Thessaloniki, Greece
e-mail: asextos@civil.auth.gr

S. Papadopoulos
e-mail: savvaspp@civil.auth.gr

Keywords Asynchronous base excitation (of bridges) · Bridge instrumentation · Bridge dynamic response · Evripos cable-stayed bridge

1 Introduction

During the last decade, time history analyses have become increasingly popular both for design and research purposes, especially for the case of complex and/or important bridges. This trend has significantly improved the analysis rigor and facilitated the consideration of various physical phenomena that were too complicated to be taken into account in the past. One of those issues, is the identification of a realistic, spatially variable earthquake ground motion (SVEGM) which can be used for the excitation of the bridge for design or assessment purposes. As it is well known, this phenomenon may affect the seismic response of long bridges, or of bridges crossing abruptly changing soil profiles; however, its potentially beneficial or detrimental impact on the final bridge performance cannot be easily assessed in advance [1–5].

One major difficulty in assessing the spatially variable patterns of earthquake ground motion is the complex wave reflections, refractions and superpositions that take place as seismic waves travel through inhomogeneous soil media. Different analytical formulations have been proposed in the past, but the inherent multi-parametric nature of wave propagation and soil-structure interaction makes it practically impossible to predict the spatially varying earthquake input along the bridge length in a deterministic manner. Dense seismograph arrays, primarily in Taiwan, Japan and the U.S., have contributed in shedding some light into this problem which can be primarily attributed to four major factors that take place simultaneously, i.e., wave passage effect, the extended source effect, wave scattering and attenuation effect [6]. The operation of these arrays, also led to the development of numerous empirical, semi-empirical and analytical coherency models, fit to represent the decaying signal correlation with distance and frequency.

Despite the significant impact of the aforementioned analytical approaches and experimental evidence, a reliable and simple methodology for the prediction of the effects of asynchronous motion on bridges is still lacking. Even modern seismic codes like Eurocode 8 deal with the problem through either simplified code-based calculations or indirect preventive measures involving larger seating deck lengths [7].

An interesting case for the study of this phenomenon using recorded data is the Evripos cable-stayed bridge, which has been permanently monitored by an accelerometer network since 1994 [8, 9]. A series of minor to moderate intensity seismic events have been recorded by this network, providing a useful set of motions recorded both in the vicinity of the structure and on specific locations on the structure and its foundation. The scope of this study therefore, is to:

- Investigate the impact of spatial variable ground motion by processing specific input motions recorded on site as the bridge, due to its overall length, is sensitive to asynchronous motion.



Fig. 1 The central section of the Evripos cable-stayed bridge

- Make use of the recorded data in order to investigate the nature of earthquake ground motion and the effects of its spatial variation on the dynamic response (in terms of forces and displacements) of the particular cable-stayed bridge.

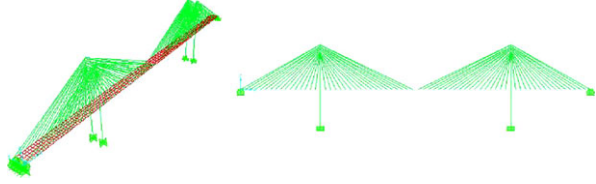
The description of the bridge, its monitoring system as well as its response under various asynchronous ground motion records, is presented in the following.

2 Description of the Evripos Cable-Stayed Bridge

The Evripos bridge, a 694.5 m long R/C structure, connects the Euboean coast in the island of Evia to the Boeotian coast in continental central Greece (Fig. 1). It comprises three parts, i.e. the central cable stayed section and two side (approaching) parts made of pre-stressed R/C beams that rest on elastomeric bearings. The central section of the bridge (Fig. 1) is divided into three spans of length 90 m, 215 m and 90 m respectively, while the deck (of 13.50 m width) is suspended by the 90 m height pylons M5 and M6 with cables. The displacements of the deck along the longitudinal direction are permitted in piers M4 and M7 while those in the transverse direction are blocked [8, 9]. In the present study, it is only the central cable-stayed section that is examined.

As already mentioned, the Evripos cable-stayed bridge behavior is constantly monitored through a special accelerometer array installed by the Institute of Engineering Seismology and Earthquake Engineering (now EPPO-ITSAK). The network is composed by four triaxial accelerometers installed at the base of the bridge, in particular, on the pile caps of piers M5 and M6 and on soil surface in areas adjacent to piers M4 and M7. There are also 31 additional uniaxial accelerometers installed on the superstructure, for system identification purposes. It is noted that all sensors have common time and common trigger settings [8, 9] thus permitting signal processing and correlation. The Finite Element model of the bridge is illustrated in Fig. 2.

Fig. 2 Finite element model of the Evripos cable-stayed bridge



3 Earthquake Strong Motion Data Available on Site

The expectation that the central cable stayed section of the bridge is asynchronously excited during an earthquake due to its significant overall length (395 m) aroused the interest in processing specific sets of records available on-site so that spatial variation of earthquake ground motion could be confirmed or not. Among the available data of seismic events that have been recorded since the installation of the accelerometers array, the recorded at the base of the piers accelerograms of the Athens earthquake (7/9/1999, M_s) which took place at a source-to-site distance of 43 km were selected and are illustrated in Fig. 3.

Firstly, the time histories were filtered, using a band-pass filter in the frequency range 0.65–25 Hz in order to remove the effects of the inertial soil bridge interaction. In order to measure the similarity of the seismic motions between all pairs of records, it is necessary to compute the lagged coherency, which indicates the degree to which two different accelerograms are related [10], according to the following expression:

$$|\bar{Y}_{jk}^M(\omega)| = \frac{|\bar{S}_{jk}^M(\omega)|}{\sqrt{\bar{S}_{jj}^M(\omega)\bar{S}_{kk}^M(\omega)}} \quad (1)$$

where \bar{S}_{jj} and \bar{S}_{kk} are the smoothed power spectral densities at the stations j and k and are given by:

$$\bar{S}_{jj}(\omega_n) = \sum_{m=-M}^{+M} W(m\Delta\omega) S_{jj}(\omega_n + m\Delta\omega) \quad (2)$$

where ω_n is the discrete frequency, $W(m\Delta\omega)$ the (Hamming) spectral window and S_{jj} the unsmoothed power spectra. \bar{S}_{jk} is the smoothed cross spectral densities between the stations j and k expressed as:

$$\begin{aligned} \bar{S}_{jk}(\omega_n) = & \frac{2\pi}{T} \sum_{m=-M}^{+M} W(m\Delta\omega) \Lambda_j(\omega_n + m\Delta\omega) \Lambda_k(\omega_n + m\Delta\omega) \\ & \times \exp\{i[\Phi_k(\omega_n + m\Delta\omega) - \Phi_j(\omega_n + m\Delta\omega)]\} \end{aligned} \quad (3)$$

where Λ_j and Λ_k are the Fourier amplitudes in stations j and k respectively and Φ_j and Φ_k are the corresponding phases. An 11-point Hamming window was used for smoothing as proposed by Abrahamson for 5 % structural damping [10, 11]. The described process was written as a GUI-based, Matlab script.

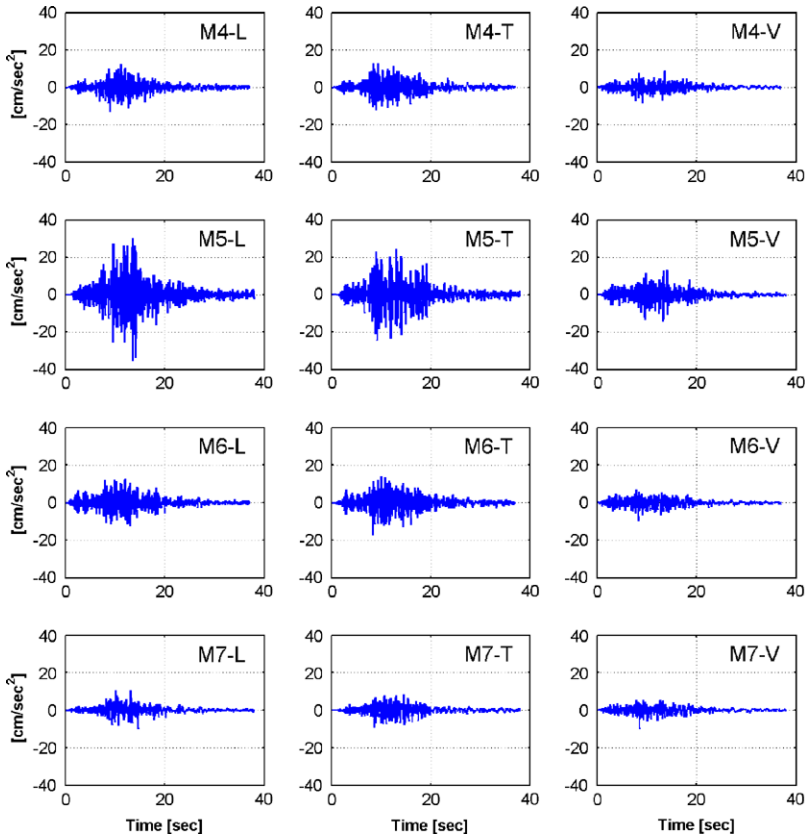


Fig. 3 Horizontal and vertical components of the strong ground motions recorded at the base of piers M4, M5, M6 and M7 due to the 1999 $M_s = 5.9$ Athens earthquake

The diagrams of lagged coherency, computed individually for all components of the records and for all pairs, are illustrated in Fig. 4 and confirm the spatially variable nature of the ground motion. As anticipated, at low frequencies and short separation distances the lagged coherency tends to unity while it decreases with increasing separation distance and frequency.

In order for the seismic motion to be able to be predicted at different stations over an extended area, several parametric coherency models have been proposed in the literature. Many of them are empirical models developed with regression fitting of different functional forms on specific data; some others are semi-empirical models the functional form of which developed with analytical procedures but their parameters were evaluated by recorded data; lastly there are also some analytical models [10].

The comparison of the computed incoherences with one of the empirical and a semi-empirical coherency model for the pairs M4-M5, M4-M6 and M4-M7 in horizontal directions is made in Fig. 5. The models used for this comparison are: the single functional form for the horizontal coherency of Abrahamson [6]:

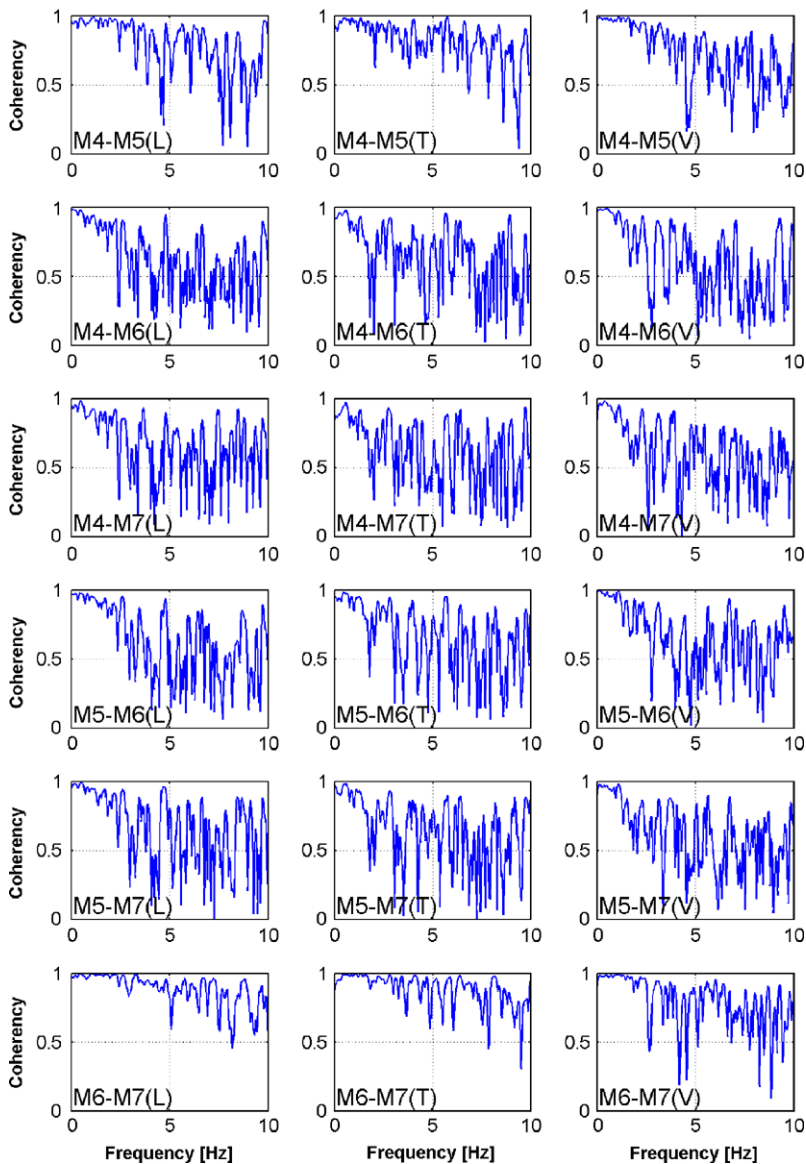


Fig. 4 Lagged coherency of motions between piers M4-M5 (90 m), M4-M6 (305 m), M4-M7 (395 m), M5-M6 (215 m), M5-M7 (90 m) and M6-M7 (90 m)

$$\begin{aligned}
 |\gamma^H(\xi, f)| = \tanh \left\{ \frac{c_1^H(\xi)}{1 + c_2^H(\xi)f + c_4^H(\xi)f^2} \right. \\
 \left. + (4.80 - c_1^H(\xi)) \exp[c_2^H(\xi)f] + 0.35 \right\} \quad (4)
 \end{aligned}$$

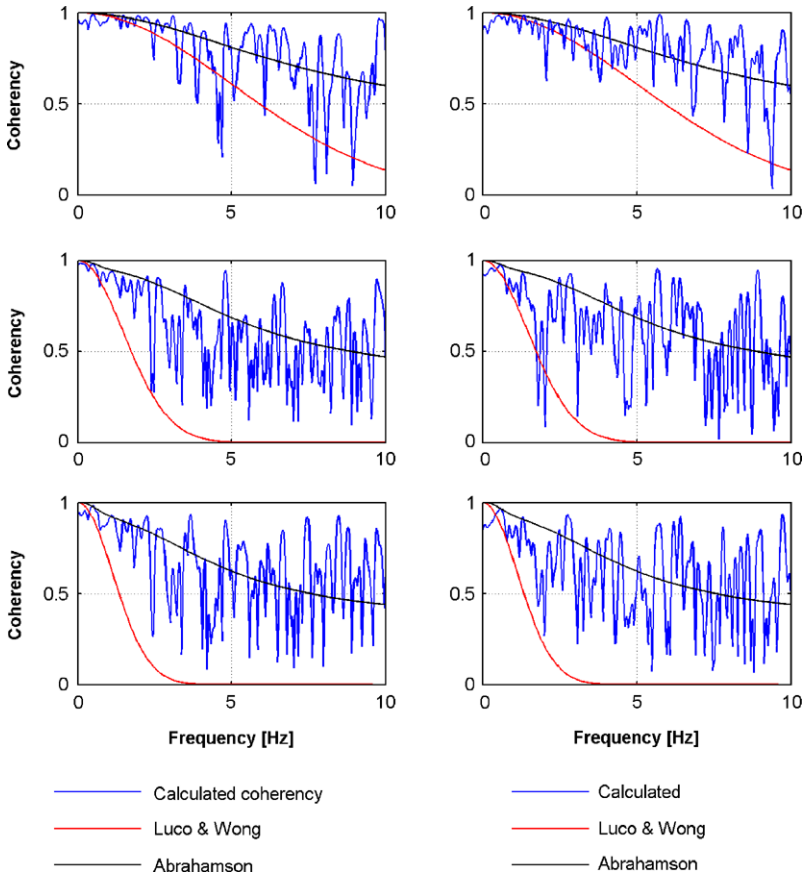


Fig. 5 Comparison between observed and predicted coherency loss for different empirical and semi-empirical models

where:

$$\begin{aligned}
 c_1^H(\xi) &= \frac{3.95}{1 + 0.0077\xi + 0.000023\xi^2} + 0.85 \exp[-0.00013\xi] \\
 c_2^H(\xi) &= \frac{0.4[1 - (1 + (\xi/5)^3)^{-1}]}{[1 + (\xi/190)^8][1 + (\xi/180)^3]} \\
 c_3^H(\xi) &= 3 \exp([-0.05\xi] - 1) - 0.0018\xi \\
 c_4^H(\xi) &= -0.598 + 0.106 \ln(\xi + 325) - 0.0151 \exp[-0.6\xi]
 \end{aligned} \tag{5}$$

and the most commonly used pattern proposed by Luco and Wong which has the form [12]:

$$|\gamma(\xi, \omega)| = e^{-\left(\frac{\nu\omega\xi}{V_s}\right)} = e^{-a^2\omega^2\xi^2} \tag{6}$$

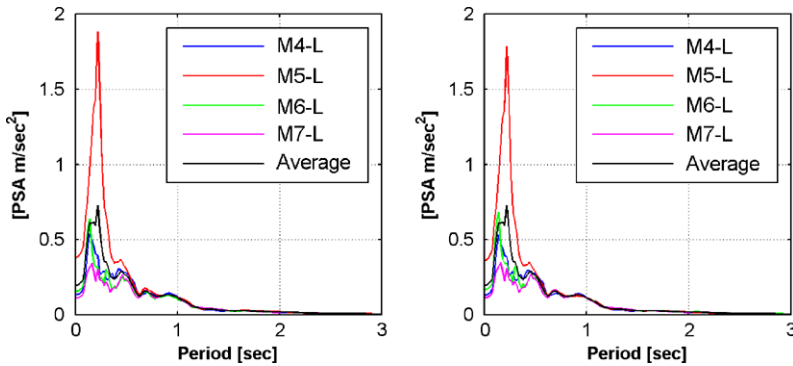


Fig. 6 5 % damped elastic response spectra of the longitudinal components of the records at piers M4-M7 compared to the scaled ones (on the *right*) at the average spectrum for $T = 1.64$ sec

where the coherency drop parameter α controls the exponential decay and ξ is the distance between two stations examined. The drop parameter is usually taken equal to $2.5 \cdot 10^{-4}$ sec/m, but in this specific case, the results are not satisfactory. On the other hand, the model of Abrahamson can predict the loss of coherency much better than Luco and Wong as illustrated in Fig. 5.

4 Analyses Performed

Most analytical or numerical studies investigating the effects of spatial variability of earthquake ground motion on the response of bridges compare the results of multiple-support excitation analysis with those of a reference condition which typically assumes synchronous excitation among all bridge supports. The comparison can then be made in terms of a ratio of the action effects (forces or displacements) of specific structural components over the response under synchronous conditions.

In the case examined herein though, the fact that the ground motions have been recorded at the bases of the four bridge piers gives the actual asynchronous excitations due to the existing seismo-tectonic and soil conditions of the site under study, but at the same time makes it difficult to the corresponding compatible “synchronous” excitation conditions. One option would have been to select one of the recorded motions and apply it synchronously at all pier supports; however, this option is limited by the fact that the available records show significant discrepancy in terms of both their PGA and spectral amplification, primarily due to local site effects at the location of pier M5 (Fig. 6).

In order to overcome this difficulty, it was decided to adopt the following procedure: strongest component of the motions recorded is in the longitudinal direction, all records (in all components) are scaled (Table 1) to the average spectral acceleration of all records at period $T = 1.64$ sec, which is the period of the highest contributing mode, activating 76 % of the mass in the longitudinal direction (Table 2).

Table 1 The scaling factors for the records at M4, M5, M6, M7 compared to the average response spectrum for $T = 1.64$ sec

Pier	M4	M5	M6	M7
Scale factor	0.977	0.947	1.069	1.014

Table 2 Dynamic characteristics (eigenfrequencies and corresponding modal contribution) of the Evripos cable-stayed bridge

Mode ID	Period	UX	UY	UZ	RX	RY	RZ
#1	2.712	0	0	6.7	1.2	2.3	0
#2	2.385	20.2	0	0	0	0	0
#3	2.061	0	58.3	0	3.4	0	47.2
#4	1.645	76.3	0	0	0	0	0
#5	1.298	0	0	6.2	1.4	5.5	0
#9	1.065	0	0	37.4	7.3	28.8	0

Then, four different “synchronous” excitation scenarios are developed, assuming each time that the scaled motions in piers M4, M5, M6 and M7 respectively, are applied uniformly at all supports. Given the aforementioned scaling, it is deemed that the four different versions of uniform excitation are compatible in terms of spectral amplification (at least at the period of vibration that is affected by the dominant earthquake component), while the fact that all the resulting scaling factors are close to unity, guarantees that the scaling-induced dispersion is limited.

Based on the above, five non-linear dynamic analyses of the Evripos cable-stayed bridge are performed using the computer program SAP2000, i.e. one using the recorded set of asynchronous motions and four considering the aforementioned compatible “synchronous” excitation scenarios. All three components of the excitations were applied simultaneously. The geometrical non-linearity induced by the bridge cables was considered assuming tension-only capabilities and the initial cable stress state due to dead loading was applied through non-linear staged-construction static analysis.

Beam elements were used to model the piers, while the bridge deck was modeled by shell elements. Piers were assumed fixed at their bases, while the supporting conditions at the two bridge edges were considered as rollers in the longitudinal direction and pinned in the transverse.

The amplitude of the seismic moments (i.e., the earthquake-induced bending moments at the bases of piers M4 and M7 and at one of the two columns at each pier M5 and M6), the displacements at the top of each pier and the displacements at the middle of the deck are examined for all asynchronous and synchronous excitation cases previously presented.

Figure 7 presents the comparison between the computed seismic moments at the base of pier M6 using the Athens 1999 (asynchronous) recorded motions, and

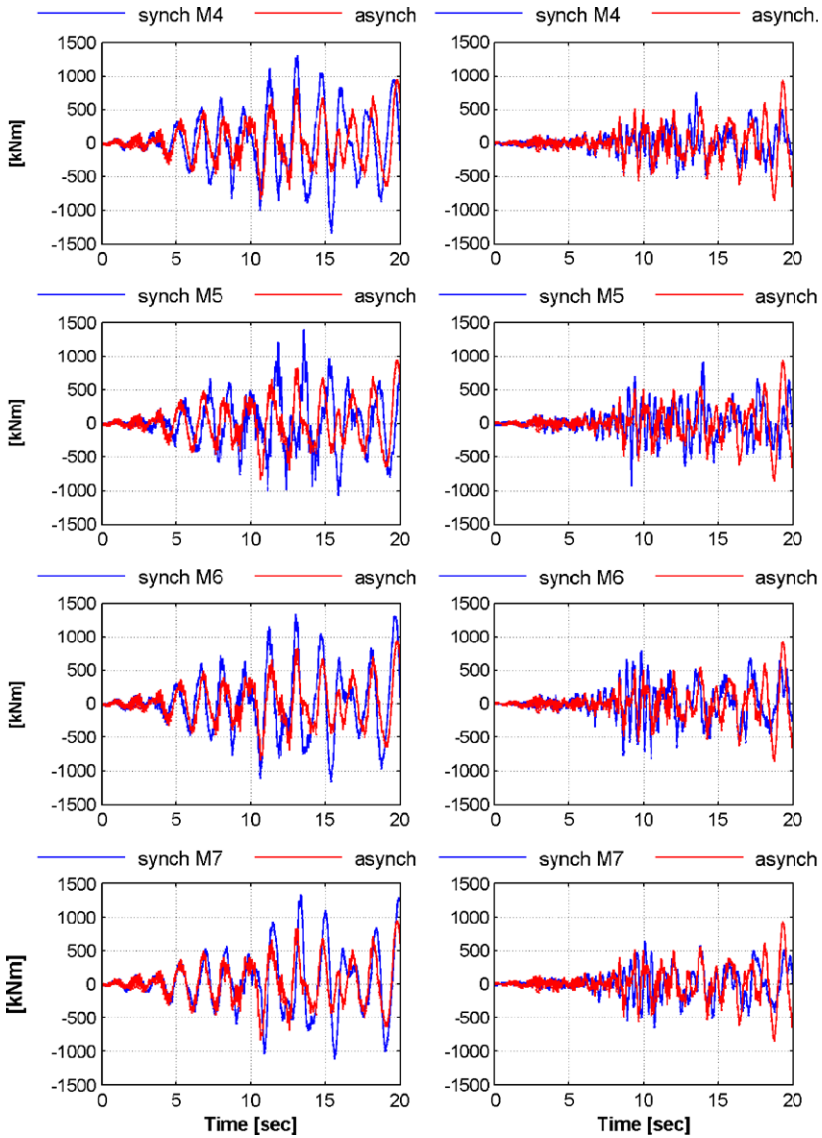


Fig. 7 Comparison of the computed seismic moments at the base of pier M6 using the Athens 1999 (asynchronous) recorded motions, with those computed through the four “synchronous” excitation scenarios (uniform application of records M4, M5, M6, M7). On the *left* the moment vector M2 is parallel to the bridge (transverse bending) while on the *right* it is normal to the bridge (M3, longitudinal bending)

those computed through the four “synchronous” excitation scenarios, that is, by the uniform application of records M4, M5, M6, and M7 respectively. The comparison of the maxima among all cases are summarized in Table 3.

Table 3 Comparison of maximum absolute earthquake induced bending moments developed in pier M6 for synchronous and asynchronous excitation (cases M4, M5, M6, M7)

Uniform excitation scenario	Case studied	Pier M5		Pier M6	
		M2 [kNm]	M3 [kNm]	M2 [kNm]	M3 [kNm]
Synch M4	Synch	1350.70	798.54	1338.30	759.11
	Asynch	833.53	743.05	949.48	943.70
	Asynch/Synch-1	-38 %	-7 %	-29 %	+24 %
Synch M5	Synch	1510.39	1008.53	1403.31	919.10
	Asynch	833.53	743.05	949.48	943.70
	Asynch/Synch-1	-45 %	-26 %	-32 %	+3 %
Synch M6	Synch	1401.33	981.36	1345.28	815.00
	Asynch	833.53	743.05	949.48	943.70
	Asynch/Synch-1	-41 %	-24 %	-29 %	+16 %
Synch M7	Synch	1314.49	849.06	1335.77	658.05
	Asynch	833.53	743.05	949.48	943.70
	Asynch/Synch-1	-37 %	-13 %	-29 %	+43 %

It can be seen that the moments M_2 developed at the base of pier M6 transversely to the bridge plane, due to the asynchronous recorded ground motions is systematically lower regardless of the “synchronous” excitation pattern adopted. As anticipated, this is more intense (approximately 32 %) for the synchronous case involving the uniform application of record M5, which, despite of the scaling to a common level of spectral amplification, still corresponds to the highest PGA among the records at all locations. On the other hand, the situation reverses for the bending moments M_3 within the bridge plane and the asynchronous excitation results in higher levels of stress in all cases, reaching 43 % increase in the extreme case of applying record M7 uniformly at all support points. The respective results for pier M5 are also summarized in Table 3. It can be seen that seismically-induced bending moments in both directions are decreased when assuming non-uniform excitation conditions independently of the scenario adopted.

As far as the displacements are concerned, the corresponding time histories are plotted in Fig. 8 and Fig. 9 for the top of pylons M5 and M6 respectively, while the maximum in time displacements for all directions are compared in Table 4 and Table 5. The respective magnitudes at the middle of the deck are summarized in Table 6. More specifically, asynchronous excitation is systematically favorable for the span middle deck displacements which are decreased up to 36 %, 45 % and 63 % along the three principal directions U_x , U_y and U_z .

The same trend is also observed for the case of the top of pylon M5—though to a lesser degree—and with the exception of a minor (6 %) increase in longitudinal displacements for one of the scenarios studied. In contrast to the above, the transverse displacements at the top of pylon M6 derived under the asynchronous

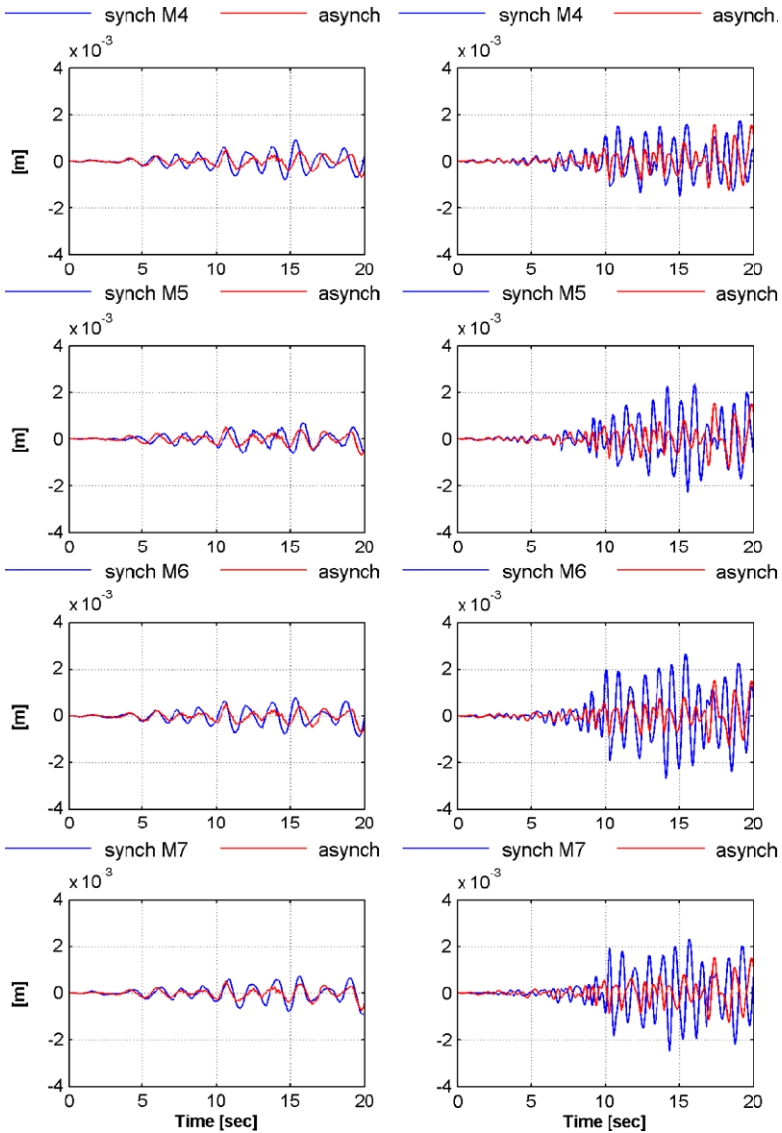


Fig. 8 Comparison of the seismic displacements at the top of pylon M5 using the Athens 1999 (asynchronous) recorded motions, with those computed through the four “synchronous” excitation scenarios (uniform application of records M4, M5, M6, M7). On the *left* displacements are in the longitudinal bridge direction while on the *right* are in transverse direction

recorded ground motions are increased compared to the synchronous case and are almost double (increased by 82 %) when compared to the uniform application of record M4. As for the vertical displacements in both pylons can either decrease or increase depending on the assumed “synchronous” scenario.

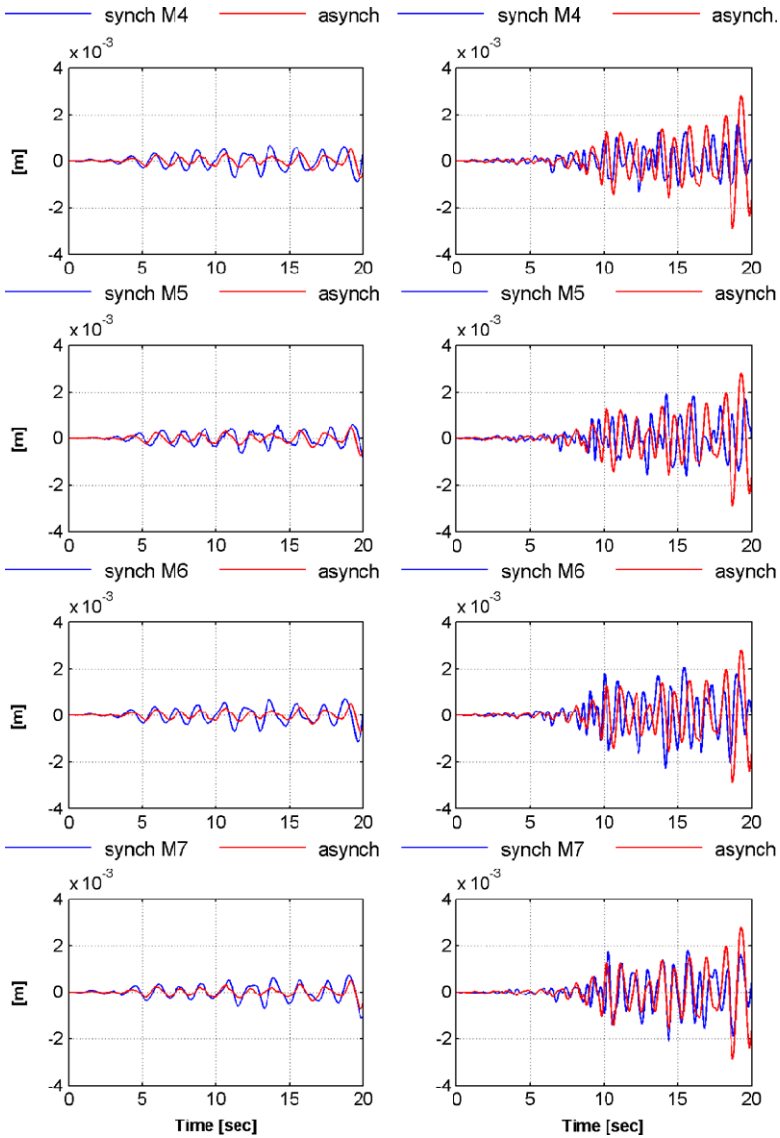


Fig. 9 Comparison of the seismic displacements at the top of pylon M6 using the Athens 1999 (asynchronous) recorded motions, with those computed through the four “synchronous” excitation scenarios (uniform application of records M4, M5, M6, M7). On the *left* displacements are in the longitudinal bridge direction while on the *right* are in the transverse direction

These results indicate that the inherently complex nature of ground motion incoherency is strongly correlated to the dynamic characteristics of the excited structure and does not systematically lead to a uniform increase or decrease of the corresponding action effects.

Table 4 Comparison of maximum absolute earthquake induced displacements [cm] developed at top of pier M5 for synchronous and asynchronous excitation (cases M4, M5, M6, M7)

Uniform excitation scenario	Case studied	U_x [cm]	U_y [cm]	U_z [cm]
Synch M4	Synch	0.09	0.18	0.05
	Asynch	0.07	0.16	0.05
	Asynch/Synch-1	-22 %	-12 %	+7 %
Synch M5	Synch	0.067	0.23	0.05
	Asynch	0.071	0.16	0.05
	Asynch/Synch-1	+6 %	-34 %	0 %
Synch M6	Synch	0.09	0.27	0.06
	Asynch	0.07	0.16	0.05
	Asynch/Synch-1	-20 %	-42 %	-14 %
Synch M7	Synch	0.09	0.25	0.05
	Asynch	0.07	0.16	0.05
	Asynch/Synch-1	-23 %	-37 %	-6 %

Table 5 Comparison of maximum absolute earthquake induced displacements [cm] developed at top of pier M6 for synchronous and asynchronous excitation (cases M4, M5, M6, M7)

Uniform excitation scenario	Case studied	U_x [cm]	U_y [cm]	U_z [cm]
Synch M4	Synch	0.09	0.16	0.04
	Asynch	0.07	0.29	0.05
	Asynch/Synch-1	-20 %	+82 %	+11 %
Synch M5	Synch	0.08	0.19	0.047
	Asynch	0.07	0.29	0.049
	Asynch/Synch-1	-10 %	+49 %	+4 %
Synch M6	Synch	0.11	0.23	0.054
	Asynch	0.07	0.29	0.049
	Asynch/Synch-1	-36 %	+28 %	-9 %
Synch M7	Synch	0.11	0.21	0.050
	Asynch	0.07	0.29	0.049
	Asynch/Synch-1	-35 %	+38 %	-2 %

Table 6 Comparison of maximum absolute earthquake induced displacements [cm] developed at the middle of the bridge deck for synchronous and asynchronous excitation (cases M4, M5, M6, M7)

Uniform excitation scenario	Case studied	U_x [cm]	U_y [cm]	U_z [cm]
Synch M4	Synch	0.11	0.14	0.16
	Asynch	0.08	0.10	0.07
	Asynch/Synch-1	-28 %	-25 %	-56 %
Synch M5	Synch	0.09	0.14	0.17
	Asynch	0.08	0.10	0.07
	Asynch/Synch-1	-15 %	-29 %	-58 %
Synch M6	Synch	0.12	0.18	0.20
	Asynch	0.08	0.10	0.07
	Asynch/Synch-1	-36 %	-45 %	-63 %
Synch M7	Synch	0.12	0.16	0.18
	Asynch	0.08	0.10	0.07
	Asynch/Synch-1	-36 %	-41 %	-60 %

5 Conclusions

The scope of this study was to examine the effects of asynchronous excitation on the Evripos cable-stayed bridge, utilizing the recorded time histories at four locations of the accelerometer network maintained by EPPO-ITSAK, due to the $M_s = 5.9$, 7/9/1999 Athens earthquake. Initially the records were filtered to remove inertial interaction effects and after that their coherency was computed for all available record pairs. Comparison of these results with two different coherency models presented in literature proved that there was a significant difference in the accuracy of the predictions of the two models, and hence the selection of a coherency model for the investigation of spatial variability of earthquake ground motion should be done with caution. A detailed finite element model of the cable-stayed bridge was developed and its response was computed using both the recorded motions and four synchronous excitation scenarios. The comparative study of the results indicates that:

- For the particular bridge studied, spatial variability of seismic ground motion has a generally favorable effect, at least on the pier base bending moments and the displacements middle of the central span deck. Apparently, the extent of this beneficial phenomenon is very much dependent on the assumptions made regarding the definition of the “synchronous” excitation, which, in contrast to the actual, recorded asynchronous case, is not obvious.

- There are specific cases (i.e., out-of-plane bending moments and displacements at the top of the two bridge pylons) where the asynchronous excitation has a clearly critical effect.

The results of the investigations of the present study indicate that the complex nature of ground motion incoherency is strongly correlated to the dynamic characteristics of the excited structure and does not systematically lead to a uniform increase or decrease of the corresponding action effects.

References

1. Burdette NJ, Elnashai AS (2008) Effect of asynchronous earthquake motion on complex bridges. II: Results and implications on assessment. *J Bridge Eng* 13:166–172
2. Deodatis G, Saxena V, Shinozuka M (2000) Effects of spatial variability of ground motion on bridge fragility curves. In: Eighth ASCE specialty conference on probabilistic mechanics and structural reliability
3. Lupoi A, Franchin P, Pinto PE, Monti G (2005) Seismic design of bridges accounting for spatial variability of ground motion. *Earthq Eng Struct Dyn* 34:327–348. doi:[10.1002/eqe.444](https://doi.org/10.1002/eqe.444)
4. Nazmy AS, Abdel-Ghaffar AM (1992) Effects of ground motion spatial variability on the response of cable-stayed bridges. *Earthq Eng Struct Dyn* 21:1–20. doi:[10.1002/eqe.4290210101](https://doi.org/10.1002/eqe.4290210101)
5. Sextos AG, Kappos AJ, Ptilakis KD (2003) Inelastic dynamic analysis of RC bridges accounting for spatial variability of ground motion, site effects and soil-structure interaction phenomena. Part 2: Parametric study. *Earthq Eng Struct Dyn* 32:629–652. doi:[10.1002/eqe.242](https://doi.org/10.1002/eqe.242)
6. Abrahamson NA (1993) Spatial variation of multiple support inputs. In: Proceedings of the 1st US seminar on seismic evaluation and retrofit of steel bridges. A Caltrans and University of California at Berkeley seminar
7. Sextos AG, Kappos AJ (2008) Evaluation of seismic response of bridges under asynchronous excitation and comparisons with Eurocode 8-2 provisions. *Bull Earthq Eng* 7:519–545. doi:[10.1007/s10518-008-9090-5](https://doi.org/10.1007/s10518-008-9090-5)
8. Lekidis V, Tsakiri M, Makra K, Karakostas C, Klimis N, Sous I (2005) Evaluation of dynamic response and local soil effects of the Evripos cable-stayed bridge using multi-sensor monitoring systems. *Eng Geol* 79:43–59. doi:[10.1016/j.enggeo.2004.10.015](https://doi.org/10.1016/j.enggeo.2004.10.015)
9. Lekidis V (2003) Investigation of the seismic response of the Evripos high bridge: experimental and analytical approach. Thessaloniki
10. Zerva A (2009) *Spatial Variation of Seismic Ground Motions: Modeling and Engineering Applications*. CRC Press, Boca Raton
11. Abrahamson NA, Schneider JF, Stepp JC (1991) Empirical spatial coherency functions for applications to soil-structure interaction analyses. *Earthq Spectra* 7:1–28
12. Luco JE, Wong HL (1986) Response of a rigid foundation to a spatially random ground motion. *Earthq Eng Struct Dyn* 14:891–908. doi:[10.1002/eqe.4290140606](https://doi.org/10.1002/eqe.4290140606)

An Efficient Beam-Column Element for Inelastic 3D Frame Analysis

Svetlana M. Kostic, Filip C. Filippou, and Chin-Long Lee

Abstract Beam-column elements with section resultant plasticity for the hysteretic behavior of the end plastic hinges are widely used for numerical simulations in earthquake engineering practice because of the good compromise between accuracy and computational cost. This chapter presents a three-dimensional inelastic beam-column element of this type with significant capabilities for the description of the global and local response of frames under monotonic and cyclic loads. In the proposed element the concept of generalized plasticity is extended to section resultants and element deformations and is used to describe the hysteretic behavior of the plastic hinges forming at the element ends. The element accounts for the interaction of the axial force with the bending moments about the principal section axes with suitably defined yield and limit surfaces that permit the description of the gradual yielding and the post-yield hardening behavior of the end sections. Comparisons of the hysteretic response of structural elements and small structural models between the proposed element and the more accurate, but computationally more expensive fiber section description of the cross section demonstrate the capabilities of the proposed model.

Keywords Nonlinear analysis · Beam-column element · Resultant plasticity · Generalized plasticity

S.M. Kostic (✉)

Faculty of Civil Engineering, University of Belgrade, Bul. Kralja Aleksandra 73, 11000 Belgrade, Serbia

e-mail: svetlana@grf.bg.ac.rs

F.C. Filippou

Department of Civil and Environmental Engineering, University of California, Berkeley, CA 94720-1710, USA

e-mail: filippou@ce.berkeley.edu

C.-L. Lee

Department of Civil and Natural Resources Engineering, University of Canterbury, Christchurch, New Zealand

e-mail: chin-long.lee@canterbury.ac.nz

1 Introduction

Nonlinear analysis methods are of increasing importance in earthquake-engineering practice with modern performance-based design codes requiring better insight into the inelastic structural behavior and more detailed information about the nonlinear structural response than traditional design procedures. In the professional practice environment the impetus to deploy more advanced and accurate analysis methods is tempered by the cost of analysis and evaluation. Because of the good compromise between accuracy and computational efficiency and the relative ease of response evaluation, frame elements are commonly used in earthquake engineering practice.

There are two basic types of nonlinear frame element, the concentrated (lumped) plasticity element and the distributed inelasticity element. In the concentrated plasticity element, the inelastic deformations arise only at the element ends, while the rest of the element behaves elastically. On the other hand, in the distributed inelasticity element, inelastic deformations may arise at any of several monitored sections along the element. With either element type the inelastic behavior of the monitored sections is described either directly with section resultant relations or with the fiber discretization of the cross section and the integration of the material response over the cross section area. The fiber section discretization offers a high level of accuracy and flexibility in modeling the 3D inelastic response of structural members, but places high demands on computer storage and memory and is computationally intensive.

Consequently, the description of the inelastic section behavior with section resultant relations is more common than the use of fiber beam column elements in the simulation of the seismic response of three dimensional structural models. If the resultant constitutive relations arise in the context of a lumped plasticity model, they represent element end force-deformation relations. This chapter uses the name *resultant plasticity model* for this type of formulation and presents a new element of this type that is based on the concept of generalized plasticity for material stress-strain response put forward by Lubliner, Aurichio and Taylor [1–3]. It overcomes the most common shortcoming of the elastic-perfectly plastic element response, the absence of gradual yielding and material hardening, while preserving the computational efficiency of elastic-perfectly plastic lumped plasticity beam-column elements.

2 Resultant Plasticity Beam-Column Elements

To date, many studies have been conducted on concentrated plasticity or point hinge beam-column elements [4–9]. Among these, the resultant plasticity beam-column elements use concepts of plasticity theory to describe the relation between basic element forces and deformations. The interaction of the axial force and bending moments about the principal axes of the cross section is described by a stress-resultant yield surface, which is identified as yield surface in the following discussion. Yield

surface equations for different types of cross section are available [4, 10–12]. Also, different strategies have been proposed for approaching the yield surface and preventing the element force path from drifting away from it. Orbison [4] used a single polynomial expression for the yield surface of wide-flange steel sections and proposed a five step procedure for mapping the element forces onto the yield surface. The algorithm is limited by the need to subdivide each increment into several sub-increments to prevent large errors. Moreover, the element cannot represent the gradual yielding and hardening at the element ends, because the end hinges are assumed to be elastic, perfectly-plastic.

Several models that improve the shortcomings of Orbison’s model were proposed in the last 15 years. The idea of loading and bounding surfaces for material plasticity by Dafalias and Popov [13] was successfully extended to concentrated and distributed plasticity beam-column elements [7, 8, 14–16]. In these models, the loading and bounding surfaces have the same shape to prevent the two surfaces from overlapping. Once the point representing the element force resultants in the force space touches the loading surface at some point A, it moves along the line connecting point A with its conjugate point A’ on the bounding surface, if plastic loading occurs.

The generalized plasticity material model by Lubliner, Aurichio and Taylor [1–3] proposes a different procedure for the gradual, asymptotic approach of the stress to the limit surface. The model is simple, does not require an expression for the limit surface and has a straightforward implementation with its dependence on two parameters with clear physical meaning. With the implementation of the return map algorithm it is also computationally very efficient.

The proposed element extends the concept of the generalized plasticity material model to element deformations and force resultants. The backward-Euler algorithm with general closest point projection [17] is adapted to the element force-deformation relation. The element accounts for isotropic and kinematic hardening and is computationally efficient because of the relative simplicity of the formulation and the quadratic convergence of the algorithm with general closest point projection.

3 Element Formulation

3.1 Basic Framework

The underlying assumption of generalized plasticity theory is the existence of two continuous real valued functions, the yield function f and limit function F in Fig. 1 [2, 3]. The yield function f encloses the elastic region forming the boundary between elastic and inelastic response:

- $f < 0 \rightarrow$ elastic state—no inelastic effects
- $f \geq 0 \rightarrow$ inelastic state—inelastic effects may or may not occur depending on loading or unloading

Fig. 1 Limit function F and yield function f

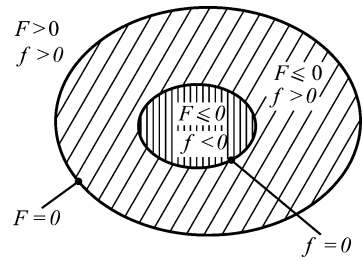
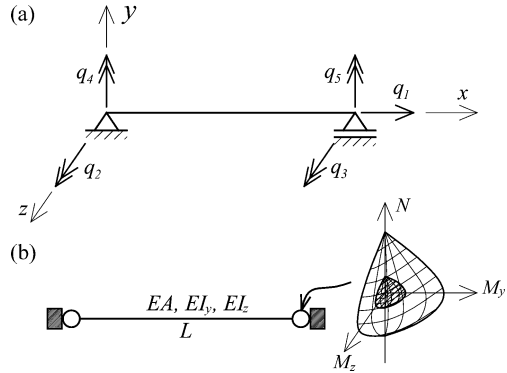


Fig. 2 (a) Basic element forces \mathbf{q} ; **(b)** End plastic hinges



The limit function F separates admissible and inadmissible stress states:

- $F \leq 0 \rightarrow$ admissible stress state
- $F > 0 \rightarrow$ inadmissible stress state

The basic forces \mathbf{q} of a three-dimensional (3D) frame element of length L without rigid body modes are shown in Fig. 2(a). The corresponding deformations are denoted with \mathbf{v} . EA denotes the axial stiffness, EI_z and EI_y the flexural stiffness about the z - and y -axis, respectively. N is the axial force, and M_z and M_y are the bending moments about the z - and y -axis, respectively. Zero-length plastic hinges may form at one or both element ends, while the rest of the element is elastic, as shown in Fig. 2(b).

In beam-column elements with stress-resultant plasticity the concepts of classical material plasticity are applied to axial force and biaxial bending moment interaction under inelastic response. The following equations govern the element behavior:

1. The element deformations \mathbf{v} are decomposed into the linear elastic contribution \mathbf{v}^e and the plastic contribution \mathbf{v}^p :

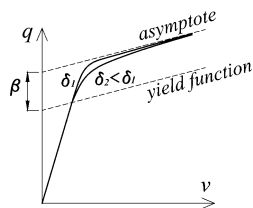
$$\mathbf{v} = \mathbf{v}^e + \mathbf{v}^p \tag{1}$$

2. A linear elastic relation is assumed between the basic element forces and the elastic deformations:

$$\mathbf{q} = \mathbf{k}_e \mathbf{v}^e = \mathbf{k}_e (\mathbf{v} - \mathbf{v}^p) \tag{2}$$

where \mathbf{k}_e is the elastic element stiffness matrix.

Fig. 3 Approach of basic force \mathbf{q} to limit surface with increasing element deformation \mathbf{v}



3. At each element end, the yield function f depends on the basic element forces \mathbf{q} , a vector \mathbf{a} describing the position of the surface center, and a hardening variable α representing isotropic hardening. The non-dimensional isotropic and kinematic hardening parameters are denoted with H_{iso} and H_{kin} , respectively. The yield function f distinguishes between elastic and inelastic states.

$$f(\mathbf{q}, \mathbf{a}, \alpha) = \Phi(\mathbf{q} - \mathbf{a}) - H_{iso}\alpha \quad (3)$$

4. The limit function F depends on the nonnegative consistency parameter λ and assumes the following form for generalized plasticity models

$$F = h(f) \frac{d}{dt}(\Phi) - \lambda \quad (4)$$

$$h(f) = \frac{f}{\delta(\beta - f) + (H_{iso} + H_{kin})\beta} \quad (5)$$

where δ and β are two non-dimensional positive constants, with δ measuring the rate of approach to the asymptotic behavior, and β measuring the distance between the yield function and the asymptote. The graphical representation of these parameters is shown in Fig. 3.

5. An associative plastic flow rule is assumed with the following evolution relation

$$\dot{\mathbf{v}}^P = \lambda \frac{\partial f}{\partial \mathbf{q}} \quad (6)$$

6. The surface motion describing the kinematic hardening mechanism is defined by the following relation:

$$\dot{\mathbf{a}} = H_{kin} \mathbf{\Pi} \dot{\mathbf{v}}^P = H_{kin} \mathbf{\Pi} \lambda \frac{\partial f}{\partial \mathbf{q}} \quad (7)$$

where $\mathbf{\Pi}$ is a scaling matrix that accounts for the different dimension of \mathbf{a} and \mathbf{v}^P . In the proposed model it has the form:

$$\mathbf{\Pi} = \text{diag} \left\{ \frac{EA}{L}, \frac{EI_z}{L}, \frac{EI_z}{L}, \frac{EI_y}{L}, \frac{EI_y}{L} \right\} \quad (8)$$

7. The simplest evolutionary equation is used for α based on the equivalent plastic strain:

$$\dot{\alpha} = \|\dot{\mathbf{v}}^P\| = \lambda \left\| \frac{\partial f}{\partial \mathbf{q}} \right\| \quad (9)$$

where:

$$\left\| \frac{\partial f}{\partial \mathbf{q}} \right\| = \left[\left(\frac{\partial f}{\partial \mathbf{q}} \right)^T \mathbf{A} \frac{\partial f}{\partial \mathbf{q}} \right]^{1/2} \quad (10)$$

with a scaling matrix \mathbf{A} defined as:

$$\mathbf{A} = \text{diag} \left\{ \frac{1}{L^2}, 1, 1, 1, 1 \right\} \quad (11)$$

8. The Kuhn-Tucker complementarity conditions are:

$$\lambda \geq 0, \quad F \leq 0, \quad \lambda F = 0 \quad (12)$$

These conditions reduce the plastic problem to a constrained optimization problem.

9. The limit equation can be written in the following form:

$$\lambda - h(f) \frac{d}{dt} (\Phi) = 0 \quad (13)$$

Integrating this equation over the time interval (t_n, t_{n+1}) , gives the discrete limit condition:

$$\Delta \lambda - h(f)(\Phi_{n+1} - \Phi_n) = 0 \quad (14)$$

3.2 Integration Algorithm

The proposed model can be transformed into a discrete constrained optimization problem by applying the implicit backward Euler numerical integration algorithm.

Assuming that the state of the element is known at time step t_n implies that the values $\{\mathbf{v}_n, \mathbf{v}_n^p, \mathbf{a}_n, \alpha_n\}$ are given. The corresponding basic forces are determined with Eq. (2):

$$\mathbf{q}_n = \mathbf{k}_e (\mathbf{v}_n - \mathbf{v}_n^p) \quad (15)$$

Under a given increment of element deformations $\Delta \mathbf{v}$ at time step t_{n+1} the total deformation is known: $\mathbf{v}_{n+1} = \mathbf{v}_n + \Delta \mathbf{v}$. The problem to be solved consists of determining the state and updating the other state variables \mathbf{v}_{n+1}^p , \mathbf{a}_{n+1} and α_{n+1} .

The application of the backward-Euler method gives:

$$\mathbf{v}_{n+1}^p = \mathbf{v}_n^p + \mathbf{g}_{n+1}(\mathbf{q}_{n+1}, \mathbf{a}_{n+1}) \Delta \lambda \quad (16)$$

$$\mathbf{a}_{n+1} = \mathbf{a}_n + H_{kin} \mathbf{\Pi} \mathbf{g}_{n+1}(\mathbf{q}_{n+1}, \mathbf{a}_{n+1}) \Delta \lambda \quad (17)$$

$$\alpha_{n+1} = \alpha_n + \left\| \mathbf{g}_{n+1}(\mathbf{q}_{n+1}, \mathbf{a}_{n+1}) \right\| \Delta \lambda \quad (18)$$

where $\Delta \lambda = \int_{t_n}^{t_{n+1}} \lambda dt$ and $\mathbf{g} = \frac{\partial f}{\partial \mathbf{q}}$. The discrete version of the Kuhn-Tucker conditions (12) is:

$$\Delta \lambda \geq 0, \quad F_{n+1} \leq 0, \quad \Delta \lambda F_{n+1} = 0 \quad (19)$$

The discrete system of equations is solved by the two-step predictor-corrector return mapping algorithm.

3.3 Return Mapping Algorithm

The return mapping algorithm is an efficient and robust integration scheme belonging to the family of elastic predictor-plastic corrector methods. In the predictor step a purely elastic trial state \mathbf{q}_{n+1}^{trial} is computed. If the trial state violates the limit condition $F \leq 0$, the element forces are corrected in the corrector step with the trial state as initial condition. Otherwise, a corrector step is not necessary, because the trial state represents the solution at time step t_{n+1} .

Since the element has two nodes, plastic deformations can arise at one or both ends. To account for this the yield functions f_1 and f_2 , limit functions F_1 and F_2 , the consistency parameters $\Delta\lambda_1$ and $\Delta\lambda_2$ and the hardening variables α_1 and α_2 are collected into vectors \mathbf{f} , \mathbf{F} , $\Delta\lambda$ and α , respectively. The diagonal 2×2 matrix composed of the value of f_1 and f_2 is denoted with $diag(\mathbf{f})$. The same convention is used for the other terms: $diag(\mathbf{F})$, $diag(\Delta\lambda)$, etc.

When both ends yield, \mathbf{g} is a 3×2 matrix, with the first column equal to $\partial_{\mathbf{q}} f_1 = \mathbf{g}_1$ and the second equal to $\partial_{\mathbf{q}} f_2 = \mathbf{g}_2$. If only one end yields, \mathbf{g} is a 3×1 vector and is equal to \mathbf{g}_1 or \mathbf{g}_2 , depending on which end yields. In this case the parameter $\Delta\Delta\lambda$ for the nonyielding node is zero.

1. Predictor step: An elastic step results by freezing the plastic flow, so that $\Delta\lambda = 0$.

$$\mathbf{q}_{n+1}^{trial} = \mathbf{k}_e (\mathbf{v}_{n+1} - \mathbf{v}_n^p) \quad (20)$$

$$\mathbf{v}_{n+1}^{p,trial} = \mathbf{v}_n^p \quad (21)$$

$$\mathbf{a}_{n+1}^{trial} = \mathbf{a}_n \quad (22)$$

$$\alpha_{n+1}^{trial} = \alpha_n \quad (23)$$

$$\mathbf{f}_{n+1}^{trial} = \mathbf{f}(\mathbf{q}_{n+1}^{trial}, \mathbf{a}_{n+1}^{trial}, \alpha_{n+1}^{trial}) = \Phi_{n+1}^{trial} - H_{iso} \alpha_{n+1}^{trial} \quad (24)$$

$$\Phi_{n+1}^{trial} = \Phi(\mathbf{q}_{n+1}^{trial} - \mathbf{a}_{n+1}^{trial}) \quad (25)$$

Once the trial state is computed, the limit condition $F \leq 0$ arising from $\Delta\lambda = 0$ reduces to the condition $\mathbf{f}_{n+1}^{trial} (\Phi_{n+1}^{trial} - \Phi_n) \leq 0$.

If this condition is satisfied, the trial state is admissible, and all state variables can be updated according to:

$$\mathbf{v}_{n+1}^p = \mathbf{v}_n^p \quad (26)$$

$$\mathbf{a}_{n+1} = \mathbf{a}_n \quad (27)$$

$$\alpha_{n+1} = \alpha_n \quad (28)$$

$$\mathbf{q}_{n+1} = \mathbf{q}_{n+1}^{trial} \quad (29)$$

$$\mathbf{k}_{n+1} = \mathbf{k}_e \quad (30)$$

If the condition $\mathbf{f}_{n+1}^{trial} (\Phi_{n+1}^{trial} - \Phi_n) \leq 0$ is not satisfied, the trial state is inadmissible, requiring a corrector step.

2. Corrector step: Setting the limit condition in Eq. (14) and the residuals $\mathbf{R}_{1,n+1}$, $\mathbf{R}_{2,n+1}$ and $\mathbf{R}_{3,n+1}$ to zero gives:

$$\mathbf{R}_{1,n+1} = -\mathbf{v}_{n+1}^p + \mathbf{v}_n^p + \mathbf{g}_{n+1} \Delta \lambda \quad (31)$$

$$\mathbf{R}_{2,n+1} = -\mathbf{a}_{n+1} + \mathbf{a}_n + H_{kin} \Pi \mathbf{g}_{n+1} \Delta \lambda_{n+1} \quad (32)$$

$$\mathbf{R}_{3,n+1} = -\alpha_{n+1} + \alpha_n + \|\mathbf{g}_{n+1}\| \Delta \lambda_{n+1} \quad (33)$$

The linearization of Eq. (14) and Eqs. (31)–(33) followed by a few numerical manipulations results in a nonlinear system of two equations for determining the parameter $\Delta \Delta \lambda$ with the following form:

$$(\mathbf{a} \Delta \Delta \lambda)(\mathbf{b} \Delta \Delta \lambda) + \mathbf{c} \Delta \Delta \lambda + \mathbf{d} = \mathbf{0} \quad (34)$$

The smallest positive solution $\Delta \Delta \lambda$ for the increment of the consistency parameter in the k -th iteration corresponds to the physically correct result.

The system can be solved with the Newton method or any other suitable algorithm for a nonlinear equation system. The solution of the linear system $\mathbf{c} \Delta \Delta \lambda + \mathbf{d} = \mathbf{0}$ can serve as initial value.

For $\delta = \mathbf{0}$ and $H_{iso} = H_{kin} = 0$ the model reduces to elastic-perfectly plastic behavior with the solution:

$$\Delta \Delta \lambda_{n+1}^{(k)} = ((\mathbf{g}_{n+1}^{(k)})^T \mathbf{A}_{n+1}^{(k)} \mathbf{g}_{n+1}^{(k)})^{-1} (\mathbf{f}_{n+1}^{(k)} - (\mathbf{g}_{n+1}^{(k)})^T \mathbf{A}_{n+1}^{(k)} \mathbf{R}_{1,n+1}^{(k)}) \quad (35)$$

where

$$\mathbf{A} = (\mathbf{k}_e^{-1} + \mathbf{Q} \Delta \lambda)^{-1} \quad \text{and} \quad \mathbf{Q} = \frac{\partial^2 f}{\partial \mathbf{q}^2}$$

The elastic-perfectly plastic solution also results when $\beta = \mathbf{0}$ and $H_{iso} = H_{kin} = 0$.

For the case that only one end yields, the system of nonlinear equations transforms into a single quadratic equation.

After finding the increment $\Delta \Delta \lambda$ from the solution of a single equation or of a system of nonlinear equations, the consistency parameter can be updated:

$$\Delta \lambda_{n+1}^{(k+1)} = \Delta \lambda_{n+1}^{(k)} + \Delta \Delta \lambda_{n+1}^{(k)} \quad (36)$$

The tangent stiffness results from the enforcement of the linearized discrete form of the limit condition. As is the case with the consistency parameter $\Delta \Delta \lambda$, when $\delta = \mathbf{0}$ and $H_{iso} = H_{kin} = 0$ or $\beta = \mathbf{0}$ and $H_{iso} = H_{kin} = 0$, the consistent tangent stiffness matrix reduces to the expression for the elastic-perfectly plastic case:

$$\mathbf{k}_{n+1} = \mathbf{A}_{n+1} - \mathbf{A}_{n+1} \mathbf{g}_{n+1} (\mathbf{g}_{n+1}^T \mathbf{A}_{n+1} \mathbf{g}_{n+1})^{-1} \mathbf{g}_{n+1}^T \mathbf{A}_{n+1} \quad (37)$$

4 Numerical Examples

The capabilities of the proposed element are assessed through the following four numerical examples. The response of the new GPNMYS element (Generalized Plasticity N - M Yield Surface) is compared with the solution of the elastic-perfectly plastic

concentrated plasticity (EPPNMYS) element [18] and the fiber hinge element [19] whose results denoted with FIBER serve as the benchmark solution. The simulations were done with FEDEASLab [20], a Matlab toolbox for nonlinear static and dynamic analysis.

4.1 Cantilever Column

The first example refers to the cantilever column in Fig. 4(a) which was the subject of an earlier study on the efficient cross section discretization for fiber beam-column elements [21, 22]. In the numerical tests, the column was subjected to a uniaxial tip translation history in test B6, and biaxial tip translation history in test B8_7 with variation of the axial force between $-0.05N_p$ and $-0.45N_p$ (Fig. 4(b) and (c)).

The response of a homogeneous column with elastic, perfectly plastic material for the distributed inelasticity fiber model with a section discretization of 288 fibers and with four Gauss-Lobatto integration points along its length is compared with the response of the concentrated plasticity elements, GPNMYS and EPPNMYS. The assumed yield function corresponds to the N - M_z - M_y interaction curve for each column end:

$$f(p, m_z, m_y) = 1.15p^2 + m_z^2 + m_y^4 + 3.67p^2m_z^2 + 3p^6m_y^2 + 4.65m_z^4m_y^2 - c \tag{38}$$

where $p = (N - a_p)/N_p$, $m_z = (M_z - a_z)/M_{pz}$, $m_y = (M_y - a_y)/M_{py}$. N_p is the plastic axial capacity, M_{pz} is the plastic moment capacity about the strong axis, and M_{py} the plastic moment capacity about the weak axis. a_p , a_z and a_y are the components of the position vector for the yield surface center in the N - M_z - M_y space.

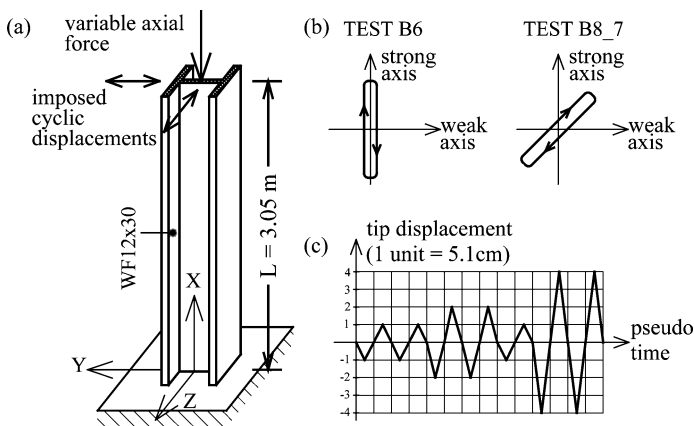


Fig. 4 (a) Cantilever column; (b) Tip displacement pattern for numerical tests B6 and B8_7; (c) Tip displacement history

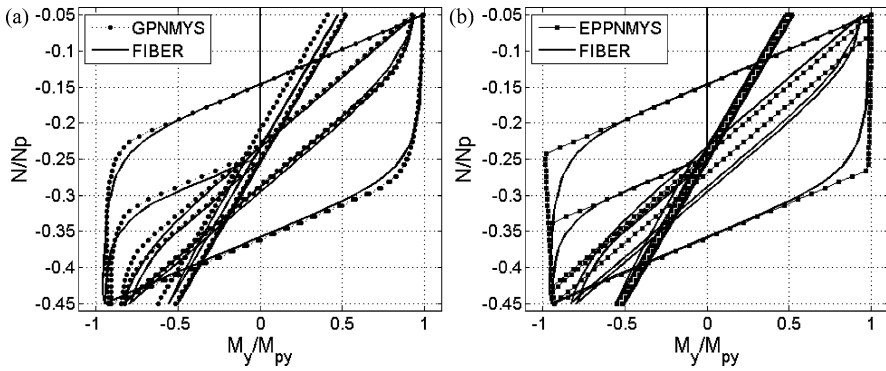


Fig. 5 Test B6: normalized bending moment—normalized axial force path (a) GPNMYS and FIBER; (b) EPPNMYS and FIBER element

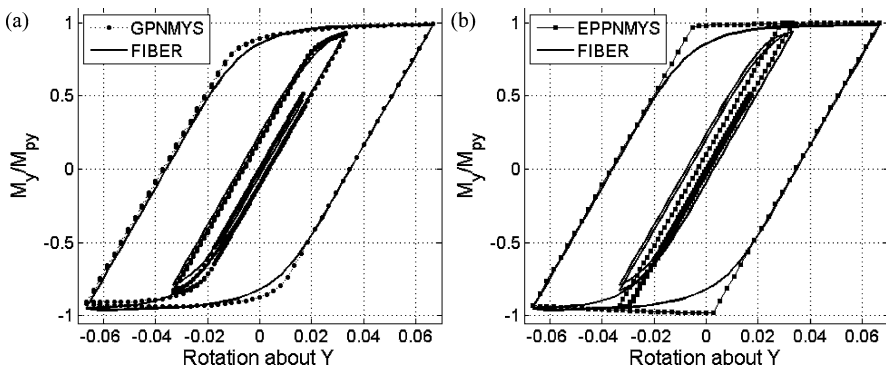


Fig. 6 Test B6: normalized bending moment—rotation relation (a) GPNMYS and FIBER; (b) EPPNMYS and FIBER element

Its displacement during loading accounts for kinematic hardening. The variable c controls the size of the yield surface. The coefficients in Eq. (38) are derived from a best fit of the yield surface of a W12×30 US steel cross section with $c = 1.0$ [4]. c is set equal to 0.3 in the GPNMYS element, and equal to 1.0 in the EPPNMYS model. Additional parameters of the GPNMYS model are: $\delta = 0.15$, $\beta = 0.70$ and $H_{iso} = H_{kin} = 0$. The simulation results are shown in Figs. 5 and 6 for Test B6 and in Figs. 7, 8, 9 and 10 for Test B8_7.

The elapsed times for the numerical tests were in the approximate ratio of 1:1.15:21 for EPPNMYS, GPNMYS and FIBER element, respectively.

To assess the ability of the GPNMYS element to represent the hardening response, the test B6 was repeated with a material having a kinematic hardening ratio of 3 % in the FIBER model. The kinematic hardening parameter H_{kin} of the GPNMYS model was set equal to 0.08, while the remaining parameters were kept at the values for the test B6 without hardening. The results are shown in Fig. 11.

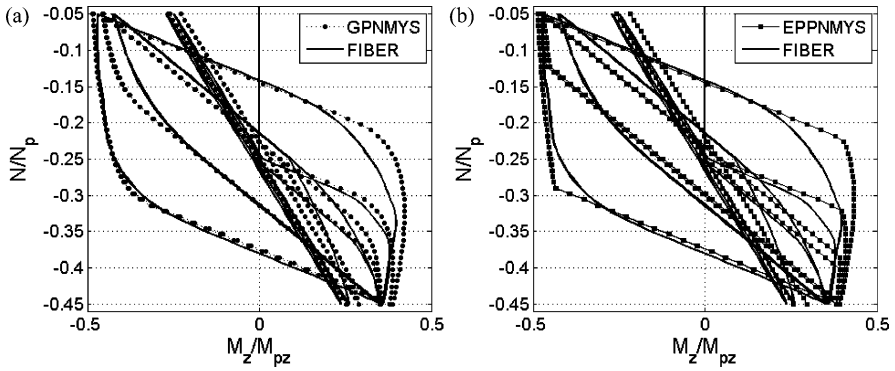


Fig. 7 Test B8_7: normalized bending moment about Z—normalized axial force path (a) GPNMYS and FIBER; (b) EPPNMYS and FIBER element

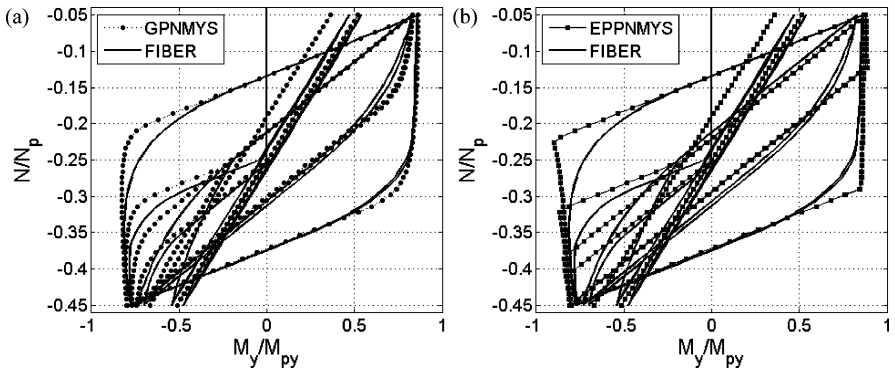


Fig. 8 Test B8_7: normalized bending moment about Y—normalized axial force path (a) GPNMYS and FIBER; (b) EPPNMYS and FIBER element

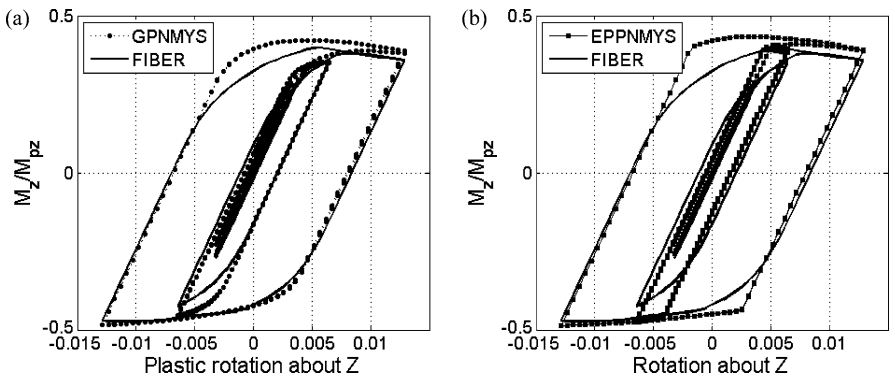


Fig. 9 Test B8_7: normalized bending moment about Z—rotation relation (a) GPNMYS and FIBER; (b) EPPNMYS and FIBER element

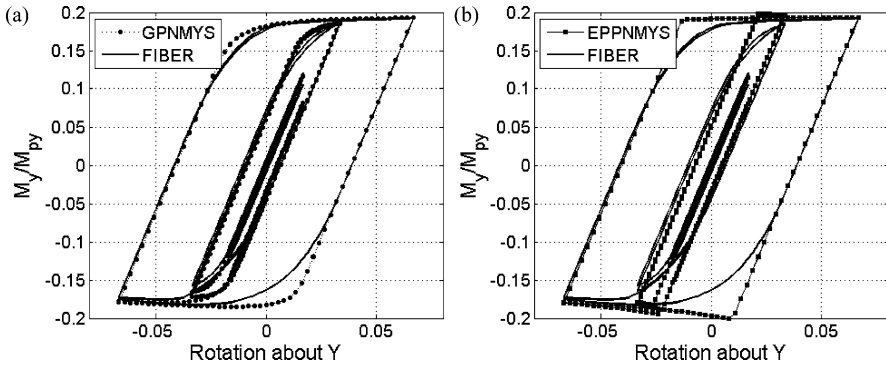


Fig. 10 Test B8_7: normalized bending moment about Y —rotation relation (a) GPNMYS and FIBER; (b) EPPNMYS and FIBER element

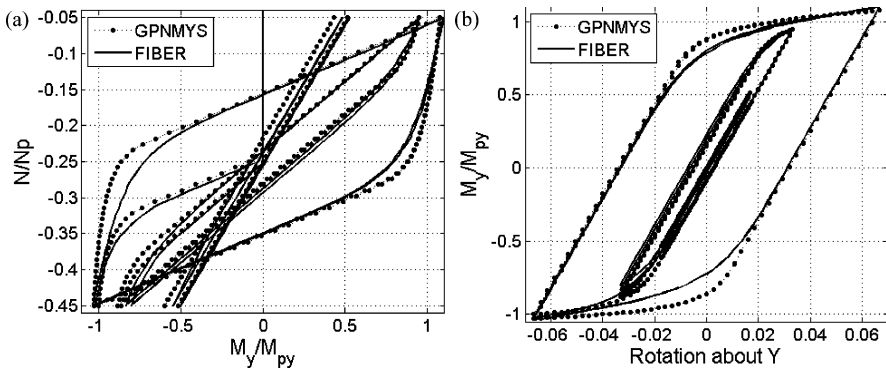


Fig. 11 Test B6 with hardening—GPNMYS and FIBER element: (a) normalized bending moment—normalized axial force path; (b) normalized bending moment about Y —rotation relation

4.2 Portal Frame Example

The second example deals with the portal frame in Fig. 12 from a study by El-Zanaty [23]. Gravity loads were applied first and kept constant while the lateral load of gradually increasing magnitude was applied. The residual stresses were not accounted for, because this effect cannot be represented with the EPPNMYS element. In the GPNMYS element this effect can be included with the size of the elastic domain [24].

The nonlinear geometry under large displacements is accounted for with the corotational formulation [25]. In the three models (GPNMYS, EPPNMYS and FIBER) a member of the portal frame is represented with one element. The material model is assumed to be elastic-perfectly plastic. Three different levels of vertical load are applied equal to 20 %, 40 % and 60 % of the ultimate vertical load

Fig. 12 El-Zanaty portal frame

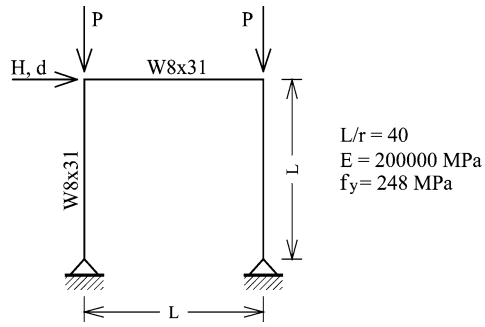
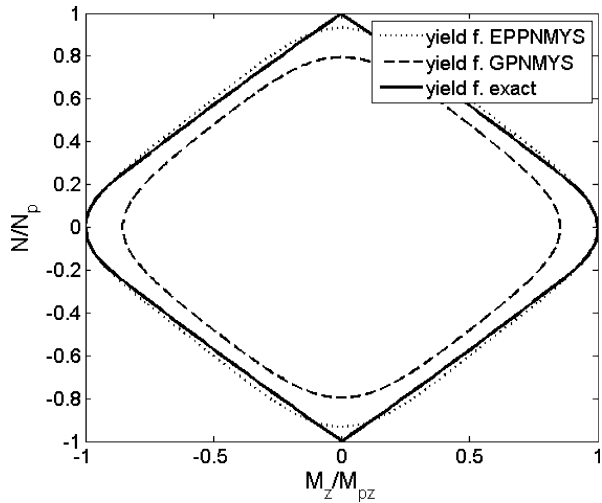


Fig. 13 Comparison of adopted $N-M_z$ yield function for EPPNMYS and GPNMYS elements with exact yield function for WF8×31 steel section



capacity of the frame. The results for bending about the major axis are given in Fig. 14.

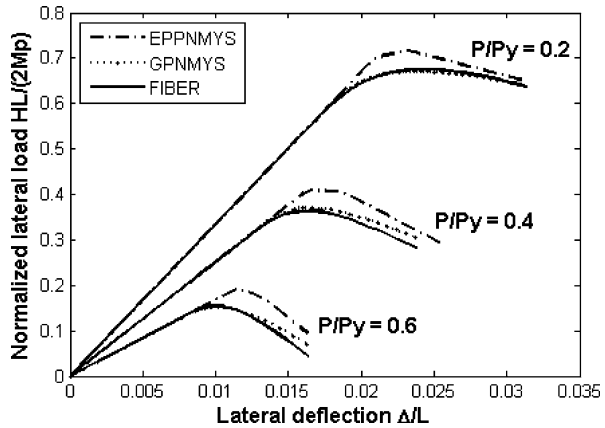
The same yield surface function as in the cantilever column example is used. For 2D bending about the strong axis it reduces to the following expression:

$$f(p, m_z) = 1.15p^2 + m_z^2 + 3.67p^2m_z^2 - c \tag{39}$$

where p and m_z are as defined earlier. The value of parameter c is equal to 1.0 in the EPPNMYS element, and equal to 0.73 for the GPNMYS element. Additional parameters of the GPNMYS model are: $\delta = 0.1$, $\beta = 0.27$. The numerically exact yield curve was established with a fiber section discretization of 288 fibers. It is contrasted with the assumed yield curves for the concentrated plasticity elements EPPNMYS and GPNMYS in Fig. 13.

As can be seen from the results, the response of the GPNMYS element is closer to the numerically exact FIBER solution on account of its ability to describe the gradual yielding of the cross section.

Fig. 14 Load-displacement response of El-Zanaty frame



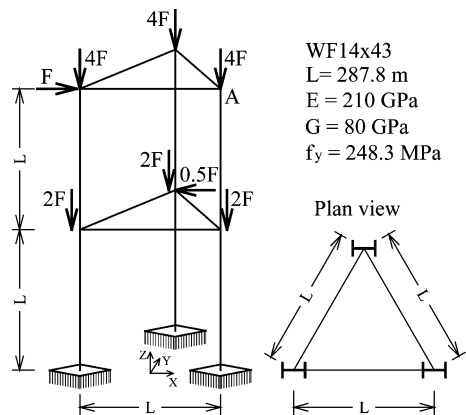
4.3 Two Story Frame Example

The third example is the two story space frame in Fig. 15 from a study by Vogel [26]. All columns and beams have a WF14×43 steel section. The frame is subjected to gradually increasing loading with the pattern in Fig. 15. The material model is elastic-perfectly plastic. The nonlinear geometry and the residual stress effects are not accounted for. As with the other examples, for the three models one element is used per member of the structural model.

For the two concentrated plasticity elements GPNMYS, EPPNMYS the yield function follows Eq. (38). The parameter c is equal to 0.7 in the GPNMYS model and equal to 1.0 in the EPPNMYS model. Additional parameters of the GPNMYS model are: $\delta = 0.02$, $\beta = 0.30$ and $H_{iso} = H_{kin} = 0$. The load-displacement response in the X-direction at point A is shown in Fig. 16.

The results with the EPPNMYS element are remarkably close to the results of the numerically exact FIBER solution, while the results of the GPNMYS element are virtually indistinguishable from the numerically exact solution.

Fig. 15 Vogel 3D frame



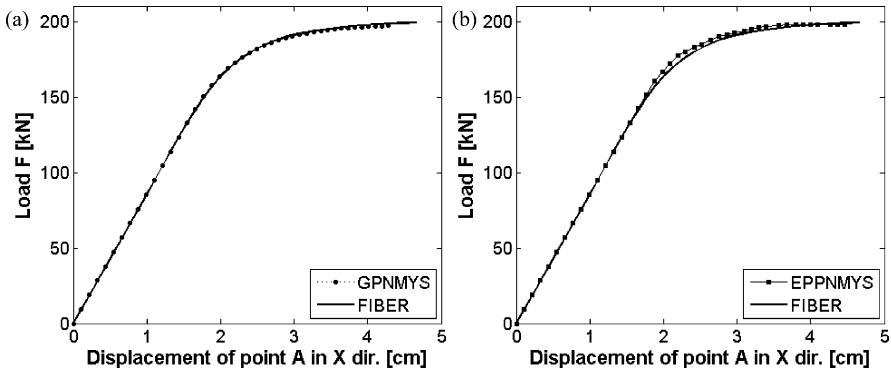
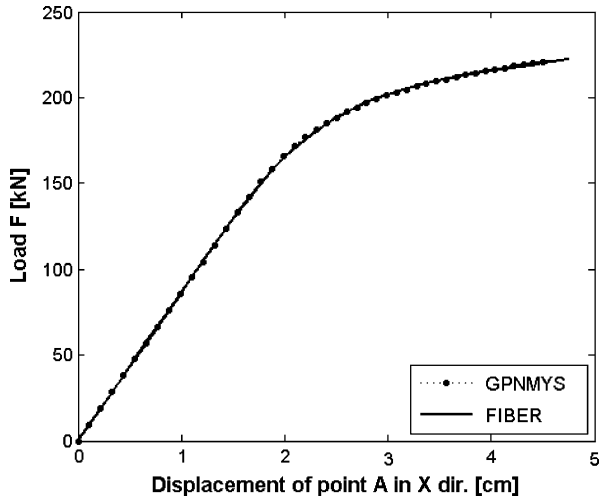


Fig. 16 Load-displacement response of Vogel frame—without material hardening: (a) GPNMYS and FIBER; (b) EPPNMYS and FIBER element

Fig. 17 Load-displacement response of Vogel frame—with isotropic hardening, GPNMYS and FIBER element



The same frame is also used to study for the effect of material hardening. Since the EPPNMYS element is not able to account for hardening, only the results of the GPNMYS element and the numerically exact FIBER element are compared. The isotropic hardening ratio is assumed equal to 3 % for the steel material in the FIBER model. The isotropic hardening parameter H_{iso} of the GPNMYS model is set equal to 0.008, while the remaining parameters are those for the case without hardening.

The results in Fig. 17 show that the solution of the GPNMYS model matches the numerically exact FIBER model response perfectly.

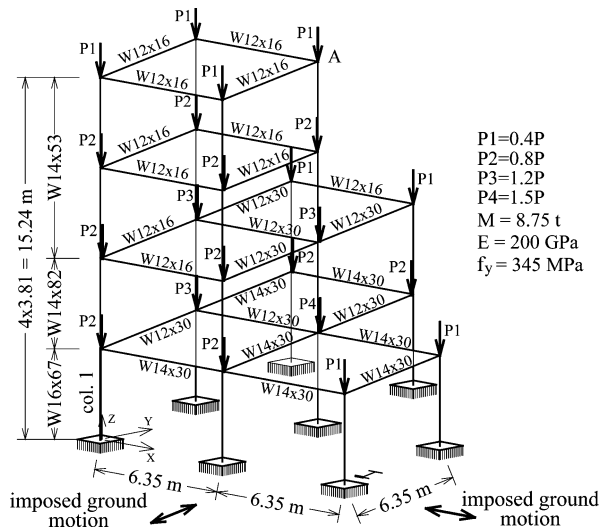
4.4 Four Story Frame Example

The last example deals with the 3D nonlinear dynamic response of the steel frame in Fig. 18 [21]. The frame was subjected first to the static gravity loading in Fig. 18 with $P = 289$ kN, and then to a biaxial ground excitation with the 1940 El Centro earthquake record scaled to a peak ground acceleration of 0.9565g.

In the three models the first story columns are modeled with the EPPNMYS, GPNMYS and FIBER elements, respectively, while the other members are assumed to remain linear elastic, so that elastic 3D frame elements can be used. The yield function and the other parameters of the EPPNMYS and GPNMYS elements are the same as for the cantilever column example without hardening. The mass is lumped at each node with a value of 8.75 t. Rayleigh damping is assumed in the analysis with a viscous damping ratio of 4 % for the first two vibration modes of the elastic structure.

The analysis results are presented in Fig. 19 and Table 1. The bending moment history for element 1 at the fixed end is shown in Fig. 19. Because of the significant overturning moment the axial compressive force of the column varies between 9 % and 48 % of the plastic axial capacity N_p . The response similarity between EPPNMYS and GPNMYS models is evident, since both concentrated plasticity elements are based on the same principles of plasticity theory. The ability to represent the gradual yielding of the cross section brings the response of the GPNMYS element closer to the numerically exact FIBER solution. For the same reason the errors of the global frame response in Table 1 in terms of the extreme roof displacements in the X- and Y-direction at point A, are smaller for the GPNMYS model.

Fig. 18 Four-story steel frame



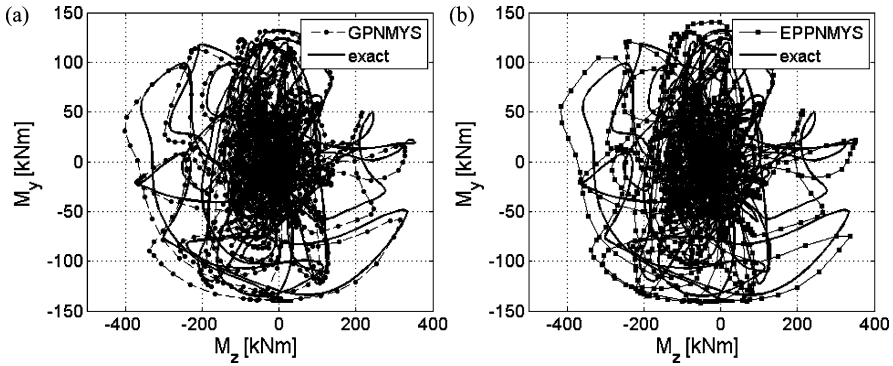


Fig. 19 Bending moment path in column 1 at fixed base: (a) GPNMYS and FIBER; (b) EPPNMYS and FIBER element

Table 1 Extreme roof displacement values at point A for the nonlinear dynamic response of the four-story steel frame to a biaxial El Centro ground acceleration history

Displacement of point A (cm)	EPPNMYS	GPNMYS	FIBER	Error (%) EPPNMYS	Error (%) GPNMYS
X direction—Max	53.39	49.74	48.75	9.52	2.03
X direction—Min	-23.60	-24.15	-24.01	1.71	0.58
Y direction—Max	37.34	36.01	37.18	0.43	3.15
Y direction—Min	-45.88	-45.00	-45.07	1.80	0.16

5 Summary and Conclusions

This chapter presented a three-dimensional nonlinear beam-column element for the simulation of the global and local response of frames under monotonic and cyclic loading. The element belongs to the family of concentrated plasticity elements, with the behavior of plastic hinges at the element ends based on yield and limit surfaces for force resultants. The inelastic response of the hinges is described by extension of generalized material plasticity concepts to force resultants. The element takes into account the interaction of the axial force with the bending moments about the principal section axes and the hardening behavior. The gradual yielding of the cross section is described by the asymptotic approach of the force resultants to the limit surface. The model is relatively simple and uses two parameters with clear physical meaning. With the implementation of the return mapping algorithm with quadratic numerical convergence it is computationally robust and very efficient.

The capabilities of the proposed element are assessed with four examples by comparing its response with the response of an elastic perfectly plastic resultant plasticity element, and with the response of a fiber beam-column element, which is assumed to represent the numerically exact solution. The proposed element proves significantly more versatile than the perfectly-plastic element for the simulation of

the hysteretic frame response under complex loading conditions without significant increase in computational effort. This effort is approximately 15 % of the computational effort of the fiber beam-column element with an adequate level of discretization. The demand on memory, data storage and data processing is also reduced significantly. The proposed element is consequently suitable for the earthquake response analysis of large frame structures under a portfolio of acceleration records, as required by current codes of performance-based design.

Acknowledgements The first author thanks the Ministry of Science of the Republic of Serbia for financial support under the project TR36046.

References

1. Lubliner J, Taylor RL, Auricchio F (1993) A new model of generalized plasticity and its numerical implementation. *Int J Solids Struct* 30(22):3171–3184
2. Auricchio F, Taylor RL (1995) Two material models for cyclic plasticity—nonlinear kinematic hardening and generalized plasticity. *Int J Plast* 11(1):65–98
3. Auricchio F, Taylor RL (1994) A generalized elastoplastic plate theory and its algorithmic implementation. *Int J Numer Methods Eng* 37(15):2583–2608. doi:[10.1002/nme.1620371506](https://doi.org/10.1002/nme.1620371506)
4. Orbison JG, McGuire W, Abel JF (1982) Yield surface applications in nonlinear steel frame analysis. *Comput Methods Appl Mech Eng* 33(1–3):557–573. doi:[10.1016/0045-7825\(82\)90122-0](https://doi.org/10.1016/0045-7825(82)90122-0)
5. Hilmy SI, Abel JF (1985) Material and geometric nonlinear dynamic analysis of steel frames using computer graphics. *Comput Struct* 21(4):825–840. doi:[10.1016/0045-7949\(85\)90159-2](https://doi.org/10.1016/0045-7949(85)90159-2)
6. Powell GH, Chen PF-S (1986) 3D beam-column element with generalized plastic hinges. *J Eng Mech* 112(7):627–641. doi:[10.1061/\(asce\)0733-9399\(1986\)112:7\(627\)](https://doi.org/10.1061/(asce)0733-9399(1986)112:7(627))
7. Hajjar JF, Gourley BC (1997) A cyclic nonlinear model for concrete-filled tubes. I: Formulation. *J Struct Eng* 123(6):736
8. Hajjar JF, Gourley BC (1997) A cyclic nonlinear model for concrete-filled tubes. II: Verification. *J Struct Eng* 123(6):745
9. Iu CK, Bradford MA, Chen WF (2009) Second-order inelastic analysis of composite framed structures based on the refined plastic hinge method. *Eng Struct* 31(3):799–813. doi:[10.1016/j.engstruct.2008.12.007](https://doi.org/10.1016/j.engstruct.2008.12.007)
10. Kitipornchai S, Zhu K, Xiang Y, Al-Bermani FGA (1991) Single-equation yield surfaces for monosymmetric and asymmetric sections. *Eng Struct* 13(4):366–370. doi:[10.1016/0141-0296\(91\)90023-6](https://doi.org/10.1016/0141-0296(91)90023-6)
11. Skallerud B (1993) Yield surface formulations for eccentrically loaded planar bolted or welded connections. *Comput Struct* 48(5):811–818. doi:[10.1016/0045-7949\(93\)90502-5](https://doi.org/10.1016/0045-7949(93)90502-5)
12. Chen WF, Atsuta T (1977) *Theory of beam-columns*. McGraw-Hill, New York
13. Dafalias YF, Popov EP (1977) Cyclic loading for materials with a vanishing elastic region. *Nucl Eng Des* 41(2):293–302. doi:[10.1016/0029-5493\(77\)90117-0](https://doi.org/10.1016/0029-5493(77)90117-0)
14. El-Tawil S, Deierlein GG (2001) Nonlinear analysis of mixed steel-concrete frames. I: Element formulation. *J Struct Eng* 127(6):647
15. El-Tawil S, Deierlein GG (2001) Nonlinear analysis of mixed steel-concrete frames. II: Implementation and verification. *J Struct Eng* 127(6):656
16. Jin J, El-Tawil S (2003) Inelastic cyclic model for steel braces. *J Eng Mech* 129(5):548–557
17. Simo JC, Hughes TJ (1998) *Computational inelasticity*. Springer, New York
18. Kostic SM, Filippou FC, Lee C-L (2009) Evaluation of resultant plasticity and fiber beam-column elements for the simulation of the 3D nonlinear response of steel structures. In: 2nd international conference on computational methods in structural dynamics and earthquake engineering—COMPdyn, Island of Rhodes, 22–24 June 2009

19. Filippou FC, Fenves GL (2004) Methods of analysis for earthquake-resistant structures. In: Bozorgnia Y, Bertero VV (eds) Earthquake engineering: from engineering seismology to performance-based engineering. CRC Press, Boca Raton
20. Filippou FC, Constantinides M (2004) FEDEASLab getting started guide and simulation examples (trans: Engineering DoCaE). University of California, Berkeley
21. Kostic SM, Filippou FC (2010) Section discretization considerations in fiber beam-column elements for nonlinear frame analysis. Pacific Earthquake Engineering Research Center, College of Engineering, University of California, Berkeley (to be published)
22. Kostic SM, Filippou FC (2012) Section discretization of fiber beam-column elements for cyclic inelastic response. *J Struct Eng* 138(5):592–601. doi:[10.1061/\(ASCE\)ST.1943-541X.0000501](https://doi.org/10.1061/(ASCE)ST.1943-541X.0000501)
23. El-Zanaty MH, Murray DW, Bjorhovde R (1980) Inelastic behavior of multistory steel frames. Univ. of Alberta, Edmonton
24. King WS, Chen WF (1994) Practical second-order inelastic analysis of semirigid frames. *J Struct Eng* 120:2156–2175
25. Crisfield MA (1991) Non-linear finite element analysis of solids and structures. Wiley, Chichester
26. Chiorean CG (2009) A computer method for nonlinear inelastic analysis of 3D semi-rigid steel frameworks. *Eng Struct* 31(12):3016–3033. doi:[10.1016/j.engstruct.2009.08.003](https://doi.org/10.1016/j.engstruct.2009.08.003)

Floor Response Spectra for Moderately Heavy Nonstructural Elements Attached to Ductile Frame Structures

Christoph Adam, Thomas Furtmüller, and Lukas Moschen

Abstract This paper presents a methodology for predicting the seismic peak response of vibratory single-degree-of-freedom (SDOF) nonstructural elements with simple measures. The non-structural elements may be attached to both elastic and ductile load-bearing frame structures. The methodology is based on modified modal superposition of floor response spectra for SDOF oscillators on SDOF supporting structures. Dynamic interaction between the substructures is considered, and thus, the peak response of moderately heavy nonstructural elements can be assessed. The presented results are based on numerical simulations involving 44 ground motion records of the ATC63 far-field set and subsequent statistical evaluation. For several example problems “exact” results are contrasted with outcomes of the proposed methodology. This comparison provides evidence that the proposed methodology delivers sufficient accurate predictions of the seismic peak response of simple vibration-prone nonstructural elements on ductile load-bearing structures.

Keywords Ductile supporting structure · Inelastic floor response spectrum · Nonstructural element · Modified modal superposition

1 Introduction

Strong motion earthquakes of the last decades have demonstrated that the seismic resistance of load-bearing structures designed according to actual guidelines is in most cases sufficient. However, very often the serviceability of buildings was significantly impaired as a consequence of severe damage of nonstructural elements.

C. Adam (✉) · L. Moschen
Unit of Applied Mechanics, University of Innsbruck, 6020 Innsbruck, Austria
e-mail: christoph.adam@uibk.ac.at

L. Moschen
e-mail: lukas.moschen@uibk.ac.at

T. Furtmüller
ThyssenKrupp Presta AG, Eschen, Liechtenstein
e-mail: thomas.furtmueller@gmail.com

Additionally to the economic loss, damaged nonstructural elements represent a substantial safety risk for people in and around those buildings subjected to seismic excitation. Examples of such elements are large antennas, suspended ceilings, partition walls, supply lines, electrical equipment, etc., i.e. all parts of the building, which do not belong to the load-bearing system. Vibration-prone nonstructural elements are particularly vulnerable to damage, because they are exposed to the amplified response of the seismic excited supporting structure. Moreover, they exhibit a significant smaller mass and stiffness than the load-bearing structure, and thus natural periods of both substructures can become tuned, i.e. closely spaced. In the literature nonstructural elements are also referred to as secondary structures/elements, or nonstructural components/containments. Synonyms for load-bearing system are primary structure/system and supporting structure.

Many rational methods have been developed in an effort to predict the dynamic response of nonstructural elements. Villaverde [1] provides a comprehensive state-of-the-art report of methods for the seismic analysis of vibration-prone nonstructural elements. However, there still exists a need for methodologies of analysis, which give an accurate prediction of the seismic response without performing expensive time history computations of the coupled system consisting of non-structural elements and the supporting structure. This can be cumbersome or even impossible, because buildings may be equipped with a large number of vibration-prone nonstructural elements. Moreover, numerical difficulties may arise due to the fact that the mass of nonstructural elements is in general much smaller than the mass of the supporting structure. Thus, most of the developed procedures are based on simplifications such as omitting the interaction between supporting structure and nonstructural element [1]. As a prominent example the floor response spectrum method is mentioned [2, 3], where the peak response of single-degree-of-freedom (SDOF) nonstructural elements is plotted against its period of vibration. Floor response spectra are in general derived without considering dynamic interaction between the substructures. Thus, when a mode of the supporting structure becomes closely spaced to the period of the nonstructural element, this approach leads to satisfactory peak response predictions only for very light nonstructural elements. A further issue is non-classical damping, because in many applications the supporting structure and the nonstructural element exhibit different inherent viscous damping [4]. As mentioned by Villaverde [1] the effect of inelastic deformations of the load-bearing structure on the dynamic response of nonstructural elements is not well understood. The results of several numerical and experimental investigations [5–12] have shown that a yielding supporting structure may have a severe impact on the dynamic response of nonstructural elements. However, only a few studies are based on a set of real ground motions, e.g. [9–12], which permits a statistical quantification of the response. Medina et al. [10, 11] introduce an acceleration modification factor to quantify the effect of inelastic deformations of earthquake excited load-bearing structures on the acceleration response of light nonstructural elements. Since their studies are restricted to light elements, they do not consider dynamic interaction between the substructures. Adam and Furtmüller [12] have assessed and quantified the

effect of dynamic interaction and tuning between inelastic SDOF supporting structures and elastic SDOF nonstructural elements. They have derived floor response spectra based on numerical simulations involving a set of 40 earthquake records.

In this study a modified floor response spectrum method is presented, where dynamic interaction between supporting structures and simple nonstructural elements is considered approximately. Thus, the response of moderately heavy nonstructural elements attached to elastic as well as inelastic multi-degree-of-freedom (MDOF) supporting structures can be predicted with simple measures. The methodology is based on the modal decomposition of the load bearing structure and floor response spectra of simple oscillators attached to SDOF supporting structures. Results of preliminary studies have been presented in [13, 14]. It is demonstrated that the proposed methodology is simple to apply and yet sufficiently accurate to estimate the seismic peak response of simple vibration-prone nonstructural elements.

2 Single-Degree-of-Freedom Supporting Structures

2.1 Structural Model and Governing Equations

In the first part of the present study the load-bearing structure is modeled as an SDOF oscillator composed of a lumped mass m_p , a viscous dashpot damper with damper constant c_p , and an elastic-plastic spring with initial stiffness k_p . A bilinear hysteretic loop of the spring according to Fig. 1(a) represents non-degrading nonlinear behavior of the supporting structure under seismic excitation. The hardening ratio between the post yielding stiffness and the initial stiffness is denoted by α . A linear elastic SDOF oscillator composed of lumped mass m_s , linear elastic spring with stiffness k_s , and viscous dashpot damper with damper constant c_s is utilized to characterize the vibration-prone nonstructural element. Connected in series both substructures form a two-degree-of freedom (2DOF) oscillator, as shown in Fig. 1(b). Base acceleration \ddot{x}_g excites the coupled system to seismic vibrations. The equations of motion of this 2DOF system, expressed by the relative displacements x_p (with respect to the base displacement x_g) and x_s (with respect to the displacement of the supporting structure $x_g + x_p$) of the lumped masses m_p and m_s , respectively, are given by

$$\begin{aligned} \begin{bmatrix} 1 + \bar{m} & \bar{m} \\ 1 & 1 \end{bmatrix} \begin{pmatrix} \ddot{x}_p \\ \ddot{x}_s \end{pmatrix} + \begin{bmatrix} 2\zeta_p\omega_p & 0 \\ 0 & 2\zeta_s\omega_s \end{bmatrix} \begin{pmatrix} \dot{x}_p \\ \dot{x}_s \end{pmatrix} + \begin{bmatrix} \omega_p^2 & 0 \\ 0 & \omega_s^2 \end{bmatrix} \begin{pmatrix} x_p \\ x_s \end{pmatrix} \\ - \begin{pmatrix} \omega_p^2 \\ 0 \end{pmatrix} x_p^{pl} = - \begin{pmatrix} 1 + \bar{m} \\ 0 \end{pmatrix} \ddot{x}_g \end{aligned} \quad (1)$$

where

$$\bar{m} = m_s/m_p, \quad \bar{m} \ll 1 \quad (2)$$

denotes the ratio of mass of the nonstructural element and of the supporting structure, which is in general significantly smaller than one: $\bar{m} \ll 1$. The natural circular

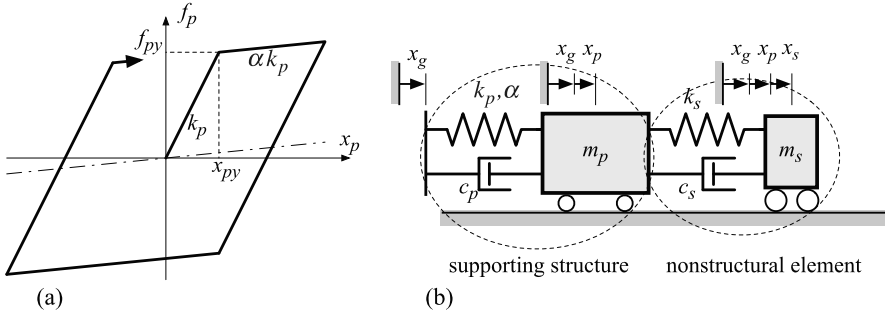


Fig. 1 (a) Bilinear cyclic behavior of the SDOF supporting structure. (b) SDOF supporting structure equipped with SDOF nonstructural element

frequencies ω_p , ω_s and damping coefficients ζ_p , ζ_s of the decoupled supporting structure and the decoupled nonstructural element, respectively, read as:

$$\begin{aligned}\omega_p &= \sqrt{k_p/m_p}, & \omega_s &= \sqrt{k_s/m_s} \\ \zeta_p &= c_p/(2\omega_p m_p), & \zeta_s &= c_s/(2\omega_s m_s)\end{aligned}\quad (3)$$

x_p^{pl} denotes the plastic part of deformation of x_p .

For a given ground motion record \ddot{x}_g the characteristic response parameters of the system according to Fig. 1(b) are the mass ratio \bar{m} , damping coefficients ζ_p , ζ_s , periods of the decoupled substructures $T_s = 2\pi/\omega_s$, $T_p = 2\pi/\omega_p$, strain hardening coefficient α , and ductility ratio μ of the supporting structure. Ductility μ characterizes the magnitude of inelastic deformations, and it is defined as the ratio of the absolute maximum relative displacement $\max|x_p|$ of the supporting structure in a single time history analysis related to the corresponding displacement x_{py} at the onset of yielding

$$\mu = \max|x_p|/x_{py}\quad (4)$$

2.2 Floor Response Spectra

In the most general approach, for a given ground motion record \ddot{x}_g the equations of motion, Eq. (1), are solved together with the constitutive equations in a nonlinear time history analysis. The results are response time histories $x_p(t)$ and $x_s(t)$.

For small mass ratios $\bar{m} \leq 10^{-3}$ the interaction between both substructures is of minor significance [6], if the natural frequencies of both substructures are detuned, i.e. ω_p and ω_s are well separated. Very small mass ratios $\bar{m} \lll 1$ may even lead to numerical instabilities in a time history analysis based on Eq. (1). Thus, in a simplified procedure the interaction between both substructures is neglected. Thereby, in a first step the response x_p of the SDOF supporting structures without attached nonstructural element is determined. Subsequently, the response x_s of the SDOF

secondary system is analyzed, where the total acceleration ($\ddot{x}_g + \ddot{x}_p$) of the mass m_p is the input excitation. This simplified approach is common in engineering practice, however, for moderately heavy nonstructural elements it leads to considerable over-conservative results, if the frequencies of the substructures are tuned.

In design practice most applications require the information of the peak acceleration and the peak displacement of the nonstructural element only. The representation of the peak response plotted against the period T_s of the nonstructural element is referred to as floor response spectrum. In the following floor response spectra for moderately heavy secondary oscillators attached to elastic and inelastic SDOF supporting structures are derived. Since the underlying system of these spectra is the 2DOF oscillator depicted in Fig. 1(b), in the following these spectra are denoted as 2DOF floor response spectra.

The seismic input of the presented spectra is based on a set of ordinary ground motions with similar overall characteristics. The selected ATC63 far-field set contains 44 ground motions (two records from 22 earthquakes), which were recorded on NEHRP site classes C (soft rock) and D (stiff soil) [15]. The records of this set originate from severe seismic events of moment magnitude between 6.5 and 7.6 and closest distance to the fault rupture larger than 10 km. Thereby, only strike-slip and reverse sources are considered.

Based on Eq. (1) for each 2DOF system with fixed parameters \bar{m} , T_p , T_s , ζ_p , ζ_s , μ , α , and each earthquake record fully coupled time history analyses are performed. Floor response spectra considering inelastic behavior of the supporting structure are derived for pre-assigned target ductilities. Thus, in each analysis the yield strength of the inelastic spring has to be determined iteratively to give this target ductility. The relative peak displacement of the nonstructural element gives for a certain set of structural parameters one value of the displacement floor response spectrum, the total peak acceleration renders one value of the acceleration floor response spectrum,

$$F_{ds,i}^{(2DOF)} = \max |x_s|_i, \quad F_{as,i}^{(2DOF)} = \max |\ddot{x}_g + \ddot{x}_p + \ddot{x}_s|_i, \quad i = 1, \dots, 44 \quad (5)$$

The statistical evaluation of the individual response spectra for each of the considered 44 ground motions leads to median, 16th percentile, and 84th percentile displacement floor response spectra $F_{ds,med}^{(2DOF)}$, $F_{ds,16}^{(2DOF)}$, $F_{ds,84}^{(2DOF)}$, and to corresponding acceleration floor response spectra. Subsequently, the focus is on median spectra.

Displacement and acceleration floor response spectra may be presented in three-dimensional form as function of the decoupled periods T_p and T_s of the supporting structure and the nonstructural element, respectively. Exemplarily, Figs. 2(a) and 2(b) show the contour plot of a median displacement and a median acceleration floor response spectrum for unlimited elastic structures with parameters $\bar{m} = 0.05$, $\zeta_p = 0.05$, $\zeta_s = 0.01$, $\alpha = 0.03$. Both figures verify that interaction between both substructures is most pronounced for $T_p \approx T_s$. Response peaks occur for unlimited elastic behavior, if period T_s is slightly larger than period T_p . While the peak acceleration becomes a maximum for very stiff substructures, peak displacements increase with growing tuned periods. The illustration of the response in terms of a contour plot provides an excellent overview of the global dynamic behavior, however, for design purposes a two-dimensional representation of floor response spectra

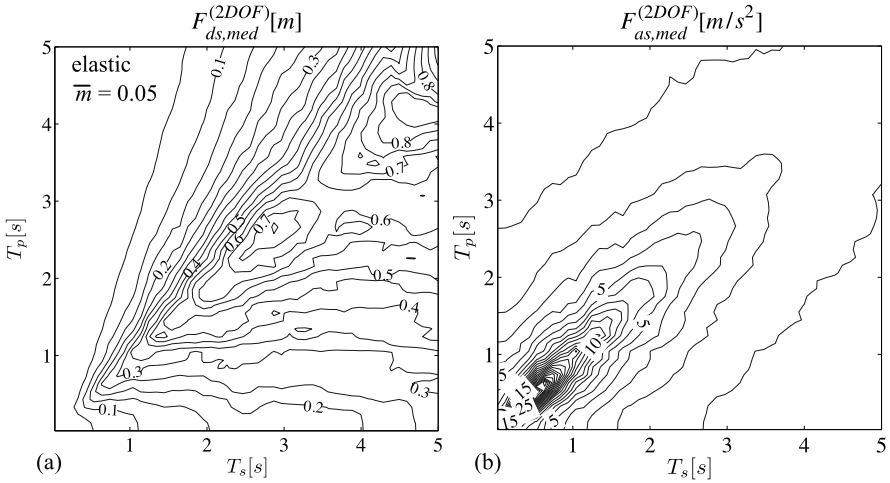
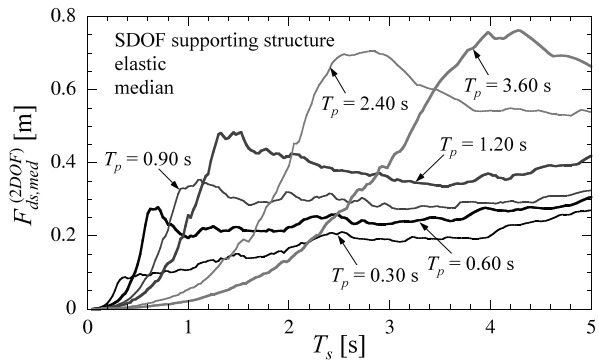


Fig. 2 (a) Displacement and (b) acceleration floor response spectra. Elastic SDOF supporting structure with the following parameters: $\bar{m} = 0.05$, $\zeta_p = 0.05$, $\zeta_s = 0.01$

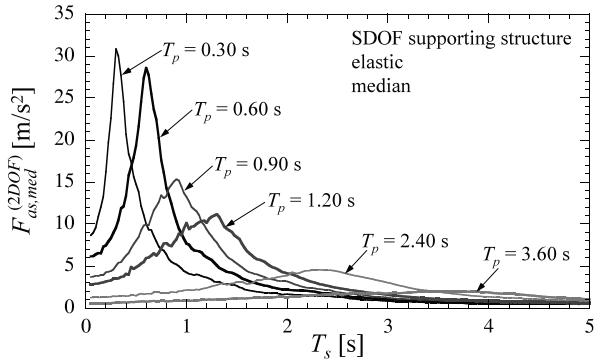
Fig. 3 Displacement floor response spectra. Elastic SDOF supporting structure with the following parameters: $\bar{m} = 0.05$, $\zeta_p = 0.05$, $\zeta_s = 0.01$. Selected periods of the supporting structure



for discrete structural periods T_p is more appropriate. Hence, in Figs. 3 and 4 for the periods $T_p = 0.30$ s, 0.60 s, 0.90 s, 1.20 s, 2.40 s, 3.60 s corresponding two-dimensional floor response spectra are depicted. They represent a vertical section in Figs. 2(a) and 2(b), respectively, at these periods.

The impact of inelastic material behavior on the response of nonstructural elements is visualized in Figs. 5, 6 and 7. Figure 5(a) represents median peak displacements of a nonstructural element attached to an elastic-plastic SDOF supporting structure with a target ductility of 4. All other parameters are the same as before. It is readily observed that inelastic deformations lead to a displacement mitigation of more than 50 % compared to the unlimited elastic response, compare Fig. 2(a) with Fig. 5(a), and Fig. 3 with Fig. 6. Moreover, the domain of resonance is shifted. For a given structural period of T_p (of the corresponding elastic system) the effective inelastic period is elongated, and thus peak displacements are shifted to larger val-

Fig. 4 Acceleration floor response spectra. Elastic SDOF supporting structure with the following parameters: $\bar{m} = 0.05$, $\zeta_p = 0.05$, $\zeta_s = 0.01$. Selected periods of the supporting structure



ues of the elastic period T_s of the nonstructural element. Figure 5(a) proves evidence that the maxima of median peak displacements constitute a plateau with almost constant peak displacements in the domain $T_s > T_p$ (i.e. on the right hand side of the diagonal $T_s = T_p$). Peak accelerations are reduced considerably compared to elastic structural behavior, however, maxima still occur at resonance of the elastic system: $T_p \approx T_s$, see Figs. 4 and 7.

Since the primary objective of the presented study is the prediction of floor response spectra for nonstructural elements attached to multi-story frame structures, 2DOF floor response spectra will not be discussed in further detail. Note that in Adam and Furtmüller [12] the effect of interaction between both substructures has been assessed and quantified based on an intensive study on 2DOF floor response spectra including inelastic deformations of the supporting SDOF structure.

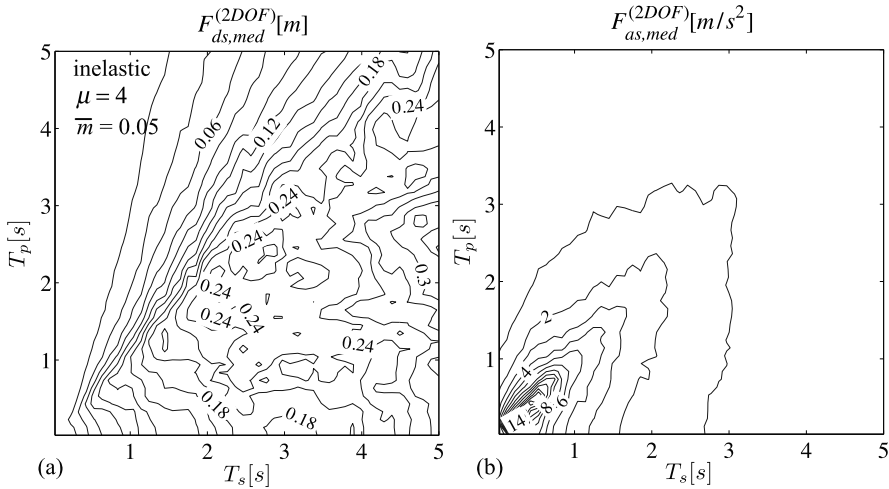


Fig. 5 (a) Displacement and (b) acceleration floor response spectra. Inelastic SDOF supporting structure with the following parameters: $\bar{m} = 0.05$, $\zeta_p = 0.05$, $\zeta_s = 0.01$, $\mu = 4$

Fig. 6 Displacements floor response spectra. Inelastic SDOF supporting structure with the following parameters: $\bar{m} = 0.05$, $\zeta_p = 0.05$, $\zeta_s = 0.01$, $\mu = 4$. Selected periods of the supporting structure

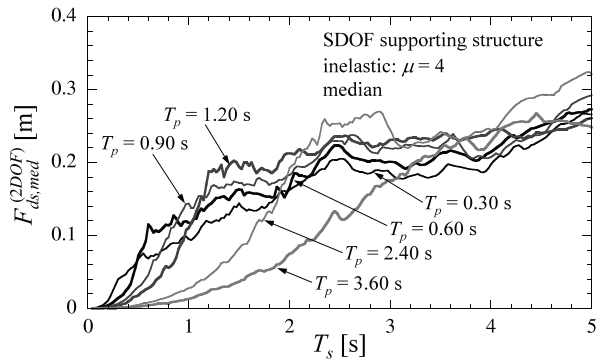
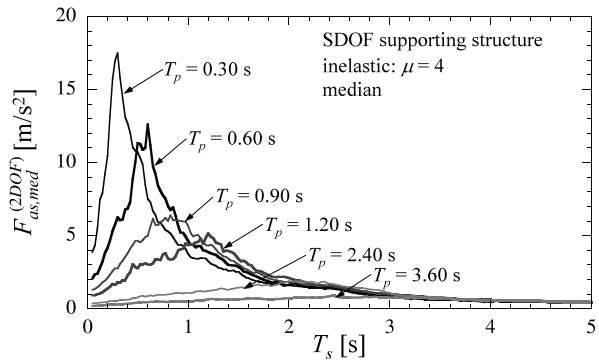


Fig. 7 Acceleration floor response spectra. Inelastic SDOF supporting structure with the following parameters: $\bar{m} = 0.05$, $\zeta_p = 0.05$, $\zeta_s = 0.01$, $\mu = 4$. Selected periods of the supporting structure



3 Multi-Degree-of-Freedom Supporting Structures

3.1 Structural Model and Governing Equations

In the second part of the present study the supporting structure is an elastic-plastic regular planar multi-story moment resisting frame structure with N stories, where the mass is lumped at story corners as shown in Fig. 8(a). The horizontal story displacements x_i , $i = 1, \dots, N$, relative to the seismic base displacement x_g are the N dynamic degrees-of-freedom of the supporting structure, which are assembled in vector \mathbf{x} . The k th floor is equipped with an elastic SDOF vibratory nonstructural element of mass m_s , stiffness k_s , and viscous damping parameter c_s . The horizontal displacement x_s of this element with respect to the displacement of the k th story ($x_g + x_k$) represents the $(N + 1)$ th degree-of-freedom of the coupled system. The coupled set of equations of motion are separated into the equations of the MDOF frame structure

$$\mathbf{M}\ddot{\mathbf{x}} + m_s(\ddot{x}_k + \ddot{x}_s)\mathbf{g}_k + \mathbf{C}\dot{\mathbf{x}} + \mathbf{K}\mathbf{x} - \mathbf{G}\boldsymbol{\varphi}^p = -(\mathbf{M}\mathbf{e} + m_s\mathbf{g}_k)\ddot{x}_g \tag{6a}$$

and of the vibratory SDOF nonstructural element

$$m_s(\ddot{x}_k + \ddot{x}_s) + c_s\dot{x}_s + k_s x_s = -m_s\ddot{x}_g \tag{6b}$$

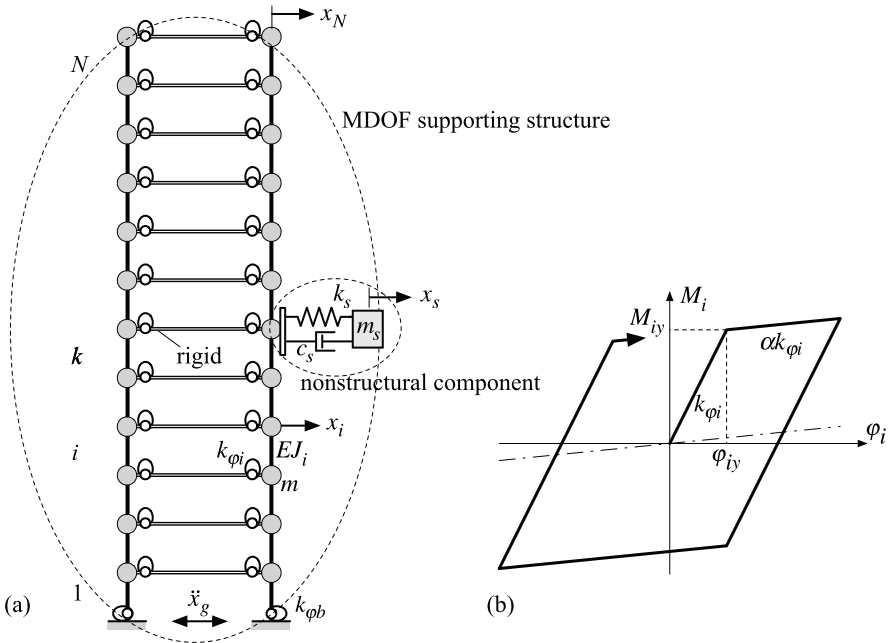


Fig. 8 (a) Generic multi-story frame structure equipped with an SDOF nonstructural element. (b) Bilinear cyclic behavior of the rotational springs

\mathbf{M} , \mathbf{C} , \mathbf{K} are the mass matrix, damping matrix, and initial stiffness matrix, respectively, dimension $[N \times N]$, of the frame structure. The damping matrix \mathbf{C} is proportional to \mathbf{M} and \mathbf{K} , which leaves the coupled system non-classically damped. Influence vector \mathbf{e} $[N]$ represents the displacements of the story masses resulting from a static unit ground displacement in direction of the seismic excitation. In the considered generic frame model inelastic deformations are confined to bilinear rotational springs located at the base and at both ends of the beams, compare with Fig. 8(a). For such a concentrated plasticity model vector $\boldsymbol{\varphi}^P$ contains the plastic chord rotations of the elastic-plastic springs. Alternatively, in a fiber model vector $\boldsymbol{\varphi}^P$ would contain the plastic curvatures, which are distributed along the frame or, in a plastic hinge model, plastic curvatures are confined to pre-selected locations of the frame. $\boldsymbol{\varphi}^P$ is of dimension $[M]$, where M is the number of discrete frame locations, which may exhibit plastic deformations. Matrix \mathbf{G} is the rectangular influence matrix of plastic spring chord rotations (plastic curvatures) of dimension $[M \times N]$. The nonstructural element is coupled to the supporting structure via the influence vector \mathbf{g}_k of dimension $[N]$, whose k th component is one, and all other components are zero. This vector identifies the location of the nonstructural element in the k th story of the load-bearing structure.

3.2 Floor Response Spectra

The evaluation of floor response spectra for vibratory nonstructural elements on inelastic multi-degree-of-freedom (MDOF) supporting structures is an expensive and time-consuming venture, in particular if interaction between the substructures cannot be neglected. It necessitates the time history solution of the complete set of coupled non-classically damped equations (6a)–(6b) together with the constitutive equations of the inelastic springs. Again, relative displacement and total acceleration floor response spectra according to Eq. (5) are derived for the ATC63-FF set of earthquake records. However, for MDOF frame systems, where inelastic deformations may occur at different stories, the definition of ductility is not unique. It must be distinguished between local ductilities, which denote the ratios of the maximum individual interstory drifts related to their corresponding values at onset of yield, and the global ductility defined as

$$\mu = \max |x_N|/x_{Ny} \quad (7)$$

$\max |x_N|$ is the absolute relative peak displacement of the roof in a single time history analysis, and x_{Ny} is the corresponding displacement at onset of yielding. In this study characterization of inelastic deformations of MDOF frame structures is based on the global ductility according to Eq. (7).

For the sake of comparison “exact” floor response spectra of nonstructural elements in MDOF supporting structures are derived for given global target ductilities. This requires a repeated solution of Eqs. (6a)–(6b) until the actual global ductility ratio matches the desired target ductility.

3.3 Simplified Prediction of Floor Response Spectra

In order to avoid such an expensive computation subsequently a methodology for the simplified prediction of the seismic peak response of the nonstructural element is established, based on 2DOF floor response spectra. Starting point of this methodology is a modal decomposition of the frame substructure displacements \mathbf{x} into the N mode shapes ϕ_n , $n = 1, \dots, N$, of this subsystem,

$$\mathbf{x} = \sum_{n=1}^N \phi_n q_n \quad (8)$$

which transforms Eqs. (6a)–(6b) into a set of N coupled modal equations with off-diagonal coefficients in the resulting modal matrices, see e.g. [9]. For modal mass ratios

$$\bar{m}_n = \frac{m_s \phi_{nk}^2}{\phi_n^T \mathbf{M} \phi_n}, \quad n = 1, \dots, N \quad (9)$$

much smaller than one, $\bar{m}_n \ll 1$, the off-diagonal coefficients become small compared to the diagonal terms. If the natural frequencies of the supporting structure

and of the nonstructural element are well separated, these coefficients may be neglected [2], and Eq. (6a) decomposes into N modal SDOF oscillator equations of motion [9]:

$$\ddot{q}_n + 2\zeta_n\omega_n\dot{q}_n + \omega_n^2(q_n - q_n^{pl}) = -\Gamma_n\ddot{x}_g, \quad n = 1, \dots, N \quad (10)$$

In Eq. (10) q_n denotes the n th modal coordinate of the stand-alone frame structure, ζ_n is the corresponding modal damping coefficient, and Γ_n represents the n th effective participation factor [16],

$$\Gamma_n = \frac{\boldsymbol{\phi}_n^T \mathbf{M} \mathbf{e}}{\boldsymbol{\phi}_n^T \mathbf{M} \boldsymbol{\phi}_n} \quad (11)$$

The inelastic portions of the modal coordinates q_n^{pl} and the vector of plastic chord rotations (or curvatures, alternatively) $\boldsymbol{\varphi}^p$ are related according to

$$q_n^{pl} = \frac{1}{\omega_n^2 \boldsymbol{\phi}_n^T \mathbf{M} \boldsymbol{\phi}_n} \boldsymbol{\phi}_n^T \mathbf{G} \boldsymbol{\varphi}^p \quad (12)$$

Note that the N Eqs. (10) are coupled through the vector of plastic deformations $\boldsymbol{\varphi}^p$.

However, if the m th mode of the supporting structure is tuned to the mode of the nonstructural element, i.e. the substructure frequencies ω_m and ω_s are closely spaced, coupling terms between these modes must be considered. Then, the following modal equations of motion of a non-classically damped 2DOF system are to be solved [9],

$$\begin{aligned} & \begin{bmatrix} 1 + \bar{m}_m & \bar{m}_m/\phi_{mk} \\ \phi_{mk} & 1 \end{bmatrix} \begin{pmatrix} \ddot{q}_m \\ \ddot{x}_s \end{pmatrix} + \begin{bmatrix} 2\zeta_m\omega_m & 0 \\ 0 & 2\zeta_s\omega_s \end{bmatrix} \begin{pmatrix} \dot{q}_m \\ \dot{x}_s \end{pmatrix} \\ & + \begin{bmatrix} \omega_m^2 & 0 \\ 0 & \omega_s^2 \end{bmatrix} \begin{pmatrix} q_m \\ x_s \end{pmatrix} - \begin{pmatrix} \omega_m^2 \\ 0 \end{pmatrix} q_m^{pl} = - \begin{pmatrix} \Gamma_m + \bar{m}_m/\phi_{mk} \\ 0 \end{pmatrix} \ddot{x}_g \end{aligned} \quad (13)$$

in addition to $(N - 1)$ SDOF modal oscillators according to Eqs. (10),

$$\ddot{q}_n + 2\zeta_n\omega_n\dot{q}_n + \omega_n^2(q_n - q_n^{pl}) = -\Gamma_n\ddot{x}_g, \quad n = 1, \dots, m - 1, m + 1, \dots, N \quad (14)$$

In (13) ϕ_{mk} is the k th component of the m th primary structure mode shape $\boldsymbol{\phi}_m$.

Inspection of Eqs. (1) and (13) reveals that the structure of the equations of motion of the real 2DOF system and of the modal 2DOF system is similar. In particular, if the mode shapes are normalized leaving their k th element equal to one, i.e. $\phi_{nk} = 1$, $n = 1, \dots, N$, both differential operators are equal. The only difference concerns the excitation. While the first of Eqs. (1) is excited by $(1 + \bar{m})\ddot{x}_g$, the corresponding expression in Eqs. (13) is $(\Gamma_m + \bar{m}_m)\ddot{x}_g$ (for $\phi_{mk} = 1$).

This observation leads to the assumption that floor response spectra based on a 2DOF oscillator according to Fig. 1(b) can be employed to estimate approximately floor response spectra of SDOF nonstructural elements attached to MDOF supporting structures as shown in Fig. 8(a). However, 2DOF floor response spectra must be modified as outlined in the following before they provide appropriate results for MDOF substructure assemblies.

In order to obtain the m th modal component of the floor response spectrum it is proposed to multiply the spectral values of 2DOF floor response spectra (where period T_p , damping coefficient ζ_p , and mass ratio \bar{m} correspond to their modal counterparts $T_m = 2\pi/\omega_m$, ζ_m , and \bar{m}_m of MDOF structure) by an effective participation coefficient $\bar{\Gamma}_m$,

$$\begin{aligned} F_{ds,med}^{(m)} &= \bar{\Gamma}_m F_{ds,med}^{(2DOF)}(\bar{m} \equiv \bar{m}_m, T_p \equiv T_m, \zeta_p \equiv \zeta_m) \\ F_{as,med}^{(m)} &= \bar{\Gamma}_m F_{as,med}^{(2DOF)}(\bar{m} \equiv \bar{m}_m, T_p \equiv T_m, \zeta_p \equiv \zeta_m) \end{aligned} \quad (15)$$

$\bar{\Gamma}_m = \bar{\Gamma}_m(T_s)$ depends on the period T_s of the nonstructural element, as discussed in the following. For rigid nonstructural elements (i.e. $T_s = 0$) its response is identical to the response of the supporting structure at the attachment point, and hence, the spectral values of 2DOF floor response spectra are to be multiplied by the effective participation coefficient $|\Gamma_m|$. At tuned periods, $T_m \approx T_s$, the interaction between q_m and x_s is strong. Particularly, the response x_s is affected by the m th modal coordinate q_m , because the corresponding primary modal mass is much larger than the secondary mass m_s . It is reasonable to multiply 2DOF floor response spectra by $|\Gamma_m|$ for $T_m \approx T_s$. However, for systems with $T_s \gg T_m$ the supporting structure is more rigid compared to the nonstructural element, and thus, the response x_s is mainly induced by \ddot{x}_g , and remains almost unaffected by the parameters of the supporting structure (such as parameter Γ_m). As a result, from these empirical considerations it is proposed to define period dependent effective participation factors $\bar{\Gamma}_m(T_s)$ according to

$$\bar{\Gamma}_1(T_s) = \begin{cases} |\Gamma_1| & 0 \leq T_s \leq \delta_1 T \\ (T_s/T_1 - \gamma_1)(|\Gamma_1| - 1)/[(\delta_1 - \gamma_1)T_1] + 1 & \delta_1 T_1 \leq T_s \leq \gamma_1 T_1 \\ 1 & T_s \geq \gamma_1 T_1 \end{cases} \quad m = 1 \quad (16a)$$

$$\bar{\Gamma}_m(T_s) = \begin{cases} |\Gamma_m| & 0 \leq T_s \leq \delta_m T_m \\ (T_s/T_m - \gamma_m)|\Gamma_m|/[(\delta_m - \gamma_m)T_m] & \delta_m T_m \leq T_s \leq \gamma_m T_m \\ 0 & T_s \geq \gamma_m T_m \end{cases} \quad m > 1 \quad (16b)$$

These effective participation factors $\bar{\Gamma}_m(T_s)$ are provided with a bar to distinguish them from the original period independent participation factors Γ_m . Up to $T_s = \delta T_m$, $\bar{\Gamma}_m(T_s)$ complies with the absolute value of the corresponding Γ_m : $\bar{\Gamma}_m(T_s) = |\Gamma_m|$. Afterwards follows a linear ramp, which ends at period $T_s = \gamma_m T_m$. As it can be seen in Fig. 9, for periods $T_s \geq \gamma_m T_m$ the effective participation factor is different for the fundamental mode ($m = 1$) and for higher modes ($m > 1$): $\bar{\Gamma}_1(T_s) = 1$ for $T_s \geq \gamma_1 T_1$, for all other modes $\bar{\Gamma}_m(T_s) = 0$. Coefficients δ_m and γ_m , $m = 1, \dots, N$

$$\begin{aligned} m = 1: \quad & \delta_1 = 1.5, \quad \gamma_1 = 5.0 \\ m > 1: \quad & \delta_m = 0, \quad \gamma_m = 3.0 \end{aligned} \quad (17)$$

are based on an empirical optimization procedure.

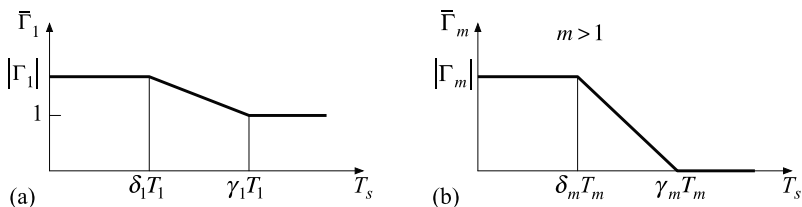


Fig. 9 Period dependent effective participation factor for (a) the fundamental mode, and (b) higher modes

Finally, an approximation of the actual floor response spectrum is determined by superposing modal 2DOF floor response spectra according to the SRSS mode superposition rule [16]

$$F_{ds,med} = \sqrt{\sum_{m=1}^{R \leq N} (F_{ds,med}^{(m)})^2}, \quad F_{as,med} = \sqrt{\sum_{m=1}^{R \leq N} (F_{as,med}^{(m)})^2} \quad (18)$$

In the modal superposition the number $R (\leq N)$ of considered modal 2DOF floor response spectra depends on the sum of the effective modal mass as proposed in earthquake engineering [16]. It is noted that the SRSS mode superposition has not been developed for absolute accelerations for which a strong correlation between modal responses is observed because of the presence of the ground acceleration component. However, here the total peak acceleration of the nonstructural element (and not of the supporting structure) is considered, where the impact of the ground acceleration is less significant. This fact is supported by the outcomes of the subsequently presented application examples.

For a series of example problems, considering various elastic and inelastic supporting structures with different modal parameters, coefficients δ_m and γ_m were derived minimizing the error of the proposed approximate floor response spectra according to Eq. (18) with respect to the exact outcome [17]. Afterwards, the mean of all individual outcomes as given in Eq. (17) was determined. In the following several example problems are presented to assess these values and the complete procedure.

3.4 Assessment and Application

Generic planar multi-story single-bay frames of N stories as shown in Fig. 8(a) serve as load-bearing structure. They are composed of elastic columns, rigid beams, and rotational springs at both ends of the beams [10, 11]. Identical point masses are assigned to each joint of the particular frame. The fundamental mode shape of the MDOF frames follows a straight line. Global cyclic response under earthquake excitation is represented by non-degrading bilinear hysteretic behavior of the rotational springs, see Fig. 8(b). Strain hardening ratio α is 0.03 for all springs. The

Table 1 Structural periods of vibration, modal mass ratios, and participation factors of selected frame structures for the first three modes

N	T_1 [s]	T_2 [s]	T_3 [s]	\bar{m}_1	\bar{m}_2	\bar{m}_3	$ \Gamma_1 $	$ \Gamma_2 $	$ \Gamma_3 $
9 stiff	0.90	0.35	0.21	0.050	0.065	0.039	1.42	0.63	0.30
9 flex.	1.80	0.71	0.42	0.050	0.065	0.039	1.42	0.63	0.30
12 stiff	1.20	0.48	0.29	0.050	0.075	0.054	1.44	0.68	0.36

spring strength is tuned to obtain simultaneous onset of yielding at all springs in a pushover analysis with linear design load pattern. This tuning provides inelastic deformations distributed in the entire structure when subjected to a severe earthquake. For inelastic supporting frame structures the global target ductility μ is selected exemplarily to be 4.5 %. modal viscous damping is assigned to each mode of the frame structure with N dynamic degrees-of-freedom. The fundamental period of vibration T_1 is 0.1N s for stiff, and 0.2N s for more flexible frame structures. On top of the frames a vibratory nonstructural element is connected, which is modeled as an elastic SDOF oscillator with light inherent damping, $\zeta_s = 0.01$. The effective fundamental modal mass ratio is $\bar{m}_1 = 0.05$ for all considered structure assemblies. In the proposed simplified analyses of floor response spectra the N th component of all mode shapes is set to 1: $\phi_{nN} = 1, n = 1, \dots, N$. In Table 1 the first three periods, the corresponding modal mass ratios, and the period independent participation coefficients are compiled for all considered frame structures.

Figures 10 and 11 represent median displacement and median acceleration floor response spectra, respectively, for a nonstructural element attached to an unlimited elastic stiff 9-story frame structure. The black full line corresponds to the results utilizing the complete set of Eqs. (6a)–(6b), i.e., full dynamic interaction between the frame structure and the nonstructural containment is considered. Figure 10 shows that the median displacement floor response spectrum exhibits a peak, where the fundamental mode of the frame is closely tuned to the mode of the nonstructural element, i.e. $T_1 \approx T_s$. The acceleration floor response spectrum in Fig. 11 shows an additional peak at the $T_2 \approx T_s$. Furthermore, the results of the proposed simplified analysis are displayed. Thereby, the contributions of three median 2DOF floor response spectra are employed, whose periods T_p and mass ratios \bar{m} correspond to the first three natural periods and modal mass ratios of the frame structure. These periods and mass ratios are: 0.90 s/0.050, 0.35 s/0.065, and 0.21 s/0.039. The corresponding 2DOF response spectra for $T_p = 0.90$ s and $\bar{m} = 0.05$ are shown in Figs. 3 and 4. The underlying 2DOF floor response spectra multiplied by the period dependent effective participation coefficients are depicted in Figs. 10 and 11 by thin lines. Their superposition according to the SRSS rule leads to the approximation of the floor response spectra shown by bold light gray lines. It can be observed that there is a good overall match between the exact solution and its approximate counterpart. As expected, the median peak displacement response can be approximated sufficiently accurate by the floor response spectrum of the fundamental mode only, see Fig. 10. This outcome supports the proposed period dependent effective participa-

Fig. 10 Displacement floor response spectra: exact, proposed approximation, and corresponding modal contributions. Elastic stiff 9-story supporting frame structure

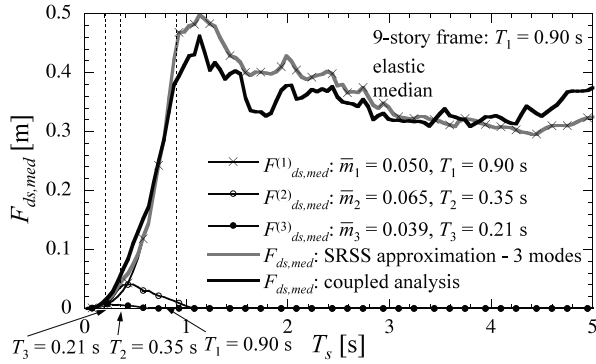
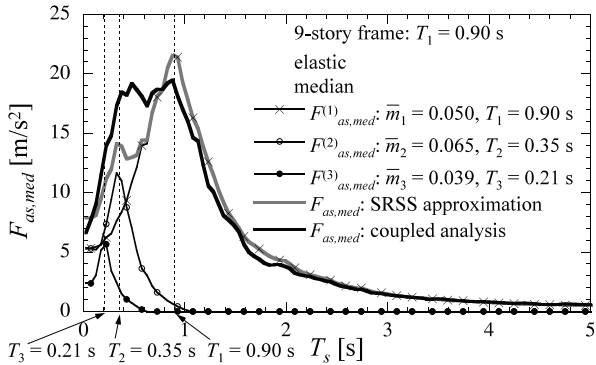


Fig. 11 Acceleration floor response spectra: exact, proposed approximation, and corresponding modal contributions. Elastic stiff 9-story supporting frame structure



tion factor $\bar{\Gamma}_1$ for the fundamental mode according to Eqs. (16a) and (17), compare also with Fig. 9(a).

However, the contributions of the second and third mode on the median acceleration floor response spectrum are essential, see Fig. 11. This figure shows that for this example problem the three mode SRSS approximation underestimates the peak acceleration response in the vicinity of the second structural mode: $T_s \approx T_2$. Thus, for this example the choice of the effective participation factor for higher modes $\bar{\Gamma}_n, n \geq 2$, according to Eqs. (16b) and (17) is not optimal. However, it is repeated that $\bar{\Gamma}_n, n \geq 2$, was determined utilizing an optimization procedure, which included various different elastic and inelastic frame structures with different fundamental periods and stories. In order to keep the procedure simple a unique $\bar{\Gamma}_n, n \geq 2$ was determined, which minimizes the average error for all considered cases.

In Figs. 12 and 13 the results of the SRSS superposition of 2DOF floor response spectra, which are multiplied by a constant (i.e. period independent) effective participation factor, are shown additionally. It is demonstrated that the resulting floor response spectra overestimate the peak response considerably. Thus, the assumption of period depending effective participation factors implemented according to Eqs. (16a)–(16b) is justified.

The effect of interaction between the supporting structure and the nonstructural element is examined in Figs. 14 and 15. Additionally, in these figures floor response

Fig. 12 Displacement floor response spectra: exact, and approximations. Elastic stiff 9-story supporting frame structure

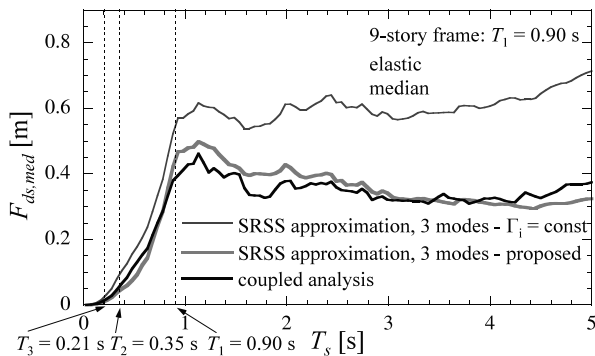
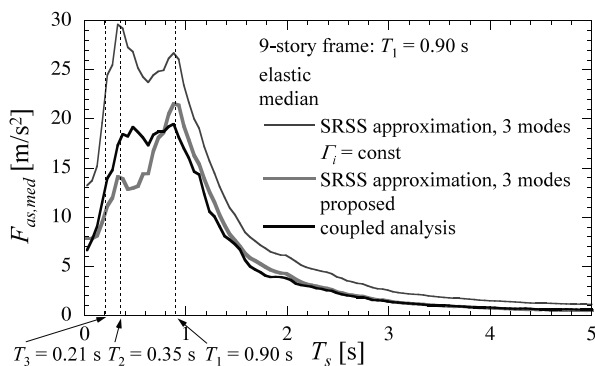


Fig. 13 Acceleration floor response spectra: exact, and approximations. Elastic stiff 9-story supporting frame structure



spectra are shown, which are generated omitting coupling between the substructures. In such a decoupled analysis the dynamic input for the nonstructural element is the seismic response of the stand-alone supporting structure at its attachment point. The results verify that this decoupled approach overestimates for the selected mass ratio the actual response by more than 100 % for closely spaced substructure periods. Thus, for the utilized mass ratio a decoupled analysis, which is common engineering practice, may lead to results much too conservative. These results confirm the proposed simplified methodology, which is simple and yet sufficiently accurate.

Next, the methodology is assessed including inelastic behavior of the supporting frame structure. The same structure as before is utilized, however the results of this example problem are based on a global ductility ratio of 4. The corresponding median displacement and median acceleration floor response spectra are presented in Figs. 16 and 17. Thereby, the outcomes of the simplified methodology are based on the modal superposition of three modified 2DOF floor response spectra. These modal contributions are graphically displayed in Figs. 16 and 17. The corresponding original 2DOF floor response spectra for the fundamental mode $T_p = 0.90$ s are illustrated in Figs. 5(a) and 5(b). Figures 16 and 17 verify that the proposed procedure approximates floor response spectra with sufficient accuracy also for inelastic behavior of the supporting structure. In contrast to results based on unlimited elastic deformations the simplified procedure underestimates slightly the median

Fig. 14 Displacement floor response spectra: exact, proposed approximation, and decoupled solution. Elastic stiff 9-story supporting frame structure

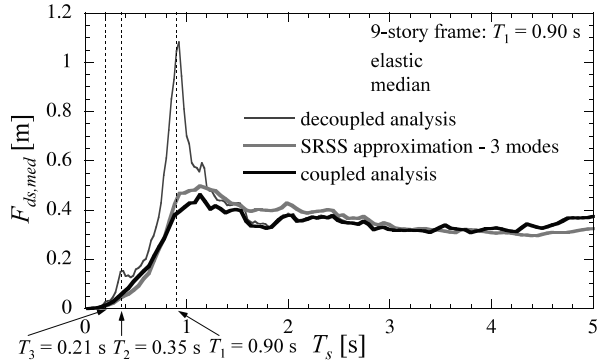


Fig. 15 Acceleration floor response spectra: exact, proposed approximation, and decoupled solution. Elastic stiff 9-story supporting frame structure

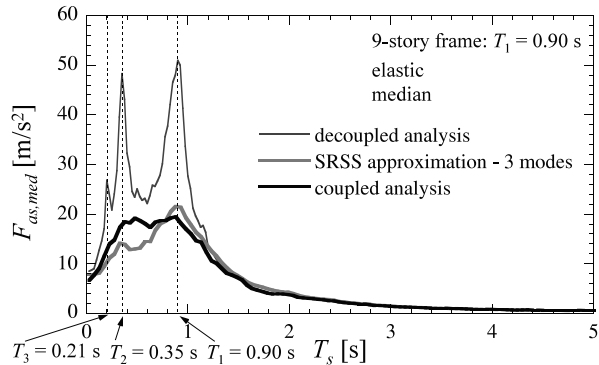
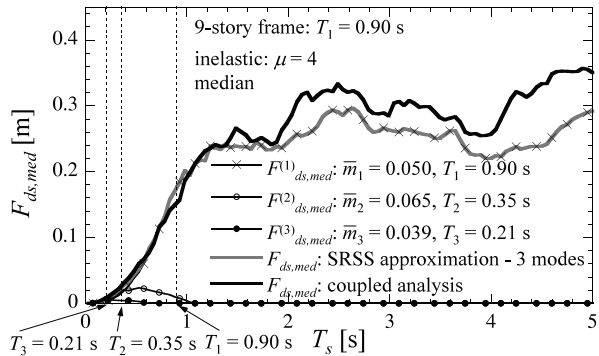


Fig. 16 Displacement floor response spectra: exact, proposed approximation, and corresponding modal contributions. Inelastic stiff 9-story supporting frame structure



peak displacement response (compare Fig. 10 with Fig. 16). In this example the superposition of modified 2DOF acceleration floor response spectra leads to a better approximation of acceleration floor response spectra than for the unlimited elastic structure, see Fig. 11 and Fig. 17. Note that ductile deformations of the supporting structure lead to energy dissipation and period elongation, and thus, floor response spectra do not exhibit pronounced peaks at tuned natural periods. For moderately heavy nonstructural elements Figs. 18 and 19 demonstrate the importance of inter-

Fig. 17 Acceleration floor response spectra: exact, proposed approximation, and corresponding modal contributions. Inelastic stiff 9-story supporting frame structure

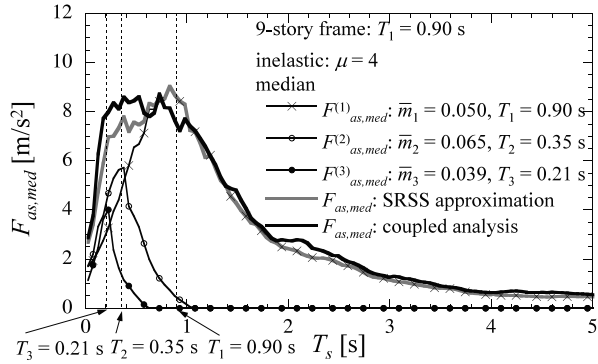


Fig. 18 Displacement floor response spectra: exact, proposed approximation, and decoupled solution. Inelastic stiff 9-story supporting frame structure

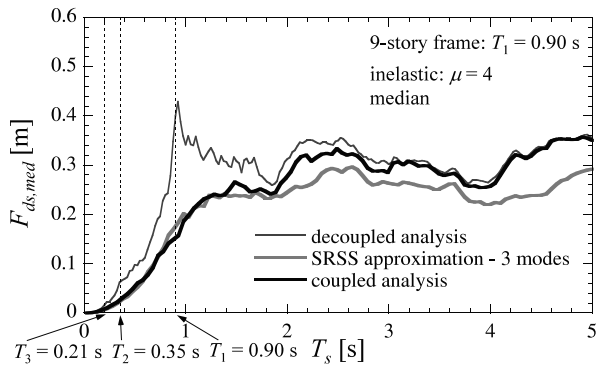
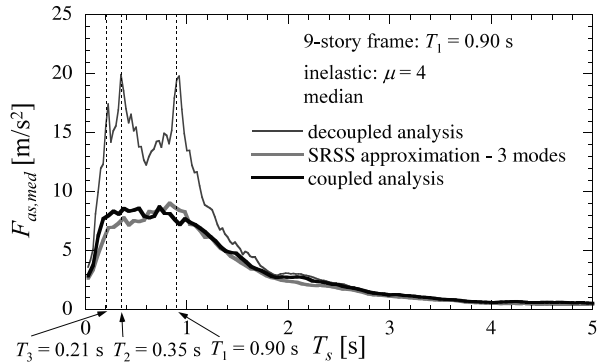


Fig. 19 Acceleration floor response spectra: exact, proposed approximation, and decoupled solution. Inelastic stiff 9-story supporting frame structure



action between an inelastic supporting structure and an elastic nonstructural element for tuned substructure periods.

Subsequently, a more flexible inelastic 9-story frame structure with a fundamental vibration period of $T_1 = 1.80$ s is considered. The global target ductility of the frame structure is again 4. The modal mass ratios and the damping coefficients are identical with the ones of the stiff frame structure ($T_1 = 0.90$ s), see Table 1. Me-

Fig. 20 Displacement floor response spectra: exact, proposed approximation, and decoupled solution. Inelastic flexible 9-story supporting frame structure

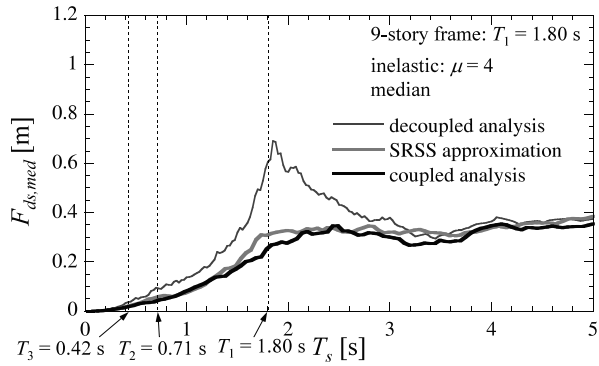
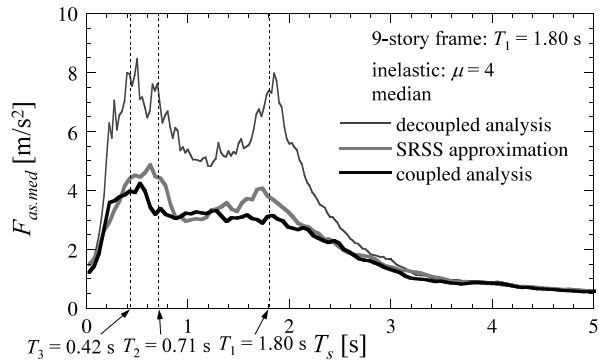


Fig. 21 Acceleration floor response spectra: exact, proposed approximation, and decoupled solution. Flexible inelastic 9-story supporting frame structure



dian floor response spectra of this structural assembly confirm previous findings, see Figs. 20 and 21. The approximation utilizing 2DOF floor response spectra leads to a satisfactory prediction of the actual median peak response.

For a 12-story supporting structure with a fundamental vibration period of $T_1 = 1.20$ s median floor response spectra are presented in Figs. 22 and 23. In this example the proposed methodology based on the first three modes leads to an excellent match compared to the exact floor response spectra. Comparison with outcomes from decoupled analyses (Fig. 23) shows the improvement of this method compared to the classic decoupled engineering approach.

4 Conclusions

In this study it was demonstrated that the seismic peak response of vibratory non-structural elements attached to plane regular multi-story frame structures can be predicted efficiently and with sufficient accuracy by modal superposition of modified floor response spectra for SDOF nonstructural elements on SDOF supporting structures. The obtained results of this study reveal that for both unlimited elastic and ductile load-bearing structures the proposed methodology captures effects of cou-

Fig. 22 Displacement floor response spectra: exact, proposed approximation, and decoupled solution. Inelastic stiff 12-story supporting frame structure

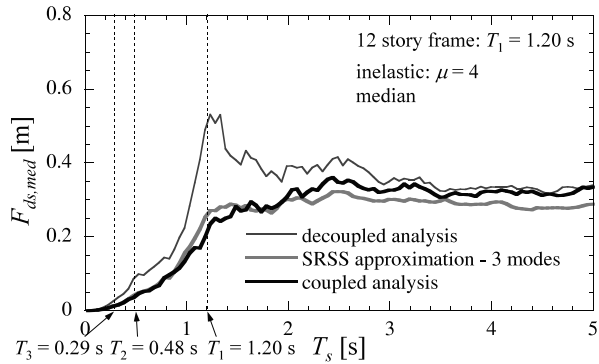
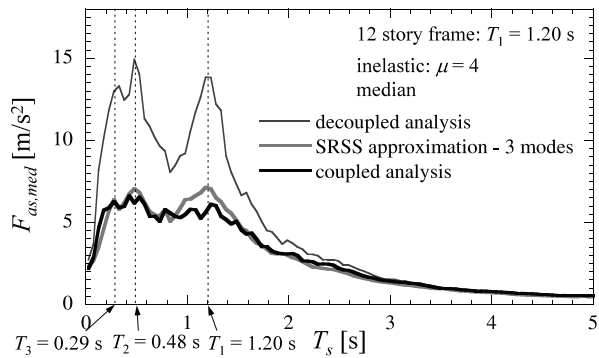


Fig. 23 Acceleration floor response spectra: exact, proposed approximation, and decoupled solution. Inelastic stiff 12-story supporting frame structure



pling, dynamic interaction, and tuning. However, it is emphasized that the proposed period-dependent effective participation factors were calibrated to results based on a far-field set of earthquake records. The application of these relations to earthquake records with other characteristics needs to be assessed in a subsequent study. In all considered example problems plastic deformations are distributed throughout multi-story supporting frame structures. Thus, the procedure was not tested for structures with highly inelastic localized deformations, which arise for example in soft story structures. Furthermore, only non-deteriorating inelastic component behavior is considered. In the near future such a procedure will become even more competitive when the underlying floor response spectra coupled 2DOF systems for various structural parameters may be found in a database available to the engineering public, which is currently compiled by the authors.

References

1. Villaverde R (2004) Seismic analysis and design of nonstructural components. In: Earthquake engineering: from engineering seismology to performance-based engineering. CRC Press, Boca Raton, pp 19-1–19-48

2. Building Seismic Safety Council (2003) NEHRP recommended provisions for seismic regulations for new buildings and other structures, FEMA-450. Federal Emergency Management Agency, Washington
3. Chen G, Wu J (1999) Transfer-function-based criteria for decoupling of secondary systems. *J Eng Mech* 125:340–346
4. Igusa T, Der Kiureghian A (1985) Dynamic characterization of two-degree-of-freedom equipment-structure systems. *J Eng Mech* 111:1–19
5. Lin J, Mahin SA (1985) Seismic response of light subsystems on inelastic structures. *J Struct Eng* 111:400–417
6. Sewell RT, Cornell CA, Toro GR, McGuire RK, Kassawara RP, Singh A, Stepp JC (1987) Factors influencing equipment response in linear and nonlinear structures. In: Wittmann FH (ed) *Trans 9th international conference on structural mechanics and reactor technology*, vol K2. Balkema, Rotterdam, pp 849–856
7. Adam C (2001) Dynamics of elastic-plastic shear frames with secondary structures: shake table and numerical studies. *Earthq Eng Struct Dyn* 30:257–277
8. Mohammed HH, Aziz TS, Ghobarah A (2004) Nonlinear experimental response of primary-secondary systems under repeated seismic excitation. In: *Proceedings of the 13th world conference on earthquake engineering*. Canadian Association of Earthquake Engineering, paper 3369, 15 pp
9. Adam C, Fotiu PA (2000) Dynamic analysis of inelastic primary-secondary systems. *Eng Struct* 22:58–71
10. Medina RA, Sankaranarayanan R, Kingston KM (2006) Floor response spectra for light components mounted on regular moment resisting frame structures. *Eng Struct* 28:1927–1940
11. Sankaranarayanan R, Medina RA (2007) Acceleration response modification factors for nonstructural components attached to inelastic moments-resisting frame structures. *Earthq Eng Struct Dyn* 36:2189–2210
12. Adam C, Furtmüller T (2008) Seismic response characteristics of nonstructural elements attached to inelastic buildings. In: Brennan MJ (ed) *Proceedings of 7th European conference on structural dynamics*, paper 120, 12 pp
13. Adam C, Furtmüller T (2008) Approximation of the seismic response of vibration prone nonstructural elements attached to multi-story frame structures. In: Yang YB et al (eds) *Proceedings of the 11th East Asia-Pacific conference on structural engineering & construction (EASEC-11)*, paper B07-22, 10 pp
14. Adam C, Furtmüller T (2008) Response of nonstructural components in ductile load-bearing structures subjected to ordinary ground motions. In: *Proceedings of the 14th world conference on earthquake engineering*, paper 05-01-0327, 8 pp
15. FEMA P-695 (2009) Quantification of building seismic performance factors. Federal Emergency Management Agency, Washington
16. Chopra AK (2007) *Dynamics of structures*, 3rd edn. Pearson Prentice Hall, Upper Saddle River
17. Moschen L (2010) Abschätzung der Erdbebenantwort schwingungsfähiger Sekundärstrukturen in ebenen Rahmentragwerken. Diploma thesis, University of Innsbruck, 66 pp (in German)

Seismic Assessment of Steel Moment Frames Using Simplified Nonlinear Models

Dimitrios G. Lignos, Christopher Putman, and Helmut Krawinkler

Abstract This chapter discusses the effectiveness of simplified nonlinear models for seismic assessment of steel moment frames using single and multi-mode nonlinear static methods. It is demonstrated that the nonlinear static procedure (NSP) has much value in understanding important behavior characteristics that are not being explored in a nonlinear response history analysis (NRHA) in which engineers usually focus on a “blind” demand/capacity assessment rather than interpretation and visualization of the steel frame behavior. It is also shown that NSP procedures have many limitations for quantitative assessment of steel moment frame demands even for low-rise frames. The conclusion is that both NSP and NRHA have intrinsic value and that it is advisable to employ a combination of both to understand seismic performance of steel moment frames and to quantify important engineering demand parameters for these lateral resisting structural systems.

Keywords Nonlinear static analysis · Higher mode effects · Component models · Nonlinear response history analysis · Performance-based earthquake evaluation

1 Introduction

In the context of Performance Based Earthquake Engineering (PBEE) a number of engineering guidelines [1–7] are currently being used for seismic evaluation and rehabilitation of steel and reinforced concrete structures. A structural engineer would

D.G. Lignos (✉)
Department of Civil Engineering and Applied Mechanics, McGill University, Montreal, QC,
H3A 2K6, Canada
e-mail: dimitrios.lignos@mcgill.ca

C. Putman
Degenkolb Engineers, Oakland, CA 94612, USA
e-mail: cputman@degenkolb.com

H. Krawinkler
Department of Civil and Environmental Engineering, Stanford University, Stanford,
CA 94305-4020, USA
e-mail: krawinkler@stanford.edu

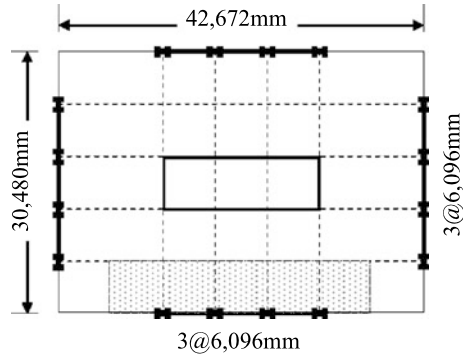
commonly evaluate the performance of a structure by using the nonlinear static procedure (NSP), which is also referred as pushover analysis (PA). In the current engineering practice in the U.S., a pushover analysis is typically based on an invariant lateral load pattern that is applied along the height of a structure. This structure is then pushed to a pre-defined target roof displacement. Many researchers have conducted extensive research on the evaluation of seismic demands of structural systems with nonlinear static procedures based on invariant load patterns, e.g., [8–12]. These studies summarize major drawbacks of these procedures to predict seismic demands of structures. Others [13–16] have conducted research on enhanced NSPs that account for higher mode effects and either retain the simplicity of invariant load patterns or employ adaptive procedures in which the lateral load pattern varies during the NSP. Typically, these methods improve the prediction of engineering demand parameters compared to the single mode PA. The value of NSP is in the fact that this procedure permits inspection of structural response. It is also a simple tool to identify critical regions of a structural system in which the potential for significant strength or stiffness discontinuities is high.

Based on FEMA-440 [5], the major differences between results obtained from NSP and nonlinear response history analysis (NRHA) are attributed to the cyclic deterioration in strength and stiffness of structural components as part of a structure [6]. These effects are typically ignored by NSP. Other reasons for observed differences between NRHA and NSP in prediction of seismic demands of a structural system are (1) inaccuracies in the prediction of the target roof displacement at which the structural response is to be evaluated, and (2) multi-degree-of-freedom (MDOF) effects. In order to improve nonlinear MDOF modeling for the estimation of the seismic response of a structural system, the National Institute of Standards and Technology (NIST) initiated a program of focused studies [17]. This chapter summarizes one of these studies, which address the minimum level of MDOF modeling sophistication and appropriateness of nonlinear methods for seismic evaluation of special steel MRFs.

2 Archetype Steel Buildings

The evaluation of the Engineering Demand Parameters (EDPs) predicted with NRHA and NSP procedures is done with a two-, four- and eight-story archetype steel building with perimeter special MRFs as their primary lateral resisting system. These archetype steel buildings were designed as part of the NIST [18] project. These structures comprise 3-bay special steel MRFs with Reduced Beam Sections (RBS) designed in accordance with AISC 358-05 [19]. A plan view of a typical archetype is shown in Fig. 1. The three steel buildings that are utilized in this study are designed based on Response Spectrum Analysis (RSA) for a seismic design category D_{max} . This corresponds to a design spectral acceleration at the short period, S_{DS} , and at a period of 1 second, S_{D1} , equal to $1.0g$ and $0.60g$, respectively. The

Fig. 1 Plan view of a typical archetype building with perimeter steel moment resisting frames (dimensions in mm)



detailed design of the archetype steel buildings is summarized in [18, 20]. In the subsequent discussion, the three special steel MRFs are denoted as 2-Story-RSA- D_{max} , 4-Story-RSA- D_{max} and 8-Story-RSA- D_{max} , respectively.

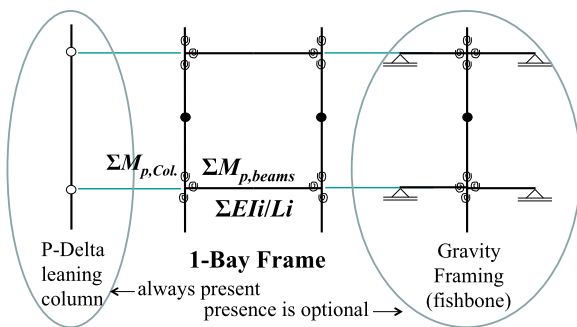
3 Modeling of Archetype Steel Moment Resisting Frames

In order to model the seismic response of the perimeter steel MRFs shown in Fig. 1, two types of two-dimensional (2-D) analytical models are developed. The first analytical model is the 3-bay model with all the components (beams, columns and panel zones) of the steel MRF explicitly modeled. The second model is a single bay simplified frame whose properties are tuned to represent the detailed steel MRF shown highlighted in Fig. 1. In both models, P-Delta effects are simulated with a leaning column that is connected to the steel MRF with axially rigid trusses. The subsequent sections discuss details of these two analytical models.

3.1 Three-Bay Steel Moment Resisting Frame Model

The steel MRF, which is highlighted in Fig. 1, is modeled in a customized version of DRAIN-2DX (Prakash et al. [21]). In this model, beams and columns are modeled with elastic beam-column elements with concentrated plastic hinge springs at their ends. These springs simulate the hysteretic response of a steel component (beam or column) subjected to cyclic loading including strength and stiffness deterioration based on the modified Ibarra-Medina-Krawinkler (IMK) deterioration model [22, 23]. Panel zone shear distortion is explicitly modeled [24]. The exact location of the RBS section is also incorporated in the model. The deterioration parameters of steel columns and beams with RBS are determined by multivariate regression equations that have been developed based on information retrieved from a recently developed database for deterioration modeling of steel components [23, 25]. These analytical models have been used extensively for quantification of building seismic performance factors using the FEMA P-695 methodology [18].

Fig. 2 Simplified model with P-Delta column and gravity framing fishbone model



3.2 Simplified Single-Bay Frame Model

To reduce the computational effort in estimating seismic demands of the steel MRFs with NRHA and evaluate the effectiveness of simpler representations of the 3-bay steel MRFs discussed in Sect. 3.1, a simplified model (see Fig. 2) is developed. In this model, a single bay frame represents the three-bay moment-resisting frame so that the overturning moment and column axial deformation effects are adequately simulated. Luco et al. [26] developed similar models for computing the seismic inelastic demands of steel MRFs. P-Delta effects are simulated with a leaning column that is always present in the numerical model. Strength and stiffness properties of the gravity framing that is not part of the moment resisting frame can be represented with the “fishbone” model shown at the right of Fig. 2. However, stiffness and strength of the gravity framing was not specifically used in the majority of the current study except for an ancillary study, which is discussed in Sect. 4.2. Lumping together multi-bay frames into a single bay frame can be accomplished by the following rules for steel beams,

$$\sum EI_i/L_i = EI/L \quad (1)$$

$$\sum M_{p,i} = M_p \quad (2)$$

in which I_i , L_i , and $M_{p,i}$ is the moment of inertia, length and plastic bending strength of the i -th beam in a story, respectively, and EI/L and M_p are the stiffness and plastic moment of the single bay beam. For steel columns,

$$\sum EI_i = 2EI \quad (3)$$

$$\sum M_{pc,i} = 2M_{pc} \quad (4)$$

in which $M_{pc,i}$ is the plastic moment of the i -th column of the multi-bay frame and M_{pc} is the plastic moment of the single bay column in the presence of an axial load. For taller steel MRFs in which overturning moment and axial deformations in columns are important, these effects can be approximated by setting L of the single bay frame equal to the distance between the end columns of the multi-bay frame; and by setting the area of the single bay column equal to the area of the end column of

the multi-bay frame. This simplification is based on the assumption that overturning effects are resisted mostly by the end columns of a steel MRF. The approximations summarized herein are reasonable if all bays of the steel MRFs are of about equal width, and become more approximate when spans of the steel MRF vary considerably. Ignoring panel zone shear deformations and using centerline dimensions for beams and columns introduce additional approximations to the analytical models. The expected gravity load that is used to simulate P-Delta effects is based on a linear combination of the dead load (D) and 25 % of the live load (L) applied uniformly at the individual floors of the structure. The tributary gravity load to the columns of the perimeter MRF was directly applied to the columns of the 1-bay frame.

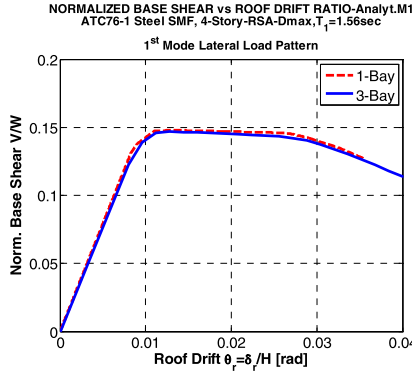
Figure 3a shows a comparison between the pushover curves of the 3-bay four-story steel MRF and the simplified 1-bay model. In this figure, the base shear V is computed from the inertial forces only (V_I) and is normalized with respect to the seismic weight W of the steel MRF. The roof drift θ_r is defined as roof displacement δ_r over the total height H of the steel MRF. As seen from this figure, the response of the 1- and 3-bay models is almost identical. The 1-bay models are implemented in the OpenSees simulation platform [27] whereas the 3-bay models are implemented in Drain-2DX [21]. The base shear histories for a single ground motion obtained from the 3-bay model developed in Drain-2DX (ATCW 3-Bay) and the 1-bay model developed in OpenSees is shown in Fig. 3b. A comparison between absolute peak overturning moments (OTM) obtained for the eight-story 3-bay and 1-bay frames is shown in Fig. 3c. These simulations are based on the FEMA P-695 [7] set of 44 ground motions for a scale factor ($SF = 2.0$). Note that a $SF = 2.0$ corresponds to approximately a maximum considered event (MCE) in California. From these comparisons shown in Fig. 3, in both static and dynamic analysis the seismic response based on the 1-bay and 3-bay models is almost identical, providing confidence in both the simulation platforms and in the ability of the simplified model to represent the response of the 3-bay steel MRF.

4 Seismic Assessment of Steel Moment Resisting frames

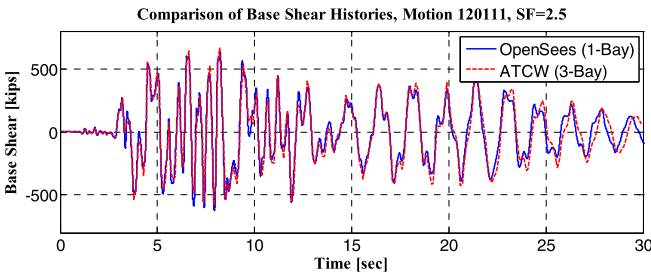
This section focuses on evaluating the seismic response of steel MRFs with the simplified models discussed in Sect. 3.2. The assessment is based on a comparison between NSP and NRHA results.

Feasibility and limitations of the NSP is illustrated with the case studies that were investigated. Since the emphasis is on simple methods that can assess multi-mode effects on the seismic response of steel frame structures the modal pushover analysis (MPA) [13] is also evaluated. Two main options are used for modeling the components of the steel MRFs discussed in Sect. 3. These options are summarized as follows:

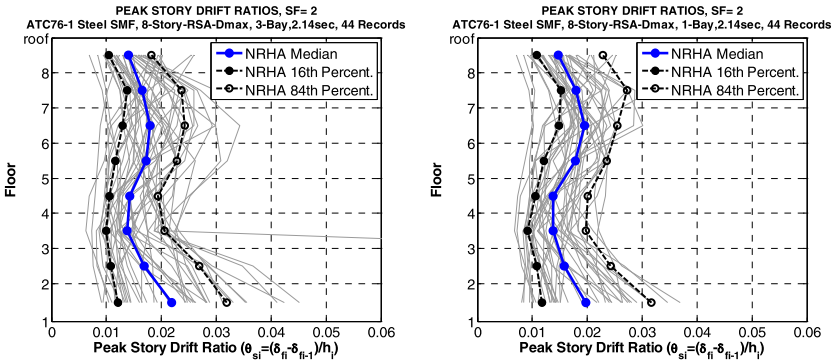
- **ASCE41:** All the steel components are modeled in accordance with ASCE/SEI 41-06 [3] utilizing the component model shown in Fig. 4a. Note that the post-capping stiffness of this model is obtained by linearly connecting peak point C



(a) Comparison of pushover curves between 1- and 3-bay models of the four-story steel MRF



(b) Base shear history of the four-story MRF models for a single ground motion

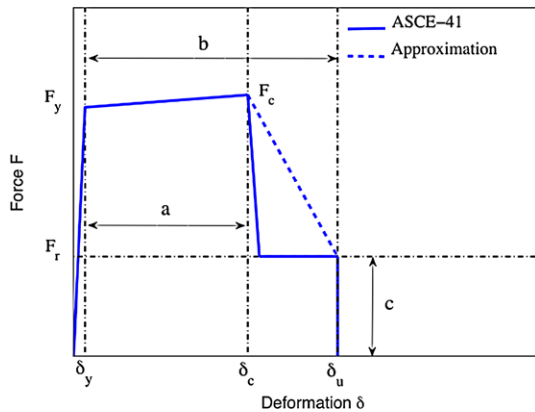


(c) Comparison of overturning moments obtained from NRHA of 3-bay and simplified 1-bay model

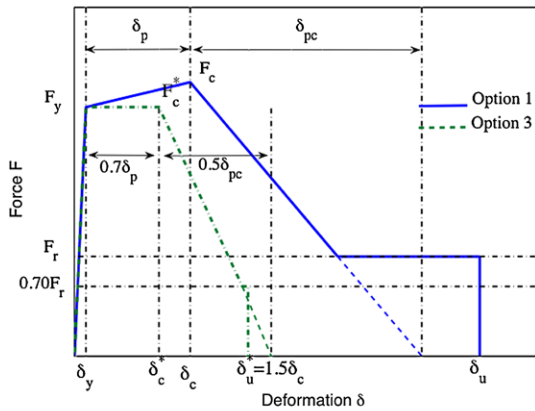
Fig. 3 Comparison of response predictions using the 3-bay and 1-bay simulation models

and point E of the generic ASCE/SEI 41-06 model. This modification is made in order to provide a better match with data and analysis models developed in the past decade [22, 23] and also to avoid numerical instability problems in the nonlinear analysis due to the sharp decreases in stiffness between time steps and force increments.

Fig. 4 Steel component models; (a) ASCE 41; (b) Modified IMK model, Options 1 and 3



(a)



(b)

- **Analyt.M1:** All the steel components are modeled with the modified IMK component model [23]. For this purpose, a monotonic backbone curve is used as shown in Fig. 4b. This option is the same as the ATC-72-1 [28] analysis Option 1. Cyclic deterioration is not reflected in the component model for monotonic response and subsequently in the NSP. However, in the NRHA the component model deteriorates cyclically based on the rules discussed in [22, 23]. For comparison purposes in the same figure we have superimposed the modified backbone curve based on the IMK model (see ATC-72 [28] analysis Option 3).

The following options are used to determine the target roof displacement for the NSP:

- **ASCE41:** The target displacement is obtained from the ASCE/SEI 41-06 [3] coefficient method.
- **EqSDOF:** The target displacement is based on the median displacement obtained from NRHA of the first mode equivalent Single-Degree-Of-Freedom (SDOF)

system. The 44 ground motions of the FEMA P-695 [7] set is used. The analysis is conducted with the IIDAP [29] tool. The properties of the equivalent SDOF are obtained from the base shear without P-Delta effects (i.e., V_I —roof displacement pushover curve). This implies that P-delta effects are accounted for approximately in the properties of the equivalent SDOF.

Note that for the MPA procedure only the Analyt.M1-EqSDOF option is explored. This implies that the pushover analysis is conducted with the Analyt.M1 model, and the target displacement for the individual modes is determined from an equivalent SDOF analysis with the analysis tool IIDAP [29]. This program computes the inelastic response of SDOF systems including cyclic deterioration in strength and stiffness. The cyclic deterioration parameter λ [25] is set equal to the median value for steel components obtained from a steel database for deterioration modeling (Lignos and Krawinkler [25]).

4.1 Single Mode Nonlinear Static Analysis Procedure

Figures 5a and 5b show the pushover curves with ($V_{I+P-\Delta}$) and without P-Delta (V_I) effects for the 4-Story-RSA- D_{max} MRF based on the ASCE-41/Analyt.M1 component models, respectively. In the same figures we have superimposed the idealized trilinear curve based on the ASCE-41-06 [3]. When the ASCE41 component model is used in the analysis, the NSP underestimates the post-yield strength and deformation capacities compared to the Analyt.M1 model. The implication is that the target roof displacements predicted from the equivalent SDOF systems (see Figs. 5c and 5d) are different for large ground motion intensities.

The use of the pushover curve based on the ASCE-41 component model (see Fig. 5a) together with the equivalent SDOF model for target displacement prediction (ASCE41-EqSDOF) may provide performance estimates that are lower than might be justifiable. For a scale factor $SF = 2.0$ the EqSDOF leads to 33 collapses, which are a direct consequence of the relatively short yield plateau obtained from using ASCE41 component models in the pushover analysis. For all options, NSP story drift predictions show a significant deviation from median NRHA values (Figs. 6a, 6b). In the inelastic range ($SF = 2.0$) drifts in the lower stories are overestimated and drifts in the upper stories are underestimated. Results are illustrated for the two- and four-story steel MRFs but the same observation applies for the eight-story MRF.

Story shear predictions for the four-story steel MRF based on the NSP show poor correlation with results from NRHA in the inelastic range ($SF = 2.0$). This can be seen in Figs. 6c and 6d. Story shears are consistently underestimated, particularly in the upper stories. The reason is the dynamic redistribution, which amplifies story shear forces compared to those obtained from a predetermined lateral load pattern. If story shear forces are an important performance consideration, then the validity

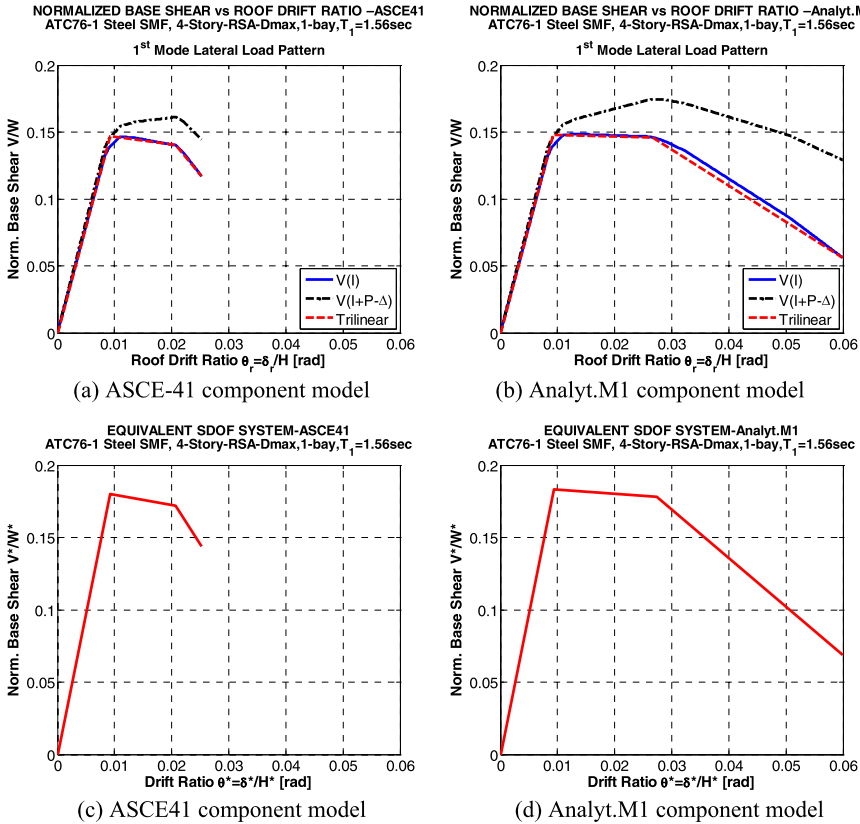


Fig. 5 Single mode pushover curves and equivalent SDOF systems for the 4-Story-RSA- D_{max} steel MRF

of quantitative values obtained from a pushover analysis diminish for this four-story steel SMF. Similar observations apply to floor OTMs, which control axial forces in columns of frame structures. In the upper stories, the NSP predictions are less than half from those obtained from NRHA (see Figs. 6e and 6f). The situation is better at the base, because absolute maximum shear forces in individual stories occur at different times. The outcome is that even for relatively low-rise steel MRF structures, NSP predictions may provide misleading quantitative information, particularly for force quantities.

The all-important issue of lateral load pattern is not explored here. Previous work [5] has addressed this issue and came to the conclusion that variations in invariant lateral load patterns do not improve the accuracy of EDP predictions. The load pattern applied in all cases discussed here is based on the elastic first mode deflected shape, as recommended in [3].

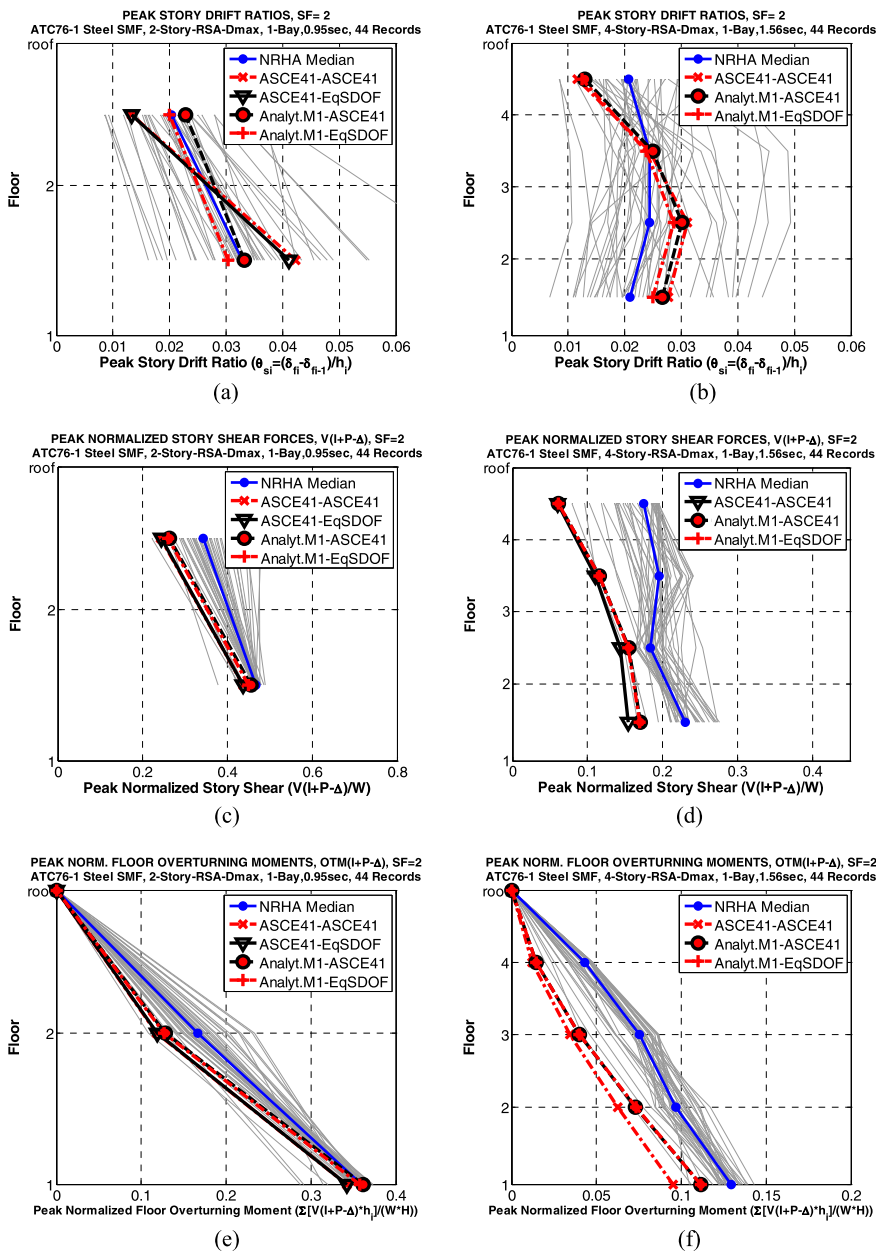


Fig. 6 Comparison between NSP and NRHA predictions for EDPs of the two- and four-story steel MRFs for SF = 2.0

4.2 Incorporation of Gravity System in the Analysis Model

The gravity system components must have sufficient strength and deformation capacity to resist tributary gravity loads at the maximum drifts computed for the lateral load resisting system. The structural engineer typically decides whether or not to include contributions of the gravity system to the lateral stiffness and strength of a building. It is recommended to incorporate the gravity system in the analytical model of the structural system because the analysis might expose weaknesses that are not evident from inspection. An incentive for incorporating the gravity system is its potential benefit in decreasing drift demands and increasing collapse capacity of a structural system. This might be particularly attractive if the pushover curve exhibits an early negative tangent stiffness that may lead to large displacement amplification or even collapse. The negative stiffness will be potentially reduced by incorporating the gravity system or might even turn into a positive stiffness (Gupta and Krawinkler [30]).

A simple way to incorporate the gravity framing is by means of the “fishbone” arrangement (see Fig. 2). In order to prevent accumulation of large axial force in the column of the fishbone, an arrangement with two beams is preferred. In this arrangement, all beams are lumped into a single beam (I/L of beam = $\sum EI_i/L_i$ of all beams), all columns are lumped into a single column (I of column = $\sum I_j$ of all columns), and all gravity connections are lumped into two connections represented by rotational springs. Beams can be usually represented by elastic elements, provided that the connections of beams to columns are weaker than the beams. The column bending strength should include the effects of tributary axial forces due to gravity loads. Post-yield properties of the columns should be based on average plastic hinge properties of the columns. For modeling of the gravity system of the 4-Story-RSA- D_{\max} steel MRF, a preliminary design of the gravity beams and columns is performed using tributary areas deduced from the plan view shown in Fig. 1. Since half of the structure is modeled, the spine (column) of the “fishbone” represents 6 gravity columns and 4 moment frame columns bending about the weak axis. The beam represents 7 gravity beams.

Shear connection properties were estimated from tests summarized in [31, 32]. The cyclic behavior of a typical steel shear tab connection is shown in Fig. 7a. The pinching04 model in OpenSees [27] is utilized to simulate the response of this connection. Because of the complex behavior of these connections, greatly simplified models may be employed that are easily utilized by the engineering profession; thus, a simple elastic-perfectly plastic spring model superimposed on the experimental results is also used (see Fig. 7a). The yield rotation for this spring is 0.008 rad. Pre- and post-capping plastic rotations θ_p , θ_{pc} are 0.10 rad and 0.15 rad, respectively. The yield strength is a compromise between positive and negative strength values that can be sustained at large inelastic rotations. This model ignores the additional strength at relatively small rotations. A comparison of pushovers without and with gravity system is presented in Fig. 7b. In this example not much is gained in pushover strength and deformation capacity by incorporating the gravity system in the analysis model.

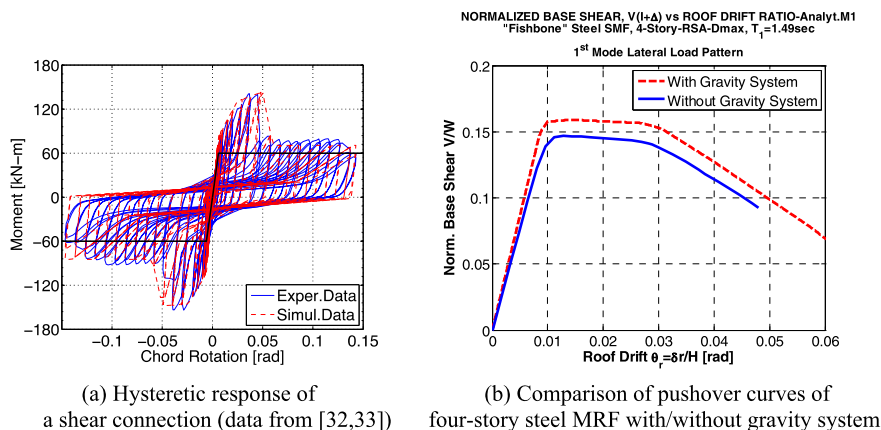


Fig. 7 Effect of gravity system on global pushover of the four-story steel MRF

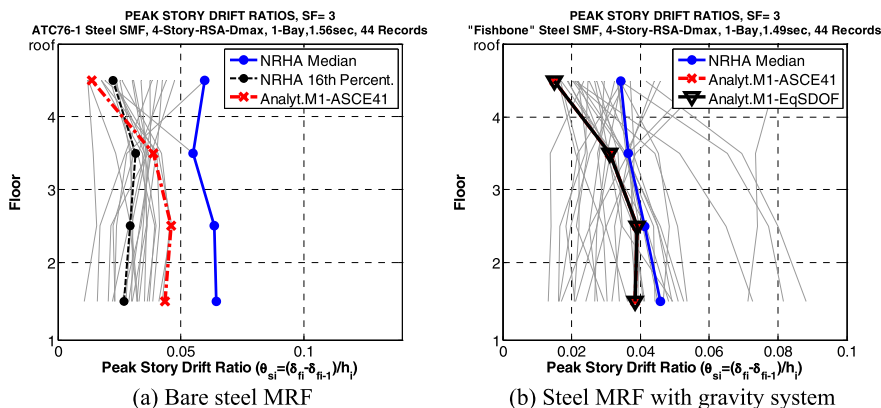


Fig. 8 Effect of gravity system on story drift ratios of the four-story MRF for SF = 3.0

The gain in peak story drift ratios when incorporating the gravity system in this example is seen in Fig. 8. This figure shows NRHA and NSP results for a ground motion scale factor $SF = 3.0$. For this scale factor, the maximum response is mostly in the negative tangent stiffness region of the pushover (roof drift > 3 % as seen from Fig. 7b). Figure 8a shows the median story drift ratios along the height of the bare four-story steel MRF for the set of 44 ground motions for $SF = 3.0$. This scale factor represents the median collapse capacity of this steel MRF, because collapse occurred under 22 out of 44 ground motions.

Incorporation of the gravity system reduced the number of collapses from 22 to 11, which has a significant effect on the probability of collapse of the steel MRF. The median roof drift is reduced from 0.049 to 0.034 rad. It is understood that the

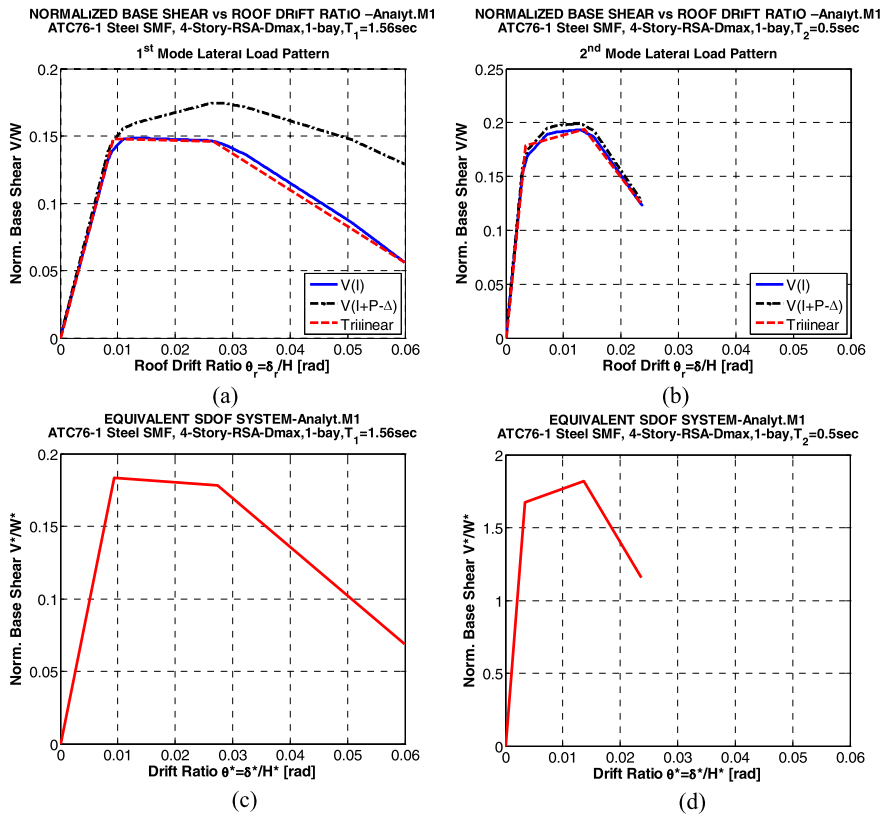


Fig. 9 Pushover curves for 1st and 2nd lateral load pattern of the 4-Story-RSA-D_{max} steel MRF together with equivalent SDOFs

observations made here are case specific, and the benefit gained from incorporating the gravity system may depend strongly on the structural configuration.

4.3 Multi-mode Nonlinear Static Procedures

The basic steps for seismic evaluation of the peak response of a steel MRF using MPA are summarized in [13, 17]. Figures 9a and 9b show the pushover curves of the four-story steel MRF using the 1st and 2nd mode lateral load patterns. The idealized equivalent SDOF systems based on the Analyt.M1 component model are shown in Figs. 9c and 9d for the 1st and 2nd mode load pattern, respectively. The IIDAP program is used to compute median displacements for the equivalent modal SDOF systems using the 44 ground motions from FEMA P695.

Goel and Chopra [33] concluded that estimates of plastic hinge rotations and member forces using MPA into the inelastic range can be improved by computing

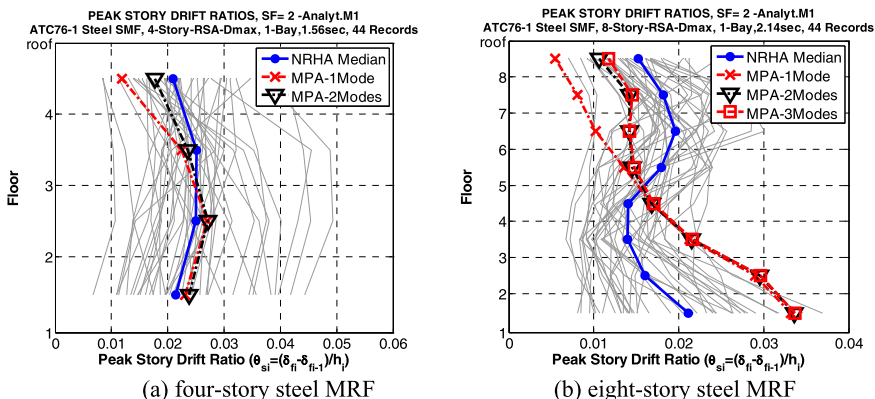


Fig. 10 Peak story drift ratios for the four- and eight-story steel MRF as predicted with NRHA and MPA for SF = 2.0

plastic hinge rotations from the total story drifts [34]. However, this will require an additional nonlinear static analysis. For the sake of simplicity, this approach was not implemented in the results presented in this section. In many cases, particularly for low-rise regular structures, the higher mode target displacement obtained from the equivalent SDOF system is less than the yield displacement, which implies that the higher mode contribution is elastic. If this is the case, all deformations and forces obtained from the MPA are modal combinations of inelastic first mode and elastic higher mode contributions. In general, this is a preferred procedure compared to the elastic response spectrum analysis (RSA) in which all modal contributions are assumed to be elastic up front [17].

The results presented in this section are for the four- and eight-story steel MRFs. Note that their seismic response has not entered the negative tangent stiffness region. The following summary observations are made on the benefits of MPA predictions for steel SMFs compared to single mode NSP predictions:

- In all cases that were investigated, the MPA led to improved EDP predictions compared to the single mode NSP options. The MPA employed here is based on the component model used in the NRHA (Analyt.M1) and on predicting modal target displacements from NRHA of equivalent modal SDOF systems.
- Incorporation of the second mode led to considerable improvement in EDP predictions. Consideration of the 3rd mode did not change the results by much even for the eight-story steel MRF (see Figs. 10, 11).
- In the case of the four-story steel MRF (see Figs. 10a, 11a, 11c) the improvement of all the story-based EDP predictions compared to NSP predictions is remarkable. In the eight-story steel MRF the MPA significantly improved the story drift ratios (Fig. 10b), shear force (Fig. 11b), and overturning moment predictions in the upper stories (Fig. 11d), compared to the single mode NSP. But predicted drifts based on MPA in the lower stories are more than 50 % larger than those obtained from NRHA for a SF = 2.0. The reason is that for this scale factor, the

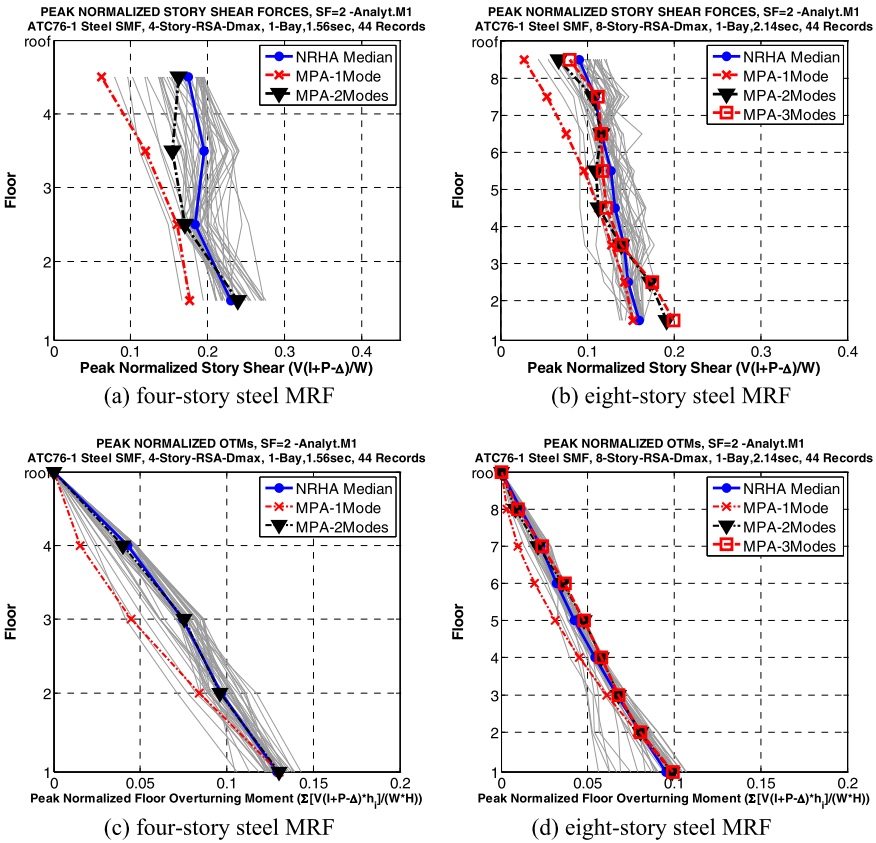


Fig. 11 Peak story shear forces and overturning moments for the four- and eight-story steel MRF as predicted with NRHA and MPA for SF = 2.0

first mode pushover shows large amplification of story drifts in the lower stories, which is not present in the NRHA. This shows the sensitivity of the predictions to invariant load patterns, which is present as much in the MPA as it is in a single mode NSP.

- The second mode contribution was elastic, which simplifies the modal combination and avoids ambiguities that might be caused by displacement reversals sometimes observed in inelastic higher mode pushover analyses.

4.4 Residual Deformations and Absolute Acceleration Demands

Figure 12 shows the residual story drift ratios and peak absolute floor accelerations along the height of the four-story steel MRF for SF = 1.0 and 2.0. It is noteworthy that the maximum absolute floor acceleration does not vary radically over the

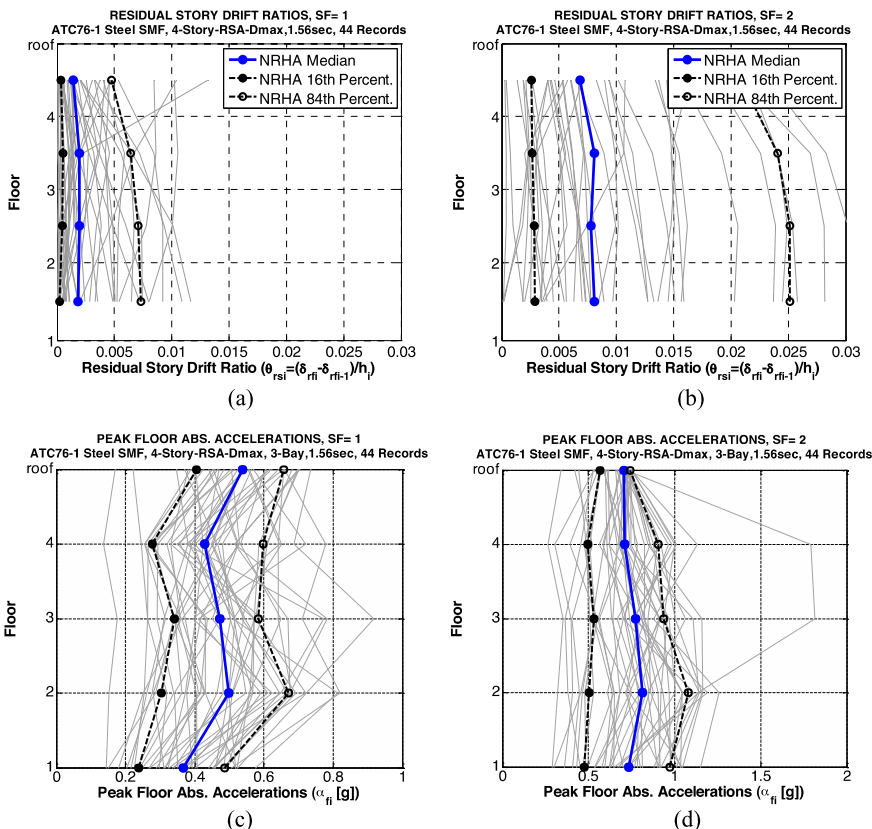


Fig. 12 Residual story drift ratios and peak floor accelerations for the four-story MRF for SF = 1.0 and 2.0

height of the four-story MRF, and that it is distributed almost uniformly over the height for a ground motion scale factor of 2.0 at which the structure responds in the highly inelastic range. Similar observations are made for the rest of the structures that are part of this study. It is a shortcoming of the NSP that it does not provide any estimation of these two important EDPs, considering the increasing importance of floor acceleration and residual drift in loss assessment of structures [35–37], and the importance of floor accelerations in estimating diaphragm forces.

5 Summary and Conclusions

This chapter presents an assessment of simplified techniques for the seismic evaluation of steel moment resisting frames. This assessment is based on direct comparisons of engineering demand parameters such as story drift ratios, story shear

forces and overturning moments of 2-dimensional models of two-, four- and eight-story archetype steel buildings as predicted with nonlinear single and multi-mode static procedures and nonlinear response history analysis. The archetype steel buildings are designed as part of NIST [18]. Detailed 3-bay models and simplified 1-bay models of the perimeter steel MRFs of these buildings are utilized, with the results produced by the two types of models being almost identical. Modeling of gravity framing can be achieved by means of a simple “fishbone” model. The main findings from the results presented here, which are representative for regular steel moment resisting frames only, are summarized as follows:

- For regular frames of four- and more stories, results from a single mode pushover analysis with an invariant load pattern do not correlate well with median results from nonlinear response history analysis. This holds true for story drifts, shear forces, and overturning moments.
- Modal Pushover Analysis leads to improved EDP predictions compared to the single mode NSP options by incorporating the second mode in the analysis in addition to the first mode. The second mode contribution is elastic for the cases evaluated in this study, which simplifies the modal combination.
- The sensitivity to invariant load patterns in single mode NSP and MPA typically leads to amplification of story drifts in lower stories compared to NRHA.
- Incorporating the gravity system into the analytical model of the structural system typically leads to a reduction in story drift ratios compared to the bare frame only. This reduction may not be very important, except when the ground motion intensity is large and collapse becomes an issue. Further studies need to be conducted to address in detail the effect of gravity system on the seismic response of steel MRFs.
- Nonlinear static analysis procedures are not capable of providing relevant information on residual drifts and floor absolute accelerations. These two EDPs are very important in loss assessment of buildings; the former for nonstructural acceleration sensitive damage, and the latter for assessing the need for demolition.
- In the authors’ opinion, the main value of a nonlinear static (pushover) analysis is to inspect the load-deformation response at a global and local level for the purpose of evaluating behavior characteristics such as the importance of P-Delta effect, global yielding, post-yield and post-capping strength and stiffness characteristics. The nonlinear static analysis is also valuable for detection of potential strength and stiffness discontinuities that might adversely affect the dynamic response of a structure. Quantification of demand parameters from pushover results is questionable for structures that have considerably higher mode effects and/or significant strength or stiffness discontinuities. Such quantification can be obtained, approximately, from NRHA using simple component models such as a bilinear hysteresis model, and a small set of spectrum-matched ground motions. More accurate assessment of demand parameters, including measures of uncertainties, will necessitate more accurate structural modeling for NRHA and ground motions that represent the intensity characteristics and record-to-record variability inherent in seismic hazard.

Acknowledgements This study relies on results obtained under Task Order 6 of the NEHRP Consultants Joint Venture (a partnership of the Applied Technology Council and Consortium of Universities for Research in Earthquake Engineering), under Contract SB134107CQ0019, Earthquake Structural and Engineering Research, issued by the National Institute of Standards and Technology. The views expressed do not necessarily represent those of the organizations identified above.

References

1. ATC (1996) Seismic evaluation and retrofit of concrete buildings. ATC 40 report, vols 1 and 2. Applied Technology Council, Redwood City
2. ASCE (2003) Seismic evaluation of existing buildings. ASCE standard ASCE/SEI 31-03. American Society of Civil Engineers/Structural Engineering Institute, Reston
3. ASCE (2007) Seismic rehabilitation of existing buildings. ASCE standard ASCE/SEI 41-06. American Society of Civil Engineers/Structural Engineering Institute, Reston
4. FEMA (1997) NEHRP guidelines for the seismic rehabilitation of buildings. FEMA 273 report, prepared by the Applied Technology Council for the Federal Emergency Management Agency, Washington
5. FEMA (2005) Improvement of nonlinear static seismic analysis procedures. FEMA 440 report, prepared by the Applied Technology Council for the Federal Emergency Management Agency, Washington
6. FEMA (2009) Effects of strength and stiffness degradation on seismic response. FEMA P-440A report, prepared by the Applied Technology Council for the Federal Emergency Management Agency, Washington
7. FEMA (2009) Quantification of building seismic performance factors. FEMA P-695 report, prepared by the Applied Technology Council for the Federal Emergency Management Agency, Washington
8. Saiidi M, Sozen MA (1981) Simple nonlinear seismic analysis of R/C structures. *J Struct Div* 107(ST5):937–951
9. Fajfar P, Gaspersic P (1996) The N2 method for the seismic damage analysis of RC buildings. *Earthq Eng Struct Dyn* 25(1):31–46
10. Lawson RS, Vance V, Krawinkler H (1994) Nonlinear static pushover analysis—why, when and how? In: *Proceedings of the 5th US conference on earthquake engineering*, Chicago, vol 1, pp 283–292
11. Bracci JM, Kunnath SK, Reinhorn AM (1997) Seismic performance and retrofit evaluation of reinforced concrete structures. *J Struct Eng* 123(1):3–10
12. Krawinkler H, Seneviratna GDPK (1998) Pros and cons of a pushover analysis for seismic performance evaluation. *Eng Struct* 20(4–6):452–464
13. Chopra AK, Goel RK (2002) A modal pushover analysis procedure for estimating seismic demands for buildings. *Earthq Eng Struct Dyn* 31(3):561–582
14. Gupta B, Kunnath SK (2000) Adaptive spectra-based pushover procedure for seismic evaluation of structures. *Earthq Spectra* 16(2):367–392
15. Sasaki KK, Freeman SA, Paret TF (1998) Multimode pushover procedure (MMP)—a method to identify the effects of higher modes in a pushover analysis. In: *Proceedings of the 6th US national conference on earthquake engineering*, Seattle
16. Antoniou S, Pinho R (2004) Development and verification of a displacement-based adaptive pushover procedure. *J Earthq Eng* 8(5):643–661
17. NIST (2010) Applicability of nonlinear multiple-degree-of-freedom modeling for design. GCR 10-917-9, prepared by the NEHRP Consultants Joint Venture for the National Institute of Standards and Technology, Gaithersburg

18. NIST (2010) Evaluation of the FEMA P-695 methodology for quantification of building seismic performance factors. GCR 10-917-8, prepared by the NEHRP Consultants Joint Venture for the National Institute of Standards and Technology, Gaithersburg
19. AISC (2005) Prequalified connections for special and intermediate steel moment frames for seismic applications. AISC 358-05, American Institute of Steel Construction, Inc, Chicago
20. Lignos DG, Putman C, Zareian F, Krawinkler H (2011) Seismic evaluation of steel moment frames and shear walls using nonlinear static analysis procedures. In: Proceedings of the ASCE structures congress, Las Vegas, April 14–16, 2011
21. Prakash V, Powell GH, Campbell S (1993) DRAIN-2DX: basic program description and user guide. Report UCB/SEMM-1993/17, University of California, Berkeley
22. Ibarra LF, Medina RA, Krawinkler H (2005) Hysteretic models that incorporate strength and stiffness deterioration. *Earthq Eng Struct Dyn* 34(12):1489–1511
23. Lignos DG, Krawinkler H (2011) Deterioration modeling of steel components in support of collapse prediction of steel moment frames under earthquake loading. *J Struct Eng* 137(10):1215–1228
24. Krawinkler H, Bertero VV, Popov EP (1975) Shear behavior of steel frame joints. *J Struct Div* 101(11):2317–2336
25. Lignos DG, Zareian F, Krawinkler H (2010) A steel component database for deterioration modeling of steel beams with RBS under cyclic loading. In: Proceedings of the ASCE structures congress, Orlando, May 12–15, 2010
26. Luco N, Mori Y, Funahashi Y, Cornell A, Nakashima M (2003) Evaluation of predictors of non-linear seismic demands using ‘fishbone’ models of SMRF buildings. *Earthq Eng Struct Dyn* 32(14):2267–2288
27. McKenna F (1997) Object oriented finite element programming frameworks for analysis, algorithms and parallel computing. PhD dissertation, University of California, Berkeley
28. PEER/ATC (2010) Modeling and acceptance criteria for seismic design and analysis of tall buildings. PEER/ATC-72-1, prepared by the Applied Technology Council in cooperation with the Pacific Earthquake Engineering Research Center, Redwood City
29. Lignos DG (2009) Interactive interface for incremental dynamic analysis, IIDAP: theory and example applications manual, version 1.1.5. Department of Civil and Environmental Engineering, Stanford University
30. Gupta A, Krawinkler H (2000) Dynamic P-Delta effects for flexible inelastic steel structures. *J Struct Eng* 126(1):145–154
31. Liu J, Astaneh AA (2000) Cyclic testing of simple connections including effects of slab. *J Struct Eng* 126(1):32–39
32. Liu J, Astaneh AA (1999) Studies and tests of simple connections, including slab effects. Report UCB/CEE-Steel-99 /01, University of California, Berkeley
33. Goel RK, Chopra AK (2005) Extension of modal pushover analysis to compute member forces. *Earthq Spectra* 21:125–140
34. Gupta A, Krawinkler H (1997) Seismic demands for performance evaluation of steel moment resisting frame structures (SAC Task 5.4.3). Report No 132, John A. Blume Earthquake Engineering Center, Stanford University, Stanford
35. Pampanin S, Christopoulos C, Priestley MJN (2002) Residual deformations in the performance-seismic assessment of frame structures. Report ROSE-2002/02, European School for Advanced Studies in Reduction of Seismic Risk, Pavia
36. Aslani H, Miranda E (2005) Probabilistic earthquake loss estimation and loss disaggregation in buildings. Report No 157, John A. Blume Earthquake Engineering Center, Stanford University, Stanford
37. Ramirez CM, Miranda E (2009) Building-specific loss estimation methods & tools for simplified performance-based earthquake engineering. Report No 173, John A. Blume Earthquake Engineering Center, Stanford University, Stanford

Preliminary Seismic Assessment Method for Identifying R.C. Structural Failures

Stylios J. Pardalopoulos, Georgia E. Thermou,
and Stavroula J. Pantazopoulou

Abstract In this chapter, an efficient method for rapid preliminary assessment of the seismic vulnerability of reinforced concrete buildings is presented. The method determines the columns' limiting shear resistance at the critical storey of the structure, by applying a *strength assessment* procedure associated with typical column details representative of the state of practice from the era of the building's period of construction and evaluates the severity of seismic displacement demand and the maximum seismic acceleration that the building can sustain by applying a *stiffness index assessment*. For application of the method, only knowledge of the basic geometric and material properties of the building is required. The proposed method is applied for verification reasons to two reinforced concrete buildings that failed during the 1999 Athens earthquake. It is shown that the proposed method can be used as a diagnostic tool for identification of both the building's fragility and the prevailing failure mechanism, allowing the engineers to immediately identify the most vulnerable buildings that are likely to collapse in a potentially strong earthquake, as well as to set objectives for their rehabilitation.

Keywords Lightly reinforced concrete · Rapid assessment · Substandard construction · Brittle failure · Buildings

1 Introduction

Recent earthquakes have repeatedly illustrated the deficiencies of brittle reinforced concrete buildings built according to earlier design codes. This class of buildings, which today represents the majority of the built environment in the greatest part

S.J. Pardalopoulos · S.J. Pantazopoulou
Dept. of Civil Engineering, Democritus University of Thrace, 67100, Xanthi, Greece

G.E. Thermou (✉)
Dept. of Civil Engineering, Aristotle University of Thessaloniki, 54124, Thessaloniki, Greece
e-mail: gthermou@civil.auth.gr

S.J. Pantazopoulou
Dept. of Civil & Environmental Engineering, University of Cyprus, Nicosia, Cyprus

of the world, is typified by a number of features such as small section columns, relatively stiff beams, inadequately confined joints and insufficient anchorage of longitudinal and transverse reinforcement. Although the application of detailed assessment procedures for seismic evaluation of every single existing structure is of vital importance, the immense volume of required work makes it seem an unrealistic scenario. This difficulty could be removed by applying a rapid evaluation procedure, where information readily available for most buildings will be used; in such a rapid assessment, critical features of the structure that render it more vulnerable could be immediately identified, thereby simplifying the process of singling out those structures that represent a major threat to human life in the event of a strong earthquake.

The objective of this study is to present a methodology where the building's geometrical characteristics, material properties and reinforcement detailing of the structural elements are considered sufficient information so as to single out the most vulnerable buildings that are likely to collapse in a potential strong earthquake, but can also be used to determine the objectives for their rehabilitation. Existing reinforced concrete buildings, "non-conforming" according to modern standards, are assessed based on prioritising of the various alternative modes of failure. Mechanisms considered refer to column flexure, degraded shear, anchorage and lap-splice development, exceedance of joint shear capacity, connection punching and reinforcement yield at the adjacent to columns beams; the rate of degradation of these mechanisms with increasing displacement amplitude and number of cycles is idealised through simplified mechanistic constructs which allows the prioritising of failure modes as degradation proceeds. Furthermore, the seismic vulnerability of this category of buildings is assessed as a function of interstorey drift demand imposed by the design earthquake [1]. For confirmation, the methodology is applied in two reinforced concrete buildings that collapsed during the 1999 Athens earthquake. Results indicated that in all cases buildings failed in a brittle manner practically prior to development of any displacement ductility (i.e. elastic-brittle damage), a conclusion compatible with the reconnaissance reports.

2 Construction Practice of Reinforced Concrete Buildings in the 1960's and 1970's

The rapid population growth and the shift from the agricultural to the industrial economy model throughout Southern Europe in the first 2/3rds of the 20th century led to massive urbanisation of cities. Multistorey reinforced concrete constructions were established as the basic building unit, as they provided capability of arranging the structural elements according to the architectural designs, short construction time, low construction cost and endurance in earthquake excitations.

In this period, construction details were not strictly addressed by the design codes, since their role in seismic response was yet to be fully understood and as such they were seldom specified in design drawings of that era. Implementation in practice was, to a large extent, determined by the experience of the labourers

and the foreman responsible for the site. Credentials were never questioned and supervision was relatively lenient. Reconnaissance studies from collapsed buildings in major earthquake events over the past 30 years suggest that specific trade practices were used throughout Southern Europe (tie patterns and spacing, layout of reinforcement), regardless of details—if any—that may have been specified in official drawings. Typical details based on the standards of the period (summarised in fib Bulletin 24 [2]) comprised smooth rectangular stirrups anchored with 90° hooks in the ends, made of StI ($f_{yk} = 220$ MPa) 6–8 mm diameter bars spaced at 250–300 mm o.c. (on centres) along the member lengths. Longitudinal reinforcement of StIII ($f_{yk} = 420$ MPa) at relatively low area ratios and concrete quality of Bn150 to Bn200 (defined as per DIN 1045, [3]) corresponding to modern concrete characteristic strengths of 12 to 16 MPa were utilised. Lap splices were unconfined whereas starter bars had arbitrary lengths. Regarding typical column section sizes those ranged between 250 and 500 mm. Beam sizes were 250 mm by 600 to 700 mm, common slab thicknesses ranged from 120 to 160 mm, reinforced with 10 mm diameter bars usually spaced at 200 mm o.c. Other features commonly reported refer to short or captive columns owing to the mixed use of the first floor of the buildings and unconfined beam-column joints particularly in connections over the perimeter of an R.C. frame building. Single column footings were mostly used and, in well-attended structures, they were joined at the column base with lightly reinforced, small section connecting beams.

Despite these systematic inadequacies, the percentage of buildings that have collapsed in major earthquakes in the Mediterranean basin is relatively low when compared to the total number of available buildings that belong to this substandard construction category; this is not the case in other parts of the world such as in Haiti [4]. One issue that can be concluded, however, from post-earthquake reconnaissance evidence and forensic evaluations of collapsed buildings which led to loss of human life, is that collapse usually occurs due to premature failure if the gravity load bearing elements of the structures, prior to attainment of the nominal yielding displacement. This is contrary to the focus of most modern assessment methodologies that are based on comparisons between ductility demand and supply. Note that the usual point of reference in these procedures is columns where transverse reinforcement is not adequate to support shear strength under displacement reversals beyond flexural yielding of the individual members of a structure. For this reason, values of rotation capacity in what is termed “non-conforming” members are usually deemed in the range of 1 % to 1.5 %. This focus could be justifiable for structures with columns where the member size (in the range of 500 mm or higher) is twice that of typical stirrup spacing used in the 1960’s, so that a nominal 45° shear plane in a column would intersect at least two stirrups. But in case of structures with smaller column sizes, in the range of 350 mm, as is often encountered in older residential buildings, the practical spacing of stirrups from the 1960’s (250 mm) could mean that a nominal potential sliding plane could be formed, intersecting no stirrup at all and therefore being unable to mobilise any form of shear resistance.

3 Method for Rapid Seismic Assessment of Reinforced Concrete Buildings

In light of the limited knowledge of actual construction details in older structures, preliminary assessment targeted toward identification of the most vulnerable buildings must necessarily rely on a marginal collection of data that is readily available, such as the overall geometric details of the structure (number of floors, floor height, floor area, location and gross geometry of load carrying members in plan), on the implicit assumption that all reinforcing details are represented by the historical construction information for the period and region of construction of the building studied. With these data, building seismic vulnerability is based on the following two criteria:

- (a) A *strength assessment criterion*, which is used to determine the weakest mechanism of resistance, likely to control the sequence of failure of the vertical elements of the structure, as well as their limiting resistance.
- (b) A *stiffness index assessment criterion*, which is used to quantify the interstorey drift demand of the critical storey of the building and the maximum ground acceleration that the building can sustain.

Strength Assessment Collapse occurs when the vertical elements of the critical floor lose their load carrying capacity. This process may be initiated either by loss of lateral load resistance of the columns, or by punching and loss of support of the floor diaphragms. Assuming the point of inflection (zero moment) at midspan of the column length, enables the establishment of a static relationship between the critical strengths of various mechanisms that could be responsible for column failure along the line of a single column and the column shear sustained when any of these phenomena is occurring: $V^{col} = (M^{top} + M^{bottom})/h_{col}$ where h_{col} is the deformable length of the column (i.e. the clear storey height, or free column length in captive columns, Fig. 1(a)). This enables using column shear as a common basis for comparison of strengths in order to establish a hierarchy of possible events that threaten the integrity of a structure under lateral sway.

The flexural shear demand associated with flexural yielding in the column ends under lateral sway, is a point of reference in the hierarchy of failure (Fig. 1(b)), as flexural yielding is the only failure mode associated with ductile member behaviour. Assuming the maximum developed stress of the column longitudinal reinforcement equals to the steel yielding stress, f_y , the flexural shear demand can be calculated according to Eq. (1), taking into consideration the column's internal force equilibrium.

$$V_{flex} = 2 \cdot M_y / h_{col} = \left[\rho_{\ell, tot} \cdot \frac{f_y}{f_c} \cdot (1 - 0.4 \cdot \xi) + v \cdot \left(\frac{h}{d} - 0.8 \cdot \xi \right) \right] \cdot \frac{b \cdot d^2 \cdot f_c}{h_{col}} \quad (1)$$

where, M_y is the flexural moment at yielding; $\rho_{\ell, tot}$ is the total longitudinal reinforcement ratio of the column; f_y is the longitudinal reinforcement yield stress;

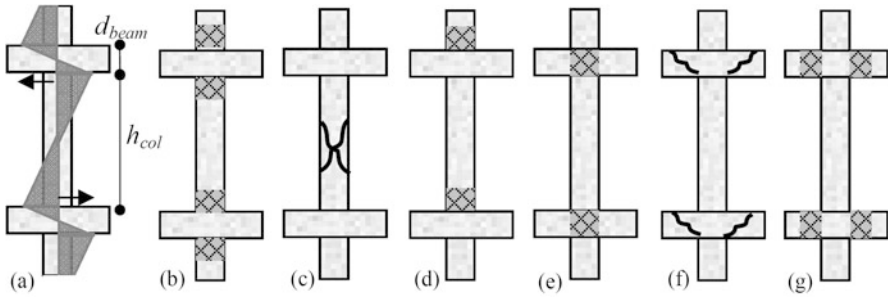


Fig. 1 Moment distribution and (b)–(f) possible failure modes of a reinforced concrete columns: (b) Flexural yielding, (c) Shear failure, (d) Bar anchorage/lap-splice failure, (e) Joint shear failure, (f) Connection punching failure, (g) Column shear limited by plastic hinging in the beams ⇒ ductile frame behaviour

f_c is the concrete compressive strength; ξ is the normalised depth of compression zone given in Fig. 2(b) as a function of $\rho_{\ell,tot}$ and the (service) axial load ratio, v , acting on the cross section ($N_{g+0.3q}/(b \cdot d \cdot f_c)$); h is the column height; d is the column effective depth; b is the column width and h_{col} is the deformable length of column (equal to free storey height or to the column length in the case of captive columns).

Lightly reinforced columns, where transverse reinforcement is not adequate to support shear strength under displacement reversals beyond flexural yielding, is a common occurrence in older structures. A first estimate of the shear strength can be obtained from the typical reinforcing details used in construction in the 1960–70’s, by considering the simple statics of a column with symmetric end conditions under lateral sway. Shear strength is supported by the stirrups that are intersected by the critical plane of diagonal tension failure. To this end, it is assumed that shear failure occurs by formation of a sliding plane inclined at an angle θ_v with respect to the longitudinal axis of the typical column (Fig. 1(c)). θ_v determines the number of stirrup legs actively participating to shear strength; based on calibration with test and analytical results it is taken equal to 30° . The concrete contribution to shear strength is accounted for by the horizontal component of a diagonal strut that carries the column axial load through the web to the support. The angle of inclination of the diagonal strut, α , is determined from the line connecting the centres of the compression zones in the opposite ends of the column (over its height), i.e. $\tan \alpha = (h - 0.8 \cdot \xi \cdot d)/h_{col} = (h/d - 0.8 \cdot \xi) \cdot d/h_{col}$ (Fig. 2(a)), where ξ is the normalised depth of compression zone at the onset of yielding (Fig. 2(b)) and h and d are the height and the effective depth of the column’s cross section. Generally, it is required that $\alpha \leq \theta_v$.

The shear force that can develop to a column at the exhaustion of its shear strength is:

$$V_v = v \cdot \tan \alpha \cdot b \cdot d \cdot f_c + A_{tr} \cdot f_{st} \cdot \frac{d - \xi \cdot d}{s} \cdot \cot \theta_v \tag{2}$$

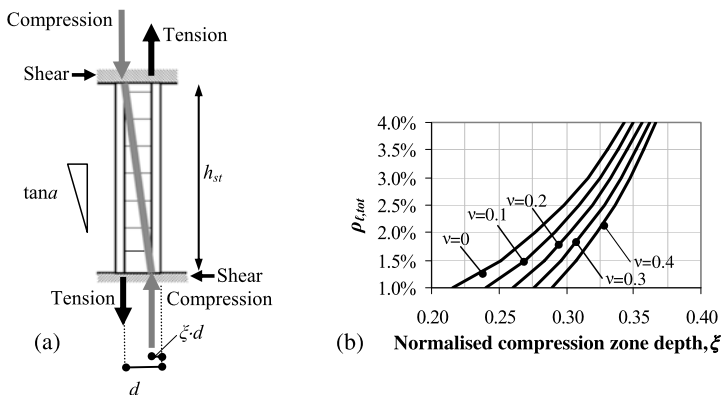


Fig. 2 (a) Lightly reinforced column model used for the methodology; (b) Relationship between ξ , $\rho_{\ell,tot}$ and normalised axial load, v , for columns at the onset of yielding

where, A_{tr} is the area of stirrup legs in a single stirrup pattern in direction normal to the splitting plane; s is the stirrup spacing and f_{st} is the stirrup yield stress.

Another possible mechanism of failure that can develop in reinforced concrete columns is anchorage failure of longitudinal reinforcement (Fig. 1(d)). Anchorage of a reinforcement bar in tension is achieved through friction, developed between the surface of the bar and the surrounding concrete. In cases of bars with ends formed as hooks, an additional constant force is added to the total anchorage capacity of the bar [5]. When the maximum anchorage force that can be developed by the bar is lower than the tension force corresponding to the bar yield, $f_y \cdot A_b$ (where A_b is the cross section area of the bar), anchorage failure is anticipated and the maximum tension force developed by the bar is limited to its maximum anchorage capacity. In this state, the column’s anchorage shear demand can be calculated according to:

$$V_a = \left[\rho_{\ell,tot} \cdot \frac{\min \left\{ \frac{4 \cdot L_a \cdot f_b}{D_b} + \alpha_{hook} \cdot 50 \cdot f_b; f_y \right\}}{f_c} \cdot \frac{b \cdot d^2 \cdot f_c}{h_{col}} \right] \cdot \left((1 - 0.4 \cdot \xi) + v \cdot \left(\frac{h}{d} - 0.8 \cdot \xi \right) \right) \quad (3)$$

where, $\rho_{\ell,tot}$ is the total longitudinal reinforcement ratio of the column; L_a is the anchorage length; f_b is the concrete bond stress, calculated according to Model Code 2010 [5] ($f_b = 2 \cdot f_{b,o}$, where $f_{b,o} = n_1 \cdot n_4 \cdot (f_c/20)^{0.5}$, $n_1 = \{1.80 \text{ for ribbed bars; } 0.90 \text{ for smooth bars}\}$, $n_4 = \{1.2 \text{ for } f_y = 400 \text{ MPa; } 1.0 \text{ for } f_y = 500 \text{ MPa}\}$). Note that the anchorage capacity of a smooth bar hook is considered equal to with that of a ribbed bar, $= 50 \cdot f_b \cdot A_b$); D_b is the diameter of longitudinal reinforcing bars; α_{hook} is a binary index (1 or 0) to account for hooked anchorages ($\alpha_{hook} = 0 \Rightarrow$ no hooks); f_y is the longitudinal reinforcement yield stress; f_c is the concrete compressive strength; ξ is the normalised depth of compression zone (Fig. 2(b)); v is the (service) axial load acting on the cross section; h is the column height; d is the column effective depth; b is the column width; h_{col} is the column’s deformable length.

Lap failure of longitudinal reinforcement bars (Fig. 1(d)) occurs when the tension force developed to the one of the two paired bars cannot be fully transferred to the other one, due to insufficient concrete bond stress. Note that laps usually occur at the lower end of the column, where starter bars from the floor below are paired with their extensions. Concrete bond stress is increased by the transversal pressure provided by the column stirrups along the lap length, whereas hook development at the ends of the lapped bars also increase the tension force that can be transferred from one bar to another. The column's shear demand at the onset of its longitudinal reinforcement bars lap capacity can be calculated as:

$$V_{lap} = \frac{\left[\min \left\{ \left(\mu_{fr} \cdot L_{lap} \cdot \left[\frac{A_{tr}}{s} \cdot f_{st} + \alpha_b \cdot (b - N_b \cdot D_b) \cdot f_t \right] \right) + \alpha_{hook} \cdot 50 \cdot N_b \cdot A_b \cdot f_b \right\}; N_b \cdot A_b \cdot f_y \right]}{d \cdot (1 - 0.4 \cdot \xi) + v \cdot b \cdot d^2 \cdot f_c \cdot (0.5 \cdot h/d - 0.4 \cdot \xi)} \cdot h_{col}/2 \quad (4)$$

where, in addition to the symbols described in previous cases, μ_{fr} is the friction coefficient ($0.2 \leq \mu_{fr} \leq 0.3$ for smooth bars; $1.0 \leq \mu_{fr} \leq 1.5$ for ribbed bars); L_{lap} is the lap length; α_b is a binary index (1 or 0) depending on whether ribbed or smooth reinforcement has been used (this variable regulates the contribution of the concrete cover); N_b is the number of tension bars; f_t is the concrete tensile strength; A_b is the area of a single tension bar.

Preservation of gravity load carrying capacity and lateral load strength in reinforced concrete frame structures under earthquake action is linked to the integrity of the beam-column joints, since these elements are part of both the vertical and the horizontal load path. Transfer of forces through the joints is necessary for the development of the flexural strengths of the adjacent beam and column elements at the joint faces. During an earthquake, the moment distribution at the element ends adjacent to the opposite joint faces, impose the development of significant shear forces in the joint core. In a new reinforced concrete construction, stirrups inside the joint act as a mechanism of confinement, preserving the integrity of the diagonal compressive stress-field, through which concrete participates to the joint shear action, while also enabling sharp force gradients along the beam and column primary reinforcements through development of high bond stresses. In an older construction, with absence of stirrups inside the joint, the integrity of the joint relies to the limited tensile strength of the joint panel. In both cases, when the shear capacity of the joint core (Eqs. (5a)–(5b)) is less than the corresponding developed shear forces, resulting from the flexural response of the adjacent to elements to the joint faces, joint failure during an earthquake (Fig. 1(e)) may be very brittle.

– For unreinforced or lightly reinforced joints:

$$V_j = \gamma_j \cdot 0.5 \cdot \sqrt{f_c} \cdot \sqrt{1 + \frac{v_j \cdot f_c}{0.5 \cdot \sqrt{f_c}}} \cdot \frac{b_j \cdot d \cdot d_{beam}}{h_{col}} \quad (5a)$$

– For well reinforced joints:

$$V_j = \left[\gamma_j \cdot 0.5 \cdot \sqrt{f_c} \cdot \sqrt{1 + \frac{v_j \cdot f_c}{0.5 \cdot \sqrt{f_c}} \cdot \frac{b_j \cdot d \cdot d_{beam}}{h_{col}}} \right] \cdot \sqrt{1 + \rho_{j,horiz} \cdot \frac{f_{st}}{f_t}} \quad (5b)$$

In Eqs. (5a)–(5b), γ_j equals 1.40 for interior joints and 1.00 for all other cases; v_j is the (service) axial load acting on the bottom of the column adjusted at the top of the joint; b_j is the joint width; d_{beam} is the beam depth; $\rho_{j,horiz}$ is the area ratio of joint horizontal reinforcement (i.e. total area of stirrup legs in the joint parallel to the plane of action, divided by $b_j \cdot d_{beam}$).

Punching shear of flat slabs in slab-column connections (Fig. 1(f)) is a failure mode associated to the concentration of shear stresses over a relatively small area, around the column. The associated column shear is estimated from equilibrium of moment transfer, $V_{pn} = M_{pn} / h_{col}$, where M_{pn} is the strength for moment transfer of the critical punching perimeter at the slab-column connection, as:

$$V_{pn} = \frac{0.12 \cdot \min \left\{ 1 + \sqrt{\frac{200}{d_{sl}}}; 2 \right\} \cdot (100 \cdot \rho_{\ell,sl} \cdot f_c)^{1/3} \cdot d_{sl} \cdot 0.25 \cdot u_{crit} \cdot (h + 4 \cdot d_{sl})}{h_{col}} \quad (6)$$

where, d_{sl} is the slab depth, $\rho_{\ell,sl}$ is the total slab reinforcement ratio at the critical punching perimeter around the column, u_{crit} .

The limiting shear strength that controls the behaviour of the column, $V_{u,lim}$, is the least value obtained from Eqs. (1)–(6), also identifying the mode of column failure, thus,

$$V_{u,lim} = \min\{V_{flex}, V_v, V_\alpha, V_{lap}, V_j, V_{pn}\} \quad (7)$$

The above scenarios, which correspond to brittle failure modes except for the column flexural yield, may be suppressed if the shear force input to the column is limited by yield of the longitudinal reinforcement of the adjacent beams (Fig. 1(g)). In this case, the limiting shear strength of the column is:

$$V_{by} = \frac{(M_{beam}^+ + M_{beam}^-)}{h_{st}} = \frac{0.85 \cdot \rho_{beam} \cdot b_{beam} \cdot d_{beam}^2 \cdot f_y^{beam}}{h_{col}} \quad (8)$$

where, ρ_{beam} is the tension longitudinal reinforcement ratio of the beam (i.e. the total longitudinal reinforcement ratio of the beam section adjacent to the column if an interior connection is considered, or in the case of exterior connections the value of the top or bottom beam reinforcement ratio (whichever is largest, since the numerator in original form of Eq. (8) is simplified to absolute maximum of M_{beam}^+ or M_{beam}^-); b_{beam} is the beam width; d_{beam} is the beam effective depth and f_y^{beam} is the yield stress of the beam longitudinal reinforcement.

Stiffness Index Assessment From the earliest earthquake studies the area ratio of the vertical load-bearing elements in a structure was used to characterise the magnitude of lateral stiffness. The first generation of Seismic Codes (up to 1950's)

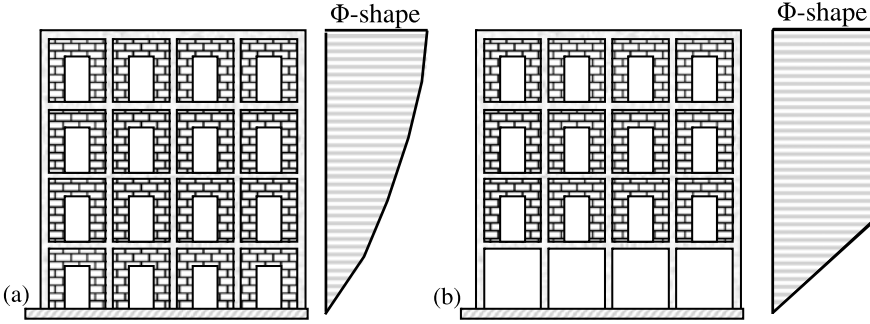


Fig. 3 Lateral displacement profiles; (a) shear-type; (b) soft-storey

required that the floor area ratio of walls should be 2%o times the number of floors in the structure. The relationship between generalised stiffness, K^* and the floor area ratios of columns, ρ_c , walls, ρ_{wc} , and infill walls, ρ_{wm} , in a multistorey structure was explored recently [1]. Next, the fundamental period of the structure, T ($T \approx 2 \cdot \pi \cdot \sqrt{[0.8 \cdot W / (g \cdot K^*)]}$), was used, in order to derive expressions for the displacement demand under the design earthquake, S_d , in terms of ρ_c , ρ_{wc} , and ρ_{wm} (where the seismic hazard is given in relative displacement vs. period spectrum coordinates). Here the Design Earthquake Spectrum of Type I, as prescribed by EC8-I [6] has been used.

Using function $\Phi_i = \sin(\pi \cdot i / (2n))$ as an approximation to the fundamental mode shape of vibration of the structure (modelling shear-type behaviour for older construction, Fig. 3) in calculating K^* and T ($= 2\pi \sqrt{[m_i / K_i \cdot \sum \Phi_i^2 / \sum (\Phi_i - \Phi_{i-1})^2]}$), where K_i and m_i are the stiffness and mass of the typical storey i), it is possible to develop generic charts of the type shown in Fig. 4 that relate drift demand in the *first* floor of the structure to a combined stiffness geometric index, k , as follows:

$$0.15 \leq T \leq 0.50: \quad \Theta_1 = 121.6 \cdot a_g \cdot n^2 \cdot \left(\frac{\gamma}{E_c \cdot k} \right) \cdot \sin\left(\frac{\pi}{2 \cdot n} \right) \quad (9a)$$

$$0.50 < T \leq 2.00: \quad \Theta_1 = 1.52 \cdot a_g \cdot \frac{n}{h_{st}^{0.5}} \cdot \left(\frac{\gamma}{E_c \cdot k} \right)^{0.5} \cdot \sin\left(\frac{\pi}{2 \cdot n} \right) \quad (9b)$$

where, a_g is the peak ground acceleration, n is the number of floors, E_c is the elastic modulus of concrete, h_{st} is the storey height and γ is the mass per unit area of the floor.

The combined stiffness geometric index, k , for dual systems is obtained from:

$$k = \rho_c + n_{wm} \cdot \rho_{wm}^e \quad (10)$$

where:

$$n_{wm} = \frac{25 \cdot E_{wm}}{E_c \cdot \left(\frac{h_{st}^2}{l_{m,ave}^2} + 2.5 \right)}, \quad \rho_{wm,i}^e = \rho_{wm,i} + \frac{\left(4 \cdot \frac{h_{st}^2}{l_{m,ave}^2} + 2.5 \right)}{\left(4 \cdot \frac{h_{st}^2}{l_{w,ave}^2} + 2.5 \right)} \cdot \frac{E_c}{E_{wm}} \cdot \rho_{wc,i}$$

For frame-structures index k is substituted by k' , defined as:

$$k' = \rho_c + \eta'_{wm} \rho_{wm}, \quad \text{where } \eta'_{wm} = \frac{10 \cdot f_{wk} \sqrt{\left(1 + \frac{h_{st}^2}{l_{w,ave}^2}\right)}}{E_c \Theta_1} \quad (11)$$

where E_c , E_{wm} are the elastic moduli of concrete and masonry, respectively, ρ_c is the columns' area ratio in the floor plan, ρ_{wm}^e , is an equivalent compound dimensionless area index that represents both masonry walls and R.C. walls expressed in terms of masonry wall properties, h_{st} is the storey height, $l_{m,ave}$, $l_{w,ave}$ are the average lengths of masonry and R.C. walls in the plane of seismic action, respectively, f_{wk} is the compressive strength of masonry and Θ_1 is the estimated chord rotation demand of the first storey.

In cases of inadequate shear resistance collapse of substandard buildings in a critical earthquake could be prevented only if the interstorey drift demand, Θ_u , in the critical floor (if the critical floor is the first floor, $\Theta_u = \Theta_{u,1}$), is less than the estimated drift at failure, Θ_{fail} . The fraction of the interstorey drift demand developed through deformation in the columns, is: $\Theta_u^c = \lambda_c \cdot \Theta_u$, where λ_c is the relative column stiffness ratio in the frame connections of the building [1]: $\lambda_c = \lambda / (1 + \lambda)$, $\lambda = \sum EI_b h_{st} / \sum EI_c L_b$, where summation refers to the number of beams (1 or 2) and columns (1 or 2) converging to the connection.

If failure occurs prior to flexural yielding of the columns, i.e., when the estimated base shear force at the occurrence of the controlling mode of failure of the column, $V_{u,lim}$ is less than the base shear corresponding to the onset of yielding of column reinforcement, $V_{y,flex}$, then the drift at failure is obtained from:

$$\begin{aligned} \Theta_{fail}^c &= \frac{V_{u,lim}}{V_{y,flex}} \cdot \Theta_{y,nom}^c = r_{u,lim} \cdot \Theta_{y,nom}^c = \Theta_{y,crit}^c \leq \lambda_c \cdot \Theta_{y,crit} \\ \Rightarrow \Theta_{fail} &= \frac{1}{\lambda_c} \cdot \Theta_{fail}^c = \frac{1}{\lambda_c} \cdot \Theta_{y,crit}^c \end{aligned} \quad (12)$$

In the above, $\Theta_{y,crit}$ is the estimated interstorey drift at longitudinal reinforcement yielding of the critical floor—for typical frame structures (with floor heights around 3 m) this is usually in the range of 0.5 %. $\Theta_{y,crit}^c$ is the average interstorey drift at longitudinal reinforcement yielding of the vertical members of the critical storey. For typical older construction (stirrups spaced at distances over 200 mm), it is shown through detailed calculation in the next section that the ratio $r_{u,lim}$ may be as low as 0.3–0.6, depending on the size of the columns for the typical details used in the period of reference (due to the widespread practice of using uniformly large stirrup spacing around 250 mm, values for the ratio are lower in the case of smaller column section sizes owing to the lower number of stirrup layers engaged by the sliding plane).

The plot in Fig. 4 has been drawn for the EC8 [6] design spectrum (Type I) using a unit value of peak ground acceleration for a period range $0.15 \leq T < 0.5$ sec (Eq. (9a)); thus, demand (ordinate in the graph) should be multiplied by the specified peak ground acceleration of the site in consideration, a_g . The plot has been derived for concrete quality C20/25 ($f'_c = 20$ MPa) and mass per unit area of the floor,

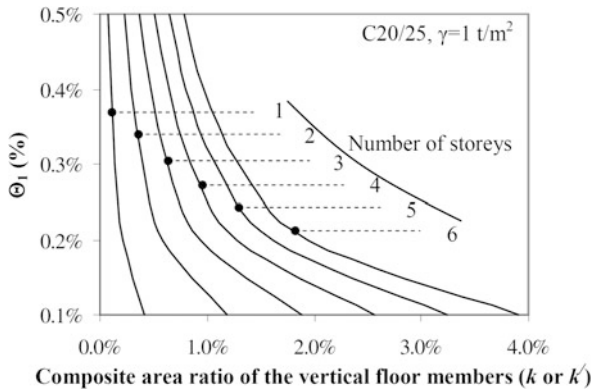


Fig. 4 Seismic vulnerability of old construction curves: relate the required composite floor area ratio of vertical members to interstorey drift demand ratio for a unit value of peak ground acceleration, $a_g = 1 \text{ m/s}^2$ and a mass per unit area of the floor, $\gamma = 1 \text{ t/m}^2$. (For any other PGA or γ value given in m/s^2 and in t/m^2 , the vertical axis should be multiplied by the product of these values (without the units); e.g. if $a_g = 0.36g = 3.53$ and $\gamma = 0.5$, then the vertical axis value should be multiplied by the product $3.53 \cdot 0.5 = 1.765$)

$\gamma = 1.0 \text{ t/m}^2$. (For a different mass value (e.g. 0.5 t/m^2), the ordinate values in the graph should be multiplied by this value. A detailed example is provided in the legend of Fig. 4.) The range of the y-axis in the plot (i.e. 1st-floor drift demand) $0.1 \% \leq \Theta_1 \leq 0.5 \%$, is defined for buildings susceptible to brittle failures: the upper limit corresponds to nominal interstorey drift at yielding for frames, whereas the baseline value of 0.1% is the estimated drift limit associated with inclined web cracking (owing to diagonal tension failure) of concrete members; it is also in the range of shear angle associated with masonry infill cracking. The chart may be used to determine the level of peak ground acceleration that may be sustained without failure, given the area ratios of the vertical, load-bearing elements in an existing structure; alternatively, it may be used to determine the required floor index so as to guide the retrofit strategy for upgrading the structure to a specified level of regional seismic demand.

4 Application of the Seismic Assessment Procedure

The proposed methodology for rapid evaluation of the limiting resistance of “non-conforming” reinforced concrete buildings through prioritising of the individual column shear strengths is tested through application to two building examples. Those buildings are field examples of structures that collapsed during the 1999 strong ground motion of Athens. Both buildings were located in the northern region of Athens, where the ground motion possessed “near-field” characteristics. The essential attributes of each building and the estimated strengths and modes of failure are studied using the expressions for strength ratios and drift demands detailed in the

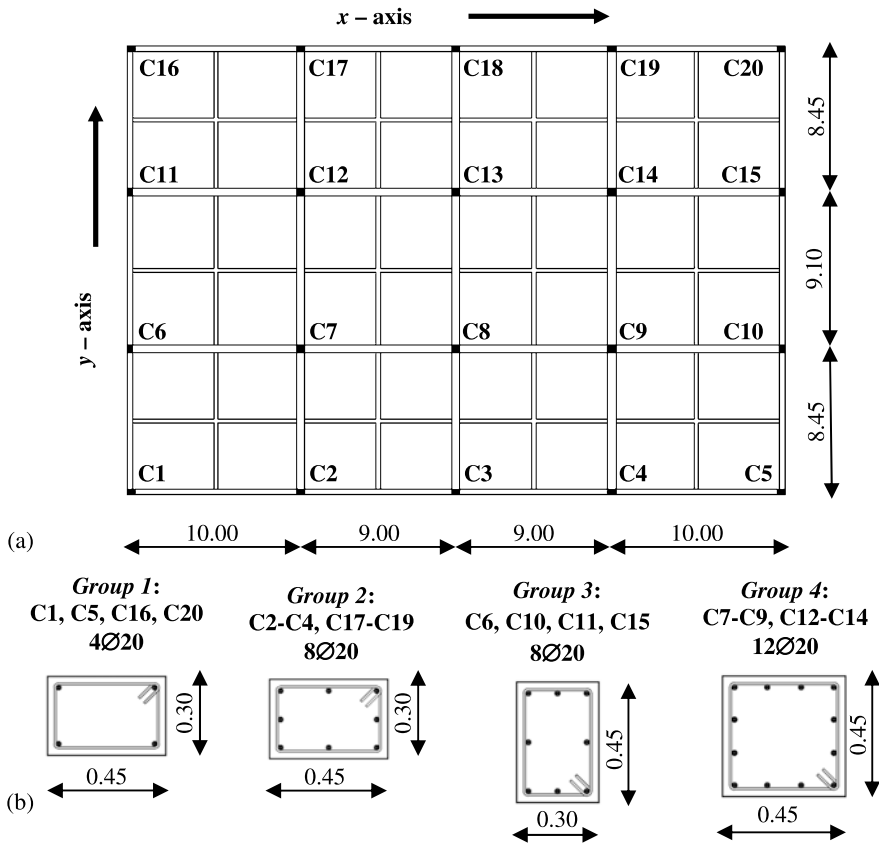
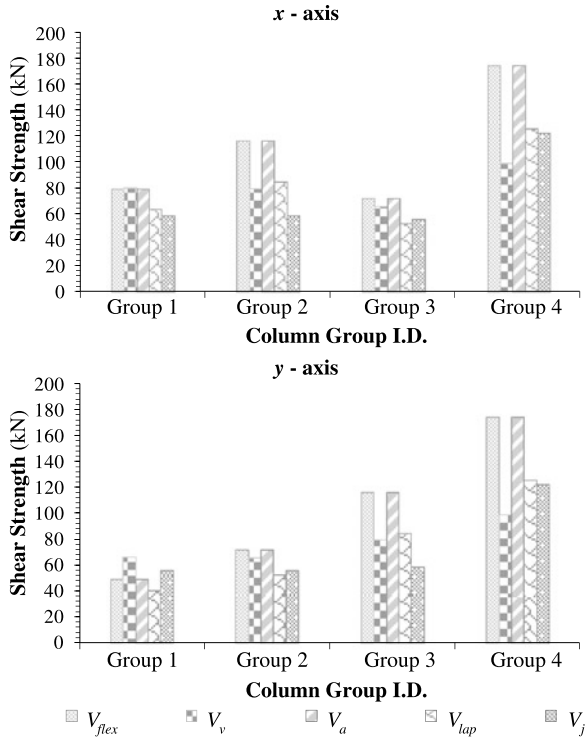


Fig. 5 (a) Plan configuration of *Building A*; (b) External dimensions and reinforcement details of the building’s columns (dimensions in m)

preceding section; the characteristics of the performance point are estimated with reference to the EC8 [6] spectrum adjusted to the level of peak ground acceleration reported for the site in consideration. The estimated performance limit state is compared with the observed behaviour based on post-earthquake reconnaissance reports.

Building A was a two-storey fully symmetric in plan, industrial building, with external plan dimensions of 38.00 m by 26.00 m (Fig. 5(a)). The first and the second storey heights were 5.40 m and 5.30 m, respectively. *Building A* was separated by seismic gaps from two adjacent wing buildings along the two smaller sides. The structural system was formed as an orthogonal grid of columns, beams and slabs, according to typical construction practice of reinforced concrete frame structures in Southern Europe. Details of the column geometry and longitudinal reinforcement are presented in Fig. 5(b). Column longitudinal bars were smooth $\varnothing 20$ mm in all cases, whereas stirrups were smooth, rectangular ties, approximately categorised based on site reconnaissance as $\varnothing 8/300$ mm. Slab thickness was

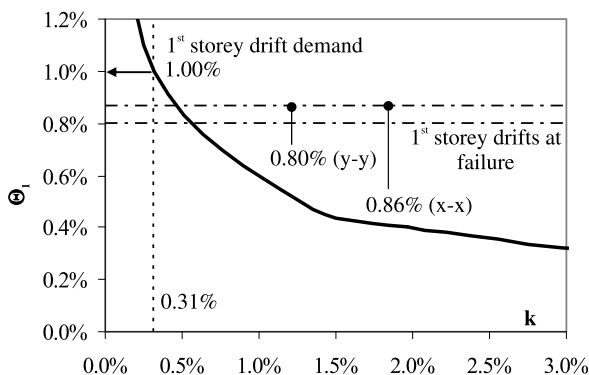
Fig. 6 Shear strength of *Building A* columns in *x* and *y* plan directions



0.15 m. All perimeter beam cross sections were 0.70 m (height) by 0.30 m (width), 0.70 × 0.45 m for beams spanning between columns and 0.70 × 0.25 m for the secondary beams. During the earthquake the building collapsed without any horizontal dislocations of its structural elements, whereas the two adjacent buildings were intact. From tests of core samples, the mean value of concrete compressive strength was determined as 24.8 MPa, whereas steel yielding and ultimate stresses were found to be for the longitudinal reinforcement 431.5 MPa and 512.0 MPa respectively and for the stirrups 402.0 and 553.0 MPa, respectively.

The results of the strength assessment of the first storey columns in *x* and *y* directions for *Building A* are presented in Fig. 6. The building’s columns were divided in four groups, according to their geometric properties (Fig. 5) and service loads, calculated according to the $g + 0.3 \cdot q$ earthquake combination. Note that shear strength at lap-splice and at anchorage of column primary reinforcement are calculated considering $L_{lap} = 20 \cdot D_b$ and $L_a = L_{lap} + d_{sl}$, respectively. Also considered was the existence of hooks in both ends of each longitudinal reinforcement bar. The prevailing failure mechanisms for all the orthogonal section columns (i.e. column groups 1, 2 and 3) was failure due to exhaustion of the lap-length development capacity of tension reinforcement when seismic action is considered in a direction parallel to the columns’ smaller side and joint shear failure when the direction parallel to the columns’ bigger side is considered. Rectangular section columns (i.e. columns

Fig. 7 Vulnerability curve of Building A



C7–C9 and C12–C14) were found vulnerable to shear failure. Shear strength at beam yielding, V_{by} , was not calculated due to insufficient information concerning the beam reinforcement. The total shear force that the first storey columns of Building A could sustain was 1386 kN and 1301 kN in x and y directions, respectively, whereas the corresponding flexural strength was estimated equal to 2346 kN and 2138 kN, respectively.

Results of the *stiffness index assessment* of the first storey columns are shown in Fig. 7. Considering mass per unit area, $\gamma = 0.66$ t/m² (derived from the $g + 0.3 \cdot q$ seismic combination), total storey mass, $m = 651.1$ t and storey stiffness, $K_x = 53161.1$ kN/m and $K_y = 52498.9$ kN/m, the estimated building period was $T_x = T_y = 1.12$ sec ($T = 2 \cdot \pi \cdot \sqrt{[m_i/K_i \cdot \sum \Phi_i^2 / \sum (\Phi_i - \Phi_{i-1})^2]}$). The vulnerability curve derived for Building A (Eq. (9b)) for a PGA value of 0.38g which is the reported site acceleration for the critical earthquake. From the floor plan of Fig. 5(a) the area ratio of vertical elements and corresponding k parameters (Eq. (10)) were estimated equal to $k = \rho_c = 0.31$ % in both x and y directions, indicated that for the estimated area ratio of the vertical members in both directions, the first storey drift demand would be $\Theta_{1,x} = \Theta_{1,y} = 1.00$ % (Fig. 7). The average nominal drift at yield, $\Theta_{y,nom}^c$, was estimated equal to 1.00 % and 0.88 % in x and y directions, respectively. Note that interstorey drift at column yielding was estimated using a “stick model” cantilever extending from the support to the point of inflection around the midheight of the column [7, 8]: $\Theta_{y,nom}^c = 1/3 \cdot \Phi_y \cdot L_s$, where $\Phi_y = 2.14 \cdot \varepsilon_{sy}/h$ (ε_{sy} is the nominal yield strain of longitudinal reinforcement). Premature failure was estimated for the columns by applying the strength criteria (Eq. (7)) in the x and y directions, respectively (Fig. 6(a)–(b)). In all column group cases the controlling limiting shear strength was smaller than the corresponding flexural shear demand (note that V_{by} was not estimated due to insufficient information), indicating brittle failure with no ductility. The average values of the first storey columns were $V_{u,lim,x}/V_{flex,x} = 0.61$ and $V_{u,lim,y}/V_{flex,y} = 0.65$ and the corresponding drifts at failure ($\Theta_{y,crit}^c = r_{u,lim} \cdot \Theta_{y,nom}^c$, Eq. (12)) were 0.61 % and 0.56 % in x and y directions, respectively. The estimated first storey drift at failure in each direction for an average value of $\lambda_c = 0.70$ is $\Theta_{fail,x} = 1/\lambda_c \cdot 0.61$ % = 0.86 % and $\Theta_{fail,y} = 1/\lambda_c \cdot 0.56$ % = 0.80 % (horizontal dashed lines). The outcome of

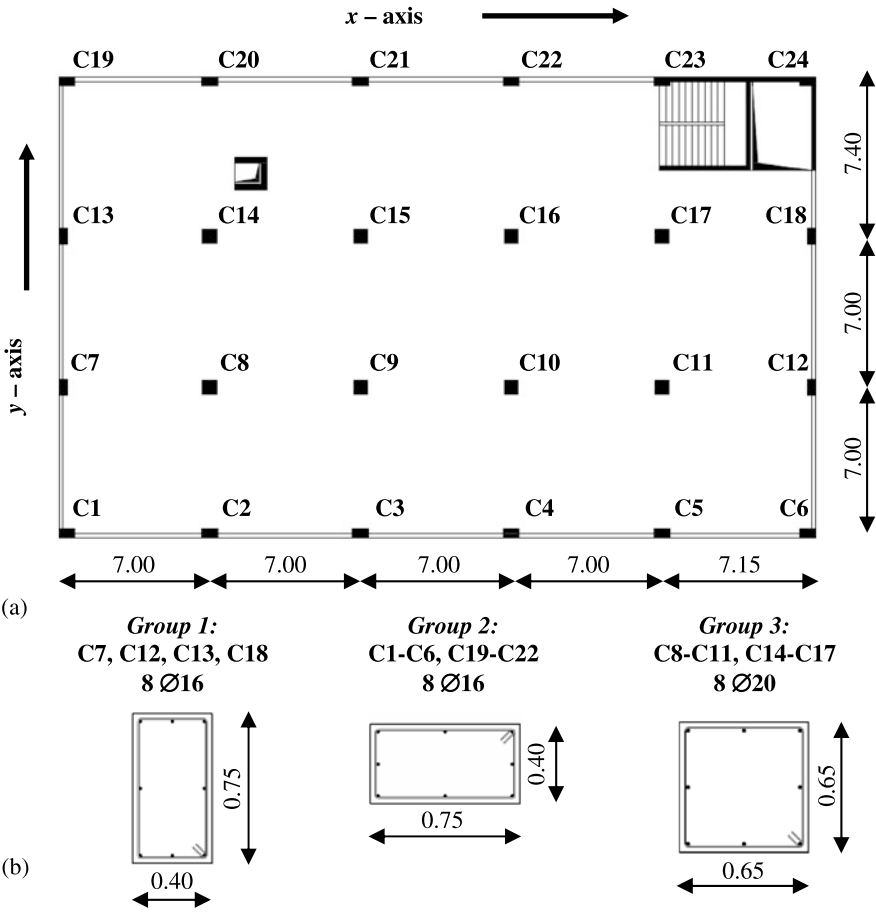
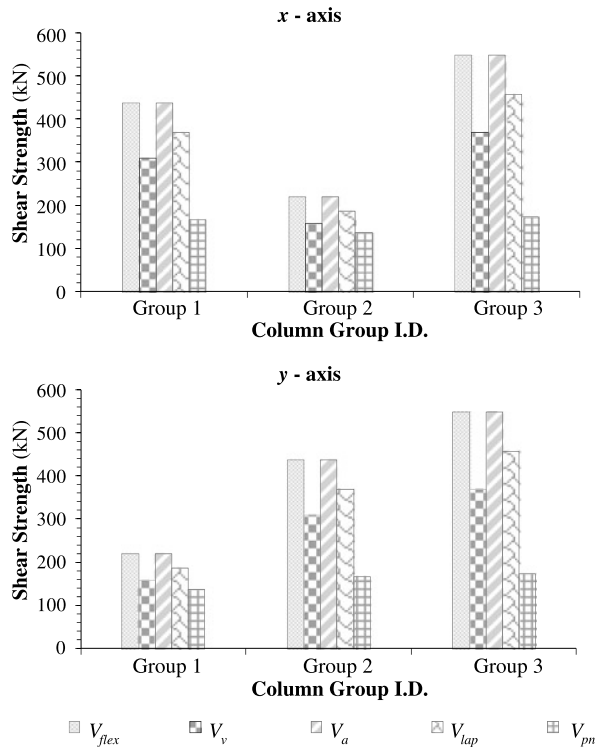


Fig. 8 (a) Plan configuration of *Building B*; (b) External dimensions and reinforcement details of the building’s columns (dimensions in m)

the *stiffness index assessment* procedure ($\Theta_{1,x} > \Theta_{fail,x}$ and $\Theta_{1,y} > \Theta_{fail,y}$) renders *Building A* susceptible to collapse in the 1999 Athens earthquake, a finding compatible with the reconnaissance report.

Building B was also an industrial building, having a 37.60 m by 22.80 m orthogonal plan (Fig. 8(a)). The building had two basements and four storeys, each 2.85 m high. The structural system comprised a grid of columns which were connected with beams only along the buildings’ perimeter, the beams having a section height of 0.60 m and 0.20 m web width. In the centre of typical floor plan, columns supported a flat-plane Zoellner system, having a thickness of 0.22 m. During the earthquake the building collapsed, except for the stairwell in the corner of the plan (Fig. 8(a)). The stairwell was connected to the building through the floor slabs which were lightly reinforced ($\rho_{\ell,sl}$ around 1.0 %). Thus the connection was deficient in its capacity to transfer the inertia forces of the diaphragm to the perimeter walls of the

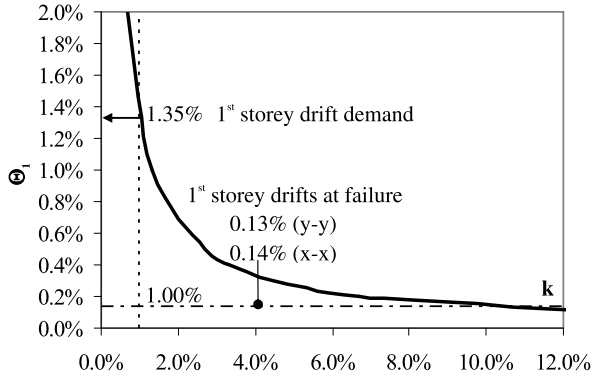
Fig. 9 Shear strength of *Building B* columns in *x* and *y* plan directions



stairwell over the 5 m long unilateral contact provided at each floor level; in light of this poor connection, mobilisation of walls in providing lateral load resistance to the building was marginal, as evidenced by the building wreckage. After tests conducted on material samples, the concrete was found to have a mean compressive strength of 20 MPa, while longitudinal reinforcement and stirrups were found to have smooth surface and were classified as S400 ($f_y = 400$ MPa) and S220 ($f_y = 220$ MPa) respectively. Column dimensions and longitudinal reinforcement details (bar diameter equal to 16 mm in all cases, except for the rectangular columns where $\varnothing 20$ mm bars were utilised) are presented in Fig. 8(b), whereas transverse reinforcement comprised $\varnothing 6/300$ mm rectangular, smooth stirrups.

To perform *strength assessment*, the building’s columns were divided in three column groups, as presented in Fig. 8, according to their geometrical properties and their service load (calculated according to the seismic combination $g + 0.3 \cdot q$). Longitudinal reinforcement bars were considered to have a lap length, L_{lap} , equal to $25 \cdot D_b$, and an anchor length, $L_a = L_{lap} + d_{sl}$, whereas hooks were considered in both ends of each bar. *Strength assessment* (Fig. 9(a)–(b)) has revealed that the prevailing failure mechanism of the first storey columns was failure due to exhaustion of slab punching strength. The total shear force that the first storey columns of *Building B* could sustain at the onset of slab punching was 3602 kN and 3422 kN in *x* and *y* directions, respectively, whereas the corresponding flex-

Fig. 10 Vulnerability curve of *Building B*



ural strength was estimated equal to 9650 kN and 8345 kN, respectively. Considering first storey total weight, $W_{g+0.3q} = 31836$ kN (total mass, $m = 811.3$ t and mass per unit area, $\gamma = 1.08$ t/m²) and storey stiffness, $K_x = 1059906$ kN/m and $K_y = 1051293$ kN/m, the estimated building period was $T_x = T_y = 0.50$ sec. The vulnerability curve of *Building B* (Fig. 10) derived from Eq. (9a), considering $a_g = 0.38g$, which was the peak ground acceleration in the Sepolia region where the building was located. The area ratios of the first storey columns was estimated equal to $k = \rho_c = 1.00\%$ in both x and y directions, thus the first storey drift demand for *Building B* would be $\Theta_{1,x} = \Theta_{1,y} = 1.35\%$. The average nominal drift at yielding of the vertical elements, $\Theta_{y,nom}^c$ ($\Theta_{y,nom}^c = 1/3 \cdot \Phi_y \cdot L_s$, $\Phi_y = 2.14 \cdot \varepsilon_{sy} / h$ [7, 8]), was estimated equal to 0.35% and 0.29% in x and y directions, respectively, whereas the failure drift of columns, $\Theta_{y,crit}^c$, was equal to less than 50% of the average nominal drift at yield ($\Theta_{y,crit,x}^c = 0.37 \cdot \Theta_{y,nom,x}^c$, $\Theta_{y,crit,y}^c = 0.41 \cdot \Theta_{y,nom,y}^c$). The first storey drift at failure, Θ_{fail} ($\lambda_c = 1.00$) (Eq. (10)), was found equal to 0.14% and 0.13% in x and y directions, respectively. Since $\Theta_{fail} < \Theta_1$, *stiffness index assessment* indicates that *Building B* is susceptible to collapse in the 1999 Athens earthquake, a finding compatible with the reconnaissance report.

5 Conclusions

A method for rapid seismic assessment of reinforced concrete buildings, based on basic data easily available for all buildings such as the building's general geometry in plan and elevation, material properties and reinforcement detailing rules representative of the period of the building's construction, was presented in this chapter. Motivation for the introduction of this method was the emerging need for a dependable tool for rapid identification of the most vulnerable buildings that are likely to collapse in the in the event of a strong earthquake, without the need of conducting time and effort consuming detailed assessment procedures, which can be applied in a second face to the selected buildings.

Privatisation of the potential failure mechanisms in the load carrying system of concrete buildings in order to calculate its limiting resistance and determination

of the building's ultimate storey drift are the two main concepts of the assessment method. Mechanisms considered refer to column flexure, shear, anchorage lap and splice development capacity, beam-column joint shear and slab punching strength in the slab-column area, as failure of vertical structural elements is directly related to building severe damage or collapse. Based on the determination of the structural system limiting strength, strength ratios are calculated for each of the principal directions of the plan, that allow to obtain the drift capacity of the building in the respective direction. Drift capacity is compared with the corresponding drift demand. When the demand exceeds the capacity prior to attainment of flexural yielding, brittle failure and collapse is anticipated. Note that through the rapid assessment method it is also possible to obtain the magnitude of displacement ductility that would be required through column retrofit, in order to eliminate the risk of collapse due to excessive displacement demand.

For verification the method is tested in two actual building examples that collapsed during the 1999 Athens earthquake. The proposed seismic assessment approach was successful in all the cases considered, in properly identifying collapse and the mode of prevailing failure. In both building cases, brittle failure modes were prioritised to occur prior to flexural yielding with premature collapse without ductility. The base shear at the onset of failure was in both cases in the range of 0.10 to 0.12 to the structural weight, underscoring the older practices where the so-called seismic coefficient used was in this range of values.

References

1. Thermou GE, Pantazopoulou SJ (2011) Assessment indices for the seismic vulnerability of existing RC buildings. *Earthq Eng Struct Dyn* 40(3):293–313
2. Federation of Structural Concrete (fib) (2003) Seismic assessment and retrofit of reinforced concrete buildings. *fib Bulletin* 42, State-of-art report prepared by Task Group 7.1
3. Deutsches Institut für Normung (DIN) (1972) *Beton und Stahlbetonbau: Bemessung und Ausführung—DIN 1045*, Berlin
4. Eberhard MO, Baldrige S, Marshall J, Mooney W, Rix GJ (2010) The M_w 7.0 Haiti earthquake of January 12, 2010. USGS/EERI Advance Reconnaissance Team, Team report V1-1
5. Federation of Structural Concrete (fib) (2010) Model code 2010. First complete draft
6. Eurocode 8 (2004) Design of structures for earthquake resistance—part 1: General rules, seismic actions and rules for buildings. EN1998-1-2004, European Committee for Standardization (CEN), Brussels
7. Priestley MJN (1998) Brief comments on elastic flexibility of reinforced concrete frames and significance to seismic design. *Bull New Zealand Natl Soc Earthq Eng* 31(4):246–259
8. Priestley MJN, Kowalsky MJ (1998) Aspects of drift and ductility capacity of cantilever structural walls. *Bull New Zealand Natl Soc Earthq Eng* 31(2):73–85

Numerical Determination of the Seismic Strength of Reinforced Concrete Shear Walls with Fractal Cracks

O. Panagouli, E. Mistakidis, and K. Iordanidou

Abstract Shear walls play an important role to the seismic strength of modern seismic resistant structures. They are designed so that they have significant bending and shear strengths and ductility. However, existing structures have lightly reinforced shear walls. In most cases, especially under cycling loading, shear cracks appear, reducing the shear capacity of the wall. Here, a typical shear wall of an existing structure is examined in which it is assumed that a crack has been formed. For the modelling of the geometry of the crack a new approach is applied, using the notion of fractal geometry. The aim of the chapter is the estimation of the post-cracking strength of the wall, taking into account the geometry of the cracks and the mixed friction-plastification mechanisms that develop in the vicinity of the crack. Due to the significance of the crack geometry a multi-resolution analysis is performed. The materials (steel and concrete) are assumed to have elastic-plastic behaviour. For concrete both cracking and crushing are taken into account in an accurate manner. On the interface unilateral contact and friction conditions are assumed to hold. For every structure resulting for each resolution of the interface, a classical Euclidean problem is solved. The obtained results lead to interesting conclusions concerning the post-cracking strength of lightly reinforced shear walls.

Keywords Lightly reinforced shear walls · Seismic strength · Fractal cracks

1 Introduction

Shear walls play a significant role to the seismic strength of structures built in seismic prone areas. Shear walls in modern structures are designed to have significant bending and shear strengths and ductility. However, shear walls in old, existing buildings have been constructed using poor materials and usually have inadequate shear strength. In such elements, shear cracks appear reducing their overall capacity. The aim of this chapter is to apply a new approach in order to estimate the

O. Panagouli · E. Mistakidis (✉) · K. Iordanidou
Laboratory of Structural Analysis and Design, Dept. of Civil Engineering, University of Thessaly,
Pedion Areos, 38334 Volos, Greece
e-mail: emistaki@gmail.com

post-cracking strength of a shear wall which is part of an existing structure, taking into account the geometry of the formed cracks. To this end, the notion of fractal geometry is applied in order to approximate the geometry of the crack.

It is well known that the geometry and structure of the interface between two solid surfaces in contact is of fundamental importance to the study of friction, wear, lubrication and also strength evaluation. Experimental studies [1–4] have shown that the fracture interfaces have irregularities of all scales, and require advanced mathematical models for their description. In general, the actual contact between two real interfaces is realized only over a small fraction in a discrete number of areas. Consequently, the real area of contact is only a fraction of the apparent area [5, 6] and the parameters of the actual contact regions are strongly influenced by the roughness of the contacting surfaces. For that, fractal contact models are suitable for the simulation of contact.

The fractal approach adopted here for the simulation of the geometry of the cracks formed in the shear wall, uses computer generated self-affine curves for the modelling of the interface roughness, which is strongly dependent on the values of the structural parameters of these curves. The computer generated interfaces, which are characterized by a precise value of the resolution δ of the fractal curve, permit the study of the interface roughness on iteratively generated rough profiles. This fact makes this approach suitable for engineering problems, since it permits the satisfactory study of the whole problem with reliable numerical calculations.

Among the aims of this chapter is to study how the resolution of a fractal interface \mathcal{F} affects the strength of a reinforced concrete shear wall element, in which it is assumed that a crack has been developed. The geometry of the crack is modelled through the application of the principles of fractal geometry. On the interface between the two cracked surfaces, unilateral contact and friction conditions are assumed to hold. The applied approach takes into account the nonlinear behaviour of the materials, including the limited strength of concrete under tension. The shear wall is subjected to shear loading. As a result of the applied approach, the contribution of the friction between the cracked surfaces is taken into account, as well as the additional strength coming from the mechanical interlock between the two faces of the crack. For every structure resulting for each resolution of the interface, a classical Euclidean problem is solved by using a variational formulation [7].

2 On the Modelling of Roughness with Fractal Interpolation Functions

The fractal nature of material damage has been a matter of a very intense research during the last three decades. The fractal nature of fracture surfaces in metals was shown more than 20 years ago by Mandelbrot et al. [1]. In this paper the authors studied the fracture of cracked surfaces in metals fractured either by tensile or impact loading, which were shown to develop fractal structure over more than three orders of magnitude. In quasi-brittle materials observations have shown that fracture surfaces display self-affine scale properties in a certain range of scales which is

in most cases very large and which greatly depends on the material micro-structure. This is true for a large variety of quasi-brittle materials such as rock, concrete, wood and ceramics [8, 9].

Fractal sets are characterized by non-integer dimensions [10]. The dimension of a fractal set in plane can vary from 0 to 2. Accordingly, by increasing the resolution of a fractal set, its length tends to 0 if its dimension is smaller than 1 (totally disconnected set), or tends to infinity if it is larger than 1. In these cases the length is a nominal, useless quantity, since it changes as the resolution increases. Conversely, the fractal dimension of a fractal set is a parameter of great importance because of its scale-independent character.

Many methods which are based on experimental or numerical calculations, such as the Richardson method [10], have been developed for the estimation of the fractal dimension of a curve. According to this method, dividers, which are set to a prescribed opening δ , are used. Moving with these dividers along the curve so that each new step starts where the previous step leaves off, one obtains the number of steps $N(\delta)$. The curve is said to be of fractal nature if by repeating this procedure for different values of δ the relation

$$N(\delta) \sim \delta^{-D} \quad (1)$$

is obtained in some interval $\delta^{(*)} < \delta < \Delta^{(*)}$. The power D denotes the fractal dimension of the profile, which is in the range $1 \leq D < 2$. The relation between the fractal dimension D of this profile and the dimension of the corresponding surface is $D_S = D + 1$ [10].

The idea of self-affinity is very popular in studying surface roughness because experimental studies have shown that usually, under repeated magnifications, the profiles of real surfaces are statistically self-affine to themselves [1, 11]. The self-affine fractals were used in a number of papers as a tool for the description of rough surfaces [12–17]. Typically, such a profile can be measured by taking height data y_i with respect to an arbitrary datum at N equidistant discrete points x_i and following the procedure presented in [18]. Here, fractal interpolation functions are used for the passage from this discrete set of data $\{(x_i, y_i), i = 0, 1, 2, \dots, N\}$ to a continuous model, where $\mathcal{F}(x_i) = y_i, i = 0, 1, \dots, N$. It has been proved [18] that there is a sequence of functions $\mathcal{F}_{n+1}(x) = (T\mathcal{F}_n)(x)$, where $T : C^0 \rightarrow C^0$ is an operator defined by:

$$\mathcal{F}_{n+1}(x) = (T\mathcal{F}_n)(x) = c_i l_i^{-1}(x) + d_i \mathcal{F}_n(l_i^{-1}(x)) + g_i \quad (2)$$

for $x \in [x_{i-1}, x_i], i = 1, 2, \dots, N$. The operator T converges to a fractal curve \mathcal{F} , as $n \rightarrow \infty$. The transformation l_i transforms $[x_0, x_N]$ to $[x_{i-1}, x_i]$ and it is defined by the relation

$$l_i(x) = a_i x + b_i. \quad (3)$$

The factors d_i are the hidden variables of the transformations and they have to satisfy $0 \leq d_i < 1$ in order for $T : C^0 \rightarrow C^0$ to have a unique fixed point. Moreover, the remaining parameters are given by the following equations:

$$a_i = (x_i - x_{i-1})/(x_N - x_0) \quad (4)$$

$$c_i = (y_i - y_{i-1})/(x_N - x_0) - d_i(y_N - y_0)/(x_N - x_0) \quad (5)$$

$$b_i = (x_N x_{i-1} - x_0 x_i)/(x_N - x_0) \quad (6)$$

$$g_i = (x_N y_{i-1} - x_0 y_i)/(x_N - x_0) - d_i(x_N y_0 - x_0 y_N)/(x_N - x_0). \quad (7)$$

The fractal interpolation functions give profiles which look quite attractive from the viewpoint of a graphic roughness simulation. In higher approximations these profiles appear rougher as it is shown in the next section where the first to fourth approximations of a fractal interpolation function are presented. Moreover, the roughness of the profile is strongly affected by the free parameters d_i , $i = 1, \dots, N$ of the interpolation functions. As these parameters take larger values, the resulting profiles appear rougher.

It must be mentioned here that an important advantage of the fractal interpolation functions presented here is that their fractal dimension can be obtained numerically [18] and is given by the relation:

$$\delta^{-D} \approx \sum_{i=1}^N |d_i| a_i^{D-1} \delta^{-D} \Leftrightarrow \sum_{i=1}^N |d_i| a_i^{D-1} = 1. \quad (8)$$

3 The Considered Wall Structure

3.1 Structural Configuration

In Fig. 1 a reinforced concrete shear wall element is presented which is assumed to be part of a typical existing structure built during the 60s or 70s. The wall is reinforced by a double steel mesh consisting of horizontal and vertical rebars having a diameter of 8 mm and a spacing of 200 mm. The quality of the steel mesh is assumed to be S220 (typical for buildings of that age). At the two ends of the wall the amount of reinforcement is higher. Four 20 mm rebars of higher quality (S400) are used, without specific provisions to increase the confinement. The thickness of the wall is 200 mm and the quality of concrete is assumed to be C16/20, typical for this kind of constructions. The wall is fixed on the lower horizontal boundary.

3.2 Simulation of the Fractal Crack

The considered shear wall is divided into two parts by a crack which is assumed that has been formed as a result of the action of an earthquake. Obviously, the depicted crack has been formed due to shear failure of concrete. For the description of the geometry of the crack, the notion of fractals is used. More specifically, the crack is assumed to be a fractal interface, described by the fixed point of a fractal interpolation

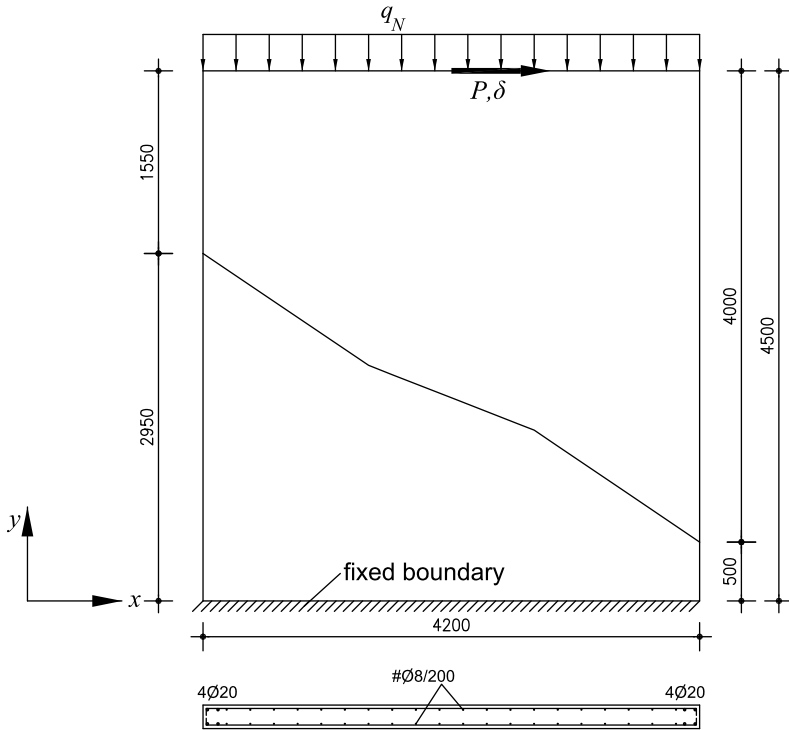


Fig. 1 The considered shear wall

function interpolating the set of data $\{(-1.0, 2.95), (0.4, 2.0), (1.8, 1.0), (3.2, 0.5)\}$. The free parameters of the fractal interpolation function are taken to have the values $d_1 = d_2 = d_3 = 0.50$.

The objective here is to estimate the capacity of the shear wall under an action similar to the one that has created the crack. For this reason, a horizontal displacement of 20 mm is applied on the upper side of the wall (see Fig. 1). Moreover, a vertical distributed loading q_N is applied on the upper horizontal boundary, creating a compressive axial loading. The resultant of this loading is denoted by N . For N six different values will be considered from 0 to 2500 kN with a step of 500 kN.

As it was mentioned in the previous section, self-affine interfaces are adopted for the interface simulation. The computer generated interfaces $\mathcal{F}_n, n = 1, 2, \dots$ are only images “pre-fractals” characterized by a precise value of the resolution of the fractal set. The resolution $\delta^{(n)}$ is related to the (n) -th iteration of the fractal interpolation function and represents the characteristic linear size of the interface. As it is shown in Fig. 2, where four iterations of a fractal interface are given, the linear size of the interface changes rapidly when higher order approximations are taken into account. It is assumed that the opposite sides of the fracture are perfectly matching surfaces, so only one side of the fracture was generated by using the described

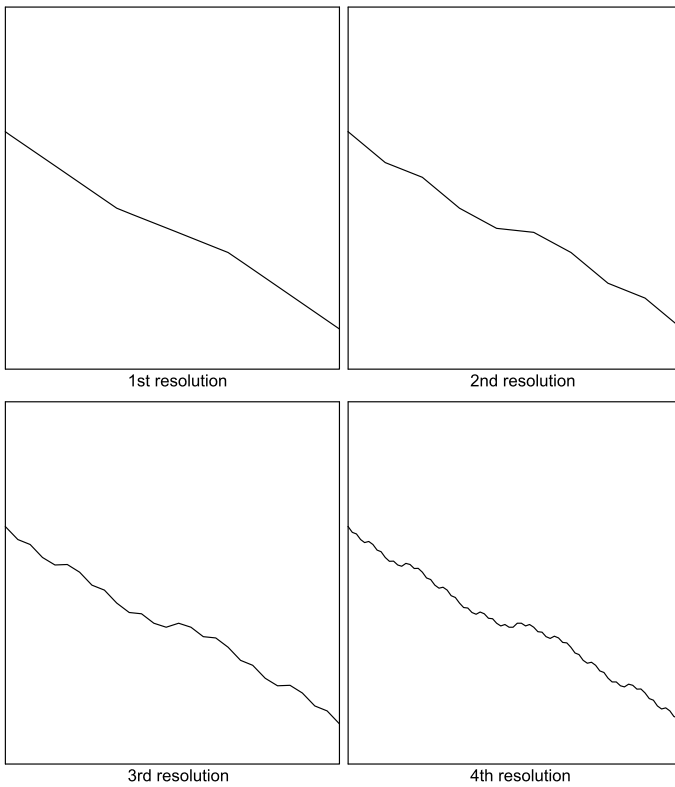


Fig. 2 The first four resolutions of the fractal crack

Table 1 Characteristics of the considered structures

Iteration (n)	Resolution $\delta^{(n)}$ (m)	Interface length $L^{(n)}$ (m)
1st	1.404	4.888
2nd	0.468	4.946
3rd	0.156	5.080
4th	0.052	5.373

fractal interpolation function. By applying relation (8) the fractal dimension of the interface studied here results to be equal to 1.369.

In Table 1 the characteristics of each resolution are presented. The resolution $\delta^{(n)}$ for each iteration (n) is given in the second column of Table 1. The last column of this table presents the total crack lengths $L^{(n)}$ in m.

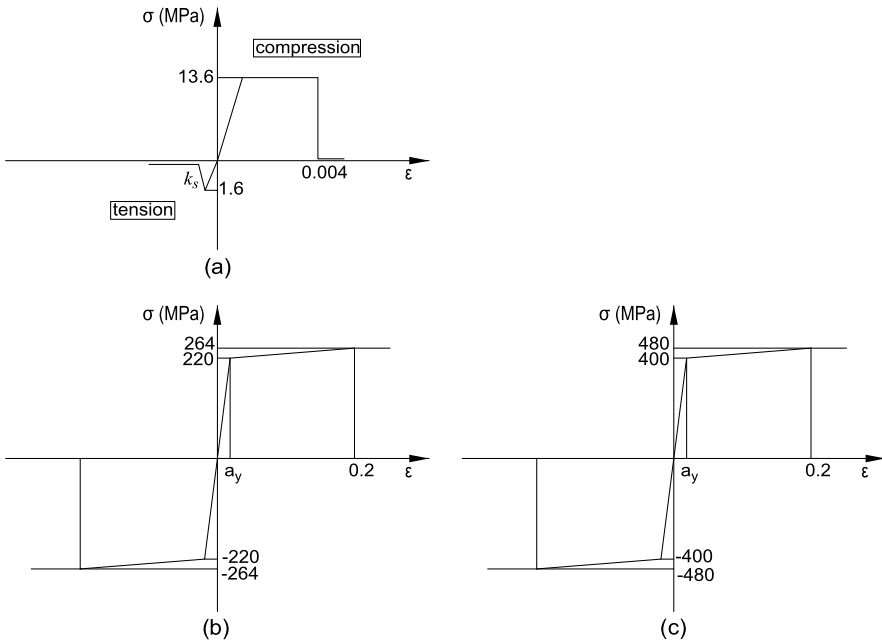


Fig. 3 The adopted materials laws (a) C16/20 concrete, (b) S220 steel, (c) S400 steel

3.3 Material Properties

The modulus of elasticity for the elements representing the mass of concrete was taken equal to $E = 21$ GPa and the Poisson’s coefficient equal to $\nu = 0.16$. The material was assumed to follow the nonlinear law depicted in Fig. 3a. Under compression, the material behaves elastoplastically, until a total strain of 0.004. After this strain value crushing develops in the concrete, leading its strength to zero. A more complicated behaviour is considered under tension. More specifically, after the exhaustion of the tension strength of concrete, a softening branch follows, having a slope $k_s = 10$ GPa. Progressively, the tension strength of concrete is also zeroed. The above unidirectional nonlinear law is complemented by an appropriate yield criterion (Tresca) which takes into account the two-dimensional stress fields that develop in the considered problem. For the simulation of cracking a smeared crack algorithm is used, in which the cracks are evenly distributed over the area of each finite element [19].

The steel rebars were modelled through two-dimensional beam elements, which were connected to the same grid of nodes as the plain stress elements simulating the concrete. At each position, the properties that were given to the steel rebars take into account the reinforcement that exists in the whole thickness of the wall. For example, the horizontal and vertical elements that simulate the steel mesh are assigned an area of 100.5 mm^2 that corresponds to the cross-sectional area of two 8 mm steel rebars. For simplicity, the edge reinforcements were simulated by a

single row of beam elements that have an area of 1256 mm^2 (i.e. $4 \times 314 \text{ mm}^2$). For the steel rebars, a modulus of elasticity $E = 210 \text{ GPa}$ was assumed. Moreover, the nonlinear laws of Figs. 3b, 3c were considered for the S220 and S400 steel qualities respectively. These laws exhibit a hardening branch, after the yield stress of the material is attained.

3.4 F.E. Discretization and Solution Procedure

For the modelling of the above problem the finite element method is used. In order to avoid a much more complicated three-dimensional analysis, two-dimensional finite elements were employed, however, special consideration was given to the incorporation of the nonlinearities that govern the response of the wall. More specifically, the mass of the concrete was modelled through quadrilateral and triangular plain stress elements. The finite element discretization density is similar for all the considered problems [20]. This rule ensures that the discretization density will not affect the comparison between the results of the various analyses that were performed.

Figure 4 depicts the finite element discretizations for the structures that correspond to the third and fourth iterations of the fractal interface. The grey lines in the finite element meshes correspond to the positions of the steel rebars. The distance between the two facing parts of the interface is only 0.1 mm. Special attention was given in the modelling so that the steel rebars retain their initial horizontal and vertical positions, i.e. no eccentricity exists between the corresponding rows of beam finite elements due to the formation of the crack.

In this chapter, only the finite element models corresponding to the 3rd and 4th approximations of the fractal crack were considered, because 1st and 2nd approximations are not meaningful from the engineering point of view.

At the interfaces, unilateral contact and friction conditions were assumed to hold. The Coulomb's friction model was followed with a coefficient equal to 0.6. At each scale, where a classical Euclidean problem is solved, a variational formulation [7] was used in order to describe the contact between the two parts of the crack.

For every value of the vertical loading N , a solution is taken in terms of shear forces and horizontal displacements at the interface, for different values of the resolution of the cracked wall and for the case of the uncracked wall. The aim of this work is to study the behaviour of the shear wall, i.e. the behaviour of the concrete and the forces in the rods, as the vertical loading and the resolution of the interface change.

Two cases are considered:

- In the first case the wall is uncracked.
- In the second case, where a fractal crack \mathcal{F} has been developed in the wall, different resolutions are taken into account in order to examine how the resolution of a fractal interface affects the strength of a reinforced concrete shear wall element.

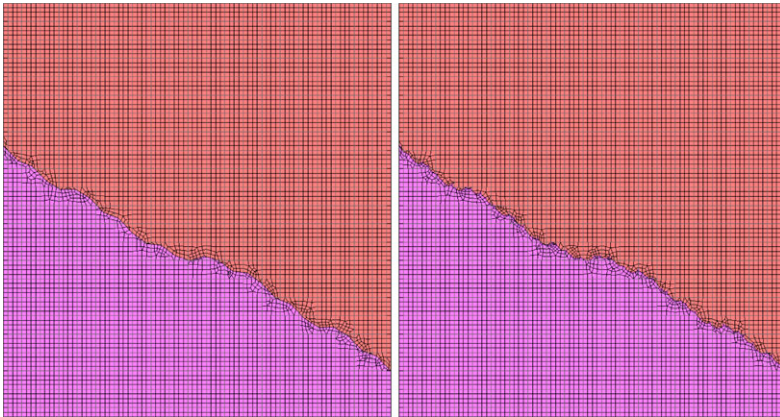


Fig. 4 F.E. discretizations for third and fourth approximations of the fractal interface

The solution of the above problems is obtained through the application of the Newton-Raphson iterative method. Due to the highly nonlinear nature of the problem, a very fine load incrementation was used. The maximum value of the horizontal displacement (20 mm) was applied in 2000 loading steps, while the total vertical loading was applied in the first load step and was assumed as constant in the subsequent steps.

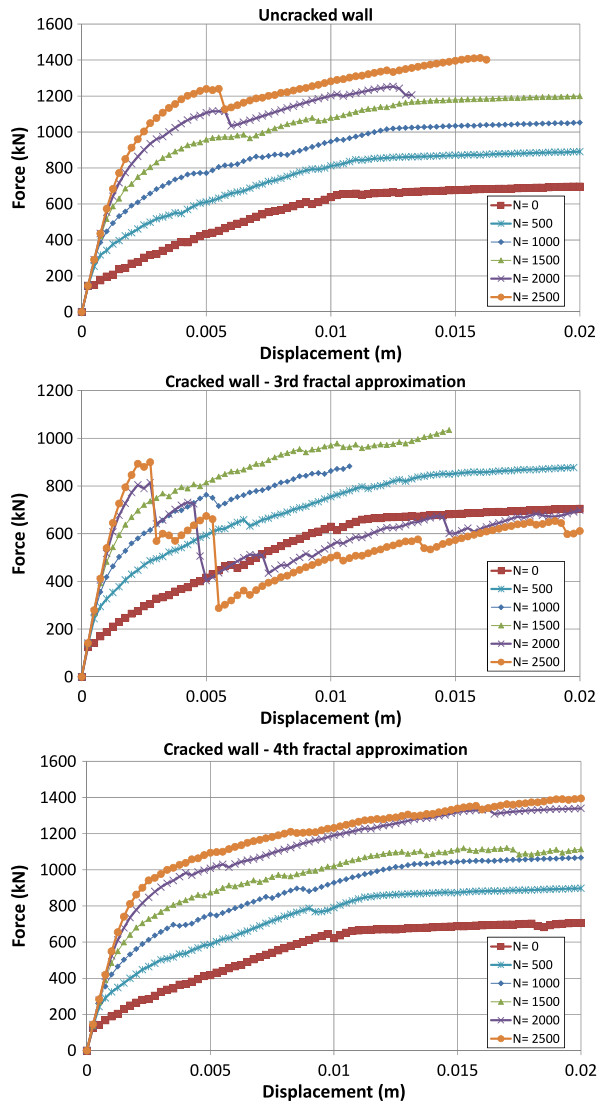
4 Numerical Results and Discussion

4.1 Overall Response

The numerical analyses yielded large quantities of results. In this section the overall response of the structures corresponding to the different fractal resolutions will be studied. Figure 5 presents the applied horizontal load verse the corresponding displacement (curves) for the different values of the vertical loading. It has to be noticed, starting from the case of the uncracked wall, that the value of the vertical loading plays a significant role. As the value of the vertical loading increases, the capacity of the wall to undertake horizontal loading increases as well. However, for the higher load values (for $N = 2000$ kN and 2500 kN), strength degradations are noticed. As it will be explained later, these degradations have their nature to the exhaustion of the shear strength of concrete. However, after this strength degradation, the resistance of the wall increases again as a result of the transfer of the loading from the concrete to the horizontal steel rebars.

Coming now to the cases of the cracked walls, the beneficial effect of the normal compressive loading is once more verified. This result holds for both the 3rd and the 4th approximations of the fractal crack but for small displacement values only. For larger displacement values, the two variants of the cracked wall behave differently.

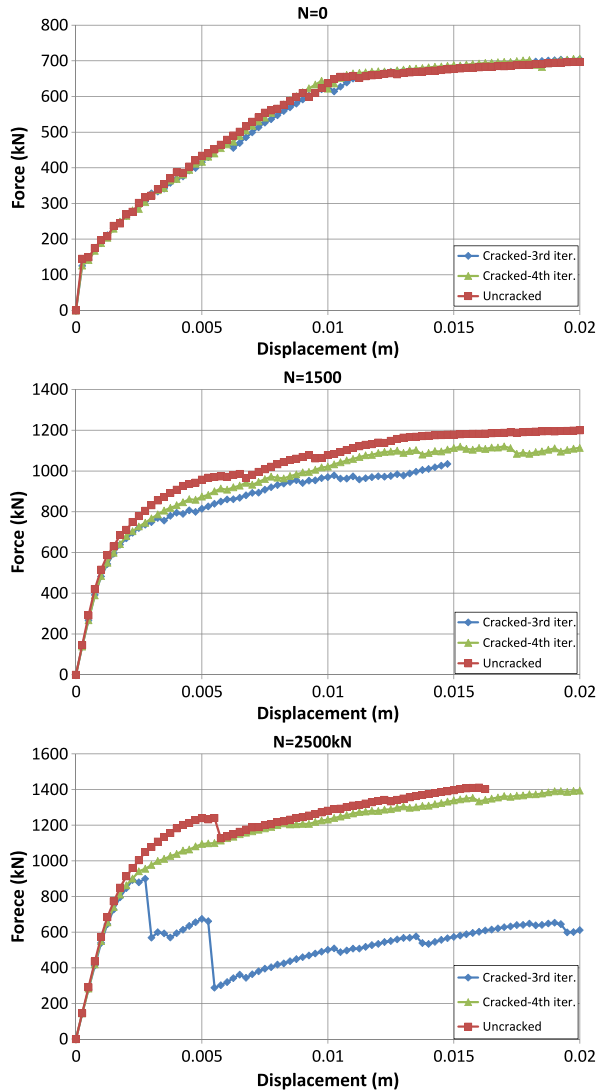
Fig. 5 Load-displacement ($P-\delta$) curves for the cases of the uncracked and cracked walls



The 4th approximation appears to have a stable behaviour without strength degradations. However, it is noticed that in the case of the 3rd approximation and for heavy axial loading, significant strength degradation takes place.

However, the most interesting case is that of the heavy axial loading ($N = 2500$ kN). First, as it is shown in Fig. 6, the behaviour of the 4th approximation of the fractal crack leads to results that are close enough to those of the uncracked wall. There exist some differences for horizontal displacements in the range of 2–6 mm. In this range the uncracked wall exhibits greater resistance. However, for 6 mm, the

Fig. 6 Comparison of the behaviour of the three variants of the examined wall for specific values of the compressive axial loading



uncracked wall appears strength degradation and after this displacement value the results of the 4th approximation of the fractal crack are again very close to those of the initially uncracked wall.

Significantly different is the case of the 3rd approximation of the fractal crack. It is noticed that although in the first loading steps the results follow closely those of the 4th approximation, after a displacement value of 3 mm significant strength degradation appears, having the form of successive vertical branches. The ultimate strength of this wall is significantly lower than the other variants.

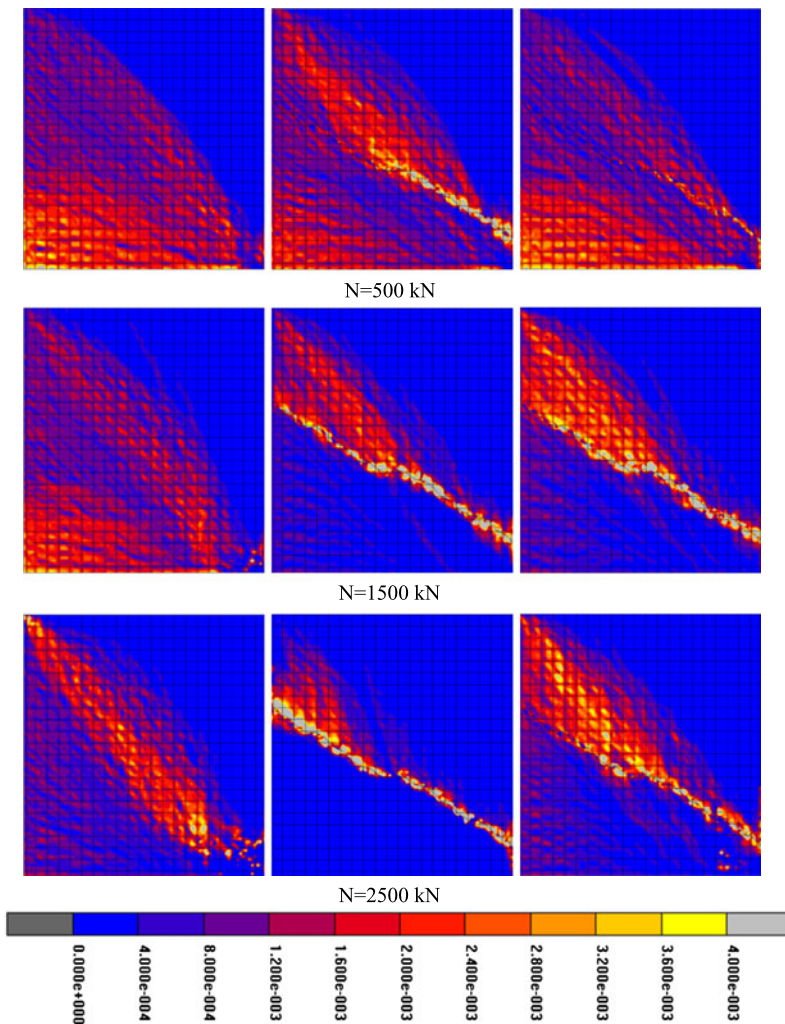


Fig. 7 Cracking strains for various values of the vertical loading, for the cases of the uncracked wall (*left column*) and the cracked walls (3rd approximation—*middle column* and 4th approximation—*right column*)

4.2 Comparison of the Differences in the Behaviour of Concrete

It is interesting to try to explain this significantly different behaviour that appears between the walls corresponding to the 3rd and 4th approximations of the fractal crack. For this reason, all the parameters affecting the behaviour of the wall will be comparatively studied in the sequel.

Figure 7 depicts the cracking strains of concrete for specific values of the axial loading. All the depicted results correspond to the end of the analysis, i.e. they have

been obtained for an applied horizontal displacement of 20 mm. First of all, it can be noticed that for low values of the axial loading, the cracking patterns that have been developed in all the studied walls are rather similar. The larger cracking strain values have their nature in the bending deformation of the wall. For moderate axial loading, the cracking patterns are quite different. The uncracked wall has again a bending type cracking pattern. The cracked walls seem to behave differently. Both of them exhibit significant cracking in the vicinity of the crack. Apart from this, shear type cracking patterns develop at the upper parts of the walls.

The above results alone cannot explain the significantly different responses that the two cracked variants of the wall exhibit. For this reason, the plastic strains of concrete are examined in the following. Figure 8 depicts the plastic concrete strains for the three different variants of the wall and for specific values of axial loading. The upper value of the presented scale corresponds actually to the crushing limit (grey values). Therefore, it can be considered that the concrete stresses in these areas are actually zero. For the uncracked wall (left column of Fig. 8) it can be noticed that the more heavily deformed region is the lower right corner. It is clear that in this case the wall exhibits a typical bending type deformation behaviour (cracking at the lower left region, crushing at the lower right corner).

On the other hand, the cracked walls seem to deform significantly in the vicinity of the crack. This phenomenon is more pronounced in the case of the 3rd approximation of the fractal wall. Especially in the case of heavy axial loading, it can be noticed that the vicinity of the crack is in crushed state, i.e. in this region the forces are transmitted solely by the steel mesh (the concrete has no ability to transfer any kind of forces). For the case of the 4th approximation, this phenomenon is rather limited, i.e. it can be concluded that in this case the crack retains partial its ability to transfer shear and compressive forces through the contact and friction phenomena that develop in the interface and through the mechanical interlocking that occurs between the two interface parts.

4.3 Developed Forces in the Steel Rebars

It is now interesting to examine the deformations that have occurred at the steel mesh. Figure 9 displays the steel mesh for the three variants of the considered wall and for different values of the vertical loading. The presented deformations correspond to the last load step and have been magnified by a factor of 10 so that the differences between the examined cases are visible.

For low vertical loading values, the deformations of the steel meshes are actually very similar. However, for moderate values of the vertical loading ($N = 1000$ kN) there exist some differences. The steel meshes of the cracked walls seem to be distorted in the vicinity of the right part of the formed crack. In this region the vertical rebars above and below the crack present an offset which can be attributed to the inability of the interface to transfer shear forces. For the case of heavy vertical loading, the situation is different again. The wall corresponding to the 4th resolution

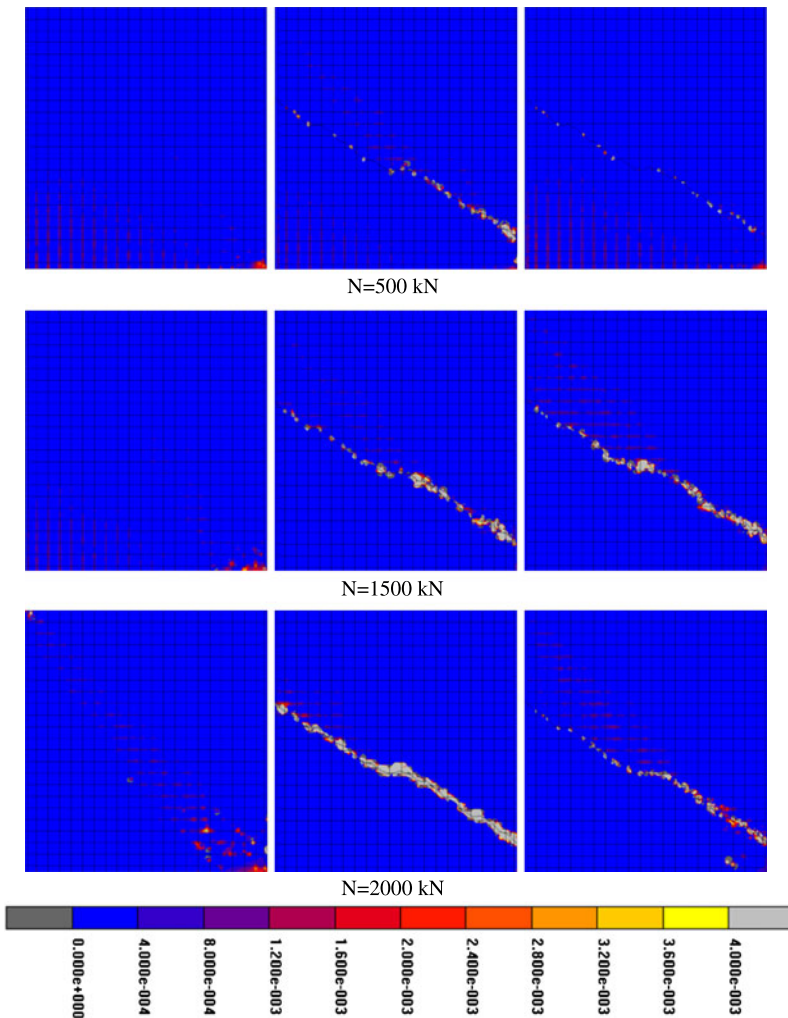


Fig. 8 Plastic strains for various values of the vertical loading, for the cases of the uncracked wall (*left column*) and the cracked walls (3rd approximation—*middle column* and 4th approximation—*right column*)

of the fractal crack has a deformation similar to that of the case of the moderate loading. However, the steel mesh of the wall corresponding to the 3rd resolution of the fractal crack exhibits significant deformations all along the crack. All the upper vertical rebars present a significant horizontal offset with respect to the lower ones. This horizontal offset is obvious even in the leftmost part of the wall. Moreover, the horizontal rebars of the upper part present a vertical offset with respect to the ones of the lower part. This deformation pattern verifies the findings that were noticed in Fig. 8 concerning the excessive strains in the vicinity of the crack (which

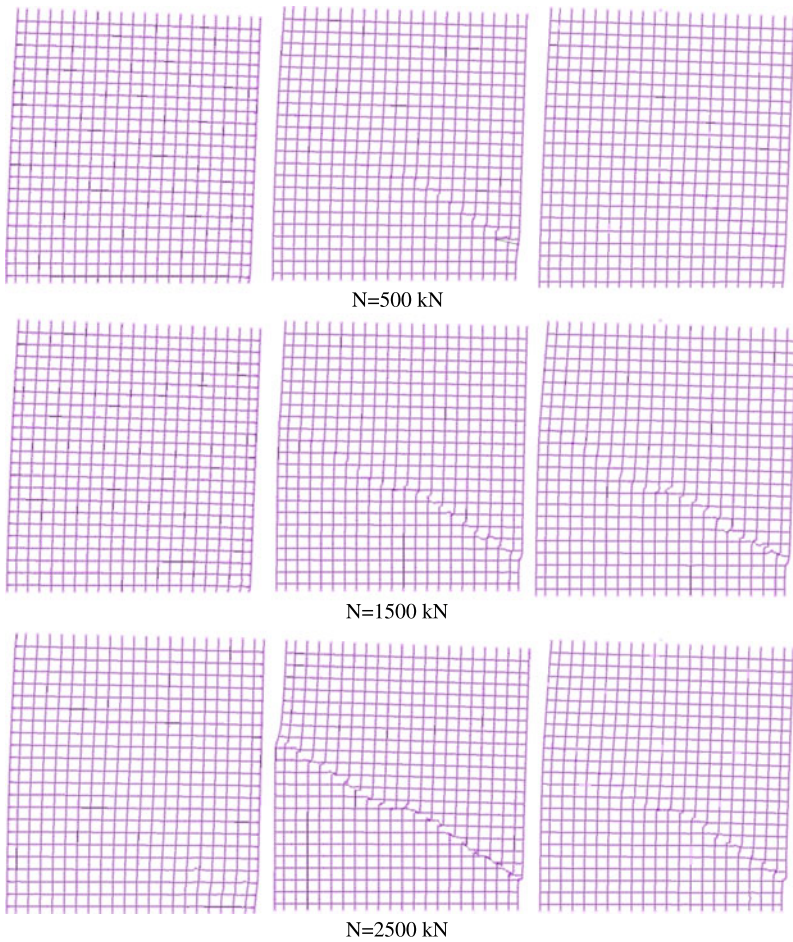


Fig. 9 Deformation of the steel mesh for various values of the vertical loading, for the cases of the uncracked wall (*left column*) and the cracked walls (3rd approximation—*middle column* and 4th approximation—*right column*)

had values well above the crushing strain limit). This deformation type of the steel mesh has its nature to the inability of the concrete to transfer any loading in this case.

In the sequel, the difference in the response between the 3rd and the 4th approximations of the fractal crack for the case of the heavy vertical loading will be explained. First of all, it has to be noticed that the higher vertical loading leads also to higher values of the horizontal loading, as it has been explained for the case of the uncracked wall. These increased horizontal forces have to be transferred from the upper part of the cracked wall to its lower part. In this respect, three mechanisms develop in order to facilitate the horizontal load transfer:

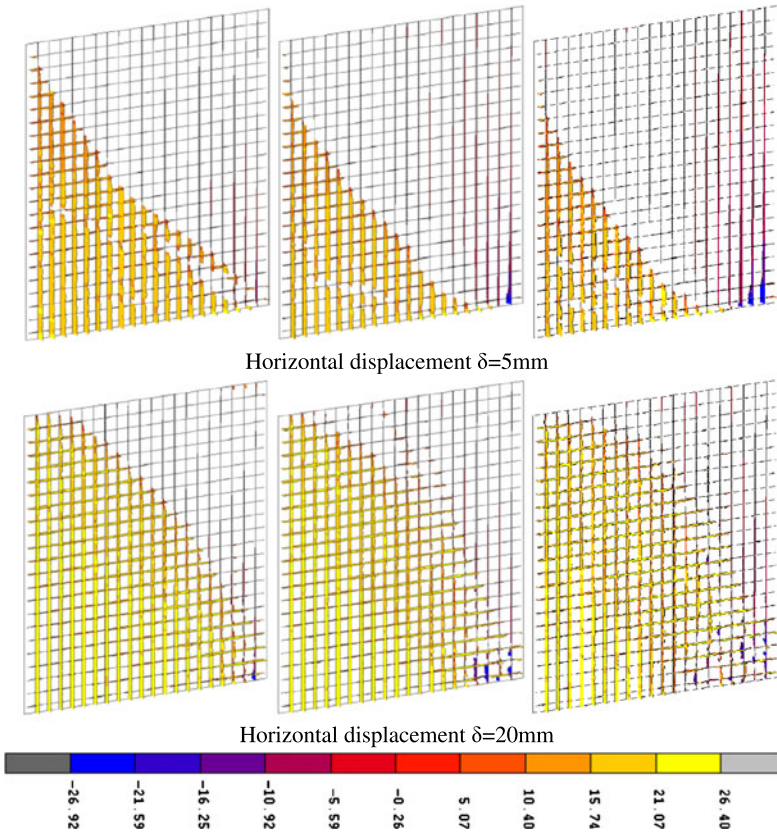


Fig. 10 Forces developed in the steel mesh for various values of the vertical loading for the uncracked wall (*left column*: $N = 500$ kN, *middle column*: $N = 1500$ kN, *right column*: $N = 2500$ kN)

- Exploitation of the tensile strength of the horizontal rebars;
- Development of friction on the part of the crack where contact forces occur;
- Mechanical interlock between the two faces of the crack.

The first two mechanisms are almost similar in both cracked walls. However, it is obvious from Fig. 6 that the higher resolution approximations of the fractal crack have improved capacity to transfer forces through the mechanical interlock mechanism. To the authors' opinion, this is the most important reason for the difference in the response between the walls corresponding to the 3rd and the 4th approximation of the fractal crack. For lower vertical load values the differences are rather limited, however, as the vertical loading increases, the response is completely different because the increased vertical forces are combined with the increased horizontal forces and "destroy" completely the vicinity of the interface.

Figures 10, 11 and 12 display the forces that develop at the horizontal and vertical rebars of the steel mesh for the three variants of the wall examined here

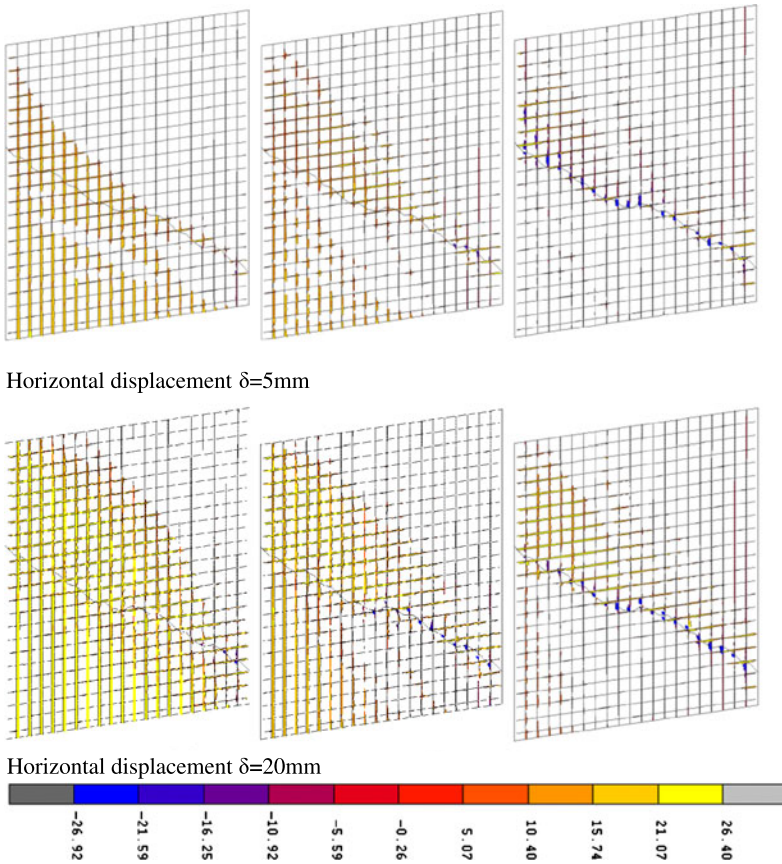


Fig. 11 Forces developed in the steel mesh for various values of the vertical loading for the 3rd approximation (left column: $N = 500 \text{ kN}$, middle column: $N = 1500 \text{ kN}$, right column: $N = 2500 \text{ kN}$)

(uncracked, 3rd approximation, 4th approximation respectively) for displacements of 5 and 20 mm. The left column of each figure corresponds to lower values of the axial loading ($N = 500 \text{ kN}$), the middle column to moderate loading values ($N = 1500 \text{ kN}$) and the right column to heavy axial loading ($N = 2500 \text{ kN}$).

For the case of the uncracked wall (Fig. 10) it is noticed that in the early horizontal loading steps ($\delta = 5 \text{ mm}$), only the vertical rebars are significantly loaded. The rebars in the left side of the wall have tensile forces while the rebars in the right side develop compressive forces, as a result of the bending of the wall. For $\delta = 20 \text{ mm}$, after the development of cracking in various parts of the initially uncracked wall, the horizontal rebars are also stressed, mainly in the areas where the corresponding cracks have reduced or zeroed the ability of concrete to transfer shear forces.

For the case of the 3rd approximation of the crack, it is noticed that the vertical rebars are stressed only for small axial loading values. For moderate and heavy

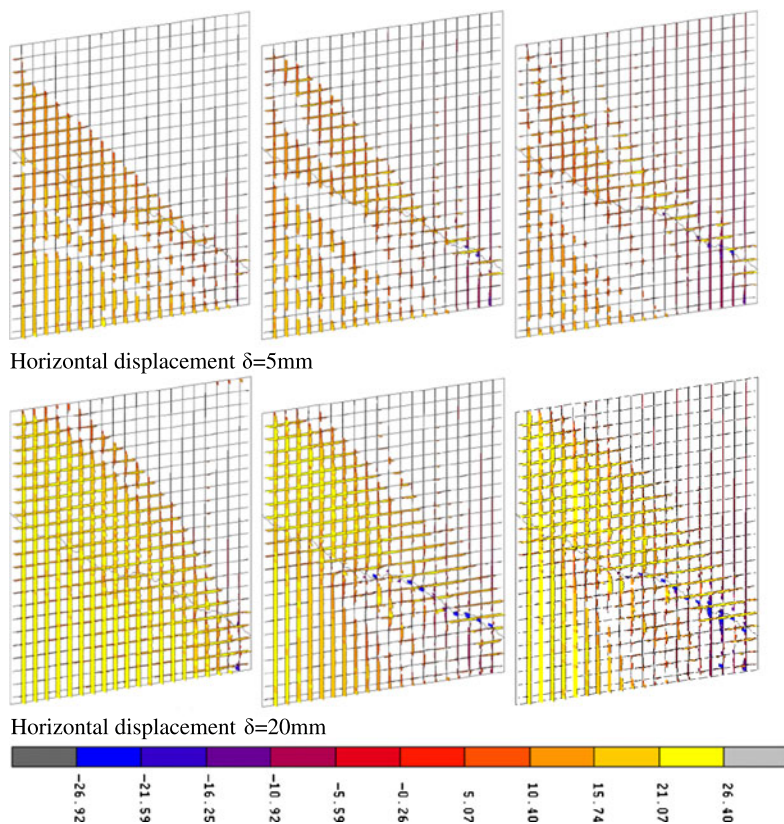


Fig. 12 Forces developed in the steel mesh for various values of the vertical loading for the 4th approximation (*left column: $N = 500$ kN, middle column: $N = 1500$ kN, right column: $N = 2500$ kN*)

axial loading, the vertical rebars are only partial stressed. It deserves to be noticed that the rebar stresses are negative in the vicinity of the crack, a fact that verifies that the concrete is unable to transfer even compressive loading. Moreover, it is noticed that the rebars of the right side of the wall do not develop compressive stresses any more, due to the fact that the magnitude of bending that develops in this case is significantly smaller than that in the case of the uncracked wall. The horizontal rebars are stressed only in specific areas, near the crack and in the regions where cracking strains have been developed. In any case, a closer look in the forces that have been developed in the rebars verifies the significantly decreased bending capacity of the specific wall.

The situation is rather different for the case of the 4th approximation of the fractal crack. The corresponding rebar forces are depicted in Fig. 12. It can easily be verified that for small values of the axial loading, the picture of the forces of the vertical rebars is quite similar to that of the uncracked wall. The same holds also for the forces of the horizontal rebars. For moderate axial load values, the forces of the

vertical rebars present discontinuities. At the right part of the crack it can be noticed that in some rebars the forces are compressive, indicating again the partial inability of the concrete in this region to transfer compressive loading. The horizontal rebars are mainly stressed in the upper part of the cracked wall and in the vicinity of the crack. Notice that this result is absolutely compatible with the remarks given for the cracked areas in Fig. 7.

5 Conclusions

In the chapter, the finite element analysis of a typical wall element was presented assuming that a certain crack has been developed as a result of an earthquake action. The crack was modelled following tools from the theory of fractals. Two different resolutions of the fractal curve were considered and their results were compared to those of the initially uncracked wall. The main finding of this work is that the cracked wall still has the capacity to sustain monotonic horizontal loading. For small axial loading values, this capacity is similar to that of the initially uncracked wall. However, for larger axial loading values, the demands increase. In this case, it seems that a more accurate modelling of the fractal crack (i.e. considering higher values of the resolution) leads to better result. Using lower resolution values, the mechanical interlock between the two faces of the crack is rather limited, leading the concrete in vicinity of the crack to overstressing and gradually to a complete loss of its capacity to sustain any kind of forces. In this case the bending capacity of the wall is significantly limited with respect to that of the uncracked concrete.

References

1. Mandelbrot B, Passoja D, Paullay A (1984) Fractal character of fractured surfaces of metals. *Nature* 308:721–723
2. Saouma VCB, Barton C, Gamaleldin N (1990) Fractal characterization of fracture surfaces in concrete. *Eng Fract Mech* 35:47–53
3. Borodich FM, Mosolov AB (1992) Fractal roughness in contact problems. *J Appl Math Mech* 56:681–690
4. Majumdar A, Tien CL (1990) Fractal characterization and simulation of rough surfaces. *Wear* 136:313–327
5. Borri-Brunetto M, Carpinteri A, Chiaia B (1999) Scaling phenomena due to fractal contact in concrete and rock fractures. *Int J Fract* 95:221–238
6. Panagouli OK, Mistakidis ES (2011) Dependence of contact area on the resolution of fractal interfaces in elastic and inelastic problems. *Eng Comput* 28(6):717–746
7. Mistakidis E, Stavroulakis G (1997) *Nonconvex optimization in mechanics. Algorithms, heuristic and engineering applications by the FEM*. Kluwer Academic, Boston
8. Mourot G, Morel S, Bouchaud E, Valentin G (2005) Anomalous scaling of mortar fracture surfaces. *Phys Rev E* 71(1):016136
9. Carpinteri A, Chiaia B, Invernizzi S (1999) Three-dimensional fractal analysis of concrete fracture at the meso-level. *Theor Appl Fract Mech* 31:163–172
10. Mandelbrot B (1982) *The fractal geometry of nature*. Freeman, New York

11. Måløy KJ, Hansen A, Hinrichsen EL, Eoux S (1992) Experimental measurements of the roughness of brittle cracks. *Phys Rev Lett* 68:213–215
12. Majumdar A, Buhushan B (1990) Role of fractal geometry in roughness characterization and contact mechanics of surfaces. *J Tribol* 112:205–216
13. Panagiotopoulos PD, Panagouli OK (1997) Fractal geometry in contact mechanics and numerical applications. In: Carpintieri A, Mainardi F (eds) *CISM-book on scaling, fractals and fractional calculus in continuum mechanics*. Springer, Berlin, pp 109–171
14. Borodich FM, Onishchenko DA (1999) Similarity and fractality in the modelling of roughness by a multilevel profile with hierarchical structure. *Int J Solids Struct* 36(17):2585–2612
15. Mistakidis ES, Panagouli OK (2002) Strength evaluation of retrofit shear wall elements with interfaces of fractal geometry. *Eng Struct* 24:649–659
16. Mistakidis ES, Panagouli OK (2003) Friction evolution as a result of roughness in fractal interfaces. *Eng Comput* 20(1):40–57
17. Chen C-J, Lee T-Y, Huang YM, Lai F-J (2009) Extraction of characteristic points and its fractal reconstruction for terrain profile data. *Chaos Solitons Fractals* 39:1732–1743
18. Barnsley M (1988) *Fractals everywhere*. Academic Press, Boston
19. deBorst R, Remmers J, Needleman A, Abellan MA (2004) Discrete vs smeared crack models for concrete fracture: bridging the gap. *Int J Numer Anal Methods Geomech* 28(7–8):583–607
20. Hu G-D, Panagiotopoulos PD, Panagouli OK, Scherf O, Wriggers P (2000) Adaptive finite element analysis of fractal interfaces in contact problems. *Comput Methods Appl Mech Eng* 182:17–37

Damage Analysis of Reinforced Concrete Structures with Substandard Detailing

Panagiotis E. Mergos and Andreas J. Kappos

Abstract The goal of this study is to investigate seismic behaviour of existing R/C buildings designed and constructed in accordance with standards that do not meet current seismic code requirements. In these structures, not only flexure, but also shear and bond-slip deformation mechanisms need to be considered, both separately and in combination. To serve this goal, a finite element model is developed for inelastic seismic analysis of complete planar R/C frames. The proposed finite element is able to capture gradual spread of inelastic flexural and shear deformations as well as their interaction in the end regions of R/C members. Additionally, it is capable of predicting shear failures caused by degradation of shear strength in the plastic hinges of R/C elements, as well as pullout failures caused by inadequate anchorage of the reinforcement in the joint regions. The finite element is fully implemented in the general inelastic finite element code IDARC2D and it is verified against experimental results involving individual column and plane frame specimens with non-ductile detailing. It is shown that, in all cases, satisfactory correlation is established between the model predictions and the experimental evidence. Finally, parametric studies are conducted to illustrate the significance of each deformation mechanism on the seismic response of the specimens under investigation. It is concluded, that all deformation mechanisms, as well as their interaction, should be taken into consideration in order to predict reliably seismic damage of R/C structures with substandard detailing.

Keywords Finite element model · Reinforced concrete · Shear-flexure interaction · Bond-slip · Substandard detailing

P.E. Mergos

Laboratory of Concrete and Masonry Structures, Department of Civil Engineering,
Aristotle University of Thessaloniki, 54124 Thessaloniki, Greece
e-mail: panmerg@yahoo.com

A.J. Kappos (✉)

Department of Civil Engineering, City University London, Northampton Sq.,
London EC1V 0HB, UK
e-mail: Andreas.Kappos.1@city.ac.uk

1 Introduction

In countries often struck by devastating earthquakes, a large fraction of the existing R/C building stock has not been designed to conform to modern seismic codes. These structures have not been detailed in a ductile manner and according to capacity design principles. Therefore, it is likely, that in case of a major seismic event, their structural elements will suffer from brittle types of failure, which may lead to irreparable damage or collapse of the entire structure.

The first step in performing a realistic seismic damage analysis is to develop an analytical model that is able to predict accurately inelastic response to seismic loading. The complexity of this problem increases significantly for non-ductile R/C structures, where, apart from flexure, shear and anchorage slip may significantly influence the final response. This is the reason why, especially for these structures, all three deformation mechanisms should be explicitly treated, while their interaction should also be taken into consideration [1].

Current research on seismic assessment of R/C structures is focused primarily on flexural response. Deformations caused by shear and bond-slip related mechanisms are either ignored or lumped into flexure [2]. However, the necessary assumptions inherent to both of these approaches may drive the assessment procedure to erroneous results. This is especially the case for 'old type' existing R/C structures, where shear and bond types of failure cannot be precluded, due to the absence of ductile detailing and capacity design.

Only a small number of studies [3–7] proposed numerical models for seismic assessment of non-ductile R/C structures, where all three deformation mechanisms are considered individually. Nevertheless, all these studies have demonstrated the importance and the advantages of treating separately all deformation components, when assessing seismic response of deficient R/C structures.

Following this approach, a new finite element model [8–11] is developed herein for examining inelastic response of R/C frames with substandard detailing. The novel feature of the proposed finite element is the fact that it is capable of modelling gradual spread of inelastic flexural and shear deformations, as well as their interaction in the end regions of R/C members. Furthermore, it is able to predict shear failures caused by degradation of shear strength in the plastic hinges of R/C elements, as well as pullout failures caused by inadequate anchorage of the reinforcement in the joint regions under general loading conditions.

The chapter starts with an analytical description of the finite element model. The element formulation, components and inherent assumptions are explained. Emphasis is placed on the ability of the numerical model to predict brittle types of failure (i.e. shear and bond). In addition, the necessary alterations to the nonlinear solution algorithms are discussed in order for the proposed beam-column element to be fully implemented in a general inelastic damage analysis finite element code.

Then, with the aim to verify the capabilities of the proposed numerical model to reproduce inelastic response of R/C buildings with deficient configuration, the proposed finite element is applied to the analysis of well documented R/C column and frame specimens subjected to cyclic or seismic loading. Analytical results are

compared with experimental recordings. It is shown that the numerical model is able to capture sufficiently experimental response in terms of strength, stiffness and displacements, and to predict reliably the prevailing mode of failure for each specimen.

Finally, parametric analyses illustrate the relative importance of each deformation mechanism on the response of the examined specimens in the elastic and inelastic range. It is shown that proper modelling of all flexibility components, as well as their interaction, is a substantial prerequisite for reliable prediction of seismic response of R/C frames built with inadequate earthquake resistant provisions.

2 Finite Element Model

2.1 General Formulation

The finite element model proposed herein for seismic damage analysis of existing RC structures is based on the flexibility approach (force-based element) and belongs to the class of phenomenological models. It consists of three sub-elements representing flexural, shear, and anchorage slip response (Fig. 1). The total flexibility matrix F_b is calculated as the sum of the flexibilities of its sub-elements and can be inverted to produce the element stiffness matrix K_b . Hence:

$$F_b = F^{fl} + F^{sh} + F^{sl} \quad (1)$$

where, F_b , F^{fl} , F^{sh} , F^{sl} are the basic total, flexural, shear and anchorage slip, respectively, tangent flexibility matrices. K_b is the basic tangent stiffness matrix of the element, relating incremental moments ΔM_A , ΔM_B and rotations $\Delta \theta_A$, $\Delta \theta_B$ at the element flexible ends A and B respectively.

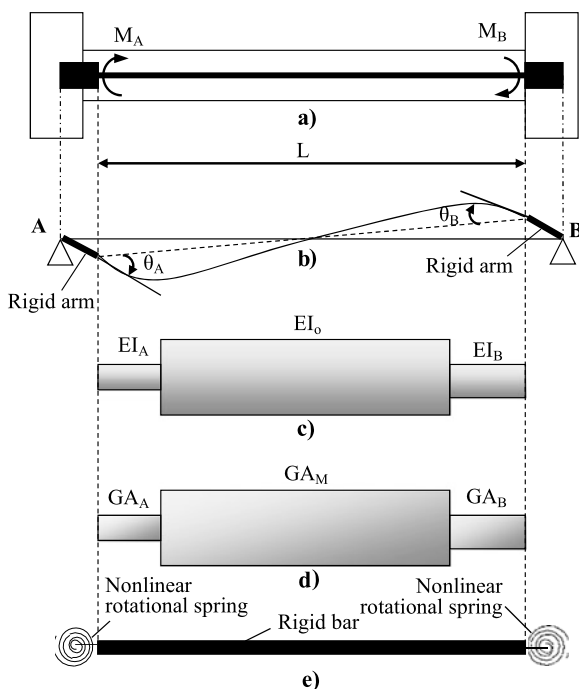
The local stiffness matrix K_e , relating displacements and forces at the element joints, is easily determined following standard structural analysis procedures. The components of the examined finite element, as well as their interaction, are described analytically in the following sections.

2.2 Flexural Sub-element

This sub-element (Fig. 1c) is used for modelling flexural behaviour of an R/C member before and after yielding of the longitudinal reinforcement. It consists of a set of rules governing the hysteretic moment-curvature (M - φ) response of the member end sections and a spread inelasticity model describing flexural stiffness distribution along the entire member.

M - φ hysteretic model (Fig. 2a) is composed by the skeleton curve and a set of rules determining response during loading, unloading and reloading. M - φ envelope curve is derived by section analysis and appropriate bilinearization. Loading response is assumed to follow the bilinear envelope curve. Unloading is based on the

Fig. 1 Proposed finite element. (a) R/C member geometry. (b) Beam-column finite element with rigid arms. (c) Flexural sub-element. (d) Shear sub-element. (e) Anchorage slip sub-element



respective Sivaselvan and Reinhorn [12] hysteretic rule adjusted for mild stiffness degradation. Reloading aims at the point with previous maximum excursion in the opposite direction.

To capture distribution of section flexural stiffness along the concrete member, a gradual spread inelasticity model is assigned [13]. Following this model, the element is divided into two inelastic end regions and one elastic intermediate zone. Stiffness along the intermediate zone is assumed to be uniform and equal to the elastic stiffness EI_o of the $M-\varphi$ envelope curve.

Stiffness distribution inside the inelastic zones depends on the loading state of the end section hysteretic response. In particular, Fig. 2b illustrates hysteretic response of four discrete sections located inside one plastic hinge region. It can be seen that when all sections remain in the strain hardening branch (loading state), flexural stiffness remains constant in the inelastic zone. However, when they are in the unloading and reloading state, stiffness varies from a minimum value $r_1 \cdot EI_o$ or $r_2 \cdot EI_o$, corresponding to the end section, to a maximum value, which is equal to EI_o . Hence, under the general assumption that the loading state of all sections of the yielded region remains the same, it may be considered that when $M-\varphi$ end section hysteretic response is on the strain hardening branch, stiffness distribution remains uniform in the inelastic zone. In the case where end-section $M-\varphi$ behaviour is in the unloading or reloading state, it is assumed that the stiffness varies linearly from end section flexural stiffness $r_1 \cdot EI_o$ or $r_2 \cdot EI_o$ to EI_o .

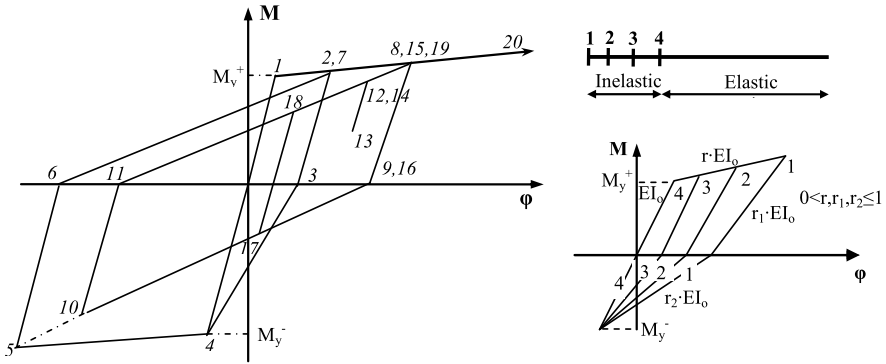
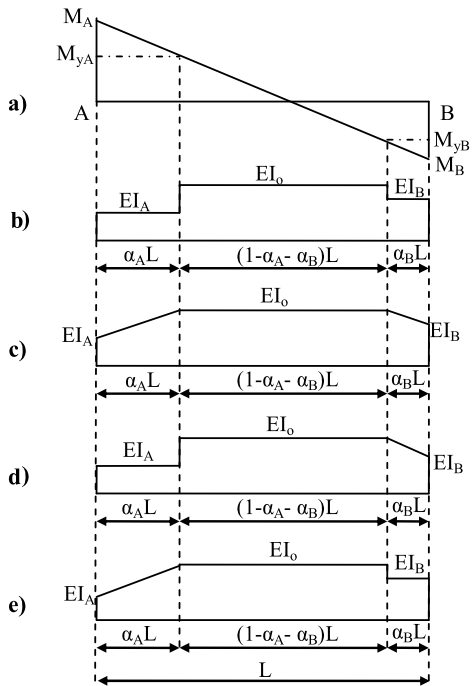


Fig. 2 (a) $M-\phi$ hysteretic model. (b) $M-\phi$ hysteretic response of four individual sections inside plastic hinges

Fig. 3 Element. (a) Bending moment diagram. (b) Stiffness distribution when ends A and B are in the loading state. (c) Stiffness distribution when ends A and B are in the unloading or reloading state. (d) Stiffness distribution when end A is in the unloading or reloading state and end B is in the loading state. (e) Stiffness distribution when end A is in the unloading or reloading state and end B is in the loading state



In accordance with the previous observations, stiffness distribution along the member may be assumed to have one of the shapes shown in Fig. 3, where L is the length of the member; EI_o is the stiffness at the intermediate part of the element and EI_A and EI_B are the current flexural rigidities of the sections at the ends A and B respectively. The flexural rigidities EI_A and EI_B are determined from the $M-\phi$ hysteretic relationship of the corresponding end sections.

Table 1 Determination of flexural flexibility matrix coefficients

Flexibility coefficient	Stiffness distribution	c_o	c_A	c_B
f_{11}	Fig. 3b	4	$12\alpha_A - 12\alpha_A^2 + 4\alpha_A^3$	$4\alpha_B^3$
f_{22}	Fig. 3b	4	$4\alpha_A^3$	$12\alpha_B - 12\alpha_B^2 + 4\alpha_B^3$
f_{12}	Fig. 3b	-2	$4\alpha_A^3 - 6\alpha_A^2$	$4\alpha_B^3 - 6\alpha_B^2$
f_{11}	Fig. 3c	4	$6\alpha_A - 4\alpha_A^2 + \alpha_A^3$	α_B^3
f_{22}	Fig. 3c	4	α_A^3	$6\alpha_B - 4\alpha_B^2 + \alpha_B^3$
f_{12}	Fig. 3c	-2	$\alpha_A^3 - 2\alpha_A^2$	$\alpha_B^3 - 2\alpha_B^2$
f_{11}	Fig. 3d	4	$12\alpha_A - 12\alpha_A^2 + 4\alpha_A^3$	α_B^3
f_{22}	Fig. 3d	4	$4\alpha_A^3$	$6\alpha_B - 4\alpha_B^2 + \alpha_B^3$
f_{12}	Fig. 3d	-2	$4\alpha_A^3 - 6\alpha_A^2$	$\alpha_B^3 - 2\alpha_B^2$
f_{11}	Fig. 3e	4	$6\alpha_A - 4\alpha_A^2 + \alpha_A^3$	$4\alpha_B^3$
f_{22}	Fig. 3e	4	α_A^3	$12\alpha_B - 12\alpha_B^2 + 4\alpha_B^3$
f_{12}	Fig. 3e	-2	$\alpha_A^3 - 2\alpha_A^2$	$4\alpha_B^3 - 6\alpha_B^2$

In the same figure, α_A and α_B are the yield penetration coefficients. The yield penetration coefficients specify the proportion of the element where the acting moment exceeds the end-section yield moment. These coefficients are first calculated for the current moment distribution from Eq. (2), where M_{yA} and M_{yB} are the respective flexural yielding moments of end sections A and B. Then, they are compared with the previous maximum penetration lengths; the yield penetration lengths cannot be smaller than their previous maximum values.

$$\alpha_A = \frac{M_A - M_{yA}}{M_A - M_B} \leq 1; \quad \alpha_B = \frac{M_B - M_{yB}}{M_B - M_A} \leq 1 \quad (2)$$

Having established the stiffness distribution along the R/C member at each step of the analysis, the coefficients of the flexibility matrix of the flexural sub-element can be derived from the general equation (3) and Table 1, determined by applying the principle of virtual work.

$$f_{ij}^fl = \frac{L}{12EI_o} (c_o + c_A \cdot \gamma_A + c_B \cdot \gamma_B); \quad \gamma_A = \frac{EI_o}{EI_A} - 1; \quad \gamma_B = \frac{EI_o}{EI_B} - 1 \quad (3)$$

2.3 Shear Sub-element

The shear sub-element (Fig. 1d) represents the hysteretic shear behaviour of the R/C member prior and subsequent to shear cracking, flexural yielding, and yielding of the shear reinforcement. Herein, this sub-element has been designed in a similar way to the flexural element described above. It consists of a set of rules determining V - γ (shear force vs. shear strain) hysteretic behaviour of the member intermediate

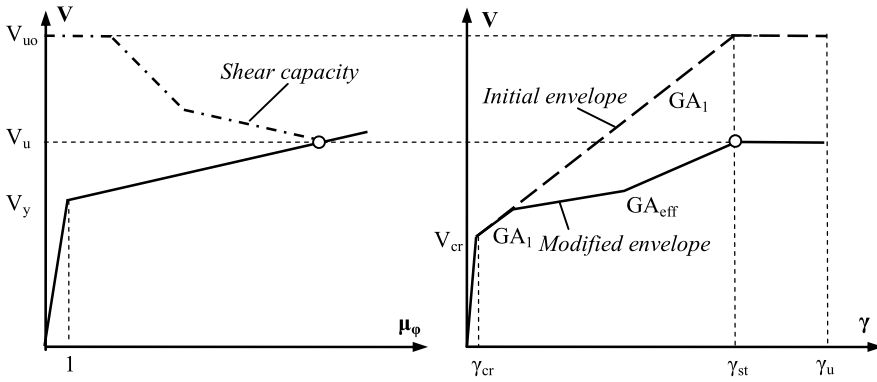


Fig. 4 (a) Flexural primary curve in terms of member shear force and curvature ductility demand of the critical cross section. (b) Shear ($V-\gamma$) primary curve before and after modelling shear-flexure interaction

and end regions, and a shear spread inelasticity model determining distribution of shear stiffness along the R/C member.

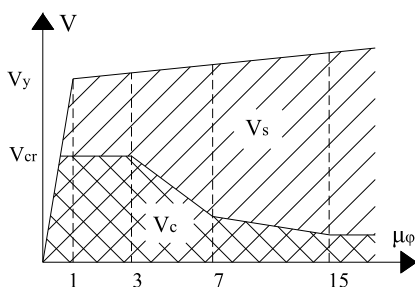
Shear hysteresis is determined by the $V-\gamma$ skeleton curve and a set of rules describing response during unloading and reloading. The primary curve is first derived without considering shear-flexure interaction effect. This initial envelope curve (Fig. 4) is valid for modelling shear behaviour outside plastic hinge regions of the R/C members.

The $V-\gamma$ initial primary curve consists of four branches (Fig. 4), but only three different slopes, as explained later on. The first branch connects the origin and the shear cracking point, which is defined as the point where the nominal principal tensile stress exceeds the mean tensile strength of concrete [14]. The second and third branches of the initial primary curve have the same slope and connect the shear cracking point to the point corresponding to the onset of yielding of transverse reinforcement, or else the point of attainment of maximum shear strength (γ_{st}, V_{uo}). The second and third branches are separated at the point corresponding to flexural yielding (γ_y, V_y). This approach is adopted in order to distinguish hysteretic shear behaviour before and after flexural yielding [8].

Initial shear strength V_{uo} is calculated by the Priestley et al. [15] approach for curvature ductility demand $\mu_\phi \leq 3$ (i.e. no strength degradation). Shear strain at stirrup yielding γ_{st} is evaluated by the truss analogy approach and two modification factors for the member aspect ratio and normalized axial load, as proposed by the writers of this study [11] on the basis of calibration studies with the experimental evidence.

The fourth branch is almost horizontal and describes shear response after yielding of transverse reinforcement and until onset of shear failure, corresponding to shear distortion γ_u . The latter distortion is established on the basis of an empirical formula proposed by the writers of this study [11] derived by experimental results coming from 25 R/C specimens failing in shear mode. The proposed formula connects γ_u

Fig. 5 Variation of shear resisting mechanisms with μ_ϕ in plastic hinges



with the level of the applied axial load, the amount of transverse reinforcement and the member shear-span.

Several studies [14–16] have demonstrated that shear strength degrades due to disintegration of the plastic hinge zones caused by inelastic flexural deformations. Furthermore, it has been shown experimentally [17, 18] that shear distortions in the plastic hinge regions may increase rapidly (“shear-flexural yielding”) subsequent to flexural yielding, despite the fact that shear force demand remains almost constant, as it is controlled by flexural yielding. The combination of these phenomena is defined herein as shear-flexure interaction effect.

In this study, a new analytical methodology is proposed for the calculation of the modified V - γ envelope curve, which accounts properly for shear-flexure interaction effect (Fig. 4). The modified envelope is employed by the proposed finite element model for the determination of shear hysteretic response inside the locations of the plastic hinges.

In accordance with truss analogy approach [19], after shear cracking, shear strain increment $\Delta\gamma_s$ is related to the additional shear force resisted by the truss mechanism ΔV_s by Eq. (4), where GA_1 is the cracked stiffness of the initial shear primary curve shown in Fig. 4.

$$\Delta\gamma_s = \frac{\Delta V_s}{GA_1} \quad (4)$$

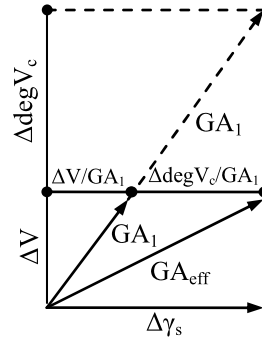
Figure 5 illustrates variation of capacity of shear resisting mechanisms (concrete V_c and truss V_s) in the plastic hinge region of a single R/C member following the Priestley’s et al. [15] shear strength approach (for clarity, contribution of axial load is lumped into V_c). It can be seen that after $\mu_\phi > 3$, V_s increases to accommodate both additional shear demand ΔV and additional deterioration of the concrete resisting mechanism $\Delta \text{deg } V_c$. Hence, ΔV_s can be considered as the sum of ΔV and $\Delta \text{deg } V_c$.

$$\Delta V_s = \Delta V + \Delta \text{deg } V_c \quad (5)$$

If GA_{eff} is the tangent stiffness of the modified shear primary curve including shear-flexure interaction effect, by definition, it yields the same increment of shear distortions $\Delta\gamma_s$ only for the applied shear force increment ΔV (without $\Delta \text{deg } V_c$), as illustrated in Fig. 6. Consequently

$$\Delta\gamma_s = \frac{\Delta V}{GA_{eff}} \quad (6)$$

Fig. 6 Determination of effective shear stiffness GA_{eff}



Combining Eqs. (4)–(6), Eq. (7) is derived for determining stiffness of the shear envelope curve after yielding in flexure. This formula shows that GA_{eff} can only be either equal or smaller than GA_1 . Equality holds only when the degradation of the concrete shear resisting mechanisms is negligible.

$$GA_{eff} = \frac{\Delta V}{\Delta V + \Delta \text{deg } V_c} \cdot GA_1 \tag{7}$$

It is important to note that, following the afore-described analytical procedure, degraded shear strength V_u [15] is always attained at shear distortion γ_{st} corresponding to stirrup yielding (Fig. 4). This observation is in accordance with truss analogy approach [19].

After determination of the V - γ envelope curves, shear hysteretic response has to be established. This behaviour is generally characterized by significant stiffness degradation and pinching. In this study, the empirical model by Ozcebe and Saatcioglu [18] (Fig. 7a) is adopted for this response, properly modified by the writers [8] in order to be incorporated in the general structural analysis framework.

After determining shear hysteretic responses, shear stiffness distribution along the R/C member has to be defined. In reality, due to shear-flexure interaction and following flexural deformations, inelastic shear strains tend to spread gradually from the member ends to the mid-span as the length of inelastic zones increases. To capture this phenomenon, a shear gradual spread inelasticity model has been first proposed by the writers of this study in [9, 11]. The model aims at monitoring variation of shear stiffness along the concrete member throughout the response.

To serve this goal, the shear sub-element is divided in two variable length end-zones, where shear-flexure interaction takes place, and an intermediate region where interaction with flexure may be disregarded. The lengths of the inelastic zones α_{A_s} and α_{B_s} of the shear sub-element are determined by the respective ones of the flexural sub-element (Fig. 7b). Hence, they are also constantly updated to capture gradual growth of the plastic hinge regions. Furthermore, the stiffness of these end-zones GA_A and GA_B are defined by the modified V - γ envelope curves (Fig. 4) calculated for the current μ_ϕ demands of the respective ends of the flexural sub-element in accordance with the analytical procedure described in the previous. Shear stiffness distribution is assumed uniform inside the inelastic zones since acting shear is uniform and all sections remain in the same V - γ loading state.

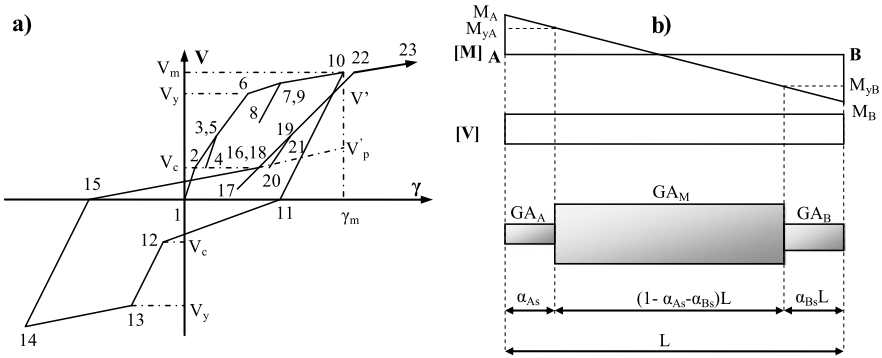


Fig. 7 (a) Shear hysteretic model. (b) Shear spread plasticity model

Shear stiffness GA_M of the intermediate part of the sub-element is also assumed uniform, but it is determined by the initial $V-\gamma$ primary curve, without considering shear-flexure interaction effect.

After having established the distribution of GA along the R/C member at each step of the analysis, the coefficients of the flexibility matrix of the shear sub-element are given by Eq. (8), determined by the principle of virtual work.

$$f_{ij}^{sh} = \frac{a_{As}}{GA_A \cdot L} + \frac{1 - a_{As} - a_{Bs}}{GA_M \cdot L} + \frac{a_{Bs}}{GA_B \cdot L} \quad (i, j = 1, 2) \quad (8)$$

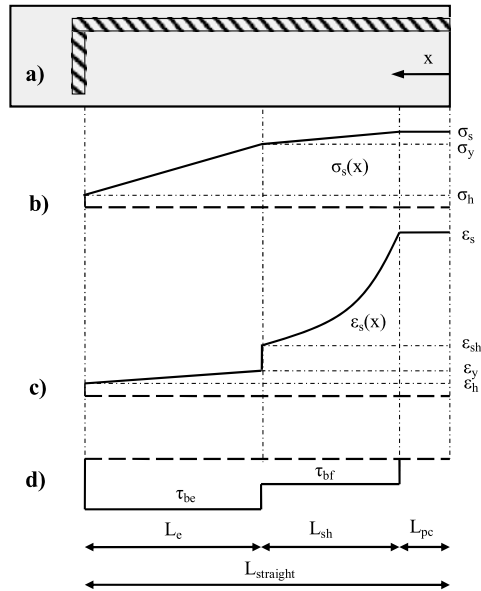
2.4 Bond-Slip Sub-element

The bond-slip sub-element accounts for the fixed-end rotations which arise at the interfaces of adjacent R/C members due to bond deterioration and the ensuing slip-page of the reinforcement anchorage in the joint regions. The proposed model consists of two concentrated rotational springs located at the member-ends; the two (uncoupled) springs are connected by an infinitely rigid bar (Fig. 1e). Following this formulation, the coefficients of the bond-slip flexibility matrix F^{sl} are given by Eq. (9), where f_A^{sl} and f_B^{sl} are the current tangent flexibilities of the concentrated rotational springs at the ends A and B respectively. These flexibilities depend on the moment-fixed end rotation ($M-\theta_{slip}$) envelope curve and the model used to represent hysteretic behaviour of each rotational spring.

$$f_{11}^{sl} = f_A^{sl}; \quad f_{22}^{sl} = f_B^{sl}; \quad f_{12}^{sl} = f_{21}^{sl} = 0 \quad (9)$$

The $M-\theta_{slip}$ skeleton curve is derived on the basis of a simplified procedure [20] assuming uniform bond stress along different segments of the anchored rebar (Fig. 8). These segments are the elastic region L_e , the strain-hardening region L_{sh} and the pullout cone region L_{pc} . The average elastic bond strength τ_{be} according to ACI 408 [21] is adopted here for the elastic region, while the frictional bond

Fig. 8 (a) Reinforcing bar with 90° hook embedded in concrete. (b) Steel stress distribution. (c) Strain distribution. (d) Bond stress distribution



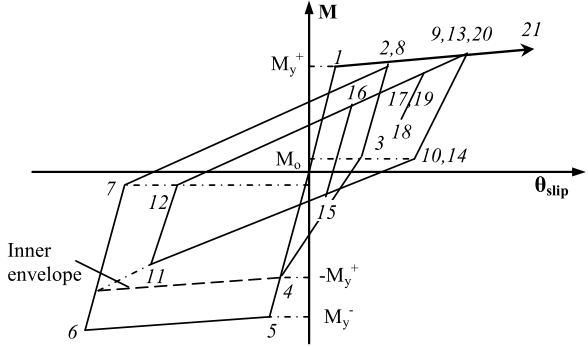
τ_{bf} according to the CEB Model Code [22] is assumed to apply within the strain-hardening region. In the pullout cone region, it is assumed that the acting bond is negligible.

For various levels of the applied end moment and using the results of $M-\varphi$ analysis, the stress σ_s and strain ε_s of the reinforcing bar at the loaded end are first determined. Then, from equilibrium and applying the assumed bond distribution, variation of reinforcing bar stress $\sigma_s(x)$ along the embedment length is defined as shown in Fig. 8b, where σ_y is the yield strength of steel and σ_h is the stress at the end of the straight part of the rebar anchorage. Then, by assigning an appropriate constitutive material law for steel [23], strain distribution $\varepsilon_s(x)$ is determined, as shown in Fig. 8c, where ε_y and ε_{sh} are the steel strains at the onset of yielding and strain hardening, respectively, and ε_h is the steel strain at the end of the straight part of the anchorage. It is important to note that post-yield nonlinearity of the material constitutive law, i.e. strain hardening, should be taken into account because it affects significantly the final results [11].

Once $\varepsilon_s(x)$ is determined, slip of the reinforcement δ_{slip} can be calculated by integration along the anchorage length of the bar. In the case of hooked bars, local slip of the hook should be added. This can be evaluated by the force acting on the hook $P_h = A_b \cdot \sigma_h$, where A_b is the area of the anchored bar, and an appropriate hook force vs. hook slip constitutive relationship [24].

Upon determination of δ_{slip} , the respective fixed-end rotation can be calculated by Eq. (10), where $(d - x_c)$ is the distance between the bar and the neutral axis.

Fig. 9 $M-\theta_{slip}$ hysteretic model



The envelope $M-\theta_{slip}$ curve constructed by the various points of the afore-described methodology is then idealized by a bilinear relationship for analysis purposes.

$$\theta_{slip} = \frac{\delta_{slip}}{d - x_c} \tag{10}$$

After establishing the envelope curve, bond-slip hysteretic behaviour (Fig. 9) is determined by adopting the respective phenomenological model of Saatcioglu and Alsiwat [25]. Additional features have been introduced by the writers to prevent numerical instabilities resulting in the implementation of the specific model in the framework of nonlinear analysis.

In R/C structures with substandard detailing, anchorage-bond failures cannot be precluded. In case of straight anchorages, bond failure takes place when the anchorage length demand L_{dem} reaches the available straight embedment length $L_{straight}$. Hence, Eq. (11) holds, where σ_{sb} is the bar stress at anchorage failure and d_b represents bar diameter. If σ_{sb} exceeds steel stress corresponding to flexural failure, then bond is not the critical mode of failure for the examined anchorage.

$$\begin{aligned} \sigma_{sb} \leq \sigma_y &\rightarrow \sigma_{sb} = \frac{4 \cdot \tau_{be'}}{d_b} \cdot L_{straight} \\ \sigma_{sb} > \sigma_y &\rightarrow \sigma_{sb} = \sigma_y + \frac{4 \cdot \tau_{bf}}{d_b} \cdot \left(L_{straight} - L_{pc} - \frac{\sigma_y \cdot d_b}{4 \cdot \tau_{be}} \right) \end{aligned} \tag{11}$$

In Eq. (11), $\tau_{be'}$ is a uniform bond strength higher than τ_{be} in order to consider the fact that for very short embedment lengths, where bond failure takes place for $\sigma_s < \sigma_y$, experimental evidence [21] shows that uniform bond strength τ_{be} underestimates significantly the available anchorage capacity. To avoid over-conservative solutions, it is proposed herein that $\tau_{be'}$ is taken by linear interpolation for $L_{straight}$ between τ_{be} corresponding to $L_y = \sigma_y \cdot d_b / (4 \cdot \tau_{be})$ and the ultimate local bond capacity τ_{bu} [22] corresponding typically to anchorage length equal to $5d_b$.

In the case of deficient end hooks, anchorage failure may be assumed to develop when the force acting on the hook reaches ultimate hook capacity P_{hu} . By equilib-

rium, Eq. (12) holds for determining σ_{sb} , where $L_{sh} = (\sigma_{sb} - \sigma_y) \cdot d_b / (4 \cdot \tau_{bf})$ and $L_d = (L_{straight} - L_{pc} - L_{sh})$.

$$\begin{aligned} \sigma_{sb} \leq \sigma_y &\rightarrow \sigma_{sb} = \frac{P_{hu} + \pi \cdot d_b \cdot \tau_{be} \cdot L_{straight}}{A_{sb}} \\ \sigma_{sb} > \sigma_y \ \& \ L_d \geq 0 \\ &\rightarrow \sigma_{sb} = \sigma_y + \frac{4 \cdot \tau_{bf}}{d_b} \cdot \left(L_{straight} - L_{pc} - \frac{(A_{sb} \cdot \sigma_y - P_{hu})}{\pi \cdot d_b \cdot \tau_{be}} \right) \\ \sigma_{sb} > \sigma_y \ \& \ L_d < 0 &\rightarrow \sigma_{sb} = \frac{P_{hu} + \pi \cdot d_b \cdot \tau_{bf} \cdot (L_{straight} - L_{pc})}{A_{sb}} \end{aligned} \quad (12)$$

3 Numerical Implementation

The finite element model, described above, requires additional modifications to the nonlinear analysis solution algorithms in order to be implemented with consistency. It is known that during nonlinear analysis the following equation is solved in incremental form.

$$K \cdot \Delta U = \Delta F \quad (13)$$

where K is the overall tangent stiffness matrix of the structure, ΔU is the vector of unknown nodal displacement increments and ΔF is the vector of the applied external load increments. The element stiffness matrices K_e are first calculated at the element level and later assembled into K .

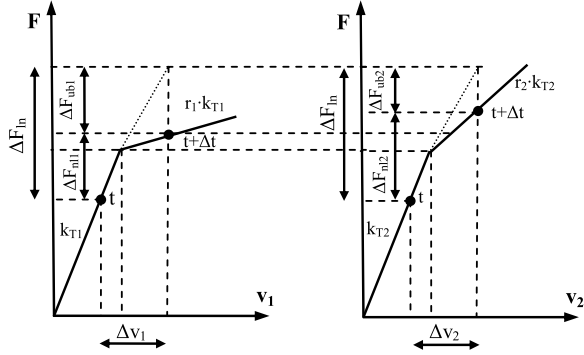
In the case of dynamic analysis, the equivalent dynamic stiffness and external load matrices must be formed. Herein, the solution of the incremental system is carried out using the unconditionally stable constant-average acceleration Newmark-Beta algorithm [26]. Viscous damping matrix is calculated by assigning the Rayleigh damping model with circular frequencies corresponding to the first and second mode of vibration.

The solution is performed assuming that the properties of the structure do not change during the analysis step. Since the stiffness of some elements is likely to change during the step t , the new configuration at $t + \Delta t$ may not satisfy equilibrium. If ΔF_{ln} is the force increment vector arising from the assumption of constant stiffness during Δt and ΔF_{nl} is the force increment vector determined by the element nonlinear hysteretic laws, then an unbalanced force vector ΔF_{ub} arises, given by the following equation

$$\Delta F_{ub} = \Delta F_{ln} - \Delta F_{nl} \quad (14)$$

Typically, in the nonlinear analysis scheme, this issue is resolved by applying the one step unbalanced force correction method [27]. According to this technique, the unbalanced force vector is subtracted from the right part of Eq. (13) at the next time step of analysis. Despite the fact that this procedure minimizes computational effort in nonlinear analysis, it cannot be applied with consistency for finite elements

Fig. 10 Unbalanced forces for two hysteretic responses coupled in series



composed by different sub-elements connected in series like the one presented in this study.

Figure 10 presents determination of unbalanced forces produced by two different hysteretic laws ($F-v_1$ and $F-v_2$), which are deemed coupled in series. The two hysteretic relationships have different elastic (k_{T1} and k_{T2}) and post-elastic stiffness ($r_1 \cdot k_{T1}$ and $r_2 \cdot k_{T2}$). It can be easily extracted that for the same force increment ΔF_{In} the restoring force increments ΔF_{n1} and ΔF_{n2} and consequently unbalanced forces ΔF_{ub1} and ΔF_{ub2} become different, resulting in loss of member equilibrium.

To overcome this problem, the ‘event to event’ solution strategy [28] is adopted herein. This method is computationally effective when multilinear models are applied to capture hysteretic response. In accordance with this procedure, the nonlinear response of the structure is subdivided into subsequent events, which mark the change of stiffness of the entire structure. Between these events, linear behaviour is considered. Hence, each analysis step is divided (when required) into sufficient number of sub-steps, until no event takes place during the last sub-step. For the finite element developed herein, as an event is prescribed every change in stiffness of all hysteretic responses of all three sub-elements of each beam-column model.

If the incremental load vector ΔF yields the deformation increment Δv_{mn} for the hysteretic response n of the element m , assuming constant stiffness, then the immediate next event force scale factor λ_{mn} corresponding to this hysteretic response is determined by

$$\lambda_{mn} = \min\left(1, \frac{v_{mne} - v_{mn}}{\Delta v_{mn}}\right) \tag{15}$$

In Eq. (15), v_{mne} is the deformation marking immediate next event and v_{mn} is the respective deformation at the beginning of the loading step. It is clear, that the immediate next event for the entire structure will correspond to the minimum value λ_{min} of all λ_{mn} . After calculating λ_{min} , the solution algorithm implemented to each nonlinear analysis step is presented in Fig. 11.

In addition to the above, following the procedure proposed in this study for determining tangent shear stiffness GA_{eff} after flexural yielding when accounting for shear-flexure interaction effect, it can be inferred by Eq. (7), that GA_{eff} becomes a function of the element shear force increment ΔV . But if it is to be applied in the

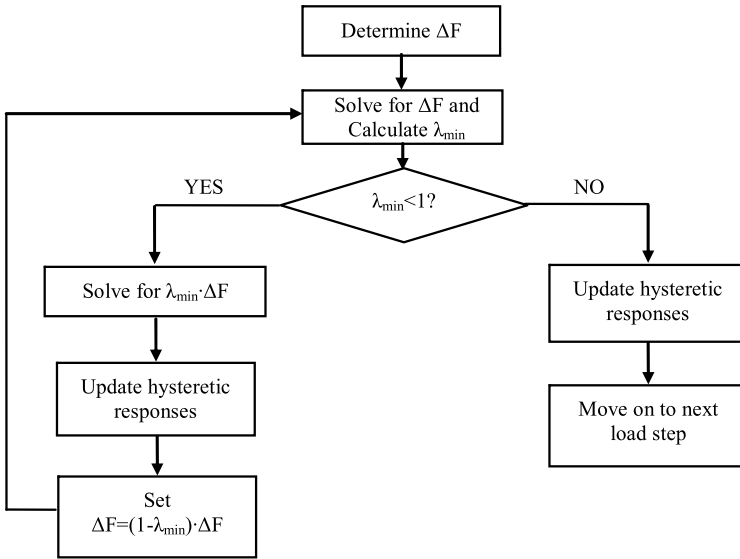


Fig. 11 Event to event solution algorithm

analytical procedure, ΔV will be influenced by GA_{eff} as well, since the latter will affect the flexibility matrix of the element. To resolve this issue, an iterative analytical scheme, applied in the respective load step of the nonlinear analysis, is proposed herein, as detailed in the algorithm shown in Fig. 12.

Applying this procedure, it was found that numerical convergence is very fast. The number of iterations may increase as the influence of shear deformations on element flexibility enhances, but the additional computational cost required in this case is justified by the significance of calculating accurately shear response.

4 Validation of the Proposed Model

The numerical model described above is implemented in the general finite element code IDARC2D developed at the State University of New York at Buffalo [29]. Then, it is validated against experimental results coming from well documented R/C column and frame specimens with substandard detailing.

In addition, parametric analyses reveal the necessity of incorporating each deformation mechanism in seismic assessment of ‘old type’ R/C structures in the linear and nonlinear range of response. To this purpose, each frame specimen is examined using four different beam-column models. The F model simulates only member flexural response. The FB model incorporates flexural and anchorage bond-slip response, while the FS one applies flexural and shear flexibility. Finally, the FSB model, which is the one proposed in this study, simulates all deformation mechanisms, as well as their interaction.

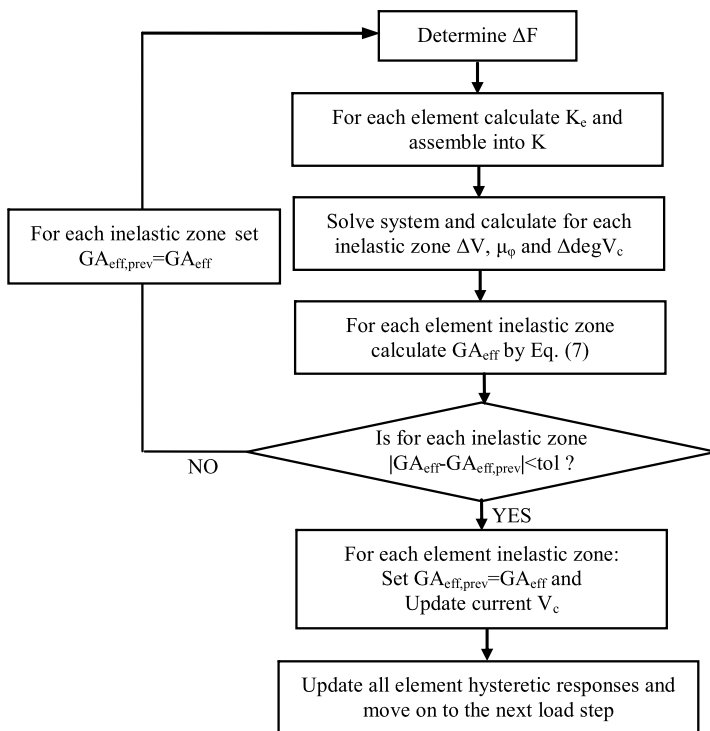


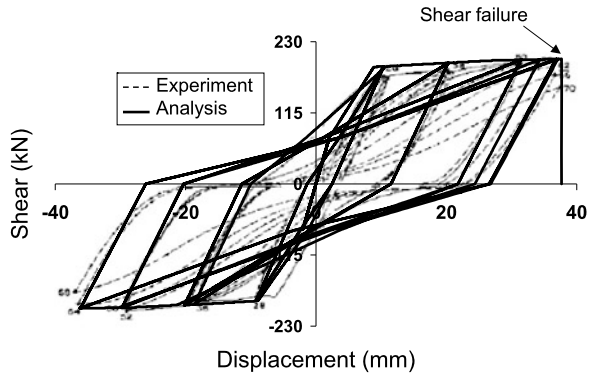
Fig. 12 Shear-flexure interaction implementation algorithm

4.1 R/C Beam Specimen R5 by Ma et al. [30]

Ma et al. [30] tested nine cantilever beams, representing half scale models of the lower story of a 20-storey ductile moment-resisting R/C office building. Herein, the specimen designated as R5 is examined. Shear span ratio was equal to 2.41. Longitudinal reinforcement consisted of 4 top and 4 bottom 19 mm bars, while volumetric ratio of transverse reinforcement was set equal to 0.31 %. Concrete strength was 31.5 MPa and yield strengths of longitudinal and transverse reinforcement were 452 MPa and 413 MPa, respectively. The specimen was subjected to a cyclic concentrated load at the free end.

Figure 13 presents lateral load vs. lateral displacement response as derived by the proposed model and as recorded experimentally. It can be seen that the analytical model reproduces sufficiently the experimental initial stiffness, lateral load capacity, and unloading stiffness. Reloading stiffness is predicted well during the early phases of inelastic response. However, as displacement demand increases, the pinching effect is underestimated leading to a small overestimation of the energy dissipation capacity of the member. It is pointed out that the displacement level at which shear failure is predicted by the analytical model correlates sufficiently well

Fig. 13 Lateral load vs. total displacement response for specimen R5 (Ma et al. [30])



with the onset of serious shear strength degradation in the experimental response ($\mu_{\Delta} \approx 4$).

Figure 14a compares shear strength predicted by Priestley’s model [15] and acting shear force as a function of the end section curvature demand. Initially, shear capacity exceeds significantly shear demand. However, due to inelastic curvature development, at the end of the analysis shear demand reaches shear capacity marking the onset of stirrup yielding. Maximum curvature demand is well predicted (experiment 0.11 rad/m and prediction 0.12 rad/m).

Figure 14b shows moment vs. fixed-end rotation hysteretic response caused by anchorage slippage as derived by the analytical model described in this study. Maximum rotation is predicted equal to 0.007 rad in both directions.

Figure 14c illustrates shear hysteretic response inside the plastic hinge region as predicted by the analytical model. It is obvious that this relationship is characterized by intense pinching effect following the hysteretic model proposed in [18]. The predicted behaviour matches adequately the experimental response with slight underestimation of the observed pinching effect [30]. Shear deformation at onset of shear failure is calculated equal to 0.043 and is in close agreement with the experimental evidence [30].

In Fig. 14c, V - γ envelope without shear-flexure interaction is also included. At the beginning, the initial envelope determines shear hysteretic response. Nevertheless, as soon as $\mu_{\varphi} > 3$, shear deformations increase more rapidly, due to interaction with flexure, and shear hysteresis separates from the initial skeleton curve. After stirrup yielding, occurring for $\gamma \approx 4 \%$, shear rigidity becomes close to zero and V - γ skeleton curve including shear-flexure interaction continues in parallel with the initial envelope.

In Fig. 14d, variation of displacement components with μ_{Δ} is presented as derived by the proposed model and experimental recordings. It can be seen that the analytical and experimental displacement patterns are in close agreement. Although shear demand after flexural yielding remains almost constant, analytically derived shear displacement increases significantly due to modelling interaction with flexure and subsequent stirrup yielding.

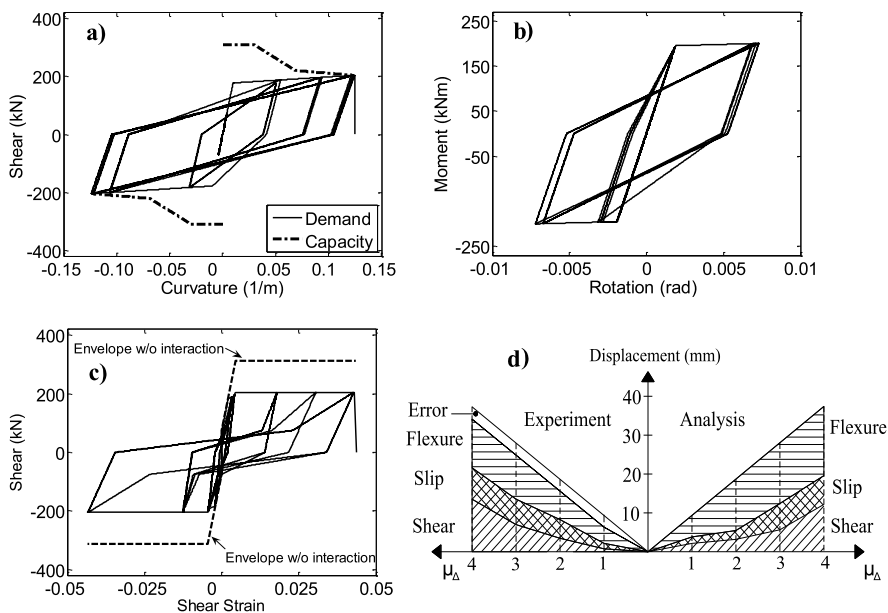


Fig. 14 (a) Shear demand and capacity as a function of the end section curvature demand. (b) Analytical $M-\theta_{slip}$ hysteresis. (c) Analytical $V-\gamma$ relationship inside the plastic hinge region. (d) Variation of member displacement components with μ_{Δ} demand as predicted by the analytical model and measured experimentally

4.2 R/C Bridge Pier Specimen HS2 by Ranzo and Priestley [31]

Ranzo and Priestley [31] tested three thin-walled circular hollow columns. Herein, the specimen designated as HS2 is examined, which was designed to fail in shear after yielding in flexure. Its outer diameter was 1524 mm and wall thickness 139 mm. The ratio of the column shear span to the section outer diameter was equal to 2.5. The normalized applied compressive axial load was 0.05. Longitudinal reinforcement ratio was 2.3 % and the volumetric ratio of transverse reinforcement 0.35 %. Concrete strength was 40 MPa and yield strengths of longitudinal and transverse reinforcement were 450 MPa and 635 MPa, respectively. Lateral actions were applied in the push and pull direction of the column for increasing levels of displacement ductility μ_{Δ} with three repeated cycles at each μ_{Δ} .

Figure 15a shows the experimental and analytical lateral load vs. total displacement response of the specimen. The analytical model captures accurately the initial stiffness, lateral strength and hysteretic response of the R/C member. More importantly, the proposed model is able to predict reasonably well the tip displacement at which onset of shear failure is developed.

This can be seen also in Fig. 15b, which compares shear strength given by Priestley's model and acting shear force as a function of the end section curvature demand. Initially, shear capacity exceeds significantly shear demand. However, due

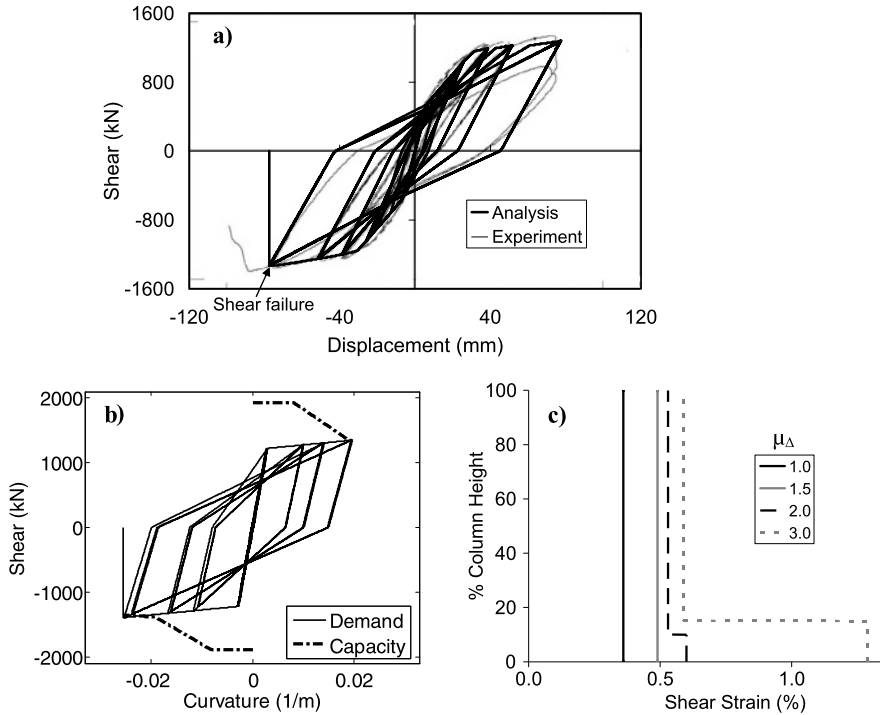


Fig. 15 Specimen HS2 (Ranzo and Priestley [31]). (a) Lateral load vs. total displacement response. (b) Shear demand and capacity as a function of the end section curvature demand. (c) Shear strain distribution for increasing displacement ductility demands

to inelastic curvature development, at the end of the analysis shear demand reaches shear capacity marking the onset of stirrup yielding. It is worth reporting that maximum curvatures predicted by the analytical model (0.019 rad/m and 0.025 rad/m in positive and negative bending respectively) correlate sufficiently with the measured ones inside the plastic hinge region (approx. 0.02 rad/m) [31].

Figure 15c illustrates shear strain distribution of the R/C column as predicted by the proposed shear sub-element for various levels of increasing μ_{Δ} . For $\mu_{\Delta} = 1.0$, shear strains remain constant along the height of the member. After $\mu_{\Delta} \geq 1.5$, a double effect is noted: First, shear strains in the inelastic zone increase more rapidly and tend to differ substantially from the ones in the intermediate part of the element due to shear-flexure interaction effect and consequent yielding of transverse reinforcement. Second, the length of the inelastic zone increases following expansion of flexural yielding towards the mid-span. By this combined effect, gradual spread of inelastic shear deformations is appropriately captured by the proposed model. At the onset of shear failure, occurring inside the plastic hinge, shear deformations are predicted equal to 0.3 % and 1.3 % outside and inside the inelastic zone, respectively. Both of these values are in good agreement with the experimental results (approx. 0.3 % and 1.2 % respectively) [31].

4.3 R/C Frame Specimen by Duong et al. [32]

This one bay, two storeys frame (Fig. 16a) was tested by Duong et al. [32] at University of Toronto. The frame was subjected to a single cycle loading. During the experiment, a lateral load was applied to the second storey beam in a displacement controlled mode, while two constant axial loads were applied to simulate the axial load effects of higher stories (Fig. 16a). During loading sequence, the two beams of the frame experienced significant shear damage (close to shear failure) following flexural yielding at their ends [32].

The finite element model applied herein for the inelastic cyclic static analysis of the frame is also shown in Fig. 16a. It consists of 4 column elements and 2 beam elements (one for each column and beam). Hence, the number of finite elements applied is minimum assuring high computational efficiency to the numerical model. The columns are supposed to be fixed at the foundation. Rigid arms are employed to model the joints of the frame.

Figures 16b, 16c compare the experimental and analytical top displacement and base shear responses obtained by the F (flexure), FB (flexure-bond) and FSB (flexure-shear-bond) finite element models. As shown in Fig. 16b, the FSB model follows closely the experimental behaviour in the whole range of response. Slight underestimation of the frame lateral stiffness takes place at the early stages of loading. This is due to the fact that pre-cracking flexural response is not modelled in this study. However, the following gradual decrease of frame stiffness is sufficiently captured by the analytical model.

At maximum displacement, the analytical model slightly overestimates load capacity (having a calculated-to-observed ratio of 1.10 in both directions). Furthermore, the analytical model predicts correctly that both beams develop shear failures after yielding in flexure.

On the other hand, the F and FB models considerably overestimate the stiffness and load carrying capacity and consequently the ability of the examined frame to dissipate hysteretic energy. For the F model, the load carrying capacity calculated-to-observed ratio is 1.30 and 1.23 in the positive and negative direction respectively. The prediction is improved with inclusion of anchorage slip effect in the FB model and the aforementioned ratio becomes 1.19 and 1.22 in the positive and negative direction.

Figure 16d presents the pushover curves obtained by the different finite element models. It can be seen that the F and FB models overestimate stiffness, load and displacement capacity. At the end of the analysis, the F and FB models overestimate load carrying capacity by 38 % and 37 % respectively. The same models overestimate displacement capacity by 52 % and 358 % accordingly. Both models erroneously predict flexural failure at the base of the frame.

The FSB model predicts correctly that shear failure is developed after yielding in flexure. However, inclusion of shear-flexure interaction effect and degradation of shear strength with curvature ductility demand affects grossly the displacement capacity predicted by this analytical model. When shear-flexure interaction is considered, ultimate displacement capacity is found 46 mm which is very close to the

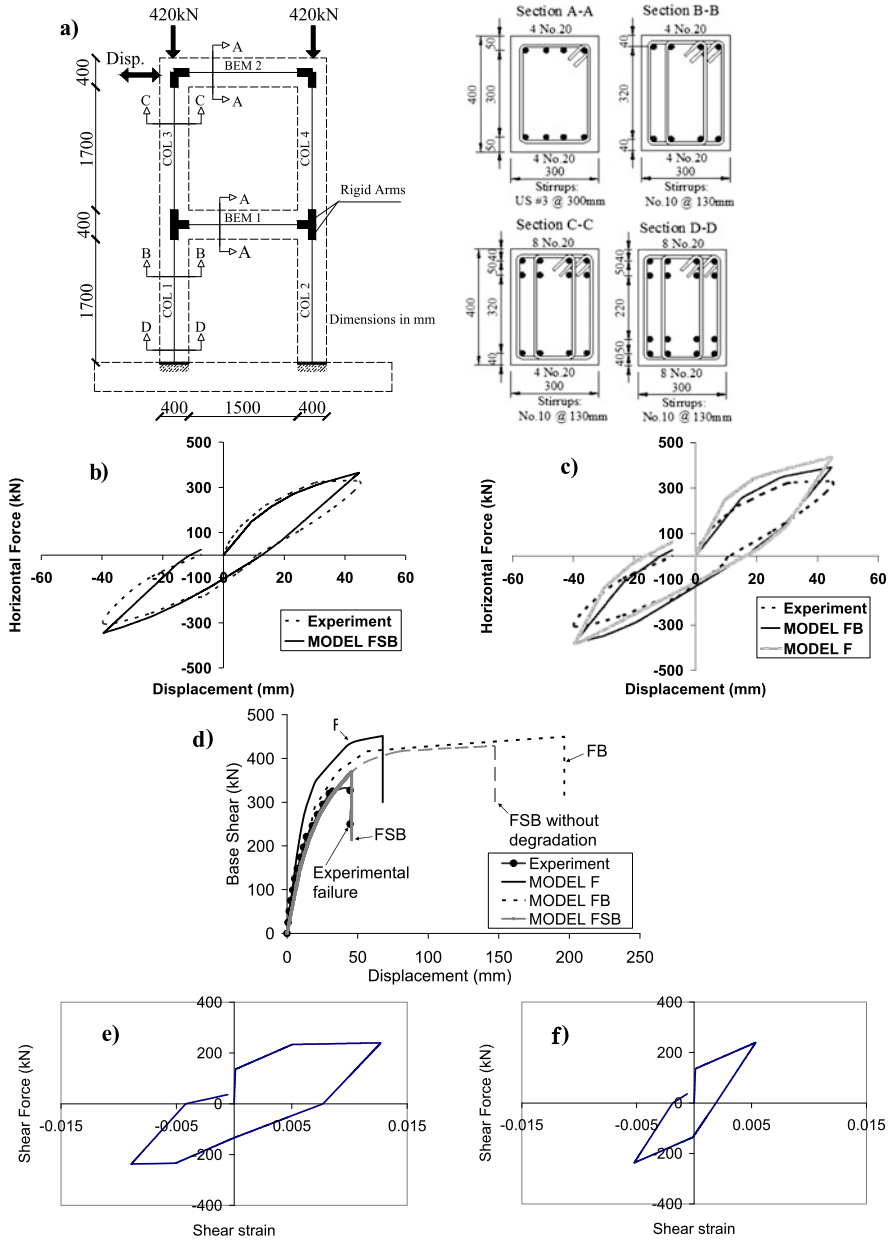


Fig. 16 (a) Duong et al. [32] frame specimen layout and applied finite element model. (b) Base shear vs. top displacement prediction by FSB model. (c) Base shear vs. top displacement predictions by F and FB models. (d) Pushover curves from different finite element models. (e) First storey beam $V-\gamma$ response inside plastic hinges. (f) First storey beam $V-\gamma$ response outside plastic hinges

44.7 mm recorded experimentally. On the other hand, if shear-flexure interaction is ignored, displacement capacity is overestimated by 228 %.

Finally, Figs. 16e and 16f present shear force-shear strain hysteresis predicted by the FSB analytical model inside and outside the plastic hinge regions for the 1st storey beam of the frame under cyclic loading. It can be seen that, due to shear-flexure interaction effect and consequent stirrup yielding, shear strains are predicted significantly higher inside than outside plastic hinges (1.26 % instead of 0.53 %), while shear force remains uniform along this RC member.

4.4 R/C Frame Specimen by Elwood and Moehle [6]

This half-scale frame specimen was constructed and tested on the shaking table at the University of California, Berkeley [6]. It comprised three columns interconnected at the top by a 1.5 m wide beam and supported at the bottom on footings (Fig. 17a). The columns supported a total mass of 31 t.

The central column was constructed with light transverse reinforcement having 90° hooks. The outside columns were detailed with closely spaced spiral reinforcement to ensure ductile response and to provide support for gravity loads after shear failure of the central column.

The specimen was subjected to one horizontal component of the ground motion recorded at Viña del Mar during the 1985 Chile earthquake (SE32 component). The normalized central column axial load was 0.10. During testing, the central column experienced a loss of lateral load capacity, due to apparent shear failure at its top, during a negative displacement cycle at approximately 17.6 sec [6].

The finite element model applied herein for the inelastic time history analysis of the frame is shown in Fig. 17a. It consists of 3 column elements and 2 beam elements (one for each member). Hence, the number of finite elements required is minimum assuring minimum computational cost.

The columns are supposed to be fixed at the foundation. Rigid arms are employed to model the joints of the frame. Rayleigh model is used for viscous damping. The equivalent viscous damping is set equal to 2 % of the critical damping for the fundamental vibration mode. The mass is assumed lumped at the top of the frame. In the following, for the calculation of the central column shear strength, the contribution of the stirrups is reduced by half to take into account their inadequate anchorage (90° hooks).

Figures 17b, 17c compare the experimental and the analytical top displacement time histories between $t = 10$ sec and onset of shear failure as predicted by the FSB and F analytical models respectively. The first 10 seconds are omitted so that the critical duration of response can be more clearly observed [6]. It is evident that the FSB analytical model predicts closely the experimental response up to onset of shear failure of the central column. On the other hand, when only flexural deformations are considered (which is the typical case for conventional inelastic analyses of R/C structures) the analysis is driven to severely erroneous results.

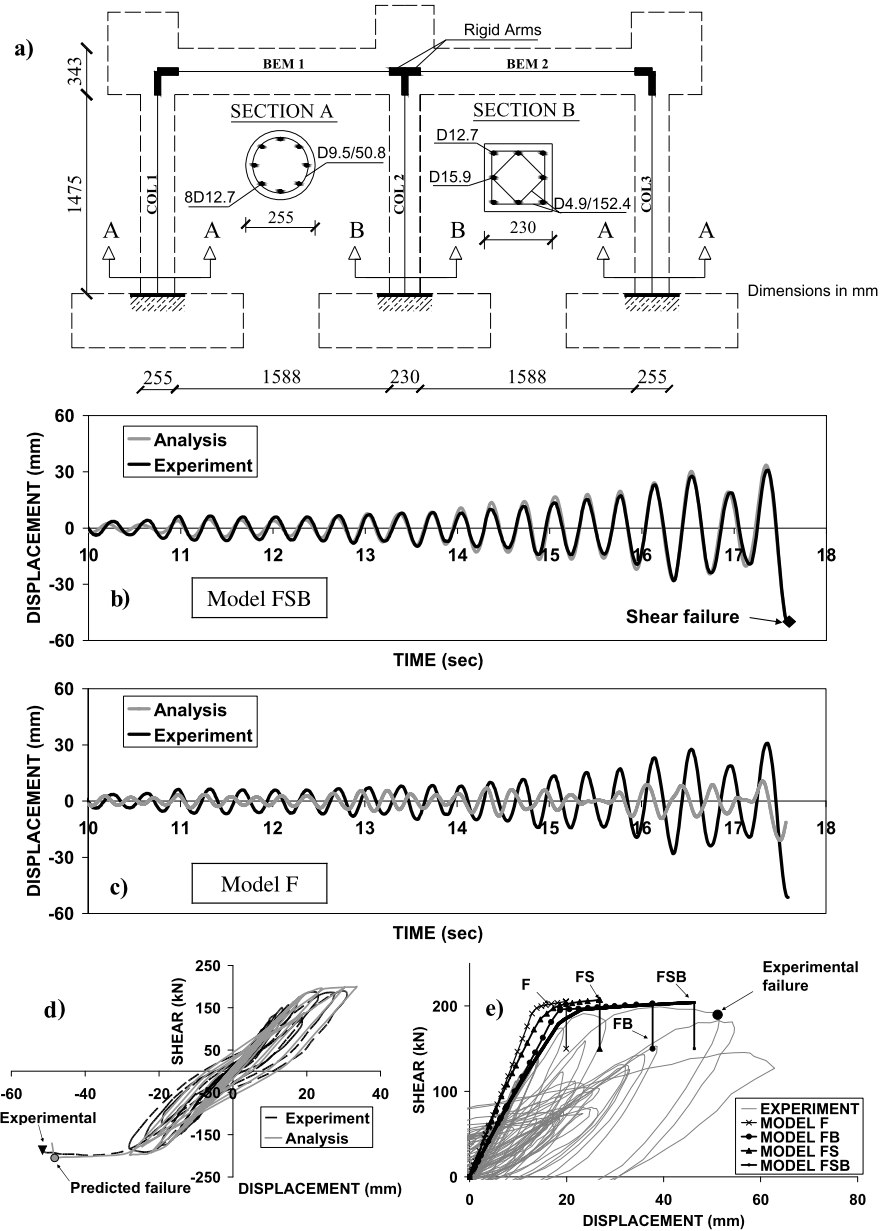


Fig. 17 (a) Elwood and Moehle [6] frame specimen layout and applied finite element model. (b) Displacement time history predicted by FSB model. (c) Displacement time history predicted by F model. (d) Frame hysteresis predicted by FSB model. (e) Pushover curves from F, FB, FS and FSB finite element models and comparison with the experimental response

In addition, Fig. 17d presents the comparison between the experimental and analytical frame hysteresis up to onset of shear failure as predicted by the FSB model. It is apparent that the model captures satisfactorily initial frame stiffness, maximum shear capacity and displacement corresponding to onset of shear failure.

Finally, Fig. 17e compares the pushover curves obtained by the four different versions of the beam-column model and the experimental response. The comparison is shown in the negative displacement direction because in this direction shear failure was detected.

The F model significantly overestimates initial frame stiffness and underestimates displacement at failure. In particular, this model predicts erroneously flexural failure at the base of the central column at a 20 mm lateral displacement.

The FS model predicts correctly the development of shear failure at the top of central column. However, it overestimates initial lateral stiffness and underestimates displacement capacity at onset of shear failure (27 mm instead of 51 mm).

The FB model provides better estimations than the two previous models. However, it overestimates frame stiffness after base shear exceeds 150 kN (onset of shear cracking) and underestimates considerably displacement at onset of lateral failure (37 mm instead of 51 mm). Moreover, a flexural failure at the base of the central column is falsely predicted.

The best estimations are provided by the FSB model which incorporates all types of deformations and represents the proposal of this study. Envelope stiffness is closely captured until maximum response. Additionally, this model predicts correctly a shear failure at the top of the central column at a 47 mm displacement, which is quite close to the experimental value.

4.5 R/C Frame Specimen by El-Attar et al. [33]

A 1/6 scale 2-storey one-bay by one-bay reinforced concrete building (Fig. 18) was tested at the Cornell University [33]. The structure was designed solely for gravity loads, without regard to any kind of lateral loads. Model structure concrete strength was 32.3 MPa and steel reinforcement yield capacity 414 MPa.

The model structure was tested using the time-scaled Taft 1952 S69E earthquake with peak ground acceleration set in increasingly higher values. After running Taft 0.45g, wide, deep cracks were observed in the beams around the locations of discontinuous positive beam reinforcement (at the joint panels), indicating bond failure and pending pullout of these bars [33].

Figure 19 compares frame response histories derived by the FSB analytical model and experimental recordings for the 0.36g peak ground acceleration. It is evident that the proposed model follows closely the experimental response after the first 1.5 sec. Small differentiations are justifiable considering the large scale (1/6) of the examined specimen.

The FSB analytical model predicts the anchorage failure of the positive reinforcement at the left end of the first storey beam for the 0.45g Taft earthquake motion. This is clear from Fig. 20 presenting hysteretic $M-\varphi$ and $M-\theta_{slip}$ responses of

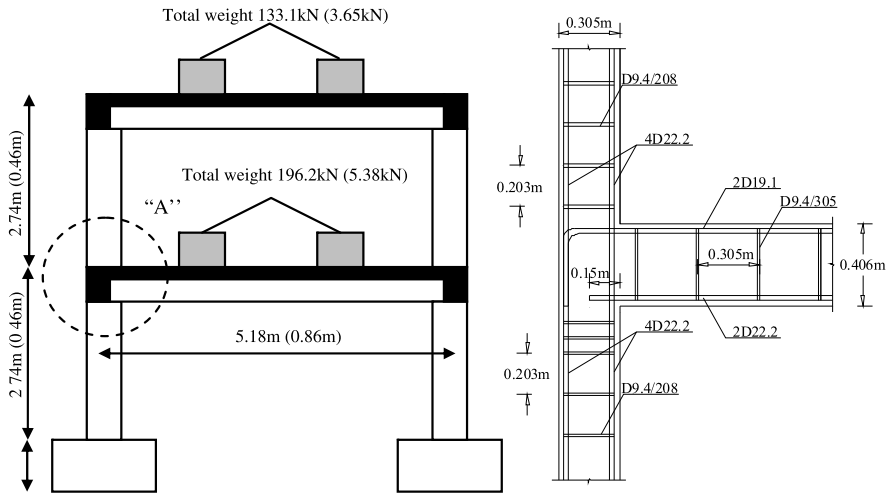


Fig. 18 El-Attar et al. [33] frame specimen configuration (values outside and inside parentheses correspond to prototype and model structure respectively)

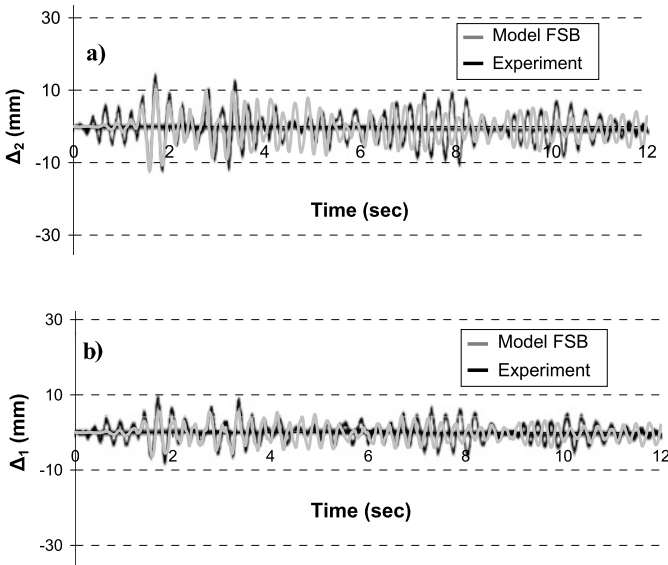


Fig. 19 Comparison of El-Attar et al. [33] frame specimen time history responses from the experimental recordings and analytical model FSB for Taft 0.36g acceleration record. (a) 2nd storey total displacement. (b) 1st storey total displacement

this end. It can be seen that while flexural response remains at the reloading stage, $M-\theta_{slip}$ first follows the reloading branch, moves on to the positive envelope curve and finally drives to failure, exceeding bottom anchorage moment capacity.

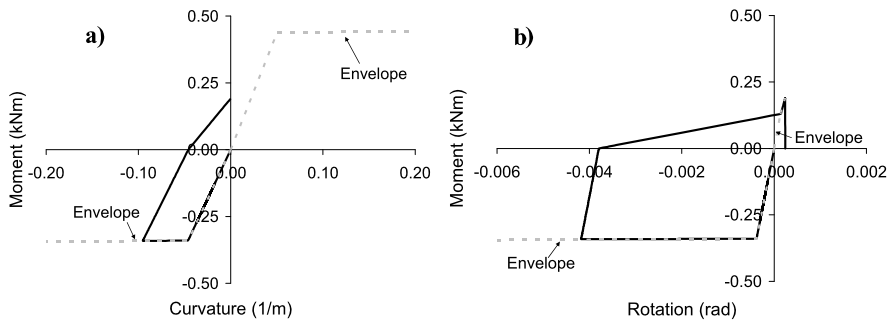


Fig. 20 Hysteretic responses of left end of the 1st storey beam of the El-Attar et al. [33] frame specimen predicted by the FSB analytical model for the 0.45g Taft acceleration record. (a) $M-\varphi$. (b) $M-\theta_{slip}$

5 Conclusions

A new beam-column model is introduced for seismic damage analysis of R/C frame structures with substandard detailing. This finite element models inelastic flexural, shear, and anchorage slip deformations, as well as their interaction, in an explicit manner. Hence, it is capable of simulating with accuracy the seismic response of R/C frames with inadequate detailing, where shear flexibility and fixed end rotations caused by anchorage slip usually play a vital role in their response. Additionally, it is able to predict, in the general case, brittle types of failure that cannot be precluded in structures, which do not conform to modern seismic guidelines. The numerical model is implemented in a general finite element code and it is validated against experimental results from well-documented column and frame specimens with brittle detailing. It is concluded that the proposed model provides accurate and reliable predictions of the frame specimen responses.

References

1. Mergos PE, Kappos AJ (2010) Seismic damage analysis including inelastic shear-flexure interaction. *Bull Earthq Eng* 8:27–46
2. CEN (Comité Européen de Normalisation) Eurocode 8 (2005) Design provisions of structures for earthquake resistance—part 3: Assessment and retrofitting of buildings (EN1998-3). Brussels
3. Pincheira J, Dotiwala F, Souza J (1999) Seismic analysis of older reinforced concrete columns. *Earthq Spectra* 15:245–272
4. Consenza E, Manfredi G, Verderame GM (2002) Seismic assessment of gravity load designed R/C frames: critical issues in structural modelling. *J Earthq Eng* 6:101–122
5. Yalcin C, Saatcioglu M (2000) Inelastic analysis of reinforced concrete columns. *Comput Struct* 77:539–555
6. Elwood K, Moehle J (2008) Dynamic collapse analysis for a reinforced concrete frame sustaining shear and axial failures. *Earthq Eng Struct Dyn* 37:991–1012

7. Sezen H, Chowdhury T (2009) Hysteretic model for reinforced concrete columns including the effect of shear and axial load failure. *J Struct Eng* 135:139–146
8. Mergos PE, Kappos AJ (2008) A distributed shear and flexural flexibility model with shear-flexure interaction for R/C members subjected to seismic loading. *Earthq Eng Struct Dyn* 37:1349–1370
9. Mergos PE, Kappos AJ (2009) Modelling gradual spread of inelastic flexural, shear and bond-slip deformations and their interaction in plastic hinge regions of R/C members. In: *Proceedings of the 2nd COMPDYN conference*, Rhodes
10. Mergos PE, Kappos AJ (2011) Seismic damage analysis of RC structures with substandard detailing. In: *Proceedings of the 3rd COMPDYN conference*, Corfu
11. Mergos PE, Kappos AJ (2012) A gradual spread inelasticity model for R/C beam-columns accounting for flexure, shear and anchorage slip. *Eng Struct* 44:94–106
12. Sivaselvan MV, Reinhorn AM (1999) Hysteretic model for cyclic behaviour of deteriorating inelastic structures. Report MCEER-99-0018, University at Buffalo, State University of New York
13. Soleimani D, Popov EP, Bertero VV (1979) Nonlinear beam model for R/C frame analysis. In: *Proceedings of 7th conference on electronic computation*, St. Louis
14. Sezen H, Moehle JP (2004) Shear strength model for lightly reinforced concrete columns. *J Struct Eng* 130:1692–1703
15. Priestley MJN, Seible F, Verma R, Xiao Y (1993) Seismic shear strength of reinforced concrete columns. Report SSRP-93/06, University of San Diego, California
16. Biskinis D, Roupakias G, Fardis MN (2004) Degradation of shear strength of R/C members with inelastic cyclic displacements. *ACI Struct J* 101:773–783
17. Oesterle RG, Fiorato AE, Aristizabal-Ochoa JD (1980) Hysteretic response of reinforced concrete structural walls. In: *Proceedings of ACISP-63: Reinforced concrete structures subjected to wind and earthquake forces*, Detroit
18. Ozcebe G, Saatcioglu M (1989) Hysteretic shear model for reinforced concrete members. *J Struct Eng* 115:132–148
19. Park R, Paulay T (1975) *Reinforced concrete structures*. Wiley, New York
20. Alsiwat JM, Saatcioglu M (1992) Reinforcement anchorage slip under monotonic loading. *J Struct Eng* 118:2421–2438
21. ACI Committee 408 (2003) Bond and development of straight reinforcement in tension. American Concrete Institute, Farmington Hills
22. CEB-FIP Model Code (1990) Model code for seismic design of concrete structures. Lausanne
23. Park R, Sampson RA (1972) Ductility of reinforced concrete column sections in seismic design. *ACI Struct J* 69:543–551
24. Soroushian P, Kienyuwa O, Nagi M, Rojas M (1988) Pullout behaviour of hooked bars in exterior beam-column connections. *ACI Struct J* 85:269–276
25. Saatcioglu M, Alsiwat JM, Ozcebe G (1992) Hysteretic behaviour of anchorage slip in R/C members. *J Struct Eng* 118:2439–2458
26. Newmark NM (1959) A method of computation for structural dynamics. *J Eng Mech Div* 89:67–94
27. Kanaan AE, Powel GH (1973) DRAIN-2D: a general purpose computer program for dynamic analysis of inelastic plane structures. Report EERC-73/06 and 73/22, University of California Berkeley
28. Golafshani AA (1982) DRAIN-2D2: a program for inelastic seismic response of structures. PhD dissertation, Department of Civil Engineering, University of California Berkeley
29. Reinhorn AM, Roh H, Sivaselvan M et al (2009) IDARC2D version 7.0: a program for the inelastic damage analysis of buildings. Report MCEER-09-0006, University at Buffalo, State University of New York
30. Ma SM, Bertero VV, Popov EP (1976) Experimental and analytical studies on hysteretic behaviour of R/C rectangular and T-beams. Report EERC 76-2, University of California Berkeley

31. Ranzo G, Priestley MJN (2001) Seismic performance of circular hollow columns subjected to high shear. Report SSRP-2001/01, University of California San Diego
32. Duong KV, Sheikh SA, Vecchio FJ (2007) Seismic behaviour of shear critical reinforced concrete frame: experimental investigation. *ACI Struct J* 104:304–313
33. El-Attar AG, White RN, Gergely P (1997) Behaviour of gravity load designed R/C buildings subjected to earthquakes. *ACI Struct J* 94:1–13

Seismic Evaluation of Existing Basement Walls

Mahdi Taiebat, W.D. Liam Finn, Alireza Ahmadnia, Elnaz Amirzehni,
and Carlos E. Ventura

Abstract Current state of practice for seismic design of basement walls is using the Mononobe-Okabe (M-O) method that is based on the Peak Ground Acceleration (PGA). The National Building Code of Canada (NBCC) has considerably changed the seismic hazard level from 10 % in 50 years in NBCC1995 to 2 % in 50 years in NBCC2010, which leads to doubling the PGA in Vancouver from 0.24g to 0.46g. The current design PGA leads to very large seismic forces that make the resulting basement walls very expensive. Because there is a little evidence of any significant damage to basement walls during major earthquakes, the Structural Engineers Association of British Columbia (SEABC) initiated a task force to review current seismic design procedures for deep basement walls. Presented in this paper are some preliminary results of the work conducted by this committee. A series of dynamic numerical analyses have been carried out on a typical basement wall designed using the M-O earth pressures with the NBCC1995 PGA for Vancouver. This wall is then subjected to three ground motions spectrally matched to the Uniform Hazard Spectrum prescribed by the NBCC2010 and the seismic performance of the wall under this level of demand has been presented and discussed. Particular attention has been given to the resulting drift ratio in the walls.

Keywords Basement wall · Seismic design · Dynamic analysis · Performance · Lateral earth pressure

1 Introduction

Basement walls constitute an integral part of tall buildings. These walls should be designed to resist the static and seismic induced lateral earth pressures. Current state of practice for design of basement walls is based on the Mononobe-Okabe (M-O) method. In this limit-equilibrium force method, the earthquake thrust acting on the wall is a function of the Peak Ground Acceleration (PGA). The seismic hazard level

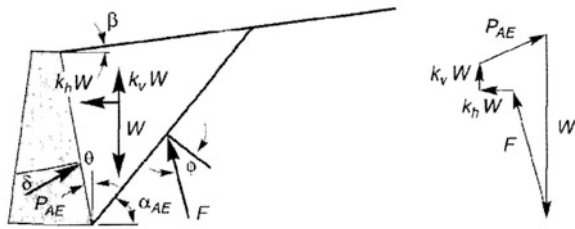
M. Taiebat (✉) · W.D. Liam Finn · A. Ahmadnia · E. Amirzehni · C.E. Ventura
Department of Civil Engineering, University of British Columbia, Vancouver, BC, Canada
e-mail: mtaiebat@civil.ubc.ca

in the 1995 edition of the National Building Code of Canada (NBCC) [1] for design of buildings had a probability of exceedance of 10 % in 50 years. The related PGA hazard under NBCC1995 is 0.24g for Vancouver area. The 2010 edition of the National Building Code of Canada [2] mandates a considerably higher seismic hazard level for design of buildings that is probability of exceedance of 2 % in 50 years. Under this hazard level, the related design PGA for Vancouver is about 0.46g that is almost doubled from the one in NBCC1995. The current design PGA leads to very large seismic forces that make the resulting basement walls very expensive. Because there is a little evidence of any significant damage to basement walls during major earthquakes, the Structural Engineers Association of British Columbia (SEABC) initiated a task force to review current seismic design procedures for deep basement walls. The authors are members of this task force committee and have carried out series of dynamic numerical analyses, using computer program FLAC [3], that take into account the flexibility and potential yielding of the wall components, as an effective procedure to study the lateral earth pressures against basement walls. To this end, a specific basement wall has been designed by the structural engineers using the current state of practice, which is based on the M-O earth pressures using the NBCC1995 PGA for Vancouver (seismic event in Vancouver with 10 % probability of exceedance in 50 years). This basement wall has then been numerically analyzed to evaluate its performance under three seismic events with 2 % probability of occurrence in 50 years for Vancouver, a higher seismic demand enforced by the NBCC2010. The seismic performance of the basement wall under this level of demand has been presented and discussed in this paper. Particular attention has been given to the resulting drift ratio in the walls. In addition, the dynamic analysis results are compared to the standard methods of determining lateral earth pressures on the wall. The results to date indicate that flexibility of the walls has important effects on the distribution of the seismic lateral pressures on the walls. This paper outlines a part of the findings in this study.

2 Background

The seismic response of retaining walls is a complex soil structure interaction problem that depends on many different factors such as the nature of the input motion, dynamic response of the backfill soil, and the flexural response of the wall. The current state of the art in engineering practice [4] is based on the studies of Okabe [5] and Mononobe and Matsuo [6] and is generally known as Mononobe-Okabe method. The M-O method is a limit-equilibrium force approach, developed by modification of Coulomb's theory for active (or passive) pressures. In this method, it is assumed that a rigid wall moves sufficiently to produce minimum active (or maximum passive) pressures. The M-O method accounts for the vertical and horizontal coefficients of acceleration induced by an earthquake. It is assumed that the soil behind the wall behaves as a rigid body so the pseudo-static acceleration can be applied uniformly throughout the mass. Therefore, in addition to the forces that exist under static conditions, the wedge is also acted upon by horizontal and vertical

Fig. 1 Forces acting on active wedge in Mononobe-Okabe analysis and force polygon illustrating equilibrium forces acting on active wedge [7]



pseudo-static forces whose magnitudes are related to the mass of the wedge by the pseudo-static accelerations $a_h = k_h g$ and $a_v = k_v g$. The forces acting on an active wedge in a dry, cohesionless backfill are shown in Fig. 1.

With the applied pseudo-static accelerations to a Coulomb active (or passive) wedge, the pseudo-static soil thrust is then obtained from force equilibrium of the wedge. The total active lateral force during earthquake, P_{AE} is expressed as

$$P_{AE} = 0.5\gamma H^2 K_{AE}(1 - k_v) \tag{1}$$

where γ is the soil density, H is the retaining wall height, and the dynamic active earth pressure coefficient, K_{AE} , is given by

$$K_{AE} = \frac{\cos^2(\phi - \theta - \psi)}{\cos^2 \theta \cos \psi \cos(\delta + \theta + \psi) \left[1 + \sqrt{\frac{\sin(\delta + \phi) \sin(\phi - \beta - \psi)}{\cos(\delta + \theta + \psi) \cos(\beta - \theta)}} \right]^2} \tag{2}$$

with ϕ and δ representing the angle of internal friction for the backfill soil and the angle of interface friction between the wall and the soil, respectively, and $\psi = \arctan[k_h/(1 - k_v)]$ with the limitation of $\phi - \beta \geq \psi$. By setting the pseudo-static accelerations to zero, Eqs. (1) and (2) will give the Coulomb static active lateral force, P_A , and the static active earth coefficient, K_A , respectively.

The M-O method only provides the total lateral force during earthquake, P_{AE} . It does not explicitly indicate anything about the distribution of lateral earth pressure from seismic events. Several studies have been conducted for investigating the distribution of the lateral earth pressures and the point of application of the resultant lateral forces, depending on the mode of deformation of the wall [8–11]. Although the Coulomb method implies that the active lateral force under static loading condition should act at a height $H/3$ above the base of the wall, experimental results suggest that it actually acts at a higher point under dynamic loading conditions.

For practical purposes, Seed and Whitman [9] proposed to separate the total (static and dynamic) active lateral force, P_{AE} , into two components; the initial static component, P_A , and the dynamic increment due to the base motion, ΔP_{AE} .

$$P_{AE} = P_A + \Delta P_{AE} \tag{3}$$

The static component of force is known to act at $H/3$ above the base of the wall with the corresponding pressure distributed linearly along the wall height as a triangle with zero pressure at the surface and a pressure equivalent to $\gamma H K_A$ at the base. As Seed and Whitman [9] stated most of the investigators agree that the increases in lateral pressure due to the base excitation are greater near the top of the wall and the

resultant interment in force acts at a height varying from $H/2$ to $2H/3$ above the base of the wall. The state of practice for design of retaining walls in Vancouver is to apply the ΔP_{AE} at height $2H/3$ above the base of the wall with the corresponding pressure distributed linearly along the wall height as an inverse triangle with zero pressure at the base of the wall and a pressure equivalent to $\gamma H(K_{AE} - K_A)$ at the ground surface. On this basis, the total active thrust will act at a height h above the base of the wall.

$$h = \frac{P_A(H/3) + \Delta P_{AE}(2H/3)}{P_{AE}} \quad (4)$$

The value of h depends on the relative magnitudes of P_A and P_{AE} and it often ends up near the mid-height of the wall.

It is important to note that the limit equilibrium-based Coulomb and M-O methods were originally developed for rigid retaining walls with sufficient rigid body displacements to mobilize the active wedge in the backfill soil. Basement walls, on the other hand, have variable degrees of flexibility and deformation at different depths. The M-O method also assumes that the movement of wall will be sufficient to produce minimum active pressure. It also assumes that the soil behind the wall acts as a rigid body and does not account for flexibility of the soil-structure system. Finally, the M-O analyses show that k_v , when taken as one-half to two-thirds the value of k_h affects P_{AE} by less than 10 %. Seed and Whitman also state in their state-of-the-art paper [9] that for most earthquakes, “. . . the horizontal acceleration components are considerably greater than the vertical acceleration components. . .”. Thus they concluded that k_v could be neglected for practical purposes. The reason for neglecting vertical loading as stated in NCHRP [4] report is generally attributed to the fact that the higher frequency vertical accelerations will be out of phase with the horizontal accelerations and will have positive and negative contributions to wall pressures, which on average can reasonably be neglected for design.

The current state of practice for design of basement walls is using the Coulomb theory and the M-O method for finding the static and total lateral thrusts, P_A and P_{AE} . It is also the current state of practice to use the PGA as the horizontal pseudo-static acceleration and zero for the vertical one for application of the M-O method in the basement wall problems. For convenience the M-O designation in this paper refers to the above mentioned procedure (including the distribution of pressures) that is an extension of the M-O method for use in practice. The wall that is analyzed in the next section has been designed based on the lateral earth pressures obtained from the M-O method.

3 Properties of the Wall

A basement wall was designed by structural engineers from SEABC specifically for this study based on the current state of practice using earth pressure derived from the pseudo-static M-O method. The PGA value of 0.24g, which corresponds to the probability of exceedance of 10 % in 50 years (NBCC1995), was used to design

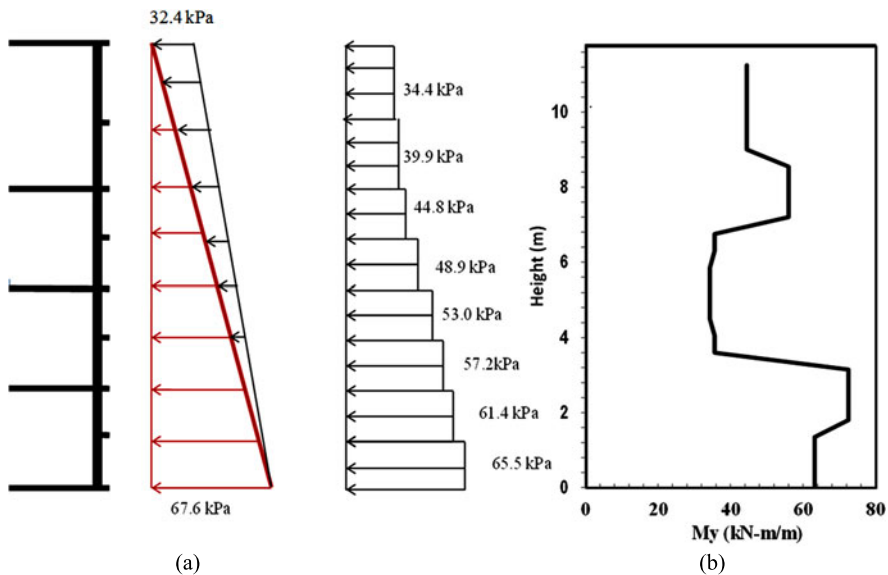


Fig. 2 (a) Distribution of the design lateral pressure along the height of the wall based on the current state of practice for a seismic hazard level of $PGA = 0.24g$ and a backfill soil with friction angle of 33° ; (b) Resulting distribution of moment resistance along the height of the wall

of this wall. The lateral earth pressure distributions (including static and seismic components) for this wall are shown in Fig. 2(a). The maximum of these total pressures or 1.5 times the static active pressures are used to find the design moments at each depth of the wall and then the wall was designed by the structural engineer for these moments in the usual manner using factored resistances of $0.85 f_y$ and $0.65 f'_c$ for steel and concrete, where f_y and f'_c are the corresponding nominal yield strengths. Finally approximately 1.3 times of the above mentioned design moments were used as the moment capacity (real member’s strength) profile along the height of the wall for evaluating the response of the wall to a suite of three ground motions, as explained in the next sections. The profile of the moment capacity along the height of this wall is shown in Fig. 1(b). Uniform properties of Moment of Inertia, $I = 0.0013 \text{ m}^4/\text{m}$, cross-section area, $A = 0.25 \text{ m}^2/\text{m}$, and Young’s modulus, $E = 2.74 \times 10^7 \text{ kN/m}^2$ are considered along the height of the basement wall.

4 Description of the Model

4.1 Model Building

Non-linear seismic response of the basement wall is analyzed by using the two-dimensional finite difference computer program FLAC. Different stages of the mod-

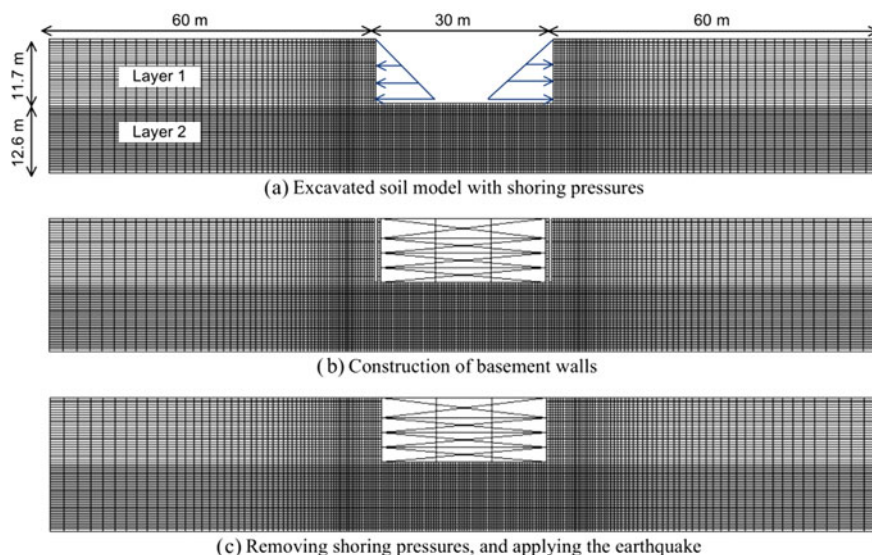


Fig. 3 Different stages of modeling procedure in FLAC

eling procedure are presented in Fig. 3. In order to ensure the proper initial stress distribution on the basement the actual construction sequence is modeled.

First, a 24.3 m deep and 150 m wide layer of soil is created and brought to equilibrium under gravity forces. The model consists of two soil layers that will be discussed further in the next section. A part of the upper soil layer is then excavated in lifts to a depth of 11.7 m and a width 30 m as shown in Fig. 3(a). As each lift was excavated, lateral pressures (shoring) are applied to retain the soil. Then as depicted in Fig. 3(b) the basement wall is constructed, the interface on the sides of the building are added, a quiet boundary is created at the base of the model and global equilibrium is re-established.

In the next stage, as shown in Fig. 3(c), the shoring pressures are removed, and load from the soil is transferred to the basement wall. The flexural behavior of the wall is modeled by an elastic-perfectly plastic beam model with yield moment equal to the corresponding moment resistance values as shown in Fig. 2(b). The connection between the structural nodes and soil grid nodes has been modeled using an interface element with an angle of friction equal to the angle of internal friction for the backfill soil ($\delta = \phi = 33^\circ$).

4.2 Properties of Soil

The response of the soil is modeled by a Mohr-Coulomb elastic, perfectly plastic constitutive model. The required model parameters are elastic shear modulus, Poisson's ratio, cohesion, and friction and dilation angles of soil. The properties used in

Table 1 Properties of the soil profile

Soil layer	Density (kg/m ³)	V_{s1} (m/s)	G_{eq}/G_{max}	Poisson's ratio	Cohesion (kPa)	Friction angle (degrees)	Dilation angle (degrees)
1	1950	200	0.3	0.28	0	33	0
2	1950	400	0.3	0.28	20	40	0

conjunction with the Mohr-Coulomb model for layers 1 and 2 of soil, as depicted in Fig. 3, are presented in Table 1.

By using the simple elastic-perfectly plastic Mohr-Coulomb material model for the soil response in seismic analysis, it is necessary to incorporate some additional damping to account for the equivalent energy dissipation during the elastic part of the cyclic loading. This damping is also required for the numerical stability of the dynamic system during the elastic part of the cyclic loading.

In order to estimate the required damping ratio and modulus reduction to represent the inelastic cyclic behavior of soils during the seismic events a set of site response analyses on an equivalent system to the free field of this problem is carried out using the equivalent-linear program SHAKE [12, 13]. In particular, a number of analyses were conducted using a suite of ground motions that matched the NBCC2010 design spectrum for Vancouver to determine effective moduli and damping of the soil layers needed for the FLAC analyses. The lower-bound modulus reduction curve and damping curve proposed by Seed et al. [14] for sands are used as shear modulus reduction curve and a damping ratio curve in SHAKE simulations. In these analyses, the maximum elastic shear modulus, G_{max} , is assumed to change with depth using the relation proposed by Robertson et al. [15] using constant stress corrected shear wave velocity of V_{s1} of 200 m/s in both soil layers.

The SHAKE analyses led to an average damping ratio of 5 % and an average shear modulus reduction factor of 0.3 ($G_{eq} = 0.3G_{max}$) for the soil layers. The shear modulus reduction factor has been used to calculate the required shear modulus for the Mohr-Coulomb model used in the FLAC analyses. In addition, a Rayleigh damping ratio of 5 % is also used in the dynamic analyses.

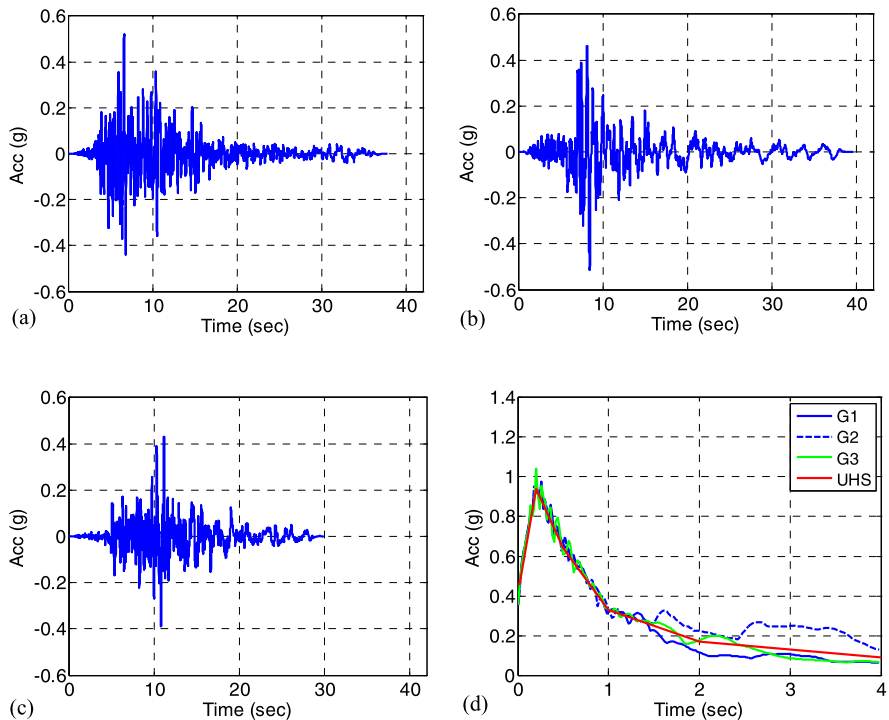
4.3 Ground Motions

Ground motions were selected from the Pacific Earthquake Engineering Research (PEER) strong ground motion database [16]. Based on the results of de-aggregation of the NBCC Uniform Hazard Spectrum (UHS) and site class C for Vancouver, candidate input motions are selected in the magnitude range $M = 6.5-7.5$ and the distance range 10–30 km using the program Design Ground Motion Library, DGML [17].

Table 2 shows the list of three ground motions selected for this study. The selected ground motions are linearly scaled to match UHS using the computer program

Table 2 List of selected ground motions

Ground motion	NGA #	Event	Year	Station	Magnitude
G1	162	Imperial Valley	1979	Calexico Fire	6.53
G2	778	Loma Prieta	1989	Hollister	6.93
G3	987	Northridge	1994	LA-Centinel	6.69

**Fig. 4** Time histories of acceleration (a–c) and response spectra (d) of ground motions G1–G3 spectrally matched to UHS in periods 0.02–1.7 sec

DGML and then spectrally matched to UHS in the period range of 0.02–1.7 sec using computer program SeismoMatch [18].

The UHS of Vancouver for a 2 % probability of exceedance in 50 years is employed as the target spectrum in this study. A very close match was achieved as shown in Fig. 4(d). Time histories of the spectrally matched motions are also shown in Figs. 4(a, b, c).

At a quiet boundary, an acceleration time history cannot be input directly because the boundary must be able to move freely to absorb incoming waves. Instead, the acceleration-time history is transformed into a stress-time history for input. For this purpose, first, the acceleration time histories are integrated to obtain velocity time

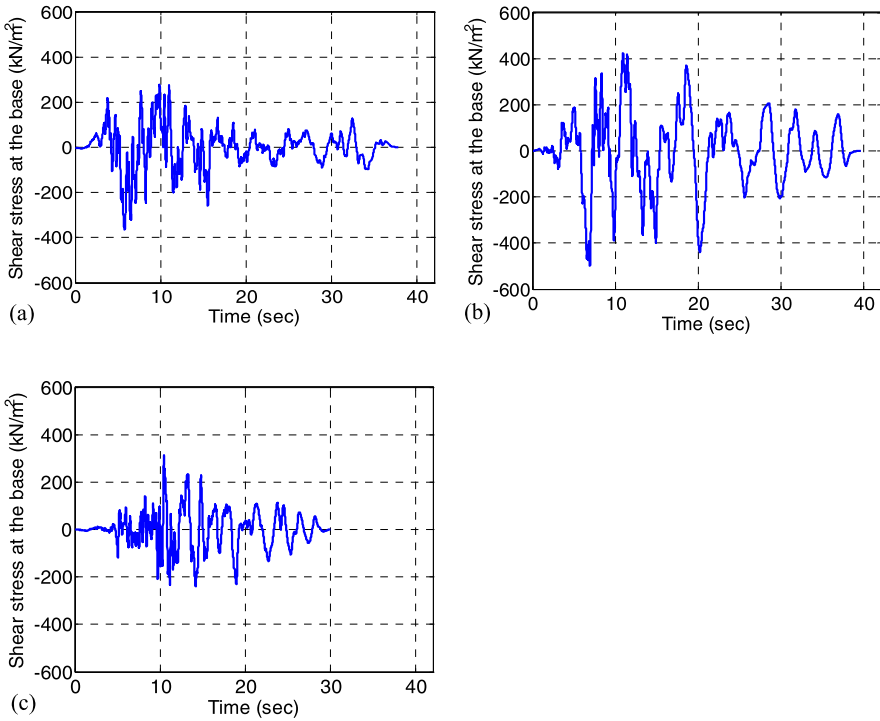


Fig. 5 Time histories of shear stress applied at the base of the model for ground motions G1–G3

histories and then the proportionality of stress to velocity in an elastic wave is used to convert the velocity to stress. The obtained stress time histories, which were applied at the base of the model, are illustrated in Fig. 5.

5 Result of Analysis

FLAC analyses were conducted to evaluate the seismic response of the basement wall. The important seismic response parameters are: (a) the magnitude and distribution of lateral earth pressures, (b) the resultant lateral force on the wall and its point of application, (c) envelopes of bending moment and shear and (d) wall deflection envelope, residual deflections, and drift ratio envelopes.

Figure 6 shows the time histories of lateral earth pressure at two different levels (L_1 and L_2) along the height of the basement wall due to the earthquake G1. As expected, the initial and final (static) lateral stresses increase by depth. At both of these levels the initial static lateral pressures (before the earthquake) is lower than the residual static lateral pressures (after the earthquake). In addition, during the seismic loading the lateral pressures in each level gradually increase from their initial values to their higher final values. The trend of this increase is slightly different

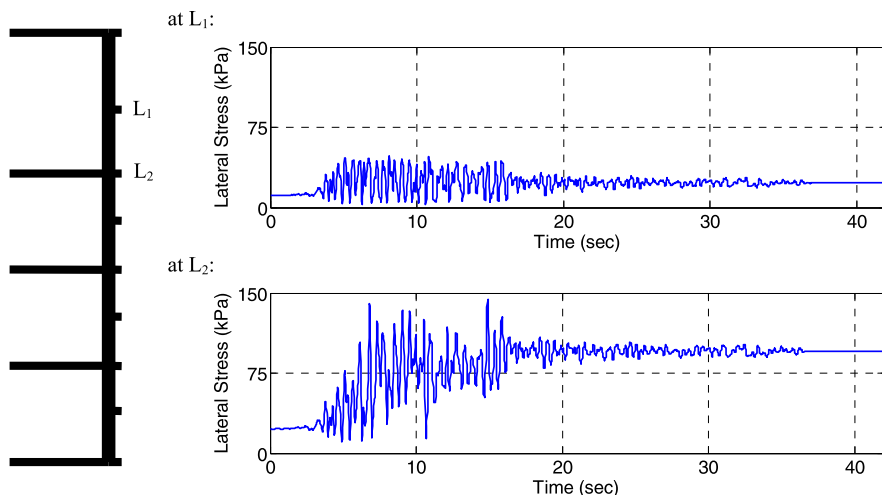


Fig. 6 Numerical results of the lateral earth pressure time histories at different locations (L_1 – L_3) along the wall under ground motion G1

for these two locations. In particular, more seismic lateral pressure is absorbed at L_2 , that is at a floor slab level with larger lateral support from the structure, than the one at L_1 which is at the mid height of the floor levels where the wall is not directly supported by the slabs.

Figure 7 shows the time histories of the resultant lateral earth force and the distance of its center of application from the base of the wall normalized with respect to the wall height (H) for three earthquakes. These figures also show the peak M-O force for a PGA of 0.46g and 0.24g, which corresponds to NBCC2010 and NBCC1995 respectively, as a baseline for comparison. Many existing walls have been designed for the hazard level of NBCC1995 and their performance at the current hazard level in NBCC2010 is a matter of concern. This was a partial motivation for the present study.

The resultant lateral force on the wall at any time is calculated by integrating the lateral stresses along the height of the wall. In addition, the corresponding moment arm is calculated to define the center of application of the resultant force. In another word, the resultant lateral earth force and its point of application are calculated for each time increment to generate the corresponding time histories of these two quantities. The presented lateral earth force time histories and their relative center of applications are from the analyses using three ground motions.

In the Mononobe-Okabe method as practiced here, the resultant force (P_{AE}) is obtained by the M-O equation based on a design PGA level. The center of application of the resultant force is calculated assuming that the resulting ΔP_{AE} is applied approximately at a distance of $0.67H$ from the base of the wall.

Figures 7(a, c, e) show that the M-O method with $\text{PGA} = 0.46g$ reasonably predicts the maximum resultant force on the basement wall. Figures 7(b, d, f) indicate that with $\text{PGA} = 0.46g$ the Mononobe-Okabe method slightly over-predicts the el-

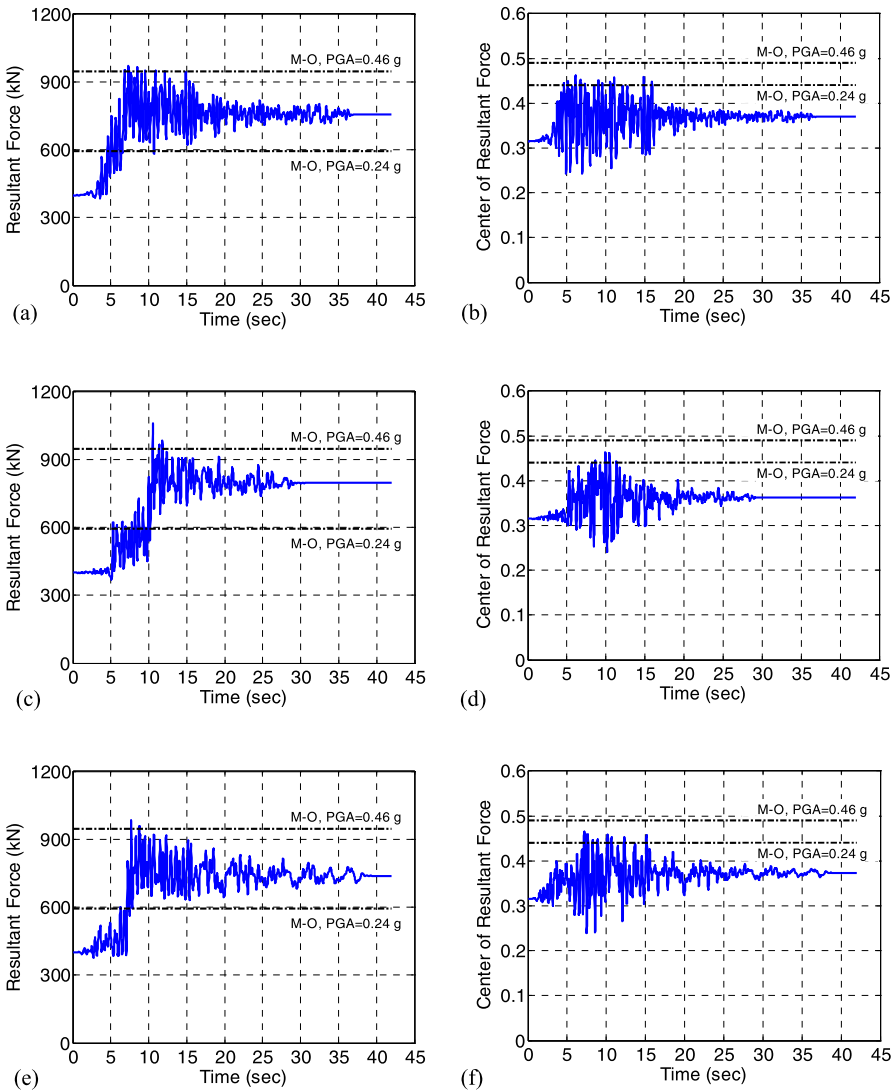


Fig. 7 Time histories of the resultant lateral earth forces and the normalized center of the resultant forces for ground motions G1 (a, b), G2 (c, d), and G3 (e, f). In these figures *dash lines* correspond to the M-O method with $PGA = 0.46g$ and $PGA = 0.24g$

evaluation of the application of the resultant lateral force on the wall at the instance of the maximum resultant force.

Figure 8 shows the maximum resultant lateral earth forces and the distance of the center of application of these forces from the base of the wall normalized respect to the wall height for all three ground motions. The corresponding results of the

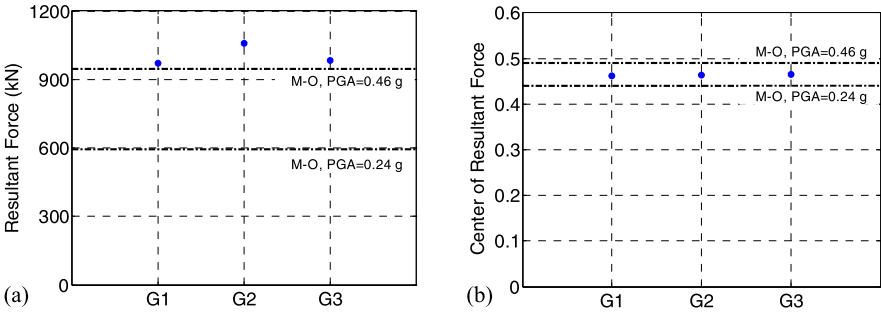


Fig. 8 Maximum resultant lateral earth forces and the corresponding normalized center of application from the base of the wall for different ground motions (G1–G3). In these figures the *dashed lines* correspond to the M-O method with PGA = 0.46g and 0.24g

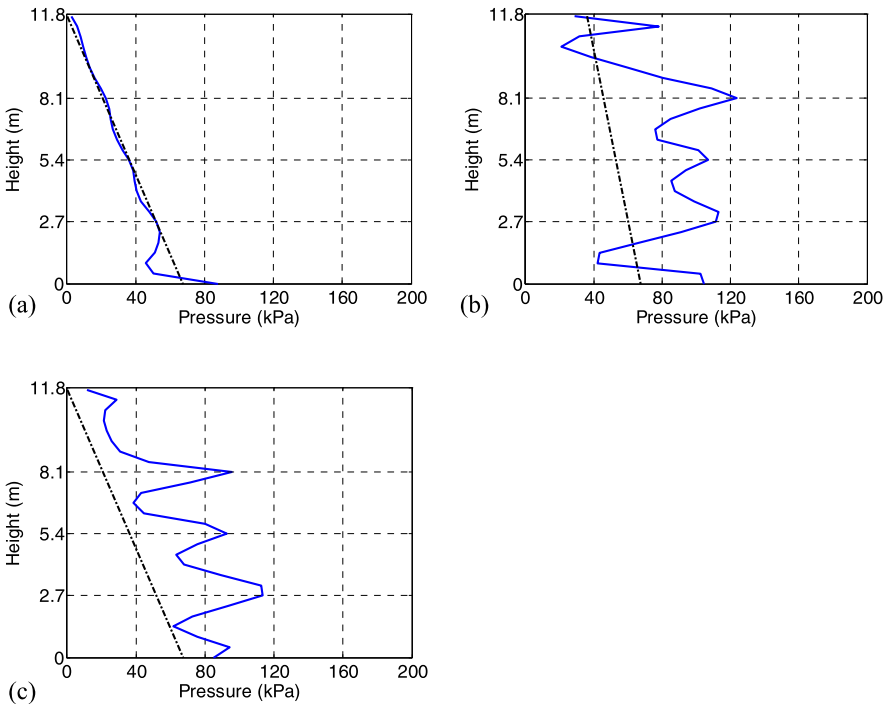


Fig. 9 Lateral earth pressure distributions along the height of the basement wall for ground motion G1; *symbols* representing the results of numerical analysis at (a) $t = 0$ sec (initial static pressures), (b) $t = 7.7$ sec (the instance of occurrence of maximum lateral earth force on the wall) and (c) $t = 37$ sec (residual static pressures), and the *dashed lines* representing the predictions from the Coulomb’s theory [for (a) and (c)] and from the M-O based method [for (b)]

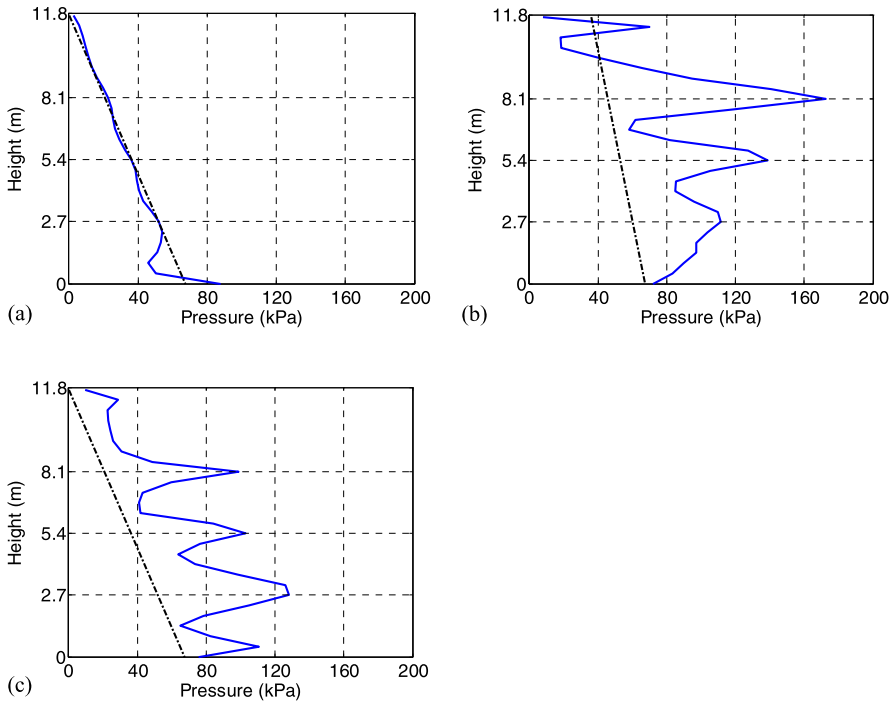


Fig. 10 Lateral earth pressure distributions along the height of the basement wall for ground motion G2; *symbols* representing the results of numerical analysis at (a) $t = 0$ sec (initial static pressures), (b) $t = 7.7$ sec (the instance of occurrence of maximum lateral earth force on the wall) and (c) $t = 37$ sec (residual static pressures), and the *dashed lines* representing the predictions from the Coulomb's theory [for (a) and (c)] and from the M-O based method [for (b)]

M-O method for $PGA = 0.46g$ and $PGA = 0.24g$ are also shown in this figures for comparison. In this method, the resultant force (P_{AE}) is obtained by the M-O equation based on a design PGA level. The center of application of the resultant force is also calculated assuming that the resulting ΔP_{AE} is applied approximately at a distance of $0.67H$ from the base of the wall. Figure 8(a) shows that the obtained maximum resultant forces from dynamic analyses are in an approximate range of the calculated maximum resultant force using the M-O method. Figure 8(b) shows that at the instance of maximum resultant force on the wall in each ground motion, the obtained distance for the center of resultant forces from dynamic analyses are consistently around mid-height of the wall, which is in a good agreement with the level calculated from the M-O based method.

Snapshots of the computed lateral earth pressure distribution along the height of the basement wall at different times are shown in Figs. 9 to 11. The results are for the analysis with ground motion G1, G2 and G3. The results of numerical analysis are presented at three different times during the analysis. Figures 9(a), 10(a) and 11(a) show the analysis results at the beginning of dynamic analysis (*symbols*) and

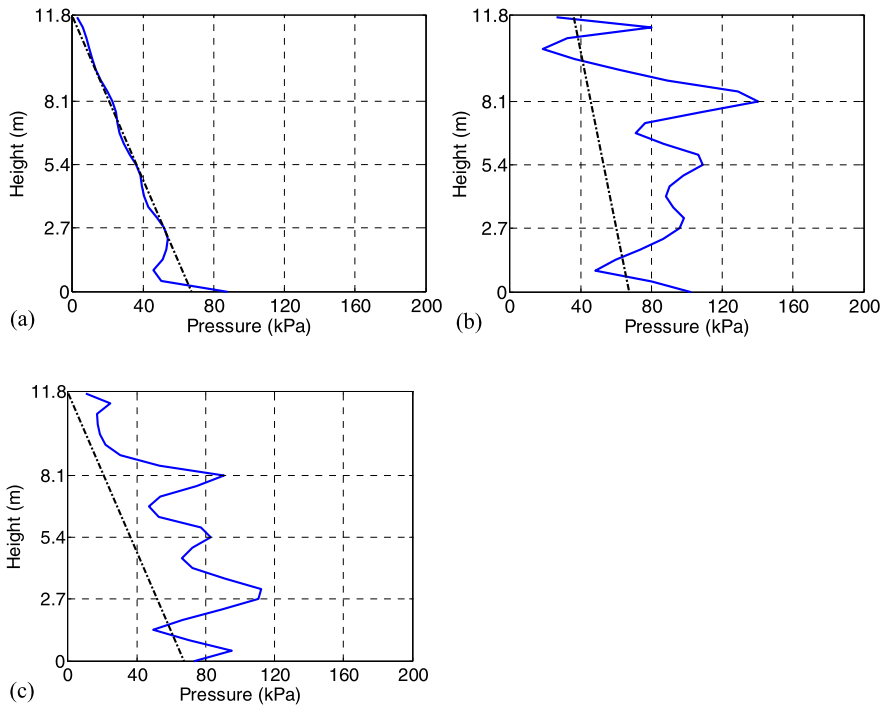


Fig. 11 Lateral earth pressure distributions along the height of the basement wall for ground motion G3; *symbols* representing the results of numerical analysis at (a) $t = 0$ sec (initial static pressures), (b) $t = 7.7$ sec (the instance of occurrence of maximum lateral earth force on the wall) and (c) $t = 37$ sec (residual static pressures), and the *dashed lines* representing the predictions from the Coulomb's theory [for (a) and (c)] and from the M-O based method [for (b)]

compare those to the suggested distribution of lateral pressures from Coulomb's theory (dashed line). The numerical analysis results at $t = 0$ sec adequately match to those obtained from the Coulomb's theory for static lateral earth pressure distribution.

Figures 9(b), 10(b) and 11(b) show that the maximum resultant earth force for the studied wall subjected to three ground motions occurs at about the peak of the input motions ($t = 7.7$ sec). Also, the lateral earth pressure profile obtained using the M-O method with the 2% in 50 year return period PGA (0.46g) are shown for comparison. The results show that the Mononobe-Okabe method, underestimates the lateral earth pressures at each floor slab level. In addition, for the top and the bottom basement stories in this study, the M-O method overestimates the lateral earth pressures on the wall between the floor slab levels, while in the other stories it underestimates the pressure on the wall.

Finally Figs. 9(c), 10(c) and 11(c) compare the residual pressures at the end of shaking when there are no dynamic effects with the suggested distribution of lateral pressures in the static case given by Coulomb's theory. It is clear that, there is a significant increase in the residual static earth pressure at the end of shaking.

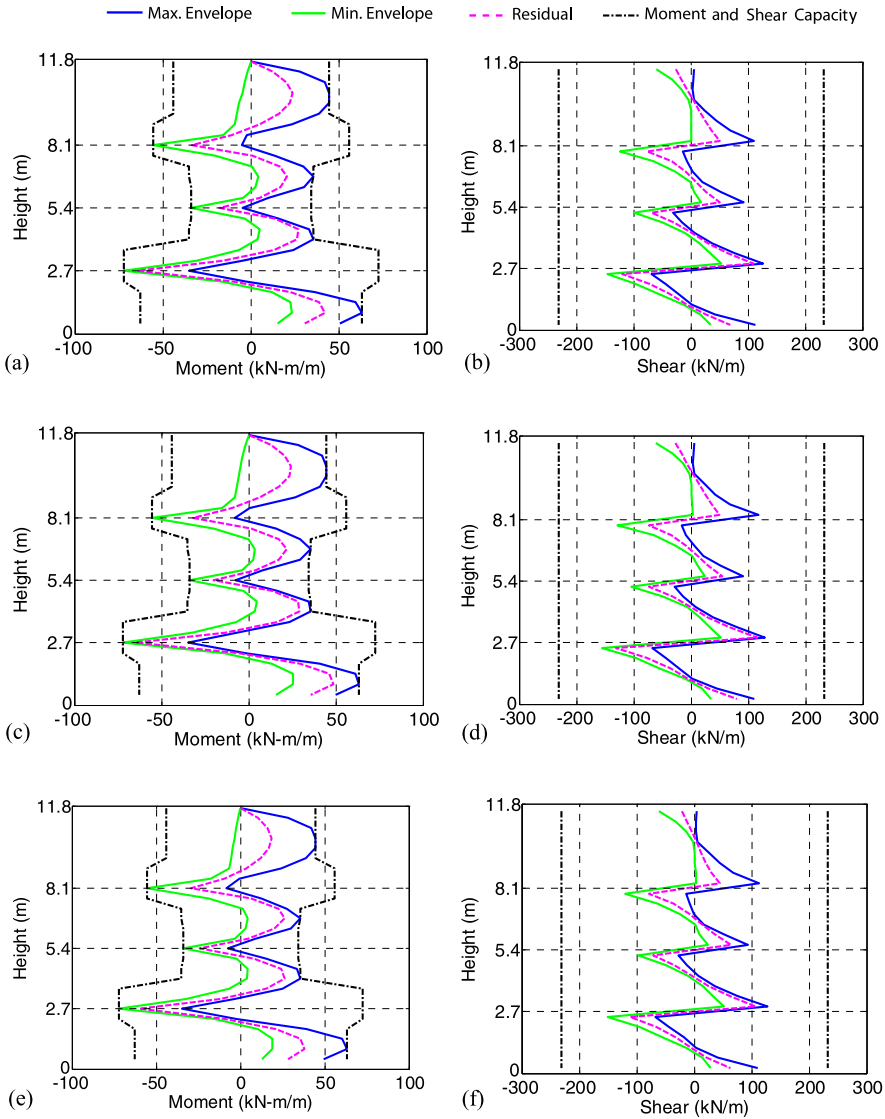
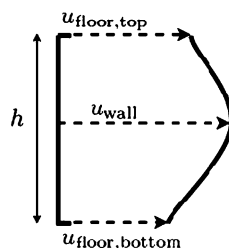


Fig. 12 The analysis results for maximum envelopes, minimum envelopes, and residual bending moments and shear forces for the basement wall subjected to ground motions G1 (a, b), G2 (c, d) and G3 (e, f)

The resulting bending moment and shear envelopes along the height of the wall using G1, G2 and G3 are presented in Figs. 12(a, c, e) and 12(b, d, f), respectively. Averages of both maximum and minimum envelopes are plotted for each wall. In this figures the limiting values of M_y and V_y correspond to the moment and shear capacity (real member’s strength) of each wall, respectively, as explained in Sect. 2.

Fig. 13 Definition of drift ratio for each story of the basement wall



As shown in Fig. 12, the basement wall designed for a hazard level of 10 % probability of exceedance in 50 years yields in moment at the mid-height of each basement story and at each floor level. The shear envelopes show that the shear demand is considerably less than the shear capacity along the height of the wall.

Following the conclusion of Fig. 12, since there is no significant difference in amount of yielding caused by different ground motions, from the engineering performance-based design standpoint, it is very important to monitor the resulting deformations and drift ratios of the wall, which is a common parameter for assessing the performance of a structure.

Drift ratio is usually defined as the relative displacement between floor levels divided by story height. The deformation or the relative displacement of the wall at the middle of each basement is calculated as the difference between the displacement of the wall at that level and the displacement of the wall at its base. Drift ratio for each story is calculated as shown in Fig. 13. The resulting drift ratio from this figure is a useful indicator to determine the amount of damage to the wall. In this figure h is the floor height, $u_{floor,top}$ and $u_{floor,bottom}$ are the wall deformations at the floor levels and u_{wall} is the deformation at the mid height of the wall (between two floors).

Drift ratio in this paper is defined in the following equation with the associated displacements patterns which are shown in Fig. 13.

$$\text{Drift Ratio} = \frac{u_{wall} - \left[\frac{u_{floor,top} + u_{floor,bottom}}{2} \right]}{0.5h} \quad (5)$$

This definition is consistent with the definition of hinge rotation used by Task Committee on Blast Resistance Design [19]. This committee related hinge rotation to structural performance. They specified two performance categories which may apply to basement walls; low and medium response categories. The Low Response Category is defined as 3.5 % drift ratio: “localized building/component damage. Building can be used; however repairs are required to restore integrity of structural envelope. Total cost of repairs is moderate”. The Medium Response Category is defined as 7 % drift ratio: “widespread building/component damage. Building cannot be used until repaired. Total cost of repairs is significant”.

The wall displacements (relative to the its base) along the height of the wall are shown in Figs. 14(a, c, e) and the associated drift ratios in Figs. 14(b, d, f). As illustrated in these figures, the relative displacements are larger between the floors and are smaller at each floor level. The results suggest that the performance of the

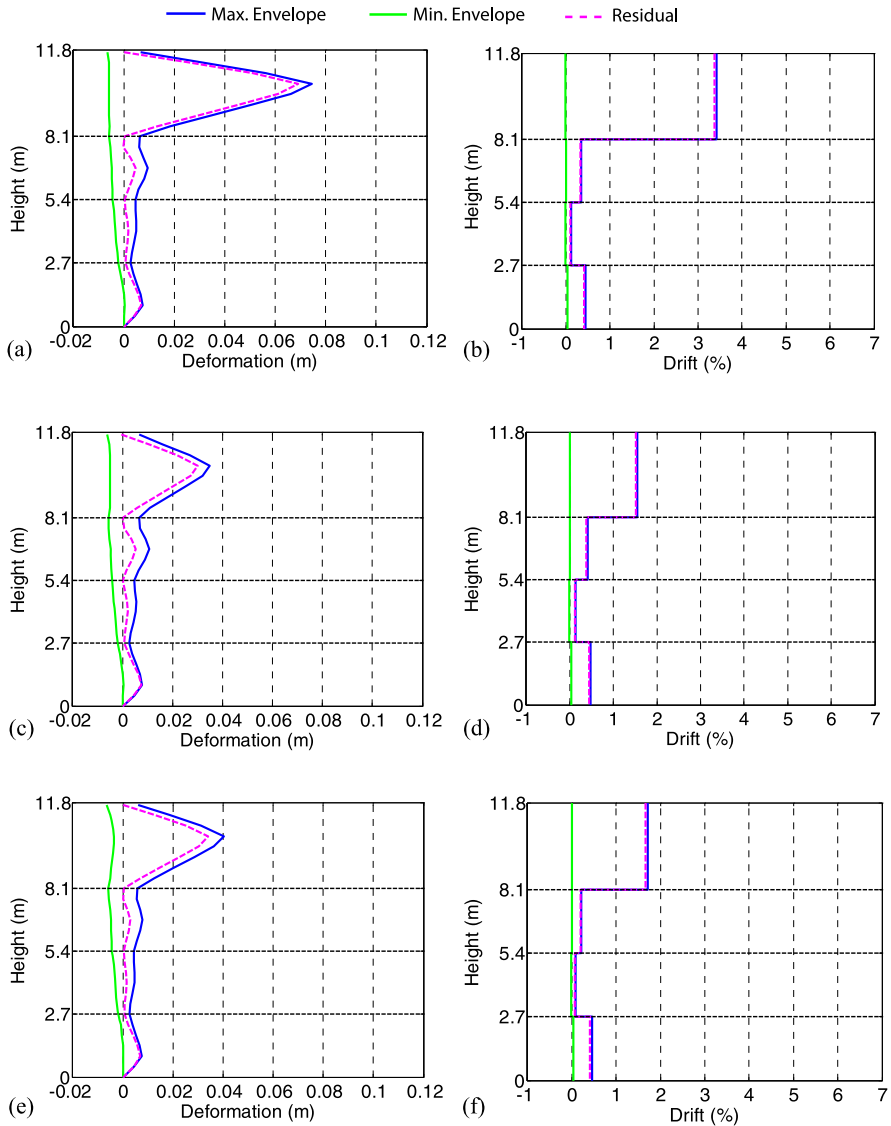


Fig. 14 The analysis results for maximum envelopes, minimum envelopes, and residual wall deformations (displacements relative to the base of the basement wall) and story drift ratios for the basement wall subjected to ground motions G1 (a, b), G2 (c, d) and G3 (e, f)

wall designed for NBCC1995 hazard PGA which is $0.24g$, seems adequate except for the first level basement in the first ground motion (Fig. 14(b)), where the drift ratio approached 3.3 %, which is almost the threshold of the low response category (3.5 %). At the rest of the basement levels the drift ratio is less than 0.5 %.

Based on the current numerical analyses, for a hazard level of 2 % in 50 years in Vancouver, design to the associated $PGA = 0.46g$ may not be warranted. An additional series of analyses is being conducted to determine at what hazard level the PGA should be selected for the M-O method to give an economical design for the 2 % in 50 years hazard. In effect, we are establishing a database for determining an appropriate effective PGA for use in M-O analysis. A problem in defining satisfactory performance in terms of drift ratios is the lack of any performance standards for basement wall in terms of drift ratios.

6 Summary and Conclusion

One of the aims of this study was to assess whether existing basement walls designed for a hazard level with 10 % probability of exceedance in 50 years (NBCC1995) in Vancouver would be safe when subjected to the higher seismic hazard level of 2 % in 50 years which is mandated by the NBCC2010. The seismic pressures against the wall for design were calculated using the M-O procedure. The walls were designed to behave elastically under these pressures. The response of the walls to higher hazard level mandated by NBCC2010 was evaluated using the computer program FLAC.

The M-O pressures for the higher hazard are approximately double the pressures used for the original design. Therefore, it was expected that the wall might yield under these elevated pressures and so a nonlinear analysis was carried out including nonlinear soil behavior and yielding of the wall. The analysis was conducted using three different input motions, all of them matched to Vancouver Uniform Hazard Spectrum in the period range 0.02–1.7 sec. The analyses show that M-O accurately predicts the peak resultant force on the wall and the point of application of the resultant force on the wall is consistently at about $0.55H$ from the base of the wall. This is the location usually assumed in British Columbia for application of M-O resultant force. However, the pressure distribution from the dynamic analysis was radically different from the linear distribution typically assumed in the practice. The total pressure during the earthquake against the top basement level is much smaller than estimated by M-O. At the end of earthquake, the residual pressure are significantly greater the Coulomb's theory.

As illustrated in Fig. 12(a), in all levels, the wall yields roughly at mid height of each floor as well at the floor levels, but on the opposite side. The behavior under shear is shown in Fig. 12(b) and it is clear that the shear demand is considerably less than the shear capacity along the height of the wall.

Figure 14 shows the deformations that occur in the wall displacements relative to the base of the wall and in terms of drift ratios. The maximum drift ratio in the first level is approximately 3.5 % for one of the motions. For the other motions the drift ratio is around 1.5 % in the top level. For the lower three basement levels the drift ratio is less than 0.5 %. These results suggest that apart from the results for motion G1 the drift ratios are in acceptable limits so the elastic design under the seismic

hazard of 10 % in 50 years is almost adequate to carry the higher hazard of 2 % in 50 years, except possibly in the upper basement level. More detailed study on this topic is underway by the authors.

Acknowledgements The materials presented in this paper are part of an ongoing study conducted by the authors as members of a task force committee for evaluation of seismic pressure on basement walls; struck by the Structural Engineers Association of British Columbia (SEABC). The authors are grateful for many constructive discussions with the Chairman of the Committee, Dr. Ron DeVall, and the committee members, Ali Amini, Don Anderson, Peter Byrne, Mat Kokan, Jim Mutrie, Ernest Naesgaard, Rob Simpson, and Doug Wallis. Support to conduct this study is provided in part by the Natural Sciences & Engineering Research Council of Canada (NSERC).

References

1. Institute for Research in Construction (1995) National Building Code of Canada. National Research Council of Canada, Ottawa
2. Institute for Research in Construction (2010) National Building Code of Canada. National Research Council of Canada, Ottawa
3. Itasca Consulting Group Inc (2008) FLAC: fast Lagrangian analysis of continua, user manual, version 6.0. Minneapolis
4. Anderson DG, Martin GR, Lam I, Wang JN (2009) Seismic analysis and design of retaining walls, buried structures, slopes, and embankments. NCHRP report 611, Transportation Research Board, Washington
5. Okabe S (1926) General theory on earth pressure. Proc Jpn Soc Civ Eng 12(1):123–134
6. Mononobe N, Matsuo H (1929) On the determination of earth pressures during earthquakes. In: Proceedings of world engineering conference, vol 9, pp 176–182
7. Kramer S (1996) Geotechnical earthquake engineering. Prentice Hall international series in civil engineering and engineering mechanics. Prentice Hall, New York
8. Prakash S, Basavanna BM (1969) Earth pressure distribution behind retaining wall during earthquakes. In: Proceedings of the fourth world conference on earthquake engineering, Santiago
9. Seed HB, Whitman RV (1970) Design of earth retaining structure of dynamic loads. In: Proceedings, specialty conference on lateral stresses in the ground and design of earth retaining structure, vol 1. ASCE/Cornell University, Ithaca, pp 103–147
10. Sherif MA, Ishibashi I, Lee CD (1982) Earth pressure against rigid retaining walls. J Geotech Eng Div 108(GT5):679–696
11. Sherif MA, Fang YS (1984) Dynamic earth pressure on walls rotating about top. Soil Found 24(4):109–117
12. Schnabel PB, Lysmer J, Seed HB (1972) Shake: a computer program for earthquake response analysis of horizontally layered sites. Report EERC 72-12, Earthquake Engineering Research Center, University of California, Berkeley
13. Idriss IM, Sun JI (1992) User's manual for SHAKE91, a computer program for conducting equivalent linear seismic response analyses of horizontally layered soil deposits. Program modified based on the original SHAKE program published in December 1972 by Schnabel, Lysmer and Seed
14. Seed HB, Wong RT, Idriss IM, Tokimatsu K (1986) Moduli and damping factors for dynamic analysis of cohesionless soils. J Geotech Eng Div 112(11):1016–1032
15. Robertson PK, Woeller DJ, Finn WD (1992) Seismic cone penetration test for evaluating liquefaction potential under cyclic loading. Can Geotech J 29:686–695
16. PEER (2011) Pacific Earthquake Engineering and Research Center, University of California, Berkeley

17. Wang G, Power M, Youngs R (2009) Design Ground Motion Library (DGML). Project 10607.000, AMEC Geomatrix Inc, Oakland
18. SeismoMatch 1.0.3, educational version. SeismoSoft Company
19. TRBRG (1997) Design of blast resistance buildings in petrochemical facilities. Report of Task Committee on Blast Resistance Design, Energy Division, ASCE

Modeling of Infilled Framed Structures

Panagiotis G. Asteris, Christis Z. Chrysostomou, Ioannis Giannopoulos,
and Paolo Ricci

Abstract This chapter presents an assessment of the behavior of infilled framed structures. The feasibility of possible immediate implementation of some recent developments both in analysis and design of infilled frames for practical design is investigated. It is now widely recognized that masonry infill panels, used in reinforced concrete (R/C) frame structures, significantly enhance both the stiffness and the strength of the surrounding frame. However, their contribution is often not taken into account because of the lack of knowledge of the composite behavior of the surrounding frame and the infill panel. Currently, Seismic Design Guidelines contain provisions for the calculation of the stiffness of solid infilled frames mainly by modeling infill walls as “diagonal struts.” However, such provisions are not provided for infilled frames with openings. The present study, based on available finite element results, proposes analytical equation for obtaining the reduction factor, which is the ratio of the effective width of a diagonal strut representing a wall with an opening over that of the solid RC infilled frame. The validity of the proposed equations is demonstrated by comparing our results, against work done by various researchers.

Keywords Infilled frames · Masonry · Seismic responses · Shear distribution · Stiffness

P.G. Asteris (✉) · I. Giannopoulos
Computational Mechanics Laboratory, Department of Civil & Construction Engineering
Educators, School of Pedagogical & Technological Education, Athens, Greece
e-mail: asteris@aspete.gr

P.G. Asteris
e-mail: pasteris@otenet.gr

C.Z. Chrysostomou
Dept. of Civil Engineering & Geomatics, Cyprus University of Technology, 3603 Limassol,
Cyprus

P. Ricci
Department of Structural Engineering, University of Naples Federico II, Naples, Italy

1 Introduction

It has been known for long that masonry infill walls affect the strength and stiffness of infilled frame structures. In seismic areas, ignoring the frame-infill panel interaction is not always on the safe side, since, under lateral loads, the infill walls dramatically increase the stiffness by acting as a compressed diagonal ‘strut/area’, resulting, thus, in a possible change of the seismic demand due to significant reduction in the natural period of the composite structural system [1, 2].

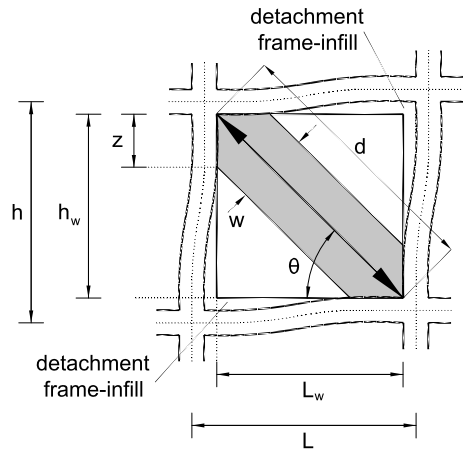
The rationale behind neglecting infill walls in the design process is partly attributed to incomplete knowledge of the behavior of quasi-brittle materials, such as unreinforced masonry (URM), of the composite behavior of the frame and the infill, as well as due to the lack of conclusive experimental and analytical results to substantiate a reliable design procedure for this type of structures, despite the extensive experimental efforts [3–10], and analytical investigations [11–23] over the past decades. Moreover, due to the large number of interacting parameters, if the infill wall is to be considered in the analysis and design stages, a modeling problem arises because of the many possible failure modes that need to be evaluated with a high degree of uncertainty. This is compounded by the presence of openings in the infills, which changes completely their behavior, and the large variety of infill walls and their dependence on local construction practices. In addition, the nonstructural nature of infills, may result in their removal in the case of building renovations, during which heavy masonry infills may be replaced by light partitions and hence change the overall behavior of the structural system with possible detrimental effects. Therefore, it is not surprising that no consensus has emerged leading to a unified approach for the design of infilled frame systems in spite of more than six decades of research. This is recognized in the engineering community and it is one of the topics that will be given priority for closer examination, so as to facilitate the inclusion of special provisions for infill walls, more detailed than the ones already included, in future amendments of the European Seismic Code. However, it is generally accepted that under lateral loads an infill wall acts as a diagonal strut connecting the two loaded corners, an approach that is only applicable to the case of infill walls without openings on the diagonal of the infill panel. The reader is referred to Moghaddam and Dowling [24], Asteris et al. [25], and Chrysostomou and Asteris [26] for an extensive review of research on testing and modeling of masonry infilled frames up to 2010.

In this chapter the macro-modeling of infilled frames is briefly presented along with a reduction parameter for the representation of infills with openings. Then some analytical studies are presented which are calibrated on experimental results, to show the effect of the openings on the period of vibration of structures and on inter-story drifts using nonlinear dynamic analysis.

2 Macro-modeling of Masonry Infill

Since the first attempts to model the response of the composite infilled-frame structures, experimental and conceptual observations have indicated that a diagonal strut

Fig. 1 Masonry infill frame sub-assembly



with appropriate geometrical and mechanical characteristics could possibly provide a solution to the problem (Fig. 1).

Early research on the in-plane behavior of infilled frame structures undertaken at the Building Research Station, Watford (later renamed Building Research Establishment, and now simply BRE) in the 1950s served as an early insight into this behavior and confirmed its highly indeterminate nature in terms solely of the normal parameters of design [27–29]. On the basis of these few tests a purely empirical interaction formula was later tentatively suggested by Wood [30] for use in the design of tall framed buildings. By expressing the composite strength of an infilled frame directly in terms of the separate strengths of the frame and infill, he short-circuited a mass of confusing detail and he recognized the desirability of a higher load factor where strengths were most dependent on the infills.

2.1 Single-Strut Models

In the early sixties, Polyakov [31] suggested the possibility of considering the effect of the infilling in each panel as equivalent to diagonal bracing, and this suggestion was later adopted by Holmes [32], who replaced the infill by an equivalent pin-jointed diagonal strut made of the same material and having the same thickness as the infill panel and a width defined by

$$\frac{w}{d} = \frac{1}{3} \tag{1}$$

where d is the diagonal length of the masonry panel. The “one-third” rule was suggested as being applicable irrespective of the relative stiffness of the frame and the infill. One year later, Stafford Smith [33], based on experimental data from a large series of tests using masonry infilled steel frames, found that the ratio w/d varied from 0.10 to 0.25. On the second half of the sixties Stafford Smith and his associates

using additional experimental data [3, 4, 34] related the width of the equivalent diagonal strut to the infill/frame contact lengths using an analytical equation, which has been adapted from the equation of the length of contact of a free beam on an elastic foundation subjected to a concentrated load [35]. They proposed the evaluation of the equivalent width λ_h as a function of the relative panel-to-frame-stiffness parameter, in terms of

$$\lambda_h = h \sqrt[4]{\frac{E_w t_w \sin 2\theta}{4EIh_w}} \quad (2)$$

where E_w is the modulus of elasticity of the masonry panel, EI is the flexural rigidity of the columns, t_w the thickness of the infill panel and equivalent strut, h the column height between centerlines of beams, h_w the height of infill panel, and θ the angle, whose tangent is the infill height-to-length aspect ratio, being equal to

$$\theta = \tan^{-1}\left(\frac{h_w}{L_w}\right) \quad (3)$$

in which L_w is the length of infill panel (all the above parameters are explained in Fig. 1). Based on experimental and analytical data Mainstone [36] proposed an empirical equation for the calculation of the equivalent strut width, given by

$$\frac{w}{d} = 0.16\lambda_h^{-0.3} \quad (4)$$

Mainstone and Weeks [37] and Mainstone [38], also based on experimental and analytical data, proposed an empirical equation for the calculation of the equivalent strut width:

$$\frac{w}{d} = 0.175\lambda_h^{-0.4} \quad (5)$$

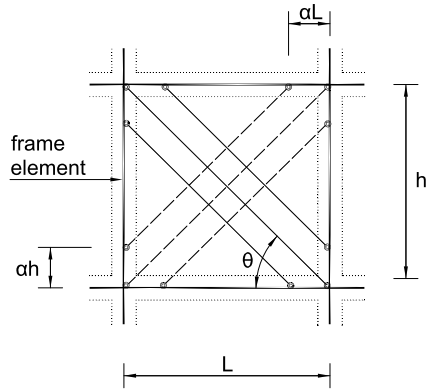
This formula was included in FEMA-274 (Federal Emergency Management Agency 1997) [39] for the analysis and rehabilitation of buildings as well as in FEMA-306 (Federal Emergency Management Agency 1998) [40], as it has been proven to be the most popular over the years. This equation was accepted by the majority of researchers dealing with the analysis of infilled frames.

2.2 Multiple Struts Models

In the last two decades it became clear that one single strut element is unable to model the complex behavior of the infilled frames. As reported by many researchers [7, 14, 41], the bending moments and shearing forces in the frame members cannot be adequately given, using a single diagonal strut connecting the two loaded corners. More complex macro-models were hence proposed, still typically based on a number of diagonal struts.

The main advantage of the multiple struts models, in spite of the increase of complexity, is the ability to represent the actions in the frame more accurately. Symakezis and Vratsanou [42] employed five parallel struts in each diagonal direction.

Fig. 2 Six-strut model for masonry infill panel in frame structures (Chrysostomou [13])



It was stressed how different compressed lengths play a significant effect on the bending moment distribution in the frame members.

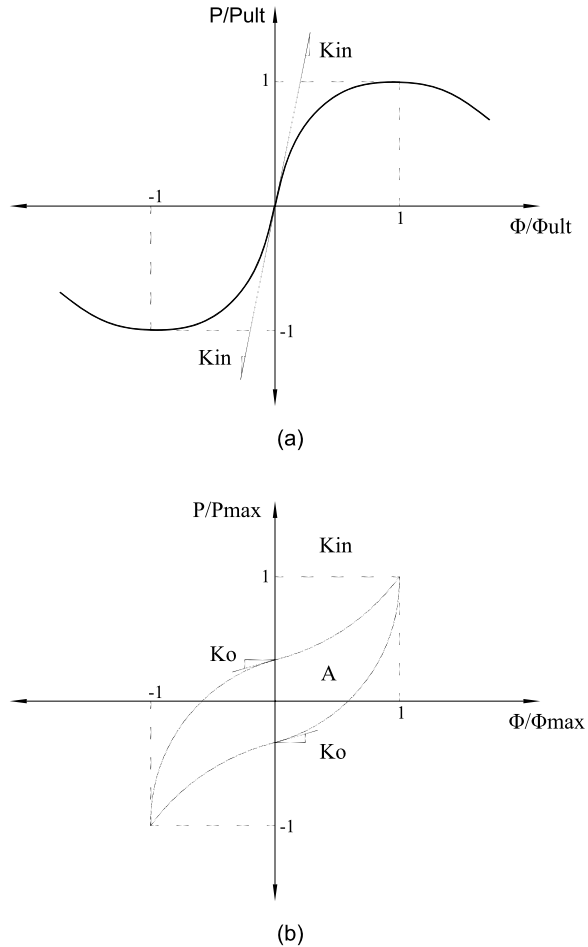
Chrysostomou [13, 15] aimed in obtaining the response of infilled frames under earthquake loading by taking into account both stiffness and strength degradation of infills. He proposed to model each infill panel by six compression-only inclined struts (Fig. 2). Three parallel struts were used in each diagonal direction and the off-diagonal ones were positioned at critical locations along the frame members. These locations are specified by a parameter α , which represents a fraction of the length or height of a panel and is associated with the position of the formation of a plastic hinge in a beam or a column. Theoretical values for this parameter are given by Liauw and Kwan [11, 43, 44]. At any point during the analysis of the non-linear response only three of the six struts were active, and the struts were switched to the opposite direction whenever their compressive force reduced to zero.

In order to conduct non-linear analysis, the force-displacement relationships corresponding to the equivalent strut model must be adequately defined. The modeling of hysteretic behavior increases not only the computational complexity but also the uncertainties of the problem [45].

In Chrysostomou’s model the hysteretic behavior of the six struts is defined by a hysteretic model, which consists of two equations. The first equation defines the strength envelope of a structural element and the second defines its hysteretic behavior. The shape of the envelope and the hysteretic loops (Fig. 3) is controlled by six parameters, all of which have physical meaning and can be obtained from experimental data. More details about the model are presented by Chrysostomou in his PhD thesis [13]. The advantage of this strut configuration over the single diagonal strut is that it allows the modeling of the interaction between the infill and the surrounding frame and it takes into account both strength and stiffness degradation of the infill, which is vital for determining the response of infilled frames subjected to earthquake load.

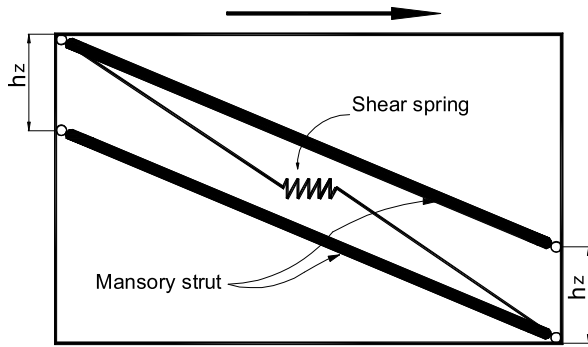
Crisafulli [47] in his PhD thesis investigated the influence of different multi-strut models on the structural response of reinforced concrete infilled frames, focusing on the stiffness of the structure and the actions induced in the surrounding frame.

Fig. 3 Strength envelope and hysteretic loop in normalized space proposed by Chrysostomou [13] (adaptation of the model for masonry walls of Soroushian et al. [46])



Numerical results, obtained from the single, two and three strut models, were compared with those corresponding to a refined finite element. The lateral stiffness of the structure was similar in all the cases considered, with smaller values for two- and three-strut models. It must be noted that, for the multi-strut models, the stiffness may significantly change depending on the separation between struts. The single strut model underestimates the bending moment because the lateral forces are primarily resisted by a truss mechanism. On the other hand, the two-strut model leads to larger values than those corresponding to the finite element model. A better approximation is obtained from the three-strut model, although some differences arise at the ends of both columns. Although the single-strut model constitutes a sufficient tool for the prediction of the overall response and the triple-strut model is superior in precision, Crisafulli adopted the double-strut model approach, accurate enough and less complicated compared to the other models.

Fig. 4 Multi-strut model proposed by Crisafulli and Carr [48] for masonry infill panel (only the struts and the shear spring active in one direction are represented)



More recently, Crisafulli and Carr [48] proposed a new macro-model in order to represent, in a rational but simple way, the effect of masonry infill panels. The model is implemented as a four-node panel element which is connected to the frame at the beam-column joints. Internally, the panel element accounts separately for the compressive and shear behavior of the masonry panel using two parallel struts and a shear spring in each direction as shown in Fig. 4.

This configuration allows an adequate consideration of the lateral stiffness of the panel and of the strength of masonry panel, particularly when a shear failure along mortar joints or diagonal tension failure is expected. Furthermore, the model is easy to apply in the analysis of large infilled frame structures. The main limitation of the model results from its simplicity, since the panel is connected to the beam-column joints of the frame, being thus not able to properly predict the bending moment and shear forces in the surrounding frame. The proposed model for masonry infill panels was implemented in RUAUMOKO [49], a computer-based analytical tool able to accurately model three dimensional structures whilst providing ancillary design data such as earthquake spectra. The proposed model has been also implemented in the program SeismoStruct [50] and numerical results were compared to experimental data by Smyrou [51] and Smyrou et al. [52], showing the accuracy of the model to evaluate the nonlinear response of the structure. Furthermore, they conducted an interesting sensitivity analysis to evaluate the relative importance of the parameters used in the model to represent the cyclic response of masonry.

3 Effect of Openings in the Lateral Stiffness of Infill Walls

Although infill walls usually have oversized openings, recent research has mainly focused on the simple case of infill wall without openings. Research on infill walls with openings is mostly analytical, restricted to special cases, and as such cannot provide rigorous comparison to actual cases because of its focus on specific materials used and specific types of openings. It is worth noting that the contribution of the infill wall to the frame lateral stiffness is much reduced when the structure is subjected to reversed cyclic loading, as in real structures under earthquake conditions.

In order to investigate the effect of openings in the lateral stiffness of masonry infill walls a finite element technique proposed by Asteris [16, 19] has been used in this chapter. The basic characteristic of this analysis is that the infill/frame contact lengths and the contact stresses are estimated as an integral part of the solution, and are not assumed in an ad-hoc way. In brief, according to this technique, the infill finite element models are considered to be linked to the surrounding frame finite element models at two corner points (only), at the ends of the compressed diagonal of the infill (points A and B in Fig. 5a). Then, the nodal displacements are computed and checked whether the infill model points overlap the surrounding frame finite elements. If the answer is positive, the neighboring points (to the previously linked) are also linked and the procedure is repeated. If the answer is negative, the procedure is stopped and the derived deformed mesh is the determined one (Fig. 5h).

Using this technique, analytical results are presented on the influence of the opening size on the seismic response of masonry infilled frames. Figure 6 shows the variation of the λ factor as a function of the opening percentage (opening area/infill wall area), for the case of an opening on the compressed diagonal of the infill wall (with aspect ratio of the opening the same as that of the infill). As expected, the increase in the opening percentage leads to a decrease in the frame's stiffness. Specifically, for an opening percentage greater than 50 % the stiffness reduction factor tends to zero.

The findings of the present parametric study using the finite-element method, lead to the following relationship for the infill wall stiffness reduction factor λ :

$$\lambda = 1 - 2\alpha_w^{0.54} + \alpha_w^{1.14} \quad (6)$$

in which α_w is the infill wall opening percentage (area of opening to the area of infill wall).

The above coefficient could be used to find the equivalent width of a strut for the case of an infill with opening by multiplying the results of Eqs. (1), (4) and (5) above. It can also be used to modify the equations of the Crisafulli model, which is described below.

4 Numerical Example

In order to illustrate the inadequacy of the single strut models to represent the structural response of infill walls with openings in frame structures, a case-study was carried out, employing a reinforced concrete frame, whereby the infill walls are modeled with each of the two approaches. For the multi-strut case the Crisafulli double-strut model has been chosen, since it is satisfactorily precise to represent accurately the local effect between the infill and the frame and less complicated than a triple-strut model. The single-strut model used is a rather 'gross' model that can be employed in commercial packages. It consists of a pair of diagonal elastic struts that are active at all times, each of which has a stiffness of 50 % of the calculated infill-wall stiffness.

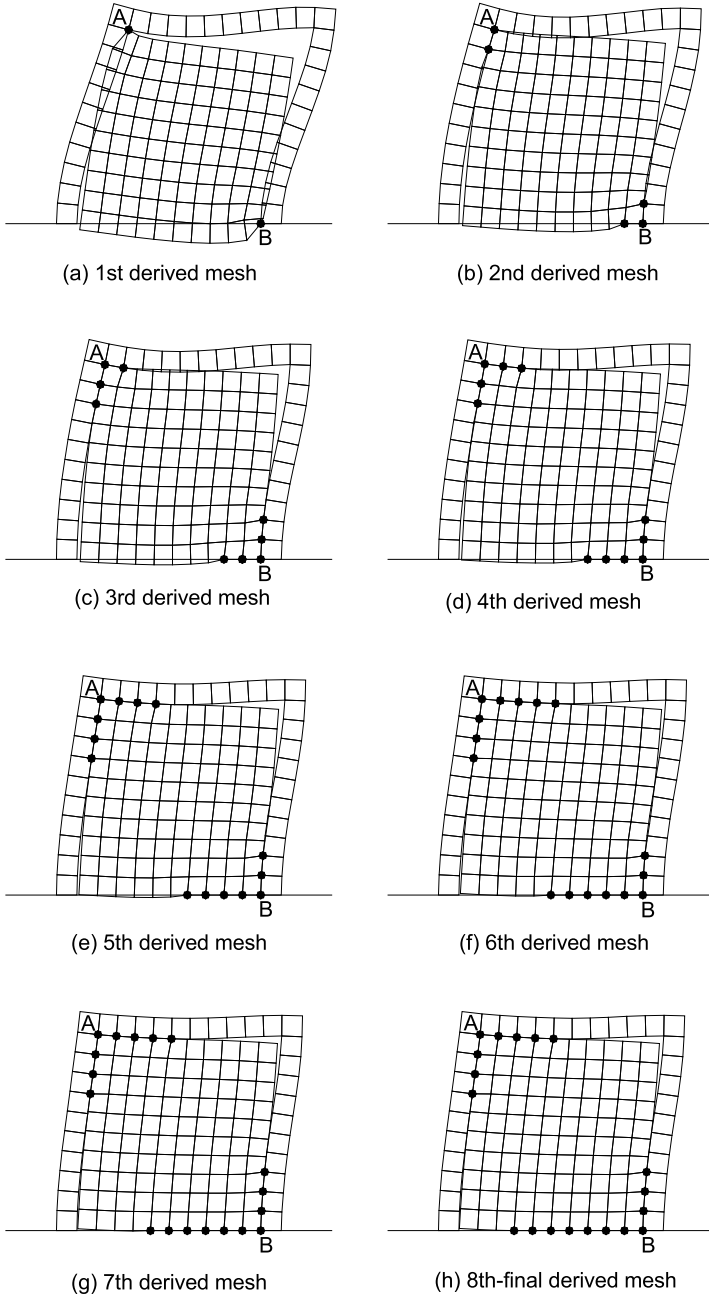
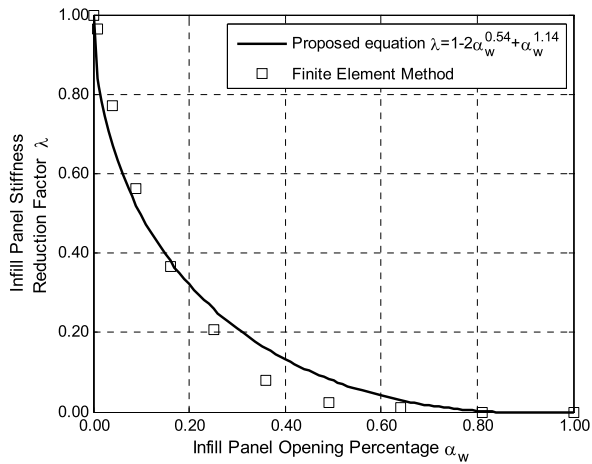


Fig. 5 Deformed meshes of an one-story one-bay infilled frame using the finite element technique proposed by Asteris [16, 19]

Fig. 6 Infill panel stiffness reduction factor in relation to the opening percentage



The relative accuracy of the models is assessed through comparison with experimental results obtained from pseudo-dynamic tests of a full-scale four-story, three-bay reinforced concrete frame, which was tested at the ELSA reaction-wall laboratory within the framework of the ICONS research program [53]. The frame was infilled with brick walls that included openings of different dimensions (Fig. 7). It can be regarded as representative of the design and construction practice of the 60's in Southern Europe, designed to withstand only vertical loads, without satisfying the modern seismic-code design-requirements.

The experimental seismic response was obtained with pseudo-dynamic testing, i.e. a step by step integration technique to compute the displacement response of the frame that was subjected to three different, numerically specified seismic records, utilizing the non-linear restoring forces actually developed during the test. The input seismic motions were chosen to be representative of a moderate-high European hazard scenario. The acceleration time-histories were artificially generated [54] and three of increasing return periods of 475, 975 and 2000 years were used for the experiment (only the first two were employed in the present study and are shown in Fig. 8).

The non-linear structural analysis program SeismoStruct [50] was employed for the analyses. SeismoStruct is an Internet-downloadable fiber-based Finite Element package capable of predicting the large displacement behavior of space frames under static or dynamic loading, considering both geometric nonlinearities and material inelasticity and fully accounting for the spread of inelasticity along the member length and across the section depth.

Section 4.1 presents a sensitivity study on the influence of the parameters controlling the hysteresis rules of the infill strut model on displacement demand. In Sect. 4.2, a comparison is made between the analysis results for the above structure using a single strut and a multi-strut model. This is done to calibrate the model based on experimental data. Then, the same frame is used but having infills with the same percentage of openings in all the panels at all floors. The analyses are used to

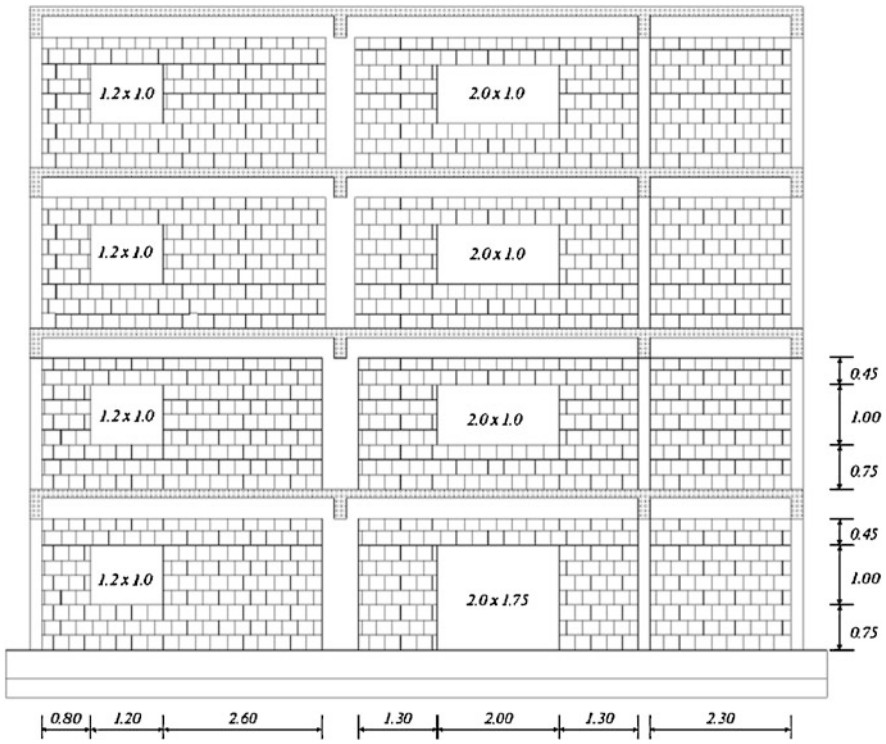


Fig. 7 Elevation view of the infilled frame—location and dimensions of openings [53]

examine the influence of openings on the period of the structure and the inter-story drift. The effectiveness of the proposed model to represent the effects of soft-stories (‘pilotis’) is also examined.

4.1 Sensitivity Analysis

In order to evaluate the importance of the empirical parameters required to define the hysteresis rules of the infill strut models, which are part of the structural model, a sensitivity analysis is carried out. The influence of a variation in each one of these parameters on the maximum top displacement recorded during the nonlinear dynamic analysis is observed. The 475 years return period acceleration time history is used for the analyses, and three different assumptions are made for the opening percentage in infill panels; (a) assuming the opening percentage in each infill panel as it is in the original tested model (original frame), (b) assuming no opening (0 % α_w frame), and (c) assuming 50 % opening percentage in all infill panels (50 % α_w frame).

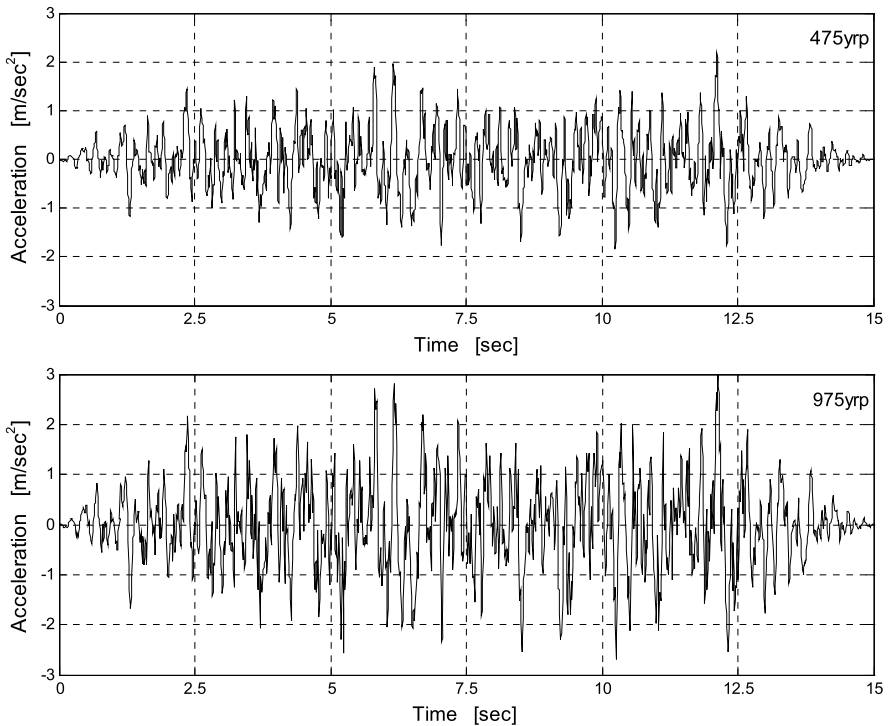


Fig. 8 Ground motion acceleration for 475 and 975 yrs

Sensitivity analysis is aimed at identifying the impact of each input variable on the structural response. It is typically used as an intermediate step when the influence of uncertainties on structural performance is investigated [55–57]. To this end, each input parameter is modeled as a random variable described by a statistical distribution, defined by a central (expected) value and an assigned variability. Then, sensitivity analysis is carried out by generating models in which a single random variable assumes a value corresponding to a selected lower or upper fractile, while the remaining variables remain to their central values, and the resulting change in the output performance parameter is observed (e.g., [57]). Note that in this case the influence of each single variable observed in sensitivity analysis not only depends on the influence of the variable on the seismic performance, but also on the assumed variability for that variable. As a matter of fact, the amount of variability assigned to the variable leads to consider—as lower and upper limits—values more or less distant from the central (median) value. A variable characterized by a lower variability will have lower and upper limit values closer to the median value, and vice versa. Hence, in this case the amount of the change in seismic performance parameter due to the change in each variable should be interpreted taking into account also the variability assigned to each variable. In the present study, attention is directly focused on the mechanical influence of each input parameter on the observed seismic per-

formance, rather than on the influence of the uncertainties affecting such parameters on seismic performance. Hence, a *parametric* sensitivity analysis is carried out, in which assumed values for the input parameters vary parametrically within a range of typically expected values. To this end, no statistical characterization of the input parameters is needed, which by the way would be not easy at all, due to the lack of specific experimental data.

Recently, sensitivity analysis has been applied to infilled RC frames [58]. In this study non-linear static pushover analyses are carried out on different structures, in order to investigate the influence of uncertain modeling parameters on seismic response parameters. One of the investigated frames is the case-study frame considered herein, in fully infilled configuration. Results highlight the strong influence of mechanical parameters defining the monotonic envelope of infill truss models on seismic performance at difference limit states, both on displacement and Peak Ground Acceleration (PGA) capacity. As far as displacement demand is concerned, as in the present study, the importance of shear stiffness and shear strength of infills is observed, through their influence on global stiffness and strength, respectively. In particular, the maximum decrease in fundamental period and the maximum increase in base shear are respectively observed with increasing shear stiffness and with increasing shear strength of infills, and vice versa. Both these increases in global stiffness and strength lead to a reduction in top displacement demand, that is, to an increase in seismic capacity (expressed as PGA) given equal the displacement capacity, within a spectral seismic assessment approach. In the present study, the sensitivity of top displacement demand to the hysteresis rules used for the infill strut model is investigated, by means of nonlinear dynamic analyses. Hence, the parameters determining such rules are assumed as input variables, as described below.

The masonry infill strut model used in the current study requires nine empirical calibrating factors to be defined. These factors have been proposed by Crisafulli [47] and are mostly related to cyclic loading rather than static monotonic loading (e.g. Push-over analysis), which has been shown that has little influence. A short description about their meaning and the ranging values is given below:

1. *Starting unloading stiffness factor* (γ_{un}) is used to define, as a proportion of its loading counterpart, the starting unloading stiffness modulus. Its value may typically vary between 1.5 and 2.5. Value used in the current study is 1.7.
2. *Strain reloading factor* (α_{re}) is employed to predict the strain at which the loop reaches the envelope after unloading. Its typical value ranges from 0.2 and 0.4. Value used is 0.2.
3. *Strain inflection factor* (α_{ch}) is utilized in the computation of the strain at which the reloading curve should feature an inflection point, effectively controlling, in this way, the loops' fatness. Its value may be found within the interval of 0.1 to 0.7. Value used is 0.7.
4. *Complete unloading strain factor* (β_a) is used in the definition of the plastic deformation after complete unloading. Its values typically range between 1.5 and 2.0. Value used is 2.0.

5. *Stress inflection factor* (β_{ch}) is employed in the computation of the stress at which the reloading curve should feature an inflection point. Its values typically range between 0.5 and 0.9. Value used is 0.9.
6. *Zero stress stiffness factor* (γ_{plr}) is utilized to define, as a proportion of its initial counterpart (E_m), the stiffness at zero stress, after complete unloading has taken place. Its values typically range between 0 and 1. Value used is 1.0.
7. *Reloading stiffness factor* (γ_{plr}) is used to define, as a proportion of its loading counterpart, the reloading stiffness modulus, after complete loading has taken place. Its values typically range between 1.1 and 1.5. Value used is 1.1.
8. *Plastic unloading stiffness factor* (e_{x1}) is employed to define, as a proportion of its loading counterpart, the unloading tangent modulus corresponding to the plastic strain. Its values typically range between 1.5 and 3.0. Value used is 3.0.
9. *Repeated cycle strain factor* (e_{x2}) is utilized in the computation of the strain that the envelope curve should reach after inner cycling. Its values typically range between 1.0 and 1.5. Value used is 1.0.

As mentioned above, a parametric type of sensitivity analysis was used to evaluate the sensitivity of the top displacement demand to the illustrated input variables. To this end, for each of the three considered types of frame (original, 0 % α_w and 50 % α_w), the top displacement was computed for the base-case model, in which case each input variable of the model was set to the previously chosen value. Then, different models were generated for each input variable assuming values varying in the above illustrated ranges, and leaving the remaining variables at the values they assume in the base-case model. Top displacement demand was computed for each one of these models, and its variability depending on the variability of each input variable was then calculated as follows:

$$\Delta_y = 100 \frac{y_{ij} - y_{bc}}{y_{bc}} (\%) \quad (7)$$

where y_{ij} is the value of the top displacement computed for the variation of the i -th input variable to the j -th assumed value, whereas y_{bc} corresponds to the value of the top displacement estimated for the base-case model. Figure 9 reports values of Δ_y for the parameters most significantly affecting the top displacement demand.

From the graphs above it can be observed that the ‘starting unloading stiffness factor’ γ_{un} is the parameter that affects the most the top displacement of the frame. The ‘strain inflection factor’ α_{ch} is the 2nd major parameter that affects the model behavior and 3rd is the ‘plastic unloading stiffness factor’ e_{x1} , which has minor effect on the results.

α_{ch} directly controls the “fatness” of the hysteresis loops in reloading phase, whereas γ_{un} and e_{x1} control the shape of the unloading curve from the envelope curve through the initial and final tangent modulus, respectively. In particular, γ_{un} provides the unloading tangent modulus as a proportion of the initial modulus of the monotonic envelope and e_{x1} controls the influence of the unloading strain (that is, the influence of the magnitude of the strain at which the unloading curve starts from the envelope curve) on the degradation of the final tangent modulus.

Fig. 9 Sensitivity analysis results of infill model parameters in terms of deviation from the original model

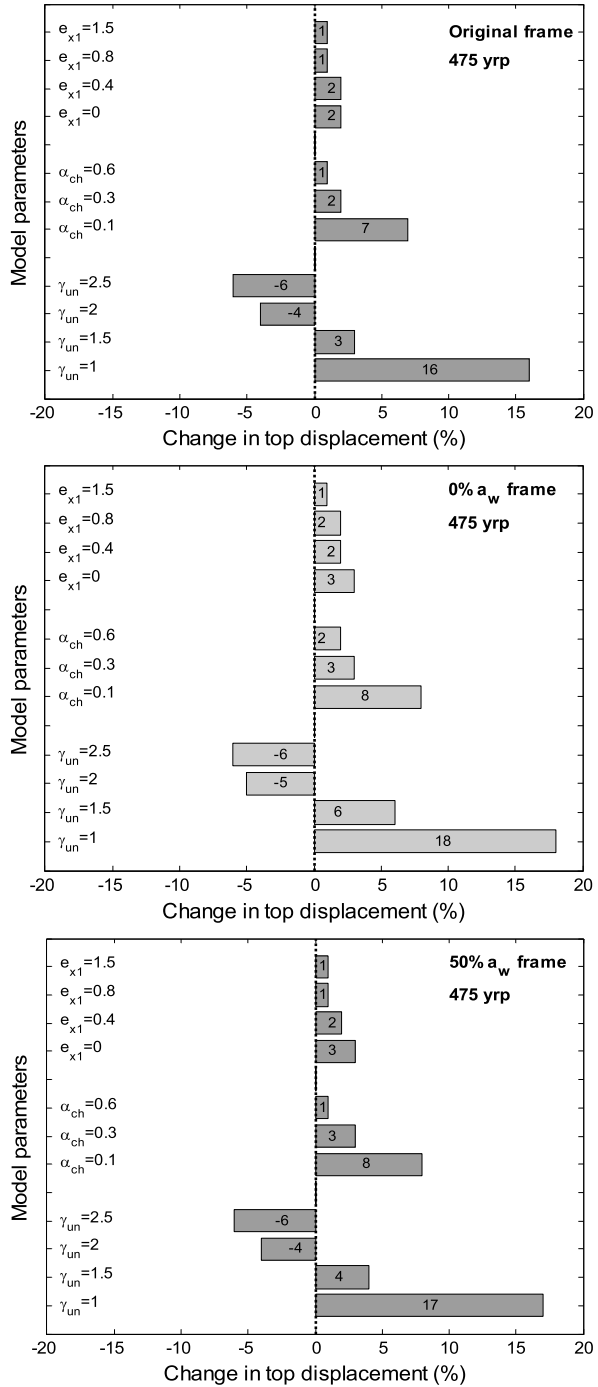


Table 1 Periods and mass contribution of bare frame model

Period [sec]	Experimental	Analytical	Mass contribution [%]
1st	0.64	0.63	83.02
2nd	0.22	0.21	10.78
3rd	0.13	0.13	3.58
4th	0.09	0.09	2.60

When these parameters decrease, hysteresis loops become less pronounced and, therefore, less energy-dissipating, thus leading to a detrimental increase in global displacement demand, as clearly shown by trends depicted in Fig. 9.

Another interesting point that is worth mentioning is that the effect of all parameters is similar regardless which frame (original, 0 % and 50 % α_w) is used each time. As opening percentage increases, the influence of infills on structural behavior should tend to decrease, and top displacement should become a little less sensitive to infill parameters, therefore also the variation in top displacement with the variation in infill parameters should tend to decrease in absolute terms. Nevertheless, this is a very slight effect, due to “weight” of infills on structural response, which remains decisive also when openings are present.

This study confirms the considerable sensitivity of seismic performance—in this case in terms of top displacement demand under a given acceleration time history—to infill characteristics. Attention is focused on hysteresis rules of infill truss model, thus highlighting the importance of a proper calibration of the parameters that control such rules.

4.2 Verification of the Numerical Model

Before proceeding with the analyses of the infilled frame, there was a need to verify the accuracy of the numerical model of the bare frame. The aim was to ensure that the numerical model, before inserting the various infill panels, represents satisfactorily the bare frame. By limiting the other parameters of uncertainty, the infilled panel model is rendered in fact the only variable, the effect of which should be examined.

An eigenvalue-modal analysis was undertaken to provide a first insight into the structure. The values of the periods of the 1st up to the 4th mode are computed and presented in Table 1, together with the experimental estimates of the natural frequencies. In order to provide data for modal identification of the bare frame, a very low intensity excitation was applied to the structure before the pseudo-dynamic test took place, similar as a non-destructive test. More details about these methods, which are based on time-domain linear models, can be found elsewhere [55].

From Table 1 above, it can be observed that the fundamental period is dominant (mass contribution 83.02 %). The value of the fundamental period for a typical 4-story building is high, reflecting the flexibility of the structure mainly due to the

absence of infill panels. By comparing the 1st period of the test frame (0.64 sec) with the fundamental period of the numerical model (0.63 sec), it is noted that there is a remarkable agreement between them. The same conclusion can be reached for the rest periods, showing the accuracy of the analytical model used.

4.3 Single Strut Model vs Multiple Struts Model

Representative numerical results obtained from the single and multi-strut models are depicted in Fig. 10 for acceleration time-histories of increasing return periods of 475 and 975 years. It can be easily concluded that the multi-strut model provides a very good fit to the experimental results and better approximation using finite elements is hardly justified. However, it should be stressed that the correct modeling of the infill required the selection of the value of a significant number of parameters, a difficult and intricate task, which is not always appropriate in everyday practice.

On the contrary, the single-strut model lacks a similar ability to represent adequately the experimental behavior, providing significantly less accurate results. This is entirely attributed to the inability of such over-simplified models to reproduce all the complex aspects of the infill walls' behavior. Similar to the above conclusions have been drawn regarding the displacement and the shear-force profiles along the height of the building.

4.4 Comparison of the Experimental and Analytical Model of the Tested Infilled Frame

After the preliminary verification of the numerical model for the bare frame, the infilled panel elements were implemented in the model. A static time-history analysis was carried out in the infilled frame with the aim to simulate the pseudo-dynamic tests conducted in the laboratory. The accuracy of the numerical model is evaluated by comparing the results of the analysis with the experimental results. The comparison was done in terms of time-history maximum inter-story drift and base shear, as can be seen in Figs. 11 and 12. In Fig. 11, the maximum experimental and numerical drifts for each story are plotted together with the drift values corresponding to three damage limit states. More details regarding these limits are described elsewhere [59]. It can be observed that for a return period of 475 years, the maximum drift values are varying close to the Immediate Occupancy (IO) limit state, while for a return period of 975 years, the peak value at the 1st story exceed the Collapse Prevention (CP) limit state. The maximum drift values are given in a tabular form as well.

In Fig. 12, a comparison in terms of time-histories, instead of comparison of the instantaneous peak values of base shear is presented; it is considered to be more

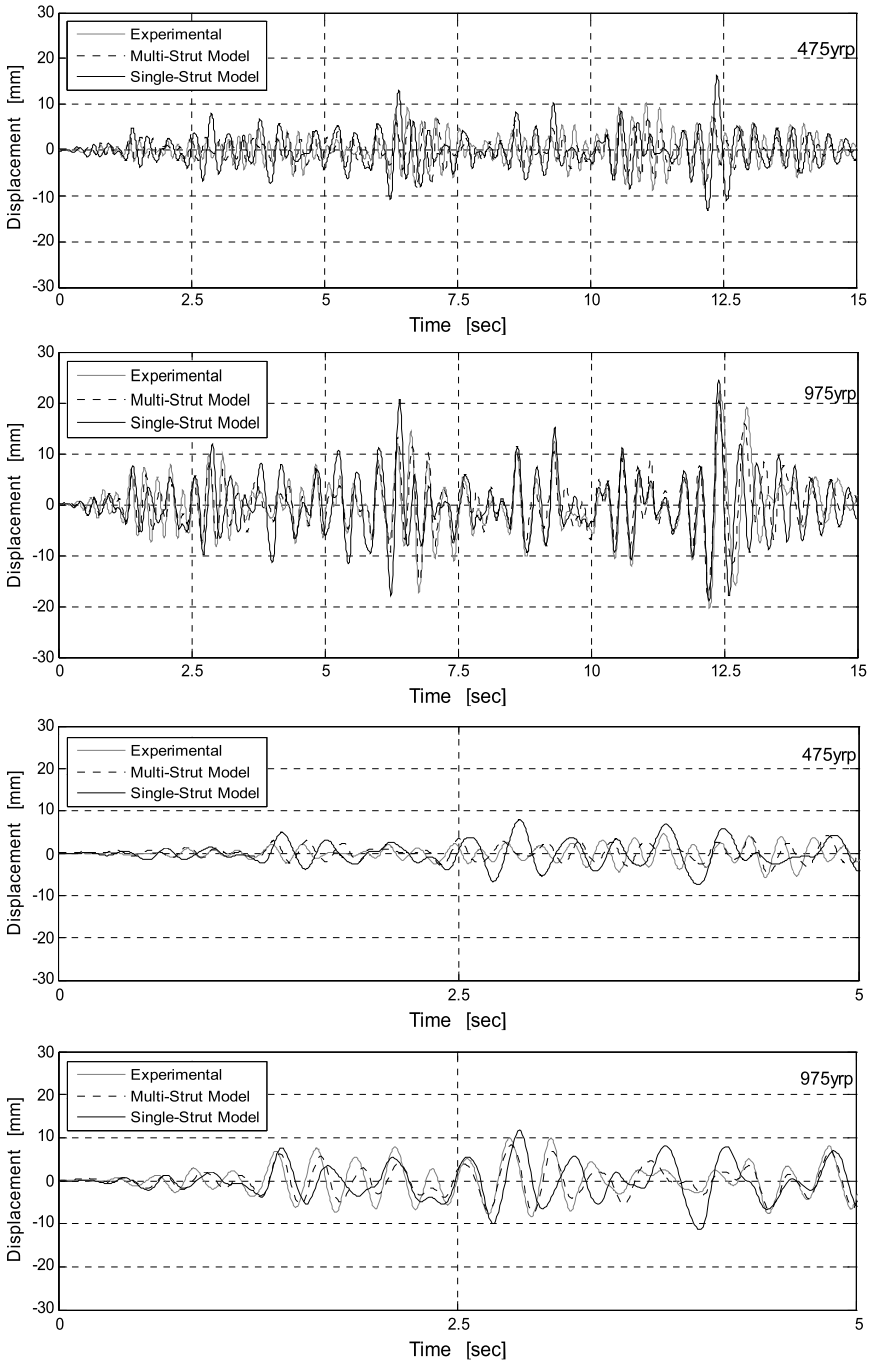
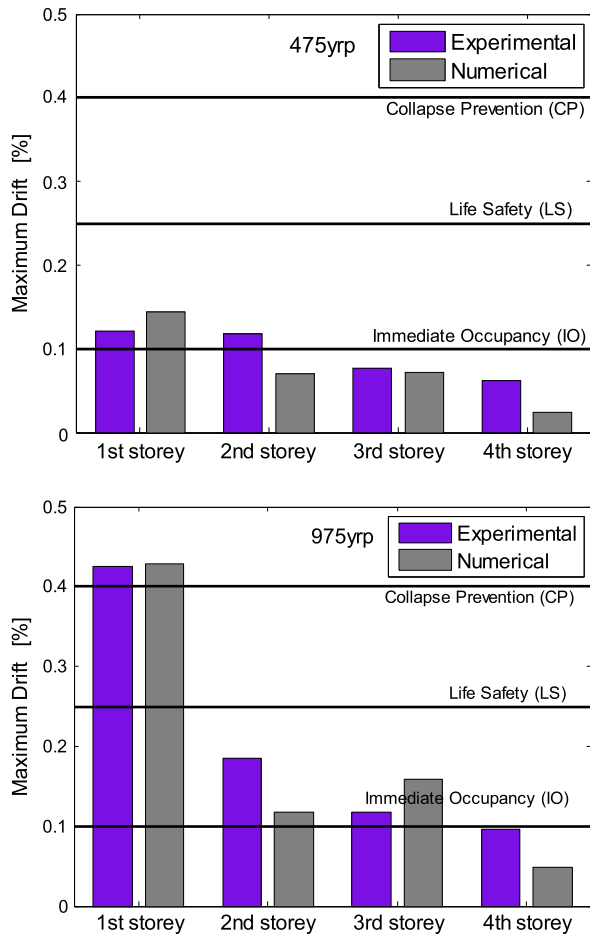


Fig. 10 Comparison of the top displacement of the infill frame and the two structural models (475 and 975 yrp record)

Fig. 11 Maximum inter-story drift for the 475 and 975 yrp tests: comparison with drift values corresponding



representative because an overall picture of the precision of the numerical model is obtained.

A first overall observation is that the analytical results demonstrate a good match with those of the experiment. Some differences are identified in several parts of the time-histories. For example, at the beginning of the time-history, corresponding to the 475 yrs record of the model, few differences occurring at the peaks of a limited of cycles are observed, while at the middle of the same records the model tends to underestimate the base shear.

4.5 Effect of Openings on Fundamental Periods

The infill wall enhances the lateral stiffness of the framed structures; however, the presence of openings within the infill wall will reduce the lateral stiffness. Figure 13

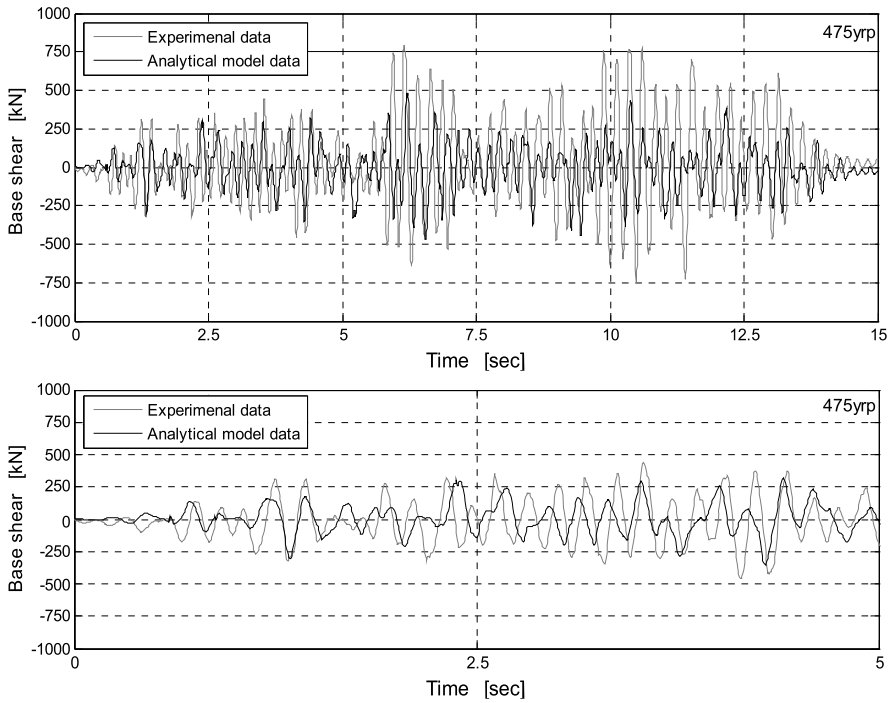
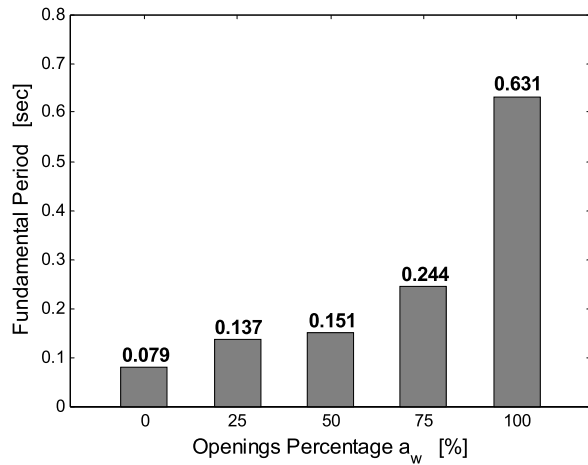


Fig. 12 Comparison of the Base Shear of the experimental infilled frame and the corresponding analytical model (475 yrp record)

Fig. 13 Variation of fundamental period with opening size

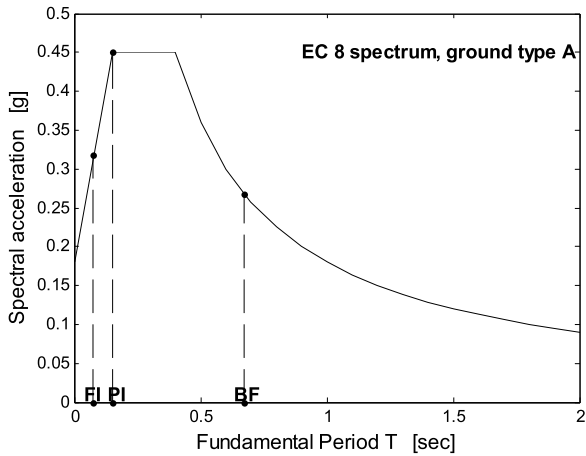


shows the variation of the fundamental period with the opening percentage. All values are also presented in a tabular form (Table 2), where the mass contribution for the fundamental period is given as well. The fundamental period increases as the

Table 2 Fundamental periods and mass contributions of various percentage openings

Openings α_w [%]	Period [sec]	Mass contribution [%]
0	0.079	59.48
25	0.137	85.76
50	0.151	88.33
75	0.244	87.26
100	0.631	83.02

Fig. 14 Elastic acceleration spectra for a 475 yrp and the fundamental periods of a fully infilled frame (FI), a partially infilled frame (PI) and a bare frame (BF)

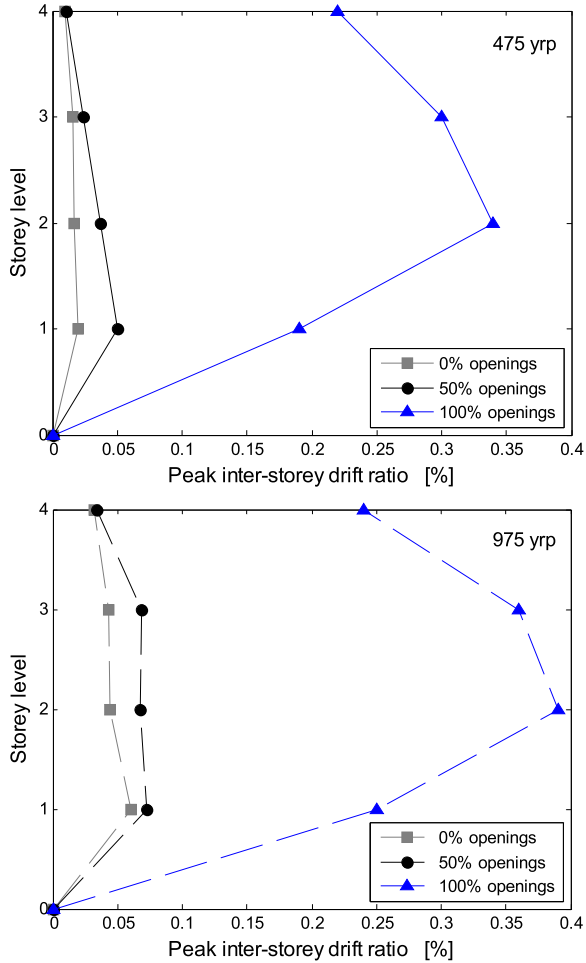


opening size increases, as expected, due to stiffness reduction of the model. Such variation of periods cannot be considered using the formulas proposed by design codes. There is no clear relationship between the opening size and the fundamental period, but the opening size does have an influence on the fundamental period of the structure.

By comparing the fundamental periods of a fully infilled (FI) and a bare frame (BF), a difference of magnitude of roughly 9 is observed, which is in agreement with the literature.

An elastic spectrum according to the standard EC 8 [60] for ground type A was chosen, as can be seen in Fig. 14. In this figure, the periods of the idealized systems representing the fully infilled frame ($T = 0.079$ s), the partially infilled frame (with 50 % of openings) ($T = 0.151$ s) and the bare frame ($T = 0.631$ s) are indicated. It can be observed that the spectral acceleration, which corresponds to the bare frame (BF), is only about half of the spectral acceleration, which corresponds to the partially infilled frame (PI) and a bit lower than the corresponding value for a fully infilled frame (FI). It is clear that such a variation of the period of vibration will have a considerable effect on the dimensioning of the infilled-frame members.

Fig. 15 Peak inter-story drift at each story level (475 and 975 yrp)



4.6 Effect of Openings on Inter-story Drift Ratios

The displacement variation along the building height is a typical way of illustrating the behavior of a building in each story. A better representation of the above is the use of the inter-story drift curve given in Fig. 15.

This figure shows the peak inter-story drift ratio during the time-history analysis. The ‘weakness’ of the second floor is more pronounced when larger openings in the infill panels are present. Three different cases of openings are illustrated and the resulting inter-story drift ratio confirms the previous statement. This figure is produced for acceleration time-histories of increasing return periods of 475 and 975 years. The 975 yrp analysis gives, as expected larger peak story drifts for all various openings. The same conclusion was reached by Dorji et al. [61], who presented the inter-story drifts ratios for three different opening percentages.

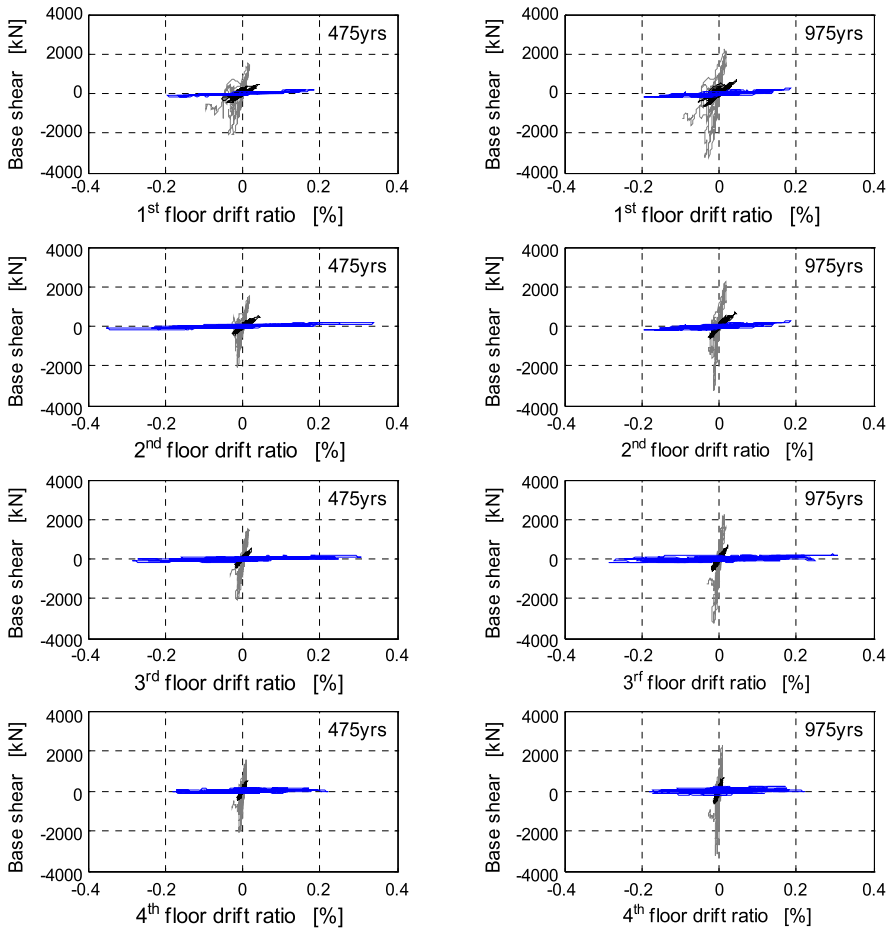


Fig. 16 Response-history of base shear with 1st, 2nd, 3rd and 4th floor drift ratio for 0 %, 50 % and 100 % open

Another way to demonstrate the influence of different percentage openings of the infilled panels is the plot of base shear vs. inter-story drifts (Fig. 16). It can be clearly seen, that the bare frame ($\alpha_w = 100\%$) has the highest inter-story drift and at the same time the lowest base shear value. On the other hand, the fully infilled frame ($\alpha_w = 0\%$) has the lowest drift-values and the highest base-shear value, which is expected.

The variation of the base shear and top displacement with different infilled panel openings (α_w) is examined in Fig. 17. A quadratic function to both data is fitted, implying the relationship between base shear and displacement. Also, the variation of base shear with the increasing opening-size of the infilled panels is similar to the variation of the stiffness reduction factor λ with the opening-size, presented in Fig. 6.

Fig. 17 Inter-story drift showing the soft-story effect after 15 load cycles (475 yrp)

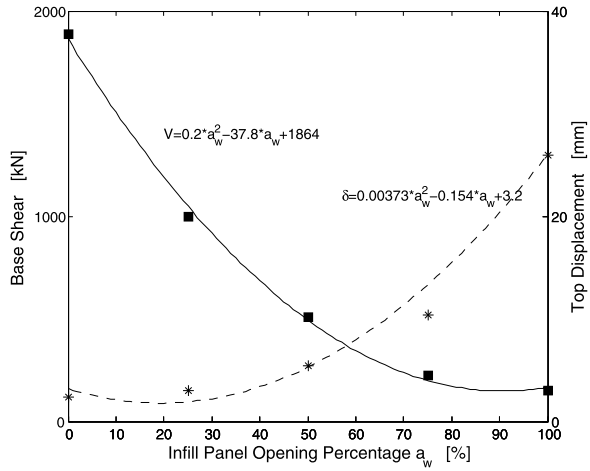
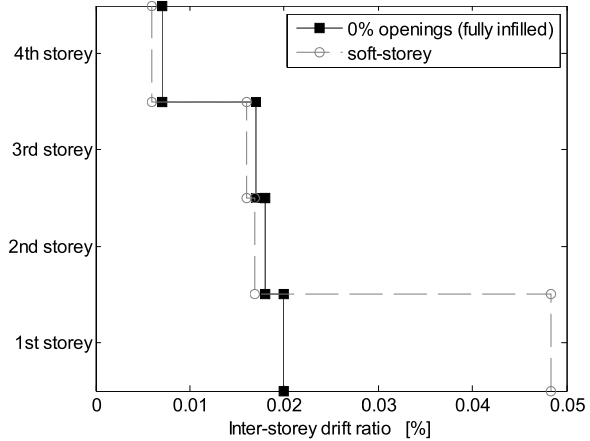


Fig. 18 Inter-story drift showing the soft-story effect after 15 load cycles (475 yrs)



The applicability of the proposed procedure for representing the openings in the walls was examined by introducing a ‘pilotis’, which may cause the soft-story phenomenon during dynamic earthquake loads. This study investigated this problem by comparing two models:

- (a) A structure with fully infilled frames throughout the height of the building.
- (b) A structure which does not have any infill at the first floor but has fully infilled frames in the rest of the floors, representing the presence of a ‘pilotis’.

From Fig. 18, which shows the peak values of inter-story drift ratios, it can be concluded that there is a strong soft-story effect, which is captured by the proposed modeling. The drift ratio value at the ground floor for case (b) is increased almost 3 times when compared to case (a).

5 Conclusions

In this chapter the attempts of researchers through many decades to model infill walls are summarized and the most commonly used macromodels are presented. One of the main difficulties to introduce infill walls, which are universally accepted as having a significant influence in the response of frames in the modeling of structures, is the absence of a way to represent openings in the infills. In this work, a reduction factor, λ , is proposed that can be used as a multiplication factor on well known equations to calculate the reduced equivalent width of compression struts, so as to be able to model infill walls with openings. The same reduction factor can be used in models of multiple-struts, so as to be able to idealize the nonlinear behavior of infill walls with openings.

Using this approach, a two-strut model, which was calibrated on experimental results, was used to examine the effects of openings on the period of vibration of infilled structures with openings and on inter-story drifts. A sensitivity analysis allowed to observe the influence of the parameters controlling the hysteresis rules of the infill strut model on the displacement demand, thus highlighting the need of paying special attention to the choice of these parameters.

It was shown that, as expected, the period of vibration of the structures is largely affected by the presences of openings, which in turn has an effect on the earthquake load that such structures will be subjected-to during an earthquake. The period of vibration of the infilled frame was found to be 9 times smaller than that of the bare frame, with the periods of vibration of the frames with openings to be in-between, but without a clear trend.

Regarding the inter-story drifts, it is shown that at the beginning of the analysis, when the infill and the structure are still in linear behavior, the bare frame has inter-story drifts of the order of 2 times larger than those of the fully infilled frame. When the structure moves into more cycles, this difference goes as high as 3 times larger.

It can be therefore concluded, that the proposed reduction factor can be used to model infill frames with openings with satisfactory results. Further work needs to be done, using a larger number of ground motions and frame configurations, so as to fully validate this methodology.

References

1. El-Dakhkhni WW, Elgaaly M, Hamid AA (2003) Three-strut model for concrete masonry-infilled frames. *J Struct Eng* 129(2):177–185
2. Kose MM (2009) Parameters affecting the fundamental period of RC buildings with infill walls. *Eng Struct* 31:93–102
3. Smith BS (1966) Behavior of square infilled frames. *J Struct Div* 92(ST1):381–403
4. Smith BS, Carter C (1969) A method of analysis for infilled frames. *Proc Inst Civ Eng* 44:31–48
5. Page AW, Kleeman PW, Dhanasekar M (1985) An in-plane finite element analysis model for brick masonry. In: *Proceedings of a session held in conjunction with Structures congress '85*, Chicago, pp 1–18

6. Mehrabi AB, Shing PB, Schuller M, Noland J (1966) Experimental evaluation of masonry-infilled RC frames. *J Struct Eng* 122(3):228–237
7. Buonopane SG, White RN (1999) Pseudodynamic testing of masonry infilled reinforced concrete frame. *J Struct Eng* 125(6):578–589
8. Santhi MH, Knight GMS, Muthumani K (2005) Evaluation of seismic response of soft-storey infilled frames. *Comput Concr* 2(6):423–437
9. Santhi MH, Knight GMS, Muthumani K (2005) Evaluation of seismic performance of gravity load designed reinforced concrete frames. *J Perform Constr Facil* 19(4):277–282
10. Asteris PG, Kakaletsis DJ, Chrysostomou CZ, Smyrou EE (2011) Failure modes of infilled frames. *Electron J Struct Eng* 11(1):11–20
11. Liauw TC, Kwan KH (1984) Nonlinear behaviour of non-integral infilled frames. *Comput Struct* 18:551–560
12. Dhanasekar M, Page AW (1986) Influence of brick masonry infill properties on the behaviour of infilled frames. *Proc Inst Civ Eng 2 Res Theory* 81:593–605
13. Chrysostomou CZ (1991) Effects of degrading infill walls on the nonlinear seismic response of two-dimensional steel frames. PhD thesis, Cornell University, Ithaca
14. Saneinejad A, Hobbs B (1995) Inelastic design of infilled frames. *J Struct Eng* 121(4):634–650
15. Chrysostomou CZ, Gergely P, Abel JF (2002) A six-strut model for nonlinear dynamic analysis of steel infilled frames. *Int J Struct Stab Dyn* 2(3):335–353
16. Asteris PG (2003) Lateral stiffness of brick masonry infilled plane frames. *J Struct Eng* 129(8):1071–1079
17. Moghaddam HA (2004) Lateral load behavior of masonry infilled steel frames with repair and retrofit. *J Struct Eng* 130(1):56–63
18. Asteris PG (2005) Closure to lateral stiffness of brick masonry infilled plane frames by P.G. Asteris. *J Struct Eng* 131(3):523–524
19. Asteris PG (2008) Finite element micro-modeling of infilled frames. *Electron J Struct Eng* 8:1–11
20. Kakaletsis DJ, Karayannis CG (2009) Experimental investigation of infilled reinforced concrete frames with openings. *ACI Struct J* 106(2):132–141
21. Asteris PG, Giannopoulos IP, Chrysostomou CZ (2012) Modeling of infilled frames with openings. *Open Constr Build Technol J* 6:81–91
22. Makarios TK, Asteris PG (2012) Numerical investigation of seismic behavior of spatial asymmetric multi-storey reinforced concrete buildings with masonry infill walls. *Open Constr Build Technol J* 6:113–125
23. Asteris PG, Cotsvos DM (2012) Numerical investigation of the effect of infill walls on the structural response of RC frames. *Open Constr Build Technol J* 6:164–181
24. Moghaddam HA, Dowling PJ (1987) The state of the art in infilled frames. ESEE research report 87-2, Imperial College of Science and Technology, Civil Engineering Department, London
25. Asteris PG, Antoniou ST, Sophianopoulos DS, Chrysostomou CZ (2011) Mathematical macromodeling of infilled frames: state of the art. *J Struct Eng* 137(12):1508–1517
26. Chrysostomou CZ, Asteris PG (2012) On the in-plane properties and capacities of infilled frames. *Eng Struct* 41:385–402
27. Thomas FG (1953) The strength of brickwork. *Struct Eng* 31(2):44–46
28. Wood RH (1958) The stability of tall buildings. *Proc Inst Civ Eng* 11:69–102
29. Mainstone RJ (1962) Discussion on steel frames with brickwork and concrete infilling. *Proc Inst Civ Eng* 23:94–99
30. Wood RH (1959) Discussion on the stability of tall buildings. *Proc Inst Civ Eng* 12:517–518
31. Polyakov SV (1960) On the interaction between masonry filler walls and enclosing frame when loading in the plane of the wall. In: Translation in earthquake engineering. Earthquake Engineering Research Institute, San Francisco, pp 36–42
32. Holmes M (1961) Steel frames with brickwork and concrete infilling. *Proc Inst Civ Eng 2 Res Theory* 19:473–478

33. Smith BS (1962) Lateral stiffness of infilled frames. *J Struct Div* 88(ST6):183–199
34. Smith BS (1967) Methods for predicting the lateral stiffness and strength of multi-storey infilled frames. *Build Sci* 2:247–257
35. Hetenyi M (1946) *Beams on elastic foundations*. University of Michigan Press, Ann Arbor
36. Mainstone RJ (1971) On the stiffnesses and strengths of infilled frames. *Proc Inst Civ Eng Suppl* (iv):57–90
37. Mainstone RJ, Weeks GA (1970) The influence of bounding frame on the racking stiffness and strength of brick walls. In: *Proceedings of the 2nd international brick masonry conference*. Building Research Establishment, Watford, pp 165–171
38. Mainstone RJ (1974) Supplementary note on the stiffness and strengths of infilled frames. Current paper CP 13/74, Building Research Station, Garston, Watford
39. Federal Emergency Management Agency (1997) NEHRP commentary on the guidelines for the seismic rehabilitation of buildings. FEMA-274, Applied Technology Council, Washington
40. Federal Emergency Management Agency (1998) Evaluation of earthquake damaged concrete and masonry wall buildings: basic procedures manual. FEMA-306, Applied Technology Council, Washington
41. Reflak J, Fajfar P (1991) Elastic analysis of infilled frames using substructures. In: *Proceedings of the 6th Canadian conference on earthquake engineering*, Toronto, pp 285–292
42. Symakezis CA, Vratsanou VY (1986) Influence of infill walls to R.C. frames response. In: *Proceedings of the eighth European conference on earthquake engineering*, Lisbon, vol 3, pp 47–53
43. Liauw TC, Kwan KH (1983) Plastic theory of infilled frames with finite interface shear strength. *Proc Inst Civil Eng 2 Res Theory* 75:707–723
44. Liauw TC, Kwan KH (1983) Plastic theory of non-integral infilled frames. *Proc Inst Civil Eng 2 Res Theory* 75:379–396
45. Klingner RE, Bertero VV (1976) *Infilled frames in earthquake-resistant construction*. Report EERC 76-32, University of California, Berkeley
46. Soroushian P, Obaseki K, Choi K-B (1988) Nonlinear modeling and seismic analysis of masonry shear walls. *J Struct Eng* 114(5):1106–1119
47. Crisafulli FJ (1997) *Seismic behaviour of reinforced concrete structures with masonry infills*. PhD thesis, University of Canterbury, Christchurch
48. Crisafulli FJ, Carr AJ (2007) Proposed macro-model for the analysis of infilled frame structures. *Bull New Zealand Soc Earthq Eng* 40(2):69–77
49. Carr AJ (2004) RUAUMOKO: inelastic dynamic analysis. Department of Civil Engineering, University of Canterbury. <http://www.ruauumoko.co.nz>
50. SeismoSoft (2009) *SeismoStruct—a computer program for the static and dynamic analysis of framed structures*. <http://www.seismosoft.com>
51. Smyrou E (2006) *Implementation and verification of a masonry panel model for nonlinear dynamic analysis of infilled rc frames*. Dissertation for the MSc in earthquake engineering, European School for Advanced Studies in Reduction of Seismic Risk (ROSE SCHOOL), Università degli Studi di Pavia
52. Smyrou E, Blandon-Uribe C, Antoniou S, Pinho R, Crowley H (2006) Implementation and verification of a masonry panel model for nonlinear pseudo-dynamic analysis of infilled RC frames. In: *Proceedings of the first European conference on earthquake engineering and seismology*, Geneva
53. Pinto A, Verzeletti G, Molina J, Varum H, Pinho R, Coelho E (1999) Pseudo-dynamic tests on non-seismic resisting RC frames (bare and selective retrofit frames). Joint Research Centre, Ispra
54. Campos-Costa A, Pinto AV (1999) European seismic hazard scenarios—an approach to the definition of input motions for testing and reliability assessment of civil engineering structures. JRC special publication X.99.XX, ELSA, JRC, Ispra
55. Dolšek M (2009) Incremental dynamic analysis with consideration of modeling uncertainties. *Earthq Eng Struct Dyn* 38(6):805–825

56. Vamvatsikos D, Fragiadakis M (2009) Incremental dynamic analysis for estimating seismic performance sensitivity and uncertainty. *Earthq Eng Struct Dyn* 39(2):141–163
57. Celarec D, Dolšek M (2010) The influence of epistemic uncertainties on the seismic performance of RC frame building. In: *Proceedings of the 14th European conference on earthquake engineering*, paper 534
58. Celarec D, Ricci P, Dolšek M (2012) The sensitivity of seismic response parameters to the uncertain modelling variables of masonry-infilled reinforced concrete frames. *Eng Struct* 35:165–177
59. ASCE Standard ASCE/SEI 41-06 (2007) *Seismic rehabilitation of existing buildings*. American Society of Civil Engineers
60. CEN (2004) *Eurocode 8: design of structures for earthquake resistance. Part I: General rules, seismic action and rules for buildings*. Brussels
61. Dorji J, Thambiratnam DP (2009) Modelling and analysis of infilled frame structures under seismic loads. *Open Constr Build Technol J* 3:119–126

Numerical Evaluation of the Seismic Efficiency of Connections of Fractures and Complements of Ancient Colonnades

Maria-Eleni Dasiou, Ioannis N. Psycharis, and Antigone Vrouva

Abstract As a common practice, restoration projects of ancient colonnades have to deal with joining together fragments of architectural members using threaded titanium bars (reinforcement) fixed into place with cement mortar. The basic criterion for the design of such connections is that, in case of a seismic event, the reinforcement should absorb the seismic energy and fail before the marble suffers any damage. For the dimensioning of these connections, the capacity design concept is usually implemented. In this chapter, the efficiency of the reinforcement of the connection calculated with this methodology is investigated for selected severe seismic excitations. The analyses were performed for two case studies with different geometries: a column of the Parthenon Pronaos and the Southern colonnade of the Ancient Agora of Kos in Greece. The induced forces were calculated using the distinct element method. The results show that the design is adequate, as the stresses induced to the reinforcement bars were always less than their ultimate strength and, in many cases, considerably less than their yield resistance as well.

Keywords Restoration of monuments · Design of connections · Fractures · Earthquake performance · Rocking

1 Introduction

Ancient colonnades consist of stone blocks of different sizes and shapes made of marble, stiff limestone or porous stone, depending on the available material in the nearby region. Typically, the blocks are not connected to each other and the structure

M.-E. Dasiou · I.N. Psycharis (✉) · A. Vrouva
School of Civil Engineering, National Technical University of Athens,
9, Heroon Polytechniou Str., Zografos, 15780, Greece
e-mail: ipsych@central.ntua.gr

M.-E. Dasiou
e-mail: medasiou@yahoo.com

A. Vrouva
e-mail: a_vrouva@hotmail.com

behaves as a system of discrete blocks, except of connectors (clamps and dowels) that are provided in certain places only. In current restoration practice, ancient mortises that are preserved in such places are used to connect the stone blocks with new clamps and dowels made of titanium. The basic principle that is followed for the design of the new connectors is that, in case of a seismic event, the connectors should absorb the seismic energy and fail before the surrounding marble suffers any damage.

Apart from the connectors, the use of titanium bars is also common for joining together fragmented ancient blocks or fragments of blocks with new complements so as to restore the unity of each discrete element of the ancient structure. The principle in designing the bars that are used as reinforcement is that those should bear the induced forces in a seismic event and maintain the discrete block as a whole, while the marble does not suffer any damage.

In general, the design of the restoration anticipates the following sequence of response: The joints between independent blocks are the first to be activated. This does not necessarily imply engagement of the connectors (clamps and dowels), because, typically, there is a gap between them and the mortises of the stones. However, forces are induced to the connections between blocks and new complements. When the movements of the blocks exceed certain values, the clamps and dowels are activated, reducing, in general, the forces applied to the restored interfaces of fracture. After the failure of the connectors (clamps and dowels), it is possible that rehabilitated members of the structure lose their integrity; in that event, the titanium bars of the reinforcement should yield prior to any other damage to the marble.

In order to follow the above-mentioned procedure for the design of the reinforcement of the complements, one should know the forces that will be induced to the connectors and the reinforcement during an earthquake. However, the calculation of these forces is not an easy task, since the response of the structure is governed by rocking and sliding of the individual stone blocks. Previous investigations [1–6] on the dynamic behavior of single freestanding columns and sub-assemblages of ancient temples have pointed out that the response of these discrete structures is highly nonlinear and very sensitive to even small changes in the parameters. Thus, the imposed excitation and the frequency content of the ground motion, the degree of the accuracy of the numerical model concerning the geometry of the structure and the assumptions adopted in the analysis (joint properties, friction coefficient, etc.) may affect significantly the results of even rigorous nonlinear analyses. For this reason, the dynamic analyses of such structures contain an inherent uncertainty and their outcomes should be used with caution.

In practice, simplified analyses are usually applied for the design of the connections that are implemented during interventions. These analyses are based on the capacity design concept, thus they end up with the maximum forces that can be developed theoretically, independently of the earthquake excitation. In this chapter, the efficiency of connections of complements, which have been designed by such methodologies, under strong earthquake excitations, is investigated. For this purpose, nonlinear numerical analyses are performed using the discrete element method and the forces induced to the reinforcements are compared with their strength.

2 Principles of Intervention

2.1 *General Philosophy*

Restoration projects nowadays follow very specific guidelines in order to ascertain the required quality of the intervention. The main scope is the minimum, yet necessary and sufficient, intervention in the monument's inherent characteristics. Of main importance is the respect for the original building techniques, the original structural system and the original materials. Authenticity is a beyond debate concern and goal of the project, in order to maintain the monument at the best possible status and to minimize the alterations. Additional requirements might be reversibility, meaning the ability to revert the monument to its previous—before the restoration—state, maintenance of the structural function and consistency of the individual architectural members.

The use of new material for the complement of missing parts of structural elements is generally restricted to the absolutely necessary and must be kept in a low proportion compared to the original material. Such decisions must not be based only on stability issues, but also take under consideration the forms and volumes, the visitor's perception of the monument and aesthetic issues. It should be kept in mind that the main "recipients" of the monuments are their visitors and that the cultural heritage that they carry is not addressed to scholars and connoisseurs only, but mainly to the public.

2.2 *Structural Restoration*

The term 'structural restoration' signifies the series of interventions that are necessary to ensure the bearing capacity of the structure and of its individual parts. To this end, restoration of the connectors between the structural elements and re-composition of the original geometry of the stone pieces that were retrieved during the excavation by connecting fragments and/or complement of stone elements is deemed necessary in many cases.

In antiquity, the connection elements were made of bronze or iron and were covered with lead, cast in the mortises, which after its congelation offered high insulation to the metallic connectors, protecting them from the oxidization and the corrosion. At the same time, the connectors, being ductile materials, contributed to the overall behavior of the structure in case of an earthquake. Two types of connectors were used: dowels, which connected elements between consequent layers along the height and resisted the shear forces; and clamps, which connected stones belonging to the same layer and prevented their relative dislocation through their tensile resistance. In the ultimate limit state, the dowels and the clamps were meant to fail before the failure of the stone.

In many restorations realized in the 19th and the 20th century, the structural steel that was used in typical constructions was applied also to monuments for the enhancement of their bearing capacity and for the connection of fragments of architectural members. The steel elements were usually cast in lead, as a follow up of the ancient practice. Cement mortars were widely used for covering mass lacks. This technique caused significant damage to the monuments, because the cast lead failed to reassure the same impermeability as the ancient one and environmental actions, due to their intense corrosive character, led to iron's oxidization and subsequently to fracture of the architectural members.

In modern restoration projects, mostly inorganic materials are adopted, in order not to provoke any additional problems in the long term. Thus, for the connections between restored members of the monument (clamps and dowels), specially formed titanium sheets are commonly used, fixed in place with the use of inorganic mortars. Similarly, for joining together fragments and/or complements, threaded titanium bars are applied.

2.3 Design of the Connections

The ancient and the new pieces are typically connected with titanium threaded bars that are inserted in properly drilled holes and fixed into place by mortar. Mortar is also used as the bonding material at the interface of the fraction. As mentioned above, a proper dimensioning of the reinforcement would require difficult nonlinear analyses, which are seldom performed in practice. Usually, analyses based on the capacity design concept are performed [7, 8], which lead to the required reinforcement for resisting the maximum forces that can be induced, without restoring completely the strength of the original material. In example, the design of the connection of fractured architraves is based on the assumption that the architrave is subjected mainly to bending under increased gravity loads by a factor about 1.50; for the connection of fragments at column drums, the required reinforcement is calculated from equilibrium conditions of the complement piece under capacity actions that include the friction forces, assuming that sliding occurs at the joint, and the ultimate resistance of any existing dowels.

3 Case Studies—Description of the Monuments

3.1 Parthenon Pronaos

The first case study concerns the restored part of the Parthenon's Pronaos, situated in the Athenian Acropolis, namely part of the prostyle (prostylon).

The structural system of the ancient temple is well known and thoroughly investigated by scholars and restorers that have studied the monument (e.g. [9]). All the

blocks were of white marble derived from the Penteli quarry. The columns were of Doric style with fluting. The prostyle had 6 columns of 12 drums each of uneven height, a capital and a three part architrave (epistyle) and bore a frieze and cornice. The connection with the walls of the main cella was realized at the level of the architraves.

The prostyle suffered extend damages due to the historical fire when the Eruli set fire to the temple and a large part of it collapsed at the bombardment during the Turkish-Venetian war. Alterations in its original structural scheme were made in various historical in-stances throughout the centuries. The former restorers stripped the monument of the additions and structural alterations that did not be-long to the original ancient plan.

In situ were preserved the first column in height of 2 drums, the second in height of only one, the third and fourth in height of 3 drums, the fifth in height of 4 drums and the sixth was complete bearing also its capital. It was decided that since a large part of the column drums rested on the ground and had been attributed to that part of the monument (22 drums and 4 capitals) a restoration was to be carried out [10, 11]. More specifically the first and second column was to be restored to the height of the 6th drum, the third to the 8th drum whereas the fourth and fifth to their full height and their capitals so as to reassemble two blocks of the fifth architrave and one of the fourth.

The columns had a base diameter of 0.82 m. The axial distance between the columns was approximately 3.6 m for the sixth and fifth and 4.2 m for the fifth and fourth and their overall height 9.39 m. The diameter of the capital was 0.625 m and its height 0.69 m, while the abacus had plan dimensions 1.65 m \times 1.65 m and height equal to 0.35 m.

In the analyses presented in this chapter, a full column with its capital is used.

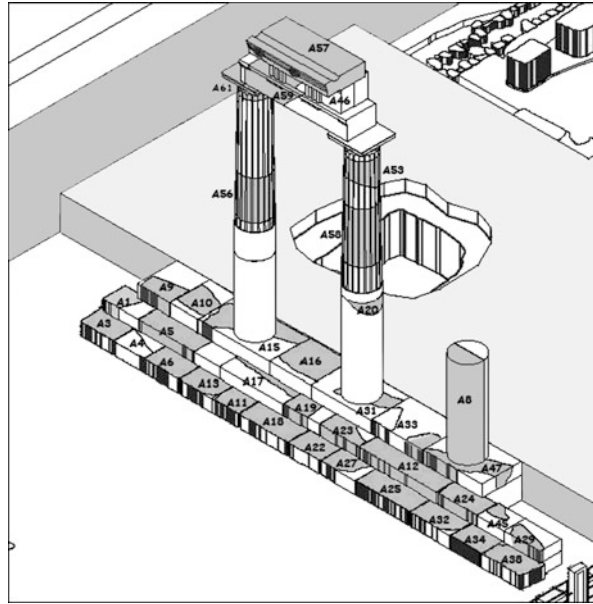
3.2 Part of the Southern Arcade (Stoa) of the Ancient Agora in the Island of Kos

The second case study is based on the part of the southern Arcade (Stoa) of the Ancient Agora in the island of Kos in Greece that has been proposed to be restored. The monument is situated in the center of the modern city of Kos.

An unexpectedly large number of structural members were found in situ. The location where the members were found and the study of the mortises of the connectors confirmed that they derived from specific parts of the building. Thus, the 'erection' of a small part of the Stoa was proposed, using a significant portion of the found ancient members.

The restoration project concerns three columns of the Stoa with the respective parts of the crepis and the entablature (Fig. 1). In this restoration, 37 from the 62 ancient members are to be used. In addition, seven new blocks are to be used to ensure the stability of the structure and, also, for aesthetic reasons.

Fig. 1 Drawing of the restoration proposal. The ancient members and fragments are shown in *gray* and the members and complements that will be made of new marble are shown in *white*



The original structure rested on a two-layer base of height 0.55 m, made of porous blocks that lied under the crepidoma (crepis). The crepis consisted of two steps and the stylobate. The first step had height 0.33 m and was made of gray limestone blocks of varying plan dimensions (their length was varying from 0.60 to 1.40 m and their width from 0.50 to 0.70 m). The second step had height 0.29 m and was made of marble blocks of the same overall dimensions. The stylobate was made of marble blocks of height 0.30 m, width about 1.00 m and varying length.

The marble columns of the Stoa were of Doric style without fluting at their lower part, up to a height of 2.07 m. The columns consisted of four drums of uneven height with base diameter 0.78 m. The axial distance between the columns was 2.66 m and their overall height was 5.61 m. The diameter of the capital was 0.635 m and its height was 0.38 m, approximately, while the abacus had plan dimensions 0.85 m \times 0.85 m and height equal to 0.11 m.

The architraves consisted of single blocks, 2.66 m in length, 0.71 m in width and 0.47 m in height. The frieze was made of blocks 1.73 m in length and 0.59 m in height that included two triglyphs and two metopes. Those blocks were either single of full width (\sim 0.47 m) or were supplemented by other blocks of approximately the same dimensions that completed the width of the layer; the latter is the case of the part of the structure that is considered in this analysis. The cornice had height 0.42 m and was projecting 0.325 m. The block that will be used in the restoration is 1.95 m long.

4 Numerical Analysis

4.1 General

The structural and the dynamic analysis of ancient temples or sub-assemblages of ancient temples differ significantly from the analysis carried out for modern structures, mainly because of their articulate construction. During a seismic event, rocking and/or sliding of the stones, independently or in groups, may occur, which results in highly nonlinear behavior [1–6]. Additionally, the response is very sensitive to the details of the geometry, the characteristics of the ground motion and the joint parameters.

The complexity and the special character of the response of the structure (rocking and sliding) create computational requirements hard to meet with the incorporation of conventional software. For the numerical analyses presented herein, the code 3DEC by Itasca Consulting Group, Inc. [12] was employed, which is based on the discrete element method. The code is designed to allow significant displacements and rotations of the blocks, even total detachment. During the calculation process, the code locates the contacts between the blocks and computes the motion of each block from the forces (normal and shear) that are developed at the joints. The contacts are divided in sub-surfaces, while various types of contact are considered (apex to apex, apex to edge etc.). In this way, rocking and sliding are accurately addressed.

The code 3DEC has been verified and calibrated for the response of ancient colonnades through comparisons of the numerical results with experimental data obtained from shaking table tests performed at the Laboratory for Earthquake Engineering of the National Technical University of Athens [2, 4–6].

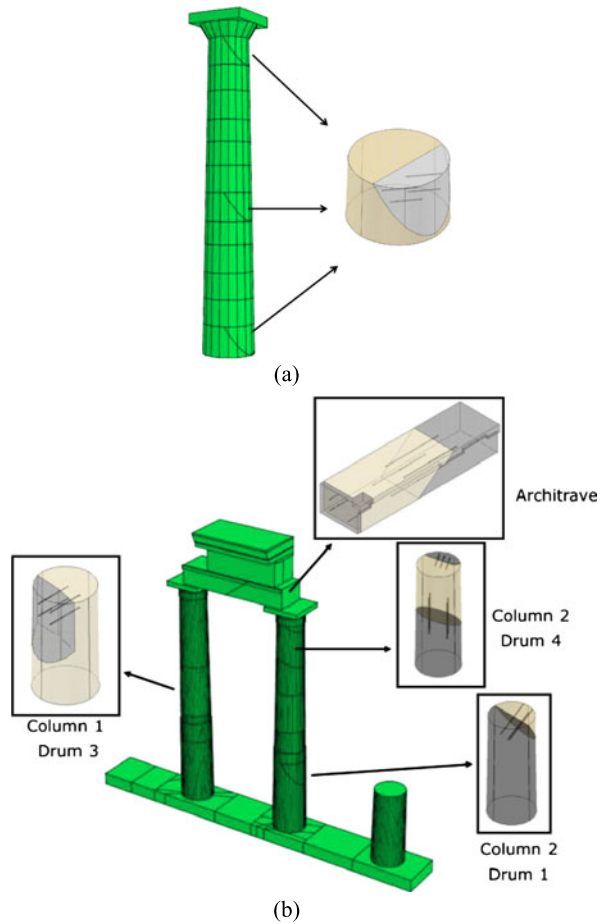
4.2 Numerical Model

Although the numerical models used in the analyses were based on the actual restoration proposals, the investigation presented herein is not meant to be applicable only to the specific cases but to evaluate the design procedure in general. The case studies were selected as typical examples, but with considerable differences in their dimensions, being thus representative of many monuments. For this reason, in the case of the column of the Parthenon fictitious complements were considered in three drums (one at the top, one at the middle and one at the base of the column) in an attempt to cover all possible situation that can be encountered in practice.

The connections between the ancient fragments and the new complements were assumed from titanium bars and were designed according to the above-mentioned methodology. The exact geometry and dimensions of the reinforcement were implemented in the numerical models (Figs. 2a and 2b).

The mortar typically used at the interfaces of the connected blocks was not considered, because its actual mechanical properties cannot be precisely defined. In addition, the dowels and the clamps were not included in the numerical model, because

Fig. 2 Numerical model of (a) the column of Parthenon Pronaos and (b) the part of the southern Arcade of the Ancient Agora [Kos] used in the analyses with 3DEC. Details of the connections considered in the model are also shown



sliding can occur before these connectors are activated, since a gap of 1 to 2 cm, not filled with mortar, is commonly left between them and the edge of the mortises. Both assumptions are to the safety side and lead to the upper limit of the forces that can be induced to the reinforcement.

The analyses were performed assuming that all the structural elements are rigid blocks. The joint properties used in the model were based on former studies [2, 4–6]: the joint stiffness was equal to 5×10^9 Pa/m in the normal direction and 1×10^9 Pa/m in the tangential direction while the friction coefficient was taken equal to 0.75. A 10 % mass-proportional damping at $f = 0.3$ Hz was also considered.

The reinforcement (titanium bars) were simulated as nonlinear springs for which the elastic stiffness, the yield force and the ultimate strain were assigned in both the axial and the shear directions. Since pullout test results were not available, the following theoretical expressions, given in [13] and proposed by 3DEC [12], were used to estimate the axial stiffness, K_a and the shear stiffness, K_s :

$$K_a = \pi \cdot k \cdot d_1 \quad (1)$$

$$K_s = E_b \cdot I \cdot \beta^3 \quad (2)$$

where d_1 is the diameter of the reinforcement; E_b is the Young's modulus of the reinforcement material; and

$$k = \left[\frac{1}{2} \cdot G_g \cdot E_b / (d_2/d_1 - 1) \right]^{1/2} \quad (3)$$

in which G_g is the shear modulus of the grout; d_2 is the diameter of the hole; I is the second moment of area of the reinforcement element; and $\beta = [K/(4 \cdot E_b \cdot I)]^{1/4}$ with $K = 2 \cdot E_g/(d_2/d_1 - 1)$.

The ultimate axial strength, P_{ult} , and the shear strength, $F_{s,b}^{\text{max}}$, of the titanium bars were calculated using the formulas proposed in [14] and [15], respectively, and adopted by 3DEC [12]:

$$P_{\text{ult}} = 0.1 \cdot \sigma_c \cdot \pi \cdot d_2 \cdot L \quad (4)$$

$$F_{s,b}^{\text{max}} = 0.67 \cdot d_1^2 \cdot (\sigma_b \cdot \sigma_c)^{1/2} \quad (5)$$

where σ_c is the uniaxial compression strength of the marble (up to a maximum value of 42 MPa); L is the bond length; and σ_b is the yield strength of the reinforcement.

4.3 Seismic Input

As mentioned above, the case studies are used as examples of typical monuments and the analyses aim at investigating the effectiveness of connections in general. For this reason, the earthquake excitations were selected to cover a wide range of recorded ground motions with different characteristics, not necessarily representative of the specific sites of the considered monuments. Ten earthquake records were selected from the strong motion data bases: Cosmos Virtual Center; Pacific Earthquake Engineering Research Center (PEER); European Strong-Motion Database (ESD); National Observatory of Athens; Institute of Technical Seismology and Earthquake Resistant Structures (ITSAK), which had different frequency characteristics. Both horizontal components of each earthquake were applied as the base excitation. The selected earthquakes and their characteristics are shown in Table 1. In Fig. 3, the time-histories of the acceleration of the components that were applied in the transverse direction are shown. The response spectra of both horizontal components are presented in Fig. 4.

5 Results

For all the titanium bars that were used in the connections, the time histories of the axial and the shear forces were obtained from the analyses. Indicative results are

Table 1 Peak ground accelerations in the two horizontal components of the earthquake records considered in the analyses

Earthquake	PGA (g)	
	Longitudinal direction	Transverse direction
Imperial Valley, 1979	0.33	0.25
Lefkada, 2003	0.34	0.42
Aigio, 1995	0.49	0.53
Athens, 1999	0.15	0.23
Kalamata, 1986	0.24	0.27
Erzincan, 1992	0.51	0.25
Gazli, 1984	0.71	0.60
Irpinia, 1980	0.36	0.25
Landers, 1992	0.15	0.17
Northridge [Sylmar], 1994	0.84	0.60

shown in Fig. 5, where the time-histories of the axial force of the four reinforcement bars that were used to connect the two fragmented pieces of the architrave beam of the colonnade in Kos (Fig. 2b) are depicted.

From these results, the efficiency factor for each bar was derived as the ratio of the maximum uniaxial stress, $\sigma_{M,max}$, that was developed during each earthquake motion over the yield stress, σ_y . The uniaxial stress was calculated using the Von Misses yield criterion:

$$\sigma_M = \sqrt{\sigma^2 + 3 \cdot \tau^2} \quad (6)$$

where σ is the axial stress of the bar and τ is the shear stress. The yield stress σ_y and ultimate stress σ_u of the threaded titanium bars were taken equal to 330 MPa and 420 MPa, respectively.

From the analyses performed, it was found that collapse of the colonnade of the Ancient Agora of Kos occurs for four of the selected earthquakes, namely: Northridge, Irpinia, Erzincan and Gazli. The collapse mechanism for the Sylmar record of the Northridge earthquake is shown in Fig. 6. Since the main scope of this re-research was to evaluate the efficiency of the design of the reinforcement of the connections assuming that collapse does not occur, these records were not further examined for the case study of the monument in Kos.

For the remaining earthquakes, the accomplished efficiency factors of each of the four reinforcement bars that were applied at the connection of the architrave of the colonnade of the Ancient Agora are shown in Fig. 7. None of the bars reached its yield strength for the earthquakes examined.

The two lower reinforcement bars (No. 1 and 2), which were in tension under gravity loads, showed an efficiency factor about 0.60, and were not much affected by the base motion. This value is close to $1/\gamma_G$, where $\gamma_G = 1.5$ is the safety factor for the gravity loads that was used for the design of these reinforcements according to the methodology described above.

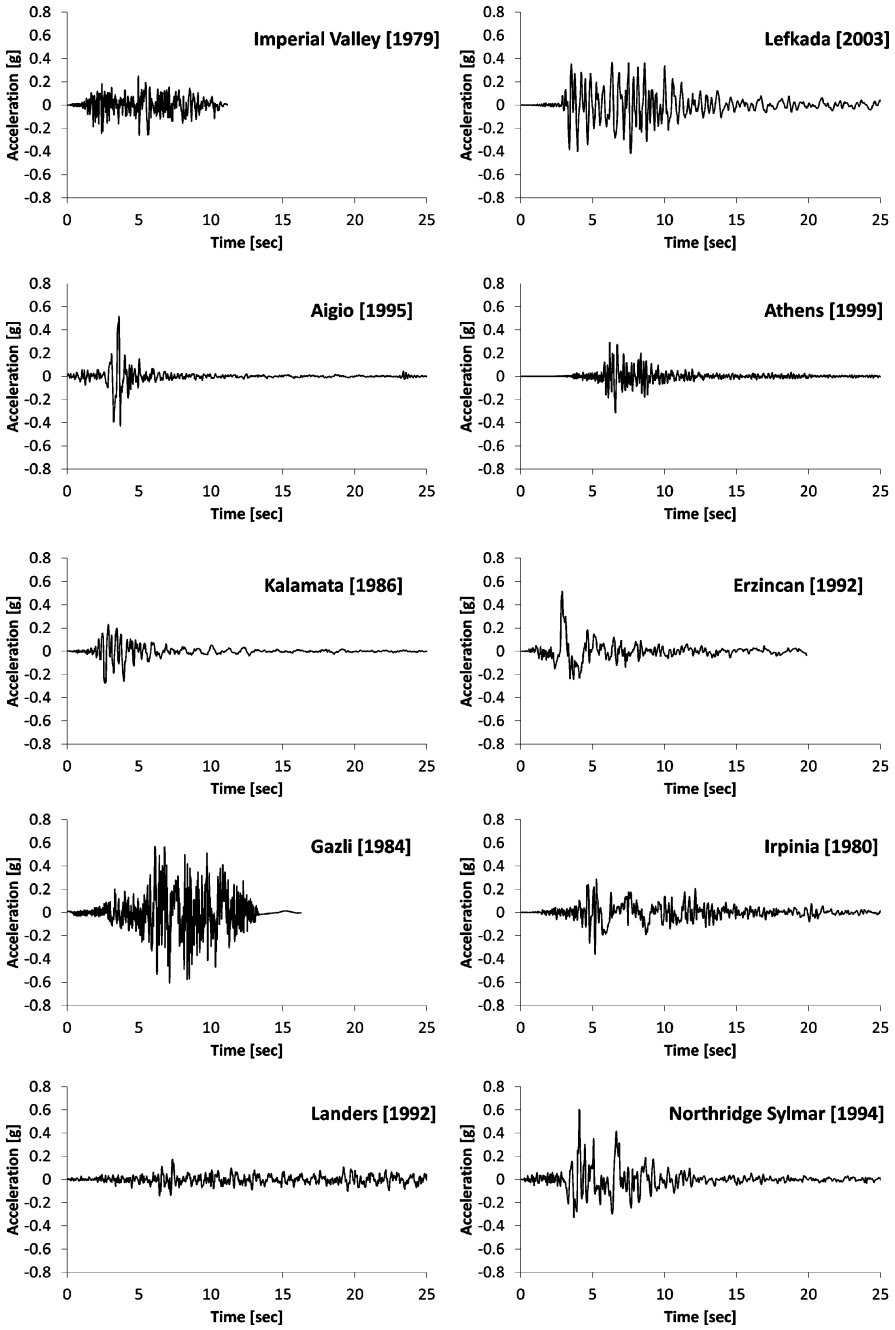


Fig. 3 Acceleration time-histories of the earthquake records applied in the transverse direction

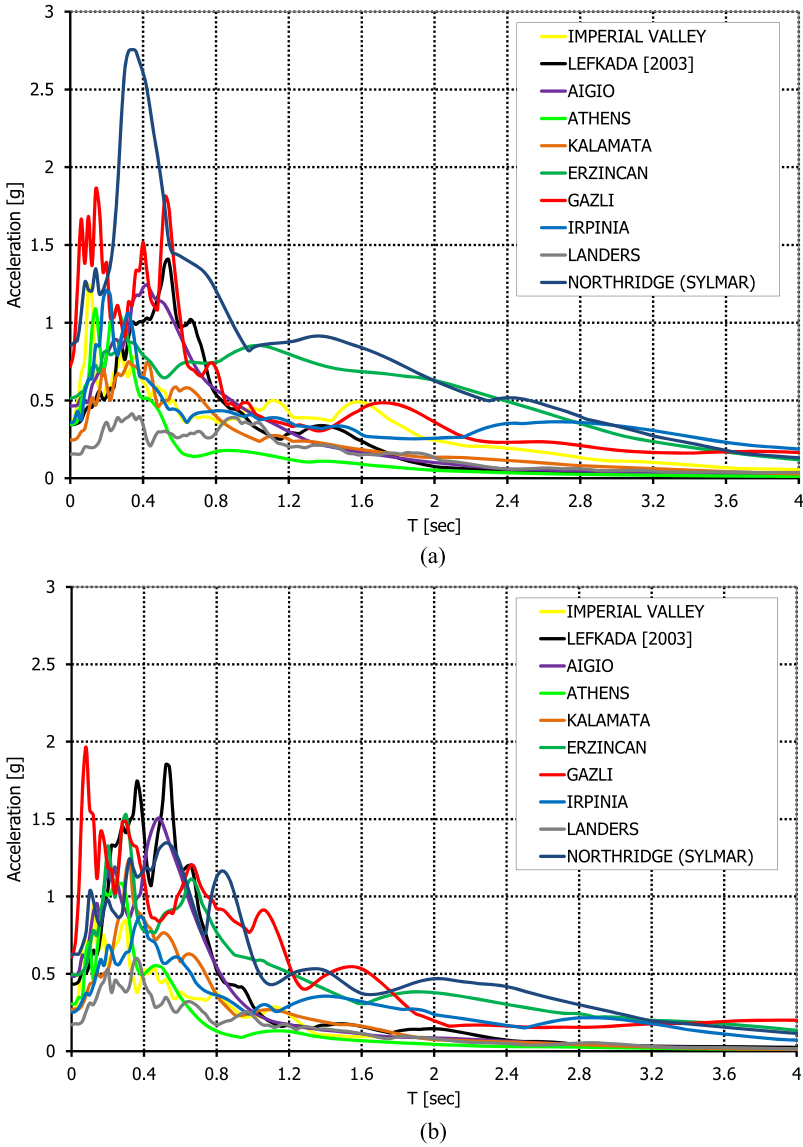
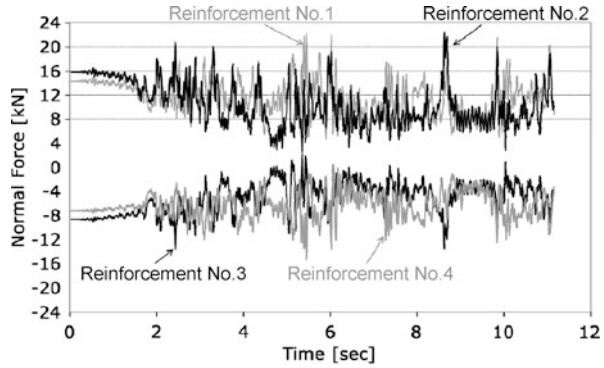


Fig. 4 Acceleration response spectra for 5 % damping of the horizontal components of the base motions that were applied in (a) the longitudinal direction and (b) the transverse direction of the structure

The upper reinforcement bars of the architrave (No. 3 and 4) were stressed significantly less for three of the earthquake excitations (Imperial Valley, Athens and Kalamata); however, large stresses were induced to these bars for the Lefkada and

Fig. 5 Time histories of the axial forces of the 4 titanium bars of the architrave connection of the colonnade in Kos for the Imperial Valley earthquake



the Aigion earthquakes, showing that large displacements occurred at the architrave during these ground motions.

Figures 8 to 13 show the efficiency factors of the reinforcement bars used for the connection of the fragments at the drums of the columns for both case studies. It can be observed that significantly different stresses were induced to the titanium bars for each type of fragmentation, depending on the place of the intervention along the height of the column.

The worst case was observed for fragments located at the bottom drum of a column (Figs. 9 and 11); in this case almost all bars yielded for most earthquake motions.

The smallest forces were induced to the connections of the uppermost drums, e.g. the third drum of column 1 of the colonnade in Kos (Fig. 8) and the 12th drum of the column of the Parthenon Pronaos (Fig. 12), where efficiency factors less than 0.70 and 0.50 respectively were achieved in most cases.

Forces close to yield were induced to the titanium bars of connections located around the middle-height of the columns, as at the fourth drum of column 2 of the colonnade in Kos (Fig. 10) and the 6th drum of the column of Parthenon (Fig. 12).

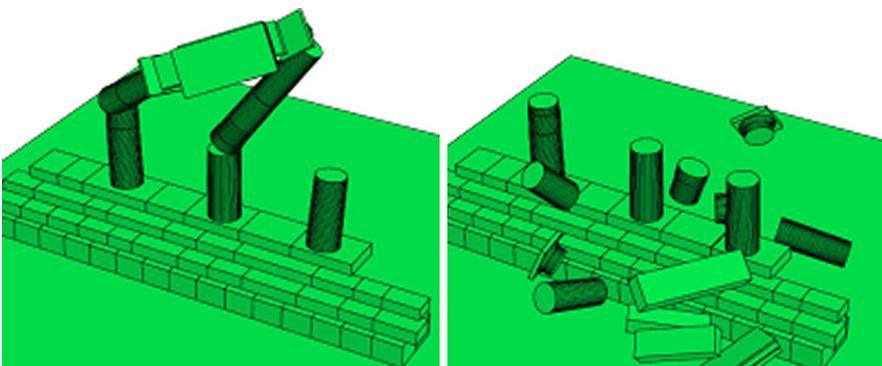


Fig. 6 Collapse mechanism of the monument in Kos for the Sylmar, Northridge, record

Fig. 7 Accomplished efficiency factors of the four titanium bars of the architrave connection of the colonnade in Kos for the five earthquake excitations that do not cause collapse of the monument

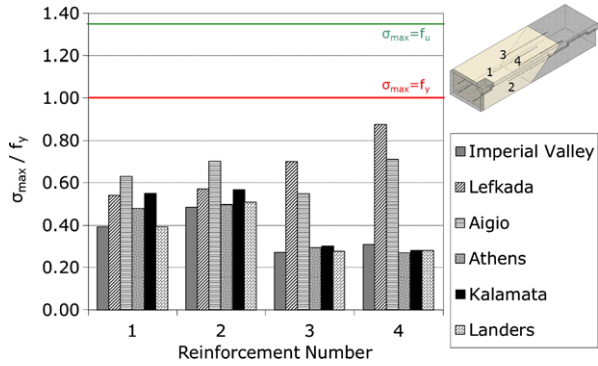


Fig. 8 Efficiency factors of the four titanium bars used for the complement of the third drum of column 1 of the colonnade in Kos for the five earthquake excitations that do not cause collapse of the monument

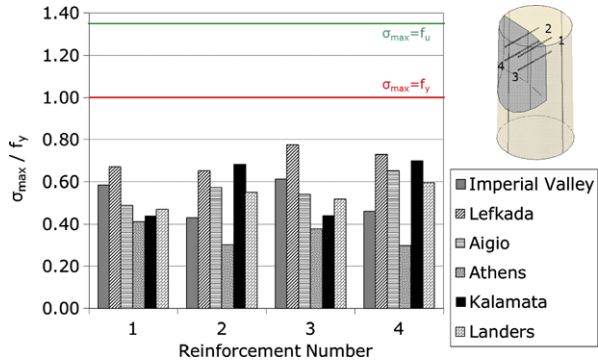
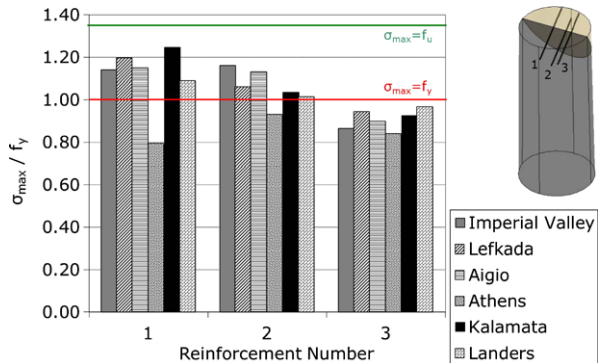


Fig. 9 Efficiency factors of the three titanium bars used for the complement of the first drum of column 2 of the colonnade in Kos for the five earthquake excitations that do not cause collapse of the monument



It should be noted that in all cases, the maximum stress was less than the ultimate limit strength of the reinforcements. In this sense, it can be said that the simplified approach for the design of the connections is, in general, adequate, although yield of the bars might occur temporarily.

It is evident from these results that both the inclination of the connection and its position along the height of the column affect significantly the forces that are induced to the reinforcement bars. The worst case concerns fragments that form a

Fig. 10 Efficiency factors of the seven titanium bars used for the complements of the fourth drum of column 2 of the colonnade in Kos for the five earthquake excitations that do not cause collapse of the monument

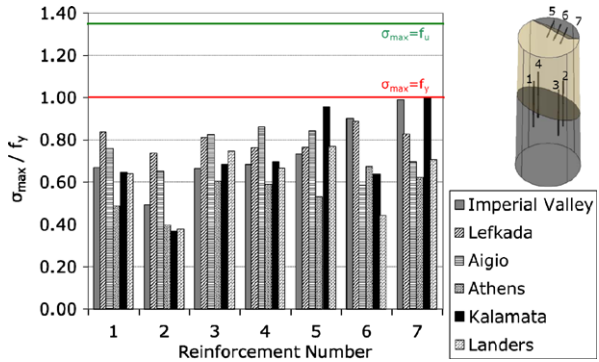


Fig. 11 Efficiency factors of the four titanium bars used for the complement of the first drum of the column of the Parthenon for the ten earthquake excitations used in the analyses

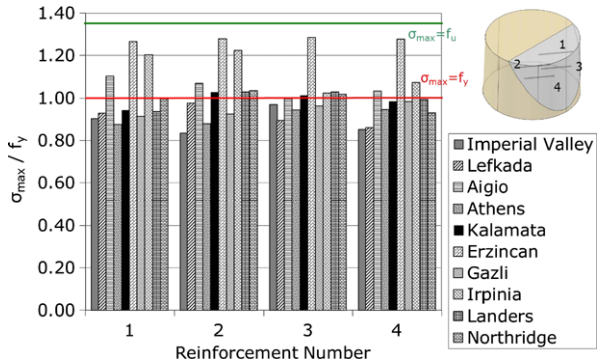
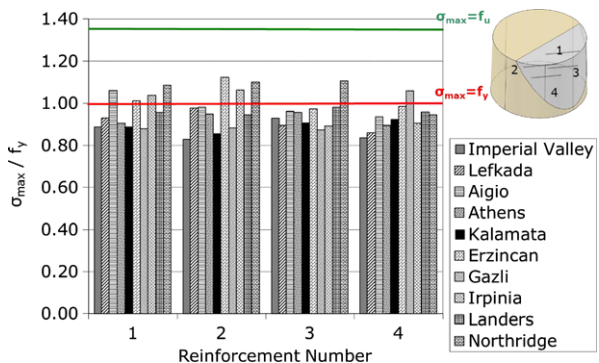


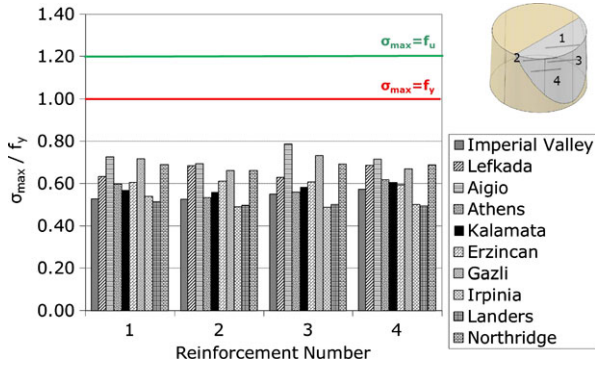
Fig. 12 Efficiency factors of the four titanium bars used for the complement of the middle (6th) drum of the column of Parthenon for the ten earthquake excitations used in the analyses



wedge and are located at the lower part of the column, where the gravity loads are larger. During rocking, large forces are developed at such connections; this was also observed in [16].

It must be noted that the obtained results concern the maximum forces that were induced to the reinforcement bars of the connections during the response of the structures examined, which, however, cannot be ascertained that they are the most adverse ones that could occur. This is because the forces that are developed at the

Fig. 13 Efficiency factors of the four titanium bars used for the complement of the last (12th) drum of the column of Parthenon for the ten earthquake excitations used in the analyses



connections of the complements depend on the “mode” in which the columns rock during the seismic excitation. The worst case is when the part of the column above the drum under consideration rocks around the edge corner of the fragment, which is not certain that occurred in the cases examined. However, the consistency of the obtained results for many earthquakes of different characteristics shows that the conclusions drawn are reliable for most of the cases that are expected to be encountered in practice.

6 Conclusions

The efficiency of the design of connections of fractured architraves or complements of drums of columns was evaluated from the results of dynamic analyses. The main conclusions drawn are:

- The simplified methodology that is used in practice for the dimensioning of the reinforcement of connections between new and old complements, which is based on the capacity design concept, was proved to be adequate, since the ultimate strength of the titanium bars was never reached. However, the yield stress can be temporarily exceeded. In most cases, though, the stresses induced to the reinforcement bars were considerably lower than the corresponding yield resistance.
- The position of the intervention and the shape of the fragment to be completed affect the forces that were induced to the connections. The most adverse situation was observed for fragments of column drums that formed a wedge and were located at the lower part of the column.

Acknowledgements Part of the research reported herein was performed in the frame-work of the structural analysis of the proposed restoration of the southern Arcade of the Ancient Agora of Kos, which was financed by the Hellenic Ministry of Culture on behalf of the Archaeological Institute of Aegean Studies of Rhodes under project EL006 “Designation of the ancient Hellenistic Agora of Kos and the medieval circumferential fortifications of the city of Kos”.

References

1. Psycharis IN, Papastamatiou DY, Alexandris A (2000) Parametric investigation of the stability of classical columns under harmonic and earthquake excitations. *Earthq Eng Struct Dyn* 29:1093–1109
2. Papantonopoulos C, Psycharis IN, Papastamatiou DY, Lemos J, Mouzakis H (2002) Numerical prediction of the earthquake response of classical columns using the distinct element method. *Earthq Eng Struct Dyn* 31:1699–1717
3. Psycharis IN, Lemos JV, Papastamatiou DY, Zambas C, Papantonopoulos C (2003) Numerical study of the seismic behaviour of a part of the Parthenon Pronaos. *Earthq Eng Struct Dyn* 32:2063–2084
4. Dasiou M-E (2007) Report in work package 7 and work package 8. Research project earthquake protection of historical buildings by reversible mixed technologies (PROHITECH)
5. Dasiou M-E, Psycharis IN, Vayas I (2009) Verification of numerical models used for the analysis of ancient temples. In: Proceedings of PROHITECH conference, Rome
6. Dasiou M-E, Psycharis I, Vayas I (2008) Seismic behaviour of ancient temples' columns and colonnades analysis. In: Proceedings of 3rd Panhellenic conference on earthquake engineering and engineering seismology, Athens, 5–7 November 2008 (in Greek)
7. Zambas C (1994) Study for the restoration of the Parthenon (vol 3b). Hellenic Ministry of Culture, Committee for the Preservation of the Acropolis Monuments
8. Ioannidou M, Paschalides V, Mentzini M (2002) Joining of fractured architraves with titanium reinforcement: new approach. In: Proceedings of the 5th international meeting for the restoration of the Acropolis monuments, Athens, 4–6 October 2002. Committee for the Preservation of the Acropolis Monuments (in Greek)
9. Orlandos A (1977) Parthenon's architecture (vol 2, part b). Archaeological Service of Athens
10. Korres M (1989) Study for the restoration of the Parthenon (vol 2, part I). Hellenic Ministry of Culture, Committee for the Preservation of the Acropolis Monuments
11. Korres M (1996) Pronaos—west wall. In: Catalogue of the exhibition “The Parthenon architecture and conservation” held at the Osaka City Museum from September 25 to October 15. Foundation for Hellenic Culture, Committee for the Conservation of the Acropolis Monuments, pp 45–47
12. Itasca Consulting Group Inc (1996) 3DEC: 3-dimensional distinct element code, theory and background
13. Gerdeen JC, Snyder VW, Viegelahn GL, Parker J (1977) Design criteria for roof bolting plans using fully resin-grouted nontensioned bolts to reinforce bedded mine roof. *US Bureau of Mines, OFR*, 46(4)-80
14. Littlejohn GS, Bruce DA (1975) Rock anchors—state of the art. Part I: Design. *Ground Eng* 8(3):25–32
15. Bjurstrom S (1974) Shear, strength on hard rock joints reinforced by grouted untensioned bolts. In: Proceedings of the 3rd international congress on rock mechanics, vol II, part B. National Academy of Sciences, Washington, pp 1194–1199
16. Stefanou I, Psycharis I, Georgopoulos I-O (2011) Dynamic response of reinforced masonry columns in classical monuments. *Constr Build Mater* 25:4325–4337 (special issue: Masonry research and practice)

Seismic Overturning of Rocking Structures with External Viscous Dampers

Elias G. Dimitrakopoulos and Matthew J. DeJong

Abstract Numerous structures exhibit rocking behavior during earthquakes and there is a continuing need to retrofit these structures to prevent collapse. The behavior of stand-alone rocking structures has been thoroughly investigated, but there are relatively few theoretical studies on the response of retrofitted rocking structures. In practice, despite the benefits of allowing rocking motion, rocking behavior is typically prevented instead of optimized. This study characterizes the fundamental behavior of damped rocking motion through analytical modeling. A single rocking block analytical model is utilized to determine the optimal viscous damping characteristics which exploit the beneficial aspects of rocking motion while dissipating energy and preventing overturning collapse. To clarify the benefits of damping, overturning envelopes for the damped rocking block are presented and compared with the pertinent envelopes of the free rocking block. Preliminary experimental work to verify analytical modeling is also presented. Finally, the same principles of controlling rocking behavior with damping are extended to a particular class of rocking problems, the dynamics of masonry arches. A pilot application of the proposed approach to masonry arches is presented.

Keywords Rocking · Overturning · Analytical dynamics · Earthquake engineering · Damping

1 Introduction

Numerous heritage structures exhibit rocking behavior when loaded dynamically, including monuments, towers, bridge piers, sculptures, etc. Recent earthquakes (e.g.

E.G. Dimitrakopoulos (✉)

Department of Civil and Environmental Engineering, Hong Kong University of Science and Technology, Clear Water Bay, Kowloon, Hong Kong
e-mail: ilias.dimitrakopoulos@gmail.com

M.J. DeJong

Department of Engineering, University of Cambridge, Trumpington Street, Cambridge, CB2 1 PZ, UK
e-mail: mjd97@cam.ac.uk

Chile and Italy) have increased world-wide incentive to retrofit such structures to avoid collapse during dynamic loading, but also to develop new design methodologies which isolate modern structures by deliberately taking advantage of rocking behavior.

Spanning a wide range of research fields, the relevant literature regarding the rocking response of the stand-alone rigid block (the simplest rocking structure) is abundant. The rocking dynamical response is highly nonlinear and extremely complex; the block displays numerous ways to overturn [1, 2] with respect to the number of the preceding impacts, and its response is highly sensitive to the characteristics of the dynamic loading. Most studies assume an idealized ground excitation in the form of a primary impulse [3] or harmonic loading [1]. The significant amount of research assuming harmonic loading may originate from the concept that a constant frequency excitation can cause resonance. However, one main advantage of the rocking system is that constant frequency rocking resonance is impossible because the natural frequency changes with rocking amplitude. Further, harmonic ground motions which could cause rocking resonance would have to have a precise time-varying frequency, and are thus extremely unlikely [4]. Rocking behavior is mostly affected by the distinct time-dependent characteristics of the ground excitation that are less relevant to the response of elastically deformable structures.

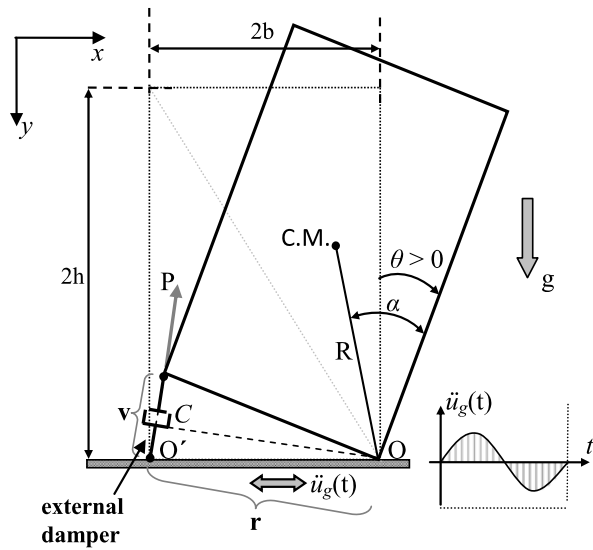
In contrast to the significant amount of research on the response of stand-alone rocking structures [5, 6], there are only a handful of theoretical studies on the response of retrofitted rocking structures [7, 8] or more complicated rocking structures ([9] and references therein). In practice, rocking behavior is typically prevented instead of limited or confined. Prevention is achieved by tying structures down, reinforcing them internally by drilling through or externally by wrapping with Fiber-Reinforce Polymers (FRP) [10].

While these methods can be effective, they can over-stiffen structures, add stress, and be destructive. In particular, Makris and Zhang [7] and Dimitrakopoulos and DeJong [11] showed that the response of the anchored rocking block can be worse than that of the pertinent stand-alone rocking block. In addition, when earthquake loading is rare and relatively minimal, as in the UK, extensive reinforcing of a vast number of structures may be economically infeasible and too invasive. Hence, application of intelligent less invasive intervention methods is sought, through confinement of the rocking response instead of prevention. This research aims to lay the foundation for the development of a new class of retrofit solutions which exploit damping systems. At the same time, this work derives from a broader study on the analysis of the dynamics [4, 9, 12] and the retrofit [11] of rocking structures.

2 Damped Rocking Motion

Motivated by the inverse effects of adding strength to the rocking block [11], this research takes an alternative approach and investigates the benefits of additional damping. Consider first the free standing rocking block of Fig. 1 (without dampers)

Fig. 1 The rocking block retrofitted with viscous dampers at its edges



subjected to a pulse-type base excitation with acceleration amplitude a_g and frequency ω_g . Assuming the coefficient of friction is high enough to prevent sliding, the rocking motion initiates when the ground acceleration \ddot{u}_g exceeds the critical value: $\ddot{u}_g \geq a_{g,\min} = g \tan \alpha$ where α is the angle of slenderness and g the gravity acceleration.

The moment equilibrium, during rocking, with respect to the pivot points O (or O' accordingly in Fig. 1) gives:

$$I_0 \ddot{\theta} + mgR \sin[\alpha \operatorname{sgn}(\theta) - \theta] = -m\ddot{u}_g R \cos[\alpha \operatorname{sgn}(\theta) - \theta] \quad (1)$$

where θ is the rocking rotation, I_0 the moment of inertia with respect to the pivot point, m the mass of the block, R the half-diagonal and $\operatorname{sgn}()$ the standard sign function. The slenderness angle is defined by $\tan \alpha = b/h$, where $2b$ is the width and $2h$ the height of the block.

To complete the description of the problem, the equation of motion is complemented with a coefficient of restitution η , defined as the ratio of the pre- and post-impact velocities, which ranges between 0 (for perfectly plastic) and 1 (for perfectly elastic impact):

$$\dot{\theta}^+ = \eta \dot{\theta}^- \quad (2)$$

The present formulation (Eqs. (1) and (2)) is valid for sufficiently slender blocks where other impact behaviors (e.g. bouncing, sliding) are assumed to be negligible.

Figure 2 presents the overturning envelopes of the rocking block, subjected to the simple trigonometric pulses shown, for different coefficients of restitution η . As expected, the coefficient of restitution affects the overturning of the rocking block only when impacts precede overturning. In other words, the energy is damped out of the stand-alone rigid block only during impact. This poses a theoretical limit to

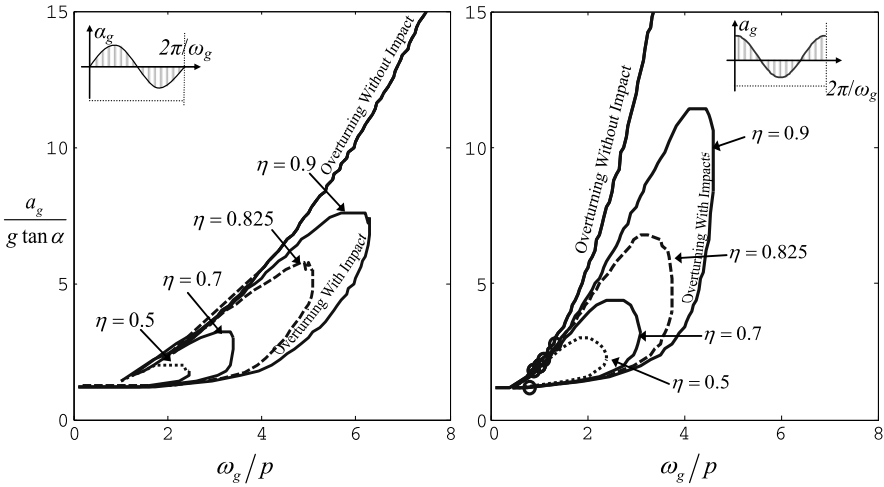


Fig. 2 Overturning envelopes of the stand-alone rocking block for different coefficients of restitution η

reducing rocking behavior by increasing energy dissipation at impact, as immediate overturning is unaffected.

2.1 Bilateral Viscous Dampers

As a first approach, consider a rigid block retrofitted with bilateral viscous dampers as in Fig. 1. The force P of a viscous linear damper is given by:

$$P = C \dot{v} \tag{3}$$

where \dot{v} is the relative velocity between the ends of the damper and C the damping constant.

Moment equilibrium of the retrofitted block (Fig. 1) during rocking gives:

$$I_0 \ddot{\theta} + mgR \sin[\alpha \operatorname{sgn}(\theta) - \theta] + P \cdot r = -m \ddot{u}_g R \cos[\alpha \operatorname{sgn}(\theta) - \theta] \tag{4}$$

where r is the lever of the damping force P .

Equation (4) can be written using Eq. (3) and geometric properties:

$$\ddot{\theta} = -p^2 \left\{ \sin[\alpha \operatorname{sgn}(\theta) - \theta] + \frac{\ddot{u}_g}{g} \cos[\alpha \operatorname{sgn}(\theta) - \theta] \right\} - p\gamma(1 + \cos\theta)\dot{\theta} \tag{5}$$

where $p = \sqrt{3g/4R}$ is the frequency parameter of the (rectangular) block, and $\gamma \doteq \frac{3}{2} \frac{C}{mp} \sin^2 \alpha$ is a dimensionless parameter that relates the damping constant C to the mass m , the slenderness α and the frequency p . The comparison of the response of the rocking block enhanced with bilateral, versus unilateral viscous dampers is offered later (Sect. 2.3) by calculating numerically the response from Eq. (5).

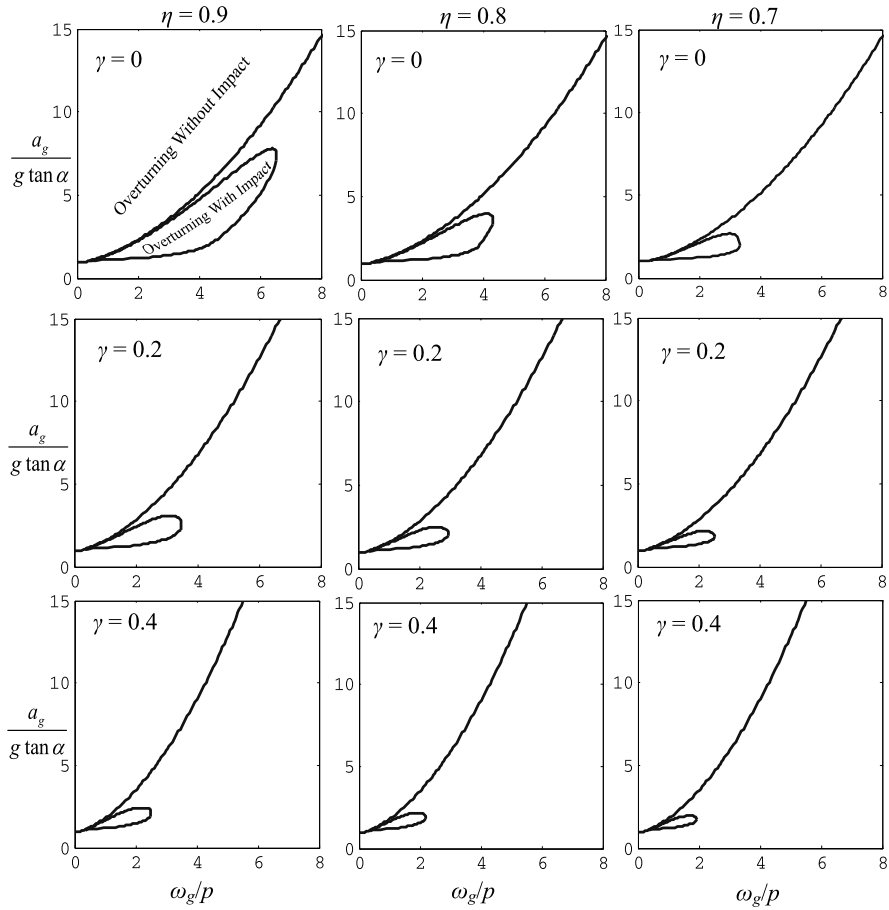


Fig. 3 Overturning envelopes of the damped rocking block under a sine pulse excitation, for different coefficients of restitution η (different columns) and different additional damping γ (different rows)

Figure 3 offers an initial general overview of the benefits of combined viscous (γ) and impact (η) damping on the response of the rocking block. The overturning envelopes of Fig. 3 describe a slender block subjected to a sine excitation. Hence, the equations of motion (Eq. (5)) have been linearized. Figure 3 shows that, in contrast to the effect of impact damping defined by the coefficient of restitution η , viscous damping is effective regardless of whether impact occurs. Figure 3 (bottom right) shows the overturning response for high viscous and high impact damping, and nears a theoretical upper limit of reducing rocking overturning by added damping, under the aforementioned assumptions.

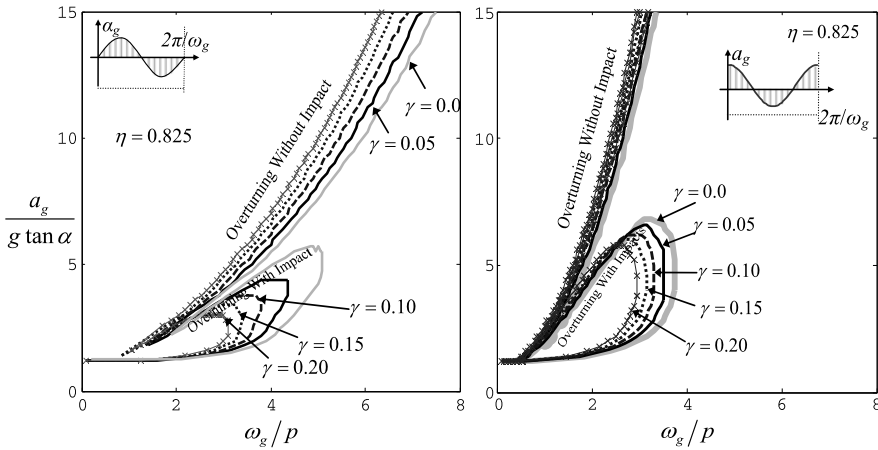


Fig. 4 Overturning envelopes for the rocking block with bilateral viscous dampers. Comparison with the stand-alone rocking block (*thick gray line*)

2.2 Unilateral Viscous Dampers

Re-centering, i.e. limiting residual displacements despite large displacement during seismic loading, is an advantage of rocking motion. However, collapse must be prevented. Thus, to limit collapse while encouraging re-centering, unilateral viscous dampers, which are activated only during uplift, are also considered. The behavior of such unilateral viscous dampers can be described with the help of an ad-hoc function $S(\theta, \dot{\theta})$ defined as follows:

$$S(\theta, \dot{\theta}) = \frac{1}{2} [\text{sgn}(\theta \cdot \dot{\theta}) + 1] = \begin{cases} 1 & \text{when uplifting} \\ 0 & \text{when restoring} \end{cases} \quad (6)$$

The equation of motion for the linear unilateral viscous damper is:

$$\ddot{\theta} = -p^2 \left\{ \sin[\alpha \text{sgn}(\theta) - \theta] + \frac{\ddot{u}_g}{g} \cos[\alpha \text{sgn}(\theta) - \theta] \right\} - p\gamma(1 + \cos \theta)S(\theta, \dot{\theta})\dot{\theta} \quad (7)$$

2.3 Response of the Damped Rocking Block to Pulse-Type Excitations

Figure 4 presents the overturning envelopes for the bilateral damping, and Fig. 5 presents the overturning envelopes for the equivalent unilateral (same γ parameter) dampers. Both figures also contain the undamped (stand-alone) rocking block envelopes. The block is excited with simple trigonometric pulses and the response is calculated by numerically solving the nonlinear differential equations of motion

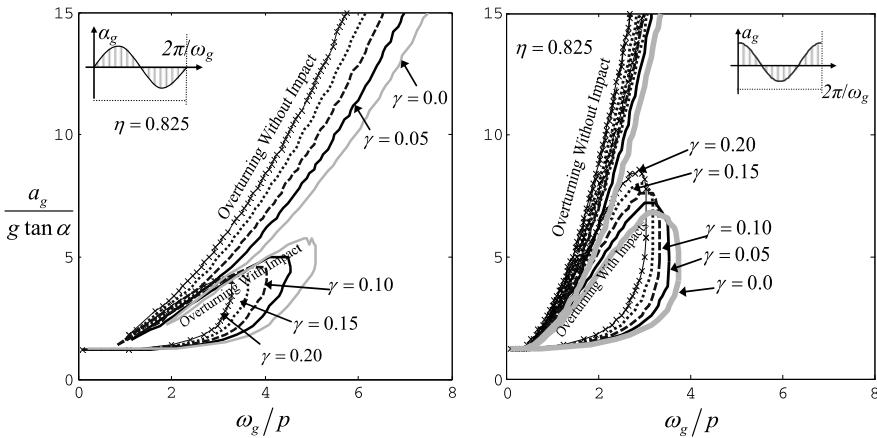


Fig. 5 Overturning envelopes for the rocking block with unilateral viscous dampers. Comparison with the stand-alone rocking block (*thick gray line*)

(Eqs. (5) and (7) respectively) assuming a constant coefficient of restitution η . The behavior is described in the dimensionless terms:

$$\frac{a_g}{g \tan \alpha}, \frac{\omega_g}{p}, \eta, \gamma = \frac{3}{2} \frac{C}{m p} \sin^2 \alpha \tag{8}$$

These dimensionless terms can be considered as an extension of the pertinent terms used for the stand-alone (undamped) rocking block which are formally derived in [12].

Similarly to the behavior of the stand-alone rocking block [12], the damped rocking block displays two different modes of overturning under a sine and a cosine pulse-excitation (e.g. Fig. 4): immediate overturning without impact and overturning with at least one impact (one in the case of a sine pulse excitation and up to 2 in the case of a cosine pulse excitation). In general and as expected, the overturning-with-impact mode is more critical since it appears for lower excitation intensities. However, unlike the case of additional strength [11], the higher the additional damping (parameter γ), the more the overturning envelopes shrink, regardless of the excitation type (sine or cosine).

In Fig. 6, the overturning envelopes for bilateral and unilateral damping are directly compared. Both unilateral and bilateral dampers have a similar beneficial effect for overturning without impact. However, there is a brief change in velocity prior to overturning during which the block tries to recover. Bilateral dampers limit this recovery, while unilateral dampers allow it, making them slightly more effective.

For overturning with impact, both damping options cause a similar beneficial shift in the minimum impulses which cause overturning (the lower limit of the overturning area shifts up and left). Comparatively, bilateral dampers provide a larger

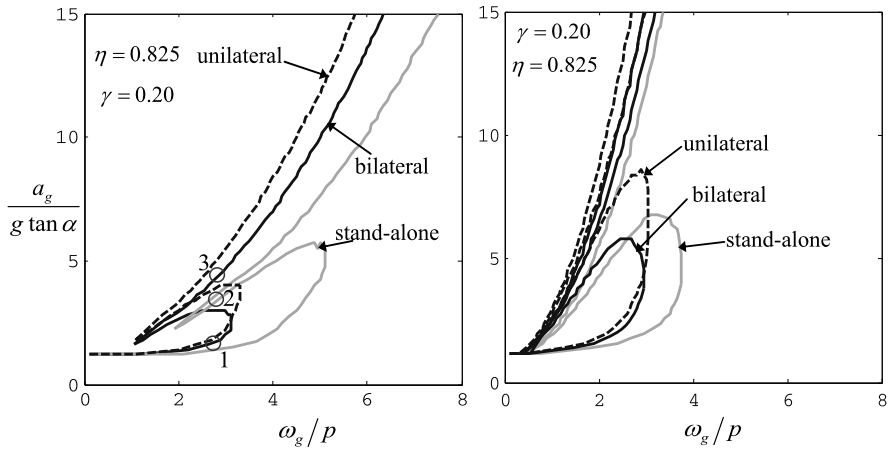


Fig. 6 Comparison of overturning envelopes for the rocking block retrofitted with bilateral and unilateral viscous dampers (*left*: sine pulse-excitation, *right*: cosine pulse-excitation)

decrease of the total overturning area through a larger downward shift in the upper limit of the overturning region. While this may be beneficial, it should be noted that the intermediate safety area, between the two overturning basins, is a result of the highly nonlinear behavior of the rocking block and is very sensitive to the characteristics of the excitation [1, 2]. Thus, from a design perspective, it is unreliable to depend on this safety region, and the lower limit is more important. Hence, both options have a remarkably similar benefit.

To further investigate the effects of adding damping and the sensitivity of the rocking response, Figs. 7 and 8 plot the time-history response (rotation and angular velocity) of the rocking block that corresponds to the points 1 to 3 in the overturning diagram (Fig. 6). For $a_g/(g \tan \alpha) = 1.8$ and 4.6 (points 1 and 3) the stand-alone and the bilaterally damped rocking block overturn, while the unilaterally damped rocking block survives. On the contrary, for $a_g/(g \tan \alpha) = 3.2$ (point 2) the opposite is true: the stand-alone and the bilaterally damped block survive, while the unilaterally damped block overturns. The response is clearly highly nonlinear, and numerous instances where either the bilateral or the unilateral damper performs better can be found. As a general rule, for a given damping parameter γ the performance of the two types of damper is comparable.

The addition of viscous dampers, realizing a nonlinear force-velocity behavior, has also been examined [11]. Again, no consistent trend has been observed regarding the comparative advantage of linear or nonlinear viscous dampers in enhancing the response of the rocking block. However, the general benefit of added damping is again evident.

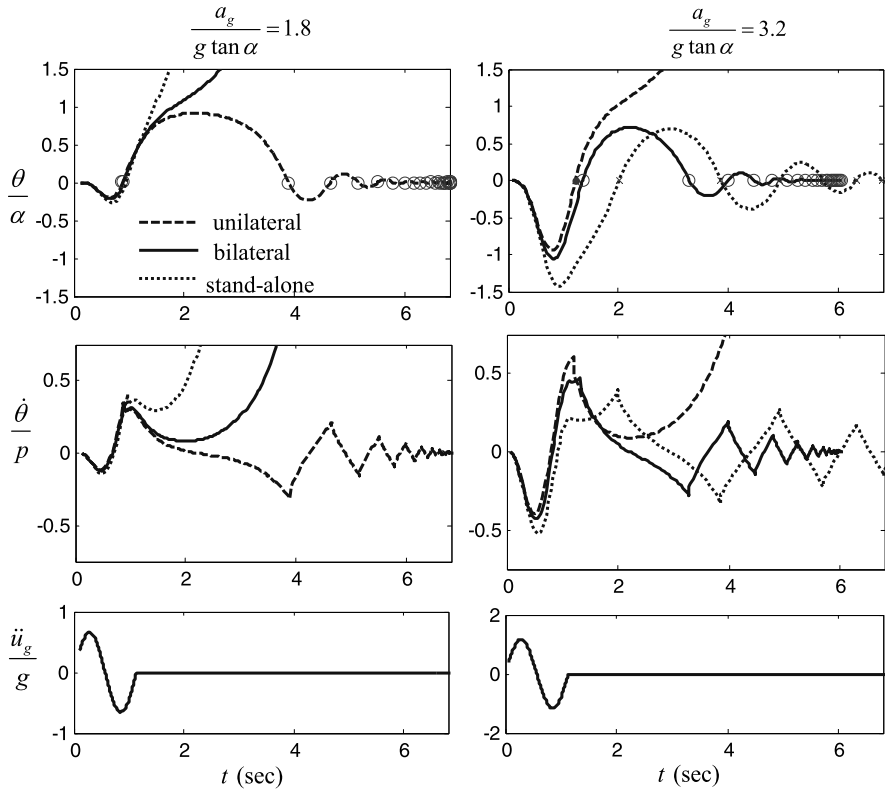


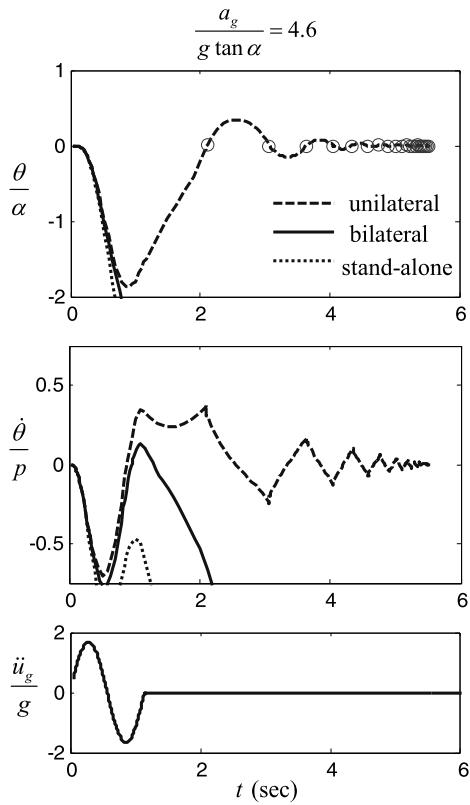
Fig. 7 Rocking rotation (*top*) and angular velocity (*middle*) time-history of the rocking block ($\omega/p = 2.75, \eta = 0.825$) excited with a sine pulse (*bottom*). The *left column* corresponds to point 1 of Fig. 6 and the *right column* corresponds to point 2 of Fig. 6

2.4 Experimental Results of the Damped Rocking Block to Pulse-Type Excitations

The damped rocking block was also investigated experimentally by shake table testing. Figure 9 (top) shows the rocking block apparatus that was mounted to the shake table. An I-beam that rocks about the ends of its flanges was used as the rocking block. Damping was applied using air dashpots attached to both sides of the block. The dashpots were only active when the block was rotating about the opposite edge. Displacement transducers were attached in parallel with the dampers to determine the rotation of the block.

Figure 9 (bottom left) exemplifies the rocking response of the block to a cosine impulse, and demonstrates relatively good agreement between experimental and analytical modeling results. Note that experiment (1) and experiment (2) indicate data from the two respective displacement transducers, indicating that the dampers were in fact only effective when rocking occurred about the opposite edge. Also note that

Fig. 8 Rocking rotation (*top*) and angular velocity (*middle*) time-history of the rocking block ($\omega/p = 2.75$, $\eta = 0.825$) excited with a sine pulse (*bottom*). These results correspond to point 3 of Fig. 6



the coefficient of restitution (η) and the damping constant (C) were determined experimentally. The air dashpot was assumed to be linear, though it is non-linear in reality, which accounts for the reduction in accuracy of predicting the response as the rocking attenuates. Further refinement of the dashpot model, as well as a general investigation of the overturning envelopes in Fig. 4, are the subject of continued research.

Figure 9 (bottom right) shows the effect of added damping on the maximum rocking response to an earthquake with a primary impulse near the beginning of the time history. The maximum rocking response decreases considerably with added damping. The maximum response is again well predicted by the analytical model.

3 Damping of Masonry Arch Rocking

The dynamics of masonry arches is a particular class of rocking problems. Under specific conditions outlined by Oppenheim [13] and DeJong et al. [14], the dynamics of the masonry arch can be captured with a single degree of freedom (SDOF)

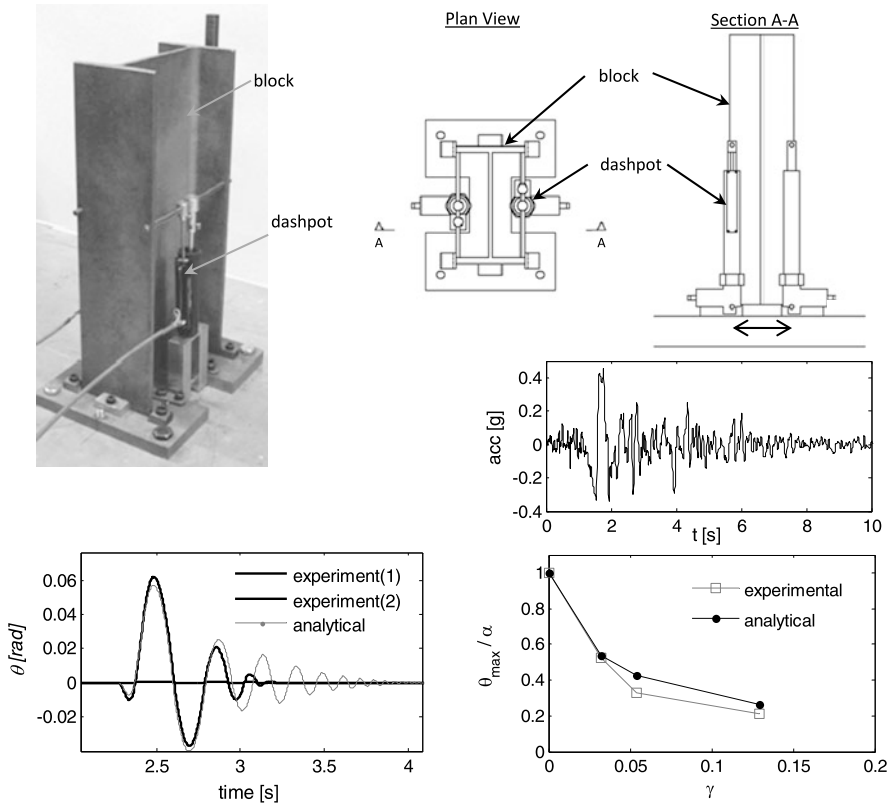


Fig. 9 Experimental setup image (top left) and diagram (top right), example comparison of experimental and analytical response (bottom left), and experimental and analytical comparison of the maximum rocking angle for the earthquake time history shown (bottom right)

model. For single pulse dominated earthquake motions, an SDOF arch model effectively predicted experimental collapse results for dry-stone masonry arches [14]. Further, arches are prolific in historic structures which stand vulnerable to seismic loading. Retrofit solutions which incorporate damping could potentially provide a viable solution for improving seismic safety. As a first approach, the same four-link mechanism model [14] is extended to account for the addition of linear viscous damping in the masonry arch. The addition of damping is initially assumed at hinging locations in the masonry arch, without considering a specific geometrical damper configuration.

The SDOF equation of motion can be derived from Hamilton’s principle and Lagrange’s equation:

$$\frac{\partial}{\partial t} \left(\frac{\partial T}{\partial \dot{\theta}} \right) - \frac{\partial T}{\partial \theta} + \frac{\partial V}{\partial \theta} = Q \tag{9}$$

The kinetic energy T and the potential energy V are given by Oppenheim [13]:

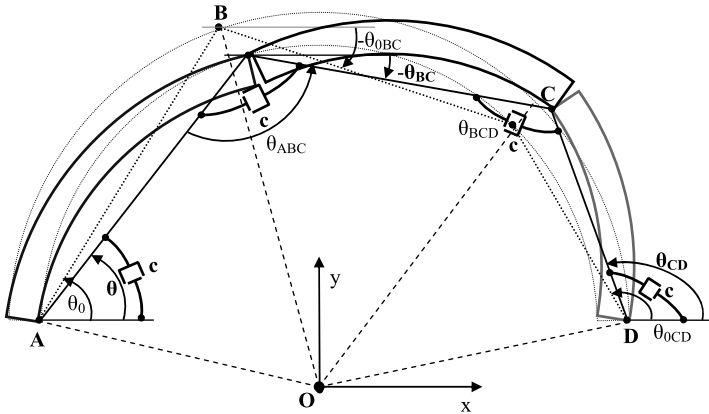


Fig. 10 The four-link kinematic mechanism of a masonry arch, during rocking under base excitation. Additional linear viscous damping is assumed at hinging locations

$$\begin{aligned}
 T = & \frac{1}{2}m_{AB}(\bar{r}_{AB}\dot{\theta})^2 + \frac{1}{2}m_{CD}(\bar{r}_{CD}\dot{\theta}_{CD}) + \frac{1}{2}I_{AB}\dot{\theta}^2 + \frac{1}{2}I_{BC}\dot{\theta}_{BC}^2 + \frac{1}{2}I_{CD}\dot{\theta}_{CD}^2 \\
 & + \frac{1}{2}[m_{BC}(\mathbf{AB}\dot{\theta})^2 + 2\mathbf{AB}\bar{r}_{BC}\cos(\theta_{AB} - \theta_{BC} - \psi_{BC})\dot{\theta}_{AB}\dot{\theta}_{BC} \\
 & + (\bar{r}_{BC}\dot{\theta}_{BC})^2] \quad (10)
 \end{aligned}$$

$$V(\theta) = g \left[\begin{aligned} & m_{AB}\bar{r}_{AB}\sin(\theta + \psi_{AB}) + m_{CD}\bar{r}_{CD}\sin(\theta_{CD} + \psi_{CD}) \\ & + m_{BC}\mathbf{AB}\sin\theta + m_{BC}\bar{r}_{BC}\sin(\theta_{BC} + \psi_{BC}) \end{aligned} \right]$$

where θ , θ_{ABC} , θ_{BCD} , θ_{CD} are the angles depicted in Fig. 10, m is the mass of the of the link indicated with subscripts, I is the moment of inertia of the of the link indicated with subscripts with respect to its center of gravity (C.G.), g is the acceleration of gravity, r_{AB} is the distance from A to the C.G. of link AB, r_{BC} is the distance from B to the C.G. of link BC, r_{CD} is the distance from D to the C.G. of link CD, ψ_{AB} is the angle enclosed between vectors \mathbf{AB} and r_{AB} (positive if counterclockwise) and angles ψ_{BC} and ψ_{CD} are defined in similar fashion.

The generalized force expression is comprised of two parts: the inertial terms due to base excitation, Q_g [13], and the additional damping forces Q_d . The work done by the non-conservative forces δW_{nc} is:

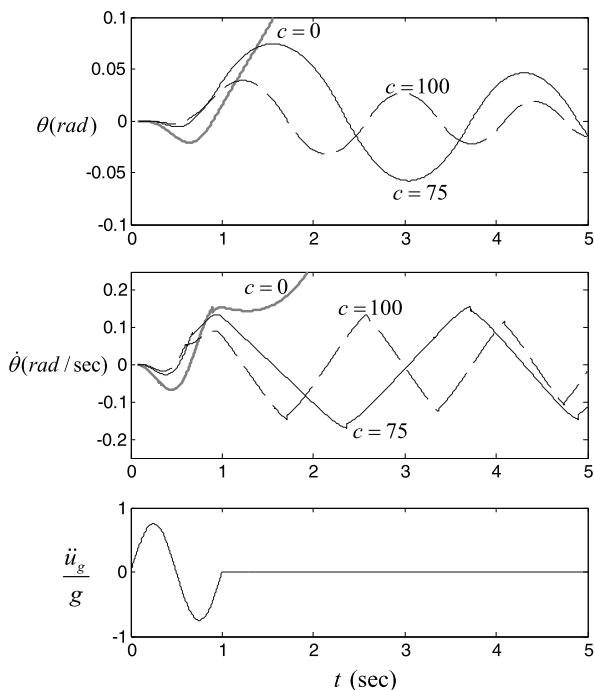
$$\delta W_{nc} = Q\delta\theta = (Q_g + Q_d)\delta\theta \quad (11)$$

where the generalized forcing due to the inertial term Q_g is:

$$Q_g = - \left(\begin{aligned} & m_{AB}\bar{r}_{AB}\sin(\theta + \psi_{AB}) + m_{CD}\bar{r}_{CD}\sin[\theta_{CD}(\theta) + \psi_{CD}] \frac{\partial\theta_{CD}}{\partial\theta} \\ & m_{BC}[\mathbf{AB}\sin\theta + \bar{r}_{BC}\sin[\theta_{BC}(\theta) + \psi_{BC}] \frac{\partial\theta_{BC}}{\partial\theta}] \end{aligned} \right) \ddot{x}_g \quad (12)$$

and the generalized forcing due to the damping force Q_d is:

Fig. 11 Rocking of a masonry arch under a sine pulse excitation (*bottom*). Rotation (*top*) and angular velocity (*middle*) about hinge A in Fig. 10. While the free rocking arch ($c = 0$) fails, the addition of damping ($c = 75, 100$ kN-m-s) prevents failure



$$\begin{aligned}
 Q_d \delta \theta &= -c \cdot \dot{\theta} \delta \theta - c \cdot \dot{\theta}_{ABC}(\theta) \delta \theta_{ABC} - c \cdot \dot{\theta}_{BCD}(\theta) \delta \theta_{BCD} \\
 &\quad - c \cdot \dot{\theta}_{CD}(\theta) \delta \theta_{CD} \quad \Rightarrow \\
 Q_d \delta \theta &= -c \left[1 + \left(\frac{\partial \theta_{BC}}{\partial \theta}(\theta) - 1 \right)^2 + \left(\frac{\partial \theta_{CD}}{\partial \theta}(\theta) - \frac{\partial \theta_{BC}}{\partial \theta}(\theta) \right)^2 \right. \\
 &\quad \left. + \left(\frac{\partial \theta_{CD}}{\partial \theta}(\theta) \right)^2 \right] \dot{\theta}(t) \delta \theta \quad \Rightarrow \quad (13) \\
 Q_d &= -c \left[1 + \left(\frac{\partial \theta_{BC}}{\partial \theta}(\theta) - 1 \right)^2 + \left(\frac{\partial \theta_{CD}}{\partial \theta}(\theta) - \frac{\partial \theta_{BC}}{\partial \theta}(\theta) \right)^2 \right. \\
 &\quad \left. + \left(\frac{\partial \theta_{CD}}{\partial \theta}(\theta) \right)^2 \right] \dot{\theta}(t)
 \end{aligned}$$

where c is the rotational damping constant (not the linear damping constant C). After extensive algebra, the equation of motion can be written in the form:

$$M(\theta)R^3\ddot{\theta} + L(\theta)R^3\dot{\theta}^2 + F(\theta)R^2g + D(\theta)R^2\dot{\theta} = P(\theta)R^2\ddot{x}_g \quad (14)$$

where $D(\theta)$ is the term introduced due to damping. Equation (14) is complicated, but it is a single degree of freedom nonlinear equation that can be solved numerically in a timely manner. Figure 11 plots the time-history response of the masonry arch described in Oppenheim [13], to a simple sine ground motion with acceleration amplitude $a_g = 0.75g$ and duration $T_g = 1.0$ sec (Fig. 11 bottom). The coefficient

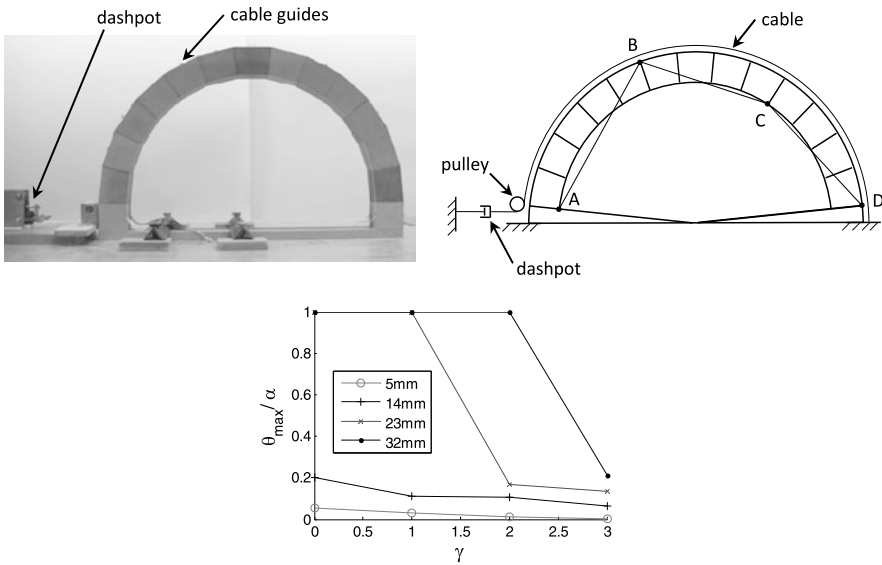


Fig. 12 Experimental setup image (top left) and diagram (top right), and the effect of increased damping on the maximum rocking response of the arch under cosine impulses with the same frequency but varying amplitude (bottom)

of restitution is taken as $\eta = 0.93$. The free masonry arch fails during rocking, while the addition of (linear) viscous damping at the hinging locations prevents failure.

The effect of added damping on the rocking response of masonry arches is also the subject of ongoing experimental investigation. Figure 12 (top) shows a schematic diagram and image of the experimental setup. Damping is applied by a single air dashpot attached to a cable which travels around the extrados of the arch. Thus, damping is effective when hinges form at the intrados of the arch, but no resistance is provided when hinges form at the extrados. For the analytical model, this means that damping is effective at hinges A and C in Fig. 10, but not at hinges B and D. In order to quantify the rotation of the arch, the linear displacement of the dashpot was measured and translated into an equivalent arch rotation θ assuming the mechanism predicted by the analytical model (see Fig. 12, top right). Figure 12 (bottom) demonstrates the beneficial effect of added damping on the arch response to impulse loading.

4 Conclusions

In this study, the consequences of adding damping to rocking structures are investigated. Interestingly, while additional damping is already implemented in practice to retrofit rocking structures, there is a lack of theoretical research on the subject.

The overturning envelopes of a rocking block retrofitted with bilateral and unilateral (activated only during uplift) linear viscous dampers, show a substantial enhancement of the behavior. As a general rule, for a given damping level, the performance of the two types of dampers is comparable. However, the unilateral damper delays the first appearance of overturning both with and without impact, but the area of overturning is larger, compared to the pertinent bilateral damper. Compared to the alternative of anchoring the rocking system, additional damping does not lead to counter effects where the behavior of the retrofitted rocking system is actually worse than that of the stand-alone system.

Experimental results for the rocking block demonstrate the benefits of added damping and indicate good agreement with analytical modeling results. Further experimental investigation is ongoing, including a more comprehensive study of maximum rocking response.

The masonry arch exemplifies an alternate type of rocking structure for which added damping might be appropriate. Stiffness compatibility is an important issue when retrofitting historic structures, and thus retrofit methods which incorporate damping and limited stiffness would be attractive. Experimental scale model testing indicates that added damping can effectively prevent collapse without over-stiffening the structure. Further investigation of combined stiffness and damping retrofit alternatives, and related practical issues, are the subject of ongoing investigation.

References

1. Hogan SJ (1990) The many steady state responses of a rigid block under harmonic forcing. *Earthq Eng Struct Dyn* 19(7):1057–1071. doi:[10.1002/eqe.4290190709](https://doi.org/10.1002/eqe.4290190709)
2. Plaut RH (1995) Fractal behavior of an asymmetric rigid block overturning due to harmonic motion of a tilted foundation. *Chaos Solitons Fractals* 7(2):177–196
3. Zhang J, Makris N (2001) Rocking response of free-standing blocks under cycloidal pulses. *J Eng Mech* 127(5):473. doi:[10.1061/\(ASCE\)0733-9399\(2001\)127:5\(473\)](https://doi.org/10.1061/(ASCE)0733-9399(2001)127:5(473))
4. DeJong MJ (2012) Amplification of rocking due to horizontal ground motion. *Earthq Spectra* 28(4):1405–1421. doi:[10.1193/1.4000085](https://doi.org/10.1193/1.4000085)
5. Housner GW (1963) The behavior of inverted pendulum structures during earthquakes (in an engineering report on the Chilean earthquakes on May 1960, Housner). *Bull Seismol Soc Am* 53(2):403–417
6. Augusti G, Sinopoli A (1992) Modelling the dynamics of large block structures. *Meccanica* 27(3):195–211. doi:[10.1007/BF00430045](https://doi.org/10.1007/BF00430045)
7. Makris N, Zhang J (2001) Rocking response of anchored blocks under pulse-type motions. *J Eng Mech* 127(5):484. doi:[10.1061/\(ASCE\)0733-9399\(2001\)127:5\(484\)](https://doi.org/10.1061/(ASCE)0733-9399(2001)127:5(484))
8. Di Egidio A, Contento A (2009) Base isolation of slide-rocking non-symmetric rigid blocks under impulsive and seismic excitations. *Eng Struct* 31(11):2723–2734. doi:[10.1016/j.engstruct.2009.06.021](https://doi.org/10.1016/j.engstruct.2009.06.021)
9. Acikgoz S, DeJong MJ (2012) The interaction of elasticity and rocking in flexible structures allowed to uplift. *Earthq Eng Struct Dyn* 41(15):2177–2194. doi:[10.1002/eqe.2181](https://doi.org/10.1002/eqe.2181)
10. Pampanin S (2006) Controversial aspects in seismic assessment and retrofit of structures in modern times: understanding and implementing lessons from ancient heritage. *Bull New Zealand Soc Earthq Eng* 39(2):120–133

11. Dimitrakopoulos EG, DeJong MJ (2012) Overturning of retrofitted rocking structures under pulse-type excitations. *J Eng Mech* 138(8):963–972. doi:[10.1061/\(ASCE\)EM.1943-7889.0000410](https://doi.org/10.1061/(ASCE)EM.1943-7889.0000410)
12. Dimitrakopoulos EG, DeJong MJ (2012) Revisiting the rocking block: closed-form solutions and similarity laws. *Proc R Soc A, Math Phys Eng Sci* 468(2144):2294–2318. doi:[10.1098/rspa.2012.0026](https://doi.org/10.1098/rspa.2012.0026)
13. Oppenheim IJ (1992) The masonry arch as a four-link mechanism under base motion. *Earthq Eng Struct Dyn* 21(11):1005–1017. doi:[10.1002/eqe.4290211105](https://doi.org/10.1002/eqe.4290211105)
14. DeJong MJ, De Lorenzis L, Adams S, Ochsendorf JA (2008) Rocking stability of masonry arches in seismic regions. *Earthq Spectra* 24(4):847. doi:[10.1193/1.2985763](https://doi.org/10.1193/1.2985763)

Innovative Computing Environment for Fast and Accurate Prediction of Approximate IDA Curves

Iztok Peruš, Robert Klinc, Matevž Dolenc, and Matjaž Dolšek

Abstract A web-based methodology for the prediction of approximate IDA curves, which was recently developed within ICE4RISK project, and demonstrated with the web application (<http://ice4risk.slo-projekt.info/WIDA>), is briefly summarized in this chapter and its applicability is presented by means of an example of a four-storey wall-equivalent dual system. The proposed methodology consists of two independent processes. The result of the first process is a response database of the single-degree-of-freedom model, whereas the second process involves the prediction of approximate IDA curves from the response database by using n -dimensional linear interpolation. The web application utilizes a response database of IDA curves, which was calculated for thirty ground motion records and the discrete values of the six parameters, which describe the period, damping and the force-displacement relationship of a building's pushover curve. The web application enables quadrilinear idealization of the pushover curve, including strength degradation. Structural collapse capacity can therefore also be estimated. Very good agreement between the computed and the approximated IDA curves was observed if the error is measured in terms of peak ground or spectral acceleration which caused selected limit state.

Keywords Performance-based earthquake engineering · Incremental dynamic analysis · Reinforced concrete building · Simplified nonlinear method · Static pushover

1 Introduction

Many simplified nonlinear methods for seismic performance assessment of buildings, which combine the nonlinear static (pushover) analysis with the procedure for determination of the target displacement, were developed in last twenty years. Most often the target displacement is defined based on the closed-form relationship between the reduction factor, ductility and the period ($R-\mu-T$), which is developed

I. Peruš · R. Klinc · M. Dolenc · M. Dolšek (✉)

Institute of Structural Engineering, Earthquake Engineering and Construction IT (IKPIR), Faculty of Civil and Geodetic Engineering, University of Ljubljana, Jamova 2, 1000, Ljubljana, Slovenia
e-mail: mdolsek@ikpir.fgg.uni-lj.si

by utilizing the seismic response of the equivalent single-degree-of-freedom model. In this case, the pushover curve is usually idealized only with a rough bi-linear force-displacement relationship. One of such procedures is embedded in the N2 method [1] which has been developed at the University of Ljubljana and implemented into the Eurocode 8 [2]. The original N2 method involves simple inelastic spectra, whereas more sophisticated relationship between reduction factor, ductility and the period can also be used. For example, inelastic spectra, which are adequate for prediction of target displacement for the reinforced concrete frames with masonry infill [3], depend on two additional parameters in comparison to that used in the original N2 method [1]. Such extension of the R - μ - T relationship enabled quadrilinear idealization of the pushover curve. However, R - μ - T relationship were determined only for a certain number of ground motion records, therefore, its extension is not trivial, since new ground motion records may cause different demand.

A step forward to a more general solution was introduced by Vamvatsikos and Cornell [4]. They developed SPO2IDA software tool that is capable of recreating the seismic behaviour of the single-degree-of-freedom (SDOF) model with quadrilinear force-displacement relationship. Based on the results of the parametric study the regression analysis was used to define each segment of the approximate 16th, 50th and 84th fractile IDA curve [5]. Since closed-form solutions for determination of target displacement as well as the SPO2IDA tool have its limitations, Han and Chopra [6] decided to determine seismic response parameters of buildings by using the IDA analyses of the SDOF systems. With this approach they eliminate an error resulting from inelastic spectra. However, pushover-based methods involve several simplifications, which are subject of debate among researchers for about 15 years. The basic assumption is that seismic response of building can be assessed based on the seismic response of an equivalent SDOF model which is determined by utilizing pushover analysis of a MDOF model. Since this assumption is straight forward, pushover-based methods was used primarily for first-mode dominated structures. Recently, the applicability of basic pushover-based methods was extended (e.g. [6–8]). These methods approximately take into account dynamic effects associated with higher modes.

As an alternative to described approaches for approximate determination of seismic response parameters, a web-based methodology for prediction of approximate IDA curves was recently introduced [9] with the aim to propose a more general yet computationally efficient method for prediction of seismic response parameters of first-mode dominated buildings. However this is not the only option for applicability of such technology. It is believed that the web-based methodology could be used in future to develop web applications for selection of ground motion records in order to facilitate use of response history analysis (i.e. for progressive IDA which involves precedence list of records [10] or for record-specific seismic performance assessment of building stock).

It was shown before that the proposed methodology for the prediction of approximate IDA curves is sufficiently accurate for the seismic performance assessment of first-mode dominated buildings, since it provide accurate estimates for the target displacement of equivalent SDOF models [9]. The objective of this chapter is to

briefly present this methodology and demonstrate the use of the web application for prediction of the approximate IDA curves of reinforced concrete structures.

2 Summary of the Web-Based Methodology and Application for Prediction of Approximate IDA Curves

The methodology which was used to develop the web-based application for determination of approximate IDA curves consists of two independent processes [9]. The first process involves determination of the response database, whereas the second process involves the prediction of approximate IDA curves from the response database. The first process is the parametric study, which is performed for the SDOF model and depends on definition of the input parameters which affect the seismic response, and definition of the discrete values of these input parameters. The usual input parameters of the parametric study are the period of the system, the parameters of the force-displacement relationship and the hysteretic behaviour, the damping, and the ground motions. It is worth emphasizing that definition of the SDOF model depends on expert judgement, since the selection of a force-displacement relationship or hysteretic behaviour of the SDOF model, which might be appropriate for simulating the global response of a specific structural type, is not trivial. Different experts may select different input parameters or discrete sets of their values. It is therefore important that the process of the parametric study is independent of the second process, since in the future many different databases may be created. The results of the parametric study can be used to create a response database, which can be established for a discrete number of input parameters of the SDOF model and for a set of ground motion records.

Since the IDA curves, which are stored in the response database, are computed for the discrete parameters of the SDOF model, the second process of the methodology involves prediction of the approximate IDA curves for any input parameter of the SDOF model. Clearly, this process is trivial if the request for the prediction of approximate IDA curves is based on the same input parameters as those for which the IDA curves are available in the response database. However, this is, in general, a very rare case. Thus the second process involves two steps: the query for appropriate IDA curves from the database, and the computation of the approximate IDA curves by the selected interpolation method. In the case of the presented methodology the n -dimensional linear (also known as multi-linear) interpolation is used by applying one-dimensional linear interpolation in each separate coordinate dimension by expression:

$$\begin{aligned}
 &IM(x_1^*, x_2^*, \dots, x_j^*, \dots, x_n^*) \\
 &= \sum_{i_1=0}^1 \sum_{i_2=0}^1 \dots \sum_{i_j=0}^1 \dots \sum_{i_n=0}^1 \\
 &\quad \left\{ IM(i_1, i_2, \dots, i_j, \dots, i_n) \cdot \prod_{j=1}^n [(1 - i_j)(1 - x_j^*) + i_j x_j^*] \right\} \quad (1)
 \end{aligned}$$

where $x_j^* \in [0, 1]$ are the normalized input coordinates of the point x_j where we seek the interpolated value $IM(x_1^*, x_2^*, \dots, x_n^*)$ and $IM(i_1, i_2, \dots, i_n)$ are values at the corners of the unit hypercube, which are available in the database.

The result of the query from the response database is a set of 2^n IDA curves, where n is the number of parameters, which define the SDOF model of the building. If the response database is computed for a sufficient number of discrete input parameters, then linear interpolation is a suitable method for determining the approximate IDA curves. It is known that equivalent SDOF models vary depending on the structural system and the material of the structure. For example, in the case of the prediction of the approximate IDA curves of a reinforced-concrete building, the force-displacement relationship can be described by the four dimensionless parameters $r_v = F_1/F_2$, $r_h = u_1/u_2$, $\mu_u = u_3/u_2$, $\alpha = -k_{pc}/k_i$, where points (u_1, F_1) and (u_2, F_2) , represent the first and second characteristic points of the idealized force-displacement relationship and roughly represent, respectively, the cracking of the concrete and, in the case of regular structures, yielding of reinforcement at the base of the columns. The displacement u_3 is related to the displacement where the strength of the structure starts degrading, while k_{pc} and k_i are, respectively, the post-capping and initial stiffness of the idealized force-displacement relationship.

3 Key Technological Principles of the Web Application

The infrastructure of the web application was built following the characteristics and the benefits of the cloud computing for the business environment—to increase IT capacity in real time and on the fly with no significant investment in new infrastructure, extensive training of personnel or licensing of the software. In addition, concepts introduced through the Web 2.0 revolution were adopted (simplicity, adaptability, remixability, openness, etc.). Discussion regarding the principles of the newly emerged technologies and their potential impact in the future can be found in [11].

There are several reasons to implement the presented methodology through the web application. Firstly, the database of the IDA curves can contain huge amount of data and as such is not appropriate for distribution. Although anyone can create his own database, it is unlikely that many researches or users will do so, since the determination of the database is computationally and time-demanding and also requires specific knowledge, which is usually not in the domain of the potential users. Therefore it is most appropriate that the database is stored and maintained in one place and can be easily accessible through the Internet.

Advantages of such environment are operating system independence, no need for installation and no maintenance cost. In addition, a web-based application can be accessed from anywhere at any time, which makes it even more attractive. The web application was built following the classic three-tier client-server architecture (Fig. 1), which enforces a general separation of three parts: client tier (also named presentation layer or, more specifically, user interface), middle tier (business logic)

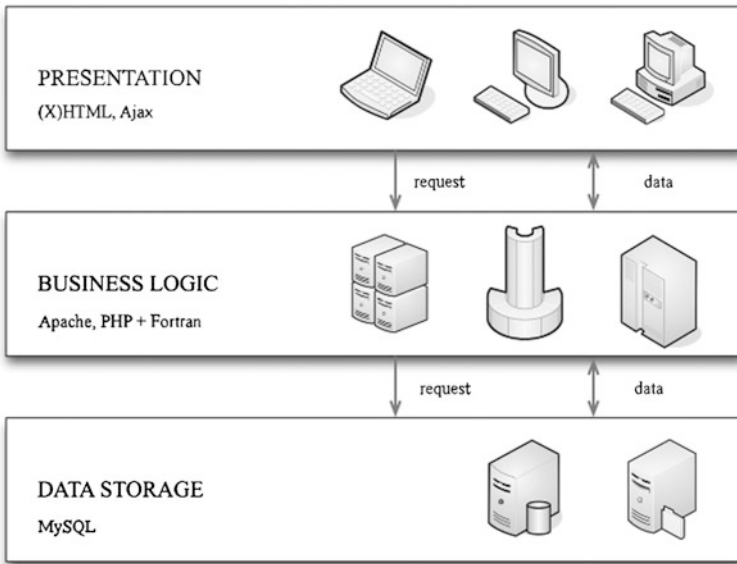


Fig. 1 Three-tier architecture of the web application

and data storage tier. The decision to adapt the three-tier client-server architecture resulted in the following advantages:

- The separation of the tiers makes it easier to modify or replace any tier (or part of the tier) without affecting the other tiers.
- Separating the application and the database functionality means better load balancing. For example, the database can reside on a completely different server.
- Adequate security policies can be enforced within the server tiers without the significant effect on the clients.

The main function of the top-most level of the application is to translate tasks and results to something the user can understand (the presentation tier of the system). In our application the presentation is disseminated through a web browser which handles web pages encoded in (X)HTML language and generated by a web server on the layer of business logic. Calls between the user interface and the web server are both synchronous and asynchronous. For asynchronous calls, Ajax web programming approach was applied.

The middle tier, the business logic layer is based on the Apache web server running on the Linux platform. Requests are handled by scripts written by using the PHP programming language which are processing input parameters, interacting with relational database, parsing results and preparing output (X)HTML pages. For mathematically advanced processing, Fortran script is used.

Data is stored in a relational database. On the basis of the excellent connectivity with the PHP programming language and the Apache web server it was decided to use the MySQL relational database. Another reason is the fact that it is open source

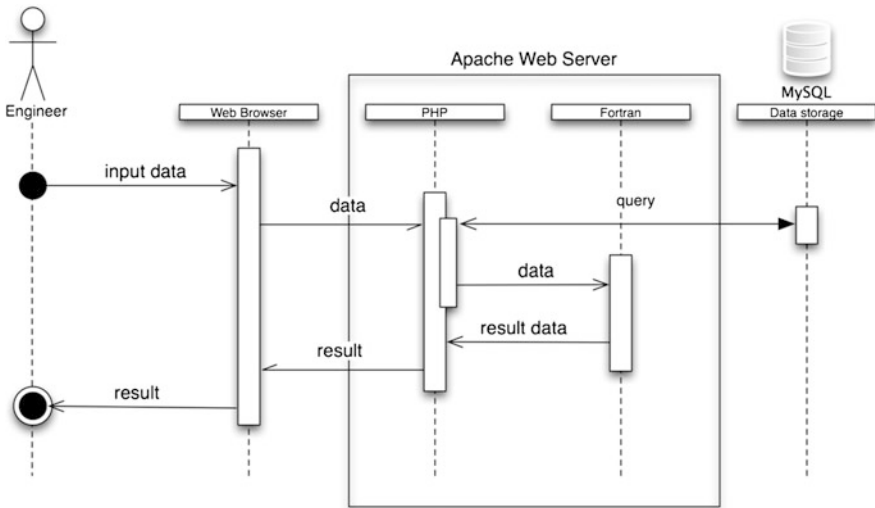


Fig. 2 The sequence diagram of the web application

software, freely available. In the test environment, the whole system resides on one server; however, the architecture is scalable so the business logic and data layer can be distributed to different physical servers if the requirements emerge. In the first iteration, the database of analysis results had approximately 5 million records spread over 2 relational tables and occupied almost 400 MB of space. However, after the normalization and optimization the database now has approximately 450,000 records in two relational tables and occupies roughly 170 MB of space. As a consequence, the calculation and response time dropped drastically from the initial 30 s to less than a few seconds (for combined input and output processing).

Details of the activities and the information passing between and within all tiers (Fig. 2) are usually completed in less than 3 seconds. The events are triggered in a following (simplified) sequence:

1. Engineer navigates to the web site of the developed application and inserts parameters of his structure to the HTML form.
2. Parameters are passed to the PHP script that builds an appropriate MySQL query and queries the MySQL database.
3. After receiving the resulting data, the data is processed and the requested parameters are saved to the file.
4. Fortran program is called and started, using saved file as an input. The result is an output file.
5. PHP script uses result data passed through the output file and process it.
6. The result is sent to the browser and stored to the result file, which is also available.
7. In parallel, PHP script is used to prepare graphs of the results and passing them to the browser.

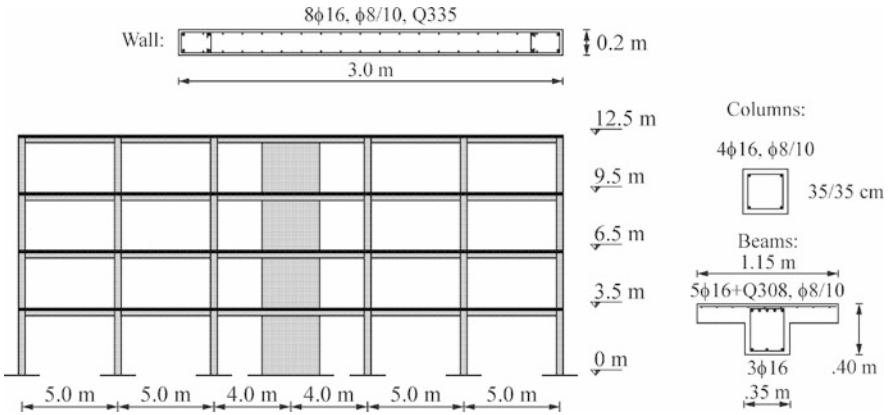


Fig. 3 The elevation and the typical reinforcement of the four-storey wall-equivalent dual structural system

4 Example

The proposed methodology and the web application for prediction of approximate IDA curves are demonstrated by means of an example of four-storey wall-equivalent dual structural system (Fig. 3). The approximate 16th, 50th and 84th fractile IDA curves have been predicted for the two intensity measures, i.e. for the peak ground acceleration a_g and for the spectral acceleration at the first mode period of the structure $S_{ae}(T_1)$, and for the two engineering demand parameters, which are the top displacement and the maximum drift. All the results are compared with those obtained by IDA. Note that the “exact” IDA curves were computed for all 30 ground motion records by assuming 2 % critical damping.

4.1 Description of the Structure, the Structural Model and the Seismic Loading

The four-storey reinforced concrete structure consists of two frames with the wall in the middle (Fig. 3). The height of the bottom storey is 3.5 m, whereas all other stories are 3 m high. The dimension of cross section of the columns is 35/35 cm. The width and height of the beams are 35 cm and 40 cm, respectively. Rather low amount of reinforcement is used for structural elements of frames since the central wall has quite high bearing capacity. Its dimension of cross section is 300/20 cm and is reinforced with the welded mesh Q335 and with $4\phi 16$ at both ends of the wall as presented in Fig. 3. The mean concrete strength and the yield strength of steel amounted 33 MPa and 400 MPa, respectively. Total mass of the structure (429 t) resulted from gravity (9 kN/m^2) and variable (2 kN/m^2) action, which were combined according to the Eurocode 8 rule. Vertical loads of beams were considered

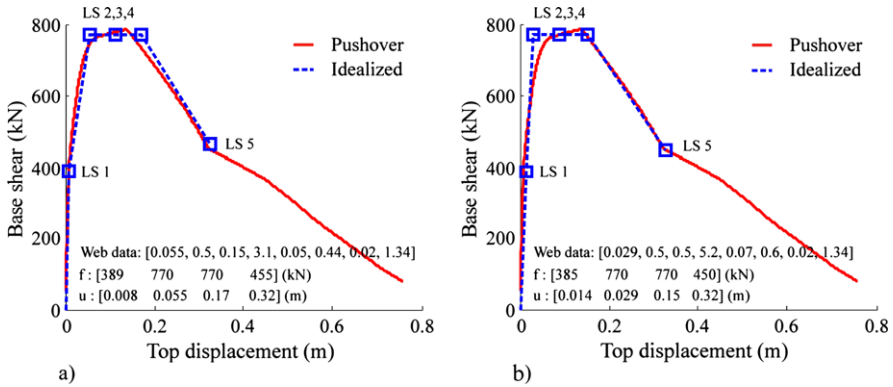


Fig. 4 The pushover curve of the dual structural system, (a) the quadrilinear and (b) trilinear idealized force-displacement relationship. Web data represents, respectively, u_2 (m), $r_v = F_1/F_2$, $r_h = u_1/u_2$, $\mu_u = u_3/u_2$, $\alpha = -k_{pc}/k_i$, T (s), ξ and Γ

being constant along the elements by assuming the effective distance between the two planar structures equal to 4 m.

A structural model of the building was prepared by using the PBEE toolbox [12], which can be applied for the seismic performance assessment of reinforced concrete (RC) buildings in conjunction with OpenSees [13]. The aim of the PBEE toolbox is to enable rapid definition of simple nonlinear structural models of RC buildings. In this case the most time-consuming part of the work involves the determination of the properties of the plastic hinges. Since the PBEE toolbox automatically generates the properties of plastic hinges, based on data regarding material strength, reinforcement and section properties, and involve function for post-processing of analysis results, its significantly facilitates use of nonlinear analyses for the purpose of seismic performance assessment or design of buildings.

4.2 Determination of Approximate IDA Curves

The input parameters which are required for the determination of the approximate IDA curves can be defined based on the results of the pushover analysis. A horizontal load pattern for pushover analysis corresponded to the product of the storey masses $m = [106 \ 106 \ 106 \ 109 \ t]^T$ and the first mode shape $\phi = [0.15 \ 0.41 \ 0.71 \ 1.0]^T$.

The pushover curve is presented in Fig. 4 where it can be observed that the maximum base shear force versus weight ratio amounts to about 18 % and that displacement capacity is rather small since at displacement 22.8 cm structure’s shear resistance is reduced for about 15 %.

The pushover curves were idealized with a quadrilinear (Fig. 4a) and trilinear (Fig. 4b) force-displacement relationship. Note that two types of idealized force-displacement relationship were selected due to the comparison reasons. In the first

case the period of the equivalent SDOF model is similar to the period of the structure since the initial stiffness of the idealized force-displacement relationship is approximately the same as that corresponded to the pushover curve, whereas in the second case the initial stiffness of the equivalent model is much smaller, which is the usual case if the seismic response parameters is determined by the pushover-based methods.

Five limit states were arbitrarily defined based on the pushover curve in order to evaluate the difference between IDA and approximate IDA. The most severe limit state (LS 5) was defined in the post-capping range and corresponded to the base shear, which is 15 % smaller than the maximum base shear. At this displacement the storey-drift ratio was approximately constant from storey to storey and amounted 1.8 %. Other limit states were defined as shown in Fig. 4, where displacement at LS 3 is mean displacement of those corresponded to the LS 2 and LS 4. The limit state LS 1 is defined at half of the maximum force of the trilinear force-displacement relationship, whereas for the case of quadrilinear force-displacement relationship, LS 1 corresponded to the first point of the idealized force-displacement relationship.

The parameters of the equivalent SDOF model can be easily computed based on the results of the pushover analysis and are also presented in Fig. 4. Note that the parameter of the force-displacement relationship as well as the period varies with respect to the quadrilinear or trilinear force-displacement relationship, while the modification factor $\Gamma = 1.34$ and the damping ratio are the same for the two cases.

The approximate IDA curves were obtained by using the web application (<http://ice4risk.slo-projekt.info/WIDA/>), as presented in Fig. 5. The result of the web application is the visual presentation of the approximate IDA curves in the browser as well as in the file, which can be downloaded for further processing. The intensity measure of the approximate IDA curves is the peak ground acceleration or spectral acceleration, which corresponds to the period of the idealized system and the selected damping. In addition to the approximate IDA curves for the given ground motion records, web application provides the 16th, 50th and 84th fractile IDA curves. Note that these fractiles can be obtained for a given engineering demand parameter (EDP) or a given intensity measure (IM). However, in our examples the fractiles are presented for a given IM, which corresponds to the usual (EDP-based) statistics of IDA.

The approximate 16th, 50th and 84th fractile IDA curves are compared with the “exact” IDA curves (Figs. 6 and 7). The spectral acceleration at first mode period and the peak ground acceleration were selected for the intensity measure as presented, respectively, in Figs. 6 and 7. In addition to the IDA curves also the points, which correspond to the arbitrarily defined limit states, are presented. Note that the five limit states were defined based on the idealized force-displacement relationship of the pushover curve, as described above and presented in Fig. 4. Therefore the limit states may not be appropriate for seismic performance assessment of the structure, but they should be understood as generic limit states with increasing levels of nonlinearity, which are defined only for the purpose of measuring the error induced by the approximate IDA curves.

ICE4RISK | Approximate IDA curves

High-throughput computing environment for seismic risk assessment

[ICE4RISK web site](#) | [Application description](#)

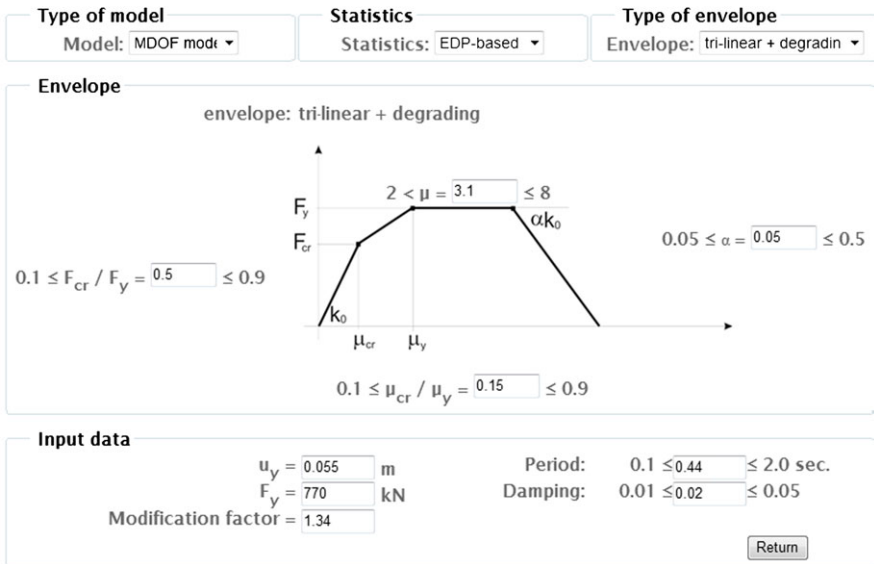


Fig. 5 The user interface of the web application (<http://ice4risk.slo-projekt.info/WIDA>) for the case of quadrilinear idealization of the pushover curve

In general quite small error is observed for the approximate 50th and 84th fractile IDA curves. However, comparison between the IDA curves for the case of trilinear force-displacement relationship, which is shown in Fig. 6b, is not considered in this observation.

A bit larger error is observed for the 16th fractile response. If the intensity measure is the spectral acceleration at the first mode period then approximate IDA underestimate 16th fractile of the global collapse capacity (Fig. 6). Quite opposite is observed for 16th fractile IDA curve if the peak ground acceleration is selected for the intensity measure (Fig. 7b). In this case the approximate IDA underestimates the 16th fractile of the engineering demand parameters but the peak ground acceleration that causes global dynamic instability is overestimated.

The large difference between the approximate IDA and IDA curves presented for the case of trilinear idealization of the force-displacement relationship (Fig. 6b) can be explained as follows. Namely, the trilinear idealization of the force-displacement relationship results in higher period of the equivalent SDOF model ($T = 0.6$ s) with respect to the first mode period of the structure ($T = 0.43$ s). Therefore comparison presented in Fig. 6b is not consistent, even misleading, since intensity measures for approximate IDA and the IDA are in fact different ($S_{ae}(T = 0.6 \text{ s}) \neq S_{ae}(T = 0.43 \text{ s})$). On the other hand this inconsistency could be partly eliminated if, for example, the intensity measure in the case of approximate IDA would be equal

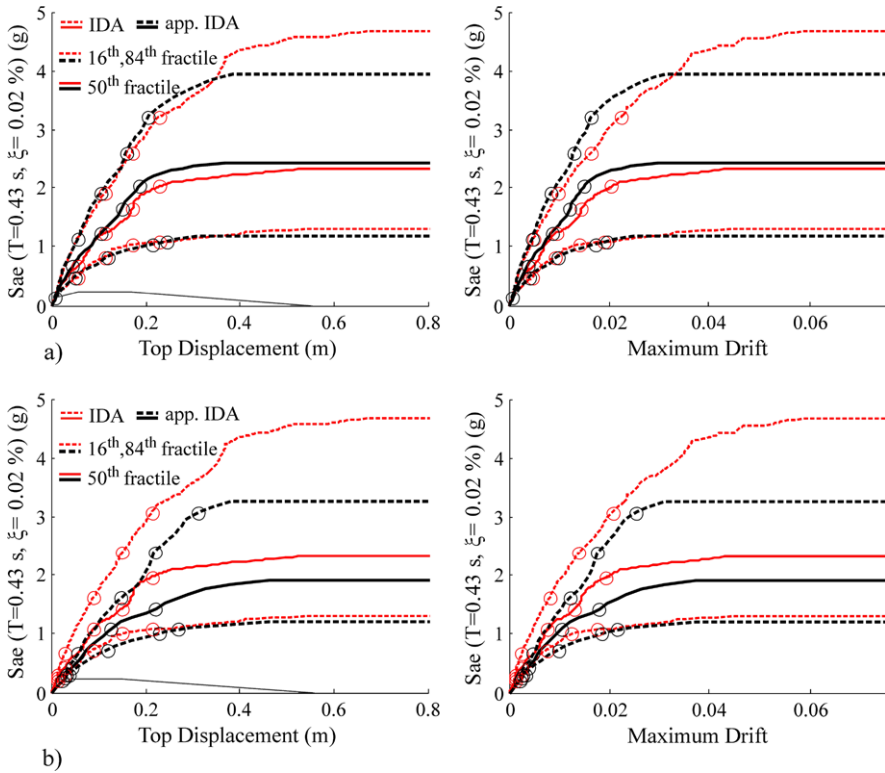


Fig. 6 Comparison between the approximate and “exact” fractile IDA curves for the top displacement and maximum drift versus the spectral acceleration at first mode period, for (a) the quadrilinear and (b) trilinear idealized force-displacement relationships. The defined limit states (LS) are also indicated

to that in IDA. Currently the web application does not have the capability to distinguish between the period of the equivalent SDOF system and the period, which is adopted for definition of intensity measure if expressed in terms of the spectral acceleration.

The three fractiles of the peak ground acceleration, which causes global dynamic instability, are predicted with high accuracy. The largest error is -6.6% (Table 1), while the average absolute error is only 3.3% . In this case both types of force-displacement relationship were capable of predicting similar results. A slightly larger error is observed for the case if the intensity measure is spectral acceleration at the first mode period ($T = 0.43$ s). The only valid comparison for this case can be made on the basis of the approximate IDA of the quadrilinear force-displacement relationship. Knowing that the spectral acceleration at only 2% damping is quite sensitive parameter, it can be concluded that $S_{ae}(T_1)$, which caused dynamic instability, is predicted with sufficient accuracy, since an average error is about 10% .

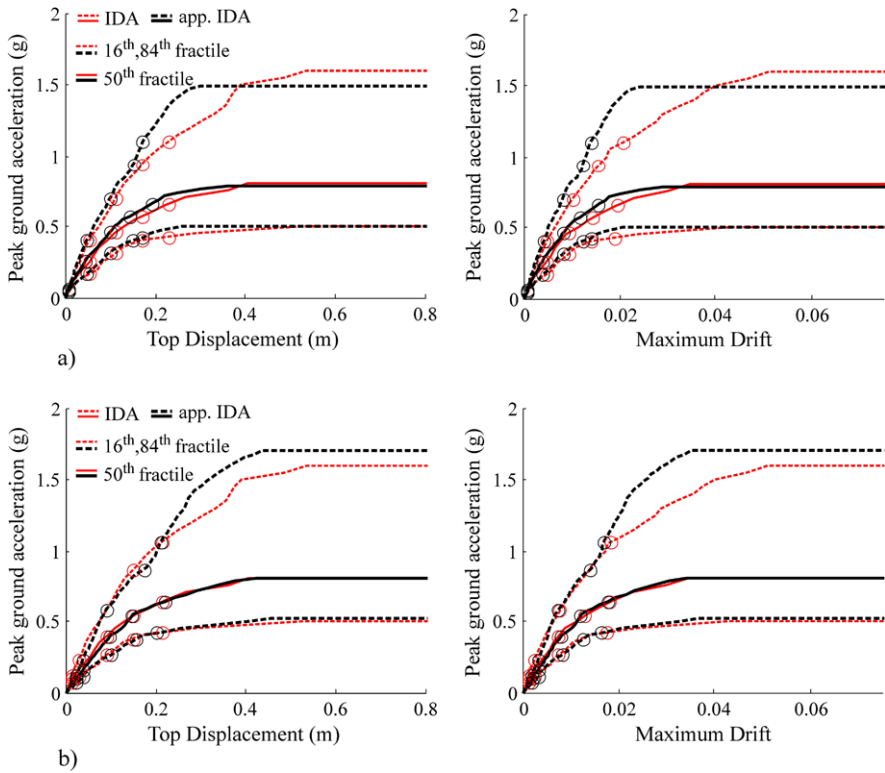


Fig. 7 Comparison between the approximate and “exact” fractile IDA curves for the top displacement and maximum drift versus the peak ground acceleration, for (a) the quadrilinear and (b) trilinear idealized force-displacement relationships. The defined limit states (LS) are also indicated

Table 1 Predicted and “exact” fractiles of the peak ground acceleration and $S_{ae}(T_1)$, which causes global dynamic instability (collapse) of the structure

Analysis and percent error	$S_{ae}(T_1)$ (g)			Peak ground acceleration (g)		
	84th	50th	16th	84th	50th	16th
IDA	1.29	2.31	4.68	0.50	0.80	1.60
App. IDA—quadr.	1.17	2.43	3.95	0.50	0.78	1.49
App. IDA—tri.	1.19	1.91	3.26	0.52	0.80	1.70
ε (%)—quadr.	-9 %	6 %	-15 %	-0.4 %	-2.1 %	-6.6 %
ε (%)—tri.	-8 %	-17 %	-30 %	4.0 %	0.5 %	6.4 %

Since displacement demand is very sensitive in the range near global dynamic instability, it is very difficult to predict it with high accuracy. Therefore also the error for predicting the limit state EDPs can be high but may still be acceptable.

Table 2 The average absolute error $E[|\varepsilon|]$ for predicted top displacement and maximum drift considering the first three limit states and all limit states. Results are presented for the case of quadrilinear force-displacement relationship of the idealized pushover curve

	$S_{ae}(T_1)$ vs. top disp.		a_g vs. top disp.	
	LS 1–3	All	LS 1–3	All
$E[\varepsilon]$	9 %	11 %	14 %	15 %
	$S_{ae}(T_1)$ vs. max. drift		a_g vs. max. drift	
$E[\varepsilon]$	9 %	13 %	16 %	18 %

For example, mean error for predicting EDPs taking into account first three limit state or all five, is presented in Table 2, for both intensity measures but only for the quadrilinear force-displacement relationship. It can be observed that error slightly increases if more severe limit states were incorporated in its calculation. However, an average error does not exceed 18 %. Note that the error is partly the consequence of the pushover-based methodology for prediction of the approximate IDA curves and partially the consequence of the n -dimensional interpolation between the IDA curves of the SDOF model, which are stored in the response database of the web application. However, the later source of error is usually small, as discussed elsewhere [9].

5 Conclusions

The web-application for the prediction of approximate IDA curves is an innovative computational tool since it enables fast and accurate prediction of seismic response parameters based on the results of pushover analysis. The advantage of the proposed methodology, which was used for development of the web application, is the systematic treatment of huge parametric studies. Namely, the response database and the procedure for determination of the approximate IDA curves based on the results stored in the database are independent. Therefore the response database can be easily upgraded with the new data, for example, by adding the response for different sets of ground motion records.

The results of the presented example have indicated that the approximate IDA curves are in very good agreement with the IDA curves for most of the presented results. It was shown that overall results are better if the approximate IDA curves are predicted by using the quadrilinear force-displacement relationship of the equivalent SDOF model. However, prediction of the top displacement and the maximum drift which correspond to severe limit states is very sensitive and therefore difficult to predict with high accuracy.

Acknowledgements The results presented in this chapter are based on work supported by the Slovenian Research Agency within the framework of the project High-throughput computing environment for seismic risk assessment (<http://ice4risk.slo-projekt.info/>) (J2-0845-0792-08). This support is gratefully acknowledged.

References

1. Fajfar P (2000) A nonlinear analysis method for performance-based seismic design. *Earthq Spectra* 16(3):573–592
2. CEN (2004) Eurocode 8: design of structures for earthquake resistance. Part 1: General rules, seismic actions and rules for buildings. EN 1998-1, European Committee for Standardisation, Brussels
3. Dolšek M, Fajfar P (2005) Simplified non-linear seismic analysis of infilled concrete frames. *Earthq Eng Struct Dyn* 34(1):49–66
4. Vamvatsikos D, Cornell CA (2006) Direct estimation of the seismic demand and capacity of oscillators with multi-linear static pushovers through IDA. *Earthq Eng Struct Dyn* 35:1097–1117
5. Vamvatsikos D, Cornell CA (2002) Incremental dynamic analysis. *Earthq Eng Struct Dyn* 31:491–514
6. Han SW, Chopra AK (2006) Approximate incremental dynamic analysis using the modal pushover analysis procedure. *Earthq Eng Struct Dyn* 35:1853–1873
7. Chopra AK, Goel RK (2002) A modal pushover analysis procedure for estimating seismic demands for buildings. *Earthq Eng Struct Dyn* 31(3):561–582
8. Kreslin M, Fajfar P (2011) The extended N2 method taking into account higher mode effects in elevation. *Earthq Eng Struct Dyn* 40:1571–1589
9. Peruš I, Klinc R, Dolenc M, Dolšek M (2013) A web-based methodology for the prediction of approximate IDA curves. *Earthq Eng Struct Dyn* 42(1):43–60. doi:[10.1002/eqe.2192](https://doi.org/10.1002/eqe.2192)
10. Azarbakht A, Dolšek M (2011) Progressive incremental dynamic analysis for first-mode dominated structures. *J Struct Eng* 137:445–455
11. Klinc R, Dolenc M, Turk Ž (2009) Engineering collaboration 2.0: requirements and expectations. *ITcon* vol 14, special issue Next generation construction IT: technology foresight, future studies, roadmapping, and scenario planning, pp 473–488. <http://www.itcon.org/2009/31>
12. Dolšek M (2010) Development of computing environment for the seismic performance assessment of reinforced concrete frames by using simplified nonlinear models. *Bull Earthq Eng* 8(6):1309–1329
13. OpenSees (2011) Open system for earthquake engineering simulation. Pacific Earthquake Engineering Research Center, Berkeley. <http://opensees.berkeley.edu/>. Accessed August 2011

Improving Static Pushover Analysis by Optimal Bilinear Fitting of Capacity Curves

Flavia De Luca, Dimitrios Vamvatsikos, and Iunio Iervolino

Abstract An improvement of codes' bilinear fit for static pushover (SPO) curves is put forward aimed at decreasing the error introduced in the conventional SPO analysis by the piecewise linear fitting of the capacity curve. In the approach proposed herein, the error introduced by the bilinear fit of the force-deformation relationship is quantified by studying it at the single degree of freedom (SDOF) system level, away from any interference from multiple degree of freedom (MDOF) effects. Incremental Dynamic Analysis (IDA) is employed to enable a direct comparison of the actual curved backbones versus their piecewise linear approximations in terms of the spectral acceleration capacity for a continuum of limit-states, allowing an accurate interpretation of the results in terms of performance. A near-optimal elastic-plastic bilinear fit can be an enhanced solution to decrease systematically the error introduced in the SPO analysis if compared to the fit approaches provided by most codes. The main differences are (a) closely fitting the initial stiffness of the capacity curve and (b) matching the maximum strength value, rather than disregarding them in favor of balancing areas or energies. Employed together with selective area discrepancy minimization, this approach reduces the conservative bias observed for systems with highly curved force-deformation backbones.

Keywords Pushover curve · Incremental dynamic analysis · Single-degree-of-freedom · Piecewise linear fit

F. De Luca (✉) · I. Iervolino

Dipartimento di Strutture per l'Ingegneria e l'Architettura, Università degli Studi di Napoli Federico II, Via Claudio 21, 80125 Naples, Italy
e-mail: flavia.deluca@unina.it

I. Iervolino
e-mail: iunio.iervolino@unina.it

D. Vamvatsikos
School of Civil Engineering, National Technical University of Athens, 9 Heron Polytechniou, 15780 Athens, Greece
e-mail: divamva@mail.ntua.gr

1 Introduction

In the last decades, improvements in the computational capabilities of personal computers have allowed the employment of nonlinear analysis methods in many earthquake engineering problems. In this framework, nonlinear static analysis is becoming the routine approach for the assessment of the seismic capacity of existing buildings. Consequently, nonlinear static procedures (NSPs) for the evaluation of seismic performance, based on static pushover analysis (SPO), have been codified for use in practice. All such approaches consist of the same five basic steps: (a) to perform static pushover analysis of the multi-degree-of-freedom (MDOF) system to determine the base shear versus displacement (e.g., roof) response curve; (b) to fit a piecewise linear function (often bilinear) to define the period and backbone of an equivalent single degree of freedom system (SDOF); (c) to use a pre-calibrated R - μ - T (reduction factor-ductility-period) relationship for the extracted piecewise linear backbone to obtain SDOF seismic demand for a given spectrum; (d) to use the static pushover curve to extract MDOF response demands; (e) finally, to compare demands to capacities; see [1] for example.

In fact, NSP is a conventional method without a rigorous theoretical foundation for application on MDOF structures [2], as several approximations are involved in each of the above steps. On the other hand, its main strength is its ability to provide nonlinear structural capacity in a simple and straightforward way.

Although several improvements and enhancements have been proposed since its introduction, any increase in the accuracy of the method is worth only if the corresponding computational effort does not increase disproportionately. Extensively investigated issues are the choice of the pattern considered to progressively load the structure and the implication of switching from the nonlinear dynamic analysis of a multiple degree of freedom (MDOF) system to the analysis of the equivalent SDOF sharing the same (or similar) capacity curve. Regarding the shape of the force distributions, it was observed that an adaptive load pattern could account for the differences between the initial elastic modal shape and the shape at the collapse mechanism [3–5]. Contemporarily, other enhanced analysis methodologies were proposed to account for higher mode effects and to improve the original MDOF-to-SDOF approximation (e.g., [6]). Regarding the demand side, efforts have been put to provide improved relationships between strength reduction factor, ductility, and period (R - μ - T relationships), to better evaluate the inelastic seismic performance at the SDOF level [7, 8].

One of the issues that have not yet been systemically investigated is the approximation introduced by the piecewise linear fit of the capacity curve for the equivalent SDOF (for some preliminary suggestions see the recent NIST GCR 10-917-9 [9] report).

The necessity to employ a multilinear fit (an inexact, yet common, expression to describe a piecewise linear function) arises due to the use of pre-determined R - μ - T relationships that have been obtained for idealized systems with piecewise linear backbones. This has become even more important recently since nonlinear modeling practice has progressed towards realistic multi-member models, which often

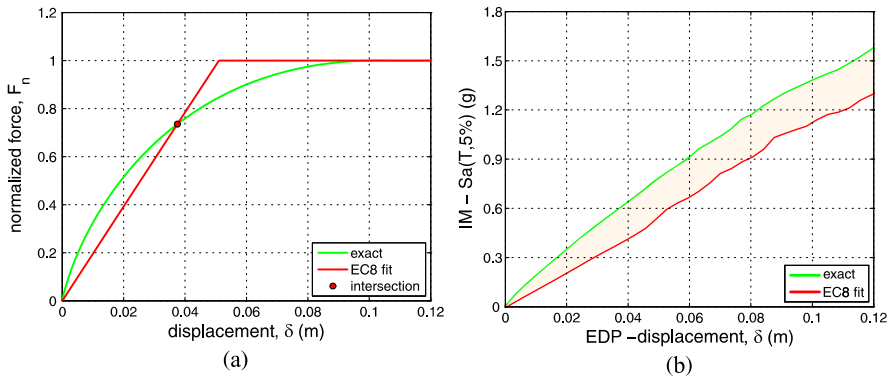


Fig. 1 (a) Example of exact capacity curve versus its elastoplastic bilinear fit according to EC8, and (b) the corresponding median IDA curves showing the negative (conservative) bias due to fitting for $T = 0.5$ s (from [18])

accurately capture the initial stiffness using uncracked section properties. The gradual plasticization of such realistic elements and models introduces a high curvature into the SPO curve that cannot be easily represented by one or two linear segments. It is an important issue whose true effect is often blurred, being lumped within the wider implications of using an equivalent SDOF approximation.

The investigation presented deals only with the bilinear approximation of the capacity curves. Although $R-\mu-T$ relationships that can capture far more complex backbones have recently appeared [10], the bilinear approach is by far the most widely employed in guidelines and literature [11–16]. The approach presented herein will be based on the accurate assessment of the effect of the equivalent SDOF fit on the nonlinear static procedure results. This can be achieved by quantification of the bias introduced into the estimate of the seismic response at the level of the SDOF itself.

Incremental dynamic analysis (IDA) [17] will be used as the benchmark method to quantify the error introduced by a bilinear fit with respect to the exact capacity curve of the SDOF. Figure 1a shows a typical example, where an elastoplastic backbone fit is used according to Eurocode 8 or EC8 [11]. While this fit approach is meant to result to an unbiased approximation in terms of seismic performance, the median IDA results of Fig. 1b show the actual error that is introduced by such code-mandated fitting rules. In most cases, they lead to an unintended and hidden bias that is generally conservative. On the other hand, this bias can become unreasonably high in many situations.

Therefore, three issues emerge for addressing: first, to develop a methodology aimed at quantifying the bias introduced by the fitting of a capacity curve; second, to assess the error introduced by the fitting rules already employed in codes and literature; third, to perform a systematical investigation aimed at providing alternative fits that can reduce this discrepancy to almost a minimum. The comparison with existing approaches will function as the benchmark to evaluate the improvement introduced by the alternative fitting rules proposed.

A near optimal solution in terms of the bilinear fit will, thus, be examined for both hardening and softening behavior. A more comprehensive solution based on a piecewise linear fit with three or four linear segments is studied in [18].

2 Methodology

The first main target is the quantification of the error introduced in the NSP-based seismic performance assessment by the replacement of the original capacity curve of the system, termed the “exact” or “curved” backbone, with a piecewise linear approximation, referred to as the “fitted” or “approximate” curve (e.g., Fig. 1a). This will enable a reliable comparison between different fitting schemes in an attempt to minimize the observed discrepancy between actual and estimated performance. In all cases, to achieve an accurate and focused comparison of just the effect of fitting, it is necessary to disaggregate the error generated by the fit from the effect of approximating an MDOF structure via an SDOF system. Thus, all the investigations are carried out entirely at the SDOF level.

An ensemble of SDOF oscillators is considered with varying curved shapes of force-deformation backbones. They are all fitted accordingly with bilinear elastic-plastic shapes. For each considered curved backbone shape, 5 % viscous damping was used and appropriate masses were employed to obtain periods of 0.2 sec, 0.5 sec, 1 sec, and 2 sec. In all cases, both the exact and the approximate system share the same mass, thus replicating the approach followed in the conventional NSP methodology (e.g., [1]).

When comparing an original system with its approximation, having a piecewise linear backbone, the same hysteretic rules are always employed, so that both systems display the same characteristics when unloading and reloading in time-history analyses. In other words, all differences observed in the comparison can be attributed to the fitted shape of the approximate backbone, obviously also capturing any corresponding differences in the oscillator period.

For each exact shape of the SDOF’s capacity curve and for each period value, several piecewise linear fit approximations have been considered according to different fitting rules. To enable a precise comparison that will allow distinguishing among relatively similar backbones in consistent performance terms, as it was previously stated, IDA is employed. Median IDA curves of the exact capacity curves and their backbones are compared according to the intensity measure given engineering demand parameters (IM|EDP) approach, see [19] and [18] for details.

To perform IDA for each exact and approximate oscillator considered, a suite of sixty ground motion records was used, comprised of both horizontal components from thirty ordinary records from the PEER NGA database. They represent a large magnitude, short distance bin having no near-source directivity or soft-soil effects. Using the hunt and fill algorithm [20], 34 runs were performed per record to capture each IDA curve with excellent accuracy. The IM of choice was the 5 %-damped spectral acceleration at the period T of the oscillator, $S_a(T)$, while the oscillator

displacement δ was used as the corresponding EDP, being the only SDOF response of interest when applying the NSP.

Once the IM and EDP are decided, interpolation techniques allow the generation of a continuous IDA curve from the discrete points obtained by the 34 dynamic analyses for each ground motion record.

The resulting sixty IDA curves can then be employed to estimate the summarized IDA curves for each exact and approximate pair of systems considered. Still, in order to be able to compare an exact system with a period T with its approximation, having an equivalent period T_{eq} , it was necessary to have their summarized IDA curves expressed in the same IM. In this case it is chosen to be $S_a(T)$; i.e., the spectral ordinate at the period of the exact backbone oscillator. Thus, while the approximate system IDA curves are first estimated as curves in the $S_a(T_{eq})-\delta$ plane, they are then transformed to appear on $S_a(T)-\delta$ axes. This is achieved on a record-by-record basis by multiplying all the $S_a(T_{eq})$ values, from the runs that comprise the i -th IDA curve, by the constant spectral ratio ($S_a(T)/S_a(T_{eq})$) that characterizes the i -th record [21].

The error due to the fitting is evaluated for every value of displacement, δ , or normalized displacement, δ_n , in terms of the relative difference between the two system median S_a -capacities, both evaluated at the period T of the exact system, as it is shown in Eq. (1).

$$e_{50}(\delta_n) = \frac{S_{a,50}^{fit}(\delta_n) - S_{a,50}^{exact}(\delta_n)}{S_{a,50}^{exact}(\delta_n)} \quad (1)$$

3 Overview of Code and Guidelines Fits

The piecewise linear fit made of two branches (bilinear) is the most common approximation adopted by codes and guidelines; unsurprisingly most $R-\mu-T$ relationships have been calibrated for such approximate backbones. Eurocode 8 [11] suggests a bilinear fit based on the equivalence of the area discrepancy above and below the fit, assuming an elastic-plastic idealized backbone for the equivalent SDOF, see Fig. 2a. This approach is similar to the original N2 method [1]. As a consequence, EC8 prescribes an $R-\mu-T$ relationship [7] based on the elastic-perfectly-plastic fit.

The EC8 approximation is fitted up to the point of attainment of a plastic mechanism (point A in Fig. 2a). The only remaining parameter to be evaluated is the yield displacement (δ_y), determined by the equivalence of the areas (or the corresponding energy). At its basis, the EC8 fitting process is not iterative. Still, an optional iterative adjustment of the fit for a given target displacement is also possible [11].

FEMA documents (FEMA 273 [12]; FEMA 356 [13]; FEMA 440 [14]) gradually upgraded the proposed piecewise linear fit by integrating rules to account for softening behavior. According to FEMA 356 [13] (see Fig. 2b), the idealized relationship is bilinear with an initial slope and a post yield slope (positive or negative) evaluated by balancing the area above and below the capacity curve up to the target displacement (δ_t) and calculating the initial effective slope at a base shear force

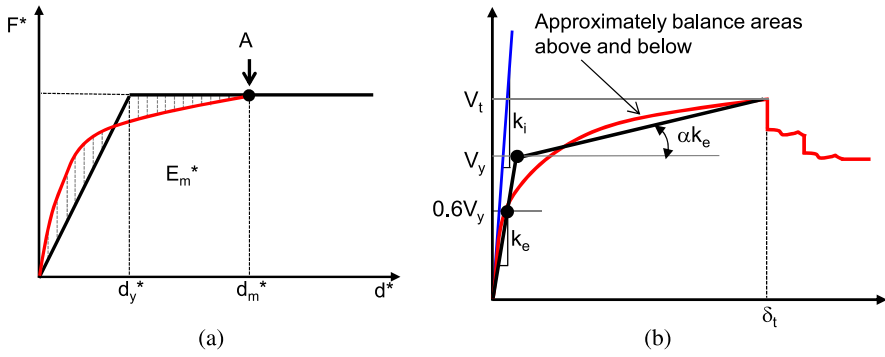


Fig. 2 Fitting procedure (a) according to EC8 [11], (b) according to FEMA 356 [13]

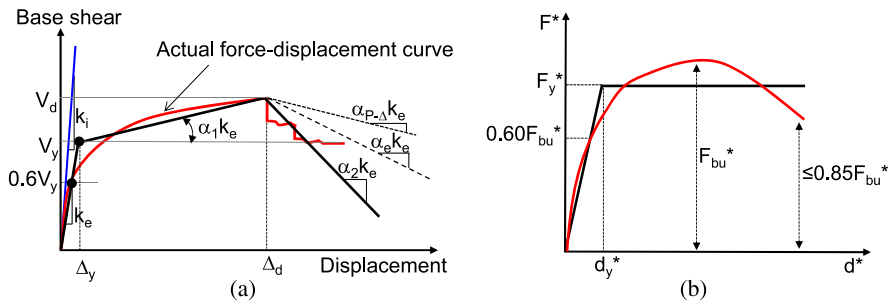


Fig. 3 Fitting procedure (a) according to FEMA 440 [14] and ASCE/SEI 41-06 [15], (b) according to Italian seismic code (CS.LL.PP. [16, 22])

equal to 60 % of the nominal yield strength. The proposed graphical procedure is iterative. All FEMA documents are based on the coefficient method for the evaluation of demand.

FEMA 440 [14], and consequently ASCE/SEI 41-06 [15] that provides exactly the same fitting method, assume the basic approach provided by FEMA 356 [13] with additional rules regarding the softening behavior, see Fig. 3a. The softening slope α_e is employed only in the evaluation of the limiting value of strength reduction factor to avoid dynamic instability, and not in determining the target displacement.

It is worth to note that α_e is evaluated according to a simplified expression, see Eq. (2), that accounts for both softening caused by $P-\Delta$ effect ($\alpha_{P-\Delta}$) and for the negative stiffness (α_2) caused by cyclic and in-cycle degradation. The *ad hoc* λ coefficient in Eq. (2) is meant to account for near-field effects.

$$\alpha_e = \alpha_{P-\Delta} + \lambda(\alpha_2 - \alpha_{P-\Delta}) \tag{2}$$

In FEMA 440 [14] it is clearly emphasized that the whole fitting procedure; in particular the definition of intersection at 60 % of V_y and the suggested values for the λ coefficient are based purely on judgment. The latter observation emphasizes

the need of a more specific investigation of the fit approach adopted. Some preliminary suggestions on this subject are provided in the recent NIST GCR 10-917-9 [9] report, while a more systematical validation on this specific issue is provided in the study herein.

Italian guidelines (CS.LL.PP. [16, 22]) suggest an elastoplastic fit that may also account for a limited softening behavior up to the point of a 15 % degradation of the maximum base shear in the capacity curve. The fit is based on the 60 % rule for the initial stiffness, in analogy with all FEMA documents. Then, an equal area criterion is applied to derive the plateau of the bilinear fit; the latter can be extended up to the point in which a 15 % degradation of the maximum base shear is reached (Fig. 3b).

The result of such an approach is that the plateau of the elastic-plastic fit is always lower than the maximum shear strength of the exact backbone. Obviously, if the structural model adopted cannot display any negative stiffness (e.g., elastic plastic behavior of the element without consideration of $P-\Delta$ effects), this fitting criterion simply becomes equivalent to FEMA provisions. The obtained bilinear fit according to the Italian code provisions is then accompanied by the classical [7] $R-\mu-T$ relationship, also employed in Eurocode 8.

4 Investigation of Bilinear Fits

Bilinear elastic-plastic or elastic-hardening fits are the fundamental force-deformation approximations employed in all NSP guidelines, as shown in the previous section. The simplicity of the bilinear shape means that the only need is to estimate the position of the nominal “yield point” and select a value for the constant post-elastic stiffness. According to codified prescriptions the general criteria followed are: (a) using the intersection at a specific point of the “exact” capacity curve, and/or (b) area balancing approaches that in turn conform to an equal energy criterion.

The definition of a near-optimal bilinear fit is attempted by a two steps process: first the definition of the proper initial slope is investigated considering generalized elastic plastic exact backbones, and then the post-elastic part is investigated considering generalized hardening and softening in the exact backbone studied. The scope of the investigation is always limited to bilinear non-softening fits.

For the first sample of generalized elastic-plastic systems studied, the stiffness becomes zero beyond a displacement of 0.10 m and the target displacement is assumed to be well into the fully plastic region. Thus, the post-elastic segment is fixed to have zero stiffness while the initial “elastic” part can be fitted at will.

In both the FEMA and EC8 fitting rules, the fitted “elastic” stiffness can be a function of the target displacement due to the area balancing used. This can make the bilinear fitting yield different results depending on the limit-state of interest and may initially put the code-mandated fits (as implemented herein) at a slight disadvantage. It will be remedied in the second part of the study where generalized elastic-hardening systems will be tackled. They have varying post-yield stiffness and lower target displacements, allowing more fitting flexibility and providing a

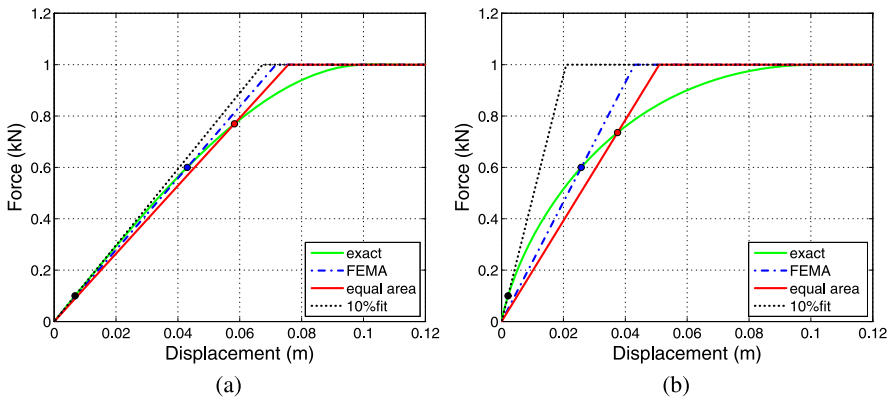


Fig. 4 Comparison of generalized elastic-plastic capacity curves and their corresponding fits having (a) insignificant versus (b) significant changes in initial stiffness (from [18])

more rigorous comparison of code fits against any proposal for a near-optimal bilinear fit in the case of non-softening “exact” capacity curves. Finally, in analogy with the approach followed by the recent Italian seismic code, also “exact” capacity curves characterized by degrading behavior will be investigated. In this latter case an elastoplastic fit is still employed and the general aim is to check up to which point in the softening range it remains accurate.

Generally, the target, herein, is the development of a simple fitting rule that performs well for a continuum of limit states. Therefore, the performance of all rules will be carefully examined even outside the immediate region of interest defined by a target displacement.

4.1 Bilinear Fits of Generalized Elastic-Plastic Systems

First a family of generalized elastic-plastic capacity curves is considered that exhibit a stiffness gradually decreasing with deformation, starting from the initial elastic and reaching zero slope. The shapes are characterized by the magnitude of the changes in stiffness. Figures 4a and 4b give an example of the shapes employed in the investigation of this family of backbones and emphasize two opposing cases. The first (Fig. 4a) is not characterized by significant curvature, while the second (Fig. 4b) shows a significant change in slope that can be representative of the behavior of a model that accounts for uncracked stiffness. The kinematic strain hardening and a moderately pinching hysteresis rule [23] are considered.

Three basic fitting rules are compared: (a) the FEMA fit (60 % rule) assuming a target displacement high enough so that the slope of the second branch of the bilinear can be assumed to be zero; (b) the EC8 fit using a simple *equal area* criterion; (c) the 10 % fit, defined so that the intersection between the capacity curve and the

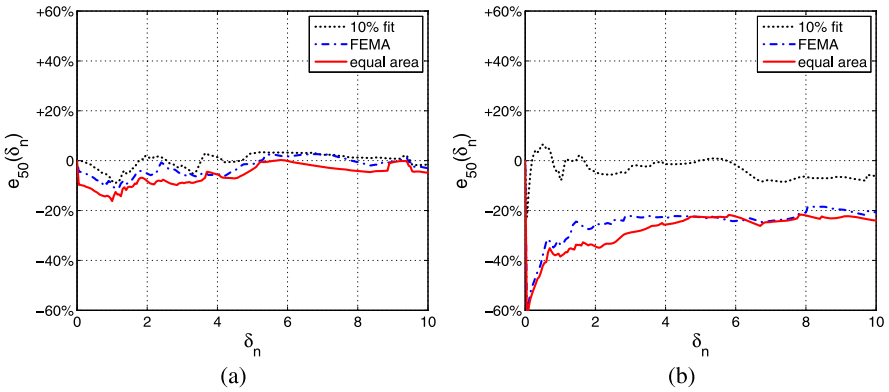


Fig. 5 Median relative error comparison between the 10 %, FEMA and equal area fits for $T = 0.2$ sec, when applied to the capacity curves of Fig. 4: (a) insignificant versus (b) significant changes in initial stiffness (from [18])

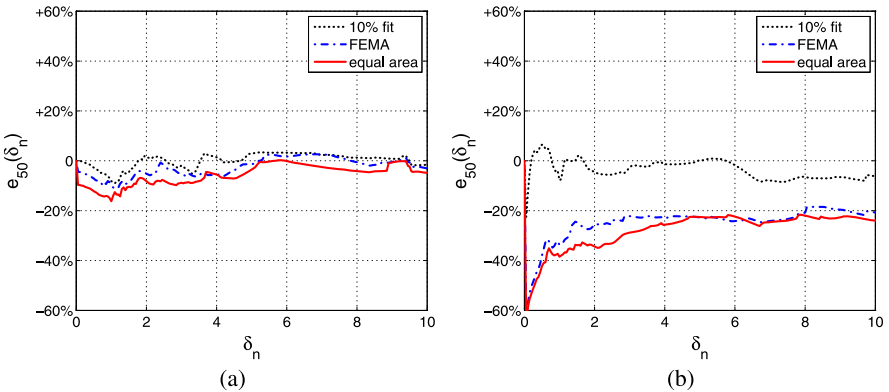


Fig. 6 Median relative error comparison between the 10 %, FEMA and equal area fits for $T = 0.5$ sec, when applied to the capacity curves of Fig. 4: (a) insignificant versus (b) significant changes in initial stiffness

fitted elastic segment is at 10 % of the maximum base shear. The latter is the proposal for a simple rule that can better capture the initial stiffness. Figure 4a shows that in the case in which the capacity curves are not characterized by significant stiffness changes at the beginning of the backbone, the three fits are very similar to each other. They differ significantly though when the initial backbone stiffness diminishes rapidly, as in Fig. 4b. In all cases the fitted post-elastic stiffness is set to zero.

As described in the methodology section, IDA is performed for each of the SDOF systems presented in Fig. 4 and for their fitted approximations for a range of periods. Figures 5 and 6 show the comparison in the median S_a -capacity for T equal to 0.2 sec and 0.5 sec, respectively, as functions of normalized displacement δ_n . The

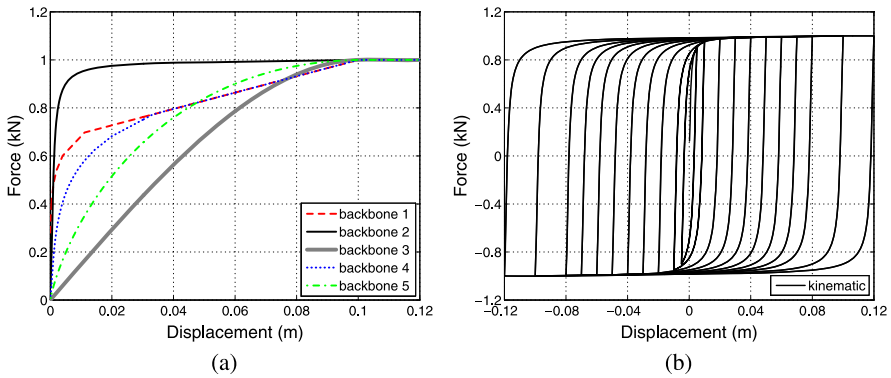


Fig. 7 (a) Backbones and (b) hysteretic behavior according to standard kinematic strain hardening rule of the generalized elastic-plastic systems considered (adapted from [18])

normalizing value is in this case equal to 0.1 m, the point in which all the backbones turn to zero stiffness. Obviously, the shape of the backbones has a significant impact. In all cases, the error becomes significant for the shape with non-trivial curved segments, the maximum error appearing at the earlier backbone segments. The 10 % fit leads to a significant decrease in the error for any deformation level, even for the highly curved shape of Fig. 4b where it clearly violates any notion of equal area (or equal energy) that seems to be prevalent in current guidelines.

The new fit introduced leads to a slightly non-conservative estimation of the capacity for displacements before the full plasticization (for δ_n up to 1) and only for short-period systems, $T = 0.2$ sec (Fig. 5). On the other hand, even in case of highly-curved backbones (Fig. 5b), only a 10 % underestimation appears at most. Conversely, it has to be noted that code approaches are always conservative for all the displacement levels and all the shapes considered, but at a cost of almost 20–40 % underestimation of capacity. The trends identified are generally confirmed for all other periods considered (T equal to 1.0 sec and 2.0 sec).

Beyond the two curved shapes shown in Fig. 4, a number of different generalized elastic-plastic shapes were also investigated. A sample of ten backbones is considered, aimed at drawing out general conclusions regarding the proposed fit. The sample consists of five different shapes (see Fig. 7a) times the two hysteretic rules. In Fig. 7b the standard kinematic strain hardening rule is shown for the five shapes considered.

Figures 8, 9, 10 and 11 show the relative error on the median S_a -capacity evaluated at each period for the 10 % fit proposed and the conventional FEMA fit. The bias is evaluated up to δ_n equal to 2, where most of the significant differences appear. This is a more focused view, compared to the two shapes in Figs. 4a and 4b where it was evaluated up to δ_n equal to 10. Figures 8 to 11 show gray dotted lines representing the error related to a specific shape of the backbone and to a specific hysteretic rule. The effect of the hysteretic rule was found to be insignificant, as

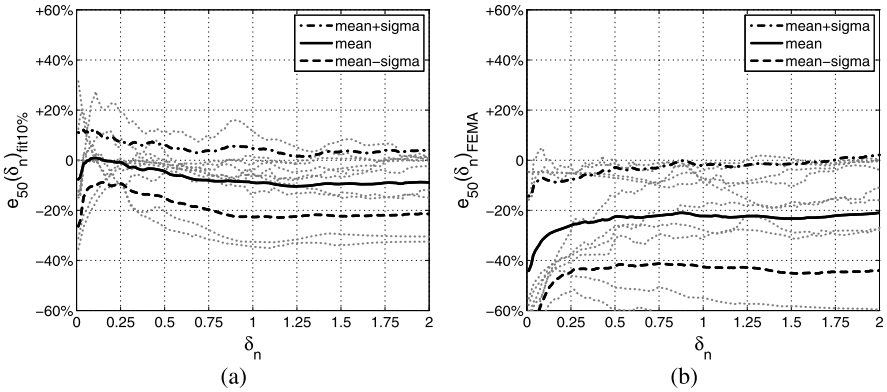


Fig. 8 The median relative error for (a) the 10 % fit and (b) the 60 % FEMA fit, $T = 0.2$ sec, in case of elastic-plastic SDOF system family (gray dotted lines) (adapted from [18])

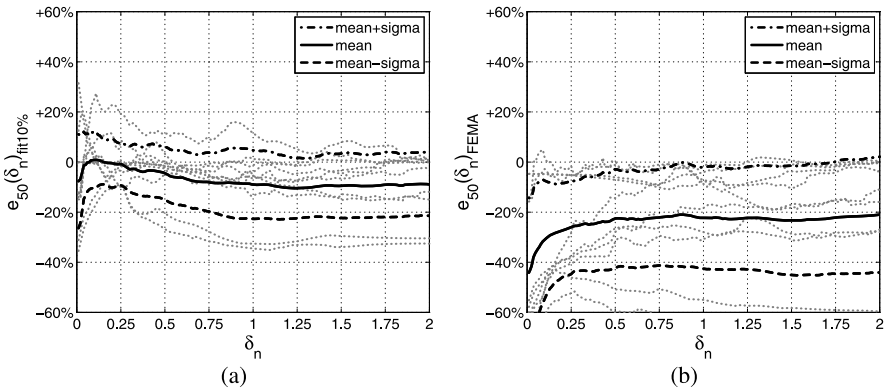


Fig. 9 The median relative error for (a) the 10 % fit and (b) the 60 % FEMA fit, $T = 0.5$ sec, in case of elastic-plastic SDOF system family (gray dotted lines)

the error depends primarily on the shape of the fit; thus the two different hysteretic behaviors have been considered together to build up a heterogeneous family of generalized elastic-plastic behavior.

The 10 % fit enjoys an insignificant bias on average for all the periods considered and the error introduced by the fit never exceeds 20 %. FEMA fit shows a strictly negative (i.e., conservative, bias of 20 % or even 60 %) depending on the shape of the original backbone. Most of the bias is concentrated at the beginning of the backbone as it was already emphasized by the examples in Figs. 5 and 6. Error comparisons for the S_a -capacity dispersion (record to record) are not shown as all fits roughly achieve similar performance. Some differences may appear in the region preceding the nominal yield point of the approximation.

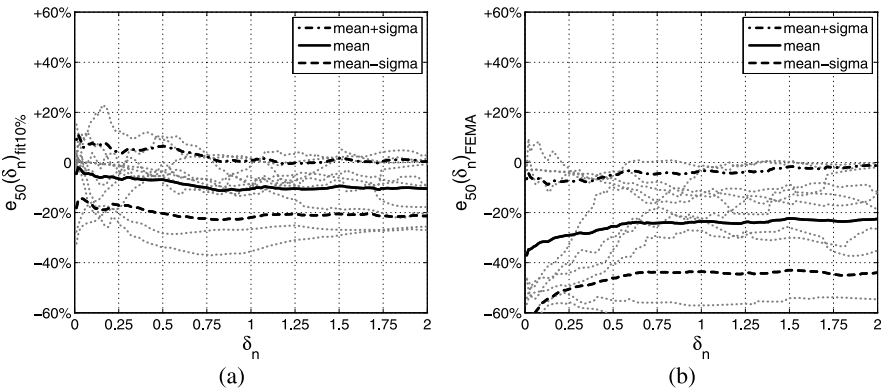


Fig. 10 The median relative error for (a) the 10 % fit and (b) the 60 % FEMA fit, $T = 1.0$ sec, in case of elastic-plastic SDOF system family (gray dotted lines) (adapted from [18])

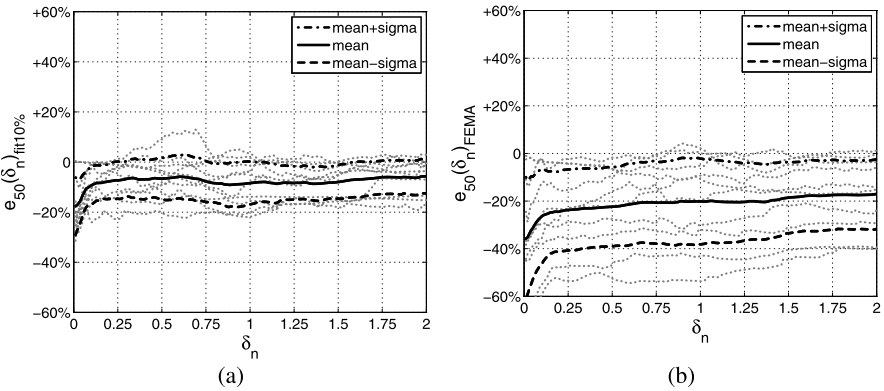


Fig. 11 The median relative error for (a) the 10 % fit and (b) the 60 % FEMA fit, $T = 2.0$ sec, in case of elastic-plastic SDOF system family (gray dotted lines)

Therein the fitted system will predict no dispersion whereas the actual one shows some small variability. Still, this is to be expected, and it is not important enough to favor one fit with respect to another.

Summarizing, it can be stated that the fit should capture as close as possible the initial stiffness of the backbone while the generally low secant stiffness assumed in most of the guidelines and codes tends to be overly-conservative. The only possible exception to this rule appears only for initially ultra-stiff systems that very quickly lose their initial properties. This is the reason why fitting the “elastic” secant at 5 % or 10 % of the maximum base shear, as opposed to 0.5 % or 1 % is considered a more robust strategy.

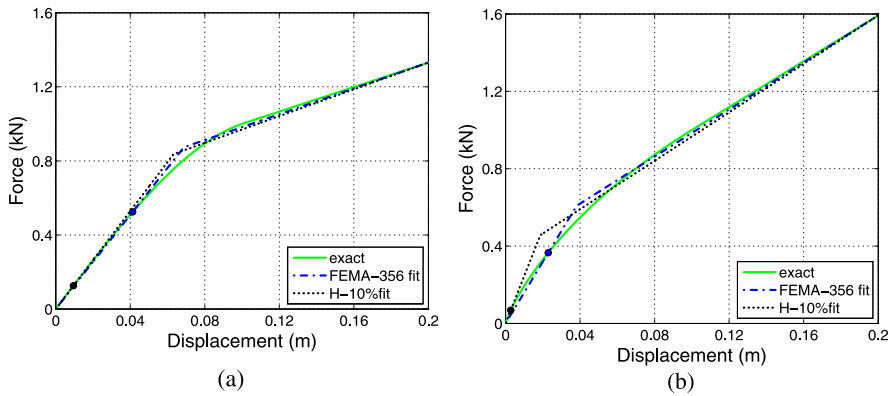


Fig. 12 Comparison of generalized elastic-hardening capacity curves and their corresponding fits having (a) insignificant versus (b) significant changes in initial stiffness (from [18])

4.2 Bilinear Fits of Generalized Elastic-Hardening Systems

The second family of shapes investigated is characterized by a generalized elastic-hardening behavior. Only the pinching hysteretic rule was considered for this family of backbones, given the insignificant differences observed earlier when compared to the kinematic hardening.

Each backbone considered was characterized by different curvatures and final hardening stiffness, allowing a wide coverage of the typical shapes that can be obtained considering different structural behaviors and modeling options.

In analogy with the two examples showed in the previous subsection, two different backbones will be presented in detail from the family considered. The first (Fig. 12a) is not characterized by significant changes in the stiffness, in contrast to the second (Fig. 12b). The target displacement is assumed to be equal to 0.2 m. The EC8 fit is not applied as it is restricted to elastic-plastic approximations which are clearly inferior for the shapes shown in Fig. 12. On the other hand, the FEMA fit rule can be applied without problems, although it might call for different approximations depending on the value of the target displacement (*FEMA-356 fit*). Still, the results and the corresponding conclusions remain the same in all cases. The alternative fit proposed, termed the *H-10 % fit* rule, determines the initial stiffness at 10 % (instead of 60 %) of the nominal yield shear defined in accordance with FEMA, while the post-elastic stiffness is determined by minimizing the absolute area discrepancy between the capacity curve and the fitted line.

The proposed H-10 % procedure came out as the simplest rule with a near-minimum error for this family of backbones. While many alternatives were considered, they are not showed herein for the sake of brevity. It has to be noted that elastic-plastic fits according to the proposal of the previous subsection have been also considered in the investigation of this family of backbones, assuming the plateau of the fit at the force corresponding to the target displacement (e.g., at 0.2 m here); even if less performing than the H-10 % fit rule, considered in the following, the still low

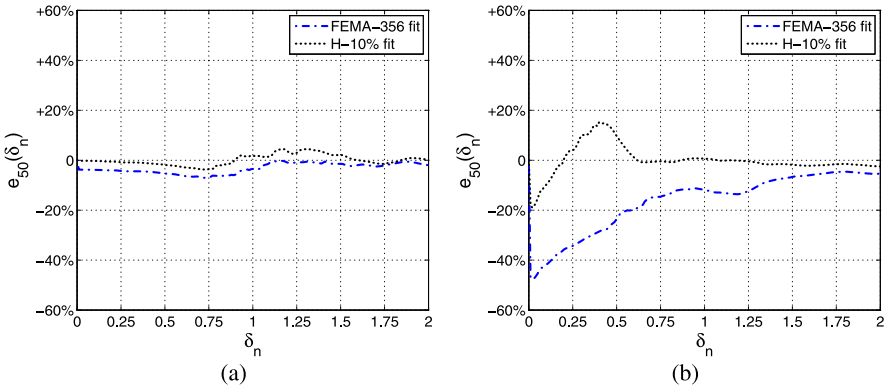


Fig. 13 Median relative error comparison between the H-10 % and FEMA fits for $T = 0.2$ sec, when applied to the capacity curves of Fig. 12: (a) insignificant versus (b) significant changes in initial stiffness (from [18])

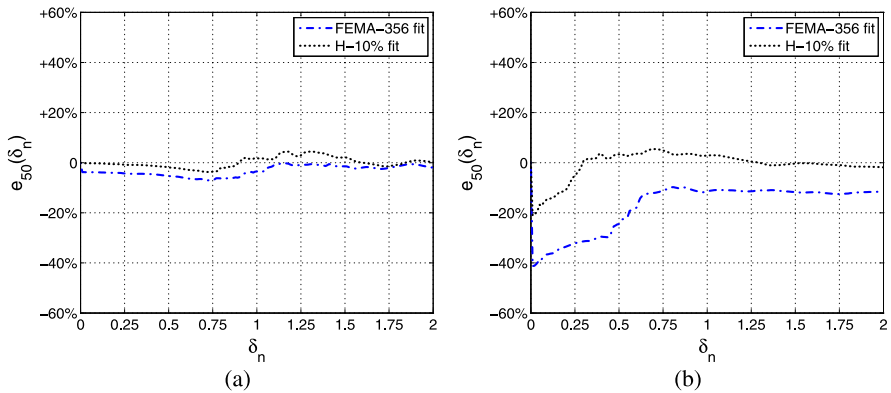


Fig. 14 Median relative error comparison between the H-10 % and FEMA fits for $T = 0.5$ sec, when applied to the capacity curves of Fig. 12: (a) insignificant versus (b) significant changes in initial stiffness

bias of those trials compared to the FEMA-356 fitting rule, enforced the general conclusion that capturing the initial stiffness is the dominant criterion that leads to a significant bias reduction with respect to actual code fit prescriptions.

The results of the two fitting procedures (*H-10 % fit* and *FEMA-356 fit*) applied to the example shapes appear in Fig. 12. Obviously, when the stiffness of the backbone is not characterized by abrupt changes in the curvature (Fig. 12a) both fits tend to be practically the same. Figures 13 and 14 show the error introduced by each fit, for both backbone shapes considered in Fig. 12, in the cases of $T = 0.2$ and 0.5 sec, respectively. In analogy with the results presented for the elastic-plastic case, most of the error is concentrated at the beginning of the backbone. In the case of the backbone with low changes in the stiffness (low curvature), it can be observed that the

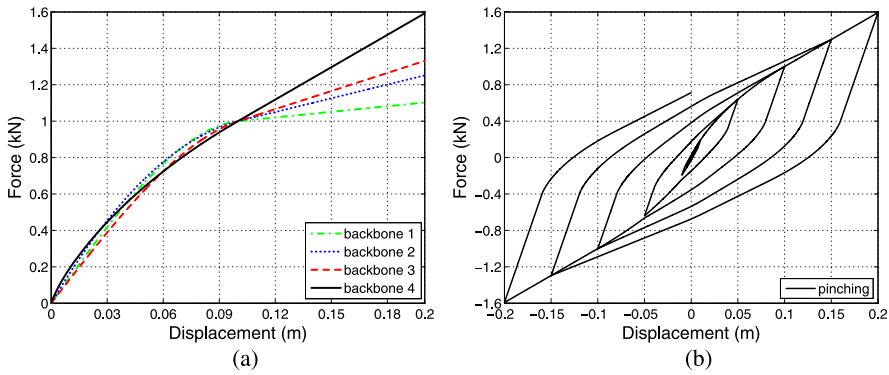


Fig. 15 Backbones (a) and hysteretic behavior according to pinching hysteresis rule (b) of the generalized elastic-hardening systems considered (adapted from [18])

error is very small and very similar for both fits. A higher curvature of the backbone increases the error introduced by the fit and emphasizes that although at the target displacement the backbones and their fits in both cases are coincident, this is not enough to guarantee the same error. The earlier fitted segments and especially the defined equivalent period can make a large difference. As the H-10 % rule manages to capture the initial stiffness better, it provides better predictive capability for higher displacements.

The evidence, again, confirms the general trend already shown in the previous subsection, that it is important to capture the initial stiffness of the capacity curve to have an unbiased fit. In this case, as well, the code approach results in a conservative error that can be over 50 % in the case of non-trivial shapes and at the lower displacement values (Fig. 12b). In the same range, the H-10 % fit leads to a slightly non-conservative solution only for the short periods ($T = 0.2$ sec), an effect that was also observed in the elastic-plastic backbone family. Otherwise, the fit remains conservative and overall it can be considered to be relatively unbiased.

In this case a sample of only four shapes is considered, the different shapes shown in Fig. 15a and the pinching hysteretic rule assumed for these backbones appearing in Fig. 15b. In Figs. 16, 17, 18 and 19 the relative errors in the median S_a -capacity, are compared for the four different periods and the different SDOF backbones. The importance of capturing the initial stiffness is highlighted by the results at each period, and the H-10 % fit leads to a small and relatively unbiased error, which seldom exceeds 10 %. In this case the sample of backbones considered for the elastic-hardening case was smaller than the elastic-plastic case, but robustness of the general results, showing the same trends in both cases, supports previous remarks. It should be noted that the results of the FEMA approximation will improve somewhat at low displacements if we refit for a lower target displacement. Still, the corresponding improvement by a similar refit of H-10 % at the target displacement nullifies this advantage, thus the general fitting hierarchy observed is maintained.

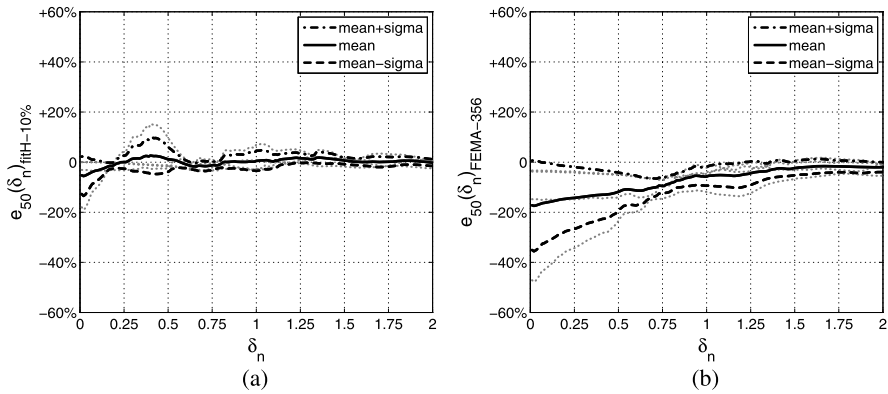


Fig. 16 The median relative error for (a) the H-10 % fit and (b) the 60 % FEMA fit, $T = 0.2$ sec, in case of elastic-hardening SDOF systems family (gray dotted lines) (adapted from [18])

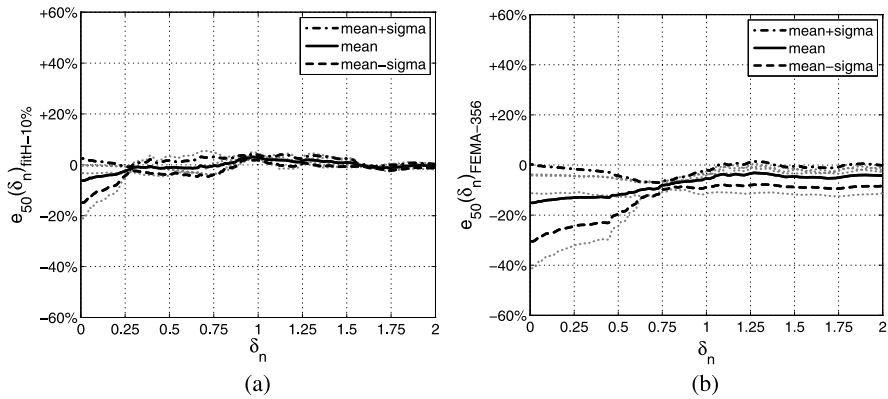


Fig. 17 The median relative error for (a) the H-10 % fit and (b) the 60 % FEMA fit, $T = 0.5$ sec, in case of elastic-hardening SDOF systems family (gray dotted lines)

4.3 Bilinear Fits of Generalized Elastic-Hardening-Softening Systems

The Italian hybrid fitting rule (CS.LL.PP. [16, 22]) is worth to be investigated, especially to check whether considerations regarding the best approach for non-softening behaviors are still reliable to capture early negative response. In other words, the general principle of getting the initial stiffness (10 % rule) is going to be checked for a backbone family of softening curves and consequently compared with the 60 % rule. In addition, the merits of balancing the mismatch areas above and below the capacity curve will also be discussed. While the Italian Code, similar to other guidelines, is concerned with providing a specialized fit for a given target point on the capacity curve. Following the methodology described in Sect. 2, herein, it will be

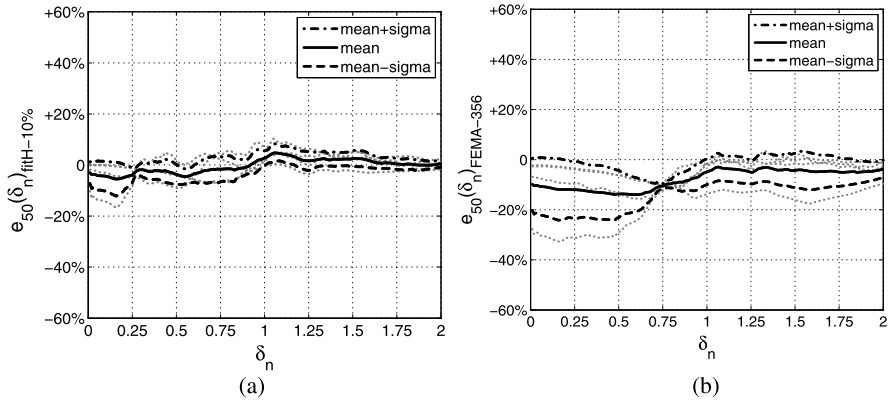


Fig. 18 The median relative error for (a) the H-10 % fit and (b) the 60 % FEMA fit, $T = 1.0$ sec, in case of elastic-hardening SDOF systems family (gray dotted lines) (adapted from [18])

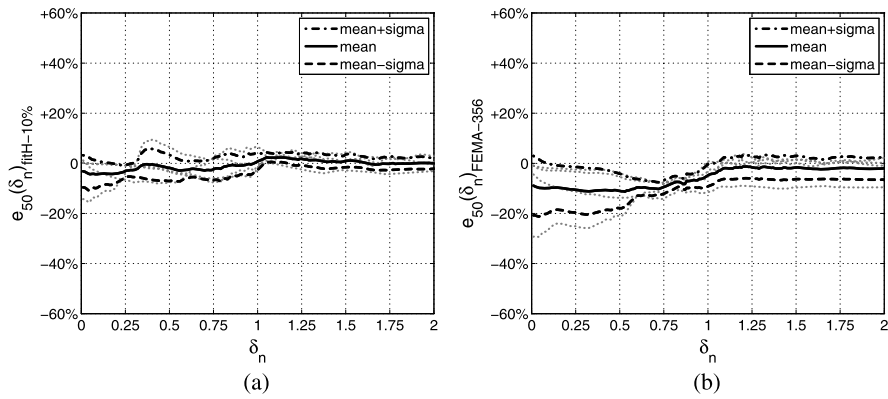


Fig. 19 The median relative error for (a) the H-10 % fit and (b) the 60 % FEMA fit, $T = 2.0$ sec, in case of elastic-hardening SDOF systems family (gray dotted lines)

sought to provide near-optimal fits for a continuum of limit states. Thus, any dependence on any specific target point on the backbone is intentionally avoided, that is, checking all possible targets at the same time. This is achieved employing a simple direct search approach, where the height of the plastic plateau for the fit is gradually moved from 80 % to 100 % of the peak shear in the exact capacity curve. Consequently, while checking for a broadly optimal fit, all possible fits that could arise from applying the Italian Code approach to different target points will be efficiently captured.

Two example backbones from the numerous tests conducted are shown in Fig. 20. They were chosen to emphasize two different softening trends, combined with different curvature changes in the initial part of the backbones: insignificant (see Fig. 20a) versus significant (see Fig. 20b). Four different fits are displayed out of

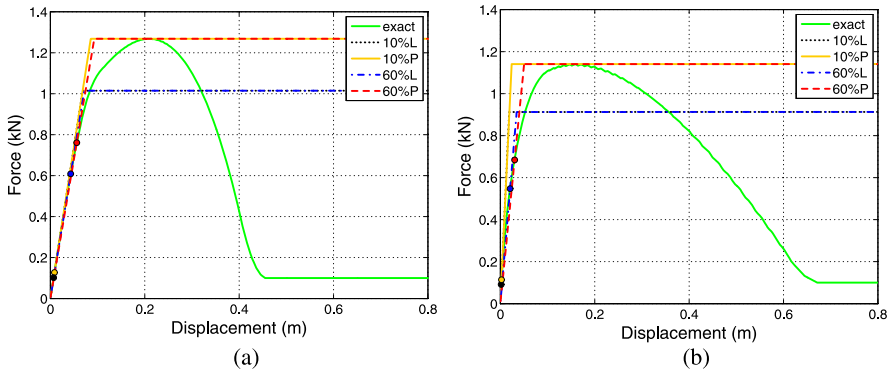


Fig. 20 Comparison of two capacity curves with softening branch and their corresponding fits having (a) insignificant versus (b) significant changes in initial stiffness (Fig. 20(b) from [18])

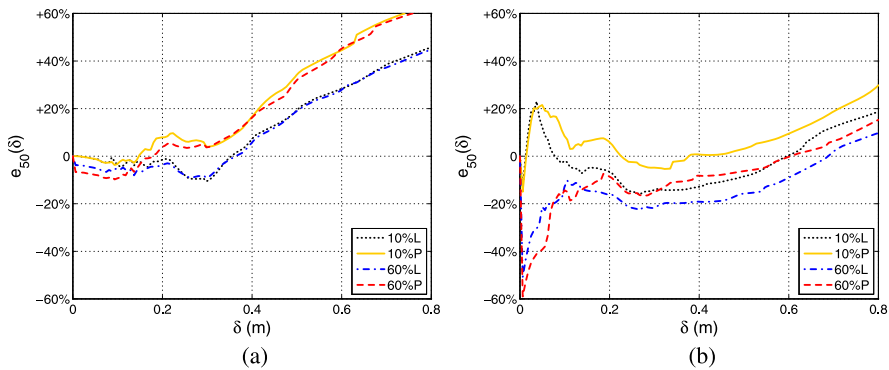


Fig. 21 Median relative error comparison between the 10%L, 10%P, 60%L and 60%P fits for $T = 0.2$ sec, when applied to the capacity curves of Fig. 20: (a) insignificant versus (b) significant changes in initial stiffness and different softening slopes (Fig. 21(b) from [18])

the large number that has been checked: the initial stiffness is fixed at 10 % or 60 % of the maximum shear combined with two plateau levels at 80 % (L) and 100 % (P) of peak shear, thus obtaining four fitting approaches named 10%L, 10%P, 60%L and 60%P, respectively. The performances of each of the four fits considered are shown in Figs. 21 and 22 for $T = 0.2$ sec and 0.5 sec, respectively.

Results show how the changes in curvature in the initial part still play an important role for fitting performances. The 10 % fit improves results as long as there are significant changes in the curvature of the exact backbone. Furthermore, catching the peak point (P versus L fits) seems to offer better performance than a lower plateau value, regardless of any area-balancing rules. The latter results are partially confirmed by the fits suggested in other studies where the maximum shear value is selected as one of the criteria for fitting softening backbones (e.g., [24]).

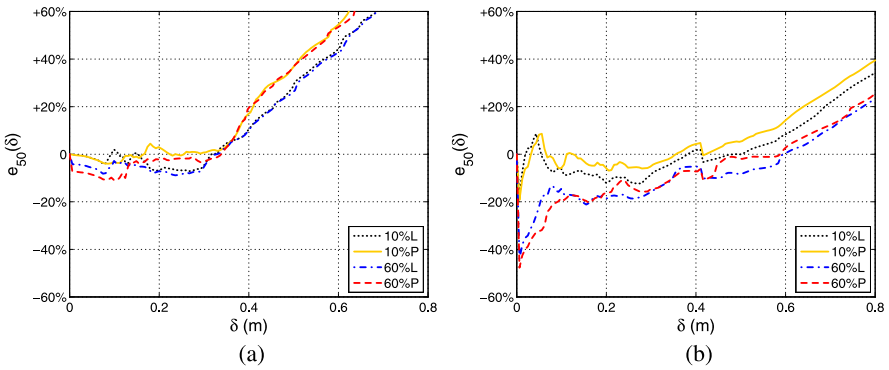


Fig. 22 Median relative error comparison between the 10%L, 10%P, 60%L and 60%P fits for $T = 0.5$ sec, when applied to the capacity curves of Fig. 20: (a) insignificant versus (b) significant changes in initial stiffness and different softening slopes

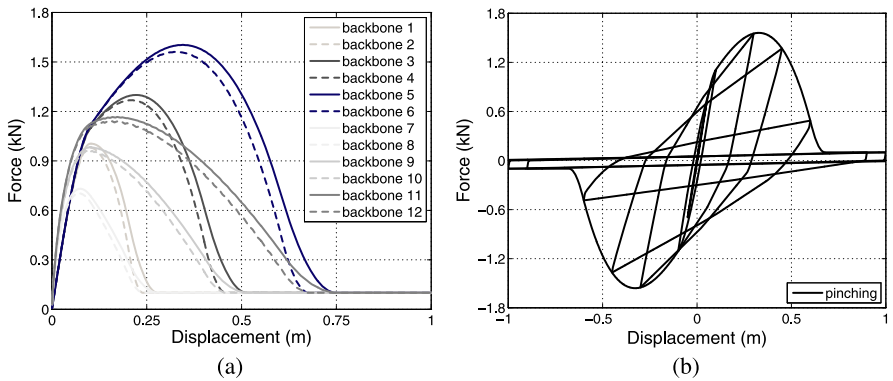


Fig. 23 Backbones (a) and example hysteretic behavior according to pinching hysteresis rule (b) of the family of capacity curves considered

For low frequencies and significant changes in the initial stiffness, the 10 % fit, in both its versions showed herein, P and L, can lead to slightly non-conservative results at the beginning of the backbone. The same effect was observed also in the case of non-softening backbones. Still, for conventional limit states of interest and for most practical applications for which a static pushover is used, the target points will not be located in this early near-elastic part of the backbone.

The fit approaches showed have been tested for a sample family of exact backbones in which curvature at the beginning and the slope of the softening have been varied. The sample family of backbones considered and their hysteresis loops are presented in Fig. 23. The median error trends of the 60%L and the 100%P fits are compared in Figs. 24, 25, 26 and 27, respectively, for the four periods considered (0.2, 0.5, 1.0 and 2.0 seconds). The error is mapped according to the characteristic points of the exact backbone; the peak point “p”, where the maximum shear

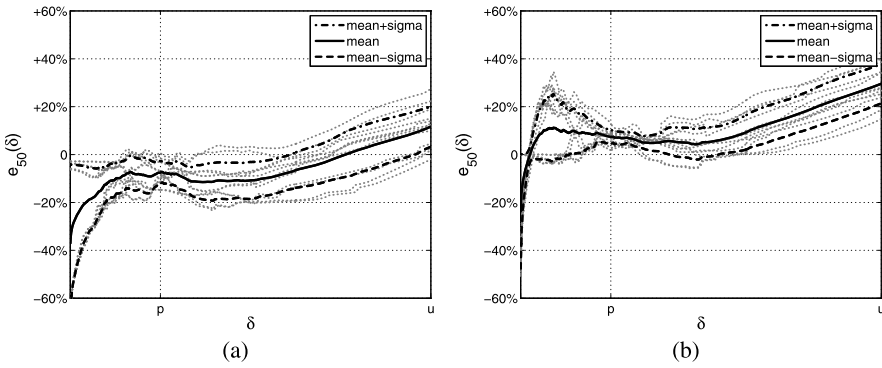


Fig. 24 The median relative error at $T = 0.2$ sec if (a) the 60%L and (b) 10%P fits are employed, respectively, for the family of capacity curves in Fig. 23 (gray dotted lines) (adapted from [18])

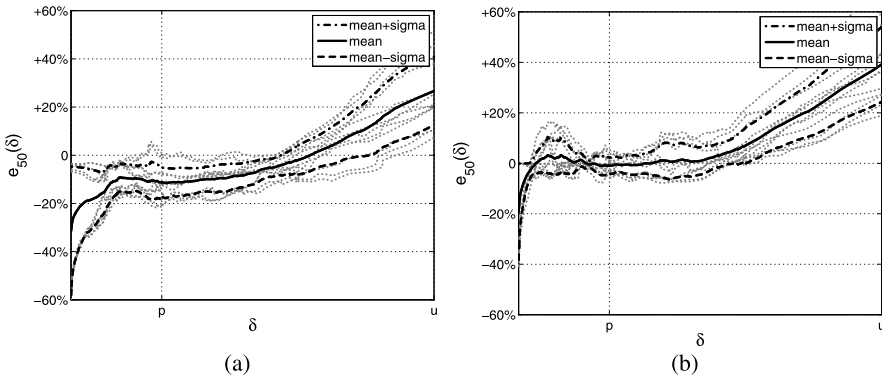


Fig. 25 The median relative error at $T = 0.5$ sec if (a) the 60%L and (b) 10%P fits are employed, respectively, for the family of capacity curves in Fig. 23 (gray dotted lines)

is attained, and the ultimate point “u”, where the exact capacity curve reaches the residual branch.

Figures 24 to 27 are meant to represent the median error to be expected when fitting a generic capacity curve with a specific rule (in this case 60%L and 100%P rules respectively). The 10%P fit is found to be an unbiased fit approach that can be extended to the mildly softening part of the backbone at each of the periods investigated, showing robust performances for this portion of backbone in a wide range of frequencies.

5 Conclusions

Structural seismic assessment based on the nonlinear static procedure is a method that, in its coded variants, has become common in the last decades among re-

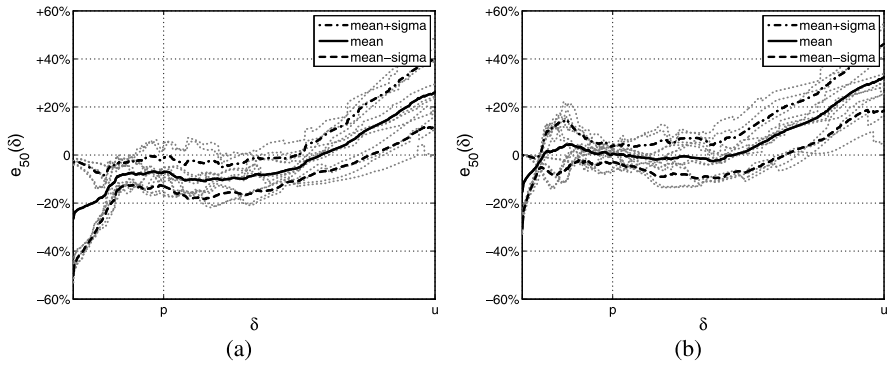


Fig. 26 The median relative error at $T = 1.0$ sec if (a) the 60%L and (b) 10%P fits are employed, respectively, for the family of capacity curves in Fig. 23 (gray dotted lines) (adapted from [18])

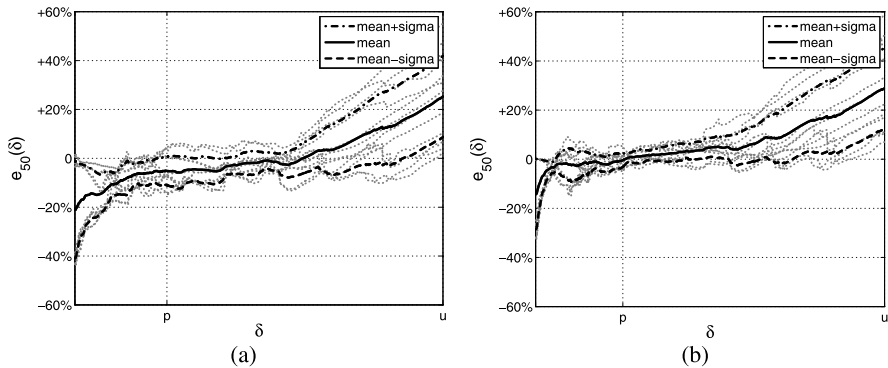


Fig. 27 The median relative error at $T = 2.0$ sec if (a) the 60%L and (b) 10%P fits are employed, respectively, for the family of capacity curves in Fig. 23 (gray dotted lines)

searchers and practitioners. It is based on the fundamental approximation that the behavior of an MDOF system can be interpreted by the response of an equivalent SDOF. This necessitates a number of approximations at various stages of the procedure. Herein, the problem of the optimal bilinear fit to be chosen as the idealized base shear-displacement curve is systematically investigated.

Assessment of different fits is achieved via incremental dynamic analysis on an intensity-measure capacity basis that allows a straightforward comparison of the performance of structural systems characterized by different periods; in this case, the period of the capacity curve and its bilinear approximation. Therefore, the approach followed allows the investigation of a continuum of limit states at the SDOF level, excluding other sources of error already investigated in detail in other studies.

The initial focus is on the non-softening behavior of the exact capacity curve to be fitted. Code fits (Eurocode 8, FEMA documents and Italian code) were found to be always characterized by a mostly conservative bias due to the enlarged equivalent

period assumed. Italian code recommendations to capture early softening behavior by means of extended elastoplastic fits are shown to result to acceptable errors when matching the maximum strength and not exceeding the displacement that corresponds to 85 % of the maximum shear.

Finally, the investigations yielded to suggest the rule of setting the elastic segment to match the initial stiffness of the exact capacity curve (e.g., fitting at 10 % of the peak base shear). A subsequent hardening segment should be fitted by minimizing the area discrepancy up to the target point, while a plastic segment should instead be set at the peak base shear value. The low bias introduced by these enhanced fit solutions is found to be an improvement with respect to existing code approaches. Essentially, such fitting rules can be assumed to be a near-optimal solution especially in the case of capacity curves with significant changes in stiffness, representative of modern modeling approaches that account for the uncracked section properties. In fact, the error introduced by a near-optimal bilinear fits does not exceed 20 %.

Furthermore, the latter results represent a step towards the definition of a fully optimized fit rule that can represent a further enhancement to be considered as an upgrade in current seismic provisions. While any enhanced three-segment piecewise linear fit that incorporates a softening branch would further improve the accuracy in the equivalent SDOF backbone, it would also require changes in the R - μ - T relationships. On the other hand, the procedures presented herein can fit seamlessly in current seismic codes without requiring any further changes.

Acknowledgements The analyses presented in the paper have been developed in cooperation with Rete dei Laboratori Universitari di Ingegneria Sismica—ReLUIS for the research program funded by the Dipartimento della Protezione Civile—Executive Project 2010–2013.

References

1. Fajfar P, Fischinger M (1988) N2—a method for non-linear seismic analysis of regular structures. In: Proceedings of the 9th world conference on earthquake engineering, Tokyo, pp 111–116
2. Krawinkler H, Seneviratna GPKD (1998) Pros and cons of a pushover analysis of seismic performance evaluation. *Eng Struct* 20:452–464
3. Bracci JM, Kunnath SK, Reinhorn AM (1997) Seismic performance and retrofit evaluation of reinforced concrete structures. *J Struct Eng* 123:3–10
4. Elnashai AS (2001) Advanced inelastic static (pushover) analysis for earthquake applications. *Struct Eng Mech* 12:51–69
5. Antoniou S, Pinho R (2004) Advantage and limitations of adaptive and non-adaptive force-based pushover procedures. *J Earthq Eng* 8:497–522
6. Chopra AK, Goel RK (2002) A modal pushover analysis procedure for estimating seismic demands for buildings. *Earthq Eng Struct Dyn* 31:561–582
7. Vidic T, Fajfar P, Fischinger M (1994) Consistent inelastic design spectra: strength and displacement. *Earthq Eng Struct Dyn* 23:507–521
8. Miranda E, Bertero VV (1994) Evaluation of strength reduction factors for earthquake-resistant design. *Earthq Spectra* 10(2):357–379

9. National Institute of Standards and Technology (NIST) (2010) Applicability of nonlinear multiple-degree-of-freedom modeling for design. Report NIST GCR 10-917-9, prepared by the NEHRP Consultants Joint Venture, Gaithersburg
10. Vamvatsikos D, Cornell CA (2006) Direct estimation of the seismic demand and capacity of oscillators with multi-linear static pushovers through incremental dynamic analysis. *Earthq Eng Struct Dyn* 35(9):1097–1117
11. Comité Européen de Normalisation (2004) Eurocode 8—design of structures for earthquake resistance. Part 1: General rules, seismic actions and rules for buildings. EN 1998-1, CEN, Brussels
12. Federal Emergency Management Agency (FEMA) (1997) NEHRP guidelines for the seismic rehabilitation of buildings. Report FEMA-273, Washington
13. Federal Emergency Management Agency (FEMA) (2000) Prestandard and commentary for the seismic rehabilitation of buildings. Report FEMA-356, Washington
14. Federal Emergency Management Agency (FEMA) (2005) Improvement of nonlinear static seismic analysis procedures. Report FEMA-440, Washington
15. American Society of Civil Engineers (ASCE) (2007) Seismic rehabilitation of existing buildings. ASCE/SEI 41-06, Reston
16. CS.LL.PP. (2008) DM 14 gennaio. Norme tecniche per le costruzioni. *Gazzetta Ufficiale della Repubblica Italiana* 29, 4/2/2008
17. Vamvatsikos D, Cornell CA (2002) Incremental dynamic analysis. *Earthq Eng Struct Dyn* 31:491–514
18. De Luca F, Vamvatsikos D, Iervolino I (2012) Near-optimal piecewise linear fits of static pushover capacity curves for equivalent SDOF analysis. *Earthq Eng Struct Dyn* 42(4):523–543
19. De Luca F (2011) Records, capacity curve fits and reinforced concrete damage states within a performance based earthquake engineering framework. PhD dissertation, University of Naples Federico II. <http://wpage.unina.it/flavia.deluca/outreach.htm>
20. Vamvatsikos D, Cornell CA (2004) Applied incremental dynamic analysis. *Earthq Spectra* 20:523–553
21. Fragiadakis M, Vamvatsikos D, Papadrakakis M (2006) Evaluation of the influence of vertical irregularities on the seismic performance of a nine-storey steel frame. *Earthq Eng Struct Dyn* 35:1489–1509
22. CS.LL.PP. (2009) Circolare 617. Istruzioni per l'applicazione delle norme tecniche per le costruzioni. *Gazzetta Ufficiale della Repubblica Italiana* 47, 2/2/2009 (in Italian)
23. Ibarra LF, Medina RA, Krawinkler H (2005) Hysteretic models that incorporate strength and stiffness deterioration. *Earthq Eng Struct Dyn* 34:1489–1511
24. Han SW, Moon K, Chopra AK (2010) Application of MPA to estimate probability of collapse of structures. *Earthq Eng Struct Dyn* 39:1259–1278

Collapse Fragility Curves of RC Frames with Varying Design Parameters

Ilias A. Gkimousis and Vlasios K. Koumousis

Abstract The inelastic behavior of reinforced concrete structures subjected to a number of strong motion excitations of escalated Intensity Measure (IM) and monitoring of characteristic Engineering Demand Parameters (EDPs) of the structure for all these different instances is presented. This provides the necessary data to estimate the overall performance of a structure at a particular site of specified seismic hazard within the framework of Incremental Dynamic Analysis (IDA). In this, generation of data regarding capacity and demand evolves following a lognormal distribution while the corresponding cumulative distribution function is used to define the corresponding fragility curves. This analysis facilitates further the deduction of statistically sound estimates of the measured parameters. The hysteretic inelastic response of reinforced concrete members, i.e. beams and columns designed on the basis of Eurocodes is of primal importance. The Bouc-Wen model, as implemented in “Plastique” code, with parameters established based on existing experimental data, is considered implementing the IDA procedure. Through this modeling, a series of plane frames of different number of spans and stories designed in a similar manner is investigated. Also, the effect of some general design code provisions on collapse capacity of these frames, such as stiffness distribution along height and strong column-weak beam design principle are examined. Numerical results are presented and their corresponding fragility curves are derived. Interesting features are revealed, regarding the effect of alternative designs on collapse capacity, which often deviate from collapse predictions made using the static pushover analysis.

Keywords Incremental dynamic analysis · Fragility curves · Probability of collapse · Redundancy · Stiffness distribution · Strong column-weak beam design principle

I.A. Gkimousis · V.K. Koumousis (✉)

Institute of Structural Analysis & Aseismic Research, National Technical University of Athens, Zographou Campus, 15780, Athens, Greece

e-mail: vkoum@central.ntua.gr

I.A. Gkimousis

e-mail: cvgkim@central.ntua.gr

1 Introduction

One of the main objectives of current earthquake-resistant design codes is to ensure increased levels of safety commencing with protection of human life during strong earthquakes, while reducing damage-repair cost for small and medium excitations for new and existing structures. This constitutes the framework of Performance Based Earthquake Engineering (PBEE) by defining performance levels which correspond to different damage situations. The level of collapse prevention for example, demands certain probability of collapse that does not exceed the acceptable limits set for this purpose. However, at the moment, code provisions are deterministic in nature, as they are based on return periods relating seismic excitation with specific levels of damage.

Hence, it becomes important to establish such probabilistic information and to follow design methods that statistically ensure the non-exceedance of the specified damage state. The Incremental Dynamic Analysis (IDA) [1, 2] addresses this issue by calculating statistical data in terms of Intensity Measure (IM) and Engineering Demand Parameters (EDPs). This is followed by a statistical analysis of the outcome and the evaluation of fragility curves [3, 4]. This procedure is capable of revealing significant probabilistic evidence of structural behavior by defining relation between probability of collapse and ground motion IM. If fragility curves are combined with seismic hazard data from a specific region of interest that combine the same IM with the seismic hazard, the Mean Annual Frequency (MAF) of exceeding a performance state is derived for the particular site.

In this work the aforementioned methodology is used to assess collapse capacity of Reinforced Concrete plane frames designed following different considerations. It should be noted that these frames are centerline models of 3D symmetrical structures with equal inertia characteristics and fixed supports. More specifically, this study focuses on the performance state of dynamic collapse by examining the effect of geometrical and structural frame parameters on the probability of collapse.

2 Analytical Procedure

2.1 Implementing IDA

In order to perform nonlinear elastoplastic dynamic analysis following the IDA method, the “Plastique” [5] program was used which employs the phenomenological Bouc-Wen hysteretic model, the parameters of which were defined as described in [6]. To establish more realistic results, as the structure approaches collapse where large displacements become significant, P - Δ effects were introduced according to [7]. This is a simple, approximate, non-iterative technique, where lateral forces are introduced to each story level due to the overturning moments caused by the movement of diaphragm masses.

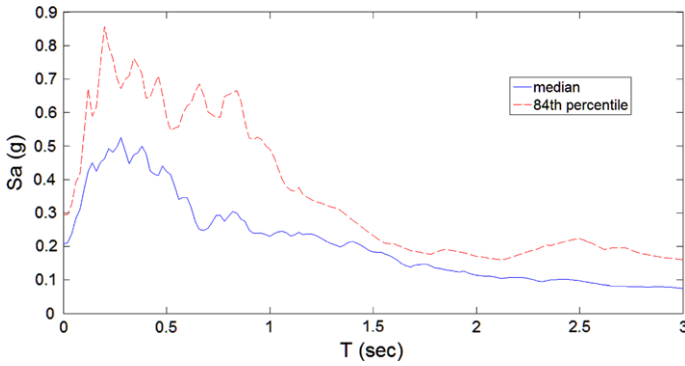


Fig. 1 Median and 84 % percentile response spectra for all twenty earthquakes

As far as IDA is concerned, as intensity measure (IM) the escalated 1st eigenmode spectral acceleration with 5 % viscous damping $S_a(T_1, 5\%)$ was selected. Respectively, the maximum interstory drift ratio is considered as the engineering demand parameter (EDP) that measures demand on different levels of structural deterioration. To save computational time the haunt and fill algorithm as the method to trace IDA curves, after repeated runs, was utilized [2]. This was parameterized properly to achieve as much accuracy as possible in the region of dynamic instability. Twenty accelerograms were appropriately selected for the analysis, corresponding to major earthquakes in California and they are listed in [2, 8]. They consist of relatively large magnitude excitations, moderate distances from fault, so as to avoid pulse excitations and near field effects [9]. In Fig. 1, the median and the 84 % percentile response spectra for all twenty excitations are presented. The only source of uncertainty used in this study is the record to record variability (aleatory uncertainty), which is sensitive to the dispersion of spectra in the region of structure's 1st eigenperiod. For the selected ground motions this dispersion in the spectral accelerations is computed in terms of the dimensionless logarithmic standard deviation of counted statistics through relation (1) and the final graph is presented in Fig. 2.

$$\sigma_{\ln, y} = \ln\left(\frac{y_{84}}{y_{50}}\right) \quad (1)$$

where, y_{50} are the median spectral values while y_{84} are the 84 % percentile spectral values for a given eigenperiod.

2.2 Statistical Evaluation

After performing the computationally demanding IDA, some very important features usually emerge with the proper statistical evaluation of the outcome. The statistical sample in this work consists of twenty spectral accelerations (S_{a_c}) where

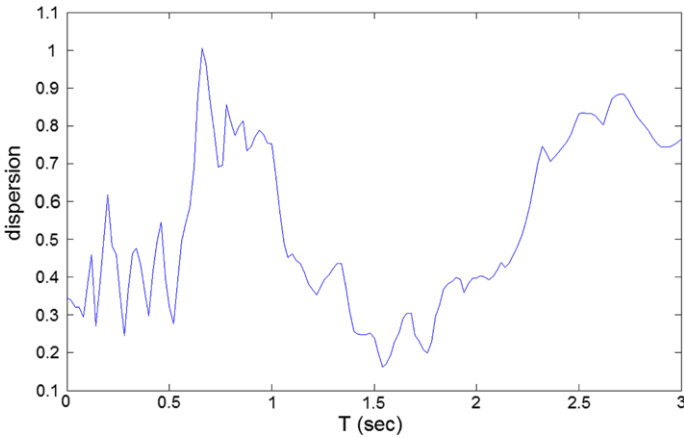


Fig. 2 Dispersion of twenty acceleration spectra for the eigenperiods of interest

dynamic collapse occurred. Collapse is considered to happen, when a global or local collapse mechanism is formed, or when maximum interstory drift ratio exceeds the value of 12 %. In order to pursue analytical calculations, a lognormal distribution is fitted to the data and by calculating its cumulative distribution function (CDF) a collapse fragility curve, based on the IM approach [3, 4], is derived as follows:

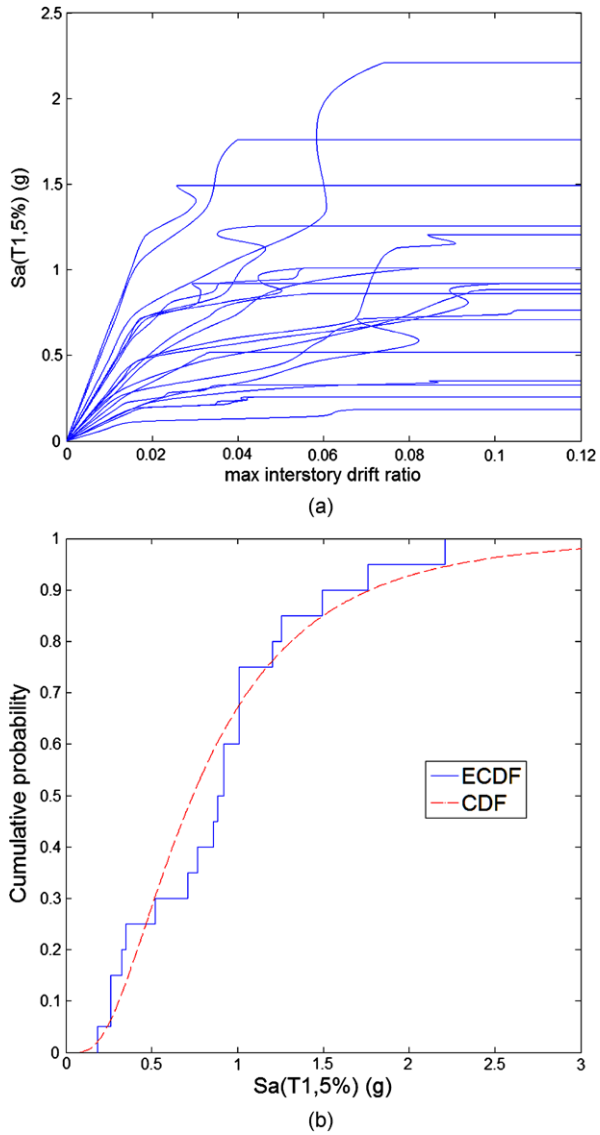
$$P[Sa_c \leq Sa] = \Phi \left[\frac{1}{\beta_{Sa,c}} \ln \left(\frac{Sa}{n_{Sa,c}} \right) \right] \tag{2}$$

where, $\beta_{Sa,c}$ is the standard deviation of the natural logarithm, while $n_{Sa,c}$ is the lognormal median of the data.

The above described steps are presented in Fig. 3, for the case of a 6-story, 2-bay plane RC frame with first eigenperiod, $T_1 = 0.639$ sec. In the figure, the lognormal distribution, fitted to the data, is presented and constitutes the fragility curve for this frame.

Furthermore, in the literature several indices are defined that can be used to quantify the stochastic nature of fragility. To determine the most representative ones, a Probabilistic Seismic Hazard Analysis (PSHA) for the seismic site of interest is required, which provides the necessary hazard spectra and hazard curves. This data, when combined with fragility curves, can reveal the very important feature of how rarely a structure may collapse when it is subjected to spectral accelerations that are possible to occur in the specific geographical region. This measure is the mean annual frequency (MAF) of collapse and its inverse is the collapse return period of the structure. In this study, the hazard curves that were implemented in the procedure are associated to the IM and are given in [10]. The indices used [11] are the median collapse spectral acceleration ($Median(Sa_c)$), the probability of collapse for the earthquake with probability of occurrence 10 %/50 years ($P_{C|10\%/50y}$), the Margin Against Collapse (MAC) for the 10 %/50 years earthquake (Eq. (3)) and the

Fig. 3 (a) All 20 IDA curves. (b) Corresponding empirical (ECDF) and analytical fragility curves (CDF)



MAF of collapse (Eq. (4)). Also, the dispersion of structural behavior according to different seismic excitations can be described through the standard deviation of the natural logarithm of the data (σ_{ln}).

$$MAC_{10\%/50\text{years}} = \frac{Median(Sa_c)}{Sa_{10\%/50\text{years}}} \tag{3}$$

where $Sa_{10\%/50years}$ is given in the hazard spectrum and defines the spectral acceleration that is expected to occur when the earthquake with probability of occurrence 10 % in 50 years strikes.

$$MAF = \lambda_c = \int_0^\infty F_{C,Sa,c}(x) |d\lambda_{Sa}(x)| \quad (4)$$

where $F_{C,Sa,c}(x)$ is the collapse fragility curve and $\lambda_{Sa}(x)$ is the ground motion hazard curve.

To complete the picture, for all the proceeding examples we present also fragility curves through a standard static pushover analysis [12]. Assuming that collapse data follows a lognormal distribution, the median value of the base shear at collapse is given from the non-linear static analysis. To transform base shear force into spectral acceleration terms, relation $Sa = V/(M_{tot} \cdot a)$ is used, where V is the collapse base shear, M_{tot} is structure's total mass and a is given as follows:

$$a = \frac{[\sum m_i \varphi_i]^2}{M_{tot} \cdot \sum m_i \varphi_i^2} \quad (5)$$

where m_i is the mass of story i and φ_i is the story ordinate value that corresponds to the 1st eigenmode.

In order to generate the fragility curve through Eq. (2) a measure of the standard deviation should also be known in advance. This information has already been extracted from the IDA procedure using the index (σ_{ln}).

3 Effect of Design Criteria in the Collapse Capacity of RC Frames

3.1 Effect of the Number of Bays and Stories

In Fig. 4, eight plane RC frames of 3 and 6 stories have been designed according to Greek codes, with number of bays ranging from 1 to 4 as presented in Table 1. In order to facilitate comparison they retain the same reinforcement in the interior and exterior columns respectively.

These frames are analyzed following the IDA method. Collapse fragility curves are produced and they are presented in Fig. 5. In Table 2 the probabilistic indices for collapse estimation have been calculated, together with measures of deformation such as the median interstory drift ratio (IDR) and the median roof drift ratio (RDR). It is important to notice that these results are meant only for comparison

Table 1 Plane frames geometrical features

Column sections (m)	Beam sections (m)	Bay length (m)	Story height (m)
0.25 × 0.25	0.30 × 0.20	4.50	3.00

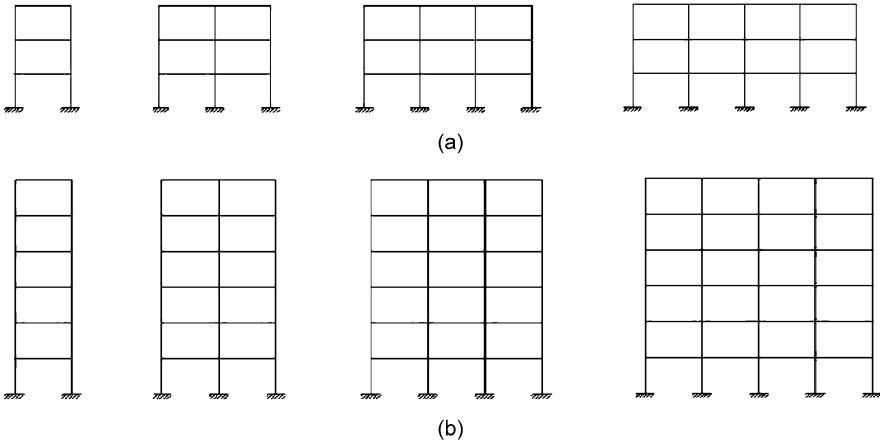


Fig. 4 (a) 3 story frames. (b) 6 story frames

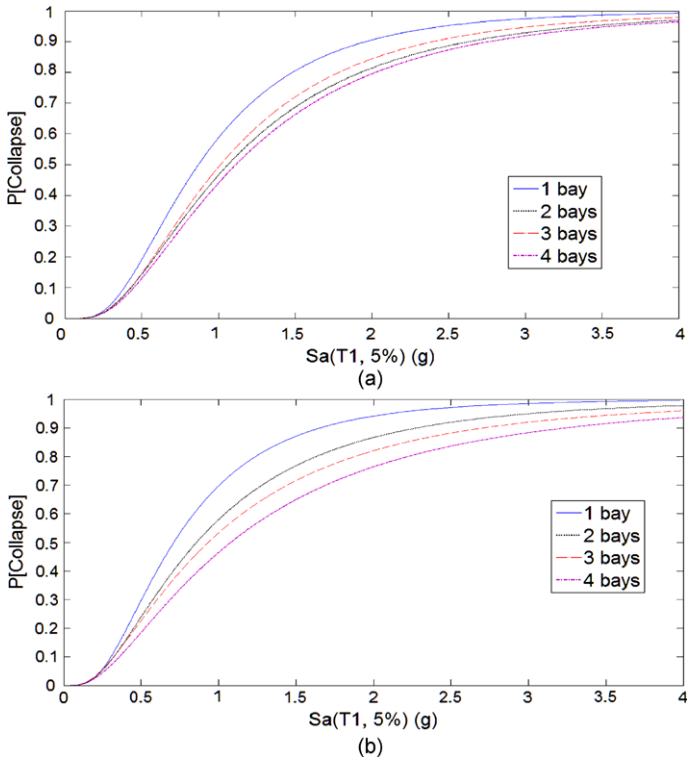


Fig. 5 (a) Collapse IDA fragility curves for 3-story frames. (b) Collapse IDA fragility curves for 6-story frames

Table 2 Collapse capacity quantification for all RC frames

Stories	Bays	T1 (sec)	Median(Sa_c)	σ_{ln}	$P_{C 10\%/50y}$	MAC	λ_c	Median (IDR)	Median (RDR)
3	1	0.324	0.87	0.63	74 %	0.67	0.0121	0.031	0.023
	2	0.349	1.06	0.70	61 %	0.82	0.0098	0.079	0.053
	3	0.357	1.02	0.67	64 %	0.78	0.0103	0.054	0.041
	4	0.362	1.12	0.71	59 %	0.86	0.0093	0.089	0.054
6	1	0.650	0.70	0.68	75 %	0.63	0.0100	0.045	0.022
	2	0.693	0.86	0.76	65 %	0.75	0.0086	0.080	0.035
	3	0.708	0.93	0.82	60 %	0.81	0.0076	0.080	0.038
	4	0.717	1.07	0.77	53 %	0.92	0.0064	0.076	0.040

between the different frames of the analysis as they appear inadequate to withstand the strong earthquakes of California being poorly designed with the minimum code reinforcement.

A basic difference between 6-story and 3-story frames is that collapse capacity does not increase with the increase of the number of bays. More specifically in the case of the 3-story frames the 2-bay frame exhibits smaller probability of collapse for the 10 %/50 years earthquake and smaller MAF of collapse than the 3-bay frame. Comparing also these two different groups of frames, the 6-story frames result into larger dispersion of the results due to the fact that their eigenperiods represent larger spectral dispersion according to Fig. 2. Also, median collapse spectral acceleration (Sa_c) takes smaller values for the 6-story frames. Although it results that with the increase of frame height collapse capacity decreases, which is anticipated as $P-\Delta$ effects becomes important and also higher axial load in columns causes their ductility to diminish, this statement can't be generalized due to the limited number of cases considered in the current study. In contrast, the MAF of collapse for the 6-story frames seems to be smaller, meaning larger collapse return periods, since smaller spectral accelerations are expected to appear in larger eigenperiods. This means that although the higher frames can't resist as large absolute accelerations, it is the shorter ones that have a greater probability to collapse during natural ground motions due to resonance. The context of Table 2 is depicted in Fig. 6.

The results of the last 2 columns in Table 2 that refer to deformations are presented in Fig. 7.

In Fig. 7c, IDR/RDR ratio depicts the degree of damage accumulation in a few stories. As the ratio becomes bigger, like in 6-story frames, it is portrayed that damage is localized in a few stories of the building, while in 3-story frames damage is almost uniformly distributed along the height. Generally, 1-bay frames develop smaller displacements and for 6-story frames they seem to stabilize when more bays are added. Also, for the same reasons that collapse capacity in terms of spectral accelerations decreases, 6-story frames don't exhibit as large demands in displacements as the 3-story frames.

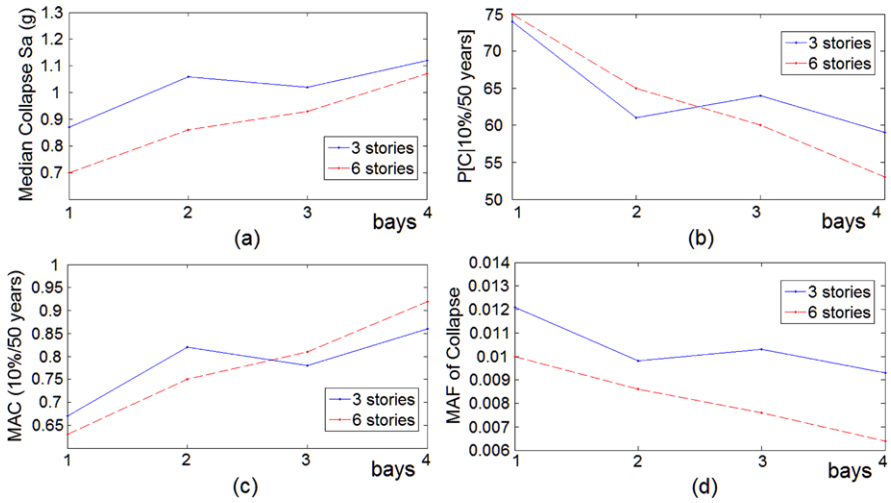


Fig. 6 Effect of the number of bays and stories in frames collapse capacity. (a) Median collapse capacity. (b) Probability of collapse for the 10 %/50 years earthquake. (c) MAC for the 10 %/50 years earthquake. (d) MAF of collapse

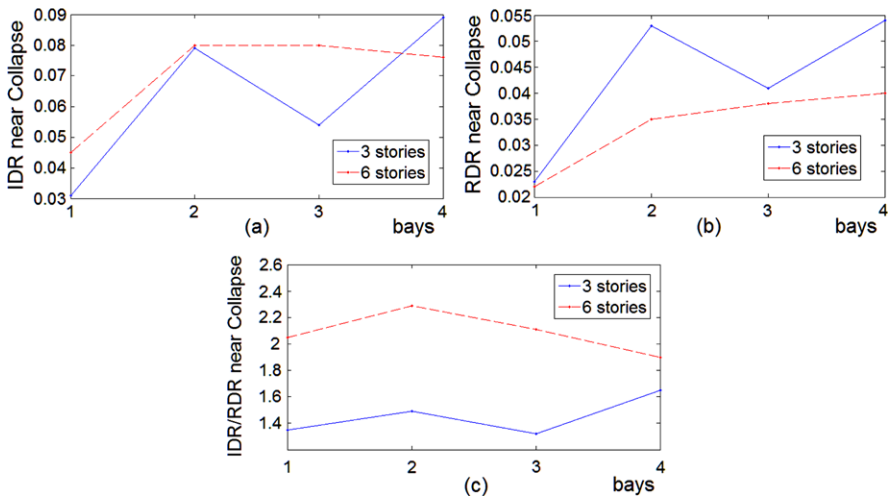


Fig. 7 Effect of the number of bays and stories in frames displacements near collapse. (a) Inter-story drift ratio (IDR). (b) Roof drift ratio (RDR). (c) IDR/RDR

From Figs. 6 and 7 it is evident that for 3-story frames, although it was expected 3-bay frame to develop higher strength against collapse than the 2-bay frame, the opposite results. This may be attributed to possible local collapse mechanisms that don't allow the structure to take advantage of its full redundancy. To elaborate more on this fact, the measure of structural redundancy as proposed by Bertero and Bert-

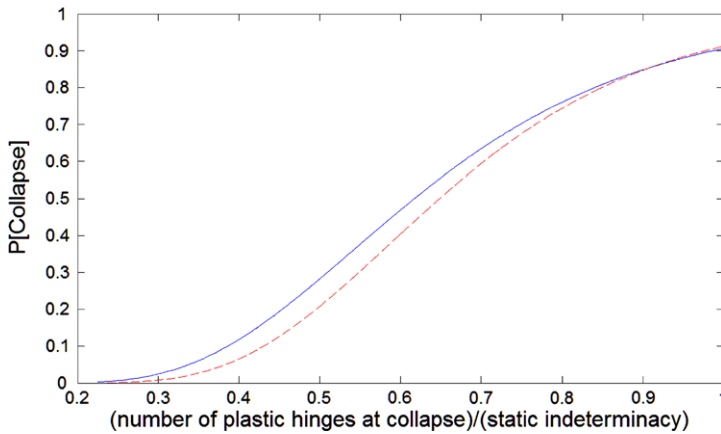


Fig. 8 Number of plastic hinges involved in collapse for 2-bays and 3-bays frames

ero [13] was investigated. This measure is the number of plastic hinges n that yield or fail at structural members ends until total collapse. So, in each single record IDA run where collapse is detected, the number of formed plastic hinges is recorded. This number is divided by the number of static indeterminacy of the structure to determine the redundancy ratio. Thus, a statistical set with 20 values is formed and the results are presented in the form of a cumulative distribution function in Fig. 8. It is clear that the 3-bay frame delays in consuming its full redundancy for a specific probability of collapse. Therefore, for a given probability of collapse, in the 3-bay frame the redundancy ratio, that expresses the regions that have yielded or failed, is smaller than the redundancy ratio in the 2-bay frame respectively; a fact that reveals the probabilistic nature of structural redundancy with respect to seismic loading.

The nonlinear modeling of structures with the notion of plastic hinge formation reveals the estimated form of collapse. For every collapse mechanism identified in each single IDA record, the number of stories involved in the mechanism is recorded and the results are presented in Table 3. A particular story is assumed to participate in the collapse mechanism when at least one plastic hinge appears either on its beams or columns.

For example in 6-story, 2-bay frame, plastic hinges are formed in the first 3 stories in 15 % of all the occasions, in the first 4 stories in 15 %, in the first 5 stories in 35 % and all stories are involved in collapse mechanism in 35 % of all the occasions. Also, the total percentage of stories where plastic hinges are formed either in their beams or columns is 82 %. Generally, from Table 3 it is observed that the distribution of plastic hinges along height is not influenced by the number of bays and that there is a tendency for concentration of damage in higher floors. There is no case of first-soft story mechanism for the 3-story frames, not first or second story mechanism for 6-story frames. The involvement of fifth and sixth story is significant, since flexural strength of columns is about 3 times higher than flexural strength of beams causing the beams in upper floors to yield earlier. Finally, percentages of stories involved in collapse for 6-story frames are clearly smaller, a fact that comes in agreement with

Table 3 Stories involved in collapse mechanism for each frame

Geometrical features		Percentages of observed plastic hinges						
Stories	Bays	Stories 1-1 (%)	Stories 1-2 (%)	Stories 1-3 (%)	Stories 1-4 (%)	Stories 1-5 (%)	Stories 1-6 (%)	Percentages of stories involved in collapse (%)
3	1	0	40	60	0	0	0	87
	2	0	25	75	0	0	0	92
	3	0	25	75	0	0	0	92
	4	0	30	70	0	0	0	90
6	1	0	0	15	15	45	25	80
	2	0	0	15	15	35	35	82
	3	0	0	10	30	35	25	79
	4	0	0	5	30	40	25	81

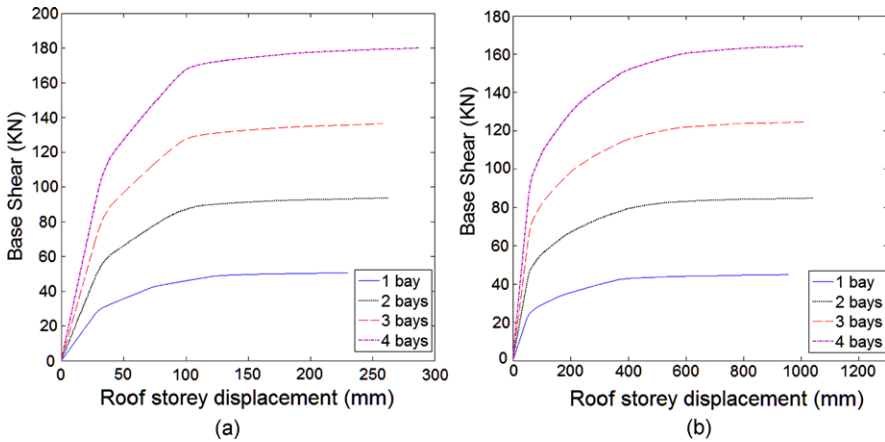


Fig. 9 (a) Pushover curves for 3-story frames. (b) Pushover curves for 6-story frames

Fig. 7c. Hence, it is evident from a different perceptive that damage concentrates in few stories in the case of the 6-story frames.

Next, the static pushover results with triangular lateral force distribution are presented in Fig. 9. The general trend is that, as the number of bays increases, redundancy also increases and the greater possibility for force redistribution exists, resulting into higher collapse base shear [14].

After estimating spectral collapse accelerations from base shears and considering the 5th column of Table 2 as standard deviations input, the following fragilities curves are determined as calculated using Eq. (2). It is clear from Fig. 10 that no conclusive remark can be drawn when a probabilistic methodology is based on static analysis with deterministic loading. This means that after regularization of the

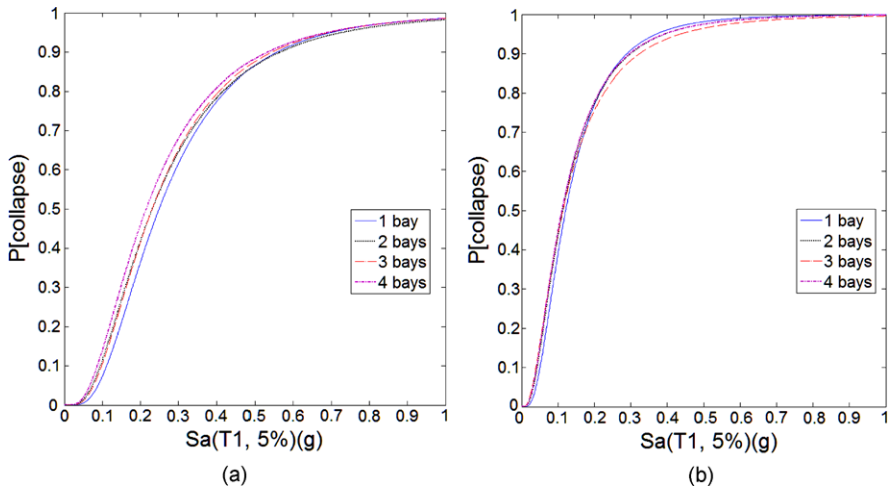


Fig. 10 (a) Collapse pushover fragility curves for 3-story frames. (b) Collapse pushover fragility curves for 6-story frames

collapse base shear with mass, all frames in each group exhibit approximately the same collapse capacity.

3.2 Effect of Stiffness Distribution Along Height

To examine the effect of stiffness distribution along the height in RC frames collapse capacity, 2 different designs of the 6-story 2-bay frames were analyzed. The study refers to typical, moment resisting frames, where mass is considered equal in all stories and distribution of stiffness between 2 consecutive stories doesn't exceed 60 % reduction. Also, the same moment of inertia is attributed to the same floor's members, as all beams and columns have the same mechanical properties. In order to quantify stiffness variation for every alternative design, the indices in Eqs. (6) to (8) are used as in [15]. These indices provide information about the form of lateral displacements, either for shear-type or flexural-type buildings. Index ρ_i is defined as the ratio of the sum of stiffness ratios of all beams at floor i to the sum of the stiffness ratios of all columns at the same floor. When ρ_i equals to zero, then pure flexural-type deformation occurs and if ρ_i becomes infinite then pure shear-type deformation occurs, while intermediate values stand for a combination of the 2 types where both beams and columns deform in flexure. Index ρ_b quantifies the variation of beam stiffness and is defined as the ratio of the sum of stiffness ratios of all beams at each floor to the sum of the stiffness ratios of all beams at the first floor. Similarly, index ρ_c is defined for columns.

$$\rho_i = \frac{\sum_{\text{story } i \text{ beams}} \frac{EI_b}{L_b}}{\sum_{\text{story } i \text{ columns}} \frac{EI_c}{L_c}} \tag{6}$$

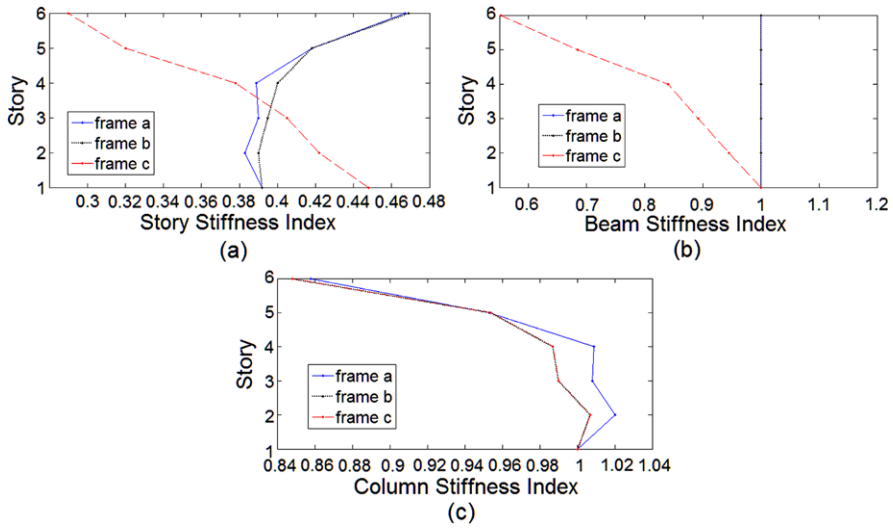


Fig. 11 Variation of stiffness along height for the 3 alternative designs. (a) Story stiffness index ρ_i . (b) Beam stiffness index ρ_b . (c) Column stiffness index ρ_c

$$\rho_b = \frac{\sum_{\text{story } i} \frac{I_b}{L_b}}{\sum_{\text{1st story}} \frac{I_b}{L_b}} \tag{7}$$

$$\rho_c = \frac{\sum_{\text{story } i} \frac{I_c}{L_c}}{\sum_{\text{1st story}} \frac{I_c}{L_c}} \tag{8}$$

In Fig. 11, the above indices are presented for the 3 frames designed to have different stiffness variation along height. Frame (a) is the 6-story, 2-bay frame presented in Sect. 3.1. This frame is designed according to Greek codes with varying column’s reinforcement along height. External columns maintain the same amount of reinforcement, while for the interior ones less steel rebars diameters are used in the 5th and 6th floor. Frame’s (b) reinforcement remains constant along height in every column so as in all stories index ρ_i to maintain approximately the same mean value with frame (a). Frame (c) is similar to frame (b), but with beam cross sectional dimensions diminishing as the number of stories increases. This variation is applied only in dimensions and not in cross section’s reinforcement so as to retain yield moment strength practically constant.

In the first two frames, that present constant beam stiffness in all stories, ρ_i index attains bigger values in upper floors as reinforcement in columns decreases. On the other hand having smaller beam cross sections in the 3rd design, index ρ_b becomes smaller as presented in Fig. 11b. In the same figure, plots for frames (a), (b) are identical as their beams are the same everywhere, while in Fig. 11c, plots for frames (b), (c) are identical as they have the same column properties. In general, variation of beams’ moment of inertia affects those frames for which beam’s rotations influence their deformation more than column’s lateral displacements.

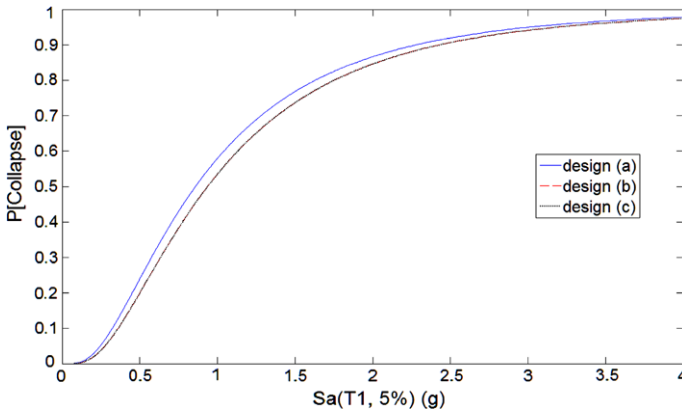


Fig. 12 Collapse IDA fragility curves of the 3 RC frames with different stiffness variation along height

Table 4 Collapse capacity quantification for the 3 different design alternatives

Frame	T1 (sec)	Median(Sa_c)	σ_{ln}	$P_{C 10\%/50y}$	MAC	λ_c	Median (IDR)	Median (RDR)
a	0.693	0.86	0.76	65 %	0.75	0.0078	0.080	0.035
b	0.694	0.94	0.74	61 %	0.82	0.0072	0.080	0.046
c	0.705	0.93	0.75	62 %	0.81	0.0072	0.076	0.035

After performing IDA for the three frames, fragility curves are determined which are presented in Fig. 12. Intuitively, one would expect that equal stiffness in each story would have forced damage to concentrate at lower floors, dictating collapse capacity to decrease. However, as it appears in Fig. 12 using the same amount of reinforcement in columns results into slight enlargement of median collapse spectral acceleration. Nevertheless, there is no more collapse capacity increase when beam cross sections vary while keeping the reinforcement and the cross section of columns constant.

Fragility behavior is quantified through evaluation of the probabilistic indices described in Sect. 2.2. The new outcomes are presented in Table 4.

In Table 4 a significant feature based on IDR/RDR ratio is displayed, which describes damage localization in specific stories. The smaller value for frame (b), meaning more similar damage distribution along height, is the main reason for the higher collapse capacity exhibited. This ratio is smaller because displacements in terms of roof drift ratio appear to be greater for frame (b) since it has less stiffness in its lower columns, thus facilitating plastic hinge formation in these critical regions. Therefore, plastic hinges at the bottom of first floor columns facilitates seismic energy dissipation and is an inevitable but positive feature for capacity design. More specifically, plastic hinge distribution at collapse is presented in Table 5. Generally, no significant differences are observed in the way that stiffness distribution

Table 5 Stories involved in collapse mechanism for each frame

Frames	Percentages of observed plastic hinges						Percentages of stories involved in collapse (%)
	Stories 1-1 (%)	Stories 1-2 (%)	Stories 1-3 (%)	Stories 1-4 (%)	Stories 1-5 (%)	Stories 1-6 (%)	
a	0	0	15	15	35	35	82
b	0	0	15	10	50	25	81
c	0	0	15	10	45	30	82

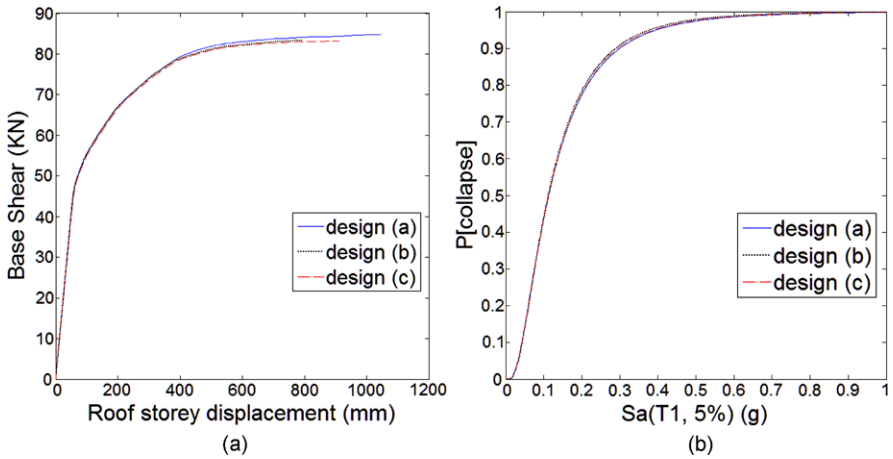


Fig. 13 (a) Pushover curves. (b) Collapse pushover fragility curves of the 3 RC frames with different stiffness variation along height

affects plastic hinge distribution. For the case of frame (b) with uniform column reinforcement, in 50 % of all the occasions plastic hinges are formed up to 5th story. Hence, it isn't the fact that more stories are involved in collapse mechanism which increases collapse capacity, but the fact that more columns participate in the mechanism dissipating more energy, as they aren't as stiff as in frame (a) where lower story columns were designed with increased reinforcement.

Similar to the previous study, fragility curves are generated from pushover analysis with the contribution of IDA to estimate dispersion in the results and the outcome is presented in Fig. 13. In this case all diagrams are almost identical, meaning that according to static analysis every alternative design has zero effect on seismic accelerations that the frame can withstand. Hence, it becomes evident that only a series of non-linear dynamic analysis with variable loading input is capable to reveal variations in structural behavior, even when small design variations are considered.

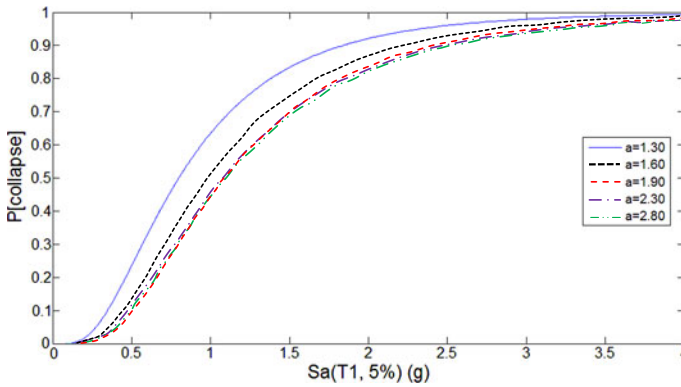


Fig. 14 Collapse IDA fragility curves for the different SCWB ratios

3.3 Effect of the Strong Column-Weak Beam Design Principle

The aim of the strong column-weak beam (SCWB) design provision is to avoid localized story mechanisms and thus attain more distributed failure mechanisms towards lateral sway. In order to study the effect of this concept, only yield moments of beams and columns are taken into account through index α [15]. This is defined as the ratio of the sum of columns yield moments to the sum of beams yield moments that are connected to a given joint:

$$\alpha = \frac{\sum M_{c,y}}{\sum M_{b,y}} \quad (9)$$

In this work, the alternative designs are based on the 3-story, 3-bay frame, where beam reinforcement remains constant and only column reinforcement varies from one design to another resulting in different α values, where index α is referred to the middle joint of the 1st floor.

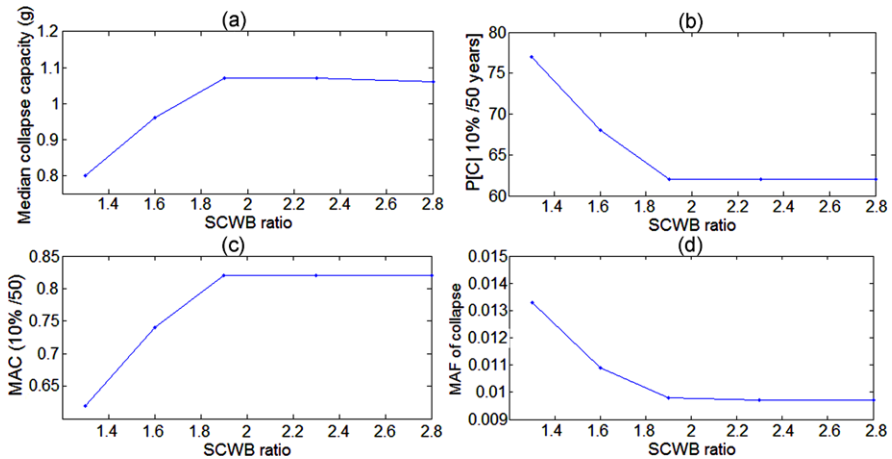
After performing IDA for all five frames, the fragility curves are determined which are displayed in Fig. 14. Also, the accompanying probability indices are provided in Table 6.

The results in Fig. 14 and Table 6 signify increased collapse strength until $\alpha = 1.90$ and after that, further increase in α does not result into higher collapse capacity, as fragility curves for $\alpha = 2.30$ and $\alpha = 2.80$ slightly differ from the fragility curve for $\alpha = 1.90$. Actually, due to larger dispersion in the last two cases, these curves present smaller collapse spectral accelerations at lower collapse probabilities. Hence, IDA defines a strength limit that can be assessed, meaning that additional reinforcement in columns has no effect except the increase in cost. For the case of the frame studied herein, this limit is accessed for $\alpha = 2$, when yield moment of columns is twice the yield moment of beams.

The results of Table 6 are displayed graphically in Fig. 15. From both Table 6 and Fig. 15 it is evident that there is an improvement by 15 % in collapse capacity from the worst to the best design. Also an improvement of 33 % at median collapse

Table 6 Collapse capacity quantification for the 5 different SCWB ratios

α	T1 (sec)	Median($S_{a,c}$)	σ_{ln}	$P_{C 10\%/50y}$	MAC	λ_c	Median (IDR)	Median (RDR)
1.30	0.386	0.80	0.65	77 %	0.62	0.0133	0.052	0.032
1.60	0.375	0.96	0.66	68 %	0.74	0.0109	0.069	0.048
1.90	0.368	1.07	0.63	62 %	0.82	0.0098	0.066	0.049
2.30	0.365	1.07	0.67	62 %	0.82	0.0097	0.076	0.056
2.80	0.363	1.06	0.68	62 %	0.82	0.0097	0.077	0.056

**Fig. 15** Effect of SCWB ratio on collapse capacity for a 3-story, 2-bay RC frame

spectral acceleration and at the margin against collapse (MAC) occurs, while the return period of collapse increases by 28 years. In terms of displacements, the frame exhibits repeatedly larger interstory and roof drifts up to $\alpha = 2.30$, while for $\alpha = 2.80$ no further increase occurs. In order to elaborate on the fact that improvement of collapse capacity is bounded up to a certain level, the results of plastic hinges distribution forming a collapse mechanism for every escalated record are listed in Table 7.

In the last column of Table 7, capacity design violation is considered to occur when a column fails prior to a beam at a given joint of the structure. Such violation can occur even if the formation of a plastic hinge at a beam isn't adequate enough to prevent a final failure at the column of the joint. As expected, more plastic hinges are formed in beams as column flexural strength increases, while the average number of total plastic hinges formed remains unaffected with SCWB ratio, meaning that only the distribution of plastic hinges changes. Also, violation of capacity design regulation percentages are reduced while this ratio gets bigger. However, for values larger than 1.90 this percentage doesn't appear to differ considerably, a fact that is also depicted by the similarity of fragility curves presented in Fig. 14. Thus, it

Table 7 Plastic hinge percentages at collapse

α	Average number of plastic hinges formed (%)	Plastic hinges percentages at columns (%)	Plastic hinges percentages at beams (%)	Capacity design violation percentages (%)
1.30	19.5	57	43	55
1.60	21	45	55	45
1.90	21	33	66	15
2.30	19.5	20	80	15
2.80	18	12	88	5

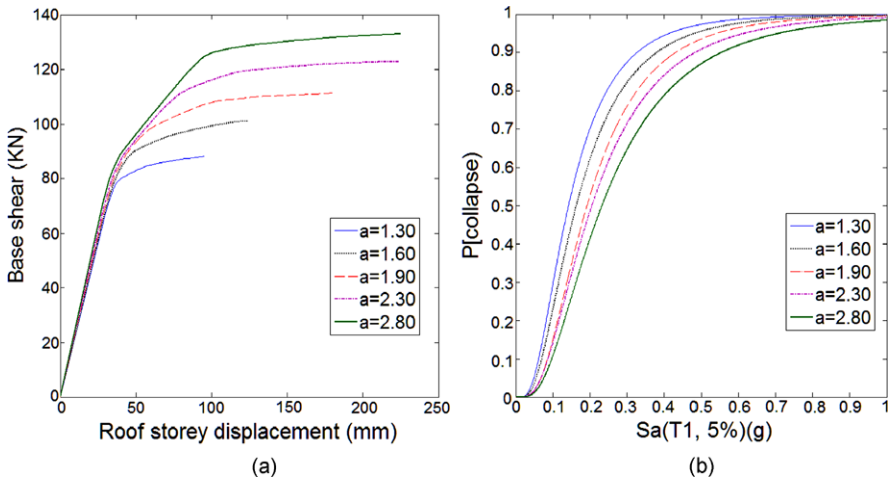


Fig. 16 (a) Pushover curves. (b) Collapse pushover fragility curves of the RC frames with different SCWB ratio

becomes evident that when capacity design provisions are in place, an optimum design with respect to the probability of collapse can be achieved.

Also, a static pushover analysis is performed for the corresponding five RC frames and the outcome is presented in Fig. 16 to depict the primal behavior to compare with IDA. Generally, the main tendency both in the pushover curves and the corresponding fragility curves is an increase of ultimate strength with the increase of column reinforcement. This fact is conflicting to the behavior revealed from IDA where a limit was observed in collapse capacity even if additional reinforcement is considered in columns. Therefore, another misleading result may come from the non-linear static analysis, while the true actual trend is revealed only by performing non-linear dynamic analysis.

An even better design can be proposed combining both beam and column flexural strength and not just considering the SCWB ratio. For example, in Fig. 17 two fragility curves are presented which refer to the same frame with $\alpha = 2.30$ and an alternative design where beams yield moment is improved with the ratio α reduced

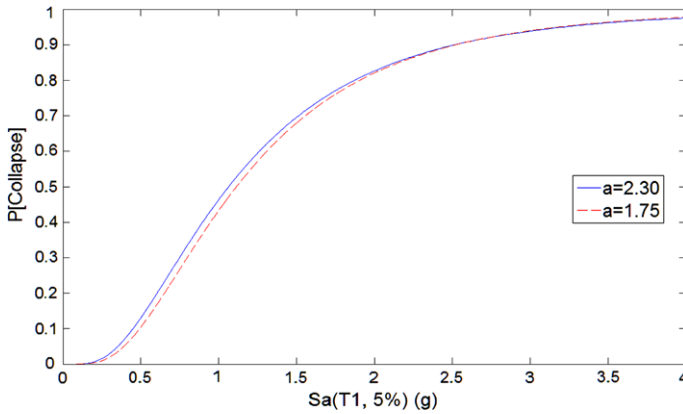


Fig. 17 Collapse IDA fragility curves for the same frame after reducing α through beam yield moment increase

to 1.75. It is clear that this alternative design increases slightly collapse capacity by increasing beam rotational capacity, justifying the claim that total structural strength is not affected only by the SCWB ratio but also by member's strength.

4 Concluding Remarks

In this work fragility curves following IDA are determined for a series of 2D RC frames to estimate the effect of variation of some of their geometrical, mechanical and design parameters on their collapse capacity. The main remarks drawn can be summarized as follows:

- For the set of frames studied in this work results between IDA and pushover analysis deviate in some cases, emphasizing the need for more realist simulation of structures under seismic excitations through a series of non-linear dynamic analysis.
- By calculating mean values for the two groups of frames concerning 6- and 3-story frames, 17 % reduction in collapse probability assuming the 10 % in 50 years earthquake occurs and 28 % reduction in terms of MAF of collapse is achieved when number of bays increases from 1 to 4.
- When stiffness distribution along height varies, probability of collapse is reduced only 3 % and MAF of collapse is improved by 8 %.
- With regard to the SCWB ratio, probability of collapse is reduced by 15 %, while MAF of collapse is reduced by 27 %. Also, an upper limit exists, beyond which collapse capacity is not improving.
- By assessing the sensitivity in collapse capacity with respect to the investigated factors, it can be concluded that a primal factor is the redundancy of the structure which appears in frames with more bays. Of equal importance is the SCWB ratio

that affects the form of collapse mechanism within the structure. Stiffness distribution along the height of the structure appears to be insignificant, suggesting constant reinforcement along the height.

- More elaborate analysis should be performed to establish more general results which should be based on more representative samples and more exhaustive variation of parameters.

References

1. Vamvatsikos D, Cornell A (2002) Incremental dynamic analysis. *Earthq Eng Struct Dyn* 31(3):491–514
2. Vamvatsikos D, Cornell A (2004) Applied incremental dynamic analysis. *Earthq Spectra* 20(2):523–553
3. Jalayer F, Cornell A (2003) A technical framework for probability-based demand and capacity factor design (DCFD) seismic formats. PEER report 2003/08
4. Zareian F, Krawinkler H, Ibarra L, Lignos D (2010) Basic concepts and performance measures in prediction of collapse of buildings under earthquake ground motions. *Struct Des Tall Spec Build* 19:167–181
5. Chatzi EN, Triantafillou SP, Koumousis VK (2005) A computer program for 3D inelastic analysis of R/C structures. In: 5th GRACM international congress on computational mechanics, Limassol
6. Charalampakis AE, Koumousis VK (2008) Identification of Bouc-Wen hysteretic systems by a hybrid evolutionary algorithm. *J Sound Vib*. doi:[10.1016/j.jsv.2008.01.018](https://doi.org/10.1016/j.jsv.2008.01.018)
7. Wilson EL, Habibullah A (1987) Static and dynamic analysis of multi-story buildings, including P - Δ effects. *Earthq Spectra* 3(2):289–298
8. Vamvatsikos D, Jalayer F, Cornell A (2003) Application of incremental dynamic analysis to an RC-structure. In: FIB symposium on concrete
9. Krawinkler H, Medina R, Alavi B (2003) Seismic drift and ductility demands and their dependence on ground motions. *Eng Struct* 25:637–653
10. Medina RA, Krawinkler H (2003) Seismic demand for nondeteriorating frame structures and their dependence on ground motions. Report No 144, John A. Blume Earthquake Engineering Center
11. Haselton C, Deierlein G (2008) Assessing seismic collapse safety of modern reinforced concrete moment-frame buildings. PEER report 2007/08
12. Shinozuka M, Feng MQ, Kim H-K, Kim S-H (2000) Nonlinear static procedure for fragility curve development. *J Eng Mech* 126(12):1287–1296
13. Bertero RD, Bertero VV (1999) Redundancy in earthquake-resistant design. *J Struct Eng* 125(1):81–88
14. Manola MM, Koumousis V (2010) The role of redundancy and overstrength in earthquake resisting design. In: 9th international congress on mechanics, Limassol
15. Zareian F, Krawinkler H (2009) Simplified performance based earthquake engineering. Report No 169, John A. Blume Earthquake Engineering Center

Seismic Risk Assessment of Italian School Buildings

Barbara Borzi, Paola Ceresa, Marta Faravelli, Emilia Fiorini,
and Mauro Onida

Abstract Most of the Italian school buildings were not designed according to seismic criteria and, therefore, they are vulnerable from a seismic point of view. A clear proof of this was the catastrophic collapse of the school at San Giuliano during the October 2002 earthquake: thirty people died, of which twenty seven were young students and one their teacher. After this seismic event, the process for identifying the most seismically vulnerable school buildings was started in Italy, with the final aim of improving their strength. Furthermore, several school buildings, mainly located in the historical town centre were damaged during the recent seismic event of L'Aquila (April 6, 2009), as reported by Salvatore et al. (Rapporto dei danni provocati dall'evento sismico del 6 aprile sugli edifici scolastici del centro storico de L'Aquila, <http://www.reluis.it>). The proposed research work was driven by the idea of defining a methodology that implements an analysis in successive steps with an increasing level of detail. Only the buildings with seismic risk higher than a given threshold go through to the following phase, so that the number of buildings analysed decreases at each phase. The implemented procedure follows some well known works published in literature (Grant et al. 2007; Crowley et al. 2008). The definition of a prioritisation scheme of intervention is strictly due to the high number of school buildings (almost 50000) that cannot be deeply analysed considering the limited resources available. The school building location, the exposure data and seismic input information are implemented in a WebGIS platform through interactive maps and tabs. By means of the developed WebGIS tools, the seismic risk analyses of the school buildings are performed and the obtained results, in terms of maps and tables, are herein presented.

Keywords Seismic risk · School buildings · Vulnerability · Conventional resistance

B. Borzi · P. Ceresa · M. Faravelli (✉) · E. Fiorini · M. Onida
European Centre for Training and Research in Earthquake Engineering (EUCENTRE),
Via Ferrata 1, 27100 Pavia, Italy
e-mail: marta.faravelli@eucentre.it

P. Ceresa
Istituto Universitario di Studi Superiori (IUSS), V.le Lungo Ticino Sforzo 56, 27100 Pavia, Italy

1 Introduction

Italian seismic provisions and seismic zonation were updated several times during the last century. Therefore, a large portion of buildings has not been designed for an adequate level of seismic resistance required under modern design provisions. The majority of the Italian school buildings are especially vulnerable to seismic ground motion since they are judged to be seismically inadequate. An ad hoc seismic risk evaluation of the school buildings becomes therefore of fundamental importance for planning an accurate retrofitting of these buildings and for the safety of their occupants.

The seismic vulnerability evaluation of the school buildings is a topic that has been discussed by several authors in the last decades. For example the SAVE project-Task 2 [1] includes the vulnerability study of public and strategic buildings located in central and southern of Italy, while the “Scuola Sicura” project [2] provides the evaluation of the structural characteristics of school buildings located in the Molise district. Also EUCENTRE research groups [3, 4] have dealt with this topic proposing methods for seismic risk assessment of school buildings and then applying them to schools located in some Italian districts. Also, a seismic testing program [5] is in progress in accordance with Italian regulations (Article 2, paragraphs 2, 3 and 4 of [6]). According to this program, schools are classified as relevant buildings in relation to the consequences of a possible collapse. Therefore seismic controls are required, with priority given to the schools in seismic zone 1 and 2. Although this program [5] had originally set the time limit for testing to 2008, later extended to 2011, the controls are not yet complete even for zone 1 and 2.

Due to the lack of available data, the studies performed in recent years haven't affected all the schools throughout the country. The previous studies were not concerned with the school buildings located in districts with low seismic hazard. However the schools located in these areas may have high levels of vulnerability having been designed in the absence of seismic regulations and this could result in a high seismic risk.

To the authors' knowledge, the study presented herein is the first where the maps of conditional probability of damage and seismic risk are obtained at a national level, since it has been carried out considering most of the Italian school buildings. The available data refer to the survey of all school buildings (“Anagrafe Edilizia Scolastica”) carried out by the Ministry of Education (“MIUR”) to identify various safety-related parameters. The collected survey forms comprise about 70 % of the Italian school buildings, and contain data that allow to identify the geographical location of the building, as well as its structural characteristics (i.e., age, number of storeys, construction type, and preservation status), its security conditions and the features of rooms and sporting facilities.

2 Adopted Procedure

This research work describes the method proposed for identifying the most seismic vulnerable Italian school buildings and for assigning priorities for the execution

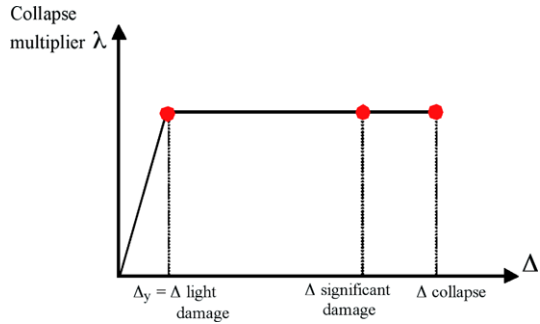
of detailed inspections and structural retrofitting measures. The adopted method is based on an initial proposal by Grant et al. [3]. It comprises multiple steps of assessment of increasing level of detail, each one substantially reducing the size of the building inventory since only the buildings most at seismic risk are considered. The procedure consists of two phases which correspond to the two levels of the available building information. In both phases, the seismic risk is defined considering the probability of reaching or exceeding given limit states by comparing the demand with the capacity in terms of displacements. The vulnerability of the school buildings is defined by computing their capacity curves (known, in the technical literature, as pushover curves). The mechanics-based methodology SP-BELA (Simplified Pushover-Based Earthquake Loss Assessment), developed for large-scale vulnerability assessment, is used for performing the simplified pushover curves [7, 8] of the analysed buildings. In the first phase of the assessment, the capacity is computed as a function of the number of storeys, structural vertical typology, and building age written in the questionnaires of the “Anagrafe Edilizia Scolastica”. Based on these data, the buildings are subdivided in classes and random populations of buildings can be generated for each building class using Monte Carlo simulation. For each randomly generated building, a simplified pushover analysis is carried out using SP-BELA (Fig. 1), leading to the definition of the displacement capacity, vibration period and viscous damping of an equivalent single degree of freedom system [7, 8].

The second phase of the procedure is based on the data collected, at Regional level, through the 2nd Level Forms [9–11] of GNDT (“Gruppo Nazionale per la Difesa dai Terremoti”). In this second phase, only masonry buildings are taken into account since the complete GNDT 2nd Level Form for reinforced concrete (RC) buildings were few and, therefore, not statistically significant, whereas they allow the calculation of the Conventional Resistance (“Resistenza Convenzionale”) for masonry buildings. The Conventional Resistance is the lateral strength of the weakest storey of the building divided by the structure seismic weight. Therefore, the difference with respect to the first phase of the procedure is that the resistance factor of the capacity curve is computed directly with the data available within the form of the reference school building and not computed for each random generated building stock representative of the reference school building class.

If the results of the seismic testing program [5] became available, it would be possible to increase the number of levels of detail.

Due to the incompleteness of the available database, the second phase of the procedure cannot be applied to the overall Italian school building stock. Therefore, the estimate of the reduction in size of the building inventory moving from the first to the second phase of the procedure cannot be carried out. The study described herein does not apply the prioritisation procedure as a whole, but represents its validation in order to identify some possible shortcomings that need improvements.

Fig. 1 Capacity curve for elastic-perfectly-plastic structural behaviour [8]



2.1 Definition of the Building Capacity

The capacity is evaluated as a function of the number of storeys, the structural typology and the year of construction. For each building class identified on the basis of this information, a sample of 1000 buildings is created by means of a Monte Carlo generation. The sample size of 1000 is considered statistically representative since its increase does not affect the final results. For RC buildings the procedure includes a simulated design with the Allowable Stress Method as this was the design method prescribed by the law prior to [12].

For each building of the sample a simplified pushover analysis is carried out using the SP-BELA methodology that allows to calculate the properties of an equivalent single degree of freedom system, such as the displacement capacity Δ , the equivalent period of vibration T and the equivalent viscous damping ξ for each limit state.

Three limit state (LS) conditions have been taken into account [13]:

- Light damage: the building can be used after the earthquake without the need for repair and/or strengthening;
- Significant damage: the building cannot be used after the earthquake without strengthening;
- Collapse: the building becomes unsafe for its occupants as it is no longer capable of sustaining any further lateral force or the gravity loads for which it has been designed.

The limit state conditions previously described can be related to specific prescriptions of Italian design code [12, 14]. In particular, the reference limit state conditions for RC buildings are defined in relation to the chord rotation. For masonry structures, the damage is usually related to interstorey drift capacity, and the limit conditions have been identified through the results of experimental tests as described in [8].

An elastic-perfectly-plastic behaviour of the structure is assumed (Fig. 1), which effectively means that, in order to define the pushover curve, only the displacement capacity Δ corresponding to the three LS and the lowest collapse multiplier λ of all the considered mechanisms need to be defined. Multiplying λ by the structure seismic weight gives the lateral strength of the weakest storey of the building.

In the first phase, the collapse multiplier λ is calculated for each of the 1000 buildings of the sample on the basis of the formulations reported in [7] for reinforced concrete buildings and in [8] for masonry buildings. In the second phase, on the other hand, the collapse multiplier λ coincides with the Conventional Resistance calculated using the data included in the GNDT 2nd Level Form for masonry buildings.

In the first phase a building class is associated to each school belonging to the database of the “Anagrafe Edilizia Scolastica” and then, for each class, a sample of buildings is generated and, for each of them, a capacity curve with different collapse multiplier and limit displacements. In the second phase, however, a building class is still associated to each building in the GNDT database (defined exclusively as a function of the number of storeys) and for each class is generated a sample of buildings, but the capacity curves are characterised by the same collapse multiplier, which coincides with the Conventional Resistance calculated using the data collected in the GNDT 2nd Level Form for the examined building, and different limit displacements.

2.1.1 Defined Classes of Buildings

In the first phase of the methodology, 47 classes of buildings (Fig. 2) have been identified in the database of the “Anagrafe Edilizia Scolastica”, based on the number of storeys, the horizontal and vertical structural typology and the year of construction.

Masonry buildings have been divided into three vulnerability classes: A = high, B = average, C = low. The three classes have been identified on the basis of the intersection of the horizontal and vertical structural typology, using the correspondence shown in Table 1. This correlation is reported in [15] and it was developed by Braga et al. [16] on the basis of the Irpinia’80 data. When there was not enough information to assign the class using the available data, a default class B was assigned. The number of storeys considered for masonry buildings is from 1 to 5.

A different criterion has been applied for the RC buildings since they are subdivided in two main classes: RC buildings that have not been seismically designed and RC buildings seismically designed. Comparing the seismic zone to which the municipality has been assigned and the period of building construction, it is possible to identify if a school building has been or not designed according to seismic design provisions. For seismically designed buildings, the seismic zone of the municipality at the period of construction has to be taken into account since it can be used, together with the provisions of the design codes of the same period, for defining the value of the design lateral force as a percentage of the total building weight. Figure 2 refers to three seismic zones in Italy, since the fourth one [17], characterised by the lowest value of seismicity, has been disregarded because it was introduced by recent regulation and not really used to design buildings so far. In SP-BELA, the buildings are designed considering only gravity-load before seismic classification. Then, following the classification and depending on the seismic zone of the municipality, a base shear coefficient, included in the design of the buildings, was

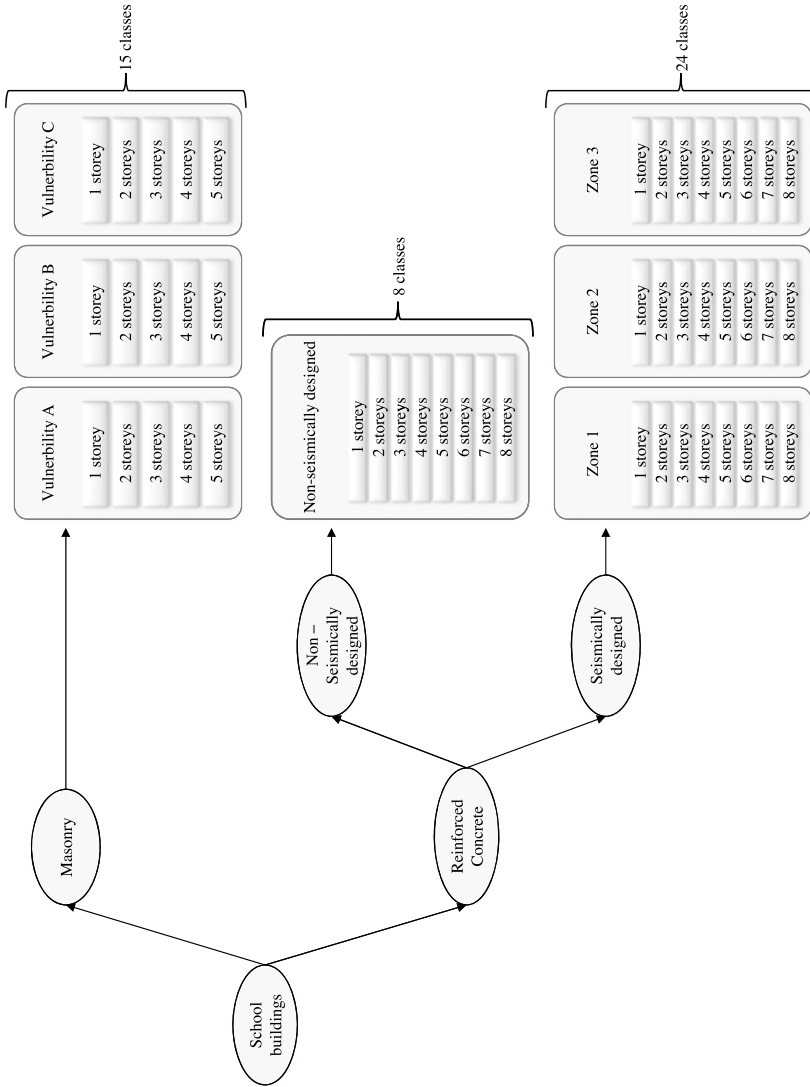


Fig. 2 Classes of buildings considered in the study

Table 1 Vulnerability classes from horizontal and vertical structural type

Horizontal	Vertical		
	stone	tuff	brick
vault	A	A	A
wood	A	A	B
iron	B	B	C
CA	B	C	C

assigned. For buildings assigned to Zone 1, this coefficient has been taken as 10 % of the weight, for buildings in Zone 2 as 7 % and in Zone 3 as 4 %. The number of storeys considered for RC school buildings is: 1, 2, 3, 4, 5, 6, 7, more or equal to 8 (Fig. 2).

The second phase of the analysis has been developed for masonry buildings only. The classes of buildings considered in this phase are only 5, depending on the number of storeys. In this case, masonry buildings were not divided into vulnerability classes because the Conventional Resistance parameter already includes information about the building vulnerability.

2.1.2 Computed Fragility Curves

As explained in Sect. 2.1.1, in phase 1 the masonry buildings were divided into three vulnerability classes: class A, B and C. The SP-BELA method does not provide fragility curves for highly vulnerable masonry buildings due to the lack of the necessary data for the description of the sample, as the only statistically significant sample available was limited to good quality masonry buildings. Also the description of the building capacity through a pushover curve does not account for the local collapse mechanisms which are the most common collapse mechanism for highly vulnerable masonry buildings. To define the fragility of highly vulnerable masonry buildings a hybrid method was therefore adopted. SP-BELA was used to define the fragility of low vulnerability masonry buildings (class C). The curve obtained for buildings of type C was then modified by including data of observed damage from recent earthquakes to obtain the fragility curves for class A and B.

Observed damage data herein included are those summarised in the damage probability matrices (DPM) published in Braga et al. [16]. Such matrices come from a statistic of post-event data collected in the municipalities affected by the 1980 Irpinia earthquake. For the evaluation of these matrices, the buildings were classified in 3 vulnerability classes (A = high, B = average, C = low). The hazard is expressed in MSK macroseismic intensity scale [18]. The DPMs consider 5 damage levels, besides the absence of damage.

The first step was to find a correspondence between the levels of damage taken into account in the DPMs and the SP-BELA limit states. It was assumed that the

Fig. 3 Fragility curves for limit state of significant damage obtained from DPM developed by Braga et al. [16] and lognormal function which best interpolates them

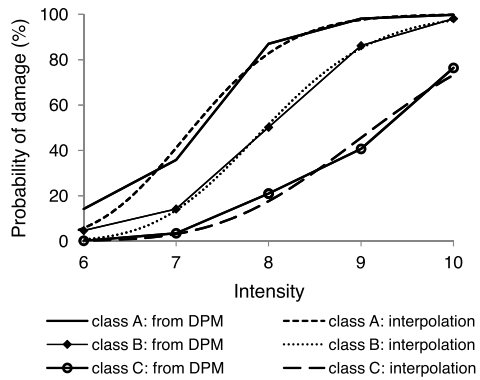


Table 2 Multiplicative coefficients that allow to obtain, for each limit state, the fragility curves for the class A and B starting from the curve obtained for the class C

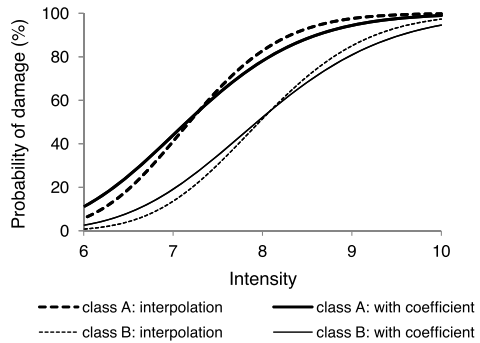
Limit state	Vulnerability class	
	A	B
Light damage	1.36	1.17
Significant damage	1.28	1.16
Collapse	1.26	1.15

damage levels 1 and 2 correspond to light damage, the level 3 corresponds to significant damage and levels 4 and 5 correspond to collapse. The DPMs developed by Braga et al. [16] were used to understand the relationship in terms of probability of damage between the three classes of masonry. Fragility curves have been defined through the best fit with a lognormal curve of the points corresponding to the damage probability matrix. Hence, the authors have assumed that the fragility curves corresponding to the different vulnerability classes are characterised by a different mean value and by the same dispersion parameter (i.e. the same coefficient of variation, CV).

Figure 3 shows the curves for the limit state of significant damage. In the aforementioned figure, a continuous line is used for the curves resulting from the discrete DPMs developed by Braga et al. [16], while the dashed lines refer to the lognormal best fit curves. The good correspondence between the curves demonstrates that the lognormal distribution is a good mathematical function to describe the probability distribution of the damage data coming from observations.

For each limit state, the ratio between the mean value of the curve for class C and the mean of the curves for class A and B was calculated. These coefficients are reported in Table 2 as a function of the limit state. In order to validate the assumption that the CV does not change from one vulnerability class to the other, Fig. 4 shows the comparison between the fragility curves for classes A and B obtained by interpolating the corresponding DPM (dashed line) and the fragility curves obtained starting from the curve for class C and modifying the average value using the coefficients shown in Table 2 (continuous line) for the significant damage limit state. Plots obtained from the curve for class C show a good approximation with those derived

Fig. 4 Fragility curves for limit state of significant damage obtained by interpolating the corresponding DPM of Braga et al. [16] and curves obtained with the calculated coefficients



by the interpolation of the DPMs. Therefore, SP-BELA fragility curves are calculated for the vulnerability class C and then those for classes A and B are obtained using the coefficients summarised in Table 2.

The fragility curves for the RC buildings were calculated only applying the mechanical method.

2.2 Conditional Probability of Damage

In SP-BELA the comparison between seismic capacity and demand is carried out in terms of displacement. The building displacement capacity has been introduced in Sect. 2.1. The seismic demand imposed by the earthquake to the structure is calculated with reference to the elastic spectrum related to the school building location, computed according to the formulation proposed in [12, 14]. This formulation has been obtained through least-square interpolation of the median acceleration spectrum derived from the probabilistic hazard study performed by DPC-INGV project [17] for a grid of points (each one at distance of 0.05 degrees) used for the whole country. The formula and the coefficients given by the Italian code [12, 14] allow the computation of the mean spectral accelerations for each point of the grid and for seismic events characterised by a return period (T_r) of 30, 50, 72, 101, 140, 201, 475, 975 and 2475 years, respectively.

In this study, the least-square interpolation method has been applied to the median acceleration spectrum (50th percentile) plus and minus one standard deviation for deriving the parameters that allow the computation of the 84th and 16th percentile spectral accelerations, respectively. Therefore, the seismic demand imposed by the earthquake to the structure is computed with respect to the 16th, 50th and 84th percentile acceleration spectra. Bedrock conditions with no topographic amplification have been assumed for the Italian territory, since no data are available at present for the evaluation of the site conditions where the school buildings are located.

The seismic demand is derived from the elastic response spectrum knowing the location of the school building, for a given return period and a selected percentile

(16th, 50th, and 84th). From SP-BELA method, the vibration period T of the building and the equivalent viscous damping ξ are computed for each limit state. Knowing the response period, the spectral ordinate is directly derived for each LS. Knowing the equivalent viscous damping, the spectra reduction factor η , used to take into account the energy dissipation capacity of a given structure for a given LS, is then computed, as suggested for instance in [19]:

$$\eta = \sqrt{\frac{7}{2 + \xi}} \quad (2.1)$$

For RC frames, the equivalent viscous damping ξ in Eq. (2.1) has been obtained as a function of the ductility, using Eq. (2.2) [19]. For masonry buildings, the damping values suggested in [20] have been adopted (5 %, 10 % and 15 %, respectively) for each limit state.

$$\xi = 0.05 + 0.565 \left(\frac{\mu - 1}{\pi \mu} \right) \quad (2.2)$$

The displacement spectral ordinates are defined starting from the spectral accelerations:

$$S_d = S_a \left(\frac{T}{2\pi} \right)^2 \quad (2.3)$$

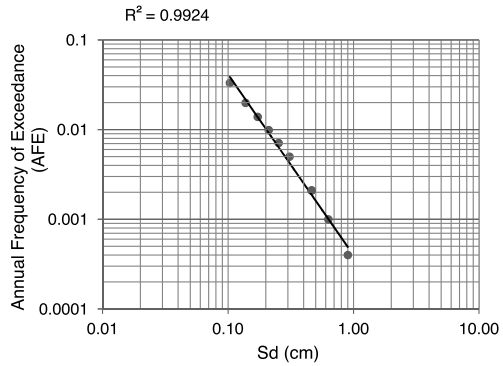
where S_d represents the displacement demand, S_a the acceleration demand and T the period of vibration of the building.

Based on the previously introduced ingredients, the conditional probability of damage, where the condition is that a given seismic event will occur, can be computed for the nine return periods T_r considered in the Italian seismic code [12]. Random populations of buildings are generated for each building class (1000 buildings for each one of the 47 classes shown in Fig. 2) using Monte Carlo simulation. The period of vibration T , the displacement capacity Δ and the ductility factor η at the three different damage limit states (Fig. 1) can be calculated for each randomly generated building through a simplified pushover analysis performed using SP-BELA (Sect. 2.1). Knowing T at each LS and for a given overdamped (using Eq. (2.1)) displacement response spectrum, the displacement demand of a given building of the random population can be predicted and compared with its limit state displacement capacity. This procedure is repeated for the 1000 buildings randomly generated for each class of school buildings (Fig. 2). The sum of all buildings whose displacement capacity is lower than the displacement demand divided by the total number of buildings gives an estimation of the probability of exceeding a given limit state. The output of these computations is the conditional probability of damage, given the occurrence of a seismic event characterised by a given return period T_r .

2.3 Computation of the Seismic Risk

The seismic risk is computed knowing the hazard curve of the place where the school building is located. Such curve gives the probability of occurrence of a given

Fig. 5 Relationship between the annual frequency of exceedance (AFE) and S_d ($T = 0.2$ sec)



level of ground shaking severity in a specific exposure time t_d . Severity can be expressed in terms of the Annual Frequency of Exceedance (AFE), which is the reciprocal of the return period T_r . The hazard curve represents the relationship between AFE and a ground motion parameter, herein assumed as the spectral displacement S_d . The logarithm of the S_d and the logarithm of the corresponding AFE ($= 1/T_r$) can be assumed to be linearly-related, at least for return periods of engineering interest. The gradient of the log-log hazard curve is named $-k$, according to the definition in Part 1 of the Eurocode 8 [21]. As an example, Fig. 5 plots the spectral ordinates S_d for a vibration period of 0.2 seconds. Since the values are linearly related, the hazard curve is defined knowing a value of S_d corresponding to a return period T_r and the slope k of the line interpolating all the other points and passing from a reference point.

The reference point is here conventionally assumed equal to the value at 475 year return period and the hazard curve is defined by the following relationship:

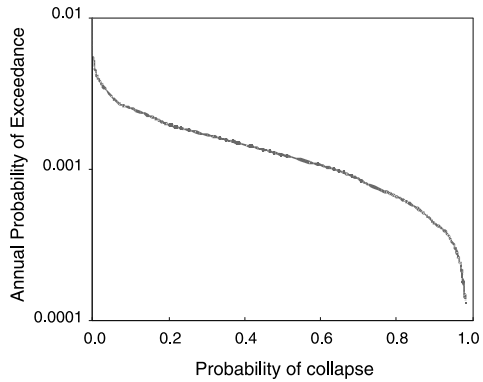
$$AFE = AFE_{475} \left(\frac{S_{d475}}{S_d} \right)^k \tag{2.4}$$

where AFE_{475} and S_{d475} are the annual frequency of exceedance and the spectral displacement corresponding to the 475 year return period, respectively.

Knowing the vibration period T of the structure, nine values of spectral accelerations S_a are computed in correspondence of the nine return periods T_r listed in [12]. Using Eq. (2.3), the S_a values are converted in spectral displacements S_d ; the next step is the derivation, in a log-log plane, of the line interpolating these points and passing for the point computed at a 475 year return period, and the slope k is finally calculated. Therefore, the hazard curve is directly derived and the displacement demand can be computed whatever return period is considered. It follows that all the events that could occur in a specific exposure time t_d can be taken into account. Hence, the seismic demand is then computed and compared with the capacity for each event, obtaining the conditional probability of exceeding a given limit state.

The seismic risk is the unconditional probability of failure the limit state conditions. For its computation, the hazard curve previously expressed as a function of the frequency has to be given in terms of probability. The occurrence of the events

Fig. 6 Exceedance curve of the collapse limit state in an exposure time of 1 year, for a given class of buildings



is assumed to follow the Poisson process, that is a memoryless distribution such that each event occurs independently of one another. Therefore, the occurrence probability (q) of an event with severity AFE, in the exposure time t_d , is given by the following equation:

$$q = 1 - e^{-t_d AFE} \tag{2.5}$$

Since AFE is related to the spectral displacement S_d according to Eq. (2.4), the probabilistic hazard curve can be expressed as a function of S_d :

$$q = 1 - e^{-t_d AFE_{475} (S_{d475}/S_d)^k} \tag{2.6}$$

Three exposure times t_d are taken into account in this study: 1 year, 10 years and 50 years. If, for example, the annual collapse risk has to be computed, the corresponding hazard curve is obtained from Eq. (2.6) with $t_d = 1$. The derived curve gives the annual probability of occurrence of an event with severity AFE expressed as a function of S_d . The hazard curve has to be related to the conditional probability of collapse, i.e. the vulnerability, where the condition is the occurrence of an event for a given return period T_r . Knowing that T_r can be expressed as a function of AFE and AFE is related to S_d according to Eq. (2.4), the conditional probability of damage is then obtained and the condition is expressed as a function of S_d . Therefore, since two curves are available—the hazard curve and the vulnerability curve—both expressed as a function of S_d , the exceedance curve of a given limit state in the exposure time t_d can be computed as a discrete function.

Shown in Fig. 6 is the exceedance curve for a exposure time t_d of 1 year and the collapse limit state. The annual seismic risk is given by the analytical integration of this curve, using the following equation:

$$\begin{aligned} \text{Seismic Risk} = \sum_{i=0}^{+\infty} & \left[\frac{APE_{2(i+1)} - APE_{2i}}{6} \right] \\ & \cdot [P_{\text{collapse}_{2i}} + 4P_{\text{collapse}_{2(i+0.5)}} + P_{\text{collapse}_{2(i+1)}}] \end{aligned} \tag{2.7}$$

where APE is the Annual Probability of Exceedance, and P_{collapse} the probability of collapse.

If the exposure time t_d is different from 1 year, the ordinates of the derived plot are the probability of exceedance in the considered t_d .

3 Available Databases

The procedure described for the evaluation of the seismic risk has been applied for processing the data of two databases: the survey forms of the “Anagrafe Edilizia Scolastica” (used in the first phase of the procedure) and the GNDT 2nd Level forms (used in the second phase of the procedure). The school buildings of the “Anagrafe Edilizia Scolastica” forms have been georeferenced based on the street address. Then, a correspondence between these buildings and the ones of the GNDT forms has been derived in order to compare the two sets of data. Since there is no a common identification to be associated to the school buildings of the two databases, the correspondence has been carried out using the geographical location. The georeferenced buildings belonging to the “Anagrafe Edilizia Scolastica” database are 49503, whereas the ones belonging to the GNDT database and with a correspondence in the first database are 3553.

3.1 School Buildings Analysed in the First Phase of the Procedure

As previously introduced in Fig. 2, the school buildings of the “Anagrafe Edilizia Scolastica” database have been subdivided in 47 classes. However, there are 17328 buildings of this database without the specification of their structural typology or the number of storeys. Therefore, the latter could not be introduced in one of the classes of Fig. 2. Hence, some assumptions have been done in order to automatically assign the needed information for classifying these school buildings. Furthermore, additional hypotheses have been required for assigning one of the two main structural typologies considered in this study (masonry and reinforced concrete) to those buildings with a mixed typology. The “reinforced concrete and masonry” or “masonry and other typology” structures have been analysed as masonry buildings, whereas the “reinforced concrete and other typology” structures have been classified as “reinforced concrete” buildings. With these assumptions, it was possible to include 7211 buildings belonging to the 17328 buildings without clear specifications. Therefore, there are 10117 school buildings of the “Anagrafe Edilizia Scolastica” database that cannot be analysed since there are no enough information for assigning a structural typology or because their assigned structural typology in the forms was “other”. Starting from the available 49503 school buildings of the “Anagrafe Edilizia Scolastica” database, the buildings analysed in the first phase of the procedure are 39386, subdivided in 19749 masonry structures and 19637 RC structures.

Figure 7a shows the map with the location of the 49503 georeferenced school buildings of the “Anagrafe Edilizia Scolastica” database, and Fig. 7b shows a bar



Fig. 7 Georeferenced school buildings (a) and their classification as a function of their structural typology (b)

chart with the numbers of buildings considered (additionally subdivided according to their structural typology) or omitted in the proposed procedure.

Figure 8 shows the distribution of buildings based on the number of storeys: almost half of all investigated school buildings are two storey structures and more than 90 % of the buildings has a number of storeys less than four.

Fig. 7 (Continued)

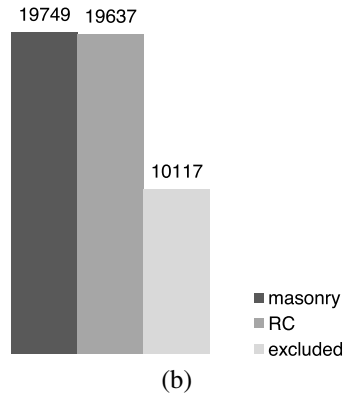


Fig. 8 Distribution of school buildings based on the number of storeys

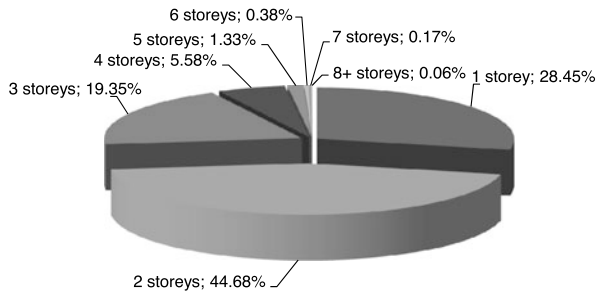


Fig. 9 Distribution of buildings according to the degree of education and the structural typology

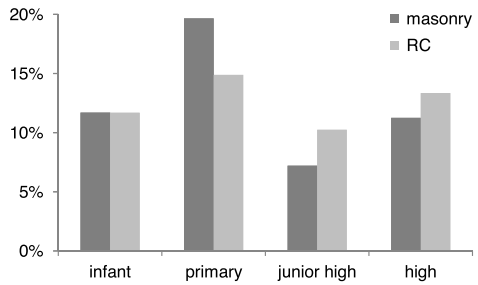
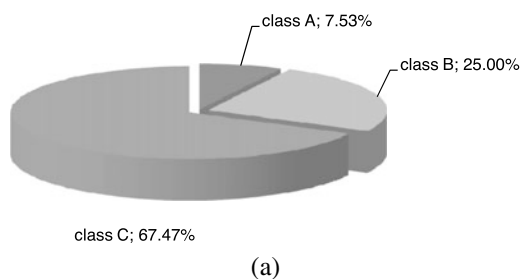


Figure 9 shows the distribution of buildings according to the degree of education and the structural typology. Primary school buildings are probably the older structures and this can justify that the majority of them has a masonry structural typology. On the contrary, the junior high and high school buildings, more recently built, are mostly in RC.

As explained in Sect. 2.1.1, masonry buildings have been divided into classes of vulnerability A, B and C as a function of horizontal and vertical structural typology. Figure 10a shows the distribution in the three vulnerability classes of 19749 masonry buildings considered in the analysis, while the map reported in Fig. 10b shows, for each district, the number of masonry school buildings in class A, B and

Fig. 10 Division into vulnerability classes for masonry school buildings in percentage (a) and in number of building for each district (b)



C, respectively. More than 60 % of the buildings is in class C, the best class. In fact school buildings have always been considered “relevant” structures and were designed with greater attention to design details.

3.2 School Buildings Analysed in the Second Phase of the Procedure

The school buildings of the GNDT database whose data of the 2nd Level forms allow the calculation of the Conventional Resistance and with a correspondence in the “Anagrafe Edilizia Scolastica” database are 3553. However, five of these masonry buildings cannot be analysed since the data of the compiled survey forms are not coherent. Therefore, the school buildings considered in the second phase of the methodology are 3548, divided in five classes according to the number of storeys (Table 3).

The map shown in Fig. 11a gives the location of the school buildings analysed in the second phase of the methodology. In addition, Fig. 11b shows the distribution of such buildings for the different seismic zones (from 1 to 3). It has to be pointed out that there are no school buildings belonging to seismic zone 4 (characterised by the smallest seismic hazard) since the compilation of the GNDT 2nd Level forms has been carried out only for the buildings located in zones with medium-high seismicity.

Table 3 Masonry school buildings analysed in the second phase of the procedure

No. of storeys	No. of buildings
1 storey	785
2 storeys	1215
3 storeys	1156
4 storeys	356
5 storeys	36

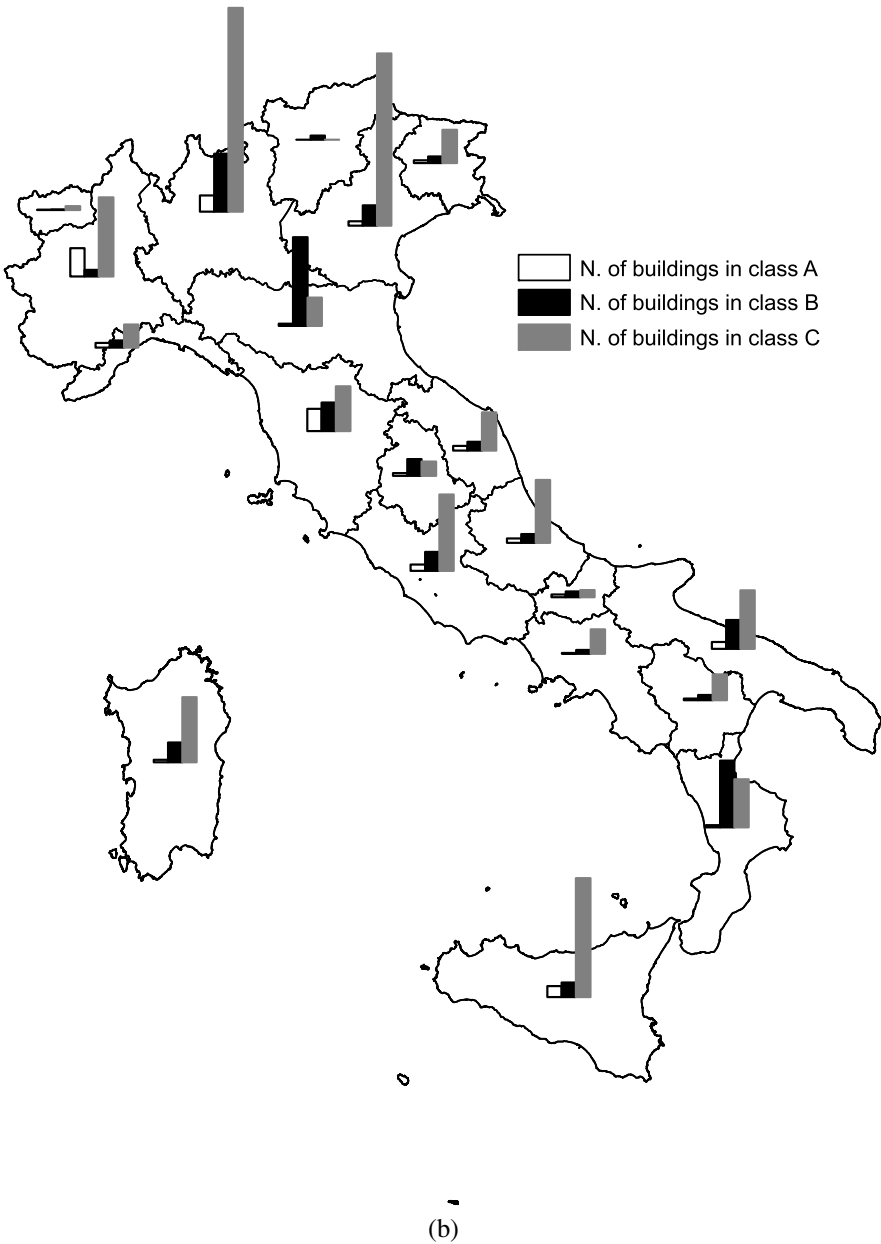


Fig. 10 (Continued)

The Conventional Resistance has been computed for each one of the 3548 school buildings previously described. Knowing this value and its correspondence with the

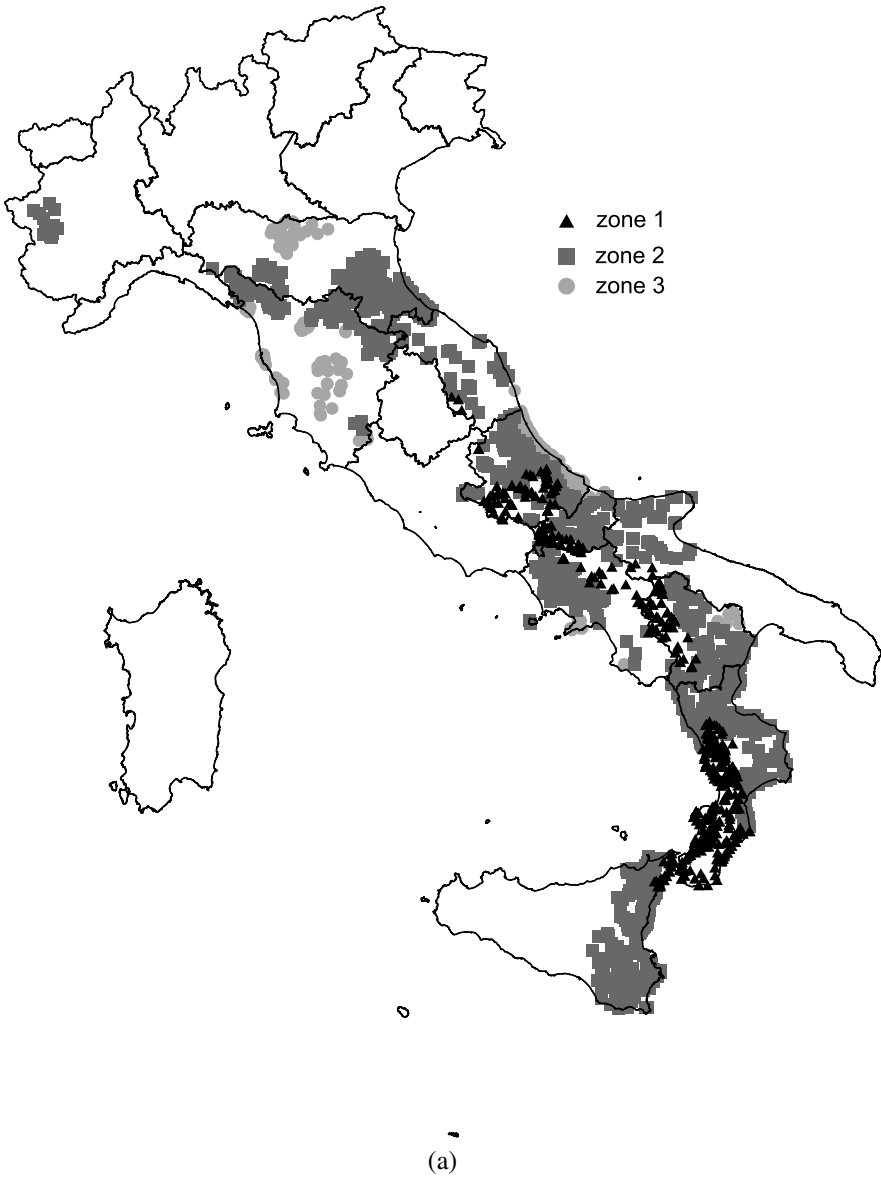
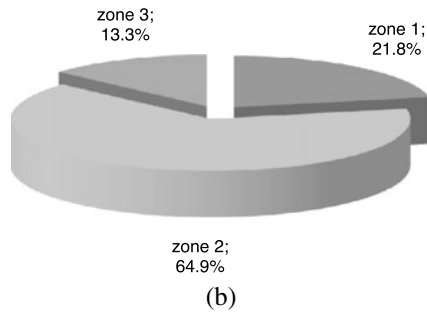


Fig. 11 School buildings analysed in the second phase of the procedure (a) and organised by seismic zone (b)

collapse multiplier λ (as anticipated in Sect. 2.1), the plateaux of the simplified capacity curve is automatically defined for each one of the analysed masonry school buildings.

Fig. 11 (Continued)



4 Discussion of the Results

In this chapter are presented the results obtained in terms of conditional and unconditional probability of damage for the three limit states considered (light damage, significant damage and collapse).

4.1 Results of the First Phase of Analysis

Figure 12a shows the conditional probability of exceeding the significant limit state for a seismic event with a 475 year return period, computed with respect to the 16th, 50th and 84th percentile acceleration spectra. The map reported in Fig. 12b shows the unconditional probability of exceeding the significant limit state calculated for three exposure times (1 years, 10 years, 50 years). This is an “unconditional” probability of damage, because it was considered the hazard curve associated with each school building, i.e. the probability that occurs a specific ground shaking in a given exposure time. The “conditional” probability of damage is a point on the fragility curve, while the “unconditional” probability derived from the integration of this curve with the hazard curve.

Masonry is the structural typology that mainly affects the results because it is very popular in Italy, even in areas of high seismicity, and masonry buildings are the most vulnerable structures. Figure 13 shows the influence of structural typology on the mean probability of damage. The mean overall value is close to the mean value for masonry buildings, particularly in districts with the highest values, while, for the districts with lower probability of damage, the mean value is equidistant from the mean values for the masonry and the RC buildings.

4.2 Correlation Between the Results Obtained in the Two Phases of the Procedure

The correlation between the results obtained in the two phases of the procedure for the 3548 masonry school buildings is plotted in Fig. 14 in terms of seismic risk for an exposure time of 50 years.

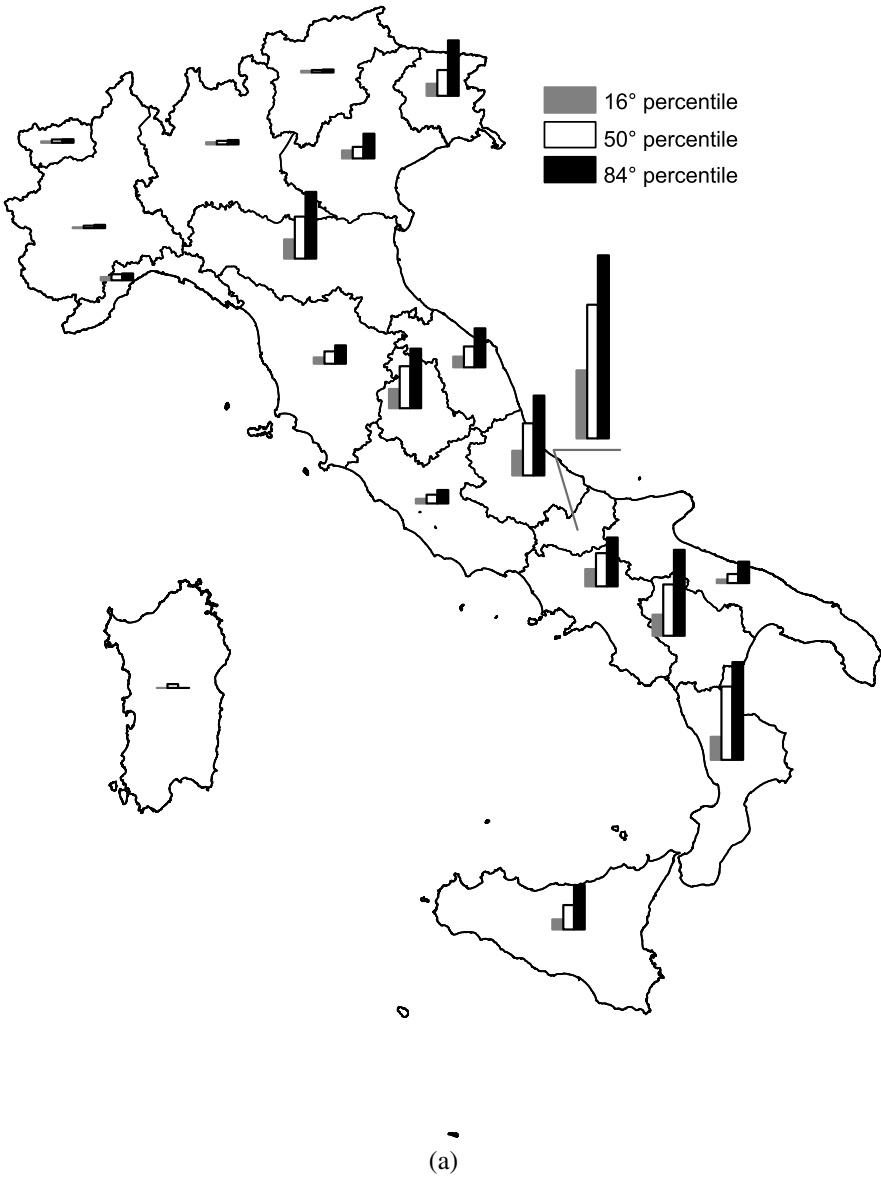


Fig. 12 Mean value for each district of the: conditional probability of exceeding the significant limit state for a 475 year return period (a) and the unconditional probability of exceeding the significant limit state (b)

Figure 14 shows that the correlation between the results of the two phases of the procedure is quite satisfactory. The points over the line of best fit represent an underestimation of the seismic risk in the first phase of the analysis. This finding could

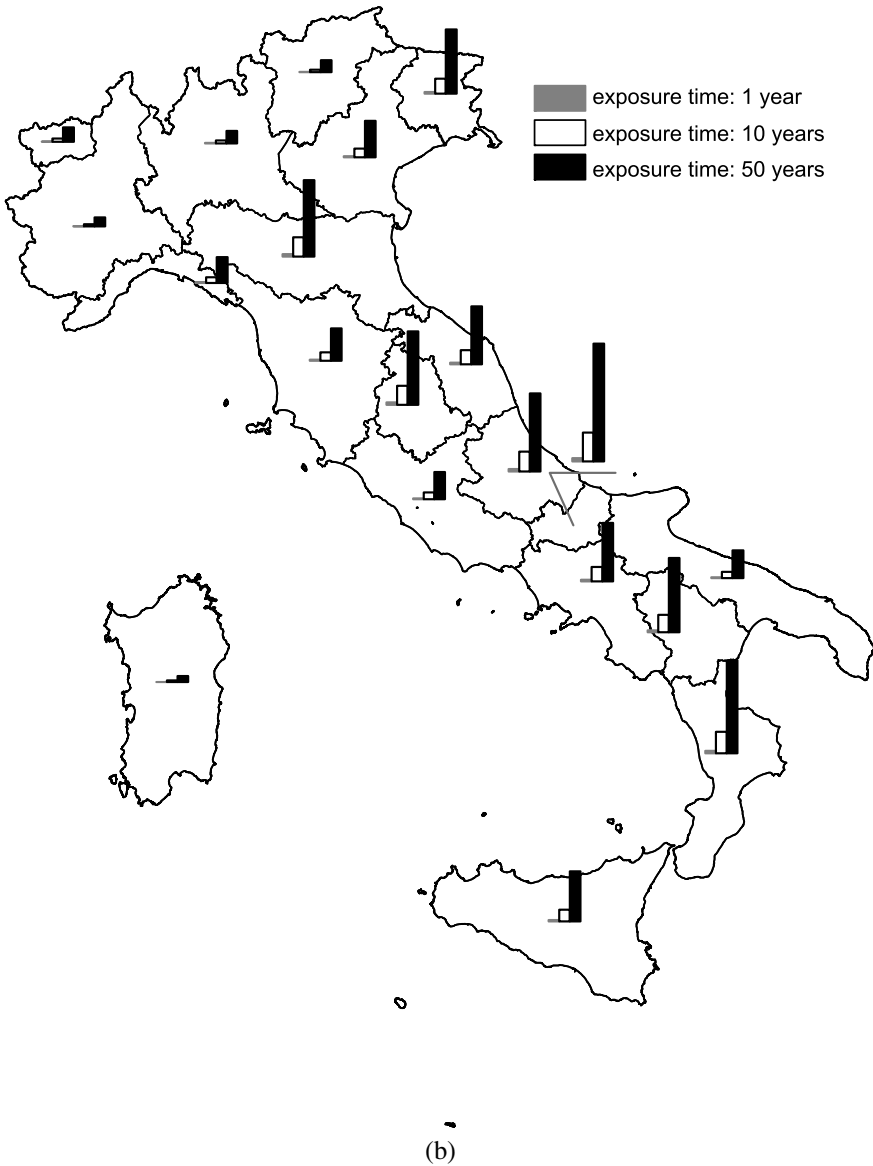


Fig. 12 (Continued)

be due to the different evaluation of the seismic vulnerability of the masonry structures. In the first phase of the procedure, SP-BELA fragility curves are calculated for the vulnerability class C and then those for classes A and B are obtained using the correction coefficients. In the second phase of the procedure, the Conventional Resistance is computed from the data of the survey forms and this resistance could

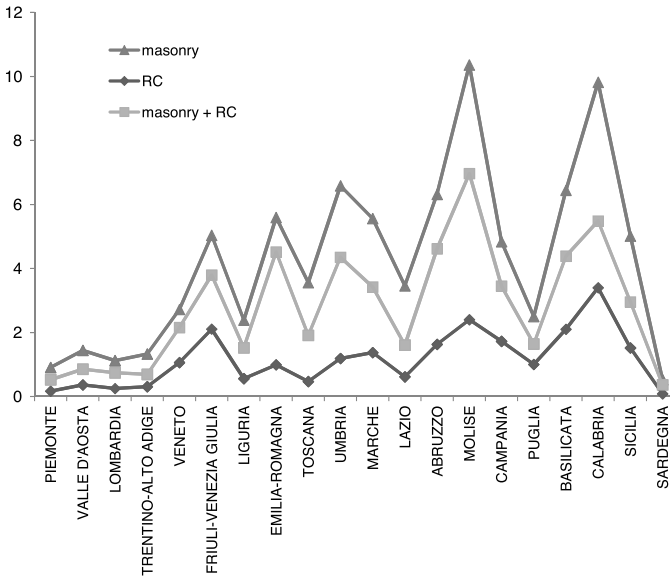
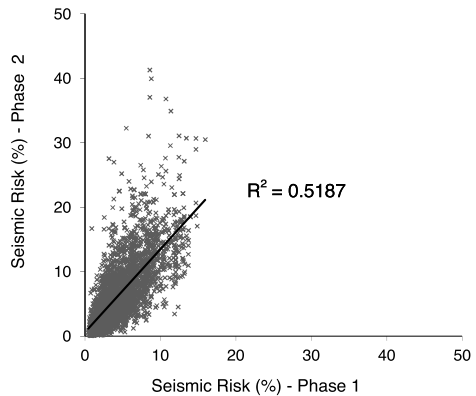


Fig. 13 Mean value for each district of the unconditional probability of exceeding the significant damage limit state for an exposure time of 50 years

Fig. 14 Correlation between the results obtained from the two phases of the proposed procedure

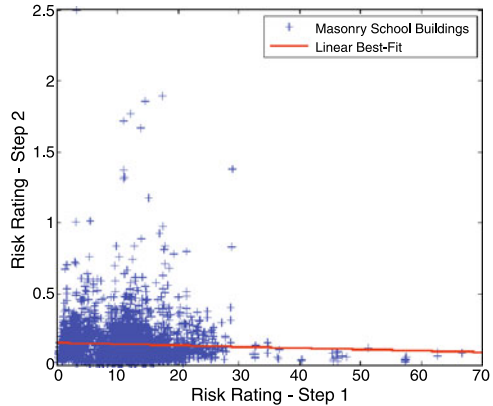


be less than the one assumed in the first phase of the procedure, leading to more vulnerable buildings.

The correlation shown in Fig. 14 is compared with that obtained from [4] for masonry buildings (Fig. 15) in the application of the multiphase methodology proposed in [3]. In the study enveloped by [4], it was used the information contained in the GNDT 1st and 2nd Level forms for schools located in central southern Italy.

Also in this case the methodology adopted is a multiphase procedure that includes two phases with increasing level of detail, where at each step the Risk Rating was calculated. The latter represents the relationship between seismic demand and

Fig. 15 Risk Rating for step 1 and for step 2 [4]



capacity. The comparison between Fig. 14 and Fig. 15 shows that the methodology proposed in this study improves the correlation between the results obtained in the two phases of analysis.

5 WebGIS

Within this study a WebGIS platform that allows, by means of interactive maps and table, to locate the Italian school buildings, to view the data collected into the database of the “Anagrafe Edilizia Scolastica” and the information related to the seismic input, has been developed.

The developed processing of data can be viewed both with a desktop GIS and with a website GIS. It was decided to produce a WebGIS platform for several reasons: it can be accessed from various Internet stations, is multi-platform i.e. its functionality does not depend on the operating system used and, finally, all users will share the server upgrade since all data and functions are centralised in a server.

In Fig. 16 is shown an example of a map in which all the Italian school buildings are localised. In addition there are two charts about the elastic spectrum and the fragility curve related to the selected school building.

The developed WebGIS allows the following operations using the tools dedicated: find a school building by own geographical attributes (district, province and municipality), choose which layer display on the map, thematise the selected layer and add a new geographical layer related to the risk analysis selected. It is possible to perform “real time” scenario analysis too, as it will be discussed in the following section.

6 “Real Time” Damage Scenario

The routines developed for the calculation of the seismic risk give the possibility of calculating real-time damage scenarios, using the seismic input obtained from

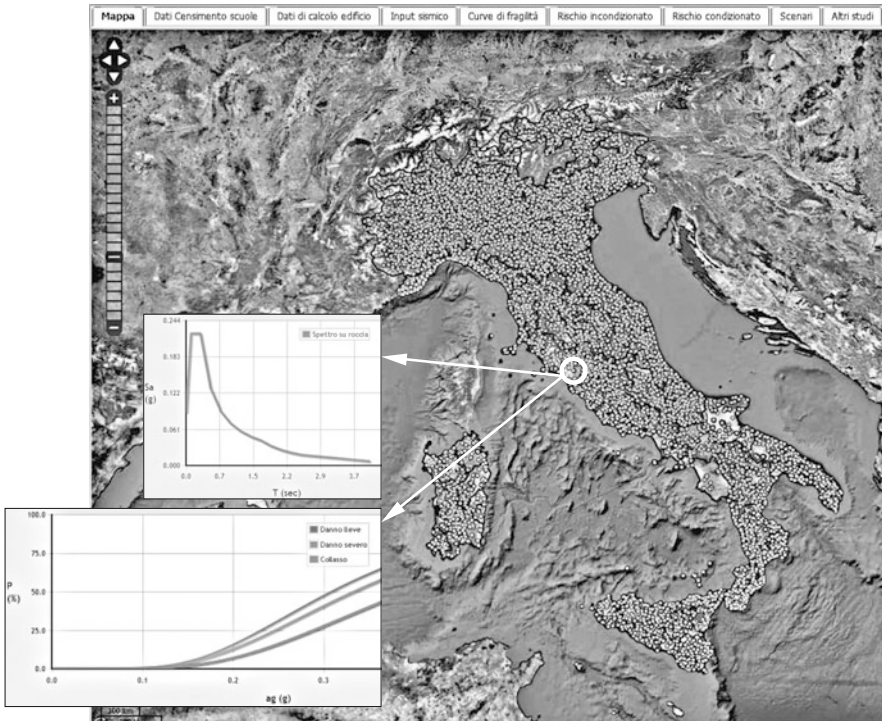


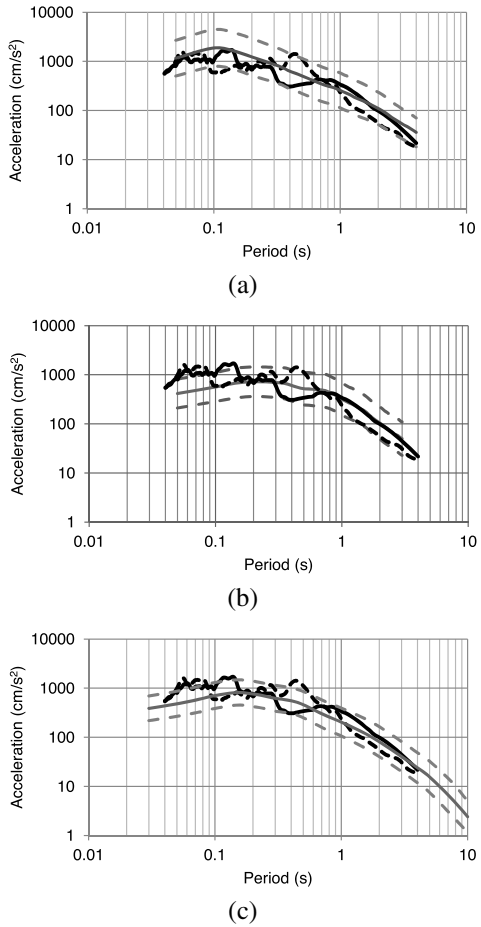
Fig. 16 Localisation of school buildings on WebGIS, spectrum and fragility curve

a selected attenuation law for a given magnitude and distance. Three attenuation relationships were selected among the most recent published in literature. Important requirements that have led to the selection were: (1) a simple form, which allows to generate a damage scenario with few input data, (2) estimate of spectral ordinates in terms of displacement or acceleration applied to both the high and low frequency, (3) good performance in terms of comparison with the spectra derived from the records of several real Italian earthquakes. The chosen laws are [22–24].

Figure 17 shows a comparison between the adopted attenuation laws and a record of the 2009 Abruzzo earthquake. The record comes from the ITACA database [25].

For the definition of the displacement spectrum which represents the demand imposed by the earthquake to the building, it is necessary to indicate, in addition to the attenuation law, the characteristics of the earthquake, such as magnitude, coordinates of the epicentre and the fault mechanism. The user must then indicate the radius within which the damage scenario has to be computed. Finally, the user must indicate the level of damage and the percentile of interest. Each created layer allows to view, on the map of Italy, the effect of the damage scenario selected for the school buildings located within the area indicated (Fig. 18).

Fig. 17 Comparison between the attenuation law [22] (a), [23] (b) and [24] (c) and the record of the 2009 Abruzzo earthquake (E-W in *bold black* and N-S in *black dashed*) of the station AQA, Mw 6.3, epicentral distance 4.6 km [25]. In *grey* the attenuation law (*dashed line* for plus or minus standard deviation)



7 Closure

The novelty of this research study is represented by the maps of seismic risk for school buildings at a national scale. These maps give an overall view for the definition of a prioritisation procedure for surveys and detailed structural retrofitting measures.

A multiphase procedure has been proposed for the evaluation of the amount of school buildings requiring additional investigations. The methodology implements two analysis phases with an increasing level of detail such that the number of buildings analysed decreases at each step since only the buildings most at risk are considered.

The generation of seismic risk maps at a national scale is an outcome of the first phase of the proposed procedure. The data used for the map generation are based on the collected survey forms of the 70 % of the Italian school buildings. However, a reduced number of school buildings (3500) was available during the second phase

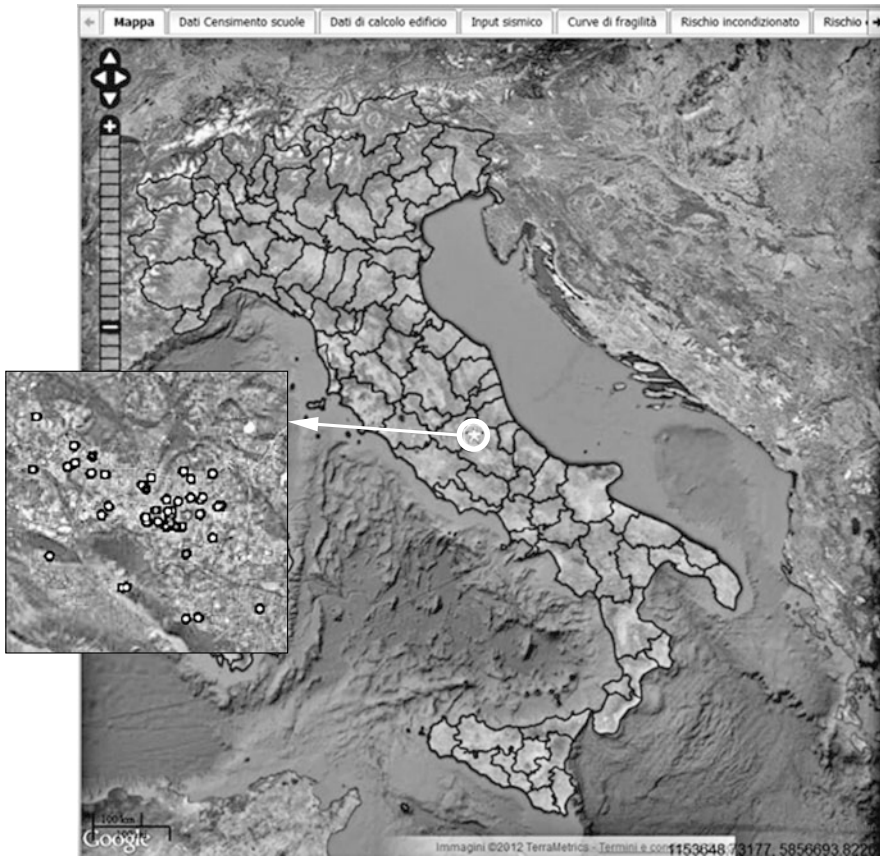


Fig. 18 Example of a damage scenario

of the procedure. In fact, additional information on the building resistance should be collected and used during this analysis phase. In this study, this information was available for the school buildings of some districts of Italy and for masonry structures only.

The analyses were implemented in a specifically developed WebGIS platform that allows, through maps and tables, to view information and perform routine calculations. Moreover, the tool developed can provide significant assistance for emergency management in the immediate post-earthquake because it is able to perform an assessment of the real-time damage scenario.

Further developments of the proposed methodology are still required. It should be extremely useful to complete the collection of the data related to the school building resistance in all Italian districts and for all the structural typologies in order to allow a more accurate estimate of the seismic vulnerability of these buildings. This will allow the application of the second phase of the procedure at a national scale.

Therefore, it would be possible to apply the proposed procedure for the identification of the school buildings requiring priority of intervention.

Acknowledgements The study presented has benefited from financial support of the Prime Minister's Office—Department of Civil Protection; this publication, however, does not necessarily reflect the views and official policies of the Department. The authors would like to thank the support of the Italian Ministry of Research and Higher Education (MIUR—Ministero dell'Università e della Ricerca) for the availability of the “Anagrafe Edilizia Scolastica” forms. In closing, the authors are very grateful to Ms Miriam Colombi for the support related to the previously published works on the same topic, Ms Antonella Di Meo for finding the correspondence between the “Anagrafe Edilizia Scolastica” forms and the GNDT 2nd Level forms and Mr Marco Pagano for georeferencing the school buildings.

References

1. Dolce M, Martinelli A (2005) *Inventario e vulnerabilità degli edifici pubblici e strategici dell'Italia centro-meridionale*, vol II, *Analisi di vulnerabilità e rischio sismico*. INGV/GNDT—Istituto Nazionale di Geofisica e Vulcanologia/Gruppo Nazionale per la Difesa dai Terremoti, L'Aquila
2. Dolce M, Masi A, Moroni C, Martinelli A, Mannella A, Milano L, Lemme A, Miozzi C (2007) *Sisma Molise 2002. Il progetto “Scuola sicura”: dall'indagine di vulnerabilità sismica alla esecuzione degli interventi*. Atti del XII convegno l'ingegneria sismica in Italia, Pisa
3. Grant DN, Bommer JJ, Pinho R, Calvi GM, Goretti A, Meroni F (2007) A prioritization scheme for seismic intervention in school buildings in Italy. *Earthq Spectra* 23(2):291–314
4. Crowley H, Colombi M, Calvi GM, Pinho R, Meroni F, Cassera A (2008) Application of a prioritization scheme for seismic intervention in schools buildings in Italy. In: *Proceedings of the 14th world conference on earthquake engineering*, Beijing
5. DPCM 21.10.2003 (2003) Disposizioni attuative dell'art. 2, commi 2, 3 e 4 dell'ordinanza del Presidente del Consiglio dei Ministri n3274 del 20 marzo 2003, recante «Primi elementi in materia di criteri generali per la classificazione sismica del territorio nazionale e di normative tecniche per le costruzioni in zona sismica». Dipartimento della Protezione Civile, GU 29.10.2003 n252
6. OPCM 20.03.2003 n3274 (2003) Primi elementi in materia di criteri generali per la classificazione sismica del territorio nazionale e di normative tecniche per le costruzioni in zona sismica. GU 08.05.2003 n105
7. Borzi B, Pinho R, Crowley H (2008) Simplified pushover-based vulnerability analysis for large scale assessment of RC buildings. *Eng Struct* 30(3):804–820
8. Borzi B, Crowley H, Pinho R (2008) Simplified pushover-based earthquake loss assessment (SP-BELA) method for masonry buildings. *Int J Archit Herit* 2(4):353–376
9. AA VV (1999) *Censimento di vulnerabilità degli edifici pubblici, strategici e speciali nelle regioni Abruzzo, Basilicata, Calabria, Campania, Molise, Puglia e Sicilia*. Dipartimento della Protezione Civile, Roma
10. AA VV (2000) *Censimento di vulnerabilità a campione dell'edilizia corrente dei centri abitati, nelle regioni Abruzzo, Basilicata, Calabria, Campania, Molise, Puglia e Sicilia*. Dipartimento della Protezione Civile, Roma
11. Zonno G coord (1999) *Rapporto finale CNR-IRRS alla Commissione Europea*. Contratto ENV4-CT96-0279, pp 95–102
12. DM 14.01.2008 (2008) *Approvazione delle nuove norme tecniche per le costruzioni*. GU 04.02.2008 n29
13. Calvi GM (1999) A displacement-based approach for vulnerability evaluation of classes of buildings. *J Earthq Eng* 3(3):411–438

14. Circolare applicativa delle NTC08 (2009) Circolare del Ministero delle Infrastrutture e dei Trasporti 2 febbraio 2009, n617 recante istruzioni per l'applicazione delle nuove norme tecniche per le costruzioni di cui al decreto ministeriale 14 gennaio 2008. Suppl ord n27 alla GU 26.2.2009 n47
15. Angeletti P, Baratta A, Bernardini A, Cecotti C, Cherubini A, Colozza R, Decanini L, Diotallevi P, Di Pasquale G, Dolce M, Goretti A, Lucantoni A, Martinelli A, Molin D, Orsini G, Papa F, Petrini V, Riuscetti M, Zuccaro G (2002) Valutazione e riduzione della vulnerabilità sismica degli edifici, con particolare riferimento a quelli strategici per la protezione civile. Rapporto finale Dipartimento della Protezione Civile—Ufficio Servizio Sismico Nazionale, Roma
16. Braga F, Dolce M, Liberatore D (1982) Southern Italy November 23, 1980 earthquake: a statistical study on damaged buildings and an ensuing review of the M.S.K.—76 scale. CNR-PFG n503, Rome
17. INGV-DPC S1 (2007) Proseguimento della assistenza al DPC per il completamento e la gestione della mappa di pericolosità sismica prevista dall'ordinanza PCM 3274 e progettazione di ulteriori sviluppi. <http://esse1.mi.ingv.it>
18. Medvedev AV, Sponheuer W (1969) Scale of seismic intensity. In: Proceedings of the 4th world conference on earthquake engineering, Santiago de Chile
19. Priestley MJN, Calvi GM, Kowalsky MJ (2007) Displacement-based seismic design of structures. IUSS Press, Pavia
20. Restrepo-Vélez LF, Magenes G (2004) Simplified procedure for the seismic risk assessment of unreinforced masonry buildings. In: Proceedings of the 13th world conference on earthquake engineering, Vancouver
21. Eurocode 8 (2004) Design of structures for earthquake resistance—part 1: General rules, seismic actions and rules for buildings. EN 1998-1:2004, Comité Européen de Normalisation, Brussels
22. Cauzzi C, Faccioli E (2008) Broadband (0.05 to 20 s) prediction of displacement response spectra based on worldwide digital records. *J Seismol* 12(4):453–475
23. Akkar S, Bommer JJ (2010) Empirical equations for the prediction of PGA, PGV, and spectral accelerations in Europe, the Mediterranean region, and the Middle East. *Seismol Res Lett* 81(2):195–206
24. Boore DM, Atkinson GM (2008) Ground motion prediction equations for the average horizontal component of PGA, PGV, and 5%-damped PSA at spectral periods between 0.01 and 10.0 s. *Earthq Spectra* 24:99–138
25. ITACA—ITalian ACcelerometric Archive. <http://itaca.mi.ingv.it/ItacaNet/>

Nonlinear Dynamic Response of MDOF Cable Nets Estimated by Equivalent SDOF Models

Isabella Vassilopoulou and Charis J. Gantes

Abstract In this work the geometric nonlinear dynamic response of saddle-shaped cable nets subjected to uniform harmonic loads is investigated. The detection of nonlinear phenomena can be realised by numerous numerical nonlinear dynamic analyses leading to diagrams of response curves. This procedure demands much computational effort for different loading amplitudes, changing the frequencies by very small steps and taking into consideration initial conditions by means of nodal initial displacements and velocities. The number of such analyses can be significantly reduced by means of an analytical solution that can provide the necessary information about the conditions for which nonlinear resonances occur. To that effect, an equivalent SDOF model is set up, and its equation of motion is found to be similar to the one of the Duffing oscillator, for which analytical solutions under primary or secondary resonances can be found in the literature. The transformation of the MDOF cable net to the SDOF one is obtained by similarity relations. The comparison between the two models by means of the steady-state amplitude of the central node demonstrates that the behaviour of the SDOF model describes satisfactorily the one of the MDOF model, predicting the dominant nonlinear phenomena.

Keywords Nonlinear dynamic response · Saddle form cable net · Equivalent SDOF model · Duffing oscillator · Similarity relations

1 Introduction

The first suspended roof was the “velarium” of the Colosseum, built in 70 B.C. in Rome (Fig. 1a). The first modern saddle-form cable net covered the Raleigh Arena in North Carolina (Fig. 1b), built in 1953, which for many years after its completion constituted an important exemplar for such structures [1].

I. Vassilopoulou (✉) · C.J. Gantes
Laboratory of Metal Structures, School of Civil Engineering, National Technical University of Athens, 9 Heroon Polytechniou Street, Zografou, 15780 Athens, Greece
e-mail: isabella@central.ntua.gr

C.J. Gantes
e-mail: chgantes@central.ntua.gr

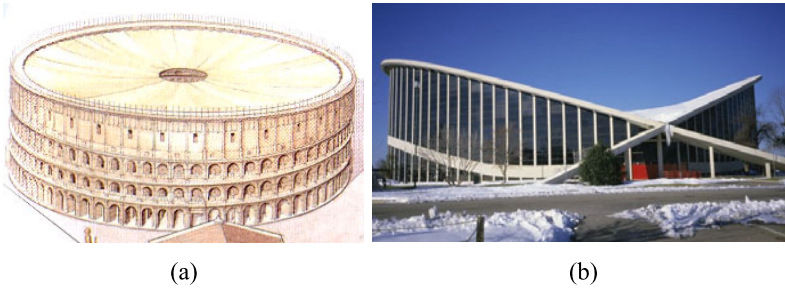


Fig. 1 (a) Schematic representation of the “velarium” of the Colosseum in Rome, Italy, (b) Raleigh Arena in North Carolina



Fig. 2 (a) Scandinavium Arena in Gothenburg, Sweden, (b) Scotiabank Saddledome in Calgary, Alberta, Canada

In Fig. 2a another pretensioned cable net is illustrated, which is the roof of the Scandinavium Arena in Gothenburg, Sweden, constructed in 1971 [2]. The saddle-shaped roof of the Scotiabank Saddledome (formerly the Pengrowth Saddledome) in Calgary, Alberta, Canada, is also an example of such systems (Fig. 2b) [3].

The Stadium of Peace and Friendship in Greece is another example of a saddle-shaped cable net [4]. It was constructed in 1983 and it was used, among other stadiums, for the Olympic Games of 2004 (Fig. 3a). The Velodrome in London is the most recent structure of that type, which hosted the Olympic track cycling events in 2012 (Fig. 3b) [5].

A cable net consists of two families of prestressed cables, the main or carrying cables, which are suspended from the highest points of the boundary ring and the secondary or stabilising ones, which are anchored at its lowest points. The difference of height between the highest or lowest points and the central node is called sag of the roof in the direction of the main or stabilising cables, respectively. The shape of the final surface produced by these two groups of cables is the saddle or the hyperbolic paraboloid, which, mathematically, is a doubly ruled surface [6]. If f_x/L_x and f_y/L_y are the sag-to-span ratios of a cable net forming a hyperbolic



Fig. 3 (a) Stadium of Peace and Friendship in Athens, Greece, (b) Velodrome in London, UK

paraboloid surface in x and y direction, respectively, the geometry of the surface can be expressed as:

$$z = \frac{4f_x}{L_x^2}x^2 - \frac{4f_y}{L_y^2}y^2 \quad (1)$$

with f_x , f_y taking always positive values. In case the sags are equal in both directions and the boundary is a cycle in plan view with $L_x = L_y = L$, the expressions giving the geometry of the structure are:

$$z = \frac{4f}{L^2}(x^2 - y^2) \quad (2)$$

$$4x^2 + 4y^2 = L^2 \quad (3)$$

Cable nets are lightweight and tensile structures. They can cover long spans without intermediate supports, carrying loads much heavier than their own weight. Their capacity to transmit loads to the supports through tension of the cables renders them very efficient systems, while their elegance due to their unusual forms and lightness is indisputable. These characteristics trigger the interest of both architects and structural engineers looking for attractive solutions to cover long-span structures such as stadiums, exhibition halls, swimming pools, hangars, ice rinks, theatres, concert halls, churches etc.

However, the price of their lightness is their low stiffness leading to large deformations. It is well known that cables change significantly their shape in order to equilibrate transverse loads, due to their lack of shear and bending rigidity [7]. Hence, an important difference is noted between the initial geometry and the deformed one and the system's stiffness changes as the loads act on the structure, leading to a so-called geometric nonlinearity. The principle of superposition is not valid for such systems and separate nonlinear analyses must be performed for each loading combination [8]. Moreover, the cables must remain in tension under any load combination, as cable slackening leads to large local deformations, sudden increase of the tension in adjacent cables and possible fatigue problems at the anchorage points. Large curvatures for both groups of cables lead to an increase of the system's stiffness for loads directed both downwards, such as snow and wind pressure, and upwards, such as wind suction. High levels of initial pretension in

the cables can also mitigate the large deflections, rendering the system sufficiently stiff [9]. Due to these two properties, cable nets are considered as weakly nonlinear systems, as opposed to single cables, which are strongly nonlinear.

In this work the dynamic behaviour of cable nets subjected to harmonic loads is investigated. Linear modal analyses are first performed in order to calculate the natural frequencies and vibration modes of the system. The response to harmonic loads is then derived by nonlinear dynamic analyses. Single results from such analyses turn out to be insufficient for detecting nonlinear dynamic phenomena and thus estimating the overall dynamic behaviour of the system and the level of its geometric nonlinearity. It is observed that such phenomena are very sensitive to the load amplitude and frequency of external excitation and to initial conditions, so that a large number of nonlinear dynamic analyses must be conducted in order to ensure that the maximum response has been obtained. Therefore, the need of an analytical solution is highlighted, leading to the concept of an equivalent single-degree-of-freedom (SDOF) model for which the analytical solution of the equation of motion can be found. The characteristics of a multi-degree-of-freedom (MDOF) cable net model are transformed to the ones of the equivalent SDOF model and the dynamic response of the former is estimated using the analytical solutions of the latter. Numerical analyses for the large cable net confirm the validity of the method.

2 Theoretical Background of Nonlinear Systems

In this section the main notions, describing the behaviour of nonlinear systems and especially cable structures, are provided in order to understand qualitative features of their dynamic response.

2.1 Nonlinear Dynamic Analysis

In nonlinear dynamics there are three main types of resonances. The first one is the external resonance, depending on the frequency of the external excitation Ω and its relation with the eigenfrequencies of the system ω . It can be distinguished into primary resonance as well as subharmonic and superharmonic resonances, called secondary resonances. The second one is the internal resonance, depending on the characteristics of the system and specifically on the relation between its natural frequencies [10]. The third one is the parametric resonance. Parametric oscillations occur when the system has time-varying (periodic) parameters. In this case the structural system can be excited by a periodic input, with frequency close to the natural frequency of the system, leading to oscillations with large amplitudes [11].

Superharmonic resonance may occur when the loading frequency can be expressed as:

$$\Omega = (1/n) \cdot \omega \quad (4)$$

where n is an integer. When the loading frequency is larger than the frequency of the system, related to it with the expression:

$$\Omega = n \cdot \omega \tag{5}$$

where n is again an integer, phenomena of subharmonic resonance may occur. In both cases, the system responds in such a way that the free oscillation term does not decay to zero in spite of presence of damping and in contrast to the linear solution [12].

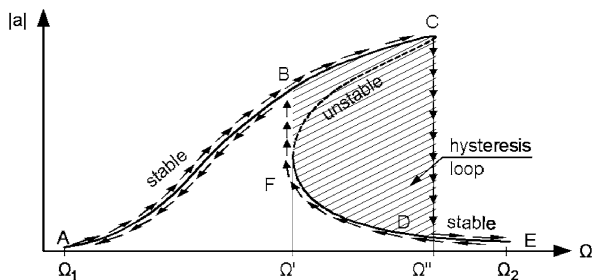
In contrast to SDOF systems, which have only a single linearised natural frequency and a single mode of motion, an n -DOF system has n linearised natural frequencies and n corresponding mode shapes (some of which can be generalised modes corresponding to repeated eigenvalues). When two or more linearised natural frequencies are commensurable or nearly commensurable, for example $\omega_2 \approx \omega_1$, $\omega_2 \approx 2\omega_1$, $\omega_2 \approx 3\omega_1$, $\omega_3 \approx \omega_2 \pm \omega_1$, $\omega_3 \approx 2\omega_2 \pm \omega_1$, $\omega_4 \approx \omega_3 \pm \omega_2 \pm \omega_1$ and so on, the corresponding modes may be strongly nonlinearly coupled, leading to internal resonances. If an internal resonance exists in a free system, energy imparted initially to one of the modes involved in internal resonance will be continuously exchanged among all modes involved in that resonance. Moreover, if a harmonic external excitation of frequency Ω acts on a MDOF system, then, in addition to all primary and secondary resonances, resonant combinations of frequencies might exist [13]. Finally, it should be mentioned that, during the internal resonances, the beat phenomenon characterises the response of the system, due to the combination of frequencies very close to each other.

The relation between oscillation amplitude and frequency is described by the response diagram in which the steady-state amplitude, denoted as a , is plotted on the vertical axis and the frequency ratio Ω/ω on the horizontal axis. A typical response curve of a nonlinear system such as a cable structure is shown in Fig. 4.

In this diagram it is observed that [14]:

- In nonlinear systems, the nonlinearity controls the oscillation amplitude. As the amplitude increases the system becomes stiffer, changing its natural frequency, and the forcing term does not remain in step with the natural oscillation.
- Observing the response curve of Fig. 4, for $\Omega < \Omega'$ a single response is expected, while for $\Omega > \Omega'$ there might be three different amplitudes of the system's response for the same forcing level and frequency. The initial conditions determine which of these potential responses is the actual response of the system. When

Fig. 4 Response diagram of a nonlinear system



only one response exists, this response is stable. When three different possible responses exist, only the oscillations with largest and smallest amplitudes are stable, while the remaining intermediate one is unstable.

- The multivaluedness of response curves due to nonlinearity leads to jump phenomena and consequently to hysteresis loops. If a force is applied to a nonlinear system, with an increasing frequency from Ω_1 to Ω_2 , the response point will move on the upper curve as far as point C, but then it will drop to point D on the lower curve and continue to point E. If the force has a decreasing frequency from Ω_2 to Ω_1 , the response amplitude will follow the curve EDF, but at point F it will jump to the upper curve at point B and continue until point A. This is in contrast to linear systems, where no hysteresis loops exist in frequency response functions, and the eventual steady states do not depend on the choice of initial conditions.

2.2 Dynamic Response of Simple Cables

The vibration modes and natural frequencies of a nonlinear system can be calculated conducting linear modal analyses. Although it is not appropriate to perform any kind of linear analysis for nonlinear systems, it is important to know their linearised frequencies in order to detect nonlinear dynamic phenomena depending on the natural frequencies of the system.

Pugsley [15] proposed semi-empirical expressions for the first three in-plane modes of a sagged suspended chain, which could represent a hanging inextensible cable without pretension. He demonstrated the applicability of the results by conducting experiments on cables, in which the sag-to-span ratio ranged from 1:10 up to about 1:4. Ahmadi-Kashani [16] compared the semi-empirical formulae of Pugsley with numerical results for a wide range of sag-to-span ratios and provided improved formulae for the estimation of the natural frequencies.

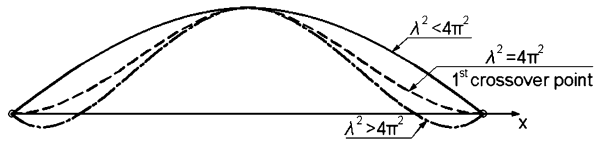
Irvine and Caughey [17] developed a linear theory for the free vibrations of a suspended cable, in which the sag-to-span ratio f/L is about 1:8 or less. They derived specific formulae for the frequencies of the in-plane and out-of-plane vibrations. They introduced the parameter λ^2 , which involves the cable geometry and elasticity and plays an important role in the cable's symmetric vibrations:

$$\lambda^2 = 64 \left(\frac{f}{L} \right)^2 \frac{EA}{H} \quad (6)$$

The values of the frequencies for the in-plane symmetric modes depend on this parameter. In particular for:

- $\lambda^2 < 4\pi^2$, the frequency of the first symmetric in-plane mode is smaller than the frequency of the first antisymmetric in-plane one and the vertical modal component of the first symmetric mode has no internal nodes with zero displacements along the span (Fig. 5).

Fig. 5 First symmetric mode for different values of the parameter λ^2



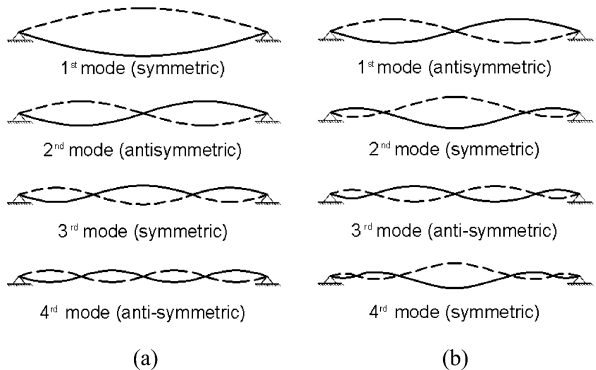
- $\lambda^2 = 4\pi^2$, the frequency of the first symmetric in-plane mode is equal to the frequency of the first antisymmetric in-plane one. This phenomenon is called crossover of modes leading to an internal resonance between these two modes and this value of λ^2 designates the first crossover point. The vertical modal component of the first symmetric mode is tangential to the profile of the cable at each support (Fig. 5).
- $\lambda^2 > 4\pi^2$, the frequency of the first symmetric in-plane mode is larger than the frequency of the first antisymmetric in-plane one and the vertical modal component of the first symmetric mode has two internal nodes with zero displacements along the span (Fig. 5).
- $\lambda^2 = 16\pi^2$, the second crossover occurs and the frequency of the second symmetric in-plane mode is equal to the frequency of the second antisymmetric in-plane one.

In general, the parameter λ^2 takes the value $(\lambda_n)^2 = (2n\pi)^2$ at the n th crossover point.

In addition, it was observed that the frequencies of the antisymmetric modes remained constant as λ^2 changed, while the frequencies of the symmetric modes changed and at the crossover points became larger than the corresponding antisymmetric ones. This was also confirmed by conducting several experiments changing the sag of the cable and observing the first symmetric and the first antisymmetric in-plane vibration modes. As shown in Fig. 6 the shape of the first and second symmetric modes changed before and after the first crossover point, while the ones of the first two antisymmetric modes remained unaltered.

Rega and Luongo [18] explored an inextensible and an elastic cable with flexible supports. They concluded that the cable extensibility plays a more important role than that of the supports in the system’s dynamic behaviour. Srinil et al. [19]

Fig. 6 First four vibration modes of a simple suspended cable (a) before crossover, (b) after crossover



studied the free vibrations of sagged flexible horizontal or inclined cables in three-dimensional motion, conducting time-history analyses. It was shown that not only the 1:1 internal resonance between symmetric and antisymmetric modes—which corresponds to the crossover or avoidance points, respectively—but mostly the 2:1 internal resonances produce hybrid profiles of the cable's vibration and enhancement of the cable tension in some time intervals.

2.3 Static and Dynamic Response of Cable Nets

In [20] Leonard gave an analytical solution for the static equilibrium of a simple cable net consisting of two crossing cables, prestressing one another and subjected to a concentrated load at their common point. Gero in [21, 22] introduced a method for the scaling of a large network to a smaller one, both having fixed cable edges. The method proposed the transformation of a network with large number of cables to a smaller one, using transformation relations and design charts that were produced for the small cable net via geometric nonlinear analyses. Using the transverse transformation relations, it was possible to evaluate the static behaviour of the large cable net.

Regarding the dynamic response of cable nets, in [23] Chisalita derived a formula for the first frequency of a simple flat cable net consisting of two cables, having the same pretension and cross-section. Leonard in [20], considering lumped or consistent masses, provided an analytical solution for the frequencies of a simple cable net with initial sag.

For multi-degree-of-freedom models numerical analyses have been conducted in order to investigate the dynamic behaviour of the system regarding the natural frequencies. In [24] a transfer matrix method was presented for calculating the natural frequencies of orthogonal flat cable nets. A boundary element approach was proposed in [25] calculating the eigenfrequencies and the mode shape of the free vibrations of flexible membranes with arbitrary shape. In [26] the authors presented a computational scheme for vibration analysis of flat cable nets consisting of highly tensioned cables and having orthogonal projections in plan.

In [27] Gambhir and Batchelor developed a finite element method for the analysis of cable nets, either flat or with initial sag, modelling the prestressed cable net as a series of finite length curved elements. Several boundary shapes were applied in order to evaluate their method. The numerical results giving the fundamental frequency of the cable net were compared with experimental ones resulting in satisfactory accuracy. In [28], they investigated the influence of the cable cross-sectional area, the initial pretension and the sag-to-span ratio on the natural frequencies of 3D cable nets.

Seeley et al. [29] studied the natural frequencies and modal shapes of a cable network with a circular plan view, forming a concave surface. The fundamental frequency of the net was described by an approximate formula depending on the sag and the sag-to-span ratio. The value of this natural frequency was proved to be

close to an average of the frequencies of the first in-plane and out-plane modes of a simple sagged cable with the same sag-to-span ratio.

Most of the pertinent publications referring to the dynamic behaviour of cable nets present new computerised methods of analysis and other numerical techniques to calculate the nonlinear dynamic response of cable networks and membranes, by solving the governing equations of motion [30–37], several of them in comparison with experimental results. In [38] a modified modal superposition method is used, appropriate for nonlinear systems, considering their geometric nonlinearities by changing the geometry under load.

Fan et al. [39] investigated the nonlinear dynamic response of a cable suspended roof during a strong earthquake. They concluded that, although there are no reports of damage in cable suspended roofs during strong earthquakes, since their natural frequencies are low in relation to the dominant earthquake frequencies, nevertheless they may lose their bearing capacity to resist vertical seismic effects, due to the nonlinear vibration of the system, which induces jump phenomena detected in the response diagrams.

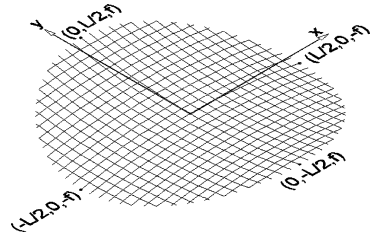
Lazzari et al. [40] proposed a numerical analysis of the wind-induced response of flexible structures, offering the advantage to capture the effects of nonlinearities of both structural and aerodynamic origins of the problem. They also studied the free vibrations of a real saddle-form cable net, its resonant behaviour and its dynamic response under wind action.

3 Modelling Issues and Assumptions

The model adopted in this investigation is a three-dimensional symmetric saddle-shaped cable net, with a circular plan view of diameter L (Fig. 7). The network consists of N cables in each direction, arranged in a quadratic grid. The sag of the roof is equal to f in both directions. All cables are modelled as straight truss elements between two adjacent intersection points. Both groups of cables have a circular cross-section with diameter D and area A , while their material is assumed to be linearly elastic with Young modulus E in tension and zero compression branch. An initial pretension equal to N_0 is introduced in all cables, rendering the net uniformly prestressed. The cable mass density is equal to m and an additional concentrated nodal mass M may also be considered. A lumped mass matrix is used for the analysis. In nonlinear dynamic analyses Rayleigh damping [41] is also introduced with a damping ratio equal to $\zeta = 2\%$, which is a common value for such structures [9]. All three translational degrees of freedom are considered as free for all internal nodes of the net, while the cable ends are modelled as pinned.

For the calculation of the natural frequencies of the system, the geometry and stiffness of the state under prestressing are considered. All analyses have been carried out with the finite element software ADINA [42, 43], which has been validated by means of comparisons with analytical solutions of simple cables and cable nets regarding the eigenfrequencies and the dynamic response to harmonic loads [44].

Fig. 7 Geometry of the cable net



4 Eigenfrequencies and Eigenmodes of Cable Nets

As explained in Sect. 2.1, the eigenfrequencies of the nonlinear system, although calculated by a modal analysis, which is a linear procedure, play an important role in its dynamic behaviour, because they are used to define nonlinear resonances. Thus, a first step to understand the dynamic response of a cable suspended roof is to calculate and study its natural frequencies and corresponding vibration modes.

Parametric analyses were conducted for a large number of cable nets with different geometrical and mechanical characteristics regarding the number of cables in each direction N , the projected diameter L , the sag-to-span ratio f/L , the initial pretension N_0 , the elastic modulus of the cable material E , the cable mass density m , the nodal concentrated mass M , the cable diameter D and thus the cross-sectional area A .

The cable net's vibration modes can be distinguished in symmetric and antisymmetric. The former ones consist of symmetric vertical components and antisymmetric horizontal components with respect to both horizontal axes x and y , while the latter ones consist of antisymmetric vertical components and symmetric horizontal components with reference to one or both horizontal axes [45]. In this work, the first four modes are thoroughly studied, which are (i) the first symmetric mode of the net, denoted as 1S, (ii) the first two antisymmetric modes with respect to one horizontal axis, which, due to the symmetry of the model, are similar, with equal eigenfrequencies and thus are treated as one mode, denoted both of them as 1A, and finally (iii) the first antisymmetric mode with respect to both horizontal axes, which is denoted as 2A. These four modes are illustrated in Fig. 8.

Looking into the eigenmodes and eigenfrequencies of the cable nets, frequency crossovers and modal transitions were detected, as also reported in Sect. 2.2 for simple suspended cables. A parameter λ^2 has been introduced for cable nets [46], similar to that for a simple cable, expressed as:

$$\lambda^2 = \left(\frac{f}{L}\right)^2 \frac{EA}{N_0} \quad (7)$$

where N_0 is the initial pretension of all cables. Small values of this parameter characterise shallow cable nets, or deep cable nets with low levels of pretension. As for the simple cable, the parameter λ^2 is proved to govern the appearance sequence of the vibration modes of the cable net [47]. Four limits of this parameter were detected regarding the modal transition and the crossover points between the first four vibration modes:

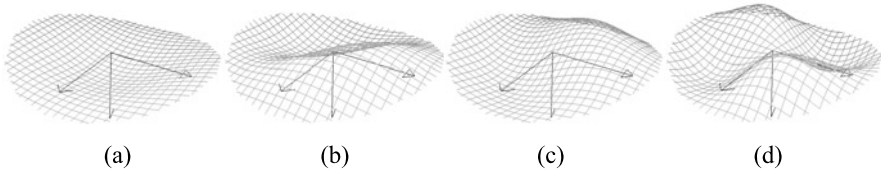


Fig. 8 The first four vibration modes of a cable net (a) 1st symmetric mode (1S), (b) and (c) 1st antisymmetric modes about one horizontal axis (1A) and (d) 1st antisymmetric mode about both horizontal axes (2A)

- (a) For $\lambda^2 \leq 0.80$, the first mode of the system is mode 1S, the second and third eigenmodes are modes 1A, while the fourth eigenmode is mode 2A: $\omega_{1S} < \omega_{1A} < \omega_{2A}$. For $\lambda^2 = 0.80$ the first crossover occurs: $\omega_{1S} = \omega_{1A}$.
- (b) For $0.80 < \lambda^2 \leq 1.00$, the relation between the natural frequencies is $\omega_{1A} < \omega_{1S} < \omega_{2A}$, meaning that modes 1A appear first, followed by mode 1S and then by mode 2A. For $\lambda^2 = 1.00$, the second crossover occurs leading to equal eigenfrequencies for modes 1S and 2A: $\omega_{1S} = \omega_{2A}$.
- (c) For $1.00 < \lambda^2 \leq 1.17$, a transition between the third and fourth eigenmodes occurs, meaning that $\omega_{1A} < \omega_{2A} < \omega_{1S}$. For $\lambda^2 = 1.17$ the natural frequencies of the first three eigenmodes are equal: $\omega_{1A} = \omega_{2A}$ (third crossover point).
- (d) For $1.17 < \lambda^2$, mode 2A becomes the first mode of the system, modes 1A become second and third, while 1S remains the fourth mode. Thus, $\omega_{2A} < \omega_{1A} < \omega_{1S}$.

The shape of the first symmetric mode changes with respect to parameter λ^2 , as described also for simple suspended cables in Sect. 2.2. Thus, for small values, smaller than 1.17, the vertical component of this mode has no internal nodes with zero displacements, for values near 1.17 the vertical modal component is tangential to the horizontal plane at the cable ends, while for large values, larger than 1.17, internal nodes with zero displacements are observed. The deformed shape of the first symmetric mode is illustrated in Fig. 9 for different values of parameter λ^2 .

Based on this study of the natural frequencies and vibration modes of a MDOF cable net, many similarities with a simple suspended cable have been observed. The appearance sequence of the modes can be predicted by a non-dimensional parameter λ^2 for cable nets, similar to the one referring to simple suspended cables. Crossover points, at which modal transition occurs, depend also on this parameter.

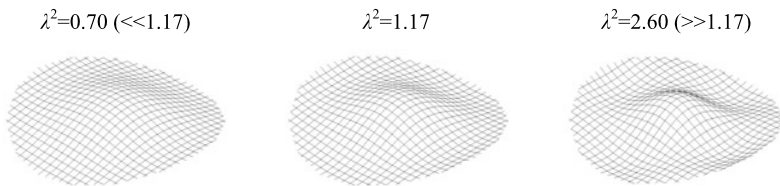


Fig. 9 First symmetric mode of a cable net

It is possible to use this parameter at a preliminary design stage, aiming at avoiding internal resonances between the first vibration modes, which may lead to oscillations of large amplitude, provoking also an unpredictable dynamic response with a continuous exchange of energy between the modes involved in resonance.

5 Dynamic Response of Cable Nets Under Harmonic Load

The authors of the present work have explored the dynamic behaviour of a damped cable net subjected to a uniform symmetric load for a wide range of values of the loading frequency, observing resonances not only for the first natural mode, but also for higher modes [46]. In [48] an undamped cable net was also analysed under a uniform harmonic load, with frequency equal to the system's eigenfrequency, accounting for fundamental resonance. Following the deformed geometry during the dynamic response revealed that not only the first symmetric mode but also higher symmetric modes are activated due to internal resonances, leading to the beat phenomena in the oscillation diagram of the net. Nevertheless, a single analysis cannot provide adequate information about the dynamic response of a nonlinear system. In general, several analyses had to be conducted for different loading frequencies changed by small steps in order to plot response curves, such as the one described in Fig. 4 and detect nonlinear phenomena.

In [44] the dynamic response a MDOF cable net subjected to uniform harmonic loads was investigated. Many nonlinear analyses were conducted in order to compose response diagrams that would prove the occurrence of nonlinear phenomena. The same procedure is followed in this section, in order to explain the importance of plotting such diagrams. Thus, a 3-dimensional cable network system, as the one described in Sect. 3, is utilised here with the characteristics listed in Table 1.

Conducting linear modal analyses the natural frequencies and vibration modes are calculated. The first symmetric mode with frequency $\omega_{1S} = 9.902 \text{ sec}^{-1}$, being the first mode of the system, is considered to be the main vibration mode of the system when it is subjected to a uniform load (Fig. 10). Knowing the eigenfrequencies of the system the loading frequencies are appropriately chosen aiming at resonances.

Table 1 Characteristics of the cable net

Number of cables N	25
Cable span L	100 m
Sag-to-span ratio f/L	1/35
Elastic modulus of cables E	165 GPa
Damping ratio ζ	2 %
Cable diameter D	50 mm
Initial cable pretension N_0	600 kN
Cable mass density m	10 Mg/m ³

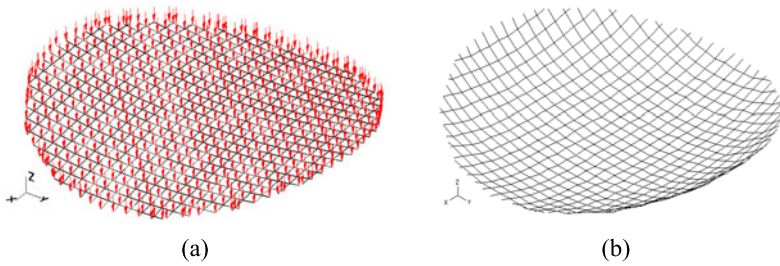


Fig. 10 (a) Uniform load, (b) magnified deformed shape for uniform load

For a uniform load distribution, as shown in Fig. 10a, with a loading amplitude $P_0 = 1.3$ kN and frequency varying between $0.90\omega_{1S}$ and $1.30\omega_{1S}$, the steady-state response amplitude of the central node with respect to the ratio of the loading frequency over the frequency of mode 1S is illustrated in Fig. 11. Bending of the response curve is observed as the maximum steady-state oscillation amplitude occurs for $\Omega/\omega_{1S} = 1.11$ and not for $\Omega/\omega_{1S} = 1.00$ as for linear systems. Jump phenomena are also noted, leading to sudden decrease of the response amplitude for a small change of the loading frequency. In addition a double response is calculated for a large range of frequency ratios, depending on the initial conditions.

For loading amplitude $P_0 = 14$ kN and frequencies between $0.30\omega_{1S}$ and $0.60\omega_{1S}$, the steady-state response is shown in Fig. 12. In this chart, the peak of the response for $\Omega = 0.36\omega_{1S}$ indicates an order-three superharmonic resonance for mode 1S. For frequency ratios different from 0.36 smaller steady-state amplitudes are observed. Thus, a small change of the loading frequency results in significantly different response amplitudes, due to superharmonic resonances.

Fig. 11 Steady-state response of the cable net under fundamental resonance for mode 1S ($P_0 = 1.3$ kN)

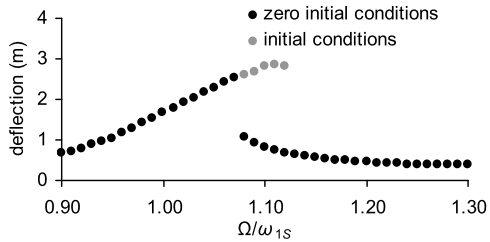
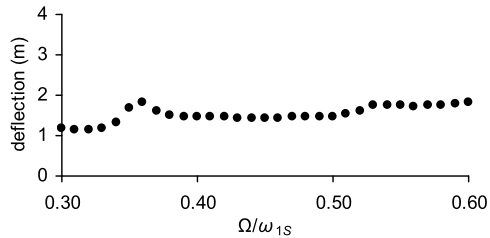


Fig. 12 Steady-state response of the cable net under superharmonic resonance for mode 1S ($P_0 = 14$ kN)



As mentioned in [49] the phenomenon of subharmonic resonance in nonlinear systems occurs for large load amplitudes, for specific initial conditions and for loading frequencies close to $2\omega_{1S}$ or $3\omega_{1S}$ but slightly larger than those, introducing a frequency detuning. In this case, it is impossible to know which load amplitude and frequency and which initial deflection and velocity can cause this kind of nonlinear resonance, because no analytical solutions are available. Thus, this case is not studied in this section.

Hence, the response to dynamic loads is proved to be highly nonlinear, characterised by superharmonic resonances, bending of the response curve, dependence on the initial conditions and jump phenomena. In the response diagrams each dot represents the steady-state deflection resulting from a single nonlinear dynamic analysis. It is noted that in order to plot such a response diagram, 41 and 31 nonlinear dynamic analyses are performed for detecting the fundamental and superharmonic resonance, respectively, changing the frequency ratio by steps of 0.01. Only by this kind of diagrams is it possible to detect the loading frequency for which nonlinear phenomena take place, changing the frequency ratio by sufficiently small steps. It is now easy to understand why single numerical analyses cannot provide sufficient information about eventual nonlinear phenomena.

6 Approximate Method of an Equivalent SDOF Cable Net

Nonlinear phenomena, such as superharmonic or subharmonic resonances, bending of the response curve and response amplitudes dependent on the initial conditions, can be detected in simple SDOF models by exploring their equation of motion. In a multi-degree-of-freedom system, for which no analytical solutions can be found, the only way to plot a response curve, which can show whether the above phenomena may occur, is by conducting a large number of nonlinear time-history analyses, for different closely spaced load amplitudes and frequencies.

As mentioned in Sect. 2.3, Gero [21, 22] presented a method to estimate the static behaviour of a large cable net, referred to as prototype, using charts that describe the behaviour of a smaller one, referred to as model, by means of the maximum deflection and cable tension. The transformation of the large structure to the smaller one was obtained by similarity relations. The proposed method was restricted to nets with fixed cable edges. The two networks should have similar geometries, with the same sag-to-span ratio, so that their corresponding quantities could also be similar.

The preliminary design method developed by Gero has been extended by the authors of this chapter to elastically supported cable network structures, by taking into consideration the characteristics of the edge ring, and more specifically its flexural stiffness $E_r I_r$ [50–52]. Thus, the ring is no longer considered as rigid, but as elastically deformable, accounting for more realistic boundary conditions for the cables. Additional charts and similarity relations have been provided for the preliminary design of the edge ring, including the sag-to-span ratio of the net as a variable in the transformation relations. This method has been further developed for the case

of dynamic response [48], providing additional similarity relations for the mass and the natural frequency of the system, for the case of fixed cable ends.

In what follows, this preliminary design method is used to transform a MDOF cable net into an equivalent SDOF cable net, in order to solve its equation of motion, find analytical solutions of the nonlinear dynamic response, estimate the nonlinear dynamic response of the large structure and thus facilitate the detection of nonlinear phenomena.

6.1 Similarity Relations

The prototype in this work is similar to the symmetric MDOF cable net described in Sect. 3. Harmonic loads, expressed as $P(t) = (P_0) \cos \Omega_p t$, are exerted vertically on every node of the net, having the same amplitude and time variation. The oscillation of the central node of the net describes its dynamic response.

The model is a SDOF cable net, shown in Fig. 13. It is the simplest possible cable net model, which is a symmetric structure consisting of two crossing perpendicular cables with the same initial pretension N_0 , material with elastic modulus E , cross-sectional diameter D and area A , unit weight ρ , equal lengths L and equal but opposite sags f . The central node is free, while the ends of the cables are fixed. The uniformly distributed mass of the cables is considered as lumped. Additional concentrated mass M can be taken into account. The total mass is attached to the central node. No local sag is produced between two adjacent nodes, as no self-weight is taken into consideration. A harmonic load $P(t) = (P_0) \cos \Omega t$ is applied on the central node.

The transformation of the characteristics of the prototype to the corresponding ones of the model is obtained by similarity relations. The relations used for this

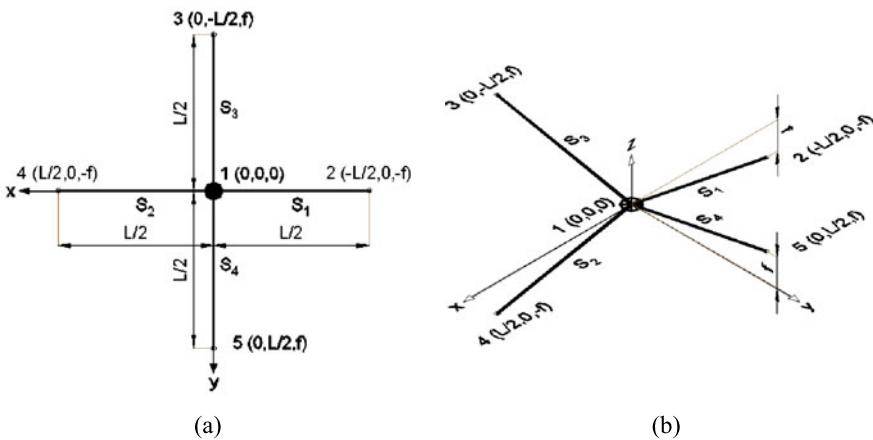


Fig. 13 Geometry of the SDOF cable net model (a) plan view, (b) perspective view

method are based on the ones provided in [48], for a cable net with fixed cable ends and are the following:

$$(P_0)_m = (P_0)_p \left(\frac{E_m}{E_p} \right) \left(\frac{L_m}{L_p} \right)^2 \left(\frac{N_p + 1}{N_m + 1} \right)^2 \sqrt{\frac{f_m/L_m}{f_p/L_p}}: \quad \text{load amplitude} \quad (8)$$

$$D_m = D_p \left(\frac{L_m}{L_p} \right) \sqrt{\left(\frac{N_p + 1}{N_m + 1} \right) \left(\frac{f_p/L_p}{f_m/L_m} \right)}: \quad \text{cable diameter} \quad (9)$$

$$A_m = A_p \left(\frac{L_m}{L_p} \right)^2 \left(\frac{N_p + 1}{N_m + 1} \right) \left(\frac{f_p/L_p}{f_m/L_m} \right)^2: \quad \text{cable cross-sectional area} \quad (10)$$

$$(EA)_m = (EA)_p \left(\frac{E_m}{E_p} \right) \left(\frac{L_m}{L_p} \right)^2 \left(\frac{N_p + 1}{N_m + 1} \right) \left(\frac{f_p/L_p}{f_m/L_m} \right)^2: \quad \text{axial stiffness} \quad (11)$$

$$(N_0)_m = (N_0)_p \left(\frac{E_m}{E_p} \right) \left(\frac{L_m}{L_p} \right)^2 \left(\frac{N_p + 1}{N_m + 1} \right): \quad \text{initial pretension} \quad (12)$$

$$\rho_m = \rho_p \left(\frac{E_m}{E_p} \right) \left(\frac{L_p}{L_m} \right)^2 \left(\frac{f_m/L_m}{f_p/L_p} \right)^2: \quad \text{cable unit weight} \quad (13)$$

$$M_m = M_p \left(\frac{E_m}{E_p} \right) \left(\frac{L_m}{L_p} \right) \left(\frac{N_p + 1}{N_m + 1} \right)^2: \quad \text{nodal mass} \quad (14)$$

$$w_{d,m} = w_{d,p} \left(\frac{L_m}{L_p} \right) \left(\frac{f_m/L_m}{f_p/L_p} \right): \quad \text{nodal dynamic deflection} \quad (15)$$

$$\omega_m = \omega_p: \quad \text{natural frequency} \quad (16)$$

$$\Omega_m = \Omega_p: \quad \text{loading frequency} \quad (17)$$

$$\zeta_m = \zeta_p: \quad \text{damping ratio} \quad (18)$$

where N is the number of cables in each direction, while the subscripts m and p refer to the model and the prototype, respectively.

6.2 Analytical Solution of a SDOF Cable Net Model

Referring to the SDOF cable net system of Fig. 13, the analytical expression of the equation of motion is reported from [44].

The length S_N of each segment at the equilibrium state under pretension is expressed as:

$$S_N = \sqrt{(L/2)^2 + f^2} \quad (19)$$

The initial length S_0 for all segments is equal to:

$$S_0 = \frac{S_N}{1 + \frac{N_0}{EA}} \quad (20)$$

Table 2 Tension components referring to the global axes

Cable	Axis x	Axis y	Axis z
1	$N_{1x} = N_1 \cdot (L/2 + u)/S_1$	$N_{1y} = N_1 \cdot v/S_1$	$N_{1z} = N_1 \cdot (f + w)/S_1$
2	$N_{2x} = N_2 \cdot (L/2 - u)/S_2$	$N_{2y} = -N_2 \cdot v/S_2$	$N_{2z} = -N_2 \cdot (f + w)/S_2$
3	$N_{3x} = N_3 \cdot u/S_3$	$N_{3y} = N_3 \cdot (L/2 + v)/S_3$	$N_{3z} = -N_3 \cdot (f - w)/S_3$
4	$N_{4x} = -N_4 \cdot u/S_4$	$N_{4y} = N_4 \cdot (L/2 - v)/S_4$	$N_{4z} = N_4 \cdot (f - w)/S_4$

If u , v and w are the displacements of the central node, referring to the global axes x , y , z , respectively, the deformed lengths of the cable segments are calculated as:

$$S_{1,2} = \sqrt{(L/2 \pm u)^2 + v^2 + (f + w)^2} \tag{21}$$

$$S_{3,4} = \sqrt{u^2 + (L/2 \pm v)^2 + (f - w)^2} \tag{22}$$

The cable tension for each deformed segment is expressed as:

$$N_i = N_0 + EA \left(\frac{S_i - S_N}{S_0} \right) \tag{23}$$

where $i = 1, 2, 3, 4$ and their components, referring to the global axes, are listed in Table 2.

The sums of forces at the central node, referring to the x , y and z global axes, are:

$$N_k = N_{1k} - N_{2k} + N_{3k} - N_{4k} \quad \text{where } k = x, y, z \tag{24}$$

Differentiating Eqs. (24) with respect to u , v and w , respectively, and considering zero displacement ($u = v = w = 0$) for the unforced and undeformed state, the stiffness coefficients at the prestressed equilibrium states are:

$$K_{x0} = K_{y0} = \frac{4 \cdot (EAL^2 + 2N_0L^2 + 8N_0f^2)}{\sqrt{(L^2 + 4f^2)^3}} \tag{25}$$

$$K_{z0} = \frac{4 \cdot (8EAf^2 + 2N_0L^2 + 8N_0f^2)}{\sqrt{(L^2 + 4f^2)^3}} \tag{26}$$

while the three corresponding natural frequencies of the system can be expressed as:

$$\omega_{x0} = \sqrt{\frac{K_{x0}}{M}} = \omega_{y0} = \sqrt{\frac{K_{y0}}{M}} \quad \text{and} \quad \omega_{z0} = \sqrt{\frac{K_{z0}}{M}} \tag{27}$$

In case a dynamic load is applied on the central node, the equations of motion of this node for the three directions of the global axes are expressed in the equilibrium state:

$$M\ddot{u} + C\dot{u} + N_{1x} - N_{2x} + N_{3x} - N_{4x} = P_x(t) \tag{28}$$

$$M\ddot{v} + C\dot{v} + N_{1y} - N_{2y} + N_{3y} - N_{4y} = P_y(t) \tag{29}$$

$$M\ddot{w} + C\dot{w} + N_{1z} - N_{2z} + N_{3z} - N_{4z} = P_z(t) \tag{30}$$

where $P_x(t)$, $P_y(t)$ and $P_z(t)$ are the three components of the external dynamic load, varying with time, referring to the global axes. The damping C is a function of the damping ratio ζ , expressed as [41]:

$$C = \zeta C_{cr} = 2\zeta M\omega_{z0} \tag{31}$$

Allowing only for vertical displacements, an external excitation $P_z(t) = P_0 \times \cos \Omega t$ is applied on the central node, with a loading frequency Ω . Substituting the expressions of the tension of the cables (Eq. (23)) and the prestressed, initial and deformed lengths (Eqs. (19)–(22)), into the vertical components of the cable tensions (Table 2), the differential equation (30) becomes:

$$\begin{aligned} M\ddot{w} + C\dot{w} + N_z &= P_z(t) \Rightarrow \\ M\ddot{w} + C\dot{w} - \frac{4EA(f+w)}{L\sqrt{1+4\frac{(f+w)^2}{L^2}}} &+ \frac{4EA(f-w)}{L\sqrt{1+4\frac{(f-w)^2}{L^2}}} + \frac{4w(EA+N_0)}{L\sqrt{1+4\frac{f^2}{L^2}}} &= P_z(t) \end{aligned} \tag{32}$$

As proved in [53], Eq. (32), developed in Taylor series, becomes similar to the equation of motion referring to a forced damped Duffing oscillator, which is thoroughly explored in the literature [49]. Thus, it can be expressed as:

$$\ddot{w} + 2\varepsilon\mu\dot{w} + \omega_{z0}^2 w + \varepsilon\alpha w^3 = P \cos(\Omega t) \tag{33}$$

where:

$$2\varepsilon\mu = \frac{C}{M} = 2\zeta\omega_{z0} \tag{34}$$

$$\varepsilon\alpha = \frac{16EA}{ML^3} \tag{35}$$

$$P = \frac{P_0}{M} \tag{36}$$

$$\omega_{z0} = \sqrt{\frac{K_{z0}}{M}} = \sqrt{\frac{4EA}{ML} \cdot \left(8\frac{f^2}{L^2} + 2\frac{N_0}{EA} - 4\frac{N_0}{EA} \frac{f^2}{L^2} \right)} \tag{37}$$

In what follows the analytical solutions of Eq. (33) under fundamental, superharmonic and subharmonic resonances are retrieved from [49] and [53]. In case of fundamental resonance the excitation is assumed to be weak, defined as:

$$P_0 = \varepsilon p_0, \quad P = P_0/M = \varepsilon p_0/M = \varepsilon p \quad \text{with } p = O(1) \tag{38}$$

A small detuning parameter σ is introduced to express the proximity of the loading frequency to ω_{z0} , such that:

$$\Omega = \omega_{z0} + \varepsilon\sigma, \quad \text{with } \sigma = O(1) \tag{39}$$

The response of the nonlinear system at steady state is:

$$w(t) = a \cos(\Omega t - \gamma) + O(\varepsilon) \tag{40}$$

where a is the amplitude of the oscillation and γ is the phase. The peak amplitude of the free oscillation term is given as:

$$a_p = \frac{p}{2\mu\omega_{z0}} \tag{41}$$

and the corresponding value of the detuning σ is:

$$\sigma_p = \frac{3\alpha a_p^2}{8\omega_{z0}} = \frac{3\alpha p^2}{32\mu^2\omega_{z0}^3} \tag{42}$$

The frequency-response curves are obtained in the form:

$$\sigma = \frac{3\alpha a^2}{8\omega_{z0}} \pm \sqrt{\frac{p^2}{4\omega_{z0}^2 a^2} - \mu^2} \tag{43}$$

Typical frequency-response curves are shown in Fig. 14.

In case of superharmonic resonance a loading frequency is considered, such that:

$$3\Omega = \omega_{z0} + \varepsilon\sigma \quad \text{with } \sigma = O(1) \tag{44}$$

The response of the nonlinear system at steady state is expressed as:

$$w(t) = a \cos(3\Omega t - \gamma) + P\left(\frac{1}{\omega_{z0}^2 - \Omega^2}\right) \cos \Omega t + O(\varepsilon) \tag{45}$$

having a term with the same frequency as the excitation and a free oscillation term whose frequency is exactly three times the frequency of the excitation. The frequency-amplitude relation for superharmonic resonance is expressed as:

$$\sigma = \frac{3\alpha \Lambda^2}{\omega_{z0}} + \frac{3\alpha a^2}{8\omega_{z0}} \pm \sqrt{\frac{\alpha^2 \Lambda^6}{\omega_{z0}^2 a^2} - \mu^2} \tag{46}$$

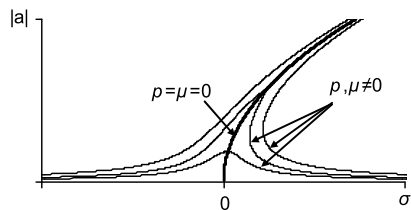
where

$$\Lambda = \frac{1}{2} P\left(\frac{1}{\omega_{z0}^2 - \Omega^2}\right) \tag{47}$$

The peak amplitude of the free oscillation term is calculated as:

$$a_p = \frac{\alpha \Lambda^3}{\mu\omega_{z0}} \tag{48}$$

Fig. 14 Fundamental resonance: Amplitude $|a|$ vs. frequency detuning σ



which depends on the cubic term coefficient α . The corresponding value of the frequency detuning σ is:

$$\sigma_p = \frac{3\alpha\Lambda^2}{\omega_{z0}} \left(1 + \frac{\alpha^2\Lambda^4}{8\mu^2\omega_{z0}^2} \right) \tag{49}$$

The maximum permissible value of Λ , given by Eq. (47) is equal to:

$$\Lambda_0 = \frac{G}{6\alpha} - \frac{4\mu\omega_{z0}}{G} \tag{50}$$

where

$$G = \left[\mu\alpha^2\omega_{z0} \left(108w_{\max} + 12\sqrt{\frac{96\mu\omega_{z0} + 81\alpha w_{\max}^2}{\alpha}} \right) \right]^{1/3} \tag{51}$$

and w_{\max} is the maximum permissible deflection corresponding to the maximum allowable cable stress which is considered in this work equal to the yield stress. A typical frequency-response curve for the case of superharmonic resonance is illustrated in Fig. 15. When conditions for superharmonic resonance hold, for excitations of large amplitude and loading frequency approximately equal to $\omega_{z0}/3$, the amplitude of the oscillation does not decay to zero, in spite of the presence of damping, in contrast to linear systems.

For subharmonic resonance the loading frequency is equal to:

$$\Omega = 3\omega_{z0} + \varepsilon\sigma, \quad \text{with } \sigma = O(1) \tag{52}$$

The frequency-amplitude relation for the subharmonic resonance is:

$$\left[\left(\sigma - \frac{9\alpha\Lambda^2}{\omega_{z0}} - \frac{9\alpha a^2}{8\omega_{z0}} \right)^2 + 9\mu^2 \right] a^2 = \frac{81\alpha^2\Lambda^2}{16\omega_{z0}^2} a^4 \tag{53}$$

Equation (53) has a double zero solution, called trivial solution ($a = 0$) and two non-zero ones, denoted as nontrivial ones. One of the two nontrivial solutions is stable and the other one is unstable. For subharmonic nontrivial solutions, it must be satisfied that:

$$\sigma \geq \frac{63\alpha}{8\omega_{z0}} \Lambda^2 + \frac{2\omega_{z0}}{\alpha} \frac{\mu^2}{\Lambda^2} \tag{54}$$

with oscillation amplitude:

$$a^2 = c \pm \sqrt{c^2 - s} \tag{55}$$

Fig. 15 Superharmonic resonance: Amplitude $|a|$ vs. frequency detuning σ

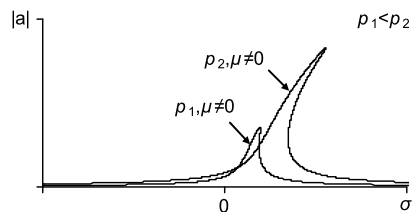
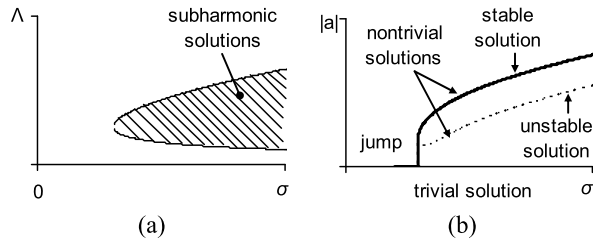


Fig. 16 Subharmonic resonance: (a) region of subharmonic solutions, (b) amplitude $|a|$ vs. frequency detuning σ



where

$$s = \frac{64\omega_{z0}^2}{81\alpha^2} \left[\left(\sigma - \frac{9\alpha\Lambda^2}{\omega_{z0}} \right)^2 + 9\mu^2 \right] \quad \text{and} \quad c = \left(\sigma \frac{8\omega_{z0}}{9\alpha} - 6\Lambda^2 \right) \quad (56)$$

The condition of inequality (54) defines a region in which subharmonic solutions appear. This region and a typical frequency-response curve for the case of subharmonic resonance are illustrated in Fig. 16, where it is obvious that subharmonic resonances require a frequency detuning $\sigma \neq 0$.

The exact value of σ that can cause this kind of resonance depends on the loading amplitude and the system’s characteristics, as determined by inequality (54). The initial conditions define the response amplitude of the system. For the trivial solution $a = 0$, the steady-state response depends only on the external load:

$$w(t) = P \left(\frac{1}{\omega_{z0}^2 - \Omega^2} \right) \cos \Omega t + O(\varepsilon) \quad (57)$$

while, for the non-trivial stable solution of a , the response of the nonlinear system at steady state is:

$$w(t) = a \cos \left(\frac{\Omega t - \gamma}{3} \right) + P \left(\frac{1}{\omega_{z0}^2 - \Omega^2} \right) \cos \Omega t + O(\varepsilon) \quad (58)$$

having a term with the same frequency as the excitation and a free oscillation term whose frequency is exactly one-third the frequency of the excitation. The existence of multiple solutions, depending on the initial conditions, renders the dynamic behaviour of the system unpredictable and in some cases with catastrophic results.

As proved in [53] the study of the SDOF cable net through the simplified model of the Duffing oscillator provides sufficiently accurate results and useful information for the conditions under which nonlinear phenomena take place.

6.3 Example 1: Cable Net with Sag-Span Ratio $f/L = 1/35$

The method of the equivalent SDOF cable net is presented here by means of the following examples. In order to reduce the scaling error, model and prototype have the same sag-to-span ratios f/L , cable span L and Young modulus E . For the first example the characteristics of the prototype are tabulated in Table 3. Based on the similarity relations of Sect. 6.1, the characteristics of the equivalent SDOF model are also listed in Table 3.

Table 3 Characteristics of prototype and model

	Prototype	Model
Number of cables N	25	1
Cable span L	100 m	100 m
Sag-to-span ratio f/L	1/35	1/35
Elastic modulus of cables E	165 GPa	165 GPa
Yield stress σ_y	1570 MPa	1570 MPa
Damping ratio ζ	2 %	2 %
Cable diameter D	50 mm	1800 mm
Initial cable pretension N_0	600 kN	7800 kN
Nodal mass M	0.151 Mg	25.52 Mg

6.3.1 Analytical Solutions for the SDOF Model

The eigenfrequency of the SDOF model is calculated from Eq. (37):

$$\omega_m = 8.22 \text{ sec}^{-1} \quad (59)$$

Accounting for a maximum cable stress equal to the yield stress, the maximum permissible deflection ($w_{\max,m}$) is calculated for the model equalling to 3.975 m corresponding to a maximum permissible static load:

$$P_{\max,m} = 10939 \text{ kN} \quad (60)$$

The maximum amplitude of the steady-state response, defined by Eq. (41), cannot be larger than the maximum permissible deflection. Thus, taking into account Eqs. (34) and (38), the threshold of the load amplitude is:

$$a_{\text{peak}} \leq w_{\max,m} \Rightarrow (P_0)_{m,\text{peak}} \leq 2M_m \zeta \omega_m^2 w_{\max,m} = 274.17 \text{ kN} \quad (61)$$

which, according to Eq. (8), corresponds to load amplitude for the MDOF cable net:

$$(P_0)_{p,\text{peak}} = (P_0)_{m,\text{peak}} \left(\frac{N_m + 1}{N_p + 1} \right)^2 = 1.62 \text{ kN} \quad (62)$$

Taking into consideration that during the transient response the deflection of the net cannot exceed the maximum permissible one, a smaller load amplitude is chosen for the prototype equal to $(P_0)_p = 1.30 \text{ kN}$, corresponding to a nodal load for the SDOF model, equal to:

$$(P_0)_m = (P_0)_p \left(\frac{N_p + 1}{N_m + 1} \right)^2 = 219.70 \text{ kN} \quad (63)$$

For this load amplitude the maximum amplitude of the steady-state response is:

$$a_{\text{peak}} = \frac{(P_0)_m}{2M_m \zeta \omega_m^2} = 3.185 \text{ m} \quad (64)$$

and the corresponding value of the detuning σ is calculated by Eq. (42):

$$\varepsilon\sigma_{peak} = \frac{3(P_0)_m^2(EA)_m}{2M_m^3\zeta^2\omega_m^5L_m^3} = 1.22 \text{ sec}^{-1} \tag{65}$$

Hence, the peak steady-state response amplitude occurs for loading frequency:

$$\Omega = \omega_m + \varepsilon\sigma = 9.44 \text{ sec}^{-1} = 1.15\omega_m \tag{66}$$

The expression of the response curve is based on Eq. (43), taking into account Eq. (35):

$$\begin{aligned} \varepsilon\sigma &= \frac{6a^2}{\omega_m} \cdot \frac{(EA)_m}{M_mL_m^3} \pm \sqrt{\frac{(P_0)_m^2}{4M_m^2\omega_m^2a^2} - (\zeta\omega_m)^2} \\ &= \left(0.12a^2 \pm \sqrt{\frac{0.27}{a^2} - 0.027} \right) \text{ sec}^{-1} \end{aligned} \tag{67}$$

while the frequency ratio is calculated as:

$$\frac{\Omega}{\omega_m} = \frac{\omega_m + \varepsilon\sigma}{\omega_m} \tag{68}$$

The corresponding response curve is plotted in Fig. 17.

The bending of the curve indicates the intense nonlinearity of the system. This bending means that jump phenomena are expected to characterise the response of the prototype, as well as multiple response amplitudes dependent on the initial conditions and existence of unstable solutions, while the maximum steady-state amplitude is predicted for frequency ratio larger than 1.

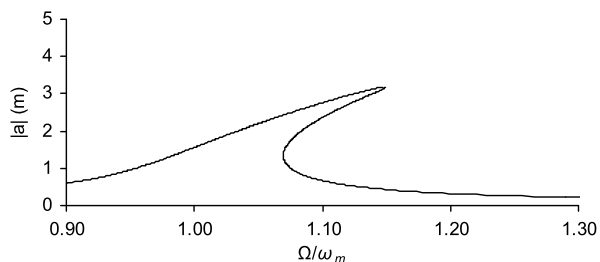
In case of superharmonic resonant conditions, the peak amplitude of the free oscillation term is expressed by Eq. (48):

$$a_{peak} = \frac{16(EA)_m}{M_mL_m^3} \cdot \frac{\Lambda^3}{\zeta\omega_m^2} = (1.954 \cdot \Lambda^3) \text{ (m)} \tag{69}$$

Assuming that the maximum steady-state amplitude must not exceed the maximum permissible deflection:

$$a + 2\Lambda = (1.954\Lambda^3 + 2\Lambda) \text{ (m)} = 3.975 \text{ m} \tag{70}$$

Fig. 17 Fundamental resonance: response curve of the SDOF model for $\zeta = 2 \%$ and load amplitude $(P_0)_m = 219.7 \text{ kN}$



the solution of Λ satisfying Eq. (70), is given by Eq. (50), taking into consideration Eq. (35):

$$\Lambda_0 = \frac{\varepsilon G \cdot M_m L_m^3}{6 \cdot 16(EA)_m} - \frac{4\zeta \omega_m^2}{\varepsilon G} = 1.003 \text{ m} \quad (71)$$

where, according to Eq. (51):

$$\varepsilon G = 20.14 \text{ sec}^{-2} \text{ m}^{-1} \quad (72)$$

Considering that the loading frequency is equal to:

$$\Omega = \omega_m/3 = 8.22/3 = 2.74 \text{ sec}^{-1} \quad (73)$$

the threshold of the load amplitude can be obtained from Eq. (47), taking into account the value of Λ_0 given by Eq. (71):

$$(P_0)_{m,peak} = 2M_m \Lambda_0 (\omega_m^2 - \Omega^2) = 3074.70 \text{ kN} \quad (74)$$

which corresponds to load amplitude for the MDOF cable net:

$$(P_0)_{p,peak} = (P_0)_{m,peak} \left(\frac{N_m + 1}{N_p + 1} \right)^2 = 18.19 \text{ kN} \quad (75)$$

A smaller load amplitude is chosen for the prototype equal to $(P_0)_p = 14 \text{ kN}$, corresponding to a nodal load for the SDOF model, equal to:

$$(P_0)_m = (P_0)_p \left(\frac{N_p + 1}{N_m + 1} \right)^2 = 2366 \text{ kN} \quad (76)$$

meaning:

$$\Lambda = \frac{(P_0)_m}{2 \cdot M_m} \left(\frac{1}{\omega_m^2 - \Omega^2} \right) = 0.772 \text{ m} \quad (77)$$

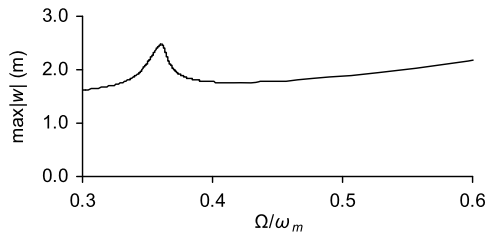
The diagram of the steady-state response is defined by Eq. (46), taking into account Eq. (35):

$$\begin{aligned} \varepsilon \sigma &= \frac{48\Lambda^2}{\omega_m} \cdot \frac{(EA)_m}{M_m L_m^3} + \frac{6a^2}{\omega_m} \cdot \frac{(EA)_m}{M_m L_m^3} \\ &\pm \sqrt{\frac{\Lambda^6}{\omega_m^2 a^2} \cdot \left(\frac{16(EA)_m}{M_m L_m^3} \right)^2 - (\zeta \omega_m)^2} \Rightarrow \\ \varepsilon \sigma &= 0.574 \text{ sec}^{-1} + 0.12a^2 (\text{sec}^{-1}) \\ &\pm \sqrt{\frac{0.022}{a^2} (\text{sec}^{-2}) - 0.027 (\text{sec}^{-2})} \end{aligned} \quad (78)$$

and the frequency detuning is calculated for a given response amplitude. The maximum possible response amplitude is expected equal to:

$$w_{\max,m} = a + 2\Lambda \quad (79)$$

Fig. 18 Superharmonic resonance: response curve of the SDOF model for $\zeta = 2\%$ and load amplitude $(P_0)_m = 2366\text{ kN}$



where Λ this time is calculated as:

$$\Lambda = \frac{(P_0)_m}{2 \cdot M_m} \left(\frac{1}{\omega_m^2 - \Omega^2} \right) = \frac{46.36\text{ m/sec}^2}{(8.22\text{ sec}^{-1})^2 - \Omega^2} \tag{80}$$

with

$$\Omega = \frac{\omega_m + \varepsilon\sigma}{3} \tag{81}$$

The response diagram is shown in Fig. 18.

Subharmonic solutions, with non-trivial amplitudes of the free oscillation term, exist only if the condition of expression (54) is satisfied:

$$\begin{aligned} \varepsilon\sigma &\geq \frac{126\Lambda^2}{\omega_m} \cdot \frac{(EA)_m}{M_m L_m^3} + \frac{M_m L_m^3}{8(EA)_m} \cdot \frac{\zeta^2 \omega_m^3}{\Lambda^2} \Rightarrow \\ \varepsilon\sigma &\geq 2.53\Lambda^2 (\text{sec}^{-1}) + \frac{0.168}{\Lambda^2} (\text{sec}^{-1}) \end{aligned} \tag{82}$$

for a given value of Λ . The load amplitude is calculated from Eq. (47):

$$\begin{aligned} (P_0)_m &= 2M_m \Lambda (\omega_m^2 - \Omega^2) \Rightarrow \\ (P_0)_m &= 51.04\text{ kN sec}^2 \text{ m}^{-1} \cdot \Lambda \cdot [(8.22\text{ sec}^{-1})^2 - \Omega^2] \end{aligned} \tag{83}$$

where

$$\Omega = 3\omega_m + \varepsilon\sigma = 24.66\text{ sec}^{-1} + \varepsilon\sigma \tag{84}$$

for a frequency detuning satisfying inequality (82), while the amplitude of the oscillation is obtained by Eq. (55):

$$\begin{aligned} a^2 &= (2.77\varepsilon\sigma - 6\Lambda^2)(m^2) \\ &\pm \sqrt{[(2.77\varepsilon\sigma - 6\Lambda^2)(m^2)]^2 - 7.66 \cdot [(\varepsilon\sigma - 2.89\Lambda^2)^2 + 0.24](m^4)} \end{aligned} \tag{85}$$

Figure 19 illustrates the curve that defines the region of subharmonic solutions, by means of Λ and $(P_0)_m$ with respect to the frequency ratio, for values of load amplitude up to the maximum permissible static one. In Fig. 20 the response amplitude is plotted with respect to the frequency ratio and the loading amplitude for values up to the maximum permissible one. It is noted that in Fig. 19a the amplitude Λ is much smaller with respect to the one of the free oscillation term, shown in

Fig. 19 Subharmonic resonance of the SDOF model: (a) A vs. frequency ratio, (b) $(P_0)_m$ vs. frequency ratio

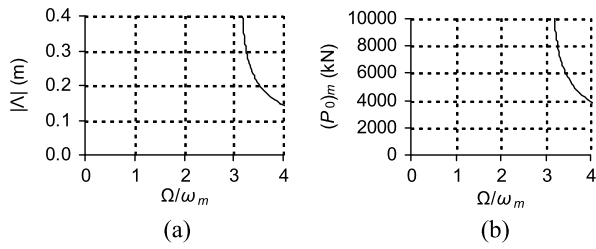


Fig. 20 Subharmonic resonance of the SDOF model: (a) response amplitude vs. frequency ratio, (b) load amplitude $(P_0)_m$ vs. response amplitude

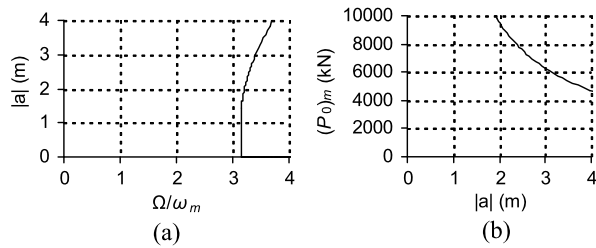


Fig. 20a, confirming that subharmonic resonances can suddenly develop vibrations with very large amplitudes leading to catastrophic results. The frequency ratios that could cause subharmonic resonance without cable failure are between 3.18 and 3.70 (Fig. 20a), resulting in oscillation amplitudes larger than 1.77 m (Fig. 20), while the load amplitude should be larger than 4732 kN (Fig. 19b and Fig. 20b), corresponding to 28 kN for the prototype.

A parametric analysis, changing the load amplitude, the frequency ratio and the initial deflection, keeping the initial velocity of the central node equal to 16 m/sec, shows that as the load amplitude increases, the minimum initial deflection and the frequency ratio that can cause subharmonic resonance decrease (Fig. 21). If, for example, the load amplitude is equal to $(P_0)_m = 9464$ kN, corresponding to 56 kN for the MDOF prototype, an initial velocity 16 m/sec, a minimum initial deflection 1.49 m and a loading frequency $\Omega = 3.32\omega_m$ constitute the conditions for subharmonic resonance. The time-history diagrams of the central node deflection, for these initial conditions and for zero initial conditions, are plotted in Fig. 22, where it is shown the increase oscillation amplitude due to subharmonic resonance.

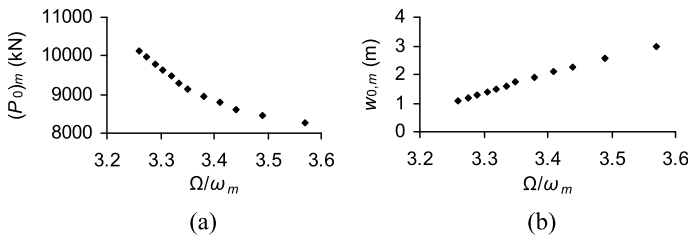


Fig. 21 Subharmonic resonant conditions for the SDOF model: (a) $(P_0)_m$ vs. frequency ratio, (b) initial deflection vs. frequency ratio

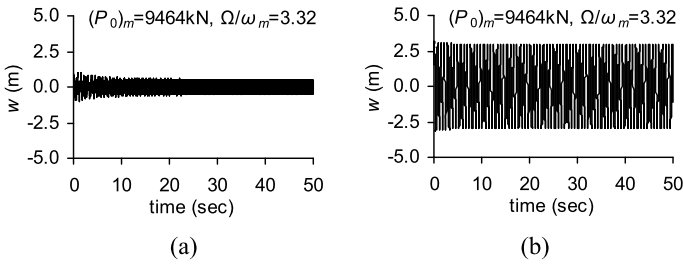


Fig. 22 Time-history diagrams of the central node deflection for $\Omega/\omega_m = 3.32$ and $(P_0)_m = 9464$ kN: (a) with zero initial conditions, (b) with initial displacement and velocity

6.3.2 Numerical Results for the MDOF Prototype

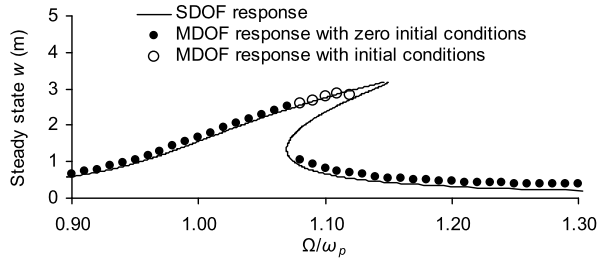
In order to evaluate the accuracy of this method, numerical analyses are conducted to calculate the dynamic response of the MDOF cable net that is the prototype for this example. The non-dimensional parameter λ^2 is:

$$\lambda^2 = \left(\frac{f}{L}\right)^2 \frac{EA}{N_0} = 0.44 < 1.17 \tag{86}$$

which means that the first mode of the system is the symmetric mode with a vertical component having no internal nodes with zero displacements. A modal analysis is performed to calculate the vibration modes and the natural frequencies of the system. The first vibration mode is the first symmetric mode (1S) with frequency $\omega_p = 9.902 \text{ sec}^{-1}$. According to similarity relation (16) the natural frequency of the model should be equal to the one of the prototype. The natural frequency of mode 1S, obtained by the equivalent SDOF model, is 17 % smaller than the one calculated by modal analysis of the MDOF system. The difference is rather large, because the difference between the model and the prototype, regarding the number of cables is also large. Nevertheless, this method is not intended to estimate with accuracy the eigenfrequency, the maximum deflection or the cable tension of the prototype, but it is rather proposed to facilitate detection of the occurrence of nonlinear phenomena.

Accounting for fundamental resonant phenomena the load amplitude of the harmonic uniform load was chosen in Sect. 6.3.1 equal to $(P_0)_p = 1.30$ kN. The load frequency varies between $0.90\omega_p$ and $1.30\omega_p$. The damping ratio, according to similarity relation (18), is considered equal to $\zeta_p = \zeta_m = \zeta = 2\%$. The amplitude of the steady-state response for the central node of the MDOF prototype with respect to the ratio of the loading frequency over the eigenfrequency is plotted in Fig. 23. In the same diagram the response of the SDOF model of Fig. 17 is also illustrated for comparison reasons. In this diagram each dot corresponds to the steady-state deflection amplitude of the central node of the MDOF system, obtained by a numerical analysis with zero initial conditions. Each circle defines the steady-state response of one numerical analysis for the MDOF system considering initial conditions. According to similarity relation (15), the nodal dynamic deflection of the prototype should approximate the one of the model. Indeed, it is noted that the equivalent SDOF model can predict with very good accuracy the response of the MDOF system.

Fig. 23 Fundamental resonance: response curve of the MDOF prototype for $\zeta = 2\%$ and load amplitude $(P_0)_p = 1.30$ kN



The bending of the response curve for the MDOF system is shown in the diagram of Fig. 23. If zero initial conditions are assumed, for frequency ratio $\Omega/\omega_p = 1.07$ the steady-state amplitude is 2.52 m, while for $\Omega/\omega_p = 1.08$ the amplitude drops suddenly to 1.06 m, thus confirming the jump phenomenon. However, if initial conditions are assumed, the amplitude of the steady-state deflection for $\Omega/\omega_p = 1.08$ is 2.62 m, verifying that the dynamic response of the MDOF prototype depends on the initial conditions. These phenomena, namely the maximum steady-state amplitude occurring for frequency ratio larger than 1, leading to the bending of the curve, the jump and the multiple response amplitudes dependent on the initial conditions, also verified by the numerical simulation, confirm the intense nonlinearity of the MDOF cable net, which was predicted by the SDOF model. Using the equivalent SDOF model, it is possible to estimate, for specific load amplitudes, the frequency ratio for which the maximum dynamic response of the MDOF system is expected.

In case of superharmonic resonance the load amplitude for the MDOF prototype is chosen in Sect. 6.3.1, equal to $(P_0)_p = 14$ kN. The load frequency varies between $0.30\omega_p$ and $0.60\omega_p$. The amplitude of the steady-state response for the central node of the MDOF prototype with respect to the frequency ratio, and the response of the equivalent SDOF model (Fig. 18) are plotted together in Fig. 24. The steady-state amplitudes estimated by the method of the SDOF model are between 25 % and 48 % larger than the ones obtained by numerical analysis. This estimation cannot be considered as satisfactory. On the other hand, the peak amplitude for frequency ratio $\Omega/\omega_p = 0.36$, predicted by the equivalent SDOF model, is verified for the prototype, confirming the occurrence of an order-three superharmonic resonance for the first symmetric mode. In addition, in Fig. 24, a second peak of the amplitude is observed for frequency ratio $\Omega/\omega_p = 0.53$ for the MDOF system, corresponding to an order-two superharmonic resonance for the same mode. In this case, the loading frequency is $\Omega = 0.53 \cdot \omega_p = 5.525 \text{ sec}^{-1} = 0.36\omega_6$, where ω_6 is the frequency of the sixth mode equal to $\omega_6 = 14.655 \text{ sec}^{-1}$. Hence, this second peak indicates also an order-three superharmonic resonance for the sixth mode being the second symmetric mode of the system. With the equivalent SDOF model having only one frequency, it is not possible to predict this second superharmonic resonance for the higher order mode. Moreover, the SDOF model, having only a cubic nonlinear term, cannot detect order-two superharmonic resonances.

Based on the parametric analysis of Sect. 6.3.1, a load amplitude equal to $(P_0)_p = 56$ kN applied on every node, with a load frequency equal to $\Omega = 3.32\omega_p$

Fig. 24 Superharmonic resonance: response curve of the MDOF prototype for $\zeta = 2\%$ and load amplitude $(P_0)_p = 14\text{ kN}$

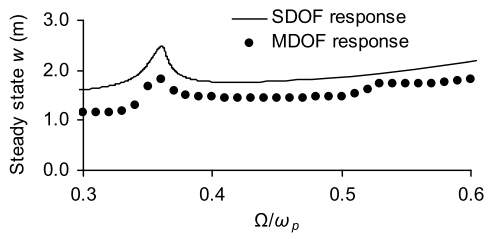
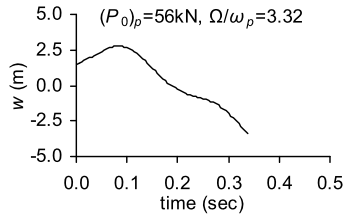


Fig. 25 Time-history response of the central node for $(P_0)_p = 56\text{ kN}$ and $\Omega/\omega_p = 3.32$



and initial conditions that correspond to an initial deflection of the central node 1.49 m and initial velocity of the same node 16 m/sec, should cause subharmonic resonance. Conducting a numerical analysis for the prototype, before the first cycle of the oscillation concludes, the nodal deflection reaches the maximum permissible one causing cable tensile failure (Fig. 25).

For smaller load amplitudes, larger initial deflection is required, and for smaller initial deflection, only larger load amplitude can cause subharmonic resonance. Both cases lead to cable tensile failure. Thus, for this cable net, with damping ratio 2 %, it is impossible for the subharmonic resonance to evolve, because the large load amplitude and the large initial conditions required for such a resonance cause cable tensile failure as soon as the vibration starts.

6.4 Example 2: Cable Net with Sag-Span Ratio $f/L = 1/20$

The range of application of this method is evaluated by means of parametric analyses. To that effect, another cable net is assumed, with a diameter $L_p = 100\text{ m}$, sag-to-span ratio equal to $f_p/L_p = 1/20$, Young modulus $E_p = 165\text{ GPa}$, and number of cables in each direction is $N_p = 25$. The nodal mass is again equal to $M_p = 0.151\text{ Mg}$. Four different cases of cable diameter D_p , and initial pretension $(N_0)_p$ are considered, accounting for three different levels of initial cable stress. The cable diameter and the initial pretension are chosen appropriately, resulting in characteristic values of the non-dimensional parameter λ^2 . The load amplitude in each case is chosen large enough to cause bending of the response curve, but sufficiently small to avoid cable tensile failure. The characteristics of the nets for these cases are tabulated in Table 4.

Following the same procedure, as described in Sect. 6.3, a damping ratio $\zeta = 2\%$ is considered and the case of fundamental resonance for the first symmetric mode

Table 4 Characteristic cases for cable net with $f/L = 1/20$ and $E = 165$ GPa

Cases	$(P_0)_p$ [kN]	D_p [mm]	$(N_0)_p$ [kN]	σ_y [MPa]	$(N_0)_p/(A\sigma_y)$	λ^2
1	1.3	40	735	1670	0.35	0.70
2	1.2	40	600	1570	0.30	0.86
3	2.0	50	600	1570	0.20	1.35
4	5.0	80	800	1570	0.10	2.59

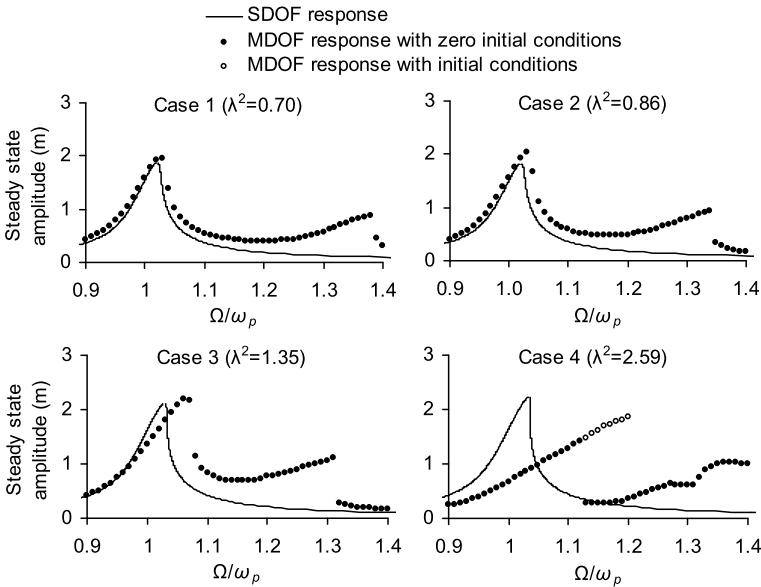
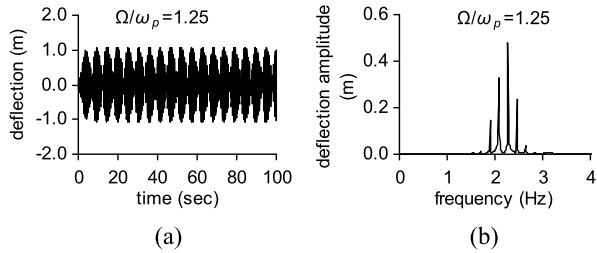


Fig. 26 Fundamental resonance: response curve of the MDOF prototypes and SDOF models

(1S) is addressed. The diagrams of the steady-state amplitude of the central node deflection of the MDOF systems, along with the ones of the equivalent SDOF cable nets, are illustrated in Fig. 26 for different frequency ratios.

In all charts, two peaks appear in the response curve of the MDOF systems. The first one, for frequency ratio close to 1, corresponds to the fundamental resonance of the first symmetric mode, while the second one describes the fundamental resonance for the second symmetric mode. The analysis of the equivalent SDOF cable net, having only one degree of freedom, cannot predict the fundamental resonance for the second symmetric mode. For the first two cases, the maximum steady-state response of the central node of the MDOF system, as well as the frequency ratio for which this occurs, are predicted with satisfactory accuracy by the method of the equivalent SDOF model. For the third case, the response diagram bends more than the one of the equivalent SDOF cable net, while for the fourth case the method does not provide accurate results. In this case, the bending of the response curve for

Fig. 27 Response diagrams of the central node deflection for $\Omega/\omega_p = 1.25$ (case 4): (a) time-history diagram, (b) response spectrum



the MDOF system is more intense and the maximum steady-state amplitude of the central node is smaller than the one predicted by the method. This occurs because for the third and fourth cases the parameter λ^2 is larger than 1.17, meaning that the first symmetric mode presents internal nodes with zero displacements, as explained in Sect. 4. Thus, the vibration mode of the SDOF cable net cannot describe well the one of the MDOF system, and the results do not show a good match. In the last two cases, following fundamental resonance for the first symmetric mode a beat phenomenon characterises the time-history diagrams of the central node deflection, meaning that more than one modes participate in the motion of the node. This occurs for frequency ratios between $\Omega/\omega_p = 1.14$ and $\Omega/\omega_p = 1.20$ for the third case and between $\Omega/\omega_p = 1.20$ and $\Omega/\omega_p = 1.40$ for the fourth case. The beat phenomenon is very intense in the fourth case, in which five symmetric modes have frequencies close to the loading frequencies, resulting in the irregular increase of the response amplitude, as shown in Fig. 26.

For example, the time-history diagram and the response spectrum of the central node deflection for frequency ratio $\Omega/\omega_{1S} = 1.25$ are plotted in Fig. 27. The beat phenomenon is obvious in the time-history diagram during the 100 seconds of the analysis, which does not decay, although damping is included. In the response spectrum, several peaks are distinguished, corresponding to the symmetric modes, proving that all symmetric modes are activated during the oscillation of the net. The activation of higher modes cannot be estimated by the equivalent SDOF cable net, having only one vibration mode.

Observing the diagrams of Fig. 26, it is worth mentioning that in order to obtain similar oscillation amplitudes, the load amplitude for the fourth case is much larger than the one of the other cases, as listed in Table 4. Thus, for the same load amplitude, larger parameters λ^2 lead to smaller oscillation amplitudes.

6.5 Evaluation of the Method

The equivalent SDOF model, having only one eigenfrequency and eigenmode, cannot detect resonances for higher modes for a MDOF cable net, or internal resonances. In addition, having only a cubic nonlinear term, it cannot predict nonlinear resonances of order-two for the large system.

The analytical solution describes the steady-state amplitude of the response but not the maximum transient one, for which a cable tensile failure is possible to occur before the steady-state response is reached. Moreover, it is provided for a vertical load applied on the central node, causing a vertical vibration. Thus, only the oscillation amplitude of the central node of the MDOF system can be estimated. Since this vertical motion corresponds to the first symmetric mode of the cable net, this method cannot assess the response of the MDOF cable net for other modal shapes, or for other spatial loading distributions, such as antisymmetric ones.

The results of this method are not satisfactory when the parameter λ^2 is larger than 1.17 for the MDOF system. In this case, the first symmetric mode of the cable net presents internal nodes with zero displacements and cannot be simulated with accuracy by the SDOF model.

Nevertheless, the advantages of this method are very important for the design of such structures. The intensity of the geometric nonlinearity of the MDOF system can be estimated very satisfactorily, by means of the bending of the response curve, the jump phenomena and the existence of double response amplitude due to the initial conditions. The loading frequency detuning, for which fundamental, superharmonic or subharmonic resonances for the first symmetric mode occur, can be found for a given load amplitude with good accuracy. Finally, the computational time required to solve the equation of motion and have an assessment of the response of the MDOF system is minimal. On the contrary, the creation of a response diagram for the MDOF system requires a large number of nonlinear dynamic analyses.

7 Summary and Conclusions

The research presented in this work aims at investigating the response of cable nets subjected to dynamic loads, focusing on the dynamic phenomena that characterise nonlinear structures. A method of an equivalent SDOF model is proposed to detect the conditions under which nonlinear dynamic phenomena take place.

Firstly, a saddle-form MDOF cable net is assumed, having a circular plan view and pinned cable ends. The first symmetric and antisymmetric vibration modes and the corresponding natural frequencies are calculated. A non-dimensional parameter λ^2 , including the sag-to-span ratio of the net and the mechanical characteristics of the cables, regarding their axial stiffness and their pretension, determines the sequence of their vibration modes, as in simple cables. For specific values of this parameter two or more vibration modes have equal frequencies although they have different shapes, leading to internal resonances. The shape of the first symmetric mode depends on λ^2 , presenting internal nodes with zero displacement for values of this parameter larger than 1.17.

Next, the steady-state response is calculated for the MDOF cable net under uniform harmonic loads, in order to plot response diagrams. The loading frequencies are chosen either close to the natural frequency of the first symmetric mode, lead-

ing to fundamental resonances, or smaller than that, accounting for superharmonic resonances. Under these conditions, although damping exists, a small change of the loading frequency may cause large difference in the steady-state oscillation amplitude, while the initial conditions influence significantly the response of the cable net, as occurs in intensely nonlinear systems. These diagrams are necessary in order to detect nonlinear dynamic phenomena, such as bending of the response curve, jump phenomena, dependence on the initial conditions and superharmonic resonances, but they require a large number of nonlinear dynamic analyses, changing the loading frequency by small steps and trying several initial conditions and loading amplitudes.

Thus, a method of an equivalent SDOF cable net model is proposed to facilitate the prediction of such nonlinear phenomena for the MDOF system. The transformation of the geometrical and mechanical characteristics from the large system to the smaller one is obtained by similarity relations. The SDOF model consists of two crossing cables, simulating the simplest cable net. The vertical displacement of the central node is the system's single degree of freedom. The analytical solution of its equation of motion provides the steady-state response amplitude under resonant conditions. The results of the SDOF model, by means of the maximum load, the maximum deflection and the loading frequency, are transformed to the ones of the MDOF system, by using the inverse similarity relations. Response diagrams are plotted for both SDOF and MDOF systems, based on the analytical solutions and conducting time-history analyses, respectively. The two responses are compared for several geometries and cable initial stresses in order to define the range of application of this method. A good agreement between the two diagrams is noted for values of parameter λ^2 smaller than 1.17. For larger values, the shape of the first symmetric mode, which is considered as the main vibration mode of the MDOF system under uniform load, presents internal nodes with zero displacements and the SDOF model cannot simulate with accuracy its oscillation.

It is also noted that, in order to have a superharmonic or a subharmonic resonance, large amplitudes of the load are required. In particular for subharmonic resonances, large initial conditions are also necessary. The combination of these two conditions leads to cable tensile failure during the transient response at the beginning of the analysis. Thus, it is unlikely for cable nets to experience subharmonic resonance.

The numerical investigation of the overall nonlinear dynamic behaviour of a MDOF system can be obtained by numerous nonlinear time-history analyses, for different load amplitudes and initial conditions, for very small time steps and frequency steps. The main advantage of this method is that it can detect the loading amplitudes and frequencies for which nonlinear phenomena occur for the MDOF cable net, constituting a useful tool for further investigation of such structures in the region of the critical loading frequency regarding fundamental and order-three secondary resonances, avoiding nonlinear phenomena.

References

1. Yeomans D (2009) *How structures work: design and behaviour from bridges to buildings*. Wiley Blackwell, Oxford
2. <http://www.arcaro.org/tension/album>
3. Majowiecki M (1994) *Tensostrutture progetto e verifica*. CREA, Genova (in Italian)
4. Alessi R, Bairaktaris D, Caridakis F, Majowiecki M, Zoulas F (1979) The roof structures of the new sports arena in Athens. In: *World congress on shell and spatial structures*, Spain, pp 6.107–6.123
5. <http://www.london2012.com>
6. Muttoni A (2011) *The art of structures: introduction to the functioning of structures in architecture*. EPFL Press, Lausanne
7. Kadlčák J (1994) *Statics of suspension cable roofs*. Balkema, Rotterdam
8. Ghali A, Neville AM, Brown TG (2003) *Structural analysis: a unified classical and matrix approach*, 5th edn. Spon Press, London
9. Buchholdt HA (1999) *An introduction to cable roof structures*, 2nd edn. Thomas Telford, London
10. Younis MI (2011) *MEMS linear and nonlinear statics and dynamics*. Springer, New York. doi:10.1007/978-1-4419-6020-7
11. Peña-Ramírez J, Fey RHB, Nijmeijer H (2012) An introduction to parametric resonance. In: Fossen TI, Nijmeijer H (eds) *Parametric resonance in dynamical systems*. Springer, New York. doi:10.1007/978-1-4614-1043-0_1
12. Jordan DW, Smith P (2004) *Nonlinear ordinary differential equations: an introduction to dynamical systems*, 3rd edn. Oxford University Press, New York
13. Kerschen G, Worden K, Vakakis AF, Golinval JC (2006) Past, present and future of nonlinear system identification in structural dynamics. *Mech Syst Signal Process* 20:505–592
14. Lakshmanan M, Murali K (1996) *Chaos in nonlinear oscillators: controlling and synchronization*. World Scientific, Singapore
15. Pugsley AG (1949) On the natural frequencies of suspension chains. *Q J Mech Appl Math* 2:412–418
16. Ahmadi-Kashani K (1989) Vibration of hanging cables. *Comput Struct* 31:699–715
17. Irvine HM, Caughey TK (1974) The linear theory of free vibrations of a suspended cable. *Proc R Soc Lond Ser A, Math Phys Sci* 341(1626):299–315
18. Rega G, Luongo A (1980) Natural vibrations of suspended cables with flexible supports. *Comput Struct* 12:65–75
19. Srinil N, Rega G, Chucheepsakul S (2003) Nonlinear interactions in the 3D free vibrations of horizontal and inclined sagged cables. In: *5th international symposium on cable dynamics*, Santa Margherita Ligure, pp 77–84
20. Leonard JW (1988) *Tension structures: behavior & analysis*. McGraw-Hill, New York
21. Gero JS (1975) The behaviour of cable network structures. Structures report SR8, University of Sydney
22. Gero JS (1975) The preliminary design of cable network structures. Structures report SR9, University of Sydney
23. Chisalita A (1984) Finite deformation analysis of cable networks. *J Eng Mech* 110:207–223
24. Dhooar BL, Gupta PC, Singh BP (1985) Vibration analysis of orthogonal cable networks by transfer matrix method. *J Sound Vib* 101:575–584
25. Katsikadelis JT, Sapountzakis EJ (1988) An approach to the vibration problem of homogeneous, non-homogeneous and composite membranes based on the boundary element method. *Int J Numer Methods Eng* 26:2439–2455
26. Zingoni A (1996) An efficient computational scheme for the vibration analysis of high tension cable nets. *J Sound Vib* 189:55–79
27. Gambhir ML, Batchelor BdeV (1977) A finite element for 3-D prestressed cable nets. *Int J Numer Methods Eng* 11:1699–1718

28. Gambhir ML, Batchelor BdeV (1979) Finite element study of the free vibration of 3D cable networks. *Int J Solids Struct* 15:127–136
29. Seeley GR, Christiano P, Stefan H (1975) Natural frequencies of circular cable networks. *J Struct Div* 101:1171–1177
30. Morris NF (1973) Dynamic response of cable networks. *J Struct Div* 100:2091–2108
31. Morris NF (1975) Modal analysis of cable networks. *J Struct Div* 101:97–108
32. Ozdemir H (1979) A finite element approach for cable problems. *Comput Struct* 15:427–437
33. Monforton GR, El-Hakim NM (1980) Analysis of truss-cable structures. *Comput Struct* 11:327–335
34. Papadrakakis M (1983) Inelastic dynamic response of cable networks. *J Struct Eng* 109:1139–1154
35. Vilnay O, Rogers P (1990) Statical and dynamical response of cable nets. *Int J Solids Struct* 26:229–312
36. Swaddiwudhipong S, Wang CM, Liew KM, Lee SL (1989) Optimal pretensioned forces for cable networks. *Comput Struct* 33:1349–1354
37. Stefanou GD (1997) The response of large cable nets to general dynamic loads based on step-by-step time integration techniques. *J IAASS* 38:53–64
38. Geschwindner LF (1981) Nonlinear dynamic analysis by modal superposition. *J Struct Div* 107:2325–2336
39. Fan J, He F, Liu Z (1997) Chaotic oscillation of saddle form cable-suspended roofs under vertical excitation action. *Nonlinear Dyn* 12:57–68
40. Lazzari M, Saetta AV, Vitaliani RV (2001) Non-linear dynamic analysis of cable-suspended structures subjected to wind actions. *Comput Struct* 79:953–969
41. Chopra AK (1995) *Dynamics of structures: theory and applications to earthquake engineering*. Prentice Hall, New York
42. ADINA (Automatic Dynamic Incremental Nonlinear Analysis) v8.4 (2006) ADINA user interface command reference manual, vol I: ADINA solids & structures model definition. ADINA R&D Inc, Watertown
43. ADINA (Automatic Dynamic Incremental Nonlinear Analysis) v8.4 (2006) Theory and modeling guide, vol I: ADINA solids & structures. ADINA R&D Inc, Watertown
44. Vassilopoulou I, Gantes CJ (2011) Nonlinear dynamic behavior of saddle-form cable nets under uniform harmonic load. *Eng Struct* 33:2762–2771
45. Vassilopoulou I, Gantes CJ (2007) Vibration modes and dynamic response of saddle form cable nets under sinusoidal excitation. In: *Geometrically non-linear vibrations of structures*. Euromech colloquium, vol 483. FEUP, Porto, pp 129–132
46. Vassilopoulou I, Gantes CJ (2007) Modal transition and dynamic nonlinear response of cable nets under fundamental resonance. In: *8th HSTAM international congress on mechanics*, Patras, vol 2, pp 787–794
47. Vassilopoulou I, Gantes CJ (2010) Vibration modes and natural frequencies of saddle form cable nets. *Comput Struct* 88:105–119
48. Vassilopoulou I, Gantes CJ (2007) Similarity relations for nonlinear dynamic oscillations of a cable net. In: *1st ECCOMAS thematic conference on computational methods in structural dynamics and earthquake engineering*, COMPDYN 2007, Rethymno, p 373 (abstract)
49. Nayfeh A, Mook DT (1979) *Nonlinear oscillations*. Wiley, New York
50. Vassilopoulou I, Gantes CJ (2002) Behaviour and preliminary analysis of cable net structures with elastic supports. In: *4th national conference on metal structures*, Patras, vol II, pp 517–525
51. Vassilopoulou I, Gantes CJ (2004) Behavior, analysis and design of cable networks anchored to a flexible edge ring. In: *IAASS symposium on shell and spatial structures from models to realization*, Montpellier, pp 212–213 (extended abstract)
52. Vassilopoulou I, Gantes CJ (2005) Cable nets with elastically deformable edge ring. *Int J Space Struct* 20:15–34
53. Vassilopoulou I, Gantes CJ (2012) Nonlinear dynamic phenomena in a SDOF model of cable net. *Arch Appl Mech* 82:1689–1703

Non-linear Model of a Ball Vibration Absorber

Jiří Náprstek, Cyril Fischer, Miroš Pirner, and Ondřej Fischer

Abstract Wind excited vibrations of slender structures such as towers, masts or certain types of bridges can be reduced using passive or active vibration absorbers. If there is available only a limited vertical space to install such a device, a ball type of absorber can be recommended. In general, it is a semi-spherical horizontal dish in which a ball of a smaller diameter is rolling. Ratio of both diameters, mass of the rolling ball, quality of contact surfaces and other parameters should correspond with characteristics of the structure. The ball absorber is modelled as a holonomous system. Using Lagrange equations of the second type, governing non-linear differential system is derived. The solution procedure combines analytical and numerical processes. As the main tool for dynamic stability investigation the 2nd Lyapunov method is used. The function and effectiveness of the absorber identical with those installed at the existing TV towers was examined in the laboratory of the Institute of Theoretical and Applied Mechanics. The response spectrum demonstrates a strongly non-linear character of the absorber. The response amplitudes at the top of a TV tower with ball absorber were reduced to 15–40 % of their original values.

Keywords Vibration ball absorber · Dynamic stability · Nonlinear vibration

1 Introduction

Passive vibration absorbers of various types are very widely used in civil engineering, especially when wind induced vibration should be suppressed. TV towers,

J. Náprstek (✉) · C. Fischer · M. Pirner · O. Fischer
Institute of Theoretical and Applied Mechanics, AS CR, Prosecká 76, Prague 9, Czech Republic
e-mail: naprstek@itam.cas.cz

C. Fischer
e-mail: fischer@itam.cas.cz

M. Pirner
e-mail: pirner@itam.cas.cz

O. Fischer
e-mail: fischero@itam.cas.cz

masts and other slender structures exposed to wind excitation are usually equipped by such devices. Conventional passive absorbers are of the pendulum type. Although they are very effective and reliable, they have several disadvantages limiting their application. First of all, they have certain requirements to space, particularly in a vertical direction. These requirements cannot be satisfied any time when an absorber should be installed as a supplementary equipment. Also horizontal construction, like foot bridges, cannot accept any absorber of the pendulum type. Another disadvantage represents a need of a regular maintenance.

Both above shortcomings can be avoided using the absorber of ball type. The basic principle comes out of a rolling movement of a metallic ball of a radius r inside of a metallic rubber coated dish of a radius $R > r$. This system is closed in an airtight case. Such a device is practically maintenance free. Its vertical dimension is relatively very small and can be used also in such cases where a pendulum absorber is inapplicable due to lack of vertical space or difficult maintenance. First papers dealing with the theory and practical aspects of ball absorbers have been published during the last decade, see [1] and [2].

Dynamics of the ball absorber is more complicated in comparison with the pendulum one. Its movement can be hardly described in a linear state although for the first view its behaviour is similar to the pendulum absorber type. A number of problems are still open being related with movement stability, bifurcations, auto-parametric resonances and at least but not last with dish and ball surface imperfections. This chapter presents basic mathematical model in 2D together with its numerical evaluation and practical application as far as to the state of the realization including some results of long-term measurements.

2 Mathematical Model in Two Dimensions

The dish is fixed to a vibrating structure. Their dynamic character is represented by a linear SDOF system represented by a mass M . Inside of a dish an internal ball m in a vertical plane is moving, i.e. 2DOF system should be investigated, as it is outlined in Fig. 1. It follows from geometric relations:

$$R \cdot \varphi = r(\psi + \varphi) \quad \Rightarrow \quad r\psi = \rho\varphi \quad (1)$$

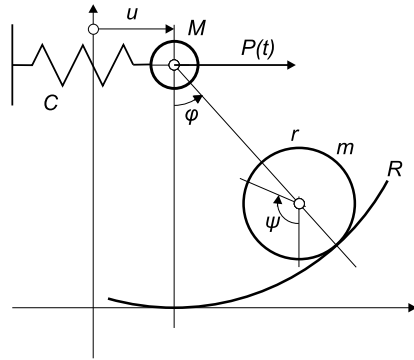
where $\rho = R - r$. It holds for vertical, or horizontal components of a displacement and velocity of the internal ball centre:

$$\left. \begin{array}{l} \text{horiz.:} \quad u + \rho \cdot \sin \varphi \quad \Rightarrow \quad \dot{u} + \rho \dot{\varphi} \cos \varphi \\ \text{vert.:} \quad \rho \cdot \cos \varphi \quad \Rightarrow \quad -\rho \dot{\varphi} \sin \varphi \end{array} \right\} \quad (2)$$

Kinetic energy of a moving system of balls m , M can be written in a form:

$$\begin{aligned} T &= \frac{1}{2}m[(\dot{u} + \rho \dot{\varphi} \cos \varphi)^2 + \rho^2 \dot{\varphi}^2 \sin^2 \varphi] + \frac{1}{2}J\dot{\psi}^2 + \frac{1}{2}M\dot{u}^2 \\ &= \frac{1}{2}(m + M)\dot{u}^2 + m\rho\dot{u}\dot{\varphi} \cos \varphi + \frac{m}{2\kappa}\rho^2\dot{\varphi}^2 \end{aligned} \quad (3)$$

Fig. 1 Basic scheme of a system



$m/\kappa = m + J/r^2 \Rightarrow \kappa = 5/7$, while the potential energy is given by an expression:

$$V = mg\rho(1 - \cos \varphi) + \frac{1}{2}Cu^2 \tag{4}$$

The damping should be introduced in a form of a simple Rayleigh function:

$$B = \frac{1}{2}(Mb_u\dot{u}^2 + mb_\varphi\rho^2\dot{\varphi}^2) \tag{5}$$

- m mass of the ball m ;
- J inertia moment of the ball m ;
- b_u, b_φ damping coefficients (logarithmic decrements).

Expressions (3), (4), (5) should be put into the Lagrange equations of the second type, see e.g. [3]:

$$\sum_{r=1}^n \left\{ \frac{d}{dt} \left(\frac{\partial T}{\partial \dot{q}_r} \right) - \frac{\partial T}{\partial q_r} + \frac{\partial V}{\partial q_r} + \frac{\partial B}{\partial \dot{q}_r} \right\} \delta q_r = P_r(t) \tag{6}$$

$$q_1 = u = \zeta \cdot \rho; \quad q_2 = \varphi; \quad P_u(t) = p(t) \cdot M\rho; \quad P_\varphi(t) = 0$$

which give the governing equations of the system:

$$\ddot{\varphi} + \kappa b_\varphi \dot{\varphi} + \kappa \omega_m^2 \sin \varphi + \kappa \ddot{\zeta} \cdot \cos \varphi = 0 \tag{7a}$$

$$\mu \ddot{\varphi} \cos \varphi - \mu \dot{\varphi}^2 \sin \varphi + (1 + \mu) \ddot{\zeta} + b_u \dot{\zeta} + \omega_M^2 \zeta = p(t) \tag{7b}$$

$$\mu = m/M; \quad \omega_M^2 = C/M; \quad \omega_m^2 = g/\rho \tag{7c}$$

Equations (7a), (7b) and (7c) describe 2D movement of a ball absorber under excitation by the force $P(t)$ at any arbitrary deviation amplitudes including incidental transition through a limit cycle towards an open regime.

3 Theoretical Analysis of the Absorber

Theoretical efficiency of the absorber will be assessed using its frequency characteristics for excitation of the mass M by harmonic force $p(t) = p_0 \cdot \sin \omega t$ simulating influence of external loading or for kinematic excitation of the same mass M .

In the later case the movement of the ball m rolling inside the dish is fully described by Eq. (7a). Should we solve the deviation $\varphi(t)$, (7b) can serve us subsequently for an evaluation of the force $p(t)$, which is necessary when the deviation $u(t) = \rho \cdot \zeta(t)$ should be achieved. To obtain frequency characteristics the harmonic excitation $\zeta(t) = \zeta_o \cos(\omega t)$ should be introduced into (7a)–(7c), which yields:

$$\ddot{\varphi} + \kappa b_\varphi \dot{\varphi} + \kappa \omega_m^2 \sin \varphi - \kappa \omega^2 \cos \varphi \cdot \zeta_o \cos \omega t = 0 \quad (8a)$$

$$\begin{aligned} \mu \ddot{\varphi} \cos \varphi - \mu \dot{\varphi}^2 \sin \varphi + (\omega_M^2 - (1 + \mu)\omega^2) \zeta_o \cos \omega t \\ - b_u \omega \cdot \zeta_o \sin \omega t = p(t) \end{aligned} \quad (8b)$$

Equation (8a) corresponds to the equation of a mathematical pendulum excited in a point of suspension. Its effective mass is increased due to a moment of inertia of the ball m by the factor $1/\kappa = 7/5$. Even in practice the movement amplitudes of this ball do not admit to linearise Eq. (8a). At least a simple Duffing non-linear form should be retained:

$$\ddot{\varphi} + \kappa b_\varphi \dot{\varphi} + \kappa \omega_m^2 \left(\varphi - \frac{1}{6} \varphi^3 \right) - \kappa \omega^2 \left(1 - \frac{1}{2} \varphi^2 \right) \cdot \zeta_o \cos \omega t = 0 \quad (9)$$

Let us concentrate in this chapter to the prior case when the excitation of a harmonic force is taken into account. As the resulting system is auto-parametric, the corresponding methods can be applied, see e.g. [4]. Expecting a single mode response, following approximate expressions for excitation and response can be written (cf. e.g. [5]):

$$\begin{aligned} p(t) &= p_0 \sin(t\omega) \\ \varphi(t) &= \alpha \sin(t\omega) + \beta \cos(t\omega) \\ \zeta(t) &= \gamma \sin(t\omega) + \delta \cos(t\omega) \end{aligned} \quad (10)$$

Having four new variables $\alpha = \alpha(t)$, $\beta = \beta(t)$, $\gamma = \gamma(t)$, $\delta = \delta(t)$ instead of two original unknowns $\varphi(t)$, $\zeta(t)$, two additional conditions can be freely chosen:

$$\dot{\alpha} \sin(t\omega) + \dot{\beta} \cos(t\omega) = 0, \quad \dot{\gamma} \sin(t\omega) + \dot{\delta} \cos(t\omega) = 0 \quad (11)$$

After substitution (10) and (11) into (7a)–(7c) and substituting the sin and cos functions by two terms of Taylor expansion, the harmonic balance procedure gives differential system for unknown amplitudes $\mathbf{X} = (\alpha, \beta, \gamma, \delta)^T$, see e.g. [6] or [7].

$$\mathbf{M}(\mathbf{X}) \dot{\mathbf{X}} = \mathbf{F}(\mathbf{X}) \quad (12)$$

The system (12) for amplitudes $\mathbf{X}(t)$ is meaningful if they are functions of a “slow time”, in other words if their changes within one period $2\pi/\omega$ are small or vanishing and individual steps of the harmonic balance operation are acceptable. The matrix \mathbf{M} and right hand side vector \mathbf{F} have the following form

$$\mathbf{M} = \begin{pmatrix} 0 & -8\frac{\omega}{\kappa} & -2\alpha\beta\omega & \omega A_\alpha \\ 8\frac{\omega}{\kappa} & 0 & -\omega A_\beta & 2\alpha\beta\omega \\ -\mu\omega A_\beta & 2\alpha\beta\mu\omega & 8(\mu+1)\omega & 0 \\ -2\alpha\beta\mu\omega & \mu\omega A_\alpha & 0 & -8(\mu+1)\omega \end{pmatrix} \quad (13)$$

$$\mathbf{F} = \begin{pmatrix} A_0(3\gamma\omega^2 - \alpha\omega_m^2) + 2\omega^2((\alpha\beta\delta + (8 - \beta^2)\gamma) - 4\frac{\alpha}{\kappa}) - 8\beta\omega b_\varphi \\ A_0(\delta\omega^2 - \beta\omega_m^2) + 2\omega^2(\alpha\gamma + \beta\delta - \frac{4}{\kappa})\beta + 8\alpha\omega b_\varphi \\ \frac{\omega^2}{6}(A_0(A_0 + 22)\beta\mu - 16(3\delta(\mu + 1) - 4\beta\mu)) + (\gamma\omega b_u + \delta\omega_M^2) \\ \frac{\omega^2}{6}(A_0(A_0 + 22)\alpha\mu - 16(3\gamma(\mu + 1) - 4\alpha\mu)) - (\delta\omega b_u - \gamma\omega_M^2 + p_0) \end{pmatrix} \quad (14)$$

where

$$A_0 = \alpha^2 + \beta^2 - 8, \quad A_\alpha = 2\alpha^2 + A_0, \quad A_\beta = 2\beta^2 + A_0$$

Determinant of the system matrix \mathbf{M} can be easily evaluated:

$$\det(\mathbf{M}) = -\frac{\omega^4}{\kappa^2}(64(\kappa - 1)\mu + \kappa\mu\Delta_1 R^2 - 64)(64(\kappa - 1)\mu + \kappa\mu\Delta_3 R^2 - 64) \\ \Delta_1 = (R^2 - 16), \quad \Delta_3 = 3(3R^2 - 16) \quad (15)$$

where $R^2 = R^2(t) = \alpha^2 + \beta^2$ is the amplitude of φ . Polynomial (15) has four roots R_1^2, \dots, R_4^2 :

$$3R_1^2 = R_2^2 = 8\left(1 - \frac{\mu + 1}{\sqrt{\kappa\mu(\mu + 1)}}\right) \\ 3R_3^2 = R_4^2 = 8\left(1 + \frac{\mu + 1}{\sqrt{\kappa\mu(\mu + 1)}}\right) \quad (16)$$

For positive μ and $0 < \kappa < 1$ are the first two roots negative, the last two roots are positive. The negative roots have not any physical meaning, whereas the positive roots form strictly decreasing functions of parameter μ . For $\kappa = 5/7$ (see (3)) it holds:

$$\lim_{\mu \rightarrow \infty} R_3^2 = \frac{8}{15}(5 + \sqrt{35}) \approx 5.82191 \\ \lim_{\mu \rightarrow \infty} R_4^2 = 8\left(1 + \sqrt{\frac{7}{5}}\right) \approx 17.4657 \quad (17)$$

With respect to the meaning of variable φ , even the lower value should not be reached in any real case.

Knowing the exact form and regularity properties of the system matrix \mathbf{M} , its inverse could be easily derived and then the normal form of the differential equation (12) can be established. However, as long as the matrix \mathbf{M} is regular, the original right hand side \mathbf{F} can be studied equivalently.

Let us consider stationary response of the system. In this case, the derivatives $d\mathbf{X}/dt$ vanish and the right hand side \mathbf{M} has to vanish too. Equation (12) degenerates to the form of:

$$\mathbf{F}(\mathbf{X}) = 0 \quad (18)$$

Thus, to identify the stationary solutions, the zero solution points of \mathbf{F} , depending on the excitation frequency and amplitude, should be traced. In the same time, the signum and the zero points of the Jacobian $\det(\mathbf{JF})$ have to be checked. Negative

value of the Jacobian for a particular point indicates that the corresponding solution is stable, whereas when Jacobian vanishes a bifurcation could occur.

The curve $\mathbf{F}(\alpha, \beta, \gamma, \delta, \omega) = 0$, projected into the planes (ω, R) or (ω, S) (for $S^2 = \gamma^2 + \delta^2$), forms the resonance curves known from the analysis of linear oscillators. However, correspondence of this curve to the original equations (7a)–(7c) is limited to the case of stationary response. It is necessary to remind, that limits of stationarity of the response cannot be determined from properties of (18) itself. The complete equation (12) has to be taken into account for this purpose.

4 Numerical Analysis

The aim of this study is a basic engineering approach demonstrating the problem as a whole from the theoretical background until realization in practice. Thus, the numerical analysis has been selected as it leads the most quickly to a basic overview about dynamic properties of a ball absorber.

With respect to actual experiences regarding passive vibration absorbers and some interesting properties of the system (7a)–(7c), following reference input data have been introduced:

$$\begin{aligned} M &= 10.0; & m &= 2.0; & \rho &= 0.71; & b_\varphi &= 0.1; & b_u &= 0.2 \\ C &= 140; & p_o &= 0.5\text{--}2.5 \end{aligned} \quad (19)$$

Several analysis procedures have been performed:

- Numerical integration of Eqs. (7a)–(7c) shows the response characteristics of the system.
- Numerical solution of Eq. (12) can help to decide if the response is stable or unstable.
- Analysis of the term $\mathbf{F}(\mathbf{X})$ given by (18) gives the resonance curve including the unstable branches.

Frequency response characteristics of Eq. (12) for the particular data is shown in Fig. 2. This non-linear equation has to be solved numerically. Starting from non-trivial initial conditions solution $\alpha(t)$, $\beta(t)$, $\gamma(t)$, $\delta(t)$ stabilizes after certain time. Mean value and standard deviation of the stabilized amplitudes $R = \sqrt{\alpha^2 + \beta^2}$ (variable φ , first row) and $S = \sqrt{\gamma^2 + \delta^2}$ (variable ζ , second row) depending on the excitation frequency ω are shown in Fig. 2. The variance of the amplitudes is shown as greyed area around the mean curve. Thus, the greyed areas indicate regions where a non-stationary solution should be expected (amplitudes R and S are not constant). It should be emphasized here, that validity of (12) in non-stationary case is limited, as it was derived with an assumption of slow time change of the amplitudes.

Utilizing Eqs. (18) and (14), the non-linear resonance curves describing the stationary response of the system (7a)–(7c) can be obtained. A set of such curves for excitation amplitudes $p_o = 0.25, 0.5, 1, 1.5, 2.5$ is shown in Fig. 3. It is obvious for

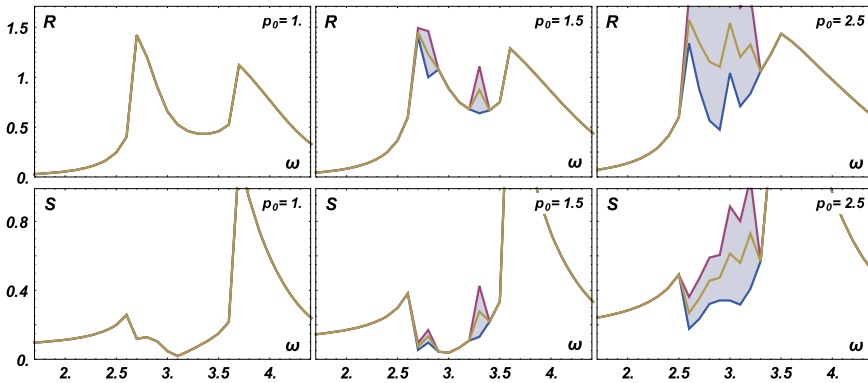


Fig. 2 Stabilized numerical solution of Eq. (12). Values of the amplitude $R = \sqrt{\alpha^2 + \beta^2}$ (variable φ , first row) and $S = \sqrt{\gamma^2 + \delta^2}$ (variable ζ , second row) are shown for three selected excitation amplitudes $p_0 = 1, 1.5, 2.5$. The excitation frequency ω is on the horizontal axis. Grey areas correspond to the frequency region of non-stationary response

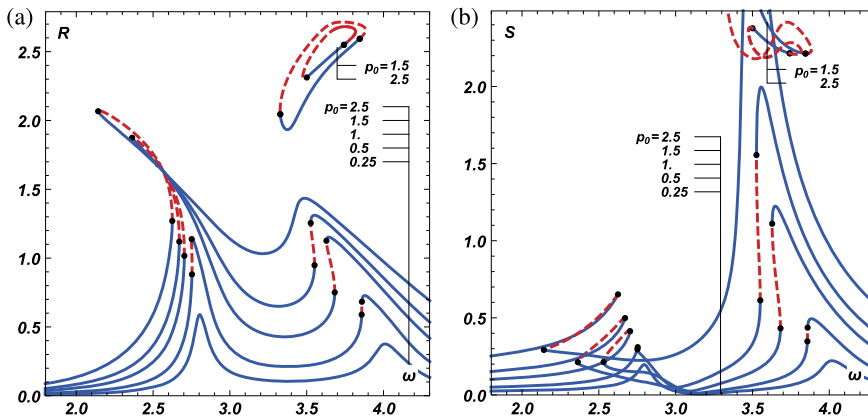


Fig. 3 Non-linear resonance curves describing the stationary response of the system computed as zero solutions of Eq. (18) for excitation amplitudes $p_0 = 0.25, 0.5, 1, 1.5, 2.5$. Stable branches are shown as solid curves, unstable parts are indicated as dashed curves. Amplitudes $R = \sqrt{\alpha^2 + \beta^2}$ are shown in the left part of the figure, amplitudes $S = \sqrt{\gamma^2 + \delta^2}$ are on the right

the first view the non-linear character manifesting oneself by a dependence of a position of extreme points on an amplitude of excitation force. This effect is visible predominantly in a neighbourhood of a conventional “linear” natural frequency of the absorber although also the second natural frequency corresponding to the original natural frequency of the structure is affected. The resonance curves are typical for a system with “softening” non-linearities. It turns out that the non-linear element represented by a ball absorber can be more effective when broad band random response should be reduced. Even better results can be expected in case of non-

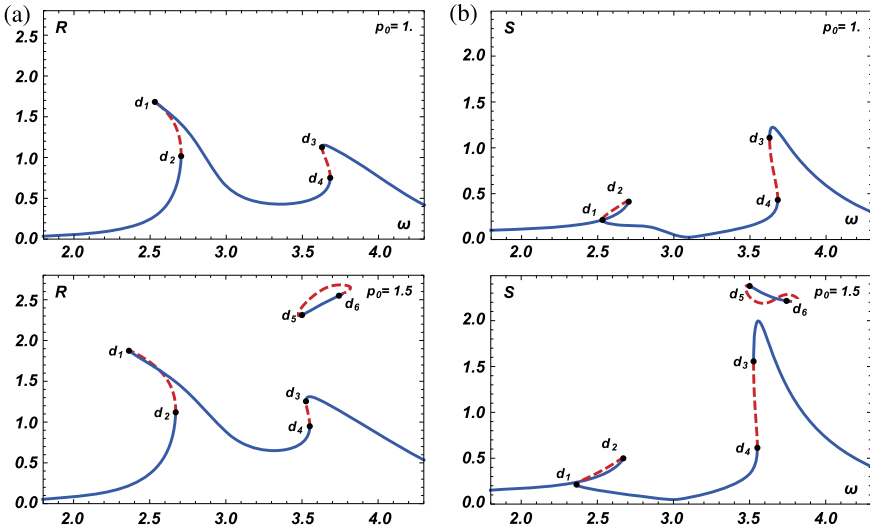


Fig. 4 Selected non-linear resonance curve for $p_0 = 1$ and $p_0 = 1.5$. (a) The case for $R = \sqrt{\alpha^2 + \beta^2}$ is on the left, (b) case for $S = \sqrt{\gamma^2 + \delta^2}$ is in the right part of the figure. Points d_1, \dots, d_6 correspond to zero points of Jacobian \mathbf{JF} and indicate change of stability properties of the curve

stationary excitation when amplitude spectrum is significantly variable in time. In such a case no doubt non-linear absorber should be preferred, while the linear one works better in cases of strong narrow band excitation mostly of deterministic character.

Let us comment the isolated curves indicating high amplitudes of response for $p_0 = 2$ and 3. Limit value for R , as it results from the roots of the $\det(\mathbf{M})$, cf. (15), is for data (19) $R < 3.22$. This limit is for the high curves in Fig. 3 still not violated. However, these curves have not any physical meaning in this case: (i) such high amplitudes of R are unrealistic, (ii) Eq. (12) was derived utilizing two terms of Taylor expansions for sin and cos functions and thus assuming only “small” amplitudes.

Let us study in more detail the stability of one particular curve from Fig. 3, the one for $p_0 = 1$. The both R and S (or φ and ζ respectively) resonance dependencies are shown in the first row of Fig. 4. The solid parts of the curves correspond to the stable solution, whereas the dashed sections correspond to the unstable solution of (18). Second row of Fig. 4 shows similar curves for higher excitation amplitude $p_0 = 1$. The isolated part of the response curve is present in this case.

Response of a real system cannot be expected to reach values of a unstable part of resonance curve. The stability of the individual sections of the curves follows from the sign of the Jacobian. Course of this value, corresponding to the curves in Fig. 4 is shown in Fig. 5a for $p_0 = 1$ and in Fig. 5b for $p_0 = 1.5$. Here the points d_1, \dots, d_4 or d_1, \dots, d_6 correspond to zero points of Jacobian \mathbf{JF} and indicate change of stability properties of the curve, cf. all parts of Fig. 4. Closed curve in the right part of Fig. 5b correspond to the isolated part of the resonance curve.

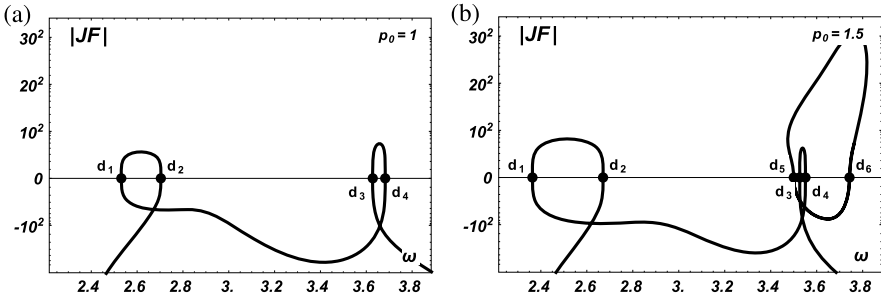


Fig. 5 Values of Jacobian determinant $\det(\mathbf{JF})$ corresponding to the stationary resonance curve for $p_0 = 1$ (a) and $p_0 = 1.5$ (b). Negative values indicate stable branches of the resonance curve and vice versa. Closed curve in the *right part* of figure (b) corresponds to the isolated part of the resonance curve, cf. second row of Fig. 4

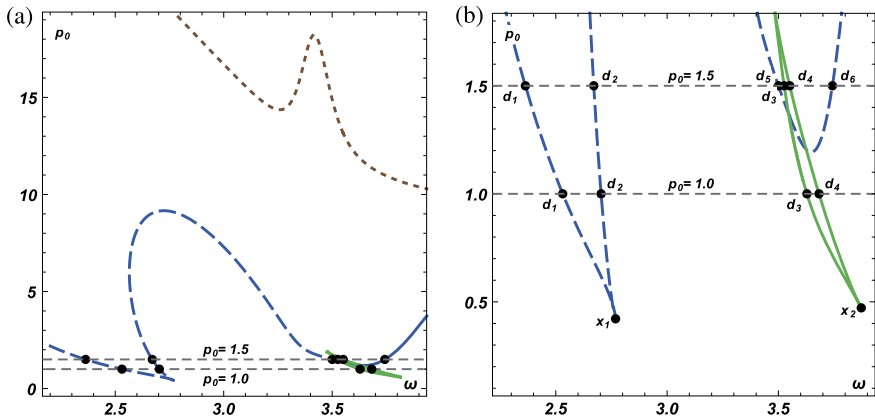


Fig. 6 (a) Position of zeroes of the Jacobian in the (ω, p_0) plane. Three different zero curves are shown as *solid, dashed and dotted lines*. (b) Zoomed view of the interesting area for $p_0 \in (0, 2)$ of figure (a). Points d_1, \dots, d_6 are indicated on the level of $p_0 = 1$ and $p_0 = 1.5$, cf. Figs. 4 and 5. Points x_1 and x_2 show the critical values of p_0 computed using Eqs. (20)–(21)

Existence of the unstable branches could serve as a characteristic of the system from the engineering point of view. It can be stated, that until the system properties (structural parameters) and the expected excitation amplitude are such that no unstable part of the resonance curve occurs, almost linear and stationary behaviour of the system can be expected. Positions of the dangerous values of the excitation amplitude p_0 depending on the excitation frequency are shown in Fig. 6. The overall situation for the system defined by values (19) is shown in the left part of the figure (a), whereas the part of realistic expected amplitudes is shown in the part (b). Positions of points d_1, \dots, d_4 corresponding to the excitation amplitude $p_0 = 1$ and d_1, \dots, d_6 for $p_0 = 1.5$ are shown in the both parts of Fig. 6.

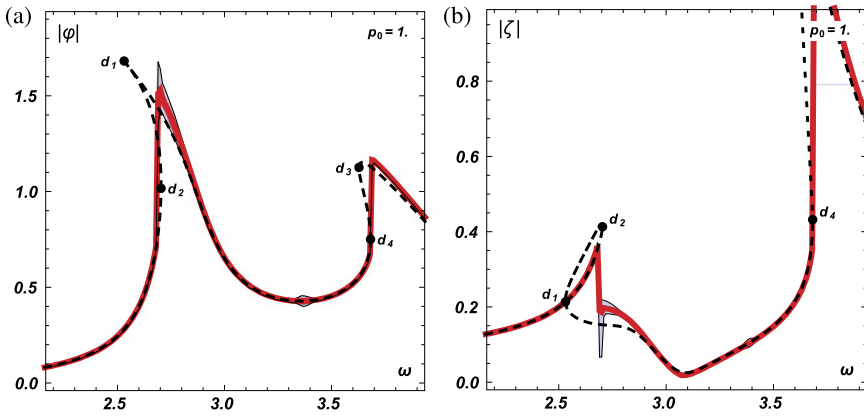


Fig. 7 Example of correspondence between stationary resonance curves computed using (14) (dashed curves) and response characteristics obtained via numerical integration of (7a)–(7c) (solid). Absolute values of the maximum, minimum and mean peak responses of φ are shown on the left and for ζ on the right. Greyed area between minima and maxima curves shows the regions of non-stationary response

The curves from Fig. 6 can be relatively easily computed from the algebraic system

$$\begin{aligned} \det(\mathbf{JF}(\mathbf{X}, \omega)) &= 0 \\ \mathbf{F}(\mathbf{X}, \omega, p_0) &= 0 \end{aligned} \tag{20}$$

Having a solution of (20) for any particular value of ω and p_0 the curves can be considered as parameter dependent $\omega(s)$ and $p_0(s)$ and traced e.g. using the arc-length method. The extremal values are then such points $(\omega(s), p_0(s))$ that

$$\partial_s \omega(s_0) = \partial_s p_0(s_0) = 0 \tag{21}$$

To cover all the extremes, the relation (21) has to be used for all interesting solutions obtained from the system (20). For data defined by (19) are the critical values of the amplitude p_0 shown in Fig. 6 as points x_1 and x_2 . Corresponding critical values of p_0 are $p_{0,x_1} = 0.421$ and $p_{0,x_2} = 0.472$ for $\omega_{x_1} = 2.77$ and $\omega_{x_2} = 3.87$.

For sake of comparison, the non-linear resonance curve for $p_0 = 1$ is shown together with result of the frequency response relation, which has been obtained using numerical integration of the original system (7a)–(7c) for excitation amplitude $p_0 = 1$. As it can be seen from Fig. 7, the agreement is rather good. Relatively low non-stationarity can be seen as the greyed areas of the curve for ω just above points d_2 and d_4 . For other excitation amplitudes the graphs resemble Fig. 3 and thus are not shown here.

It appears, that increasing the excitation amplitude over a certain limit a domain of unstable chaotic response to deterministic excitation emerges. It does not reveal that this domain increases significantly when random instead of deterministic excitation is applied. Nevertheless a presence of chaotic response domain is for the sake

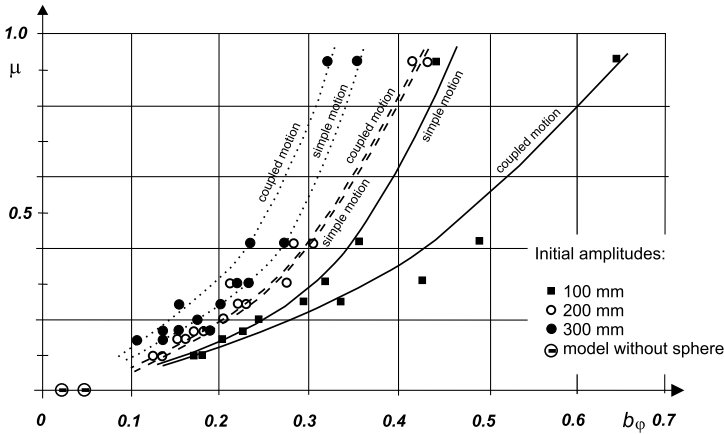


Fig. 8 Logarithmic decrement b_ϕ plotted against the mass-ratio μ for different initial amplitudes

of the structure, as the effective response amplitudes are decreasing under these circumstances due to the rapid increase of the entropy of the response probability density.

On the other hand it is necessary to remain realistic. During testing in laboratory many effects corresponding to various critical and post-critical effects have been observed which are not yet described and quantified theoretically.

5 Application of Basic Theory and Experiment

First of all two practical knowledge resulting from laboratory experiments and in situ measurements (see [8]) should be mentioned.

As regards the damping, the use of the logarithmic decrement as the measure of damping does not correspond very well to the non-linear nature of the phenomenon. However, a comparison of the behaviour of different physical models which were examined is very useful. Figure 8 shows the value of the logarithmic decrement b_ϕ of the model plotted against the absorber-mass ratio μ , see (7c). The model was put into vibration by initial deflection from its equilibrium position. In this figure diagrams for several values of initial displacement have been plotted. It can be seen that the model without ball ($\mu = 0$) has the damping nearly 0.02 (the point on the horizontal axis $\mu = 0$), while adding ball the damping reaches 0.17–0.25 (the points on the horizontal axis $\mu = 0.2$, curves valid for simple motion) i.e. nearly 8 times more. Similar effect appears also on conventional pendulum absorbers. For details, see [1].

The influence of inclination was also tested on the model, involving the case when the dish of the absorber exercises the rotation about the horizontal axis, coupled with its horizontal translation. The most unfavourable case was tested, i.e. when the frequency of dish inclination approaches the natural frequency of the ball rolling

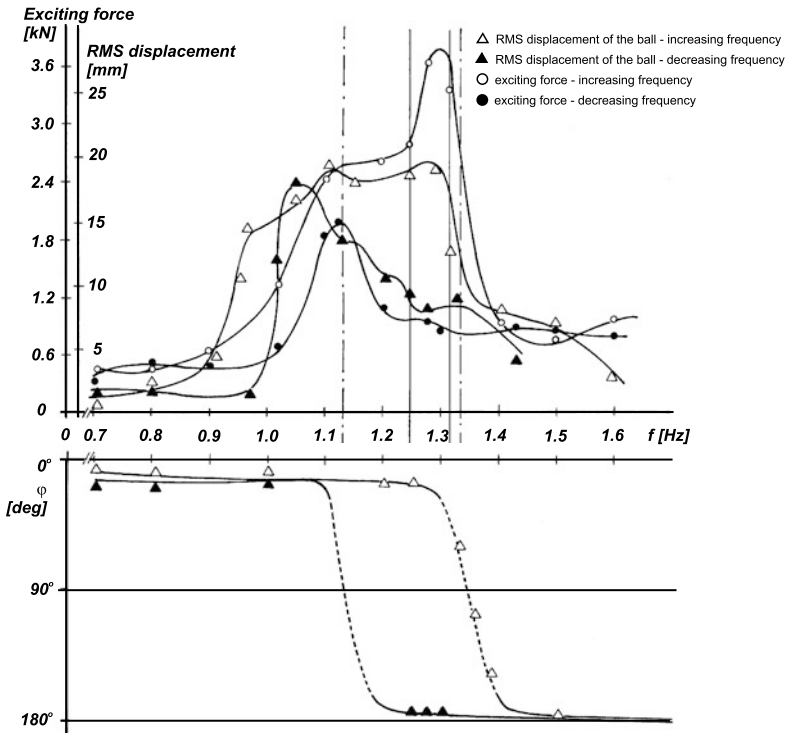


Fig. 9 Experimental resonance curves of exciting force and of ball m response

inside the dish (ω_m). No unfavourable increase of the amplitudes of the ball was observed.

The function and effectiveness of vibration ball absorber was described in detail in [2]. Now we shall describe the experiments made in the laboratory. The dish was fastened to a table supported by nine steel balls enabling the excitation of its movement by one, possibly two mutually perpendicular forces. The forces were supplied by one (uniaxial excitation) or two (biaxial excitation) MTS cylinders (jacks) via arms. The “position control” regime was selected in which the excited movement displacement was constant within a frequency range $\omega \in (4.40\text{--}9.40 \text{ s}^{-1})$. Excitation force amplitude was variable being a function of excitation frequency. Two series of experiments have been done. The first one with the internal side of the dish with rubber covering layer and the second one without this covering.

During the excitation by one harmonic force, the excitation frequency was varied within the range $\omega \in (4.40\text{--}9.40 \text{ s}^{-1})$ in steps of $\Delta\omega = 0.5$, and in the resonance domain in steps of $\Delta\omega = 0.25$. The duration of one step was 30 seconds, the transition from one step to another 15 seconds. Seven amplitudes of table displacements ranging from 1 mm to 7 mm were applied. As an example (table displacement amplitude $u_o = 4 \text{ mm}$), Fig. 9 shows the resonance curves of the ball m and dish movement depending on frequency of the excitation force, when the dish is without rubber

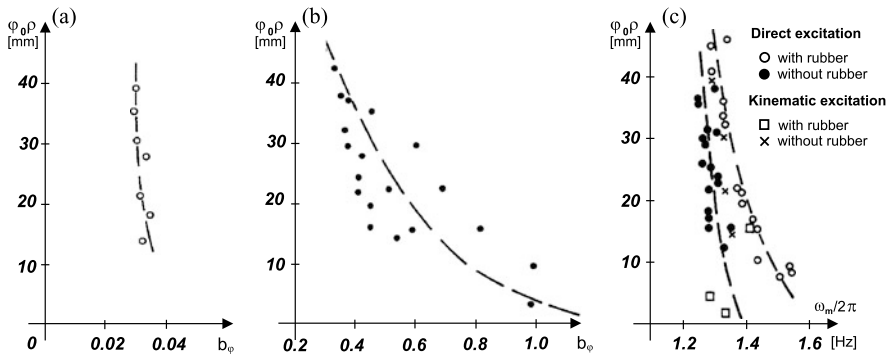


Fig. 10 (a) and (b) Relation of logarithmic decrement b_φ and amplitude $\varphi_0 \cdot \rho$ of the ball m . (c) Relation of natural frequency ω_φ and amplitude $\varphi_0 \cdot \rho$ of the ball m

coating (another plot applies for the state with coating). Figure 9 shows also the phase shift of the ball and the dish displacement in the excitation direction, once again for the increasing as well as decreasing excitation frequency, see the bottom part in Fig. 9. Two jumps of phase shift (increase or decrease) within the range $(0-2\pi)$ can be observed in a neighbourhood of the frequency corresponding with the biggest excitation force values.

The ball, although subjected to uniaxial excitation, performed a movement which comprised also a component deviating from the direction of excitation. This complex 3D ball movement appeared in the dish without rubber lining. The response spectrum contains peaks different from excitation frequency, particularly outside the resonance domain and corresponding rather with multiples of the natural frequency of the linearized system. It is another evidence of significant non-linear character of the system, which manifests this time by super-harmonics of the response.

Relation of logarithmic decrement of the damping and the amplitude $\varphi_0 \cdot \rho$ of the dish is presented in Figs. 10a, 10b, while the relationship of the natural frequency of the ball (moving on steel and on rubber coating respectively) on the amplitude $\varphi_0 \cdot \rho$ has been outlined in Fig. 10c.

6 Practical Realization

The ball absorber was used recently on two TV towers in the Czech Republic to suppress wind excited vibration (Figs. 11a, 11b). Both towers under observation showed two dominant natural frequencies before absorber has been installed $\omega_{(1)} = 7.98 \text{ s}^{-1}$, $\omega_{(2)} = 10.68 \text{ s}^{-1}$ (nearly identical for both towers). Corresponding natural modes and the amplitude of vibration in wind of mean velocity 8–15 m/s are plotted in Fig. 11c. The response amplitude at the top of the tower is 10.65 mm, while that at the RC platform level 0.273 mm. Four legs of the steel lattice part were recently strengthened.

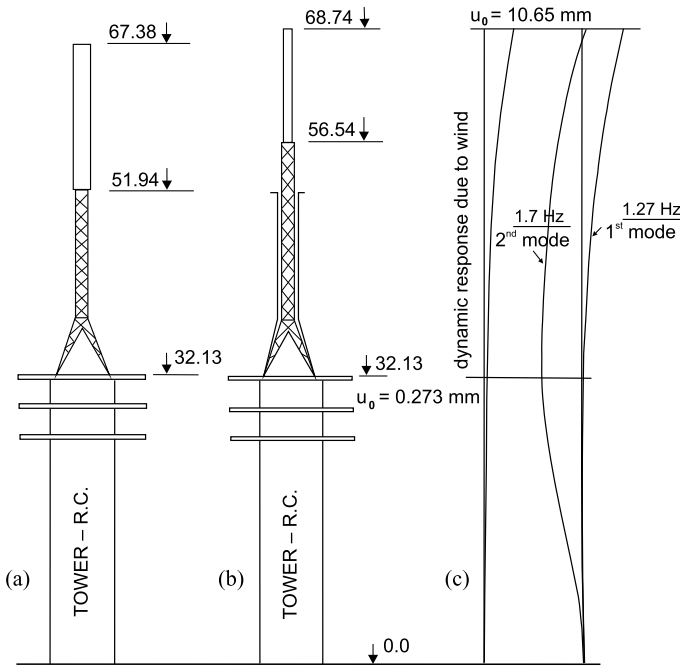


Fig. 11 TV towers, their two lowest natural modes and amplitudes of wind induced vibrations

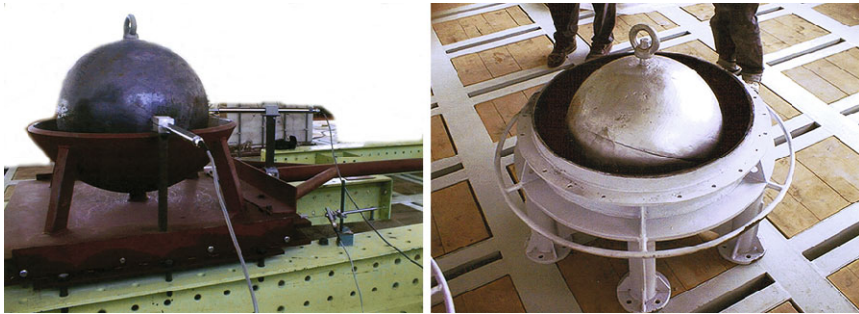


Fig. 12 Ball absorber intended for a TV tower

The ball absorber before the mounting on the top of the tower presents the photo in Fig. 12. The most important numerical results demonstrating the absorber efficiency in dimension-less values are outlined in Table 1. The efficiency has been evaluated for the most important frequencies using records of the long term measurements. For evaluation of absorber efficiency the following parameters has been introduced:

$$\varepsilon_x = \frac{f \cdot G_x(f)}{\sigma_x^2}; \quad \varepsilon_y = \frac{f \cdot G_y(f)}{\sigma_y^2} \quad (f = \omega/2\pi)$$

Table 1 Ball absorber efficiency

Frequency (Hz/s ⁻¹)	Without absorber		With absorber		Ratio with/without absorber	
	X	Y	X	Y	X	Y
0.90/5.65	0	0.0948	0	0.2031	–	2.14
1.27/7.98	19.064	3.279	0.271	0	0.0142	–
1.70/10.68	0	7.382	0	0.466	–	0.0632

$X = f \cdot G_x(f)/\sigma_x^2; \quad Y = f \cdot G_y(f)/\sigma_y^2$

$G_x(f)$, or $G_y(f)$ power spectral density of the tower top displacement in directions x , or y ;
 σ_x^2 , or σ_y^2 RMS of the tower top displacement in respective directions x , or y .

The scale of the response is presented in a form of a comparison of the values $\varepsilon_x, \varepsilon_y$ valid for the state without absorber (columns 2 and 3) and with absorber (columns 4 and 5), while columns 6 and 7 represent ratio of with/without absorber for respective directions. In particular, both columns 6 and 7 demonstrate high efficiency of the installed vibration absorber of ball type.

7 Conclusions

The vibration absorber of a ball type has been introduced. The basic Lagrangian analytical theory of non-linear behaviour has been done. Very wide numerical investigation reveals that the non-linear character of this device is an important factor influencing significantly its dynamic properties and practical efficiency. It turns out, that the non-linear character making the form of resonance curves dependent on the excitation amplitude leads to better efficiency in comparison with linear mechanism. For the same reason also chaotic component of the response can occur in certain frequency domains which increases significantly the efficiency of this device due to higher energy loss. Laboratory tests of a ball vibration absorber with the dish without and with rubber coating have demonstrated several aspects of real operation of the damper. They have also proved the effectiveness of the damper and the influence of the rubber coating. With respect to laboratory tests and long-term in situ measurements can be concluded that the ball vibration absorber is a simple nearly maintenance free low cost device with very small vertical dimensions. For these properties it is very convenient for application especially in cases when broad band excitation of random character prevails and when very limited space is available.

The same experiments gave many results demonstrating various processes of stability loss and transition into various post-critical states under certain conditions. These phenomena remained without adequate theoretical explanation and without

any assessment of influence onto damping properties. Therefore an intensive theoretical investigation should be provided. Detailed stability analysis is necessary to enable a reliable description of post-critical regimes, bifurcation points and corresponding transition effects involving the damping process. Also random parametric excitation and stochastic imperfection influence should be carefully studied.

Acknowledgements A kind support of the Czech Scientific Foundation No. 103/09/0094, Grant Agency of the ASCR Nos. A200710902, A200710805 and RVO 68378297 institutional support are gratefully acknowledged.

References

1. Pirner M (1994) Dissipation of kinetic energy of large-span bridges. *Acta Tech CSAV* 39:407–418
2. Pirner M, Fischer O (2000) The development of a ball vibration absorber for the use on towers. *J Int Assoc Shell Spat Struct* 41(2):91–99
3. Hamel G (1978) *Theoretische Mechanik*. Springer, Berlin
4. Tondl A (1994) *Quenching of self-excited vibrations*. Academia, Prague
5. Xu Z, Cheung YK (1994) Averaging method using generalized harmonic functions for strongly non-linear oscillators. *J Sound Vib* 174(4):563–576
6. Ren Y, Beards CF (1994) A new receptance-based perturbative multi-harmonic balance method for the calculation of the steady state response of non-linear systems. *J Sound Vib* 172(5):593–604
7. Náprstek J, Fischer C (2009) Auto-parametric semi-trivial and post-critical response of a spherical pendulum damper. *Comput Struct* 87(19–20):1204–1215
8. Náprstek J, Pirner M (2002) Non-linear behaviour and dynamic stability of a vibration spherical absorber. In: Smyth A et al (eds) *Proceedings of the 15th ASCE engineering mechanics division conference*. Columbia University, New York, CD ROM, paper #150

Evaluation of Response of an Isolated System Based on Double Curved Surface Sliders

Chiara Casarotti, Marco Furinghetti, and Alberto Pavese

Abstract Nowadays, the use of seismic isolation within the Italian and European context is gaining more and more acknowledgement, thanks to the high level of protection from the earthquake damage which can be guaranteed. However, the installation of devices within complex structural systems may influence the actual response due to the random variation of the installation and operating conditions with respect to the theoretical model. It is then of paramount importance a proper assessment of the overall isolating system response, considering the variability of the construction conditions. The main objective of the present work is to study the response of a particular installation system for Double Curved Surface Sliders (DCSS) for buildings with large plan development in case of construction defects related to the non-perfect co-planarity of the devices. A case study is presented, in which the effects of randomly simulated construction defects are analyzed. Preliminary results showed that the simulated construction defects have only limited influence on the global hysteretic behaviour of the system and that the simultaneous loss of contact may occur only for a limited number of devices. On the other hand, the effects of the vertical and horizontal force redistribution may cause important increase of the actions locally induced in the base connecting slab and create an eccentricity of the resultant horizontal force.

Keywords DCSS · Curved surface sliders · Seismic isolation · Double friction pendulum · Construction defects · Variable boundary conditions

C. Casarotti (✉) · M. Furinghetti
European Centre for Training and Research in Earthquake Engineering, via Ferrata 1,
27100 Pavia, Italy
e-mail: chiara.casarotti@eucentre.it

M. Furinghetti
e-mail: marco.furinghetti@eucentre.it

A. Pavese
Structural Mechanics Department, University of Pavia, via Ferrata 1, 27100 Pavia, Italy
e-mail: a.pavese@unipv.it

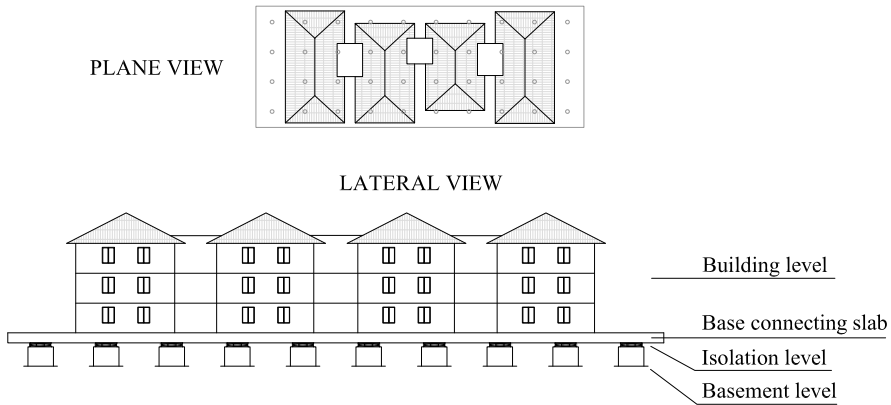


Fig. 1 Schematic model of the studied isolated system

1 Introduction

Nowadays, the use of seismic isolation within the Italian and European context is gaining more and more acknowledgement (e.g. Dolce et al. [1], Calvi et al. [2]). The recent coming into force of the European Code for antiseismic devices (CEN [3]) witnesses such increasing trend and highlights the importance of a major attention to all the aspects related to the response of the installed isolators.

Concerning the response of friction devices, a number of studies has been formerly conducted on curved surface sliders with single sliding surface (Tsopeles et al. [4], Almazan and De La Llera [5–7], Benzoni and Casarotti [8], among the others), and then on the most recent double and triple sliding surfaces sliders (Constantinou [9], Fenz and Constantinou [10, 11]). Such studies highlighted features and advantages of the technology, from the theoretical, modelling and experimental point of view, at least concerning the radial motion of the single device.

However, the installation of complex isolation systems and the actual operating conditions of installed devices often differ from the ideal theoretical model. In particular, when several devices are installed to work in parallel, the possibility of random variations in the installation conditions of each single device may arise issues regarding the response of the isolation system as a whole.

The main objective of the present endeavour is to study a particular isolation scheme for buildings with large plan development (i.e. systems consisting of several isolators supporting a base connection slab upon which the building is located, Fig. 1), in order to evaluate the influence of defects related to non-parallel sliding surfaces. Such kind of defects can be generated by phenomena of deferred concrete creep or simply by construction errors: if isolators sliding plates are non perfectly horizontal, for a given slab displacement each device will encounter a differential vertical displacement: as a consequence, some device can loose contact and localized stresses can be induced in the slab. This in turn causes a redistribution of the vertical reactions and consequently of the horizontal forces throughout the whole system.

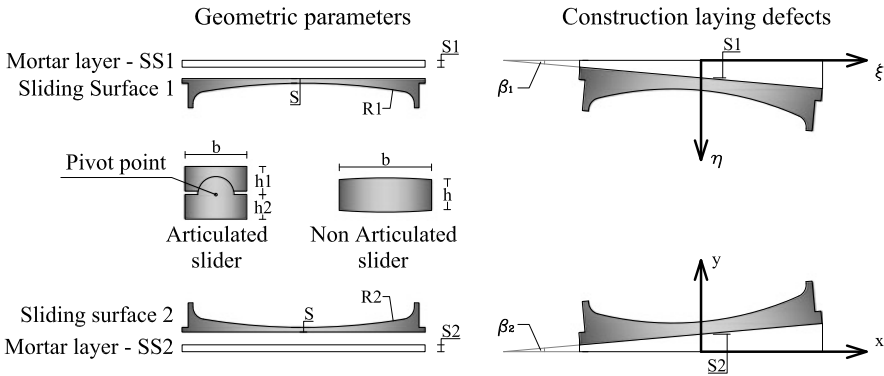


Fig. 2 Base model (Fenz and Constantinou [10], *left*), and geometric scheme for the model with non-articulated slider and construction laying defects (*right*)

Firstly, a geometrical model of the single isolator has been defined, analyzing the geometry of each component, in order to obtain the value of the vertical displacement of the device for a given value of horizontal displacement. Subsequently, the interaction among the different devices and the base slab has been modelled, by developing a f.e.m. code able to simulate the varying conditions of the system (contact-no contact condition). Finally, a case study is presented, in which construction defects have been simulated randomly on the different isolators for a large number of analysis, in order to evaluate the consequences of construction laying defects at both global and local level.

Preliminary results showed that the simulated construction defects have only limited influence on the global hysteretic response of the system, and that the simultaneous detachment of isolators during the motion occurs only for a limited number of devices. On the other hand, the effects of the vertical and horizontal force redistribution may cause important increase of the actions locally induced in the slab (in terms of shears and bending moments) and create a global torsion effect on the system, due to the eccentricity of the horizontal resultant force.

2 Mechanical Model for Double Curved Sliding Surface Isolator with Non-articulated Slider and Non-parallel Sliding Surfaces

The Double Curved Surface Slider (DCSS) consists of two stainless-steel concave sliding surfaces, each characterized by a curvature radius R_1 and R_2 , separated by an articulated slider which allows differential rotations of the upper and lower part of the slider (Fig. 2, left). The two sliding interfaces can feature different dynamic friction coefficients μ_1 and μ_2 . In some device, the slider can be non-articulated.

As well described in [9, 10], the equivalent oscillation period of the device is a function of the curvature radii of the surfaces and of the dimension of the slider:

$$T = 2\pi \sqrt{\frac{R_{eq}}{g}} = 2\pi \sqrt{\frac{R_1 + R_2 - h_1 - h_2}{g}} \quad (1)$$

When the device is installed, two layers of mortar constitute the interface between the device and the construction system in which it is installed. If such layers are not perfectly plane, issues may rise related to non-parallel sliding surfaces of the device.

In the present work, the model for the DCSS isolator with non-articulated slider and construction defects is developed, based on the plane model of the DCSS with articulated slider studied by Fenz and Constantinou [9, 10].

In the developed geometrical model, no relative rotation between the two units of the slider is imposed, while the construction laying defects are modelled in terms of non-perfect planarity of the layers of mortar, i.e. as inclinations β_1 and β_2 of the sliding surfaces with respect to the horizontal direction (Fig. 2, right).

The developed geometrical model allows to obtain the vertical displacement of the isolator upper surface as a function of the total horizontal displacement u between the two sliding surfaces, and of the two angles.

The inclinations of the sliding surfaces are described in terms of change of coordinates of the respective centre of curvature. The new coordinates of the sliding surfaces centres, in the respective reference system (Fig. 3), are expressed as:

$$\begin{cases} C_1^{\xi\eta} = [(s + R_1) \sin \beta_1; s_1 + (s + R_1) \sin \beta_1] \\ C_2^{xy} = [(s + R_2) \sin \beta_2; s_2 + (s + R_2) \sin \beta_2] \end{cases} \quad (2)$$

Referring to Fig. 3, the angles θ_1 and θ_2 of the axis of the two units of the slider with respect to the vertical axis are expressed as:

$$\begin{cases} \vartheta_1 = \arcsin\left(\frac{u_1 - C_{1\xi}}{R_1 - h_1}\right) \\ \vartheta_2 = \arcsin\left(\frac{u_2 - C_{2x}}{R_2 - h_2}\right) \end{cases} \quad (3)$$

where C_{1x} and C_{2x} are the x -coordinates of the sliding surfaces centres, and u_1 and u_2 the relative horizontal displacement between the sliding surfaces and the pivot point (Fig. 3).

By imposing equal to zero the relative rotation of the two axis of the units composing the slider (i.e. $\theta_1 = -\theta_2$), and with the relation among both the relative displacements u_1 and u_2 and the total horizontal displacement u_{TOT} ($u_2 - u_1 = u_{TOT}$), a linear system is obtained, which allows to express the values of u_1 and u_2 as a function of u_{TOT} and of the geometric characteristics of the device:

$$\begin{cases} u_1 = \frac{C_{1x}(R_2 - h_2) + C_{2x}(R_1 - h_1)}{R_1 + R_2 - h_1 - h_2} - u_{TOT} \frac{R_1 - h_1}{R_1 + R_2 - h_1 - h_2} \\ u_2 = u_{TOT} + u_1 \end{cases} \quad (4)$$

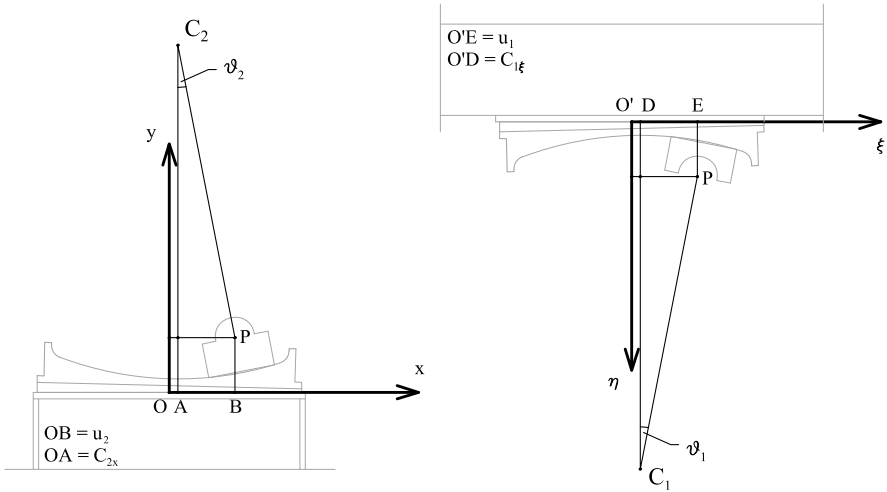


Fig. 3 Construction laying defects: definition of the relative displacements

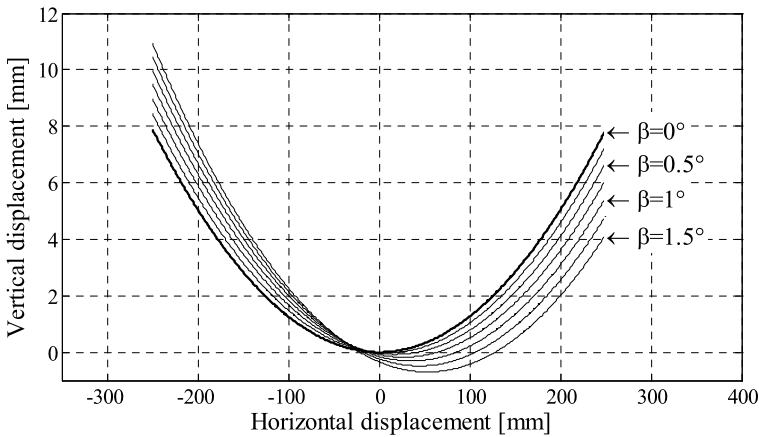


Fig. 4 Example of vertical displacements versus horizontal displacements for inclined upper plate

Once obtained u_1 and u_2 , the height of the extrados of the device can be calculated with the equations of the circumferences modelling the two sliding surfaces. Figure 4 shows an example of the profiles of vertical displacement versus horizontal displacement for the device considered in the case study of the next paragraphs, for different inclinations of the upper surface (i.e. with $\beta_1 \neq 0$ and $\beta_2 = 0$).

To compute the force response of the isolator, a standard hysteretic model has been implemented (e.g. [9, 10]), in which the force is a function of the displacement, the vertical load, the equivalent radius of curvature and the friction coefficient.

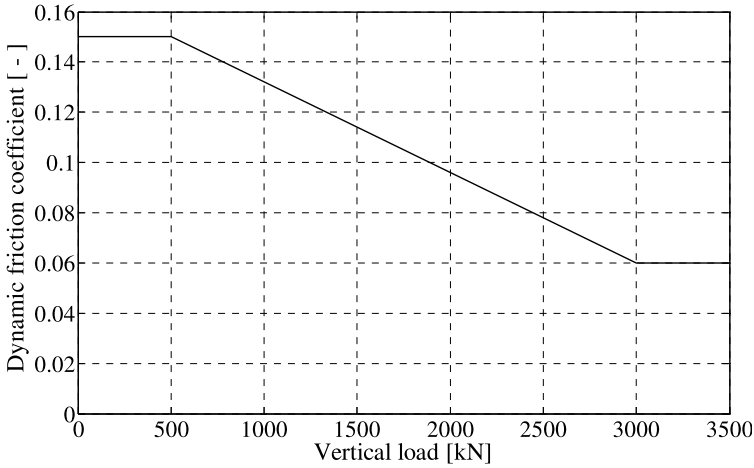


Fig. 5 Dynamic friction coefficient-vertival load variation curve

cient. Since it is well known that for common sliding materials, the friction coefficient μ is a decreasing function of the acting pressure [11], a simplified relationship for the variability of the dynamic friction coefficient as a decreasing function of the vertical load has been assumed (Fig. 6), based on the several tests carried out at the EUCENTRE TREES Lab (Pavia, Italy) on full scale devices. At this stage of the work, the curve has been assumed linear for sake of simplicity.

3 The Variable Boundary Condition Code (VBC)

The interaction among the different devices and the base slab has been modelled, by developing a f.e.m. code able to simulate the varying contact-no contact condition of the isolators (Variable Boundary Conditions code, VBC).

The code flowchart is illustrated in Fig. 6: at each loading step, devices still in contact and devices which have lost contact are identified, and the total system stiffness matrix is accordingly updated at each new configuration.

The first step of the program is the analysis of the system configuration corresponding to zero horizontal displacement. Using for each device the geometric model shown in the previous paragraph, the ideal situation of infinitely rigid slab is first studied, with an algorithm able to identify the plane determined by the three devices containing the vertical resultant application point, and with z -coordinate equal or greater than the other isolators (i.e. the three isolators bearing the infinitely rigid plate). Starting from the ideally rigid slab condition, the real deformation of the plate is then obtained by the implementation of the finite element problem: modelling the plate with its actual stiffness, the vertical load is applied by steps, checking that reactions are purely compressive and that there is no penetration between the plate and

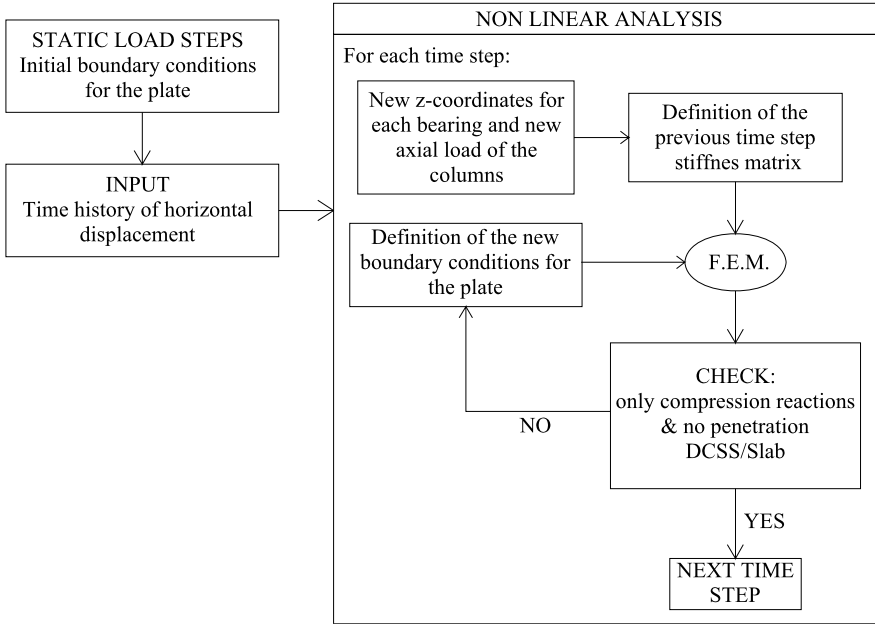


Fig. 6 Flowchart of the VBC code

the isolators. Once defined the zero-displacement deformed shape, the horizontal displacement is stepwise applied to the slab, considering the effects of a simplified dynamic interaction of the building, as described in what follows.

3.1 Modelling Detail

The weight of the plate is considered as evenly distributed over the entire surface, while the loads (static and dynamic) transmitted by the building are modelled in terms of concentrated vertical forces imposed to the isolated slab, according to the influence area of each building column. The dynamic response of the system has been represented in a simplified way, by imposing a sinusoidal displacement time history directly to the isolated plate, simulating the dynamic testing of the system. The period of the input waveform is equal to the oscillation period of the isolation system, calculated as a function of the equivalent radius of the devices.

The dynamic interaction between the building and the isolation system has been simulated by considering the isolated building as an equivalent SDOF of given mass and period. The total base shear V_b is estimated by integrating the equation of motion of a SDOF oscillator of an assumed equivalent height h_{eq} . The generated overturning moment M_{OVI} is computed and used in turn to obtain the axial load variation

Fig. 7 Overturning moment and axial load variations *x*-direction analyses

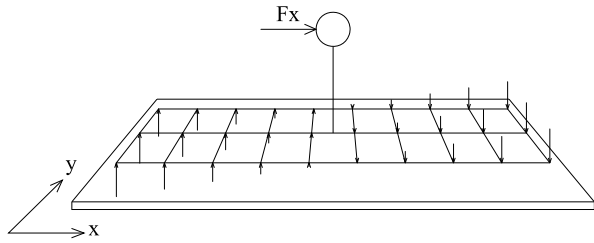
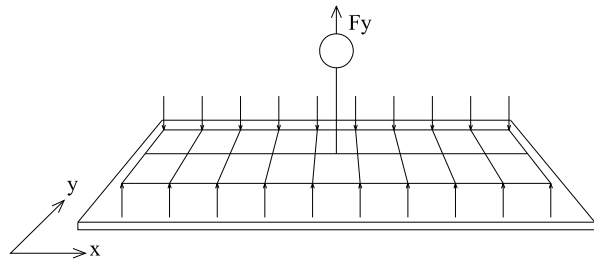


Fig. 8 Overturning moment and axial load variations *y*-direction analyses



P_i on the building columns acting on the slab for the *x* and *y* motion directions, respectively (Figs. 7 and 8):

$$M_{ovt}(t) = V_b(t)h_{eq} \tag{5}$$

$$P_{i-x_{motion}} = \frac{M_{ovt}(t)}{\sum x_j^2} x_i \tag{6}$$

$$P_{i-y_{motion}} = \frac{M_{ovt}(t)}{\sum y_j^2} y_i$$

where x_i, y_i are the coordinates of the columns, measured with respect to the centre of mass of the building. For each value of horizontal displacement and axial load variation, the new z_i coordinates of the isolators are calculated based on the described DCSS model and imposed to the plate only for the isolators still in contact at the previous time step (i.e. corresponding to the compression reactions). Then, boundary conditions are newly updated, considering at each iteration only the isolators still in contact. According to the axial load acting on each isolator and to the actual position, the corresponding reaction force is step by step computed for each device.

4 Case Study

The analyzed case study consists of a reinforced concrete frame structure, built on a slab of thickness 0.5 m, placed on a grid of 10 by 4 DCSS isolators with non-articulated slider. The plan view and a section of the system is shown in Fig. 9. The weight of the plate is 12.5 kN/m², while the building static vertical loads on the base

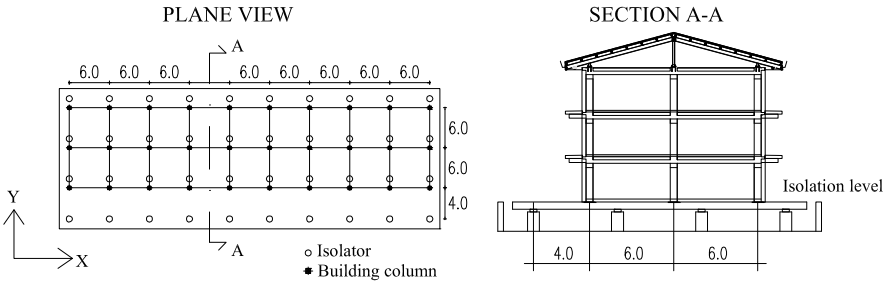


Fig. 9 Schematic view of the studied isolating system

Table 1 Static vertical load transmitted by the building columns on the base slab [kN]

Corner column	Edge column	Internal column
280.4	560.8	1121.6

slab are listed in Table 1, according to the position of the building columns. The geometric and mechanic characteristics of the DCSS are shown in Table 2 (geometric quantities refer to Fig. 2).

The input for the analysis is a sinusoidal displacement imposed to the plate (simulating the dynamic testing of the system, [12]), with amplitude of 260 mm and period of 4 s, i.e. equal to the system design displacement and isolation period, respectively. For the dynamic interaction, the building has been modelled as a SDOF with period equal to 0.48 s, 5 % damping, and h_{eq} of about 7 m (2/3 of the height).

The construction laying defects have been simulated by considering for each device the sliding surface inclinations β_1 and β_2 (Fig. 2) as varying parameters, randomly selected within an established range of variation, for a total of 135 and 125 configurations in the x and y direction of motion analysis, respectively. In order to maintain the maximum generality and to minimize the imposed a priori information, parameter distributions have been assumed uniform and independent. Wide variation ranges were intentionally considered ($\pm 1.5^\circ$, which is far beyond the allowed installation tolerances) in order to evaluate the consequences in extreme conditions: an inclination of 1.5° corresponds to a total offset of almost 2 cm over a length of 70 cm, which is the order of magnitude of the isolator base.

Table 2 Geometric characteristics of the isolator

$R_1 = R_2$	$s_1 = s_2$	b	h	s	$\mu_1 = \mu_2$
2024 mm	15 mm	335.44 mm	66.31 mm	20 mm	Variable with vertical force

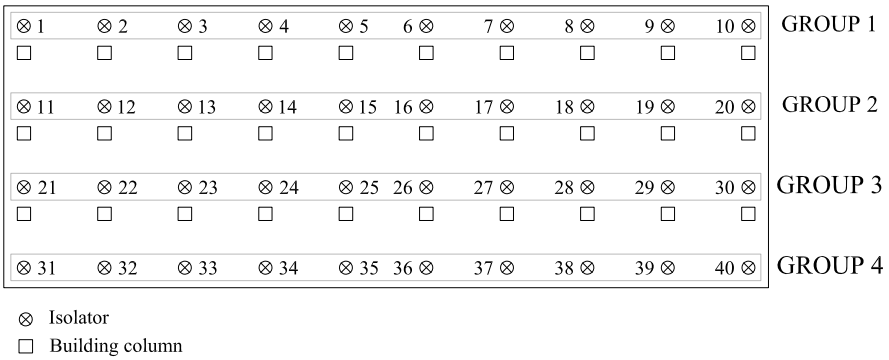


Fig. 10 Nomenclature of the devices

5 Numerical Results

Results are presented in comparison to the reference configuration 0, which is the ideal situation with isolators having perfectly horizontal sliding plates. At a global level, results are shown in terms of analysis of devices which loose contact, of global hysteretic response of the system and of eccentricity of the horizontal resultant force, while at a local level the variation of vertical loads and the moments induced in the slab are analyzed. The isolators labels and groups are illustrated in Fig. 10, according to their position with respect to the building columns. For the considered case study, it has been seen that isolators belonging to the same line (groups 1 to 4, Fig. 10) feature similar response.

5.1 Global Response

Figures 11 and 12 show the number of devices which simultaneously lost contact at each value of horizontal displacement, for the x and y direction of motion, respectively: averagely less than 5 DCSS out of 40 have lost the contact at the maximum displacement.

Figures 13 and 14 show, for the motion in the x and y direction, the rate of contact loss of each device during the analyses, i.e. the rate of the cases in which an isolator loses contact at least once during motion: it is evident the similar response of isolators belonging to the same alignment. This is due to the position of the building: the most external line (group 4) has in fact the highest probability of detachment, while group 2, which is the closest line to the building centre of mass, is the most stable.

Table 3 shows the values of frequency of contact loss per group of isolators at the maximum displacement, across all the analyses.

The total base shear as a function of the horizontal displacement is shown for both directions of motion in Fig. 15: the effects of the construction errors result in a

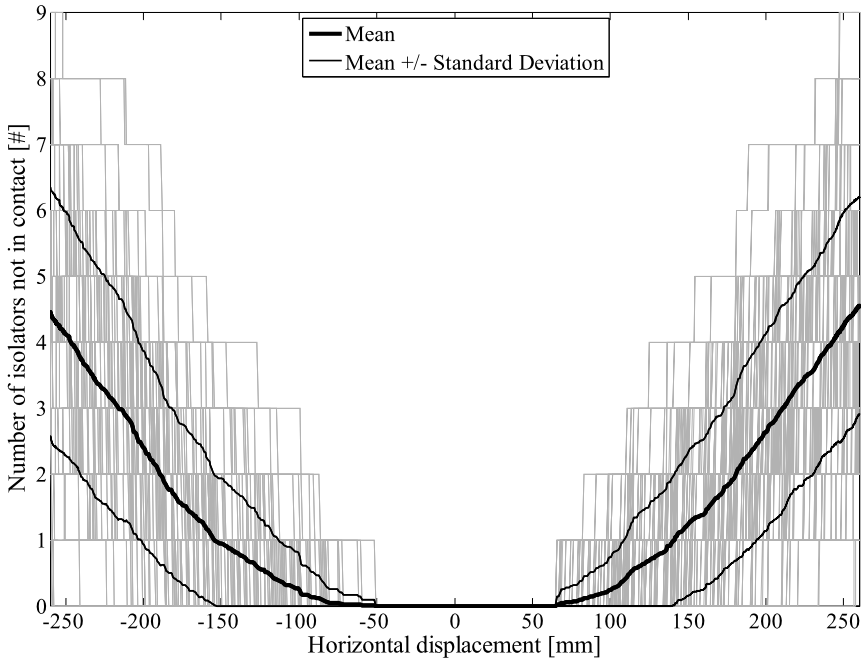


Fig. 11 Number of isolators simultaneously detached (motion in the x direction)

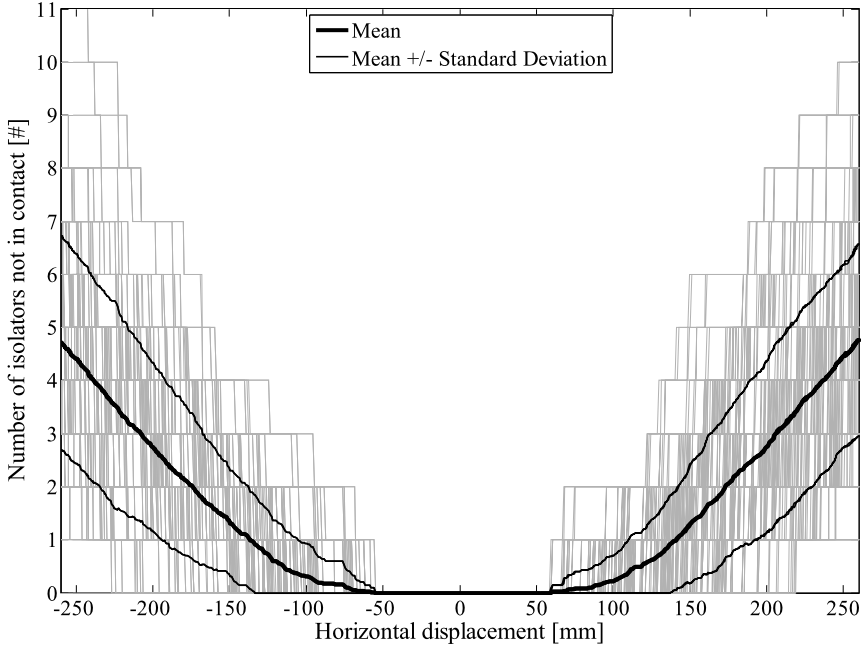


Fig. 12 Number of isolators simultaneously detached (motion in the y direction)

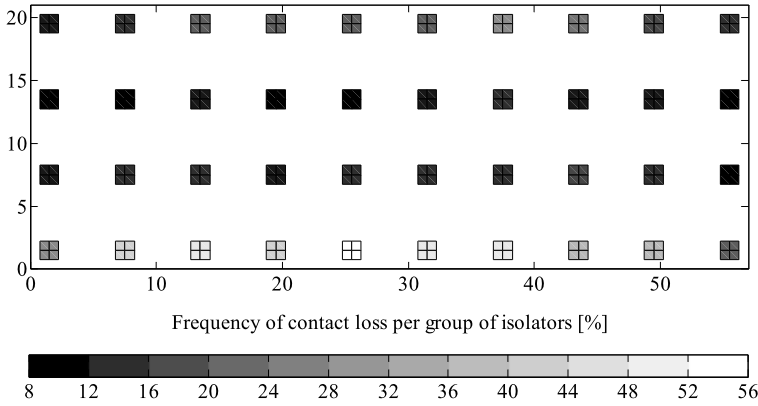


Fig. 13 Rate of cases in which an isolator loses contact at least once during the motion (*x* direction)

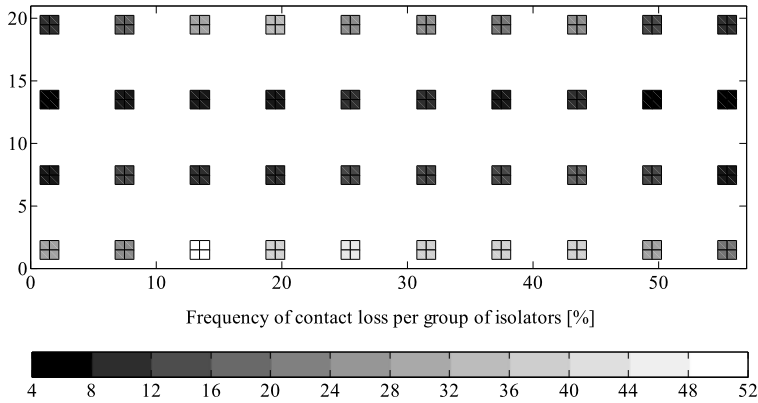


Fig. 14 Rate of cases in which an isolator loses contact at least once during the motion (*y* direction)

Table 3 Frequency of no-contact across all the analyses, at the maximum displacement

	Group 1	Group 2	Group 3	Group 4
Motion <i>x</i>	14.48 %	5.75 %	9.18 %	20.41 %
Motion <i>y</i>	13.56 %	6.44 %	9.28 %	23.12 %

limited reduction of the hysteresis loop. This is due to the redistribution of vertical loads among the isolators still in contact, which increase their reactions less than proportionally, due to the varying friction coefficient. Moreover, isolators not in contact do not contribute to the dissipative behaviour, globally resulting in a lower horizontal force resultant.

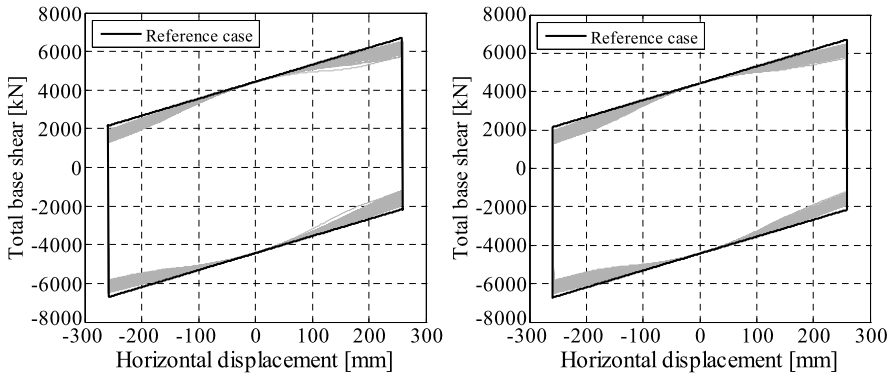


Fig. 15 Global hysteresis cycles for the x (left) and y (right) direction of motion

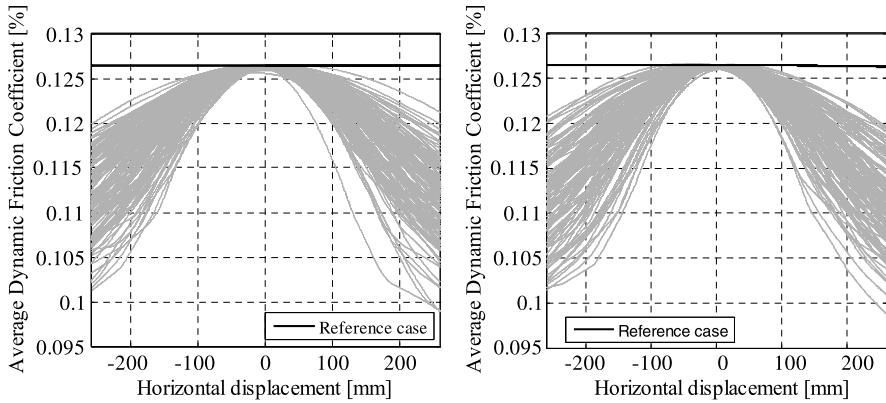


Fig. 16 Average dynamic friction coefficient for the x (left) and y (right) direction of motion

The same observation can be drawn observing the trend of the apparent global friction coefficient, idealizing the whole isolation system as an equivalent DCSS device with a weighted average dynamic friction coefficient. The average value of the dynamic friction coefficient μ_{av} has been calculated at each time step, according to the following equation:

$$\mu_{av}(t) = \frac{\sum_{i=1}^{N_{isolators}} \mu_i(V_i(t), t) \cdot V_i(t)}{\sum_{i=1}^{N_{isolators}} V_i(t)} \tag{7}$$

where $V_i(t)$ is the vertical reaction on the i -th device, and μ_i is the corresponding dynamic friction coefficient calculated according to the law illustrated in Fig. 5. In Fig. 16 the graphs of μ_{av} as a function of the horizontal displacement are reported for both the motion directions: due to the decreasing dynamic friction coefficient, the system base shear decreases at the maximum displacement, with respect to the reference configuration, resulting to be less dissipative.

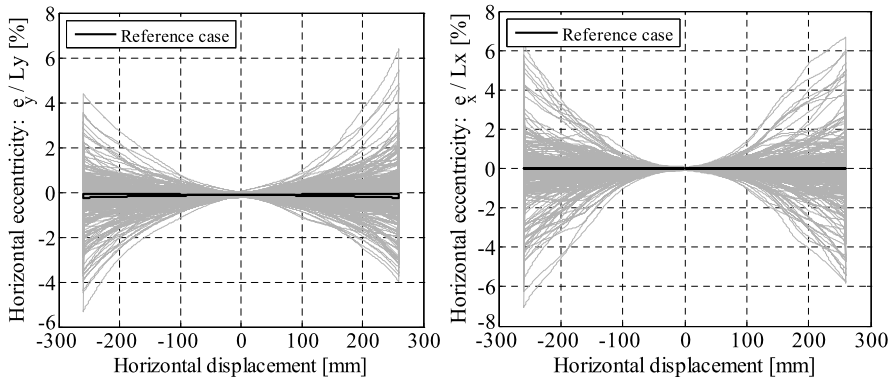


Fig. 17 Horizontal eccentricity for the x (left) and y (right) direction of motion

Finally, the horizontal eccentricity of the DCSS resultant reaction with respect to the system centre of mass has been roughly evaluated. Figure 17 illustrates the values of the eccentricity as a function of horizontal displacement. Values of eccentricity are normalized with respect to the related plan dimension of the base slab (L_x and L_y):

$$E_i = \frac{e_i}{L_i} [\%] \quad (i = x, y) \quad (8)$$

For both directions of motion, at the maximum displacement, the normalized maximum eccentricity is about the 7 %. It has to be noted that the considered motion is unidirectional and the device model is plane: in order to evaluate the importance of torsional effects, the actual eccentricity should be evaluated with a proper tridimensional model of the device.

5.2 Local Response

The vertical load variation for each device at the maximum displacement, for both the motion directions, is evaluated as:

$$\text{Var}_{ij} = \frac{V_{ij} - V_{i0}}{V_{i0}} [\%] \quad (9)$$

where V_{i0} represents the reaction at the i -th isolator of the reference case, and V_{ij} is the reaction of the j -th analysis. Figures 18 and 19 show the distribution of the vertical load variation for the four alignments of isolators. The histograms represent the rate of variation of the vertical reactions with respect to the reference case, and confirm what already observed. Because of the larger distance from the application point of the vertical load resultant, the outer rows of isolators, in particular group 4, are characterized by more dispersed axial load variations, thus by the highest frequency of contact loss, whereas internal groups (e.g. group 2) are less susceptible to

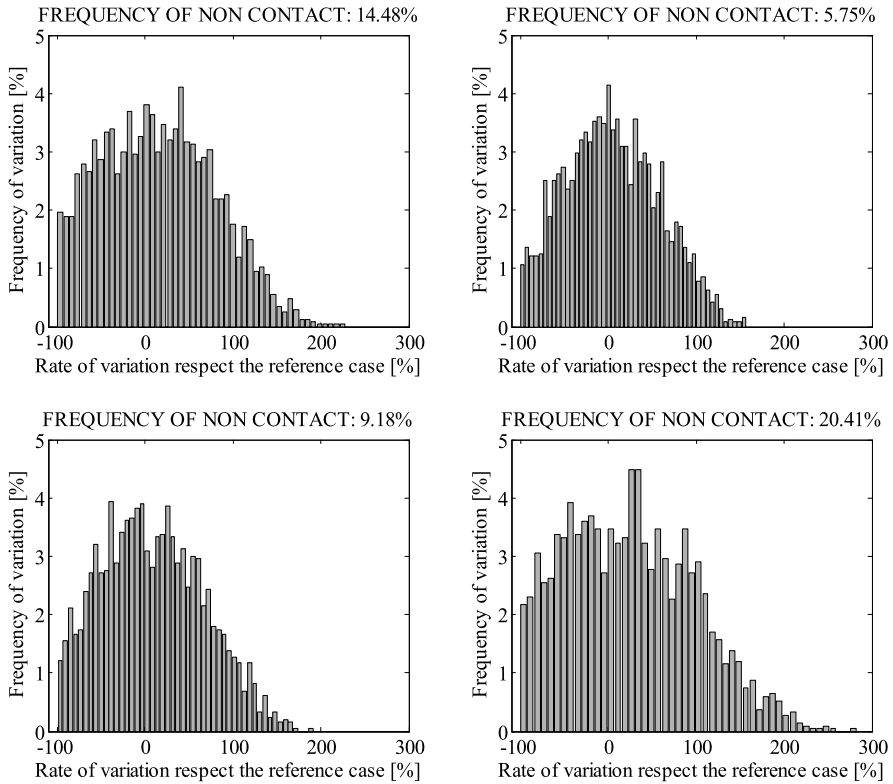


Fig. 18 Vertical load variations at maximum displacement, isolators rows 1 to 4 (x-motion)

important axial load variation and thus to detachment. It is possible to see that compressive load can increase more than twice with respect to the reference situation.

Figures 20, 21, 22 and 23 present the bending moments induced in the base slab at the isolator locations: results are shown for both the main bending moments and for the two directions of motion. It can be seen that the mean value and the reference value approximately coincide, but the actual values are greatly dispersed, especially for the internal alignments of isolators (from isolator #11 to isolator #30). This is due to the fact that, when an isolator loses contact, the plan dimensions of the corresponding slab field doubles, increasing the induced bending action. Such effect is more important for central devices since they are subject to larger vertical loads, but are not aligned to the central columns of the building.

6 Concluding Remarks

A particular isolation scheme for buildings with large plan development has been studied, consisting of a connecting base slab isolated by several DCSS devices upon

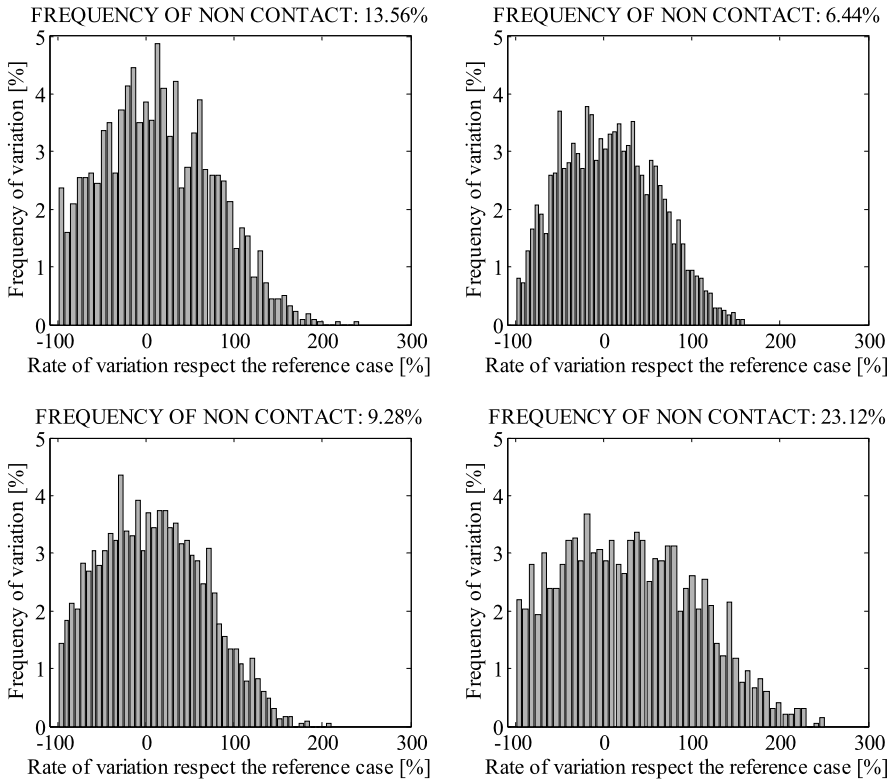


Fig. 19 Vertical load variations at maximum displacement, isolators rows 1 to 4 (y-motion)

which the structure is built. In particular, the possibility of construction laying defects of the isolators is analyzed, in order to evaluate the influence on the system response of non-parallel sliding surfaces and to estimate the related effects with respect to the idealized configuration with perfectly horizontal sliding surfaces.

In order to study the problem, a plan geometric model of a single device has been first developed, considering the real geometry of each component, and modelling the defects in terms of inclination of the two sliding surfaces of the device. A f.e.m. code has been implemented, able to simulate the interaction between the devices and the base slab upon which the building is constructed, including the variability of the boundary conditions of the plate in case of isolators losing contact during the motion.

A case study has been analyzed, with different configurations simulating random defects in the isolators. The inclinations of the sliding surfaces of each device constituted the varying parameters of the analyses, randomly selected within an uniform distribution range. Such a range has been assumed intentionally larger than admitted tolerances ($\pm 1.5^\circ$), in order to evaluate the consequences in extreme conditions. A total of 260 different configurations have been simulated, partly analyzed in the *x*-motion and partly in the *y*-motion.

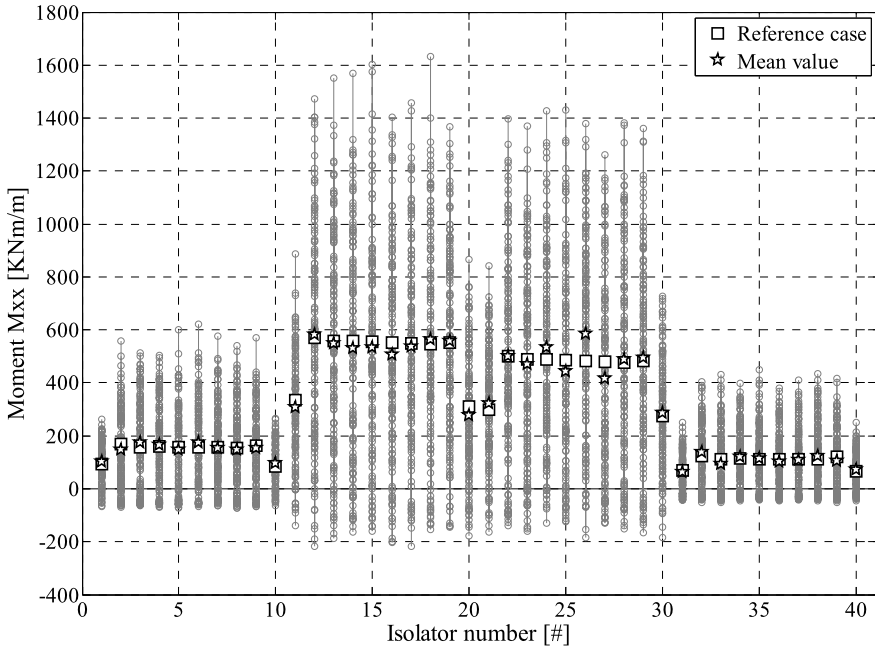


Fig. 20 Moment M_{xx} for each isolator (motion in the x direction)

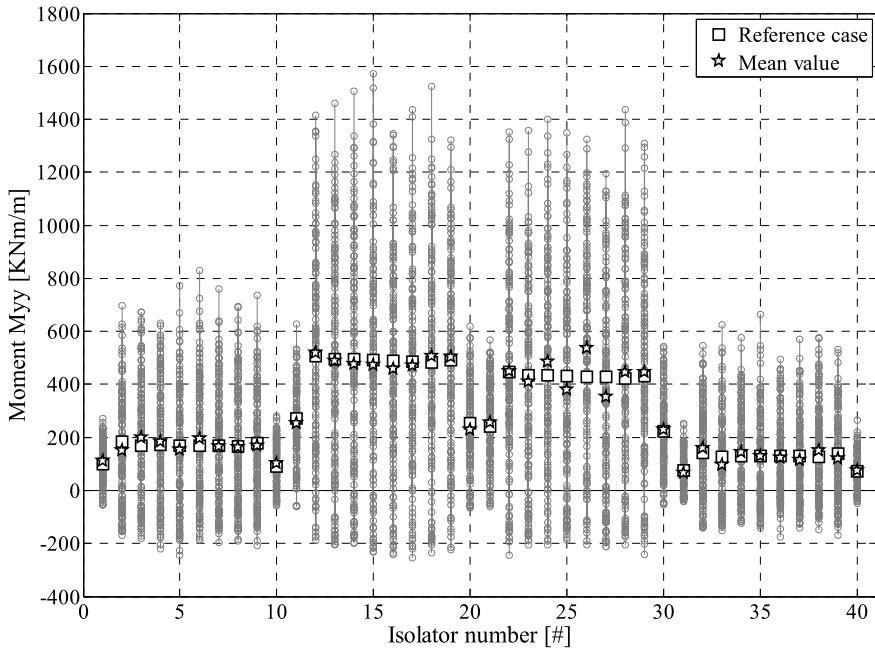


Fig. 21 Moment M_{yy} for each isolator (motion in the x direction)

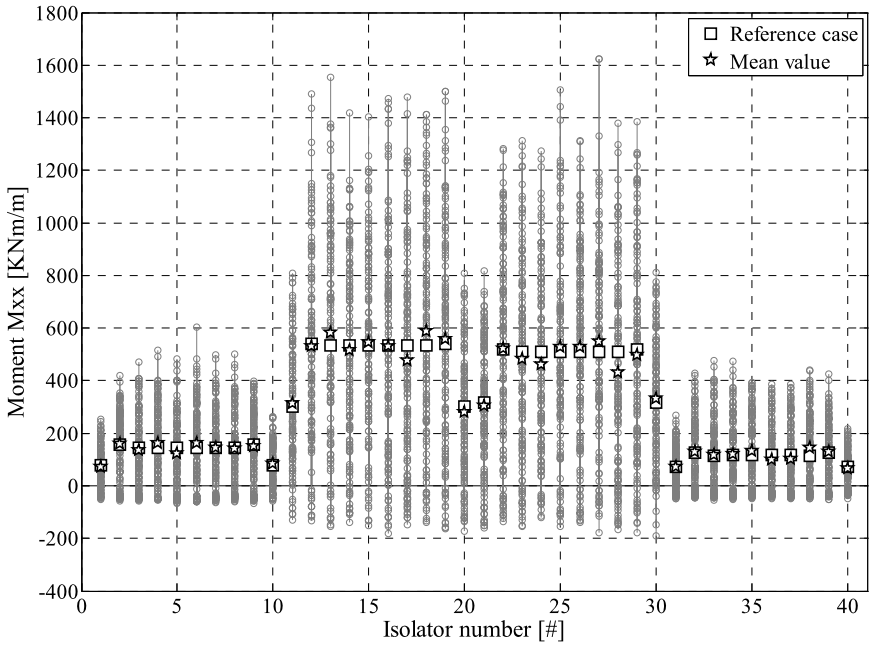


Fig. 22 Moment M_{xx} for each isolator (motion in the y direction)

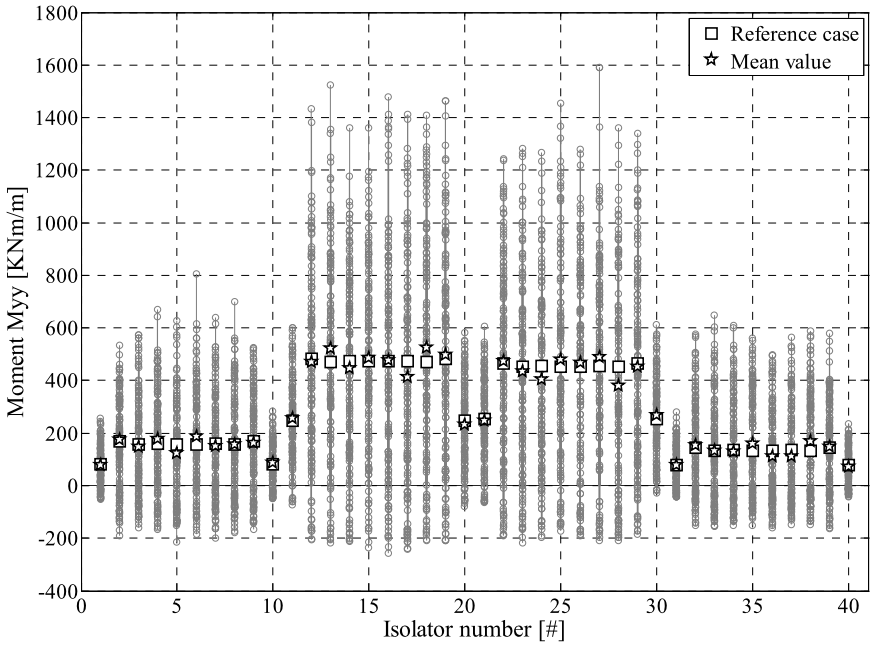


Fig. 23 Moment M_{yy} for each isolator (motion in the y direction)

The results of the numerical analyses showed that installation defects can influence the response of the isolated building more importantly at a local rather than at a global level. Results have been compared to the “ideal” reference case, corresponding to isolators with perfectly horizontal sliding surfaces. From the global point of view it was observed that:

- the dissipative behaviour is moderately reduced, due to the detachment of some device and to the redistribution of the vertical load among devices still in contact, considering the dependence of the friction coefficient on the vertical load. The average dynamic friction coefficient in fact decreases at increasing horizontal displacement.
- at the maximum displacement, the horizontal eccentricity of the system reaches values close to the 7 %. The actual effects of such eccentricity have still to be evaluated, with a proper tridimensional model of the devices, which is currently under development.
- the rate of devices losing contact during the motion is a function of the relative position of the isolator alignments with respect to the building. As expected, the rows of isolators close to the centre of mass of the building have the lowest probability of losing contact, while external rows are the most susceptible to detachment.
- for the considered case study, featuring some degree of asymmetry of the building location with respect to the plate, no more than 5 devices out of 40 loose contact simultaneously during the motion.

From the local point of view the analyses showed that:

- the construction defects may result in localized concentration of vertical loads on occasion importantly larger than those of the reference situation.
- the loss of contact of some device may result in important increase of the bending actions locally induced in the base slab.

From a merely structural point of view, the location of columns close to the devices would allow a more direct transmission of the vertical loads, thus reducing the risk of detachment of the isolators and the localization of important stress levels in the slab.

The natural development of the current endeavour is the implementation of a 3-D model of the DCSS isolator, to be employed in further analyses on a wider number of case studies, with different characteristics in terms of structural configurations, isolation scheme, plan development, number of storeys and materials.

Acknowledgements Part of the current work has been carried out under the financial support of the Italian Civil Protection, within the framework of the Executive Project 2008-2014 (Project e2—Bearings and isolation systems: characterization of existing typologies and development of innovative prototypes). Such support is gratefully acknowledged by the authors. The authors would also like to thank the Cariplo Foundation, for the contribution within the project 2008-2295.

References

1. Dolce M, Cardone D, Ponzo FC, Di Cesare A (2010) *Progetto di edifici con isolamento sismico*, 2nd edn. IUSS Press, Pavia
2. Calvi GM, Pietra D, Moratti M (2010) Criteri per la progettazione di dispositivi di isolamento a pendolo scorrevole. *Prog Sism* 3:7–30
3. CEN (2009) European code UNI EN 15129:2009, Anti-seismic devices
4. Tsopelas P, Constantinou MC (1996) Experimental study of FPS system in bridge seismic isolation. *Earthq Eng Struct Dyn* 25:65–78
5. Almazan JL, De La Llera C (2002) Analytical model of structures with frictional pendulum isolators. *Earthq Eng Struct Dyn* 31:305–332
6. Almazan JL, De La Llera C (2003) Physical model for dynamic analysis of structures with FPS isolators. *Earthq Eng Struct Dyn* 32:1157–1184
7. Almazan JL, De La Llera C (2003) An experimental study of nominally symmetric and asymmetric structures isolated with the FPS. *Earthq Eng Struct Dyn* 32:891–918
8. Benzoni G, Casarotti C (2008) Performance of lead-rubber and sliding bearings under different axial load and velocity conditions. Report SRMD2006/05-rev3, Department of Structural Engineering, University of California, San Diego, La Jolla
9. Constantinou MC (2004) Friction pendulum double concave bearing. NEES report. <http://nees.buffalo.edu/docs/dec304/FP-DC%20Report-DEMO.pdf>
10. Fenz D, Constantinou MC (2006) Behaviour of the double concave friction pendulum bearing. *Earthq Eng Struct Dyn* 35:1403–1424
11. Fenz D, Constantinou MC (2007) Spherical sliding isolation bearings with adaptive behavior: theory. *Earthq Eng Struct Dyn* 37:163–183
12. Costruttori for C.A.S.E. (2010) *L'Aquila il progetto C.A.S.E., complessi antisismici sostenibili ed ecocompatibili*. IUSS Press, Pavia

Numerical Investigation of the Effectiveness of Rubber Shock-Absorbers as a Mitigation Measure for Earthquake-Induced Structural Poundings

Panayiotis C. Polycarpou and Petros Komodromos

Abstract Very often, especially in densely-resided areas and city centers, neighboring buildings are constructed very close to each other, without sufficient clearance between them. Thus, during strong earthquakes, structural poundings may occur between adjacent buildings due to deformations of their stories. Furthermore, in the case of seismically isolated buildings, pounding may occur with the surrounding moat wall due to insufficient seismic gap at the base of the building. The current study presents a simple but efficient methodology that can be used to numerically simulate the incorporation of rubber layers between neighboring structures with relatively narrow seismic gaps in order to act as collision bumpers and mitigate the detrimental effects of earthquake-induced poundings. The efficiency of this potential impact mitigation measure is parametrically investigated considering both cases of conventionally fixed-supported and seismically isolated buildings subjected to various earthquake excitations. The results indicate that under certain circumstances the incorporation of rubber bumpers in an existing seismic gap can reduce the amplifications of the peak responses of the structures due to pounding.

Keywords Pounding · Mitigation · Shock-absorber · Bumper · Earthquake · Impacts

1 Introduction

Very often, especially in densely-resided areas and city centers, neighboring buildings are constructed very close to each other without sufficient clearance between them. Therefore, during strong earthquakes, structural poundings may occur between adjacent buildings, due to deformations of their stories. Consequences of such pounding incidences, ranging from local light damage to severe structural damage

P.C. Polycarpou · P. Komodromos (✉)
Department of Civil and Environmental Engineering, University of Cyprus, 75 Kallipoleos Str.,
P.O. Box 20537, 1678 Nicosia, Cyprus
e-mail: komodromos@ucy.ac.cy

P.C. Polycarpou
e-mail: ppanikos@ucy.ac.cy

Fig. 1 Damage of a four-story conventional building due to pounding with its adjacent two-story building, during the L'Aquila earthquake in Italy, in April 2009 [8]



or even collapse, have been observed and reported in past strong earthquakes [1–4]. In case of structural pounding, both floor accelerations and interstory deflections may be significantly amplified, threatening the functionality and the contents of the building [5–7]. The photograph in Fig. 1 shows a pounding incidence between two neighboring buildings, as reported from an EERI/PEER reconnaissance team after the L'Aquila earthquake, which hit Central Italy in April 2009 [8]. During that seismic event, the roof of a 2-story building hit an adjacent 4-story structure causing significant damage to the columns of the latter at that level. Nevertheless, the third and the fourth stories of the building experienced essentially no damage. The confinement of the damage of the 4-story building at the level of impact indicates the destructive effect of structural pounding.

Moreover, pounding may also occur in cases of seismically isolated buildings when the available width of the provided seismic gap around them is limited, due to the large horizontal relative displacements at the isolation level during very strong seismic excitations [7].

At the pounding floors, short-period impulses of high amplitude are observed in the acceleration response, while their amplitude is affected by the impact stiffness. The presence of high spikes in the acceleration response due to poundings is a very critical issue, especially for buildings that may house sensitive equipment. Therefore, it is very important to consider impact mitigation measures that could be employed in practice.

Certain mitigation measures have already been proposed, by other researchers who investigated this problem in buildings and bridge decks, in an effort to alleviate the detrimental effects of structural poundings [9]. One of the proposed measures is the incorporation of layers of soft material, such as elastomeric material, on certain

locations, where impact is likely to happen, in order to act as a shock-absorber. In order to assess the effectiveness of such an impact mitigation measure, proper numerical simulations and parametric studies can be performed, considering various types and configurations of structures under different dynamic excitations. However, the behavior of rubber shock-absorbers under impact loading must be sufficiently well modeled. Undoubtedly the most precise simulation would be the development of a detailed finite element model using special elements and material laws to properly represent the non-linearity of the problem. Nevertheless, such simulations are computationally very demanding and cannot be effectively employed for a parametric investigation of the problem. Therefore, an impact model should be used in numerical simulations of simple multi-degree of freedom dynamic systems, which will be able to provide, with sufficient accuracy, the pounding forces considering the usage of rubber shock-absorbers at impact locations. This paper presents a simple but efficient methodology for simulating the behavior of rubber bumpers of certain thickness and material properties.

2 Impact Modeling

Usually, in numerically simulated dynamic systems, such as multistory buildings under earthquake excitations, structural impact is considered using force-based methods, also known as “penalty” methods. These methods allow relatively small interpenetration between the colliding structures, which can be justified by the local deformability at the point of impact. The interpenetration depth is used along with an impact-stiffness coefficient, representing an impact spring, to calculate the impact forces that act on the colliding structures, pushing them apart. Based on the mathematic relation between the impact force and the interpenetration depth, the impact models can be classified as linear and non-linear models. Furthermore, some models assume that an impact dashpot acts in parallel to the contact spring in order to take into account the energy that is dissipated during an impact [10].

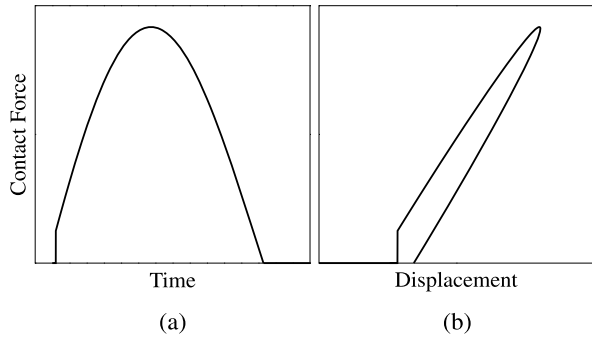
2.1 Concrete-to-Concrete Impacts

In the current study, impacts between concrete surfaces are simulated assuming a linear impact spring and an impact dashpot exerting, in parallel, impact forces to the colliding structures whenever their separation distances are exceeded. In particular, when a contact is detected, the impact force is estimated at each time-step using the following formulas [7]:

$$F_{imp}(t + \Delta t) = \begin{cases} k_{imp} \cdot \delta(t) + c_{imp} \cdot \dot{\delta}(t) & \text{when } F_{imp}(t) > 0 \\ 0 & \text{when } F_{imp}(t) \leq 0 \end{cases} \quad (1)$$

where $\delta(t)$ is the interpenetration depth, $\dot{\delta}(t)$ is the relative velocity between the colliding bodies, k_{imp} is the impact spring's stiffness and c_{imp} is the impact damping

Fig. 2 The linear viscoelastic impact model



coefficient. The latter is computed according to the following formulas, provided by Anagnostopoulos [6]:

$$c_{imp} = 2 \cdot \xi_{imp} \sqrt{k_{imp} \cdot \frac{m_1 \cdot m_2}{m_1 + m_2}} \quad (2)$$

$$\xi_{imp} = -\frac{\ln(COR)}{\sqrt{\pi^2 + (\ln(COR))^2}} \quad (3)$$

In the previous formulas, m_1 , m_2 are the masses of the two bodies and COR is the coefficient of restitution, which depends on the plasticity of the impact and is defined as the ratio of relative velocities after and before impact. Its value rates between 0, which corresponds to totally plastic impact (without rebound) and 1, which represents the case of elastic impact. An estimated value of the coefficient of restitution has to be provided by the user, taking into account the geometry and materials characteristics at the vicinity of the impact. For example, the value of the COR , for the case of structural pounding between concrete structures, is commonly selected to be between 0.5 and 0.7. Actually, the above impact model (Fig. 2) is a small variation of the classical linear viscoelastic impact model that had been initially proposed by Anagnostopoulos [1], in which the tensile forces that arise at the end of the restitution period are omitted and a small plastic deformation is introduced, which increases the available clearance between the buildings.

2.2 Modeling of Rubber Bumpers

A significant part of this numerical problem has to do with the simulation of the behavior of rubber bumpers under impact loading. Anagnostopoulos [6] simulated the usage of a soft material that acted as a shock absorber by simply considering a decreased impact stiffness value for the linear viscoelastic impact model that was used for the simulation of poundings of buildings in series. That research work demonstrated that the use of bumpers may reduce, in some cases, the response due to poundings, although the maximum response values remain higher than the corresponding case without poundings.

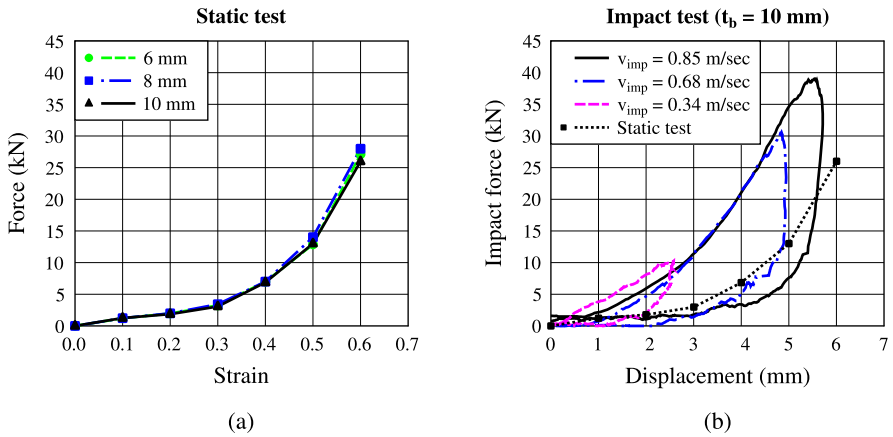


Fig. 3 Experimental results, involving both (a) static and (b) impact tests of rubber shock absorbers, obtained from Kajita et al. [15]

Jankowski et al. [11] numerically simulated the use of several devices to mitigate structural pounding among bridge segments during earthquakes. That research work examined the case of using dampers and stiffeners, as connectors of the segments in series, or rubber bumpers to absorb impact energy between girders. The rubber bumpers in that case were simulated using a linear spring-dashpot element and the results showed that the incorporation of such devices may substantially reduce the overall response due to poundings.

However, the usage of linear impact models for simulating the response of rubber during impact loading does not seem to be the most suitable, considering the stress-strain curves obtained from experiments [12–15]. In particular, static and dynamic compressive tests of rubber reveal an exponential relationship between compressive load and displacement, as shown in the plots of Fig. 3. Therefore, it would be more appropriate to simulate the incorporation of rubber-bumpers by using a non-linear impact model. Furthermore, since a rubber shock-absorber has a finite thickness, there is a possibility to reach its ultimate compressive strain during severe impacts, whereas the impact stiffness should represent the material behind the rubber (e.g. concrete) and not the rubber bumper, since the ultimate strain of the rubber is exceeded.

In a relevant research work [16, 17], regarding the usage of rubber bumpers as an impact mitigation measure for earthquake-induced poundings of seismically isolated buildings, a non-linear impact model with hysteretic damping has been proposed and verified. That simple and efficient impact model is also used in the simulations performed in the present research work. The impact force during the approaching phase is provided by the formula:

$$F_{imp}^A = \begin{cases} k_{imp} \cdot \delta^n & \text{for } \delta < \delta_u \\ k_{imp} \cdot \delta_u^n + k_{imp_PY} \cdot (\delta - \delta_u) & \text{for } \delta > \delta_u \end{cases} \quad \text{when } \dot{\delta} > 0 \quad (4)$$

while during the restitution phase the impact force is computed by the expression:

$$F_{imp}^R = k_{imp} \cdot \delta^n \cdot (1 + C_{imp} \cdot \dot{\delta}) \quad \text{for } \dot{\delta} < 0 \quad (5)$$

In Eq. (4), k_{imp} is the impact stiffness, δ is the indentation and n is the impact exponent ($n > 1$). The impact stiffness is given by the following expression:

$$k_{imp} = \alpha \cdot k_{st} = \alpha \cdot \frac{A \cdot K_r}{d^n} \quad (6)$$

where k_{st} is the bumper's static stiffness and $\alpha > 1$ is a multiplier that ranges usually between the values of 2 to 2.5 as it was found from relevant experiments [15]. A is the contact area of the bumper, d is the bumper's thickness and K_r expresses the material stiffness. The unknown parameters that have to be determined in Eq. (6) are the material stiffness K_r and the exponent n . The values of both parameters depend on the material characteristics and, therefore, their evaluation can be done experimentally. In particular, a static test curve of a rubber specimen (see for example Fig. 3(a)) can be approximated with an exponential curve of the form:

$$f(x) = c \cdot x^b \quad (7)$$

In this way, c can represent k_{st} , while b can represent the exponent n . Then, the material stiffness can be calculated by substituting these values in Eq. (6) and solving for K_r . After obtaining the material properties K_r and n , the impact stiffness of any rubber bumper with the same material and any dimensions can be calculated using Eq. (6). In the current study, those values have been estimated, based on relevant experiments from the literature [15] and the process is presented in Sect. 2.3.

Equation (4) takes into account the case of exceeding the ultimate compressive strain of the material, during the approach phase, as it is assumed that after a certain indentation, δ_u , which corresponds to the ultimate compressive capacity of the rubber bumper, the exponential trend becomes a linear trend with a linear post-yield stiffness, k_{imp_PY} .

The damping term C_{imp} in Eq. (5) is given by the formula [18]:

$$C_{imp} = \frac{(1 - COR^2)}{2 \cdot v_{imp}} \cdot \frac{\ln^3(COR)}{COR \cdot (2 + \ln^2(COR) - 2 \cdot \ln(COR)) - 2} \quad (8)$$

where v_{imp} is the impact velocity, which is the relative velocity of the two bodies just before impact.

The force-time and force-displacement diagrams of the proposed non-linear model for simulating the response of rubber bumpers under impact loading are shown in Fig. 4. Figure 5 demonstrates the same diagrams in the case of exceeding the ultimate compressive capacity of the bumper for three different values of the coefficient of restitution.

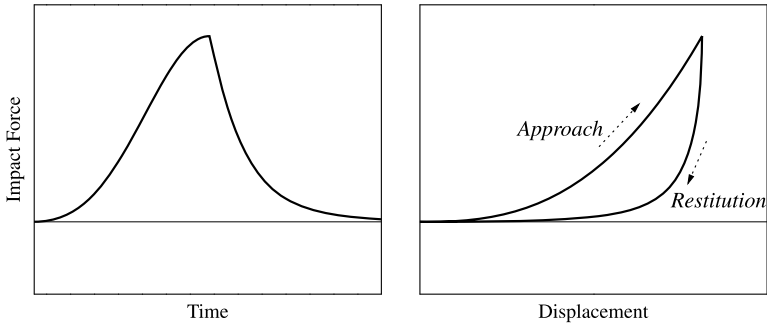


Fig. 4 Force-displacement diagram of the non-linear impact model with hysteretic damping

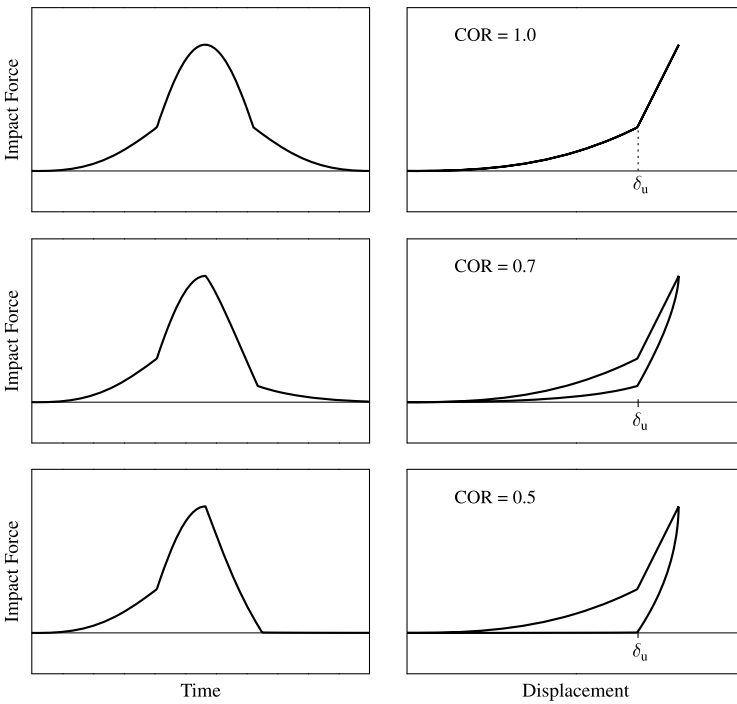


Fig. 5 Impact force in terms of time and displacement in the case of exceeding the ultimate compressive strain capacity of the rubber bumper

2.3 Validation and Parameters' Determination Based on Experimental Data

In order to validate the accuracy of the proposed non-linear hysteretic impact model, the load-displacement curves obtained from the collision tests, conducted by Kajita

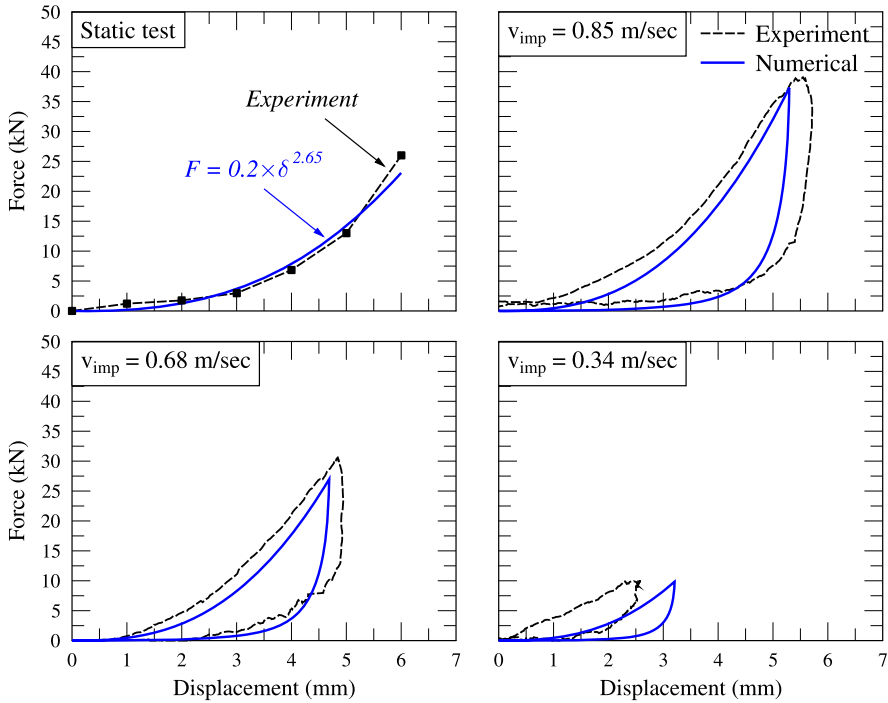


Fig. 6 Comparison between experimental and numerical force-displacement diagrams of a 10 mm thick rubber shock-absorber for various impact velocities

et al. [15], are compared with the corresponding results from numerical analyses, simulating the impact of two free bodies and considering the proposed impact model. The estimation of the impact parameters is based on the static load-displacement curve of the rubber that was used in the experiments. In particular, the static test curve is approximated with an exponent $n = 2.65$ and a static stiffness $k_{st} = 0.2 \text{ kN/mm}^{2.65}$. Consequently, considering the dimensions of the shock-absorber that was used in the experiments ($40 \times 40 \times 10 \text{ mm}$) and substituting to Eq. (6), the material's stiffness K_r is found to be equal to 55835 kN/m^2 . The strain-rate multiplier α is taken to be equal to 2.25 and, therefore, the impact stiffness for the dynamic response is calculated through Eq. (6) to be equal to $0.45 \text{ kN/mm}^{2.65}$. The energy loss during similar impact tests was found to be around 40 % to 50 % of the initial kinetic energy when using the rubber shock-absorbers [12]. Accordingly, the coefficient of restitution is assumed to be equal to 0.5 for the simulations. Nevertheless, the value of the coefficient of restitution, in the proposed impact model, does not affect the value of the maximum impact force, but only the trend of the restitution phase, determining the hysteretic energy loss.

The plots in Fig. 6 present the experimental results from Kajita et al. [15] in comparison with the corresponding numerical results, obtained from the performed simulations considering the proposed non-linear hysteretic impact model for the

Table 1 Impact parameters for the cases without and with rubber bumper

Property	No bumper	With bumper
Impact model	Linear	Non-linear
Exponent (n)	1.0	2.65
Impact stiffness (k_{imp})	2500 kN/mm	0.36 kN/mm ^{2.65}
Coefficient of Restitution (COR)	0.6	0.5
Bumper thickness (d)	–	5 cm
Bumper’s max strain (δ_u/d)	–	0.8
Post-yield impact stiffness (k_{imp_PY})	–	2500 kN/mm

simulation of the rubber bumpers. In particular the force-displacement diagrams are presented for the static test and three different impact velocities, considering an impact shock-absorber of 10 mm thick attached between two colliding masses of 300 kg each. It is observed that the trends obtained from numerical analysis, using the proposed impact model, are very well correlated with the corresponding experimental data. Specifically, there is a good approximation of the maximum impact force as well as the shape and size of the hysteresis loop of the proposed impact model with the corresponding experimental results.

3 Numerical Example Considering Two Rigid Bodies

In order to examine the effect of using a rubber shock-absorber on the computed responses after impact, a simple numerical example of two free rigid bodies of equal masses that collide with a constant relative velocity has been performed. Two different circumstances were considered regarding the area of contact. In the first case, concrete-to-concrete impact was considered and the modified linear viscoelastic impact model was used (Eq. (1)). In the second case a rubber bumper 5 cm thick was assumed to be incorporated at the area of contact, which is simulated using the non-linear impact model with hysteretic damping (Eqs. (4) and (5)). The impact parameters, used in both cases, are provided in Table 1. The masses of the two colliding rigid structures are assumed to be 320 ton each, while two different values of impact velocity were used; specifically 0.5 and 1.0 m/sec.

Figure 7 demonstrates the load-displacement diagrams for the two cases of the impact velocity and for both cases of with and without the use of the rubber bumper. The results show that the indentation, which represents the local deformation at the vicinity of impact, is much larger in the case of having the rubber shock-absorber due to the reduced impact stiffness. Furthermore, in the case of the relatively high impact velocity of 1.0 m/sec, the deformation exceeds the maximum compressive capacity of the 5 cm thick rubber bumper and the impact force begins to rise rapidly, since the post-yield linear impact stiffness is used.

The plots in Fig. 8 show the impact force, relative velocity and acceleration time-histories for the same cases. It is evident that the use of the rubber bumper elongates

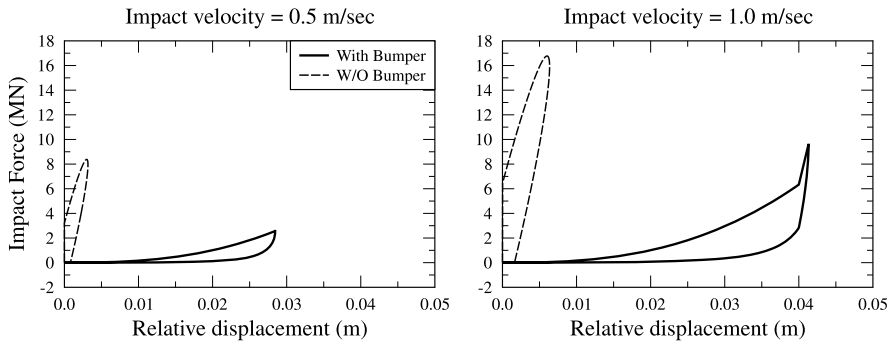


Fig. 7 Impact force-displacement diagram for the cases of two impacting rigid bodies, with and without the incorporation of a rubber bumper and for two different values of the impact velocity

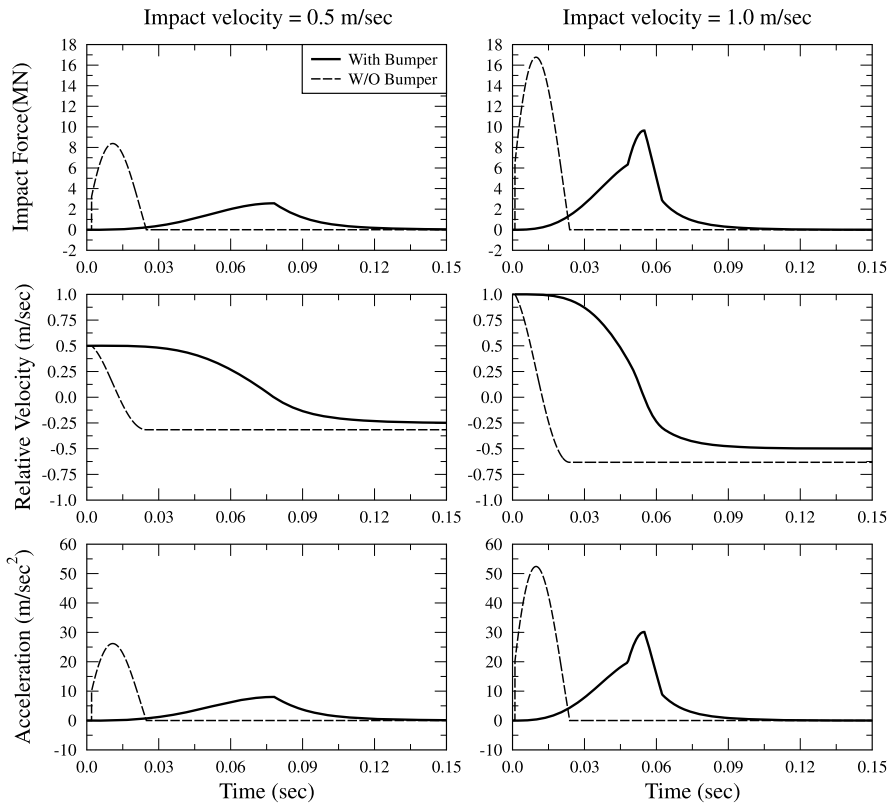


Fig. 8 Impact force, relative velocity and acceleration time-histories for the case of two impacting rigid bodies, with and without the incorporation of a rubber bumper and for two different cases of the impact velocity

the duration of impact and reduces both the maximum impact force and the maximum acceleration. The ratio between the relative velocity after and before impact is equal to the coefficient of restitution used in the corresponding impact model, which verifies the correctness of the two impact models used in the simulations.

4 Application Example Using a Seismically Isolated Building

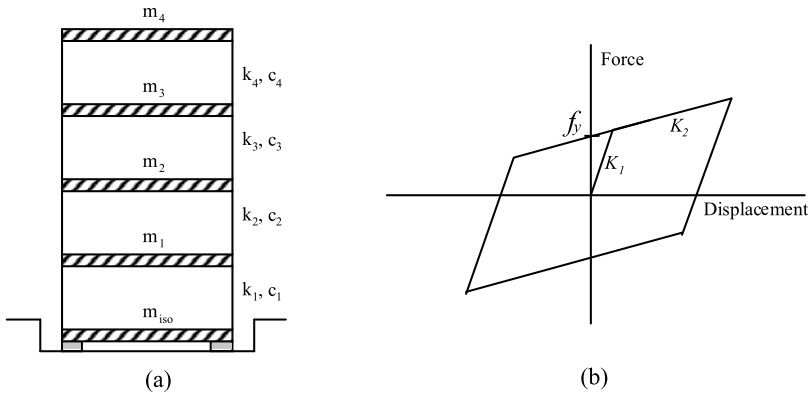
Next, a practical example is presented in order to assess the effectiveness of rubber shock absorbers as an impact mitigation measure for cases of narrow seismic gap sizes around a seismically isolated building. For the numerical simulations, a specialized software application has been developed using modern object-oriented programming in order to efficiently perform dynamic analyses of both conventionally fixed-supported and seismically isolated buildings in two dimensions, modeling the consideration of potential poundings with adjacent structures.

Here, a 4-story seismically isolated building is considered, assuming shear-beam behavior for the superstructure and bilinear behavior for the base isolation system (Fig. 9). The initial seismic gap around the building is considered to be equal to 25 cm. The same building is considered under a second configuration, where rubber shock-absorbers of 5 cm thick are attached around the building at the isolation level, with a clearance of 20 cm.

For the case without the use of bumpers, where the building hits against the surrounding moat wall (concrete-to-concrete impact) the linear viscoelastic impact model is used with an impact stiffness of 2500 kN/mm and a coefficient of restitution equal to 0.7. In the case of incorporating the rubber shock-absorbers, the proposed non-linear hysteretic impact model is used with an exponent $n = 2.65$, $k_{imp} = 0.36 \text{ kN/mm}^{2.65}$ and a $COR = 0.45$. The impact stiffness of the bumpers was calculated using Eq. (6), considering four pieces of rubber with an area of 15 cm \times 15 cm each, attached at each side of the seismically isolated building (Fig. 10). The Sylmar Converter Station record ($PGA = 0.897g$) of the Northridge 1994 earthquake ($M_w = 6.7$) is used as the ground excitation for the simulations. For the seismically isolated building under consideration, the maximum induced unconstrained displacement at the isolation level due to this earthquake record is 31.67 cm.

Figure 11 presents the acceleration time-histories at the base of the seismically isolated building, where poundings occur, for both cases, without and with bumpers. Although that in the case of having bumpers the available clearance is reduced from 25 cm to 20 cm, it is observed that the maximum acceleration response is lower than the corresponding peak acceleration without bumpers. In particular, the high spikes in the acceleration response seem to be eliminated due to the usage of the rubber shock absorbers.

This can be explained by observing the impact force time-history as presented in Fig. 12. Specifically, the plot indicates that the impact forces in the case of adding bumpers, not only become smaller but also the duration of the impact is longer, smoothening the acceleration response at the corresponding floor level.

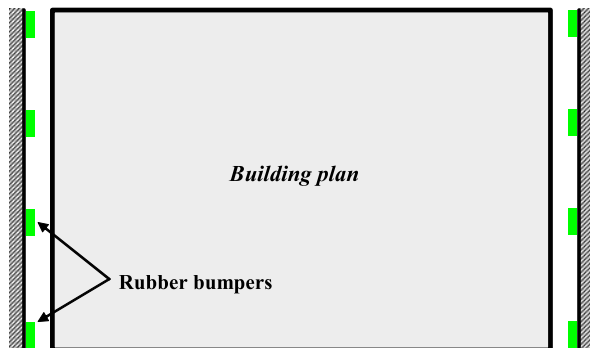


Parameter	Value
<u>- Superstructure's characteristics:</u>	
Story stiffness (k_i)	600 MN/m
Story mass (m_i)	320 ton
Top story mass (m_n)	250 ton
Superstructure's damping ratio (ξ_{sup})	2%
<u>- Isolation system:</u>	
Mass at isolation level (m_{iso})	320 ton
Viscous damping ratio (ξ_{iso})	5%
<u>- Bilinear characteristics of the isolation system:</u>	
Initial stiffness (K_1)	200 MN/m
Post yield stiffness (K_2)	25 MN/m
Characteristic strength (f_y)	$0.1 \times W_{tot}^*$

* W_{tot} = total weight of the building

Fig. 9 (a) Model of a seismically isolated building; (b) Bilinear model of the isolation system behavior; (c) Characteristics of the considered seismically isolated building

Fig. 10 Locations of rubber shock absorbers in a plan view of the building



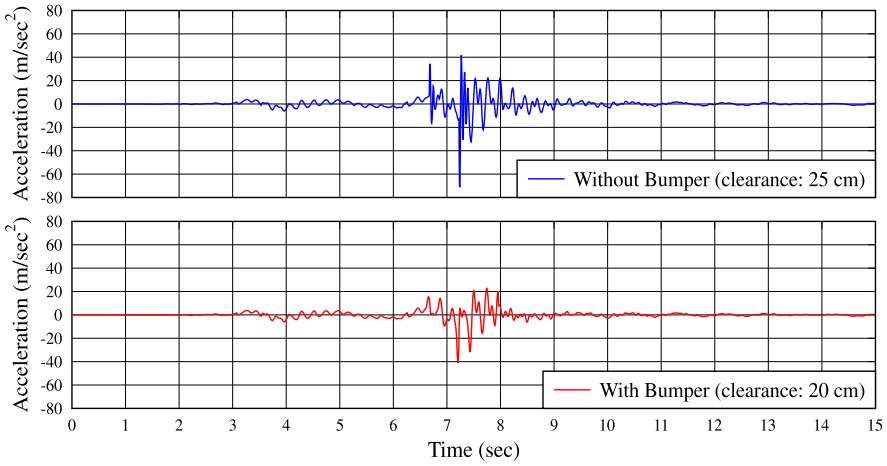


Fig. 11 Differences on the acceleration time-history at the isolation level due to the attachment of 5 cm wide rubber shock absorbers the impact locations

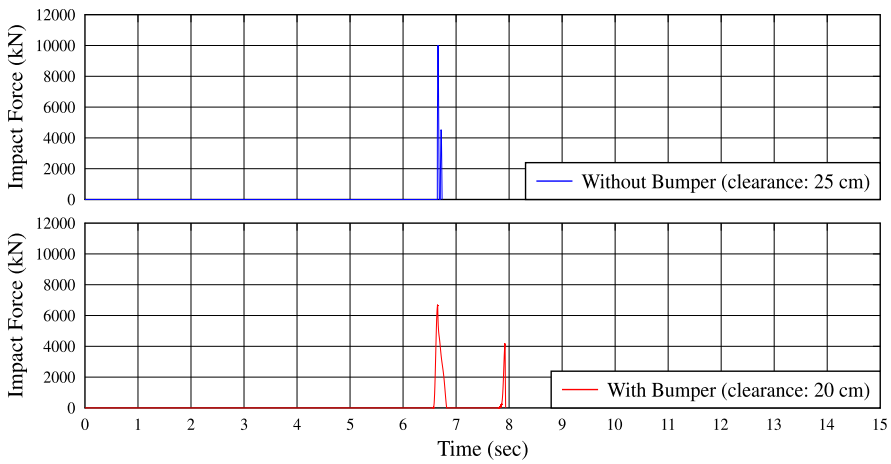


Fig. 12 Differences on the impact force time-history at the isolation level due to the attachment of 5 cm wide rubber shock absorbers at the impact locations

Figure 13 displays the maximum responses at all floors of the seismically isolated building for the two configurations examined, i.e. with and without rubber bumpers, as well as the case of having a seismic gap of 20 cm without using bumpers. While for the case of reducing the seismic gap size to 20 cm without adding any bumpers, the response is substantially amplified, no significant increase of the maximum interstorey deflections or the maximum floor acceleration at the upper floors were observed due to the decreased gap size when rubber bumpers are used. On the contrary, the maximum interstorey deflection at the first story, which is the largest among all

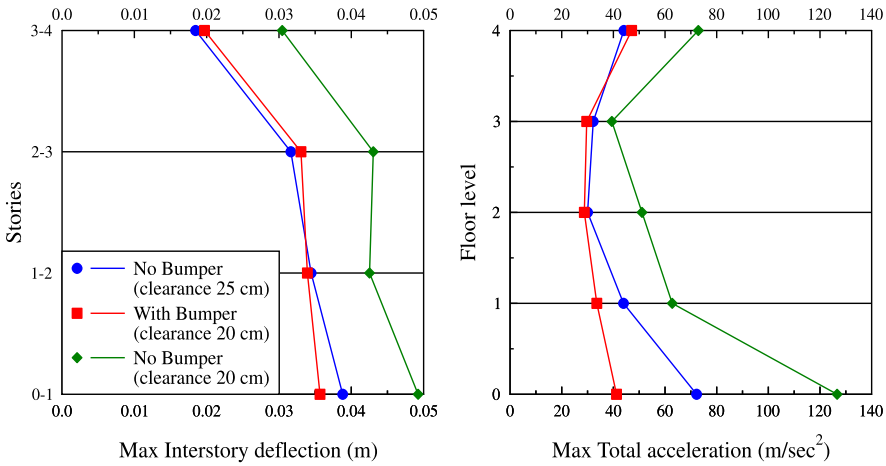


Fig. 13 Differences on the maximum responses of the seismically isolated building due to the attachment of 5 cm wide rubber shock absorbers at the impact locations

stories, slightly decreases after the incorporation of the rubber. Nevertheless, it has to be mentioned that these observations concern only the specific earthquake excitation and the specific seismically isolated building. There is a need for further investigation, performing numerous simulations considering different characteristics of the structures and different earthquake records, where the effectiveness of such impact mitigation measures will be more generally assessed.

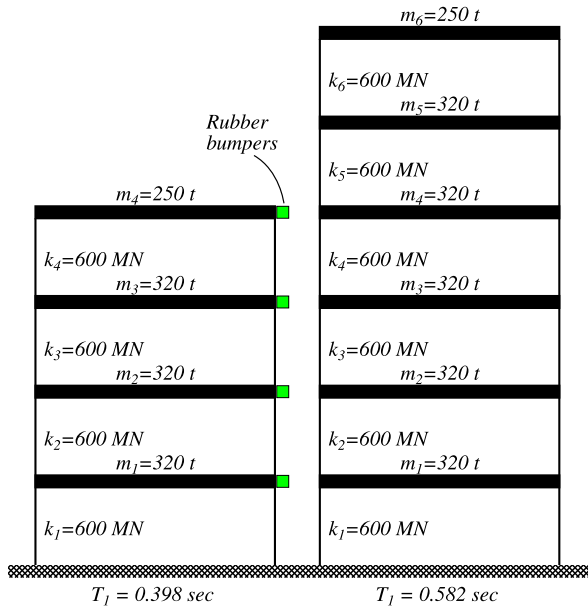
5 Application Example and Parametric Analyses Considering Two Conventional Fixed-Supported Buildings

Next, another example is presented to examine also the case of using rubber shock absorbers as an impact mitigation measure for cases of narrow seismic gap sizes between adjacent multistory conventionally fixed-supported buildings. Again, the simulated buildings are modeled in 2D as multi-degree of freedom (MDOF) systems, with shear-beam behavior and the masses lumped at the floor levels, assuming linear elastic behavior during earthquake excitations.

A 4-story and a 6-story fixed-supported buildings are considered in series for the performed simulations, as shown in Fig. 14. Each floor has a lumped mass of 320 ton, except of the top floor where a mass of 250 ton is considered. Each story has a horizontal stiffness of 600 MN, while a constant viscous damping ratio of 5 % has been considered for both buildings. The floors of the neighboring buildings are assumed to be at the same levels.

For the particular structural system, the performed analysis examined whether the incorporation of rubber bumpers at the locations of potential impacts, which

Fig. 14 The two multistory buildings considered in the simulations and their structural properties



reduces the available seismic gap width, would be beneficial for the colliding buildings or not. For the performed simulations, 5 cm thick bumpers were assumed to be installed at all floor levels, as shown in Fig. 14. Therefore, by applying the rubber shock-absorbers at the side of the one of the two buildings, the existing seismic gap size reduces by 5 cm, when compared with the case without the bumper. Consequently, the results obtained from the simulations considering the use of rubber bumpers are compared with the corresponding results from the case without bumpers but with a clearance that is 5 cm wider. In the performed parametric analyses, the available seismic gap was varied in the range of 5 to 25 cm, which corresponds to a clearance width of 0 to 20 cm in the case of incorporating rubber bumpers.

In order to investigate the effect of the earthquake characteristics, three different seismic records (Table 2) from relatively strong and widely-known earthquakes were selected and used as ground excitations.

Plots in Fig. 15 demonstrate the effect of using rubber bumpers on the computed response of the 4-story and the 6-story buildings, in terms of the size of the seismic gap for the Kobe earthquake record. In particular, the plots present the amplification

Table 2 Earthquake records that were used in the simulations

Earthquake	M_w	Recording station	PGA (g)
Kobe, Japan 1995	6.9	0 KJMA	0.821
Northridge, USA 1994	6.7	74 Sylmar—Converter	0.897
San Fernando, USA 1971	6.6	Pacoima Dam, S16	1.170

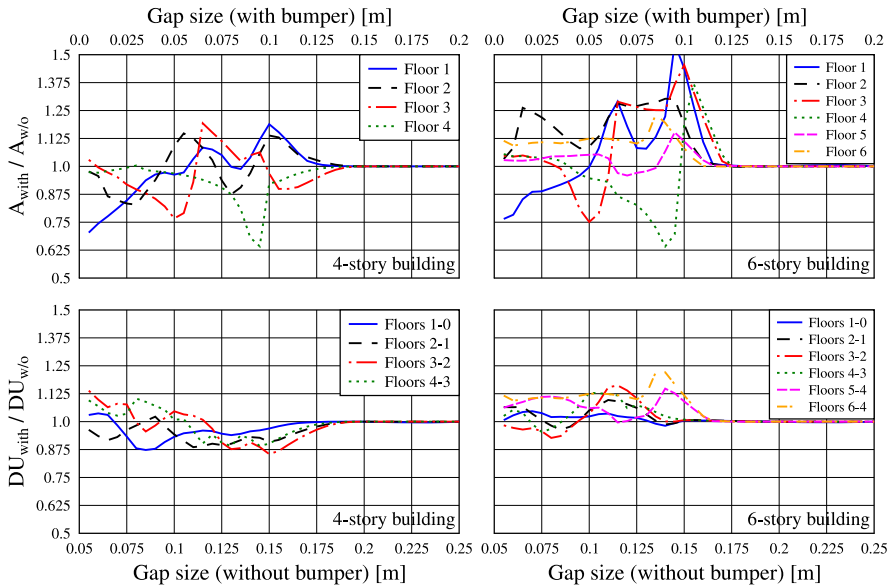


Fig. 15 Amplification of the peak floor accelerations and interstory deflections of the 4-story and the 6-story buildings, due to the usage of rubber shock-absorbers, in terms of the width of the seismic gap, considering the Kobe earthquake record

of the peak floor accelerations and peak interstory deflections due to the incorporation of rubber shock-absorbers with a thickness of 5 cm, between the two buildings. The amplification of the response is defined as the ratio of the response obtained after the incorporation of rubber bumpers, which unavoidably reduce the available clearance, to the corresponding response, without the usage of bumpers. Therefore, the usage of rubber bumpers has beneficial effects on the corresponding response quantity when the amplification ratio value is smaller than 1.0.

The results indicate that the size of the seismic gap affects the effectiveness of the rubber bumpers in a different manner on each floor and for each building. For example, the peak floor acceleration at the 4th floor of the 4-story building is reduced after the incorporation of the bumper almost for all seismic gap sizes, while at the same time the peak acceleration at the 2nd floor of the 6-story building amplifies up to 30 %. Moreover, the maximum interstory deflections are not affected in the same way with the floor accelerations, since the latter may be amplified after the use of the rubber bumper, while the former are reduced for a certain gap size. Nevertheless, peak floor accelerations seem to be more sensitive to the use of bumpers than interstory deflections, since the variations of the curves in the plots of Fig. 15 are more pronounced in the former case.

In order to be able to provide the computed results from all three earthquake records in the same plots, the mean peak responses among all floors of the buildings are computed and plotted in Fig. 16. Specifically, these plots demonstrate, in a more general form, the effect of applying rubber bumpers of 5 cm thick inside the

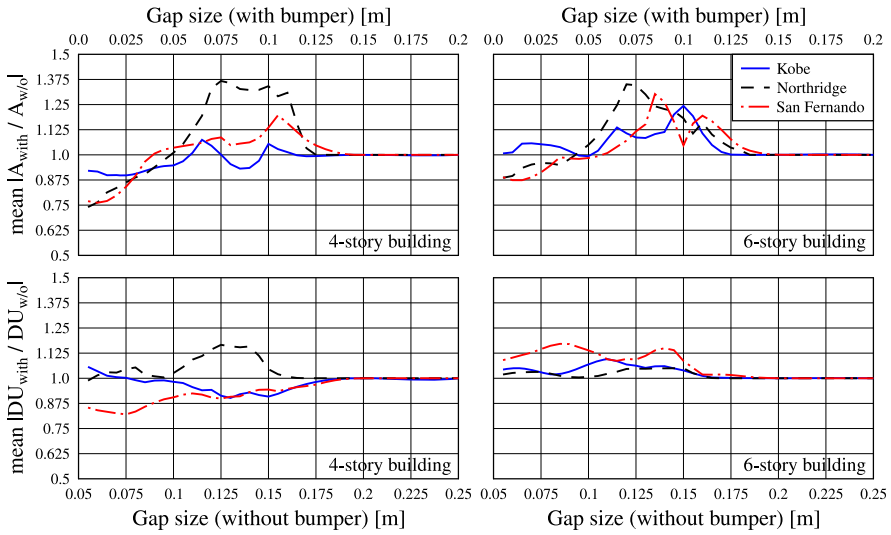
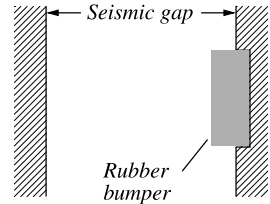


Fig. 16 Mean values of the peak responses among all floors of the 4-story and the 6-story buildings, due to the usage of rubber shock-absorbers, in terms of the width of the seismic gap

Fig. 17 Attachment of a rubber shock-absorber in a cavity on the building’s wall



available gap on the overall seismic response of the two buildings. It is observed that the characteristics of the earthquake excitation affect the effectiveness of this kind of an impact mitigation measure, in combination with the size of the available clearance. It can be also observed that, under the considered circumstances, the incorporation of such a shock-absorber amplifies, in most of the times, the response, especially in the case of the 6-story building. However there are some cases of relatively narrow gap sizes in which the usage of rubber bumpers seems to be beneficial.

In the previously presented simulations, it has been assumed that, after the attachment of rubber bumpers on the side of the seismically isolated building, the reduction of the available clearance from the surrounding moat wall equals to the corresponding thickness of the bumpers. However, the rubber bumpers could be attached in small cavities on the buildings’ walls, taking full advantage of the compressible width of the rubber, as shown in Fig. 17, without unnecessarily decreasing further the width of the seismic gap. For example, if the thickness of a rubber bumper is 5 cm and its maximum compressive strain equals 0.8, then the compressible width δ_u of the bumper is 4 cm. Therefore, if the particular, 5 cm thick shock-absorber

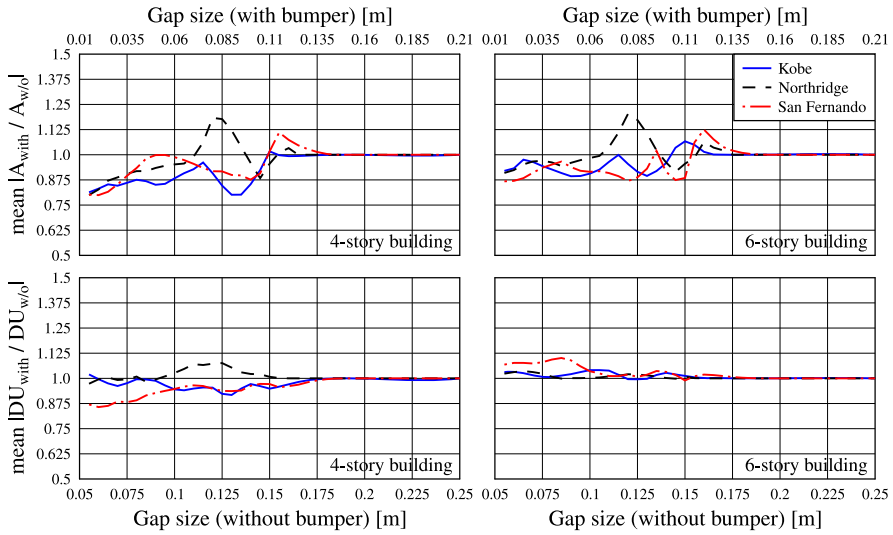


Fig. 18 Mean values of the peak responses among all floors of the 4-story and the 6-story buildings, due to the usage of rubber shock-absorbers, in terms of the width of the seismic gap, with 1 cm cavity (full advantage of bumper effective thickness, i.e. 4 cm)

is attached in a cavity that is 1 cm deep, its effective width of 4 cm can be fully utilized, without unnecessarily decreasing further the width of the available seismic gap by 1 cm.

The above technique seems to be quite efficient since the corresponding amplification ratios due to the incorporation of the bumpers, shown in Fig. 18, are substantially reduced in relation to those of Fig. 16.

6 Conclusions

In the current chapter, we have focused on the numerical simulation of rubber shock absorbers that can be used as an impact mitigation measure for earthquake-induced structural pounding. A new non-linear hysteretic impact model has been proposed for the simulation of the dynamic behavior of rubber bumpers under impact loading. The accuracy of the proposed impact model was found to be very satisfactory compared to relevant experimental results that are available in the literature. The proposed impact model has been used in two numerical examples—involving a seismically isolated building and two conventional adjacent multistory buildings, respectively—in order to assess the effectiveness of such impact mitigation measure.

The performed simulations indicate that the incorporation of rubber shock-absorbers to an existing seismic clearance can reduce the peak responses of the pounding structures, under certain circumstances. Specifically, the high spikes that are observed in the acceleration time-history of the impacting floor level are reduced

in the case of the seismically isolated building after the incorporation of the rubber shock absorbers. However, the effectiveness of the bumpers depends on the existing gap size in combination with the earthquake characteristics and the structural properties (e.g. number of stories). The attachment of the bumper in cavities on the building's wall, taking full advantage of the whole compressible width of the rubber, improves their efficiency.

Nevertheless, it has to be mentioned that the above observations concern only the specific earthquake excitations, structural properties and arrangement of buildings. There is a need for further investigation, performing numerous simulations considering different characteristics of the structures, more buildings and earthquake records, where the effectiveness of such impact mitigation measures will be more generally assessed.

Note This chapter is based on a paper included in the proceedings of the 3rd International Conference on Computational Methods in Structural Dynamics and Earthquake Engineering (COMPADYN 2011), which are available at: <http://congress.cimne.com/eccomas/proceedings/compdyn2011/> and as an e-book at: [http://www.eccomas.org/cvdata/cntr1/spc26/dtos/web/\\$modir/ThematicConf//COMPADYN-2011—Proceedings.pdf](http://www.eccomas.org/cvdata/cntr1/spc26/dtos/web/$modir/ThematicConf//COMPADYN-2011—Proceedings.pdf).

Acknowledgements This research work is co-funded by the European Regional Development Fund and the Republic of Cyprus through the Research Promotion Foundation ($\Delta\text{I}\Delta\text{AKT}\Omega\text{P}/0609/39$).

References

1. Anagnostopoulos SA (1995) Earthquake induced poundings: state of the art. In: Duma G (ed) 10th European conference on earthquake engineering. Balkema, Rotterdam
2. Bertero VV (1987) Observations on structural pounding. In: Proceedings of the international conference on Mexico earthquakes. ASCE, Mexico City, pp 264–278
3. Benuska L (ed) (1990) Loma Prieta earthquake reconnaissance report. Rep No 90-01, Earthquake Engineering Research Institute (EERI), Oakland
4. Youd TL, Bardet J-P, Bray JD (eds) (2000) Kocaeli, Turkey, earthquake of August 17, 1999 reconnaissance report. Publ No 00-03, Earthquake Engineering Research Institute (EERI), Oakland
5. Papadrakakis M, Mouzakis H (1995) Earthquake simulator testing of pounding between adjacent buildings. *Earthquake Engineering and Structural Dynamics* 24:811–834
6. Anagnostopoulos SA (1988) Pounding of buildings in series during earthquakes. *Earthquake Engineering and Structural Dynamics* 16:443–456
7. Komodromos P, Polycarpou PC, Papaloizou L, Phocas MC (2007) Response of seismically isolated buildings considering poundings. *Earthquake Engineering and Structural Dynamics* 36:1605–1622
8. Earthquake Engineering Research Institute (EERI) (2009) L'Aquila, Italy earthquake clearinghouse—observations from EERI/PEER team. <http://www.eqclearinghouse.org/italy-090406/>
9. Warnotte V, Stoica D, Majewski S, Voiculescu M (2007) State of the art in the pounding mitigation techniques. *Intersections/Intersectii* 4(3):102–117.

10. Polycarpou PC, Komodromos P (2010) On the numerical simulation of impacts for the investigation of earthquake-induced pounding of buildings. In: The tenth international conference on computational structures technology (CST2010), Valencia, 14–17 September
11. Jankowski R, Wilde K, Fujino Y (2000) Reduction of pounding effects in elevated bridges during earthquakes. *Earthquake Engineering and Structural Dynamics* 29:195–212
12. Kajita Y, Nishimoto Y, Ishikawa N, Watanabe E (2001) Energy absorption capacity of the laminated fiber reinforced rubber installed at girder ends. In: High performance materials in bridges. International conference on high performance materials in bridges, Kona, Hawaii, pp 183–192. doi:[10.1061/40691\(2003\)17](https://doi.org/10.1061/40691(2003)17)
13. Kawashima K, Shoji G, Koshitoge M, Shimanoe S (2002) Design of an earthquake-resistant expansion joint with unseating prevention system. In: FIB congress, Osaka, E-282 (CD-ROM)
14. Shim VPW, Yang LM, Lim CT, Law PH (2004) A visco-hyperelastic constitutive model to characterize both tensile and compressive behavior of rubber. *J Appl Polym Sci* 92:523–531
15. Kajita Y, Kitahara T, Nishimoto Y, Otsuka H (2006) Estimation of maximum impact force on natural rubber during collision of two steel bars. In: First European conference on earthquake engineering and seismology (1st ECEES), Geneva, September 3–8
16. Polycarpou PC, Komodromos P (2009) Simulating the use of rubber shock absorbers for mitigating poundings of seismically isolated buildings during strong earthquakes. In: 2nd international conference on computational methods in structural dynamics and earthquake engineering (COMPDYN 2009), Rhodes, 22–24 June
17. Polycarpou P, Komodromos P (2011) Numerical investigation of potential mitigation measures for poundings of seismically isolated buildings. *J Earthq Struct* 2(1):1–24
18. Polycarpou PC, Komodromos P (2012) A nonlinear impact model for simulating the use of rubber shock absorbers for mitigating the effects of structural pounding during earthquakes. *Earthq Eng Struct Dyn* 42(1):81–100. doi:[10.1002/eqe.2194](https://doi.org/10.1002/eqe.2194)

Seismic Design Methodology for Control of 3D Buildings by Means of Multiple Tuned-Mass-Dampers

Oren Lavan and Yael Daniel

Abstract In this chapter, an efficient design methodology which sizes, tunes and allocates multiple tuned-mass dampers in 3D irregular structures is presented. The proposed methodology is based on an iterative analysis/redesign algorithm which, while using two steps in each iteration, allows obtaining a very efficient amount of added dampers' mass while converging to an allowable response of the structure. This performance-based design methodology is simple, relies on analysis tools only, and is fast converging, all of which make it very attractive for practical use.

Keywords Seismic control · Tuned mass dampers · Dynamic vibration absorbers · Fully stressed design · Multiple mode vibration · Irregular structures

1 Introduction

For many years, life-safety was the major goal of seismic design. In the early 1990's a shift in the philosophy of seismic design had begun. The new emerging philosophy, performance-based design, allows for the design of structures to a higher level than the minimum required by older codes. That is, a limit on the allowable damage (structural or even nonstructural) under a given level of seismic risk could be assigned. Damage to structural components is often linked to inter-story drifts, when considering damage due to maximal responses. When considering damage to acceleration sensitive non-structural elements, total accelerations (which are accelerations in respect to an inertial frame of reference, also referred to as absolute accelerations) produced during the ground-motion are of most interest. Total acceleration levels are also very important when considering the comfort level of human occupancy. In addition, total accelerations have an effect on base-shear and overturning moments [1].

O. Lavan (✉) · Y. Daniel
Faculty of Civil and Environmental Engineering, Technion—Israel Institute of Technology,
Technion City, Haifa 32000, Israel
e-mail: lavan@tx.technion.ac.il

Y. Daniel
e-mail: yaeldan@tx.technion.ac.il

These responses could effectively be controlled using energy dissipation devices, also termed passive control. Those include viscous and visco-elastic dampers, as well as metallic and friction hysteretic dampers [1, 2]. Another device to be used herein is the Tuned-Mass-Damper (TMD). Details about TMDs and their applications may be found in the fine works [1, 3–6], only to name a few.

The use of TMDs for the reduction of responses of tall buildings due to wind loadings became widespread [7–9]. With efficient seismic design strategies, those devices may be attractive for multi-hazard mitigation of both winds and earthquakes. While wind-induced vibrations are usually dominated by a single mode, using TMDs for seismic structural protection is more complicated. In seismic vibrations, no single distinct frequency dominates the behavior, but rather many frequencies, including the ones of higher modes. Many researchers are therefore hesitant in using TMDs for seismic structural applications [10–14]. It should be noted that most of those works use only a single TMD tuned to a fundamental frequency. In addition, a TMD relies on tuning the device's natural frequency as to suppress the vibration of the structure, based on the structure's natural frequencies. However, if detuning occurs, the device loses much of its efficiency.

One solution to these drawbacks may be found in active or semi-active TMDs (ATMDs or SATMDs), whose frequencies may be altered at each moment [15–18]. Active control, however, requires an external power source to be activated, which may be costly and may force a reliability issue during an actual earthquake. Another possible solution may be achieved using multiple TMDs (MTMDs), each tuned to a different frequency. This may lead to a solution that controls various frequencies for various modes of the structure. Those TMDs could also be distributed along the structure and located at locations which will optimize the control of the structure. In addition, each TMD that is aimed at controlling a certain mode of the structure could be split to several TMDs, each tuned to a slightly different frequency within a bandwidth close to the natural frequency of the main system, thus reducing the detuning effect and allowing design robustness (for example [19]). The idea of using MTMDs tuned to various natural frequencies of the structure and distributed along its height is not new. Clark [20] indicated that a single TMD cannot significantly reduce the motion created due to seismic excitations, while MTMDs can substantially reduce motion. Moon [21, 22] shows a practical application of vertically-distributed MTMDs in tall buildings for reducing wind-induced vibrations, and offers a method of distributing them by mode shape. In his work, dampers are located at the perimeter in the space between the inner and outer façade layers in double skin façade systems, as their vibrations are in the direction perpendicular to the edge of the floor. In the methodology presented herein a somewhat different approach is taken, as the dampers' vibrations are in parallel to the floor edge. This allows a better control of torsional response as well as larger strokes for the dampers.

Several methodologies for the optimal design of a single passive TMD for MDOF structures exist, each using a different objective function [8, 23–25]. Hadi and Arfiadi [26] use an H_2 performance index to retrieve the optimal parameter of a TMD added to a MDOF structure. H_2 and H_∞ optimization criteria are also widely used in ATMD problems (for example [27]). The H_2 approach minimizes a weighted average of the weighted sum of responses at various locations, and the control energy

input. In the case of passive control, however, the control energy input is not a relevant cost measure. The H_∞ approach, on the other hand, minimizes the worst case energy attenuation of the controlled output with respect to an excitation of a given energy. Here, however, the characteristics of the input motion expected at the site where the structure is located are not considered. It should be emphasized that both approaches make use of smeared measures of the controlled responses rather than limiting each local response separately. In buildings in general, however (see for example [28, 29]), and in the case of irregular buildings in particular, it is highly important to limit each local response separately. In addition, both approaches do not target an allowable response limit. In the context of the last two highly important issues, Bounded State Control (BSC) seems more appropriate since local states are each bounded to allowable limits [28, 29].

Bounded State Control algorithms can be roughly categorized into two groups. The first relies on a train of high energy pulses of control forces (e.g. [29, 30] and references therein) while the second makes use of a continuous control law (e.g. [31–33]). While may be attractive in the application of an active control system, the pulse control strategies are not likely to be implemented by passive means. The methods that make use of continuous control laws, on the other hand, usually require formal optimization.

There are not many methodologies available for the design of MTMDs of various frequencies and locations in seismic application. In their pioneering work, Chen and Wu [34] use a frequency based transfer function as a response measure of the multi-modal vibration problem of structures. Rather than solving a formal optimization problem, they use a sequential search technique in order to allocate multi-modal MTMDs. A pre-assumed number of TMDs is sequentially added at locations where the location index (which, for example, can be the location of maximal root-mean-square (RMS) acceleration prior to placement of each damper) is optimal in each sequence. Luo et al. [35] also dealt with the multi-modal vibration problem of structures using MTMDs. In their work, a dynamic magnification factor (DMF) of the first mode obtained based on the transfer function of the structure's response in frequency domain is minimized. Constraints on the DMFs of other modes are also considered. Lin et al. [36] proposed a two-stage frequency-domain based optimal design of MTMDs taking into consideration both the structural response and the TMD stroke, and found that there is a good balance between limiting the TMD stroke and not substantially compromising on structural response. Fu and Johnson [37] suggest using passive MTMDs with a vertical distribution of mass, where each story is assigned with one TMD of which its parameters (mass, stiffness and inherent damping) are optimized as to minimize the sum of inter-story drifts. The optimization problem is solved using a pattern-search, and a local minimum is obtained. While the above methodologies present a huge step forward, there is still no methodology that leads to a desired performance under a realistic representation of the ground motion hazard, in small computational efforts while using analysis tools only.

This chapter presents a simple frequency-domain performance-based methodology for solving the allocation and sizing problem of multi-modal MTMDs in

structures undergoing seismic excitations. The objective function minimizes the total mass of all added TMDs. Constraints are added to limit the total accelerations experienced at the edges of the floors in the direction parallel to each edge. The methodology is based on a simple iterative analysis/redesign procedure where first, an analysis is performed for a given design and then redesign of the TMDs is performed according to recurrence relations. The redesign first determines the mass of all dampers at a given location based on RMS acceleration (peak acceleration could be indirectly used). Then this mass is distributed between dampers tuned to various frequencies. The methodology is based on the simple optimal design parameters of TMDs presented by Den-Hartog [3] and Warburton [4] to successfully reduce the acceleration demands within the structure. The advantages of the proposed methodology is its simplicity, relying on analyses tools only, it is performance-based—catered to serve any desirable performance, and its fast convergence.

2 Problem Formulation

2.1 Equations of Motion

The second-order differential equations of motion can be represented in state-space notation (e.g. [29]). Here:

$$\begin{aligned}\dot{\hat{\mathbf{x}}}(t) &= \mathbf{A} \cdot \hat{\mathbf{x}}(t) + \mathbf{B} \cdot a_g(t) \\ \mathbf{y}(t) &= \mathbf{CC} \cdot \hat{\mathbf{x}}(t)\end{aligned}\quad (1)$$

where $\hat{\mathbf{x}}^T = [\mathbf{x}^T \ \dot{\mathbf{x}}^T]$; $\mathbf{x} \in R^N$, $\hat{\mathbf{x}} \in R^{2N}$ is the state variable vector, $\mathbf{x}(t)$ is the displacement vector between the DOFs and the ground, $a_g(t)$ is the ground-motion's acceleration, a dot represents the derivative with respect to time, and $\mathbf{y}(t)$ is the output vector of the system. For responses of relative displacements (absolute accelerations will be accounted for later), the matrices \mathbf{A} , \mathbf{B} and \mathbf{CC} are defined as following:

$$\mathbf{A} = \begin{bmatrix} \mathbf{0}_{N \times N} & \mathbf{I}_{N \times N} \\ -\mathbf{M}^{-1}\mathbf{K} & -\mathbf{M}^{-1}\mathbf{C} \end{bmatrix} \quad \mathbf{B} = \begin{bmatrix} \mathbf{0}_{N \times 1} \\ -\mathbf{e} \end{bmatrix} \quad \mathbf{CC} = [\mathbf{I}_{N \times N} \quad \mathbf{0}_{N \times N}] \quad (2)$$

where \mathbf{M} , \mathbf{C} and \mathbf{K} are the mass, inherent damping and stiffness matrices of the structure according to the chosen N degrees-of-freedom (DOFs), respectively, \mathbf{e} is the excitation direction vector with values of zero and one, \mathbf{I} is the identity matrix and $\mathbf{0}$ is a zero matrix of appropriate dimensions, as noted.

2.2 Performance Measures

Often, the leading criterion for design of buildings in general and 3D irregular tall buildings in particular, is serviceability of the structure. Here, high absolute acceleration levels might also cause damage to equipment within the structure [1, 34]. In

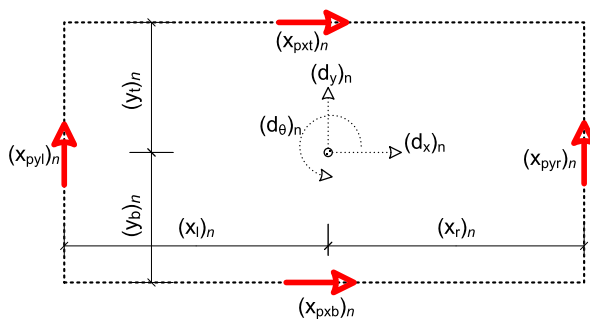


Fig. 1 Definition of dynamic DOFs and peripheral coordinates of the n th floor

addition, High absolute accelerations imply high inertia forces, hence high forces on the structural system, including foundations. Moreover, humans are prone to feel sickness and highly suffer once absolute acceleration levels exceed a certain limit. Therefore, in this chapter, absolute acceleration levels were chosen as the performance measure which should be controlled during an earthquake.

The cost of the MTMD damping system and retrofit is directly influenced by the amount of added mass. As more mass is added to the structure, there is need in more material of the damper, the damping system takes up a larger space and more gravitational forces (which the structure has to support) are added. Therefore, the added mass of all TMDs was chosen as the measure of cost-efficiency of the damping system.

2.3 Problem Formulation

An optimization problem with the objective of minimizing the total amount of added mass is formulated. The constraints allow for performance-based design by limiting the acceleration levels at all peripheral locations. Those peripheral locations are shown in Fig. 1 as: $(x_{pyl})_n$, $(x_{pyr})_n$, $(x_{pxt})_n$ and $(x_{pxb})_n$, and are the peripheral coordinates in the “y”, “y”, “x” and “x” directions, at the left, right, top and bottom edges of floor n , respectively. The remaining variables will be explained subsequently. That is, the constraints are on the total accelerations at the edges of all floors in the directions parallel to each edge. The optimization problem is thus formulated as:

$$\begin{aligned} \min J &= \sum_l^{\text{all locations}} \sum_f^{\text{all frequencies}} (\mathbf{m}_{\text{TMD}})_{l,f} \\ \text{s.t. } \max_{eq} \left(\max_t \left((\ddot{\mathbf{x}}_p^t(t))_l \right) \right) / a_{\text{all}}^t &\leq 1.0 \quad \forall l = 1, 2, \dots, N_{\text{locations}} \end{aligned} \tag{3}$$

where $(\mathbf{m}_{\text{TMD}})_{l,f}$ is the mass of the TMD located at peripheral location l tuned to frequency f , $\max_{eq} \left(\max_t \left((\ddot{\mathbf{x}}_p^t(t))_l \right) \right)$ is the envelope of peak total acceleration in

time at each location, l , under all considered earthquakes, a_{all}^t is the allowable total acceleration, and $N_{locations}$ is the number of locations to be constrained ($= 4N_{floors}$ where N_{floors} is the number of floors). The peripheral locations, l , are ordered such that the vector of peripheral coordinates is $\mathbf{x}_p = [\mathbf{x}_{pyl}^T \ \mathbf{x}_{pyr}^T \ \mathbf{x}_{pxt}^T \ \mathbf{x}_{pxb}^T]^T$ (see also Fig. 1). It should be noted that with a slight modification, the methodology to follow could also constrain the total accelerations of the floors' corners in any direction, if desired.

Due to the frequency-tuning nature of the MTMD allocation problem, an alternative formulation in the frequency domain is used. Here, the objective function does not change, but the constraints are on RMS accelerations rather than peak envelope accelerations. The allowed values for the RMS total accelerations are properly scaled so as to lead to the desired allowable peak accelerations in time of Eq. (3). Therefore, the optimization problem now takes the following form:

$$\begin{aligned} \min J &= \sum_l^{\text{all locations}} \sum_f^{\text{all frequencies}} (\mathbf{m}_{TMD})_{l,f} \\ \text{s.t. } RMS((\ddot{\mathbf{x}}_p^t)_l) / a_{all}^{RMS} &\leq 1.0 \quad \forall l = 1, 2, \dots, N_{locations} \end{aligned} \quad (4)$$

where a_{all}^{RMS} is the allowable RMS total acceleration and $RMS((\ddot{\mathbf{x}}_p^t)_l)$ is the root mean square of the total acceleration at location l (the l th term of $RMS(\ddot{\mathbf{x}}_p^t)$). Such reference to a component of a vector or a matrix, i.e. $(\cdot)_l$, will be used throughout this chapter.

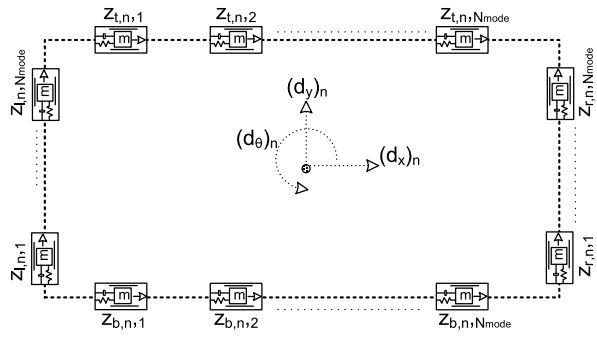
3 Proposed Solution Scheme

3.1 Fully-Stressed Design (FSD)

Fully-stressed design date back to the early 1900 where it was shown that “A statically determined framework of included figure is the most economic form of a framework of given indeterminate figure for the support of a given loading” [38]. In this problems, the weight of all members of a specific truss were minimized for a given allowable stress of each member. For that problem, it had been widely accepted that the optimal design yields a: statically determinate fully stressed design, with members out of the design having strains smaller than the allowable. Later, this design was shown to fulfill the Karush-Kuhn-Tucker conditions and therefore be an optimal design (e.g. [39]).

Recently, it was shown that some dynamic optimal designs also possess “fully stressed” characteristics. Levy and Lavan [40] considered the minimization of total added viscous damping to frame structures subjected to ground accelerations, while constraining various inter-story responses. Their optimal solutions attained by formal optimization indicated that: “At the optimum, damping is assigned to stories for which the local performance index has reached the allowable value. Stories with no

Fig. 2 Locations of TMDs at the floor n and their associated z DOFs



assigned damping attain a local performance index which is lower or equal to the allowable.” That is, the optimal solutions attained “fully stressed” characteristics.

Based on this knowledge and the past experience of the authors in other, similar, problems, it is conjectured here that the optimal solution to MTMD allocation and sizing in structures (the solution of Eq. (4)) possesses FSD characteristics, i.e.:

At the optimum, TMDs are assigned to peripheral locations for which the RMS total acceleration has reached the allowable value under the considered input acceleration PSD. In addition, at each location to which TMDs are added, TMDs of a given frequency are assigned only to frequencies for which the output spectral density is maximal.

TMDs are to potentially be added at the edges of the floors, working in parallel directions to these edges (Fig. 2). The coordinates “ z ” in Fig. 2 will be explained subsequently.

The conjecture is made up of two stages. The first imposes that for all peripheral locations with masses within the design, the total acceleration equals the allowable one, while all peripheral locations with zero added mass (outside the design) have an acceleration equal to or less than the allowable. This is illustrated on the left-hand side of Fig. 3, which presents the concept on a selected peripheral frame. Here, the 6th floor is the only one to be dampened (i.e. $\sum_f (\mathbf{m}_{TMD})_{6,f} \neq 0$), as it is the only floor to reach the allowable RMS acceleration. The second stage of the conjecture imposes that for all dampers at a peripheral location where the acceleration equals the allowable one, the output spectral densities are maximal (and equal) at all frequencies where a TMD tuned to dampen those frequencies was added. As for masses outside of the design at this DOF, the output spectral density at the frequencies those TMDs are set to dampen less than maximal. This is illustrated on the right-hand side of Fig. 3 where $(\mathbf{R}_{\ddot{x}_p}(\omega))_l$ is the output spectral density for the total acceleration at the location l ($= 6$ in Fig. 3). As can be seen, $(\mathbf{m}_{TMD})_{6,1}$ and $(\mathbf{m}_{TMD})_{6,2}$ are the only ones with a mass larger than zero as their output spectral densities, $(\mathbf{R}_{\ddot{x}_p}(\omega))_6$, are largest. If desired to constrain the corners’ total accelerations, dampers would be added to the direction that contributes more to the acceleration (between x and y).

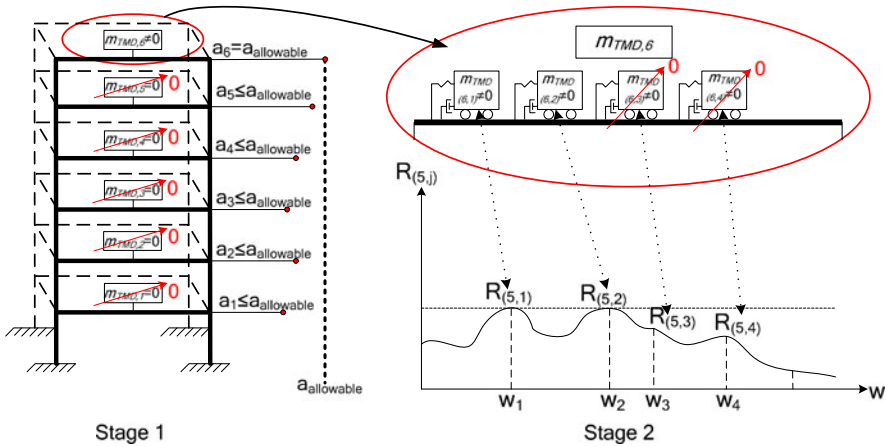


Fig. 3 Illustrations of the first part of the conjecture (left) and the second part of the conjecture (right)

For practical reasons, it is reasonable to assume that the tuning frequencies are in the vicinity of the bare structure’s frequencies, rather than searching for them among all possible frequencies. Thus, the tuning of TMDs could be in relation to the bare structure’s natural frequency.

3.2 Analysis/Redesign Algorithm

Solutions to optimization problems, which possess fully stressed characteristics, are efficiently achieved iteratively using a two step algorithm in each iteration cycle. In the first step, an analysis is performed for a given preliminary design, whereas in the second step the design is changed using a recurrence relationship that targets fully stressedness. The recurrence relation can be generally written as:

$$x_l^{(n+1)} = x_l^{(n)} \cdot \left(\frac{p_l^{(n)}}{p_l^{allowable}} \right)^P \tag{5}$$

where x_l is the value of the design variable associated with the location l , p_l is the performance measure of interest for the location l , $p_l^{allowable}$ is the allowable value for the performance measure, n —the iteration number and P —a convergence parameter. Fully stressedness is obtained from using Eq. (5) since upon convergence one of the following must take place. Either $x_l^{(n+1)} = x_l^{(n)}$ giving $p_l^{(n)} = p_l^{allowable}$, or $x_l^{(n+1)} = x_l^{(n)} = 0$ giving $p_l^{(n)} \leq p_l^{allowable}$.

Such analysis/redesign procedure will be utilized here to attain fully stressed designs where the mass, frequency and locations of MTMDs within framed structures is to be determined.

4 Design Methodology

The proposed design methodology relies on the analysis/redesign procedure which leads to the FSD criteria presented above. The proposed methodology is summarized in the following flowchart. Following the flowchart is an extensive elaboration of each step, including the equations referred to within the flowchart.

4.1 Stepwise Flowchart

Initial actions

1. Determine the mass, stiffness and inherent damping matrices of the structure. Decide on allowable RMS accelerations, which should represent the desired peak total acceleration.
2. Determine the natural frequencies and mode shapes of the structure.
3. Decide on an input PSD, which should represent an ensemble of chosen ground-motions (see example). For each DOF, evaluate the total acceleration transfer function in frequency domain using Eq. (8), transform this transfer function into peripheral coordinates using Eq. (10) and determine the peripheral output spectral density using Eq. (11). The peripheral RMS acceleration is derived from Eq. (12).
4. Add N_{mode} (N_{mode} being the number of modes potentially damped) TMDs at each peripheral coordinate, each tuned to one frequency of the structure, with the initial properties described in Eqs. (14), (17) and (19).

Iterative action

5. Update the mass, stiffness and damping matrices of the structure with the added damping system, using Eqs. (20)–(25).
6. Re-evaluate the RMS accelerations excited within the structure using Eqs. (8)–(12). Notice that for Eq. (8) the expressions $\mathbf{M}^{-1}\mathbf{K}$ and $\mathbf{M}^{-1}\mathbf{C}$ are taken from Eqs. (26) and (27), to avoid singularity.
7. Redesign the mass of each TMD according to the recurrence formulas given in Eqs. (28) and (29). Accordingly, reevaluate the stiffness and damping coefficient of each TMD using Eqs. (15)–(19).
8. Repeat steps 5 to 7 until convergence of the mass is reached.
9. Validate the results using time-history analysis and the selected set of ground-motions.
10. If desired, the allowable RMS acceleration may be scaled according to the reduction of envelope peak acceleration determined in step 9 and the allowable peak acceleration in time domain, using Eq. (30), followed by repeating steps 5–9 until fully satisfied.

Step 1 The structure's mass, damping and stiffness matrices are assembled. A desired maximal RMS acceleration (representing the desired peak total acceleration) is chosen. As it is desired to control peripheral responses (which include the largest

responses within floor limits in the “ x ” and “ y ” directions), a coordinate transformation from floor DOFs to peripheral coordinates is performed as follows:

$$\mathbf{x}_p = \mathbf{T} \cdot \mathbf{x} \quad (6)$$

where $\mathbf{x} = [\mathbf{d}_x^T \ \mathbf{d}_y^T \ \boldsymbol{\theta}^T]^T$ and the transformation matrix \mathbf{T} is:

$$\mathbf{T}_{(4 \cdot N_{floors} \times 3 \cdot N_{floors})} = \begin{bmatrix} \mathbf{0}_{(N_{floors} \times N_{floors})} & \mathbf{I}_{(N_{floors} \times N_{floors})} & \text{diag}(\mathbf{x}_l)_{(N_{floors} \times N_{floors})} \\ \mathbf{0}_{(N_{floors} \times N_{floors})} & \mathbf{I}_{(N_{floors} \times N_{floors})} & \text{diag}(\mathbf{x}_r)_{(N_{floors} \times N_{floors})} \\ \mathbf{I}_{(N_{floors} \times N_{floors})} & \mathbf{0}_{(N_{floors} \times N_{floors})} & -\text{diag}(\mathbf{y}_t)_{(N_{floors} \times N_{floors})} \\ \mathbf{I}_{(N_{floors} \times N_{floors})} & \mathbf{0}_{(N_{floors} \times N_{floors})} & -\text{diag}(\mathbf{y}_b)_{(N_{floors} \times N_{floors})} \end{bmatrix} \quad (7)$$

where N_{floors} is the number of floors, N is the number of DOFs and \mathbf{x}_l , \mathbf{x}_r , \mathbf{y}_t , and \mathbf{y}_b are the distances from the DOFs’ coordinate system’s origin to the left, right, top and bottom edges, ordered from first to top floor, as shown for the story n in Fig. 1.

Step 2 Solution of the eigenvalue problem determines the structure’s natural frequencies and mode shapes.

Step 3 A power spectral density (PSD), representing a set of relevant ground motions, for the input acceleration is selected. Examples of such input spectra are stationary white-noise, which gives a constant PSD, and the Kanai-Tajimi PSD [41]. Additional PSDs for ground-motional modeling can be found in Nagarajaiah and Narasimhan [42] and in Agrawal et al. [43]. For each DOF, the transfer function of total acceleration of the bare frame is evaluated using Eq. (8). For total accelerations it can be shown that the appropriate transfer vector, $\mathbf{H}_{\ddot{\mathbf{x}}_t}(j\omega)$, is:

$$\mathbf{H}_{\ddot{\mathbf{x}}_t}(j\omega) = -\mathbf{M}^{-1} \cdot (j\omega\mathbf{C} + \mathbf{K}) \cdot \mathbf{H}_x(j\omega) \quad (8)$$

where $j = \sqrt{-1}$ and $\mathbf{H}_x(j\omega)$ is the displacement transfer vector [44], given by:

$$\mathbf{H}_x(j\omega) = \mathbf{C}\mathbf{C} \cdot (j\omega\mathbf{I} - \mathbf{A})^{-1} \cdot \mathbf{B} \quad (9)$$

This transfer function is transformed to peripheral coordinates using:

$$\mathbf{H}_{\ddot{\mathbf{x}}_p}(j\omega) = \mathbf{T} \cdot \mathbf{H}_{\ddot{\mathbf{x}}_t}(j\omega) \quad (10)$$

where $\mathbf{H}_{\ddot{\mathbf{x}}_p}(j\omega)$ is the structure’s transfer function of total accelerations in peripheral coordinates. The output spectral densities of the peripheral accelerations, $(\mathbf{R}_{\ddot{\mathbf{x}}_p}(\omega))_l$, are evaluated using:

$$(\mathbf{R}_{\ddot{\mathbf{x}}_p}(\omega))_l = |(\mathbf{H}_{\ddot{\mathbf{x}}_p}(j\omega))_l|^2 \cdot S(\omega) \quad (11)$$

where $S(\omega)$ is the input PSD, $|(\mathbf{H}_{\ddot{\mathbf{x}}_p}(j\omega))_l|^2 = (\mathbf{H}_{\ddot{\mathbf{x}}_p}(j\omega))_l \cdot (\mathbf{H}_{\ddot{\mathbf{x}}_p}^*(j\omega))_l$ where $(\mathbf{H}_{\ddot{\mathbf{x}}_p}(j\omega))_l$ is the l th term of $\mathbf{H}_{\ddot{\mathbf{x}}_p}(j\omega)$, $(\mathbf{H}_{\ddot{\mathbf{x}}_p}^*(j\omega))_l$ is its complex conjugate.

The mean-square response is obtained by evaluating the area under the output spectral density curve [45]. Thus, the root-mean-square (RMS) of total accelerations

at peripheral coordinate l , $RMS(\ddot{\mathbf{x}}_p^l)_l$, taking into consideration the contribution of all frequencies to the total response, is derived using:

$$RMS(\ddot{\mathbf{x}}_p^l)_l = \sqrt{2 \cdot \int_0^\infty (\mathbf{R}_{\ddot{\mathbf{x}}_p}(\omega))_l d\omega} \quad (12)$$

Step 4 If for any peripheral coordinate, l , the RMS acceleration obtained is larger than the allowable RMS acceleration, MTMDs are added to suppress the acceleration produced. Each TMD of mass $(\mathbf{m}_{TMD})_{l,f}$ is assigned with a DOF for its displacement relative to the ground, $(\mathbf{z})_{l,f}$. Here, the subscript l stands for its location while the subscript f stands for its frequency. At each location, N_{mode} TMDs are added, to suppress N_{mode} original frequencies of the structure, where N_{mode} is the number of modes to potentially be controlled. Thus, generally a total of $N_{mode} \cdot N_{locations}$ dampers are potentially added (Fig. 2). Note that the order of DOFs in the damped structure is:

$$\tilde{\mathbf{x}} = \begin{bmatrix} \mathbf{d}_x^T & \mathbf{d}_y^T & \boldsymbol{\theta}^T & (\mathbf{z})_{1,1} & (\mathbf{z})_{2,1} & \cdots & (\mathbf{z})_{N_{locations},1} \\ \cdots & (\mathbf{z})_{1,N_{mode}} & (\mathbf{z})_{2,N_{mode}} & \cdots & (\mathbf{z})_{N_{locations},N_{mode}} \end{bmatrix}^T \quad (13)$$

Note also that those two vectors are organized such that the component l of \mathbf{z} relates to the displacement of a TMD that is attached to the floor at the location of the component l of \mathbf{x}_p , i.e. the locations l are corresponding in those two vectors.

The initial properties of each such damper are obtained based on a SDOF system representing the damped mode. For simplicity, in this work, Den-Hartog's properties [3] were chosen. These properties were derived for the optimal reduction of mass displacement of a SDOF system under external sinusoidal loading. They were later shown to also reduce the maximum total acceleration response of the mass of a SDOF system undergoing a harmonic base excitation [4]. It should be noted that with the proposed scheme, any different set of chosen properties can be easily used. In the case of optimal Den-Hartog properties the properties are evaluated as follows:

1. The initial mass of each TMD is taken as certain predetermined percentage of the structure's mass (say 1 %), divided equally between the dampers situated at the same location, by:

$$(\mathbf{m}_{TMD})_{l,f} = \frac{0.01}{N_{mode}} \cdot M_{structure} \quad (14)$$

where l represents the damper's location, f represents the mode dampened and $M_{structure}$ is the structure's total mass. The mass ratio $(\boldsymbol{\mu}_{TMD})_f$ of all TMDs tuned to frequency f equals the ratio between the effective TMD mass of all TMDs tuned to frequency f and the f th modal mass of the structure. This mass ratio is defined as:

$$(\boldsymbol{\mu}_{TMD})_f = \frac{\boldsymbol{\phi}_f^T \cdot \mathbf{T}^T \cdot \mathbf{D}((\mathbf{m}_{TMD})_f) \cdot \mathbf{T} \cdot \boldsymbol{\phi}_f}{\boldsymbol{\phi}_f^T \cdot \mathbf{M}_{original} \cdot \boldsymbol{\phi}_f} \quad (15)$$

where $\boldsymbol{\phi}_f$ is the f th mode-shape of the bare structure, $[\mathbf{M}_{original}]$ is the bare frame's mass matrix, \mathbf{T} is the transformation matrix of Eq. (7), and $\mathbf{D}((\mathbf{m}_{TMD})_f)$ is a diago-

nal matrix with the terms $(\mathbf{m}_{\text{TMD}})_{1:N_{\text{locations}},f}$ sitting on the diagonal in the order of TMD DOFs, as in Eq. (13).

2. The stiffness of each TMD is based on the frequency of the mode which the TMD is set to dampen. This frequency is:

$$(\omega_{\text{TMD}})_f = \frac{(\omega_n)_f}{1 + (\mu_{\text{TMD}})_f} \quad (16)$$

where $(\omega_n)_f$ is the frequency f to be dampened. The compatible stiffness is:

$$(\mathbf{k}_{\text{TMD}})_{l,f} = (\mathbf{m}_{\text{TMD}})_{l,f} \cdot ((\omega_{\text{TMD}})_f)^2 \quad (17)$$

3. The damping ratio of each TMD is obtained:

$$(\xi_{\text{TMD}})_f = \sqrt{\frac{3 \cdot (\mu_{\text{TMD}})_f}{8 \cdot (1 + (\mu_{\text{TMD}})_f)^3}} \quad (18)$$

and the matching damping coefficient is:

$$(\mathbf{c}_{\text{TMD}})_{l,f} = 2 \cdot (\mathbf{m}_{\text{TMD}})_{l,f} \cdot (\xi_{\text{TMD}})_f \cdot (\omega_n)_f \quad (19)$$

Step 5 The mass, damping and stiffness matrices of the structure are updated with the damping system in place. The new mass matrix is:

$$\mathbf{M} = \begin{bmatrix} [\mathbf{M}_{\text{original}} + \mathbf{B}_{\text{dm}}^T \mathbf{m}_{\text{TMD}} \mathbf{B}_{\text{dm}}] & \mathbf{0} \\ \mathbf{0} & [\mathbf{m}_{\text{TMD}}] \end{bmatrix} \quad (20)$$

where $[\mathbf{M}_{\text{original}}]$ is the bare frame's mass matrix and $[\mathbf{m}_{\text{TMD}}]$ is a diagonal matrix with the terms $(\mathbf{m}_{\text{TMD}})_{l,f}$ sitting on the diagonal in the order of TMD DOFs, as in Eq. (13). The matrix \mathbf{B}_{dm} is a transfer matrix, used to add the mass of TMDs to the mass of the structure perpendicular to their original DOF (i.e. if a certain damper is used to reduce vibration in the “y” direction, and thus its DOF is in the “y” direction, the mass of that TMD is added to the mass of the structure in the “x” direction of the story where it is situated). It is given by:

$$\mathbf{B}_{\text{dm}}^T = \begin{bmatrix} 1 & \cdot & \cdot & \cdot & \cdot & \cdot & N_{\text{mode}} \\ \mathbf{T}_{\mathbf{m}}^T & \cdot & \cdot & \cdot & \cdot & \cdot & \mathbf{T}_{\mathbf{m}}^T \end{bmatrix} \quad (21)$$

where:

$$\mathbf{T}_{\mathbf{m}}(4 \cdot N_{\text{floors}} \times 3 \cdot N_{\text{floors}}) = \begin{bmatrix} \mathbf{I}(N_{\text{floors}} \times N_{\text{floors}}) & \mathbf{0}(N_{\text{floors}} \times N_{\text{floors}}) & \mathbf{0}(N_{\text{floors}} \times N_{\text{floors}}) \\ \mathbf{I}(N_{\text{floors}} \times N_{\text{floors}}) & \mathbf{0}(N_{\text{floors}} \times N_{\text{floors}}) & \mathbf{0}(N_{\text{floors}} \times N_{\text{floors}}) \\ \mathbf{0}(N_{\text{floors}} \times N_{\text{floors}}) & \mathbf{I}(N_{\text{floors}} \times N_{\text{floors}}) & \mathbf{0}(N_{\text{floors}} \times N_{\text{floors}}) \\ \mathbf{0}(N_{\text{floors}} \times N_{\text{floors}}) & \mathbf{I}(N_{\text{floors}} \times N_{\text{floors}}) & \mathbf{0}(N_{\text{floors}} \times N_{\text{floors}}) \end{bmatrix} \quad (22)$$

The damping matrix of the damped frame is constructed as:

$$\mathbf{C} = \begin{bmatrix} [\mathbf{C}_{\text{original}} + \mathbf{B}_{\mathbf{d}}^T \mathbf{c}_{\text{TMD}} \mathbf{B}_{\mathbf{d}}] & [-\mathbf{B}_{\mathbf{d}}^T \mathbf{c}_{\text{TMD}}] \\ [-\mathbf{c}_{\text{TMD}} \mathbf{B}_{\mathbf{d}}] & [\mathbf{c}_{\text{TMD}}] \end{bmatrix} \quad (23)$$

where $[\mathbf{C}_{\text{original}}]$ is the bare frame's inherent damping matrix and $[\mathbf{c}_{\text{TMD}}]$ is a diagonal matrix with the terms $(\mathbf{c}_{\text{TMD}})_{l,f}$ sitting on the diagonal in the order of DOFs as

in Eq. (13). The matrix \mathbf{B}_d is a transfer matrix, used to assign the TMDs within the structure.

$$\mathbf{B}_d^T = \begin{bmatrix} 1 & \cdot & \cdot & \cdot & \cdot & \cdot & N_{mode} \\ \mathbf{T}^T & \cdot & \cdot & \cdot & \cdot & \cdot & \mathbf{T}^T \end{bmatrix} \quad (24)$$

The stiffness matrix of the damped frame is constructed similarly as:

$$\mathbf{K} = \begin{bmatrix} [\mathbf{K}_{original} + \mathbf{B}_d^T \mathbf{k}_{TMD} \mathbf{B}_d] & [-\mathbf{B}_d^T \mathbf{k}_{TMD}] \\ [-\mathbf{k}_{TMD} \mathbf{B}_d] & [\mathbf{k}_{TMD}] \end{bmatrix} \quad (25)$$

where $[\mathbf{K}_{original}]$ is the bare frame's stiffness matrix and $[\mathbf{k}_{TMD}]$ is a diagonal matrix with the terms $(\mathbf{k}_{TMD})_{l,f}$ sitting on the diagonal in the order of DOFs as in Eq. (13).

Step 6 The peripheral RMS accelerations of the damped frame at all coordinates are evaluated using frequency-domain analysis based on Eqs. (8)–(12), using the newly-updated matrices. As the computation of the transfer functions involve inversion of the mass matrix, and some TMD masses may get very small during the design process, singularity issues may occur. To avoid those, the expressions $\mathbf{M}^{-1}\mathbf{K}$ and $\mathbf{M}^{-1}\mathbf{C}$ used in Eq. (2) are evaluated as follows:

$$\mathbf{M}^{-1}\mathbf{K} = \begin{bmatrix} (\mathbf{M}_{original} + \mathbf{B}_{dm}^T \mathbf{m}_{TMD} \mathbf{B}_{dm})^{-1} \cdot (\mathbf{K}_{original} + \mathbf{B}_d^T \mathbf{k}_{TMD} \mathbf{B}_d) \\ -\boldsymbol{\Omega}_{TMD}^2 \mathbf{B}_d \\ \dots \\ -(\mathbf{M}_{original} + \mathbf{B}_{dm}^T \mathbf{m}_{TMD} \mathbf{B}_{dm})^{-1} \mathbf{B}_d^T \mathbf{k}_{TMD} \\ \boldsymbol{\Omega}_{TMD}^2 \end{bmatrix} \quad (26)$$

where $\boldsymbol{\Omega}_{TMD}^2$ is a diagonal matrix with the terms $((\omega_{TMD})_{l,f})^2$ sitting on the diagonal in the order of DOFs given in Eq. (13), and:

$$\mathbf{M}^{-1}\mathbf{C} = \begin{bmatrix} (\mathbf{M}_{original} + \mathbf{B}_{dm}^T \mathbf{m}_{TMD} \mathbf{B}_{dm})^{-1} \cdot (\mathbf{C}_{original} + \mathbf{B}_d^T \mathbf{c}_{TMD} \mathbf{B}_d) \\ -\boldsymbol{\Omega}_{TMD} \boldsymbol{\xi}_{TMD} \mathbf{B}_d \\ \dots \\ -(\mathbf{M}_{original} + \mathbf{B}_{dm}^T \mathbf{m}_{TMD} \mathbf{B}_{dm})^{-1} \mathbf{B}_d^T \mathbf{c}_{TMD} \\ \boldsymbol{\Omega}_{TMD} \boldsymbol{\xi}_{TMD} \end{bmatrix} \quad (27)$$

where $\boldsymbol{\Omega}_{TMD} \boldsymbol{\xi}_{TMD}$ is a diagonal matrix with the terms $2 \cdot (\boldsymbol{\xi}_{TMD})_{l,f} \cdot (\omega_n)_f$ sitting on the diagonal in the order of DOFs given in Eq. (13).

Step 7 Each TMD's mass is re-determined using two stages. First, the total mass of all dampers at a certain location is determined. This is followed by the distribution of that mass between all TMDs at the same location, having various tuning frequencies. This is done according to the recurrence relationships described below. Following the change in mass, the stiffness and modal damping ratio of each TMD are also updated while keeping the Den-Hartog principles intact, using Eqs. (15)–(19). The two-stage analysis/redesign procedure is carried out iteratively, in the following way.

Stage 1 The first stage of redesign includes the evaluation of the total mass of all TMDs at a certain location, which promises the existence of the first part of the conjecture. This is formulated using:

$$(\mathbf{m}_{\text{TMD,total}}^{(n+1)})_l = \sum_{f=1}^{\text{all frequencies}} (\mathbf{m}_{\text{TMD}}^{(n+1)})_{l,f} = \sum_{f=1}^{\text{all frequencies}} (\mathbf{m}_{\text{TMD}}^{(n)})_{l,f} \cdot \left(\frac{\text{RMS}(\ddot{\mathbf{x}}_p^{(n)})_l}{a_{\text{all}}^{\text{RMS}}} \right)^P \quad (28)$$

where $(\cdot)^{(n)}$ is the value at iteration n , $(\mathbf{m}_{\text{TMD,total}}^{(n+1)})_l$ is the total mass of all dampers at location l , and P is a constant which influences the convergence and convergence rate. A large P will result in a faster but less stable convergence of the above equation. Based on the authors' experience, a P in the range of 0.1–2.0 should be satisfying in terms of stability, convergence and fair amount of iterations.

Stage 2 In the second stage of redesign, the total mass obtained at each location is distributed between N_{mode} dampers (dampening modes $(\omega_n)_f$) at that same location l , promising the existence of the second part of the conjecture, using the following:

$$\begin{aligned} (\mathbf{m}_{\text{TMD}}^{(n+1)})_{l,f} &= (\mathbf{m}_{\text{TMD}}^{(n)})_{l,f} \left(\frac{\sqrt{(\mathbf{R}_{\dot{\mathbf{x}}_p}^{(n)})((\omega_n)_f)_l}}}{\max_f \left(\sqrt{(\mathbf{R}_{\dot{\mathbf{x}}_p}^{(n)})((\omega_n)_f)_l} \right)} \right)^P \\ &\times \frac{(\mathbf{m}_{\text{TMD,total}}^{(n+1)})_l}{\sum_{f=1}^{\text{all frequencies}} (\mathbf{m}_{\text{TMD}}^{(n)})_{l,f} \left(\frac{\sqrt{(\mathbf{R}_{\dot{\mathbf{x}}_p}^{(n)})((\omega_n)_f)_l}}}{\max_f \left(\sqrt{(\mathbf{R}_{\dot{\mathbf{x}}_p}^{(n)})((\omega_n)_f)_l} \right)} \right)^P} \end{aligned} \quad (29)$$

where $(\mathbf{R}_{\dot{\mathbf{x}}_p}^{(n)})((\omega_n)_f)_l$ is the component of $\mathbf{R}_{\dot{\mathbf{x}}_p}^{(n)}(\omega)$ at the location l evaluated at $\omega = (\omega_n)_f$.

The analysis/redesign procedure is continued until convergence. It shall be noted that each iteration cycle may result in either a bigger or smaller mass.

Rationale: Upon convergence, i.e. when values at the iteration $n + 1$ are equal to the corresponding values at the iteration n , Eq. (28) is satisfied under one of two conditions. That is, either $\sum_{f=1}^{\text{all frequencies}} (\mathbf{m}_{\text{TMD}}^{(n+1)})_{l,f} = \sum_{f=1}^{\text{all frequencies}} (\mathbf{m}_{\text{TMD}}^{(n)})_{l,f} \neq 0$ and thus $\text{RMS}(\ddot{\mathbf{x}}_p^{(n+1)})_l = \text{RMS}(\ddot{\mathbf{x}}_p^{(n)})_l = a_{\text{all}}^{\text{RMS}}$, or $\text{RMS}(\ddot{\mathbf{x}}_p^{(n+1)})_l = \text{RMS}(\ddot{\mathbf{x}}_p^{(n)})_l \leq a_{\text{all}}^{\text{RMS}}$ and then $\sum_{f=1}^{\text{all frequencies}} (\mathbf{m}_{\text{TMD}}^{(n+1)})_{l,f} = \sum_{f=1}^{\text{all frequencies}} (\mathbf{m}_{\text{TMD}}^{(n)})_{l,f} = 0$. This portrays fully-stressedness in total accelerations, i.e. the first part of the conjecture. Equation (29), on the other hand, portrays fully-stressedness in frequency response. Here, taking the sum of each side of the equation with respect to f implies that the sum of masses of TMDs at the location l and iteration $n + 1$ equals the desired total mass from the first stage, $(\mathbf{m}_{\text{TMD,total}}^{(n+1)})_l$, or $\sum_{f=1}^{\text{all frequencies}} (\mathbf{m}_{\text{TMD}}^{(n+1)})_{l,f} = (\mathbf{m}_{\text{TMD,total}}^{(n+1)})_l$.

This is actually attained using the fraction on the right-hand side of Eq. (29), which is constant for all f 's. The remaining part of Eq. (29) has a similar structure to that of Eq. (28). That is, upon convergence, either $(\mathbf{m}_{\text{TMD}}^{(n+1)})_{l,f} = (\mathbf{m}_{\text{TMD}}^{(n)})_{l,f} \neq 0$ and thus $\sqrt{(\mathbf{R}_{\dot{\mathbf{x}}_p}^{(n)}((\omega_n)_f))_l} = \max_f \sqrt{(\mathbf{R}_{\dot{\mathbf{x}}_p}^{(n)}((\omega_n)_f))_l}$, or $\sqrt{(\mathbf{R}_{\dot{\mathbf{x}}_p}^{(n)}((\omega_n)_f))_l} \leq \max_f \sqrt{(\mathbf{R}_{\dot{\mathbf{x}}_p}^{(n)}((\omega_n)_f))_l}$ and then $(\mathbf{m}_{\text{TMD}}^{(n+1)})_{l,f} = (\mathbf{m}_{\text{TMD}}^{(n)})_{l,f} = 0$. This portrays fully-stressedness in frequency response, i.e. the second part of the conjecture. It should be noted that the normalization of $\sqrt{(\mathbf{R}_{\dot{\mathbf{x}}_p}^{(n)}((\omega_n)_f))_l}$ with respect to $\max_f \sqrt{(\mathbf{R}_{\dot{\mathbf{x}}_p}^{(n)}((\omega_n)_f))_l}$ has no effect on the results of this equation and is done here only for clarification of the rationale behind Eq. (29).

Step 8 Repeat steps 5 to 7 until convergence of the mass is reached.

Step 9 After the process has converged, the retrofitted frame's response is validated using time history analysis and the chosen ensemble of ground motions.

Step 10 If the percent of reduction in RMS acceleration and the envelope peak accelerations are not be entirely compatible, a modification of the allowable RMS acceleration may be performed so as to scale these two frequency/time domain measures, using the following:

$$a_{\text{all},l}^{\text{RMS}} = a_{\text{all}}^t \cdot \frac{RMS((\ddot{\mathbf{x}}_p^t)_l)}{\max_{eq}(\max_t((\ddot{\mathbf{x}}_p^t(t)))_l)} \quad \forall l = 1, 2, \dots, N_{\text{locations}} \quad (30)$$

where: $a_{\text{all},l}^{\text{RMS}}$ is the modified allowable RMS acceleration to be used in the frequency-domain analysis.

Once the allowable RMS acceleration is modified, steps 5–9 are repeated until the reduction in peak acceleration is as desired.

5 Example

The following 8-story asymmetric RC frame structure (Fig. 4) introduced by Tso and Yao [46] is retrofitted using MTMDs for an excitation in the “y” direction. A uniform distributed mass of 0.75 ton/m² is taken. The column dimensions are 0.5 m by 0.5 m for frames 1 and 2 and 0.7 m by 0.7 m for frames 3 and 4. The beams are 0.4 m wide and 0.6 m tall. 5 % Rayleigh damping for the first and second modes is used. A 40 % reduction of the peripheral peak total acceleration obtained in the bare structure is desired. Hence, initially, an allowable peripheral RMS acceleration of 60 % of the maximal peripheral RMS acceleration of the bare structure is adopted. The response is analyzed under a Kanai-Tajimi PSD with parameters fitted to the average FFT values of a chosen ensemble of ground-motions (SE 10 in 50). The design variables are the locations and properties of the individual tuned mass dampers. The dampers are to potentially be located in the peripheral frames, where they are most effective, and as the excitation is in the “y” direction only, dampers

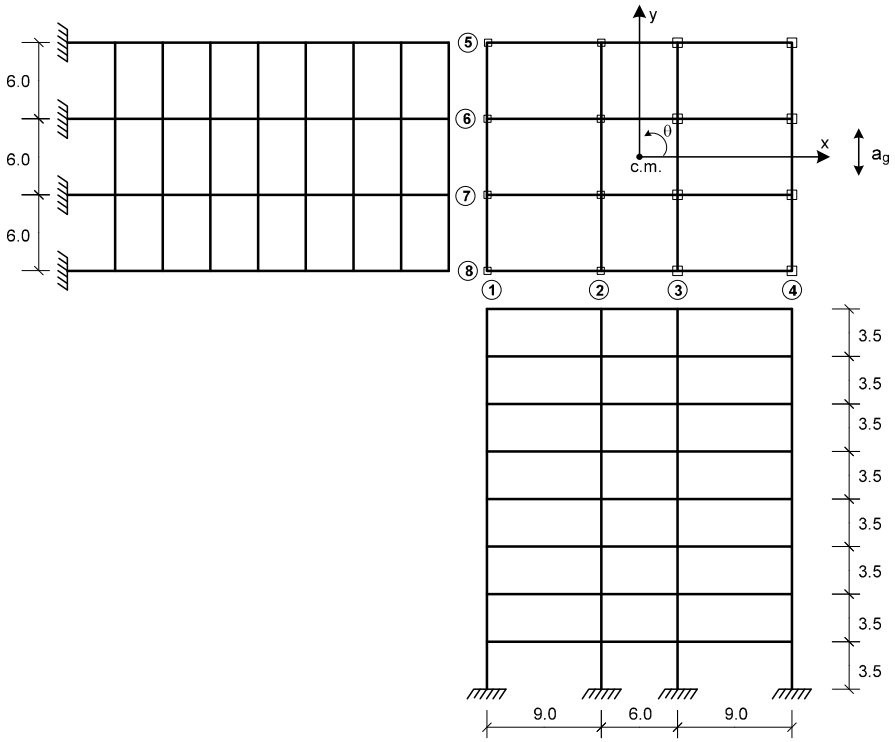


Fig. 4 Eight-story asymmetric structure

Table 1 Frequencies of the structure

Mode No.	Angular frequency (rad/sec)	Mode direction
1	5.135	x
2	5.463	y, θ
3	7.087	y, θ
4	16.240	x
5	16.938	y, θ
6	22.407	y, θ
7	29.649	x
8	29.876	y, θ
9	40.918	y, θ
10	44.770	y, θ

will be assigned only to peripheral frames 1 and 4, to dampen frequencies of modes which involve “ y ” and “ θ ”. The ‘stepwise flowchart’ described above is closely followed to optimally design the MTMDs.

Fig. 5 Peripheral RMS accelerations of bare structure (*continuous*) and allowable values (*dashed*)

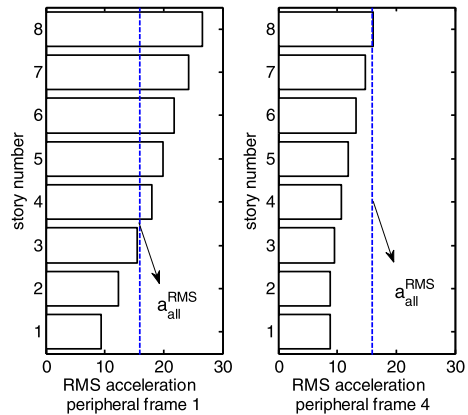
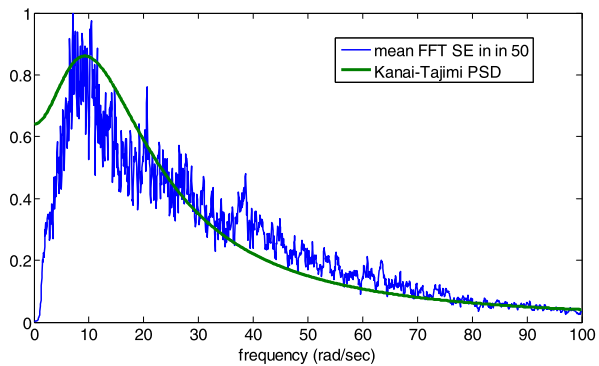


Fig. 6 Chosen input power-spectral-density



Step 1 The mass, inherent damping and stiffness matrices of the frame in the dynamic DOFs shown in Fig. 1 were constructed.

Step 2 The natural frequencies, of the structure were determined. The first 10 frequencies are presented in Table 1.

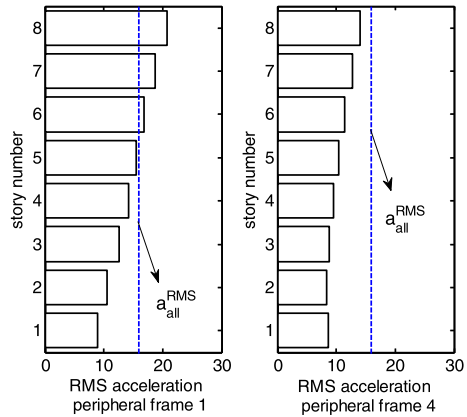
Step 3 The RMS accelerations of the undamped building at the peripheral frames in the “y” direction are presented in Fig. 5. Those were obtained using the Kanai-Tajimi PSD with parameters: $\omega_g = 13$ rad/sec, $\xi_g = 0.98$ and $S_0 = 1$. Those parameters were determined by fitting the parameters ω_g and ξ_g to a spectrum of mean FFT values of the SE 10 in 50 ground-motion ensemble, scaled to $S_0 = 1.0$ (see Fig. 6). The actual value of S_0 has no effect since the allowable RMS acceleration is determined by the percentage of reduction desired. The allowable RMS acceleration for all peripheral accelerations was earlier adopted as 60 % of the maximum peripheral RMS acceleration of the bare frame, giving: $a_{all}^{RMS} = 15.95$. It is assumed, as a first guess, that a similar reduction would be achieved in the envelope peak acceleration in time domain.

Step 4 160 TMDs were added, as a first guess, with initial properties as given in Table 2. Those are comprised of 10 dampers each tuned to a different mode

Table 2 Initial properties of TMDs

No. TMD	Mode to dampen	Initial mass (ton)	Initial natural frequency (rad/sec)	Initial damping ratio
1–16	2	2.592	5.37	0.0788
17–32	3	2.592	6.89	0.1004
33–48	5	2.592	16.64	0.0795
49–64	6	2.592	21.78	0.0998
65–80	8	2.592	29.34	0.0805
81–96	9	2.592	39.79	0.0989
97–112	10	2.592	43.94	0.0816
113–128	12	2.592	60.28	0.0822
129–144	13	2.592	62.30	0.0983
145–160	15	2.592	77.55	0.0826

Fig. 7 Peripheral RMS accelerations of structure with initial TMDs (*continuous*) and allowable values (*dashed*)



frequency (of modes related to “y” and “θ”) at each of the 16 peripheral locations of frames 1 and 4.

Step 5 The mass, stiffness and damping matrices were updated.

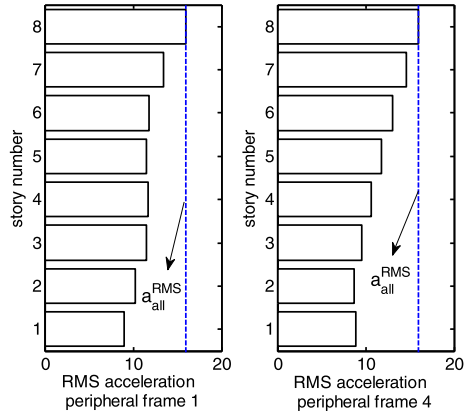
Step 6 With the newly-updated matrices and the same PSD input, new peripheral RMS accelerations, shown in Fig. 7 (for frames 1 and 4), were evaluated using Eqs. (8)–(12). Peripheral accelerations smaller than the allowable, were attained for all floors of frames 5 and 8 (see Fig. 4 for frame numbering).

Step 7 The problem has not converged, and thus the TMDs’ properties were altered, using the recurrence relations of Eqs. (28) and (29), while using $P = 2$ as the convergence parameter, giving updated total masses at each DOF. For example, the newly updated mass of all TMDs at floor 1 of peripheral frame 1 is: $m_{TMD,1}^{(1)} = 2.592 \cdot (\frac{9.41}{15.92})^2 = 0.906$ for a RMS total acceleration of 9.41 at that location (frame 1, 1st floor) after adding initial TMDs (Fig. 7). The total mass of

Table 3 Total mass of TMDs upon convergence

Floor	Total mass frame 1 (ton)	Total mass frame 4 (ton)
1-7	0	0
8	112.69	6.25

Fig. 8 Peripheral RMS accelerations of structure with final TMDs (*continuous*) and allowable values (*dashed*)



each peripheral coordinate was then distributed between the 10 dampers at the same location using Eq. (29).

Step 8 Iterative analysis/redesign as described in Eqs. (28) and (29) while altering the mass of the damper is carried out until convergence to allowable levels. Upon convergence the dampers’ total mass at each location are shown in Table 3.

TMDs with non-zero properties were located at frames number 1 and 4, both at the 8th floor, which is the top floor of each peripheral frame. The final properties of each added TMD are shown in Table 4. For frame number 1, the TMDs are set to dampen mode 2, while for frame number 4, the TMDs are set to dampen modes 2 and 3. Finally, an analysis of the retrofitted structure yields the peripheral RMS accelerations shown in Fig. 8.

All 4 assigned TMDs add up to 4.59 % of the original structure’s mass. As can be seen, only floors who had reached the maximum allowable RMS total acceleration (Fig. 8) were assigned with added absorbers (Table 4), making the solution obtained a FSD.

Table 4 Final properties of added TMDs

Frame	Floor	Mode to dampen	Final mass (ton)	Final stiffness (kN/m)	Final damping ratio
1	8	2	112.69	2472.15	0.1983
4	8	2	5.69	124.89	0.1983
4	8	3	0.55	27.72	0.0209

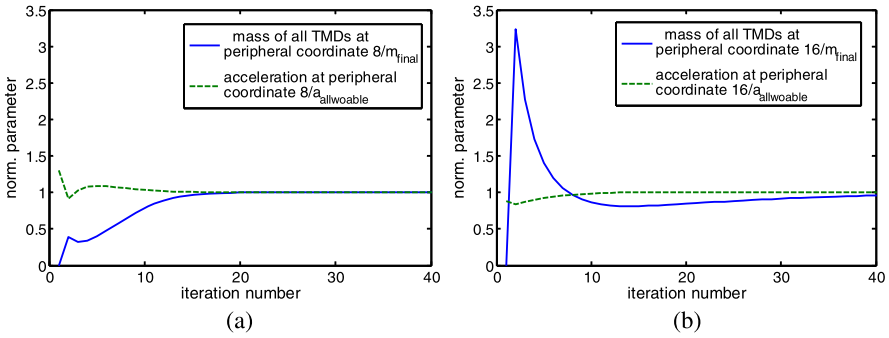


Fig. 9 Convergence of sum of masses and RMS acceleration at (a) 8th floor of peripheral frame number 1 and (b) 8th floor of peripheral frame number 4

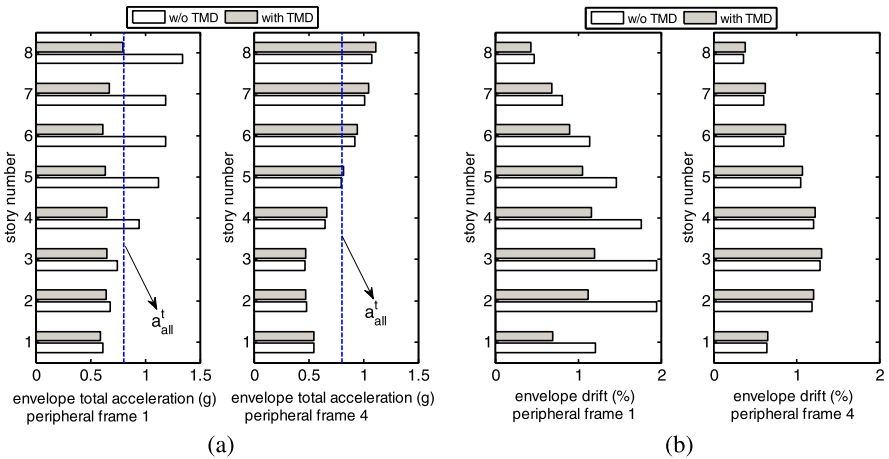


Fig. 10 Peripheral envelope (a) accelerations and allowable values (*dashed*) and (b) drifts of the bare and damped structure under the SE 10 in 50 ground motion ensemble

Figure 9 presents the convergence of the design variables (masses) and the performance measure (acceleration). As can be seen in Fig. 9, although the initial guess was very far from optimum, convergence is practically reached within less than 40 iterations.

Step 9 The retrofitted structure was examined using time-history analysis under the SE 10 in 50 ensemble of real recorded earthquakes, scaled by a factor of 0.8, to check the validity of the solution obtained. The results of the envelope peak peripheral total accelerations and inter-story drifts of frames 1 and 4 obtained using time-history analysis are shown in Fig. 10. Smaller accelerations were attained in frames 5 and 8.

The results reveal that for this ensemble, the envelope maximum total acceleration of all locations of the bare structure was at the 8th floor of frame number 1,

Table 5 Final properties of added TMDs

Frame	Floor	Mode to dampen	Final mass (ton)	Final stiffness (kN/m)	Final damping ratio
1	8	2	114.18	2397.4	0.2062
4	8	2	115.81	2431.7	0.2062

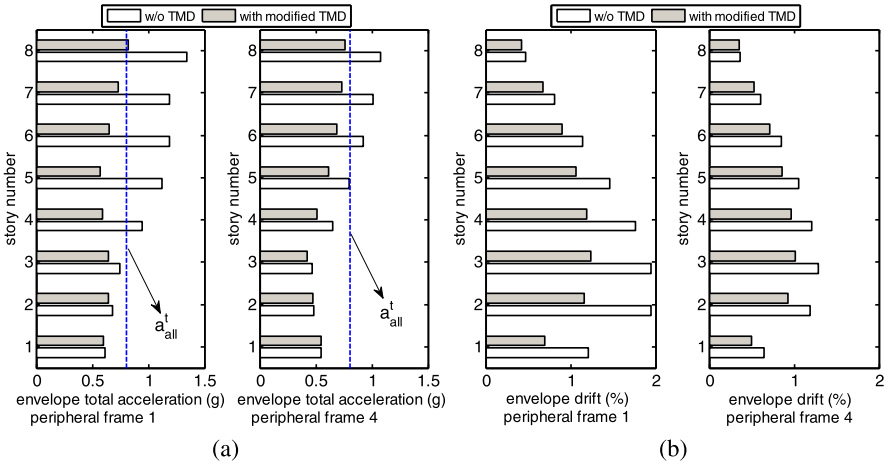


Fig. 11 Peripheral envelope (a) accelerations and allowable values (*dashed*) and (b) drifts of the bare and 3rd-time modified damped structure under the SE 10 in 50 ground motion ensemble

equaling 1.34g, while the envelope maximum total acceleration of all locations of the damped structure was 1.11g (8th floor of frame 4). This represents a 17% reduction in acceleration response, not so close to the desired reduction of 40% in maximum response.

Although reducing the drifts was not part of the design process, it can be seen that these too were appreciably reduced. The maximum peripheral drift of all locations was reduced from 1.95% in the bare structure to 1.30% in the damped structure.

Step 10 For a more accurate design, the allowable RMS total acceleration of each story is modified to better reflect the allowable peak acceleration, using Eq. (30).

In this case, a 40% reduction in envelope peak acceleration is desired, thus $a_{all}^t = 0.6 \cdot \max_l(\max_{eq}(\max_t(\ddot{x}_p^t(t)_{bare-frame}))_l)) = 0.6 \cdot 1.34 = 0.804g$. For example, for location 8 (frame 1, 8th floor): $a_{all,8}^{RMS} = 0.804 \cdot \frac{15.952}{0.795} = 16.15$. Using this modification, the analysis/redesign process (steps 5–9) is repeated until convergence is once again reached. After convergence, the total mass was increased to 8.36% of the structure’s mass. The modified retrofitted structure was again examined using time-history analysis under the SE 10 in 50 ensemble scaled by a factor of 0.8. The reduction between maximal envelope acceleration of all floors of the bare and damped structure was increased to 34.8%. The results can be modified yet again using step 10. After the third modification, the added mass of all TMDs increased to 8.87% (see Table 5), while the envelope peak total acceleration equaled 0.82g,

representing a 39.0 % reduction in response, which is very close to the desired reduction of 40 %. The results of the envelope peak peripheral total accelerations and inter-story drifts of frames 1 and 4 obtained using time-history analysis are shown in Fig. 11.

6 Conclusions

This chapter presented an analysis/redesign-based methodology for efficiently allocating, sizing and tuning multiple TMDs in 3D irregular structures.

As was shown, using the proposed analysis allows reducing absolute accelerations to a desirable level, allowing for performance-based design. This is done while using several TMDs located at different places and tuned to several frequencies.

The proposed methodology is general, and is thus suitable for use in all types of structures, regardless of the amount of irregularity.

The advantages of this methodology are its simplicity of use and relying solely on analysis tools to solve the allocation and sizing problem, with no assumptions or pre-selection of any design variable. These advantages make the proposed methodology very attractive and efficient for practical use.

If found that detuning of the TMDs due to yielding of the structure may be apparent, a TMD located at location l tuned to dampen mode f can be split into several smaller TMDs, each with a slightly different frequency within a bandwidth close to the natural frequency f of the main system. Thus reduction of the detuning effect and design robustness could be achieved. This could be done a-priori and taken into account in the design methodology. In cases where the damped structure is not brought to behave linearly, and damage to the structural system is apparent, the natural frequencies of the structure may change considerably. In those cases, a design according to the proposed scheme, combined with the use of semi-active TMDs (for example, [15–17]) which allow the simple change of the TMD's tuning, while still keeping the control system's low-cost, could be beneficial.

References

1. Soong TT, Dargush GF (1997) *Passive energy dissipation systems in structural engineering*. Wiley, Chichester
2. Christopoulos C, Filiatrault A (2006) *Principles of supplemental damping and seismic isolation*. IUSS Press, Milan
3. Den-Hartog JP (1940) *Mechanical vibrations*, 2nd edn. McGraw-Hill, New York
4. Warburton GB (1982) Optimum absorber parameters for various combinations of response and excitation parameters. *Earthquake Engineering and Structural Dynamics* 10:381–401
5. Housner GW, Bergman LA, Caughey TK, Chassiakos AG, Claus RO, Masri SF, Skelton RE, Soong TT, Spencer BF, Yao JTP (1997) Structural control: past, present and future. *J Eng Mech* 123(9):897–971
6. Kelly SG (2000) *Fundamentals of mechanical vibrations*, 2nd edn. McGraw-Hill, Boston
7. McNamara RJ (1977) Tuned mass dampers for buildings. *J Struct Div* 103:1785–1798

8. Luft RW (1979) Optimum tuned mass dampers for buildings. *J Struct Div* 105:2766–2772
9. Wiesner KB (1979) Tuned mass dampers to reduce building wind motion. In: ASCE convention and exposition, Boston, pp 1–21
10. Gupta YP, Chandrasekaran AR (1969) Absorber system for earthquake excitation. In: Proceedings of the 4th world conference on earthquake engineering, Santiago, vol II, pp 139–148
11. Kaynia AM, Veneziano D, Biggs JM (1981) Seismic effectiveness of tuned mass dampers. *J Struct Div* 107:1465–1484
12. Sladek JK, Klingner RE (1983) Effect of tuned-mass dampers on seismic response. *J Struct Div* 109:2004–2009
13. Chowdhury AH, Iwuchukwu MD, Garske JJ (1985) The past and future of seismic effectiveness of tuned mass dampers. In: Proceedings of the second international symposium on structural control, Ontario, pp 105–127
14. Rasouli SK, Yahyai M (2002) Control of response of structures with passive and active tuned mass dampers. *Struct Des Tall Spec Build* 11:1–14
15. Nagarajaiah S, Sonmez E (2007) Structures with semiactive variable stiffness single/multiple tuned mass dampers. *J Struct Eng* 133(1):67–77
16. Nagarajaiah S (2009) Adaptive passive, semiactive, smart tuned mass dampers: identification and control using empirical mode decomposition, Hilbert transform, and short-term Fourier transform. *Struct Control Health Monit* 16:800–841
17. Roffel AJ, Lourenco R, Narasimhan S (2010) Experimental studies on an adaptive tuned mass dampers with real-time tuning capability. In: ASCE 19th analysis & computation specialty conference, pp 314–324
18. Abdel-Rohman M (1984) Optimal design of active TMD for buildings control. *Build Environ* 19(3):191–195
19. Xu K, Igusa T (1992) Dynamic characteristics of multiple substructures with closely spaced frequencies. *Earthquake Engineering and Structural Dynamics* 21:1059–1070
20. Clark AJ (1988) Multiple passive tuned mass dampers for reducing earthquake induced building motion. In: Proceedings of the 9th world conference on earthquake engineering, Tokyo-Kyoto, vol V, pp 779–784
21. Moon KS (2010) Vertically distributed multiple tuned mass dampers in tall buildings: performance analysis and preliminary design. *Struct Des Tall Spec Build* 19:347–366
22. Moon KS (2010) Integrated damping systems for tall buildings: vertically distributed TMDs. In: 2010 ASCE structures congress, pp 3122–3131
23. Wirsching PH, Campbell GW (1974) Minimal structural response under random excitations using vibration absorber. *Earthquake Engineering and Structural Dynamics* 2:303–312
24. Sadek F, Mohraz B, Taylor AW, Chung RM (1997) A method of estimating the parameters of tuned mass dampers for seismic applications. *Earthquake Engineering and Structural Dynamics* 26:617–635
25. Lee CL, Chen YT, Chung LL, Wang YP (2006) Optimal design theories and applications of tuned mass dampers. *Eng Struct* 28:43–53
26. Hadi MNS, Arfiadi Y (1998) Optimum design of absorber for MDOF structures. *J Struct Eng* 124(11):1272–1280
27. Spencer BF, Suhardjo J, Sain MK (1994) Frequency domain optimal control strategies for aseismic protection. *J Eng Mech* 120(1):135–158
28. Soong TT (1988) State of the art review—active structural control in civil engineering. *Eng Struct* 10:74–84
29. Soong TT (1990) Active structural control: theory and practice. Longman Scientific & Technical, Harlow
30. Prucz Z, Soong TT, Reinhorn AM (1985) An analysis of pulse control for simple mechanical systems. *J Dyn Syst Meas Control* 107:123–131
31. Chuang CH, Wu DN (1996) Optimal bounded-state control with applications to building structure. *Optim Control Appl Methods* 17:209–230
32. Chuang CH, Wu DN, Wang Q (1996) LQR for state-bounded structural control. *J Dyn Syst Meas Control* 118:113–119

33. Del Grosso A, Zucchini A (1995) Bounded-state active control of structures: a set-theoretic approach. *Smart Mater Struct* 4:A15–A24
34. Chen G, Wu J (2001) Optimal placement of multiple tune mass dampers for seismic structures. *J Struct Eng* 127(9):1054–1062
35. Luo X, Ma R, Li G, Zhao D (2009) Parameter optimization of multi-mode vibration control system. In: *International conference of measuring technology and mechatronics automation*. IEEE Comput Soc, Los Alamitos, pp 685–688
36. Lin CC, Wang JF, Lien CH, Chiang HW, Lin CS (2010) Optimum design and experimental study of multiple tuned mass dampers with limited stroke. *Earthquake Engineering and Structural Dynamics* 39:1631–1651
37. Fu TS, Johnson EA (2011) Distributed mass damper system for integrating structural and environmental control in buildings. *J Eng Mech* 137(3):205–213
38. Cilley FH (1900) The exact design of statically indeterminate frameworks, an exposition of its possibility but futility. *Trans ASCE* 43:353–407
39. Levy R (1985) On the optimal design of trusses under one loading condition. *Q Appl Math* 43(2):129–134
40. Levy R, Lavan O (2006) Fully stressed design of passive controllers in framed structures for seismic loadings. *Struct Multidiscip Optim* 32:485–498
41. Kanai K (1957) Semi-empirical formula for the seismic characteristics of the ground. *Bull Earthq Res Inst Univ Tokyo* 35:309–325
42. Nagarajaiah S, Narasimhan S (2006) Smart base-isolated benchmark building. Part II: Phase I sample controllers for linear isolation systems. *Struct Control Health Monit* 12:589–604
43. Agrawal AK, Xu Z, He WL (2006) Ground motion pulse-based active control of a linear base-isolated benchmark building. *Struct Control Health Monit* 13:792–808
44. Kwakernaak H, Sivan R (1991) *Modern signals and systems*. Prentice Hall, Englewood Cliffs
45. Newland DE (1993) *An introduction to random vibrations, spectral & wavelet analysis*. Prentice Hall, Harlow
46. Tso WK, Yao S (1994) Seismic load distribution in buildings with eccentric setback. *Can J Civ Eng* 21:50–62

Comparison of Innovative Base Isolation Retrofitting Technology with Conventional Retrofitting of Existing Buildings

Mikayel Melkumyan

Abstract Three remarkable projects on retrofitting by base isolation of the existing buildings are described in the chapter. One of them is retrofitting of a 5-story stone apartment building in Armenia. The operation was made without resettlement of the occupants. World practice provides no similar precedent in retrofitting of apartment buildings. The other project is retrofitting of the 60 years old 3-story stone school building also in Armenia. This building has historical and architectural value. Unique operations which were carried out in order to install the isolation system within the basement of this building and to preserve its architectural appearance are described. The third project is development of the design on retrofitting by base isolation of the 180 years old historical building of the Iasi City Hall in Romania. The structural concept of retrofitting is described and detailed results of the earthquake response analysis for two cases, i.e. when the building is base isolated and when it has a fixed base, are given. For all three buildings comparative analyses of the cost of innovative base isolation retrofitting technology vs. the costs of the different methods of conventional retrofitting are carried out and presented.

Keywords Existing buildings · Base isolation · Innovative technology · Retrofitting · Conventional retrofitting · Comparison of technologies · Base isolated building · Fixed base building · Comparison of responses · Linear analysis · Non-linear analysis

1 Innovative Base Isolation Retrofitting Technology for the Existing Buildings with Stone Bearing Walls

Isolation of structures from horizontal ground motions is gradually becoming a more common method of providing protection from earthquake damage. By reducing the seismic forces transmitted, isolation protects the contents and secondary structural

M. Melkumyan (✉)

Armenian Association for Earthquake Engineering (AAEE), 1st lane of Nansen st. 6, 0056, Yerevan, Armenia

e-mail: mmelkumi@yahoo.com

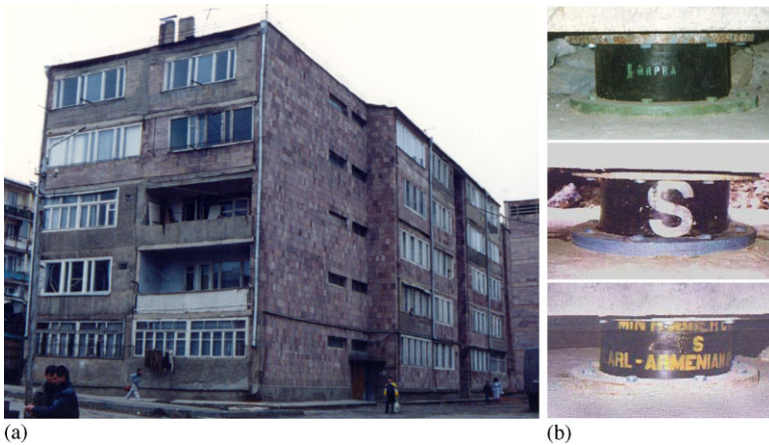


Fig. 1 General view of the retrofitted by base isolation existing 5-story stone apartment building (a) and fragments of its isolation system (b)

features as well as the main structure; the safety of occupants and passers-by is thus also enhanced. Moreover, it is practicable to design the isolation system so that the structure responds elastically to the design level earthquake. Thus repair cost should be greatly reduced and continued serviceability of the structure assured [1]. The rehabilitation of existing structures by the insertion of isolators at foundation level has been carried out on historic buildings in California such as the Oakland City Hall, San Francisco City Hall [2, 3], Salt Lake City and County Building [4, 5]. For these, isolation may provide the only viable means that is not unduly intrusive and damaging for the appearance of the building. Together with that the retrofitting technique using base isolation has great potential for rehabilitation of ordinary civil structures such as apartment blocks. The first retrofit of stone apartment building of series 1A-450 has been carried out in Armenia [6, 7].

1.1 Innovative Base Isolation Retrofitting Technology for the Existing Five-Story Stone Apartment Building

Buildings on typical design of series 1A-450 have been erected in all regions of Armenia. They have the plan dimensions 52×15 m, symmetrical about the center of the long side and the bearing walls with 45–50 cm of thickness located mainly in transverse direction. The horizontal stiffness in the longitudinal direction is provided partly by the R/C frames with strong beams and columns, made inside the body of walls, and by longitudinal walls at the edge parts of the buildings.

The developed structural concept aims at retrofitting an existing building by means of seismic isolators using simple working technology [8]. This is a unique pioneering seismic isolation project introduced for an existing 5-story stone building (Fig. 1).

The idea is to supply this building with seismic isolation in the foundation by gradually cutting the isolators into the walls at the level of foundation upper edge by means of a two-stage system of R/C beams. Base isolation method for existing buildings with bearing walls (Patent of the Republic of Armenia #579) that envisions placing of seismic isolators at the level of the foundation or the basement solves the problem as shown in Fig. 2.

It is very important that openings in walls are made so that two adjacent openings are not made simultaneously; parts of walls existing between seismic isolators should be cut off beginning from the middle of building plan. This operation was made without re-settlement of the dwellers. The world practice has had no similar precedent in retrofitting of apartment buildings.

The project was implemented in 1995–1996, was financed by the World Bank and co financed by UNIDO. The high damping rubber bearings (HDRB) for this retrofit project were designed with significant help and support of the UK based Malaysian Rubber Producers' Research Association (MRPRA). To implement the project 60 HDRBs were used, 28 bearings have been manufactured in MRPRA and 32 in Malaysia by Min Rubber Products Sdn. Bhd. and Sime Engineering Rubber Products Sdn. Bhd.

HDRBs are a simple economical means of providing isolation. They have the low horizontal stiffness required to give a long vibration period (typically 2 s) to the structure when mounted on the bearings. Their vertical stiffness is high, thus minimizing any rocking of the structure during an earthquake. The damping needed to limit the displacement of the structure and reduce the response at the isolation frequency is incorporated into the rubber compound so that there are generally no needed auxiliary dissipation devices. The bearings can be designed to withstand safely the large horizontal displacements imposed during an earthquake. The service life of the bearings is expected to be several decades [9], and they should require no maintenance. There has been much emphasis on the suitability of base isolation for critically important structures such as hospitals and emergency centers. The protection of both structure and contents, however, would be advantageous for civil structures such as apartment blocks.

The isolators are located by upper and lower recesses provided by annular steel rings bolted to outer steel plates which are connected to the reinforcement in the upper continuous and lower foundation beams; the isolators themselves are not bolted to the structure. This method of connection helps to minimize the cost of the isolators themselves and simplifies their installation on site. Because the bearing is simply located in a recess, no tapped holes for bolted connections are needed in the end-plate. The side, top and bottom rubber cover layers ensure the steel plates are protected from corrosion. In the considered existing building the bearings were not be located in an enclosed, heated basement, but would be exposed to the outside environment. The severe winter weather at the site meant that particular attention had to be paid to the low temperature crystallization resistance of the rubber compound.

The plan of foundation is given in Fig. 3, along with the location of the HDRBs and the total static load on each. The range of the vertical loads on bearings is

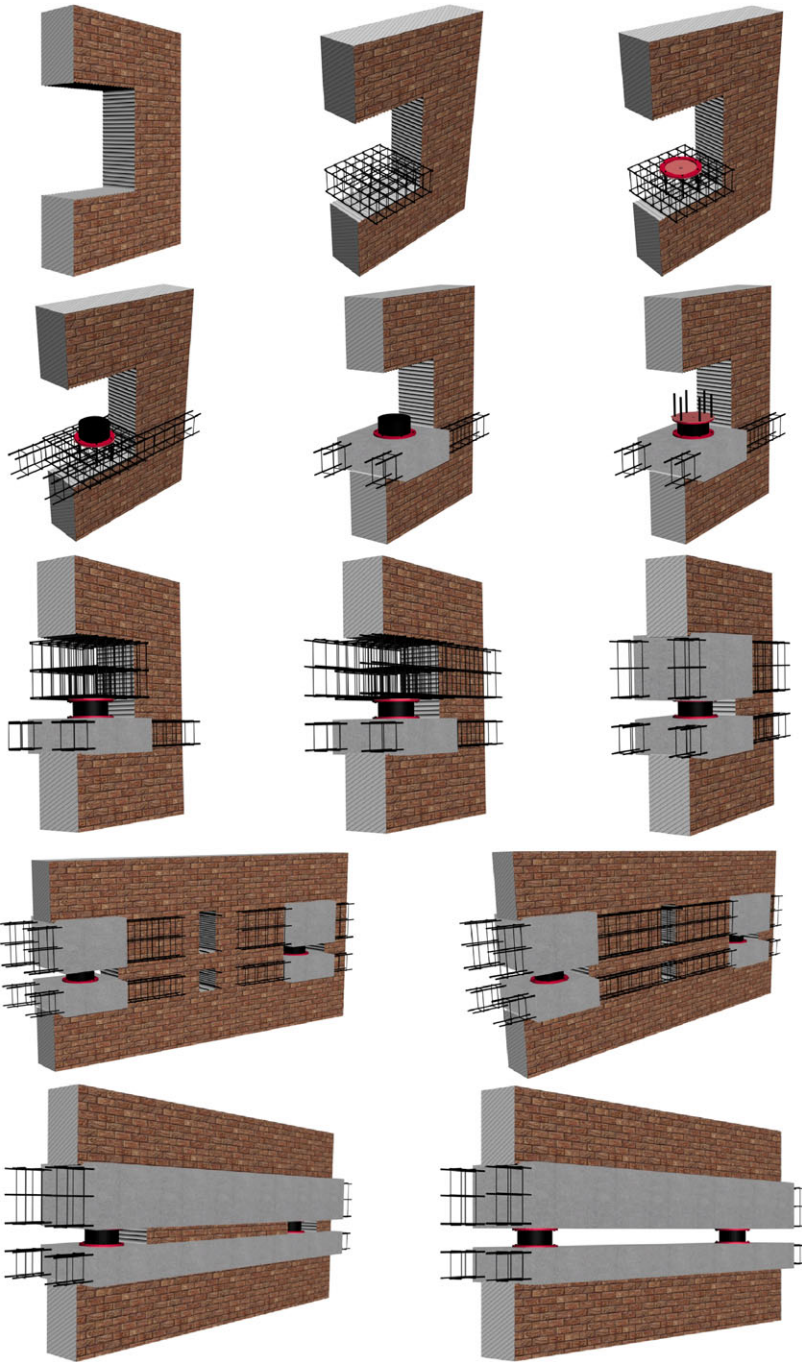


Fig. 2 Stages of installation of seismic isolation system in the existing building with stone bearing walls

Table 1 Parameters of isolation bearings

Bearing type	Hard	Soft	
Horizontal stiffness, kN/mm	0.81	0.58	
Design vertical load, kN	820	590	
Design horizontal displacement, mm	130	130	
Max. horizontal displacement, mm	195	195	
Max. static vertical load, kN	900	680	
Vertical loads (kN) at max horizontal displacement:	Max.	1240	980
	Min.	440	140
Rubber shear modulus, ^a MPa	0.97	0.69	
Static compressive stress (max), MPa	8.7	6.5	
Critical load (kN)	3260	2360	
Load for internal plate yield (kN)	4800	4800	
Horizontal displacement, mm, at onset of roll-out:			
for design vertical load	300	300	
for min. vertical load	260	196	
Nominal vertical stiffness, ^b kN/mm	400	310	

^aAt 100 % strain, 0.5 Hz

^bEstimated using shear rubber modulus in this table and a bulk modulus of 2500 MPa

1.2 Retrofitting by Base Isolation of the Existing Three-Story Stone School Building

The considered in this section building (school #4 in the city of Vanadzor) has historical and architectural value for the city. Taking this into account the financing organization—“Caritas Switzerland”—has agreed with the proposal to retrofit this building by base isolation. Below the unique operations, which were carried out in order to install seismic isolation bearings in the considered building are described in detail. The project on retrofitting the school #4 building was initiated by “Caritas Switzerland” in 2001. At that time the donor had carried out the feasibility study and was supposed to start the project using conventional design. The reason for making such a decision was in wide application of conventional retrofitting in the country and also in the unawareness of the donor about retrofitting by base isolation that has been already implemented with high efficiency in the same city.

The school is a 3-story 60 years old building with thick bearing walls constructed using tuff stones. Actually this building is a non-engineered structure with wooden floors. The design for conventional retrofitting of this school envisaged strengthening of bearing walls by reinforced concrete jackets and by construction of R/C frames in addition to the existing walls in order to decrease the distance between the existing walls. Also it was envisaged to replace the wooden floors by the R/C slabs. However, “Caritas Switzerland” being approached with a new proposal to use

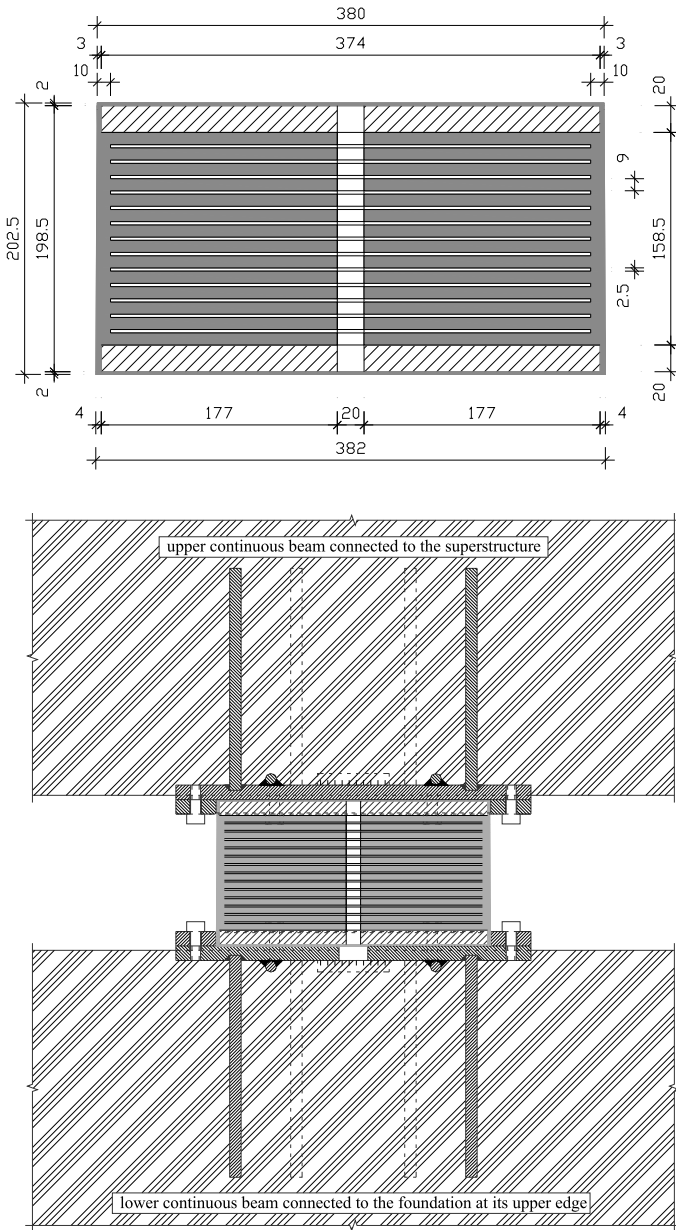


Fig. 4 Geometrical dimensions of the designed HDRB for existing 5-story stone apartment building and location of HDRB by upper and lower recesses provided by annular steel rings bolted to the outer steel plates connected to reinforcement in the upper continuous and lower foundation beams

Fig. 5 General view of the retrofitted by base isolation 3-story school building



base isolation for retrofitting of the school instead of conventional retrofitting had changed its initial decision. The following advantages were taken into account: high reliability, lower cost and reduced duration of construction in comparison with conventional retrofitting as well as preservation of the architectural view of the building.

School building (Fig. 5) has mainly a Π -shape plan and has load-bearing walls located in transverse and longitudinal directions. The thickness of bearing walls in the basement is varying from 600 mm to 1150 mm and in the floors above ground is varying from 600 mm to 700 mm. There is a school sport hall located between the axes A–C and 5–6. The height of the sport hall is equal to the height of the basement plus the height of the first floor. This, as well as the Π -shape plan, causes significant asymmetry to the building relative to the longitudinal axis D. Actually the plan of the building in the limits of the basement and the first floor is almost rectangular while the plans of the second and third floors are of Π -shape.

The school building had survived the 1988 Spitak earthquake and fortunately the effect of this earthquake on the building was not very damaging. The building received inclined cracks mainly in the walls located around the staircases with the evaluated damage extent between 2 and 3. Therefore, it was decided to strengthen parts of the existing damaged walls by cement injection and/or by reinforced concrete jackets and also to replace the wooden floors by the R/C slabs. These operations were made simultaneously with installation of the base isolation system on the level of the school basement.

Seismic isolation interface for the school building was created in the middle part along the height of the school basement [10]. This approach has conditioned some differences in retrofitting of the school building in comparison with the described above retrofitting of the apartment building. In the case of the school building the lower continuous beams were structurally connected to the bearing walls of the basement. This has given the possibility to strengthen the bearing walls by means of the lower continuous beams before cutting the building and passing its weight through the seismic isolators to the bearing walls of the basement. Such structural solution permits to reliably carry the concentrated vertical loads by the bearing walls of the basement.

For the given project the medium damping rubber bearings from neoprene have been designed and tested locally. An isolation frequency again was chosen equal

to 0.5 Hz. For the design level earthquake and damping in the isolation system of 8–9 % the calculated horizontal displacement was equal to 140 mm. The maximal horizontal displacement was equal to 210 mm. Geometrical dimensions are the same as given in Fig. 4. The other main parameters of the designed MDRBs are as follows: horizontal stiffness— 0.81 ± 0.1 kN/mm; vertical stiffness— ≥ 300 kN/mm; rubber shear modulus— 0.97 ± 0.15 MPa; critical vertical load—4500 kN; vertical load at max horizontal displacement—1500 kN.

The isolators in the school building were also located by the upper and lower recesses, however, the annular steel rings in this case were bolted directly to the anchors. The outer steel plates were also modified and instead of 20 mm thick plates the 6 mm plates were envisaged (Fig. 6). The given modifications in the design of the isolators' sockets have brought to significant reduction of steel consumption. Figure 6 also shows the cross-sections of the basement bearing wall in the place where isolator is installed between the lower and upper pedestals and where there is no isolator but the lower and upper continuous beams are seen from both sides of the bearing wall. All together 41 MDRBs had been manufactured by the Yerevan Factory of Rubber Technical Articles (YFRTA) for retrofitting of school building. The plan of location of seismic isolators on the lower continuous beams is shown in Fig. 7.

For the considered building, which has historical and architectural value the technique of installation of seismic isolators has especially important meaning. First of all an infringement of the external view of the building should not take place under any circumstances. Secondly, no one stone of the façade should fall down during making openings in the bearing walls.

There are three different cases of making openings in the existing walls of the basement, which were mainly used at the retrofitting of the building [11]. The relatively simple case is the one, when the opening has the part of existing wall above it (Fig. 8). In this case there is no need to put any additional supports, as the strength of the wall is sufficient in order to avoid falling. When the opening is made, the lower reinforcement frame of the lower pedestal with the isolator socket can be placed and after that binding reinforcement lower frames are passed along both sides of bearing wall through the frame of the lower pedestal (Fig. 9).

At the next step the concrete of the lower pedestal is casted, the isolator is installed (Fig. 10a) and above it the upper socket and the reinforcement frame of the upper pedestal are placed. Then the binding reinforcement upper frames are passed through the reinforcement frame of the upper pedestal along both sides of existing bearing wall (Fig. 10b). After casting the concrete of the upper pedestal all lower and upper pedestals should be connected to each other forming a two-stage system of R/C continuous beams (Fig. 11).

More complicated case of making openings is when any of existing beams or girders is crossing the space of the opening. In this case one of the ends of the existing beam loses its support (Fig. 12) and it is necessary to create temporary supports in order to carry dead load of the existing building. The operation should be made very carefully in order to avoid any damages in the superstructure after making openings in the existing walls. It is important to make all operations described

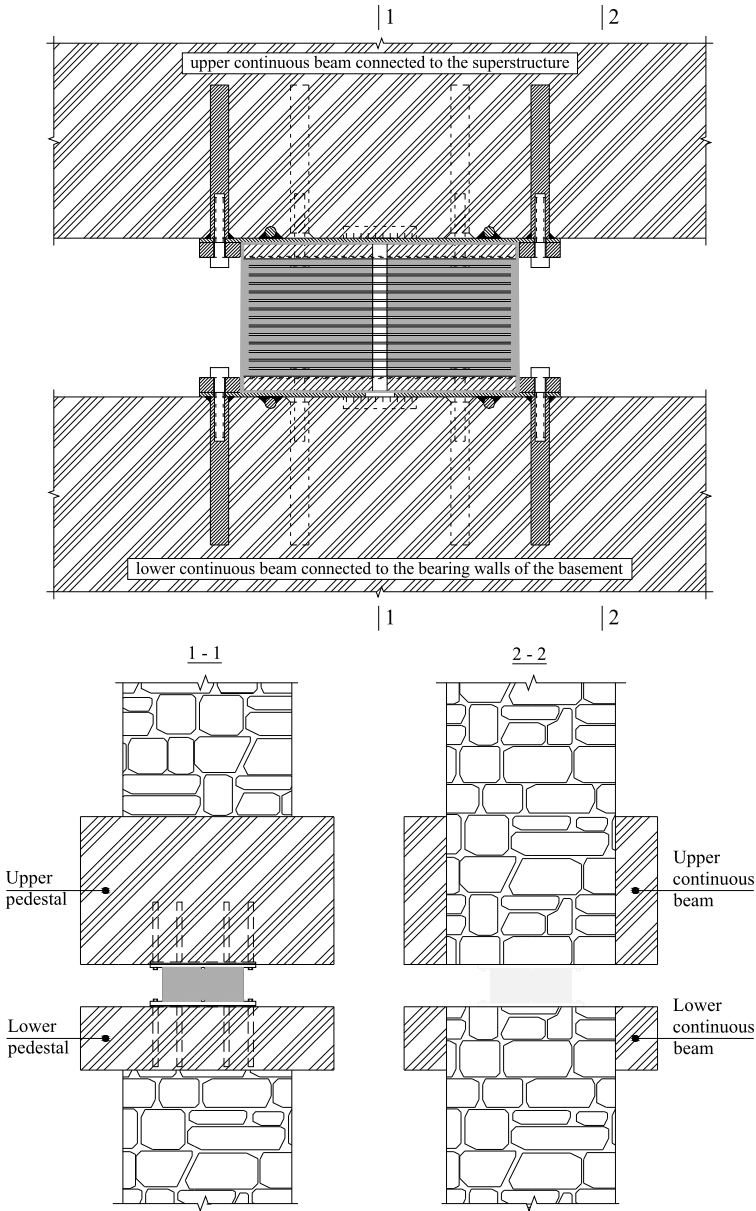


Fig. 6 Location of MDRB by upper and lower recesses provided by annular steel rings bolted to the anchors connected to the upper and lower continuous beams in school building

above as quickly as possible. Therefore, for such cases everything should be prepared in advance and after casting the concrete the temporary supports should be taken out only when concrete gets about 70 % of its strength. Sometimes it is neces-

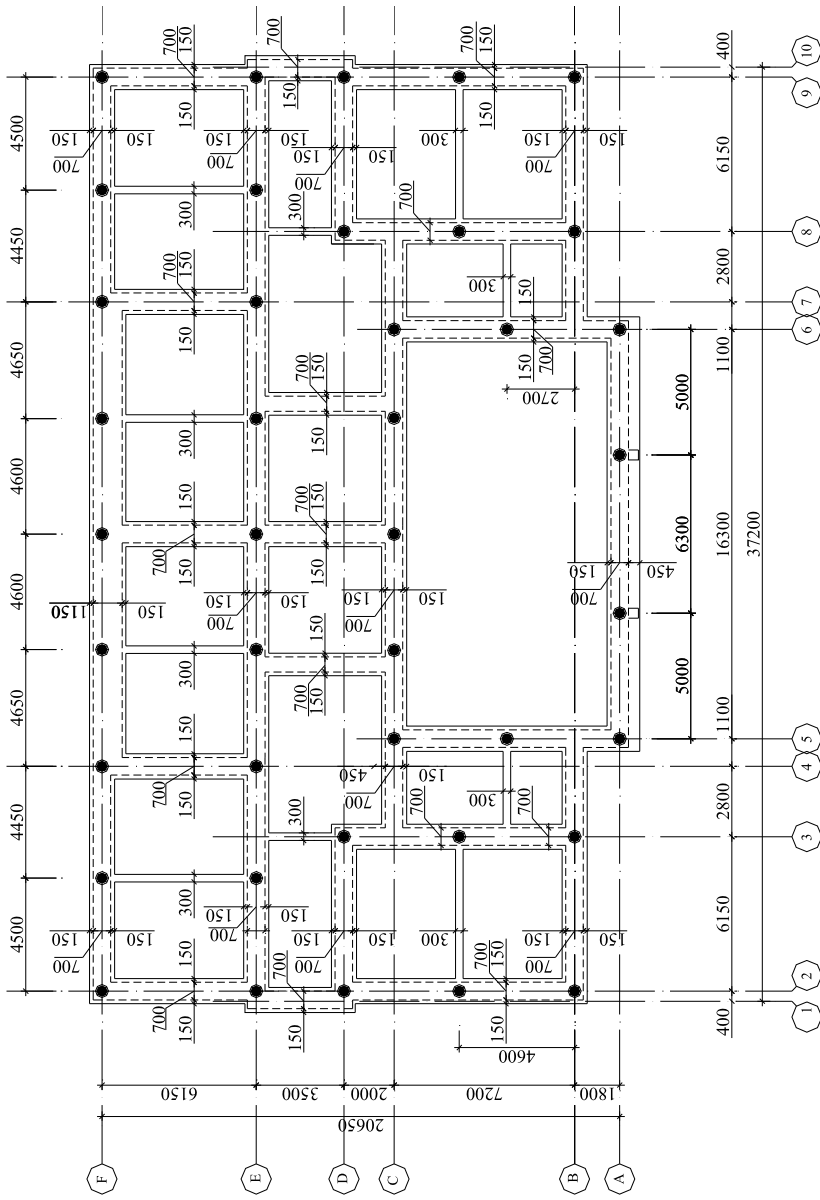


Fig. 7 Plan of MDRBs' location on the lower continuous beams in the basement of the school building

Fig. 8 Retrofitting of existing 3-story stone school building: the case when the opening has the part of the existing wall above it



sary to install temporary supports inside the opening in the plane of existing walls. In this case the supports should be prepared from steel, as after casting the concrete they will remain in the lower and upper pedestals. Later the parts of such supports between pedestals should be cut.

Most complicated case is the one when the opening does not have any part of existing wall above it. For school building such cases happened at the entrance when openings should be made just beneath the columns and the arches. Before starting to make openings the arches must be temporarily supported (Fig. 13a). Then gradually the opening under the column should be made. With this purpose, at the beginning the part of the foundation only under the one quarter of the column section should be taken out (Fig. 13b). This will allow installing under the column a mechanical jack. After that the other part of foundation under another quarter of the column section can be demolished.

When this work is finished a temporary support under the one half of the column section should be installed and the mechanical jack can be taken out (Fig. 14a). Then again gradually the foundation under the other half of the column section should be demolished and this part of the column section also should be temporarily supported. In cases like this the reinforcement frames of the lower



Fig. 9 The views of the lower reinforcement frames of the lower pedestal installed in the opening together with the isolator socket

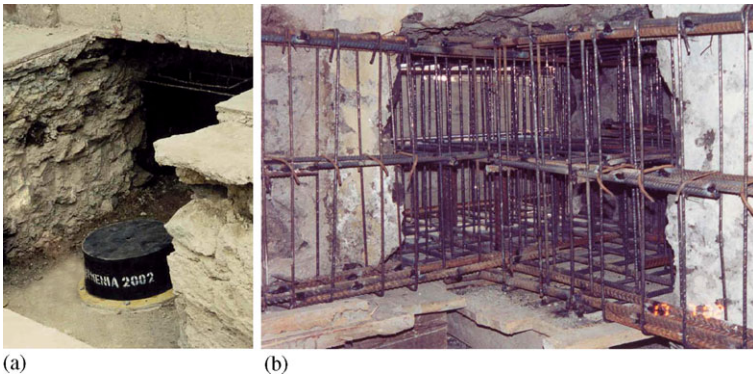


Fig. 10 The view of the isolator installed in the socket after casting the concrete of the lower pedestal (a), and of the upper reinforcement frame installed in the opening together with the upper socket and with the binding reinforcement upper frames (b)



Fig. 11 The views of a two-stage system of R/C continuous beams, which separate the building from its foundation and create the seismic isolation system



Fig. 12 Existing beam is crossing the space of the opening and supported by temporary columns

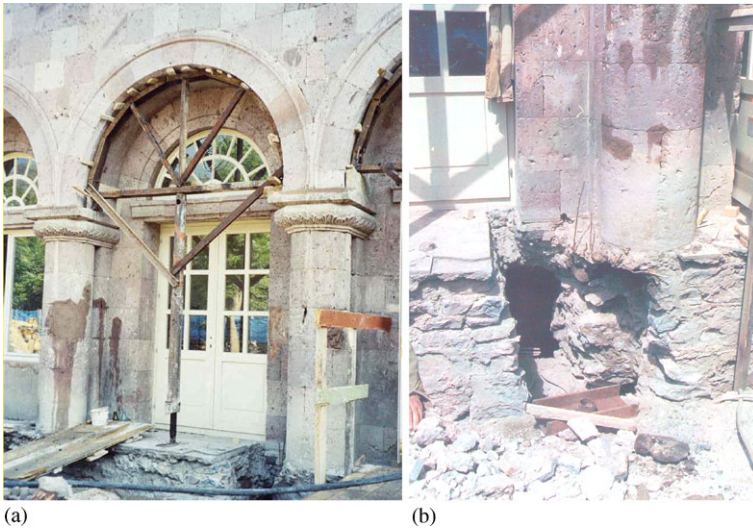


Fig. 13 Temporary support under the existing arches (a) and the part of the foundation under the one quarter of the column section is taken out (b)

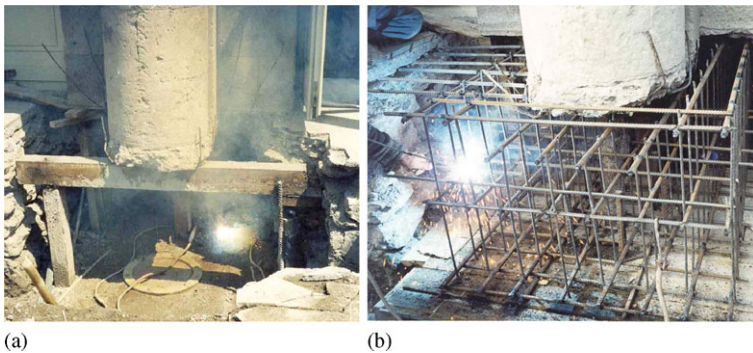


Fig. 14 Temporary support under the one half of the existing column section (a), and existing column and the wall behind it are supported temporarily and the reinforcement frame of the upper pedestal is installed (b)

and upper pedestals cannot be prepared in advance and should be made in situ (Fig. 14b).

The following operations are similar to those described above. However, during every step of implementation of such complicated cases of retrofitting it is necessary to take care of the condition of the existing structures not permitting development of any damages as these structures are part of the valuable architectural appearance of the building.



Fig. 15 Views of the Iasi City Hall building

1.3 Design for Retrofitting by Base Isolation of the Existing Cultural Heritage Iasi City Hall Building (Iasi County, Romania)

Experience accumulated in Armenia in retrofitting of existing buildings including those of historical and architectural value created a good basis for participation in the international competition announced by the Government of Romania for development of the design on retrofitting by base isolation of the 178 years old historical building of the Iasi City Hall (Fig. 15). Design was developed in cooperation with Romanian company MIHUL S.R.L. It was approved by the Technical Committee for Seismic Risk Reduction (TCSRR, a body especially created by the Government of Romania) on June 1, 2009.

The structural system consists of un-reinforced masonry walls with primarily wood horizontal diaphragms. The thicknesses of the interior and exterior walls vary between 40 to 60 cm and up to 100 cm respectively. Stone foundations have been provided under the masonry bearing walls. The building suffered repairable damage after the 1977 Vrancea earthquake. Thus, the bearing walls were repaired by grout injection, reinforced concrete slabs replaced damaged floors, and the tall chimneys were anchored in place using steel ties. The Iasi City Hall is located in the seismic zone C, and based on Romanian Building Code P100-92, the expected peak ground acceleration for that zone is $0.2g$. The soil in the vicinity of the building is classified as stiff clay sensitive to moisture; the ground water table is approximately 6 m below surface [12]. However, the TCSRR has requested to accept the peak ground acceleration (PGA) for retrofitting design of the Iasi City Hall building equal to $0.28g$. TCSRR had justified its request mentioning that either for the 100 years mean recurrence interval $0.2g$ PGA shall be multiplied by the importance factor 1.4 according to the Romanian seismic code in force P100-1/2006 or for the 475 years mean recurrence interval PGA at Iasi City, estimated by Probabilistic Seismic Hazard Assessment for Vrancea earthquakes is also equal to $0.28g$.

The key objective of the given work was elaboration of structural concept and the design of retrofitting by base isolation of the Iasi City Hall building, which will ensure cost-effectiveness of the construction works, high reliability of the structure and preservation of the historical and architectural value of this building.

Base isolation method for an existing building with bearing walls that envisions placing of seismic isolators at the level of basement solves the problem according to the innovative technology described in Sects. 1.1 and 1.2. It is known that the City Hall building does not have a basement under its whole area. Only a partial basement exists under a part of the building between the axes 3–5 and K–P, as well as the axes 5–8 and M'–N. It was proposed based on the accumulated experience [8, 11, 13] on retrofitting of the similar buildings by base isolation to extend the basement throughout the whole building built surface.

This will require to excavate the soil from the inside of the building and to bare the existing foundation walls. Obviously, that these walls before creation of the isolation system must be thoroughly cleaned and washed from the remainders of soil and then adequately strengthened. The suggested structural solution provides for jacketing of the natural stone walls of foundations. The typical thickness of concrete utilized for the jacketing of masonry walls is 5 cm. There is no need for increasing of the thickness of jacketing as in base isolated structures significant reduction of the shear forces takes place. For the same reason there is also no need for cementitious injection of the basement walls. By implementing the shotcrete 5 cm thickness of jacketing could be achieved easily. However, TCSRR was insisting on increasing of the thickness of R/C jacket and on increasing of the diameter of reinforcing bars in the jacket. Therefore, finally the thickness of the basement walls jackets was increased from 5 cm to 8 cm and the diameter of reinforcing bars of the jackets steel meshes of 150×150 mm was increased from 5 mm to 8 mm. Also at the level of the basement floor a R/C slab with the thickness of 10 cm was additionally designed. Nevertheless, it was mentioned by the designers that the need in such a slab and in increasing of the jacket's thickness is questionable and not justified.

The new approach on installation of clusters of seismic isolators which was successfully implemented in many buildings in Armenia was also proposed for retrofitting of the Iasi City Hall building (Fig. 16). Immediately above the seismic isolation plane a 150 mm thick reinforced concrete slab, which will cover the basement, was also proposed. This approach will significantly increase the reliability of the whole structure (building plus the isolation system), will bring to increased rigidity of the superstructure (the part of the building above the isolation plane) and will bring to more uniform distribution of seismic forces on isolators.

By implementing the suggested base isolation method a new basement will be created. The height of that basement under the slab is 1.85 m, however under the upper beam of isolation system the height is 1.3 m (Fig. 17). The height of the basement is limited because of the deepness of the foundation walls. This deepness was discovered in situ through excavation of soil along one of the exterior walls of the building and was equal to 2.4 m approximately. According to the Romanian Codes at least 0.4 m of the foundation walls should remain in the soil. Therefore, the basement could be designed with the mentioned height only. Of course, such a basement cannot be considered as a luxury premise, but it can be successfully used for many purposes. At the same time the height of the existing basement will not be changed/reduced.

Regarding the bearing walls above the isolation interface it is suggested to execute local strengthening of walls where local cracks exist by cement injection in

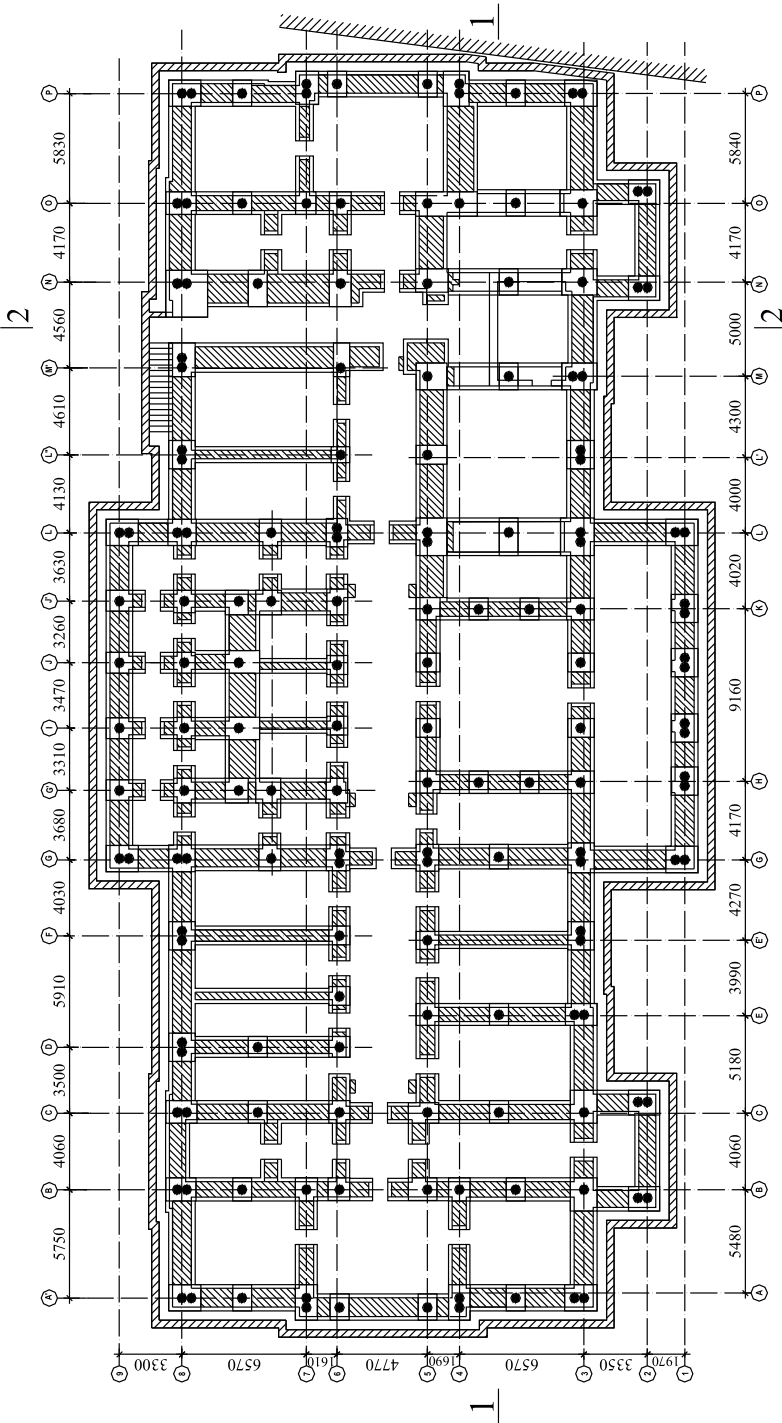


Fig. 16 Plan of location of seismic isolators on the level of the newly created basement highlighting the lower pedestals under the isolators and the lower continuous beams along the whole perimeter of the bearing walls

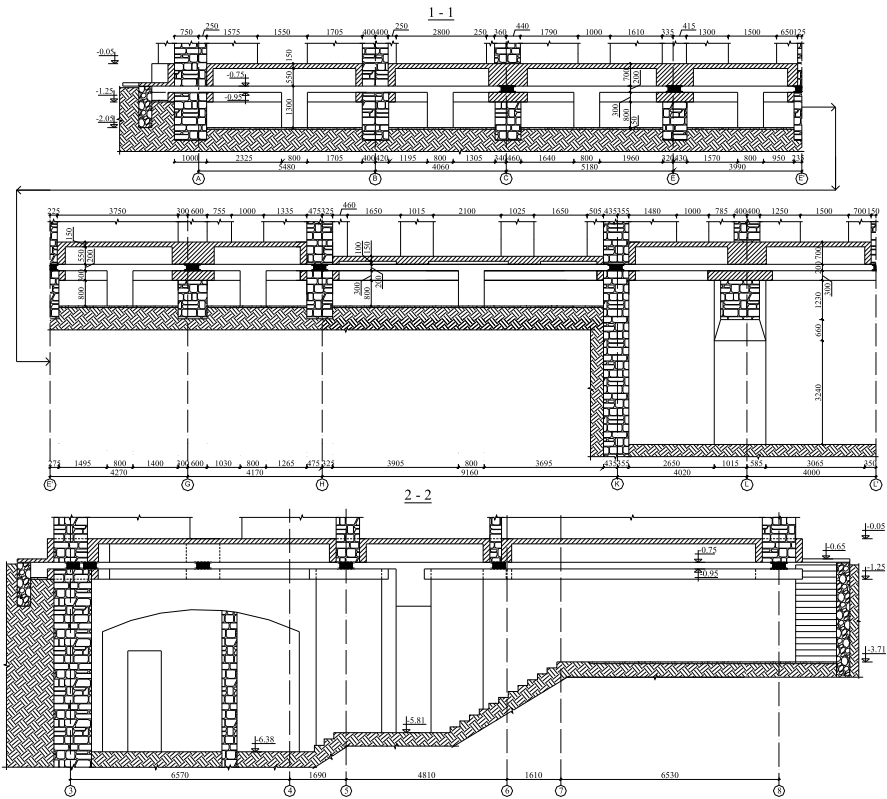


Fig. 17 Longitudinal (1–1) and transverse (2–2) vertical elevations of the basement and isolation system of the building according to the developed structural solution

the cracks and by fixing here of 6 mm steel clamps and plastering those parts. This is just a constructive measure, which is actually not required by carried out calculations. Despite this TCSR has requested to change the mentioned clamps by the steel meshes of 100 × 100 mm with the reinforcing bars of diameter 8 mm.

In order to develop the retrofitting design the Iasi City Hall building was analyzed under the seismic impacts with PGA equal to 0.28g following the request of TC-SRR. This committee has also mentioned that according to the Code P100-1/2006 the demand spectral displacement at the period of vibrations of base isolated building equal to 2.0 sec and the damping ratio of 5 % for Iasi is 27 cm. Therefore, it was suggested by designers to accept the value of the actual damping ratio for seismic isolators equal to 15 % [14]. In this case according to the Annex A of P100-1/2006 the mentioned displacement demand shall be recomputed and reduced by a factor of 0.707 ($27 \times 0.707 = 19.09$ cm). Period of vibrations of the base isolated Iasi City Hall building, as it is given in [15], is the same in longitudinal (X) and in transverse (Y) directions and is equal to 2.13 sec. This means that the calculated displacement demand will actually be equal to $2 : 2.13 \times 19.09 = 17.92$ cm. TCSR has also men-

tioned that “Good practice and the international codes request a total displacement for design increased by 50 % with respect to displacement demand”. Satisfying this requirement the final value of a total displacement $D = 17.92 \times 1.5 = 26.88$ cm was accepted for retrofitting design of the Iasi City Hall building.

However, the statement given by TCSR for a total displacement seems weak and not justified. In Science and Engineering such statements are not acceptable as they are not clear and are made without any references. Also when it is stated as “Good practice . . .” shall someone understand that there is a “Better practice . . .” or “Best practice . . .” and what has to be done in these cases? Most probably the absence of the extensive experience on base isolation in Romania is forcing the members of TCSR to require an over designed isolation system, which will bring to artificial increase of the cost of retrofitting of the Iasi City Hall building. Is there a need for that? Those countries, which are currently extensively using seismic isolation technologies for retrofitting or for new construction like Japan [16], Russia [17], China [18], Italy [19], Armenia [13], and others are constantly reporting on reliability and cost effectiveness of these technologies.

If it is so then why seismic isolation should be expensive in Romania? There is a risk that in case of artificial increase of retrofitting cost the Iasi City Hall, being over designed, will become the first and the last building retrofitted by base isolation following the sad experience of USA where because of similar extremely high conservatism seismic isolation is actually dying. But TCSR was arbitrarily requesting to significantly increase the values of PGA and of design displacement of isolation system. This was forcedly done in the design with the understanding that it will raise the cost of retrofitting works unnecessarily.

Earthquake response analysis of the building was carried out by SAP2000 non-linear program. The design model was developed using different types of finite elements for walls, floor slabs and seismic isolators. The non-linearity was considered only for seismic isolators because for cases like Iasi City Hall building there is no need to apply non-linearity to superstructure. For the linear model the isolators are given the effective stiffness equal to 0.81 kN/mm. For non-linear model the isolators have initial stiffness equal to 3 kN/mm and post yield stiffness equal to 0.81 kN/mm.

For the analysis TCSR has requested to select only those acceleration time histories which “. . . characterized by a corner period of response spectra T_c close to the value of 0.7 sec. The design accelerograms might be also compatible with local soil condition in Iasi, as those conditions have been experienced during the Vrancea 1986 and 1990 earthquakes”. Finally 9 accelerograms were selected and scaled to acceleration 0.28g: 4.03.1977 Vrancea earthquake, EW direction at Buc-INCERC station ($T_c = 0.78$); 30.05.1990 Vrancea earthquake, EW direction at Buc-Magurele station ($T_c = 0.64$); 30.08.1986 Vrancea earthquake, NS direction at Iasi station ($T_c = 0.44$); 30.08.1986 Vrancea earthquake, EW direction at Iasi station ($T_c = 0.36$); 31.05.1990 Vrancea earthquake, EW direction at Iasi station ($T_c = 0.40$); 30.08.1986 Vrancea earthquake, NS direction at Istrita station ($T_c = 0.62$); 31.05.1990 Vrancea earthquake, EW direction at Istrita station ($T_c = 0.64$); 30.08.1986 Vrancea earthquake, NS direction at Muntele Rosu station ($T_c = 0.70$); 30.05.1990 Vrancea earthquake, EW direction at Muntele Rosu station ($T_c = 0.72$).

Table 2 The average results of the linear and non-linear earthquake response analyses of the base isolated Iasi City Hall building using 9 acceleration time histories scaled to 0.28g

Level	Longitudinal (X) direction			Transverse (Y) direction		
	Displacement, mm	Acceleration, g	Shear force, kN	Displacement, mm	Acceleration, g	Shear force, kN
First floor slab	118.50	0.13		118.01	0.13	
Ground floor slab	117.43	0.13		116.80	0.13	
Top of isolators	116.40	0.13		116.42	0.13	
Bottom of isolators	0.12	0.28		0.11	0.28	
Foundation	0.00	0.28	15031	0.00	0.28	15025
			Linear analysis			
First floor slab	151.35	0.09		151.48	0.09	
Ground floor slab	150.72	0.08		148.77	0.09	
Top of isolators	148.54	0.08		147.61	0.08	
Bottom of isolators	0.55	0.28		0.52	0.28	
Foundation	0.00	0.28	19132	0.00	0.28	19000
			Non-linear analysis			

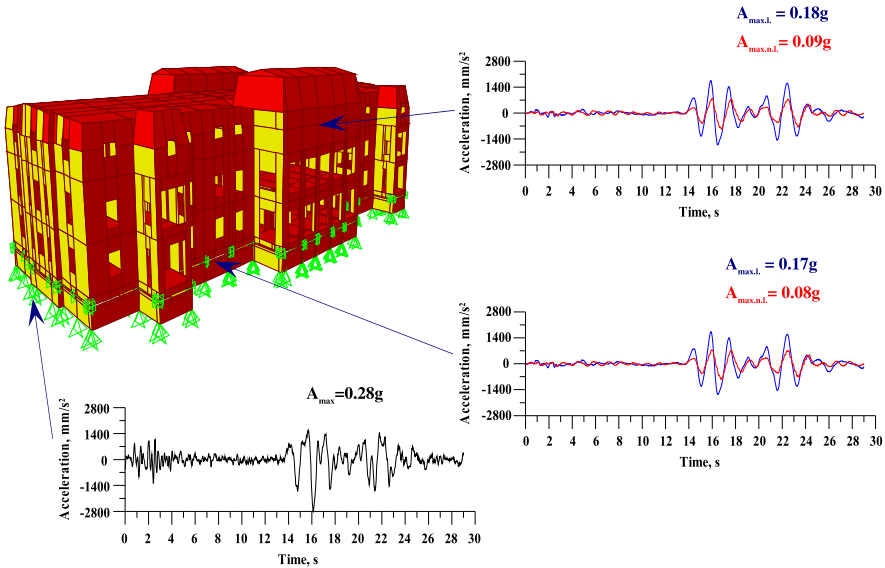


Fig. 18 Comparison of the response accelerations on the levels of the top of isolators and of the slab of conference hall by the linear and non-linear analyses in longitudinal direction using 30.08.1986, NS Muntele Rosu

The following results of calculations were obtained: periods of vibrations in X and Y directions are equal to each other and equal to 2.13 sec; floor accelerations along the height of superstructure in both directions are the same and are equal to 0.085g in average, which means that thanks to application of base isolation the input PGA of 0.28g decreases by about 3.3 times; in none of the isolators the vertical force exceeds 1500 kN; superstructure is moving in horizontal direction as an absolutely rigid body without any overturning and this as well as the above results underline the high effectiveness of the implemented base isolation system.

Also it should be mentioned that at small deformations, which correspond to the wind impact, the initial stiffness of rubber bearings is much higher than their effective stiffness and, thus, the ability of the system to provide an intrinsic restraint against wind loading is confirmed. Structural elements above and below the isolation interface are working only in elastic stage. In comparison with the linear analysis non-linear analysis brings to increase (27 %) of average displacement of isolation system and to decrease (35 %) of average floor accelerations above it. Other average results of calculations by linear and non-linear versions are given below in Table 2. Figure 18 visually illustrates the reduction of input acceleration in the superstructure of the base isolated Iasi City Hall in longitudinal direction under the impact of the 30.08.1986 Vrancea earthquake acceleration time history, NS direction recorded at Muntele Rosu station accelerogram with $T_c = 0.7$ sec.

To the best demonstration of the effectiveness of the proposed retrofitting by base isolation the Iasi City Hall building was also analyzed as a fixed base structure using

Table 3 The average results of earthquake response analyses of the fixed base Iasi City Hall building using 9 acceleration time histories scaled to 0.28g

Level	Longitudinal (X) direction			Transverse (Y) direction		
	Displacement, mm	Acceleration, g	Shear force, kN	Displacement, mm	Acceleration, g	Shear force, kN
First floor slab	13.26	1.04		12.81	1.18	
Ground floor slab	7.16	0.66		6.82	0.63	
Basement slab	0.55	0.28		0.62	0.28	
Foundation	0.00	0.28	58583	0.00	0.28	62605

the same selected acceleration time histories. The obtained average results are given in Table 3.

It is easy to notice that in base isolated building the maximum average story drift of superstructure is equal to 1.67 mm while in fixed base building this value reaches to 6.23 mm, which is about 3.7 times bigger. The checked stress-strain states show that the fixed base building must be totally strengthened. Otherwise the fixed base building will not resist the earthquake with PGA of 0.28g and even 0.2g.

In the same time the retrofitting of this building by base isolation excludes the necessity of strengthening of superstructure. As an example, Fig. 19 presents the distribution of in-plane direct stresses and of in-plane shear stresses over the surface of the wall along the axis G for fixed base and base isolated buildings and Fig. 20 visually illustrates amplification of the input acceleration along the height of the fixed base building in longitudinal direction under the impact of the 30.08.1986 Vrancea earthquake acceleration time history, NS direction recorded at Muntele Rosu station.

2 Retrofitting by Base Isolation vs. Conventional Retrofitting

Conventional retrofitting techniques to be applied for existing buildings most probably are not acceptable in Armenia and generally in developing low income countries as such techniques require huge investments including those related to the resettlement of residents. However, still conventional retrofitting is used much more widely and frequently than innovative retrofitting which is conditioned by the lack of knowledge and by conservatism of engineers/designers, developers and building owners. Nevertheless, their vision of the philosophy of retrofitting/strengthening of existing buildings should be and will be changed in the course of time as little by little with more and more applications of innovative retrofitting technologies it become obvious that such technologies are incomparably more effective and reliable structurally and more cost efficient.

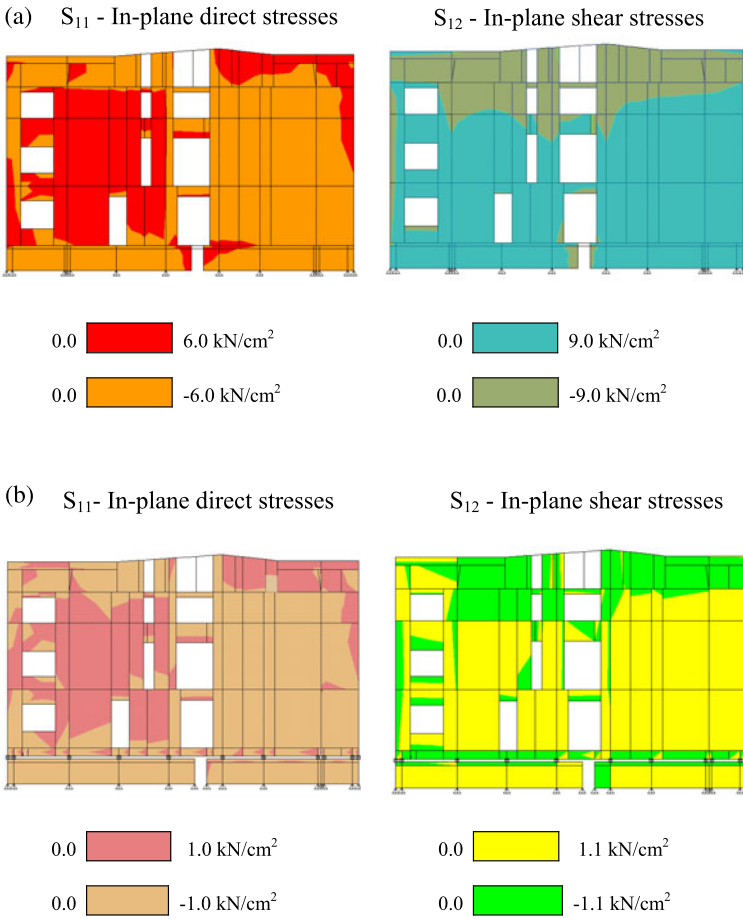


Fig. 19 Stress distribution over the wall along the axis G for fixed base (a) and for base isolated buildings (b)

2.1 Comparison of Retrofitting Technologies in Armenia

Conventional strengthening/retrofitting techniques are including: stiffening existing wooden floors and roofs by covering them with a layer of reinforced concrete; insertion of reinforced concrete ring-beams into the inner face of external walls at floor and eaves level to tie vertical and horizontal elements together; strengthening of walls (mainly when cracked) by cement injection or by adding a thin layer of cement render reinforced with steel mesh on either side of the wall, etc.

In [20] it is mentioned that in rare instances, base isolation has been used to protect the structure from the ground shaking, but this is very expensive. This statement is not always true and is not reflecting real situation in every country where seismic (base or roof) isolation is widely implementing. For example in Armenia

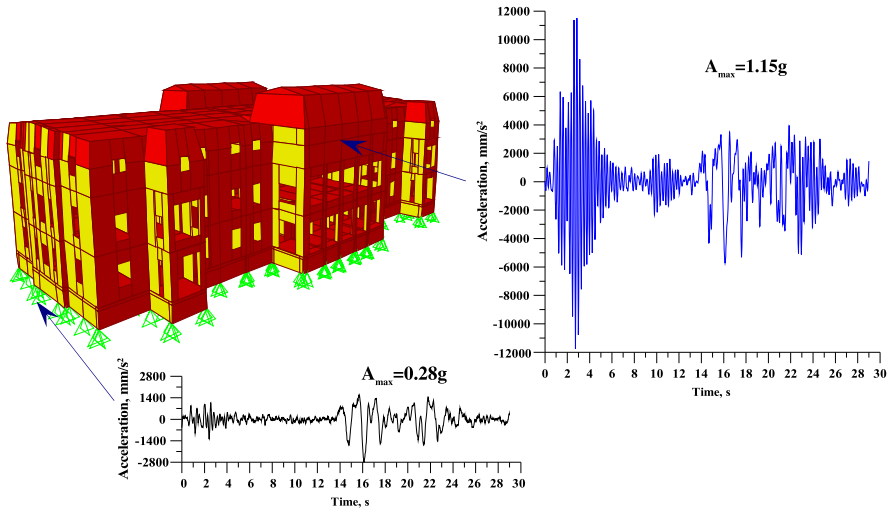


Fig. 20 Response acceleration at the top (the slab of conference hall) of fixed base building in longitudinal direction using 30.08.1986, NS Muntele Rosu accelerogram with $T_c = 0.7$ sec

due to seismic isolation the cost of retrofitting is about 2.0 times less in comparison with the cost of conventional retrofitting. In this regard an interesting analysis was carried out by one of the Armenian design company “Project-6” LLC (Director G. Gulanyan). With participation of the author of this paper the company has analyzed and compared the cost of strengthening of existing stone apartment buildings of series 1A-450 by different methods (Table 4). It was assumed that the cost of the most expensive method of traditional strengthening comprises 100 %.

From Table 4 it follows that in Armenia the cost of innovative method of strengthening/retrofitting of stone apartment buildings with application of base isolation is 2.5 times less in average in comparison with the cost of traditional methods of retrofitting. And this is of course with consideration of the cost of seismic isolation rubber bearings but without consideration of the cost of evacuation of tenants. It is easy to understand that evacuation of tenants requires huge additional investments in order to provide evacuated tenants with temporary shelters, water, sewer, electricity and relevant infrastructure. Consideration of these additional investments makes in absolutely clear and obvious that at least in those earthquake prone countries where progressive thinking of designers/engineers, developers, building owners and decision-makers, as well as progressive codes are exist and also where it is possible manufacturing or importing low-cost seismic isolators the preference should be given to the innovative methods of retrofitting with application of base isolation. In the result of its analysis “Project-6” had concluded that the most cost effective technique for strengthening of existing buildings is base isolation in combination with cement injection or with polymer-cement slurry injection for total or local strengthening of the damaged bearing walls.

Table 4 Comparison of the cost of strengthening of existing stone apartment buildings of series 1A-450 by different methods

Method of strengthening	Cost in %	Needed action
Traditional method with application of reinforced concrete jackets, frames and floor slabs. This method is applicable for buildings with damage extent from 2 to 3 ^a	100	Evacuation of tenants, move out furniture
Traditional method with application of only reinforced concrete frames. This method is applicable for buildings with damage extent from 1 to 2	43	Evacuation of tenants
Innovative method with application of base isolation and local strengthening of walls only by reinforced concrete jackets. This method is applicable for buildings with damage extent from 2 to 3 ^a	37	Without evacuation of tenants, partial move of furniture
Innovative method with application of base isolation and total strengthening of walls by cement injection. This method is applicable for buildings with damage extent from 2 to 3	31	Without evacuation of tenants, partial move of furniture
The same as previous but with local strengthening of wall by cement injection for buildings with damage extent from 1 to 2	27	Without evacuation of tenants, partial move of furniture
The same as previous without touching the superstructure for buildings with damage extent from 0 to 1	21	Without evacuation of tenants

^aThis method can also be applied for buildings with damage extent 4, however, with due regard of economic and social factors

Above several remarkable projects on retrofitting by base isolation are described. One of them is retrofitting of the existing stone apartment building of series 1A-450 in the city of Vanadzor. This project is an actual example of cost effectiveness of retrofitting by base isolation vs. conventional retrofitting. The cost of retrofitting of this building defined in the result of competitive bidding is equal to 165.600 USD including the cost of rubber bearings. Other two similar buildings in the same city were retrofitted conventionally. One was retrofitted with application of reinforced concrete jackets and frames and it cost is equal to 340.000 USD. The other one was retrofitted by insertion only of reinforced concrete horizontal ring-beams and vertical columns into the external and internal bearing walls and it cost is equal to 294.200 USD. These actual examples prove ones again that substantial saving (about 2.0 times) could be achieved thanks to application of base isolation. Also this innovative technology allows avoiding infringement of the external and internal views of the buildings which is extremely important especially at seismic protection of historic buildings and structures of cultural heritage like, for example, the above described building of Iasi City Hall.

Fig. 21 View of “Georghe Pirvan” Museum, Bârlad constructed in 1880



Fig. 22 View of Palace of “Alexandru Ioan Cuza” University of Iasi which was constructed in two stages: first in 1894 and then in 1928–1934



Fig. 23 “Alexandru Ioan Cuza” University of Iasi building “D” constructed in 1880 and improved in 1938



2.2 Comparison of Retrofitting Technologies in Romania

Special analysis was carried out by the second author of this paper in order to reveal cost effectiveness of retrofitting by base isolation of the buildings that represent an architectural monument. Four buildings were considered which were strengthened conventionally (Figs. 21, 22, 23 and 24) and the results were compared with those obtained in retrofitting design of Iasi City Hall by application of base isolation.

Fig. 24 School Inspectorate of Iasi building “A” constructed at the beginning of the 20th century



Structural systems of these buildings as well as of the Iasi City Hall building are similar. They have bearing walls made of brick on the continuous stone masonry foundation. Their floors are made of wooden beams but above the basements (if there are) the floors are made of small brick arches. The shaped limestone of foundations is walled up with dirty sand and lime mortar. The compressive strength of brick corresponds to the grade of 25–50 and of mortar—to the grade of 4–10.

In the considered buildings there were inclined cracks observed along the height of the bearing walls with the opening of 1–3 mm. Most of them occurred around the windows and doors as a possible result of the earthquake impact. Also cracks are usually increase in their number, length and openings by the uneven settlements of the ground under the foundation because of wetting or exceeding its local bearing capacity.

Conventional strengthening of these buildings included reinforced concrete jacketing of foundations with the thickness of 8–20 cm and the execution of reinforced concrete belts at the bottom and at the top of foundations. Sometimes the belts were designed larger at the bottom to increase the width of foundations. Above the foundations the strengthening included:

- injection of all the cracks with additive cement;
- reinforced concrete jacketing of the bearing walls by shotcrete in 2–3 layers;
- introduction of a system of reinforced concrete elements (additional shear walls, columns, belts);
- reinforced concrete framing of the door and window openings connected to the walls' jackets;
- execution of a continuous belts at the top of the walls;
- replacing the wooden floors by the reinforced concrete slabs, etc.

The major inconvenience of these strengthening systems is the need to remove and restore all the architectural elements inside and outside the building and replacing the original fresco plaster of the monument. In many cases these original elements cannot be removed, and these will require restoration after the next severe earthquake that will affect the building.

Actually the cost of retrofitting of the considered buildings of cultural heritage consists of the cost of structural strengthening and of total architectural restoration,

Table 5 Retrofitting costs for different buildings of cultural heritage/architectural monuments in Romania

Name of the building	Type of retrofitting	Cost of structural strengthening, €/sqm	Cost of architectural restoration, €/sqm	Total cost of retrofitting, €/sqm
“Georghe Pirvan” Museum, Bârlad	conventional	230	260	490
Palace of “Alexandru Ioan Cuza” University of Iasi	conventional	240	250	490
“Alexandru Ioan Cuza” University of Iasi building “D”	conventional	230	240	470
School Inspectorate of Iasi building “A”	conventional	230	240	470
Iasi City Hall	base isolation	204	115	319

which is not the case in retrofitting by base isolation. During the retrofitting by base isolation the original architectural elements, frescoes, etc. are preserved in high proportion and they may need only local intervention with incomparably lower costs. At the conventional retrofitting a very difficult task is restoration of the original finishes that requires high qualified manpower to execute the plasterwork of architectural elements, mosaics, shaping the stones, etc. Table 5 gives the information on retrofitting costs for all considered buildings.

Comparison of the values given in Table 5 shows significant difference in the costs of innovative retrofitting vs. conventional retrofitting. The average cost of structural strengthening by conventional methods is equal to 233 €/sqm which is higher than the cost of retrofitting by base isolation (including the cost of seismic isolators) by 1.14 times. For architectural restoration these figures are 248 €/sqm and 2.16 times, respectively. Thus, finally retrofitting by base isolation costs 1.5 times less than conventional retrofitting. However, above was mentioned that in the retrofitting design for Iasi City Hall many additional strengthening measures were envisaged by the requests of TCSRR which actually have artificially increased the cost of retrofitting by base isolation. If to take this into account one can definitely say that cost savings would be much more and the figure of 1.5 may be closer to 2.0 what was obtained for ordinary buildings in Armenia.

3 Conclusions

New unique, innovative and cost-effective non-conventional seismic protection methods based on the application of seismic isolation systems have been developed and introduced into construction practice by the author of this chapter. Three remarkable projects on retrofitting by base isolation of the existing buildings are

described. The operations on two of them were made without resettlement of the occupants. World practice provides no similar precedents in retrofitting of apartment and school buildings.

Retrofitting of the existing buildings by base isolation enabled to preserve the buildings' exterior appearance and to avoid marring their architectural features. Thanks to the seismic isolation there was no need to carry out overall strengthening of the superstructure. Only minimum structural measures were taken in superstructures of the considered buildings to meet the requirements of the seismic building codes in force. Reliability of the buildings retrofitted with application seismic isolation is considerably higher than with conventional strengthening.

The cost of retrofitting of the buildings of cultural heritage generally consists of the cost of structural strengthening and of total architectural restoration, which is not the case in retrofitting by base isolation. During the retrofitting by base isolation the original architectural elements, frescoes, etc. are preserved in high proportion and they may need only local intervention with incomparably lower costs. At the conventional retrofitting a very difficult task is restoration of the original finishes that requires high qualified manpower to execute the plasterwork of architectural elements, mosaics, shaping the stones, etc.

The cost of retrofitting by base isolation is proved to be much lower than the cost of traditional strengthening technologies. Based on the performed calculations, analysis and design it is confirmed that in Armenia the cost of innovative method of strengthening/retrofitting of stone buildings with application of base isolation is 2.5 times less in average in comparison with the cost of traditional methods of retrofitting. In Romania retrofitting by base isolation of the buildings of cultural heritage costs 1.5–2.0 times less than conventional retrofitting.

The above figures obtained without consideration of the cost of evacuation of occupants. Their evacuation requires huge additional investments in order to provide them with temporary shelters, water, sewer, electricity and relevant infrastructure. Consideration of these additional investments makes in absolutely clear and obvious that at least in those earthquake prone countries where progressive thinking of designers/engineers, developers, building owners and decision-makers, as well as progressive codes are exist and also where it is possible manufacturing or importing low-cost seismic isolators the preference should be given to the innovative methods of retrofitting with application of base isolation.

References

1. Fuller K, Lim C, Loo S, Melkumyan M, Muniandy K (2000) Design and testing of high damping rubber earthquake bearings for retrofit project in Armenia. In: Balassanian S, Cisternas A, Melkumyan M (eds) Earthquake hazard and seismic risk reduction. Kluwer Academic, Dordrecht, pp 379–385
2. Walters M, Honeck B, Elsesser E (1995) Use of seismic isolation in new and retrofit construction. In: Proceedings of the joint ASME/JSME pressure vessels and piping conference, seismic, shock and vibration isolation, Honolulu, vol PVP319, pp 31–38

3. Naaseh S (1995) Seismic retrofit of San Francisco City Hall: the role of masonry and concrete. In: Proceedings of the 3rd national concrete masonry engineering conference, San Francisco, vol 2, pp 769–795
4. Skinner R, Robinson W, McVerry G (1993) An introduction to seismic isolation. Wiley, New York
5. Ehrenkrants Group, Burtch Beall, EW Allen and Associates, Forell/Elsesser Engineers and SSD Inc (1986) Base isolation study for the renovation of the city and county building. Report, Salt Lake City
6. Melkumyan M (1994) Base isolation retrofit project in Armenia. In: Proceedings of the UNIDO workshop on use of natural rubber based bearings for earthquake protection of small buildings, Jakarta
7. Melkumyan M (2002) Seismic isolation of civil buildings in Armenia. *Prog Struct Eng Mater* 4(4):344–352
8. Melkumyan M (1997) The use of high damping rubber isolators to upgrade earthquake resistance of existing buildings in Armenia. In: Proceedings of the international post-SMiRT conference seminar on seismic isolation, passive energy dissipation and active control of seismic vibrations of structures, Taormina, pp 861–867
9. Fuller K, Roberts A (1997) Longevity of natural rubber structural bearings. In: Proceedings IRC 97, Kuala Lumpur, pp 777–787
10. Melkumyan M, Käppeli G, Khalatyan R, Hovivyan H (2003) Application of seismic isolation for retrofitting of existing 3-story stone building of the school #4 in the city of Vanadzor, Armenia. In: Proceedings of the 8th world seminar on seismic isolation, energy dissipation and active vibration control of structures, Yerevan, pp 557–565
11. Melkumyan M, Hovivyan H, Movsessyan L, Terjanyan S (2003) Technique of installation of seismic isolation bearings in an existing building with historical and architectural value. In: Proceedings of the 8th world seminar on seismic isolation, energy dissipation and active vibration control of structures, Yerevan, pp 629–641
12. Miyamoto K, Gilani A (2007) Base isolation for seismic retrofit of structures, application to a historic building in Romania. In: Seismic risk reduction, proceedings of the international symposium, Bucharest, pp 585–592
13. Melkumyan M (2007) Base and roof isolation for earthquake retrofitting and protection of existing buildings in Armenia. In: Proceedings of the international symposium on seismic risk reduction (the JICA cooperation project in Romania), Bucharest, pp 593–600
14. Melkumyan M, Hakobyan A (2005) Testing of seismic isolation rubber bearings for different structures in Armenia. In: Proceedings of the 9th world seminar on seismic isolation, energy dissipation and active vibration control of structures, Kobe, vol 2, pp 439–446
15. Melkumyan M, Gevorgyan E (2009) Structural concept on retrofitting by base isolation and analysis of the Iasi City Hall historical building in Romania. In: Proceedings of the international conference on protection of historical buildings by reversible mixed technologies, Rome
16. Fujita T (1999) Demonstration of effectiveness of seismic isolation in the Hanshin-Awaji earthquake and progress of applications of base-isolated buildings. In: Report on 1995 Kobe earthquake by INCEDE, ERC and KOBEnet. IIS, University of Tokyo—Voluntary information network for earthquake disaster mitigation, Serial 15, pp 197–216
17. Smirnov V, Eisenberg J, Zhou F, Chung Y, Nikitin A (2000) Seismoisolation for upgrading of an existing historical building in Irkutsk-City, Siberia, Russia. In: Proceedings of the 12th world conference on earthquake engineering, Auckland, Paper 0962
18. Zhou F, Liu W, Xu Z (2004) State of the art on application, R & D and design rules for seismic isolation and energy dissipation in China. In: Proceedings of the 8th world seminar on seismic isolation, energy dissipation and active vibration control of structures, Yerevan, pp 174–186
19. Martelli A, Forni M, Rizzo S (2008) Seismic isolation: present application and perspectives. In: Proceedings of the international workshop on base isolated high-rise buildings, Yerevan, pp 1–26
20. Coburn A, Spence R (2002) Earthquake protection, 2nd edn. Wiley, New York

Preliminary Design of Seismically Isolated R/C Bridges—Features of Relevant Expert System and Experimental Testing of Elastomeric Bearings

George C. Manos and Stergios A. Mitoulis

Abstract Seismically isolated R/C bridges is the target of an expert system based on the current design provisions of Eurocode 8, Part 2, which aims to facilitate their preliminary design. The expert system and the developed software includes a series of checks provided by Eurocode 8 (Part 2), in order to ensure the satisfactory seismic “optimum” performance of the selected isolation scheme. In doing so, the software accesses a specially created database of the geometrical and mechanical characteristics of commercially available cylindrical or prismatic elastomeric bearings, that can be easily enriched by relevant data from laboratory tests on isolation devices. The basic assumption included in the software is modeling the seismic response of an isolated bridge as a S.D.O.F. system. The features of this expert system are presented and discussed. Moreover, results from a number of tests are also included, indicative of the quality control procedure, specified by International Standard ISO 22762-1 (2005).

Keywords Bridges · Seismic isolation · Knowledge-based systems · Software · Preliminary design · Testing of elastomeric bearings

1 Introduction

1.1 Performance of Bridges During Earthquakes and Base Isolation

The basic principle of conventional earthquake resistant design is to ensure an acceptable safety level, while avoiding collapse and loss of life. This approach can be considered adequate for most types of structures. However, for important structures, such as bridges, higher level of performance is required, as bridges should maintain emergency communications even after severe earthquakes. Over the last 20 years,

G.C. Manos (✉) · S.A. Mitoulis
Laboratory of Strength of Materials and Structures, Department of Civil Engineering,
Aristotle University of Thessaloniki, Thessaloniki, Greece
e-mail: gcmayos@civil.auth.gr

Fig. 1 Rupture of elastomeric bearings during the Tohoku 2011 earthquake in Japan



a lot of research has been conducted in order to raise the safety level, while keeping construction costs reasonable. Seismic isolation has had numerous applications during recent decades [1–3], especially in important structures such as bridges, which should maintain the emergency communications, with appropriate reliability, after the design seismic event [4]. One of the goals of the seismic isolation is to shift the fundamental frequency of a structure away from the dominant frequencies of earthquake ground motion [5, 6]. The other purpose of an isolation system is to provide an additional means of energy dissipation, thereby reducing the transmitted acceleration of the deck, which represents the critical structural element of the bridges, [7].

There are many cases of damage to bridges in the past earthquakes all over the world. Bridges are particularly vulnerable to damage and collapse when subjected to earthquake motion due to the fact that their earthquake resisting system has low hyperstatic redundancy. Considerable efforts have been made in the past two decades to develop improved seismic isolation design procedures for new bridges [8–10] and comprehensive retrofit guidelines for existing bridges [11]. The suitability of a particular arrangement and type of isolation system will depend on many factors including the span, number of continuous spans, and seismicity of the region [12–14], frequencies of vibration of the relatively severe components of the earthquake, maintenance and replacement facilities.

Rubber bearings including elastomeric bearings and seismic isolators are installed to improve the seismic performance of bridges either alone or combined with a variety of damping devices [7]. In Japan as well as in other countries around the world, such bearings were installed as part of retrofitting schemes aimed to upgrade the seismic safety of various types of bridges [15]. During past earthquakes, there was no report of significant damage of rubber bearings and their high deformation performance protected the function of bridges [9]. During the recent devastating Tohoku 2011 earthquake elastomeric bearings generally performed quite well under the extreme ground motions in the majority of the cases, although elastomeric bearings ruptured in some bridges as shown in Fig. 1; see also Figs. 8b and 9b as well as the relevant material in [16]. A number of bridges were damaged by the subsequent tsunami (Fig. 2); for this type of action elastomeric bearings and the way they are installed do not protect the bridge deck from floating away. The current research aims to provide a tool that can be utilized in the preliminary design of

Fig. 2 Failure of a bridge due to the tsunami during the Tohoku 2011 earthquake in Japan



seismically isolated bridges through an expert system specially developed for this purpose. The field of application of this expert system, which is based on the provisions of Eurocode 8 relevant to actions generated from earthquake ground motions (not tsunami), is either newly designed bridges or the upgrading of existing bridges. It must be pointed out that the quality control of such isolation devices is of the utmost importance. Specifications for testing of the materials for the production of these isolation devices as well as of the devices themselves are described in detail [14, 17]. Furthermore, this expert system aims to serve as a tool for facilitating the designer in trying various isolation schemes and not for replacing his engineering judgment.

The modeling of seismic isolation devices is described by Eurocode 8-Part 2 as well as in [3]. A number of issues are related to the employment of isolation systems. Among these, the modeling of isolators, namely the commonly adopted force-displacement relationship of the devices, represents an approximation that changes with aging and temperature [18]. Hence, an assumption is made in the expert system, as will be outlined in the following, for simplifying the modeling of the response of the isolated structure (simplified model) (i.e. bridge).

Some of the material in this chapter is also included in a preliminary work by Manos et al. [19].

1.2 Current Code Provisions Related to the Design of Base Isolated Bridges

Seismic design of structures, in general, involves the conceptual, preliminary and final design [20], the latter being typically prescribed in detail, for most conventional structures, by the existing seismic code requirements (see above). The conceptual design, however, is not, and cannot easily be, encapsulated in codes' provisions; hence, it relies heavily on engineering judgment, expertise and experience. It is therefore quite often the case that the final design, although completely covered by detailed seismic code provisions, is essentially driven by the choices initially made. The same design process described above is also followed in the case of bridge

structures, independently of whether they are typical, short highway overpasses or more complex, long and/or curved bridges. Such bridges, although appearing to be relatively simple structures compared to some irregular buildings, may be designed with numerous different configurations depending on a set of performance (in terms of safety and serviceability), economic (including maintenance), constructability or even aesthetic criteria. This gives the designer the flexibility to choose among various structural configurations, and especially among different strategies for the support of the deck on the abutments and piers; a decision related to the use of monolithic or bearing-type connections. On the other hand, the process to select the desired dimensions and the number of the bearings to be used at each support is often time consuming, as it commonly leads to iterative calculations and numerical analyses [6] and multiple design checks against target code-based criteria concerning both the maximum bearing strain and the overall performance of the bridge structure [4, 21].

In general, it can be claimed that no comprehensive procedure has been presented to date for the optimal (i.e., cost-effective), preliminary design of seismically isolated highway overpasses and bridges. To this end, the present study aims to facilitate the designer of typical overpass configurations in selecting from a smaller, filtered sample of “eligible” bearing sections, and quickly spot the preferable combination of bearing size, type, number, location and cost at minimal computational effort. The decision-making system developed is based on multiple code-based performance criteria [4, 21], statistics arising from the construction of 40 km of bridges along the 680 km, newly built, Egnatia Highway in northern Greece, engineering judgment and recent research findings as well as ad-hoc laboratory testing, conducted for the purpose of this study. The particular process is also integrated and implemented in a user-friendly software, which permits the quick selection of the bearing scheme for given structural systems and seismic conditions. An effort was made to cover the majority of realistic overpass and simple bridge configurations, and a wide variety of steel laminated elastomeric bearing sections which are most commonly adopted for practical purposes [7, 22]. The structure of both the expert system and the software developed for the preliminary design of base-isolated bridges, together with their validation against more rigorous numerical analysis procedures, is presented in a summary form.

2 Principles of Seismic Isolation of Bridge Systems and Current Code Provisions

2.1 Preliminary Design

In Europe, seismic isolation of bridges is performed according to the Eurocode 8-Part 2 and more specifically according to clause 7, which refers to the basic requirements and compliance criteria, analysis procedures and the verification of the isolating system. Annexes J and K of the Eurocode 8-Part 2 also make reference

to the laboratory tests required in order to determine the variation of the design properties of the seismic isolator units and to verify the elastomeric bearings under seismic design situations. Similar provisions exist in the United States [21]. The Bridge Engineer is also given the choice between commercially available bearings or any other, experimentally tested, rubber bearing suitable for seismic isolation.

In most practical cases, the preliminary design of seismically isolated bridges can be performed using the response spectrum analysis framework prescribed by Eurocode 8, for a simple rigid deck finite element model which adequately provides a first estimate of the bearings' size, number and configuration. It is noted herein, that the rigid deck model is valid for most of the straight isolated bridges with continuous deck, at least in the longitudinal direction, in which the deck actually "floats" along the isolation pier-deck interface. In the transverse direction, however, the deck is in most cases restrained by stoppers (i.e., seismic links) which prevent excessive transverse deck displacements. In both cases though, as long as the displacements are kept below a prescribed magnitude, the system can be reliably assumed to be a single degree of freedom (S.D.O.F.).

The process for the design of the seismic isolation of the above bridges, considering a S.D.O.F. response, usually follows a series of simple steps, which are not prescribed by most codes [4, 21] with the exception of the Indian code specifications [23], but results from fundamentals of the dynamics of structures:

Calculation of the weight of the bridge per unit length according to the code provisions for the combination of the dead and permanent loading of the bridge (i.e., according to [5] and partly from the variable vertical loading (i.e., 0.2 for highway or 0.3 for railway bridges according to [4]) initial selection of the bearings' cross section, the total height of the elastomer and the number of the bearings per support, calculation of the total effective stiffness K_{tot} of the isolation system in the longitudinal direction of the bridge, calculation of the effective longitudinal period of the bridge as $T_{eff} = 2 \cdot \pi \cdot \sqrt{\frac{m_{tot}}{K_{tot}}}$, where m_{tot} is the total mass of the bridge, calculation of the seismic displacement $d_{Ed,x}$ of the deck in the longitudinal direction, by using the elastic spectrum of the code, according to Eurocode 8 specific guidance for seismically isolated bridges and performing a final check to judge the bearing adequacy according to code-based performance criteria.

The most common engineering practice for the final design of the aforementioned bridge systems is given in the following with emphasis on the commonly used Low Damping Rubber Bearings (LDRB).

2.2 Final Design

The techno-economical selection of an LDRB bridge isolation system is made so as to satisfy all the design constraints arising from safety-oriented code provisions, but also to maximize performance at the lowest possible cost. This is a complicated problem and, depending on the structural configuration of the bridge, the designer

has many design alternatives which require an iterative procedure, involving the repeated analysis and the design of the bridge isolation system until both criteria, i.e. code requirements that ensure both safety and cost-effectiveness, are simultaneously satisfied. Typically, the designer selects an acceptable isolation system for the bridge without considering all the possible combinations of bearing type, size and configuration, and without knowing whether the system selected was the best possible balance between cost and performance. Furthermore, most bridge isolation systems use bearings that are manufactured by international companies. In addition, due to the complexity of the above process and although permissible according to the codes, in most cases the designers are reluctant to use experimentally tested products of the local industry, hence, they lean primarily towards commercially manufactured products of the international market.

3 The Proposed Expert System

The methodology presented herein for the preliminary design of base isolated bridges is described in some detail. The methodology applies to all bridges isolated with low damping steel laminated elastomeric bearings (LDRBs), with the exception of cases where monolithic pier-deck or abutment-deck connections are combined with bearing-type pier-deck connections. The verification of the methodology is not presented in detail in this paper as it was done elsewhere [14]; it was shown that satisfactory results are obtained for straight bridges. The structure of the expert system can be summarized in the following three steps.

3.1 Step 1: User Input

A database of commercially available and experimentally tested elastomeric bearings is first compiled consisting of bearings' properties, (i.e. shear stiffness G), shape (i.e., rectangular or circular), rubber and steel plate thickness, height, and width, overall area (A) and dimensions (B_x , B_y or D). Possible bridge structural systems, characterized by different number and length of middle and central spans (L_1 or L_2), that define the total bridge length (L_{tot}) and the mass per unit length (m), as well as initial configurations of n bearings are herein defined by the designer (see Fig. 17). Seismic hazard is also considered with the most commonly used parameters in mind, i.e. the design seismic acceleration (S_a), soil type and the importance factor of the bridge under study.

3.2 Step 2: Decision Process

The second step of the methodology includes the necessary and basic calculations and checks for the seismically isolated bridge. The designer decides the acceptable

range for bearing compression (σ_e) where a minimum of 2.0 MPa and a maximum value of 5.0 MPa are proposed by the system itself according to [24]. The limit for the bearing's compression ensures that friction will be adequate to avoid the sliding of the bearing during seismic shear loading, whereas the upper limit is given to ensure that the shear strain due to the interaction between the neoprene and the steel plates under compression will remain at acceptable limits (i.e., $\varepsilon_{c,d} \leq 2.5$ according to Eurocode 8 Part 2). It is noted that this limitation is optional, in the sense that it is not explicitly imposed by the codes, however, it is good common practice. For instance, the vast majority of the bearings used in isolated bridges recently built along the Egnatia Highway in Greece have been designed not to exceed 5.0 MPa in compression. As such, the compression criterion is adopted as the first filter applied to all the bearings checked.

Based on the mass of the bridge, the compression stress (σ_e) is derived as a ratio of the total vertical load acting on each bearing (P_i) over its own area (A). The criterion proposed by Eurocode 8-Part 2 for the calculation of the maximum effective normal stress of the bearing is herein adopted:

$$\sigma_e \leq \frac{2 \cdot b_{min}}{3 \cdot t_t} \cdot G \cdot S_{min} \quad (1)$$

where σ_e is maximum effective normal stress of the bearing, b_{min} is the minimum dimension of the bearing, t_t is the total thickness of the elastomeric, G the shear modulus of the elastomer and S_{min} the minimum shape factor of the bearing layers.

It is noted that this criterion has to be applied to every single eligible bearing, in this case, stored in an external database as will be described in Sect. 3.1. All bearings that pass this filter are marked as “potentially eligible” and proceed to the next check.

By respecting the desired configuration of the bearings as set by the designer at the beginning of the process, for each bearing that has passed the previous check, the total isolation system stiffness (K_{tot}), its effective period (T_{eff}) and spectral displacement (d_{Ed}) are defined and each bearing is separately checked against seismic actions. The criterion used herein is strain-based, checking the horizontal shear deflections of the bearing given the computed level of vertical loading.

All the bearings that passed the above initial screening process are checked against a set of code-prescribed criteria, involving the normalized shear strain of the bearing due to (a) seismic loading, (b) vertical loading and (c) rotation. Herein, the criterion prescribed in Eurocode 8 is adopted, according to which the maximum total shear strain $\varepsilon_{t,d}$ of the equivalent single degree of freedom system of the seismically isolated bridge should not exceed:

$$\varepsilon_{t,d} \leq 6.0 \quad (2)$$

where:

$$\varepsilon_{t,d} = \varepsilon_{s,d} + \varepsilon_{c,d} + \varepsilon_{a,d} \quad (3)$$

and $\varepsilon_{s,d}$ is the shear strain due to the total design seismic displacement, $\varepsilon_{c,d}$ is the shear strain due to compression and $\varepsilon_{a,d}$ is the shear strain due to angular rotation.

The latter is clearly the less critical [4]. Shear strain due to the vertical load combination $\varepsilon_{c,d}$ is of the order of 0.70 for a maximum effective normal stress of the bearing that remains below 5.0 MPa as described above.

The second criterion [4, 14] is that the seismically induced shear strain $\varepsilon_{s,d}$ should be limited to:

$$\varepsilon_{s,d} \leq 2.0 \quad (4)$$

The shear strain of the bearing due to seismic load is computed again for the equivalent single degree of freedom system of the isolated bridge based on its dynamic characteristics and seismic response. Equation (4) can be written in terms of the displacement d_{Ed} of the system under study as:

$$\varepsilon_{s,d} = \frac{d_{Ed}}{t_t} \quad (5)$$

where t_t is the total thickness of the elastomeric and $d_{Ed} = \sqrt{d_{Ed,x}^2 + d_{Ed,y}^2}$ the S.R.S.S. combination of the two horizontal components of seismic displacement. It is noted that, in many practical cases, $d_{Ed,y}$ is negligible, as the transverse movements of the deck are restrained by seismic links. Moreover, it was found that the shear strain due to the total design seismic displacement expressed in Eq. (5) is more critical than the $\varepsilon_{t,d} \leq 6.0$ criterion of Eq. (2) at least for cases where the compressive stress σ_e is kept within the proposed limits (i.e., $2.0 < \sigma_e < 5.0$ MPa).

4 Experimental Testing

An experimental investigation was carried out aiming at establishing the mechanical characteristics of elastomeric bearings locally produced. For this purpose a series of standard tests was performed at the Laboratory of Strength of Materials and Structures of Aristotle University according to the International Standard [17]. Initially, these tests were used as qualification tests for the materials used in the production; that is the neoprene, the steel plates and the adhesion materials and processes. These tests are presented in a summary form and discussed in what follows. Next, in an effort to study the influence of certain parameters in the mechanical characteristics of these elastomeric bearings, the vulcanization process was investigated. Finally, compression and shear tests were also conducted with elastomeric bearings as will be presented in the following subsections.

4.1 Tensile Cyclic Tests of the Neoprene

Eleven tests were performed with frequencies varying from 0.25 Hz to 4.0 Hz. At the end of the series the specimens failed at maximum axial strain 400 % and maximum axial stress 8 MPa. At fracture the specimen underwent approximately 500

Fig. 3a Tensile cyclic tests with 200 % strains

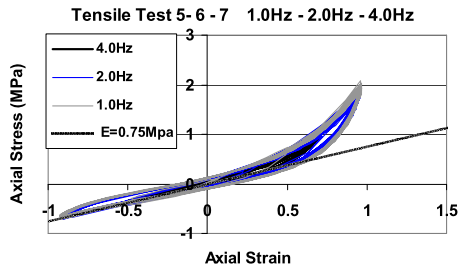
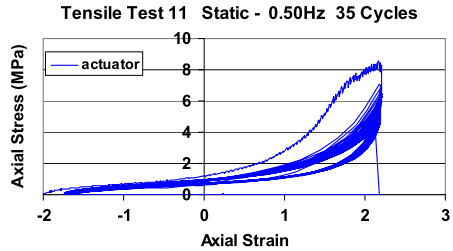


Fig. 3b Tensile cyclic tests with 400 % strains that lead to the fracture of the specimen



cycles. The approximate Young’s modulus was found to be equal to 0.75 MPa. At high levels of axial strain (more than 100 %) this value was more than double. At even higher levels of strain this value was further increased. At the initial static load-unload cycles there was a considerable difference in the load-unload path that tended to become less pronounced when the loading cycles increased in numbers. There was no noticeable influence on the behavior of the specimen arising from the frequency of the loading. The cyclic loading was introduced from an initial condition that was the result of preloading it with 50 % of the target maximum strain level. Figure 3a depicts the test results for maximum target strain 200 % whereas Fig. 3b depicts similar results for maximum target strain 400 % which resulted in the fracture of the test specimen.

4.2 Shear Cyclic Tests of Unit Slices of Elastomeric Bearings

Shear cyclic tests of specimens made of two unit slices were performed according to the International Standard [17]. For the prismatic specimens each unit slice included a layer of elastomer and two steel plates from a bearing with plan dimensions 200 mm × 200 mm. The dimensions of each slice of elastomer were 200 mm × 200 mm and 7.62 mm thickness for the orthogonal specimens (Fig. 4a); for the cylindrical specimens the diameter of the elastomer was 250 mm and its thickness 7.62 mm (Fig. 4b) with the appropriate steel plating. Thus, the tested specimens were formed by two slices of elastomer and four steel plates. Each steel plate had a thickness of 2.94 mm and sufficient dimensions in plan to have the elastomer attached and to provide enough room for the loading arrangement. Figures 4c, 5a

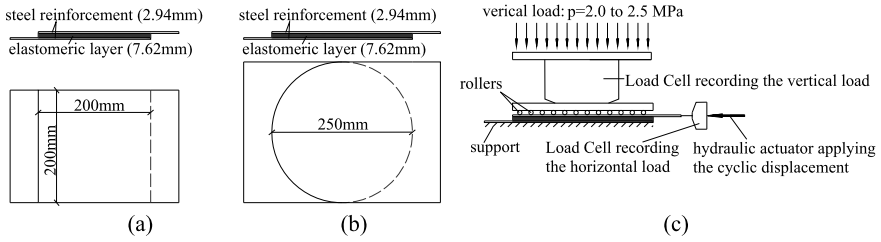


Fig. 4 Cross sections and plan views of: (a) rectangular specimens ($200 \times 200 \times 13.5$ (7.62) mm) and (b) cylindrical specimens ($\varnothing 250 \times 13.5$ (7.62) mm), (c) testing arrangement

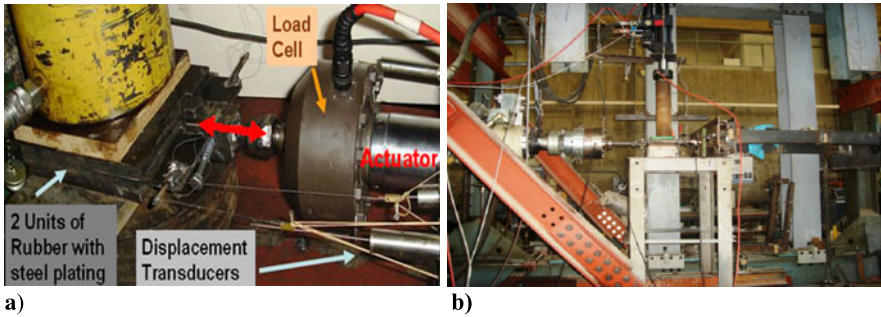


Fig. 5 Loading arrangement of a unit slice with the simultaneous application of a compressive stress field

and 5b depict the used loading arrangement. The final slice-specimen was of prototype dimensions as to be in plan a one to one representation of elastomeric bearings produced by the same process; that is employing a number of such identical unit slices and building it up to the desired height. A dynamic actuator was utilized to introduce a series of imposed cyclic shear strain loading to the specimens (see Fig. 5). Initially, the series of tests did not exceed a maximum strain level of 100 %. Next, a series of similar tests introduced maximum shear strain levels larger than 100 % up to the failure of the specimen that appeared in the form of the debonding of the elastomer from the steel plating (see Figs. 1, 8b and 9b). In what follows typical tests results are presented in brief.

4.2.1 Shear Cyclic Tests with Strain Amplitude Lower than 100 %

Both orthogonal as well as cylindrical geometry elastomeric specimens were tested during this sequence. Throughout all the tests the applied load producing the shear strains was monitored together with the corresponding displacements of the specimen that were utilized to deduce the applied shear stress and shear strain levels to the specimen. At the same time, the applied vertical load, normal to the slices of neoprene, was recorded and checked for any significant variations; the objective

Fig. 6a Shear cyclic test results for shear strain amplitude 75 % and frequencies 0.1 Hz, 0.5 Hz and 1.0 Hz

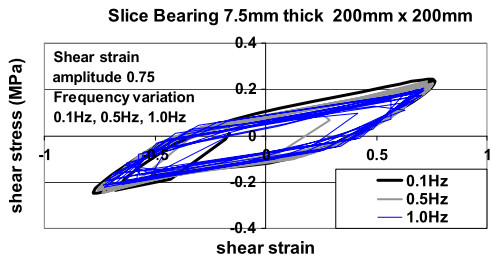
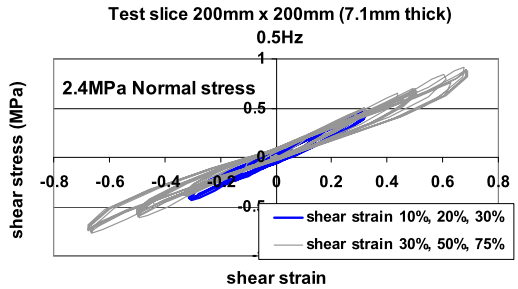
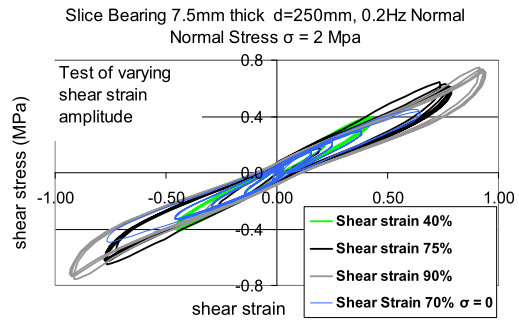


Fig. 6b Shear test results for frequency 0.5 Hz and shear strain amplitude from 5 % to 75 % slice with the simultaneous application of a compressive stress field



in this case being to keep the vertical load almost constant at the range of 2.0 to 2.5 MPa throughout all tests. These cyclic tests were performed for the following combinations: 3–11 cycles for each test, with temperature 23 degrees Celsius and cyclic loading varying with frequency 0.2 Hz. The shear strain amplitude was varied from 5 % to 75 % in the following steps: 5 % (0.38 mm), 10 % (0.76 mm), 25 % (1.91 mm), 50 % (3.81 mm), and 75 % (5.72 mm). An increase in the shear stiffness was observed when the cyclic shear strain became larger than 75 %. Subsequent tests that followed the initial tests with shear strain amplitudes varying again in the range from 5 % to 75 % exhibited an increase in the shear stiffness when they are compared with the results of the initial shear tests. Again, the specimen exhibited a stable performance throughout the increasing shear strain amplitude from 5 % to 75 % during these subsequent tests. Additional tests were also performed with the same specimens whereby the studied variable this time was the frequency of imposing the shear strain, keeping the maximum target strain amplitude constant and equal to 75 %. The corresponding results are depicted in Fig. 6a. In this case, the specimen’s performance was examined for loading frequencies equal to 0.1 Hz, 0.5 Hz and 1.0 Hz. As can be seen from this figure no significant variation in the performance of the specimen could be observed from the obtained response whereby the loading frequency was varied from 0.1 Hz to 1.00 Hz. An additional specimen of the same geometry and produced by the same process was tested by the loading arrangement shown in Fig. 5b. This time, apart from imposing the shear strain levels of continuously increasing amplitude, the specimen was placed under a constant compressive stress field normal to the horizontal plane of the elastomer (σ_e). This stress field corresponded to an equivalent compressive stress equal to 2.4 MPa. The frequency of the cyclic load was equal to 0.5 Hz and the shear strain amplitude was

Fig. 7 Cylindrical bearing slice specimen $d = 250$ mm with a variation on the shear strain amplitude up to 90 % and the normal stress amplitude (σ_e) from 0 to 2.0 MPa



continuously increasing from 10 % to 75 %. The summary results of this test are depicted in Fig. 6b. An increase in the stiffness and a decrease in the equivalent damping ratio is evident when the specimen is subjected to the previously described compressive stress field of 2.4 MPa equivalent uniform stress normal to the elastomer. However, this observation should not be generalized; as was shown from the measurements of another investigation [14, 25] further increase in this compressive stress field has the opposite effect.

Similar observations can be drawn from the shear test results obtained from the cylindrical geometry specimens. Typical shear test results are depicted in Fig. 7 for a cylindrical bearing slice specimen ($d = 250$ mm) with a variation on the shear strain amplitude up to 90 % and the normal stress amplitude (σ_e) from 0 to 2.0 MPa.

4.2.2 Shear Cyclic Tests with Strain Amplitude Higher than 100 %

The previously described loading sequences were repeated again with unit slice elastomeric specimens of the orthogonal and cylindrical geometry being loaded this time with shear strain amplitudes higher than 100 % up to the failure of the specimen. Two distinct loading arrangements were again adopted. First, the shear strains were introduced without the application of compressive load normal to the horizontal plane of the elastomer (Fig. 8a) whereas in the second case a vertical load was applied and kept constant producing an equivalent uniform compressive stress normal to the plane of the elastomer in the range of 2.0 to 2.5 MPa (Fig. 4c). Figure 8b depicts a typical failing mode during this loading process without the presence of the compressive stress field. Figure 9a depicts the load-unload behavior of this test with large shear strains without the application of compressive normal stress; Fig. 9b shows the resulting debonding of the elastomer from the steel plating at the end of this loading sequence. The levels of shear strain ranged from 100 % and gradually increased to 275 %. It can be observed that for shear strain levels lower than 200 % the specimen's behavior remains stable even for this demanding test that corresponds to an elastomeric bearing that does not have the beneficial stabilizing effect of the compressive stress field normal to the slices of the elastomer within the bearing. The maximum shear stress capacity reached for this specimen a value equal to 1.7 MPa; this occurred for a maximum strain level equal to 275 %.

Fig. 8a Loading the unit slice specimen without the presence of the compressive stress field

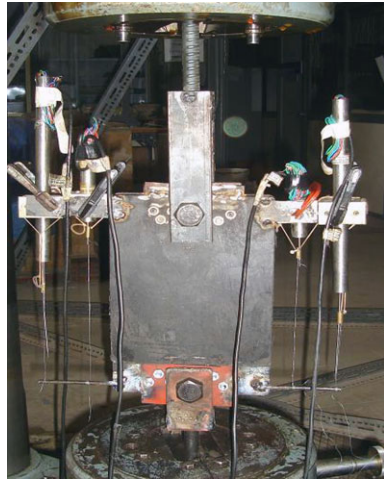


Fig. 8b Failing mode of the unit slice specimen without the presence of the compressive stress field



The load-unload behavior of the specimen with the simultaneous application of continuously increasing shear strains and an imposed compressive stress field normal to the elastomer equal to 2.0 MPa is shown in Fig. 10a; Fig. 10b shows the resulting debonding of the elastomer from the steel plating at the end of this loading sequence. When no compressive field was applied, the level of shear strain reached first a maximum strain equal to 250 % whereby the maximum shear stress was observed equal to 1.6 MPa; then for larger shear strain amplitudes the bearing capacity degrades and the specimen reaches its debonding failure mode. The maximum shear stress, when the 2.0 MPa compressive field was applied, reached a maximum value equal to 2.4 MPa for a shear strain level equal to 275 %. Then for higher shear strain levels the bearing capacity degrades and the specimen reaches its debonding failure mode. From the comparison of the performance of the specimens with and without

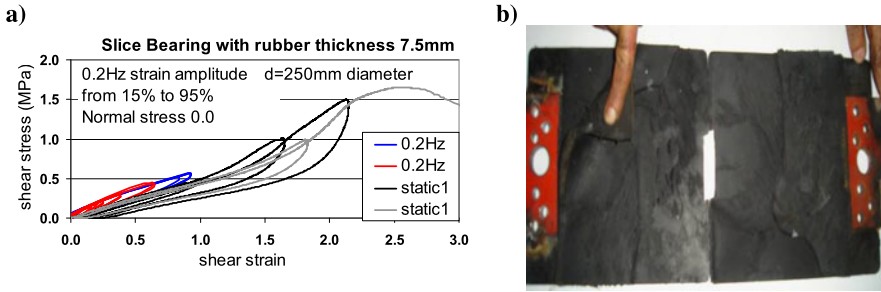


Fig. 9 Shear stress-strain response of the sliced elastomeric specimens up to failure for strains in the region of 300 % with $\sigma_e = 0.0$ MPa (a) together with the debonding of the elastomer from the steel plating at the end of this loading sequence (b)

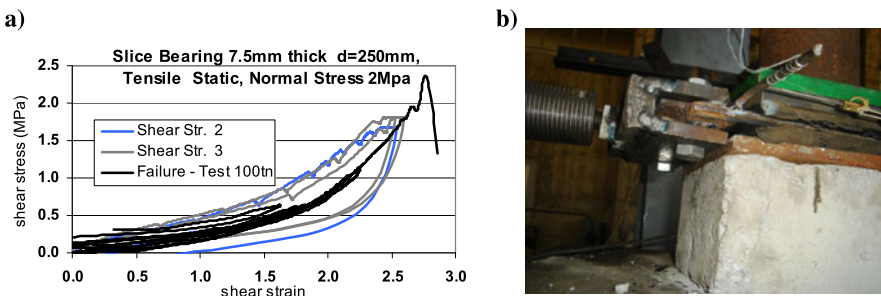


Fig. 10 Shear stress-strain response of the sliced elastomeric specimens up to failure for strains in the region of 300 % with $\sigma_e = 2.0$ MPa (a) together with the failing mode of the unit slice specimen with the presence of the compressive stress field (b)

the compressive stress field (Figs. 9a and 10a) it can be seen that the most severe test is that without the normal compressive stress field. It corresponds to an elastomeric bearing that does not have the beneficial stabilizing effect of the compressive stress field normal to the slices of the elastomer.

4.3 Tests with Elastomeric Bearings

After completing an extensive sequence of tests with the slices of the elastomeric bearings, aiming to improve and validate the production process, another sequence of tests was conducted with elastomeric bearings of certain geometry as will be described in the following subsection. This series of tests had as an objective to study the compression and shear behavior of these elastomeric bearings in time and examine the influence on the behavior of an artificial aging process that these bearings were subjected to by keeping them in specific heating conditions for a certain time. Two different elastomeric bearings were examined; the first was a square bearing

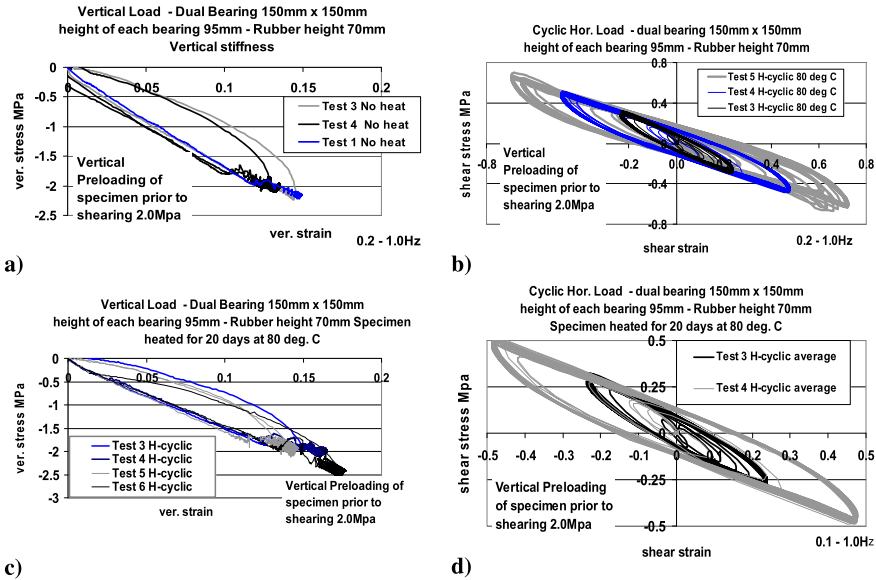


Fig. 11 Results from compression as well as from combined pre-compression and shear for the elastomeric specimen 150 mm × 150 mm before and after the artificial aging

with dimensions 150 mm × 150 mm in plan and a height of 95 mm. The clear thickness of the elastomer was 70 mm with two layers of elastomer and a thickness of the steel plating equal to 10 mm for the outer plates and 5 mm for the middle plate. The second elastomeric bearing was again of orthogonal geometry with dimensions 200 mm × 250 mm in plan having six layers of elastomer. All the steel plating was 3.5 mm thick. Two specimens of this bearing were examined; the first had a thickness of the elastomer equal to 72 mm (thick) whereas the second specimen had a thickness of the elastomer equal to 57 mm. These specimens were subjected to vertical loading tests as well as to tests that combined a vertical preloading condition, that resulted in an axial compressive field of approximately 2.0 MPa, with a horizontal dynamic load, which produced the desired level of shear strain. The loading arrangement that was utilized is in accordance with the International Standard ISO 22762-1.

4.3.1 Tests with Elastomeric Bearings 150 mm × 150 mm

Initially, this elastomeric bearing specimen was tested in compression and then in combined pre-compression of 2.0 MPa and in shear without any artificial aging (23rd September 2008). Then, the same specimen was heat treated for 20 days in a temperature equal to 80 °C and after cooling it was subjected again to the same loading sequence; e.g. in combined pre-compression of 2.0 MPa and in shear (11th

Fig. 12 Comparison of the vertical stress-strain response before and after artificial aging

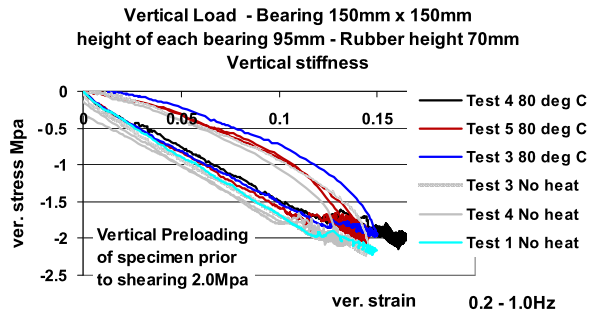
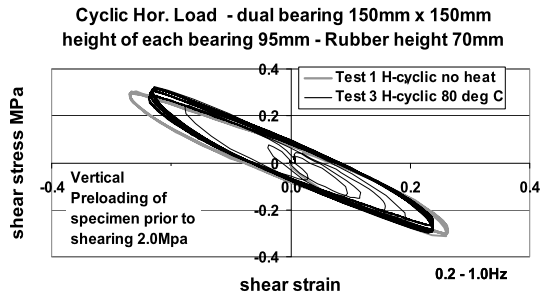


Fig. 13 Comparison of the shear stress-strain response before and after artificial aging



November 2008). During the shear tests, cyclic load was applied with varied frequencies in the range of 0.1 Hz to 1.0 Hz. Figures 11a and 11c depict the vertical stress-strain diagram for this specimen before and after the heat treatment whereas Figs. 11b and 11d depict the shear stress-strain diagram for the same specimen that was first subjected to pre-compression of 2 MPa and then to shear strain; again this test was conducted before (Fig. 11b) and after (Fig. 11d) the described heat treatment.

In Fig. 12 the comparison of the vertical stress-strain response for this elastomeric bearing specimen before and after artificial aging is shown. As can be seen, this artificial aging process resulted in a small decrease in the vertical stiffness for this elastomeric bearing. In Fig. 13 the effect of the artificial aging is depicted by comparing the cyclic shear stress-strain response before and after the heat treatment. As can be seen in this figure, this artificial aging process resulted in a very small increase in the shear stiffness for this bearing.

4.3.2 Tests with Elastomeric Bearings 250 mm x 200 mm

All the tests for this elastomeric bearing were conducted at the “new” strong reaction frame of the Laboratory of Strength of Materials and Structures of Aristotle University which houses a dynamic actuator with capabilities of ±1000 kN in load and ±250 mm in displacement and includes servo-electronic control in order to perform dynamic tests in real-time. Figure 14 illustrates a view of this strong reaction frame together with the placement of the elastomeric bearing in this loading

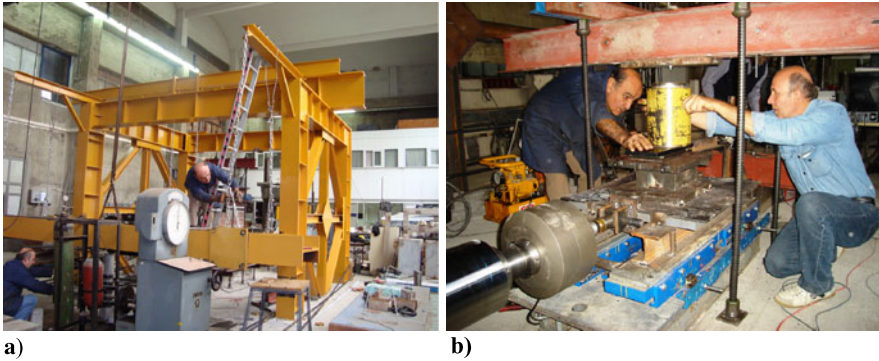


Fig. 14 The strong reaction frame of Aristotle University (a) and the 250 mm × 200 m elastomeric bearing tested at this strong reaction frame (b)

arrangement being supported by a special sliding device with very low coefficient of friction.

One important issue that is of great interest is the longevity of the rubber structural bearings [26]. The influence of aging on the important mechanical properties of the bearings examined in the laboratory was approximated through artificial aging. Initially, this elastomeric bearing specimen was tested in compression and then in combined pre-compression of 6.0 MPa and in shear without any artificial aging. Then the same specimen was heat treated for 21 days in a temperature equal to 75 °C and after cooling it was subjected again to the same loading sequence; e.g. in combined pre-compression of 6.0 MPa and in shear. During the shear tests, cyclic load was applied with varied frequencies in the range of 0.1 Hz to 0.2 Hz. Figures 15 and 16 include summary results of these tests for the specimen with the relatively thick layers of the elastomer (72 mm total elastomer thickness). In Fig. 15 the comparison of the vertical stress-strain response for this elastomeric bearing specimen before and after artificial aging is shown. As can be seen, this artificial aging process resulted in a small decrease in the vertical stiffness for this bearing. In Fig. 16 the effect of the artificial aging is depicted by comparing the cyclic shear stress-strain response before and after the heat treatment. As can be seen in this figure, this artificial aging process resulted again in a small decrease in the shear stiffness for this bearing.

5 Particulars of the Expert System

In what follows the particulars of this expert system will be described in a summary form. Full details are presented in Manos et al. [14].

Fig. 15 Comparison of the vertical stress-strain response before and after artificial aging

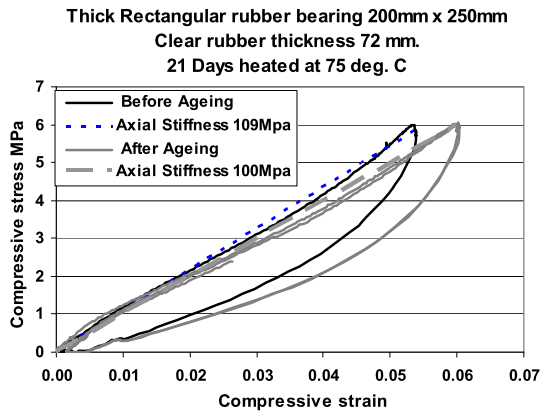
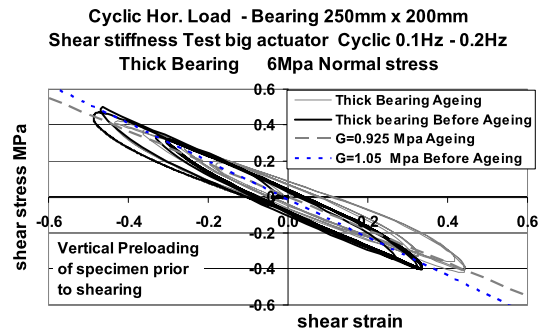


Fig. 16 Comparison of the shear stress-strain response before and after artificial aging



5.1 Structure of the Data Base

The above decision-making system was integrated and implemented in a computer software to facilitate the process and visualize the results in a way useful to the designer. As already mentioned, a database of 260 bearings available on the international market is developed in Microsoft Access using three distinct relational tables containing the necessary fields to describe the bearing geometry and capacity.

5.2 Embedment of Non-commercial Bearings After Laboratory Testing

It is noted that the database, which is part of the software, has the ability to be enriched by experimentally verified bearings. This was done for three additional bearings, produced by a local industry, which have been subjected to an extensive testing performed at the Laboratory of Strength of Materials of Aristotle University Thessaloniki. As already mentioned, the experimental study of the present investigation followed the specifications of the International Standards, which refer to the

properties of the materials of which the elastomeric bearings are composed. These tests involved quality control, vulcanization procedures and construction guidelines and were performed with samples of elastomeric slices taken from the production process. Then, a sequence of prototype tests according to [4] were applied to a series of steel laminated elastomeric bearings produced by the local industry.

The influence of the normal stress level, shear strain amplitude, frequency of shear stress loading and artificial aging was investigated. From such tests, the effective shear stiffness and the equivalent effective damping can be deduced together with their variation; the measured values can become input parameters for the developed software [14].

5.3 User Input

The primary input of the software refers to Step 1 of the proposed methodology and is made through a user-friendly interface, which manages previous and new bridge seismic isolation alternative solutions as these are progressively created by the user. A new project, that is a new preliminary design of isolation system requires the following input parameters:

(a) *Selection of structural system and bearing type*: The software can be used for the preliminary design of the seismic isolation system of bridges up to four spans, as shown in Fig. 17. The weight of the superstructure, which essentially controls the vertical load on the bearings, is either given by the designer as it is possible that the deck section has been selected before the selection of the isolation system or is estimated by the knowledge-based software for three typical deck types: a box girder section, a voided-slab deck or a deck with precast and pre-stressed I-beams.

(b) *Desirable bearing type and configuration*: The cross-section of the bearing (namely, rectangular or circular) can also be selected at this stage. With pre-stressed and precast I-beam bridge decks, the number of bearings on each support (pier or abutment) is based on the number of the longitudinal beams. In a cast-in-situ box girder or slab-type bridge deck, the number of bearings per support can be decided by the designer as a function of the dimensions of the pier's cap and the anticipated response of the isolated deck as well as using the software. The shear modulus of the bearings is automatically set by the program based on the manufacturer's specifications or any other experimentally justified value for the case of non-commercial bearings after appropriate testing. It is noted that the value suggested by Eurocode 8 [4] is 1.0 MPa. Eurocode 8 also provides a lower and upper limit of 0.9 MPa and 1.5 MPa.

(c) *Level of seismic demand*: The user defines the level of seismic demand, based on the elastic response spectrum of Eurocode 8-Part 1, the relevant soil classification and importance factor and a peak ground acceleration of 0.16, 0.24 and 0.36; the latter being an open parameter to potentially comply with various levels of seismic hazard in other countries.

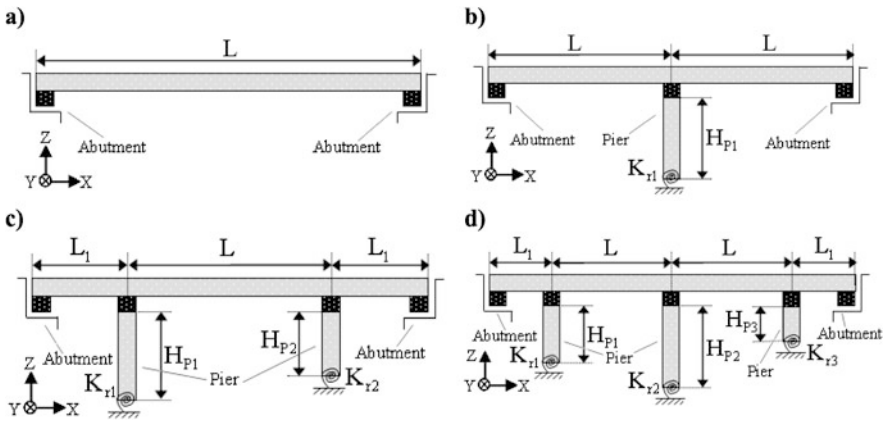


Fig. 17 Typical bridge types (geometries) with: (a) one, (b) two, (c) three or (d) four spans

5.4 Decision Process

The system automatically checks all bearings stored in the database against compression (through the resulting shear strain in the bearing) and the shear strains produced by the earthquake loading based on the compression and shear strain criteria described in Sect. 3.2 and then ranks all eligible bearings that have passed the above checks according to the Optimal Performance criterion (Eq. (6) in Ref. [14]). The results are illustrated in a graph of the $OP_{(i)}$ ratios with the section geometry. The same graph also illustrates the individual safety criterion value ($SC_{(i)}$) and total costs ($CC_{(i)}$) in order to facilitate the designer when making selections based on purely safety or cost criteria. The software also provides in a tabular form the following summary results: (a) the maximum displacement of the deck subjected to the design seismic action, and (b) the aforementioned safety criterion values, cost ratios and optimal performance indicators. Apart from the graph and the table, the software provides an output interface for each eligible bearing, showing the main dynamic characteristics of the analyzed bridge system, i.e. the effective stiffness of the resulting isolating system, the total weight of the superstructure, the effective period of the bridge, the design acceleration at the specific period and the design seismic displacement.

5.5 Assumptions and Limitations

The simplified analysis performed in the software considering the rigid deck model for the bridge, is applicable when the total mass of the piers is less than 20 % of the total bridge mass, as prescribed by Eurocode 8. The bridges under design should also be straight or have small curvature in plan and small longitudinal inclination. The software can be used in all isolated bridges with low damping elastomeric bearings that are bearings with an effective damping not larger than 6 %. However, the

validity of the software for high damping rubber bearings (HDRBs) is being currently investigated. As already mentioned, the software is developed for the preliminary design of the isolation of bridges with up to four spans.

The flexibility of the foundation, the piers and the deck in both the longitudinal and transverse direction of the bridge was taken into account in the revised version of the software. The flexibility of the foundation is a user input for all the piers. The influence of the other two parameters (flexibility of the piers and the deck) were extensively investigated as described in the next sections of the paper.

Another assumption of the software concerns the bearings used for the support of the deck to the piers and abutments. The software can consider several bearings per support either the same or different number of bearings on each pier or abutment-support. This number has no limit because of the calculation procedure used in the software. The software, however, considers that the bearings are all the same type, for example, they have the same cross-section area and the same total thickness of the elastomeric layers along the deck.

Concerning the seismic action, the software considers that the bridge is isolated in both the longitudinal and the transverse direction of the bridge as the software deals with the simultaneous action of longitudinal and transverse earthquake motion. The response of the bridge in the transverse direction can be assumed to be restrained by seismic links, which join the deck with the piers' heads.

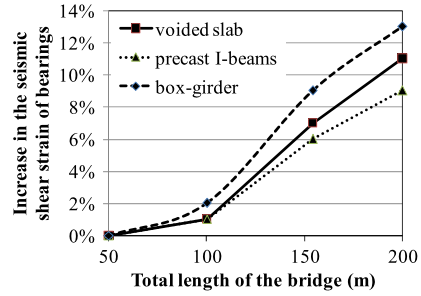
6 Additional Features of the Expert System

In what follows additional features of this expert system will be described in a summary form. These features were not included in the previous work by Manos et al. [14]. They represent an extension of this work that has been completed recently.

6.1 *The Effect of Piers' Flexibility in the Longitudinal Direction*

In the initial version of the software [14], an assumption was made that the flexibility of the piers is negligible when compared to the flexibility of the isolator units for horizontal seismic loads. In this section, the flexibility of the piers in the longitudinal direction is examined. Five different pier sections with variable dimensions in-plan and four different pier heights were considered in this parametric numerical study. The pier sections represent typical cross sections that are employed in the design of medium span bridges. The expert system utilizes a relatively simple rationale to select certain geometry of the pier cross-sections, for each one of the given choices. The user also has the option to select for each pier cross-section the governing dimensions and the pier's height. In this parametric study the height of the piers was set to have values of 8, 10, 15 or 20 meters. The stiffness of the piers is in general considerably larger than the stiffness of the isolator system. The simplified approach for approximating the longitudinal stiffness of the piers that was

Fig. 18 Increase of the maximum shear strain response of the isolator system when the flexibility of the deck in the transverse direction is considered



incorporated in the expert system was checked by 3-D numerical simulations [27] of the pier-isolator-deck system which was subjected to horizontal forces applied in a static manner at the center of mass of the bridge deck. It was confirmed that this approximate methodology results in estimates of the horizontal displacements at the top of the piers that are in very good agreement with the corresponding pier deflections as predicted by the 3-D rigorous numerical simulations. The parametric numerical study covered a substantial number of bridge systems, with a variety of pier sections and with pier height ranging from 6 to 20 meters and bridge total lengths from 50 to 200 meters. By examining bridges that have all the other parameters the same and differ only as to the stiffness of the piers, e.g. by employing different pier sections, with different dimensions and different heights, thus with different longitudinal pier stiffness, the following conclusions were made. For the seismic force response, when the longitudinal stiffness of the piers is decreased, the isolator bearing shear strain demands ε_s are increased. It was found from the examined cases (variation of the pier's height from 10 m to 20 m) that such a decrease in the pier's stiffness can lead to an increase of up to 18 % of the bearings' earthquake shear strain demand (ε_s).

6.2 Flexibility of the Deck Considering the Piers to be Stiff

The influence of the flexibility of the deck on the design of the seismic isolation system was studied for four different deck lengths 50, 100, 150 and 200 meters and three different deck cross sections, (a) Box Girder Deck Section, (b) Voided-slab Deck Section and (c) Precast I beam Deck Section. The piers were considered to be stiff. The inclusion of the transverse flexibility of the deck results in eigen-period values of the isolated bridge system in the transverse direction, as predicted by the 3-D numerical model, up to 3 % larger (for total deck length 200 meters) than the corresponding values resulting from the S.D.O.F. approximation, which forms the basis of the expert system. The influence of the deck's flexibility in the transverse direction on the maximum shear strain response of the isolation system is depicted in Fig. 18.

The increase of this maximum shear strain response is shown in this figure for three distinct deck systems; these are (a) Box Girder Deck Section, (b) Voided-slab

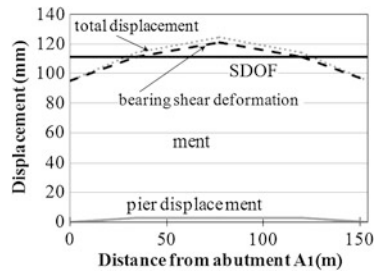
Deck Section and (c) Precast I beam Deck Section. For all three deck systems the total deck length is varied from 50 m to 200 m. As can be seen, the increase in the maximum shear strain response of the isolation system for a box girder deck section with 200 m total length reaches approximately 13 % compared with the corresponding maximum shear strain response of the isolation system of the same bridge where this deck flexibility is ignored. As expected, this influence decreases rapidly for total deck lengths smaller than 150 m (e.g. up to 2 % for total length 100 m, irrespective of the type of deck). Moreover, this influence also becomes smaller when the deck is a “Voided-slab Deck Section” (11 % for 200 m) than a “Box Girder Deck Section” (13 % for 200 m); in turn this influence becomes even smaller when a “Precast I beam Deck Section” is considered (9 % for 200 m). Hence, it is proposed to amplify by 13 % the maximum shear displacement response found by the initial version of the expert system, which is based on the S.D.O.F. approximation ignoring such deck flexibility influences. In this conservative way, the influence of most practical cases of deck flexibility in the transverse direction could be dealt with.

6.3 Piers’ Flexibility in the Transverse Direction

The influence of the flexibility of the piers in the transverse direction on the maximum shear strain response of the isolation system is studied here. In this parametric study, five different pier types were considered, combined with two different bearing sections that were found by the initial version of the expert system to be the first two choices. The flexibility of the deck in the transverse direction, which was examined on its own in the previous section, is also included here. From a large number of numerically simulated cases the results from two distinct cases are discussed next. The transverse displacement response is studied for a box-girder bridge having a total length of 150 m with either relatively flexible piers or relatively stiff piers in the transverse direction; this is plotted in Fig. 19 for the case of relatively stiff piers in the transverse direction. The 3-D simulation predicted displacement response at the top of the piers and the abutments is plotted in this figure with the solid gray line (pier displacements), whereas the displacement of the deck in the same locations is plotted with the dotted line. The shear displacement response of the isolators in these locations is plotted with the dashed line whereas with the solid black line is plotted the shear displacement response of the isolators for a system where the transverse flexibility of the piers is ignored. The latter values are predicted by the S.D.O.F. approximation included in the initial version of the expert system. The following observations can be made on the basis of these results:

- As can be seen in Fig. 19 for the case of relatively stiff piers in the transverse direction, the resulting maximum shear displacement response of the isolator system in this case, when the flexibility of the piers in the transverse direction is considered, is larger than the corresponding values predicted by the S.D.O.F.

Fig. 19 The response (displacements) in the transverse direction of the bridge when stiff piers are utilized in the transverse direction



approximation included in the initial version of the expert system. The shear displacement response of the isolators is mainly influenced in this case from the flexibility of the deck, which was examined in the previous subsection, rather than the flexibility of the piers. The increase in the maximum shear displacement response is of the order of 9 % in this case, as was already discussed in Sect. 6.2. Hence, as already mentioned in this section, it is proposed to amplify by 12 % the maximum shear displacement response found by the expert system, which is based on the S.D.O.F. approximation ignoring such deck flexibility influences. In this conservative way, the influence of most practical cases of deck flexibility in the transverse direction could be dealt with.

- For the case of relatively flexible piers in the transverse direction, the resulting maximum shear displacement response of the isolator system in this flexible-pier case, when the flexibility of the piers in the transverse direction is considered, is smaller than the corresponding values predicted by the S.D.O.F. approximation included in the initial version of the expert system. The shear displacement response of the isolators is mainly influenced in this case from the flexibility of the piers rather than the flexibility of the deck, which was discussed in the previous section. The decrease in the maximum shear displacement response is of the order of 10 % in this case. Thus, when the flexibility of the piers is ignored, as is the case in the S.D.O.F. approximation, the resulting choice of isolators is on the conservative side. Based on this finding no alteration of the S.D.O.F. approximation is proposed at this stage regarding the influences arising from the transverse flexibility of the piers.

7 Verification of Results for the Design of a Real Bridge

The methodology described above and the software developed were validated by extensive 2-D and 3-D parametric numerical simulations of bridges with the same geometry and structural system that can be selected through the options included in this software, as explained before. Moreover, this validation process was extended to include the case of a real bridge (Fig. 20).

The bridge adopted as the case study is a simplified version of the Araithos-Peristeri bridge described by [28], already constructed along the Egnatia Highway in northern Greece. The simplified system consists of four spans, that is the maximum

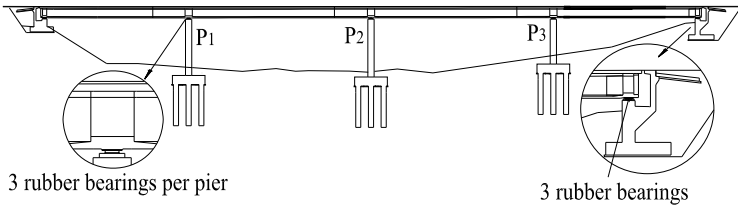


Fig. 20 Longitudinal section of the simplified Araithos-Peristeri Bridge

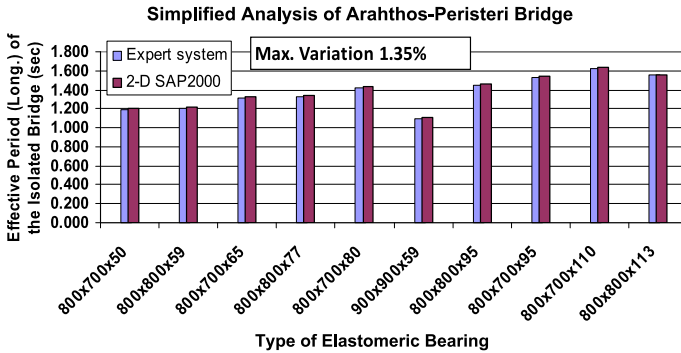


Fig. 21 Comparison of the effective periods (T_{eff}) of the isolated bridge calculated by the software developed and by the more rigorous dynamic analysis with FE SAP 2000

number of spans that are supported by the software (Figs. 17 and 20), as opposed to the six spans of the real structure, and a total length equal to 154.0 meters. Three bearings were selected for supporting the deck on each abutment and pier to avoid extensive rejection of bearing sections due to high compression. The length of the central span is $L = 43.00$ meters, the length of the end spans $L_1 = 34.00$ meters, the shape of the bearings is rectangular, soil type was taken corresponding to class B according to the Eurocode 8, the design ground acceleration was taken equal to $0.16g$, the importance factor was assumed to be $\gamma_I = 1.30$, the maximum allowable compression was set equal to 5.00 MPa and the minimum compression to 2.00 MPa, the shear modulus of the elastomeric bearings was assumed to be $G = 1.0$ MPa and the deck mass was estimated as $m = 308.40$ kN/meter.

As described above, the validation procedure then followed two discrete steps. First, the effective period of the S.D.O.F. system was computed and was compared with more rigorous eigen-value analysis, with the aid of the finite element software SAP 2000 [25]. This is presented in Fig. 21.

The validity of the S.D.O.F. assumption in the longitudinal direction for the particular bridge system was verified because the maximum deviation between the S.D.O.F. simplification and the fundamental period of the structure of the M.D.O.F. system did not exceed 1.35 %, and this was deemed acceptable for preliminary design purposes. Next, the predicted by the S.D.O.F. approximation of the maximum

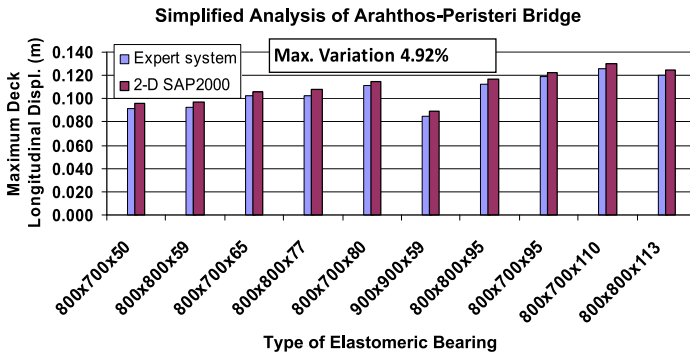


Fig. 22 Comparison of the max. Deck displacement of the isolated bridge calculated by the software developed and by the more rigorous dynamic analysis with FE SAP 2000

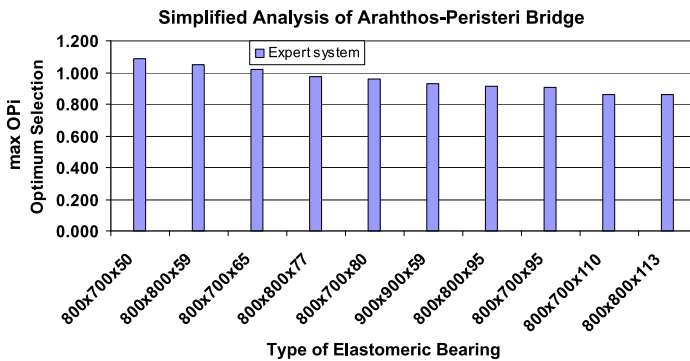


Fig. 23 Bearings that passed the software tests. Plotted are the values of Optimal Performance ratio

deck horizontal seismic displacement response is compared with the corresponding values obtained through the more rigorous numerical analysis, as shown in Fig. 22. Again, the validity of the S.D.O.F. approximation for this particular bridge is verified because the observed differences between the corresponding values did not exceed 4.92 %. For both Fig. 21 and Fig. 22 the dimensions of each bearing are plotted in the abscissa (namely, rectangular bearings with dimensions B_x , B_y and thickness of the elastomer t_e , e.g. equal to 800, 700 and 50 mm respectively).

The application of the methodology as implemented through the software of the expert system, resulted in 29 design alternatives (namely, eligible bearing sections) for the isolation system of the bridge that were all acceptable, namely, corresponding to a safety criterion value greater than one (1.0) as defined by Eq. (4). To facilitate the final choice, the first ten (10) of these eligible bearings are plotted in Fig. 23 according to the value of the Optimal Performance ratio, $OP(i)$, as defined by Eq. (6) in Ref. [14]. The bearing with the highest value of this ratio is plotted at the further left of this plot. Consequently, the choice of such an “optimum” bearing scheme

will be the one with the highest Optimal Performance ratio value. This choice is not based on the minimum cost, which, however, is indicated separately by the cost criterion values ($CC(i)$), if the designer prefers to base his choice on the cost rather than the optimal performance. All the bearing schemes offered as designer's choice comply with the safety code requirements, described by Eq. (4).

8 Concluding Remarks

- The expert system developed for the preliminary design of the seismic isolation of bridges, assumed to respond as S.D.O.F. systems, is presented and discussed in this paper. The proposed methodology is based on the current design provisions of Eurocode 8. The methodology of this expert system is also implemented in software whose efficiency is validated through more rigorous 2-D and 3-D M.D.O.F. parametric numerical analyses as well as by using the case of a real bridge.
- It is evident that the prediction success of the preliminary design process, that is proposed here, heavily relies on the extent of the contribution of the fundamental mode in the longitudinal direction, which, when dominant, yields the S.D.O.F. simplification as reasonable assumption.
- The initial version of the expert system did not include any influence arising from either the flexibility of the piers in the longitudinal or transverse direction or the flexibility of the deck.
- The current investigation revealed that by not accounting for the flexibility of the piers the expert system predictions of the maximum shear strain response of the isolators is on the conservative side by a small margin and as such these predictions can be considered satisfactory.
- On the contrary it was found that the contribution of the flexibility of the deck on the maximum shear strain response of the isolators cannot so easily be neglected. Hence, it is proposed to amplify by 13 % the maximum shear displacement response found by the initial version of expert system, which is based on the S.D.O.F. approximation ignoring such deck flexibility influences. In this conservative way, the influence of most practical cases of deck flexibility in the transverse direction could be dealt with.
- The software that is based on this expert system permits the investigation of hundreds of bearing solutions. The eligible bearing hierarchy provided through the proposed safety over cost (Optimal Performance) criterion, provides a significantly large number of potential design alternatives to be considered for the final selection. In this way, the proposed process can be seen as an effective preliminary design tool, believed to lead to the quicker and more reliable estimate of the optimal bearing selection and seismic response of bridges, assumed to respond as S.D.O.F. systems, either in the stage before its final design or when such an existing bridge is checked for upgrading its seismic performance using such an isolation scheme.

Acknowledgements This research was partially conducted in the framework of the Regional Innovation Pole of the Region of Central Macedonia in northern Greece, established in 2006 in the city of Thessaloniki. The project was partially funded by the General Secretariat of Research and Technology of the Greek Ministry of Development; its support is gratefully acknowledged.

References

1. Kelly JM, Buckle IG, Koh CG (1986) Mechanical characteristics of base isolation bearings for a bridge deck model test. Report UCB/EERC-86/11, Earthquake Engineering Research Center, University of California, Berkeley
2. Kelly JM (1986) Aseismic base isolation: a review and bibliography. *Soil Dyn Earthq Eng* 5(4):202–216
3. Kelly JM (1997) Earthquake resistant design with rubber. Springer, Santa Clara. ISBN 3540761314, 9783540761310
4. Eurocode 8 (2004) Design of structures for earthquake resistance—part 2: Bridges. DRAFT No 3
5. Eurocode 8 (2004) Design of structures for earthquake resistance—part 1: General rules, seismic actions and rules for buildings. DRAFT No 3, European Committee for Standardization
6. Naeim F, Kelly JM (1999) Design of seismic isolated structures. From theory to practice. Wiley, New York
7. Kunde MC, Jangid RS (2003) Seismic behavior of isolated bridges: a state-of-the-art review. *Electron J Struct Eng* 3:140–170
8. Kawashima K (2004) Seismic isolation of highway bridges. *J Jpn Assoc Earthq Eng* 4(3):283–297 (special issue)
9. Kawashima K (2012) Damage of bridges due to the 2011 great east Japan earthquake. In: Proceedings of the international symposium on engineering lessons learned from the 2011 great east Japan earthquake, Tokyo, March 1–4, pp 82–101
10. Public Works Research Institute (1995) Study on seismic response characteristics of Menshin bridges based on measured records. Technical memorandum of PWRI, No 3383, Public Works Research Institute
11. Dicleli M, Mansour M, Constantinou M (2005) Efficiency of seismic isolation for seismic retrofitting of heavy substructured bridges. *J Bridge Eng* 10(4):429–441
12. Manos GC, Mitoulis S, Kourtidis V, Sextos A, Tegos I (2007) Study of the behavior of steel laminated rubber bearings under prescribed loads. In: Proceedings of 10th world conference on seismic isolation, energy dissipation and active vibrations control of structures, Istanbul, May 2007
13. Manos GC, Sextos A, Mitoulis S, Kourtidis V, Geraki M (2008) Tests and improvements of bridge elastomeric bearings and software development for their preliminary design. In: Proceedings of 14th world conference on earthquake engineering, Beijing
14. Manos GC, Mitoulis SA, Sextos A (2012) A knowledge-based software for the design of the seismic isolation system of bridges. *Bull Earthq Eng* 10:1029–1047. doi:[10.1007/s10518-011-9320-0](https://doi.org/10.1007/s10518-011-9320-0)
15. Hoshikuma J, Zhang G, Sakai J (2012) Seismic behavior of retrofitted bridges during the 2011 great east Japan earthquake. In: Proceedings of the international symposium on engineering lessons learned from the 2011 great east Japan earthquake, Tokyo, March 1–4, 2012, pp 1323–1332
16. Buckle I, Yen W-HP, Marsh L, Monzon E (2012) Implications of bridge performance during great east Japan earthquake for U.S. seismic design practice. In: Proceedings of the international symposium on engineering lessons learned from the 2011 great east Japan earthquake, Tokyo, March 1–4, 2012, pp 1363–1374
17. International Standard ISO 22762-1 (2005) Elastomeric seismic protection isolators—part 1: Test methods. International Organization for Standardization

18. Constantinou MC, Tsopeles P, Kasalanati A, Wolff ED (1999) Property modification factors for seismic isolation bearings. Report MCEER-99-0012, Multidisciplinary Center for Earthquake Engineering Research, Buffalo
19. Manos GC, Mitoulis SA, Sextos A (2011) Preliminary design of seismically isolated R/C highway overpasses—features of relevant software and experimental testing of elastomeric bearings. In: Papadrakakis M, Fragiadakis M, Plevris V (eds) Proceedings of the conference on computational methods in structural dynamics and earthquake engineering, Corfu, 26–28 May 2011. <http://congress.cimne.com/eccomas/proceedings/compdyn2011>
20. Pracasa Rao AVNS (1992) BEAS: expert system for the preliminary design of bearings. Technical note. *Adv Eng Softw* 14(2):163–166
21. AASHTO (2001) Recommended LRFD guidelines for the seismic design of highway bridges. Based on: NCHRP 12-49, Comprehensive specification for the seismic design of bridges, revised LRFD design specifications (seismic provisions), third draft of specifications and commentary, March 2001
22. Faravelli L (2001) Modelling the response of an elastomeric base isolator. *J Struct Control* 8(1):17–31
23. Bansal G (2006) Bridge bearings. Indian Railways Institute of Civil Engineering (IRICEN), Pune
24. Abe M, Yoshida J, Fujino Y (2004) Multi-axial behaviors of laminated rubber bearings and their modeling. I: Experimental study. *J Struct Eng* 130(8):1119–1132
25. Ryan KL, Kelly JM, Chopra AK (2004) Experimental observation of axial load effects in isolation bearings. In: Proceedings of 13th world conference on earthquake engineering, Vancouver, August 2004, No 1707
26. Fuller KNG, Roberts AD (1997) Longevity of natural rubber structural bearings. In: International rubber conference. Kuala Lumpur, 6–9 October
27. Computers and Structures Inc (2002) SAP 2000. Nonlinear ver 11.0.4. User's reference manual, Berkeley
28. Mitoulis SA, Tegos IA, Stylianidis K-C (2010) Cost-effectiveness related to the earthquake resisting system of multi-span bridges. *Eng Struct* 32(9):2658–2671

Soft Computing in Structural Dynamics

T. Burczyński, R. Górski, A. Poteralski, and M. Szczepanik

Abstract The paper is devoted to new computational techniques in structural dynamics where one tries to study, model, analyse and optimise very complex phenomena, for which more precise scientific tools of the past were incapable of giving low cost and complete solution. Soft computing methods differ from conventional (hard) computing in that, unlike hard computing, they are tolerant of imprecision, uncertainty, partial truth and approximation. The paper deals with an application of the bio-inspired methods, like the evolutionary algorithms (EA), the artificial immune systems (AIS) and the particle swarm optimisers (PSO) to optimisation problems. Structures considered in this work are analysed by the finite element method (FEM) and the boundary element method (BEM). The bio-inspired methods are applied to optimise shape, topology and material properties of 3D structures modelled by the FEM and to optimise location of stiffeners in 2D reinforced plates modelled by the coupled BEM/FEM. The structures are optimised using the criteria dependent on frequency, displacements or stresses. Numerical examples demonstrate that the methods based on the soft computation are effective for solving computer aided optimal design problems.

Keywords Soft computing · Evolutionary algorithm · Artificial immune system · Particle swarm optimiser · Optimisation · Finite element method · Boundary element method · Dynamics

1 Introduction

Structures are frequently subjected to dynamic loads and it is very important to analyse their transient dynamic response. Important properties of vibrating structures are

T. Burczyński (✉) · R. Górski · A. Poteralski · M. Szczepanik
Institute of Computational Mechanics and Engineering, Silesian University of Technology,
Konarskiego 18a, 44-100 Gliwice, Poland
e-mail: Tadeusz.Burczynski@polsl.pl

T. Burczyński
Institute of Computer Science, Cracow University of Technology, Warszawska 24,
31-155 Cracow, Poland
e-mail: tburczyn@pk.edu.pl

M. Papadrakakis et al. (eds.), *Computational Methods in Earthquake Engineering*,
Computational Methods in Applied Sciences 30, DOI [10.1007/978-94-007-6573-3_24](https://doi.org/10.1007/978-94-007-6573-3_24),
© Springer Science+Business Media Dordrecht 2013

eigenfrequencies. The dynamic response or natural frequencies of structures can be established by changing shape, topology and material properties of structures. Another possibility of the response improvement is applying stiffeners. The choice of their number, properties and location in a structure decides about the effectiveness of reinforcement. Reinforced structures are often used in practice because they are resistant, stiff and stable. A typical area of application of such structures is an aircraft industry, where light, stiff and highly resistant structures are required. Many aircraft elements are made as thin panels reinforced by stiffeners.

Dynamic response of structures with an arbitrary geometry, material properties and boundary conditions can be obtained by carrying out laboratory tests but they are usually very expensive and time consuming. In order to reduce costs and time, computer simulations are performed instead of experimental investigations. As a result, dynamic quantities of interest like displacements, velocities, accelerations, forces, stresses, etc., can be determined. The most versatile methods of analysis of structures subjected to arbitrary static and time dependent boundary conditions are the finite element method (FEM) and the boundary element method (BEM). The coupling of these methods is very desirable in order to exploit their advantages. Optimal properties of dynamically loaded structures can be searched using the computer aided optimisation tools.

In the present paper, the coupling of the FEM and BEM with the bio-inspired methods in optimisation of dynamically loaded structures is presented. The evolutionary algorithms (EA), the artificial immune systems (AIS) and the particle swarm optimisers (PSO) are used to optimise shape, topology and material properties of 3D freely vibrating structures and 2D dynamically loaded stiffened plates. The former are analysed by the FEM and the latter by the coupled BEM/FEM.

2 Soft Computing Methods

Soft computing techniques resemble human reasoning more closely than traditional techniques, which are largely based on conventional logical systems or rely heavily on the mathematical capabilities of a computer. These computing techniques are often used to complement each other in applications. It should be pointed out that simplicity and complexity of systems are relative, and certainly, most successful mathematical modelling of the past have also been challenging and very significant.

Unlike hard computing schemes, which strive for exactness and for full truth, soft computing techniques exploit the given tolerance of imprecision, partial truth, and uncertainty for a particular problem. Another common contrast comes from the observation that inductive reasoning plays a larger role in soft computing than in hard computing.

Three important soft computing methods used in the paper are:

- Evolutionary Computations (EC),
- Artificial Immune Systems (AIS),
- Particle Swarm Methods (PSM).

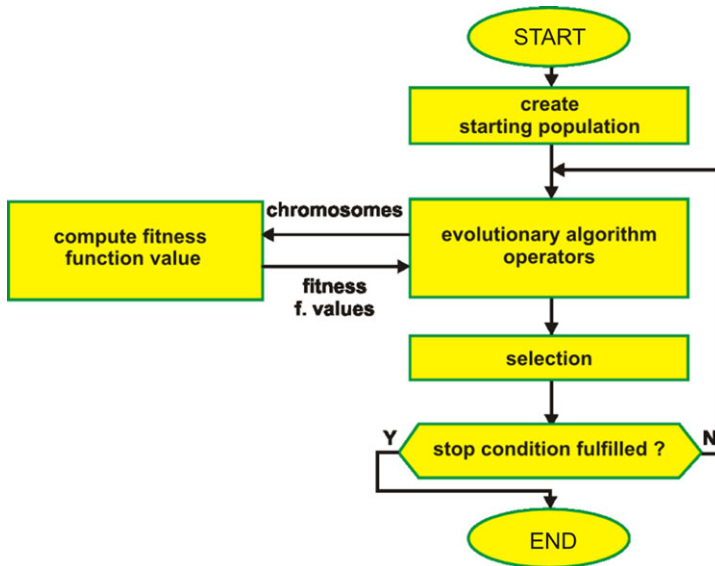


Fig. 1 A flowchart of an evolutionary algorithm

2.1 Evolutionary Computations (EC)

Evolutionary algorithms [1, 2] are algorithms searching the space of solutions and they are based on the analogy to the biological evolution of species. Like in biology, the term of an individual is used, and it represents a single solution. Evolutionary algorithms operate on populations of individuals, so while the algorithm works, all the time we deal with a set of problem solutions. An individual consists of chromosomes. Usually it is assumed that an individual has one chromosome. Chromosomes consist of genes which are equivalents of design variables in optimisation problems. The adaptation is computed using a fitness function. All genes of an individual decide about the fitness function value. A flowchart of an evolutionary algorithm is presented in Fig. 1.

In the first step, an initial population of individuals is created. Usually, the values of genes of particular individuals are randomly generated. In the next step, the fitness function value for each individuals is computed. Then, evolutionary operators change genes of the parent population individuals. They are then selected for the offspring population, which becomes the parent population and the algorithm is continuing iteratively till the end of the computation. The termination condition of the computation can be formulated as the maximum number of iterations.

In evolutionary algorithms the floating-point representation is applied, which means that genes included in chromosomes are floating-point numbers. Usually the variation of a gene value is limited.

A single-chromosome individual (called a chromosome) ch_i , $i = 1, 2, \dots, N$, where N is the population size, may be presented by means of a column or line

Fig. 2 Structure of an individual

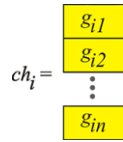
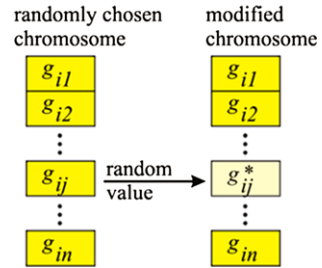


Fig. 3 A diagram of a uniform mutation



matrix, whose elements are represented by genes g_{ij} , $j = 1, 2, \dots, n$, where n is the number of genes in a chromosome. The sample chromosome is presented in Fig. 2.

Evolutionary operators change gene values like the biological mechanisms of mutation and crossover. Different kinds of operators are presented in publications, and the basic ones are:

- uniform mutation,
- mutation with Gaussian distribution,
- boundary mutation,
- simple crossover,
- arithmetical crossover.

A uniform mutation changes the values of randomly chosen genes in randomly selected individual. The new values of genes are drawn in such a way that they fulfil constraints imposed on the variation of the gene values. The diagram of how an operator works is presented in Fig. 3.

A mutation with Gaussian distribution is an operator changing the values of genes randomly, similarly to uniform mutation. New values of the genes are created by means of random numbers with Gaussian distribution. The operator searches the individual's surrounding.

A boundary mutation (Fig. 4) operates similarly to a uniform mutation, however, new values of the genes are equal to the left or right value from the gene variation range (left or right constraint on gene values).

A simple crossover is an operator creating an offspring on the basis of two parent individuals. A cutting position is drawn (Fig. 5), and a new individual consists of the genes coming partly from the first and partly from the second individual.

An arithmetical crossover has no biological counterpart. A new individual is formed similarly to a simple crossover, on the basis of two parent individuals, however, the values of the individual's genes are defined as the average value of the parent individuals' genes (Fig. 6).

Fig. 4 A diagram of a boundary mutation

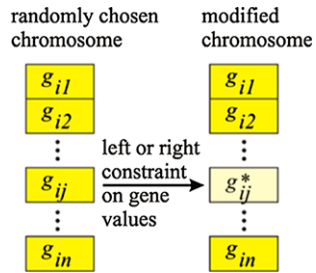


Fig. 5 A diagram of a simple crossover

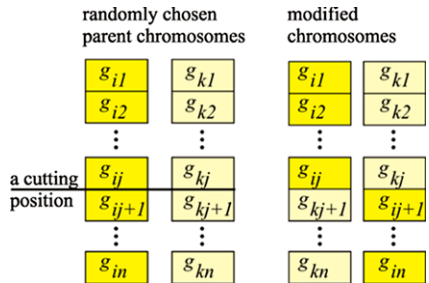
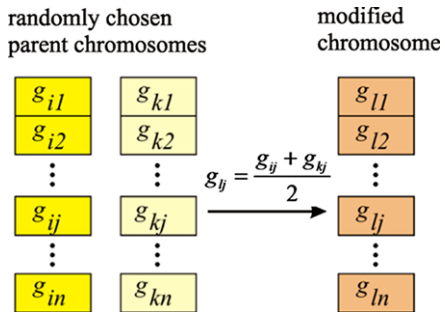


Fig. 6 A diagram of an arithmetical crossover



An important element of an evolutionary algorithm is the mechanism of selection. The probability of the individual’s survival depends on the value of the fitness function. Ranking selection is performed in a few steps. First, the individuals are classified according to the value of the fitness function, then a rank value is attributed to each individual. It depends on the individual’s number and the rank function. The best individuals obtain the highest rank value, the worst obtain the lowest one. In the final step individuals for the offspring generation are drawn, but the probability of drawing particular individuals is closely related to their rank value.

2.2 Artificial Immune Systems (AIS)

The artificial immune systems (AIS) are developed on the basis of a mechanism discovered in biological immune systems [3]. An immune system is a complex system which contains distributed groups of specialised cells and organs. The main purpose of the immune system is to recognise and destroy pathogens—funguses, viruses, bacteria and improper functioning cells. The lymphocytes cells play a very important role in the immune system. The lymphocytes are divided into several groups of cells. There are two main groups B and T cells, both contains some subgroups (like B-T dependent or B-T independent). The B cells contain antibodies, which could neutralise pathogens and are also used to recognise pathogens. There is a big diversity between antibodies of the B cells, allowing recognition and neutralisation of many different pathogens. The B cells are produced in the bone marrow in long bones. A B cell undergoes a mutation process to achieve big diversity of antibodies. The T cells mature in thymus, only T cells recognising non-self-cells are released to the lymphatic and the blood systems. There are also other cells like macrophages with presenting properties, the pathogens are processed by a cell and presented by using MHC (Major Histocompatibility Complex) proteins. The recognition of a pathogen by B cell (Fig. 7a) is performed in a few steps (Fig. 7). First, the B cells or macrophages present the pathogen to a T cell using MHC (Fig. 7b), the T cell decides if the presented antigen is a pathogen. The T cell gives a chemical signal to B cells to release antibodies. A part of stimulated B cells goes to a lymph node and proliferate (clone) (Fig. 7c). A part of the B cells changes into memory cells, the rest of them secrete antibodies into blood. The secondary response of the immunology system in the presence of known pathogens is faster because of memory cells. The memory cells created during primary response, proliferate and the antibodies are secreted to blood (Fig. 7d). The antibodies bind to pathogens and neutralise them. Other cells like macrophages destroy pathogens (Fig. 7e). The number of lymphocytes in the organism changes, while the presence of pathogens increases, but after attacks a part of the lymphocytes is removed from the organism.

The artificial immune systems [4–7] take only few elements from the biological immune systems. The most frequently used are the mutation of the B cells, proliferation, memory cells, and recognition by using the B and T cells. The artificial immune systems have been used to optimisation problems in [8], classification and also computer viruses recognition in [4]. The cloning algorithm presented by von Zuben and de Castro [6, 8] uses some mechanisms similar to biological immune systems to global optimisation problems. The unknown global optimum is the searched pathogen. The memory cells contain design variables and proliferate during the optimisation process. The B cells created from memory cells undergo mutation. The B cells evaluate and better ones exchange memory cells. In Wierzczoń [9] version of *Clonalg* the crowding mechanism is used—the diverse between memory cells is forced. A new memory cell is randomly created and substitutes the old one, if two memory cells have similar design variables. The crowding mechanism allows find-

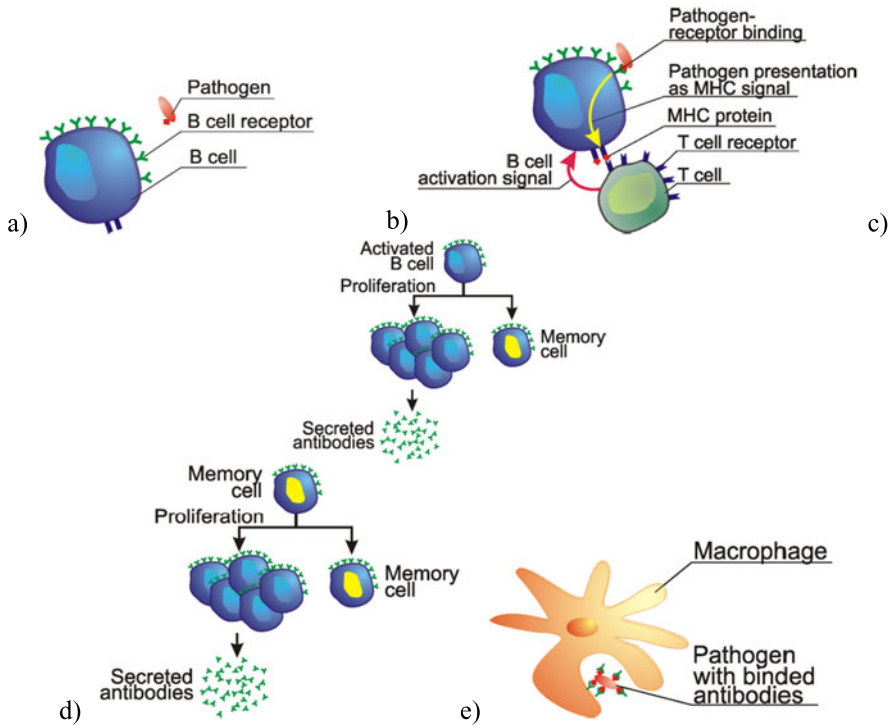
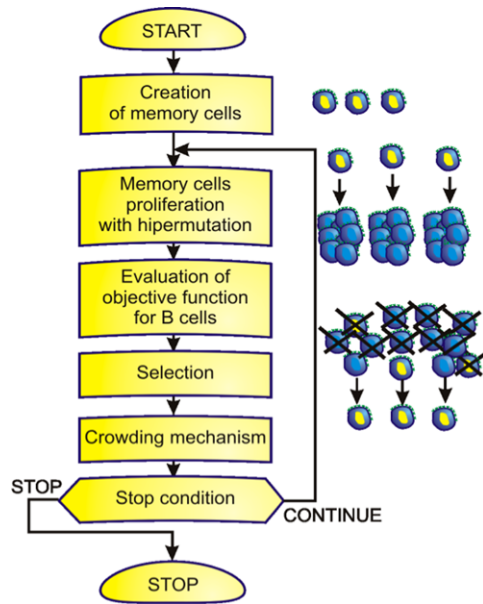


Fig. 7 An immune system: (a) a B cell and pathogen, (b) the recognition of pathogen using B and T cells, (c) the proliferation of activated B cells, (d) the proliferation of a memory cell—secondary response, (e) pathogen absorption by a macrophage

ing not only the global optimum but also other local ones. The presented approach is based on the Wierzchoń [9] algorithm, but the mutation operator is changed. The Gaussian mutation is used instead of the nonuniform mutation in the presented approach.

A flowchart of an artificial immune system is presented in Fig. 8. The memory cells are created randomly. They proliferate and mutate creating B cells. The number of clones created by each memory cell is determined by the memory cells objective function value. The objective functions for B cells are evaluated. The selection process exchanges some memory cells for better B cells. The selection is performed on the basis of the geometrical distance between each memory cell and B cells (measured by using design variables). The crowding mechanism removes similar memory cells. The similarity is also determined as the geometrical distance between memory cells. The process is iteratively repeated until the stop condition is fulfilled. The stop condition can be expressed as the maximum number of iterations.

Fig. 8 An artificial immune system



2.3 Particle Swarm Methods (PSM)

The particle swarm algorithms [10], similarly to the evolutionary and immune algorithms, are developed on the basis of the mechanisms discovered in the nature. The swarm algorithms are based on the models of the animals social behaviours: moving and living in the groups. The animals relocate in the three-dimensional space in order to change their stay place, the feeding ground, to find the good place for reproduction or to evading predators. We can distinguish many species of the insects living in swarms, fishes swimming in the shoals, birds flying in flocks or animals living in herds (Fig. 9).

A simulation of the bird flocking was published in [10]. They assumed that this kind of the coordinated motion is possible only when three basic rules are fulfilled: collision avoidance, velocity matching of the neighbours and flock centring. The computer implementation of these three rules showed very realistic flocking behaviour flaying in a three-dimensional space, splitting before obstacle and rejoining again after missing it. The similar observations concerned the fish shoals. Further observations and simulations of the birds and fishes behaviour gave in effect more accurate and more precise formulated conclusions [11]. The results of this biological examination were used by Kennedy and Eberhart [12], who proposed Particle Swarm Optimiser—PSO. This algorithm realises directed motion of the particles in n -dimensional space to search for solution for n -variable optimisation problem. PSO works in an iterative way. The location of one individual (particle) is determined on the basis of its earlier experience and experience of whole group (swarm). Moreover, the ability to memorise and, in consequence, returning to the areas with convenient properties, known earlier, enables adaptation of the particles to the life

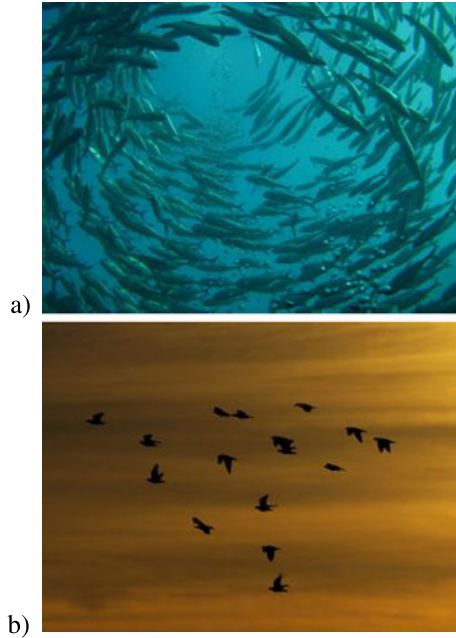
Fig. 9 Particles swarms:

(a) fish shoal

(<http://www.sxc.hu/photo/1187373>),

(b) bird flock

(<http://www.sxc.hu/photo/1095384>)



environment. The optimisation process using PSO is based on finding the better and better locations in the search-space (in the natural environment that are for example hatching or feeding grounds).

The algorithm with continuous representation of design variables and constant constriction coefficient (constricted continuous PSO) has been used in presented research. In this approach each particle oscillates in the search space between its previous best position and the best position of its neighbours, with expectation to find new best locations on its trajectory. When the swarm is rather small (swarm consists of several particles or tens of particles) it can be assumed that all the particles stay in a neighbourhood of the currently considered one. In this case we can assume the global neighbourhood version and the best location found by swarm so far is taken into account—current position of the swarm leader (Fig. 10).

The position of the i -th particle is changed by stochastic velocity v_{ij} , which is dependent on the particle distance from its earlier best position and position of the swarm leader. This approach is given by the following equations:

$$v_{ij}(k + 1) = wv_{ij}(k) + \phi_{1j}(k)[q_{ij}(k) - d_{ij}(k)] + \phi_{2j}(k)[\hat{q}_{ij}(k) - d_{ij}(k)] \quad (1)$$

$$d_{ij}(k + 1) = d_{ij}(k) + v_{ij}(k + 1), \quad i = 1, 2, \dots, m; \quad j = 1, 2, \dots, n \quad (2)$$

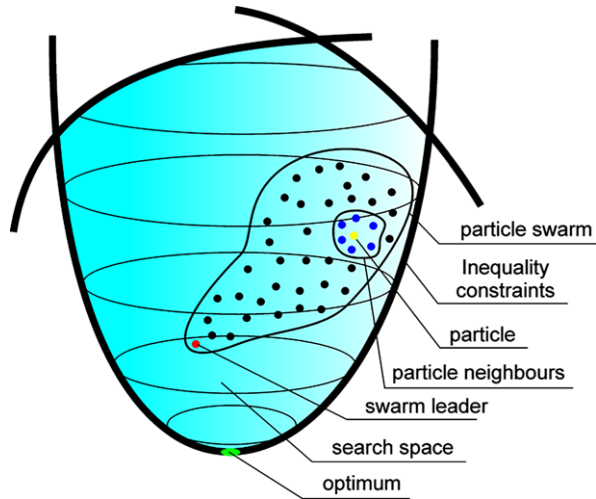
where:

$$\phi_{1j}(k) = c_1r_{1j}(k); \quad \phi_{2j}(k) = c_2r_{2j}(k),$$

m number of the particles,

n number of design variables (problem dimension),

Fig. 10 The idea of the particle swarm

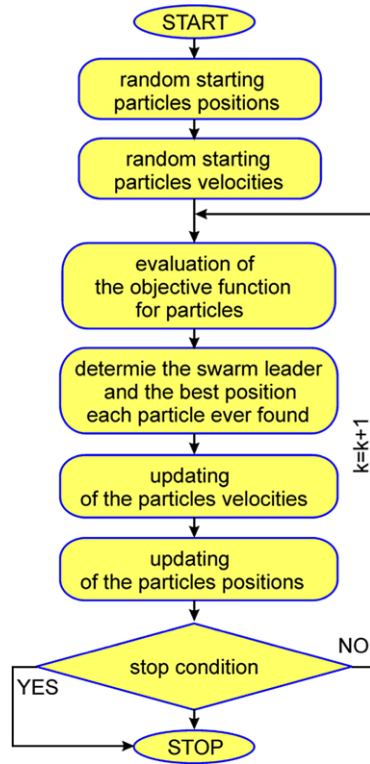


- w inertia weight,
- c_1, c_2 acceleration coefficients,
- r_1, r_2 random numbers with uniform distribution $[0, 1]$,
- $d_{ij}(k)$ position of the i -th particle in k -th iteration step,
- $v_{ij}(k)$ velocity of the i -th particle in k -th iteration step,
- $q_{ij}(k)$ the best found position of the i -th particle found so far,
- $\hat{q}_{ij}(k)$ the best position found so far by swarm—the position of the swarm leader,
- k iteration step.

The velocity of i -th particle is determined by three components of the sum in Eq. (1). The first component $wv_{ij}(k)$ plays the role of the constraint to avoid excessive oscillation in the search space. The inertia weight w controls the influence of particle velocity from the previous step on the current one. In this way this factor controls the exploration and exploitation. Higher value of inertia weight facilitates the global searching, and lower—the local searching. The inertia weight plays the role of the constraint applied for the velocities to avoid particles dispersion and guarantees the convergence of the optimisation process. The second component $\phi_1(k)[q_{ij}(k) - d_{ij}(k)]$ realises the cognitive aspect. This component represents the particle distance from its best position found earlier. It is related to the natural inclination of the individuals (particles) to the environments where they had the best experiences (the best value of the fitness function). The third component $\phi_2(k)[\hat{q}_{ij}(k) - d_{ij}(k)]$ represents the particle distance from the position of the swarm leader. It refers to the natural inclination of the individuals to follow the other which achieved a success.

The flowchart of the particle swarm optimiser is presented in Fig. 11. At the beginning of the algorithm the particle swarm of assumed size is created randomly. Starting positions and velocities of the particles are created randomly. The objective function values are evaluated for each particle. In the next step the best positions of

Fig. 11 Particle swarm optimiser—block diagram



the particles are updated and the swarm leader is chosen. Then the particles velocities are modified by means of Eq. (1) and particles positions are modified according to Eq. (2). The process is iteratively repeated until the stop condition is fulfilled. The stop condition is typically expressed as the maximum number of iterations.

The general effect is that each particle oscillates in the search space between its previous best position (position with the best fitness function value) and the best position of its best neighbour (relatively swarm leader), hopefully finding new best positions (solutions) on its trajectory, what in whole swarm sense leads to the optimal solution.

3 Soft Computing in Optimisation of Dynamically Loaded Structures

3.1 Evolutionary Generalized Optimisation of Structures Modeled by the FEM [13]

Consider a structure which, at the beginning of an evolutionary process, occupies a domain Ω_0 (in E^3), bounded by a boundary Γ_0 . The domain Ω_0 is filled by a elastic

homogeneous and isotropic material of a Young’s modulus E_0 and a Poisson ratio ν . The 3D structures are considered in the framework of the linear theory of elasticity. During the evolutionary process the domain Ω_t , its boundary Γ_t and the field of Young’s modulus $E(x, y, z) = E_t$ and $(x, y, z) \in \Omega_t$ can change for each generation t (for $t = 0$, $E_0 = \text{const}$). The evolutionary process proceeds in an environment in which the structure fitness is described by maximisation of the objective functions:

- (a) maximisation of the first eigenfrequency

$$\max(\omega_1) \tag{3}$$

with a constraint imposed on the volume of the structure

$$\begin{aligned} V &\equiv |\Omega| \\ V &\leq V^{\max} \end{aligned} \tag{4}$$

- (b) maximisation of the difference between first, second and third eigenfrequency

$$\max[(\omega_2 - \omega_1) + (\omega_3 - \omega_2)] \tag{5}$$

with a constraint imposed on the volume of the structure (4);

- (c) maximisation of the difference between first, second, third eigenfrequency and forced vibration frequency ω_{forced}

$$\max[|\omega_1 - \omega_{forced}| + |\omega_2 - \omega_{forced}| + |\omega_3 - \omega_{forced}|] \tag{6}$$

with a constraint imposed on the volume of the structure (4).

The distribution of Young’s modulus $E(x, y, z)$, $(x, y, z) \in \Omega_t$ in the structure is described by a hyper surface $W(x, y, z)$, $(x, y, z) \in H^3$. The hyper surface $W(x, y, z)$ is stretched under $H^3 \subset E^3$ and the domain Ω_t is included in H^3 , i.e. $(\Omega_t \subseteq H^3)$.

The shape of the hyper surface $W(x, y, z)$ is controlled by genes g_j , $j = 1, 2, \dots, N$ (where N is a number of design variables), which create a chromosome

$$ch = \langle g_1, g_2, \dots, g_j, \dots, g_N \rangle \tag{7}$$

Gene values are described by the function $W(x, y, z)$ in interpolation nodes (control points) $(x, y, z)_j$, i.e. $d_j = W[(x, y, z)_j]$, $j = 1, 2, \dots, N$.

The following constraints are imposed on genes

$$g_j^{\min} \leq g_j \leq g_j^{\max} \tag{8}$$

where g_j^{\min} and g_j^{\max} are the minimum and the maximum value of the gene, respectively.

The assignation of Young’s moduli to each finite element Ω_e , $e = 1, 2, \dots, R$ (where R is a number of finite elements) is performed by the mapping:

$$E_e = W[(x, y, z)_e], \quad (x, y, z)_e \in \Omega_e, \quad e = 1, 2, \dots, R \tag{9}$$

It means that each finite element can have different material.

When the value of Young’s modulus for the e -th finite element is within the interval $0 \leq E_e < E_{\min}$, the finite element is eliminated and the void is created,

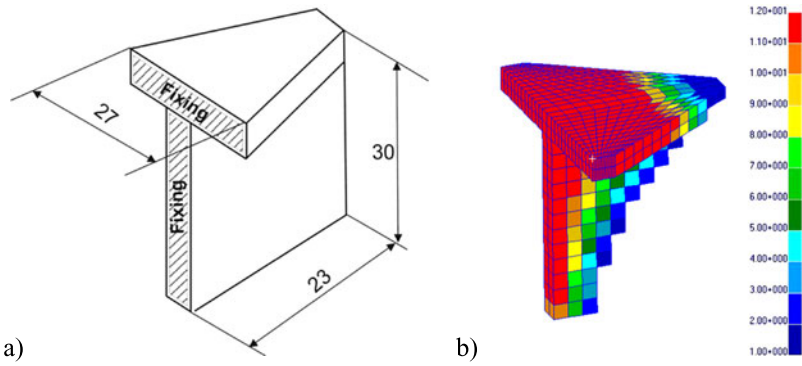


Fig. 12 A 3D bracket: (a) dimensions in [mm], (b) distribution of Young's moduli

Table 1 Input data

Minimal Young's modulus	Maximal volume
$0.4 \times 2 \times 10^5$ MPa	4000 mm ³

Table 2 Parameters of evolutionary algorithm













Number of genes	27
Number of generations	2000
Number of chromosomes	100
Probability of cloning	10 %
Probability of uniform mutation	5 %
Probability of boundary mutation	2 %
Probability of simple crossover	10 %
Probability of arithmetical crossover	10 %

otherwise the finite element has the value of the Young's modulus within the interval $E_{\min} \leq E_e < E_{\max}$. As a result, shape, topology and material properties of the structure are changed simultaneously [14] and this procedure is called *evolutionary generalised optimisation*.

Example 1 (Maximisation of the first eigenfrequency of a 3D bracket) A 3D bracket fixed as shown in Fig. 12a is optimised using evolutionary algorithm. The criterion of optimisation is maximisation of the first eigenfrequency. The design variables are the control points of the hyper surface which decides about the distribution of Young's moduli of the structure. The best solution obtained after 88 generations is presented in Fig. 12b. Table 1 contains constraints of the problem. The Poisson's ratio is constant ($\nu = 0.3$). The parameters of evolutionary algorithm are presented in Table 2.

The distribution of Young's moduli are grouped for twelve different materials shown in Table 3.

Table 3 The distribution of Young’s moduli

Range of Young’s moduli E (MPa)	Material no.	Colour	Range of Young’s moduli E (MPa)	Material no.	Colour
80000 - 90000	1		140000 - 150000	7	
90000 - 100000	2		150000 - 160000	8	
100000 - 110000	3		160000 - 170000	9	
110000 - 120000	4		170000 - 180000	10	
120000 - 130000	5		180000 - 190000	11	
130000 - 140000	6		190000 - 200000	12	

Example 2 (Maximisation of the difference between first, second and third eigenfrequency of a rectangular prism) A 3D structure in the form of a rectangular prism fixed as shown in Fig. 13a is optimised using evolutionary algorithm. The criterion of optimisation is maximisation of the difference between first, second and third eigenfrequencies. The design variables are the control points of the hyper surface which decides about the distribution of Young’s moduli of the structure. The best solution obtained after 169 generations is shown in Fig. 13b in which distribution of Young’s moduli can be seen. Table 4 contains constraints of the problem. The Poisson’s ratio is constant ($\nu = 0.3$). The parameters of evolutionary algorithm are presented in Table 5.

Fig. 13 A rectangular prism: (a) dimensions in [mm], (b) distribution of Young’s moduli

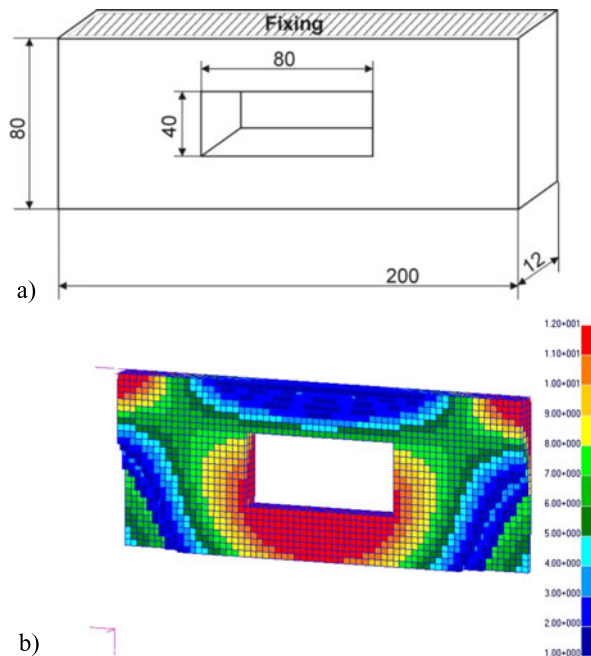


Table 4 Input data

Minimal Young’s module	Maximal volume
$0.4 \times 2 \times 10^5$ MPa	4.8×10^4 mm ³

Table 5 Parameters of evolutionary algorithm

Number of genes	27
Number of generations	2000
Number of chromosomes	100
Probability of cloning	10 %
Probability of uniform mutation	5 %
Probability of boundary mutation	2 %
Probability of simple crossover	10 %
Probability of arithmetical crossover	10 %

The distribution of Young’s moduli are grouped for twelve different materials shown in Table 6.

Example 3 (Maximisation of the difference between first, second and third eigenfrequency and forced vibration frequency of a rectangular prism) The example concerns optimisation of a 3D structure from the previous example (Fig. 13a) using evolutionary algorithm. The criterion of optimisation is maximisation of the difference between first, second and third eigenfrequencies and a forced vibration frequency (150 Hz). The design variables are the control points of the hyper surface which decides about the distribution of Young’s moduli of the structure. The best solution is obtained after 134 generations and it is presented in Fig. 14. Table 7 contains constraints of the problem. The Poisson’s ratio is constant ($\nu = 0.3$). The parameters of evolutionary algorithm are presented in Table 8.

The distribution of Young’s moduli are grouped for twelve different materials shown in Table 9.

Table 6 The distribution of Young’s moduli







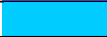





Range of Young’s moduli E (MPa)	Material no.	Colour	Range of Young’s moduli E (MPa)	Material no.	Colour
80000 - 90000	1		140000 - 150000	7	
90000 - 100000	2		150000 - 160000	8	
100000 - 110000	3		160000 - 170000	9	
110000 - 120000	4		170000 - 180000	10	
120000 - 130000	5		180000 - 190000	11	
130000 - 140000	6		190000 - 200000	12	

Fig. 14 Distribution of Young's moduli for a rectangular prism

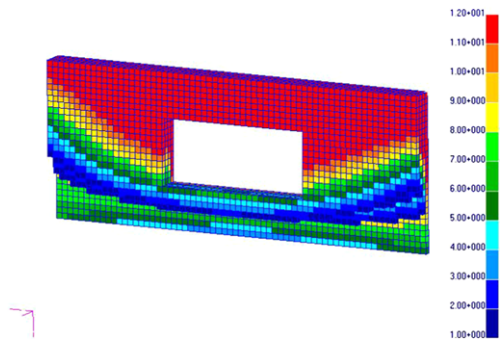


Table 7 Input data

Minimal Young's modulus	Maximal volume
$0.4 \times 2 \times 10^5$ MPa	80000 mm ³

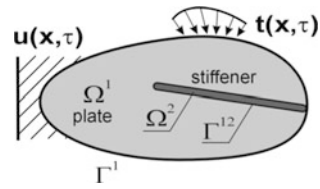
Table 8 Parameters of evolutionary algorithm

Number of genes	27
Number of generations	2000
Number of chromosomes	100
Probability of cloning	10 %
Probability of uniform mutation	5 %
Probability of boundary mutation	2 %
Probability of simple crossover	10 %
Probability of arithmetical crossover	10 %

Table 9 The distribution of Young's moduli

Range of Young's moduli E (MPa)	Material no.	Colour	Range of Young's moduli E (MPa)	Material no.	Colour
80070.2 - 90064	1	Dark Blue	140035 - 150029	7	Light Green
90064.4 - 10005	2	Blue	150029 - 160023	8	Yellow
100058 - 110053	3	Light Blue	160023 - 170018	9	Orange
110053 - 120047	4	Cyan	170018 - 180012	10	Dark Orange
120047 - 130041	5	Green	180012 - 190006	11	Red
130041 - 140035	6	Light Green	190006 - 200000	12	Dark Red

Fig. 15 Reinforced plate subjected to dynamic loads



3.2 Bio-inspired Optimisation of Structures Modelled by the Coupled BEM/FEM

A two-dimensional, homogeneous, isotropic and linear elastic deformable body with boundary Γ_1 and occupying domain Ω_1 , is considered. The body is modelled as a plate in plane stress or strain and it is reinforced by the stiffener occupying domain Ω_2 . The body is supported (displacements $u(x, \tau)$ are known at a part of the outer boundary) and subjected to dynamic tractions $t(x, \tau)$ (where τ is time), applied at the outer boundary, as shown in Fig. 15.

The plate is modelled by the boundary element method (BEM) [15] and the stiffener by the finite element method (FEM) using beam finite elements, attached along the Γ_{12} boundary (the interface). A perfect bonding between the plate and the stiffener is assumed. The whole structure is analysed by the coupled BEM/FEM and the subregion method [16]. The method allows modelling of bodies with many plate subdomains and stiffeners of different properties. The numerical equations, which are written for each plate and beam subdomain separately, are coupled using displacement compatibility conditions and traction equilibrium conditions at all nodes along the common boundaries.

A set of algebraic equations for the plate in Fig. 15 has the following form:

$$[M^1 \quad M^{12}] \begin{Bmatrix} \ddot{u}^1 \\ \ddot{u}^{12} \end{Bmatrix} + [H^1 \quad H^{12}] \begin{Bmatrix} u^1 \\ u^{12} \end{Bmatrix} = [G^1 \quad G^{12}] \begin{Bmatrix} t^1 \\ t^{12} \end{Bmatrix} \quad (10)$$

where: M is a mass matrix, H and G are the BEM coefficient matrices, u and \ddot{u} are displacement and acceleration vectors, respectively, t is a vector of tractions applied at the outer boundary or at the interface. The superscripts denote the matrices, which correspond to the outer boundary or the interface.

The equation of motion for the stiffener in Fig. 15 in a matrix form is:

$$M^{21} \ddot{u}^{21} + K^{21} u^{21} = T^{21} t^{21} \quad (11)$$

where: K is the FEM stiffness matrix, T is a matrix, which expresses the relationship between the FE nodal forces and the BE tractions. The latter matrix allows treatment the finite element region as an equivalent boundary element region.

If the structure is subjected to time dependent boundary conditions, the dynamic interaction forces between the plate and the stiffener act along the interface. These tractions are treated as body forces distributed along the attachment line and they are unknowns of the problem. The displacement compatibility conditions and the traction equilibrium conditions at the nodes along the interface are:

$$u^{12} = u^{21}; \quad t^{12} = -t^{21} \quad (12)$$

Fig. 16 Reinforced rectangular plate

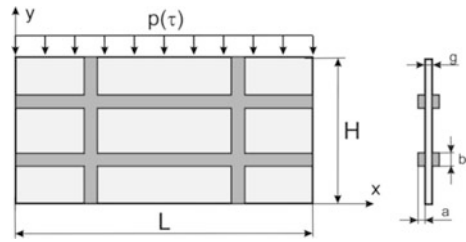
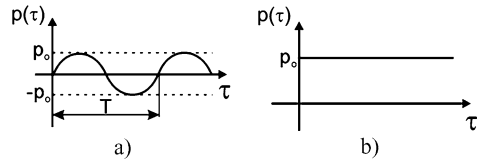


Fig. 17 Dynamic loadings: (a) sinusoidal, (b) Heaviside



If the above conditions are taken into account in equations for the plate (10) and stiffener (11), the following system of equations for the whole structure is obtained:

$$\begin{bmatrix} M^1 & M^{12} \\ 0 & M^{21} \end{bmatrix} \begin{Bmatrix} \ddot{u}^1 \\ \ddot{u}^{12} \end{Bmatrix} + \begin{bmatrix} H^1 & H^{12} & -G^{12} \\ 0 & K^{21} & T^{21} \end{bmatrix} \begin{Bmatrix} u^1 \\ u^{12} \\ t^{12} \end{Bmatrix} = G^1 t^1 \quad (13)$$

The unknowns are displacements and tractions on the external boundary and at the interface in each time step.

Example 4 (Reinforced rectangular plate) Optimisation of a reinforced rectangular plate (Fig. 16) is performed by means of AIS, PSO and EA. The plate is dynamically loaded and it is reinforced by the frame-like structure composed of straight beams. The plate and the stiffeners are modelled by the boundary elements and beam finite elements, respectively. Different kinds of load and support are considered. The structure before optimisation (the reference plate) is shown in Fig. 16.

The length and the height of the plate is \$L = 10\$ cm and \$H = 5\$ cm, respectively. The thickness of the plate is \$g = 0.25\$ cm, the dimensions of beams cross-section are \$2a = 0.5\$ cm and \$b = 0.5\$ cm. The material of the plate and frame is aluminium and the mechanical properties are: modulus of elasticity \$E = 70\$ GPa, Poisson’s ratio \$\nu = 0.34\$ and density \$\rho = 2700\$ kg/m³. The material is homogeneous, isotropic and linear elastic and the plane stress is assumed. The uniformly distributed load is applied at the upper edge of the plate. Two kinds of time dependent loads are considered (see Fig. 17): (a) the sinusoidal load \$p(\tau) = p_0 \sin(2\pi\tau/T)\$ with the period of time \$T = 20\pi\$ \$\mu\$s, and (b) the Heaviside load \$p(\tau) = p_0 H(\tau)\$. The value of the load in both cases is \$p_0 = 10\$ MPa. The time of analysis is \$600\$ \$\mu\$s and the time step \$\Delta t = 2\$ \$\mu\$s.

Three different supports are considered (see Fig. 18):

- (a) support A—the plate is fixed on the left and right edge,
- (b) support B—the plate is supported at two segments, each of 0.5 cm long,
- (c) support C—the plate is fixed at the bottom edge.

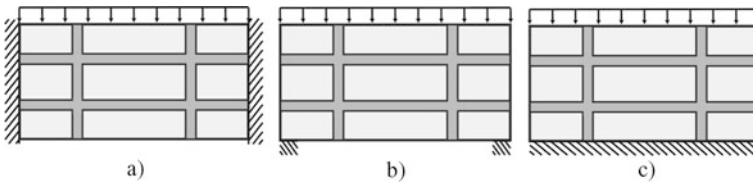
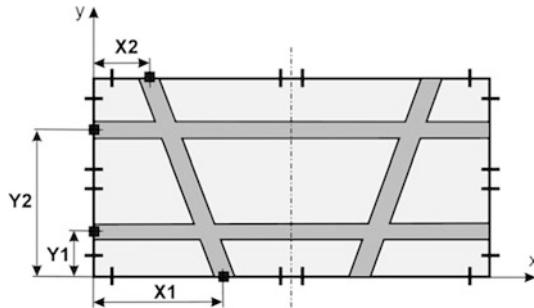


Fig. 18 Types of supports: (a) support A, (b) support B, (c) support C

Fig. 19 Design variables and constraints



The optimal positions of stiffeners are searched in order to maximise stiffness of the plate. The maximal dynamic vertical displacement on the loaded edge is minimised. Because of symmetry of the structure and boundary conditions, only a half of the structure is considered. The number of design variables defining the position of the frame is 4: X_1 , X_2 , Y_1 and Y_2 (see Fig. 19). The longer beams are parallel to the x axis. The end points of beams can move along the edges of the plate within the constraints, as shown in Fig. 19. The constraints on design variables are imposed: X_1 and X_2 variables are within the range of 0.5 to 4.75 cm, Y_1 of 0.5 to 2.25 cm and Y_2 of 2.75 to 4.5 cm. The parameters of AIS are: the number of memory cells and the clones is 6, the crowding factor and the Gaussian mutation is 0.5. The parameters of EA are: the number of chromosomes is 20, the probability of the Gaussian mutation is 0.5, the probability of a simple and arithmetic crossover is 0.05. The parameters of PSO are: numbers of particles is 20, inertia weight is 0.73 and two acceleration coefficients are 1.47.

The total number of boundary and finite elements in the BEM/FEM analysis is 120 and 120, respectively (each horizontal and vertical beam is discretized into 40 and 20 finite elements, respectively). The number of boundary and finite elements during the optimisation is constant.

The values of design variables obtained by AIS, PSO and EA for the plate subjected to the sinusoidal load, the Heaviside load and for three kinds of supports, are presented in Table 10. The results obtained by three different methods are almost the same (with the accuracy to two decimal places they are identical). The values of J_0 and J (where: J_0 and J is the objective function for the reference and the optimal plate, respectively) and the reduction $R = (J_0 - J)/J_0 \cdot 100\%$, are also presented.

A significant reduction R , resulting in the improvement of dynamic response of the optimal plates in comparison with the initial designs, can be observed. The op-

Table 10 Values of design variables, J and R

Load	Support	Design variables [cm]				J_0 [10^{-4} cm]	J [10^{-4} cm]	R [%]
		X1	X2	Y1	Y2			
AIS, PSO and EA								
Sinusoidal	A	4.75	2.86	0.88	2.75	89	76	15
	B	4.75	1.81	0.57	2.75	92	73	21
	C	1.20	1.82	0.50	2.75	82	62	24
Heaviside	A	0.50	4.75	0.50	4.50	112	91	19
	B	4.75	1.41	0.50	4.50	211	149	29
	C	0.50	2.20	1.70	2.80	49	42	14

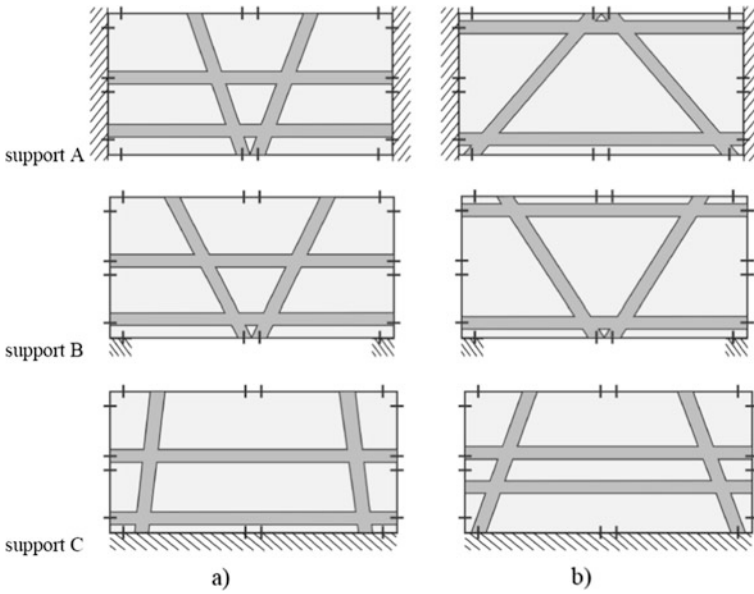


Fig. 20 Optimal plates subjected to dynamic loads: (a) sinusoidal, (b) Heaviside

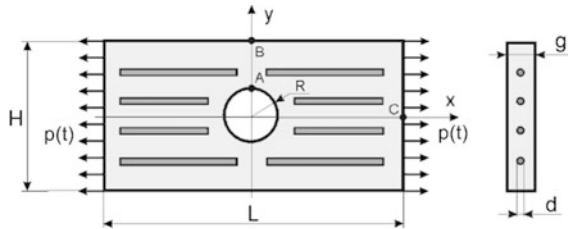
timal structures for different kinds of supports and for the sinusoidal and the Heaviside loads are shown in Fig. 20a and Fig. 20b, respectively. It can be seen that in the present example most of constraints are active.

The number of fitness function evaluations by three different bio-inspired algorithms used in this example is presented in Table 11. It can be observed that the number of fitness function evaluations for obtaining the final design variables and the corresponding fitness functions presented in Table 11 is different and depends on the applied load and support. Generally, the efficiency of the AIS and the PSO is similar and much better for this particular example, than the efficiency of the EA.

Table 11 Efficiency of bio-inspired methods

Load	Support	Fitness function evaluations		
		EA	AIS	PSO
Sinusoidal	A	2515	588	360
	B	3705	714	440
	C	1952	756	520
Heaviside	A	303	483	60
	B	1526	441	120
	C	2797	924	580

Fig. 21 Reinforced plate with a hole



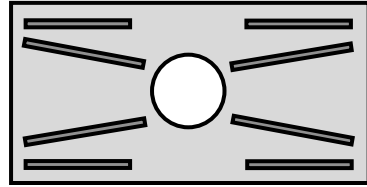
Example 5 (Reinforced plate with a hole) Optimisation of a rectangular reinforced plate with a hole (Fig. 21) is performed by means of PSO with the same parameters as in Example 4. The plate is dynamically loaded and it is reinforced by 8 symmetrically distributed rods of circular cross-section. The plate and the reinforcing rods are modelled by the boundary elements and beam finite elements, respectively. The structure before optimisation (the reference plate) is shown in Fig. 21.

The plate is stretched by a uniformly distributed load applied at its left and right edge. The dynamical load is defined by the Heaviside impulse $p(t) = p_0H(t)$, the value of the load is $p_0 = 10$ MPa. The time of analysis is $T = 300 \mu s$ and the time step $\Delta t = 3 \mu s$. The length and the height of the plate and the hole radius is $L = 10$ cm, $H = 5$ cm and $R = 1$ cm, respectively. The thickness of the plate is $g = 1$ cm and the diameter of each rod is $d = 0.3$ cm. Distance between the rod axes for the reference plate is 1 cm, the length of the shorter and longer rods is 3 cm and 4 cm, respectively. Distance between the end points of the rods to the left or right edge of the plate is 0.5 cm. The plane stress is assumed. The materials of the plate (p) and stiffeners (s) are epoxy and steel, respectively. They are homogeneous, isotropic and linear elastic. The values of mechanical properties are: modulus of elasticity $E_p = 4.5$ GPa and $E_s = 210$ GPa, Poisson's ratio $\nu_p = 0.37$ and $\nu_s = 0.3$, density $\rho_p = 1160$ kg/m³ and $\rho_s = 7860$ kg/m³.

The optimal location of reinforcement in the interior of the plate is searched and the following objective function J is minimised:

$$J = \int_0^T \frac{|\sigma_x^A(t)|^2}{\sigma_0} dt \tag{14}$$

Fig. 22 Optimal location of rods in the plate



where $\sigma_x^A(t)$ is the x -component of stress at the point A (see Fig. 21), σ_0 is a nominal stress at the weakened cross-section, defined as the ratio of the applied load to the area of this cross-section, T is a time of analysis.

The objective function (14) is minimised with respect to design variables (X_{ij} , Y_{ij} , $i, j = 1, 2$), defining the coordinates of the j -th end point of the i -th rod. It is assumed that during optimisation the reinforcement is symmetrical with respect to two symmetry axes. Thus only a quarter of the plate with two rods is modelled (the appropriate boundary conditions at the symmetry axes are assumed) and the number of design variables is 8.

The constraints on design variables are imposed. The distance between the rods and the outer boundary (of the quarter of the plate) cannot be lower than 0.5 cm. The intersection of rods is not allowed.

The total number of boundary and finite elements in the BEM/FEM analysis is 92 and 64, respectively (each rod is discretized into 32 finite elements).

For this example five tests were performed and similar results were obtained. The values of design variables for the optimal solutions, rounded off to two decimal places, are: $X_{11} = 0.97$ cm, $Y_{11} = 1.03$ cm, $X_{12} = 4.50$ cm, $Y_{12} = 1.50$ cm, $X_{21} = 1.57$ cm, $Y_{21} = 2.00$ cm, $X_{22} = 4.50$ cm and $Y_{22} = 2.00$ cm. The optimal structure is shown in Fig. 22.

4 Conclusions

In the paper, the formulation and application of the finite element method, the boundary element method and the bio-inspired methods to optimisation of shape, topology and material properties of dynamically loaded structures for different criteria of optimisation is presented. The bio-inspired methods can be simply implemented because they need only the values of objective functions. An important feature of these approaches is a strong probability of finding the global optimal solutions. The described approaches are free from limitations of classic gradient optimisation methods.

In the presented approach, shape, topology and material optimisation is performed simultaneously for 3D freely vibrating structures analysed by the finite element method. The optimal location of reinforcement is searched in order to increase a stiffness or strength of dynamically loaded reinforced plates analysed by the coupled boundary/finite element method. As a result of optimisation, a significant improvement of dynamic response is obtained, in comparison with initial designs.

Coupling of finite or boundary element method and the bio-inspired algorithms give an effective and efficient alternative optimisation tool, which enables solving a large class of the optimisation problems of mechanical structures. Numerical examples confirm the efficiency of the proposed optimisation method and demonstrate that the methods based on soft computing are effective techniques for solving computer aided optimal design problems. Generally, for the considered numerical examples, the efficiency of the artificial immune systems and the particle swarm optimiser's is better than the evolutionary algorithms.

Acknowledgements This work was supported by the Polish Ministry of Science and Higher Education under the research grant.

References

1. Arabas J (2001) Lectures on evolutionary algorithms. WNT, Warsaw (in Polish)
2. Michalewicz Z (1996) Genetic algorithms + data structures = evolutionary algorithms. Springer, Berlin
3. Ptak M, Ptak W (2000) Basics of immunology. Jagiellonian University Press, Cracow (in Polish)
4. Balthrop J, Esponda F, Forrest S, Glickman M (2002) Coverage and generalization in an artificial immune system. In: Proceedings of the genetic and evolutionary computation conference, GECCO 2002. Morgan Kaufmann, New York, pp 3–10
5. de Castro LN, Timmis J (2003) Artificial immune systems as a novel soft computing paradigm. *Soft Comput* 7(8):526–544
6. de Castro LN, Von Zuben FJ (2001) Immune and neural network models: theoretical and empirical comparisons. *Int J Comput Intell Appl* 1(3):239–257
7. Poteralski A, Szczepanik M, Dziatkiewicz G, Kuś W, Burczyński T (2011) Immune identification of piezoelectric material constants using BEM. *Inverse Probl Sci Eng* 19(1):103–116
8. de Castro LN, Von Zuben FJ (2002) Learning and optimization using the clonal selection principle. *IEEE Trans Evol Comput* 6(3):239–251 (special issue on artificial immune systems)
9. Wierzchoń ST (2001) Artificial immune systems, theory and applications. Akademicka Oficyna Wydawnicza EXIT, Warsaw (in Polish)
10. Reynolds CW (1987) Flocks, herds, and schools, a distributed behavioral model. *Comput Graph* 21:25–34
11. Heppner F, Grenander U (1990) A stochastic nonlinear model for coordinated bird flocks. In: Krasner S (ed) *The ubiquity of chaos*. AAAS, Washington
12. Kennedy J, Eberhart RC (1995) Particle swarm optimisation. In: Proceedings of IEEE international conference on neural networks. IEEE Press, Piscataway, pp 1942–1948
13. Burczyński T, Poteralski A, Szczepanik M (2003) Genetic generation of 2-D and 3-D structures. In: Second MIT conference on computational fluid and solid mechanics. Massachusetts Institute of Technology, Cambridge
14. Burczyński T, Poteralski A, Szczepanik M (2007) Topological evolutionary computing in the optimal design of 2D and 3D structures. *Eng Optim* 39(7):811–830
15. Dominguez J (1993) Boundary elements in dynamics. Computational Mechanics Publications, Southampton
16. Fedelinski P, Gorski R (2006) Analysis and optimization of dynamically loaded reinforced plates by the coupled boundary and finite element method. *Comput Model Eng Sci* 15(1):31–40

Optimal Design of RC Frames Using Nonlinear Inelastic Analysis

Bora Gencturk and Kazi Ashfaq Hossain

Abstract Recent earthquakes, especially those in Chile (2010) and Christchurch (2011), have demonstrated the unexpected performance of buildings designed according to modern seismic design codes. These incidents strengthen the cause for moving towards performance-based design codes rather than serviceability and strength design. This chapter deals with optimal design of RC frames, a widely used structural type around the world, considering both the initial cost and structural performance as problem objectives. Initial cost comprises the total cost of materials and workmanship for structural components, while structural performance is measured by a two-level approach. First, each design is checked for acceptability according to existing codes, and next performance is quantified in terms of maximum inter-story drift obtained from nonlinear inelastic dynamic analysis. This multi-objective, multi-level approach allows one to investigate the implications of the selection of design parameters on the seismic performance while minimizing the initial cost and satisfying the design criteria. The results suggest that structural performance varies significantly within the acceptable limits of design codes and lower initial cost could be achieved for similar structural performance.

Keywords Reinforced concrete · Inelastic dynamic analysis · Structural optimization · Taboo search · Pareto front

1 Introduction

Structures have been traditionally designed to withstand applied loads and deformations, with appropriate factor of safety, which they may experience throughout their

B. Gencturk (✉)

Department of Civil and Environmental Engineering, University of Houston,
N107 Engineering Building 1, Houston, TX 77204-4003, USA
e-mail: bgencturk@central.uh.edu

K.A. Hossain

Department of Civil and Environmental Engineering, University of Houston,
E131 Engineering Building 2, Houston, TX 77204-4003, USA
e-mail: kahossain@uh.edu

service life. These designs are commonly based on code requirements, contemporary practices, and subjective judgment and experience of the personnel involved in the design process. After the 1994 Northridge earthquake in the United States, it has been observed that the structures that comply with the code requirements, although achieved life safety objective, sustained significant damage resulting in major economic losses. The Northridge earthquake has been the main stimulus in the United States for moving towards performance-based seismic design (PBSD) codes. These initiatives resulted in a series of notable documents: ATC-40 [1], FEMA-273 [2] and FEMA-356 [3] which were more recently converted to a standard in ASCE-41 [4].

Cost reduction has always been an objective in engineering design. In a typical residential/office building the cost of structural components is relatively low compared to those of mechanical, electrical, plumbing and non-structural features. Nevertheless, reducing the initial structural cost is important both from financial and sustainability standpoints. The latter is associated with the use of non-renewable earth resources, CO₂ emission and other negative impacts on the environment. This chapter is an attempt to tie cost savings with quantifiable structural performance during earthquakes in an optimization framework for reinforced concrete (RC) buildings. Initial cost is evaluated based on the cost of materials and labor for structural components. Structural response is, on the other hand, quantified using nonlinear inelastic dynamic analysis in order to gain insight on expected performance which goes beyond what existing code regulations can provide. As such, the proposed framework falls within PBSD with an extension to include optimization to understand and guide the decision making process.

After a literature review on cost optimization of RC structures, the subsequent sections outline the essential steps of the proposed framework through an example application: definition of the seismic hazard and selection of earthquake ground motions for nonlinear inelastic dynamic analysis, modeling, structural analysis and evaluation of initial cost, structural optimization, and processing of results and decision making.

2 Literature Review

This chapter concerns the optimal design RC buildings considering the initial cost. As a result, in the following sections, after a brief summary of weight optimization studies, which mainly target steel structures, a detailed review of previous studies on initial cost optimization of RC buildings is provided.

2.1 Weight Optimization

Several studies in literature aimed at minimizing the weight of the structure based on the assumption that the cost is directly proportional to the weight ([5–13] among

others). Although this is, for the most part, true for steel structures, it is difficult to make such a correlation for RC structures. Therefore, studies on weight-optimal design of concrete structures are limited in comparison. These studies can be primarily divided into component-level and whole-structure optimization.

Weight optimal design of RC beam elements was performed by Chung and Sun [14]. The beam thickness and reinforcement area were considered as design variables with constraints on deflection, stress, and section sizes. Incremental finite element technique was used to unify structural weight optimization with structural analysis, design, and sensitivity analysis. Sequential linear programming (SQP) algorithm was used to incorporate material nonlinearity in the formulation. Karihaloo and Kanagasundaram [15] used linear and nonlinear programming techniques to solve weight minimization problem of statically indeterminate beams with constraints on normal and shear stresses. While, Karihaloo and Kanagasundaram [16] proposed minimum-weight design of elastic plane frames under multiple loads taking into account the effects of buckling and transverse deflections. Under certain assumptions, the optimization problem was reduced to a non-linear programming (NLP) problem, which was solved using several methods: sequential convex programming (SCP), sequential linear programming (SLP), and sequential unconstrained minimization technique (SUMT).

2.2 Cost Optimization

Although material weight contributes to a major part of the total cost of a structure, weight optimization does not take into account other significant cost components such as labor cost and cost of formwork. Materials are the major cost component for steel structures and the initial cost can be represented in terms of material weight. Unlike steel structures, cost optimization is more appropriate for concrete structures due to use of multiple materials. Hence, costs of concrete, reinforcing steel, labor and formwork need to be considered. Numerous studies have been performed on cost optimization of RC beams, columns, slabs and frames. These studies are grouped based on the number of objectives (single vs. multiple) and the optimization approach (mathematical programming-based, gradient-based or heuristic), and reviewed in this section.

2.2.1 Single-Objective and Mathematical Programming-Based Optimization

The objective function for the single-objective cost optimization problems is typically chosen as the initial cost of the structure comprising material and construction costs. Design variables comprise section sizes and reinforcement ratios for all the members. Various structural performance metrics as defined in the building codes are selected as constraints. Earlier attempts in structural optimization of building frames were more oriented towards the use of non-heuristic optimization techniques.

An exhaustive review of literature on mathematical programming-based optimization can be found in [17].

Mathematical programming methods (or direct methods) are mostly linear and nonlinear programming techniques, which have been successfully applied to cost optimal design of RC structures. These methods were found to perform satisfactorily for limited number of design variables and constraints. Several notable studies used mathematical programming for cost optimization of RC structures [18–28].

2.2.2 Single-Objective and Gradient-Based Optimization

Mathematical programming optimization had less success in addressing feasible solutions for realistic optimization problems. On the contrary, gradient-based methods (or indirect) methods are found to be more efficient for large-scale optimization problems by taking into account numerous design variables and constraints. Use of gradient-based methods requires the existence of continuous derivatives of both the objective function and the constraints. For this reason, in most cases, analytical formulations are adopted to evaluate performance metrics. Below is a review of selected studies on optimization of RC structures using gradient-based methods.

Cheng and Truman [29] developed a framework for optimal design of RC and steel structures using optimality criteria (OC) approach. Structural assessment was performed using elastic static and dynamic analysis. In order to meet the requirement of the used optimization algorithm, discrete member properties were converted to continuous variables. Structural weight (or cost) was chosen as the objective function subject to constraints on displacements. Moharrami and Grierson [30] used OC method to determine the optimum cross-sectional dimensions and longitudinal reinforcement of the components of RC buildings subject to constraints on strength and stiffness. Costs of concrete, steel and formwork formed the objective function. Performance of the structure under gravity and static lateral loads was considered and evaluated based on the prevailing code requirements. The results indicated that OC method converges smoothly to least-cost design and the final design is independent of the initial selection of the design variables.

Adamu and Karihaloo [31, 32] used discretized continuum-type optimality criteria (DCOC) for cost minimal design of RC beams with freely varying or uniform cross-sections along the span. Limiting values were applied on deflections, bending and shear strengths with bounds on design variables. The results were compared with those computed using continuum-type optimality criteria (COC) in another paper [33]. In a separate study the authors used the same criteria for RC frames with columns under uniaxial and biaxial bending actions [34, 35]. Design variables included width and depth of the members and reinforcing steel ratio. Deflection, bending and shear strengths were chosen as constraints. Fadaee and Grierson [36] investigated the effects of combined axial load, biaxial moments and biaxial shear on three-dimensional RC elements. OC method was used for optimizing the sections sizes and reinforcement areas. Chan [37] investigated optimal lateral stiffness design of tall RC and steel buildings using the OC method. The objective was to

minimize the cost subject to lateral drift, stiffness and serviceability constraints. Constructability and practical sizing of members were also taken into consideration. The proposed method was applied to an 88-story building.

Chan and Zou [38] utilized the principle of virtual work to generate elastic and inelastic drift response of RC building. Response spectrum and nonlinear pushover analyses were used respectively to produce those responses. The formulation was based on OC approach. A two-phase optimization approach was adopted. In the first phase, optimum member sizes were obtained through elastic design optimization. In the second phase, reinforcement ratios were found for previously determined sections through inelastic design optimization. In another study, Zou and Chan [39] used OC method to minimize the construction cost of RC buildings subject to constraints on lateral drifts. Response spectrum and time history loading were applied based on Chinese seismic design code. Lateral drift response was formulated based on the principle of virtual work. Multiple earthquake loading conditions were taken into consideration for optimal sizing of members. Chan and Wang [40] investigated the cost optimization of tall RC buildings subject to constraints on maximum lateral displacement and interstory drift. Member sizes were designed based on OC approach. Zou [41] proposed an optimization technique for base-isolated RC buildings based on OC method. Similar to the author's previous studies, lateral drift response was formulated based on the principle of virtual work. The underlying assumption of this study was that all the members of the superstructure behave linear elastically while the isolation system behaves nonlinearly.

2.2.3 Single-Objective and Heuristic Optimization

In spite of being computationally efficient, gradient-based approaches have limited scope because both the zeroth and at least first order derivatives of the objective function and the constraints are needed. In addition, the search domain needs to be continuous, which prevents the use of discrete design variables such as the reinforcing steel areas (or ratios). To circumvent these problems, researchers used the method of virtual work to explicitly define the objective function and constraints. The review in the previous section indicates that OC was preferred as the gradient-based optimization algorithm in most studies. Recent advancement in computational tools, on the other hand, enables researchers to include computationally costly analysis methods, such as static pushover analysis and dynamic time history analysis in structural optimization problems, through finite element modeling. However, in most cases conventional gradient-based algorithms cannot be used because the continuity of functions or their derivatives may not exist. By using heuristic approaches, this problem can be overcome. Furthermore, heuristic algorithms can effectively find global minima, while gradient-based algorithm might be trapped at a local minimum.

Genetic algorithm (GA) was first used as a technique to solve engineering optimization problem by Goldberg and Samtani [42]. Based on his study, many researchers successfully employed GA for design optimization of structures. A com-

prehensive review of studies related to structural optimization based on GA is available in [43]. Choi and Kwak [44] created a database of different RC sections sorted from the least to most resistance for obtaining optimum member design. A two-step algorithm, which involved finding the continuous and discontinuous solution from the database, was used. Design variables were reduced to a single one by using section identification numbers. Optimization of the entire structure was proposed by combining individually optimized elements. Similarly, Lee and Ahn [45] developed a data set containing section properties of frame elements in a feasible range while performing discrete optimization of RC plane frames based on GA. The semi-infinite search space was converted to a finite one by using the data sets, which were further modified and reduced based on the provisions of existing code regulations on reinforcement area and configuration. Camp et al. [46] investigated material and construction cost minimization of RC frames based on GA. Serviceability and strength constraints were used to satisfy the code requirements that are incorporated in the algorithm as penalty functions.

Balling and Yao [47] used a multi-level approach for design optimization of RC concrete frames. RC frame optimization was identified to be more complicated than steel frames because of the problems with reinforcement design. The optimization of reinforcement detailing was simultaneously conducted with the optimization of cross-sectional dimensions. This approach enabled the investigation of the effect of reinforcement topology, bar selection, bar positioning, cutoff and bend points, and stirrups and ties. A simplification was made based on the assumptions that either the lower bound of reinforcement area or strength would govern the optimum design. Similarly, Rajeev and Krishnamoorthy [48] considered discrete design variables for detailing and placing of reinforcement in RC frames as opposed to traditional practice of selecting steel area as continuous design variables that required rounding up to realistic constructible values.

Govindaraj and Ramasamy [49] studied the cost optimal design of continuous RC beams based on GA. Only the cross sectional dimensions of beams were considered as design variables in order to reduce computational costs. Constraints were applied on strength, serviceability, ductility, durability as per Indian standards. Detailing of reinforcement was accounted for in a sub-level optimization problem. Saini et al. [50] performed cost-optimal design of singly and doubly reinforced concrete beams subjected to uniformly distributed and concentrated loads based on artificial neural networks (ANN). To bypass trapping of ANN in local minima, GA was used to optimize the architecture and user defined parameters. The limit state design and the optimization were performed with constraints on moment capacity, actual deflection and durability along with other geometric constraints according to Indian standards.

Sahab et al. [51] proposed a two-stage hybrid optimization algorithm based on modified GA and applied this algorithm to perform cost optimization of RC flat slab buildings. In a similar study, Sahab et al. [52] presented multi-level optimization procedure for RC flat slab building. Column layouts along with section sizes and number of reinforcing bars were obtained through exhaustive search, whereas the hybrid optimization algorithm was used to find section sizes. Constraints were applied based on the design regulations. In a different study, in order to reduce the

computational costs in finding optimal design of structures subjected to earthquake loads, Salajegheh et al. [53] combined two artificial intelligence strategies: radial basis function (RBF) neural networks and binary particle swarm optimization (BPSO), and proposed a hybrid optimization method.

Leps and Sejnoha [54] implemented augmented simulated annealing method for optimizing shape, bending and shear reinforcement of RC structures, simultaneously. An example was presented for a continuous beam. Rao and Xiong [55] proposed a new hybrid GA where GA was applied to determine the feasible search region that contains the global minimum. The optimum solution was obtained through an integrated algorithm comprising hybrid negative sub-gradient method and discrete one-dimensional search. An example was presented for optimal design of an RC beam. Ahmadi-Nedushan and Varaee [56] applied Particle Swarm Optimization (PSO) method to one-way RC slabs with different support conditions. The total cost of the slab was selected as the objective function subject to constraints on strength, ductility and serviceability as recommended in the design code. A dynamic multi-stage penalty function was chosen which transforms the constrained problem to an unconstrained one by penalizing the impractical points on the search space. El Semelawy et al. [57] found optimum values of slab thicknesses, number and sizes of tendons, and tendon profiles of pre-stressed concrete flat slabs based on modern heuristic optimization techniques. A general and flexible tool was developed that could handle real life problems. Costs of concrete and tendons were included in the objective function. Results suggested that the consideration of a second objective function (distance from constraints) would make the optimization technique more efficient.

Fragiadakis and Papadrakakis [58] studied deterministic and reliability based optimization for designing RC frames against seismic forces and found the latter to be more feasible in terms of economy and flexibility of design. Non-linear response history analysis was performed for structural performance assessment. The objective was to obtain improved performance against earthquake hazards with minimal cost. Evolutionary algorithm (EA) was used to solve the optimization problem. Three hazard levels and several limit states from serviceability to collapse prevention were considered. In order to reduce the computational time, fiber-based beam-column elements were used only at the member ends, and inelastic dynamic analysis was performed only if non-seismic checks performed through a linear elastic analysis were met.

2.2.4 Multi-Objective Optimization

In most studies on single-objective optimization, the merit function was selected to minimize the cost of the structure through optimal material usage. Alternative designs were explored to obtain the optimal solution. Hence, single-objective optimization methods usually provide just one optimal solution. Decision makers either have to accept or reject the optimum design. On the other hand, multiple merit functions, which are related to decision making process, are taken into consideration

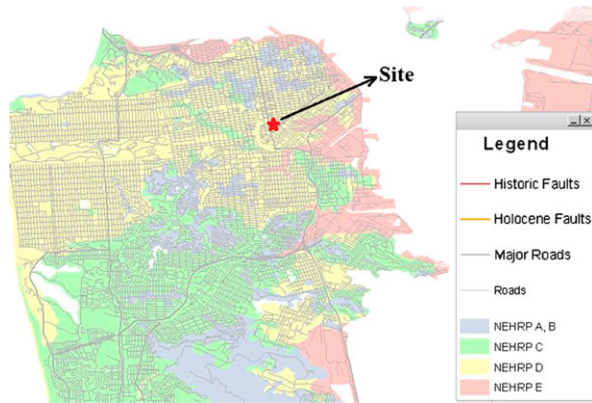
in multi-objective optimization. It offers decision makers the flexibility to select the “best” (or most suitable) option from a number of equivalent solutions based on their priorities and judgments. Hence, several studies formulated multi-objective optimization problem by modifying existing algorithms to account for multiple objective functions.

Ang and Lee [59] formulated an integrated framework for optimization of RC buildings with respect to minimum life-cycle cost criteria. Life-cycle cost included initial costs from materials, labor, and construction together with probable damage cost from future earthquake hazards. By applying the minimum life-cycle cost criteria, constraints for the allowable risk of fatality were measured. Li and Cheng [60] incorporated damage-reduction based structural optimization algorithm into seismic design of RC frames. Initial costs and total expected loss formed the objective function. A simplified approach for reliability analysis was adopted along with a tailored enumeration technique. Findings included improved seismic performance of damage-reduction-based design over traditional design, on the grounds of several metrics such as life-cycle cost, structural responses against extreme earthquakes and reliability of the weakest story based on the drift.

Lagaros and Papadrakakis [61] compared two design approaches: based on European seismic design code and performance-based design (PBD) for three-dimensional RC frames. The considered two objective functions were the initial construction cost and maximum inter-story drift. Linear and nonlinear static analyses were performed for European code based and PBSO, respectively. Three performance objectives corresponding to three hazard levels were considered. EA was used for optimization. Design based on Eurocode was found to be more vulnerable to future earthquakes. Zou et al. [62] used OC method to minimize the initial material cost and life-cycle damage cost of RC frames in a multi-objective optimization framework for performance based earthquake engineering (PBEE). Optimal member sizes were determined through elastic response spectrum analysis in the first stage of optimization. In the second stage, static pushover analysis was performed to find the reinforcement ratios. Fragiadakis and Lagaros [63] presented an alternative framework for PBSO of structures. Particle swarm optimization algorithm was adopted. The formulation could account for any type of analysis procedure (linear or nonlinear, static or dynamic). Initial cost or lifetime seismic loss could be selected individually or together to define the objectives of the problem. Both deterministic and probabilistic design procedures were incorporated. A number of limit states from serviceability to collapse prevention were selected for probabilistic design.

Paya et al. [64] used cost, constructability, sustainability (environmental impact), and safety as the four objective functions while performing structural optimization of RC frames based on multi-objective simulated annealing (MOSA). Design was performed according to Spanish code. Pareto optimal set of solutions were obtained. Mitropoulou et al. [65] used life-cycle cost assessment (LCCA) to evaluate the designs based on a prescriptive and performance-based methodology. Initial construction cost was minimized in the former case; while, in the latter case, life-cycle cost was considered as an additional objective function, turning the problem into a multi-objective one. Incremental dynamic analysis (IDA) and nonlinear static pushover

Fig. 1 Soil profile in San Francisco Bay area [68]



analysis were performed for structural assessment. Various sources of uncertainty were taken into consideration for seismic demand and structural capacity.

3 Seismic Hazard and Earthquake Ground Motions

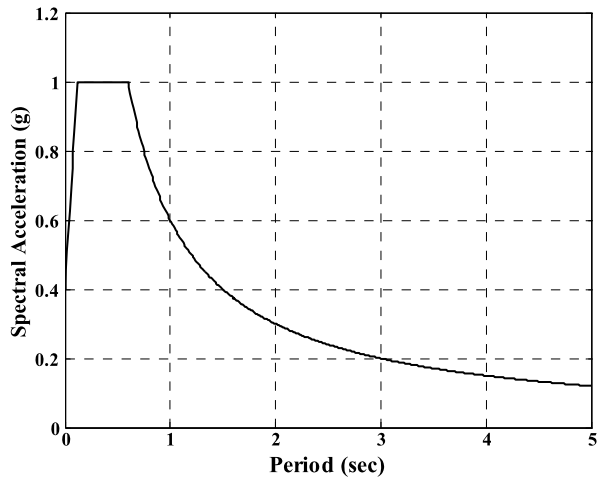
3.1 Definition of Seismic Hazard

For the example application in this study, the design spectrum is derived according to ASCE 7-10 [66]. A site is selected at the intersection of Market Street and Van Ness Avenue in San Francisco, California with coordinates $37^{\circ} 46' 29.67''$ N, $122^{\circ} 25' 10.12''$ W. The soil type at the location is determined as site class D according to the NEHRP [67] scale as shown in Fig. 1. Design spectral response acceleration parameters at short periods, S_{DS} , and at a period of one second, S_{D1} , are taken as $1g$ and $0.6g$, respectively. The design response spectrum is computed based on ASCE 7-10 section 11.4.5. The calculated design spectrum, shown in Fig. 2, is used for selecting the earthquake ground motions as described in the next section.

3.2 Selection and Spectrum Matching of the Earthquake Ground Motions

For nonlinear inelastic analysis of the structural frames, the seismic response history procedures of ASCE 7-10 are followed. Accordingly, three earthquake ground motions are selected from the database of Pacific Earthquake Engineering Research (PEER) Center [69]. In order to conform to the requirements of ASCE 7-10 on

Fig. 2 Design spectrum at the selected site



ground motion selection, spectrum matching is utilized. The fundamental period of the frames change during optimization because of the changing decision variables (i.e. section sizes and reinforcement ratios). Based on eigenvalue analysis of a typical frame considered in this example (see Sect. 4.1), the fundamental period is estimated as 0.5 seconds. ASCE 7-10 requires the ground motions be scaled such that the average value of the five percent damped response spectra for the suite of motions is not less than the design response spectrum for periods ranging from $0.2T$ – $1.5T$, where T is the fundamental period of the structure. For the typical frame mentioned above, the period range suggested by ASCE 7-10 is 0.1–0.75 seconds. Given that the fundamental period of the frames will change during the optimization process, spectrum matching is performed for 0–1 seconds to be conservative. Note that spectrum matching (rather than acceleration scaling) is utilized here as this approach results in less record-to-record variability in structural response [70, 71].

In spectrum matching process, target spectrum is defined as the ASCE 7-10 design spectrum for the period range from 0 to 1 seconds while the spectra of the original ground motions are retained for larger periods. This approach ensures that unrealistic high period oscillations are not introduced into the spectrum compatible ground motions by matching outside the period range that is relevant to the frames considered here. Spectrum matching is performed using the modified version of the RSPMatch software [72] described in [70]. The plot of design spectrum along with the spectra of the selected ground motions before and after spectrum matching is shown in Fig. 3, while the acceleration time histories are shown in Fig. 4. The spectrum compatible time histories in Fig. 4(b) are used for nonlinear inelastic dynamic analysis.

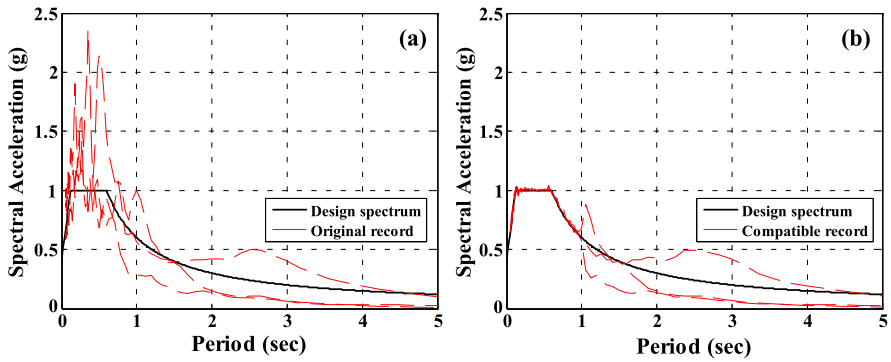


Fig. 3 Acceleration response spectrum of (a) original, and (b) spectrum compatible ground motion records

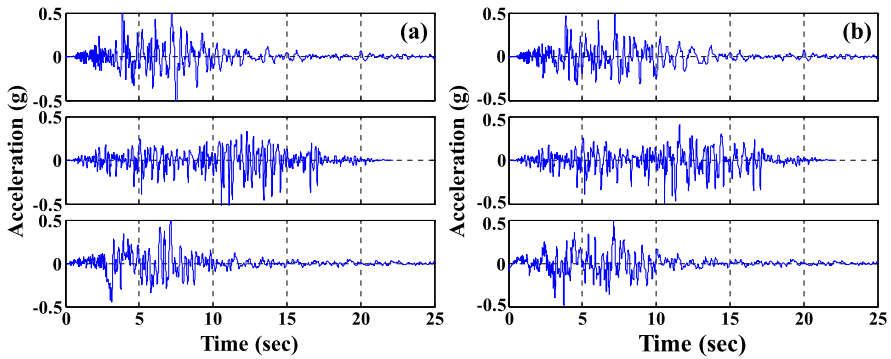


Fig. 4 (a) Original, and (b) spectrum compatible ground motions

4 Modeling, Structural Analysis and Initial Cost

4.1 Structural Frames

The four-story three-bay reinforced concrete structural frame, shown in Fig. 5, is chosen for performing the design optimization. Story height and bay width of the frame as well as the initial cross sections and initial reinforcement ratios of all the members are selected based on the archetype design (ID 1008) in [73]. Initial column sizes are 558.8 mm × 558.8 mm (22 in × 22 in) with total longitudinal reinforcement ratios varying from 1.13 % to 1.63 % depending on the story level and column type (exterior or interior). Typically, reinforcement ratios are higher in the interior columns. All beams are assigned a cross sectional dimension of 558.8 mm × 609.6 mm (22 in × 24 in). Unlike the original archetype design, same reinforcement ratios are used at both tension and compression sides of a beam which are reduced gradually with increasing floor level from 0.83 % (first floor level) to 0.45 %

Fig. 5 The structural frame used for the example optimization problem

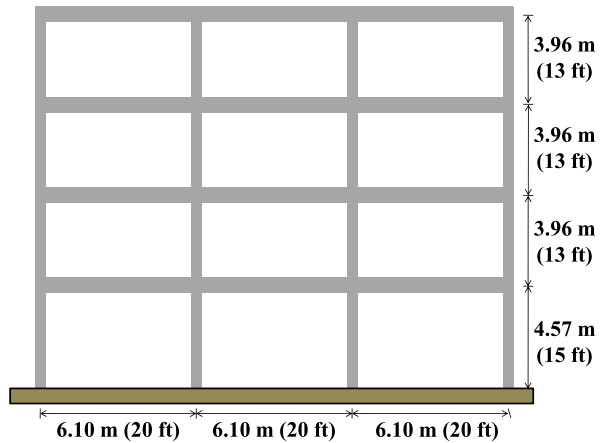
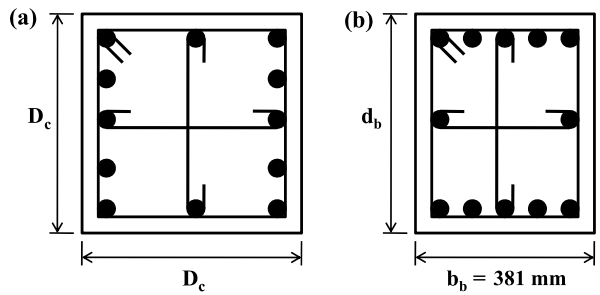


Fig. 6 Typical cross sections of (a) columns and (b) beams



(roof level). Beam stirrups and column stirrups are spaced at 127 mm (5 in) with total reinforcement ratios of 0.33 % and 0.7 %, respectively. The design inter-story drifts at each story ranged between 0.6 % and 1.2 %.

In order to minimize the search space, only the most important parameters are taken into consideration. The following assumptions are made in selecting design variables are: (i) all columns have the same dimensions, (ii) constant reinforcement ratio is maintained throughout a beam or a column, (iii) beam depths and reinforcement ratios change every two floors, (iv) beam width at every floor is fixed to 381 mm (15 in), and (v) shear reinforcement ratios or stirrups are not considered as design variables; rather these are designed based on elastic analysis. Most of these assumptions are also needed for construction feasibility and applied in real projects. It is also assumed that all beams and columns contain fixed number of longitudinal and transverse bars with predefined reinforcement configurations. The column and beam sections used for optimization are shown in Fig. 6.

Based on these assumptions, seven design variables are selected: column width, reinforcement ratios of exterior and interior columns, depth and reinforcement ratio of first two story beams, and depth and reinforcement ratio of top two story beams. A range of discrete values is assigned for each of these design variables, which are listed in Table 1. The bounds of these values comply with ACI 318-11 [74]. All

Table 1 Design variables and ranges for the considered structural frames

Design variables	Values
Width of columns (mm)	381, 508, 635, 762, 889, 1016
Reinforcement ratio of external columns	0.01, 0.02, 0.03, 0.04, 0.05, 0.06
Reinforcement ratio of internal columns	0.01, 0.02, 0.03, 0.04, 0.05, 0.06
Depth of first two story beams (mm)	381, 508, 635, 762, 889, 1016
Reinforcement ratio of first two story beams	0.005, 0.01, 0.015, 0.0175, 0.02, 0.025
Depth of top two story beams (mm)	381, 508, 635, 762, 889, 1016
Reinforcement ratio of top two story beams	0.005, 0.01, 0.015, 0.0175, 0.02, 0.025

possible combinations of these design variables generate 279,936 cases, which set up the search space for this optimization problem.

The gravitational loads for the considered space (interior) frame include a floor dead (including self-weight) and live loads of 8379 N/m² (175 psf) and 2394 N/m² (50 psf), respectively. The equivalent lateral load method, which is one of the recommended procedures of ASCE 7-10 [66], is used for defining the earthquake loads in elastic analysis. Lateral loads are computed according to ASCE 7-10 section 12.8.1. The response modification factor (R), overstrength factor (Ω_0), and deflection amplification factor (C_d) corresponding to a special moment resisting frame are used, which are 8, 3 and 5.5, respectively. Effective seismic weight of the frame is taken as the full dead load plus 25 % of the live load. Based on the seismic design coefficients and the seismic weight, design seismic base shear is found to be 360.3 kN (81 kips). The total base shear is then distributed at each floor level by assuming an inverted triangular (code suggested) distribution. The approximate fundamental period of the structure for the initial section sizes and reinforcement ratios is calculated as 0.58 seconds.

4.2 Evaluation of Structural Capacity and Earthquake Demand

Structural capacity and earthquake demand are evaluated using two different analysis techniques. A linear elastic analysis is performed and design checks are made according to ACI 318-08 [75] and IBC 2009 [76]. All the load combinations (including the seismic effects) stipulated in these regularity documents are taken into account. Additionally, P-Delta effects are accounted for in the analysis and design checks. The structural capacity is not measured based on a specific response quantity; on the contrary, a combination of decision variables is categorized into a binary variable of acceptable/unacceptable (pass/fail) based on the serviceability and

Table 2 Cost items

Item	Unit	Cost (\$/unit)
Material costs		
Steel (longitudinal), A615 grade 40	metric ton	1018.5
Steel (transverse), A615 grade 40	metric ton	1253.8
Concrete, ready mix (35 MPa)	m ³	145.2
Cast-in-place concrete forming	m ²	29.6
Labor costs		
Placing steel (longitudinal) in beams	metric ton	806.9
Placing steel (transverse) in beams	metric ton	2050.3
Placing steel (longitudinal) in columns	metric ton	948.0
Placing steel (transverse) in columns	metric ton	2182.6
Placing concrete	m ³	64.2
Placing concrete forming	m ²	110.3

strength checks. If a combination of decision variables does not satisfy any of the code requirements it is classified as unacceptable.

Earthquake demand on the other is evaluated through a nonlinear inelastic dynamic time history analysis using the fiber-based finite element analysis program ZEUS NL [77]. The structural frames are modeled using displacement-based beam-column elements with cubic shape functions [78, 79]. Concrete [80] and reinforcing steel [81] are modeled using the existing models ZEUS NL materials library. Geometric nonlinearity is taken into account in the dynamic analysis. A response history analysis is performed under each of the three spectrum compatible earthquake records shown in Fig. 4(b) and the earthquake demand is measured in terms of the maximum absolute interstory drift at any of the columns. Interstory drift is selected here as the response metric to measure the earthquake demand for being closely related to the development of P-Delta instability (a system level indicator), and to the amount of local deformation imposed on the vertical elements and beam column connections (component level indicators).

4.3 Calculation of Initial Cost

The cost of materials (concrete, reinforcing steel and formwork) and labor (placing) are considered here for the initial cost calculation of the structural frames. The cost items are estimated based on 2011 Building Construction Cost Data [82] and provided in Table 2. The details of initial cost calculation can be found in [83].

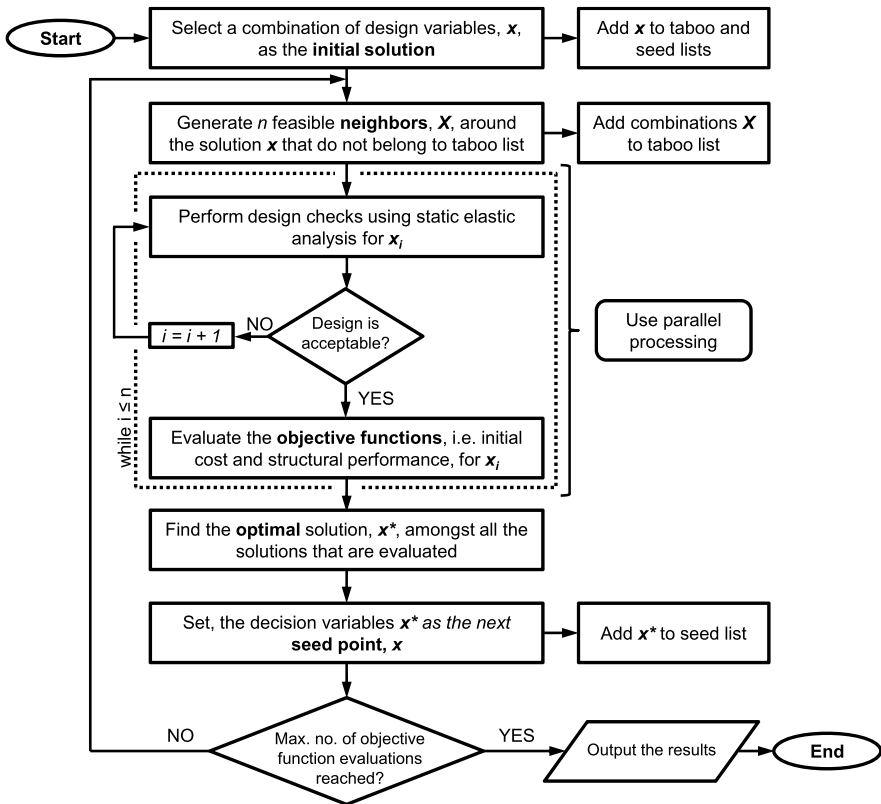
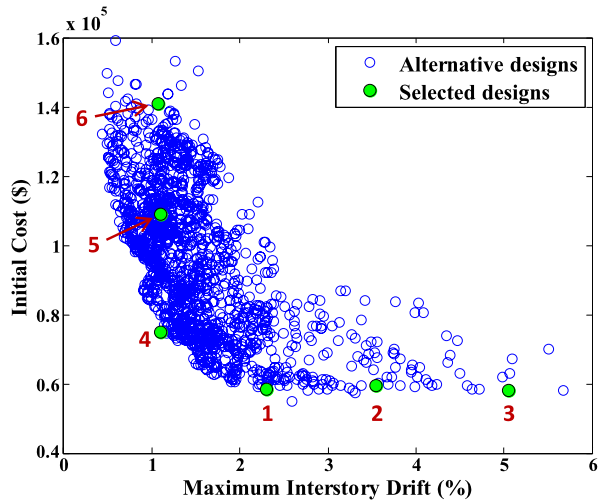


Fig. 7 Flowchart of the structural optimization approach

5 Structural Optimization

As discussed earlier, design optimization of RC structures is a challenging task, especially when inelastic dynamic analysis is used to evaluate the performance metrics. To partially overcome this problem a two level approach is adopted here. First, an elastic static analysis is performed for a combination of design variables. All the design checks, as mentioned in Sect. 4.2, are performed according to selected regulatory documents. If the design is classified as acceptable, inelastic dynamic time history analyses are performed under the three spectrum compatible ground motions. The maximum of the maximum interstory drifts obtained from the three analyses is used as one of the objectives (structural performance). On the contrary if the design is classified as unacceptable, the structural performance objective is set to a large value so that this combination of design variables is penalized and not further considered by the optimization algorithm. The other objective is defined as the initial cost. Both objectives are only evaluated if the selection of design variables is acceptable. The flowchart of the optimization procedure is provided in Fig. 7.

Fig. 8 Results of multi-objective optimization in the solution space



Taboo search (TS) algorithm is used to obtain the optimal solutions for the multi-objective optimization problem considered here. TS algorithm has been applied to various structural optimization problems and it has been showed to be very effective in solving combinatorial optimization problems with nonlinear objective functions and discontinuous derivatives [83–86]. TS employs a neighborhood search technique to sequentially move from a combination of design variables \mathbf{x} (i.e. section sizes and reinforcement ratios) that has a unique solution \mathbf{y} (initial cost and maximum interstory drift), to another in the neighborhood of \mathbf{y} until some termination criterion is reached. To explore the search space, at each iteration TS selects a set of neighboring combinations of decision variables using some optimal solution as a seed point. Usually, a portion of the neighboring points is selected randomly to prevent the algorithm being trapped at a local minimum. TS algorithm uses a number of memory structures to keep track of the previous evaluation of objective functions and constraints. The most important memory structure is called the taboo list, which temporarily or permanently stores the combinations that are visited in the past. TS excludes these solutions from the set of neighboring points that are determined at each iteration. The existence of the taboo list is crucial to the optimization problem considered here because the evaluation of objective functions and/or constraints are computationally costly.

6 Results and Discussion

The results of structural analysis are shown in the solution space (initial cost vs. maximum interstory drift) in Fig. 8. Note that each circle in Fig. 8 represent a combination of the decision variables and all the points satisfy the design checks according to ACI 318-08 [75]. Before all, the most important conclusion from these

Table 3 Cost and performance comparisons of alternative designs

Design numbering according to Fig. 8	Design variables						Total cost (\$)	Maximum interstory drift (%)	Fundamental period (sec)
	Depth of columns (mm)	Reinforcement ratio of external columns	Reinforcement ratio of internal columns	Depth of first two story beams (mm)	Reinforcement ratio of first two story beams	Depth of top two story beams (mm)			
1	508	0.02	0.02	508	0.025	508	58544	2.308	1.01
2	508	0.03	0.03	508	0.0175	381	59595	3.543	1.06
3	508	0.02	0.02	635	0.015	381	57922	5.054	0.94
4	635	0.02	0.02	762	0.0175	635	74754	1.097	0.62
5	889	0.06	0.01	635	0.0175	635	109111	1.102	0.54
6	1016	0.05	0.04	635	0.01	1016	140966	1.077	0.42

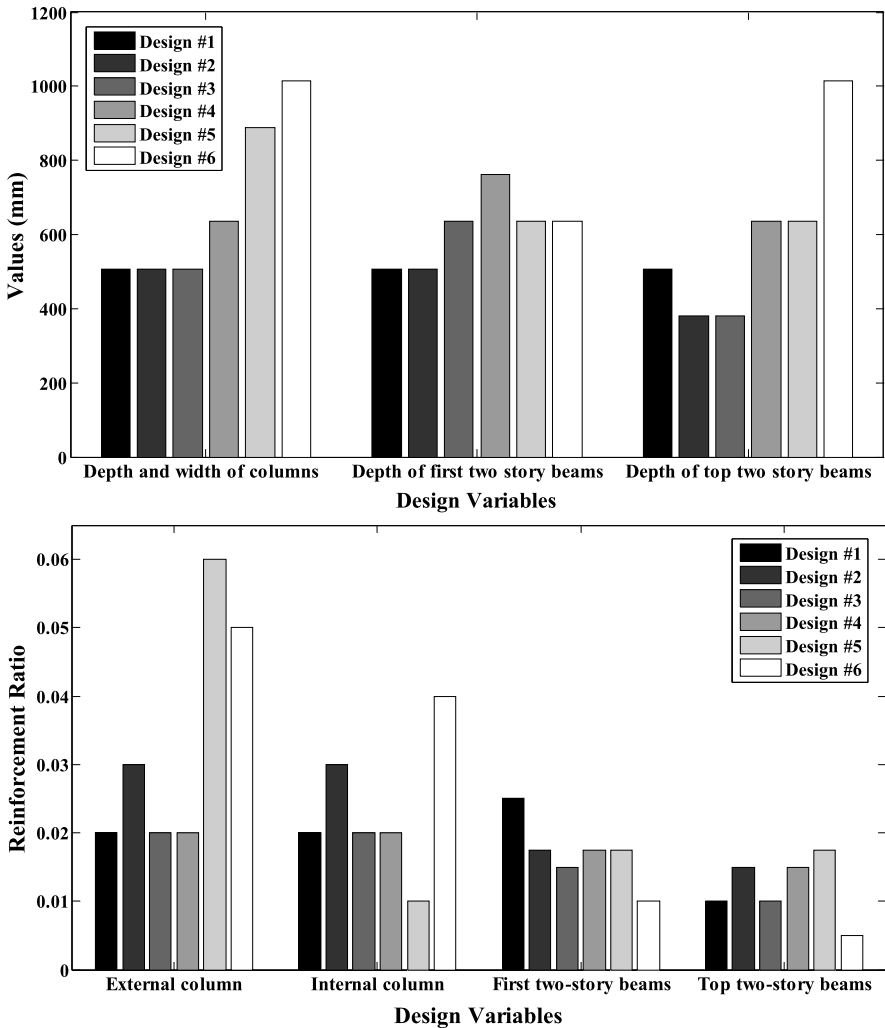
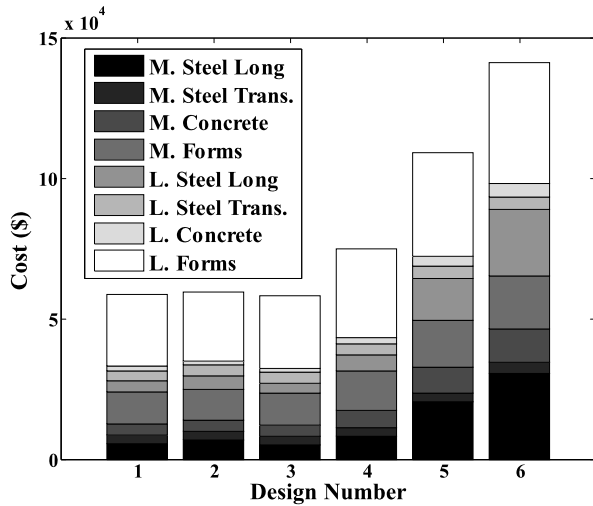


Fig. 9 Comparison of design variables for the similar cost and similar performance cases

results is that although the design satisfies the code regulations, significant variation in structural performance could be observed depending on the selection of design variables. In several cases the maximum interstory drift reaches or exceeds five percent, which can be detrimental for the vertical load carrying system and may result in partial or total collapse of the building if sufficient ductility and load carrying capacity at large displacement are not provided. Notwithstanding significant changes to seismic design codes since 1994 Northridge earthquake, these results suggest that even if we can ensure collapse prevention in most cases, there is a good chance that we will observe unexpected structural performance by a number of structures which

Fig. 10 Breakdown of initial cost: designs 1–3 and 4–6 show similar cost and similar performance cases, respectively



may have severe consequences such as deaths, injuries, and direct and indirect economic losses.

Among all the alternative designs, six are selected in order to assess the contribution of each design variable to the total cost or structural performance. The selected solutions are identified in Fig. 8 and corresponding decision variables are shown in Table 3 along with total cost and maximum interstory drift. For the first three designs (rows of Table 3), the total initial costs are very close, whereas maximum interstory drifts vary significantly. While for the last three designs, the opposite is true. The comparison of design variables for the selected solutions is provided in Fig. 9. For the first two designs, the dimensions of all the members are identical except for the depth of the top two story beams, which is observed to affect significantly the maximum interstory drift. Similarly, for third design, the critical parameter that governs the performance is the beam sectional property (i.e. reinforcement ratio) in top two stories. Apparently, reinforcement ratios of the columns do not have much impact on the drift performance in these cases. It can be observed from the cost breakdown shown in Fig. 10 that each cost component contributes consistently to the total cost across these design alternatives.

The last three design alternatives have very similar drift performances while the total costs are significantly different. These results again confirm that a decrease in section dimensions or reinforcement ratios of columns can be compensated by increasing the depth of the beams (see Fig. 9). These results also shed light on selection of proper design variables in seismic design for both performance and cost. It is clear from Fig. 10 that there are significant differences in total cost, mostly due to material and labor cost of longitudinal steel, although all three design alternatives results in similar structural performance. The labor cost of formwork contributes the most to the total initial cost in all the cases; on the contrary, the labor cost of concrete has the lowest contribution. Finally, it is seen in last column of Table 3 that the fundamental period of the frames changes considerably by changing decision

variables; however, it still remains within 0–1 seconds, which is the range selected for spectrum matching of earthquake ground motions.

7 Future Research Directions

Optimal seismic design of RC building is a challenging task, mainly due to associated computational cost and difficulty in defining performance objectives. In addition to section sizes, and reinforcement ratios, reinforcement topology needs to be optimized as well. With increasing design variables, the search space grows rapidly resulting in excessive computational demand, especially when rigorous structural analysis approaches such as the nonlinear inelastic dynamic analysis is used. Thus, there is a need to develop methods for identifying design variables that are practical for engineers and that govern the seismic response.

Other performance definitions such as lifetime economic losses, deaths and injuries should also be included among the objectives of the optimization problem. It is likely that these additional layers of computation will reduce the efficiency of optimization algorithms; therefore, proper techniques should be developed to test and overcome these potential problems. The uncertainty in structural response due to sources such as the variation in material properties, effects of non-structural components, errors in analysis models and inherent randomness in ground motion processes should also be incorporated in structural optimization.

8 Conclusions

In this chapter we have attempted to lay out a framework for cost optimal seismic design of RC buildings. The novelty of the proposed approach is the multi-objective, multi-level investigation. The former is by consideration of both the initial cost and structural performance, while the latter is due to a two-level structural assessment where each design alternatives is first assessed for code compliance and then performance is quantified using rigorous structural analysis. The framework is applied to a four-story three-bay RC building. The results support the potential use of the proposed approach in decision making process where both initial cost and structural performance is considered at the same time while complying with the code requirements. The shortcomings of the approach mainly stemming from the high computational demand and negligence of uncertainty need to be addressed in future studies.

References

1. ATC (1996) Seismic evaluation and retrofit of concrete buildings. Report ATC-40, Applied Technology Council

2. FEMA (1997) NEHRP guidelines for the seismic rehabilitation of buildings, FEMA 273. Federal Emergency Management Agency, Washington
3. FEMA (2000) Prestandard and commentary for the seismic rehabilitation of buildings, FEMA 356. Federal Emergency Management Agency, Washington
4. ASCE/SEI (2007) Seismic rehabilitation of existing buildings. American Society of Civil Engineers, ASCE/SEI 41-06, Reston
5. Feng TT, Arora JS, Haug EJ (1977) Optimal structural design under dynamic loads. *Int J Numer Methods Eng* 11(1):39–52
6. Cameron GE, Chan CM, Xu LEI, Grierson DE (1992) Alternative methods for the optimal design of slender steel frameworks. *Comput Struct* 44(4):735–741
7. Camp C, Pezeshk S, Cao G (1998) Optimized design of two-dimensional structures using a genetic algorithm. *J Struct Eng* 124(5):551–559
8. Pezeshk S (1998) Design of framed structures: an integrated non-linear analysis and optimal minimum weight design. *Int J Numer Methods Eng* 41(3):459–471
9. Li G, Zhou R-G, Duan L, Chen W-F (1999) Multiobjective and multilevel optimization for steel frames. *Eng Struct* 21(6):519–529
10. Memari AM, Madhkhan M (1999) Optimal design of steel frames subject to gravity and seismic codes' prescribed lateral forces. *Struct Multidiscip Optim* 18(1):56–66
11. Foley CM, Schinler D (2003) Automated design of steel frames using advanced analysis and object-oriented evolutionary computation. *J Struct Eng* 129(5):648–660
12. Lagaros ND, Fragiadakis M, Papadrakakis M, Tsompanakis Y (2006) Structural optimization: a tool for evaluating seismic design procedures. *Eng Struct* 28(12):1623–1633
13. Liu M, Burns SA, Wen YK (2006) Genetic algorithm based construction-conscious minimum weight design of seismic steel moment-resisting frames. *J Struct Eng* 132(1):50–58
14. Chung TT, Sun TC (1994) Weight optimization for flexural reinforced concrete beams with static nonlinear response. *Struct Multidiscip Optim* 8(2):174–180
15. Karihaloo BL, Kanagasundaram S (1987) Optimum design of statically indeterminate beams under multiple loads. *Comput Struct* 26(3):521–538
16. Karihaloo BL, Kanagasundaram S (1989) Minimum-weight design of structural frames. *Comput Struct* 31(5):647–655
17. Sarma KC, Adeli H (1998) Cost optimization of concrete structures. *J Struct Eng* 124(5):570–578
18. Hill LA (1966) Automated optimum cost building design. *J Struct Div* 92(6):247–264
19. Cohn MZ (1972) Optimal limit design for reinforced concrete structures. In: International symposium on inelasticity and nonlinearity in structural concrete, Waterloo, pp 357–388
20. Krishnamoorthy CS, Munro J (1973) Linear program for optimal design of reinforced concrete frames. *Proc Int Assoc Bridge Struct Eng* 33:119–141
21. Cauvin A (1979) Nonlinear elastic design and optimization of reinforced concrete frames. In: CSCE ASCE ACI CEB international symposium, University of Waterloo, Ontario, pp 197–217
22. Gerlein MA, Beaufait FW (1980) An optimum preliminary strength design of reinforced concrete frames. *Comput Struct* 11(6):515–524
23. Kirsch U (1983) Multilevel optimal design of reinforced concrete structures. *Eng Optim* 6(4):207–212
24. Cohn MZ, MacRae AJ (1984) Optimization of structural concrete beams. *J Struct Eng* 110(7):1573–1588
25. Huan Chun S, Zheng C (1985) Two-level optimum design of reinforced concrete frames with integer variables. *Eng Optim* 9(3):219–232
26. Krishnamoorthy CS, Rajeev S (1989) Computer-aided optimal design of reinforced concrete frames. In: Ramakrisnan CV, Varadarajan A (eds) International conference on engineering software, Narosa, New Delhi
27. Hoit M (1991) Probabilistic design and optimization of reinforced concrete frames. *Eng Optim* 17(3):229–235

28. Al-Gahtani AS, Al-Saadoun SS, Abul-Feilat EA (1995) Design optimization of continuous partially prestressed concrete beams. *Comput Struct* 55(2):365–370
29. Cheng FY, Truman KZ (1985) Optimal design of 3-D reinforced concrete and steel buildings subjected to static and seismic loads including code provisions. Final report series 85-20, prepared by University of Missouri-Rolla, National Science Foundation, US Department of Commerce, Washington
30. Moharrami H, Grierson DE (1993) Computer-automated design of reinforced concrete frameworks. *J Struct Eng* 119(7):2036–2058
31. Adamu A, Karihaloo BL (1994) Minimum cost design of RC beams using DCOC. Part I: Beams with freely-varying cross-sections. *Struct Multidiscip Optim* 7(4):237–251
32. Adamu A, Karihaloo BL (1994) Minimum cost design of RC beams using DCOC. Part II: Beams with uniform cross-sections. *Struct Multidiscip Optim* 7(4):252–259
33. Adamu A, Karihaloo BL, Rozvany GIN (1994) Minimum cost design of reinforced concrete beams using continuum-type optimality criteria. *Struct Multidiscip Optim* 7(1):91–102
34. Adamu A, Karihaloo BL (1995) Minimum cost design of RC frames using the DCOC method. Part I: Columns under uniaxial bending actions. *Struct Multidiscip Optim* 10(1):16–32
35. Adamu A, Karihaloo BL (1995) Minimum cost design of RC frames using the DCOC method. Part II: Columns under biaxial bending actions. *Struct Multidiscip Optim* 10(1):33–39
36. Fadaee MJ, Grierson DE (1996) Design optimization of 3D reinforced concrete structures. *Struct Multidiscip Optim* 12(2):127–134
37. Chan CM (2001) Optimal lateral stiffness design of tall buildings of mixed steel and concrete construction. *Struct Des Tall Spec Build* 10(3):155–177
38. Chan CM, Zou XK (2004) Elastic and inelastic drift performance optimization for reinforced concrete buildings under earthquake loads. *Earthq Eng Struct Dyn* 33(8):929–950
39. Zou X-K, Chan C-M (2004) An optimal resizing technique for seismic drift design of concrete buildings subjected to response spectrum and time history loadings. *Comput Struct* 83(19–20):1689–1704
40. Chan CM, Wang Q (2006) Nonlinear stiffness design optimization of tall reinforced concrete buildings under service loads. *J Struct Eng* 132(6):978–990
41. Zou XK (2008) Integrated design optimization of base-isolated concrete buildings under spectrum loading. *Struct Multidiscip Optim* 36(5):493–507
42. Goldberg DE, Samtani MP (1987) Engineering optimization via genetic algorithm. In: Will KM (ed) Ninth conference on electronic computation, New York
43. Pezeshk S, Camp CV (2002) State of the art on the use of genetic algorithms in design of steel structures. In: Burns SA (ed) Recent advances in optimal structural design. American Society of Civil Engineers, Reston
44. Choi CK, Kwak HG (1990) Optimum RC member design with predetermined discrete sections. *J Struct Eng* 116(10):2634–2655
45. Lee C, Ahn J (2003) Flexural design of reinforced concrete frames by genetic algorithm. *J Struct Eng* 129(6):762–774
46. Camp CV, Pezeshk S, Hansson H (2003) Flexural design of reinforced concrete frames using a genetic algorithm. *J Struct Eng* 129(1):105–115
47. Balling RJ, Yao X (1997) Optimization of reinforced concrete frames. *J Struct Eng* 123(2):193–202
48. Rajeev S, Krishnamoorthy C (1998) Genetic algorithm-based methodology for design optimization of reinforced concrete frames. *Comput-Aided Civ Infrastruct Eng* 13(1):63–74
49. Govindaraj V, Ramasamy JV (2005) Optimum detailed design of reinforced concrete continuous beams using genetic algorithms. *Comput Struct* 84(1–2):34–48
50. Saini B, Sehgal VK, Gambhir ML (2007) Least-cost design of singly and doubly reinforced concrete beam using genetic algorithm optimized artificial neural network based on Levenberg-Marquardt and quasi-Newton backpropagation learning techniques. *Struct Multidiscip Optim* 34(3):243–260
51. Sahab MG, Ashour AF, Toropov VV (2005) A hybrid genetic algorithm for reinforced concrete flat slab buildings. *Comput Struct* 83(8–9):551–559

52. Sahab MG, Ashour AF, Toropov V (2005) Cost optimisation of reinforced concrete flat slab buildings. *Eng Struct* 27(3):313–322
53. Salajegheh E, Gholizadeh S, Khatibinia M (2008) Optimal design of structures for earthquake loads by a hybrid RBF-BPSO method. *Earthq Eng Eng Vib* 7(1):13–24
54. Leps M, Sejnoha M (2003) New approach to optimization of reinforced concrete beams. *Comput Struct* 81(18–19):1957–1966
55. Rao SS, Xiong Y (2005) A hybrid genetic algorithm for mixed-discrete design optimization. *J Mech Des* 127(6):1100–1112
56. Ahmadi-Nedushan B, Varae H (2011) Minimum cost design of concrete slabs using particle swarm optimization with time varying acceleration coefficients. *World Appl Sci J* 13(12):2484–2494
57. El Semelawy M, Nassef AO, El Damatty AA (2012) Design of prestressed concrete flat slab using modern heuristic optimization techniques. *Expert Syst Appl* 39(5):5758–5766
58. Fragiadakis M, Papadrakakis M (2008) Performance-based optimum seismic design of reinforced concrete structures. *Earthq Eng Struct Dyn* 37(6):825–844
59. Ang AHS, Lee J-C (2001) Cost optimal design of R/C buildings. *Reliab Eng Syst Saf* 73(3):233–238
60. Li G, Cheng G (2003) Damage-reduction-based structural optimum design for seismic RC frames. *Struct Multidiscip Optim* 25(4):294–306
61. Lagaros ND, Papadrakakis M (2007) Seismic design of RC structures: a critical assessment in the framework of multi-objective optimization. *Earthq Eng Struct Dyn* 36(12):1623–1639
62. Zou XK, Chan CM, Li G, Wang Q (2007) Multiobjective optimization for performance-based design of reinforced concrete frames. *J Struct Eng* 133(10):1462–1474
63. Fragiadakis M, Lagaros ND (2011) An overview to structural seismic design optimisation frameworks. *Comput Struct* 89(11–12):1155–1165
64. Paya I, Yepes V, Gonzalez-Vidoso F, Hospitaler A (2008) Multiobjective optimization of concrete frames by simulated annealing. *Comput-Aided Civ Infrastruct Eng* 23(8):596–610
65. Mitropoulou CC, Lagaros ND, Papadrakakis M (2011) Life-cycle cost assessment of optimally designed reinforced concrete buildings under seismic actions. *Reliab Eng Syst Saf* 96(10):1311–1331
66. ASCE (2010) Minimum design loads for buildings and other structures. American Society of Civil Engineers, ASCE 7-10, Reston
67. FEMA (2003) NEHRP recommended provisions for seismic regulations for new buildings and other structures, FEMA 450, part 1: Provisions. Federal Emergency Management Agency, Washington
68. USGS (2009) Soil type and shaking hazard in the San Francisco Bay area. US Geological Survey. <http://earthquake.usgs.gov/regional/nca/soiltype/>. Accessed February 1, 2011
69. PEER (2005) Pacific Earthquake Engineering Research (PEER) Center: NGA database. <http://peer.berkeley.edu/nga/>. Accessed January 1, 2009
70. Hancock J, Watson-Lamprey J, Abrahamson NA, Bommer JJ, Markatis A, McCoyh E, Mendis R (2006) An improved method of matching response spectra of recorded earthquake ground motions using wavelets. *J Earthq Eng* 10(Suppl 1):67–89
71. Al Atik L, Abrahamson N (2010) An improved method for nonstationary spectral matching. *Earthq Spectra* 26(3):601–617
72. Abrahamson NA (1993) Non-stationary spectral matching program RSPMatch, user's manual
73. Haselton CB, Deierlein GG (2007) Assessing seismic collapse safety of modern reinforced concrete moment frame buildings. Report No 156, The John A. Blume Earthquake Engineering Center, Department of Civil and Environmental Engineering, Stanford University, Palo Alto
74. ACI (2011) Building code requirements for structural concrete (ACI 318-11) and commentary. American Concrete Institute, Farmington Hills
75. ACI (2008) Building code requirements for structural concrete (ACI 318-08) and commentary. American Concrete Institute, Farmington Hills
76. ICC (2009) International building code. International Code Council, Washington

77. Elnashai AS, Papanikolaou VK, Lee D (2010) ZEUS NL—a system for inelastic analysis of structures, user's manual. Mid-America Earthquake (MAE) Center, Department of Civil and Environmental Engineering, University of Illinois at Urbana-Champaign, Urbana
78. Izzuddin BA, Elnasahi AS (1993) Adaptive space frame analysis, part II: A distributed plasticity approach. *Proc Inst Civ Eng, Struct Build* 99:317–326
79. Izzuddin BA, Elnasahi AS (1993) Eulerian formulation for large-displacement analysis of space frames. *J Eng Mech* 119(3):549–569
80. Martínez-Rueda JE, Elnashai AS (1997) Confined concrete model under cyclic load. *Mater Struct* 30(3):139–147
81. Ramberg W, Osgood WR (1943) Description of stress-strain curves by three parameters. Technical note 902, 1943-07, National Advisory Committee for Aeronautics, Washington
82. RS Means (2011) Building construction cost data 2011 book. RS Means, Reed Construction Data, Kingston
83. Gencturk B (2013) Life-cycle cost assessment of RC and ECC frames using structural optimization. *Earthq Eng Struct Dyn* 42(1):61–79
84. Bland J (1998) Structural design optimization with reliability constraints using taboo search. *Eng Optim* 30(1):55–74
85. Manoharan S, Shanmuganathan S (1999) A comparison of search mechanisms for structural optimization. *Comput Struct* 73(1–5):363–372
86. Ohsaki M, Kinoshita T, Pan P (2007) Multiobjective heuristic approaches to seismic design of steel frames with standard sections. *Earthq Eng Struct Dyn* 36(11):1481–1495

Nonsmooth and Nonconvex Optimization for the Design and Order Reduction of Robust Controllers Used in Smart Structures

A.J. Moutsopoulou, A.T. Pouliezios, and G.E. Stavroulakis

Abstract H-infinity controller design for linear systems is a difficult, nonconvex typically nonsmooth optimization problem when the controller is fixed to be of order less than the one of the open-loop plant, a requirement with some importance in embedded smart systems. In this paper we use a new Matlab package called HIFOO, aimed at solving fixed-order stabilization and local optimization problems; it is based on a new hybrid solution algorithm. The problem is to reduce the vibration of the smart system using H-infinity control and nonsmooth optimization.

Keywords Fixed-order controller design · H-infinity control · Nonconvex optimization · Nonsmooth optimization · Smart structures · Robust structural control

1 Introduction

A composite beam laminated with piezoelectric sensors and actuators and subjected to external loads is considered as a model example in this paper. The governing equation of the beam is formulated. Finite elements are used to approximate the dynamic response of the beam. Vibration control problem for flexible structure is considered and performance specification is stated in terms of a disturbance attenuation requirement for external disturbances. H-infinity (H_∞ control strategy) is applied to

A.J. Moutsopoulou (✉)

Department of Civil Engineering, Technological Educational Institute of Crete, 71004 Heraklion, Greece

e-mail: amalia@staff.teicrete.gr

A.T. Pouliezios · G.E. Stavroulakis

Department of Production Engineering and Management, Technical University of Crete, 73100 Chania, Greece

A.T. Pouliezios

e-mail: tasos@dpem.tuc.gr

G.E. Stavroulakis

e-mail: gestavr@dpem.tuc.gr

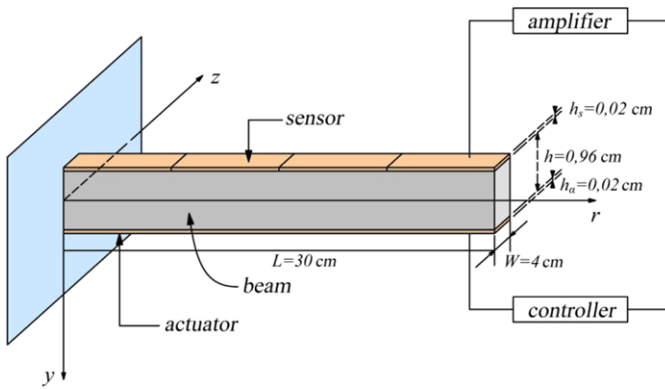


Fig. 1 Smart beam

solve the posed problem. Considering the uncertainty, which arises from neglecting higher order, dynamics, insufficient knowledge of the real plant parameters, external disturbances and measure noise, H_∞ robust controller is designed [1–5].

By using the classical approach a H_∞ controller of order equal to 36 has been found. The fact that controller order, which is equal to the order of the system, is relatively higher than the order of classical controllers such as PI and LQR has led a number of researchers to develop order reduction algorithms. The most widely used such algorithm, known as HIFOO, has been implemented in a Matlab environment, and is the one used in the following procedure [6–10].

HIFOO is a public-domain Matlab package initially designed for H_∞ fixed-order controller synthesis, using nonsmooth nonconvex optimization techniques. It was later on extended to multi-objective synthesis, including strong and simultaneous stabilization under H_∞ constraints. HIFOO relies upon HANSO, a general purpose implementation of an hybrid algorithm for nonsmooth optimization, mixing standard quasi-Newton and gradient sampling techniques. The acronym HIFOO stands for H_∞ fixed order optimization, and the package is aimed at designing a stabilizing linear controller of fixed order for a linear plant in standard state-space configuration while minimizing the H_∞ norm of the closed-loop transfer function.

2 Mathematical Modelling

A cantilever slender beam with rectangular cross-sections is considered. Four pairs of piezoelectric patches are embedded symmetrically at the top and the bottom surfaces of the beam, as shown in Fig. 1.

The beam is from graphite-epoxy T300-976 and the piezoelectric patches are PZT G1195N [5, 11]. The top patches act like sensors and the bottom like actuators. The resulting composite beam is modelled by means of the classical laminated technical theory of bending. Let us assume that the mechanical properties of both

Table 1 Parameters of the composite beam

Parameters	Values
Beam length, L	0.3 m
Beam width, W	0.04 m
Beam thickness, h	0.0096 m
Beam density, ρ	1600 kg/m ³
Young's modulus of the beam, E	1.5×10^{11} N/m ²
Piezoelectric constant, d_{31}	254×10^{-12} m/V
Electric constant, ξ_{33}	11.5×10^{-3} V m/N
Young's modulus of the piezoelectric element	1.5×10^{11} N/m ²
Width of the piezoelectric element	$b_S = b_A = 0.04$ m
Thickness of the piezoelectric element	$h_S = h_A = 0.0002$ m

the piezoelectric material and the host beam are independent in time. The thermal effects are considered to be negligible as well [12, 13].

The beam has length L , width W and thickness h . The sensors and the actuators have width b_S and b_A and thickness h_S and h_A , respectively. The electromechanical parameters of the beam of interest are given in Table 1.

2.1 Reduced Model of the Piezoelectric Composite

In order to derive the basic equations for piezoelectric sensors and actuators (S/As), we assume that:

- The piezoelectric S/A are bonded perfectly on the host beam;
- The piezoelectric layers are much thinner than the host beam;
- The piezoelectric material is homogeneous, transversely isotropic and linearly elastic;
- The piezoelectric S/A are transversely polarized (in the z -direction) [5, 13].

Under these assumptions the three-dimensional linear constitutive equations are given by [1, 9],

$$\begin{Bmatrix} \sigma_{xx} \\ \sigma_{xz} \end{Bmatrix} = \begin{bmatrix} Q_{11} & 0 \\ 0 & Q_{55} \end{bmatrix} \left(\begin{Bmatrix} \varepsilon_{xx} \\ \varepsilon_{xz} \end{Bmatrix} - \begin{bmatrix} d_{31} \\ 0 \end{bmatrix} E_z \right) \tag{2.1}$$

$$D_z = Q_{11}d_{31}\varepsilon_{xx} + \xi_{xx}E_z \tag{2.2}$$

where σ_{xx} , σ_{xz} denote the axial and shear stress components, D_z , denotes the transverse electrical displacement; ε_{xx} and ε_{xz} are a axial and shear strain components; Q_{11} , and Q_{55} , denote elastic constants; d_{31} , and ξ_{33} , denote piezoelectric and dielectric constants, respectively. Equation (2.1) describes the inverse piezoelectric effect and Eq. (2.2) describes the direct piezoelectric effect. E_z , is the transverse

component of the electric field that is assumed to be constant for the piezoelectric layers and its components in xy -plane are supposed to vanish. If no electric field is applied in the sensor layer, the direct piezoelectric equation (2.2) gets the form,

$$D_z = Q_{11}d_{31}\varepsilon_{xx} \quad (2.3)$$

and it is used to calculate the output charge created by the strains in the beam [2].

2.2 Equations of Motion

The length, width and thickness of the host beam are denoted by L , b and h . The thickness of the sensor and actuator is denoted by h_S and h_A . We assume that:

- The beam centroidal and elastic axis coincides with the x -coordinate axis so that no bending-torsion coupling is considered;
- The axial vibration of the host beam centreline is considered negligible;
- The displacement field $\{u\} = (u_1, u_2, u_3)$ is obtained based on the usual Timoshenko assumptions [14],

$$\begin{aligned} u_1(x, y, z) &\approx z\varphi(x, t) \\ u_2(x, y, z) &\approx 0 \\ u_3(x, y, z) &\approx \omega(x, t) \end{aligned} \quad (2.4)$$

where φ is the rotation of the beams cross-section about the positive y -axis and w is the transverse displacement of a point of the centroidal axis ($y = z = 0$).

The strain displacement relations can be applied to Eq. (2.4) to give,

$$\varepsilon_{xx} = z \frac{\partial \varphi}{\partial x}, \quad \varepsilon_{xz} = \frac{\partial \omega}{\partial x} \quad (2.5)$$

We suppose that the transverse shear deformation ε_{xx} is equal to zero [14].

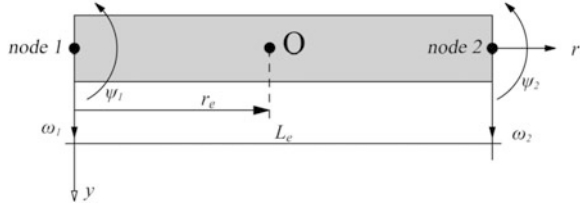
In order to derive the equations of the motion of the beam we use Hamilton's principle,

$$\int_{t_2}^{t_1} (\delta T - \delta U + \delta W) dt = 0 \quad (2.6)$$

where T [15] is the total kinetic energy of the system, U is the potential (strain) energy and W is the virtual work done by the external mechanical and electrical loads and moments. The first variation of the kinetic energy is given by,

$$\begin{aligned} \delta T &= \frac{1}{2} \int_V \rho \left\{ \frac{\partial u}{\partial t} \right\}^r \left\{ \frac{\partial u}{\partial t} \right\} dV \\ &= \frac{b}{2} \int_0^L \int_{-\frac{h}{2}-h_A}^{\frac{h}{2}+h_S} \rho \left(z \frac{\partial \varphi}{\partial t} \delta \frac{\partial \varphi}{\partial t} + \frac{\partial \omega}{\partial t} \delta \frac{\partial \omega}{\partial t} \right) dz dx \end{aligned} \quad (2.7)$$

Fig. 2 Beam finite element



The first variation of the potential energy is given by,

$$\begin{aligned} \delta U &= \frac{1}{2} \int_V \delta\{\varepsilon\}^T \{\sigma\} dV \\ &= \frac{b}{2} \int_0^L \int_{-\frac{h}{2}-h_A}^{\frac{h}{2}+h_s} \left[Q_{11} \left(z \frac{\partial \omega}{\partial x} \delta \right) \left(z \frac{\partial \omega}{\partial x} \right) \right] dz dx \end{aligned} \tag{2.8}$$

If the load consists only of moments induced by piezoelectric actuators and since the structure has no bending twisting couple then the first variation of the work has the form [15],

$$\delta W = b \int_0^L M^A \delta \left(\frac{\partial \varphi}{\partial x} \right) dx \tag{2.9}$$

where M^A is the moment per unit length induced by the actuator layer and is given by,

$$M^A = \int_{-\frac{h}{2}-h_A}^{-\frac{h}{2}} z \sigma_{xx}^A dz = \int_{-\frac{h}{2}-h_A}^{-\frac{h}{2}} z Q_{11} d_{31} E_z^A dz \left(E_z^A = \frac{V_A}{h_A} \right) \tag{2.10}$$

2.3 Finite Element Formulation

We consider a beam element of length L_e , which has two mechanical degrees of freedom at each node: one translational ω_1 (respectively ω_2) in direction z and one rotational φ_1 (respectively φ_2), as it is shown in Fig. 2. The vector of nodal displacements and rotations q_e is defined as [2],

$$q_e^r = [\omega_1, \psi_1, \omega_2, \psi_2] \tag{2.11}$$

The beam element transverse deflection $\omega(x, t)$ and the beam element rotation $\psi(x, t)$ of the beam are continuous and they are interpolated within the beam by using Hermitian linear shape functions H_i^ω and H_i^ψ as follows [4],

$$\begin{aligned} \omega(x, t) &= \sum_{i=1}^4 H_i^\omega(x) q_i(t) \\ \psi(x, t) &= \sum_{i=1}^4 H_i^\psi(x) q_i(t) \end{aligned} \tag{2.12}$$

This classical finite element procedure leads to the approximate (discretized) variational problem. For a finite element the discrete differential equations are obtained by substituting the discretized expressions (2.12) into Eqs. (2.7) and (2.8) to evaluate the kinetic and strain energies. Integrating over spatial domains and using the Hamilton principle (2.6) the equation of motion for a beam element are expressed in terms of nodal variable q as follows [3, 5, 11],

$$M\ddot{q}(t) + D\dot{q}(t) + Kq(t) = f_m(t) + f_e(t) \quad (2.13)$$

where M is the generalized mass matrix, D the viscous damping matrix, K the generalized stiffness matrix, f_m the external loading vector and f_e the generalized control force vector produced by electromechanical coupling effects. The independent variable $q(t)$ is composed of transversal deflections ω_1 and rotations ψ_1 , i.e., [16]

$$q(t) = \begin{bmatrix} \omega_1 \\ \psi_1 \\ \vdots \\ \omega_n \\ \psi_n \end{bmatrix} \quad (2.14)$$

where n is the number of nodes used in analysis. Vectors ω and f_m are positive upwards. To transform to state-space control representation, let (in the usual manner),

$$\dot{x}(t) = \begin{bmatrix} q(t) \\ \dot{q}(t) \end{bmatrix} \quad (2.15)$$

Furthermore to express $f_e(t)$ as $Bu(t)$ we write it as f_e^*u where f_e^* the piezoelectric force is for a unit applied on the corresponding actuator, and u represents the voltages on the actuators. Furthermore, $d(t) = f_m(t)$ is the disturbance vector [17]. Then,

$$\dot{x}(t) = \begin{bmatrix} O_{2n \times 2n} & I_{2n \times 2n} \\ -M^{-1}K & -M^{-1}D \end{bmatrix} x(t) + \begin{bmatrix} O_{2n \times 2n} \\ M^{-1}f_e^* \end{bmatrix} u(t) + \begin{bmatrix} O_{2n \times 2n} \\ M^{-1} \end{bmatrix} d(t) \quad (2.16)$$

$$\begin{aligned} &= Ax(t) + Bu(t) + Gd(t) = Ax(t) + \begin{bmatrix} B & G \end{bmatrix} \begin{bmatrix} u(t) \\ d(t) \end{bmatrix} \\ &= Ax(t) + \tilde{B}\tilde{u}(t) \end{aligned} \quad (2.17)$$

The previous description of the dynamical system will be augmented with the output equation (displacements only measured) [2],

$$y(t) = [x_1(t) \quad x_3(t) \quad \cdots \quad x_{n-1}(t)]^T = Cx(t) \quad (2.18)$$

In this formulation u is $n \times 1$ (at most, but can be smaller), while d is $2n \times 1$. The units used are compatible for instance m, rad, sec and N.

3 Design Objectives and System Specifications

For the description of system uncertainties the known from the control theory Δ technique is used. With this technique, which will be outlined later, the uncertainties are introduced in the system as additional feedback branches, similarly to the introduction of control branches. The robust control design tries then to design the optimal control feedback under perturbation coming from the worst uncertainty feedback (for details [12]).

The structured singular value of a transfer function matrix is defined as,

$$\mu(M) = \begin{cases} \frac{1}{\min_{k_m} \{\det(I - k_m M \Delta) = 0, \bar{\sigma}(\Delta) \leq 1\}} \\ 0, & \text{if no such quantity is defined} \end{cases} \quad (3.1)$$

In words it defines the smallest structured Δ (measured in terms of $\bar{\sigma}(\Delta)$) which makes $\det(I - M\Delta) = 0$: then $\mu(M) = 1/\bar{\sigma}(\Delta)$. It follows that values of μ smaller than 1 are desired (the smaller the better: a larger variation is allowed) [12].

3.1 Design Objectives

Design objectives fall into two categories:

Nominal performance

1. Stability of closed loop system (plant + controller).
2. Disturbance attenuation with satisfactory transient characteristics (overshoot, settling time).
3. Small control effort.

Robust performance

4. (1)–(3) above should be satisfied in the face of modelling errors [12].

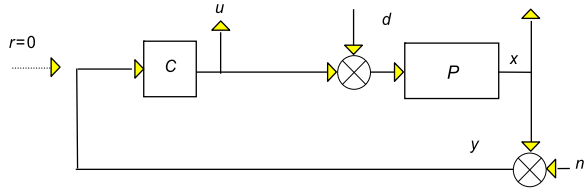
3.2 System Specifications

To obtain the required system specifications to meet the above objectives we need to represent our system in the so-called (N, Δ) structure. To do this let us start with the simple typical diagram of Fig. 3. In this diagram there are two inputs, d (disturbances) and n (noise), and two outputs, u (control vector) and x (state vector). In what follows it is assumed that,

$$\left\| \begin{matrix} d \\ n \end{matrix} \right\|_2 \leq 1, \quad \left\| \begin{matrix} u \\ x \end{matrix} \right\|_2 \leq 1 \quad (3.2)$$

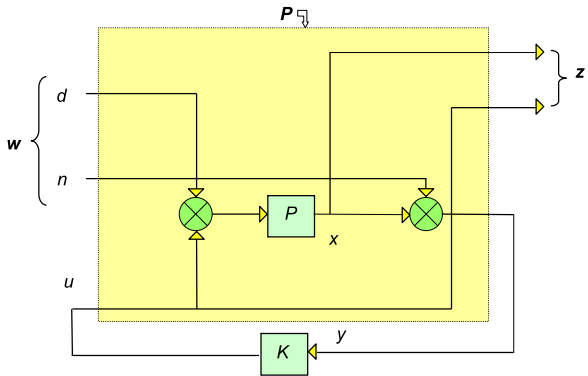
If that's not the case, appropriate frequency-dependent weights can transform original signals so that the transformed signals have this property.

Fig. 3 Classical control block diagram



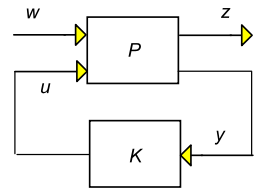
Redrawing Fig. 3 in frequency domain we get Fig. 4:

Fig. 4 Detailed two-port diagram



or in less detail Fig. 5,

Fig. 5 Two-port diagram



with,

$$z = \begin{bmatrix} u \\ x \end{bmatrix}, \quad w = \begin{bmatrix} d \\ n \end{bmatrix} \tag{3.3}$$

where z are the output variables to be controlled, and w the exogenous inputs.

Given that P has two inputs and two outputs it is, as usual, naturally partitioned as,

$$\begin{bmatrix} z(s) \\ y(s) \end{bmatrix} = \begin{bmatrix} P_{zw}(s) & P_{zu}(s) \\ P_{yw}(s) & P_{yu}(s) \end{bmatrix} \begin{bmatrix} w(s) \\ u(s) \end{bmatrix} \stackrel{op}{=} P(s) \begin{bmatrix} w(s) \\ u(s) \end{bmatrix} \tag{3.4}$$

Furthermore,

$$u(s) = K(s)y(s) \tag{3.5}$$

Substituting (3.5) in (3.4) gives the closed loop transfer function $N_{zw}(s)$,

$$N_{zw}(s) = P_{zw}(s) + P_{zu}(s)K(s)(I - P_{yu}(s)K(s))^{-1}P_{yw}(s) \tag{3.6}$$

4 Controller Synthesis

It is possible to approximately synthesize a controller that achieves given performance in terms of the structured singular value μ .

In this procedure known as $(D, G\text{-}K)$ iteration (2.14) the problem of finding a μ -optimal controller K such that $\mu(\mathcal{F}_u(F(j\omega), K(j\omega))) \leq \beta, \forall \omega$, is transformed into the problem of finding transfer function matrices $D(\omega) \in \mathcal{D}$ and $G(\omega) \in \mathcal{G}$, such that,

$$\sup_{\omega} \bar{\sigma} \left[\left(\frac{D(\omega)\mathcal{F}_u(F(j\omega), K(j\omega))D^{-1}(\omega)}{\gamma} - jG(\omega) \right) (I + G^2(\omega))^{-\frac{1}{2}} \right] \leq 1, \quad \forall \omega \tag{4.1}$$

Unfortunately this method does not guarantee even finding local maxima. However for complex perturbations a method known as $D\text{-}K$ iteration is available (also implemented in Matlab) [11, 12]. It combines H_{∞} synthesis and μ -analysis and often yields good results. The starting point is an upper bound on μ in terms of the scaled singular value,

$$\mu(N) \leq \min_{D \in \mathcal{D}} \bar{\sigma}(DND^{-1}) \tag{4.2}$$

The idea is to find the controller that minimizes the peak over frequency of its upper bound, namely,

$$\min_K \left(\min_{D \in \mathcal{D}} \|DND^{-1}\|_{\infty} \right) \tag{4.3}$$

by alternating between minimizing $\|DND^{-1}\|_{\infty}$ with respect to either K or D (while holding the other fixed) [12, 18, 19].

1. *K-step.* Synthesize an \mathcal{H}_{∞} controller for the scaled problem $\min_K \|DN(K) \times D^{-1}\|_{\infty}$ with fixed $D(s)$.
2. *D-step.* Find $D(j\omega)$ to minimize at each frequency $\bar{\sigma}(DND^{-1}(j\omega))$ with fixed N .
3. Fit the magnitude of each element of $D(j\omega)$ to a stable and minimum phase transfer function $D(s)$ and go to Step 1.

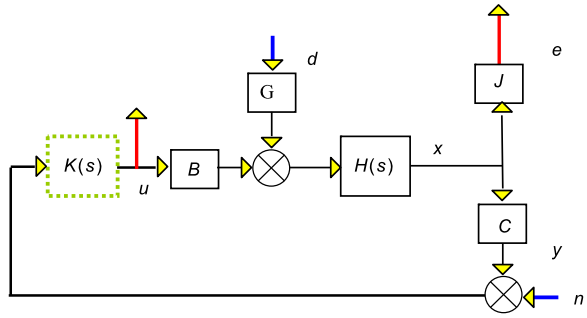
5 Relation to the Beam Control Problem

Our aim is to find the appropriate N matrix, as defined in (3.6). To this aim it is useful, to derive the input-output relations for the original model,

$$\begin{bmatrix} u \\ e \end{bmatrix} = F(s) \begin{bmatrix} d \\ n \end{bmatrix} \Rightarrow z = F(s)w \tag{5.1}$$

as depicted in Fig. 6, where the beam is described by,

Fig. 6 Beam with controller



$$\dot{\mathbf{x}}(t) = A\mathbf{x}(t) + [B \quad G] \begin{bmatrix} \mathbf{u}(t) \\ \mathbf{d}(t) \end{bmatrix} \tag{5.2}$$

$$\Rightarrow H(s) = (sI - A)^{-1} \tag{5.3}$$

and J is used to pick up those states that we are interested in regulating (may be different from y). In most of the displacements at the four nodes of the discretized structure are assumed to be measured i.e. J will be,

$$J = \begin{bmatrix} 1 & 0 & 0 & 0 & 0 & 0 & 0 & 0 & 0 & 0 & 0 & 0 & 0 & 0 & 0 \\ 0 & 0 & 1 & 0 & 0 & 0 & 0 & 0 & 0 & 0 & 0 & 0 & 0 & 0 & 0 \\ 0 & 0 & 0 & 0 & 1 & 0 & 0 & 0 & 0 & 0 & 0 & 0 & 0 & 0 & 0 \\ 0 & 0 & 0 & 0 & 0 & 0 & 1 & 0 & 0 & 0 & 0 & 0 & 0 & 0 & 0 \end{bmatrix} \tag{5.4}$$

To continue, use appropriate weighting and redraw Fig. 6 to fit our problem:

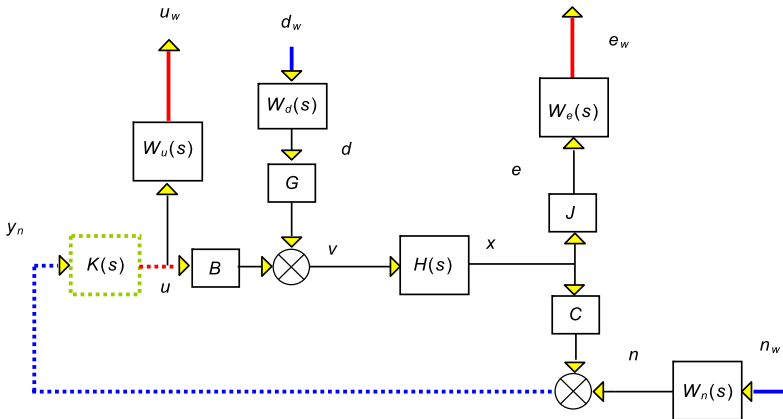
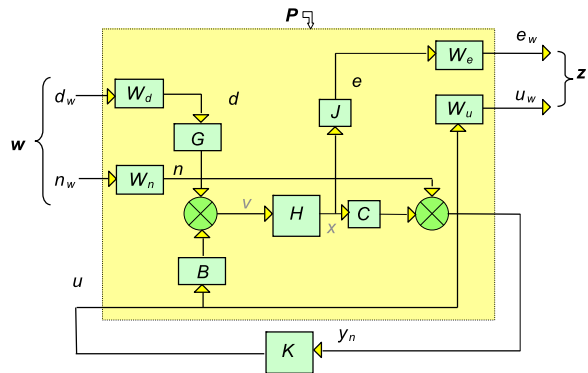


Fig. 7 Weighted block diagram for the beam problem

Then redraw Fig. 7 as a two port diagram, similar to Fig. 8:

Fig. 8 Two port diagram for the beam problem



In Fig. 8 x, v are auxiliary signals. We are looking for,

$$Q_{zw}(s) = P_{zw}(s) + P_{zu}(s)K(s)(I - P_{yu}(s)K(s))^{-1}P_{yw}(s) \quad (5.5)$$

such that,

$$z = Q_{zw}w = F_1(P, K)w \quad (5.6)$$

We need to find $P(s)$. The necessary transfer functions are,

$$\begin{aligned} e_w &= W_e J x = W_e J H v = W_e J H (G W_d d_w + B u) \\ &= W_e J H G W_d d_w + W_e J H B u \end{aligned} \quad (5.7)$$

$$u_w = W_u u \quad (5.8)$$

$$\begin{aligned} y_n &= C x + W_n n_w = C H v + W_n n_w = C H (G W_d d_w + B u) + W_n n_w \\ &= C H G W_d d_w + C H B u + W_n n_w \end{aligned} \quad (5.9)$$

Combining all these gives,

$$\begin{bmatrix} u_w \\ e_w \\ y_n \end{bmatrix} = \begin{bmatrix} 0 & 0 & \vdots & W_u \\ W_e J H G W_d & 0 & \vdots & W_e J H B \\ \cdots & \cdots & \cdots & \cdots \\ C H G W_d & W_n & \vdots & C H B \end{bmatrix} \begin{bmatrix} d_w \\ n_w \\ \vdots \\ u \end{bmatrix} \quad (5.10)$$

or,

$$\begin{bmatrix} z \\ y_n \end{bmatrix} = \begin{bmatrix} P_{zw} & P_{zu} \\ P_{yw} & P_{yu} \end{bmatrix} \begin{bmatrix} w \\ u \end{bmatrix} \quad (5.11)$$

where,

$$\begin{aligned} P_{zw} &= \begin{bmatrix} 0 & 0 \\ W_e J H G W_d & 0 \end{bmatrix}, & P_{zu} &= \begin{bmatrix} W_u \\ W_e J H B \end{bmatrix} \\ P_{yw} &= \begin{bmatrix} C H G W_d & W_n \end{bmatrix}, & P_{yu} &= C H B \end{aligned} \quad (5.12)$$

One more step is needed, however to get the Q_{ij} 's. We do this using

$$\begin{bmatrix} u \\ e \end{bmatrix} = \begin{bmatrix} (I - K C H B)^{-1} K C H G & (I - K C H B)^{-1} K \\ J (I - H B K C)^{-1} H G & J (I - H B K C)^{-1} H B K \end{bmatrix} \begin{bmatrix} d \\ n \end{bmatrix} \quad (5.13)$$

and noting that,

$$\begin{aligned}
 d &= W_d d_w, & n &= W_n n_w, & e_w &= W_e e, & u_w &= W_u u \\
 \begin{bmatrix} u \\ e \end{bmatrix} &= \begin{bmatrix} W_u^{-1} u_w \\ W_e^{-1} e_w \end{bmatrix} = F(s) \begin{bmatrix} d \\ n \end{bmatrix} = F(s) \begin{bmatrix} W_d d_w \\ W_n n_w \end{bmatrix} \Rightarrow \\
 \begin{bmatrix} u_w \\ e_w \end{bmatrix} &= \begin{bmatrix} W_u & \\ & W_e \end{bmatrix} F(s) \begin{bmatrix} W_d & \\ & W_n \end{bmatrix} \begin{bmatrix} d_w \\ n_w \end{bmatrix}
 \end{aligned} \tag{5.14}$$

or,

$$\begin{aligned}
 \begin{bmatrix} u_w \\ e_w \end{bmatrix} &= \begin{bmatrix} W_u(I - KCHB)^{-1}KCHGW_d & W_u(I - KCHB)^{-1}KW_n \\ W_eJ(I - HBKC)^{-1}HGW_d & W_eJ(I - HBKC)^{-1}HBKW_n \end{bmatrix} \\
 &\times \begin{bmatrix} d_w \\ n_w \end{bmatrix}
 \end{aligned} \tag{5.15}$$

Let us insert the previous matrices in,

$$z = Q_{zw}w \quad \text{or} \quad \begin{bmatrix} u \\ e \end{bmatrix} = \begin{bmatrix} Q_{11} & Q_{12} \\ Q_{21} & Q_{22} \end{bmatrix} \begin{bmatrix} d \\ n \end{bmatrix} \tag{5.16}$$

To express P in state space, form the natural partitioning,

$$P(s) = \left[\begin{array}{c|cc} A & B_1 & B_2 \\ \hline C_1 & D_{11} & D_{12} \\ C_2 & D_{21} & D_{22} \end{array} \right] = \begin{bmatrix} P_{zw}(s) & P_{zu}(s) \\ P_{yw}(s) & P_{yu}(s) \end{bmatrix} \tag{5.17}$$

(where the packed form has been used), while the corresponding form for K is,

$$K(s) = \left[\begin{array}{c|c} A_K & B_K \\ \hline C_K & D_K \end{array} \right] \tag{5.18}$$

Equation (5.18) defines the equations,

$$\begin{aligned}
 \dot{x}(t) &= Ax(t) + \begin{bmatrix} B_1 & B_2 \end{bmatrix} \begin{bmatrix} w(t) \\ u(t) \end{bmatrix} \\
 \begin{bmatrix} z(t) \\ y(t) \end{bmatrix} &= \begin{bmatrix} C_1 \\ C_2 \end{bmatrix} x(t) + \begin{bmatrix} D_{11} & D_{12} \\ D_{21} & D_{22} \end{bmatrix} \begin{bmatrix} w(t) \\ u(t) \end{bmatrix}
 \end{aligned} \tag{5.19}$$

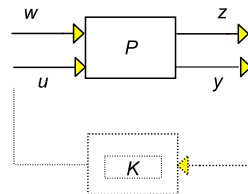
and,

$$\dot{x}_K(t) = A_K x_K(t) + B_K y(t) \tag{5.20}$$

$$u(t) = C_K x_K(t) + D_K y(t) \tag{5.21}$$

To find the matrices involved, we break the feedback loop and use the relevant equations, see Fig. 9:

Fig. 9 Open loop structure



To get the structure in state space form, relate the inputs, outputs, states and input/output to the controller:

$$\begin{aligned}
 \dot{x}_F &= Ax_F + (Gd + Bu), & x &= Ix_F \\
 \dot{x}_u &= A_u x_u + B_u u, & u_w &= C_u x_u + D_u u \\
 \dot{x}_e &= A_e x_e + B_e Jx, & e_w &= C_e x_e + D_e Jx \\
 \dot{x}_{nw} &= A_{nw} x_{nw} + B_{nw} n_w, & n &= C_{nw} x_{nw} + D_{nw} n_w \\
 \dot{x}_{dw} &= A_{dw} x_{dw} + B_{dw} d_w, & d &= C_{dw} x_{dw} + D_{dw} d_w \\
 & & y &= Cx + n
 \end{aligned} \tag{5.22}$$

Let,

$$x = \begin{bmatrix} x_F \\ x_u \\ x_e \\ x_{nw} \\ x_{dw} \end{bmatrix}, \quad y = y, \quad w = \begin{bmatrix} d_w \\ n_w \end{bmatrix}, \quad z = \begin{bmatrix} u_w \\ e_w \end{bmatrix}, \quad u = u \tag{5.23}$$

Substituting the internal signals d, n, e and x from (5.22), yields,

$$\begin{aligned}
 \begin{bmatrix} \dot{x}_F \\ \dot{x}_u \\ \dot{x}_e \\ \dot{x}_{nw} \\ \dot{x}_{dw} \end{bmatrix} &= \begin{bmatrix} A & 0 & 0 & 0 & GC_{dw} \\ 0 & A_u & 0 & 0 & 0 \\ B_e J & 0 & A_e & 0 & 0 \\ 0 & 0 & 0 & A_{nw} & 0 \\ 0 & 0 & 0 & 0 & A_{dw} \end{bmatrix} \begin{bmatrix} x_F \\ x_u \\ x_e \\ x_{nw} \\ x_{dw} \end{bmatrix} \\
 &+ \begin{bmatrix} GD_{dw} & 0 \\ 0 & 0 \\ 0 & 0 \\ 0 & B_{nw} \\ B_{dw} & 0 \end{bmatrix} \begin{bmatrix} d_w \\ n_w \end{bmatrix} + \begin{bmatrix} B \\ B_u \\ 0 \\ 0 \\ 0 \end{bmatrix} u
 \end{aligned} \tag{5.24}$$

$$\begin{bmatrix} u_w \\ e_w \end{bmatrix} = \begin{bmatrix} 0 & C_u & 0 & 0 & 0 \\ D_e J & 0 & C_e & 0 & 0 \end{bmatrix} \begin{bmatrix} x_F \\ x_u \\ x_e \\ x_{nw} \\ x_{dw} \end{bmatrix} + 0 \begin{bmatrix} d_w \\ n_w \end{bmatrix} + \begin{bmatrix} D_u \\ 0 \end{bmatrix} u \tag{5.25}$$

$$y = \begin{bmatrix} C & 0 & 0 & C_{nw} & 0 \end{bmatrix} \begin{bmatrix} x_F \\ x_u \\ x_e \\ x_{nw} \\ x_{dw} \end{bmatrix} + \begin{bmatrix} 0 & D_{nw} \end{bmatrix} \begin{bmatrix} d_w \\ n_w \end{bmatrix} + 0u \tag{5.26}$$

Therefore the matrices are:

$$A_1 = \begin{bmatrix} A & 0 & 0 & 0 & GC_{dw} \\ 0 & A_u & 0 & 0 & 0 \\ B_e J & 0 & A_e & 0 & 0 \\ 0 & 0 & 0 & A_{nw} & 0 \\ 0 & 0 & 0 & 0 & A_{dw} \end{bmatrix} \quad (5.27)$$

$$B_1 = \begin{bmatrix} GD_{dw} & 0 \\ 0 & 0 \\ 0 & 0 \\ 0 & B_{nw} \\ B_{dw} & 0 \end{bmatrix}, \quad B_2 = \begin{bmatrix} B \\ B_u \\ 0 \\ 0 \\ 0 \end{bmatrix}$$

$$C_1 = \begin{bmatrix} 0 & C_u & 0 & 0 & 0 \\ D_e J & 0 & C_e & 0 & 0 \end{bmatrix}, \quad D_{11} = 0, \quad D_{12} = \begin{bmatrix} D_u \\ 0 \end{bmatrix} \quad (5.28)$$

$$C_2 = [C \ 0 \ 0 \ C_{nw} \ 0], \quad D_{21} = [0 \ D_{nw}], \quad D_{22} = 0 \quad (5.29)$$

As can be seen, in this configuration the size of the state vector is $16 + 4 + 4 + 4 + 8 = 36$ (16 is the size of the state vector, 4 is the size of the disturbance and of the noise and 8 is the size of the errors). This (36) will also be the size of the controller model $K(s)$. This number will be decreased, if some weight matrices are constant, by their corresponding order.

6 Results for H_∞ Control

In the simulations that follow the disturbance is the first mechanical load, i.e. 10 N at the free end of the beam,

$$f_m(t) = 10 \text{ N} \quad (6.1)$$

Figure 10 shows the displacement time history at all nodal points of the beam, with and without control. Results are satisfactory, as recovery time is about 0.005 sec. We observe vibration reduction of 95 %.

Figure 11 displays the angle of rotation time history at all beam nodal points, with and without control, using H_∞ , angle of rotation tends to vanish completely.

In Fig. 12 actuator voltage is plotted for all beam nodal points. Voltage lies below 500 V, witch is the piezoelectric limit.

In the simulations that follow the disturbance is the sinusoidal load

$$f_m(t) = q_0(t) \quad (6.2)$$

$$q_0(t) = 10 \sin(0.01t) \quad (6.3)$$

In Fig. 13 displacement time history is presented for all four nodes of the beam, with and without control. We observe vibration reduction of 90 %. By employing the H_∞ control, vibration reduction is achieved; while the voltage applied is significantly lower that 500 V, which is the piezoelectric limit (Fig. 14).

Figure 15 shows the variation of angle of rotation for the four beam nodes, with and without control. Using H_∞ , angle of rotation tends to vanish completely.

Fig. 10 Displacement at beam nodal points, with and without control, for the first mechanical loading

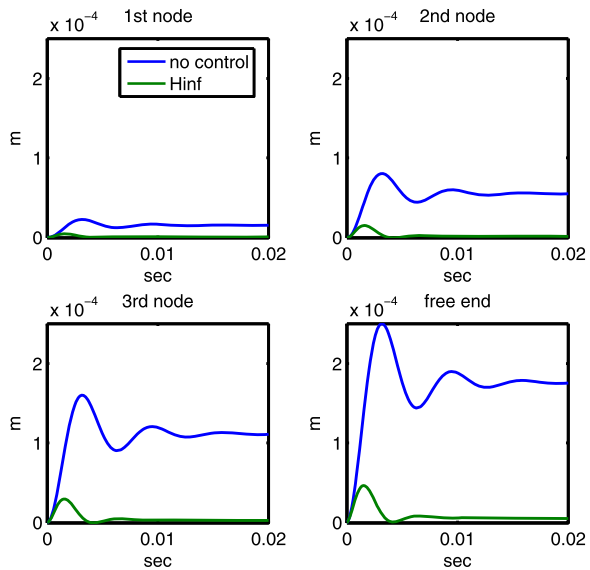
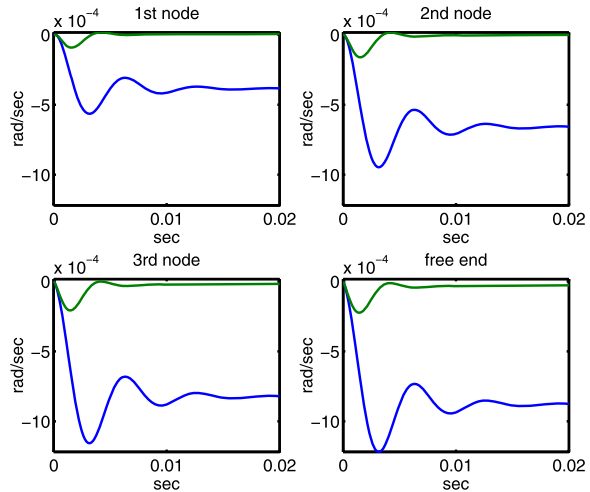


Fig. 11 Angle of rotation at beam nodal points, with and without control, for the first mechanical loading



7 Order Reduction of Controller H_∞

The H_∞ controller found is order 36. The fact that controller order, which is equal to the order of the system, is relatively higher than the order of classical controllers such as PI and LQR has led a number of researchers to develop order reduction algorithms. The most widely used such algorithm, known as HIFOO, has been implemented in a Matlab environment, and is the one used in the following procedure [8, 9].

Fig. 12 Control produced voltage at beam nodal points

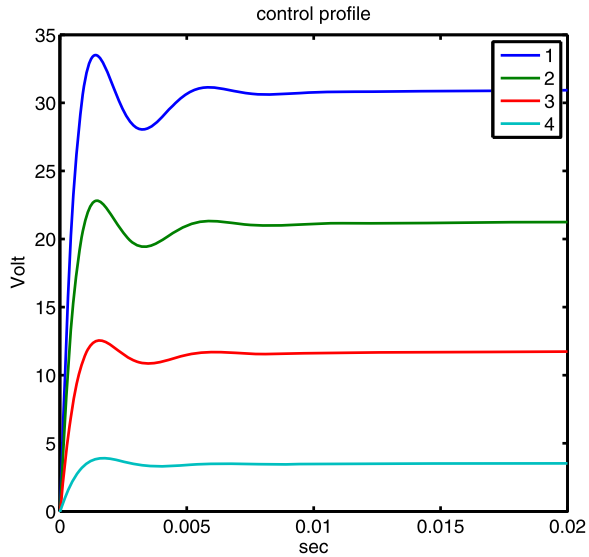
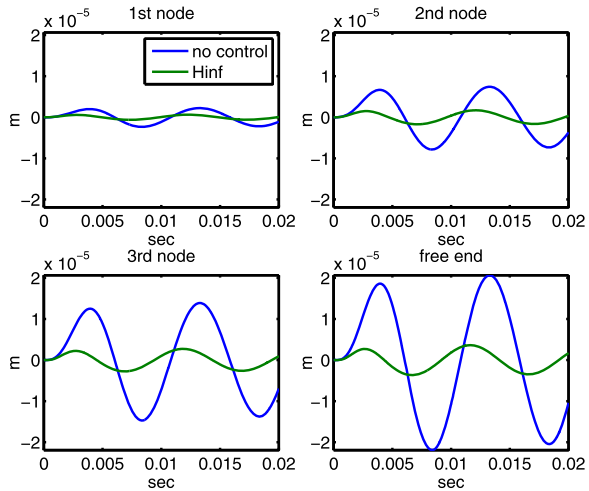


Fig. 13 Displacement at beam nodal points, with and without control, for the second mechanical loading



The general problem is to compute a controller of reduced order $n < 36$ while retaining the performance of the H_∞ criterion as well as the behaviour of a full order controller for the given system [7, 8].

As already mentioned that, the state space equations of our system are

$$\begin{aligned} \dot{x}(t) &= Ax(t) + B_1w(t) + B_2u(t) \\ z(t) &= C_1x(t) + D_{11}w(t) + D_{12}u(t) \\ y(t) &= C_2x(t) + D_{21}w(t) + D_{22}u(t) \end{aligned} \tag{7.1}$$

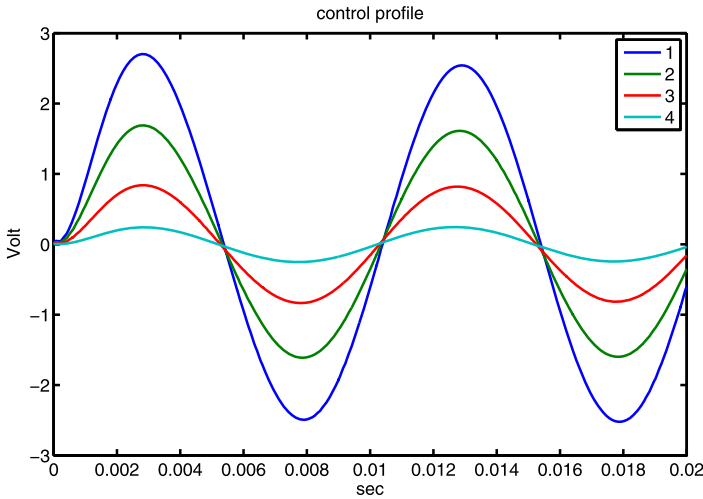
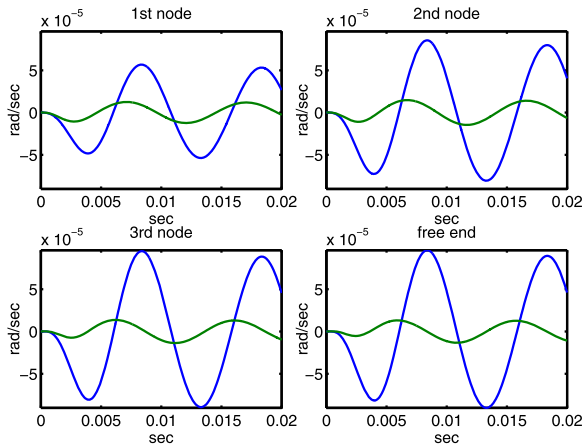


Fig. 14 Control produced voltage at beam nodal points, for the second mechanical loading

Fig. 15 Angle of rotation at beam nodal points, with and without control, for the second mechanical loading



and the state space equations for the controller K are

$$\begin{aligned} \dot{x}_K(t) &= A_K x_K(t) + B_K y(t) \\ u(t) &= C_K x_K(t) + D_K y(t) \end{aligned} \tag{7.2}$$

Let $\alpha(X)$ be the spectral abscissa of a matrix X that is the maximum real part of its eigenvalues. Then, we require not only that $\alpha(A_{CL}) < 0$, where A_{CL} is the closed-loop system matrix, but that $\alpha(A_k) < 0$ as well. The feasible set of A_k , that is the set of stable matrices, is not a convex set and has a boundary that is not smooth [6, 10].

The HIFOO procedure has two phases: stability and performance optimization [9, 20]. In the stability phase, HIFOO attempts to minimize

$$\max(\alpha(A_{CL}, \varepsilon\alpha(A_{CL}))) \quad (7.3)$$

where ε is a positive parameter that will be described shortly, until a controller is found for which this quantity is negative, that is the controller is stable and makes the closed-loop system stable. In case it is unable to find such a controller, HIFOO terminates unsuccessfully.

In the performance optimization phase, HIFOO searches for a local minimizer of

$$f(K) = \begin{cases} \infty & \text{if } \max(\alpha(A_{CL}, \varepsilon\alpha(A_K))) \geq 0 \\ \max(\|T_{zw}\|_\infty, \varepsilon\|K\|_\infty) & \text{otherwise} \end{cases} \quad (7.4)$$

where

$$\|K\|_\infty = \sup_{R_{s=0}} \|C_K(sI - A_K)^{-1}B_K + D_K\|_2 \quad (7.5)$$

The introduction of ε is motivated by the fact that the main design objective is to attain closed-loop system stability and to minimize $\|T_{zw}\|_\infty$, by demonstrating that ε should be relatively small; the term $\varepsilon\|K\|_\infty$, however, prevents the controller H_∞ norm from becoming too large, in which case the stability constraint by itself would not exist. Given that it is preceded by the stability phase, the performance optimization phase is initialized with a finite value of $f(K)$. Consequently, when it reaches a value of K for which $f(K) = \infty$, that value is rejected, since an objective reduction is sought at each iteration [9, 20].

8 Results Using Controller HIFOO

As mentioned before, the HIFOO controller is implemented in Matlab by way of appropriate routines. It is called in the following manner:

$$\text{Kfoo} = \text{hifoo}(\text{plant}, 2)$$

where `plant` is the system description in the form of Eqs. (7.1), and $n = 2$ is controller order.

The resulting controller is described in state space in similar manner as H_∞ , i.e.

$$\begin{aligned} \dot{x}_K(t) &= A_K x_K(t) + B_K y(t) \\ u(t) &= C_K x_K(t) + D_K y(t) \end{aligned} \quad (8.1)$$

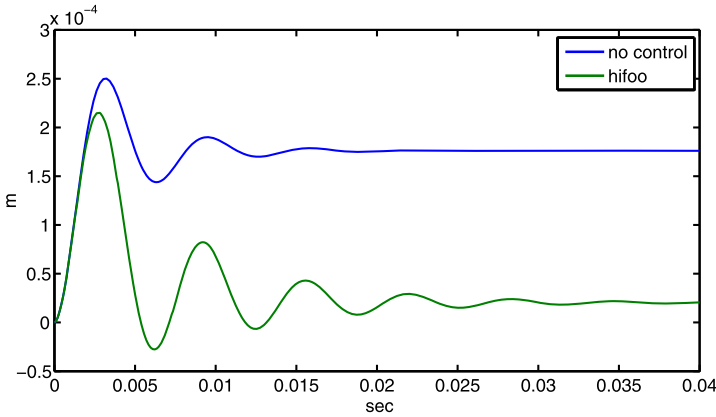


Fig. 16 Beam free end displacement, with and without HIFOO control, for the first mechanical input

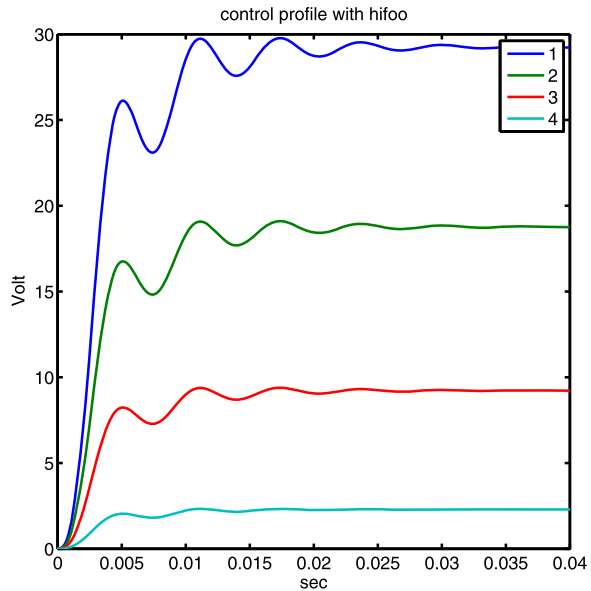
The controller state space equation is given by relation (7.5), where controller matrices are equal to

$$\begin{aligned}
 A_K &= \begin{bmatrix} 728.1 & -5034 \\ 207.5 & -1408 \end{bmatrix} \\
 B_K &= \begin{bmatrix} 212.8 & 811.6 & 1716 & 2810 \\ -164.9 & -637.2 & -1348 & -2207 \end{bmatrix} \\
 C_K &= \begin{bmatrix} 1557 & -916.7 \\ 1013 & -592.3 \\ 517 & -297.9 \\ 144.3 & -82.59 \end{bmatrix} \\
 D_K &= \begin{bmatrix} 36.1 & 136.6 & 287.1 & 468.3 \\ 23.5 & 87.69 & 186.5 & 303 \\ 12.12 & 44.12 & 93.39 & 154.3 \\ 4.204 & 12.53 & 26.92 & 43.51 \end{bmatrix}
 \end{aligned} \tag{8.2}$$

For the purpose of comparison of HIFOO controller performance to that of H_∞ , the beam free end response is examined, for the first and third mechanical input.

For the first mechanical input, equilibrium recovery time for the free end is 0.03 sec, as shown in Fig. 16, and maximum upward displacement is 2×10^{-4} , while steady state error is 10^{-7} . The maximum produced voltage for the control of the end node is 30 V, as shown in Fig. 17. Using H_∞ the free end restores equilibrium within 0.02 sec, as shown in Fig. 10, and its maximum upward displacement is 0.3×10^{-4} , while steady state error is 10^{-9} . The maximum produced voltage is 35 V, as shown in Fig. 12. Therefore, the HIFOO controller exhibits slightly inferior results with respect to all criteria, higher steady state error, longer equilibrium recovery time and larger upward displacement; however, it has lower energy demand and lower order.

Fig. 17 Stress at beam nodal points, using HIFOO, for the first mechanical input



It can be observed that by using the HIFOO controller, a reduction of system controller order is achieved, while beam position is controlled with node displacements of order of 10^{-7} . The H_∞ criterion performance is thus retained while a lower order controller is used.

The steady state error is 3×10^{-5} , while using the H_∞ controller it is 0.5×10^{-5} (Fig. 16). The maximum produced voltage for the HIFOO controller is 30 V; the respective value is 35 V for the H_∞ controller [19]. In other words, beam adjustment to its equilibrium position is achieved with a lower order controller that requires lower voltage.

9 Conclusions

A finite element based modelling technique for the determination of the smart system was presented. Firstly we examine the H_∞ criterion. The advantage of the H_∞ criterion is in its ability to take into account in the computations the worst result of uncertain disturbances or noise in the system. It is possible to synthesize an H_∞ controller which will be robust with respect to a predefined number of uncertainties in the model. The results are very good: the oscillations were suppressed, with the piezoelectric components' voltages within their endurance limits.

Using nonsmooth and nonconvex optimization we reduce the order of the H_∞ controller. The good performance of the controller was made even for a lower order of the system. We reduce vibration with small recovery time and the piezoelectric patches in their endurance limits.

References

1. Balamurugan V, Narayanan S (2002) Finite element formulation and active vibration control study on beams using smart constrained layer damping (SCLD) treatment. *J Sound Vib* 249(2):227–250
2. Foutsitzi G, Marinova D, Hadjigeorgiou E, Stavroulakis G (2002) Finite element modelling of optimally controlled smart beams. In: 28th summer school: Applications of mathematics in engineering and economics, Sozopol
3. Foutsitzi G, Marinova D, Hadjigeorgiou E, Stavroulakis G (2003) Robust H_2 vibration control of beams with piezoelectric sensors and actuators. In: Proceedings of physics and control conference (PhyCon03), St Petersburg, 20–22 August, vol I, pp 158–163
4. Miara B, Stavroulakis G, Valente V (2007) Topics on mathematics for smart systems. In: Proceedings of the European conference, Rome, 26–28 October 2006. World Scientific, Singapore
5. Moutsopoulou A, Pouliezios A, Stavroulakis GE (2008) Modelling with uncertainty and robust control of smart beams. In: Topping BHV, Papadrakakis M (eds) Proceedings of the ninth international conference on computational structures technology. Civil Comp Press, Stirling, Paper 35
6. Burke J, Overton ML (2001) Variational analysis of non-Lipschitz spectral functions. *Math Program* 90:317–352
7. Burke J, Lewis A, Overton ML (2005) A robust gradient sampling algorithm for nonsmooth nonconvex optimization. *SIAM J Optim* 15:751–779
8. Burke J, Henrion D, Lewis A, Overton ML (2006) Stabilization via nonsmooth, nonconvex optimization. *IEEE Trans Autom Control* 51:1760–1769
9. Burke J, Henrion D, Lewis A, Overton ML (2006) HIFOO a Matlab package for fixed-order controller design and H_∞ optimization. In: IFAC symposium on robust control design, Toulouse. <http://www.cs.nyu.edu/overton/papers/pdf/hifoo-rocond.pdf>
10. Hinrichsen D, Pritchard AJ (2005) Mathematical systems theory I: modelling, state space analysis, stability and robustness. Texts in applied mathematics, vol 48. Springer, New York
11. Packad A, Doyle J, Balas G (1993) Linear, multivariable robust control with a m perspective. *J Dyn Syst Meas Control* 115(2b):310–319 (50th anniversary issue)
12. Pouliezios A (2006) MIMO control systems, class notes. <http://pouliezios.dpem.tuc.gr>
13. Stavroulakis GE, Foutsitzi G, Hadjigeorgiou E, Marinova D, Baniotopoulos CC (2005) Design and robust optimal control of smart beams with application on vibrations suppression. *Adv Eng Softw* 36(11–12):806–813
14. Friedman J, Kosmatka K (1993) An improved two node Timoshenko beam finite element. *Comput Struct* 47:473–481
15. Tiersten HF (1969) Linear piezoelectric plate vibrations. Plenum, New York
16. Zhang N, Kirpitchenko I (2002) Modelling dynamics of a continuous structure with a piezoelectric sensor/actuator for passive structural control. *J Sound Vib* 249:251–261
17. Sisemore C, Smaili A, Houghton R (1999) Passive damping of flexible mechanism system: experimental and finite element investigation. In: The 10th world congress of the theory of machines and mechanisms, Oulu, vol 5, pp 2140–2145
18. Yang SM, Lee YJ (1993) Optimization of non collocated sensor, actuator location and feedback gain and control systems. *Smart Mater Struct* 8:96–102
19. Zhang X, Shao C, Li S, Xu D (2001) Robust H_∞ vibration control for flexible linkage mechanism systems with piezoelectric sensors and actuators. *J Sound Vib* 243(1):145–155
20. Millston M (2006) HIFOO 1.5: structured control of linear systems with a non trivial feedthrough. MS thesis, Courant Institute of Mathematical Sciences, New York University

A Risk-Based Decision Making Methodology for Planning and Operating Safe Infrastructure Systems Against Various Hazards

Yiannis Xenidis and Demos C. Angelides

Abstract Decision-making for infrastructure systems is a difficult task to perform because of the complexity and the variety of the types of risks that may occur in the different phases of the life-cycle of an infrastructure system. To overcome these difficulties a new methodology for a risk-based decision making for planning and operating infrastructure systems is proposed. This methodology integrates: (i) the variability of impact upon risk occurrence, (ii) the available risk-response strategies, and (iii) the preference of the decision maker over these strategies with regard to the criticality of the various impacts upon risk occurrence. The proposed methodology considers four risk-response strategies, namely: (a) acceptance, (b) mitigation, (c) transfer, and (d) avoidance. Three approaches are applied, in order to determine the preference margins between these strategies: (i) compliance with regulations and specifications, (ii) determination based on data elaboration, and (iii) subjective judgment. Once, the expected value of the impact upon risk occurrence is estimated, the decision maker is capable to decide for the respective risk-response. An application example is presented as a proof-of-concept of the proposed methodology.

Keywords Risk · Infrastructure · Decision making · Life-cycle · Resilient systems

1 Introduction

Infrastructure systems are characterized of great interdependencies, which are mostly identifiable, yet difficult to model. Therefore, their efficiency in improving everyday life for people, as well as their contribution to the economy and societal wealth can only partially be estimated by traditional tools and techniques. These estimations become even more difficult when risks of all kinds of nature are considered. Natural hazards like floods become more intensive due to climate

Y. Xenidis (✉) · D.C. Angelides

Aristotle University of Thessaloniki, University Campus, 54124, Thessaloniki, Greece
e-mail: ioxen@auth.gr

D.C. Angelides

e-mail: dangelid@civil.auth.gr

changes, while earthquakes still remain difficult to foresee. Infrastructure reliability and functionality are very critical and require appropriate risk response strategies, which can successfully ensure the long-term sustainability of infrastructure systems.

The introduction of the concept of resilience for infrastructure systems constitutes a new and rapidly evolving approach that provides a different perspective to the design and monitoring of infrastructure systems [1, 2]. Resilience may be, generally, considered as a system property that allows a quick recovery after a major risk occurrence [3, 4]. The recovery can be, generally, defined as a stable system's state that allows operation to a specific service level depending on the system. Therefore, resilience does not imply a full system recovery, but rather the necessary one that ensures continuity of the system's functionality to predetermined and required levels. A comprehensive analysis of the resilience concept can be found in [4].

Measuring resilience is a difficult task, because it requires a good insight of the system's structure and operation [5]. When the system is complex and prone to inherent uncertainties with regard to its function, measuring resilience becomes a, really, rough work to do. On the other hand, while resilience is inherent to the system, there is a definite interaction between the system and the system's environment that renders the process of recovery, not solely dependent on the system's resilience, but also on the actions that aim to alleviate the risk impact, which are normally decided in the framework of a risk response action plan. Therefore, a system's safety against stresses (occurred risks) is a combination between several parameters and hardly a system's property [6].

A complementary approach to resilience measurement for ensuring infrastructure system's functionality is the application of the proper risk-response strategies against anticipated risks. A properly designed and applied risk-response strategy that successfully corresponds to the system's requirements for recovery facilitates and accelerates the system's reaction against the damage from the occurred risk. Risk-response strategies can be decided through various decision making methods; however, most of them present two serious limitations when they are considered for application in infrastructure systems: (a) they do not address, in any way, the systems' characteristics to the decision making process and (b) they treat systems' complexity in a rather descriptive, than analytic fashion. The following section presents some well-established and widely applied decision making methods and argues about their limitations for infrastructure systems.

This chapter presents a risk-based decision making approach that aims at providing risk-response decisions for infrastructure systems that consider both the systems' characteristics and the system's complexity. The first feature, i.e. the systems' characteristics, is introduced in an indirect way; a risk analysis that may be performed by any traditional or innovative method produces the values of risks that the system is prone to. However, since the risk value is considered as the expected value of a risk impact and this impact is directly related to the system's characteristics, it is inferred that in an indirect way these characteristics are addressed to the decision making process. The second feature, i.e. the system's complexity, is introduced

by the comparison of the best risk-response decisions for different criteria and the homogenization of these decisions to one that optimally responds to all criteria simultaneously. The final output is a single decision for responding to a specific risk that the system faces.

The chapter is structured in the following way: (a) Sect. 2 presents the complexity and characteristics of infrastructure systems, (b) Sect. 3 presents groups of decision-making methods with potential application to infrastructure systems, (c) Sect. 4 describes the theoretical concept of the proposed risk-based decision making approach and presents an application example as a proof-of-concept and to facilitate understanding and demonstrate the mode of application, and (d) Sect. 5 concludes and discusses about the limitations, perspectives and future work towards the improvement of the proposed approach.

2 Complexity and Characteristics of Infrastructure Systems

The term infrastructure includes certain characteristics that despite various definitions constitute a common ground for the stakeholders involved, i.e. public agencies, professional and financial organizations, academia, and, of course, the end-users. Fulmer in [7] quotes some definitions that, as he concludes, share the characteristics of interrelated systems, physical components and societal needs; therefore, he provides the following broad—yet meaningful—definition of infrastructure: “*the physical components of interrelated systems providing commodities and services essential to enable, sustain, or enhance societal living conditions*”.

These interrelated systems that include from transportation, energy, water and waste management, and communications works to industrial facilities, hospitals, schools, social welfare facilities, museums, and stadiums, typically consist components of greater networks that span extensive geographic scales and operate in a highly complicated and interdependent mode. The importance of certain among others infrastructure systems for a society and economy, as well as, their complexity, in terms of comprised components renders them the critical infrastructure of a society.

Infrastructure constitutes an asset with a long-term horizon that is rarely replaced as a whole after the completion of its life-cycle; in fact, infrastructure is not replaced at all. Interventions that aim to maintain or expand its operational capacity to the future are feasible for individual components of the infrastructure system. That prolongation of the functionality of infrastructure in different time-periods leads to variations of economic, technological and operational lives of the infrastructure components, which increases complexity in infrastructure operation and maintenance.

Having identified, in brief, the main characteristics of infrastructure systems, the next step is to investigate the decision-making methods, which are potentially applicable to problems related to these systems.

3 Decision-Making Methods and Their Limitations for Infrastructure Systems

Many decision making methods have been developed that present different levels of complexity and suitability for the various decision making problems. From basic methods that apply to everyday life's occasions to more sophisticated ones that are introduced in the cases of complex problems, there are two main approaches in the philosophy of the decision making: (a) the decision is made based on the preference of the expected output compared to the expected outputs of other decision alternatives or (b) the decision is made based on the problem's analysis that clearly suggests the best treatment for the problem in hand.

In order to select the appropriate decision-making method for a specific type of problem it is a prerequisite to understand the nature of the problem. Decisions regarding infrastructure have a simultaneous impact to multiple levels: a financial decision reflects to the operational and technical capacity of the infrastructure, while a technical decision affects the operational standards and has financial implications, etc. The interdependencies among the infrastructure systems are very well highlighted in [8]:

- A. Functional interdependencies, which include serial functioning (i.e. the function of one component requires input from another) or overlapping functioning among system components.
- B. Physical interdependencies, which include the share of physical attributes, such as distribution channels built in a building's wall.
- C. Budgetary interdependencies, which include various funding schemes in terms of structure and stakeholders.
- D. Market and economy interdependencies, which include cross-sector interactions in an economic framework.
- E. Legal and regulatory interdependencies, which include shared means of governing infrastructure systems.

In [9] Müller is cited for suggesting that infrastructure must be placed in a comprehensive context including, except from the physical (technical) assets, the non-technical ones, i.e. the operational techniques, the organizational aspects and the service-related processes.

In the following subsections some well-established methods that constitute the state-of-the-art in decision making are very briefly described, in order to provide the basis for consideration of their efficiency for infrastructure systems.

3.1 Elementary Methods

Elementary methods are mostly applied to relatively simple decision making problems and they do not require either special knowledge or specific skills. "Pros and

Cons” and “weighted Pros and Cons” methods rate the advantages and the disadvantages between alternative decisions and the alternative that presents the strongest pros and the weakest cons prevails [10].

Plus/Minus/Interesting method introduces except from pros and cons, the probable impact of the alternative decisions and through simple numerical rating it does not only suggest an optimum decision among alternatives, but also examines whether the selected alternative: (a) shall improve the decision situation and (b) is applicable or not [11].

Payoff matrices are used in combination with optimistic, realistic or pessimistic criteria (e.g. maximax-minimin, Hurwicz criterion, maximin-minimax) to identify the best tradeoff between a decision and its output [12].

Conjunctive and disjunctive methods evaluate decision alternatives by comparison to a given threshold and only those alternatives that reach a satisfactory level compared to the threshold are acceptable for implementation [13].

The above methods are not designed for complex problems; therefore their structure prevents their application to such problems. With the exception of conjunctive and disjunctive methods, the rest of the others fail to address the system’s characteristics to the decision making process in a systematic or quantified way.

3.2 Graphical Methods

Graphical methods comprise influence diagrams (fault-trees, event-trees, and cause and effect diagrams) and decision-trees. They incorporate uncertainty by assigning probabilities to the different decision nodes and they can map system’s processes. However, there are two major limitations for application to infrastructure systems:

- A. They are highly impractical for complex systems. The complexity due to the operations and the interdependencies between infrastructure systems and the excessive data over their performance, which can be available through the implementation of appropriate, modern monitoring systems result to a difficulty to apply traditional methods such as probabilistic risk assessment, especially for decision-making [14]. This difficulty is mainly due to the unavoidable due to complexity, discrete calculations of risks for specific infrastructure components and their propagation through, e.g. decision-trees, which results to an incremental assessment that the more complicated the system is, the more time-consuming it gets.
- B. The system’s mapping is deterministic, i.e. each branch of a tree describes a “road map” from the initial event (decision) to the final output, which is stable and independent from interdependencies and unexpected events. This deterministic mapping is unable to capture simultaneous, multi-components failures caused by hazards, such as, for example, natural disasters, while—at the same

time—it hardly provides useful information on the performance of the system’s individual components [14].

Both limitations render graphical decision making methods inappropriate for application to infrastructure systems’ decision situations.

3.3 Multi-attribute Utility Theory (MAUT) Methods

MAUT is a theoretical framework that can deal with complex decision problems that feature a large number of criteria and decision alternatives. MAUT methods are characterized from the use of utility functions that express the preference of the decision maker over the various decision criteria for different decision alternatives. The final decision is selected through a process that utilizes dimensions-free scales that allow for comparison between different, in nature, criteria. A great number of methods and techniques are based on MAUT such as SMART, Generalized means, UTA, AHP, etc. The main limitation of these methods, which is systemic and related to the methodological approach, is that the decision criteria are weighted according to the preference of the decision maker and the final decision is made based on the aggregate of the products between these weights and the expected values of the decision’s output for the criteria. This approach overlooks the actual impact of a decision and instead it correlates it with the factual (quantitative) or judgmental (qualitative and mostly subjective) preference of the decision maker. The importance of this limitation can be understood by the following examples:

- Example A: Tom decides to go to the movies and he has to choose between two options (AL_1 and AL_2) based on the criteria of distance from home (DH) and time of the movies start off (TS). According to his preferences by using any MAUT method, the final decision will come up to a problem generally described in the following equations:

$$AL_1 = w_{DH} \times DH_1 + w_{TS} \times TS_1 \quad (1)$$

$$AL_2 = w_{DH} \times DH_2 + w_{TS} \times TS_2 \quad (2)$$

In Eqs. (1) and (2), w_{DH} and w_{TS} are Tom’s weights (preferences) for each decision he used. The maximum value between AL_1 and AL_2 indicates the optimum decision for Tom. However, this optimum decision does not, in fact, consider the real values of the criteria (i.e. real distance, real start off time), but, only, some weighted values that reduce or increase the real ones according to Tom’s preferences.

- Example B: A public authority decides to take measures to increase the safety of a bridge against earthquake. The appropriate measures result to two options and they are evaluated based on the criteria of bridge functionality and technical reliability (after the application of the measures). In this example, the relativity, which is an inherent feature in decisions drawn through MAUT methods may easily alter the real data and result to doubtful decisions.

The systemic limitation of MAUT methods that has been identified and described above, along with certain other limitations that each one of the methods discretely suffers from, renders them questionable for application to infrastructure systems, where real values of impact from a risk or stress should not be altered for the process of decision making.

3.4 Outranking Methods

Outranking methods may also be applied to complex systems and they also use weights for the different decision criteria; however, they are significantly different to MAUT methods. The most important difference is that outranking methods do not evaluate the alternatives based on a maximum score over certain criteria with different preferences, but, instead, they make pair wise comparisons between alternatives based on actual measurements. Outranking methods, such as ELECTRE and PROMETHEE methods, are able to compare any two different alternatives fully or partially, in the case where there are no available data or information for all the criteria used. Application of these methods results to a ranking between them and the first alternative in this ranking is the selected decision. The main limitations of outranking methods are: (a) complexity, (b) requirement of a strong mathematical background for application, and (c) computational limits, i.e. these methods are not applicable for decision problems with many alternatives. These limitations render outranking methods questionable for application to infrastructure systems.

3.5 Statistical Learning Theory Methods

Statistical learning theory methods have, also, been applied for decision-making in infrastructure systems. They can be considered as a complement to graphical methods that incorporate a probabilistic computational framework and, provided that they are carefully applied they can supply results at the system-level, which can be supportive for decision-making [14]. Their main drawback is the capacity they can exhibit, which is strongly dependent to the available data in hand. The dependence of statistical methods to the quality of data is an inherent difficulty that significantly affects their accuracy, as well as, their capacity to predict, which is restricted to the limits defined by previously recorded incidents of risk occurrences. Given the complexity and dynamic nature of infrastructure systems, statistical learning theory methods may be considered as hard to apply in this field.

4 A New Approach for Risk-Based Decision Making for Resilient Systems

In the previous section the current practice in decision making was briefly discussed and the main findings were that for various reasons the existing methods present significant limitations for application to infrastructure systems. Effective decision-making methods for infrastructure systems need to address the methodological challenges referred to [15]:

- A. The complexity of infrastructure, which is traced in many levels: from the multiple dependencies between system components to the multiple operational outcomes from the combination of the various technologies and material characteristics including the economic and organizational implications.
- B. The interdependencies of infrastructure systems components that form a complex network of interactions with direct implications both inside and outside the system.
- C. The comprehensive approach for risk-based decision-making that is required, irrespectively, of sector particularities.
- D. The identification and treatment of the various risk perceptions that the different stakeholders in infrastructure systems present.
- E. The lack of adequate data to apply, safely, a decision-making process.
- F. The homogenization to a single scale of the various impacts from the occurrence of a single or various risks. As consequences vary, it is required to establish a common ground of assessing various losses, which are not directly comparable inter se. The use of comparators such as economic value is not always applicable (e.g. human loss, environmental degradation, etc.).

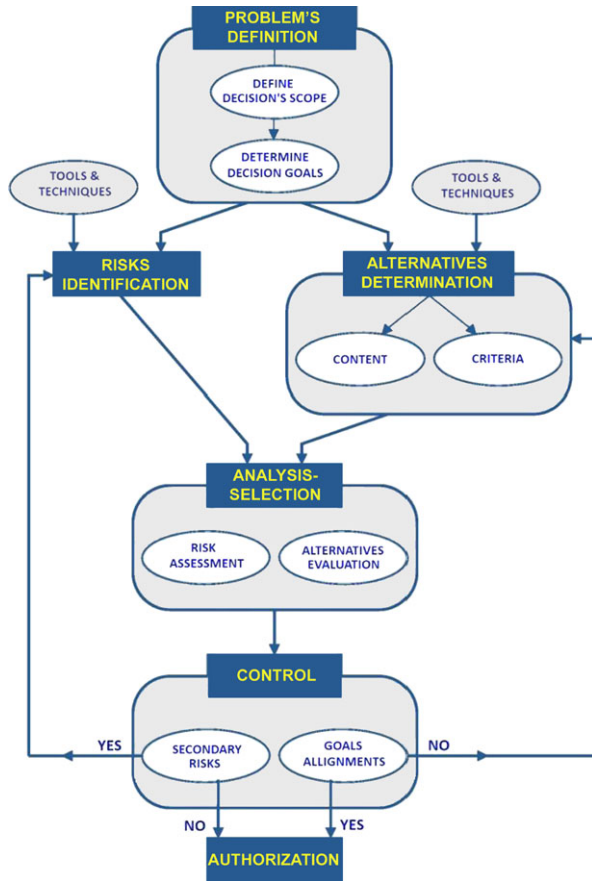
A new approach that can effectively address the above-mentioned challenges and overcome the limitations recorded in the previous section is presented and demonstrated thereafter, through an application example.

4.1 Risk-Based Decision Making Process

Risk-based decision making is a process that should follow certain steps (sub-processes) as illustrated in Fig. 1.

The first step is the problem's definition, which includes the clear and concise determination of the involved stakeholders' requirements. Given these requirements, the scope of the decision is defined and the determination of the respective goals to attain is achieved. Once, the decision situation problem is clearly defined, the next steps are to identify both the involved risks and the alternative decisions that can potentially serve the achievement of the goals set in the previous step. The alternative decisions must be well described in terms of their content, i.e. required processes, expected impact, etc., as well as criteria that are, one by one, associated to the predetermined goals. Both processes are performed through appropriate

Fig. 1 Risk-based decision making process flowchart



tools and techniques, which are extensively used in risk analysis and scenario analysis (e.g. Delphi method, SWOT analysis, information gathering techniques, etc.). The analysis that considers, simultaneously, the outputs of the previous steps, i.e. the risks and the alternative decisions, results through risk assessment and alternatives evaluation to the selection of the best decision in terms of satisfaction of the stakeholders' requirements. This decision is then checked for goals alignment and secondary risks that may arise upon its application and if the control results are acceptable then it is approved, while if not, the whole process is repeated from step 2, until it reaches acceptance.

In this chapter, a new methodology is proposed that complies with the generic risk-based decision making process, as described above, and achieves to integrate the various strategies that are optimum for each different impact upon the occurrence of a specific risk to one single strategy that best confronts simultaneously all the different impacts on the system. In order to facilitate understanding, the methodology is presented through an application example.

4.2 *The Proposed Methodology Through an Example of Application*

Suppose an infrastructure system that is of critical importance for the economic and social life of a specific area. Such a system may be a highway road, an airport, a wind farm, a public service building, etc. Infrastructure systems during their life-cycle are prone to several and different risks that can cause severe damages once they occur. Examples of such risks are all the types of failure caused by a natural hazard (earthquake, flood, fire, etc.), material failure, terrorist act, etc. The potential occurrence of one of these risks results to certain damages that are evaluated in a different way among those affected (stakeholders) by the risk event. Therefore, at every stage when a decision is required for the determination of the appropriate risk response strategy, the latter depends on the requirements and specifications set by these stakeholders.

In the case of a nuclear power plant, for example, the main priority is set to supply energy with a steady rate through a safe production process. The achievement of these goals must be ensured against a wide range of risks during the operation of the power plant. An example of one of these risks is recorded in Table 1.

Table 1 presents a hypothetical record in a risk inventory used for risk identification. The identified risk, given in the second row of the table, is classified and analyzed in terms of: (a) the factors that lead to its occurrence, (b) the symptoms (components) that are visible in different levels of risk occurrence and (c) the impact, which is the result of the risk event upon occurrence. This type of inventory along with certain innovative notions such as the “component” term is based on research performed by Angelides et al. [16].

The alternative decisions that need to be investigated, in relation to the identified risk, in order to determine the optimum among them that ensures the achievement of the decision’s goals (i.e. constant energy supply in an environmental friendly mode) are: (a) risk acceptance, (b) risk mitigation, (c) risk transfer, and (d) risk avoidance. These alternatives are essentially the recommended risk response strategies proposed by the Project Management Body of Knowledge [17], which apply, in general, to all types of projects or situations. Table 2 provides a detailed description of the alternative decisions in terms of content, required processes, and expected impact adjusted to the example of application.

Table 1 A record of a risk for a power plant

Code	TECH 1.1
Name	Risk of failure due to earthquake
Class	Technical
Factors	Heavy earthquake loads that exceed the facilities’ structural strength
Components	Cracks in walls, deformations, production fall
Impact	Repair costs, loss of revenue, injuries, fatalities, pollutants emissions

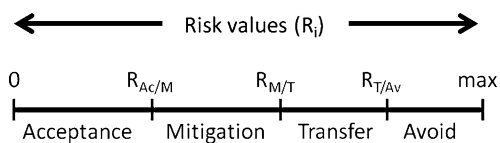
Table 2 Alternative decisions for dealing with the risk of failure due to earthquake for a power plant

Alternative decision	Risk acceptance	Risk mitigation	Risk transfer	Risk avoidance
Content description	A decision that aims at assuming liability for the negative impact upon risk occurrence. Recommended for insignificant risks.	A decision that aims at the reduction of the risk to an acceptable threshold.	A decision that aims at shifting to a third party, the negative risk impact, along with ownership of the response. Risk transfer only indirectly deals with risk.	A drastic decision that aims to eliminate either the risk factors or the risk impact. It involves even project cancellation. Recommended for very significant risks.
Application mode	Establish a contingency reserve to use in case of failure.	Reinforce critical elements of the structure. Design an action plan for quick response.	Insurance. Performance bonds. Guarantees. Risk transfer contracts.	Establishment of the facilities to a non-seismic area. Change of goals.
Expected impact	Undertake the cost for the system's recovery after the occurrence of the risk.	Limit the negative effect to an acceptable level.	Ensure compensations from a third party for the harmed stakeholders in case of failure.	Eliminate risk.

The alternative risk response strategies analyzed in Table 2 may be quantified either according to regulations, specifications, and legal frameworks or based on the strategy and policy of the organization that operates the power plant.

The criteria over which the alternative decisions are evaluated need to be consistent with the final decision's goals. They also need to be of quantitative nature, in order to define the thresholds that will constitute the boundaries of transition between the alternative decisions. These boundaries, in fact, define the ranges that correspond to the respective risk response strategies or, in other words, all the estimated risks define a range from zero value to a maximum value, which is further divided to smaller ranges that each one of them corresponds to the respective decision alternative. A generic example of the quantified relation between the risks and the risk response strategies is illustrated in Fig. 2.

Fig. 2 Quantification of the alternative decisions for one decision criterion



For the example under study, the following criteria are set:

- Minimization of the compensation costs due to a system’s failure (SCC). The quantification of the alternative decisions with regard to the SCC criterion may be based on: (a) the risk analysis that is conducted by the facility’s administration, and (b) the attitude towards risks that the facility’s administration adopts. However, there are also cases where a regulatory approach defines the liabilities in case of nuclear plants accidents. Such a case is the Price-Anderson Act in USA that ensures the availability of certain amounts of money that must be used in case of accidents in nuclear power plants [18]. Figure 3 illustrates numerically the alternative decisions for the example under study based on the Price-Anderson Act’s provisions [18]. In specific: (a) the amount of \$830 thousand, which is the average annual premium for a single-unit reactor site has been considered as the limit between the “Risk acceptance” and the “Risk mitigation” alternatives, (b) the amount of \$375 million, which is the annual premium paid by the nuclear power plant’s owners in private insurance for offsite liability coverage for each reactor unit has been considered as the limit between the “Risk mitigation” and the “Risk transfer” alternatives, (c) the amount of \$12 billion, which is the maximum level that the industry self-insurance fund can reach, in order to be readily available for losses exceeding the \$375 million threshold, has been considered as the limit between the “Risk transfer” and the “Risk avoidance” alternatives, and (d) the amount of \$600 billion, which is the cost of the Chernobyl nuclear accident—the most catastrophic in many terms including monetary—according to estimates [19], has been considered as the final threshold.

Any risk R that has a value R_{C_i} with regard to the SCC criterion results to the respective alternative decision according to the following relations:

$$[0, 600 \times 10^9] = \Theta^C, \quad C_i \in \Theta^C \tag{3}$$

$$\forall R_{C_i} \in [0, 830 \times 10^3] \rightarrow \text{Risk acceptance} \tag{4}$$

$$\forall R_{C_i} \in [830 \times 10^3, 375 \times 10^6] \rightarrow \text{Risk mitigation} \tag{5}$$

$$\forall R_{C_i} \in [375 \times 10^6, 12 \times 10^9] \rightarrow \text{Risk transfer} \tag{6}$$

$$\forall R_{C_i} \in [12 \times 10^9, 600 \times 10^9] \rightarrow \text{Risk avoidance} \tag{7}$$

In Fig. 3, “Ac” stands for “Risk acceptance”, “M” stands for “Risk mitigation”, “T” stands for “Risk transfer”, and “Av” stands for “Risk avoidance”. It should be noted that the ranking of the alternatives is consistent with the risk impact. Therefore, it is assumed that the smaller impact is manageable for the decision maker (risk acceptance), while the larger impact is intolerable for both the decision maker and any third party (risk avoidance).

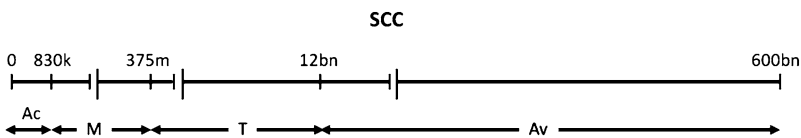


Fig. 3 Quantification of the alternative decisions for the SCC decision criterion

- Prevention of human injury or fatality (HIF). The quantification of the alternative decisions with regard to the HIF criterion may vary in terms of the adopted approach. One way, for example, is to apply threshold values, which are drawn from the legal framework that regulates the health and safety issues in each case. Another well-established approach is to evaluate the severity of a non-fatal accident according to the hours or days of absence from work [20]. Specific thresholds stand to differentiate between non-injuries, light injuries, fair, and severe injuries. The case of human loss is, of course, the worst scenario and the upper boundary in the HIF criterion. In the case of the presented example in this paper, the alternative decisions for the HIF criterion are distinguished based on the impact of exposure to radiation on humans. The values are drawn from [21] and they correspond to the following conditions: (a) 2 mSv (millisievert) is the annual amount of radiation that humans are exposed to in the natural environment, (b) 100 mSv is the quinquennial-annual amount of radiation that could be recommended for workers in related occupations, (c) 1000 mSv is the single dose that, although not fatal, could have adverse effects (e.g. sickness, nausea, etc.) for a human’s health, and (d) 5000 mSv is the single dose that could be fatal for half of those exposed to it within a month. Any exposure to radiation in doses higher than 5000 mSv results to fatalities within certain time periods (the highest the dose, the fastest the fatality). Figure 4 illustrates the numerical representation of the alternative decisions for this criterion. The notations in Fig. 4 are identical to the respective in Fig. 3.

Any risk R that has a value R_{HL_i} with regard to the HIF criterion results to the respective alternative decision according to the following relations:

$$[0, 5.000] = \Theta^{HL}, \quad HL_i \in \Theta^{HL} \tag{8}$$

$$\forall R_{HL_i} \in [0, 2] \rightarrow \text{Risk acceptance} \tag{9}$$

$$\forall R_{HL_i} \in [2, 100] \rightarrow \text{Risk mitigation} \tag{10}$$

$$\forall R_{HL_i} \in [100, 1.000] \rightarrow \text{Risk transfer} \tag{11}$$

$$\forall R_{HL_i} \in [1.000, 5.000] \rightarrow \text{Risk avoidance} \tag{12}$$

Again, as in the case of the SCC criterion, the ranking of the alternatives is consistent with the risk impact. Therefore, it is assumed that the smaller impact is manageable for the decision maker (risk acceptance), while the larger impact is intolerable for both the decision maker and any third party (risk avoidance).

- Prevention of environmental pollution (ENP). The quantification of the alternative decisions with regard to the ENP criterion can be based on the correspondence of radiation releases to the International Nuclear Event Scale (INES) [22]. Based on the values given in [23] and INES, the numerical example illustrating the ENP criterion is presented in Fig. 5. The notations in this figure are identical to the respective in Figs. 3 and 4.

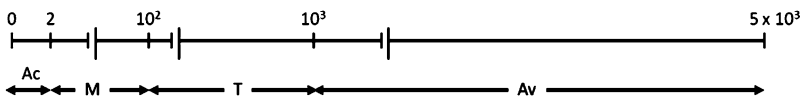


Fig. 4 Quantification of the alternative decisions for the HIF decision criterion

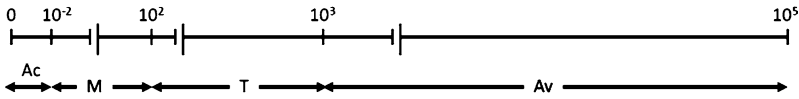


Fig. 5 Quantification of the alternative decisions for the ENP decision criterion

Any risk R that has a value R_{E_i} with regard to the ENP criterion results to the respective alternative decision according to the following relations:

$$[0, 10^5] = \Theta^E, \quad E_i \in \Theta^E \tag{13}$$

$$\forall R_{E_i} \in [0, 10^{-2}] \rightarrow \text{Risk acceptance} \tag{14}$$

$$\forall R_{E_i} \in [10^{-2}, 10^2] \rightarrow \text{Risk mitigation} \tag{15}$$

$$\forall R_{E_i} \in [10^2, 10^3] \rightarrow \text{Risk transfer} \tag{16}$$

$$\forall R_{E_i} \in [10^3, 10^5] \rightarrow \text{Risk avoidance} \tag{17}$$

The same assumption made in the previous two criteria concerning the ranking of the alternatives stands for this criterion as well.

Once, the evaluation criteria of the alternative decisions are determined, the risk-based decision making process steps to the next stage, which is the analysis, based on actual risk estimations and the evaluation of the decision alternatives. It is important to notice that the process assumes the interdependency of the criteria. This assumption, although not always valid, does not reduce the effectiveness of the methodology, since the integration to one decision is independent of the interdependency between the criteria.

Risk quantification can be generally performed by Eq. (18).

$$\text{Risk} = E[h] = \int h(\theta) \times p(\theta) d(\theta) \tag{18}$$

where θ denotes the uncertainty that characterizes the risk occurrence, which is expressed by a probability density function $p(\theta)$, while the overall impact upon risk occurrence can be measured by a Risk Consequence Measure $h(\theta)$. Equation (18) expresses the expected value of the risk, which is a well-established approach on the field for risk quantification. This expected value in the case of the example under study must be estimated for the three different criteria. Therefore, the identified risk (Risk of failure due to earthquake) must be quantified in terms of impact to the system's recovery costs, the human losses and the environmental pollution. This quantification is performed by proper adjustment of Eq. (18). The mathematical expression for each case is given in Eqs. (19)–(21):

$$R_{C_i} = \int h_{C_i}(\theta) \times p(\theta) d(\theta) \tag{19}$$

$$R_{HL_i} = \int h_{HL_i}(\theta) \times p(\theta) d(\theta) \tag{20}$$

$$R_{E_i} = \int h_{E_i}(\theta) \times p(\theta) d(\theta) \tag{21}$$

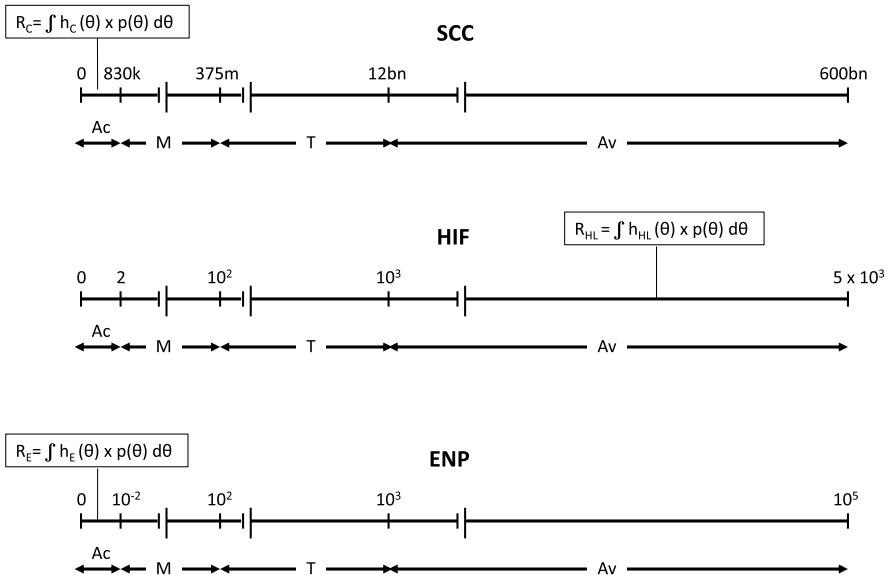


Fig. 6 Assignment of risk values to the alternative decisions ranges per criterion

In Eqs. (19)–(21), h_{C_i} measures in monetary terms the impact of the risk occurrence with regard to the SCC criterion, h_{HL_i} measures in mSv, the impact of the risk occurrence with regard to the HIF criterion, and h_{E_i} measures in mSv/h the impact of the risk occurrence with regard to the ENP criterion. Provided that the necessary data for the values in Eqs. (19)–(21) are available, the equations result to specific values that can be placed in the respective ranges of the previously defined alternative decisions for each criterion. Figure 6 illustrates graphically an example of this step of the process. As shown there, for the example under study, the same risk requires three different decisions, for the three different decision criteria respectively: (a) the proper decision with regard to the SCC criterion is “Risk acceptance”, (b) the proper decision with regard to the HIF criterion is “Risk avoidance”, and (c) the proper decision with regard to the ENP criterion is “Risk acceptance”. It is obvious that if the analysis would indicate, also, “Risk acceptance” for the HIF criterion, then the decision maker would decide this alternative for the specific risk. However, in this case the decision maker needs to compare the alternative decisions for each criterion and select the most appropriate one that satisfies simultaneously all the criteria. While in the case of the example, the selection of “Risk avoidance” may be considered “an easy choice”, since preventing human loss is a top priority, the general approach requires an objective way to compare all the alternatives for all the criteria between them.

Due to the fact that different measures are used for each criterion, it is essential to transform the different scales from the three criteria to one single scale, in order to allow comparison between the alternative decisions. This can be easily achieved by dividing the values of the boundaries between the alternative decisions to the

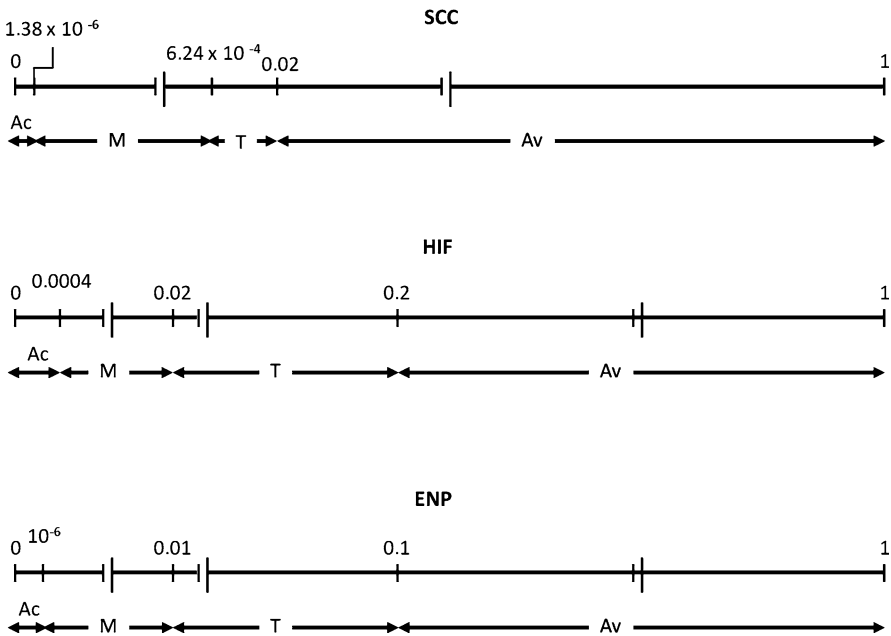


Fig. 7 The dimensions-free scales for each criterion for the example under study

maximum value of the risk for each criterion. Essentially, the original scales are transformed to dimensions-free scales in the interval $[0, 1]$, where 0 corresponds to the minimum value of the risk, 1 corresponds to the maximum value of the risk, and the values in between correspond to the boundaries of the alternative decisions. Figure 7 graphically illustrates the dimensions-free scales for each criterion (the scales of the axes are approximate due to design limitations).

Another critical issue, which should be considered for the appropriate comparison between the alternative decisions, is the preference of the decision maker for the various alternatives for each criterion. For example, as stated above, it can be, generally, expected that there is a stronger preference to avoid human loss compared to the preference of spending a large amount for maintenance costs to reduce the risk of failure due to earthquake. However, it is not easy to generalize a preference, e.g. of taking measures for environmental protection (risk mitigation for the ENP criterion) compared to a fair amount of equipment replacement costs (risk acceptance for the SCC criterion). Therefore, a systematic way that will denote preference of the decision maker of the alternative decisions evaluated over different criteria is required. The proposed approach is based on the concept of utility, which addresses the preference of the decision maker between different alternative decisions. Utility theory has been used extensively with many variations in the field of decision making [24–26].

For each criterion of the alternative decisions, the decision maker defines the appropriate utility function that best represents his preference considering the

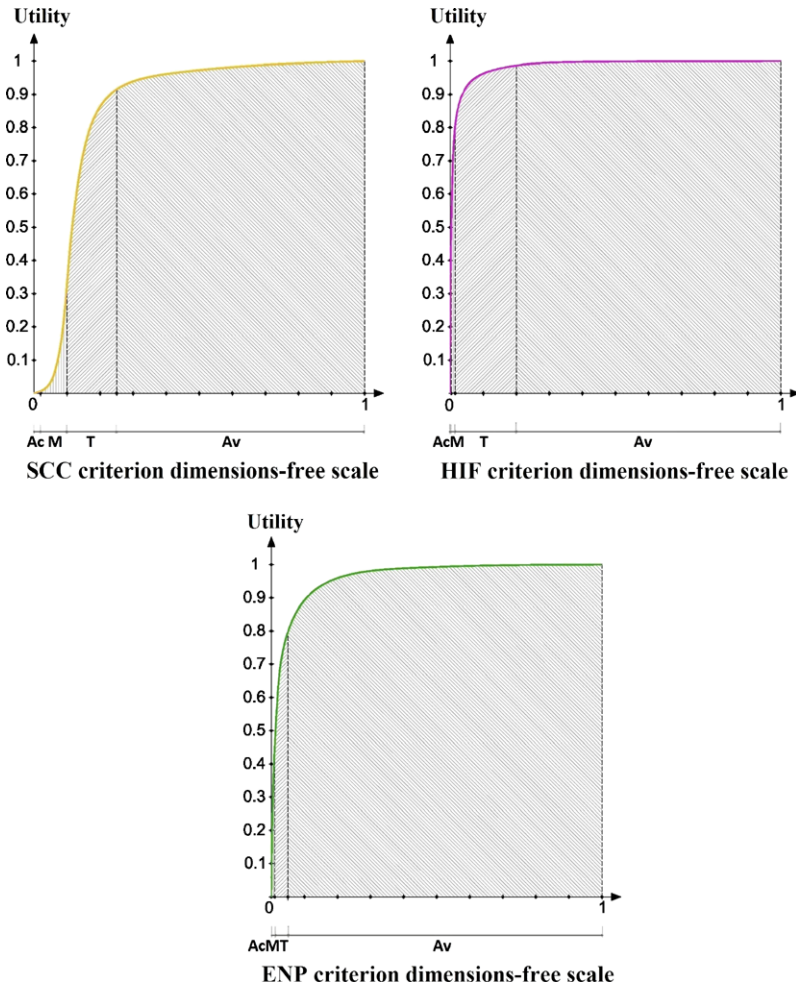


Fig. 8 Calculations of the utilities of the alternative decisions for each criterion

parameter of risk. The utility functions are defined in the set $[0, 1]$ as they are in concordance with the dimensions—free scales for each criterion. Since the boundaries for each alternative decision are known from the previous steps, the overall preference of each different alternative is calculated by the area defined by the function’s curve, the x axis and the utility values for each boundary value of the alternative decision. Figure 8 illustrates a graphical example of this calculation and the numerical results are presented in Table 3.

The calculation of utilities for each alternative decision per criterion facilitates the comparison of the alternatives and consequently the decision making process for the decision maker. Concerning the example under study, the risk analysis indicated a risk acceptance for the SCC and ENP criteria, and risk avoidance for the

Table 3 Utility values for the alternative decisions for each criterion

Criterion	Alternative decision	Utility
SCC	Risk acceptance	0.00058
	Risk mitigation	0.07361
	Risk transfer	1.13112
	Risk avoidance	7.33324
HIF	Risk acceptance	0.01106
	Risk mitigation	0.08325
	Risk transfer	1.76021
	Risk avoidance	7.98551
ENP	Risk acceptance	0.00001
	Risk mitigation	0.02922
	Risk transfer	0.27364
	Risk avoidance	9.29736

HIF criterion (see Fig. 6). An objective comparison between the two alternative decisions, which is based on the numerical results that are presented in Table 3, clearly suggests the “risk avoidance” decision as the most preferable (the one that corresponds to the maximum utility value).

Some interesting observations of the numerical results in Table 3 prove the logical consistency of the approach:

- In the case where each of the three criteria corresponds to a different alternative decision the most risk averse decision of all three always predominates.
- The HIF criterion, compared to the other two criteria consistently presents greater utility values for the same alternative decision. This is not the case only for the “risk avoidance” decision between the HIF and ENP criteria; however it is not unreasonable to consider a human injury or fatality as less important compared to an incident of major environmental pollution with long-term catastrophic effects on every form of life.

5 Conclusions

Infrastructure systems are very critical for the society and the economy. In a challenging situation with severe risks of different nature and magnitude, it becomes crucial to define those limit states of the systems that will ensure functionality and serviceability right after the occurrence of a risk and a fast system recovery to the operational levels before the occurrence of the risk.

Resilience is a concept that responds to the above requirements. However, due to the high complexity of infrastructure systems and their interdependencies both between the system’s parameters and between the system and its environment, the

measurement of resilience becomes a very difficult task to perform. A complementary approach, which indirectly provides estimation for the system's resilience is the application of the proper risk-response strategies against anticipated risks. Therefore, appropriate decision making is required.

Currently, several decision making methods and techniques exist that are well-established and in some cases, they are very sophisticated, in terms of methodological approach or mathematical background. However, they all present various limitations both in general and for application to infrastructure systems, in particular.

This chapter presents a methodology for risk-based decision making that is characterized by the following features:

- It considers the variability of impact upon risk occurrence by using appropriate risk values, which are estimated for each criterion under study. Instead of the traditional approach, that of integrating different risk values to a single one that, allegedly, denotes an overall risk value, the proposed methodology utilizes actual risk values that correspond to the different decision criteria.
- It involves the preference of the decision maker not in a way that alters the evaluation criteria of the decision as is done in MAUT methods, but, rather, in a way that is restricted to the expression of tolerance of certain risk events in case they occur. This means that the boundaries for the alternative decisions with regard to different stresses are predefined and constant, regardless of the risk event and any per case variation of the preference of the decision maker.
- It compares preference of decisions instead of preference of alternatives. This means that the risk analysis that precedes the decision making process provides results that directly indicate the appropriate decision regarding a specific criterion and then these decisions are compared and the most preferred is selected.
- It involves risk-response strategies for which the decision maker has decided that they respond to the system's requirements for increasing resilience.

The proposed methodology allows the overcoming of some limitations of well-established decision making methods in the problem of deciding the appropriate risk-response strategies for infrastructure systems. In this way, it becomes a potentially valuable tool for an indirect definition of resilience in these highly complex systems, which are prone to various failures that occur simultaneously under a single or multiple stresses.

Acknowledgements This work has been supported by the Project "Integrated European Industrial Risk Reduction System (IRIS)", No. CP-IP 213968-2, funded by the European Union FP7. The authors, also, acknowledge the valuable contribution of Mrs. A. Skiadopoulou, who actively supported this research work and co-authored the paper that provided the basis for this chapter.

References

1. Vugrin ED, Warren DE, Ehlen MA, Camphouse RC (2010) A framework for assessing the resilience of infrastructure and economic systems. In: Gopalakrishnan K, Peeta S (eds) Sustainable and resilient critical infrastructure systems: simulation, modeling, and intelligent engineering. Springer, Berlin, pp 77–116

2. CIP program discussion paper series (2007) Critical thinking: moving from infrastructure protection to infrastructure resilience. George Mason University
3. Gao F (2010) The proposed resilience analysis methodology and its application to the Suskwater pumping station. MSc thesis, Department of Mechanical Engineering, University of Saskatchewan, Saskatoon
4. Hollnagel E, Woods DD, Leveson N (eds) (2006) Resilience engineering: concepts and precepts. Ashgate, Aldershot
5. Nemeth CP (2008) Resilience engineering: the birth of a notion. In: Hollnagel E, Nemeth CP, Dekker S (eds) Resilience engineering perspectives: remaining safe to the possibility of failure, vol I. Ashgate, Aldershot, pp 3–9
6. Hollnagel E, Woods DD (2006) Epilogue: resilience engineering precepts. In: Hollnagel E, Woods DD, Leveson N (eds) Resilience engineering: concepts and precepts. Ashgate, Aldershot
7. Fulmer JE (2009) What in the world is infrastructure? PEI Infrastructure investor, pp 30–32
8. Zhang P, Peeta S (2011) A generalized modeling framework to analyze interdependencies among infrastructure systems. *Transp Res, Part B, Methodol* 45(3):553–579
9. Nielsen SB, Elle M (2000) Assessing the potential for change in urban infrastructure systems. *Environ Impact Asses Rev* 20(3):403–412
10. Baker D, Bridges D, Hunter R, Johnson G, Krupa J, Murphy J, Sorenson K (2001) Guidebook to decision making methods. WSRC-IM-2002-00002, Department of Energy, USA
11. De Bono E (1992) Serious creativity: using the power of lateral thinking to create new ideas. Harper Collins, New York
12. Skiadopoulou AS (2010) Risk-based decision making. MSc thesis, Department of Civil Engineering, Aristotle University of Thessaloniki, Thessaloniki (in Greek)
13. Fülöp J (2005) Introduction to decision making methods. Working paper 05-6, Laboratory of Operations Research and Decision Systems, Computer and Automation Institute, Hungarian Academy of Sciences, Budapest
14. Guikema SD (2009) Natural disaster risk analysis for critical infrastructure systems: an approach based on statistical learning theory. *Reliab Eng Syst Saf* 94(4):855–860
15. Utne IB, Hokstad P, Kjolje G, Vatn J, Tondel IA, Bertelsen D, Fridheim H, Rostum J (2008) Risk and vulnerability analysis of critical infrastructures—the DECRIS approach. SAMRISK, Oslo
16. Angelides D, Xenidis Y, Loukogeorgaki E, Vrakas D, Diamantoulaki I (2010) Development of the risk paradigm: the risk assessment tool [presentation]. IRIS European research project, WP-4 meeting, Bucharest, March 29–30, 2010
17. Project Management Institute (2008) A guide to the project management body of knowledge, 4th edn. Project Management Institute, Newtown Square
18. United States National Regulatory Commission (2011) Fact sheet on nuclear insurance and disaster relief funds. <http://www.nrc.gov/reading-rm/doc-collections/fact-sheets/funds-fs.html>. Accessed 30 March 2012
19. Cooper M (2011) Nuclear liability: the market-based, post-Fukushima, case for ending Price-Anderson. In: Bulletin of the atomic scientists, web edition. <http://www.thebulletin.org/web-edition/features/nuclear-liability-the-market-based-post-fukushima-case-ending-price-anderson>. Accessed 30 March 2012
20. United States Department of Labor, Occupational Safety & Health Administration (2003) Voluntary protection programs (VPP): policies and procedures manual. http://www.osha.gov/pls/oshaweb/owadisp.show_document?p_id=2976&p_table=DIRECTIVES#appendixA. Accessed 20 October 2010
21. The Guardian (2011) Radiation exposure: a quick guide to what each levels means. <http://www.guardian.co.uk/news/datablog/2011/mar/15/radiation-exposure-levels-guide#data>. Accessed 14 March 2012
22. International Atomic Energy Agency (2009) INES—the international nuclear and radiological event scale user’s manual, 2008 edn. International Atomic Energy Agency, Vienna

23. Hoetzlein RC (2011) Fukushima radiation—comparison map. <http://www.rchoetzlein.com/theory/2011/fukushima-radiation-comparis>. Accessed 14 March 2012
24. Von Neumann J, Morgenstern O (1944) Theory of games and economic behavior, 3rd edn. Princeton University Press, Princeton
25. Keeney RL, Raiffa H (1976) Decisions with multiple objectives: preferences and value trade-offs. Wiley, New York
26. Jacquet-Lagreze E, Siskos Y (1982) Assessing a set of additive utility functions for multicriteria decision making: the UTA method. *Eur J Oper Res* 10(2):151–164

On Practical Performance of a Technique for More Efficient Dynamic Analysis in View of Real Seismic Analysis of Bridge Structures

Aram Soroushian, Akbar Vasseghi, and Mahmood Hosseini

Abstract Time history analysis is a broadly accepted versatile approach, for real seismic analyses. In the most general case, time history analysis is based, on time integration, for which, the computational cost might be intolerable. For reducing the computational cost, a technique is recently proposed, based on replacing the digitized excitations, with excitations, digitized, at larger steps. After several successful implementations, of the technique, arriving at a deeper insight, into the practical performance, is the objective, here. Attention is paid to the significant role of bridges, at major earthquakes, and, a multi-span concrete bridge, designed according to the existing codes, and later upgraded laterally, by nonlinear steel shear keys, is selected. By carrying out time integration analyses, against earthquakes in consistence with the design codes, it is demonstrated that: (a) implementation of the technique can be well effective in reducing the computational costs of real seismic analyses, (b) when the nonlinearities are not severe, the effect of nonlinearity on the performance is trivial, (c) the assumptions, essential, in order to implement the technique, can be simplified, for seismic analyses.

Keywords Structural dynamic analysis · Time integration · Step size · Accuracy · Computational cost · Strong ground motion · Structural design codes

1 Introduction

In order to protect buildings, bridges, infrastructures, lifelines, etc., against earthquakes, the structures need to be designed properly, taking into account the details of structural dynamic behaviours. National and international seismic codes permit simplified analyses, for some cases [1–3]. Nevertheless, the most broadly implemental approach, for analyzing structures seismic behaviours, is to discretize the

A. Soroushian (✉) · A. Vasseghi · M. Hosseini
Structural Engineering Research Centre, International Institute of Earthquake Engineering and Seismology (IIEES), Tehran, Iran
e-mail: aramsoro@yahoo.com

A. Soroushian
e-mail: a.soroushian@iiees.ac.ir

mathematical models, in space, and try to solve the resulting semi-discretized equations of motion [4–6],

$$\mathbf{M}\ddot{\mathbf{u}}(t) + \mathbf{f}_{\text{int}} = \mathbf{f}(t), \quad 0 \leq t < t_{\text{end}} \tag{1}$$

considering the initial conditions,

$$\begin{aligned} \mathbf{u}(t = 0) &= \mathbf{u}_0 \\ \dot{\mathbf{u}}(t = 0) &= \dot{\mathbf{u}}_0 \end{aligned} \tag{2}$$

$$\mathbf{f}_{\text{int}}(t = 0) = \mathbf{f}_{\text{int}_0}$$

and, if existing, the additional constraints [4–9]

$$\begin{aligned} \mathbf{Q}_1 &= 0 \\ \mathbf{Q}_2 &\leq 0 \end{aligned} \tag{3}$$

In Eqs. (1)–(3), t and t_{end} represent the time and the duration of the dynamic behaviour, \mathbf{M} is the mass matrix, $\mathbf{f}(t)$ and \mathbf{f}_{int} stand for the vectors of excitation and internal force, $\mathbf{u}(t)$, $\dot{\mathbf{u}}(t)$, and $\ddot{\mathbf{u}}(t)$, respectively denote the unknown vectors of displacement, velocity, and acceleration, \mathbf{u}_0 , $\dot{\mathbf{u}}_0$, and $\mathbf{f}_{\text{int}_0}$, define the initial status of the model (regarding the essentiality, of considering $\mathbf{f}_{\text{int}_0}$, in Eq. (1), also see [7, 10]), and \mathbf{Q}_1 and \mathbf{Q}_2 imply some restricting conditions, e.g. additional constraints, in problems, involved in impact or elastic-plastic behaviour [11, 12]. For the general case, when the damping is un-classical, the natural frequencies are very close, or the behaviour is nonlinear, time integration is the superior analysis approach. As a brief review on time integration, the analysis starts from the initial conditions (when needed, after implementing appropriate starting procedures, e.g. see [13]), and proceeds, with a march, throughout the integration interval, and determining the unknowns, i.e. displacements, velocities, and internal forces, at distinct consecutive integration stations (see Fig. 1). Because of the complexity of exact integration formulation [14, 15], the mathematical relations leading to the determination of the unknowns, are algebraic approximations, implying the implemented integration method (e.g. Houbolt method [13, 16, 17], Newmark family [18], the central difference method [19]), and the nonlinearity solution methods (in nonlinear problems) [20], e.g. Newton Raphson, modified Newton Raphson, arc-length, and fractional-time-stepping [20–25].

In view of the approximation and the computational expensiveness, originated in the step-by-step nature, of time integration, special attention is being paid to the number and size of integration steps. The integration step size, Δt , is introduced

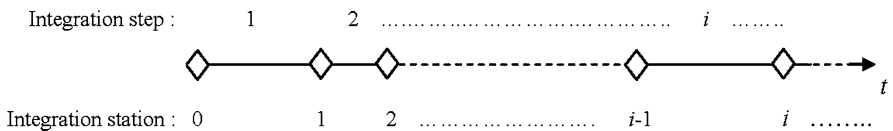


Fig. 1 Typical arrangement of the steps and stations in time integration analyses

[26], as a parameter, by changing which, the sizes of integration steps (see Fig. 1) change uniformly, throughout the integration interval (when the steps are equally sized, Δt equals the actual size of the integration steps). Apparently, any change in Δt implies an adverse change in computational cost, and affects the accuracy. Regarding the latter, the fundamental essentiality of approximate analyses is convergence [26–31], which, in time integration analyses, results in the relation, below:

$$\lim_{\Delta t \rightarrow 0} R_{app} = R \tag{4}$$

In Eq. (4), R stands for an arbitrary component of the response, \mathbf{R} , and R_{app} implies the approximate value computed for R . From Eq. (4), it is reasonable to consider the computed responses, more accurately (in an overall sense), when, Δt is smaller. Therefore, in general, more accuracies and less computational costs do not come together, and hence, the selection of Δt is crucial, from the standpoints of computational cost and accuracy. For cases, with equally-sized integration steps, a comment, for assigning appropriate values to Δt [21, 32–34], is as noted below:

$$\begin{aligned} \Delta t &= \text{Min}\left(\frac{T}{10}, \Delta t_s, \Delta t_r\right) \quad \text{for linear problems} \\ \Delta t &= \text{Min}\left(\frac{T}{100}, \Delta t_s, \Delta t_r\right) \quad \text{for nonlinear problems} \end{aligned} \tag{5}$$

In Eqs. (5), T is the smallest dominant period of oscillations, Δt_s (generally equal to infinity) stands for the largest Δt , providing numerical stability, and Δt_r is the step size, according to which, we like to record the computed responses.

In seismic analyses, the $\mathbf{f}(t)$, in Eq. (1), originates in strong ground motions, generally, as a function of the ground acceleration $\ddot{u}_g(t)$, i.e.

$$\mathbf{f}(t) = - \begin{bmatrix} \alpha_1 \\ \alpha_2 \\ \vdots \\ \alpha_N \end{bmatrix} \ddot{u}_g(t) \tag{6}$$

where, α_i is a constant real number, depending on the structural model; and, denoting the number of degrees of freedom [4, 6], by N , for many cases,

$$\alpha_1 = \alpha_2 = \dots = \alpha_N = 1 \tag{7}$$

In general, $\ddot{u}_g(t)$, is available, as a digitized record, e.g. see [14, 32, 33, 35], leading to the replacement of Eqs. (5) with:

$$\begin{aligned} \Delta t &\leq \text{Min}\left(\frac{T}{10}, \Delta t_s, \Delta t_r, \Delta t_f\right) \quad \text{for linear problems} \\ \Delta t &\leq \text{Min}\left(\frac{T}{100}, \Delta t_s, \Delta t_r, \Delta t_f\right) \quad \text{for nonlinear problems} \\ \Delta t &= \frac{\Delta t_f}{m}, \quad m \in \mathbb{Z}^+ \end{aligned} \tag{8}$$

where, Δt_f stands for the step size, by which, \ddot{u}_g is recorded, and m is the smallest positive integer, resulting in a value for Δt , satisfying the first two relations, in Eqs. (8). When, Δt_f is the governing term, in Eqs. (8), i.e.

$$m = 1, \quad \Delta t = \Delta t_f < \text{Min}\left(\frac{T}{10 \text{ (or 100)}}, \Delta t_s, \Delta t_r\right) \quad (9)$$

some computational cost is being spent, not, for the accuracy of integration, but, for considering the total strong ground motion, and preserving the accuracy of the analysis. The significance, of this computational cost, highlights, when the structural model is large, complicated, and nonlinear, and the restrictions existing on computational facilities, cause the additional computational cost to be intolerable.

Based on the fact that Eqs. (8) and (9) are valid, for analyses, against general digitized excitations, a technique is recently proposed, for replacing the digitized excitations, with excitations, digitized, at larger steps [26]. The replacement is computationally cheap, and when considering the new excitations, instead of the original excitations, the responses differ, from the responses, computed, by conventional integration, only negligibly. The issue of the accuracy is discussed indirectly, in view of convergence [26], and is demonstrated numerically, via the implementation, of the technique, in seismic analyses, of many structural systems [26, 36–49]. The results were all adequate, and even better, compared to that provided by other very recent techniques [33, 50–54]. In continuance, herein, attention is paid to bridges, and the performance, of the technique, regarding real bridges structural dynamic analyses.

Bridges can be considered as lifeline structural systems, with crucial role, before occurrence of earthquakes (and any other natural disaster), regarding regular lives and performance of social systems, and, after earthquakes, regarding the save and rescue programs. As structural systems, the behaviours of bridges can be studied, in view of, the model, typically, stated in Eqs. (1)–(3). The performance of the technique, regarding the analyses, is briefly addressed, in a paper, presented, at the COMPDYN 2011 conference [36] (the paper is available at <http://cogress.cimne.com/eccomas/proceedings/compdy2011/> and as an ebook at [http://www.eccomas.org/cvdata/cntr1/spc26/dtos/web/\\$modir/ThematicConf//COMPDYN-2011—Proceedings.pdf](http://www.eccomas.org/cvdata/cntr1/spc26/dtos/web/$modir/ThematicConf//COMPDYN-2011—Proceedings.pdf)). Herein, through a more detailed and practical study, the performance of the technique is examined in linear and nonlinear seismic analyses of bridge structural systems, against several major earthquakes, consistent, with the design codes (in the sense that both the code and the records are associated with an identical region). Regarding the consistency, it is worth noting that, in spite of all the studies on the recently proposed technique [26, 36–49], this, and the very recent MSc thesis [47], on multi-storey buildings, are the first publications, at which, the earthquakes and design codes are being set consistently. A bridge structural system is once considered, as conventionally designed (according to the existing codes [55]), and then, again, after being laterally upgraded, by some nonlinear steel shear keys. In Sect. 2, the recently proposed technique is briefly reviewed. In Sect. 3, the two structural models, together with four strong ground motions are

introduced. In Sect. 4, the results, obtained, from the implementation of the technique, in seismic analyses, are reported. The observations and the implementation of the technique, in real analyses, are discussed, in Sect. 5, and finally, with a brief review, on the achievements, the chapter is concluded, in Sect. 6.

2 The Recently Proposed Technique

As implied, in Sect. 1, the recently proposed technique replaces the original digitized records, with records, digitized, at larger steps, such that, the computational costs reduce considerably, while the losses of the analyses accuracies are negligible. The basis, of the replacement, is responses second order of convergence [26, 45, 56, 57], and, the resulting new record, $\tilde{\mathbf{f}}$, can be obtained from:

$$\begin{aligned}
 t_i = 0: & \quad \tilde{\mathbf{f}}_i = \mathbf{f}(t_i) \\
 0 < t_i < t_{end}: & \quad \tilde{\mathbf{f}}_i = \frac{1}{2}\mathbf{f}(t_i) + \frac{1}{4n'} \sum_{k=1}^{n'} [\mathbf{f}(t_{i+k/n}) + \mathbf{f}(t_{i-k/n})] \\
 t_i = t_{end}: & \quad \tilde{\mathbf{f}}_i = \mathbf{f}(t_i)
 \end{aligned} \tag{10}$$

In Eqs. (10), n' has the definition below:

$$\begin{aligned}
 t = \Delta t: & \quad n' = n - 1 \\
 \Delta t < t < t_{end} - \Delta t: & \quad n' = \begin{cases} \frac{n}{2} & n = 2j \quad j \in \mathbb{Z}^+ \\ \frac{n-1}{2} & n = 2j + 1 \quad j \in \mathbb{Z}^+ \end{cases} \\
 t = t_{end} - \Delta t: & \quad n' = n - 1
 \end{aligned} \tag{11}$$

and n stands for the integer multiplier, representing the enlargement of the excitation steps, such that the enlarged step size does not dominate Eqs. (8) (see Fig. 2). The three assumptions to be fulfilled, before implementing the technique, are as noted below [26, 45] (the first two assumptions are also implied in Fig. 3):

1. Both the excitation steps, and the integration steps, are equally sized,

$$\begin{aligned}
 \forall i, j: \quad \Delta t_{f_i} = \Delta t_{f_j} = \Delta t_f > 0 \\
 \forall i, j: \quad \Delta t_i = \Delta t_j = \Delta t > 0
 \end{aligned} \tag{12}$$

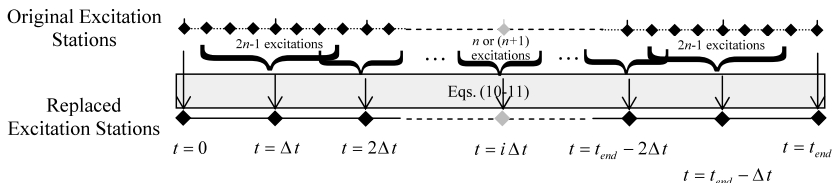


Fig. 2 Replacement of the original excitation with the new excitation [26]

- ◇ Integration (and excitation) stations
- ◆ Excitation stations at known constant steps
- ◈ t_{end} (located before the last integration station)

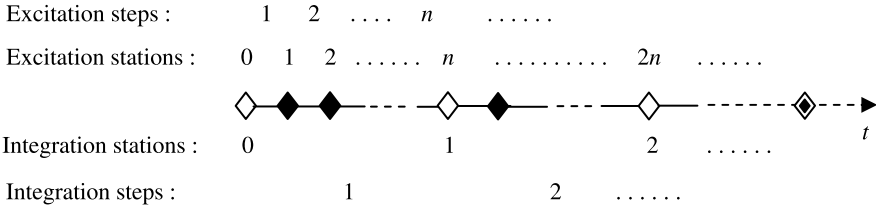


Fig. 3 Schematic illustration of the first two assumptions essential in implementation of the recently proposed technique

2. The excitation steps are embedded by the integration steps (the first time station, i.e. t_0 , is a station, for both excitation and integration),

$$\exists n \in Z^+ : \frac{\Delta t}{f \Delta t} = n < \infty \tag{13}$$

3. The $\mathbf{f}(t)$ in Eq. (1) is a digitized representation of an actual excitation, smooth [58, 59], with respect to time, i.e.,

$$\begin{aligned} \mathbf{f}(t) &= \mathbf{g}(t)\delta(t - i \Delta t_f), \quad i = 0, 1, 2, \dots \\ \mathbf{g}(t) &: \text{ actual excitation} \\ \delta(t - i \Delta t_f) &= \begin{cases} 1 & t = i \Delta t_f \\ 0 & t \neq i \Delta t_f \end{cases} \end{aligned} \tag{14}$$

And finally, the computational procedure stated briefly in [26], and, in an extended way, in [45], is as noted below:

- (a) Assign to n and Δt , the largest values, satisfying:

$$\begin{aligned} \Delta t = n \Delta t_f &\leq \text{Min} \left(\frac{T}{10}, \Delta t_s, \Delta t_r \right) \quad \text{for linear problems} \\ \Delta t = n \Delta t_f &\leq \text{Min} \left(\frac{T}{100}, \Delta t_s, \Delta t_r \right) \quad \text{for nonlinear problems} \\ \Delta t &\leq t_{end}, \quad n \in Z^+ = \{1, 2, 3 \dots\} \end{aligned} \tag{15}$$

- (b) If $n = 1$, $\tilde{\mathbf{f}} = \mathbf{f}$; and if $n \neq 1$, determine $\tilde{\mathbf{f}}$, from Eqs. (10) and (11).
- (c) Compute the approximate response of the problem, defined in Eqs. (1)–(3), by conventional time integration analysis, after replacing the \mathbf{f} with $\tilde{\mathbf{f}}$.

Meanwhile, in view of the step-by-step nature of time integration, the procedure above, issues affecting the computational costs, and the fact that, for nonlinear anal-

yses, larger integration steps cause more computational cost, for modelling the nonlinearities (see [8, 29, 30, 60–62]), the expected reduction, of computational cost, C_R , satisfies:

$$C_R \cong \frac{n-1}{n} (\%) \quad \text{for linear problems} \quad (16)$$

$$C_R < \frac{n-1}{n} (\%) \quad \text{for nonlinear problems}$$

where, the amount of smallness (in the inequality) depends on the problem and the severity of the nonlinear behaviour (for the latter, see for instance [63, 64]).

3 Structural Systems

3.1 The Bridge Models

Consider a three-span concrete bridge. The structural model is introduced, in Fig. 4. The superstructure consists of a 25 centimetres thick concrete slab with 11.8 metres width and five reinforced concrete girders. The girders are connected by transverse diaphragms, at mid-span and each end, and are simply-supported, on 400×400 millimetres steel reinforced elastomeric bearings. Each bearing consists of two exterior layers, with 6 millimetres thickness, four interior layers, with 12 millimetres thickness, and five 2 millimetres steel reinforcement. The stiffness related properties, of the bearings, are as noted below [65]:

$$\begin{aligned} \text{Vertical stiffness:} & \quad 3227000 \text{ kN/m} \\ \text{Shear stiffness:} & \quad 5220 \text{ kN/m} \\ \text{Rotational stiffness:} & \quad 1420 \text{ kNm/rad} \\ \text{Torsional stiffness:} & \quad 118 \text{ kNm/rad} \end{aligned} \quad (17)$$

The substructure consists of two closed end seat type abutments and two interior bents. Each bent consists of three concrete columns, each, with 7.75 metres height and 1.2 metres diameter. The abutments are assumed rigid (see Fig. 4 and [65]). The finite element model is consisted, of frame elements, for the girders and shell elements, for the superstructure slab. The shell elements are vertically offset, to be located, at their correct positions, and the columns are modelled, fixed, at the pile cap interface (see Fig. 4(d)). The elastomeric bearings are modelled, as spring elements, with properties, as stated, in Eqs. (17). The lateral connections, between the super-structure and sub-structure, are, once, considered fixed, by using two conventional concrete shear keys, and once, are upgraded, by replacing the concrete shear keys, with steel shear keys, at each interior bent, and abutment. Behaving nonlinearly, the steel shear keys are modelled, as nonlinear springs, in the lateral direction (the axial forces are kept negligible). The plots, in Fig. 5, define the springs

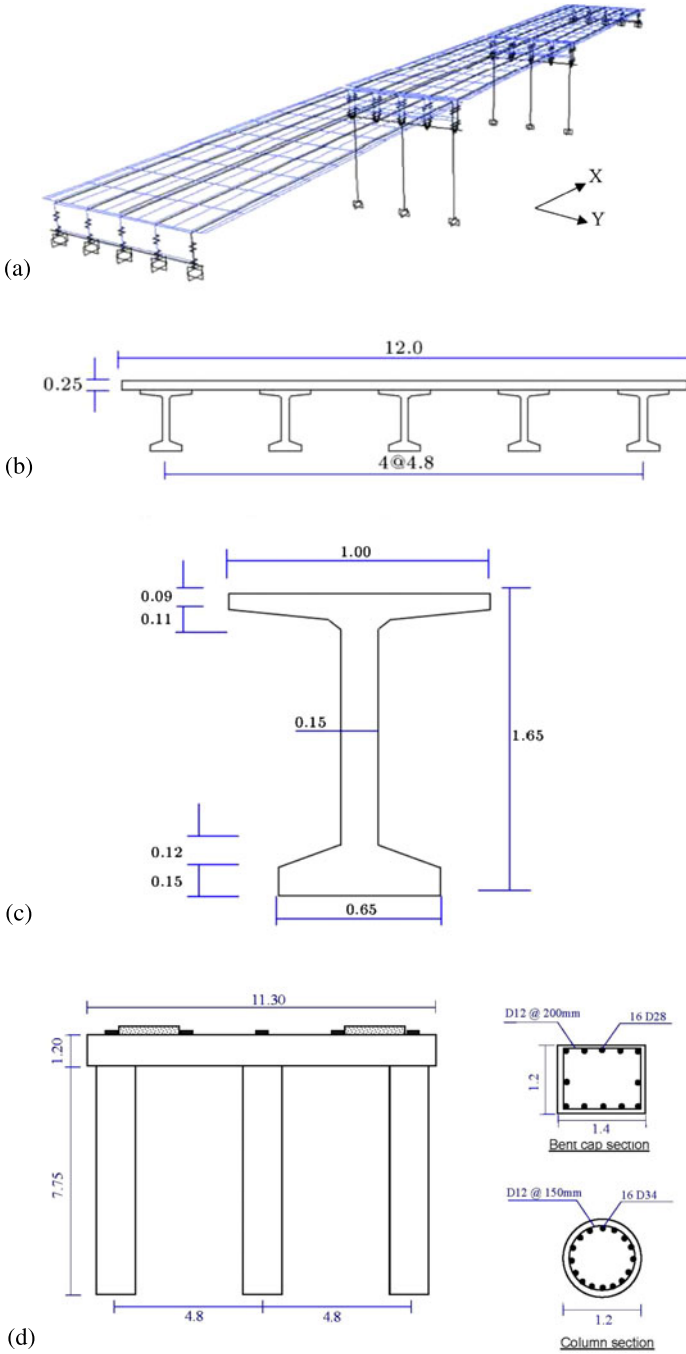
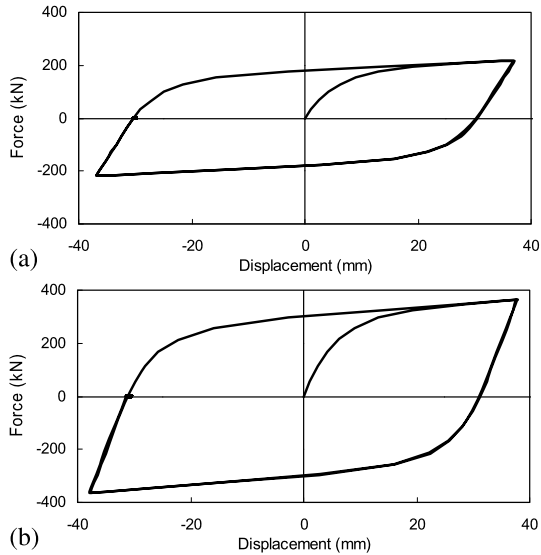


Fig. 4 The main structural model: (a) Finite element model; (b) Cross section of superstructure; (c) Typical cross section of concrete girder; (d) Interior bent

Table 1 Wen plasticity parameters for the shear keys

Shear key	Linear stiffness (N/m)	Yield force (N)	α	β
Abutment	33833	186000	1	0.03
Bent cap	56388	310000	1	0.03

Fig. 5 Load deformation curves for the springs defining the steel shear keys in the upgraded bridge model: (a) abutments; (b) bent cap

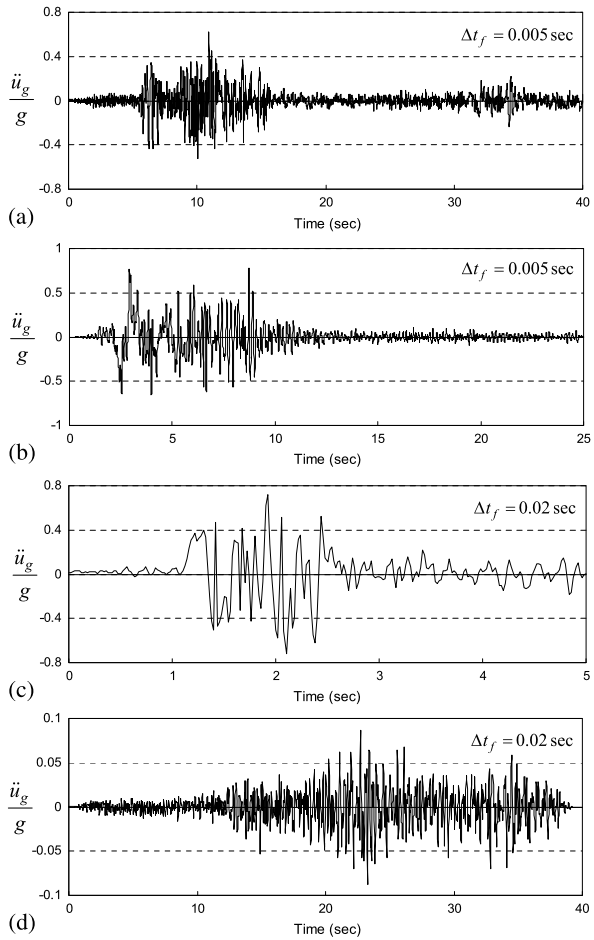


of the upgraded model, where, the material nonlinearity is according to the Wen plasticity model [65, 66], with the parameters, stated in Table 1 [65]. And, finally, it should be noted that, conventionally, the damping is considered viscous and equal to 5 %.

3.2 The Strong Ground Motions

The conventionally designed and laterally upgraded bridge structural systems, explained above, are subjected to four of the most major earthquakes, in the country (Iran). The earthquake records are depicted in Fig. 6 ($g = 9.81 \text{ m/sec}^2$). Since, the bridge design, and models, under consideration (introduced in Sect. 3.1), are typical in Iran, and similar to general anti-seismic standards and codes, the purpose, of the implemented seismic design code [55], is protection against the earthquakes, in the region, we can consider the selections here, and in Sect. 3.1, consistent, and implying a real engineering case. Accordingly, the implementation of

Fig. 6 Strong motion records for four major earthquakes in Iran: (a) Abbar (1990); (b) Bam (2003); (c) Naghan (1977); (d) Tabbas (1978) [67]



the technique in the analyses and the resulting numerical observations would be practical.

4 Numerical Study

4.1 The Problems

In view of Eqs. (1)–(3), the technique, reviewed, in Sect. 2, and the design and excitations, introduced, in Sect. 3, the performance, of the technique, is studied, in this section, with regard to twelve problems, eight linear and four nonlinear. The problems are introduced in Table 2 (also see Fig. 4(a), where, the original and upgraded bridge structural systems are identical in the X direction).

Table 2 Description of the problems under study

Problem	Bridge model	Excitation	Direction of the excitation
1	Original	Fig. 6(a)	X
2	Original	Fig. 6(b)	X
3	Original	Fig. 6(c)	X
4	Original	Fig. 6(d)	X
5	Original	Fig. 6(a)	Y
6	Original	Fig. 6(b)	Y
7	Original	Fig. 6(c)	Y
8	Original	Fig. 6(d)	Y
9	Upgraded laterally	Fig. 6(a)	Y
10	Upgraded laterally	Fig. 6(b)	Y
11	Upgraded laterally	Fig. 6(c)	Y
12	Upgraded laterally	Fig. 6(d)	Y

4.2 The Details of the Analyses, the Results, and a Brief Discussion

The technique [26] is implemented, in average acceleration [18, 32] time integration analysis, of the twelve problems, addressed, in Table 2 (average acceleration is the integration method recommended for nonlinear analyses [21]). For the last four problems, the nonlinearity solution method and tolerance (for relative errors) [20] are respectively set to be the modified Newton Raphson method [21–24] and 10^{-4} (a value conventional in practical analyses). The total base shear and the deck displacement at the top of a column (both in the direction of the ground acceleration) are considered, as the responses to be monitored. According to the procedure of the recently proposed technique [26, 45], the value of the parameter n , of the technique, is set, as noted, in the second row of Table 3. Nevertheless, since, the nonlinear parts of Eqs. (5) and (8) are not reliable (see [68]), for a more comprehensive study, the values, noted, in the third row, of Table 3, which are the consequence of disregarding nonlinearity, are, in this study, implemented in the analyses. The time integration analyses are carried out, leading to the responses, reported, in Figs. 7–18, and Table 4. The reduction of computational cost is addressed, in the last row of Table 3,

Table 3 Values assigned to the parameter n and the associated reduction of computational cost

	Problem					
	1, 2	3, 4	5, 6	7, 8	9, 10	11, 12
n (proposed)	5	2	5	2	1	1
n (implemented)	5	2	5	2	5	2
Reduction of computational cost (%)	~80	~50	~80	~50	28	9

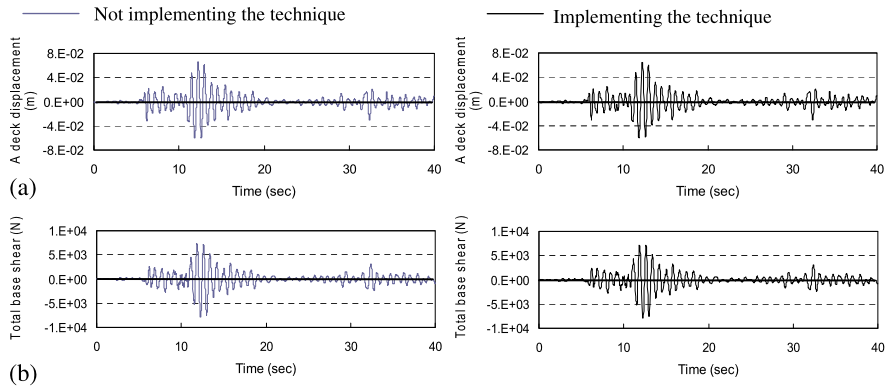


Fig. 7 Responses for Problem 1: (a) deck displacement; (b) total base shear

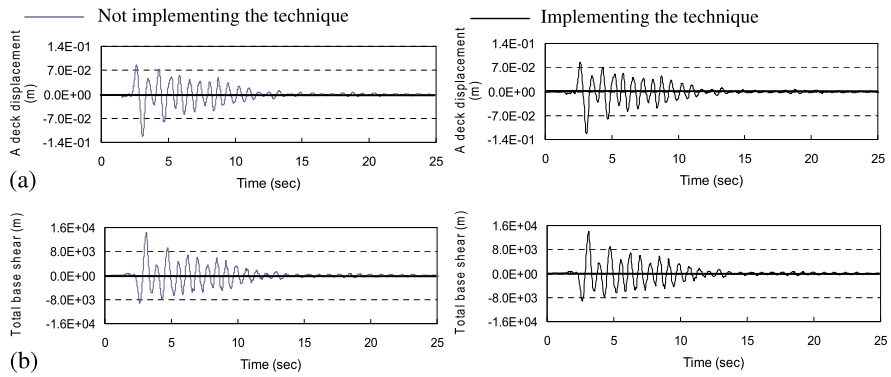


Fig. 8 Responses for Problem 2: (a) deck displacement; (b) base shear

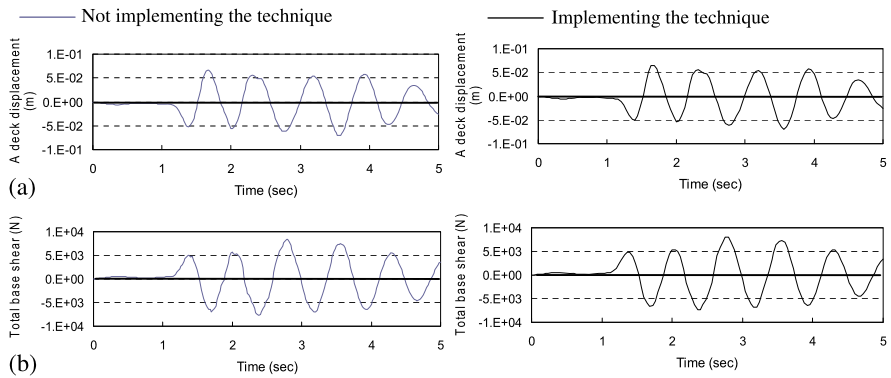


Fig. 9 Responses for Problem 3: (a) deck displacement; (b) base shear

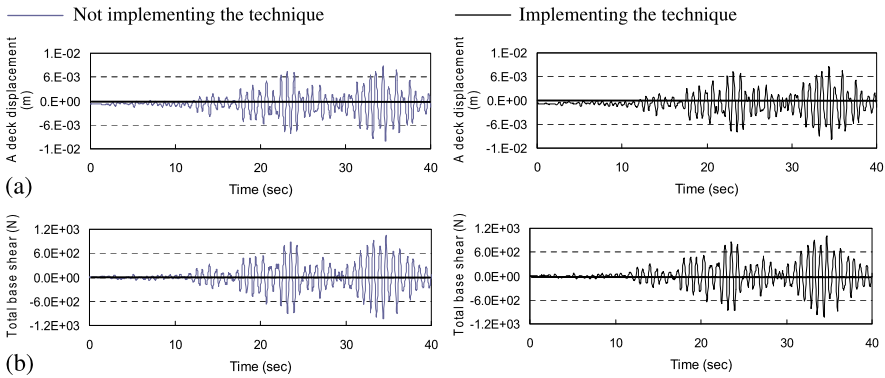


Fig. 10 Responses for Problem 4: (a) deck displacement; (b) base shear

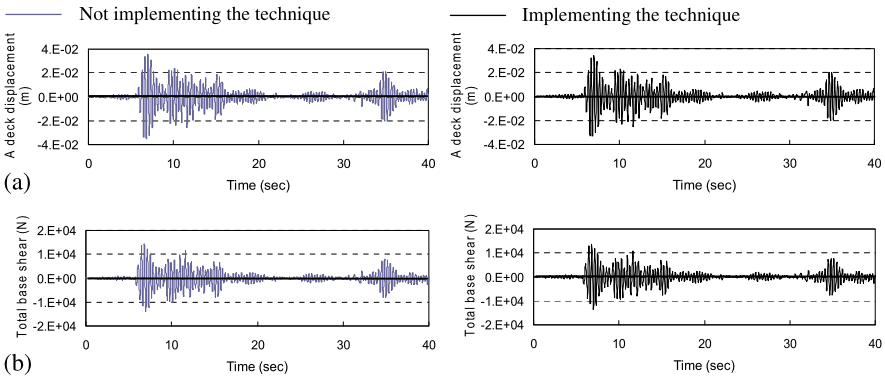


Fig. 11 Responses for Problem 5: (a) deck displacement; (b) base shear

and, for the sake of completeness, the original excitations are compared, with the replaced excitations, in Fig. 19.

Apparently, the carried out numerical investigation is an evidence, for the good practical performance, of the recently proposed technique. Specifically, it is notable that in twenty two of the twenty four graphs, in Figs. 7–18, the consequences of implementing and not implementing the technique are pictorially identical, and hence, are depicted separately (Figs. 13 and 17 are the figures displaying slight deviation, from conventional analyses, when implementing the recently proposed technique); see also Table 4; and this is while, the graphs at the right are depicted via very less points (compared to those at left). Numerically, in view of Tables 3 and 4, while, the decrease of cost is more than or equal to 50 %, the loss of accuracy is less than 15 %, implying arriving at a significant practical achievement. Any ambiguity regarding an effect, on $f(t)$, similar to that regarding the computed responses, reported in Figs. 7–18 (and consequently no specific achievement by the recently proposed technique) can be resolved, with close attention to Fig. 19, where, it is apparent

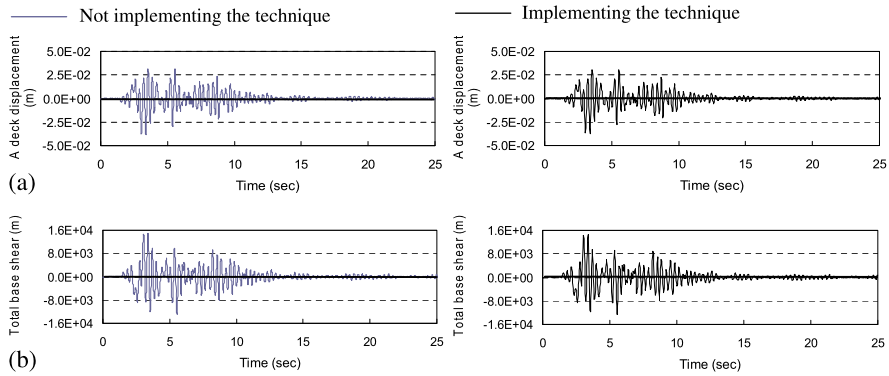


Fig. 12 Responses for Problem 6: (a) deck displacement; (b) base shear

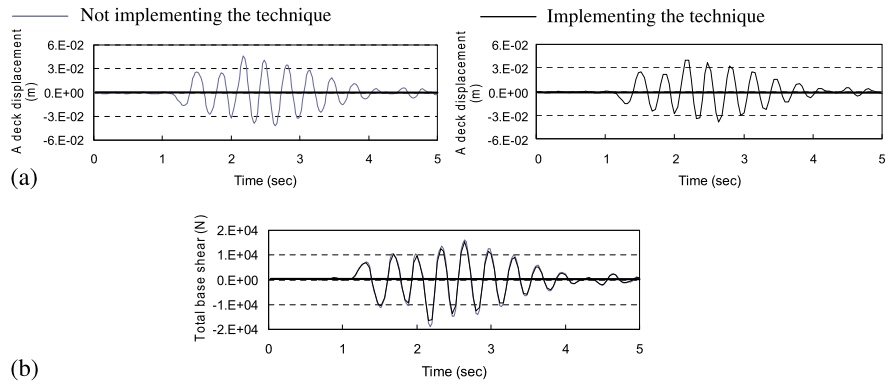


Fig. 13 Responses for Problem 7: (a) deck displacement; (b) base shear

that the two graphs, in each figure, can be pictorially recognized; see Fig. 19(c). It is also worth noting that, for the nonlinear cases, the values assigned to n , are much larger than those proposed, by the computational procedure, of the technique ($n = 1$) [26, 45]; see Table 3, and the losses of accuracies are still negligible; see Figs. 15–18 and Table 4.

5 Complementary Discussions

The two bridge structural models and the four strong ground motions, addressed, in Sects. 3 and 4, are set consistently, i.e. they are associated with one region. This, besides the fact that the selected strong ground motions are of the most severe earthquakes, in the region, provides a good evidence for the adequate performance, of the recently proposed technique, in real seismic analyses, specifically, regarding, multi-span concrete bridges. Since, structural designs, and hence the codes, affect

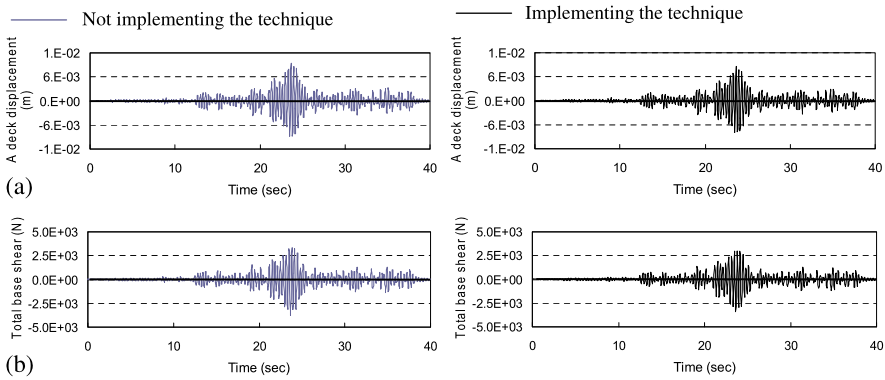


Fig. 14 Responses for Problem 8: (a) deck displacement; (b) base shear

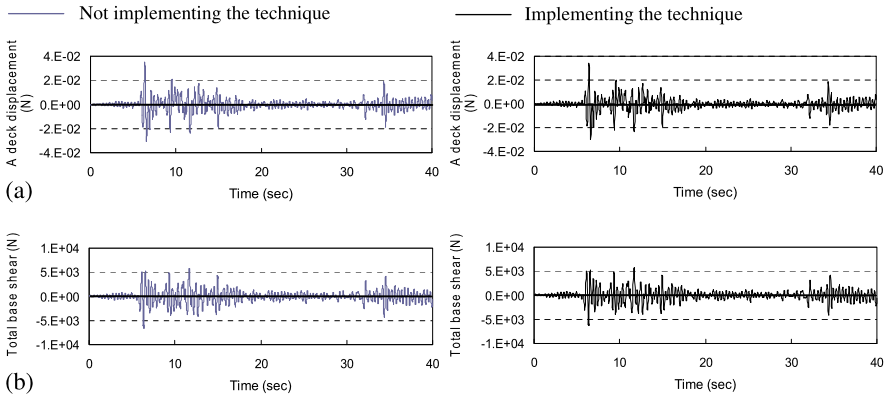


Fig. 15 Responses for Problem 9: (a) deck displacement; (b) base shear

the T in Eqs. (5) and (8), and strong ground motion records affect the Δt_f , in the same equations, it sounds reasonable to expect observations, conceptually similar to those displayed in Figs. 7–18, in repetition, of the study, with other consistent seismic codes and strong ground motions, likely, as a subject for further research.

Moreover, in view of Figs. 11–18, and Table 4, different from the past studies [26, 44, 45], the performance of the recently proposed technique is almost alike, in presence, and absence, of nonlinearities. In other words, for real nonlinearities, occurring, in multi-span concrete bridges analyses and designs, the performance of the recently proposed technique, in nonlinear time integration analyses, can be as successful as in linear analyses (also see the values of n in Table 3). For overcoming the discrepancy between the observations, we can simply consider the severity of nonlinear behaviour (see [63, 64]), as the effectual parameter diminishing the performance, of the technique, in presence of nonlinear behaviours, sufficiently low, in this study. In more detail, by comparing Figs. 11–14 (corresponding to Problems 5–8), with Figs. 15–18 (corresponding to Problems 9–12), the nonlinearities, in the

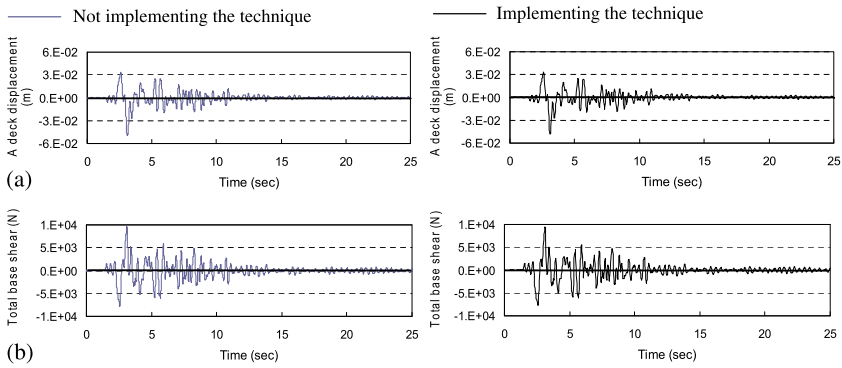


Fig. 16 Responses for Problem 10: (a) deck displacement; (b) base shear

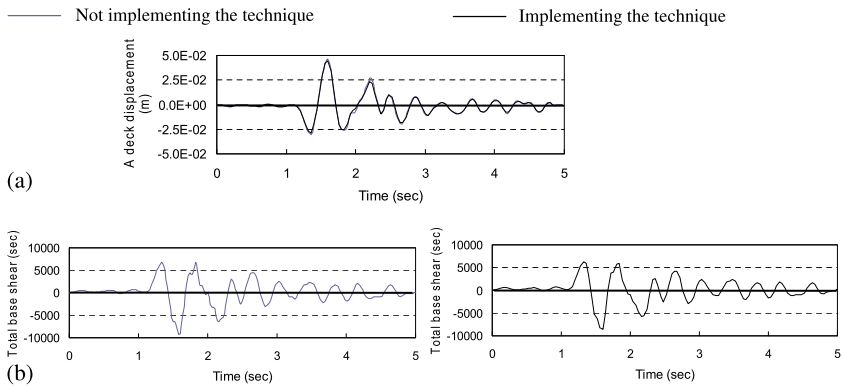


Fig. 17 Responses for Problem 11: (a) deck displacement; (b) base shear

examples, presented, are not very severe (see also [26, 44, 45]; this has caused the small influence of the nonlinearity on the performance, apparent, in the last row, of Table 3. This is in agreement with the literature existing regarding nonlinear analysis [8, 9, 69, 70].

From a practical point of view, the performance, of the technique, depends also on its versatility, and, the capability to simply control the accuracy of the computed results (to be later implemented in engineering designs or scientific interpretations). Regarding the versatility, the three assumptions, reviewed, in Sect. 2, are set, for general digitized excitations. For seismic analyses, which is the concern here, considering the existing instrumentation, e.g. see [35], and the fact that the records are resulted, from earthquakes, and earthquakes are natural phenomena, the first part of the first assumption and the third assumption are inherently valid. This is consistent with the past studies [36–49], not restated here, for the sake of brevity. And, with regard to practical control of the accuracies, in view of the literature, on general numerical analysis [31, 71] and those existing on time integration analyses [31, 62, 72],

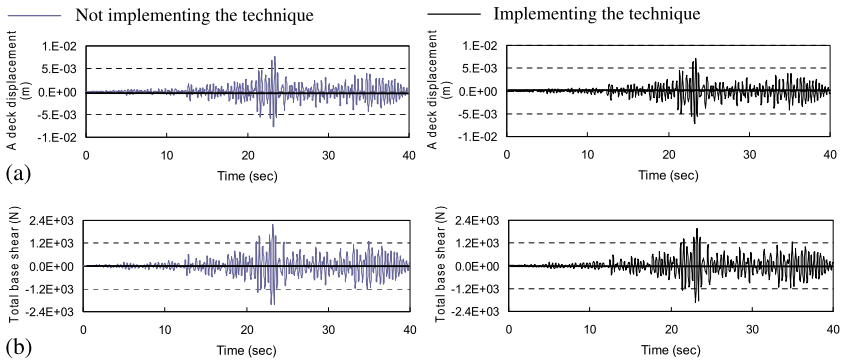


Fig. 18 Responses for Problem 12: (a) deck displacement; (b) base shear

Table 4 Sacrifice of accuracy in the problems under study (%)

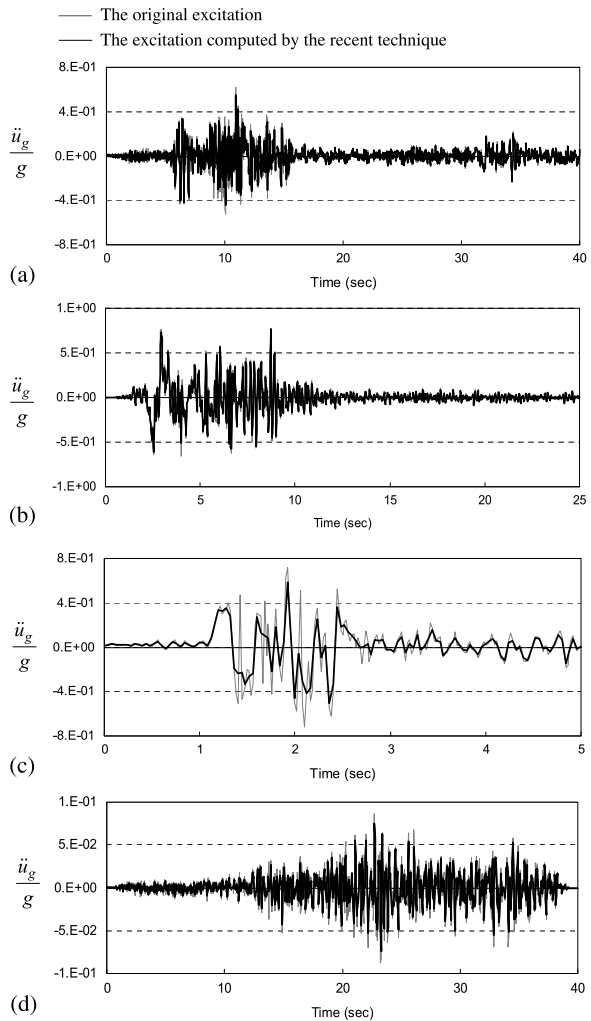
Problem	Maximum deck displacement	Maximum total base shear
1	0.81	0.20
2	0.66	1.22
3	1.60	3.32
4	2.67	2.29
5	2.70	4.72
6	3.30	2.27
7	14.19	12.87
8	8.71	8.26
9	2.29	3.57
10	2.02	2.39
11	3.94	7.56
12	6.36	9.56

we can test the accuracies, by comparing the results, with the results, obtained, from analyses with smaller (conventionally half) integration steps. In implementation of the recently proposed technique [26, 45], the integration steps are sized $n \Delta t_f$, i.e.

$$\Delta t = n \Delta t_f, \quad n \in \mathbb{Z}^+ - \{1\} \tag{18}$$

In repetition of the analyses, with smaller steps, e.g. $\frac{\Delta t}{2}$, however, the term, at the right hand side of Eq. (18), to be decreased, is the Δt_f . To explain better, in view of the formal definition of error [73], the practical purpose, of controlling the accuracy is comparing the response, with the exact response, and, as stated above, the approach is to compare the responses with more accurate responses. However, by changing the value assigned to n (the term, besides Δt_f , at the right hand side of Eq. (18)), the accuracy changes only compared to the responses obtained from the analysis carried out with steps equal to Δt_f , not with respect to the exact responses.

Fig. 19 Influence of the recently proposed technique on different earthquakes strong ground motion records: (a) Abbar (1990); (b) Bam (2003); (c) Naghan (1977); (d) Tabbas (1978)



Therefore, we would rather not evaluate the accuracy, by changing the value assigned to the parameter n .

6 Conclusion

In order to study the performance of a recent computational cost reduction technique for time integration analyses, in real cases, attention is paid to the crucial role of bridges, in natural disasters. A typical multi-span concrete bridge is considered, in two structural cases (original and upgraded with nonlinear elements), and subjected to four major earthquakes, consistent with the design code. The analyses are carried out, with the Newmark average acceleration method, and the modified New-

ton Raphson method (with a nonlinearity tolerance equal to 10^{-4}), for nonlinearity iterations, once, conventionally, when not implementing the recently proposed technique [26], and then again, when, implementing the technique. As expected, the responses obtained, after implementing the technique in time integration analysis, are very close, to the responses resulted from the conventional analyses (with steps, equal to Δt_f); and, the associated computational costs are considerably less. Based on these observations, supported with some complementary discussions, the main achievements are:

1. When, the strong ground motions are consistent with the design codes (in the sense that both are from one region), the performance of the recently proposed technique can be reasonable, specifically, regarding multi-span concrete bridges. This is an evidence, better than those, presented, in the past studies [26, 37–45], for the adequacy of the technique, when implemented in real analyses against seismic forces.
2. In the range of nonlinearity severities occurring in real analyses and designs of multi-span bridges, we might be able to disregard nonlinearities in implementation of the recently proposed technique; the reduction of the computational costs would be less than those in linear problems.

In addition, for seismic analyses, the assumptions, to be satisfied, in order to implement the technique, can be practically reduced to the two assumptions, below:

- (a) the integration steps need to be equally sized, throughout the analysis interval,
- (b) the values assigned to the integration step size, need to be smaller than the values recommended, for the integration step size, in the literature, and meanwhile larger than the strong ground motion digitization steps, by an integer multiplier, great than one.

Acknowledgements The authors sincerely appreciate the kind attention and patience of the editor and co-editors and their colleagues, regarding both the starting paper presented at COMPDYN 2011 conference, in Corfu, and meanwhile, at the different stages resulting in this chapter. The support of the International Institute of Earthquake Engineering and Seismology (IIEES) regarding the project number 7510, which is carried out in this institute, and is a major reference of the study reported in this chapter, is also sincerely acknowledged.

References

1. International Conference of Building Officials (1997) UBC—uniform building code
2. International Code Council (2003) IBC—international building code
3. Building and Housing Research Center (BHRC) (2007) Iranian code of practice for seismic resistant design, Standard No 2800-05
4. Argyris J, Mlejnek JP (1991) Dynamics of structures. Elsevier, Amsterdam
5. Belytschko T, Liu WK, Moran B (2000) Non-linear finite elements for continua and structures. Wiley, New York
6. Henrych J (1990) Finite models and methods of dynamics in structures. Elsevier, Amsterdam
7. Soroushian A (2003) New methods to maintain responses' convergence and control responses' errors in the analysis of nonlinear dynamic models of structural systems. PhD dissertation, University of Tehran (in Persian)

8. Soroushian A, Wriggers P, Farjoodi J (2005) On practical integration of semi-discretized non-linear equations of motion. Part 1: reasons for probable instability and improper convergence. *J Sound Vib* 284:705–731
9. Soroushian A, Wriggers P, Farjoodi J (2013) On practical integration of semidiscretized non-linear equations of motion: proper convergence for systems with piecewise linear behavior. *J Eng Mech* 139:114–145
10. Gavin H (2001) Structural dynamics. Class notes CE 283, Duke University
11. Wriggers P (2002) Computational contact mechanics. Wiley, New York
12. Hughes TJR, Pister KS, Taylor RL (1979) Explicit-explicit finite elements in nonlinear transient analysis. *Comput Methods Appl Mech Eng* 17/18:159–182
13. Soroushian A, Farjoodi J (2008) A unified starting procedure for the Houbolt method. *Commun Numer Methods Eng* 24:1–13
14. Chopra AK (1995) Dynamics of structures: theory and application to earthquake engineering. Prentice Hall, New York
15. Gupta AK (1992) Response spectrum method: in seismic analysis and design of structures. CRC Press, Boca Raton
16. Houbolt JC (1950) A recurrence matrix solution for the dynamic response of elastic aircraft. *J Aeronaut Sci* 17:540–550
17. Katona MG, Zienkiewicz OC (1985) A unified set of single step algorithms. Part 3: the beta-m method, a generalization of the Newmark scheme. *Int J Numer Methods Eng* 21:1345–1359
18. Newmark NM (1959) A method of computation for structural dynamics. *J Eng Mech* 85:67–94
19. Clough RW (1973) Numerical integration of equations of motion. Lectures on finite element methods in continuum mechanics, University of Alabama
20. Allgower EL, Georg K (1980) Numerical continuation methods, an introduction. Springer, New York
21. Bathe KJ (1996) Finite element procedures. Prentice Hall, New York
22. Crisfield MA (1997) Nonlinear finite element analysis of solids and structures. Advanced topics, vol 2. Wiley, Chichester
23. Cook RD, Malkus DS, Plesha ME, Witt RJ (2002) Concepts and applications of finite element analysis. Wiley, New York
24. Zienkiewicz OC, Taylor RL, Zhu JZ, Nithiarasu P (2005) The finite element method. Elsevier, Amsterdam
25. Soroushian A (2010) An enhanced fractional-time-stepping method for structural dynamics. In: Proceedings of the 17th international congress on sound & vibration, International Institute of Acoustics and Vibration (IIAV), Cairo
26. Soroushian A (2008) A technique for time integration with steps larger than the excitation steps. *Commun Numer Methods Eng* 24:2087–2111
27. Henrici P (1962) Discrete variable methods in ordinary differential equations. Prentice Hall, New York
28. Strikwerda JC (1989) Finite difference schemes and partial differential equations. Wadsworth & Brooks/Cole, Belmont
29. Wood WL (1990) Practical time stepping schemes. Clarendon, Oxford
30. Belytschko T, Hughes TJR (1983) Computational methods for transient analysis. Elsevier, Amsterdam
31. Soroushian A, Wriggers P, Farjoodi J (2009) Asymptotic upper-bounds for the errors of Richardson extrapolation with practical application in approximate computations. *Int J Numer Methods Eng* 80:565–595
32. Clough RW, Penzien J (1993) Dynamics of structures. McGraw-Hill, Singapore
33. Soroushian A (2009) Time integration with step sizes less depending on the steps of excitation: I. SDOF systems. Report 7509-P89-1, Structural Engineering Research Center (SERC), IIEES, Tehran (in Persian)
34. McNamara JF (1974) Solution schemes for problems of nonlinear structural dynamics. *J Press Vessel Technol* 96:149–155

35. Havskov J, Alguacil G (2005) Instrumentation in earthquake seismology (modern approaches in geophysics). Springer, Dordrecht
36. Soroushian A, Hosseini M, Vasseghi A (2011) On the performance of a technique for more efficient time integration when applied to bridge structures seismic analysis. In: Proceedings of the 3rd ECCOMAS thematic conference on computational methods in structural dynamics and earthquake engineering (COMPdyn 2011), Corfu
37. Soroushian A (2010) On practical performance of a technique recently proposed for time integration analysis with less computational cost. In: Proceedings of the 17th international congress on sound & vibration (ICSV17), Cairo
38. Nateghi F, Yakhchalian M (2011) On less computational costs for analysis of silos seismic behaviors by time integration. In: Proceedings of the 3rd ECCOMAS thematic conference on computational methods in structural dynamics and earthquake engineering (COMPdyn 2011), Corfu
39. Bahar O, Ramezani S (2011) Faster time integration analysis for building structures subjected to 3-component earthquakes. In: Proceedings of the 3rd III ECCOMAS thematic conference on computational methods in structural dynamics and earthquake engineering (COMPdyn 2011), Corfu
40. Soroushian A, Aziminejad A (2011) A more efficient seismic analysis of tall buildings by implementing a recently proposed technique. In: Proceedings of the 6th international conference seismology and earthquake engineering (SEE6), Tehran
41. Soroushian A (2011) A comparison between two methods for disregarding excitation steps in seismic analyses. In: Proceedings of the 6th international conference seismology and earthquake engineering (SEE6), Tehran
42. Soroushian A, Saaed A, Arghavani M, Rajabi M, Sharifpour MM (2011) Less computational costs in the analysis of seismic behaviours by time integration. In: Proceedings of the 10th biennial conference on vibration problems (ICoVP-2011), Prague
43. Nateghi F, Yakhchalian M (2011) An investigation into the effectiveness of a technique proposed for reducing computational cost of time integration in the analysis of silos seismic behaviors. In: Proceedings of the 11th US national congress on computational mechanics (11th USNCCM), Minneapolis
44. Soroushian A (2011) On the performance of a recent technique for more efficient time integration in severe seismic conditions. In: Proceedings of the 2011 international conference on advances in structural engineering and mechanics (ASEM'11), Seoul
45. Soroushian A (2011) Direct time integration with steps larger than the steps by which the excitations are digitized. Report 7510, Structural Engineering Research Center (SERC), IIEES, Tehran (in Persian)
46. Soroushian A, Sabzei A, Reziakolaei AY (2013) On the performance of a technique for reducing the computational cost of time history analyses when applied to mid-rise buildings. In: Proceedings of the 7th national congress on civil engineering (7NCCE 2013), Zahedan (in Persian)
47. Sabzei A (2013) A study on the performance of a recent technique for less computationally expensive seismic analyses when applied to linear analysis of conventional multi-storey buildings. MSc thesis, International Institute of Earthquake Engineering and Seismology (IIEES) (in Persian)
48. Reziakolaei AY, Sabzei A, Soroushian A (2013) On the performance of a structural analysis cost reduction technique when applied to residential buildings. In: Proceedings of the 4th ECCOMAS thematic conference on computational methods in structural dynamics and earthquake engineering (COMPdyn 2013), Kos
49. Sabzei A, Reziakolaei AY, Soroushian A (2013) More versatility for an integration step size enlargement technique in time integration analysis. In: Proceedings of the 4th ECCOMAS thematic conference on computational methods in structural dynamics and earthquake engineering (COMPdyn 2013), Kos

50. Saaed A (2012) A technique for faster time integration of MDOF structural systems based on using larger time interval in step by step integration. MSc thesis, International Institute of Earthquake Engineering and Seismology (IIEES) (in Persian)
51. Faroughi A, Hosseini M (2011) Simplification of earthquake accelerograms for quick time history analyses by using modified inverse Fourier transform. In: Proceedings of the 12th East-Pacific conference on structural engineering and construction (EASEC), Hong Kong
52. Hosseini M, Mirzaei I (2012) Simplification of earthquake accelerograms for rapid time history analysis based on the impulsive load concept. In: Proceedings of the 10th international congress on computational mechanics (WCCM2012), Sao Paulo
53. Rajabi M (2011) A new method for less expensive seismic analysis of SDOF structural systems. MSc thesis, International Institute of Earthquake Engineering and Seismology (IIEES) (in Persian)
54. Sharifpour MM (2013) A method for faster direct time integration analyses of systems subjected to ground strong motions. MSc thesis, Science and Research Branch, Islamic Azad University West Azerbaijan (in Persian)
55. Bureau of Technical Execution System (2008) The Iranian code of practice for the analysis and design of concrete bridges. Office of Deputy for Strategic Supervision, Tehran
56. Hughes TJR (1987) The finite element method: linear static and dynamic finite element analysis. Prentice Hall, New York
57. Penry SN, Wood WL (1985) Comparison of some single-step methods for the numerical solution of the structural dynamic equation. *Int J Numer Methods Eng* 21:1941–1955
58. Brown JW, Churchill RW (1993) Fourier series and boundary value problems. McGraw-Hill, Singapore
59. Greenberg MD (1978) Foundations of applied mathematics. Prentice Hall, New York
60. Zhou KK, Tamma KK (2004) A new unified theory underlying time dependent first-order systems: a prelude to algorithms by design. *Int J Numer Methods Eng* 60:1699–1740
61. Schueller GI, Pradlwarter HJ (1999) On the stochastic response of non-linear FE models. *Arch Appl Mech* 69:765–784
62. Soroushian A, Farjoodi J (2003) More reliable responses for time integration analyses. *Struct Eng Mech* 16:219–240
63. Soroushian A, Farjoodi J, Mehrazin H (2004) A nonlinearity measure for piece-wisely linear structural dynamic models. In: Proceedings of the 11th international congress on sound and vibration (ICSV11), St Petersburg
64. Soroushian A, Farjoodi J, Mehrazin H (2006) A new measure for the nonlinear behavior of piece-wisely linear structural dynamic models. In: Proceedings of the 13th international congress on sound and vibration (ICSV13), Vienna
65. Vasseghi A (2011) Energy dissipating shear key for precast concrete girder bridges. *Sci Iran* 18:296–303
66. Wen YK (1976) Method of random vibration of hysteretic systems. *J Eng Mech* 102:249–263
67. Building and Housing Research Center. Collection of strong ground motion records
68. Soroushian A (2010) On the performance of a conventional accuracy controlling method applied to linear and nonlinear structural dynamics. In: Proceedings of the 17th international congress on sound & vibration (ICSV17), Cairo
69. Xie YM, Steven GP (1994) Instability, chaos, and growth and decay of energy of time-stepping schemes for nonlinear dynamic equations. *Commun Numer Methods Eng* 10:393–401
70. Gratsch T, Bathe KJ (2005) A posteriori error estimation techniques in practical finite element analysis. *Comput Struct* 83:235–265
71. Collatz L (1960) The numerical treatment of differential equations. Springer, Berlin
72. Ruge P (1999) A priori error estimation with adaptive time-stepping. *Commun Numer Methods Eng* 15:479–491
73. Ralston A, Rabinowitz P (1978) First course in numerical analysis. McGraw-Hill, New York

Author Index

A

Adam, Christoph, 69
Ahmadnia, Alireza, 177
Amirzehni, Elnaz, 177
Angelides, Demos C., 591
Asteris, Panagiotis G., 197

B

Borzi, Barbara, 317
Burczyński, T., 521

C

Casarotti, Chiara, 397
Ceresa, Paola, 317
Chrysostomou, Christis Z., 197

D

Daniel, Yael, 437
Dasiou, Maria-Eleni, 225
DeJong, Matthew J., 243
De Luca, Flavia, 273
Dimitrakopoulos, Elias G., 243
Dolenc, Matevž, 259
Dolšek, Matjaž, 259

F

Faravelli, Marta, 317
Filippou, Filip C., 49
Fiorini, Emilia, 317
Fischer, Cyril, 381
Fischer, Ondřej, 381
Furinghetti, Marco, 397
Furtmüller, Thomas, 69

G

Gantes, Charis J., 345
Gencturk, Bora, 545

Giannopoulos, Ioannis, 197
Gkimousis, Ilias A., 297
Górski, R., 521

H

Hossain, Kazi Ashfaq, 545
Hosseini, Mahmood, 613

I

Iervolino, Iunio, 273
Iordanidou, K., 129

K

Kappos, Andreas J., 149
Karakostas, Christos, 33
Klinc, Robert, 259
Komodromos, Petros, 417
Kostic, Svetlana M., 49
Koumousis, Vlasios K., 297
Krawinkler, Helmut, 91

L

Lavan, Oren, 437
Lee, Chin-Long, 49
Lekidis, Vassilios, 33
Liam Finn, W.D., 177
Lignos, Dimitrios G., 91

M

Manos, George C., 491
Melkumyan, Mikayel, 461
Mergos, Panagiotis E., 149
Mistakidis, E., 129
Mitoulis, Stergios A., 491
Moschen, Lukas, 69
Moutsopoulou, A.J., 569
Mylonakis, George E., 1

N

Náprstek, Jiří, [381](#)

O

Onida, Mauro, [317](#)

P

Panagouli, O., [129](#)

Pantazopoulou, Stavroula J., [111](#)

Papadopoulos, Savvas, [33](#)

Parashakis, Haralambos, [1](#)

Pardalopoulos, Stylianos J., [111](#)

Pavese, Alberto, [397](#)

Peruš, Iztok, [259](#)

Pirner, Miroš, [381](#)

Polycarpou, Panayiotis C., [417](#)

Poteralski, A., [521](#)

Pouliezos, A.T., [569](#)

Psycharis, Ioannis N., [225](#)

Putman, Christopher, [91](#)

R

Ricci, Paolo, [197](#)

Rovithis, Emmanouil, [1](#)

S

Sextos, Anastasios, [33](#)

Soroushian, Aram, [613](#)

Stavroulakis, G.E., [569](#)

Szczepanik, M., [521](#)

T

Taiebat, Mahdi, [177](#)

Thermou, Georgia E., [111](#)

V

Vamvatsikos, Dimitrios, [273](#)

Vasseghi, Akbar, [613](#)

Vassilopoulou, Isabella, [345](#)

Ventura, Carlos E., [177](#)

Vrouva, Antigone, [225](#)

X

Xenidis, Yiannis, [591](#)